KfK 5389
August 1994

Proceedings of the German-Japanese Symposium on Multi-Phase Flow

Karlsruhe, Germany, August 23 – 25, 1994

Compiled by
U. Müller, T. Saito, K. Rust
Institut für Angewandte Thermo- und Fluiddynamik

Kernforschungszentrum Karlsruhe

KERNFORSCHUNGSZENTRUM KARLSRUHE

Institut für Angewandte Thermo- und Fluiddynamik

KfK 5389

PROCEEDINGS

of the

GERMAN-JAPANESE SYMPOSIUM ON MULTI-PHASE FLOW

KARLSRUHE, AUGUST 23 - 25, 1994

compiled by

U. Müller
T. Saito ★
K. Rust

★ The University of Tokyo, Japan
Department of Mechanical Engineering

Kernforschungszentrum Karlsruhe GmbH, Karlsruhe

PREFACE

Multi-phase flow with and without heat transfer has proved to be a true interdisciplinary science of paramount importance in industrial application such as power, refrigeration, process, petroleum, and environmental technologies. In general, any economical and ecological industrial development will benefit from improvements of understanding and proper utilization of multi-phase flow phenomena.

The first German-Japanese Symposium on Multi-phase Flow has been organized to provide a forum for experts of the two highly industrialized countries to discuss recent experimental and theoretical investigations and to exchange informations and opinions about further developments and research requirements in this wide field of engineering application of ever growing importance. Moreover, the meeting is intended to renew and to initiate personal contacts among the participants of both countries which in turn may form a basis for future co-operations or even research agreements. The 44 invited contributions to the symposium mainly focus on the measuring, understanding, and modeling of phenomena in gas-liquid two-phase flow and gas-liquid-solid three-phase flow. In particular the following aspects are addressed: Fundamental experiments in two-phase flow, instrumentation and measuring technique in two-phase flow, boiling and critical heat flux, stability of two-phase flow, condensation and evaporation phenomena, two-phase flow in pumps and cavitation, multi-component and three-phase flow, multi-phase flow modeling, and multi-phase flow in light water reactors. Actually, the sessions of the symposium are arranged under these topics within the proceedings.

Mr. Klaus Rust took all the responsibility for the technical organization of the meeting program and the handling of the papers to produce the proceedings. He did it do with scientific competence and enthusiasm. Mrs. Doris Köhler arranged lecture rooms and accommodations for the participants and organized special events such as technical and sightseeing tours as well as the social program. It is our particular desire to thank both of them for their invaluable help.

The conference fee could be kept at a modest level due to the generous financial funding provided by the Kernforschungszentrum Karlsruhe (KfK) which we gratefully acknowledge. The Japan Society for the Promotion of Science (JSPS) and the Deutsche Forschungsgemeinschaft (DFG) provided financial support for some research work reported in the proceedings and co-sponsored this meeting by reimbursing the travel expenses of several participants. This assistance is also appreciated.

Karlsruhe, August 22nd, 1994

Ulrich Müller
Kernforschungszentrum Karlsruhe

Takamoto Saito
The University of Tokyo

TABLE OF CONTENTS

Fundamental Experiments on Two-phase Flow

Instrumentation and Measuring Technique in Two-phase Flow

Boiling and Critical Heat Flux

Stability of Two-phase Flow

Condensation and Evaporation Phenomena

Two-phase Flow in Pumps and Cavitation Phenomena

Multi-component and Three-phase Flow

Multi-phase Flow Modeling

Multi-phase Flow in Light Water Reactors

Heat and Mass Transfer from a Single one- and multi-component Droplet to a gas flowing at low Reynolds number

Daidžić N., Domnick J., Durst F.

Lehrstuhl für Strömungsmechanik, Universität Erlangen-Nürnberg,
Cauerstr. 4, D-91058 Erlangen, Germany

ABSTRACT

A *film* theory of heat and mass transfer during single- and multi component droplet evaporation is presented. Single droplet evaporation measurements are performed in an acoustic levitator. With this levitator, a stable levitation of liquid droplets within a limited range of levitation power and spheroidal aspect ratio is possible under terrestrial conditions. As a result of the periodic acoustic power distribution the levitated droplet is surrounded by induced convection currents, called outer acoustic streaming, which may be represented by an effective *Reynolds* number. Enhanced heat and mass transfer rates are represented with effective *Nußelt* and *Sherwood* numbers. A second additional enhancement of heat and mass transfer is caused by droplet shape oscillations. Oscillatory motion of the air in the immediate neighborhood of droplet is characterized by an *oscillation Reynolds* number. Both effects, acoustic streaming and droplet shape oscillations, may significantly improve heat and mass transfer rates. Instantaneous droplet sizes and oscillation amplitudes in a standing-wave-levitator were measured with a so-called laser-shadow extinction method and with a CCD camera. Measurements of evaporation rates of single droplets show that pure liquids follow perfectly the D^2-*law* of evaporation, whereas water-ethyl-sucrose and other mixtures exhibit the expected non-linear behavior.

1 INTRODUCTION

Numerous applications of spray technologies are related to the process of droplet evaporation, e.g. spray drying and cooling, spray combustion or spray painting. Achievable overall heat and mass transfer rates can be exceptionally high due to the high area to volume ratio of the droplet ensemble forming the spray. The technical reason to let droplets evaporate may be quite different. In spray drying, also in some painting processes, different evaporation velocities of certain components are used to change the properties of the droplets in a well defined manner, while in combustion processes evaporating liquid fuel droplets represent one step to achieve a uniform distribution of burning gases. Although these processes are governed by the evaporation of single droplets, reliable measurements of single droplet evaporation rates are rare. This is mainly because such measurements require to suspend droplets and keep them fixed in a certain position. This was not possible until different levitating techniques were developed, of which the most important are: electrodynamic levitation, radiation levitation and acoustic levitation.

The acoustic levitation, which will be treated in the present investigation, has been mainly used in space processing and, more recently, under terrestrial conditions for the levitation of droplets immersed in another liquid, (see *Marston and Apfel* [12]). Due to the small density differences between homogeneous and dispersed phase, droplets reached sizes up to a few centimeters at relatively low levitation power. Experimental investigations in gas-liquid systems were performed by *Trinh and Hsu Chaur-Jian* [15]. However, these investigations focused on droplet oscillations and stability.

Downing [6] measured the evaporation of droplets suspended in a free jet of dry, vapour-free air flowing at 1 m/s in upward direction. For hexan droplets, he obtained a linear decay of the square of the droplet diameter as a function of time. This result was confirmed by the measurements of *Ravindran et al.* [13], in which evaporation rates of single submicron droplets suspended in an electric

field were determined. Also, a perfect linearity between the droplet surface decrease versus time was found by *Davis and Ray* [5] for dibutyl sebacate (DBS) in nitrogen and by *Zhang and Davis* [16] for n-hexadecane droplets in helium and nitrogen. More recently *Renz et al.* [14] measured droplet evaporation in stagnant and flowing gases. For the stagnant case the D^2-*law* of evaporation was approved using different n-heptane and n-decane mixtures. In contrast to these previous results, which were obtained for very small droplets in the size range between 1 and 100 μm, the present investigation focuses on droplet sizes between 0.5 and 2 mm.

As a result of the periodic excitation in the standing-wave-levitator the levitated droplet experiences certain enhanced convective flows, which result in improved heat and mass transfer. It is well known that for pure molecular transport of species and thermal energy *Sherwood* and *Nußelt* number equals two. Even when the surrounding fluid moves relative to the droplet at a sufficiently low *Reynolds* number ($\mathcal{R}e \ll 1$), the *Sherwood* number is approx. two. At somewhat higher *Reynolds* numbers or, more appropriately, at higher *Peclet* numbers, the *Sherwood* number depends on $\mathcal{P}e$. There exists fairly reliable data for the limiting cases of $\mathcal{P}e \to 0$ and $\mathcal{P}e \to \infty$, but for $\mathcal{P}e = O(1)$, few data exists [16]. In addition, an influence of droplet oscillations on enhanced heat and mass transfer rates has been studied as well.

An additional problem which exists in acoustic levitation is the occurrence of a spheroidal shape of levitated droplets. In acoustic levitation this shape represents the equilibrium state resulting from the axial acoustic radiation pressure and the radial *Bernoulli* force [10]. Stable terrestrial drop levitation is possible just bellow the pressure nodes of an acoustic standing wave within a limited range of levitation power and spheroidal aspect ratios. Deformed droplets have a somewhat larger surface area which results in increased heat and mass transfer rates.

The aim of this work is to demonstrate the use of acoustic levitation for the investigation of single droplet evaporation rates and to present basic results of the influence of the acoustic streaming (micro-convection) and droplet oscillations on measured evaporation rates. A new on-line technique, the so-called laser-shadow extinction method for droplet size, oscillation amplitude and frequency measurements is introduced.

2 EXPERIMENTAL SETUP AND INSTRUMENTATION

In Fig. 1 the test-rig for the droplet evaporation and oscillation measurements is shown. It consists of the ultrasonic levitator for stable terrestrial droplet positioning, the laser-shadow extinction layout for droplet size, eigenfrequency and deformation measurements, the CCD and high-speed cameras for visualization of droplet oscillations, deformations, break-up and internal circulation and the data acquisition unit consisting of a PC computer, A/D converters, oscilloscope, signal generator, etc.

2.1 Acoustic levitation

An acoustic (ultrasonic) radiation-pressure is used to trap a droplet at a stable position and to drive it into oscillations. A detailed description of the method and the apparatus has been given in *Daidžić et al.* [3]. A body placed in a acoustic field will experience a force on it owing to the relative motion of the body and the fluid elements in the medium. This force arises from the scattering of the sound wave from the body and is equal to the rate of change of momentum through any surface enclosing the body. The acoustic radiation pressure is defined as the time-averaged momentum flux at any point. The Force on small isolated droplets in an ultrasonic standing wave is large enough to levitate them against the gravitational acceleration. For the case of a plane standing wave where $v = \hat{v}_{max} \sin(kz)\cos(\omega t)$ and $p = \hat{p}_{max} \cos(kz)\sin(\omega t)$, the force on a small liquid droplet in gaseous medium is [10, 11]

$$F(\Delta z,\, R) = \frac{5}{8} \cdot k \cdot \rho_0 \hat{v}_{max}^2 \cdot V_l \cdot f_1(x) \cdot \sin(2\,k\,\Delta z) = \rho_l V_l g \qquad k = \frac{2\pi}{\lambda} = \frac{\omega}{c} \tag{1}$$

Under zero gravity conditions the liquid sample will be positioned exactly at the pressure node of the standing ultrasonic wave ($\Delta z = 0$), while under terrestrial conditions the droplet weight will be

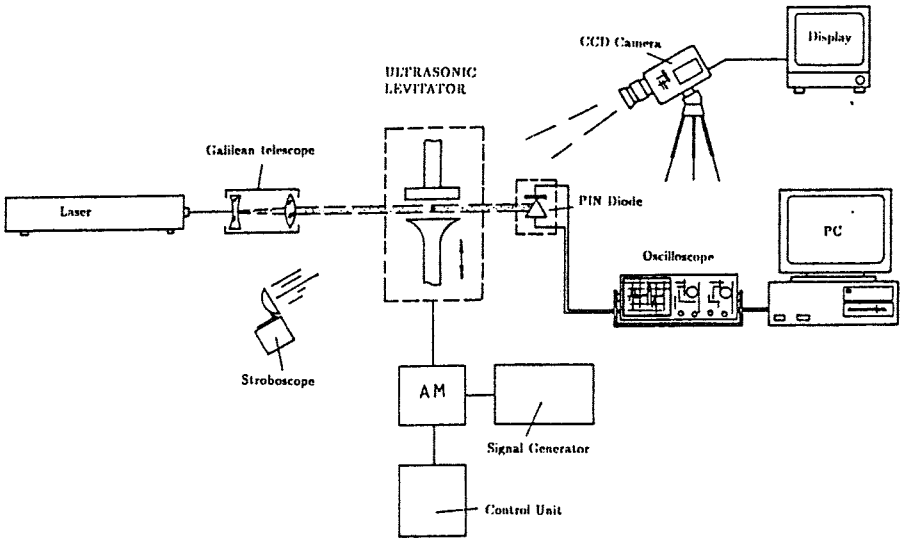

Figure 1: Experimental setup for droplet evaporation and oscillation measurements

compensated at a downwards displacement Δz

$$\Delta z = \frac{1}{2\,k} \sin^{-1}\left[\frac{8}{5} \cdot \frac{\rho_l \cdot g}{k} \cdot (\rho_0\, \hat{v}_{max}^2)^{-1} \cdot f^{-1}(x)\right] \leq \frac{\lambda}{8} \tag{2}$$

The influence of the droplet size on acoustic force is considered in two force factors

$$f_1(x) = \frac{3}{x^2}\left(\frac{\sin x}{x} - \cos x\right) \qquad f_2(x) = \frac{2.29}{x}\left(\frac{\sin x}{x} - \cos x\right) \qquad x = \frac{2\pi D}{\lambda}$$

where $f_1(x) = 0$ indicates that droplets with $D > 0.715\lambda$ cannot be levitated [10]. The optimal positioning range, with the smallest acoustic power requirement exists for $D \approx \lambda/3$ and is obtained by minimizing Eq. (1). Note that $\lim_{x\to 0} f_1(x) = 1$.

A periodic acoustic power distribution in a standing wave will induce micro-convection around a levitated droplet. A time modulation of the acoustic pressure intensity will provide a periodic squeezing action to drive steady-state shape oscillations. The acoustic levitator used in this work, operating with a carrier frequency of 56 kHz, was supplied by *Battelle-Frankfurt*. The distance between the two plates could be adjusted to achieve a standing ultrasonic wave with 3 to 5 force-free velocity anti-nodes between them. After optimizing the settings of the levitator for a given droplet size, the droplets were placed manually into these velocity anti-nodes by a μl-syringe. With this levitator it was not difficult to distort a spherical droplet into an oblate spheroid as the acoustic pressure is increased. The prolate-biased initial deformation was however not obtainable with current levitator. An amplitude-modulation of the carrier ultrasonic frequency was used in order to excite droplet oscillations.

2.2 Droplet size and deformation measurements with a CCD camera

The straightforward way to obtain droplet sizes is visualization. Due to its relatively large size it was easy to visualize droplets while levitating. Due to the acoustic radiation pressure, the shape of the droplets in the levitator was always oblate. The acoustic radiation pressure (levitation power) was adjusted to the minimum in order to minimize the spheroidal deformation, while still having a stable position. It can be assumed that the equilibrium spheroid is an ellipsoid of revolution with two main axis equal $A = C$ and $A > B$. This should be a good estimate for the oblate spheroid shape. The equivalent diameter of the droplet is accordingly $\overline{D} = \sqrt[3]{A^2 \cdot B}$. The relation between the nondimensional squared diameter and an elapsed time was fitted with the linear curve $D^{*2} = a^2 - K^* \cdot t$, ($D^2$-*law*), where $a^2 \leq 1$ is an initial nondimensional diameter squared which does not influence the value of K^*. Note that a^2 is obtained from fitting and not from initial measurements.

2.3 Laser-shadow extinction method

Measurements of droplet frequency, size, and amplitude of oscillations were performed by means of the laser-shadow extinction method, as shown schematically in Fig 2. The suspended isolated droplet is placed in the path of a collimated He-Ne laser beam. The initial laser beam diameter (0.6 mm) was expanded through a Galilean telescope yielding a *Rayleigh* range of about 2.5 m and a spot size of 3.8 mm. The laser light is collected in a direct forward scattering arrangement and collimated through a 3.3 mm aperture to a PIN diode with an active rectangular surface of 41 mm^2. Due to the highly stabilized droplet position in the levitator, it is possible to obtain a 'shadow' of the droplet in the forward direction. This shadow, which is causing an intensity deficit due to the light that is scattered and absorbed by the droplet, is detected by a PIN diode. Due to the high bandwidth of the PIN-diode, its output signal represents an instantaneous measure for the light intensity. The PIN diode is connected to an oscilloscope and to a PC computer with an A/D converter. Changes of the voltage obtained from the PIN diode are related to the droplet sizes and oscillations as shown by *Daidžić et al.* [3, 4]. A soft quadratic nonlinearity between detected laser light intensity and the surface deformation is found. However, for deformations smaller then ($\epsilon < 0.4$) linear relation gives good approximation. Since only the signal amplitude is available it is not possible to simultaneously measure spherical droplet size and initial deformation. However, using a calibration, a unique relation between droplet size, deformation and detected intensity could be established.

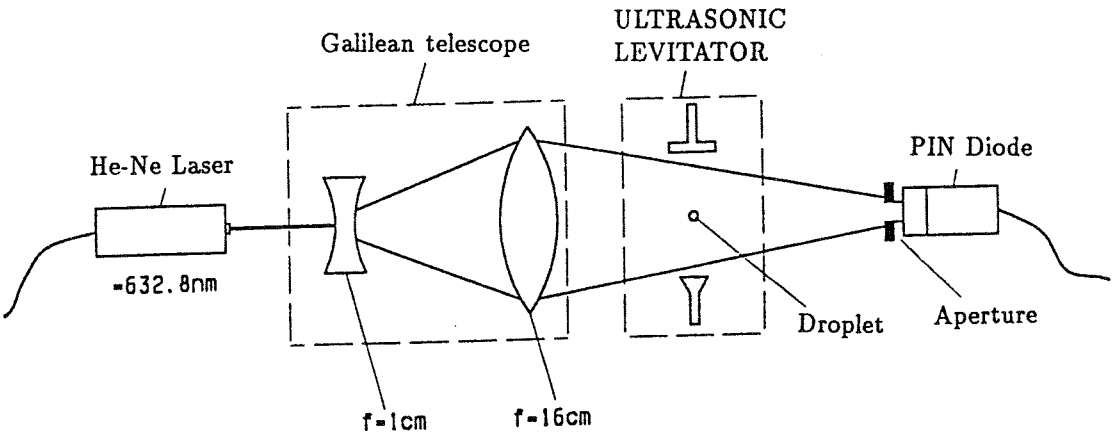

Figure 2: Laser-shadow extinction method

It is assumed that the laser possesses a proper *gaussian* intensity distribution (TEM_{00} mode). Since the droplets are very large compared to the wavelength of the laser light, diffraction effects could be neglected. Furthermore, measurements showed that the contribution of laser light going directly through the center of the droplet is less than 0.5 % of the total intensity. Since droplets were always oblate deformed a spherical mean droplet radius R_0 can be determined from the following implicit equation [3]

$$\left[I^* \left(1 - e^{-2a^2/w_a^2}\right) + e^{-2a^2/w_a^2}\right] - \left[1 - \left(\frac{R_0}{w_d}\right)^2 \cdot \epsilon_2\right] e^{-2R_0^2/w_d^2} = 0 \qquad (3)$$

where

$$\epsilon_2 = 2\frac{1-e}{2e+1} \leq 0 \qquad e = \frac{a}{b} = \frac{1-\epsilon_2/2}{\epsilon_2+1} \geq 1$$

and a and b are the half-axis of the oblate spheroid. It was found, that the agreement between the droplet sizes determined through the laser-shadow method, the visualization technique and the liquid volume injected by the μl-syringe always stayed within $\pm$ 3 % for droplet diameters exceeding 1 mm.

3 THEORETICAL CONSIDERATIONS

The evaporation of droplets can be generally described with heat and mass balance equations. In the present analysis the *infinite conductivity model* of droplet evaporation was used. This approach is valid if the *Biot* number is very small (say $\mathcal{B}i < 0.1$). In such a case we may use lumped parameter analysis and avoid the use of partial differential equations. We may write the mass conservation equation in an integral form

$$\frac{dM}{dt} = \frac{d}{dt}\left(\frac{4}{3}\pi r_s^3 \rho_l\right) = -\dot{m} \qquad [kg/s] \tag{4}$$

where r_s is the actual droplet radius and $\dot{m}$ is the evaporation mass rate. Measurements of the evaporation rates of liquids, burning of droplets, sublimation of solids, etc., have shown that the droplet diameter, after an initial transient period (heat-up), diminishes with time according to the relationship [1, 7, 8]

$$D^2 = D_0^2 - K \cdot t \tag{5}$$

where D_0 is the initial droplet diameter, and K the *evaporation constant.* Such a steady-state analysis facilitates the study of droplet evaporation. In order to derive this relation we shall perform a further reduction of the mass conservation equation. Manipulation of Eq. (4) leads to

$$\frac{d(D_s^2)}{dt} = -K \qquad \text{where} \qquad K = \frac{4 \cdot \dot{m}}{\pi D_s \rho_l} \qquad [m^2/s] \tag{6}$$

if $\dot{m} \propto D_s$, as it was usually observed in the measurements. This is the well known D^2-*law*, with the solution given by Eq. (5). The D^2-*law* is the simplest possible model describing droplet evaporation. Basic assumptions built into this theory are given elsewhere [7, 8]. In dimensionless form the D^2-*law* yields

$$D^* = \left(\frac{D_s}{D_0}\right)^2 = 1 - K^* \cdot t = 1 - \frac{t}{\tau} \tag{7}$$

where $K^* = K/D_0^2$ has the dimension $[s^{-1}]$ and the droplet lifetime τ is defined for $D_s = D^* = 0$, as $\tau = D_0^2/K = 1/K^*$.

3.1 Film theory of droplet evaporation

The mass transfer between a droplet and the surrounding gas occurs due to a certain concentration gradient. In order to explain simultaneous heat and mass transfer the so-called *film* [1] theory will be employed. The film theory assumes that the heat and mass transfer resistance between the surface and the gas is concentrated within a fictional gas film of constant thickness. The temperature and species composition along the surface, as well as at the external boundary of the film, are uniform. Formally, this requires very large *Peclet* numbers, which, for most practical situations, means very large *Schmidt* numbers for any finite *Reynolds* number. Surprisingly, this approximation is often reasonable down to *Schmidt* numbers in the order of unity [2]. The thickness of the film is determined from the requirement that the rates of a purely molecular transport by thermal conduction or diffusion through the film must be equal to the actual intensity of the convective heat or mass transfer between the surface and the surrounding. However, it should be noted that the *Stefan* flow results in the thickening of the film. In such sense we may define fictional external radii for heat and mass transfer of the spherical droplet as [1]

$$r_{f,T_0} = \frac{r_s \mathcal{N}u_0}{(\mathcal{N}u_0 - 2)}; \qquad r_{f,M_0} = \frac{r_s \mathcal{S}h_0}{(\mathcal{S}h_0 - 2)} \tag{8}$$

where $\mathcal{N}u_0$ and $\mathcal{S}h_0$ are the standard *Nußelt* and *Sherwood* number for a solid nonevaporating sphere which can be calculated from the standard correlations for the sphere in the convective field. It follows that the film thickness becomes infinite for $\mathcal{N}u_0$ and $\mathcal{S}h_0$ numbers close to 2. If there is no convection, neither natural nor forced, the mass transfer is pure diffusional in the radial direction only giving $\mathcal{S}h = 2$ [2, 3].

To include the effects of *Stefan* flow, we introduce some modified values of the *Nußelt* and *Sherwood* numbers, i.e. $\mathcal{N}u^*$ and $\mathcal{S}h^*$, which are substituted in Eq. (8) to provide the correct values of the film radii

$$r_{f,T} = \frac{r_s \mathcal{N}u^*}{(\mathcal{N}u^* - 2)}; \qquad r_{f,M} = \frac{r_s \mathcal{S}h^*}{(\mathcal{S}h^* - 2)} \tag{9}$$

Note that $\mathcal{N}u^*$ and $\mathcal{S}h^*$ should not be confused with the actual *Nußelt* and *Sherwood* numbers of an evaporating droplet which will be designated as $\mathcal{N}u$ and $\mathcal{S}h$. To take into consideration the effects of *Stefan* flow, i.e. surface blowing due to the convective mass transfer, we introduce the correction factors [3]

$$F_T = \frac{\delta_T}{\delta_{T_0}} = \frac{\mathcal{N}u_0 - 2}{\mathcal{N}u^* - 2} = F(B_T) \qquad F_M = \frac{\delta_M}{\delta_{M_0}} = \frac{\mathcal{S}h_0 - 2}{\mathcal{S}h^* - 2} = F(B_M)$$

which represent the relative change of the film thickness due to the *Stefan* flow. B_T and B_M are heat and mass transfer numbers. The modified *Nußelt* and *Sherwood* numbers may be expressed as

$$\mathcal{N}u^* = 2 + \frac{\mathcal{N}u_0 - 2}{F_T} \qquad \mathcal{S}h^* = 2 + \frac{\mathcal{S}h_0 - 2}{F_M} \tag{10}$$

Note that $\mathcal{N}u^* \to \mathcal{N}u_0$ and $\mathcal{S}h^* \to \mathcal{S}h_0$ as $F_M, F_T \to 1$. The expressions for F_T and F_M will be considered later. The following relation between *Sherwood* and *Nußelt* numbers exists

$$\mathcal{S}h_0 \geq \mathcal{S}h^* \geq \mathcal{S}h \qquad \mathcal{N}u_0 \geq \mathcal{N}u^* \geq \mathcal{N}u$$

The mass concentration of the vapour in the mixture is defined as

$$Y_i = \frac{M_i}{\sum_{i=1}^{n} M_i} \qquad \text{with} \qquad \sum_{i=1}^{n} Y_i = 1 \qquad (0 \leq Y_i \leq 1)$$

Consider now the control spherical surface of radius r so that $r_s < r < r_f$. The mass flow of vapour through this surface is given by [1, 7, 8]

$$J_v = 4\pi r^2 j_m = 4\pi r^2 \Big[\underbrace{-\rho_m \mathcal{D}_m \frac{dY_v}{dr}}_{\text{diffusion}} + \underbrace{\rho_m u_{r,m} Y_v}_{\text{convection}} \Big] \tag{11}$$

where $j_m = \rho_m u_{r,m} = \rho_v u_{r,v} + \rho_a u_{r,a}$, is the specific mass flux of vapour/air mixture on the droplet surface, Y_v is the mass concentration of the vapour phase, $u_{r,m}$ is the radial velocity of the mixture (*Stefan* flow), ρ_m is the mixture density, $\mathcal{D}_m$ is the binary diffusion coefficient of vapour in air. Under steady-state conditions in the gas phase, the total vapour mass flow rate equals the vaporization rate ($\dot{m}$), what implies $J_v = \dot{m} = 4\pi r^2 \rho_m u_{r,m}$. On the other hand, the vaporization rate, $\dot{m}$, is independent of the radius $r_s < r < r_f$ (the same mass rate leaving the surface at r_s must go through the surface at r_f). Using the definition of the *Spalding mass transfer number* B_M,

$$B_M = \frac{Y_s - Y_\infty}{1 - Y_s} \qquad 0 \leq B_M < \infty$$

The mass concentration of the vapour in a mixture is

$$Y_v = \frac{p_v M_v}{p_v M_v + (p_m - p_v) M_a} = \left[1 + \left(\frac{p_m}{p_v} - 1 \right) \frac{M_a}{M_v} \right]^{-1}$$

For water droplets in air the water-vapour pressure may be approximated with

$$p_v(T) = 602.63 \cdot RH \cdot e^{[19.7(1 - 273.15/T)]} \qquad 273.15 \leq T \leq 323.15\,K \quad 0 \leq RH \leq 1 \qquad [Pa]$$

After integrating Eq. (11), we obtain

$$\dot{m} = 2\pi r_s \overline{\rho}_m \overline{\mathcal{D}}_m \mathcal{S}h^* \ln(1 + B_M) \tag{12}$$

where $\overline{\rho}_m$ and $\overline{\mathcal{D}}_m$ are the average values of the mixture density and the binary diffusion coefficient throughout the film, respectively. The accuracy of the evaporation rate is heavily depending on the choice of the values $\overline{\rho}_m$ and $\overline{\mathcal{D}}_m$. According to *Abramzon et al.* [1], the best results are obtained using the *one-third* rule of *Sparrow* and *Gregg*, where average properties are evaluated at the following reference temperature and species mass fraction

$$T_r = T_s + \frac{T_\infty - T_s}{3} = \frac{2}{3} T_s + \frac{1}{3} T_\infty \qquad Y_r = Y_s + \frac{Y_\infty - Y_s}{3} = \frac{2}{3} Y_s + \frac{1}{3} Y_\infty$$

The mass flux of the evaporating species leaving the surface is

$$J_{v,s} = 2\,\pi\, r_s\, \overline{\rho}_m\, \overline{\mathcal{D}}_m\, \mathcal{S}h\, B_M = \dot{m} \tag{13}$$

where the actual *Sherwood* number is defined as (see ref. [3])

$$\mathcal{S}h = -\frac{2\,r_s}{Y_s - Y_\infty} \left.\frac{dY}{dr}\right|_{r_s} \tag{14}$$

Combining Eqs. (10), (12) and (13), we obtain the following relationship

$$\mathcal{S}h = \mathcal{S}h^* \frac{\ln(1+B_M)}{B_M} = \left[2 + \frac{\mathcal{S}h_0 - 2}{F(B_M)}\right] \frac{\ln(1+B_M)}{B_M} = 2\,\frac{\ln(1+B_M)}{B_M} + \frac{\mathcal{S}h_0 - 2}{F(B_M)} \frac{\ln(1+B_M)}{B_M} \tag{15}$$

In the case of pure diffusion the vapour mass flux is given by $(J_{v,diff})_s = 2\pi r_s \overline{\rho}_m \overline{\mathcal{D}}_m \mathcal{S}h (Y_s - Y_\infty) = \dot{m}$, where $\mathcal{S}h = \mathcal{S}h^* = \mathcal{S}h_0 = 2$ [3]. This means that for pure diffusion no *Stefan* flow exists. From the point of view of *film* theory, the *Stefan* flow affects the transfer rate in two different ways. First, it distorts the temperature and concentration profiles in the film leading to the appearance of the natural logarithm $ln(1+B)$ in the driving force of the process. Second, the film thickness increases in the case of evaporation.

The total heat flux through the control surface (from surrounding to droplet) is expressed with [1, 3]

$$4\,\pi\, r^2\, \overline{\lambda}_m \frac{dT}{dr} = \dot{m} \left\{ \frac{\dot{Q}_L}{\dot{m}} + [r(T_s) + \overline{c}_{p,v}\,(T - T_s)] \right\} \tag{16}$$

where $r(T_s) = h_v''(T_s) - h_v'(T_s)$ is the latent heat of evaporation. If we introduce an effective latent heat of evaporation $L(T_s) = r(T_s) + \dot{Q}_L/\dot{m}$, and integrating Eq. (16) within the limits of the thermal film thickness, we obtain (see ref. [3])

$$\dot{m} = \pi\, D_s \left(\frac{\overline{\lambda}_m}{\overline{c}_{p,v}}\right) \mathcal{N}u^* \cdot \ln(1 + B_T) \tag{17}$$

where the *Spalding heat transfer number* [1, 8], defined as

$$B_T = \frac{\dot{m}\,\overline{c}_{p,v}\,(T_\infty - T_s)}{r(T_s) + \dot{Q}_L} = \frac{\overline{c}_{p,v}\,(T_\infty - T_s)}{r(T_s) + \frac{\dot{Q}_L}{\dot{m}}} = \frac{\overline{c}_{p,v}\,(T_\infty - T_s)}{L(T_s)}$$

represents the ratio between the heat necessary to superheat the vapour and the total heat supplied to the droplet surface. Comparing the right hand sides of Eqs. (12) and (17), we obtain the following relation between the heat and mass transfer number

$$B_T = (1 + B_M)^\phi - 1$$

where

$$\phi = \frac{\overline{c}_{p,v}\overline{\rho}_m\overline{\mathcal{D}}_m}{\overline{\lambda}_m} \cdot \frac{\mathcal{S}h^*}{\mathcal{N}u^*} = \frac{\overline{c}_{p,v}}{\overline{c}_{p,m}} \cdot \frac{\mathcal{S}h^*}{\mathcal{N}u^*} \cdot \frac{1}{\overline{Le}} \qquad \text{and} \qquad \overline{Le} = \frac{\overline{\mathcal{S}c}}{\overline{\mathcal{P}r}} = \frac{\overline{\lambda}_m}{\overline{c}_{p,m}\overline{\rho}_m\overline{\mathcal{D}}_m} = \frac{\overline{a}_m}{\overline{\mathcal{D}}_m}$$

In the case of steady-state evaporation (no heat-up) the heat flux into the droplet interior equals zero $\dot{Q}_L = 0$. If we use Eq. (17), the heat transfer rate to a droplet per unit surface area and per unit time, is

$$\dot{q} = \frac{\dot{m}\, r}{\pi\, D_s^2} = \frac{r(T_s)}{D_s} \left(\frac{\overline{\lambda}_m}{\overline{c}_{p,v}} \right) \mathcal{N}u^* \cdot \ln(1 + B_T)$$

and after some reductions and the help of Eq. (10) the actual *Nußelt* number becomes

$$\mathcal{N}u = \frac{\alpha\, D_s}{\overline{\lambda}_m} = \frac{\dot{q}\, D_s}{\overline{\lambda}_m\, (T_\infty - T_s)} = \mathcal{N}u^* \frac{\ln(1 + B_T)}{B_T} = 2\, \frac{\ln(1 + B_T)}{B_T} + \frac{\mathcal{N}u_0 - 2}{F(B_T)} \frac{\ln(1 + B_T)}{B_T}$$

3.2 Evaporation rate calculations

To find the correction factors F_M, F_T for the film thickness *Abramzon et al.* [1] considered the model problem of the laminar boundary layer flow past a vaporizing wedge. In the case of isothermal surface and constant physical properties of the fluid, the problem has a self similar solution and the correction factors do not depend on the local *Reynolds* number. It was found that values of F_M, F_T are practically insensitive to the *Schmidt* and *Prandtl* numbers. *Abramzon et al.* assumed that this solution may be applied also to the spherical film around the evaporating droplet. The relative change of the diffusional film thickness is expressed as

$$F(B) = (1 + B)^{0.7}\, \frac{\ln(1 + B)}{B} = (1 + 0.2\, B) + O(B^2) \tag{18}$$

where $F(B)$ is an universal function. As *Abramzon et al.* stated, $F(B)$ increases from 1 to 1.279 as B grows from $B = 0$ to $B = 8$. In the interval $8 \leq B \leq 20$, the values of $F(B)$ remain practically constant. *Faeth* [7] argued that the actual *Sherwood* number can be written as $\mathcal{S}h = [2 \ln(1 + B_M)/B_M]$. However, for finite B_M this expression leads to *Sherwood* numbers which are smaller than 2. Moreover, for very large B_M, it predicts $\mathcal{S}h \to 0$. This relation can be obtained as a limiting case of Eq. (15), when $\mathcal{S}h_0 = 2$ ($\mathcal{R}e = 0$). Strictly speaking this relation is correct only for vanishing B_M. Before, we learned that the smallest *Sherwood* number is reached by pure diffusion and has a minimum value of two. On the other hand, it was already pointed out that the logarithmic nature of the driving potential for the mass and/or heat transfer is a direct consequence of the *Stefan* flow (blowing). Blowing of the surface may occur by evaporation processes. In case of very small mass transfer number, we have $\lim_{B_M \to 0} [\ln(1 + B_M)/B_M] = 1$ and $F_M \to 1$, and the expected result for pure diffusion, $\mathcal{S}h = 2$ is obtained. Indeed, diffusion is represented by the infinitesimal mass transfer number, $B \to 0$ (dY is the driving potential). The same analysis is valid for the *Nußelt* number. This means that for higher mass/heat transfer numbers B, the *Stefan* flow induces a small-scale motion in the immediate surrounding of droplet with an effective *Reynolds* number larger than zero and $\mathcal{S}h_0$, $\mathcal{N}u_0 > 2$. The actual *Sherwood* number can be written in a different form

$$\mathcal{S}h = [\mathcal{S}h_0 + 2(F_M - 1)] \cdot (1 + B_M)^{-0.7} = [\mathcal{S}h_0 \cdot (1 - 0.7 B_M) + 0.4\, B_M] + O(B_M^2) \tag{19}$$

A similar equation may be obtained for the actual *Nußelt* number. Substituting the modified *Sherwood* number defined by Eq. (10) into Eq. (12), the vaporization rate or the mass flux of the evaporating species could be written as

$$\dot{m} = \pi\, D_s\, \overline{\rho}_m\, \overline{\mathcal{D}}_m \left[2 + \frac{\mathcal{S}h_0 - 2}{F_M} \right] \ln(1 + B_M)$$

or for small B_M, $\dot{m} = \pi D_s \overline{\rho}_m \overline{\mathcal{D}}_m \mathcal{S}h_0 B_M$, to the second order in B_M and $\mathcal{S}h_0 = O(1)$. The most simple models of evaporation assume the values of heat and mass transfer numbers to be equal, i.e. $B_M = B_T = B$. This assumption is valid only if $\phi = 1$. For averaged *Lewis* numbers equal one, we have $\overline{c}_{p,v}/\overline{c}_{p,m} \cdot \mathcal{S}h^*/\mathcal{N}u^* = 1$. If additionally, the heat capacities of mixture and vapour are approx. equal, then $\mathcal{S}h^* = \mathcal{N}u^*$, which shows the equivalency of the heat and mass transport.

We have proved that the mass flux of the evaporating liquid is proportional to the droplet diameter ($\dot{m} \propto D_s$), see Eq. (12). In this case the D^2-*law*, Eq. (5), is valid and the droplet surface decreases proportionally with elapsed time. Using the assumption that $B_M = B_T = B$ and Eqs. (6), (10), (12) and (15), then the evaporation constant could be expressed as

$$K = \frac{8\,\overline{\lambda}_m}{\overline{c}_{p,v}\,\rho_l} \cdot \ln(1+B) + \frac{4\,\overline{\lambda}_m}{\overline{c}_{p,v}\,\rho_l}\,(\mathcal{N}u_0 - 2) \cdot B \cdot (1+B)^{-0.7} \tag{20}$$

In the case of stagnant droplets in an environment without natural or forced convection, ($\mathcal{R}e = 0, \mathcal{N}u_0,\ \mathcal{S}h_0 = 2$), a naive substitution will give the evaporation constant as $K = \frac{8\overline{\lambda}_m}{\overline{c}_{p,v}\rho_l} \cdot \ln(1+B)$, [7, 8]. However, this leads to erroneous results. For small $B < 1$ and $\mathcal{N}u_0,\ \mathcal{S}h_0 = O(1)$ the second term in Eq. (20) is of the same order as the first term and, therefore, it cannot be neglected. In addition, we already have shown that for pure diffusion no *Stefan* flow exists and the logarithmic nature of the mass/heat transfer potential vanishes. Expanding the expression for K in Eq. (20) in absolutely convergent series for small driving potentials $B < 1$, in terms of B, we may write with the second-order accuracy

$$K = \frac{4\,\mathcal{N}u_0\,\overline{\lambda}_m}{\overline{c}_{p,v}\,\rho_l} \cdot B + O(B^2) \qquad \text{or} \qquad K = \frac{4\,\mathcal{N}u_0\,\overline{\rho}_m\,\overline{\mathcal{D}}_m}{\rho_l} \cdot B + O(B^2) \qquad B < 1$$

We could also use $\mathcal{S}h_0$ instead of $\mathcal{N}u_0$. The mass transfer number $B < 1$, if $Y_s < 0.5 + Y_\infty$. Since B is a constant at the wet bulb state, it is indicated that K is constant as well. The effective *Sherwood* (or *Nußelt*) number can be now calculated as

$$\mathcal{S}h_0 = \mathcal{N}u_0 = \frac{\overline{c}_{p,v}\,\rho_l}{4\,\overline{\lambda}_m\,B} \cdot K = \frac{\rho_l}{4\,\overline{\rho}_m\,\overline{\mathcal{D}}_m\,B} \cdot K \qquad B < 1,\ \ \mathcal{S}h_0,\ \mathcal{N}u_0 > 2 \quad = O(1)$$

and using Eq. (19), the actual *Sherwood* number becomes

$$\mathcal{S}h = \left[\frac{\overline{c}_{p,v}\,\rho_l}{4\,\overline{\lambda}_m\,B} \cdot K \cdot (1 - 0.7\,B) + 0.4\,B\right] + O(B^2) \qquad = O(1) \tag{21}$$

We can now formulate D^2-*law*, Eq. (6), over $\mathcal{S}h$ number as

$$\frac{d(D_s^2)}{dt} = -K = -\frac{4 \cdot \overline{\lambda}_m \cdot B \cdot (\mathcal{S}h - 0.4\,B)}{\overline{c}_{p,v} \cdot \rho_l \cdot (1 - 0.7\,B)} \qquad [m^2/s] \tag{22}$$

With Eq. (21) a method of determining *Sherwood* or *Nußelt* numbers from measured evaporation constants and known material properties is presented. The average mixture properties for the reference conditions are calculated according to the standard additive rules. Reference temperature and species mass fraction are obtained from the *one-third* rule of *Sparrow* and *Gregg* [1].

3.3 Acoustic streaming

The scattering of acoustic waves on droplet surfaces induces a motion of the surrounding fluid. Such a small-scale motion is called acoustic streaming. The theory of acoustic streaming is treated by *Lee* [9]. In our study, we focus on the representation of such a small-scale motion with an effective *Reynolds* number. However, the question appears how to correlate such micro-convections with the standard relations for the convective heat and mass transfer coefficients. Several analysis of mass transfer to or from spheres at higher *Reynolds* numbers have been made using either the potential flow theory or boundary layer theory (*Frössling, Ranz and Marshall*) [2]. The potential flow theory yields expressions for $\mathcal{S}h$ involving $\mathcal{P}e^{1/2}$, while boundary layer theory involves $\mathcal{R}e^{1/2}\mathcal{S}c^{1/3}$.

The convective heat and mass transfer ($\mathcal{N}u_0, \mathcal{S}h_0$) between a solid nonvaporizing spherical particle and a flowing fluid may be estimated according to *Clift et al.* [1, 2, 3]. *Kronig and Bruijsten* (1951) used singular perturbation methods to obtain solutions for $\mathcal{S}h_0$ valid up to $\mathcal{P}e = O(1)$, $\mathcal{S}h_0 = 2 +$

$\frac{1}{2}\mathcal{P}e + \frac{581}{1920}\mathcal{P}e^2 + \cdots$, where $\mathcal{R}e\mathcal{S}c$ or $\mathcal{R}e\mathcal{P}r$ are *Peclet* numbers $\mathcal{P}e$ for mass and heat transfer. *Schmidt* numbers for water, ethyl and n-decane are in the order of one, $\mathcal{S}c = O(1)$, (0.612 for water, 1.29 for ethyl and 2.574 for n-decane). *Zhang and Davis* [16] proposed the following relation for intermediate *Peclet* numbers

$$\mathcal{S}h_0 = 2 + \left[\frac{1}{(0.5\mathcal{P}e + 0.3026\mathcal{P}e^2)^n} + \frac{1}{(1.008\mathcal{P}e^{1/3})^n}\right]^{-1/n} \tag{23}$$

where the best fit of experimental data is obtained for $n = 3$, although $n = 2$ fits almost as well. *Zhang and Davis* [16] performed evaporation measurements of single droplets suspended freely in an electrodynamic chamber. Convective transfer was established with the laminar jet flow of either nitrogen or helium. They found that for $\mathcal{P}e = 10$, *Sherwood* number does not exceed 4.

As a result of the acoustic energy distribution around the levitated droplet its equilibrium temperature will rise slightly above the environmental temperature T_∞ [11]. In our levitation device droplets experience temperature increase of 0.45°C. *Lierke* [11] found an empirical correlation for enhanced heat and mass transfer of levitating water droplets in air

$$0.95\,\mathcal{N}u = \mathcal{S}h = 2 + 0.172\,\mathcal{R}e \qquad \text{for} \quad \mathcal{R}e \leq 2.5 \tag{24}$$

$$0.95\,\mathcal{N}u = \mathcal{S}h = 1.56 + 0.55\sqrt{\mathcal{R}e} \qquad \text{for} \quad \mathcal{R}e > 2.5 \tag{25}$$

Lee [9] defined the acoustic streaming *Reynolds* number as $\mathcal{R}e = D \cdot v_{eff}/\nu = 2\hat{v}_{max}^2/(\omega \cdot \nu)$, where the effective flow velocity around the levitated droplet is defined with $v_{eff} \approx 2/(k \cdot D) \cdot \hat{v}_{max}^2/c = 2\hat{v}_{max}^2/(D \cdot \omega)$. The velocity amplitude is $\hat{v}_{max} = 122.1 \cdot \sqrt{D/f_2(x)}$ where D is in meters. After some substitutions the acoustic streaming *Reynolds* number becomes $\mathcal{R}e = 4746 \cdot D/[f \cdot \nu \cdot f_2(x)]$. If droplets around the optimal size are levitated it follows that $f_2(x) \approx 1$ and $\mathcal{R}e \approx 11.1$ ($f = 57.2$ kHz, $\nu = 1.57 \cdot 10^{-5}$ m^2/s) which leads to $\mathcal{S}h \approx 3.4$. In this case the effective velocity is $v_{eff} \approx 8.3$ cm/s and the velocity amplitude is $\hat{v}_{max} \approx 5.5$ m/s. If we apply Eq. (23) of *Zhang and Davis* for a water droplet with $\mathcal{P}e = 6.8$, the *Sherwood* number becomes approximately 3.9 which is about 15% higher than predicted above. The actual *Sherwood* number is somewhat smaller.

To determine augmented *Sherwood* and *Nußelt* numbers by the method developed here, we will start with Eq. (21). Measuring K in an ultrasonic levitator and estimating mass/heat transfer numbers and the physical properties of the liquids used will give the prediction of the augmented *Sherwood* and/or *Nußelt* number. Then, an effective *Reynolds* number can be found from Eq. (23), assuming that *Schmidt* and/or *Prandtl* numbers are known. The *film* theory developed here gives $\mathcal{S}h = 3.31$ for $K = 1.75 \cdot 10^{-9}$ m^2/s, ($\overline{c}_{p,v} = 1865$ J/kg K, $\overline{\lambda}_m = 0.0245$ J/s m K, $B = 0.01$, $\rho_l = 10^3$ kg/m^3, $M_a = 28.96$, $M_v = 18$, $p_m = 101.33$ kPa, $RH = 0.3$, $T = 293.15$ K, $Y_s = 0.0144$), which is only 2.7% less then the result obtained by *Lierke*. The method given in Eq. (21) is very sensitive to an accurate estimate of the physical properties. For many materials these properties are very difficult to find or still non-existing. However, this method has the major advantage that it is based on theoretical analysis of evaporation processes where only the evaporation constant K has to be measured.

3.4 Enhanced evaporation due to droplet oscillations

During droplet oscillations the host fluid is also set in motion which additionally improves heat and mass transfer. The micro-convection effect produced by droplet shape oscillations is very similar to one produced by acoustic streaming, since in both cases a host fluid is set in oscillatory motion resulting in increased *Sherwood* and *Nußelt* numbers. We will now present a simple model for estimation of an effective oscillatory *Reynolds* number. The *Sherwood* and/or *Nußelt* number can be than calculated according to Eq. (25) or directly with our method by measuring the evaporation constant of oscillating droplets. If we assume the oscillations are harmonic with amplitudes $x = |\epsilon_n|\, R\, \cos(\omega_n t + \phi)\, P_n(\cos\theta)$, then the characteristic velocity of oscillations becomes $v = \dot{x} = -|\epsilon_n|\, R\, \omega_n\, \sin(\omega_n t + \phi)\, P_n(\cos\theta)$. After an appropriate averaging over time (RMS) and over zonal *Legendre* polynomials, we can define the mean *Reynolds* number

$$\mathcal{R}e = \frac{\overline{v} \cdot \overline{x}}{\nu} = \frac{4\,\omega_n \cdot |\epsilon_n|^2 \cdot R^2}{\nu} = \frac{8 \cdot |\epsilon_n|^2 \cdot R^2}{\delta_s^2}$$

where $\delta_s = (2\nu/\omega)^{1/2}$ is the characteristic length of the oscillatory flow and represents the penetration depth of oscillations. It is usually called the *Stokes layer*. If we use the *Rayleigh-Lamb* equation for inviscid, incompressible droplet oscillations [3],

$$\omega_n = \sqrt{n\,(n-1)\,(n+2)\,\frac{\sigma}{\rho_l\,R^3}} \qquad (n = 2, 3, \ldots)$$

the *Reynolds* number of oscillatory motion becomes after some reductions

$$\mathcal{R}e = 4 \cdot |\epsilon_n|^2 \cdot \left(\frac{\sigma \cdot R}{\rho_l \cdot \nu^2}\right)^{1/2} \cdot Z_n \qquad \text{where} \qquad Z_n = \sqrt{n\,(n-1)\,(n+2)} \tag{26}$$

For a 1 mm water droplet oscillating in the second mode (n=2) with $\epsilon_2 = 0.1$ ($\sigma = 0.072$ N/m, $\rho_l = 10^3$ kg/m^3, $\nu = 15.7 \cdot 10^{-6}$ m^2/s), we obtain a *Reynolds* number of 1.92 and, according to Eq. 24, a *Sherwood* number of 2.33. This short analysis showed that the mass transfer rate is increased by 16.5% in the case of oscillating compared to stagnant droplets. As one can see from Eq. 26, the oscillating *Reynolds* number increases with the square of the oscillation amplitude $|\epsilon_n|$ and with $n^{3/2}$. For the same data as before but for droplets oscillating in the fourth mode the *Reynolds* number will be three times larger ($\mathcal{R}e = 5.48$), and the *Sherwood* number, according to Eq. 25, would increase to $\mathcal{S}h = 2.85$ which represents a 42.4 % higher evaporation rate. A possible droplet rotation in the ultrasonic levitator and the consequent evaporation enhancement, which could not be controlled, can be treated in a similar manner as droplet oscillations. However, the effect of rotation was found to be small compared to other effects due to a relatively low rotation frequency (5-10 Hz).

Still unresolved remains the question how joint acoustic streaming and droplet oscillations influence the evaporation process. Probably there is some coupling between these phenomena yielding a complex estimate of the effective *Reynolds* number and consequently the enhanced heat and mass transfer rates. However, we can measure its joint influence and, with the *film* theory developed herein, the *Sherwood* number may be estimated.

4 EXPERIMENTAL RESULTS

In this section, we will present experimental results of droplet evaporation rates. This will include single- and multi-component droplets. In addition the effects of acoustic streaming and droplet oscillations will be presented. The liquids used in this study vary from highly volatile n-octane and ethyl to low-volatile n-hexadecane. The theoretical considerations derived before will be discussed here. The verification of the experimental results will be made whenever it is possible but, in many cases, it was not possible to find all necessary material properties. Two different acquisition techniques have been used to obtain discrete droplet diameters in time, i.e. the evaporation history; the flow visualization with CCD camera and the newly developed laser-shadow extinction method.

4.1 Evaporation measurements

In Fig. 3 the evaporation histories of 5 μl water and n-decane droplets are shown. These measurements were performed with the laser-shadow method. Although the sizes differ by one order of magnitude the evaporation rates for n-Decane are in good agreement with the results obtained by *Renz et al.* [14]. The evaporation constant for water was $K = 1.498 \cdot 10^{-9}$ m^2/s at $t = 22°$C and $RH = 0.26$. For n-decane, $K = 0.949 \cdot 10^{-9}$ m^2/s at $t = 22°$C was measured. Of course the measurements were repeated many times in order to get statistically averaged values. Care must be taken in analysing evaporation rates of water droplets since they strongly depend on the relative humidity.

In Fig. 4 the evaporation histories of water, ethyl and different sucrose-mixtures are compared. Clearly, the evaporation histories for the sucrose mixtures can be divided into three different stages. In a first stage, the evaporation rates of the sucrose-water (LSG 4 and 9) and sucrose-ethyl (LSG 13) mixtures are almost identical to those of pure water and ethyl, respectively. This is followed by a second stage,

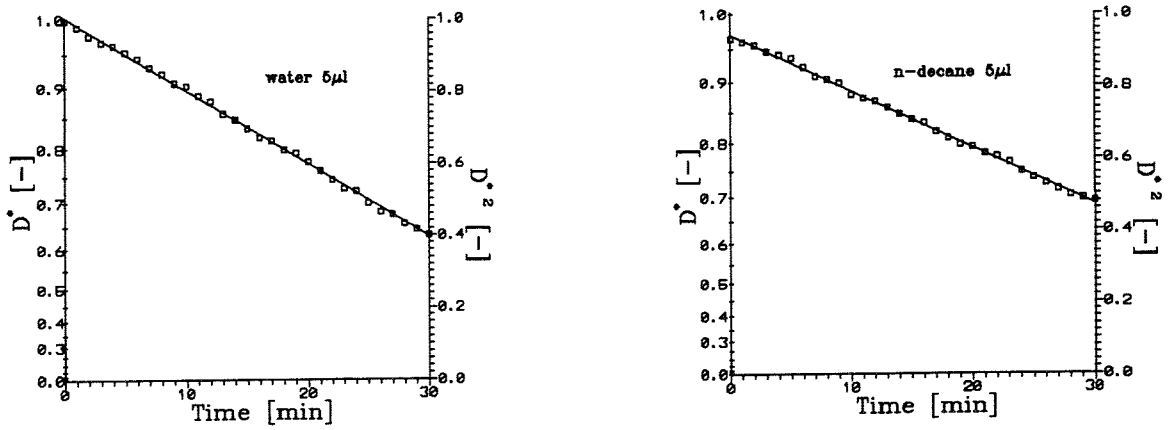

Figure 3: Evaporation history of 5 μl water and n-decane droplet.

where the curves start to deviate from the straight line, connecting to stage three, where almost linear curves can be recognized again, but on a lower level. Especially for water-sucrose solutions the final evaporation rates are very low. Here, crystallization of sugar occurs. For these measurements, the CCD camera visualization technique was used. The surface area decrease with time for mixtures may be written as $D^2 = D_0^2 - K(t) \cdot t$, where $K(t)$ is very complex function depending on the mutual nonlinear interactions between the components of the mixture.A theoretical analysis of the evaporation of multi-component liquids is actually under progress, consisting of a perturbation analysis of the nonlinear interaction between different mixture components.

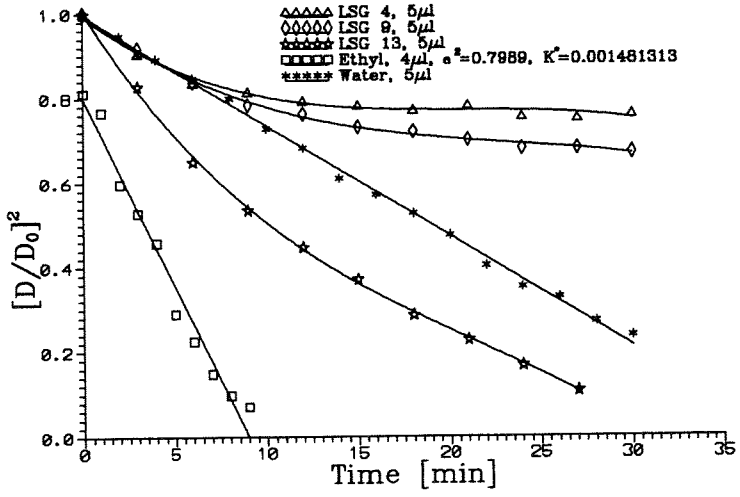

Figure 4: Evaporation rates of water, ethyl and sucrose-mixtures droplets (LSG).

In Fig. 5 the dependence of the evaporation constant on the acoustic power (which is proportional to the acoustic radiation pressure) is shown. The point of zero power was obtained by extrapolating measured data with a linear fit, i.e. $K \cdot 10^9 = 0.393 + 0.458 \cdot P$ for a 2 μl n-decane droplet. In the same figure the similar dependence for 2 μl water droplet is shown, yielding the linear relation $K \cdot 10^9 = 0.563 + 0.155 \cdot P$, where P is in Watts and K in m^2/s. If we use Eq. (22) and put $\mathcal{S}h = 2$ for $RH_\infty = 0.6$ ($\overline{\lambda}_m = 0.0215$, $\overline{c}_{p,v} = 1865$, $B = 0.0065$), we obtain a value of $K = 0.603 \cdot 10^{-9}$ m^2/s which is about 6.6% higher than the experimental result for pure diffusion. For the case of pure diffusion $\mathcal{S}h = 2$ of water droplets in air with relative humidity $RH_\infty = 0.3$ the evaporation constant becomes $K = 1.221 \cdot 10^{-9}$ m^2/s. As we already pointed out the accurate calculation of evaporation rates is very sensitive to a correct use of the physical properties of the water-vapour/air mixture. The moisture control was not used which additionally influences the uncertainty of the measurements.

In Fig. 6 the dependence of the initial oblate-biased static deformation on the acoustic power measured

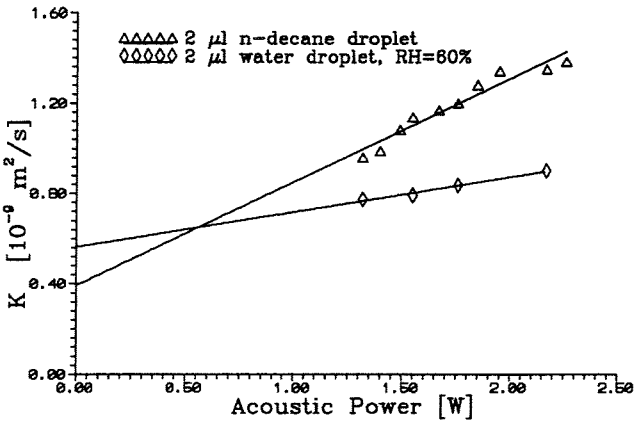

Figure 5: Dependence of the evaporation constant on the acoustic power measured for a 2 μl n-decane and water droplet ($RH = 0.6$)

for a 2 μl n-decane and water droplet is presented. Due to these static deformations the droplet surface area increases and, hence, higher evaporation rates follow. However, enhanced evaporation is only with smaller part influenced by larger surface area. Dominant part comes from more developed velocity profiles around a droplet. The experimental results were fitted with a second-order polynom yielding $a/b = 0.9991 + 0.00487 \cdot P + 0.1039 \cdot P^2$, with P in [W]. For 2 μl water droplet, we obtained $a/b = 0.9995 + 0.03586 \cdot P + 0.0449 \cdot P^2$. Initial deformation aspect ratio a/b can be calculated according to *Trinh et al.* [15]

$$\frac{a}{b} = \frac{r(\pi/2)}{r(0)} = \frac{1 + \frac{3}{64\sigma} \cdot R \cdot P_s^2 \cdot \beta_0 \left[1 + \frac{7}{5}(kR)^2\right]}{1 - \frac{6}{64\sigma} \cdot R \cdot P_s^2 \cdot \beta_0 \left[1 + \frac{7}{5}(kR)^2\right]}$$

For these calculations the RMS pressure amplitude P_s measurements with a probe microphone would have been necessaru, which however, have not been performed within this study.

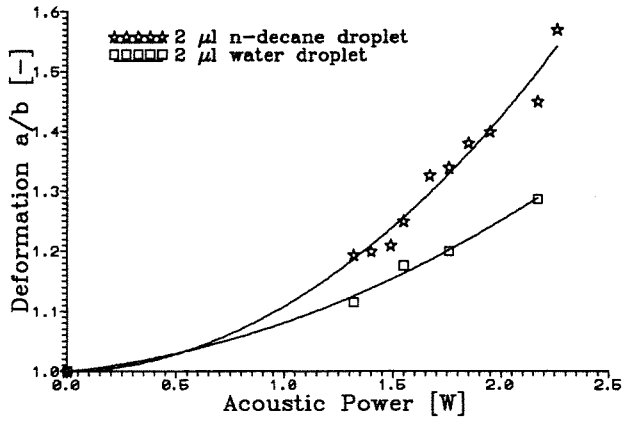

Figure 6: Dependence of the initial oblate-biased static deformation on the acoustic power measured for a 2 μl n-decane and water droplet

Let us now show the results of mass transfer rates for oscillating droplets. In Fig. 7 the evaporation histories for 2 μl n-decane droplets and enhancement of *Sherwood* numbers due to oscillations are presented. It is a remarkable result to notice how much the the evaporation rates are influenced by droplet shape oscillations. In the case of a 0.8 mm n-decane droplet ($V = 2$ μl) oscillating in second mode with $|\epsilon_2| = 0.1$, the experimental value yields 12.6 % higher evaporation rate than in case of no oscillations. Calculations gives $\mathcal{R}e = 1.17$ and $\mathcal{S}h = 2.2$, and a relative increase in mass transfer of about 10 %. As one can see the agreement with the experimental result is good. For same droplet size but, oscillating in fourth mode with $|\epsilon_4| = 0.13$ the experimental value yields 42 %

higher *Sherwood* number than no oscillations case. Calculations gives *Reynolds* number of 5.93 and *Sherwood* number 2.89 presenting a relative increase of $\approx$ 45 %. This result is in good agreement with the experimental result as well. During the measurements the resonance frequency increases due to droplet size decrease caused by evaporation. The frequency change due to evaporation was thoroughly investigated by *Daidžić* [3, 4].

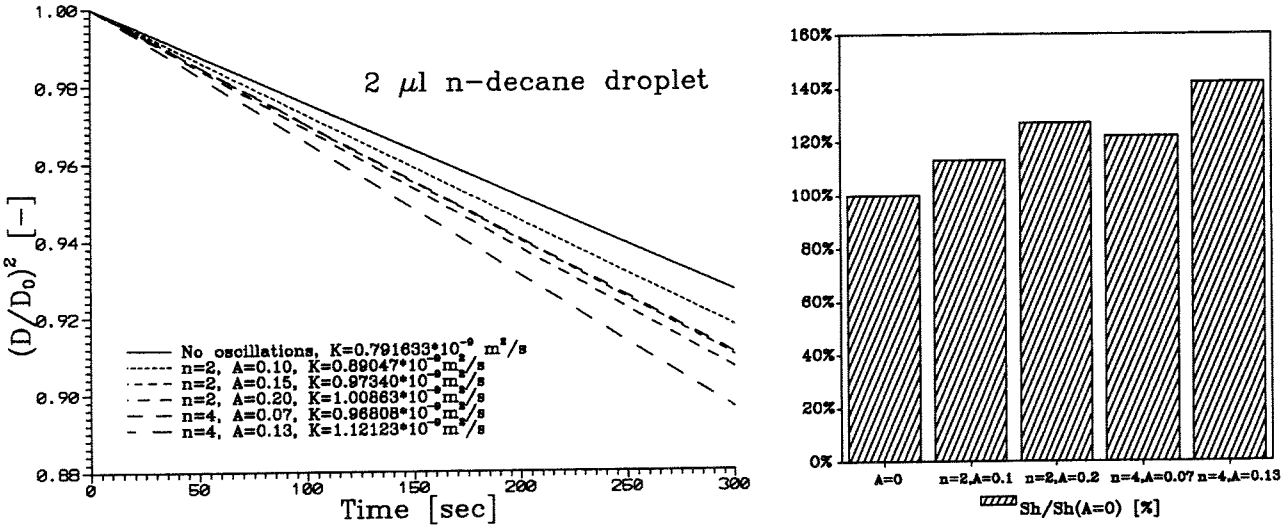

Figure 7: Evaporation rates for 2 μl n-decane droplets in case of axial symmetric oscillations and Sherwood numbers ratios

5 CONCLUSIONS

Theoretical considerations of the film theory showed previous erroneous conclusions based on the fact that pure diffusion and *Stefan* flow can co-exist with the consequence that the actual *Sherwood* number becomes smaller than two. It is shown that in the limiting case for stagnant droplet, with negligible *Stefan* flow effect, the convective transfer numbers must vanish as well and that.

By means of an ultrasonic levitator, first evaporation measurements of single droplets have been performed. The measurements have been made by either a laser-shadow extinction method or a visualization technique. With pure liquids the measurements are in perfect agreement with the well known D^2-*law*, i.e. the surface of the droplets decreases linearly with time. For water-ethyl-sucrose mixtures the expected non-linear behaviour was found, characterized by a fast evaporation of the high-volatile components and a final slow or even diminishing evaporation due to starting crystallization of the sucrose. Mutual interaction between different components evaporation rates is responsible for this nonlinearity. A perturbation analysis for mixtures with small amount of second component should give a reliable agreement with the experimental results. This will be the subject of further theoretical investigations on multi-component droplet evaporation.

It was found that acoustic streaming and droplet shape oscillations may significantly improve heat and mass transfer rates. This is specialy interesting for models of spraying systems where turbulence effects and droplet oscillations may play important role in the final droplet size distributions. So far, the combination of the ultrasonic levitation principle with new measuring techniques for instantaneous droplet sizes has proven to deliver reliable results of the evaporation rates. Even an acoustic levitation influence convective mass transfer it can still be used for pure diffusion measurements by extrapolating measured data for different acoustic powers to zero power case. Such data on pure diffusion make then possible to extract binary diffusion constant for different mixtures and combinations of liquids and gaseous hosts. Evaporation measurements in controlled environmental conditions will be the subject of future investigations which is of special interest for levitation of water droplets.

References

[1] Abramzon B., Sirignano W.A. *Approximate Theory of a Single Droplet Vaporization in a Convective Field: Effects of Variable Properties, Stefan Flow and Transient Liquid Heataing* Proc. 2nd. ASME-JSME Thermal Engng. Joint Conf., **1**, pp. 11-18, (1987)

[2] Clift R., Grace J.R., Weber M.E. *Bubbles, Drops, and Particles* Academic Press, New York, 1978.

[3] Daidžić N., Stadler R., Melling A. *Droplet evaporation and deformations in an amplitude modulated ultrasonic field* Report LSTM 373A/TEN/93, Lehrstuhl für Strömungsmechanik, Universität Erlangen-Nürnberg, Erlangen, September 1993.

[4] Daidžić N., Stadler R., Domnick J. *Experimental Techniques for Measurements of Droplet Evaporation* ICLASS 94, 6^{th} International Conference on Liquid Atomization and Spray Systems, 18-22 July 1994, Rouen, France, (1994)

[5] Davis E,J., Ray A.K. *Single Aerosol Particle Size and Mass Measurements Using an Electrodynamic Balance* Journ. Colloid and Interface Sci., **75**, No. 2, pp. 566-576, (1980)

[6] Downing C.G. *The Evaporation of Drops of Pure Liquids at Elevated Temperatures: Rates of Evaporation and Wet-bulb Temperatures* A.I.Ch.E. Journal, **12**, No. 4, pp. 760-766, (1966)

[7] Faeth G.M. *Current Status of Droplet and Liquid Combustion* Prog. Energy Combustion Sci., **3**, pp. 191-224, (1977)

[8] Law C.K. *Recent Advances in Droplet Vaporization and Combustion* Prog. Energy Combustion Sci., **8**, pp. 171-201, (1982)

[9] Lee C.P. *Outer Acoustic Streaming* Annual Report October 1, 1990 - December 31, 1991, Center for Microgravity Research and Applications (VUMRA), School of Engineering, Vanderbilt University, Nashville, Tennessee, USA, (1991)

[10] Lierke E.G., Grossbach R., Flögel K., Clancy P. *Acoustic Positioning for Space Processing of Materials Science Samples in Mirror Furnaces* Proc. IEEE Ultrasonic Symposium, pp. 1129-1139, (1983)

[11] Lierke E.G. *Acoustic Levitation - a Spinoff from Space* (to be published) 1994

[12] Marston P.L., Apfel R.E. *Acoustically Forced Shape Oscillations of Hydrocarbon Drops Levitated in Water* J. Colloid and Interface Science, **68**, No. 2, pp. 280-286, (1979)

[13] Ravindran P, Davis E.J., Ray A.K. (1979) *Diffusivities of Low-Volatility Species in Light Gases* AIChE Journal, **25**, No. 6, pp. 966-975

[14] Renz U., Breuer A., Klingsporn M. *Strahlausbreitung und Tropfenverdampfung bei der dieselmotorischen Einspritzung*, Kolloquium des SFB 224 der RWTH Aachen, 11-12 März 1993

[15] Trinh E.H., Hsu Chaur-Jian *Equilibrium shapes of acoustically levitated drops* J. Acoust. Soc. Am., **79**, No. 5, pp. 1335-1338, (1986)

[16] Zhang S.H., Davis E.J. *Mass Transfer from a Single Micro-Droplet to a Gas Flowing at Low Reynolds Number* Chem. Eng. Comm., **50**, pp. 51-67, (1987)

REPRODUCTIVE ACCURACY OF SELECTED VOID FRACTION CORRELATIONS FOR HORIZONTAL FLOW AND VERTICAL UPFLOW

R. Diener, L. Friedel

Technische Universität Hamburg-Harburg
Arbeitsbereich Strömungsmechanik
Postfach 21050, D-21071 Hamburg, Deutschland
Telephone: (040) 7718-3252, Facsimile: (040) 7718-2573

ABSTRACT

Several mean void fraction correlations have been proposed in the past. Indeed, they differ with respect to the physical parameters included, the underlying data basis, the model assumptions etc. Their predictions also considerably deviate from each other. Thus, the rational choice of an appropriate model is not straightforward.

On the basis of a large mean void fraction data bank, containing experimental results for vertical upward and horizontal pipe flow, some specific correlations have been checked for their predictive accuracy in relation to each other and in view of a generally accepted level of permissible inaccuracy.

The selection of the correlations for the relative ranking is based on the definition of a set of physically indispensable equation variables and the inclusion of some theoretical limits, which have to be met by the relationships.

The authoritative criteria for the ranking are dimensionless statistical parameters describing the scatter of the differences between the measured and the calculated values of the mean void fraction and of the two-phase mixture density. In detail, the standard deviations of the logarithmic and absolute deviations are used with the same weight.

The comparison confirmed that most of the void fraction correlations either reproduce the mean void fraction or the mean density with a rather acceptable accuracy. All in all, Rouhani's first correlation and the older HTFS-Alpha model are the only ones meriting a general recommendation in the case of horizontal and vertical upward flow.

INTRODUCTION

The mean void fraction is—amongst others—necessary for predicting the gravitational and the momentum pressure change, the latter if using a heterogeneous flow model. Several mean void fraction correlations are described in the literature, which—again amongst others—differ with respect to the physical model assumptions, the underlying data basis and the physical parameters included. As a consequence, their predictions also considerably deviate from each other and the choice of an appropriate model is, therefore, very often a matter of feeling.

In this study the merits of several well known mean void fraction correlations, if used for reproducing measured mean void fraction and mean mixture density data during horizontal flow and vertical upflow, are checked. In this respect, the separate evaluation of the predictive accuracy for mean void fraction and mean mixture density seems to be necessary, since it can

not be expected that a correlation correctly predicting mean void fraction data provides the same accuracy regarding the mean mixture density. In view of the vast amount of correlations advocated in the literature the methods finally considered emerged from a pre-examination; only those including certain authoritative independent parameters as equation variables and mathematically the (in practice) most significant limiting values of the mean void fraction have been selected.

First, the interactions between the independent parameters and the mean void fraction are defined and, thereby, the limiting conditions for the maximum and minimum mean void fraction to be fullfilled by the correlations are delineated and the correlations are selected. Next, the database is described in global terms and the statistical dimensionless numbers used for characterization of the average predictive accuracy are justified. Finally, the average predictive accuracy of the selected void fraction correlations are given on the basis of the values of the statistical numbers. Therewith, it is discerned between their merits, if reproducing mean void fraction and mean mixture density data respectively.

1. DEFINITIONS AND VALIDITY RANGES

The definitions used in the following read: The mean void fraction is the ratio between the flow area occupied by gas or vapour [1] and that of the total flow area. It is a time and area average of the distribution across the flow cross section.

$$\varepsilon = \frac{A_G}{A_G + A_F}$$

Differentiation is made between the (self adjusting) mean void fraction and the (intentionally adjustable) volumetric flow quality as on average the (mean) phase velocities differ. The latter is defined as the ratio of the vapour volume flow rate to the total volume flow rate of the two-phase mixture.

$$\dot{\varepsilon} = \frac{\dot{V}_G}{\dot{V}_G + \dot{V}_F}$$

Analogously, the ratio of the corresponding mass flow rates can be defined as the mass flow quality.

$$\dot{x} = \frac{\dot{M}_G}{\dot{M}_G + \dot{M}_F}$$

With these parameters the (graphic but non measurable) slip as the ratio of the mean velocities of both phases reads

$$S = \frac{\bar{w}_G}{\bar{w}_F} = \frac{\dot{\varepsilon}}{1-\dot{\varepsilon}} \frac{1-\varepsilon}{\varepsilon} = \frac{\dot{x}}{1-\dot{x}} \frac{1-\varepsilon}{\varepsilon} \frac{\rho_F}{\rho_G} \quad .$$

The void fraction and both qualities are defined within the limits of zero for liquid flow and unity for vapour flow respectively. In the case of a so-called homogeneous flow the mean void fraction and the volumetric flow quality are identical. With respect to a definition of the attainable magnitude of the slip, the starting point of the assessment is the pressure difference forcing the mixture through a horizontal flow channel. By assuming equal local pressure in

[1] In following the expression "vapour" will be used instead of "gas or vapour". Moreover, "mass flow quality" and "mean mixture density" will often be replaced by "quality" and "mean density".

both phases at any flow position the vapour phase must flow with a higher average velocity than the liquid because of its smaller specific weight and lower specific phase friction. In vertical upward flow this tendency will be amplified by the buoyancy. Thereby, the slip can only take values in excess of or equal to unity for vertical upward flow and horizontal flow.

$$S \geq 1$$

The mean mixture density is obtained by the void fraction weighted density of both phases. For an infinite short tube length it is calculated by

$$\bar{\rho} = \varepsilon \cdot \rho_G + (1 - \varepsilon) \cdot \rho_F$$

The limits of the mean density are given by the densities of vapour and liquid phase.

$$\rho_G \leq \bar{\rho} \leq \rho_F$$

2. INDEPENDENT PARAMETERS FOR THE MEAN VOID FRACTION

It is well accepted that the authoritative independent parameters influencing the mean void fraction are flow direction, mass flow rates of both phases, macroscopic phase state properties as density, dynamic viscosity and surface tension, characteristic dimensions of the flow cross section and gravitational acceleration [1]. Depending on the combination of these parameters different flow patterns adjust themselves, for instance bubble, slug and annular flow. Indeed, here the flow patterns are not considered as independent parameters as they set automatically in as a function of these. Additionally, the effects of mean wall roughness or physicochemical properties of the mixture as well as of the type of generation of the two phase flow should be negligibly small in view of the large pipe flow velocities usually prevailing and, thus, they remain secondary parameters.

The effect of the flow direction on the mean void fraction also seems to be negligibly small. In horizontally directed two-phase flow neither the buoyancy of the vapour phase nor the gravity of the liquid phase influence the global motion of the mixture, because in each case no force component is acting in flow direction. Only the vertical arrangement of the phases can be influenced in case of low (mean) velocities. In vertical upward flow the velocity of the lighter phase is increased due to the effect of buoyancy and, as a consequence, the mean void fraction is lower than in the case of horizontal flow at equal flow and operation conditions. However, the deviations diminish with higher velocities and pressures, in detail, as soon as the ascending velocity of a single bubble or of a bubble bulk in proportion to the transport velocity will be negligibly small.

Subsequently, the effect on the mean void fraction by changing only one independent parameter and keeping the others constant is analysed. With respect to an intentional restriction of the number of correlations to be checked, it is necessary to weight the individual importance of the remaining, not yet classified parameters. However, this can only be carried out on the basis of narrow parameter ranges, due to the complicated interactions between the two phases, which can only be overlooked or be valid within a specific flow regime. Herewith, for a simplification of the analysis the mass flow rates of the phases are replaced by the total mass flux and the quality. With this usual artificial comprehension, the specific effect of the total mass flow rate on the mean void fraction will be greatly reduced, while the flow quality as a not directly measurable and, thus, defined quantity, though very illustrative, will become a

dominant primary parameter. Furthermore, the densities and viscosities of both phases are summarized in the density and viscosity ratio, ρ_F/ρ_G and η_F/η_G.

Disregarding in the following the flow direction, the quality and the density ratio remain as primary parameters considerably affecting the mean void fraction. With increasing quality a greater amount of vapour flows through the tube cross section, whereas the liquid volume flow is correspondingly reduced and the mean void fraction rises. Due to the same reason an increasing density ratio, for instance as a consequence of a pressure reduction, causes higher mean void fractions, too. At a constant quality, a higher mass flux contributes to a more homogeneous flow due to a more intensive momentum exchange between the phases and, thus, a moderately higher mean void fraction.

As long as the tube diameter is assumed to be an order of magnitude larger than the maximum bubble diameter, an increase in tube diameter would promote phase separation and, hence, smaller mean void fractions would be obtained.

At common operating conditions the dynamic viscosity of the vapour phase varies in very small ranges, so that the mean void fraction should not be affected to a considerable degree by changing this property. For this reason, only the change of the liquid phase dynamic viscosity will be considered. A higher liquid viscosity effects larger friction forces between liquid and tube wall as well as higher drag forces between the phases. As a consequence, the friction forces prevailing in the first case lead to a lower liquid velocity gradient at the wall boundary layer and simultaneously to a higher liquid velocity in the core allowing, thus, for a higher vapour velocity, too. The mean void fraction then adjusts itself to lower values. In parallel, higher drag forces occurring between the phases cause a decrease of slip, which now would reduce the mean void fraction. The dominance of one of these tendencies depends—amongst others—on the degree of wetting of the tube wall with liquid and on the size of the interface between liquid and vapour phase. Usually, it is assumed that the increasing friction forces at the wall are the dominant forces so that the mean void fraction would be lowered by the increase of the liquid viscosity. However, in mist or bubble flow containing a large amount of small particles it can be assumed that the drag forces between the phases dominate. As a result, the mean void fraction would then increase with higher liquid viscosity.

The influence of the surface tension will be first considered on the basis of a single bubble in a stationary system. Its volume will grow with increasing surface tension, at the same time the equatorial bubble area decreases in relation to the bubble volume with increasing bubble size. If this tendency is also valid in a first approximation in flowing two-phase mixtures, then with increasing bubble size or surface tension the number of bubbles would reduce and the mean void fraction should slightly decrease.

All in all, as a rule the mass flow quality and the density ratio should influence the mean void fraction to a higher extent than the mass flux or the viscosity ratio. Both latter mentioned parameters, however, are considered to be more important than the surface tension, the hydraulic diameter or the—here not defined—physicochemical properties.

In the following selection of the correlations only the quality and the density ratio are considered as indispensable equation variables. Subsequently, the maximum attainable values of the void fraction as a function of these primary parameters are discussed.

3. LIMITING VALUES OF THE MEAN VOID FRACTION

The mean void fraction approaches to zero, if the two-phase flow changes to single-phase liquid flow and correspondingly it approaches unity in case of single-phase vapour flow:

$$\lim_{\dot{x}\to 0} \varepsilon = 0 \qquad \text{and} \qquad \lim_{\dot{x}\to 1} \varepsilon = 1$$

The density ratio can only assume values between unity, if reaching the thermodynamic critical pressure, and infinity for instance under vacuum conditions. In the first case, the flow can be considered as homogeneous or single fluid flow. Moreover, the volumetric flow quality then equals to the mass flow quality. With this condition, also the mean void fraction will assume the value of the quality. If, on the contrary, the density ratio approaches an infinite value, then the volumetric vapour flow rate reaches a value of nearly unity. Since the vapour phase velocity is first restricted by the speed of sound, the slip can not grow unrestrictedly and, therefore, the mean void fraction approaches unity, too:

$$\lim_{\frac{\rho_F}{\rho_G}\to 1} \varepsilon = \dot{\varepsilon} = \dot{x} \qquad \text{and} \qquad \lim_{\frac{\rho_F}{\rho_G}\to \infty} \varepsilon = \dot{\varepsilon} = 1$$

On the basis of these limiting conditions and assuming that the slip can take only values greater than or equal to unity during horizontal and vertical upward flow the allowable range of the mean void fraction can be defined in dependence of the mass flow quality and the volumetric flow quality. For horizontal and vertical upward flow the values of the mean void fraction range between the limiting conditions of the quality and the volumetric flow quality, Fig. 1.

The final selection of the correlations is based on the incorporation of the limits of single-phase liquid and vapour flow into the void fraction correlation. The consideration of the density ratio as equation variable is regarded as further, but secondary criterion, because seldom pressure conditions like vacuum or near critical pressure occur in technical practice.

4. MODEL SELECTION

In the following, the most often used and cited correlations in the literature are checked in view of the implementation of the limiting conditions of a void fraction of zero and unity, Tab. 1. Out of these 26 models only 13 correlations were selected for further consideration. According to the fullfilling of the limiting conditions at least within a range of $\pm$ 0.005 these were proposed by HTFS [2,3], Chexal et al. [4], Nabizadeh [5], Premoli et al. [6], Huq [7], Melber [8], Löscher and Reinhardt [9], Kowalczewski [10], Smith [11], Sonnenburg [12] and Rouhani [13,14]. Herewith, the methods developed by Chexal et al., Nabizadeh, Sonnenburg and Rouhani are based on the drift flux model developed by Zuber and Findlay [15] and Behringer [16] respectively. The models proposed by Kowalczewski, Löscher and Reinhardt, Premoli et al., Smith, Melber and HTFS do not base on a specific flow model, they resemble more to a mathematically optimized correlation. Huq's correlation is analytically derived by considering the limiting conditions applied to the slip.

The specific parameters considered in the 13 correlations can be taken from Tab. 2. All models include mass flow quality and alternatively the density ratio or the critical pressure

ratio and the overwhelming majority also considers for mass flow rate and diameter. The drift flux correlations and the model of Premoli et al. account for the surface tension, too, the viscosity ratio is only included in the models of HTFS and in the correlation of Premoli et al. Obviously, only the correlations of Sonnenburg and Premoli et al. take all of the authoritative parameters into consideration, whereas the equation developed by Huq and the model of Smith only respect for the density ratio and the quality.

5. MEAN VOID FRACTION DATA BANK

A data bank with more than 24000 experimental results was used for the evaluation of the predictive accuracy. These data largely cover the most important parameter ranges. The variances of the governing parameters are listed in Tab. 3. The data consist of single-component systems, whereby measurements in water and refrigerant R12 two-phase flow dominate, and two-component systems, mostly consisting of water/air data. In the case of the two-component mixtures the ranges of mass flow rate, density and viscosity ratio as well as of the diameter are more spread than for single-component mixtures.

6. PREDICTIVE ACCURACY

The average predictive accuracy of the selected correlations is based on the values obtained for the scatter of the logarithmic ratios and the scatter of the absolute deviations between the experimental and calculated values, Tab. 4. Moreover, the average of the logarithmic ratios characterizing the average under- or overprediction of the experimental values is depicted for the sake of completeness. The advantages of using these parameters are already discussed by Friedel [17], Govan [18] and Schmidt [19] and showed in the past to allow for a balanced description of the merits of each correlation.

At first, the predictive accuracy of mean void fraction correlations for water/steam and water/air mixtures was investigated, Tab. 5a and b. This was carried out separately, because the correlations developed by Chexal et al., Kowalczewski and Löscher and Reinhardt in their original version are not suitable for predicting the mean void fraction and the mean densities in any two-phase system. Altogether, the prediction of water/air void data is marginally not as exact possible as for water/steam mixtures, but in total satisfying with an average accuracy of about 20%. The small difference may be attributed to the larger parameter ranges exhibited during water/air flow. All in all, both correlations proposed by Rouhani and the (older) correlation of HTFS-Alpha predict the measured mean void fraction distinctly better than the others. On considering the mean density, again, the models developed by Rouhani, both HTFS correlations as well as the methods developed by Chexal et al., Nabizadeh and Premoli et al. perform rather well. However, in the case of water/air flow no correlation provides really satisfactory results. The logarithmic scatter of the best correlation still amounts to non acceptable 60%.

In the following assessment of the correlations, if coping with the whole data material, the methods developed by Melber and Smith, which do not provide comparatively accurate predictions for the mean void fraction and the mean density, and the models proposed by Chexal et al., Kowalczewski and Löscher and Reinhardt, the use of which—as stated above—is restricted to specific two-phase mixtures, no longer are considered.

On comparing Tab. 6a, b and c exhibiting the mean values for the characteristic numbers, if

the (remaining) correlations are applied to the whole data in single-component systems, the models developed by HTFS provide the best predictions for the mean void fraction as well as for the mean density, whereat the HTFS-Alpha equation is more accurate than the newer HTFS correlation. This correlation also allows for adequate good prediction, if applied to two-component mixtures, although Rouhani's first correlation is in the prediction of the mean density really—on average—slightly more accurate. The accuracy of the mean void fraction predictions of the other model developed by Rouhani is comparable to this obtained by using HTFS-Alpha regarding its logarithmic scatter, but the absolute scatter is considerably higher. This indicates that mainly the relative high mean void fraction data will be inaccurately reproduced. As a consequence, the prediction of the mean density is rather uncertain. The reason for the difference between the quality of the predictions of the calculated mean void fractions and the mean densities is discussed in the appendix.

Considering only experimental data of two-component mixtures with mass fluxes higher than 100 kg/(m^{2}s), then Rouhani's second model provides the best predictions for the mean void fraction. From this follows that the comparatively large absolute scatter, which results if all data are considered in the evaluation, can be attributed to a systematic underprediction of the mean void fraction by this correlation, if data with low mass fluxes and high qualities are included. Rouhani's second model is the only one here taking into consideration the influence of the diameter, so it could be expected to give relative good predictions in parameter ranges with great variation of the diameter. However, these data exist only for small mass fluxes (<100 kg/(m^{2}s)), which are not separately discussed here. All in all, the logarithmic scatter by using Rouhani's second correlation obtained under low mass flux conditions is not considerably lower than that produced with the first Rouhani model. Therefore, it can be argued that the influence of the diameter will be overpredicted by using the second method of Rouhani, at least in conjunction with small mass flux conditions.

The model developed by Huq provides as accurate predictions as those obtained by using the correlations of HTFS and Rouhani for measured data with mass fluxes in excess of 100 kg/(m^{2}s). In case of mass fluxes lower than 50 kg/(m^{2}s), this model yields results, which are overpredicted by an order of magnitude. This is due to the fact that the mass flux is not included in this model as equation variable. For purpose of demonstration in Fig. 2 the mean void fraction for two-component systems, at mass fluxes of less than 50 kg/(m^{2}s) and in excess of 2000 kg/(m^{2}s), are plotted against the predictions obtained by using HTFS-Alpha and Huq's model. This plot reveals the marginal differences in predicting the void fraction under high mass flux conditions and the obviously considerable differences in accuracy, if predicting mean void fraction in cases where the mass fluxes are smaller than 50 kg/(m^{2}s).

All in all, in the standard case of predicting the mean void fraction or the mean two phase mixture density the HTFS-Alpha model should be preferred. In case that this correlation is not accessible the next most general and accurate equation is Rouhani's first, which leads under certain parameter combinations to slightly superior but also to distinctly less accurate predictions.

CONCLUSIONS

The average predictive accuracy of 13 out of 26 well known mean void fraction correlations has been checked on the basis of a data bank with about 24000 experimental results obtained with single- and two-component mixtures. The HTFS-Alpha correlation and Rouhani's first version provide the most accurate predictions for the mean void fraction and the mean density.

NOMENCLATURE

A	Flow cross section
C_0	Distribution parameter
d	Diameter
g	Acceleration of gravity
f	Number of equation variables
$\dot{m}$	Mass flux
n	Number of measurements
p	Pressure
p_{crit}	Critical pressure
S	Slip
S_{abs}	Absolute scatter
S_{ln}	Logarithmic scatter
$\dot{V}$	Volumetric flow rate
$\bar{w}$	Mean velocity
$w_{G,Dr}$	Drift velocity
$\dot{x}$	Mass flow quality
$\bar{X}_{ln}$	Average of logarithmic ratios
$X_{i,abs}$	Absolute deviation between measured and predicted value
$X_{i,ln}$	Logarithmic ratio between measured and predicted value

Greek Symbols

ε	Mean void fraction
$\dot{\varepsilon}$	Volumetric flow quality
η	Dynamic viscosity
ρ	Density
σ	Surface tension

Indices

F	Liquid
G	Gas or vapour

REFERENCES

[1] Friedel, L., "Gasgehaltsänderungen in horizontaler und in aufwärts- und abwärtsgerichteter Gas-/Dampf-Flüssigkeitsströmung bei Variation der unabhängigen Einflußgrößen", in: Chem.-Ing. Techn. 53, 9, pp.750–751 (1981).

[2] Collier, J.G., Claxton, K.T. and Ward, J.A.: "HTFS correlations for two-phase pressure drop and void fraction in tubes", HTFS Design Report 28, Part 4 (1972), (commercial in confidence).

[3] Whalley, P.B. and Ward, J.A.: "The calculation of void fraction in two phase flow", HTFS Design Report 28, Part 4 (1981), (commercial in confidence).

[4] Chexal, B., Horowitz, J. and Lellouche, G.: "An assessment of eight void fraction models for vertical flows", EPRI/NSAC-107 (1986).

[5] Nabizadeh, H.: "Modellgesetze und Parameteruntersuchungen für den volumetrischen Dampfgehalt in einer Zweiphasenströmung", EIR-Bericht 323 (1977).

[6] Premoli, A., Francesco, D. and Prina, A.: "An empirical correlation for evaluating two-phase mixture density under adiabatic conditions", Paper European Two-Phase Flow Group Meeting, Mailand (1970).

[7] Huq, R.: "An analytical two-phase flow void prediction method", Paper 90-1738, AIAA/ASME 5th Joint Thermophysics and Heat Transfer Conf., Seattle (1990).

[8] Melber, A.: "Experimentelle und theoretische Untersuchungen über den Druckabfall von Zweiphasenströmungen in beliebig geneigten Rohren", Ph. D. Thesis, TH Darmstadt (1989).

[9] Löscher, K. and Reinhardt, W., "Der Schlupf bei ausgebildeter adiabater Einkomponenten-Zweiphasenströmung dampfförmig-flüssig im horizontalen Rohr", in: Wiss. Z. TH Dresden 22, 5, pp.813–819 (1973).

[10] Kowalczewski, P.P.: "Two-phase flow in an unheated and heated tube", Ph. D. Thesis, ETH Zürich (1964).

[11] Smith, S.L., "Void fractions in two-phase flow: A correlation based upon an equal velocity head model", in: Proc. Instn. Mech. Engrs. 184, 36, pp.647–657 (1969/70).

[12] Sonnenburg, H.G.: "Entwicklung eines umfassenden Drift-Flux-Modells zur Bestimmung der Relativgeschwindigkeit zwischen Wasser und Dampf", GRS-A-1752 (1991).

[13] Rouhani, S.Z. and Axelsson, E., "Calculation of void volume fraction in the subcooled and quality boiling regions", in: Int. J. Heat and Mass Transfer, 14, pp.383–393 (1969).

[14] Rouhani, S.Z.: "Modified correlations for void and two-phase pressure drop", AE-RTV-841 (1974).

[15] Zuber, N. and Findlay, J., "Average volumetric concentration in two-phase flow systems", in: J. Heat Transfer 87, pp.453–463 (1965).

[16] Behringer, H., "Die Strömung von Flüssigkeits-Gasgemischen in senkrechten Rohren", in: Z. Ges. Kälte-Ind. 43, 3, pp.55–58 (1934).

[17] Friedel, L., "Kriterien für die Beurteilung der Vorhersagegenauigkeit von halbempirischen Berechnungsmodellen", in: Chem.-Ing.-Techn. 53, 1, p.59 (1981).

[18] Govan, A.H.: "A note on statistical methods for comparing measured and calculated values", HTFS RS767-1, pp.315–323 (1988).

[19] Schmidt, J.: "Berechnung und Messung der Druckänderungen über scharfkantige, plötzliche Rohrerweiterungen und -verengungen bei Gas/Dampf-Flüssigkeitsströmung", VDI-Fortschrittsbericht 236 (1993).

[20] Ahmad, S.Y., "Axial distribution of bulk temperature and void fraction in a heated channel with inlet subcooling", in: J. Heat Transfer 92, pp.595–609 (1970).

[21] Armand, A.A. and Treschev, G.G.: "Investigation of the resistance during the movement of steam-water mixtures in a heated boiler pipe at high pressures", AERE Lib/Trans. 816 (1959).

[22] Bankhoff, S.G., "A variable density single-fluid model for two-phase flow with particular reference to steam-water flow", in: J. Heat Transfer 82, pp.265–276 (1960).

[23] Baroczy, C.J., "A systematic correlation for two-phase pressure drop", in: Chem. Engng. Prog. Symp. Ser. 62, 64, pp.232–249 (1966).

[24] Chawla, J.M., "Flüssigkeitsinhalt in Rohren für Flüssigkeits-Gas-Gemische bei der Zweiphasenströmung", in: Chem.-Ing.-Techn. 31, 5/6, pp.328–330 (1969).

[25] Dix, G.E.: "Vapor void fraction for forced convection with boiling and low flow rates", Ph D Thesis, Univ. of California, Berkeley (1971).

[26] Glahn, U.H. von: "An empirical relation for predicting void fraction with two-phase steam water flow", NASA TN-D-1189 (1962).

[27] Grieb, G., "New slip correlation for forced convection two-phase flow" in: Nucl. Energ. 28, pp.155–160 (1989).

[28] Hughmark, G.A., "Holdup in gas-liquid flow", in: Chem. Engng. Progr. 58, 4, pp.62–65 (1962).

[29] Jones, A.B.: "Hydrodynamic stability of a boiling channel", KAPL-2290 (1961).

[30] Lockhart, R.W. and Martinelli, R.L., "Proposed correlation of data for isothermal two-phase two-component flow in pipes", in: Chem. Eng. Progr. 45, pp.39–45 (1949).

[31] Marchaterre, J.F. and Hoglund, B.M., "Correlation for two-phase flow", in: Nucleonics 20, p.142 (1962).

APPENDIX

Mathematical derivation for the explanation of the differences in the predictive accuracies of the mean void fraction and mean density data

As a rule the mean void fraction correlations are optimized in order to give the most accurate prediction of the mean void fraction. According to the magnitude of the mean void fraction and the density ratio the deviation of the predicted mean mixture density from the experimental value will be differently affected by an error of the mean void fraction prediction. With the definition of the mean mixture density and the assumption that the deviations $d\rho_F$ and $d\rho_G$ are comparatively small to that of the mean void fraction, the relative deviation of the mean mixture density reads in dependence of the relative deviation of the mean void fraction as:

$$\frac{\Delta\bar{\rho}}{\bar{\rho}} = \frac{\Delta\varepsilon}{\varepsilon}\left(1+\frac{1}{\varepsilon}\left(1+\frac{1}{\varepsilon}\left[1/\left(\rho_G/\rho_F-1\right)\right]\right)\right)^{-1}$$

For a constant density ratio and small void fractions it follows

$$\frac{\Delta\bar{\rho}}{\bar{\rho}} < \frac{\Delta\varepsilon}{\varepsilon} ,$$

whereas for a high void fraction it is valid

$$\frac{\Delta\bar{\rho}}{\bar{\rho}} > \frac{\Delta\varepsilon}{\varepsilon} .$$

This implies that the prediction of the mean mixture density can be very inaccurate in the case of two-phase flow with a high quality and a high mean void fraction respectively.

Correlations proposed by S.Z. Rouhani

$$\varepsilon = \frac{\dot{x}}{\rho_G} \Big/ \left[C_0\left(\frac{\dot{x}}{\rho_G}+\frac{1-\dot{x}}{\rho_F}\right)+\frac{w_{G,Dr}}{\dot{m}}\right]$$

$$w_{G,Dr} = \left(1,18/\sqrt{\rho_G}\right)\left(g\,\sigma\left(\rho_F-\rho_G\right)\right)^{0.25}\cdot\left(1-\dot{x}\right)$$

Rouhani I: $$C_0 = 1+0,2\cdot\left(1-\dot{x}\right)$$

Rouhani II: $$C_0 = 1+0,2\cdot\left(1-\dot{x}\right)\cdot\left(g\cdot d\right)^{0.25}\cdot\left(\rho_F/\dot{m}\right)^{0,5}$$

Author	Limiting condition	
	$\lim \varepsilon = 0$ $\dot{x} \to 0$	$\lim \varepsilon = 1$ $\dot{x} \to 1$
Ahmad	+	-
Armand/Treschev	+	-
Bankhoff	-	-
Baroczy	-	-
Chawla	-	-
Chexal et al.	+	+
Dix	-	-
v. Glahn	-	+
Grieb	+	-
HTFS-ALPHA	+	+
HTFS	+	+
Hughmark	-	-
Huq	+	+
Jones	+	-
Kowalczewski	+	+
Lockhart/Martinelli	+	-
Löscher/Reinhardt	+	+
Nabizadeh	+	+
Marchaterre/Hoglund	-	-
Melber	+	+
Rouhani I	+	+
Rouhani II	+	+
Premoli et al.	+	+
Sonnenburg	+	+
Smith	+	+
Zuber/Findlay	+	-

Tab. 1: Some void fraction correlations for horizontal and vertical upward flow from the literature and the state of implementation of the limiting conditions (+ indicates void fraction is at least within $\pm$ 0.005 of the limiting condition)

Basis	Author	Parameter							
		$\dot{x}$	ρ_f/ρ_g	p/p$_{crit}$	$\dot{m}$	d	η_f/η_g	σ	flow direction
Drift-Flux Model	Rouhani I	+	+	-	+	-	-	+	-
	Rouhani II	+	+	-	+	+	-	+	-
	Nabizadeh	+	+	-	+	+	-	+	-
	Chexal et al.	+	+	+	+	+	-	+	+
	Sonnenburg	+	+	-	+	+	+	+	+
Correlation	Kowalczewski	+	-	+	+	+	-	-	-
	Melber	+	+	-	+	+	-	-	+
	Löscher et al.	+	-	+	+	+	-	-	-
	HTFS-ALPHA	+	+	-	+	-	+	-	-
	HTFS	+	+	-	+	-	+	-	+
	Huq	+	+	-	-	-	-	-	-
	Premoli et al.	+	+	-	+	+	+	+	-
	Smith	+	+	-	-	-	-	-	-

Tab. 2: Parameters of the selected correlations

Parameter		System	
		Single-component	Two-component
Quality	[-]	0 - 1	0 - 1
Mass flux	$[kg/(m^2s)]$	8 - 4115	1 - 9087
Pressure	[bar]	1 - 180	1 - 197
Density ratio	[-]	2 - 24708	5 - 10712
Viscosity ratio	[-]	2 - 28	6 - 3115
Diameter	$[10^{-3}m]$	2 - 60	9 - 1067
Surface tension	$[10^{-3}N/m]$	2 - 405	21 - 469
Two phase mixtures		H_2O D_2O R113 R12.R22 Na.K.Hg	Hg/N_2 H_2O/Air Hydrocarbon/Air H_2O/Gas Alcohol/Gas
Number of data		9827	14521

Tab. 3: Parameter ranges of the void fraction data and two-phase systems

Statistical number	Definition
Scatter of logarithmic ratios	$S_{ln} = e^{\sqrt{\frac{\sum_{i=1}^{n} X_{i,ln}^2}{n-f-1}}} - 1$
	$X_{i,ln} = ln \frac{Y_{i,exp}}{Y_{i,calc}}$
Scatter of absolute deviations	$S_{abs} = \sqrt{\frac{\sum_{i=1}^{n} X_{i,abs}^2}{n-f-1}}$
	$X_{i,abs} = Y_{i,exp} - Y_{i,calc}$
Average of logarithmic ratios	$\bar{X}_{ln} = e^{\frac{1}{n}\sum_{i=1}^{n} X_{i,ln}} - 1$

Tab. 4: Definition of dimensionless statistical numbers used to characterize the average predictive accuracy of the models

Author	Mean void fraction $\bar{X}_{ln}$ [%]	S_{ln} [%]	S_{abs} [−]	Mean density $\bar{X}_{ln}$ [%]	S_{ln} [%]	S_{abs} $[kg/m^3]$
HTFS	-5.2	21.3	0.074	-0.3	28.7	57
HTFS-Alpha	-3.9	**20.6**	**0.068**	-1.9	26.6	**53**
Rouhani I	-9.0	22.8	0.080	3.8	32.5	63
Rouhani II	-7.5	21.9	0.080	-0.6	46.5	64
Sonnenburg	-5.4	22.8	0.085	2.2	53.1	68
Huq	-5.6	24.4	0.083	-2.5	31.8	64
Nabizadeh	6.0	22.4	0.075	-6.7	**24.3**	58
Premoli et al.	-11.1	26.3	0.088	6.3	30.2	67
Smith	-7.1	25.1	0.085	-0.5	30.1	65
Chexal et al.	-3.6	26.3	0.078	4.2	24.7	59
Kowalczewski	4.6	22.9	0.082	-9.8	31.5	64
Löscher/Reinhardt	-7.2	26.3	0.088	-3.5	31.3	67
Melber	-13.8	28.1	0.109	33.9	61.1	86

Tab. 5a: Average accuracy of mean void fraction and mixture density prediction for water/steam mixtures on the basis of 4471 data points

Author	Mean void fraction $\bar{X}_{ln}$ [%]	S_{ln} [%]	S_{abs} [−]	Mean density $\bar{X}_{ln}$ [%]	S_{ln} [%]	S_{abs} $[kg/m^3]$
HTFS	3.8	42.3	0.114	-11.4	78.3	114
HTFS-Alpha	-2.0	27.9	0.107	1.3	74.4	108
Rouhani I	-6.9	**23.8**	**0.102**	7.1	**59.6**	**102**
Rouhani II	5.2	26.9	0.126	-26.7	129.4	126
Sonnenburg	-3.4	33.0	0.121	59.6	216.8	121
Huq	-16.1	66.9	0.160	33.8	83.1	160
Nabizadeh	21.4	53.5	0.136	8.9	78.7	137
Premoli et al.	-11.8	57.5	0.137	11.4	65.9	137
Smith	-20.1	76.5	0.168	32.5	72.4	168
Chexal et al.	5.3	55.4	0.118	18.5	85.4	118
Melber	-24.6	79.4	0.217	185.4	337.2	217

Tab. 5b: Average accuracy of mean void fraction and mixture density prediction for water/air mixtures on the basis of 10991 data points

Author	Mean void fraction $\bar{X}_{ln}$ [%]	S_{ln} [%]	S_{abs} [−]	Mean density $\bar{X}_{ln}$ [%]	S_{ln} [%]	S_{abs} $[kg/m^3]$
HTFS	-5.8	22.9	0.096	9.4	39.8	150
HTFS-Alpha	-5.3	**22.2**	**0.092**	0.7	**36.1**	144
Rouhani I	-8.1	24.8	0.102	11.3	43.9	180
Rouhani II	-5.9	23.6	0.104	3.9	52.2	**118**
Sonnenburg	-4.8	23.7	0.106	15.6	74.7	138
Huq	-6.3	25.7	0.111	10.6	55.3	229
Nabizadeh	2.6	25.7	0.111	3.8	67.7	156
Premoli et al.	-10.5	26.9	0.150	21.3	50.2	202

Tab. 6a: Average predictive accuracy for single-component mixtures on the basis of 9827 data points

Model	Mean void fraction $\bar{X}_{ln}$ [%]	S_{ln} [%]	S_{abs} [−]	Mean density $\bar{X}_{ln}$ [%]	S_{ln} [%]	S_{abs} $[kg/m^3]$
HTFS	0.5	37.7	0.109	-12.9	79.1	**161**
HTFS-Alpha	-6.1	31.8	**0.107**	1.3	73.9	216
Rouhani I	-10.5	**31.7**	0.112	7.7	**61.7**	281
Rouhani II	0.5	31.9	0.131	-29.1	144.7	190
Sonnenburg	-6.2	35.6	0.131	60.9	210.6	165
Huq	-13.5	50.8	0.144	34.7	86.9	413
Nabizadeh	14.4	46.4	0.129	9.6	75.3	184
Premoli et al.	-11.6	46.1	0.129	15.2	70.9	283

Tab. 6b: Average predictive accuracy for two-component mixtures on the basis of 14521 data points

Author	Mean void fraction $\bar{X}_{ln}$ [%]	S_{ln} [%]	S_{abs} [−]	Mean density $\bar{X}_{ln}$ [%]	S_{ln} [%]	S_{abs} $[kg/m^3]$
HTFS	-0.5	30.2	0.101	1.6	**50.2**	**168**
HTFS-Alpha	-6.9	31.5	0.104	14.7	56.5	236
Rouhani I	-10.3	30.4	0.110	15.7	50.9	310
Rouhani II	-4.5	**28.9**	**0.100**	-5.7	57.9	186
Huq	-8.9	31.6	0.108	14.5	55.3	451

Tab. 6c: Average predictive accuracy for two-component mixtures and mass fluxes in excess of 100 kg/m²s on the basis of 11394 data points

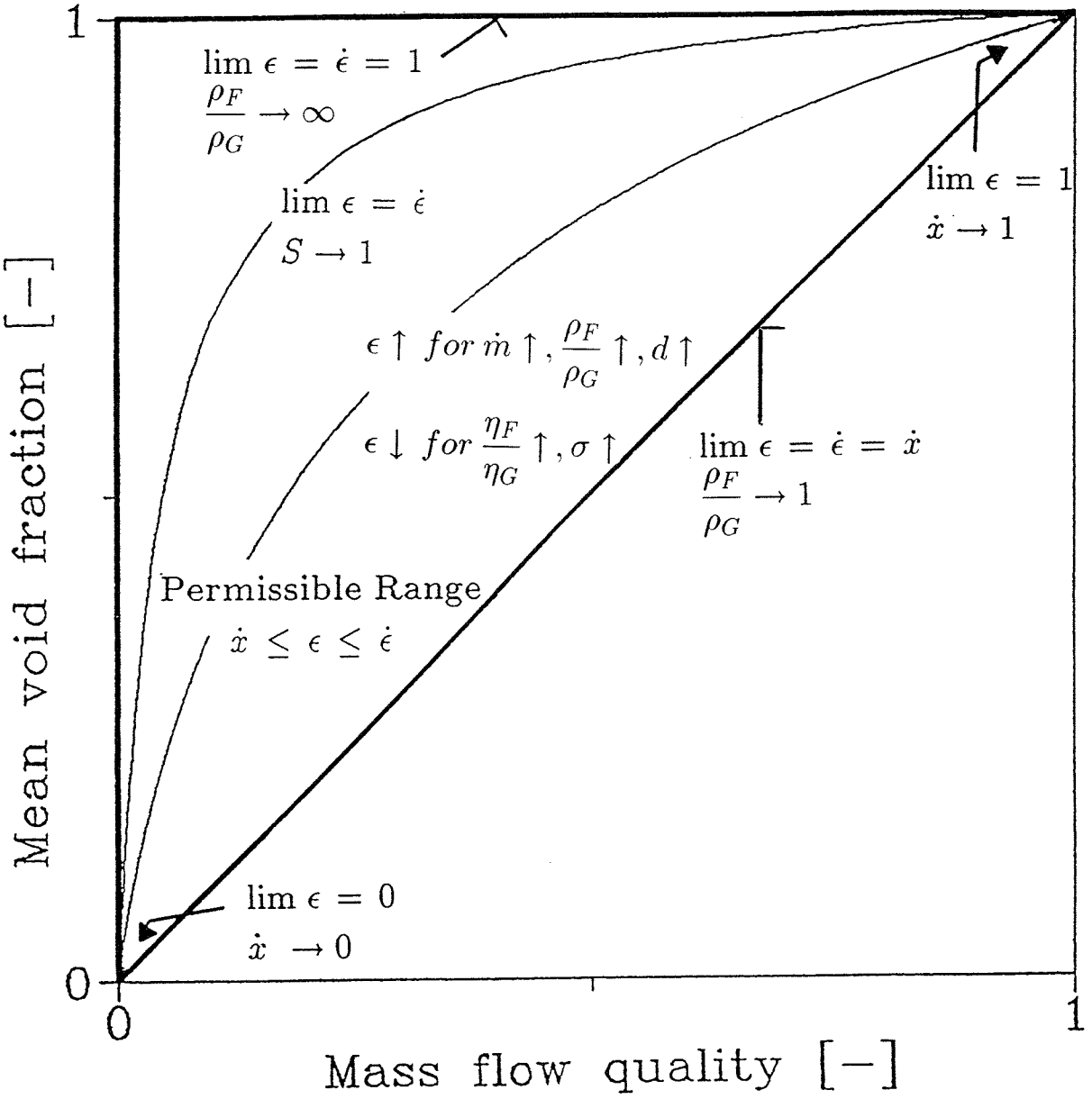

Fig.1: Limits of the mean void fraction as a function of mass flow quality and density ratio

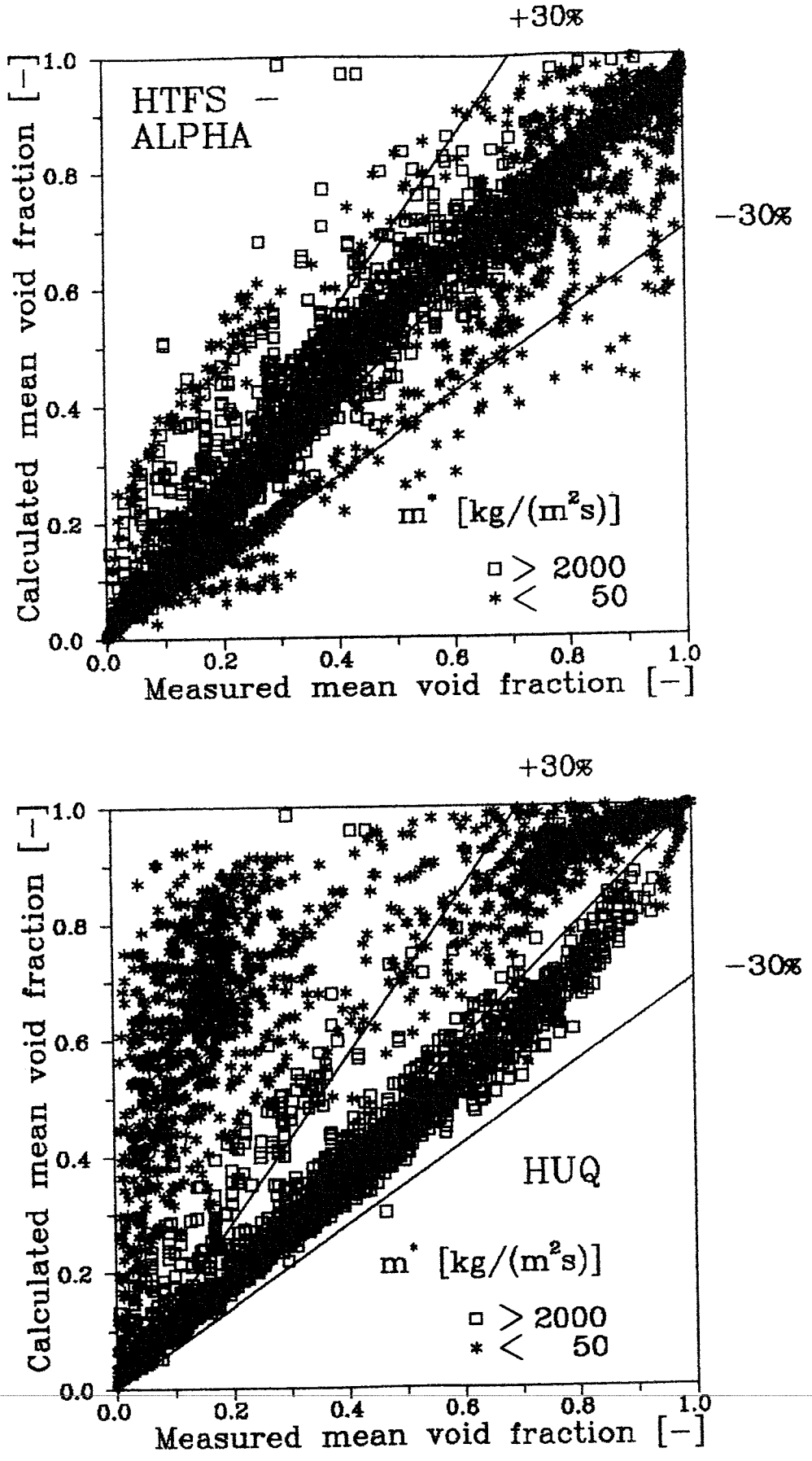

Fig.2: Reproduction of the two-component data by the correlations of HTFS-ALPHA and HUQ

EFFECT OF BUBBLE SIZE ON PHASE DISTRIBUTION IN VERTICAL BUBBLE FLOW

G. Matsui and H. Monji

Institute of Engineering Mechanics
University of Tsukuba
Tsukuba 305, Japan

ABSTRACT

Structural characteristics of bubble flow have been studied by experimenting with nitrogen gas-water bubble flow in a square duct and a round tube. It was found that coring, sliding, or uniform bubble flow in the vertical test section under the same flow condition exhibits characteristic behavior of phase distribution, turbulence, and bubble motion depending on the size and distribution of bubbles. In order to investigate still more phase distribution characteristics in detail, the effect of mixing methods on the phase distribution was experimentally investigated with upward nitrogen gas-water bubble flow under the condition of fixed flow rates using a laser Doppler anemometer and a double-sensor conductance probe system. The effect of bubble size on the phase distribution was able to be investigated by changing the injection method. The experimental results show that the diameter of the gas injection hole influences the phase distribution through the bubble size. The location of the injection hole and the direction of injection do not influence the phase distribution of fully developed bubble flow. The transitive equivalent bubble size from the coring bubble flow to the sliding bubble flow corresponds to the bubble shape transition. The analytical results show that the phase distribution may be predictable if the phase profile is judged from the bubble size.

NOTE: *This paper had not been received before the Proceedings were assembled. If received on or before August 23, 1994, handouts will be given to each participant of the Symposium.*

STATISTICAL PARAMETER CHARACTERISTICS OF GAS-PHASE FLUCTUATIONS IN GAS-LIQUID TWO-PHASE FLOW

G. Matsui and H. Monji

Institute of Engineering Mechanics
University of Tsukuba
Tsukuba 305, Japan

ABSTRACT

The gas-phase fluctuations or the corresponding quantity, such as the differential pressure fluctuations, are often used to in the statistical methods of gas-liquid two-phase flow pattern identification. It was success in experiments to identify the flow patterns using statistical parameters of the differential pressure fluctuations. The statistical parameters (the average, the standard deviation, the coefficient of skewness, and the coefficient of excess) of the gas-phase fluctuations characterized the flow patterns. However, the characteristics of the statistical parameters are not well known analytically. Therefore, the purpose of this study is to show the relation between the flow pattern and the statistical parameters and to make the characteristics of the statistical parameters clear. The wave forms of the gas-phase fluctuations are assumed on the basis of the experimental data to calculate the statistical parameters. The statistical parameters are able to be obtained analytically and the functional relations between two statistical parameters are given. The functions of statistical parameters show the specific forms corresponding to the idealized gas-phase fluctuations, i.e., the idealized flow patterns. For example, the relation of the average to the standard deviation is a circle equation and the relation between the coefficients of the skewness and the excess is a quadratic equation. The obtained functions of the parameters have the similar characteristics of the statistical parameters to the experimental results. The results show that the gas-phase fluctuations characterize the statistical parameters.

NOTE: *This paper had not been received before the Proceedings were assembled. If received on or before August 23, 1994, handouts will be given to each participant of the Symposium.*

A PROPOSAL FOR TREATMENT OF TURBULENT MIXING IN A TWO-PHASE SUBCHANNEL FLOW

Y. Sato, A. Kawahara and M. Sadatomi

Kumamoto University, Department of Mechanical Engineering
Kurokami 2-39, Kumamoto 860, Japan
Telephone:(96)344-2111, Facsimile:(96)345-1598

ABSTRACT

We propose a practical method for the treatment of turbulent mixing rate in a two-phase subchannel flow. Based on the assumption that the fundamental modes of the inter-subchannel fluid transfer are turbulent mixing, void drift and diversion cross flow, the turbulent mixing rate is considered to be equal to that in the equilibrium state that the flow will attain. The applicability of the method is examined by experiments concerning the axial variation of tracer concentration in a non-equilibrium flow. A good agreement is seen between the calculations and the measurements.

1. INTRODUCTION

Subchannel analysis is a practical method for predicting local densities of coolant and a safety margin against critical heat flux in a water cooled nuclear reactor. In this analysis, the flow passage is divided into a number of subchannels, formed between fuel rods or between rods and the wall of the shroud tube, and then the flow rate, void fraction and enthalpy in each subchannel are computed from the conservation equations of mass, momentum and energy. In writing each equation, the inter-subchannel fluid transfer is taken into account.

The inter-subchannel fluid transfer therefore plays an important role in a subchannel analysis. On the early stage, it was expressed by two mechanisms, the turbulent mixing and the cross flow, both of which were separable ones, e.g., the COBRA [1] and the HAMBO [2,3]. Since Lahey and Schraub [4] reported phenomena of non-uniform distribution of flow parameters in a rod bundle even in the absence of lateral pressure gradient, the cross flow in two-phase flow conditions has further been subdivided into void drift and diversion cross flow. If the turbulent mixing, the void drift and the diversion cross flow are the basic inter-subchannel fluid transfer mechanisms and independent of each other, a reasonable subchannel analysis becomes promising. In reality, however, such subdivision is still a hypothesis which has not been supported satisfactorily by experiments.

A subchannel experiment in a rod bundle system is unsuitable for observation of the inter-subchannel fluid transfer mechanisms, because a two-phase flow within such a system is so complicated that the local flow behavior can not be specified. On the other hand, it is effective to perform experiments by use of a channel in much simpler geometry than a rod bundle, focussing on a specific mechanism. And, flow parameters such as mass velocities and void fraction in such a channel can be varied easily in relatively wider ranges. So, basic knowledge of two-phase subchannel flow characteristics have been increased by such experiments [5-10].

Based on the assumption that the basic modes of the inter-subchannel fluid transfer in a two-phase subchannel flow are turbulent mixing, void drift and diversion cross flow, we propose a practical method which permits the turbulent mixing to be treated independently of other cross flows, and examine its applicability by an experiment in this study. The experiment has been performed in a geometrically simple channel consisting of two subchannels, under the condition that there was no pressure difference between the subchannels. The turbulent mixing and the cross flow due to void drift alone were, as a result, coexistent in a flow observed. In the experiment, axial variations in material concentration for both gas and liquid phases were determined by use of a

tracer method. The obtained data are presented, and comparisons between the data and the calculations based on the proposal are made in this paper.

2. FLOW CONDITIONS AND MODES OF INTER-SUBCHANNEL FLUID TRANSFER

Two-phase subchannel flows can be classified into equilibrium flows and non-equilibrium flows. In an equilibrium flow, no net volume exchange takes place across the subchannel boundary for each phase. The flow rates of both gas and liquid phases in each subchannel then do not vary in the axial direction. In a non-equilibrium flow, on the contrary, flow redistributions occur along the channel axis so as for the flow to approach the equilibrium state. The inter-subchannel fluid transfer causes such subchannel flow conditions and vice versa.

As mentioned in the Introduction, turbulent mixing, void drift and diversion cross flow have been used as an explanation for the inter-subchannel fluid transfer in the literature, for example, Lahey and Moody [11]. The definitions of the respective terms are as follows.
- Turbulent mixing is mass and volume exchanges of the respective phases across a subchannel boundary due to turbulent fluctuations. By this mixing, neither net mass transfer nor net volume transfer results between the subchannels.
- Void drift is a phenomenon of the cross flow resulting from the tendency of a two-phase flow in an attempt to attain an equilibrium state [12]. This cross flow can occur even in the absence of a lateral pressure gradient, in the sense of a time-averaged value, and causes net transport of the fluids from one subchannel to an adjacent one.
- Diversion cross flow is a cross flow in a non-equilibrium flow arising from lateral pressure gradients. Such pressure gradients are induced by a change in the subchannel geometry or by obstructions such as spacers.

If the turbulent mixing, the void drift and the diversion cross flow are considered to be independent modes, the inter-subchannel fluid transfer can be described simply by linear superimposition of their effects. However, there has been no evidence to support the above statement. This is because the determination of turbulent mixing rate in a non-equilibrium flow is far the most difficult. The turbulent mixing rate is defined as the fluid mass flux exchanged at a subchannel boundary or the rate of the fluid mass exchanged between subchannels per unit axial length. Here, we propose a practical method which enable us to give the turbulent mixing rate in a non-equilibrium flow. The method is stated below using Table I in which the relation between flow conditions and the modes of the inter-subchannel fluid transfer is shown:

(1) In an equilibrium flow, the inter-subchannel fluid transfer is the turbulent mixing itself, and hence a direct determination of turbulent mixing rate is experimentally possible only for an equilibrium flow.

Table I Relation between flow conditions and modes of inter-subchannel fluid transfer

Flow conditions	ISFT*) modes
(1) Equilibrium flow	(Turbulent mixing)
(2) Non-equilibrium flow without lateral pressure gradient	(Turbulent mixing) + (Void drift)
(3) Non-equilibrium flow with lateral pressure gradient	(Turbulent mixing) + (Void drift) + (Diversion cross flow)

*) 'ISFT' is an abbreviation for 'inter-subchannel fluid transfer'.

(2) In a non-equilibrium flow without lateral pressure gradient, it can be considered as the inter-subchannel fluid transfer that void drift and turbulent mixing are coexistent, being superimposed on each other. In addition, we assume that the turbulent mixing rate is equal to the value in the equilibrium state that the flow under consideration reaches. The turbulent mixing rate can thus be provided even such a non-equilibrium flow.

(3) In a non-equilibrium flow with lateral pressure gradient, it is also considered that the turbulent mixing, the void drift and the diversion cross flow are coexistent. Similarly to the above treatment (2), the turbulent mixing rate is assumed to be equal to that in the equilibrium flow condition.

3. EXPERIMENT

3.1 Outline

We conducted an experiment to see whether the proposal stated above is acceptable, laying emphasis on the turbulent mixing and the void drift alone. The experiment was performed in non-equilibrium flows in the absence of lateral pressure gradient, and the study was made by comparing the calculation with the experiment about the axial variation of tracer concentration.

Assumptions made for the present calculation are as follows.

1. A flow is one-dimensional, steady, two-component flow in each subchannel.
2. The cross-sectional area of each subchannel is constant in the axial direction.
3. A time-mean pressure differential between the adjacent subchannels does not exist. The diversion cross flow is then absent.
4. The turbulent mixing rate in a non-equilibrium flow is equal to the value in the equilibrium state that the flow attains (the present proposal).

Consider the tracer mass conservation in the control volume shown in Fig.1. Subchannel-i is interconnected to subchannel-j through a gap of S_{ij} in clearance. The axial node distance of the control volume is ΔZ. For subchannel-i, the discretized form of mass conservation equation for the tracer in the k-phase is expressed by

$$A_i G_{ki}(n) C_{ki}(n) - (G_{kij})_{VD} S_{ij} \Delta Z C_{kVD} - G_k' S_{ij} \Delta Z \left\{ C_{ki}(n+\tfrac{1}{2}) - C_{kj}(n+\tfrac{1}{2}) \right\} - A_i G_{ki}(n+1) C_{ki}(n+1) = 0 \quad (1)$$

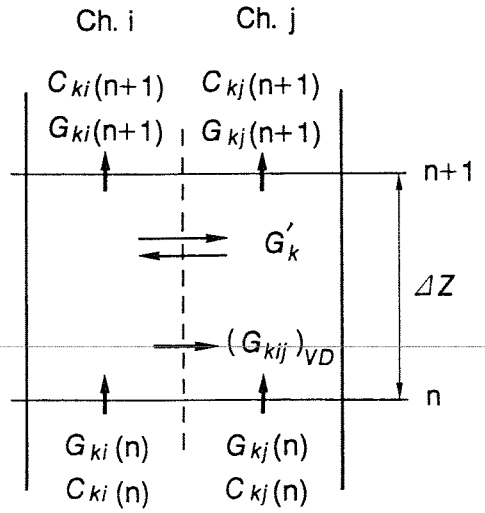

Fig.1 Control volume

where G and C are the mass flux and the tracer concentration, respectively. The second term on the left hand side is the contribution of void drift. The subscript "VD" denotes void drift. Since the cross flow due to void drift is unidirectional, C_{kVD} is given as

$$C_{kVD} = C_{ki}(n+\tfrac{1}{2}) \quad \text{when} \quad (G_{kij})_{VD} > 0 \quad ; \text{i.e. outward flow} \tag{2}$$

and

$$C_{kVD} = C_{kj}(n+\tfrac{1}{2}) \quad \text{when} \quad (G_{kij})_{VD} < 0 \quad ; \text{i.e. inward flow} \tag{3}$$

The third term of Eq.(1) expresses the contribution of turbulent mixing. G'_k is the mass flux exchanged between the subchannels. When the concentration is reduced with respect to the mean concentration C_k, $C^*_{ki}(n)=C_{ki}(n)/C_k$, Eq.(1) can be rearranged as

$$C^*_{ki}(n+1) = \frac{A_i G_{ki}(n) C^*_{ki}(n) - (G_{kij})_{VD} S_{ij} \Delta Z C^*_{kVD} - G'_k S_{ij} \Delta Z \left\{ C^*_{ki}(n+\frac{1}{2}) - C^*_{kj}(n+\frac{1}{2}) \right\}}{A_i G_{ki}(n+1)} \tag{4}$$

The mean concentration is the value averaged over the entire flow, and is then defined as

$$C_k = \frac{C_{ki}(n) A_i G_{ki}(n) + C_{kj}(n) A_j G_{kj}(n)}{A_i G_{ki}(n) + A_j G_{kj}(n)} \tag{5}$$

$(G_{kij})_{VD}$, the lateral mass flux due to void drift from subchannel–i to subchannel–j, can be correlated with the change in mass flow rate in subchannel–i,

$$(G_{kij})_{VD} = \frac{A_i G_{ki}(n) - A_i G_{ki}(n+1)}{S_{ij} \Delta Z} \tag{6}$$

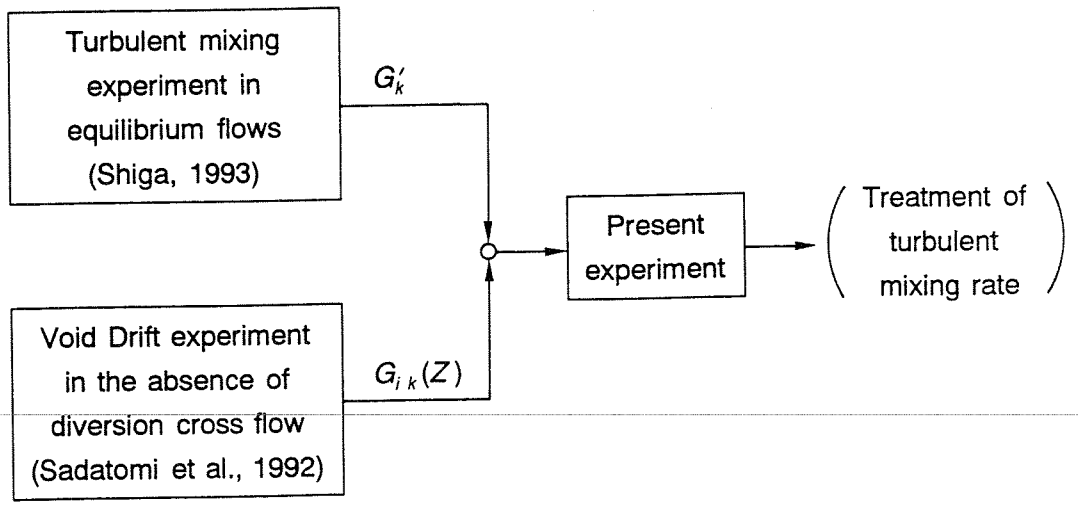

Fig.2 Relation between the previous experiments and the present experiment

Equation (4) together with Eqs.(2),(3),(5) and (6) gives a variation of the tracer concentration along the channel, if the mass flow distribution and the turbulent mixing rate are known.

In the experiment, variations of the tracer concentration for both phases were measured simultaneously in the absence of the diversion cross flow, using a two component two-phase air-water system. The test section was a geometrically simple channel made up of two subchannels alone. Prior to the present experiment, we had made two experiments on turbulent mixing and void drift using the same system. First, turbulent mixing rates for both air and water had been measured in equilibrium flows [13]. And second, for several churn-turbulent flows, data on the flow redistributions due to void drift had been obtained [14]. Such experimental information were used in this study as shown in Fig.2.

3.2 Test channels

Figure 3 shows the cross section of the two test channels used in the series of our studies. One is referred to as Ch.E-F in which the two circular subchannels of different diameter, 20.0 mm and 16.0 mm, are interconnected through a gap of 1.0 mm in clearance and 3.0 mm in width. The other is referred to as Ch.F-F made up of two identical circular subchannels of 16.0 mm I.D. The gap size is 1.0 mm in clearance and 3.0 mm in width. These two test channels were machined from transparent acrylic slabs, and polished to get smooth inner walls. There were two reasons for choosing a circular cross section as the subchannel geometry. First, fabrication of the channel is easy. And second, it is expected that, since the flows in the subchannels may become similar to those in a circular pipe, the void fraction and the pressure drop in each subchannel would be predicted by the respective correlations proposed so far for a circular pipe flow.

3.3 Test rig and experimental procedure

An essential part of the test rig is shown in Fig.4. The test channel was divided into three sections from the bottom to the top; a entry section (#4), a test section (#5), and a discharge section (#6). The cross-sectional shape of the three sections was the same except for the gap portion. In the entry and the discharge sections, there was no gap between the subchannels to avoid the lateral movement of the fluids. After metering the inlet flow rates by calibrated turbine flowmeters and rotameters, we introduced water and air to the mixers (#3) located at the bottom end of the respective subchannels. The flow rates of water and air introduced in each subchannel were set so that no lateral pressure difference between subchannels occurred in the test section. A water-air mixture flowed upward in the entry section, 2 m in length, and then entered the test section, 2 m in length. In the test section, the flow rates of both phases in each subchannel varied in the axial direction due to void drift. Such flow redistributions had already been determined in the previous experiment [14].

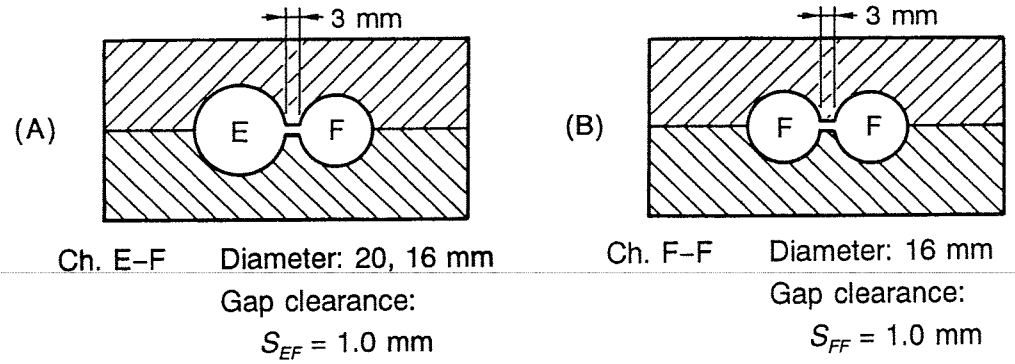

Fig.3 Cross section of the test channel

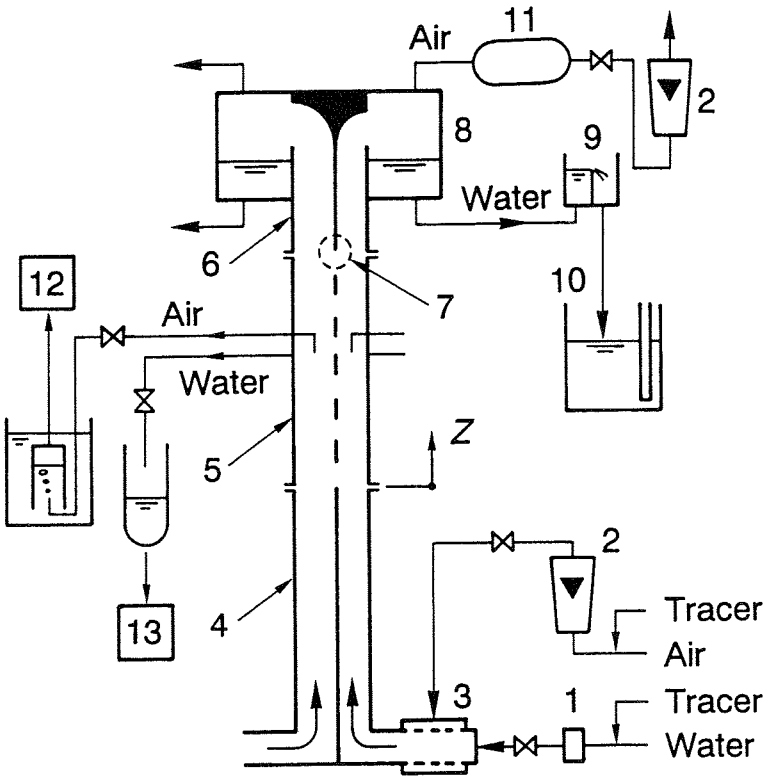

1. Turbine flowmeter
2. Rotameter
3. Mixer
4. Entry section
5. Test section
6. Discharge section
7. Knife edge
8. Separator
9. Weir
10. Metering tank
11. Surge tank
12. Gas chromatograph
13. Spectrophotometer

Fig.4 Test rig

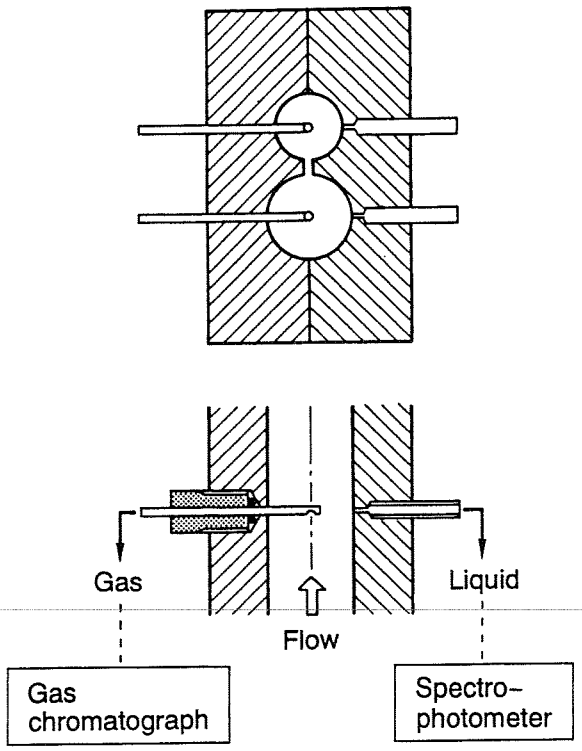

Fig.5 Sampling system

In order to prevent the diversion cross flow due to lateral pressure difference between the subchannels, the following two conditions were imposed:
(1) In the entry section, the pressure gradient in each subchannel had to be the same.

$$\left(\frac{dP}{dZ}\right)_E = \left(\frac{dP}{dZ}\right)_F \tag{7}$$

(2) At both the inlet and outlet ends of the test section, the time averaged pressures in each subchannel had to be identical.

$$P_E(0) = P_F(0), \qquad P_E(Z) = P_F(Z) \tag{8}$$

In order to check that the flow satisfies these conditions, we monitored a pressure differential between the subchannels by differential pressure transducers, and confirmed that the time averaged pressure difference was within ±30 Pa in the entry section and within ±20 Pa in the test section.

After setting a flow in a required condition, each tracer was injected continuously into one subchannel at a far upstream location of the mixer, and the axial variations of the tracer concentration in both subchannels were determined by sampling the respective fluids (Fig.4). In each run, a tracer was injected alternately in each subchannel in order to examine the cross flow in detail. Methane and aqueous solution of acid orange II were used as the tracers for air and water, respectively. Four sampling points were arranged along the channel. A schematic of the fluid sampling system is shown in Fig.5. Water was sampled from the wall region, while air from the core region, and the tracer concentrations were determined with a spectrophotometer and with a gas chromatograph, respectively. From the previous experiment [13] it had been confirmed that a tracer concentration at the above sampling points for both phases was nearly equal to the cross-sectional averaged value in each subchannel.

Table II shows the experimental conditions for two test runs. Data listed are : the gap clearance between the subchannels, S_{ij}, the volumetric fluxes of gas and liquid for the channel as a whole, j_G and j_L, the ratio of volume flow rate of the gas phase in subchannel-E (or in subchannel-F1 of Ch.F-F) to that in the whole channel at the inlet of the test section, $Q_{GE}(0)/Q_G$ (or $Q_{GF1}(0)/Q_G$), the turbulent mixing rates of gas and liquid phases if the flow is in equilibrium, $W'_G=G'_GS_{ij}$ and $W'_L=G'_LS_{ij}$, and the system pressure, P_{sys}. The data on W'_G and W'_L were obtained experimentally for the equilibrium flows [13].

In addition, the flow redistribution data in each run, $Q_{Gi}(Z)/Q_G$ and $Q_{Li}(Z)/Q_L$, which will be displayed as the curves in Figs.6 and 7 along with the results, were determined in advance [14], as mentioned previously.

Table II Experimental conditions

Run	Ch.	S_{ij}	j_L	j_G	$Q_{Gi}(0)/Q_G$	W'_L	W'_G	P_{sys}
		mm	m/s	m/s		kg/(m·s)	kg/(m·s)	kPa
1	E-F	1.0	1.50	4.0	0.50	0.157	x10^{-3} 1.07	127
2	F-F	1.0	1.00	3.3	0.70	0.103	1.06	122

4. RESULTS AND DISCUSSION

Figures 6(A) and 6(B) are the results for Run 1, showing the axial variations of tracer concentration of the liquid phase and the gas phase, respectively. The test channel used was Ch.E–F, the volumetric fluxes were j_L=1.5 m/s and j_G=4.0 m/s, the average void fraction for the whole channel was nearly equal to 0.58, and the flow pattern was churn flow.

Attention is first directed to the uppermost graph of Fig.6(A), in which the flow redistributions of both phases are plotted as the axial variation of volume flow rate ratio, $Q_E(Z)/Q$. Circular and triangular symbols indicate the gas phase and the liquid phase, respectively. Each line drawn through data points is the best fitted curve, from which the distributions of lateral mass flux due to void drift and tracer concentrations have been calculated. We can see that the flow rate for both phases tended to approach the respective equilibrium values when going downstream, and that, in this run, the cross flow due to void drift took place from subchannel–F to subchannel–E for the gas phase and vice versa for the liquid phase.

The axial tracer concentration profiles of the liquid phase are presented in the middle graph and the lowermost graph in Fig.6(A). The former corresponds to a case where the tracer was injected

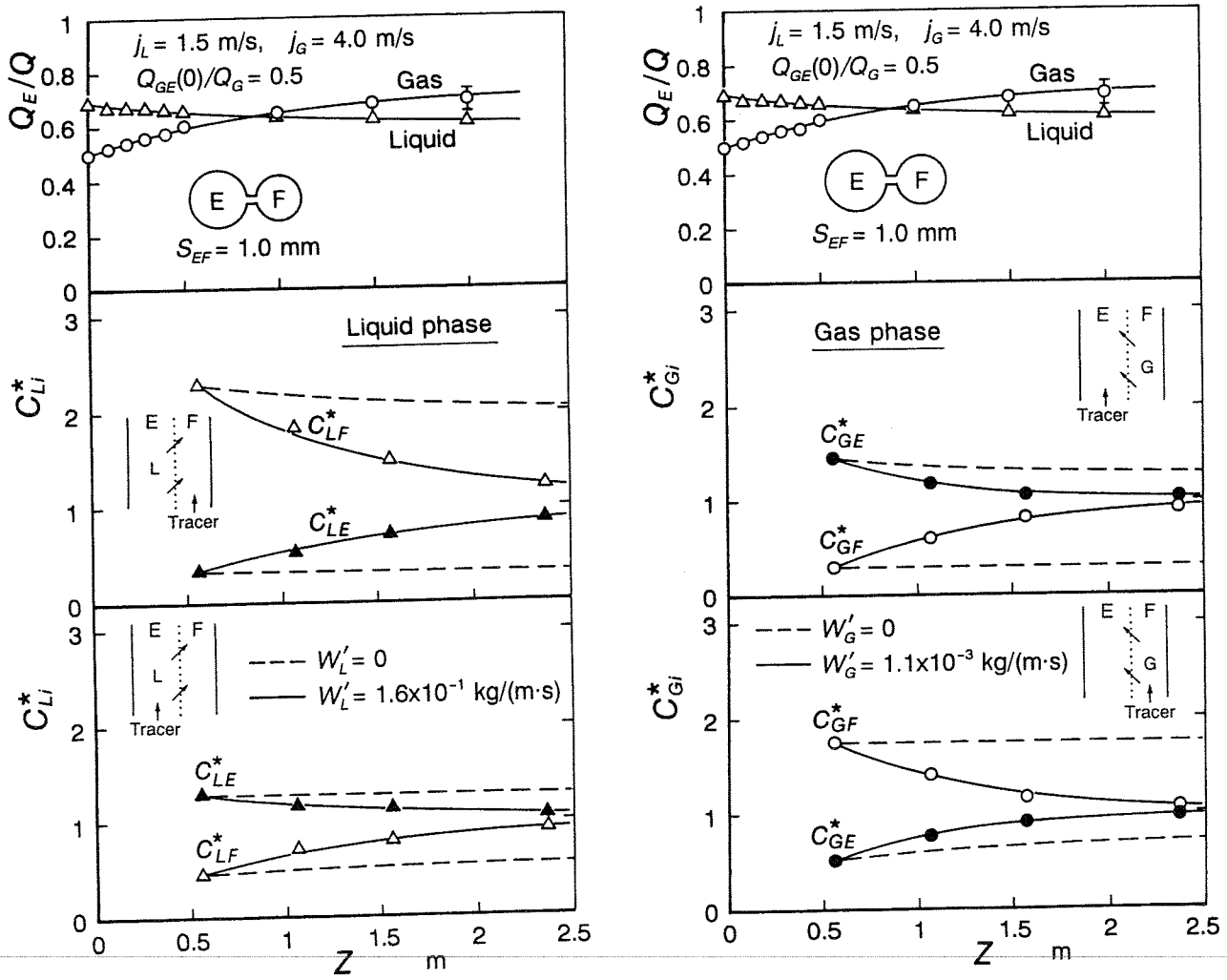

(A) Liquid phase (B) Gas phase

Fig.6 Axial tracer concentration profiles obtained from Run 1: (A) Liquid phase and (B) Gas phase

into subchannel-F, whereas the latter to the other case where the tracer was injected into subchannel-E. The ordinate of these graphs is the reduced concentration, $C^*_{Li}(Z)$. The solid line and the dashed line represent the calculated values considering and neglecting turbulent mixing, respectively. Immediately after the inlet of the test section, there was a entry region of a subchannel flow of this system. Its axial length was about 0.5 m in this flow. Thus, the data was obtained in the region beyond such the entry region. Figure 6(B) displays the axial profiles of tracer concentration for the gas phase in the same flow. The experimental errors of C^*_{Li} and C^*_{Gi} were estimated to be within ±5% and ±9%, respectively.

In the same way, Figs.7(A) and (B) show the results obtained for Ch.F-F under the flow rate conditions of j_L=1.0 m/s and j_G=3.3 m/s, at $Q_{GF1}(0)/Q_G$=0.7. The flow redistribution process approaching Q_{F1}/Q=0.5 can be seen for both phases, since the two subchannels are identical. The axial length of a entry region was about 0.3 m in this flow.

Consideration is given to comparisons between the measurements and the calculations of the axial tracer concentration. In each figure, solid lines correspond to the calculated values with taking account of turbulent mixing, while dashed lines correspond to the value without taking account of turbulent mixing (W'_k=0). The calculations have been made by Eq.(4) together with Eqs.(2),(3) and

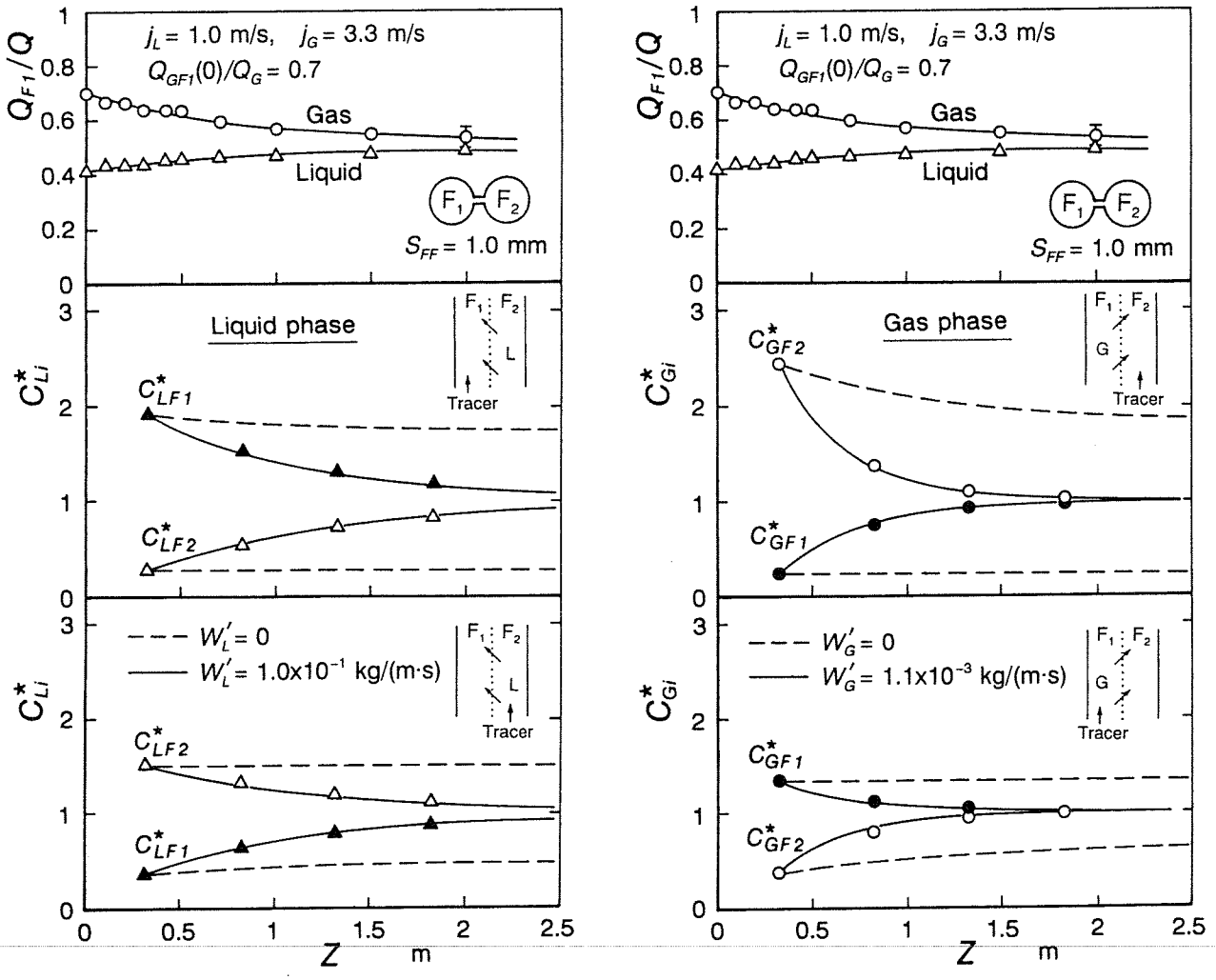

(A) Liquid phase (B) Gas phase

Fig.7 Axial tracer concentration profiles obtained from Run 2: (A) Liquid phase and (B) Gas phase

(6). A large disparity between a dashed line and the corresponding data points indicates the decisive effect of turbulent mixing on the fluid transfer across the subchannel boundary. Regarding the treatment of turbulent mixing in the calculation, the turbulent mixing rate has been taken to be the value in the equilibrium flow condition that the flow would attain. Every solid line is seen to be in good agreement with the experimental data for both phases and for both Ch.E–F and Ch.F–F, irrespective of the side of subchannels into which a tracer was injected.

From the comparisons, we conclude that the turbulent mixing and the void drift can be treated as independently coexistent, and that the turbulent mixing rate in a non–equilibrium flow can be considered to be equal to the value in the equilibrium state that the flow under consideration will attain.

5. SUMMARY

Based on the assumption that the basic modes of the inter–subchannel fluid transfer in a two–phase subchannel flow are turbulent mixing, void drift and diversion cross flow, we have proposed a method for the treatment of the turbulent mixing rate in a non–equilibrium flow. That is, the turbulent mixing rate in such a flow is considered to be equal to the value in the equilibrium state that the flow will attain.

The applicability of the proposed method was examined by experiments using a simple vertical channel consisting of two subchannels. The experiments were performed for churn flows in a vertical two–phase air–water system. The observed flows were non–equilibrium churn flows in the absence of diversion cross flow. Variations of tracer concentration along the channel were measured, and comparisons were made between the measurements and the calculations about the axial variation of the tracer concentration. The calculated values were in close agreement with the measurements. As a result, we conclude that the proposed method is applicable to a flow in which the diversion cross flow is absent. As to whether the method is practical and reasonable also in a flow with diversion cross flow, further studies are necessary. Models to predict the turbulent mixing rate in an equilibrium two–phase subchannel flow need to be developed.

NOMENCLATURE

A	=	flow area, m^2
C	=	tracer concentration, kg of tracer / kg of fluid
C^*	=	reduced concentration
D	=	diameter, m
G	=	mass flux, $kg/m^2 \cdot s$
G'	=	mass flux exchanged between subchannels due to turbulent mixing, $kg/m^2 \cdot s$
G_{ij}	=	lateral mass flux due to cross flow from subchannel–i to subchannel–j, $kg/m^2 \cdot s$
j	=	volumetric flux (= Q/A), m/s
p	=	pressure, Pa
Q	=	volume flow rate, m^2/s
S	=	gap clearance, m
W'	=	turbulent mixing rate, $kg/m \cdot s$
Z	=	axial length, m

Subscripts

E, F, i, j	=	subchannel identifiers
EQ	=	equilibrium flow
G	=	gas phase
k	=	index of phase, k = G or k = L
L	=	liquid phase
VD	=	void drift

REFERENCES

[1] D.S. Rowe, "Crossflow Mixing between Parallel Flow Channels during Boiling - Part 1 : Computer Program for Coolant Boiling in Rod Arrays", Pacific Northwest Laboratory, BNWL-371 PT.1(1967).

[2] R.W. Bowring, "HAMBO : A Computer Programme for the Subchannel Analysis of the Hydraulic and Burnout Characteristics of Rod Clusters - Part 1 : General Description", AEE Winfrith, AEEW-R524(1967).

[3] R.W. Bowring, "HAMBO : A Computer Programme for the Subchannel Analysis of the Hydraulic and Burnout Characteristics of Rod Clusters - Part 2 : The Equations", AEE Winfrith, AEEW-R582(1968).

[4] R.T. Lahey, Jr. and F.A. Schraub, "Mixing, Flow Regime, and Void Fraction for Two-Phase Flow in Rod Bundles", in: Proceedings of the Symposium on Two-Phase Flow and Heat Transfer in Rod Bundles, ASME Winter Annual Meeting, Los Angeles, pp.1-14(1969).

[5] T. van der Ros, "On Two-Phase Flow Exchange between Interacting Hydraulic Channels", Doctoral Thesis of Engineering Science, Eindhoven University of Technology, The Netherlands, Report WW015-R160(1970).

[6] K.F. Rudzinski, K. Singh, and C.C. St. Pierre, "Turbulent Mixing for Air-Water Flows in Simulated Rod Bundle Geometries", in: The Canadian Journal of Chemical Engineering, 50, pp.297-299(1972).

[7] J.M. Gonzalez-Santalo and P. Griffith, "Two-Phase Flow Mixing in Rod Bundle Subchannels", ASME Paper 72-WA/NE-19, pp.1-13(1972).

[8] M. Shoukri, H. Tawfik, and A.M.C. Chan, "Two-Phase Redistribution in Horizontal Subchannel Flow - Turbulent Mixing and Gravity Separation", in: International Journal of Multiphase Flow, 10, 3, pp.357-369(1984).

[9] A. Tapucu, M. Geçkinli, N. Troche and R. Girard, "Experimental Investigation of Mass Exchanges between Two Laterally Interconnected Two-Phase Flows", in: Nuclear Engineering and Design, 3, 105, pp.295-312(1988).

[10] Y. Sato and M. Sadatomi, "Two-Phase Gas-Liquid Flow Distributions in Multiple Channels", in: Proceedings of 3rd Japan-US Seminar on Two-Phase Flow Dynamics, Ohtsu, Japan, pp.15-20(1988).

[11] R.T. Lahey, Jr. and F.J. Moody, "The Thermal-Hydraulics of a Boiling Water Nuclear Reactor", American Nuclear Society, La Grange Park, Ill(1979).

[12] R.T. Lahey, Jr., B.S. Shiralkar, D.W. Radcliffe and E.E. Polomik, "Out-of Pile Subchannel Measurements in a Nine-Rod Bundle for Water at 1000 psia", in: Progress in Heat and Mass Transfer, VI, G. Hetzroni et al Eds., Pergamon Press pp.345-363(1972).

[13] E. Shiga, "Subchannel Crossflow of Two-Phase Mixture", Master's Thesis, Department of Mechanical Engineering, Kumamoto University, (in Japanese), (1993).

[14] M. Sadatomi, A. Kawahara and Y. Sato, "Flow Redistribution due to Void Drift of Two-Phase Flow in a Multiple Channel Consisting of Two Subchannels", in: Proceedings of the 2nd JSME-KSME Thermal Engineering Conference, Kitakyushu, Japan, pp.239-244(1992).

PHASE DISTRIBUTION IN INCLINED TUBE BUNDLE GEOMETRIES

A. Serizawa[1], K. Huda[1], I. Kataoka[2], O. Takahashi[1], and Z. Kawara[1]

[1] Department of Nuclear Engineering
Kyoto University
Yoshida, Sakyo-ku, Kyoto 606, Japan

[2] Institute of Atomic Energy
Kyoto University
Gokasho, Uji-shi, Kyoto 611, Japan

ABSTRACT

It is now believed that the local structure of a gas-liquid two-phase flow around inverted U-tube bundle is a primary cause of the mechanical vibration of the tube bundle which happened some years ago in the PWR steam generator at the Mihama-2 nuclear power reactor in Japan, followed by a serious tube break accident. However, up to now, our knowledge of the external flows over the inverted U-tube bundle is quite limited both experimentally and theoretically, which prevents us from an accurate prediction of such two-phase flow induced vibration.

The present work is therefore concerned with systematic measurements of local flow structures of air-water two-phase flow such as phase distribution, bubble number density and bubble velocity, and also with visual observation of the interactions between the bubbles and vortex sheddings, mainly in bubbly and churn turbulent flow regions, in inclined tube bundle geometries which simulate the inverted U-tube bundle in PWR steam generator. One of the purposes is to obtain the comprehensive data base with which we can discuss some important phenomena to clarify the mechanisms involved. The measurements were carried out both in in-line and staggered tube arrangements of 26 rods of 10 mm in outer diameter in vertical upward flow in a 220 x 220 mm^2 x 1040 mm long acrylic square duct. The inclination angle was varied from horizontal to 75 degrees from horizontal. The results indicated a significant difference between the cases of in-line and staggered tube arrangements. Detailed results will be presented at the Symposium.

NOTE: *This paper had not been received before the Proceedings were assembled. If received on or before August 23, 1994, handouts will be given to each participant of the Symposium.*

NON-INTRUSIVE MEASUREMENT OF DYNAMIC BEHAVIOR OF A LIQUID FILM FLOW

A. Serizawa, K. Nagane, T. Kamei, O. Takahashi, and Z. Kawara

Department of Nuclear Engineering
Kyoto University
Yoshida, Sakyo-ku, Kyoto 606, Japan

ABSTRACT

Dynamic behavior of the liquid films formed on nuclear fuel rods is a key parameter to determine the CHF during postulated loss-of-coolant accidents in boiling water reactors. Specifically, the effects of the spacers on film and liquid droplets behavior are one of the unknows which are relevant in numerical prediction of core channel thermal hydraulics. With these held in mind, we developed non-intrusive techniques to measure the dynamic behavior of the liquid film thickness, the surface characteristics, and in particular the behavior of the liquid droplets.

Firstly, we developed a pulse-echo technique using a 200 MHz ultrasonic wave applied to an air-water stratified flow in a horizontal square channel. The results indicated an excellent agreement with those obtained with a laser displacement gauge. However, this method inevitably includes some application limits in spatial resolution such as the minimum sensitive area, time resolution such as the minimum measurable film thickness, and in the reflection angle at the film surface. Discussions will be presented based on our results concerning its applicability for practical uses.

Secondly, we will mention the results obtained using computer aided fluorescence technique for visualization. In this technique, we used a fluorescence-water solution flow which is excited by a sheetwise argon-laser. The cross-sectional views taken by a video camera was analyzed by a personal computer to obtain three-dimensional images. This technique is more appropriate to measure the local flow structures of an annular-dispersed flow caused by an obstacle in the flow.

NOTE: *This paper had not been received before the Proceedings were assembled. If received on or before August 23, 1994, handouts will be given to each participant of the Symposium.*

USE OF PHASE-DOPPLER ANEMOMETRY FOR CHARACTERIZING THE MASS TRANSFER IN A FINE BUBBLE SWARM

FRANZ BISCHOF[1], FRANZ DURST[2], MARTIN SOMMERFELD[2], TOSHIHIKO SHAKOUCHI[3],

[1]ATZ-EVUS
Applikations- und Technikzentrum
Kropfersrichter Straße 6-8 92237 Sulzbach-Rosenberg; Germany
Telephone: (09661)60694, Facsimile: (09661)6889

[2]Lehrstuhl für Strömungsmechanik
Universität Erlangen-Nürnberg
Cauerstr. 4; 91058 Erlangen; Germany
Telephone: (09131)859501/02, Facsimile: (09131)859503

[3]Dept. of Mechanical Engineering
Mie University
Kamihama-cho 1515, Tsu-shi, Mie 514; Japan
Telephone: 0592-31-9384, Facsimile: 0592-31-9471

ABSTRACT

The aeration of liquids by gases is of great importance for a number of technological processes in industry. For this reason, the mass transfer and the coalescence behaviour of fine bubbles with diameters of about 0.5mm was studied in tap water and in the presence of different surfactants. For the production of gas bubbles, a novel, microporous membrane was used. The experiments were performed using a bubble column with a diameter of 14cm and a height of 70cm. For measuring the mass transfer of oxygen from the air bubbles into the surrounding water, oxygen probes were used. The application of Phase-Doppler Anemometry (PDA) allowed for the registration of coalescence behaviour, bubble size distribution, and corresponding bubble velocity. In combination with results obtained from single bubble measurements, very good agreement between mass transfer coefficients could be found. The knowledge of bubble velocity was very important and had to be taken into consideration because the velocity of bubbles was more than double within the bubble swarm compared to that of a free rising bubble.

1. INTRODUCTION

The aeration of liquids by gases is of great importance for a number of processes in technological industries. Therefore gas-liquid contacting equipments are gaining in importance for many production processes, such as oxidations with air or pure oxygen, absorptions, desorptions and biochemical processes (fermentation, waste-water treatment). In most of these processes an adequate mass transfer rate from the gas to liquid phase must be obtained. Much of the performance of such gas-liquid reactors is mainly influenced by the specific interfacial area, which in turn is determined by the bubble size distribution and the gas hold-up. Moreover, bubble coalescence has a strong influence on both parameters.

Many of the described processes take place in the presence of surfactants which can considerably influence the mass transfer process. These substances can be formed by the process itself or by pollution of the mulitphase system and are known to be concentrated at the surface of the gas bubbles (Meijboom and Vogtländer, 1974). Thus, the rise velocity (Godbole et al., 1984; Koide et al., 1976), the mass transfer coefficient (Bischof et al., 1991; Nitsch and Weber, 1976; Caskey et al., 1973), and the coalescence behaviour of gas bubbles (Drogaris and Weiland, 1983; Liepe, 1988) are altered in comparison to a clean fluid. The knowledge of the coalescence process is therefore of great importance. Traditionally, bubble coalescence phenomena have been studied in two ways. Either for a swarm of bubbles in a gas-liquid contacting equipment (i.e. Sztatecsny et al., 1977; Zlokarnik, 1978) or considering only a pair of bubbles (Lessard and Zieminski, 1971; Sagert and Quinn, 1976). Attempts to describe the coalescence process with a mathematical model have yielded only limited success (Marrucci, 1969).

The present study considers the influence of anionic and non-ionic surfactant concentration on the interfacial area and, hence, the coalescence behaviour and the mass transfer characteristics in a bubble column which is aerated with very fine bubbles in the range of about 0.2mm to 0.7mm.

2. EXPERIMENTAL FACILITY

The experiments concerning the mass transfer were performed using a bubble column with a diameter of 14cm and a height of 70cm (see Fig. 1). A microporous membrane was used in the present study to produce the bubbles. The membrane was mounted into a special aeration device between two perforated plates. Recent developments showed that by using elastic and microporous membranes, very small bubbles in the range of 0.2 to 0.7mm can be produced (Bischof and Sommerfeld, 1991). This aerator with an area of 30% of the bubble column

(1) air
(2) nitrogen
(3) pressure regulator
(4) gas flow controller
(5) gas pipe
(6) body for column
(7) screws
(8) aerator
(9) plexiglas column
(10) micro pump
(11) bubble trap
(12) oxygen probe
(13) DC power supply
(14) A/D-converter
(15) computer
(16) oxygen gauge
(17) water supply
(18) valve
(19) outlet for water
(20) pressure probe
(21) device for pressure probe

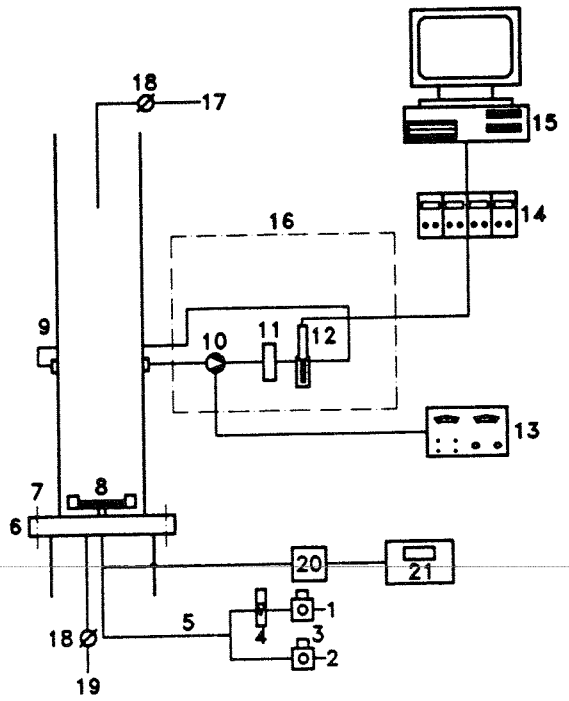

Figure 1: Schematic diagram of experimental facility

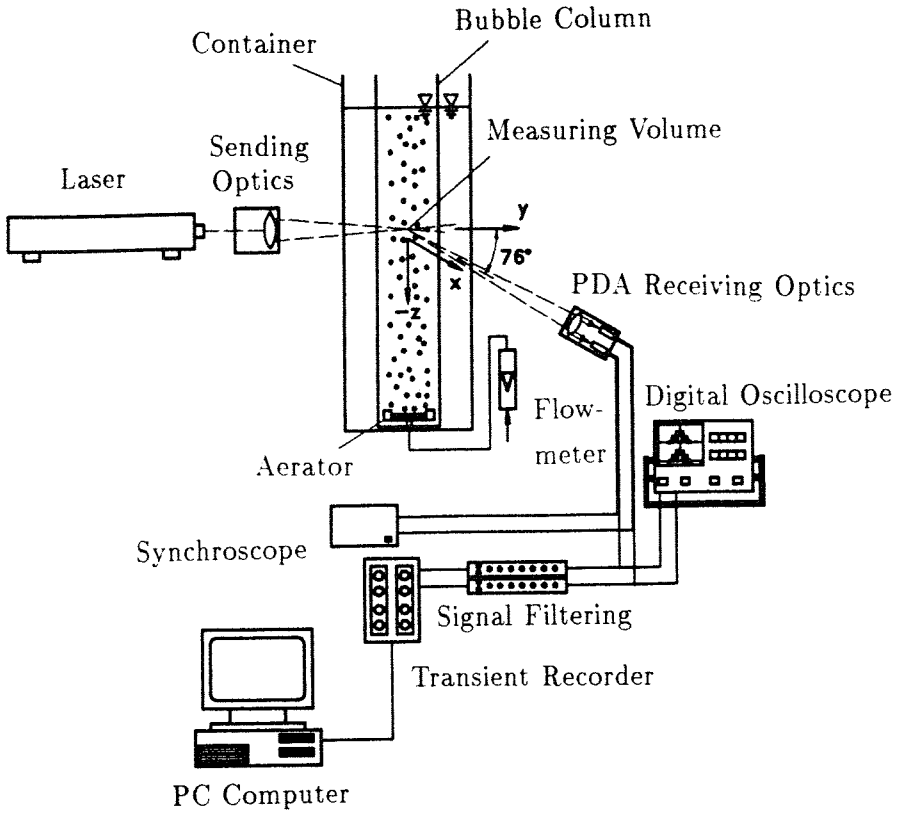

Figure 2: Schematic diagram of PDA-system for measuring bubble size and rise velocity of bubbles

cross-sectional area was placed at the bottom of the bubble column. The bubble colunm was filled with tap water where surfactants were added at different concentrations.

For the measurement of oxygen concentrations dissolved in the water, a device for sampling test water and feeding it to an oxygen probe was installed directly on the column wall at a height of 35cm. The oxygen probe was connected to a computer by an A/D converter and the results were processed by a software-program and the time dependent oxygen concentration of the test liquid was recorded. Furthermore, the oxygen input was measured, whereby the ratio of oxygen to water volume and aeration time was obtained. Additionally, the aeration constant, i.e. the product of specific mass transfer area and mass transfer coefficient was calculated.

For a complete characterization of the mass transfer as well as the gas hold-up, the gas-liquid interfacial area, the temperature, and the surface tension were measured. For the determination of the interfacial area a PDA-system was used and simultaneously bubble sizes and rise velocity of bubbles were measured (Durst and Zare, 1975). The optical and electronic components of the PDA-system are shown in Fig. 2. The characteristics of the PDA-system are given in Tab. 1.

At eight different heights above the aerator data were sampled. Because of the construction of the aerator, it was not possible to set the first measuring point directly above the aerotor. Thus the first measuring location was at a distance of 3mm above the aerator, and was defined to be reference location. For the evaluation of the data 5000 single bubbles were recorded for each measuring point. This led according to a data rate of 2 Hz to a measuring period of about 7 hours for one experimental condition. The gas flow rates were choosen to be the same as those used for the investigations of the mass transfer (Bischof et al., 1993). To study

Sending side:	
Wave length of laser	632.8 nm
Beamdiameter	1.1 mm
Focal length	365 mm
Beam distance	21 mm
Diameter of measuring volume	391 μm
Length of measuring volume	12.6 mm
Shift frequency	0.2 MHz
Conversion factor	11.0 m/s / MHz
Recieving side:	
Off-axis angle	76°
Focal length	1000 mm
Distance between detectors (APD)	20 mm
Pinhole	200 μm
Transformation ratio	6.25:1
Conversion factor	0.2 1/μm

Table 1: Characteristic data of the PDA-system

the influence of surfactants on mass transfer an ionic surfactant, namely Marlophor, was used with a concentration of 2.5ppm, 5.0ppm and 10.0 ppm. As a non-ionic surfactant 'Rewomid' was used with a concentration of 5.0ppm. Both surfactants are expected to be found in the influent of a sewage water treatment plant.

2.1 Evaluation procedure

In the following figures 3 and 4 original results are given. The information about different bubble sizes (D10, D20, D30) charaterizes the bubble size related to lenght, arae, and volume. The value for 'Sauter Mean' represents the Sauter-diameter and gives the ratio of $D30^3/D20^2$. Deviations of the number mean values for bubble size and bubble velocity are represented by $DRMS$ and RMS. Both investigations were taken within a time period of 2 months and show the stability of bubble production over a long time period, and the high accuracy of PDA-measurements.

Fig. 4 shows, that there is an insignificant larger bubble size and bubble velocity for the non-ionic surfactant Rewomid at a height of z=100mm above the aerator. Fig. 3 demonstrats, that the bubble size ranges between 60μm and 985μm, whereby most of the bubbles have a size between 155μm and 450μm. The rise velocity of the bubbles corresponding to their size is given as a black line and indicates a strongly increase with increasing bubble size.

The interfacial area a resulted from the mean Sauter-diameter d_{32} together with the gas hold-up ϵ_g according to the following equation:

$$a = \frac{6 \cdot \epsilon_g}{d_{32}(1 - \epsilon_g)} \tag{1}$$

The height of water level before and during aeration was measured to yield the gas hold-up ϵ_g.

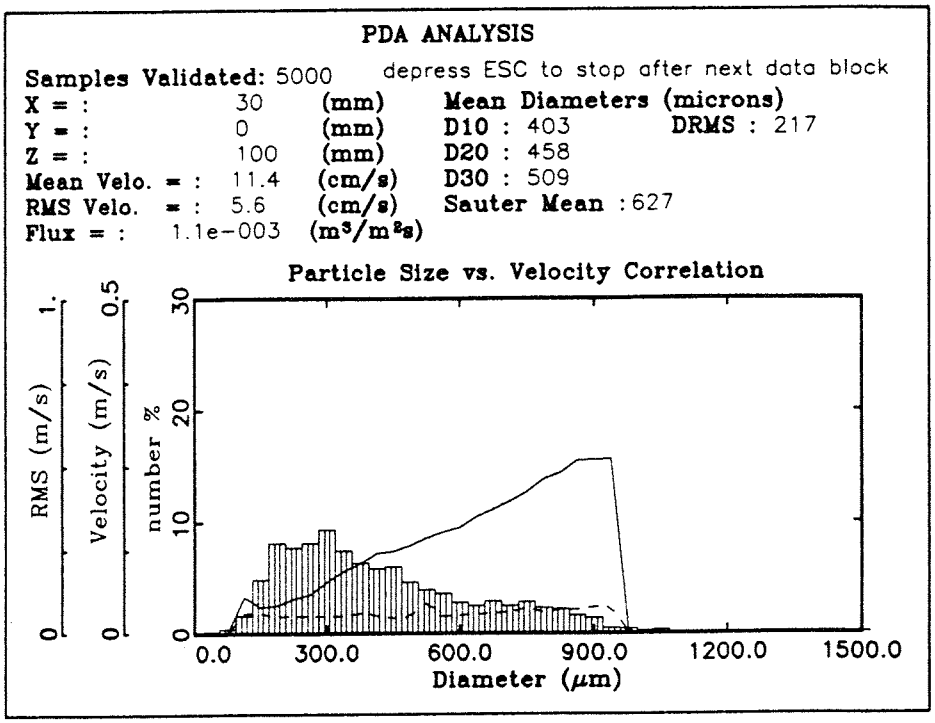

Figure 3: PDA-result with gas flow rate of 10 l/h; 5ppm Marlophor; z=100 mm

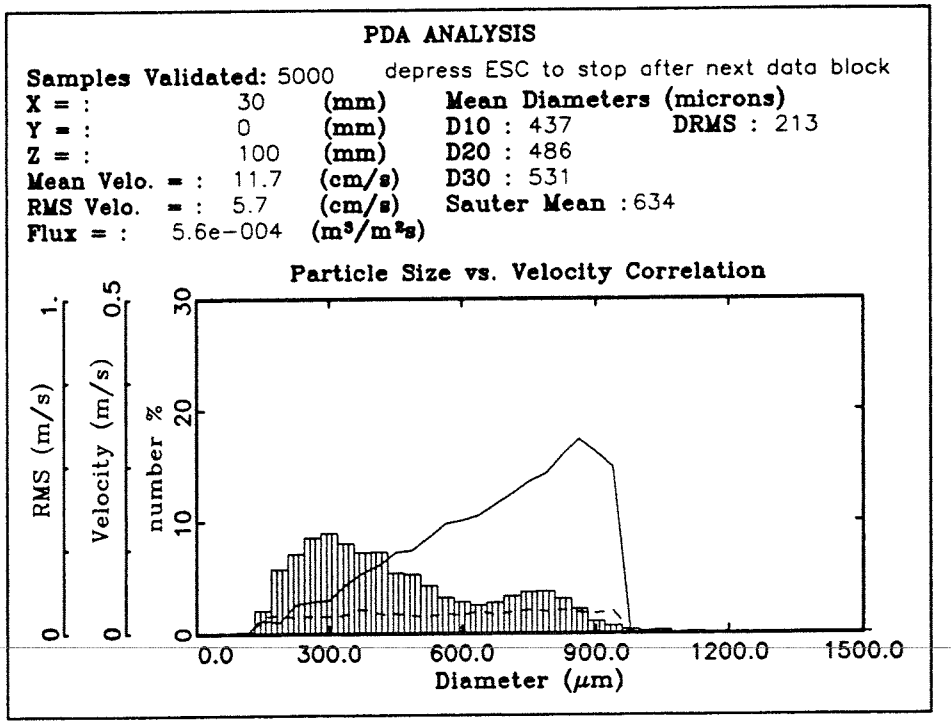

Figure 4: PDA-result with gas flow rate of 10 l/h; 5ppm Rewomid; z=100 mm

3. RESULTS

3.1 Coalescence Phenomena

To allow a direct comparison of the present study with measurements carried out for different sized single bubbles (see Bischof, 1994) we have choosen the bubble diameter D10. The results of the measurements in tap water give the change in bubble size and rise velocity in dependence of gas flow rate and height above the aerator (see Fig. 5). With increasing gas

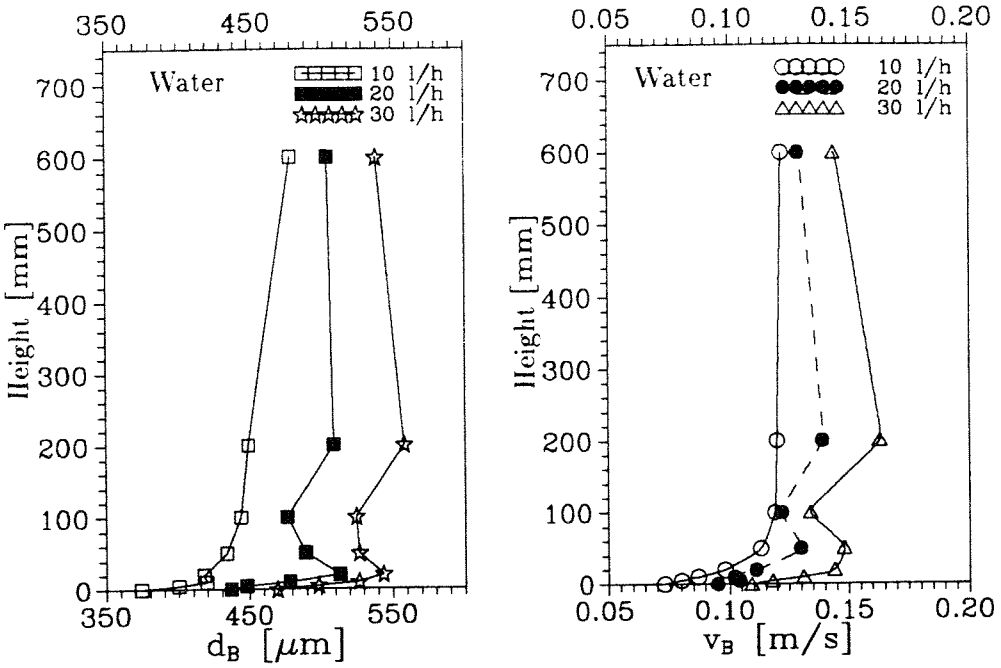

Figure 5: Mean values of bubble size and rise velocity for different gas flow rates

flow rate an increase in bubble size can be observed; additionally, the rise velocity is increased. Moreover, the comparison between the both diagrams in Fig. 5 indicate the strong correlation between bubble size and bubble velocity. Close to the aerator the coalescence between the bubbles takes place, hence the strongest change in bubble size is observed up to a height of 200mm. Thereafter, the coalescence probability becomes very small and an almost constant bubble size and bubble velocity is observed. In the case of surfactans, which were dissolved in the liquid, coalescence occures only within the first 100mm above the aerator. To have a better resolution of the range near the aerator the following diagramms give data only up to a height of z=100mm. In tap water, within the first 20mm coalescence results in a strong increase of bubble size (Fig. 6). At a gas flow rate of 10l/h the initially produced bubble size is enlarged for 13%; at 20l/h enlargement of 17% takes place, and about 16% of enlargement is found at a gas flow rate of 30l/h (always related to the initially produced bubble size).

The results for the presence of surfactants are given comprehensively in Fig. 7. Similar to the results for tap water, the bubble size and velocity strongly increase just above the aerator, within the first 200mm. In general, the maximum bubble size is reduced with an increase of surfactant concentration. This implies that the coalescence probability is reduced with increasing surfactant concentration.

The mean values of the Sauter-diameter, resulting from all the measurements are given in Fig. 8. At higher gas flow rates a larger Sauter-diameter is obtained within the bubble

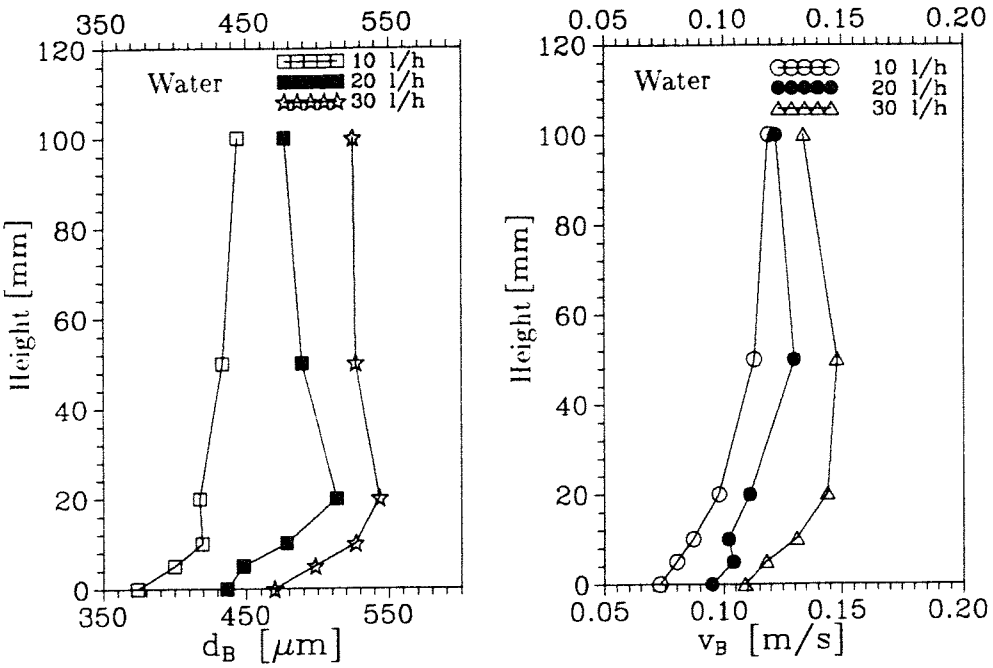

Figure 6: Mean bubble size and rise velocity for different gas flow rates; higher resolution of coalescence phenomena nearby the aerator

column. This is related to the larger initial bubble size obtained with increasing gas flow rate for the most types of aerators. But clearly, it can be seen. that there is a reduction in bubble size in the presence of surfactants. This reduction of bubble size is correlated with the concentration of the surfactant. and has a maximum of about 6% for a gas flow rate of 20l/h and a surfactant concentration of 10ppm.

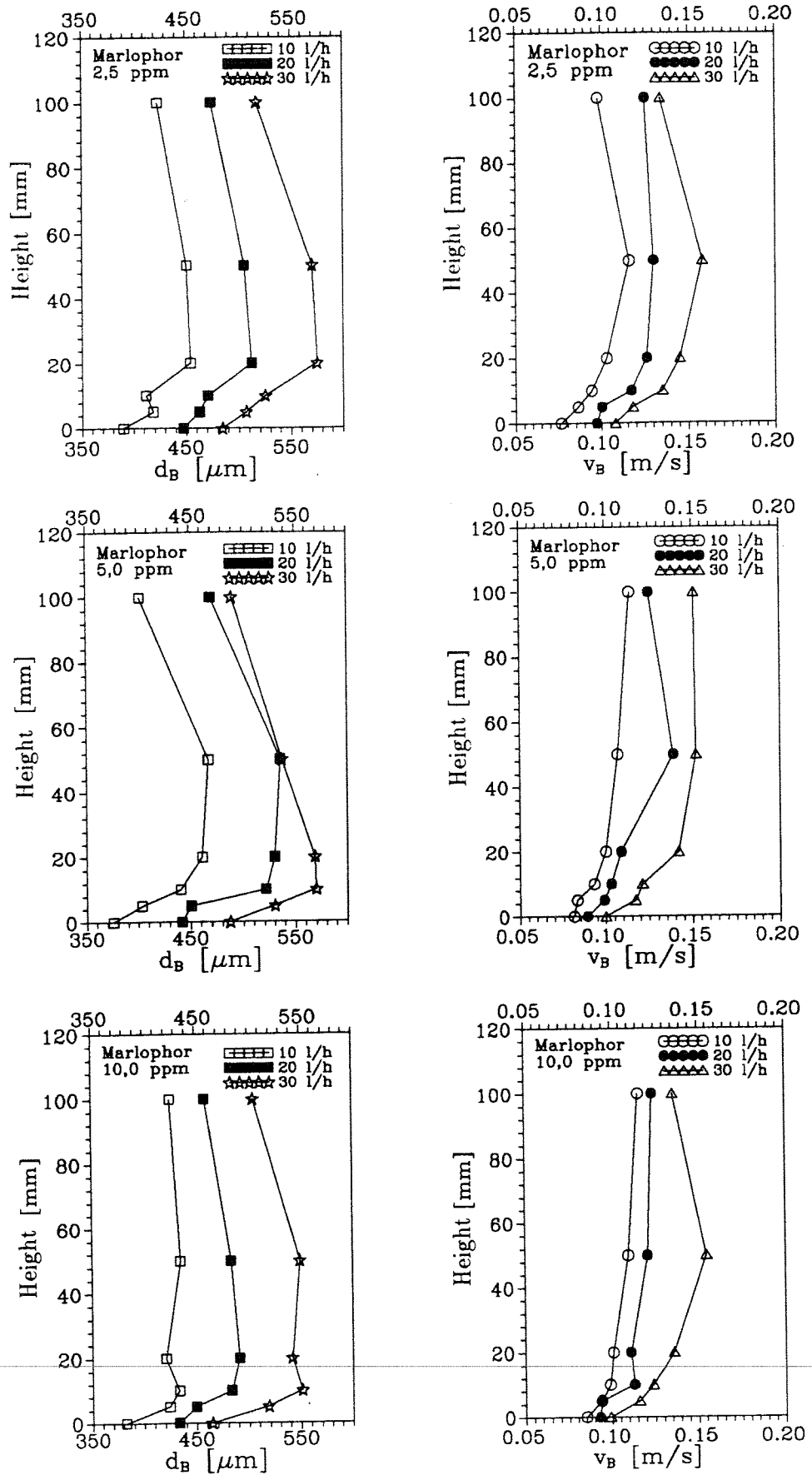

Figure 7: Influence of surfactant concentration on bubble size (left column) and bubble rise velocity (right column)

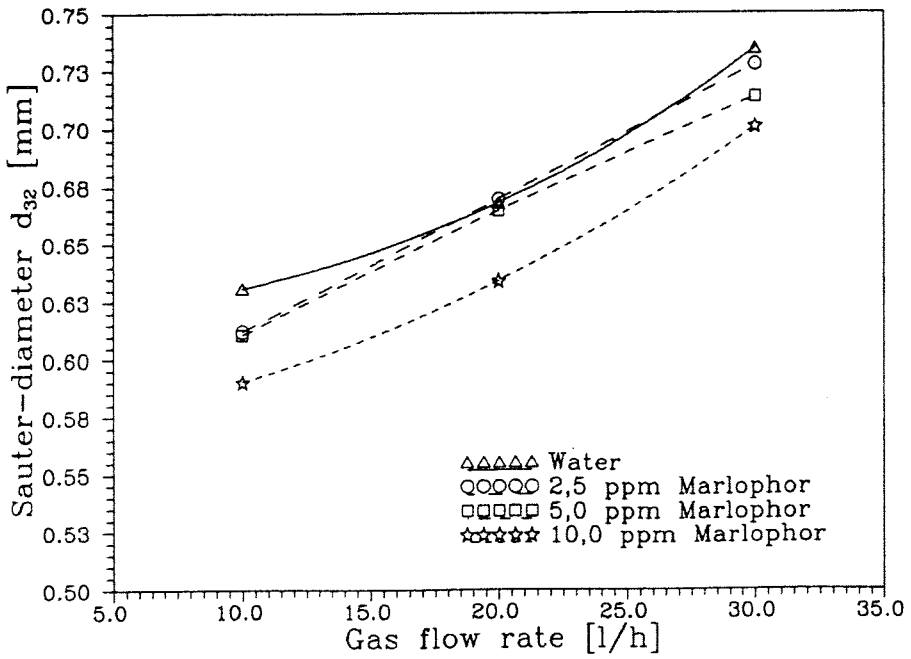

Figure 8: Mean Sauter-diameter d_{32} in dependence on gas flow rate and concentration of surfactants

3.2 Interfacial Area

The gas-liquid interfacial area represents the total surface area of all gas bubbles contained per unit volume of liquid. Therefore, this value and the mass transfer coefficient are the most relevant parameters for an optimization of the mass transfer. The influence of an increased air flow rate on the interfacial area in a bubble column aerated by a pouros membrane can be described as follows:

- A large air flow rate increases the void fraction and, therefore, also the interfacial area.
- Since the increase of air flow rate is achieved by applying higher aeration pressures, larger bubbles are usually produced which yield a lower interfacial area compared to small bubbles.
- For an increasing air flow rate, the number of bubbles per unit volume is increased whereby also the probability of coalescence is rising. This results again in a reduction of the interfacial area.

The calculated interfacial mass transfer area according to equation (1) gives the results shown in Fig. 9. In the case of tap water the interfacial area remains almost constant with increasing gas flow rate. This implies that, although the gas hold-up is increasing, coalscence effects result in larger bubbles and a decreasing bubble number density. Hence, the interfacial area is not enlarged with gas flow rate.

For the surfactant solutions the interfacial area remains larger compared to that in tap water at all gas flow rates. This is a result of the reduced coalescence probability in surfactant solutions. With increasing gas flow rates, a strong increase of the interfacial area, compared to that for tap water, can be observed for the ionic surfactant Marlophor. Already a concentration of 10ppm surfactant leads to an enlargement of the interfacial area of 20% at only

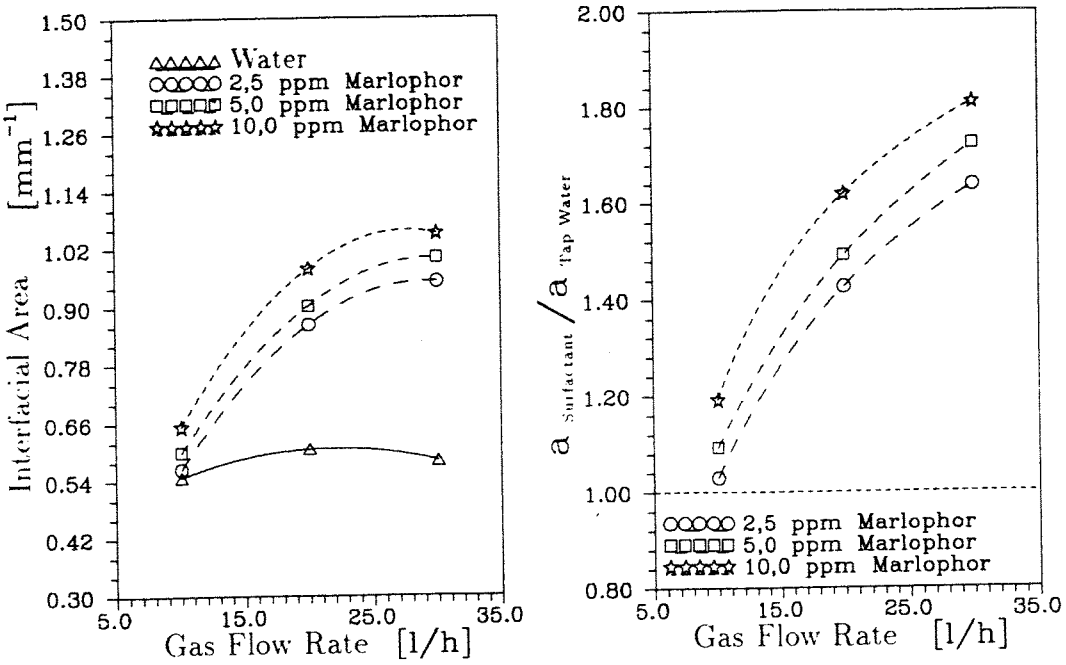

Figure 9: Variation of interfacial area a by gas flow rate and concentration of surfactants (left: interfacial area; right: normalized interfacial area

10l/h. The enlargement of the interfacial area is strongly dependent on the concentration of the surfactants, and Fig. 9 shows that with higher concentration of surfactants, a higher interfacial area can be obtained. The right diagram in Fig. 9 shows the relative enlargement of interfacial area compared to the situation in tap water. It is obvious from this figure that there is an enlargement of 80% at a gas flow rate of 30l/h, and for a concentration of 10ppm Marlophor.

3.3 Mass Transfer Studies

In general, the mass transfer from gas bubbles into the surrounding water can be described as:

$$\frac{dc}{dt} = k_l a \cdot (c_s - c_l)$$

This equation states that the temporal increase of the oxygen concentration within a liquid is directly proportional to the interfacial area a, to a concentration difference in the water (c_s represents the saturation concentration of oxygen, c_l represents the the oxygen concentration in the liquid) and to a mass transfer coefficient k_l denoting the mass transfer velocity. The product of $k_l a$ was measured with our oxgen probe and Fig. 10 gives the results where the ratio of the $k_l a$–value in the surfactant solution to the $k_l a$–value in tap water is plotted. With increasing flow rate the $k_l a$–values increase for all considered surfactant concentrations. Similar to the trends observed for the interfacial area, the behaviour for the $k_l a$–values can be described in the case of the ionic surfactant (Fig. 10). For low surfactant concentration (i.e. 2.5ppm Marlophor) the $k_l a$–values are smaller than those in tap water for all flow rates. At a flow rate of 5l/h the $k_l a$–values are reduced with increasing surfactant concentration while for higher flow rates the opposite is the case. Moreover, at higher surfactant concentrations the $k_l a$–values become larger than those in tap water at a certain flow rate. The non–ionic

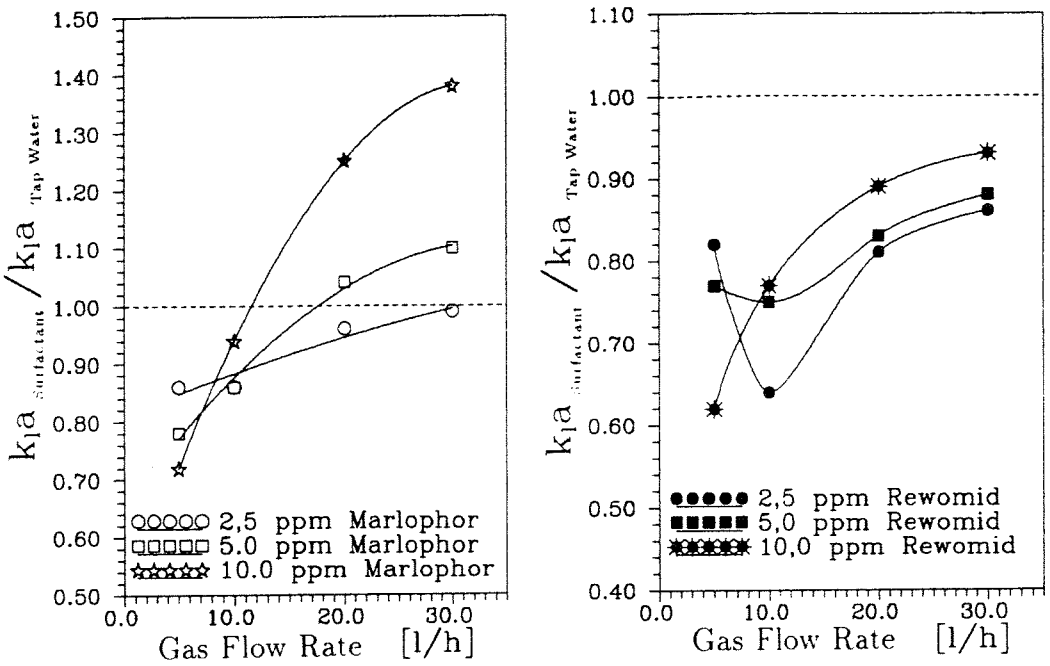

Figure 10: Influence of surfactants Marlophor (left) and Rewomid (right) on mass transfer

surfactant Rewomid shows a similar behaviour, but there is no enlargement of the total mass transfer compared to that in tap water.

Based on experimental data obtained from different sized single bubbles (see Bischof, 1994), the above result can be explained as follows. Due to the accumulation of surfactant molecules on the bubble surface the mass transfer coefficient k_l is in a similar way for both surfactants. This leads to the conclusion that the increase of interfacial area in the presence of a non-ionic surfactant is much smaller than for an ionic surfactant. Additionally, the mean Sauter-diameter for the non-ionic surfactants was smaller.

Taking into consideration the interfacial area a that was measured with the PDA-system, and the integral mass transfer coefficient $k_l a$ that was measured with oxygen probes, it is now possible, to calculate the mass transfer coefficient k_l for a single bubble. Additionally, we have to provide the average rise velocity of the corresponding bubble size, ascending in the bubble swarm. This information is necessary to compare the mass transfer coefficient of a freely rising single bubble with that of a bubble rising in a swarm. An accurate determination of bubble size and rise velocity is only possible by the use of PDA. Fig. 11 shows the correlation between the mean rise velocity of a bubble in the bubble swarm to that of a free rising bubble. The rise velocity of a bubble in a swarm is more than twice as much as that of a single bubble. This increase is also obvious from Fig. 11 (left diagram), showing the increase of the rise velocity with increasing gas hold-up. Furthermore, this result demonstrates the enlargement of the gas hold-up from 5% to 11% for a surfactant concentration of 10ppm in the water. Taking into consideration the rise velocity for the average diameter of bubbles in the bubble swarm, this value has to be multiplied with the k_l-value, which was evaluated from the measured $k_l a$-values. This procedure leads to the result shown in Fig. 12. This figure also contains a theoretical result obtained according to Brauer, (1971), which is valid for the considered bubble size range:

$$Sh = 2 + 9.45 \cdot 10^{-4} Re^{1.07} Sc^{0.888}$$

The calculated values for the mass transfer coefficient k_l show very good agreement with the

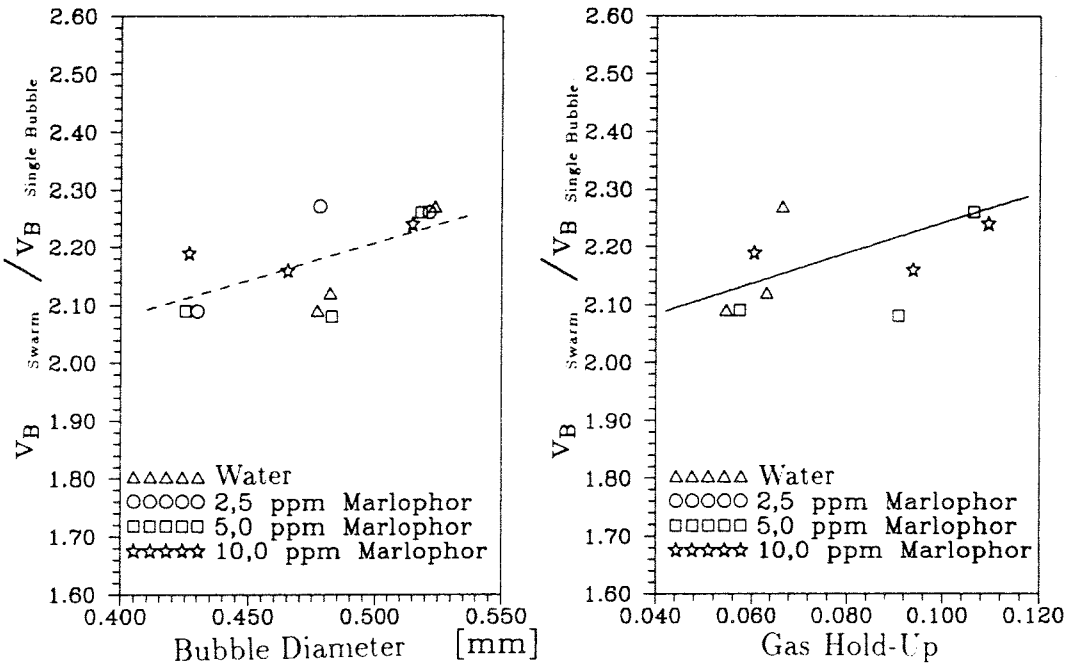

Figure 11: Increase of rise velocity of a bubble ascending in a bubble swarm compared to rise velocity of a freely rising single bubble

theoretical approach with consideration of the mean rise velocity in the bubble swarm. Good agreement between the experimental data from single bubble measurements (Bischof, 1994) and the measurements in the bubble column is also obtained. The mass transfer behaviour of a single bubbles, therefore, does not change in a swarm of fine bubbles. Difficulties of former experimental works can be explained by the missing knowledge of rise velocity of bubbles in a bubble swarm. Hence, the non intrusive PDA measuring technique allows for novel appli-

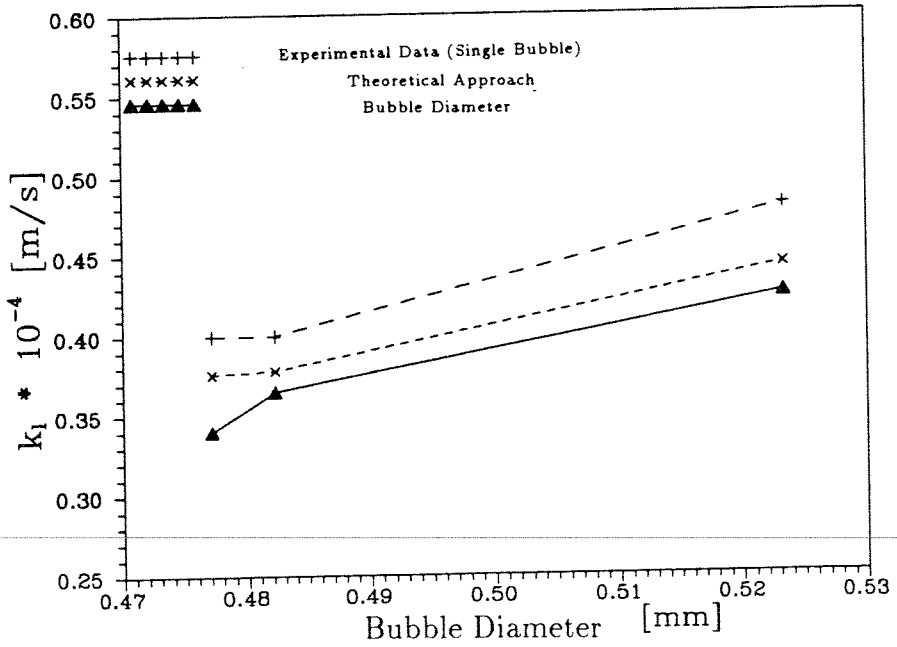

Figure 12: Comparison of experimentally investigated k_l-values for a free rising bubble (Bischof, 1994) with a bubble ascending in a bubble swarm for tap water

cations to basic research in the field of mass transfer from bubbles.

4. Conclusion

Measurements of bubble size distributions with PDA at different heights above the aerator yielded a deep insight into coalescence phenomena. It was demonstrated that coalescence occurs near the aeration system. The presence of surfactants, however, changes the behaviour of the bubble swarm. The PDA-measurement showed that the mean Sauter-diameter of the bubbles decreased with increasing surfactant concentration. In addition, the gas hold-up was enlarged, and the resulting interfacial area increased largely depending on the gas volume flow rate. The results revealed a strong influence of the molecular form of the surfactant where the ionic build-up surfactant showed generally a larger influence compared to the nonionic surfactant.

The experimental studies presented in this paper revealed that two effects determine the effectiveness of the mass transfer. On the one hand the accumulation of the surfactants molecules reduces the mass transfer coefficient and on the other hand, the reduction of coalescence probability increases the resulting mass transfer area (interfacial area) and, hence, the overall mass transfer. It could be demonstrated that these two competing effects result in completely different mass transfer characteristics for different surfactants. For certain flow conditions the overall mass transfer of oxygen was higher in the presence of surfactants compared to that in pure tap water. Furthermore, the results of these investigations showed clearly that it is not sufficient to carry out measurements with only one gas flow rate for studying the influence of surfactants on the efficiency of an aeration system.

NOMENCLATURE

Bischof,F., 1994, 'Untersuchung der Blasenbildung und des Stoffaustausches unter dem Einfluß oberflächenaktiver Stoffe und gelöster Gase', Dissertation, Universität Erlangen

Bischof,F., and Sommerfeld,M., 1991, 'Studies of the bubble formation process for optimization of aeration systems,' Proceedings, International. Conference on Multiphase Flows '91, Tsukuba, Japan, pp. 383-386.

Bischof,F., Sommerfeld,M., and Durst,F., 1991, 'The determination of mass transfer rates from individual small bubbles,' Chemical. Engineering. Science, Vol. 46,pp. 3115-3121.

Bischof,F., Sommerfeld,M., and Durst,F., 1993, 'Behaviour of fine dispersed bubbles in solutions with surfactants', Proceedings of the ASME, FED-Vol. 165, Gas-Liquid Flows, pp. 131-136

Brauer,H., 1971, ' Stoffaustausch einschließlich chemischer Reaktion', Verlag Sauerländer, Aarau und Frankfurt

Cackey,J.A., Michelsen,D.L., and To,Y.P., 1973, 'The effect of surfactant hydrophilc groups on gas absorption rate,' Journal of Colloid and Interface Science, Vol. 42, No. 1

Durst,F., and Zare,M., 1975, 'Laser-Doppler measurements in Two-Phase Flows', Proc. of LDA-75 Symp., Technical University of Denmark, 430-435

Drogaris,G., and Weiland,P., 1983, 'Coalescence behaviour of gas bubbles in aqueous solutions of n-alcohols and fatty acids,' Chemical Engineering Science, Vol. 38, pp. 1501-1506.

Godbole,S.P., Joseph,S., Shah,Y.T., and Clarr,N.L., 1984. 'Hydrodynamics and mass transfer in a bubble column with an organic liquid,' Canadian Journal of Chemical Engineering, Vol. 62, pp 440-445.

Koide, K., Hayashi,T., Sumino, K., and Iwamoto,S., 1976. 'Mass transfer from single bubbles in aqueous solutions of surfactants,' Chemical Engineering Science, Vol. 31, pp. 963-967

Lessard,R.R., and Zieminski,S.A., 1971. 'Bubble coalescence and gas transfer in aqueous electrolytic solution,' Industrial Engineering Chemical Fundamentals, Vol. 10, pp. 260-269.

Liepe,F., 1988. 'Verfahrenstechnische Berechnungsmethoden Teil 4: Stoffvereinigen in fluiden Phasen; Ausrüstungen und ihre Berechnungen.' VEB Deutscher Verlag für Grundstoffindustrie, Leipzig.

Marrucci,G., 1969. 'A theory of coalescence,' Chemical Engineering Science, Vol. 24, pp. 975-982.

Meijboom,F.W., and Vogtländer,J.G., 1974, 'The influence of surface active agents on mass transfer from gas bubbles in a liquid-1.' Chemical Engineering Science, Vol.29, pp. 857-861.

Nitsch,W., and Weber,G., 1976. 'Die Aufhebung der adsorptiven Stoffübergangshemmung im Bereich der kritischen Micellbildungskonzentration,' Chemie Ingenieur Technik, Vol 48, pp. 715-723.

Sagert,N.H., and Quinn,M.J., 1976. 'Foams,' Proceedings of Symposium, Akers, ed., Academic Press, London, New York, San Francisco, pp. 147ff.

Sztatecsny,K., Vafopulos,I., and Moser,F., 1977, "Der Einfluß von Tensiden auf den Stoffübergang in begasten Reaktoren," Chemie Ingenieur Technik, Vol. 49, p. 583.

Zlokarnik,M., 1980, 'Koaleszenzphänomene im System gasförmig/flüssig und deren Einfluß auf den O2-Eintrag bei der biologischen Abwasserreinigung,' KA-Korrespondenz Abwasser, Vol. 27, pp. 728-734.

DEVELOPMENT OF IMPROVED PDAS FOR MULTIPHASE FLOWS

G. Brenn, F. Durst, A. Melling, T.-H. Xu and M. Ziema

Lehrstuhl für Strömungsmechanik
Universität Erlangen-Nürnberg, Germany
Cauerstr. 4, D-91058 Erlangen
Telephone: (09131) 85-9500, Facsimile: (09131) 85-9503

ABSTRACT

The development of phase Doppler anemometry for multiphase flows at the Lehrstuhl für Strömungsmechanik aims to improve the accuracy of size measurements of particles (or bubbles) and to permit measurements with particles of unknown refractive index.

With the conventional PDA, the Gaussian beam defect can cause erroneous measurements if a particle of size comparable to the probe volume penetrates the half probe volume opposite the detectors, where non-uniform illumination of the particle induces mixing of the refracted and the reflected rays on the detectors. A new PDA system, which combines a planar optical layout with a phase difference estimation only from the centre of the burst signals, enables a complete elimination of the Gaussian beam defect.

In three-phase flows of gas bubbles and solid (transparent) particles in a liquid, signals from the gas and solid phases with widely separated refractive indices are readily distinguishable. Linear signal phase shift-size relationships with slopes of opposite sign are obtainable for each discrete phase of the mixture. Where the refractive indices are rather close, e.g. in interacting sprays of two different fluids, an extended PDA with a second receiving optics is used to measure a second phase shift. The phase shift ratio is ideally a function of refractive index only, but in practice a refined evaluation method is needed to extract the refractive index accurately and to distinguish between signals from the different fluids.

1 INTRODUCTION

The principles of phase Doppler anemometry for determining velocity and size distributions of suspended spherical particles were first presented in [1]. Subsequent contributions, for example [2, 3, 4], have assisted the development of commercial instruments from four manufacturers. For many significant applications, such instruments provide reliable measurements for spherical particles of known refractive index and diameters exceeding about 5 μm. Improvements to the phase Doppler anemometer are nevertheless desirable to increase the accuracy of particle size determination under certain conditions, for application with particles of unknown refractive index or in multiphase flows, and for accurate determination of particle concentration. This paper presents contributions to improvements in the first two of these respects. Following a brief description of a standard PDA system in section 2, the planar phase Doppler anemometer and its advantages in reducing the particle trajectory effect on the accuracy of particle sizing are discussed in section 3. The extended phase Doppler anemometer (EPDA) and its application for particle sizing and the identification of particles of differing refractive index are then described in section 4. Concluding remarks are given in section 5.

2 CONVENTIONAL PHASE DOPPLER ANEMOMETER

The principles of the conventional phase Doppler anemometer have been described in several papers, for example those cited in section 1. For this paper it suffices to characterize the conventional optical system (Fig. 1) by three angles, namely the half-angle α between the incident laser beams in the $x-z$ plane, the off-axis angle ϕ of the receiving optics in the $y-z$ plane, and the elevation angles ψ_u and

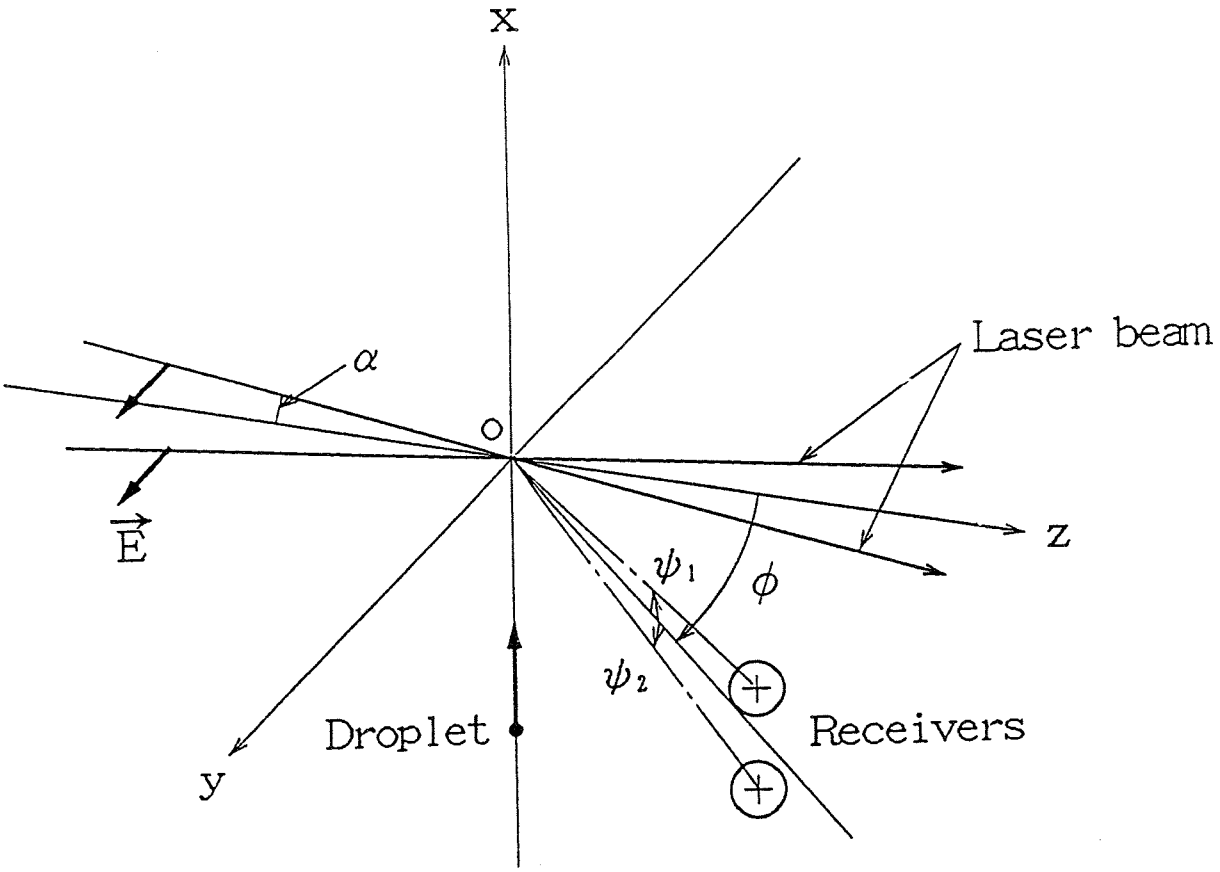

Figure 1: Conventional PDA optical layout and the coordinate system used.

ψ_d of the two detectors. The detectors are normally located symmetrically above and below the $y-z$ plane, i.e. $\psi_u = \psi_d = \psi$. In the conventional arrangement, therefore, the off-axis and elevation angles lie in mutually perpendicular planes.

When a particle passes through the measuring volume, the incident light is split into reflected, refracted and higher-order refracted rays. For purely reflecting and purely refracting particles which are larger than the wavelength of light, the phase shift Φ between two signals collected at the receiving optics may be given as follows:

$$\Phi = F(m)d_p \tag{1}$$

where d_p is the particle diameter.

Under the geometrical approximation of scattering from a spherical particle, the transfer function F may be expressed by the following relations [4] which are simple, yet accurate enough for most practical applications.

For refracting particles,

$$F = -\frac{2km \sin\alpha \sin\psi}{\sqrt{2\,(1+\cos\alpha\cos\psi\cos\phi)\left[1+m^2-m\sqrt{2(1+\cos\alpha\cos\psi\cos\phi)}\right]}} \quad . \tag{2}$$

For reflecting particles,

$$F = \frac{2k \sin\alpha \sin\psi}{\sqrt{2(1-\cos\alpha\cos\psi\cos\phi)}} \quad . \tag{3}$$

Since the phase shifts have opposite signs for the two types of particles, this sign can be utilized to distinguish refracting from reflecting particles. For measurements in a mixture of reflecting and refracting particles, the optical system should be so designed that the reflecting particles produce phase signals within the range $(0, 180°)$ and the refracting particles exhibit a phase in the range $(0, -180°)$. This subdivision of the complete period of phase $(0°, 360°)$ necessarily reduces the sensitivity of individual measurements by one-half.

Since Eqs. (2) and (3) are independent of the particle diameter, Eq. (1) illustrates the essential linearity of the phase shift-particle diameter relation for the phase Doppler anemometer for suitably selected optical parameters. Most commercial PDA systems have 3 detectors rather than 2, in order to eliminate possible 2π ambiguity for large particles in Eq. (1). In this paper attention will be directed to two-detector receiving optics, in order to emphasize the essential differences between the conventional PDA and the planar and extended PDAs in sections 3 and 4 respectively.

3 PLANAR PHASE DOPPLER ANEMOMETER

3.1 Theoretical Analysis

A major uncertainty of the conventional PDA is the Gaussian beam defect (trajectory effect) described in [5]. If a large particle penetrates the half probe volume opposite from the detectors, the Gaussian intensity profile of the incident beams causes a non-uniform illumination on the particle and induces reflected and refracted rays with roughly equal intensities on the detectors. This effect can result in a remarkable deviation of the diameter-phase difference relationship, Eq. (1), from linearity, thus causing errors in size measurements. This deviation is both particle size and trajectory dependent, so it is not possible to make corrections according to theoretical calculations of the trajectory effect during signal processing.

Numerical studies of the Gaussian beam defect have been reported in [6, 7, 8]. Figure 2 presents a numerical simulation result based on the generalized Lorenz-Mie theory for different locations of a 40μm water droplet in an 80μm probe volume, presented as a phase difference map. There is almost no phase difference dependence on the x location, since the iso-phase difference lines are parallel to the x-axis, i.e. perpendicular to the LDA-fringes. The computed phase difference is also constant for $y > 0$, but is strongly dependent on y for $y < 0$, i.e. in the half probe volume opposite from the detectors.

Based on these studies a new planar PDA optical set-up (Fig. 3) was proposed in [5], aimed at a complete elimination of the Gaussian beam defect. The two laser beams, their electric vectors and the two detectors are all in the x-z-plane. The off-axis angle ϕ is zero. The elevation angles ψ_1 and ψ_2 of the detectors have about the same magnitude as the off-axis angle in a conventional layout.

A numerical investigation of this optical set-up, for a water drop of diameter 52 μm crossing a probe volume of 80 μm diameter, is presented in Fig. 4a as a map of the phase difference between the two elementary detectors in the detection unit. It is seen that the iso-phase difference lines are rotated by 90° as compared with Fig. 2 and, hence, lie parallel to the LDA-fringes. The signal phase is no longer a function of location y but becomes a function of location x, when $x > 0$. The Gaussian beam effect has not been removed, but its influencing zone has been moved from the half probe volume $y < 0$ to the half $x > 0$. When a particle crosses the LDA-fringes along a trajectory parallel to the x-axis in the positive x-direction the front part of the burst comes from the half probe volume $x < 0$ where the

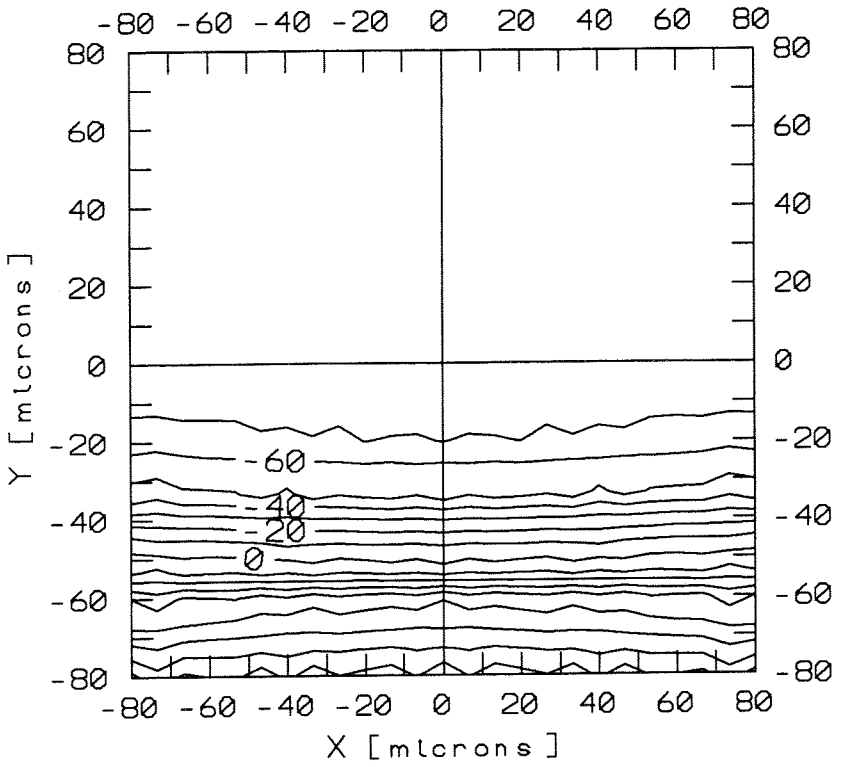

Figure 2: Simulated phase difference map. $w_0 = 40\mu$m, $\alpha = 0.9°, \phi = 30°, \psi_u = 4.1°, \psi_d - 4.1°$.

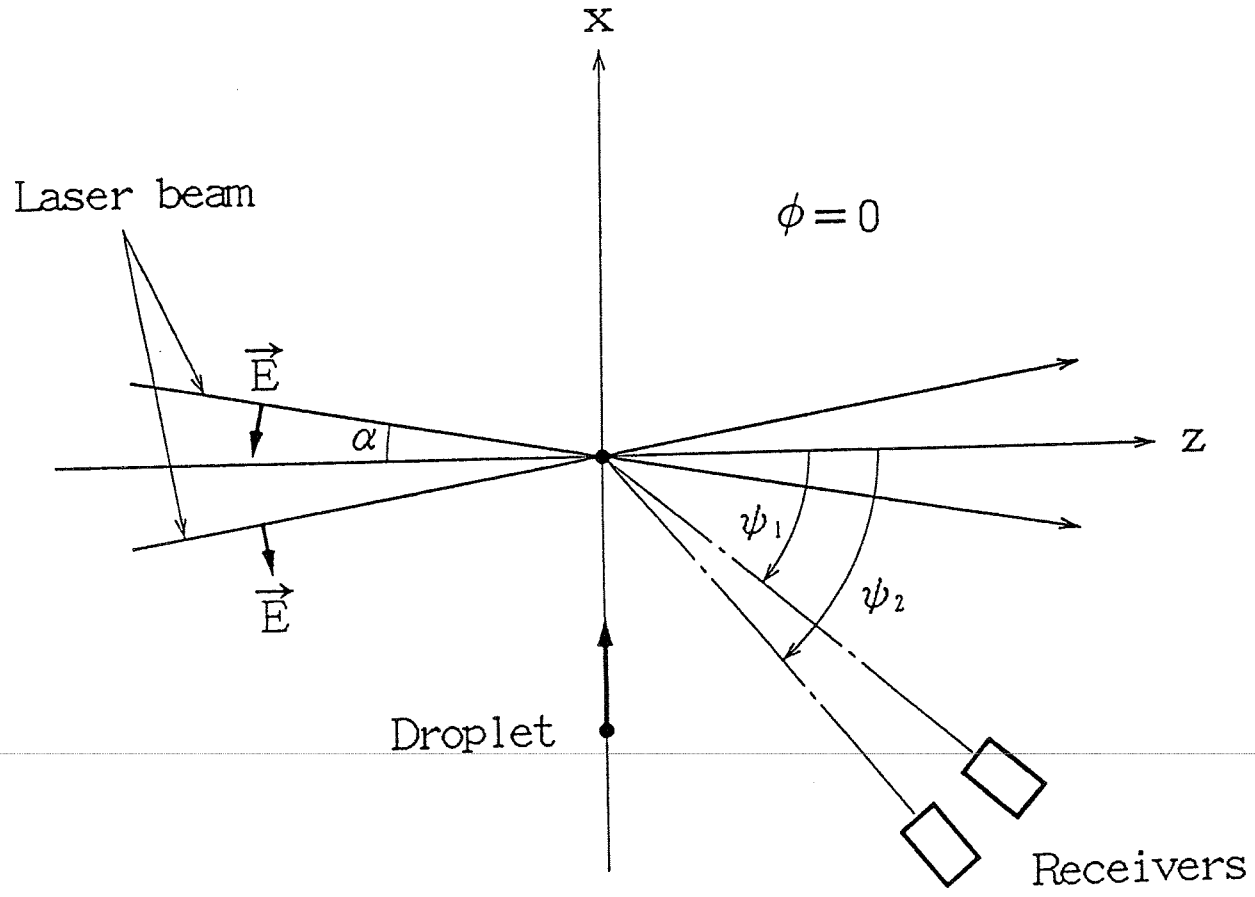

Figure 3: Planar PDA optical layout.

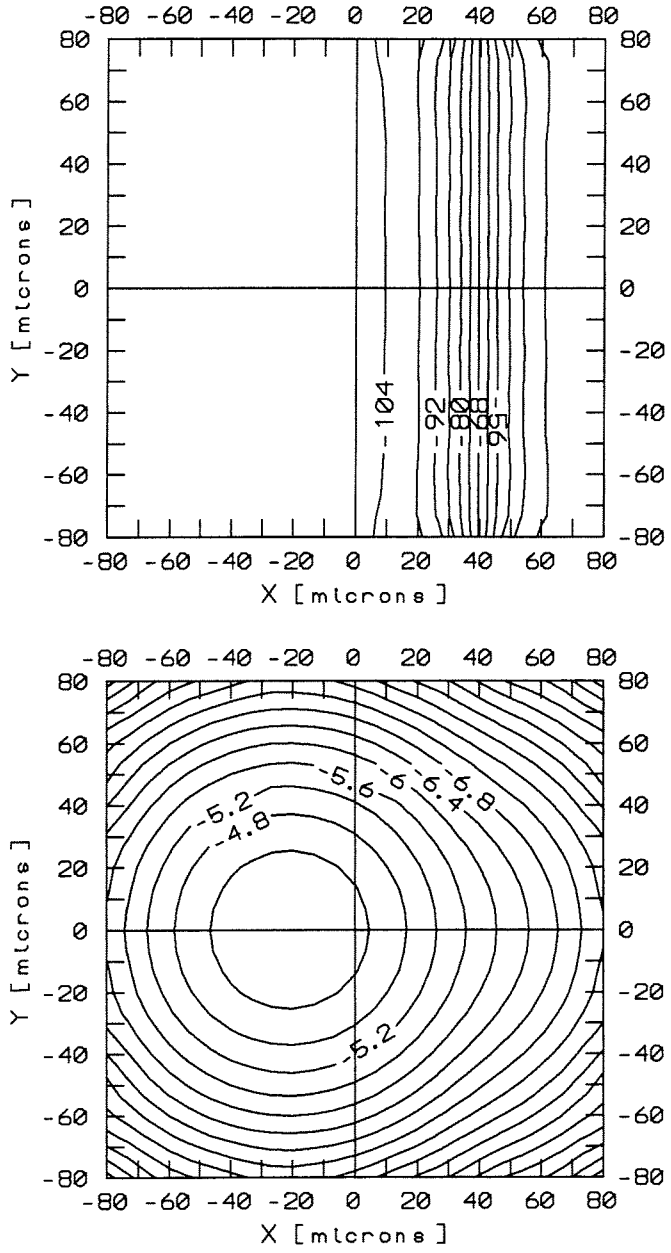

a)

b)

Figure 4: Map of a) phase difference [deg] and b) signal intensity [log(W)]. $d_p = 52\mu$m, $w_0 = 40\mu$m, $\alpha = 2.04°, \psi_u = 26.31°, \psi_d = 33.69°$.

intensity gradient of the incident Gaussian beams has no influence on the signal phase. By processing this part of the signal only, the phase measurement can be free of the Gaussian beam defect.

Figure 4b presents the relevant iso-signal intensity lines. Corresponding to the amplitude of the filtered signal, the signal intensity is defined as the product of the pedestal value and the visibility [9]. Note that the particle position for the maximum intensity is not at the geometrical centre of the probe volume but is displaced about 20μm towards the negative x side on which the detector is placed. The peak of a burst thus appears in the "front half" of the signal with respect to the particle position in the probe volume, if the particle is moving towards the positive x direction. Due to this feature, it is enough to process a part of the signal around the peak of the burst to obtain the phase difference expected from the predominant refractive scattering process.

3.2 Experimental Verification

Experimental verifications of the numerical results were made with monodisperse water droplets using a TSI-3450 aerosol generator. A transmitting optics consisting of a 12mW He-Ne laser, a collimator, a TSI beam splitter, two polarization rotators, a beam spacer and a front lens was set up and arranged with an INVENT receiving optics unit as in Figure 3. The optical parameters of this set-up are those given in Table 1. The PDA signals, filtered with an INVENT PDA filter, were digitized with

Table 1: Optical parameters used in the experiment.

Wavelength of laser λ	0.6328 μm
Half-angle of beams α	2.04°
Beam-waist radius w_0	64μm
Elevation angle ψ_1	33.69°
Elevation angle ψ_2	26.31°
Receiving-cone half-angle	2.77°

a LeCroy-9400 digital oscilloscope and processed by using the zero-crossing method which enables an analysis of the phase difference variation inside a burst. The accuracy of the analysis was ensured in the experiments by sampling at a frequency about 130 times higher than the Doppler frequency.

A typical recorded Doppler burst and the corresponding instantaneous phase difference are presented in Fig. 5. This burst signal was produced by a 95μm droplet moving towards the positive direction along the x-axis through a probe volume of diameter 128 μm. The burst signal presented in Fig. 5a is a filtered signal from the detector placed at the elevation angle 33.69°. The signal from the other detector ($\psi = 26.31°$) was very similar except for a slightly larger amplitude and is not presented here. Together with the experimental results for the signal intensity and the phase difference, results of a simulation are also plotted in Fig. 5 for comparison. The simulations were made for different locations along the x-axis using a computer code based on the generalized Lorenz-Mie theory.

As theoretically predicted, the phase difference evolution in the burst can be roughly split into two parts: (i) nearly constant phase difference for $0 < t < 2.2 \times 10^{-5}$s and (ii) strongly varying phase for $t > 2.2 \times 10^{-5}$s. Part (i) corresponds to the particle in the probe volume region that is close to the detector ($x < 25\mu$m) and is slightly larger than half of the probe volume. The peak of the recorded burst appears in this part, and it is seen in Fig. 5 that the recorded signal envelope is in very good agreement with the numerical prediction. Around the peak, the measured phase difference is 188°. By using a phase factor of 2.044°/μm, based on geometrical optics, the corresponding droplet diameter is 92μm, close to the nominal diameter 95μm for the TSI-3450 aerosol generator. The numerical computation predicts a slight increase of the phase difference with time, from 192° at $t = 0$ to 196° at $t = 2 \times 10^{-5}$s. In the experiment, however, around the peak of the burst, the phase difference is rather constant.

Part (ii) corresponds to the particle in the probe volume region $x > 25\mu$m, where the phase difference evolution shows the Gaussian beam effect. Although in this region there are differences

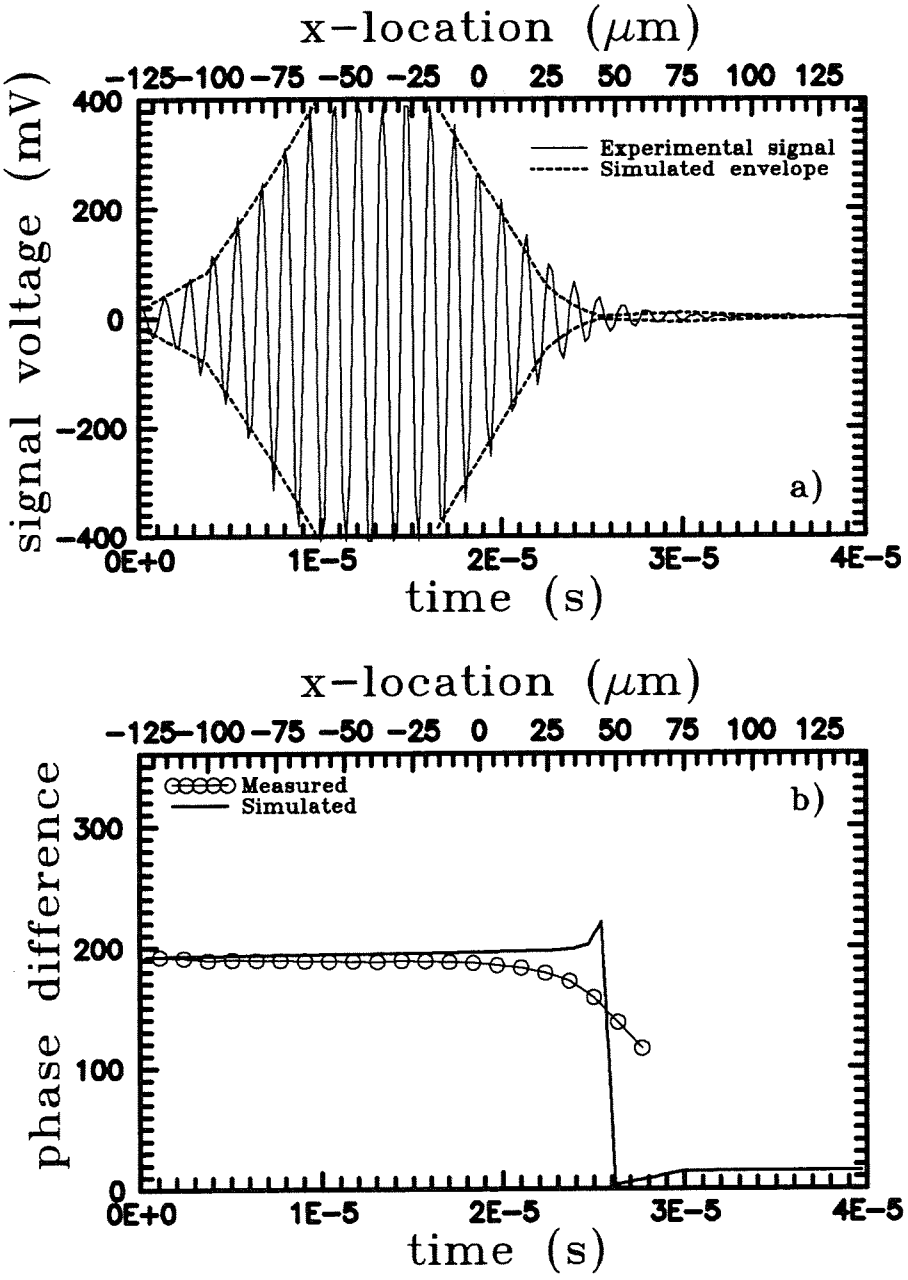

Figure 5: Phase difference evolution inside a burst. Droplet diameter 95μm.

between the experimental results and the numerical computations, there exist two important common features. Firstly, both of the curves show that the rapid evolution in the phase difference begins approximately at the time $t = 2.2 \times 10^{-5}$s, corresponding to the particle location 25μm. Secondly, the signal intensity in part (ii) is low and decreases rapidly with time. The influence of the Gaussian intensity profile is in fact limited to the last cycles of the detectable part of the burst.

Experimental studies for the evolution of phase difference and signal intensity were made for various droplet sizes in the range of 43μm to 168μm, i.e. $w_0/3$ to 1.3 w_0, where w_0 is the radius of the probe volume at the $1/e^2$ intensity level. It was confirmed for all these droplet sizes that the phase difference curves always have a long constant part followed by a short rapidly varying part as in the 95μm droplet case. Fig. 6 shows a comparison of the measured diameter with the diameter calculated

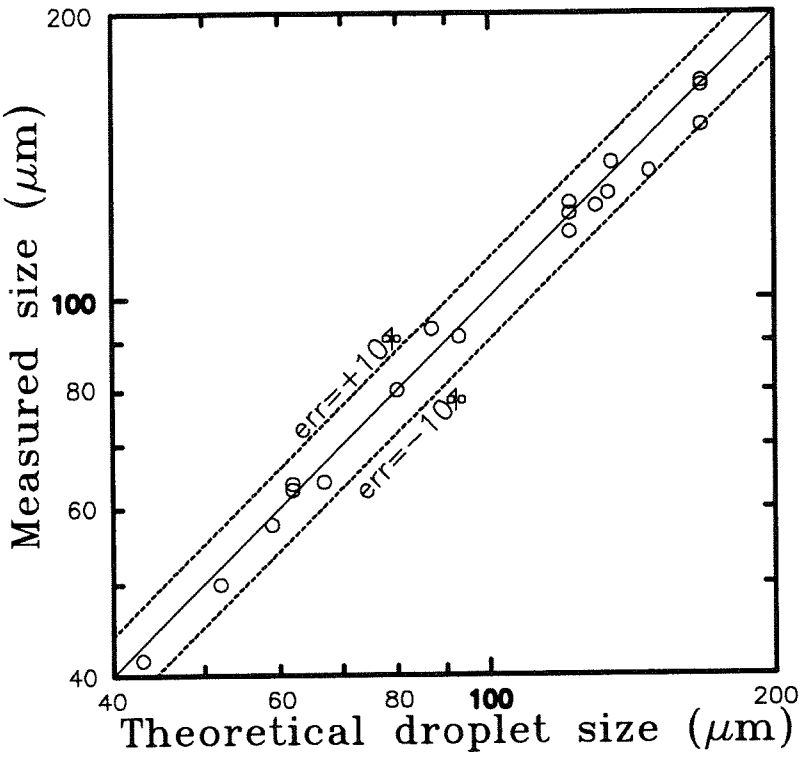

Figure 6: Comparison of measured droplet size with theoretical values.

from the oscillation frequency and liquid flow rate of the TSI aerosol generator. Each point in the plot corresponds to the measurement of a single droplet. The scatter, attributable to uncertainty in the droplet sizes from the TSI aerosol generator and to error in the PDA measurements, is within ±10% for all tests.

The numerical results given in Fig. 4 illustrate the most important characteristic of the planar optical layout, namely that for all particle trajectories with the maximum intensity inside the region $x < 0$, the measured particle sizes are the same. Although the simulations were made only for particles in the x-y-plane, the z location of a particle should have no influence on the signal phase because the intensity gradient along the length of the probe volume is low. This was confirmed experimentally, using a 2-dimensional traversing system (resolution 10μm) to position the droplet trajectory at different y and z locations respectively, for 95μm water droplets moving parallel to the x-axis. The measurements were made over a range of ±120μm in the y direction and ±0.8 mm in the z direction with a stepwidth of 10μm and 100μm respectively, until the signal-to-noise ratio was too low for signal processing. The results verified that there is no trajectory effect in either y or z directions even for trajectories that are very far from the probe centre.

3.3 Alternative Operation Mode of Conventional PDA

It can be deduced from Fig. 2 that if a particle moves parallel to the y-axis instead of the x-axis in a standard PDA optical configuration the signal phase difference inside the burst should vary with time in the same manner as that in a planar optical layout. Around the signal intensity maximum the phase difference should again be constant. With the incorporation of the signal processing method used for planar PDA, the Gaussian beam defect could therefore be eliminated for a standard PDA. This PDA optical layout, however, is suitable only for 2D-PDA systems with frequency shift because in this case the main flow direction is parallel to the LDA-fringes. The concept has been experimentally verified and a detailed analysis can be found in [10].

4 EXTENDED PHASE DOPPLER ANEMOMETER

4.1 EPDA Principles

Many multiphase flow applications involve the measuring problem that the refractive index of the light scattering particles is not known. Flows of this type may occur in mixing sprays or in environments with unknown temperature. In this case, with a normal PDA system particle diameters cannot be determined, as the phase factor relating the measured phase shift to the particle diameter is a function of the refractive index of the particle, if the light scattering is dominated by refraction.

In order to solve this problem, the extended PDA technique (EPDA) has been developed [4]. With an extended PDA, which typically is a four-detector system, Doppler signals are detected at two different scattering angles simultaneously, thus giving two different phase shifts for each detected sample droplet. A sketch of an EPDA setup is shown in Fig. 7.

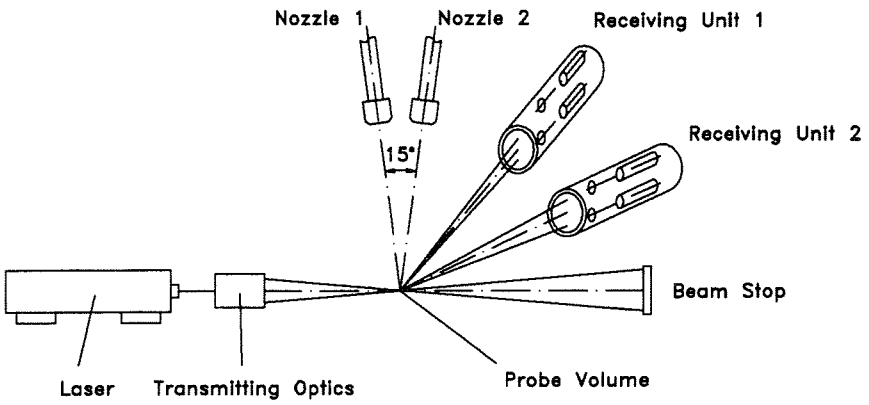

Figure 7: EPDA set-up with receiving optics units at scattering angles of 60° and 30°. In the diagram the plane of the nozzles is rotated by 90° for clarity.

The basic idea of the technique, making use of the laws of geometrical optics, is to generalize Eq. (1) to the form

$$\Phi_i = F_i(m, \alpha, \psi_i, \phi_i) \cdot d_p \tag{4}$$

using detectors at the two different scattering (off-axis) angles ϕ_1 and ϕ_2 and to calculate the ratio of the phase shifts. As the particle diameter d_p cancels out, the obtained equation

$$\frac{\Phi_1}{\Phi_2} = \frac{\sin\psi_1}{\sin\psi_2} \left(\frac{(1+\cos\alpha\cos\psi_2\cos\phi_2)\{1+m^2-m[2\,(1+\cos\alpha\cos\psi_2\cos\phi_2)]^{1/2}\}}{(1+\cos\alpha\cos\psi_1\cos\phi_1)\{1+m^2-m[2\,(1+\cos\alpha\cos\psi_1\cos\phi_1)]^{1/2}\}} \right)^{1/2} \tag{5}$$

gives the relation between the ratio of the measured phase shifts and a quantity depending only on the refractive index of the scattering particle and the geometrical parameters of the EPDA setup. The equation in the present form is only valid for symmetrical arrangements of the photodetectors with respect to the plane ψ=0 and for sufficiently small angles α and ψ.

Solving this equation with respect to the refractive index m, and dropping the physically irrelevant solution of the second order equation, we obtain the solution

$$m = -\frac{1}{2}\frac{\sqrt{f_2} - A\sqrt{f_1}}{A-1} + \frac{1}{2}\sqrt{\left(\frac{\sqrt{f_2} - A\sqrt{f_1}}{A-1}\right)^2 - 4} \quad , \tag{6}$$

where

$$f_1 = 2\,(1 + \cos\alpha \cos\psi_1 \cos\phi_1) \tag{7}$$

$$f_2 = 2\,(1 + \cos\alpha \cos\psi_2 \cos\phi_2) \tag{8}$$

$$A = \left(\frac{\Phi_1}{\Phi_2}\frac{\sin\psi_2}{\sin\psi_1}\right)^2 \frac{f_1}{f_2} \quad . \tag{9}$$

This equation provides real solutions only for non-vanishing denominators and for positive square root arguments, thus involving the validation criterion

$$\sqrt{\frac{f_2}{f_1}}\sqrt{\frac{\sqrt{f_2}-2}{\sqrt{f_1}-2}} \leq \frac{\Phi_1}{\Phi_2} < \sqrt{\frac{f_2}{f_1}} \quad . \tag{10}$$

4.2 Application of EPDA to Mixing Sprays

In a study of the mixing between two sprays, simulating the interaction which might occur between neighbouring liquid jets from a multi-hole Diesel injector, the EPDA was used to identify the origin (spray 1 or spray 2) of the detected droplets and to determine their sizes and velocities. The droplets were coded according to their refractive indices m, using demineralized water (m = 1.334) and a water-sucrose solution (m = 1.421) in the simulation for the two sprays. For these fluids, the angles of the EPDA optical system were optimized as follows: half beam-crossing angle α = 1.69°, elevation angle of the photodetectors ψ = 3.69° and scattering angles ϕ_1 = 60°, ϕ_2 = 30°. With these angles the limits for the allowable values of the phase shift ratio are

$$0.566 \leq \frac{\Phi_1}{\Phi_2} < 1.115 \quad .$$

Before undertaking measurements with mixing sprays, the EPDA technique was used to measure the refractive index of monodisperse droplets, i.e. droplets with known and constant diameter. This test showed that the accuracy of the alignment of the receiving optics units, in particular the positioning of the four photodetectors, is the crucial point of the technique. The measured phase shifts for each sample particle satisfy Eq. (5) and lead to the correct diameter measurement only if alignment tolerances are kept very small. Misalignments lead to broad refractive index distributions - even for one-component monodisperse droplet streams. A well aligned system gives results as shown in Fig. 8 for demineralized water droplets with a diameter of 71.8 μm. The correct refractive index measured with a refractometer is m = 1.334. The deviation of the mean value of the refractive index distribution measured by EPDA from the correct value is −0.6 %. The normalized standard deviation of the distribution is $7.8 \cdot 10^{-3}$. Standard deviations down to $5.5 \cdot 10^{-3}$ are achievable.

With an EPDA system adjusted according to the above mentioned criteria, the refractive index distributions in polydisperse mixing sprays produced with domestic oil burner nozzles were measured. The spray nozzles were arranged symmetrically with respect to the plane of the crossing laser beams of the EPDA system and inclined at 7.5° each against the plane (Fig. 7). Measurements were carried out at the 25 points of a square 5 × 5 grid. The refractive index distribution measured at a point 15 mm off the centre of the grid at a distance of 90 mm from the nozzle exits is shown in Fig. 9. The

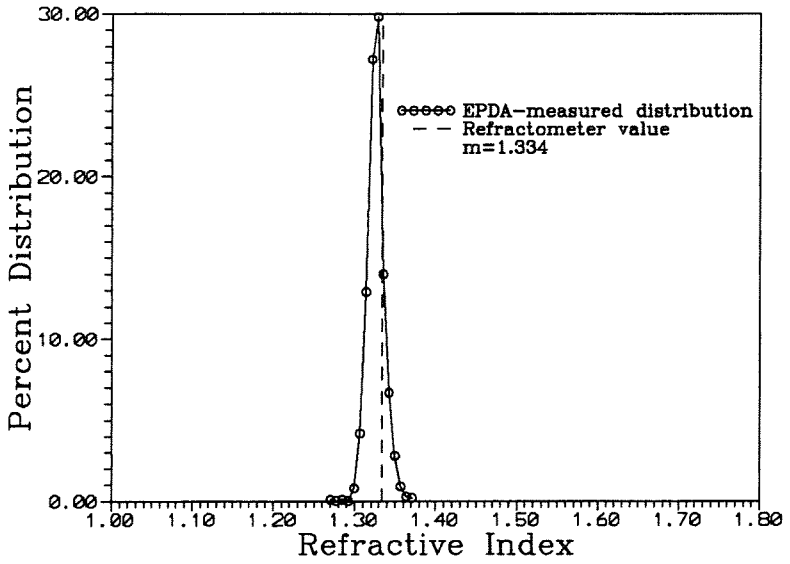

Figure 8: Refractive index distribution in a stream of monodispersed water droplets. The normalized standard deviation of the distribution is $7.8 \cdot 10^{-3}$, the mean value is 1.326.

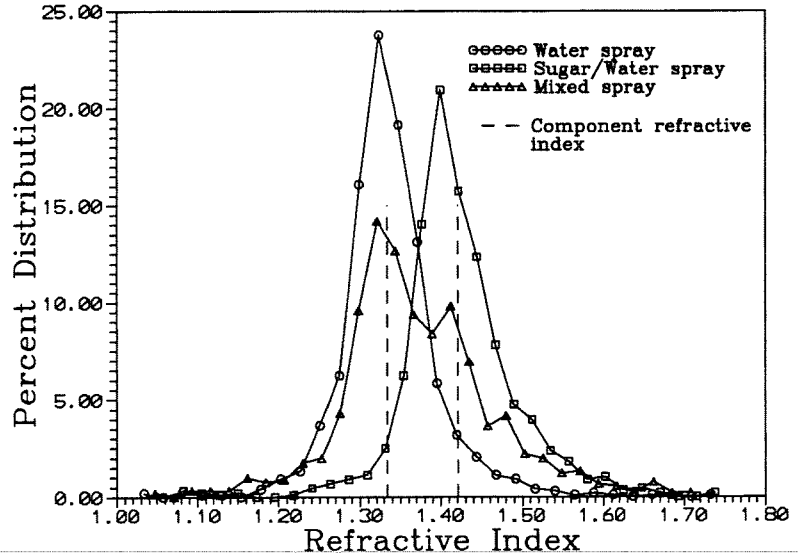

Figure 9: Refractive index distributions in two polydisperse sprays and in mixing sprays. The two peaks of pure component droplets in the mixed case can clearly be seen.

distributions for the two pure single sprays have normalized standard deviations of about $5.0 \cdot 10^{-2}$. The distribution for the mixed sprays case indicates the presence of pure water and pure sugar water droplets in the mixing zone of the sprays, represented by the two peaks of the distribution. The pure polydisperse sprays yield quite broad refractive index distributions which overlap. Mixed droplets formed by the coalescence of droplets from each of the two sprays would have intermediate refractive indices. It is, however, difficult to identify whether such droplets exist.

The measurements confirm the capability of the EPDA technique to detect particles with different refractive index even in polydisperse sprays, but the resolution of the refractive index needs to be improved.

5 CONCLUDING REMARKS

At LSTM Erlangen, research activities with phase Doppler anemometry include on the one hand the application of state-of-the-art anemometers (either commercial products or instruments developed in-house) to sprays, bubbly flows or the transport of particles. On the other hand, the further development of the phase Doppler technique is a continuing objective. For both types of activity, the analysis of the light scattering process using computer programs based on Mie scattering theory or generalized Lorenz-Mie theory is an essential complement to the experiments, to ensure an optimized choice of the instrument parameters and the operation of the PDA within the linear range of the phase shift-particle diameter relationship.

In this paper, examples of this combined approach have been shown for the development of the planar and extended versions of the phase Doppler anemometer. The advantage of this approach is particularly clear for the planar PDA, where the theoretical analysis indicated the occurrence of the Gaussian beam defect and suggested a method to avoid it. The effect and the remedy were then confirmed experimentally. The application of the extended PDA was also supported by an analysis of the scattering process, although in this case the geometrical optics approximation was adequate to suggest an appropriate measuring procedure to identify various refractive indices.

The combined application of analysis and experimentation will continue to be used at LSTM, both to achieve further improvements in the planar PDA and EPDA and to assist the development of PDA techniques for accurate determination of particle concentration and the sizing of sub-micrometer particles.

References

[1] Durst, F. and Zar, M.: "Laser Doppler measurements in two-phase flows", in Proc. LDA-Symposium Copenhagen, p. 403-429 (1975).

[2] Bachalo, W.D. and Houser, M.J.: "Phase/Doppler spray analyzer for simultaneous measurements of drop size and velocity distributions", in Optical Engineering **23**, p. 583-590 (1984).

[3] Saffman, M., Buchhave, P. and Tanger, H.: "Simultaneous measurements of size, concentration and velocity of spherical particles by a laser Doppler method", in 2nd Int. Symp. on Application of Laser Anemometry to Fluid Mechanics, Lisbon (1984).

[4] Naqwi, A., Durst, F. and Liu, X.-Z.: "Extended phase Doppler system for characterization of multiphase flows", in Part. Part. Syst. Charact. **8**, p. 16-22 (1991).

[5] Aizu, Y., Durst, F., Gréhan, G., Onofri, F. and Xu, T.-H.: "PDA-system without gaussian beam defects", in 3rd Int. Conf. Optical Particle Sizing, Yokohama, p. 461-470 (1993).

[6] Gréhan, G., Gouesbet, G., Naqwi, A. and Durst, F.: "Evaluation of a phase Doppler system using generalized Lorenz-Mie theory", in Int. Conf. on Multiphase Flows'91, Tsukuba, Japan, p. 291-296 (1991).

[7] Gréhan, G., Gouesbet, G., Naqwi, A. and Durst, F.: "On elimination of the trajectory effects in phase Doppler systems", in 5th European Symposium Particle Characterization (PARTEC 92), Nrnberg, p. 309-318 (1992).

[8] Gréhan, G., Gouesbet, G., Naqwi, A. and Durst, F.: "Trajectory ambiguities in phase Doppler systems: use of polarizers and additional detectors to suppress the effect", in Sixth International Symposium on Application of Laser Techniques to Fluid Mechanics, Lisbon (1992).

[9] Adrian, R.J. and Earley, W.L.: "Evaluation of laser-Doppler velocimeter performance using Mie scattering theory", in T.&A.M. Report n°479, Department of Theoretical and Applied Mechanics, University of Illinois, Urbana-Champaign, USA (1986).

[10] Xu, T.-H. and Tropea, C.: "Improving performance of 2D Phase-Doppler Anemometer, submitted to Measurement Science and Technology" (1994).

A NEW MEASUREMENT TECHNIQUE FOR DROPLET DIAMETERS AND DROPLET VELOCITIES

M. Boddem and D. Mewes

Institut für Verfahrenstechnik der Universität Hannover

Callinstraße 36, 30167 Hannover, Federal Republic of Germany

Telephone: (0511) 762-3828, Facsimile: (0511) 762-3031

ABSTRACT

A new measuring technique for the simultaneous measurement of the diameter of droplets and the velocity of droplets is presented. The range of application is for droplet diameters $d_p > 1000$ µm and droplet velocities $v_p < 5$ m / s. The new measuring technique is based on the refraction of laser light at the surfaces of the droplet. The intensity of the refracted light is recorded. The diameter of the droplet can be derived from the intensity of the light by the laws of the geometrical optics. The maximum margin of error of the droplet diameter measurement is less than 8%. A laser beam with a tubular characteristic is used. So, the measurement of the droplet velocity by two characteristic time intervals is possible. The maximum margin of error of the droplet velocity measurement is less than 4%. It is shown, that the simultaneous measurement of droplet sizes and velocities in a swarm by the new measurement technique is working.

1. INTRODUCTION

In many technical applications of two-phase flows, dispersed flow regimes are observed. Knowing the distribution of the size and the velocity of the particles is important to determine the heat and mass transfer in many processes. There is a need to have a measuring technique for velocities and sizes of bubbles and droplets. In the literature, many techniques have been proposed [1,2]. They can be divided in intrusive and non-intrusive techniques. The intrusive techniques are usually optical or electrical probes. In combination with the cross correlation method, it is possible to derive the particle sizes and velocities by using two equal probes mounted in the two phase flow. Generally, only chord lengths of the bubbles and droplets are measured and a statistical correction has to be carried out to get the particle diameter distribution. In some applications intrusive measuring techniques are not accessible. In this case the non-intrusive techniques have to be employed. Many non-intrusive techniques are based on the Doppler-effect. Especially the Laser-Doppler-Anemometry (LDA) in combination with blockage time or light barrier techniques is well established [3]. Just as the LDA the Phase-Doppler-Anemometry, where the phase shift of the signal is used to determine the particle size, is employed in some technical or scientific applications [4,5].

Only a few techniques allow to measure particle sizes in the range greater than $d_p = 1000\mu m$. The measuring techniques not using the Doppler-effect can be distinguished between the photographic methods like Particle-Image-Velocimetry (PIV) or holography and those using the signals of scattered or reflected light of a light beam. The use of PIV is limited to applications with good optical accessibility. There are also still problems with image processing and threshold definitions.

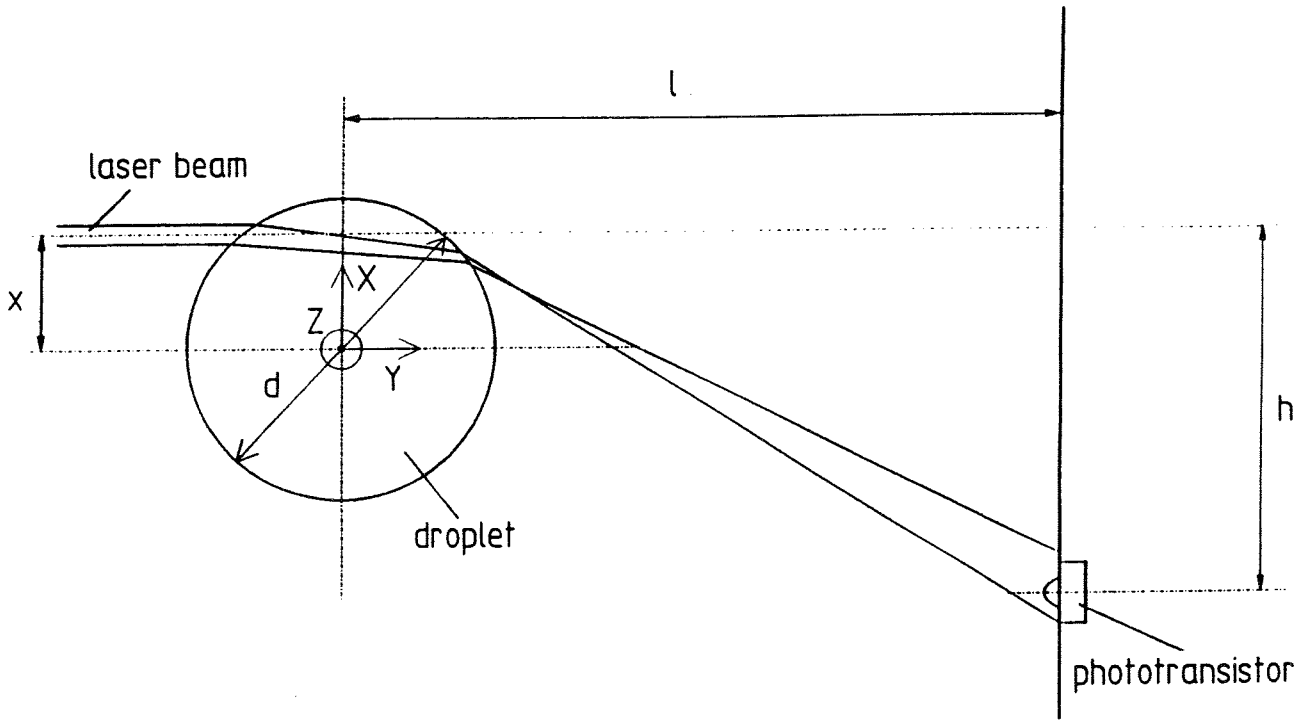

Figure 1: The geometrical relations of the experimental set-up.

There have been some publications about new measuring techniques for the simultaneous measurement of size and velocity of drops with diameters in the range of $d_p = 1000\,mm$ up to $d_p = 5000\,\mu m$ [6]. Most of these techniques use the blockage time method and so there is always a dependency between the measurement of particle velocity and particle size.

The new measuring technique is based on the refraction of laser light at the surface of droplets. The intensity of the refracted light is recorded as a function of time. It has been tested for droplet diameters in the range of $d_p = 1000\,\mu m$ up to $d_p = 6000\,\mu m$ and velocities up to $v_p = 5$ m/s.

2. THE MEASUREMENT OF DROPLET DIAMETERS

The geometrical relations of the set-up are shown in Fig. 1. A light beam is passing the droplet. It is refracted two times at the surface of the droplet. Thus it is deflected and expanded. The light beam is projected in a plane at the distance l and the height h. The height is a function of the droplet diameter d_p, the horizontal distance l, the refraction indices n_i of the phases and the distance x between the centre of the droplet and the laser beam. The height h can be calculated by the laws of the geometrical optics

$$h = x' - (l - y')\tan[2(\alpha - \beta)] \tag{1}$$

with

$$x' = \frac{d_p}{2}\sin(2\beta - \alpha) \qquad \text{and} \qquad y' = \frac{d_p}{2}\cos(2\beta - \alpha)\ . \tag{2}$$

In Eq. (2), the angles α and β are

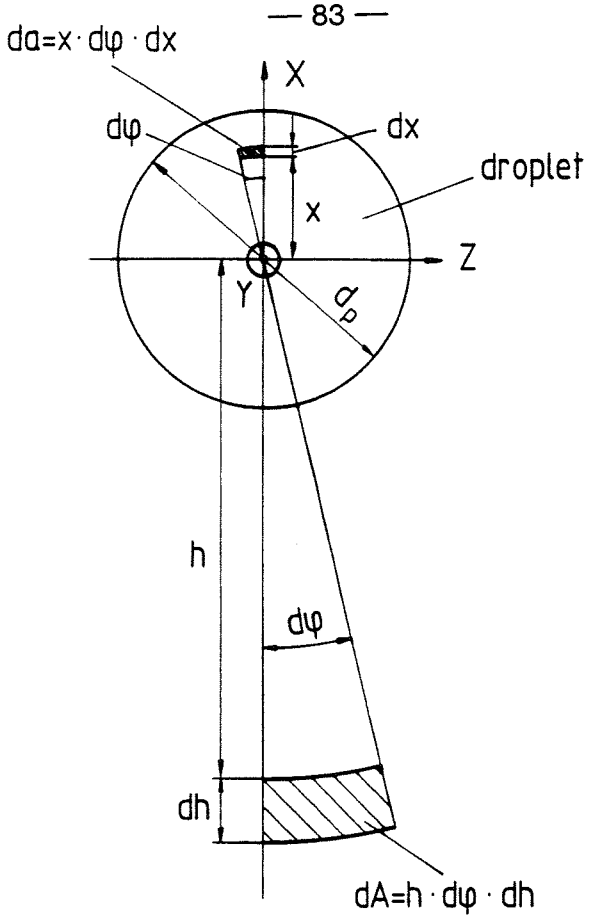

Figure 2: The expansion of an infinitesimal small element of the cross sectional area of the laser beam.

$$\alpha = \arcsin\frac{2x}{d_p} \quad \text{and} \quad \beta = \arcsin\left(\frac{2x}{d_p}\frac{n_1}{n_2}\right) \quad , \tag{3}$$

where n_1 and n_2 are the refraction indices of the surrounding medium and the droplet. Using Eq. (1), the expansion of the light beam in the x-y-plane is $\frac{dh}{dx}$. If the expansion in the y-z-plane is $\frac{df}{dz}$, the 3-dimensional expansion of the laser beam is

$$\frac{dA}{da} = \frac{dh}{dx}\frac{df}{dz} \quad . \tag{4}$$

The expansion $\frac{df}{dz}$ can easily be calculated. In Fig. 2, the geometric relations of the projection of the beam in the x-z-plane are shown. The infinitesimal distances dz and df can be written as

$$dz = x \cdot d\varphi \tag{5}$$

and

$$df = h \cdot d\varphi \quad . \tag{6}$$

This leads to

$$\frac{df}{dz} = \frac{h}{x} \qquad (7)$$

The 3-dimensional expansion of the laser beam is

$$\frac{dA}{da} = \frac{dh}{dx} \cdot \frac{h}{x} \qquad (8)$$

Equation (8) can be derived analytically. It can't be solved for the diameter d_p of the droplet. For ratios $l^* = \frac{l_d}{h} >> 1$, simplifications are possible. The distance x becomes zero and the expansion of the laser beam is symmetric to the y-axis. It can be rewritten as

$$\frac{dA}{da} = \left(\frac{dh}{dx}\right)^2 \qquad (9)$$

The derivation $\frac{dh}{dx}$ becomes

$$\left.\frac{dh}{dx}\right|_{x=0} = \frac{4l}{d_p}\left(\frac{n_1}{n_2} - 1\right) \qquad (10)$$

The ratio between the intensity in the laser beam I_0 and the measured intensity in the projection plane I_m is

$$\frac{I_0}{I_m} = \left(\frac{dh}{dx}\right)^2 = \frac{16\,l}{d_p^2}\left(\frac{n_1}{n_2} - 1\right)^2 + \frac{4\,l}{d_p}\left(\frac{n_1}{n_2} - 1\right) + 1 \qquad (11)$$

For ratios $l^* >> 1$, Eq. (11) results in

$$d_p = C\sqrt{I_m} \qquad (12)$$

with

$$C = 4l\left(\frac{n_1}{n_2} - 1\right)\frac{1}{\sqrt{I_0}} \qquad (13)$$

C is a constant and has to be evaluated by a calibration of the measuring device.

3. MEASUREMENT OF THE DROPLET VELOCITY

If the diameter of the laser beam is known, the velocity of the droplet can be calculated by

$$v_p = \frac{d_0}{t_t}\,, \qquad (14)$$

with t_t as the total time during which the droplet passes the laser beam and d_0 as the diameter of the laser beam.

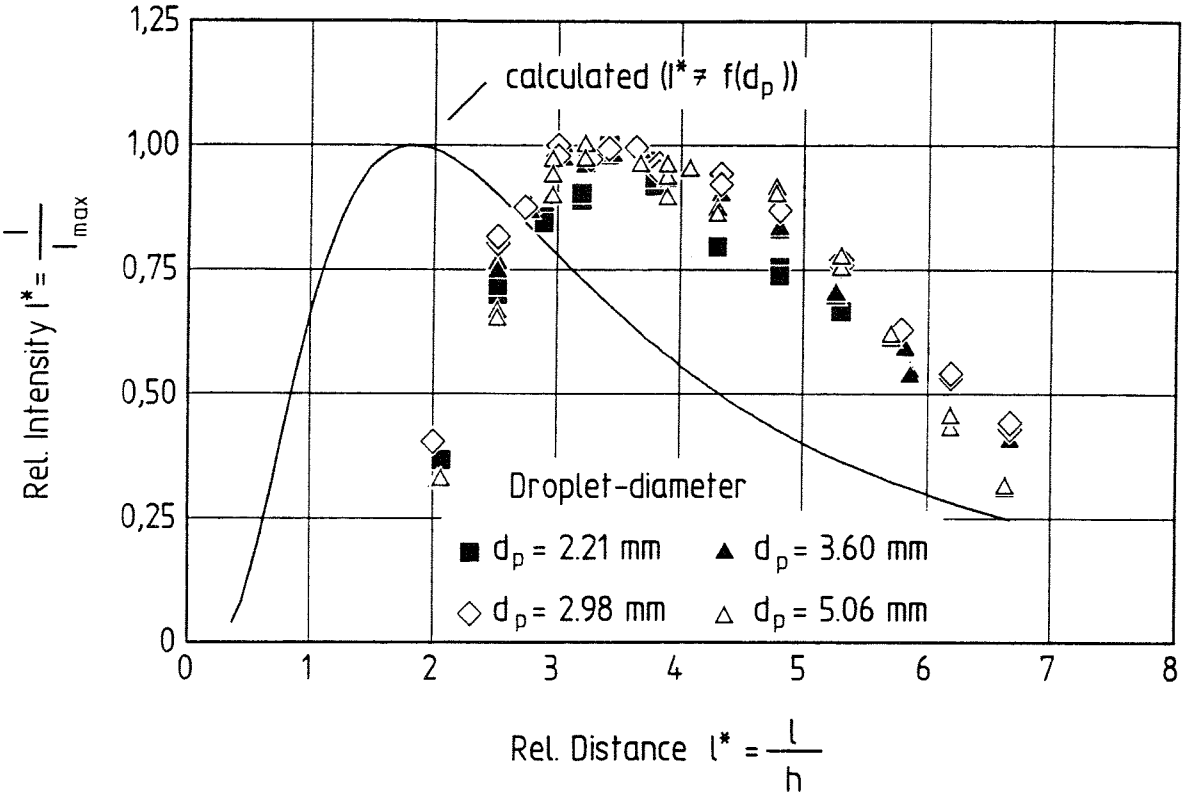

Figure 3: The influence of the length l* on the measured intensity I*.

In practice, it can't be ensured, that the droplets pass the centreline of the laser beam with the constant distance l to the photo transistor. If the droplet passes the laser beam beside the centreline, the chord length d_c of the intersection between the droplet's trajectory and the laser beam's cross sectional area is smaller than the diameter of the laser beam. The duration of the signal at the photo transistor t_t is smaller and the calculated value of the velocity v_p is higher than the real velocity. Because the intensity distribution in the cross section of the laser beam corresponds to the Gaussian distribution, the intensity decreases with increasing distance between the centreline and the trajectory of the droplet. Due to this, the measured droplet diameters are smaller than the real diameters.

The distance l between the droplet and the photo transistor has a strong influence on the measured intensity, too. It is possible to eliminate these influences by suitable arrangements.

4. ADVANCED OPTICAL ARRANGEMENT

The influence of the distance l on the intensity of the laser light at the photo transistor is shown in Fig. 3 for different droplet diameters. The related intensity $I^* = I/I_{max}$ is shown as a function of the related distance $l^* = l/h$. The measured values for different droplet diameters have a common maximum at $l^* = 3.3$. The maximum of the calculated function is at $l^* = 1.9$. The difference between the measured and the calculated values can be explained by the simplifications made with respect to the reflection of the light at the surface of the droplets. For small ratios of l^*, the fraction of reflected light increases. Due to this, the maximum of the measured values is shifted to higher values of l^*.

The influence of the distance l^* on the intensity at the photo transistor is minimal at the maximum of I^*. By adequate measures, the influence can be minimised. If the length of the laser beam is

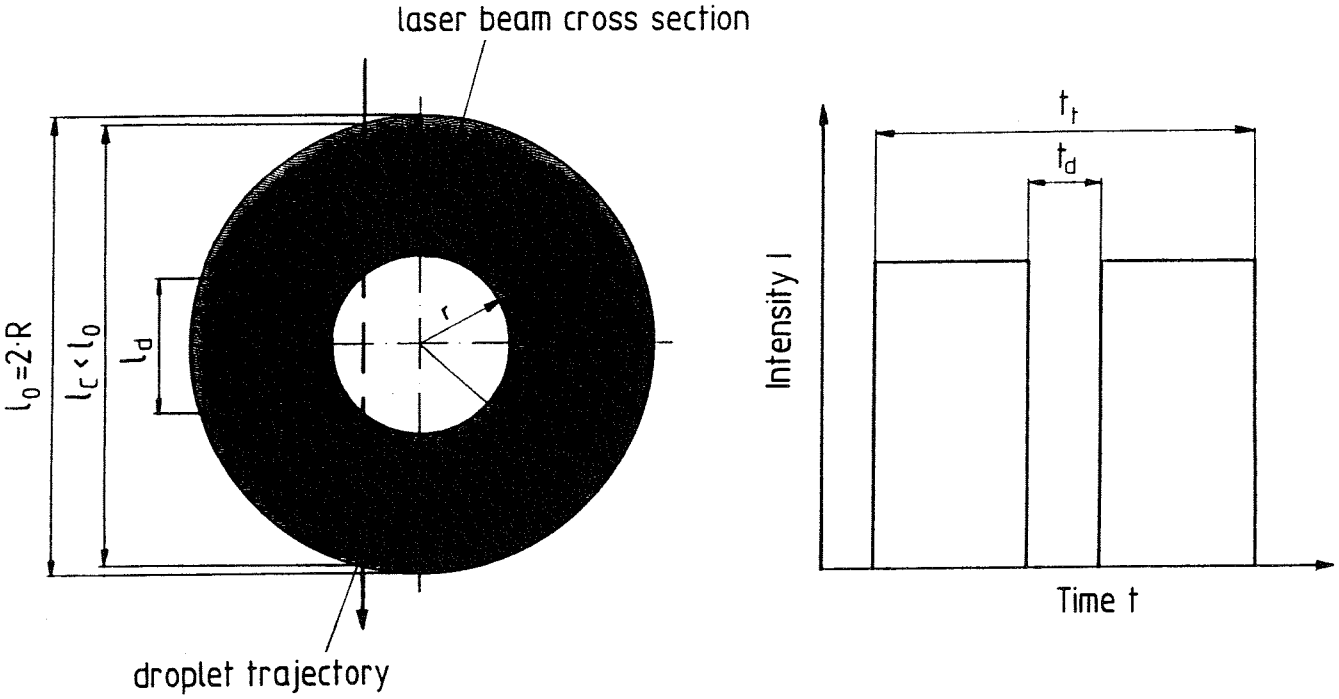

Figure 4: The geometrical relations of the cross sectional area of the tubular beam.

limited and the photo transistor is placed in the distance of $l^* = 3.3$, there is a range of I^*, in which measurements with a suitable accuracy can be conducted.

As shown above, using a normal laser beam leads to problems in measuring diameters and velocities of the droplets. For the new measuring technique, a tubular laser beam is formed by a system of lenses and a special optical aperture with a dark spot in the centre. The cross sectional area of the beam is annular and the intensity distribution is homogeneous. In Fig. 4, the cross section of the laser beam, a trajectory of a droplet through the beam and the corresponding signal at the photo transistor as a function of time are shown. The trajectory is beside the centreline of the laser beam. For the calculation of the velocity of the droplet, it is essential to know the chord length $l_c \leq l_0$. The signal at the photo transistor has two characteristic periods: The time t_t, during which the droplet passes the whole laser beam and the time t_d, during which the droplet passes the dark core of the laser beam. The ratio of the times $\frac{t_d}{t_t}$ is equal to the ratio of the lengths $\frac{l_d}{l_c}$ at the trajectory of the droplet. Here, l_d is the length of the chord through the dark core region of the laser beam. The length of the chord through the whole laser beam can be calculated by

$$l_c = 2\cdot\sqrt{\frac{\left(r^2-R^2\right)}{\left(\frac{t_d}{t_t}\right)^2-1}} \quad . \tag{15}$$

In Eq. (15), R is the radius of the whole beam and r is the radius of the dark core of the beam. The velocity of the droplet is

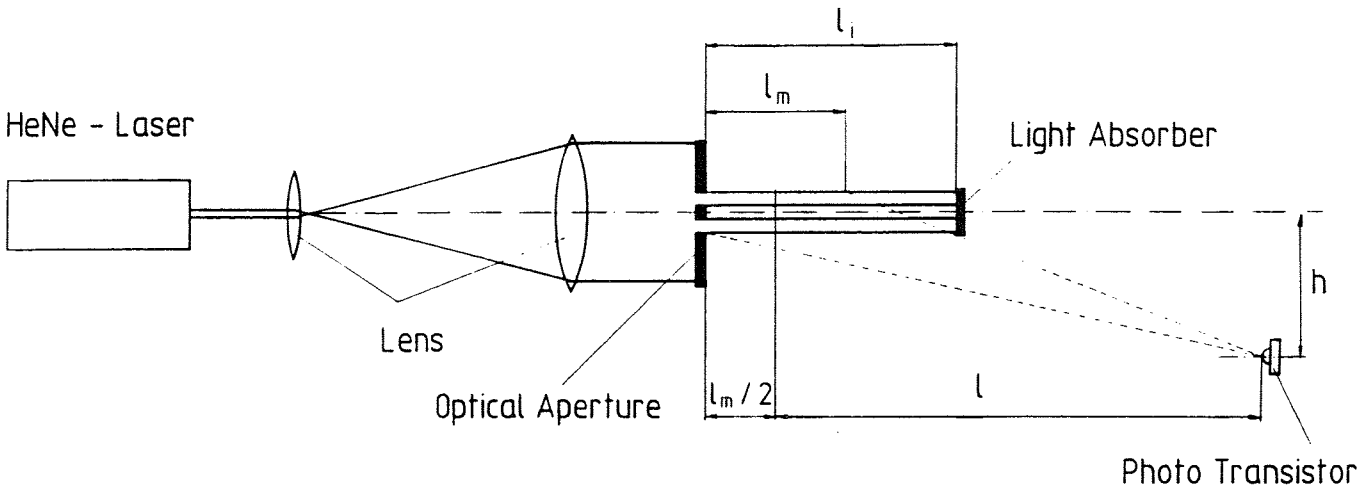

Figure 5: The experimental set-up.

$$v_p = \frac{l_e}{t_t} \quad . \tag{16}$$

Because the intensity distribution in the annular cross section of the beam is homogeneous, the measurement of the diameter of the droplet is independent of the location of the trajectory of the droplet.

The experimental set-up used in this investigations is shown on principle in Fig. 5. The light of the laser is expanded by a combination of lenses. With the optical aperture, the peripheral zones of the beam are cut off. Only the centre region of the Gaussian beam, in which the intensity is nearly constant, passes the aperture. Because of the dark spot in the middle of the aperture, the beam becomes tubular. Interrupting the beam at the distance l_i leads to a clearly defined measuring volume. The application of the photo transistor at the distance $l = 90\,mm$ and the height $h = 27\,mm$ ensures the optimal geometric configuration of $l^* = 3.3$.

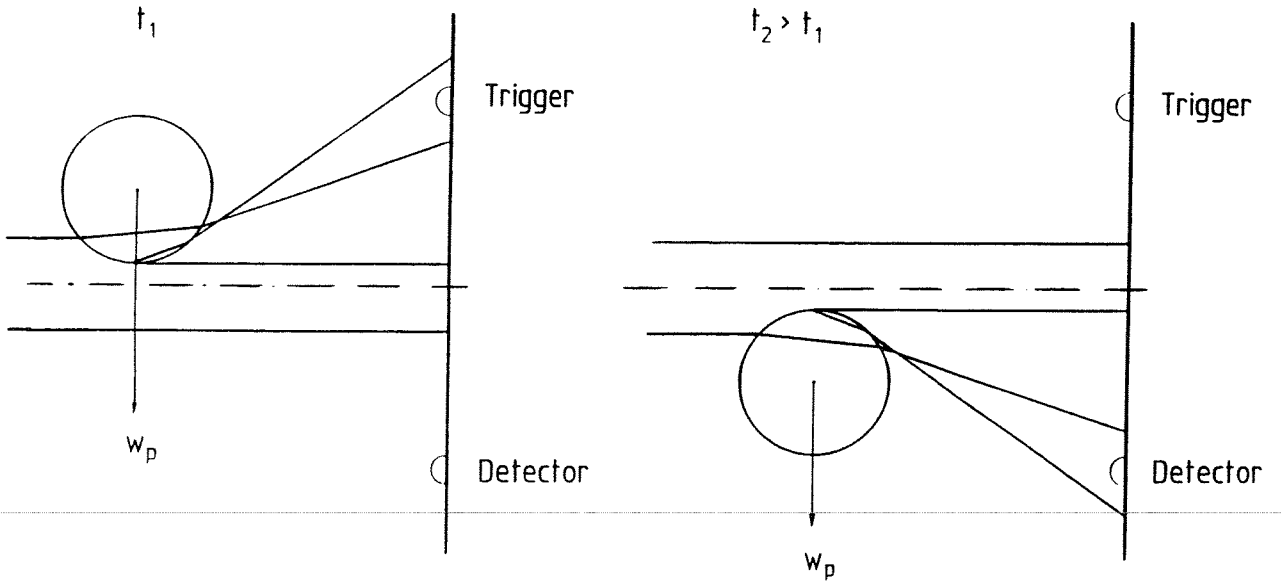

Figure 6: The configuration of the trigger and the data acquisition photo transistor.

5. DATA ACQUISITION

The duration of the signal at the photo transistor is dependent on the velocity of the droplets and the diameter of the beam. In the special case, the new measuring technique is designed for, the velocities are less than $v_p = 5$ m/s. The total time t_t is expected to be $t_t \geq 1$ ms. The acquisition of the signal is conducted by a standard A/D-converter board installed in a Personal Computer. The sampling rate is $f_s = 62.5$ kHz. The data acquisition is started by a trigger. The trigger photo transistor is mounted above the data acquisition photo transistor. The geometrical configuration is shown in Fig. 6. It can be seen, that the deflected light beam first passes the trigger photo transistor. If the intensity measured at the trigger is higher than the threshold, the data acquisition starts.

The signal measured for a droplet passing the laser beam near the centreline is shown in Fig. 7. The intensity of the laser light at the photo transistor is proportional to the voltage U measured at the photo transistor. The course of the signal is similar to a double square wave. The times t_d and t_t can be measured. The discrimination of the starting times $t_{t,s}$and $t_{d,s}$ and the ending times $t_{d,e}$ and $t_{t,e}$ is done by the calculation of the points with maximal and minimal slope. So the time measurement is independent of the intensity of the signal and due to this independent of the size of the droplets. The criteria, the course of the signal has to fulfil for a consideration, are :

- There must be a period, in which the signal is less than 25% of the maximum value. This corresponds to a droplet passing the dark core region of the laser beam.
- The ratio of the time differences $\frac{t_{d,s} - t_{t,s}}{t_{t,e} - t_{d,e}}$ must be in the range between 0.9 and 1.1. If this criterion is not fulfilled, the signal is asymmetric due to partial screening of the laser light by other droplets or the droplet is outside the measuring volume: The distance l_p between the droplet and the photo transistor is less than $(1 - \frac{l_m}{2})$.
- The ratio of the times $\frac{t_{d,s} - t_{d,e}}{t_{t,s} - t_{t,e}}$ must be less than the ratio of the radii $\frac{r}{R}$ but greater than zero.

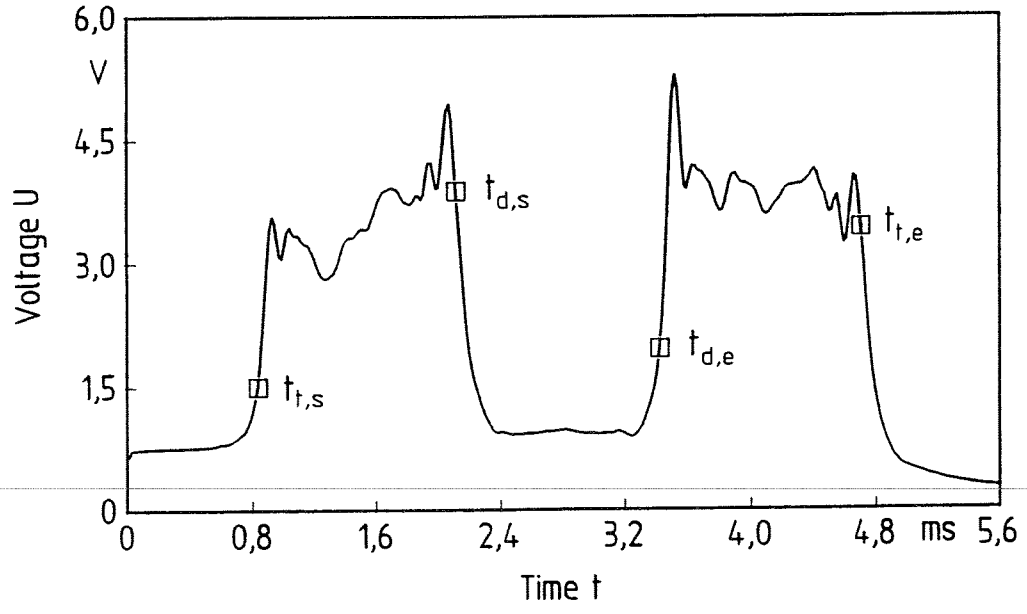

Figure 7: The signal of a droplet passing the dark core region of the laser beam.

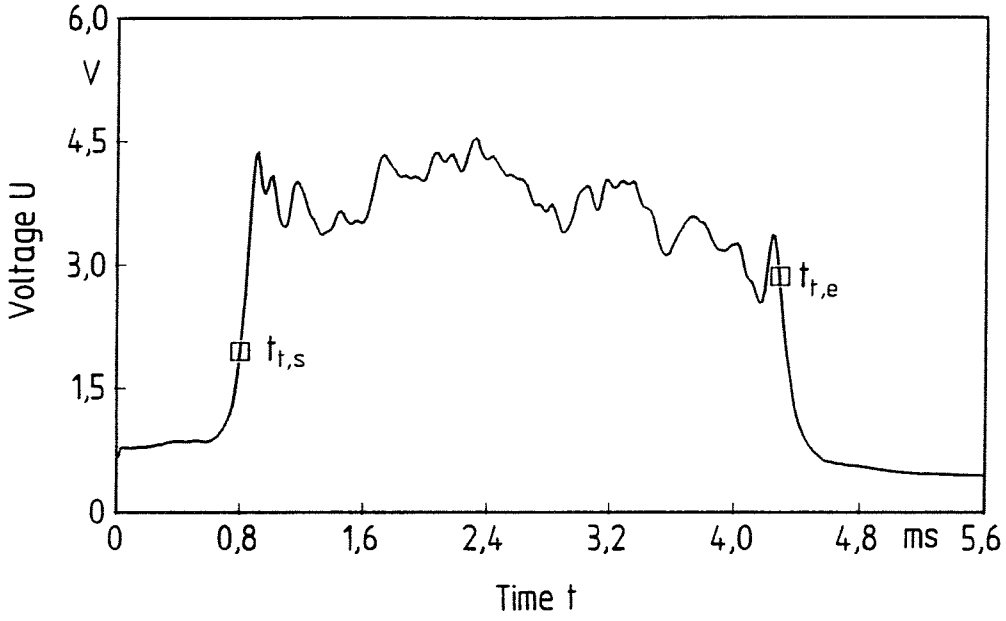

Figure 8: The signal of a droplet passing the beam beside the dark core region.

If one of these criteria is not fulfilled, the signal will not be considered to calculate the size and the velocity of the droplet.

The signal of a droplet passing the laser beam beside the dark core region is shown in Fig. 8. The course of the signal is similar to a single square wave. Already the first criterion is not fulfilled. The trajectory of the droplet is identified to be beside the dark core region of the laser beam.

For the measurement of the droplet sizes, the intensity of the signal is averaged between the times $t_{t,s}$and $t_{d,s}$ and the times $t_{d,e}$ and $t_{t,e}$.

6. EXPERIMENTAL RESULTS

To calibrate the new measuring technique, the results of the measurements of droplet diameters and droplet sizes have to be compared with reliable data. This means, a second measuring technique with a known high accuracy has to be available. Water and air are used as the two phases during the calibration of the measuring technique.

Single droplets are generated by cannulas, which can be positioned in different heights above the laser beam. The velocity of the droplets is dependent of the height of the cannulas. The cannulas are moved by a simple construction to ensure, that the trajectories of the droplets are statistical distributed across the cross section of the laser beam.

For the calibration of the droplet size measurement, the droplets are weighted. The diameter d_p of the droplet is

$$d_p = \sqrt[3]{\frac{6M_p}{\pi\rho_w}} \quad . \tag{17}$$

In Eq. (17), M_p is the mass of the droplet and ρ_w is the density of water. In Eq. (12), it has been shown, that the diameter of the droplet is proportional to the square root of the measured intensity at

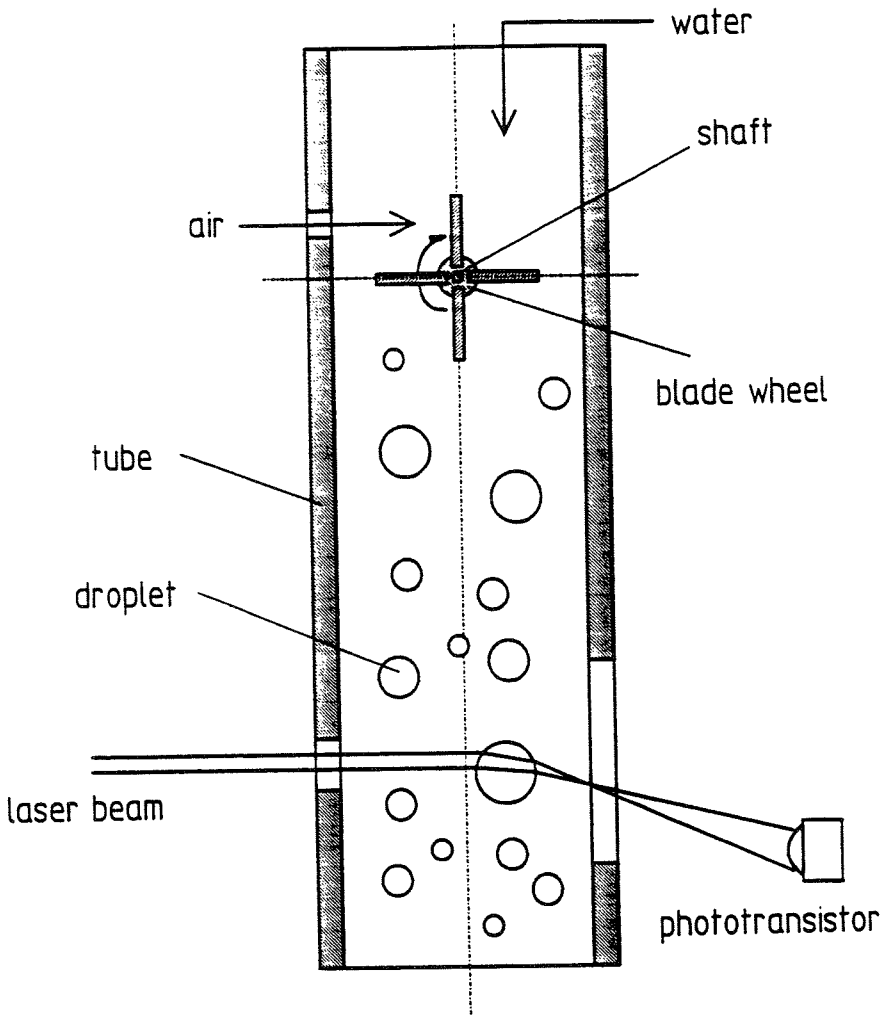

Figure 9: The device for the creation of a swarm of droplets.

the photo transistor for $l^* >> 1$. As shown above, in the experimental set-up l^* is only in the range of 3.3. Equation (12) has to be rewritten with a second calibration factor:

$$d_p = C \sqrt[E]{I_m} \quad . \tag{18}$$

In Eq. (18), the constant C and the exponent E have to be evaluated by calibration. From the calibration data it can be seen, that the exponent E is strongly dependent on the ratio l^*. The data obtained for $l^* = 3.3$ are best fitted by $E = 2.35$. The constant C has to be evaluated each time the experimental set-up has been adjusted. The maximum margin of error of the measurement of droplet sizes in the range of $1\ \text{mm} \le d_p \le 6\ \text{mm}$ has found to be less than ±8%.

It is not possible to measure the velocity of the droplets at the same time and same location with a second, reliable measuring technique. So, the instationary equation of motion has been solved for each droplet diameter and falling height used in the calibration. The maximum margin of error of the measurement of droplet velocities in the range up to $v_p = 5\ \text{m/s}$ has found to be less than ±4%.

To test the new optical measuring technique in a swarm of droplets, a simple device has been built. It is shown on principle in Fig. 9. It consists of a blade wheel which is driven by an air stream. A small amount of water is delivered on the wheel. At the circumference droplets with different sizes are built. The droplets fall down and some of them pass the measuring volume of the laser beam. In Fig. 10, the probability density of the droplet sizes is shown. The measured diameters of the droplets are in the range of $d_p = 1.5\,\text{mm}$ up to $d_p = 8.5\,\text{mm}$. The mean value is $d_p = 3.4\,\text{mm}$. The distribution of the droplet sizes is Gaussian type.

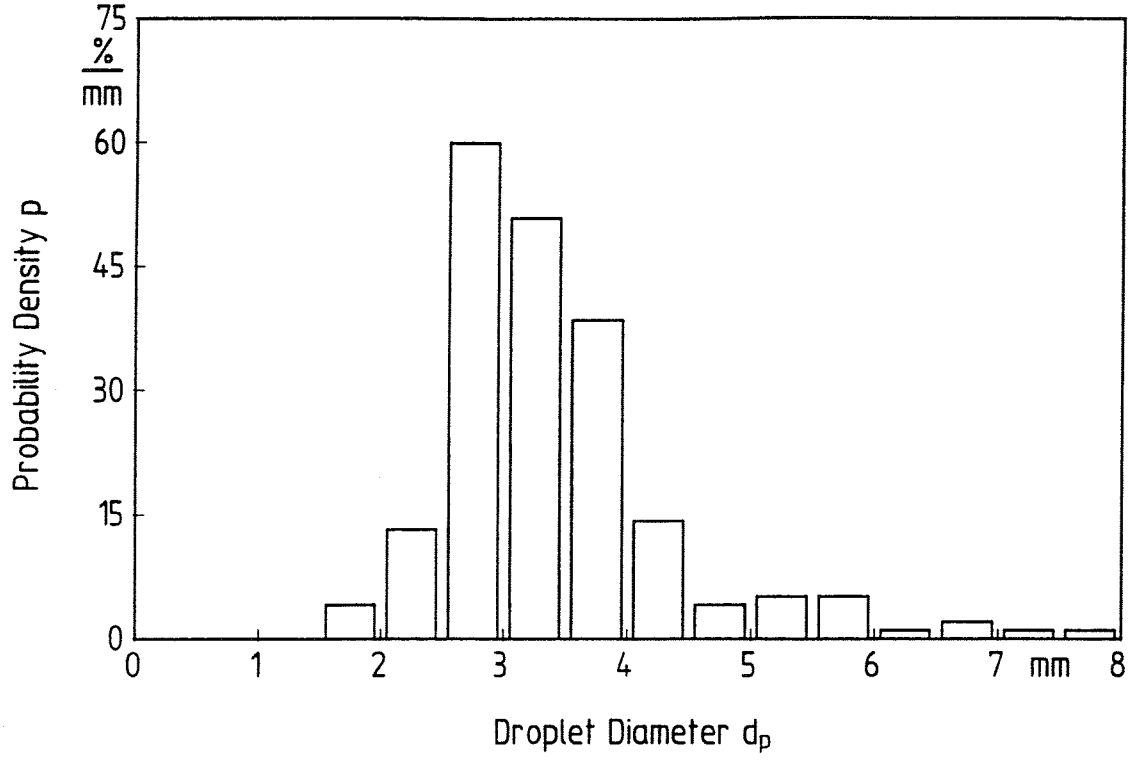

Figure 10: The probability density distribution of the droplet sizes.

The probability density of the velocity of the droplets is shown in Fig. 11. The measured velocities are in the small range of $v_p = 1.9\,m/s$ up to $v_p = 2.6\,m/s$. The mean value is $v_p = 2.15\,m/s$. The small range of the velocity of the droplets is due to the kind of droplet formation. The droplets are formed at the circumference of the blade wheel, where the velocity is nearly constant.

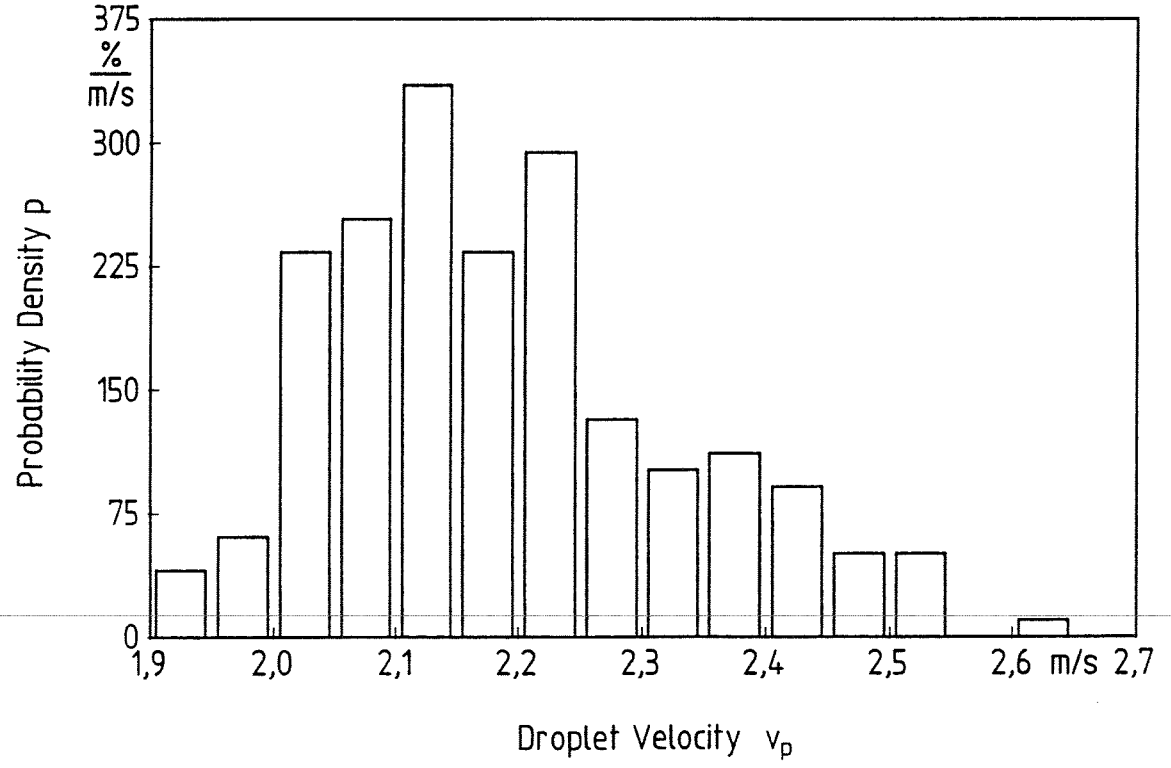

Figure 11: The probability density distribution of the droplet velocities.

7. CONCLUSIONS

A new measuring technique has been presented for the difficult task to measure droplet sizes in the range above $d_p = 1\,mm$. The simultaneous measurement of the velocity of the droplets is possible. It has been shown, that the new measuring technique is working. The main advantages are the easy set-up, the non-expansive data acquisition, the independent measurement of sizes and velocities of drops and the potentiality of the measuring technique. In a next step, the measurement of two velocity components is available by measuring the time delay of the signals at the trigger photo transistor and data acquisition photo transistor.

For a better optical accessibility, the measuring device will be miniaturised using semi conductor lasers. The length of the whole device will be in the range of less than 200 mm. Using fibre optics is the second possible step to expand the range of application.

NOMENCLATURE

a	=	area in the laser beam, m^2
A	=	area in the projection plane, m^2
C	=	constant, $m^2/\sqrt{W}$
d	=	diameter, m
E	=	constant, dimensionless
f	=	frequency, 1/s
h	=	height, m
I	=	intensity of the light, W/m^2
l	=	length, m
l*	=	length, dimensionless
n	=	refraction index, dimensionless
p	=	probability density, 1/mm (s/m)
r	=	inner radius of the beam, m
R	=	outer radius of the beam, m
t	=	time, s
v	=	velocity, m/s
x	=	x-coordinate, m
X	=	x-axis
y	=	y-coordinate, m
Y	=	y-axis
z	=	z-coordinate, m
Z	=	z-axis
α	=	angle
β	=	angle

SUBSCRIPTS

c	=	chord
d	=	dark core
e	=	end
i	=	interruption
m	=	measuring
max	=	maximum
p	=	particle
s	=	sampling

s	=	start
t	=	total
w	=	water
0	=	initial value
1	=	phase 1
2	=	phase 2

REFERENCES

[1] D. Barschdorff and D. Wetzlar: "On-Line Measurement Methods of Single Component Velocities in Two-Phase Flow Systems", in: Technology of Turbine Plant Operating with Wet Steam; BNES, London (1988).

[2] G. Hetsroni: "Handbook of Multiphase Systems", McGraw-Hill, New York (1982).

[3] S.L. Lee and S.K. Cho: "Simultaneous Measurement of Size and Two-Velocity Components of Large Droplets in a Two-Phase Flow by Laser-Doppler-Anemometry", in: Measuring Techniques in Gas-Liquid Two-Phase Flows, IUTAM Symposium Nancy/France, J.M. Delhaye and G.Cognet, Eds., Springer Berlin, p.149 (1983).

[4] M. Saffmann, "Phasen-Doppler-Methode zur optischen Partikelgrößenmessung", in: Technisches Messen 56, 7/8, p.298 (1989).

[5] K. Bauckhage, "Anwendungstechnische Aspekte zur Phasen-Doppler-Methode in der Partikelmeßtechnik", in: Technisches Messen 56, 5, p.222 (1989).

[6] R. Semiat and A.E. Dukler, "Simultaneous Measurement of Size and Velocity of Bubbles and Drops: A New Optical Technique", in: AIChE Journal 27, 1, p.148 (1981).

A NEW MEASURING SYSTEM FOR THE DETERMINATION OF LOCAL PARAMETERS OF GAS-LIQUID TWO-PHASE FLOW AND SOME APPLICATIONS

A. Schmitt and R. Loth

Fachgebiet Energietechnik und Reaktoranlagen, Technische Hochschule Darmstadt,
Petersenstraße 30, 64287 Darmstadt, Germany

ABSTRACT

To determine local parameters of gas-liquid two-phase flow (i.e. local void fraction, bubble frequency and velocity) an innovative measuring system, based on the idea of decentralized signal processing, was developed. For demonstration purposes, up to six sensors (fiber-optical probes) were applied simultaneously. Each sensor was connected to a high-performance microprocessor - a transputer - via an analog to digital converter for on-line evaluation of the sensor signal and for on-line correction of errors of measurement. Moreover, a self-adapting measuring system was realized. The new system was utilized to determine radial profiles of local parameters of gas-liquid two-phase flow in a vertically arranged sudden pipe expansion. Analysing the local phase function with methods of fractal geometry, it could be shown that gas-liquid two-phase flow exhibits a fractal character.

1. INTRODUCTION

Local parameters of gas-liquid two-phase flow, e.g. local void fraction, local bubble frequency and local bubble velocity, are very important for the improvement of two-phase flow models (two-fluid models). Local parameters are often determined with small, needle-shaped sensors, which are parts of a measuring system.

Conventional measuring systems exhibit various shortcomings. For example, they often require supplementary devices for the on-line evaluation of the obtained data. Simultaneous collection and processing of the signals of several sensors usually reduce the performance of a conventional system. As an example, the sampling frequency normally drops with the number of sensors in use. Also, on-line correction of errors of measurement is not possible but with needle-sensors in general a variety of errors are introduced. Moreover, a conventional measuring system is unable to identify a change of the operating conditions and it is not able to react adequately.

2. TRANSPUTER-BASED MEASURING SYSTEM

A measuring system, which does not exhibit the shortcomings mentioned, was newly developed [1]. For demonstration purposes several sensors were applied simultaneously. The underlying idea of the system is to equip every sensor with separate computing power in order to realize an efficient and flexible decentralized signal processing.

Therefore every sensor is associated with both, its own analog to digital converter (ADC) and its own transputer. Transputers are high-performance microprocessors, which are capable of parallel data processing due to special hard- and software features. The transputers were linked together to a network.

Figure 1 depicts the basic idea of the so-called transputer-based measuring system. In a test section "sudden expansion", exemplarily synchronous processing of the signals of six sensors is shown. The present hardware configuration of the system allows a maximum sampling frequency of 125 kHz, independent of the actual number of sensors. This frequency could be increased by using different ADCs.

3. TEST SECTION "SUDDEN EXPANSION" AND EXPERIMENTAL CONDITIONS

The new measuring system was applied to distinct gas-liquid two-phase flows of different media (air/water, steam/water and gas/liquid refrigerant). The experiments summarized in this paper primarily were conducted in an air-water loop under atmospheric conditions with a vertical test section "sudden expansion" as shown in Fig. 2. A maximum of six fiber-optical probes was in use simultaneously. The sensors comprised two types, different in the orientation of the tip (see next section).

Experiments for nine quasi-steady flow conditions (Fig. 3) are discussed here. Except flow condition E_1 the flow patterns observed agreed with those shown in the flow map by [2]. This map is based on the superficial velocities and was derived for a pipe diameter of $d^* = 0.05$ m, while in our case $d = 0.04$ m. In accordance with these authors, in the "bubble (I)"-flow regime occasionally Taylor-type bubbles were observed. Those were spaced axially very regularly and reached lengths up to $2d$.

4. FIBER-OPTICAL SENSORS AND SIGNAL PROCESSING

The measuring principle of fiber-optical sensors is based upon the behaviour of light at an interface of two media with different refractive indices (Fig. 4). It is expressed by Snell's or Descartes' law [3]; [4]. A quartz step-index fiber is led inside a steel tube through a casing. At the sensor-tip, the fiber and a capillary tube are glued together, grinded and polished. Wedge and cone tips with an angle of 90° were used. The sensor-tip shown in Fig. 4 faces the main flow direction. Such sensors are referenced as type-I, probes with their tip rectangular to that flow direction as type-II.

A gaseous medium (in the scope of that paper: air) causes a higher signal in form of an output voltage, a liquid medium (water) a lower (for details see [1]). Filming the physical situation at and around the sensor-tip with a high-speed video system served as reference for the interpretation of the signal delivered by the sensor.

In our case the sensor signal comprised two parts: The "base level" (tip fully immersed in liquid) and deviations from that level that were termed "bubble-signals", understood to hold for all kinds of bubbles. By using a single threshold technique (Fig. 5), the signal of each probe was processed to determine the following local parameters (note however that besides the single threshold technique any signal processing technique may be set up):

The local phase function [17] was obtained by comparing each digitalized signal with a software-selectable threshold value: If the signal exceeded the threshold, it was presumed that gas phase was detected, otherwise liquid phase. The local gas residence time $T_{gi}(r')$, $i = 1, 2, ..., N_b(r')$ started when the signal delivered by the sensor exceeded the threshold value for the i *th* time. It ended when the signal level fell below the threshold again. From the number of gas residence times $N_b(r')$ detected during a measurement of duration T the local bubble frequency was determined:

$$f_b(r') = N_b(r')/T. \tag{1}$$

The local void fraction is given by [5]

$$\alpha(r') = \sum_{i=1}^{N_b} T_{gi}(r')/T \ . \tag{2}$$

These local parameters can be evaluated on-line with our system.

Here not further mentioned, the local bubble velocity can also be determined from the signals of the two sensors before the expansion, using a cross-correlation technique.

The signal delivered by a fiber-optical probe was strongly influenced by the flow condition as depicted from Fig. 6, showing time-traces of the output voltage. That dependence of the sensor signal was supposed to relate on micro physical effects such as liquid films on the sensor-tip [1]; [4]. To interpret the sensor signal and to choose an appropriate threshold, calibration experiments were conducted. Based on the results of these experiments, the threshold value was placed 0.5% above the maximum value of the noise bandwidth of the base level.

5. RESULTS OF CALIBRATION EXPERIMENTS

The video system worked as reference system well for all flow conditions but those with the highest superficial gas velocity where analysing video frames was impossible because of dense bubble bulks. The main results obtained, especially for type-I sensors are (for details see [1]):

a) The fiber-optical probes used exhibit a "field of sensitivity" (also found by [6] and [7]). This field axially extended at least two tip diameters (i.e. 1 mm) in front of the tip. While the sensor signal mainly results from the phase of the medium at the surface of the tip, it can also be influenced by other effects, e.g. like the approach of a reflecting interface. In case the sensor-tip was immersed in liquid, in general a "pre-signal", due to reflection, was measured which may (as shown in Fig. 7) falsify the evaluation of local parameters.

b) Errors of measurement may also arise from other sensor-induced effects such as: the tangential "scratching" of Taylor(-type) bubbles along a type-I sensor, at radial positions near the wall; the formation of drops at the tip of a sensor type-I, which is hulled by a long Taylor bubble; the low bubble-signals itselves e.g. at flow conditions E_1 and E_2. It was found that these effects depend on the flow condition. By means of the frequency function of the signal amplitude, groups of conditions yielding the same effects could be identified.

c) For most of the flow conditions examined, typical bubble-signals were detected.

d) The increasing slope of a bubble-signal qualitatively corresponded to the slope obtained during "dewetting-experiments". In these experiments the remainder of a liquid film at the surface of the sensor-tip was seen to be able to temporarily increase the optical quality of the tip, presumably by evening out anomalies, resulting in a maximum of the rising signal slope.

6. APPLICATION OF THE TRANSPUTER-BASED MEASURING SYSTEM

To prove the performance and the flexibility of the new measuring system, the system was applied to measure local parameters of two-phase flow under various circumstances. In that paper three applications will be presented.

6.1 Measurement of Radial Profiles of the Local Void Fraction

The system was used to measure radial profiles of the local void fraction on-line, both before and after the expansion (Fig. 8; only profiles measured with type-I sensors are shown). The void-profiles in the lower part of that figure approximately are symmetrical with respect to the

centerline of the pipe and have the general form of a parabola for almost all the flow conditions considered. Only for the flow condition E_1 (finely dispersed bubble (II)), a maximum of the void-profile was measured close to the pipe wall. The profiles in the upper part of Fig. 8 measured with two different sensors (note that the superficial velocities apply to the area of the test section before the expansion) are nearly identical for a given flow condition. Thus it was deduced that the results obtained were independent of a special sensor.

The profiles presented here were discussed in detail by [1], who also shows local bubble frequency profiles. It was found that the measured profiles of local parameters in general exhibit deviations from the real situation due to errors of measurement, resulting from sensor-induced effects as previously mentioned. The determination of the local bubble velocity experimentally was also achieved. Moreover, the accuracy of the measuring system was determined. Integration of radial void-profiles yielded a mean gas mass-flux that in an optimal case was accurate in the order of a few percent.

6.2 On-line Correction of Errors of Measurement

The measuring system was used to correct on-line errors of measurement of local parameters. A measurement at flow condition E_7 is considered. From Fig. 9 radial profiles of local parameters, obtained before the expansion, are depicted. On the left part of that figure standard signal processing (single threshold technique see Section 4), was used. The local void fraction was underestimated by sensor type-I for $r' > 0.5$. On the contrary the local bubble frequency was overestimated by both sensors all over the cross-section, as was confirmed by reference measurements. The errors for the type-I sensor were mainly due to the scratching of Taylor(-type) bubbles along its tip and capillary tube. Besides, similar effects were detected for type-II sensor, falsifying the bubble frequency profile obtained with that sensor.

A (selected) modified threshold method was set up to correct on-line the errors mentioned. The underlying idea of this method is to connect all periods of the sensor signal that belong to the same bubble. The algorithm is presented in detail by [1]. Its application (right part of Fig. 9) led to a correct, uniform bubble frequency profile between 2 and 3 Hertz, independent of the sensor type. However, in correcting the local void fraction measured with the sensor of type-I, only partial progress was achieved, because a parameter to be chosen was not optimized.

For an effective correction of errors of measurement, an algorithm adapted to the flow condition (also to the sensor type) should be used. The choice of an appropriate correction algorithm could be achieved automatically by an adaptive measuring system, which identifies the flow condition before setting up the algorithm.

6.3 Adaptive Measuring System

To prove that our system can be used to form an adaptive system, a simple example was realized. An adaptive system is understood to be able to react on changing conditions that may take part during experiments, under the scope of a well-defined measuring task.

In particular, the transputer-based measuring system was programmed to determine the threshold for all fiber-optical sensors automatically. For this purpose, first the maximum of the liquid level delivered by every probe was evaluated. The threshold was then adjusted according to every maximum. So the system is able to react on a change of the liquid level value of every sensor, which may be due to damage of or deposits on the sensitive sensor-tip. This realization of an adaptive system was motivated by the experiences obtained in a large-scale experiment, where an aggressive flow medium caused erosion of many sensor-tips used, but the threshold could not be adapted during the experiment.

7. ANALYSIS WITH METHODS OF FRACTAL GEOMETRY

Data obtained with the new measuring system (and with a second, commercial system) was further evaluated with methods of fractal geometry. The term fractal geometry was coined by [8] and means "irregular or fragmented". Fractal geometry is closely related to the theory of nonlinear dynamics and only in recent years was spread to broader public (see e.g. [9]). First applications of fractal geometry to two-phase flow were reported by [10] and [11]. The former group examined with it the length of liquid slugs in horizontal two-phase flow. The latter group examined the pressure drop e.g. by evaluating fractal dimensions in phase space representation. [1] applied methods of fractal geometry to the local phase function. That local parameter was measured in the upstream part of the test section "sudden expansion" and in another pipe-test section of constant diameter (d^{**} = 0.01 m; also arranged vertically, upward air-water flow under atmospheric conditions). Analysis was conducted in physical space representation [12]; [13].

From the time trace of the local phase function a set of points "M" was chosen (in Fig. 10 that set results from the gas phase), and the box-counting method was applied. By that method the space in which the set of points is embedded (in our case a line segment) is completely covered with boxes. For each box-radius l the number $N(l, M)$ is counted, which is needed to cover the set of points. In the limit of vanishing box-radii the (infinite) set of generalized dimensions D_q [14] is defined as

$$D_q = \lim_{l \to 0} \log Z_q / \log l = \lim_{l \to 0} [1/(q-1)] \left[\log \sum_{i=1}^{N(l, M)} p_i^q(l) \right] / \log l, \; q \neq 1. \tag{4}$$

The probabilities $p_i(l)$ are obtained from

$$p_i(l) = n_i / n_M, \tag{5}$$

n_M being the total number of the elements of the set M and n_i the number of points covered by the i *th* box.

Each realized flow condition (Table 1) corresponded to another flow regime. The flow conditions in this table (C corresponding to the constant diameter pipe) are sorted from left to right with respect to a rising local void fraction. This local parameter, like the local phase function, was measured in the center of the test sections. The volume flux of the phases mostly was much better than ±2%. For each flow condition, at least 8000 bubble-signals were collected and appropriately corrected.

Figure 11 illustrates the results of the box-counting method for flow condition E_7. Two distinct regions can be identified: The interval $\log l \in [1, 4.5]$, in which the scaling-behaviour clearly depends on the parameter q, and the subsequent interval (which extends to $\log l \approx 7$ not shown in the figure) showing no such dependence. In the latter, the gradient common to all curves is one. This means that e.g. in lapses of time twice as long, the gas phase is detected twice as often. At flow condition E_7, $10^{4.5}$ samples equal about 4 seconds.

A scaling behaviour depending on the parameter q is typical for (multi-) fractals. For all flow conditions examined, these regions comprise at least two decades on the abscissa. The time trace of the local phase function, evaluated with respect to the gas phase, for the flow conditions investigated thus can be considered being a fractal. The same holds for its inverse, i.e. if instead of the gas phase the liquid phase is utilized. Because of the embedding-theorem of nonlinear dynamics [15], the (vertical) two-phase flows discussed are considered to be fractals. With the results of [11] (horizontal two-phase flow) this is assumed to hold for two-phase flow generally.

The generalized dimensions D_q were evaluated from the gradient of the curves $\log Z_q$ versus $\log l$ within subdomains of the regions showing fractal-like behaviour. Finally, the so-called D_q-curves were obtained by plotting the generalized dimensions D_q vs q (Fig. 12). For each of the

flow conditions examined, a distinct D_q-curve results. Particularly, the value of the fractal dimension D_0 varies with flow condition and thus for different flow patterns. With table 1 it is evident that a higher value of the fractal dimension correlates with a higher value of the local void fraction.

A two-phase flow whose D_q-curve has been derived, may be modelled by a simple multi-fractal of known iteration rule, as it was reported by [16] and [13] for the rate of dissipation of turbulent kinetic energy. Perhaps in the long range it is possible to develop new theoretical models based on fractal geometry. [10] gave an example in describing the distribution of slug lengths.

8. CONCLUSION

The newly developed measuring system proved to be well suited for the determination of local parameters of gas-liquid two-phase flow. Moreover, the new system is independent of the type of sensors used and of the number of sensors. Also it is flexible in applying different methods of signal processing. The system may be configured to fulfill best the needs of a measuring task. The innovative idea of the transputer-based measuring system thus provides a flexible, efficient tool for further application.

The results obtained with the methods of fractal geometry indicate that the generalized dimensions (which were evaluated in physical space representation), especially the fractal dimension D_0, may contribute to the characterization of flow conditions and the related flow pattern. Additional examinations with methods of fractal geometry and nonlinear dynamics should be conducted, to provide a broader data base. In particular it should be examined, whether an intrinsic time-scale of two-phase flow is expressed by that box-radius where the curves log Z_q versus log l no longer depend on the parameter q (Fig. 11).

ACKNOWLEDGEMENT

This investigation was supported by the "Bundesminister für Forschung und Technologie" through research project No. 1 500 885.

REFERENCES

[1] Schmitt, A., "Untersuchungen zur Bestimmung lokaler Parameter von Flüssigkeits-Gas-Zweiphasenströmungen mit einer neuentwickelten Meßkette", Dissertation TH Darmstadt (to be published 1994).

[2] Taitel Y., Bornea D. and Dukler A. E., "Modelling Flow Pattern Transitions for Steady Upward Gas-Liquid Flow in Vertical Tubes", in: AIChE Journal 26, No. 3, pp. 345 - 354 (1980).

[3] Galaup J.-P. and Delhaye J.-M., "Utilisation de sondes optiques miniatures en écoulement diphasique gaz-liquide", in: la houille blanche 1, pp. 17 - 29 (1976).

[4] Abuaf N., Jones O. C. and Zimmer G. A., "Optical probe for local void fraction and interface velocity measurements", in: Rev. Sci. Instrum. 49, No. 8, pp. 1090 - 1094 (1978).

[5] Galaup J.-P., "Contribution to the study of methods for measuring two-phase flow", Diss. Scientific and Medical University of Grenoble and National Polytechnic Institute of Grenoble (1975).

[6] Hinata, S., "A Study on the Measurement of the Local Void Fraction by the Optical Fiber Glass Probe", in: Bulletin of JSME 15, pp. 1228 - 1235 (1972).

[7] Cartellier A., "Optical Probes for local void fraction measurements: Characterization of performance", in: Rev. Sci. Instrum. 61, No. 2, pp. 874 - 886 (1990).

[8] Mandelbrot, B. B.: "Die fraktale Geometrie der Natur", Birkhäuser-Verlag, Basel, Boston (1987).

[9] Takayasu, H.: "Fractals in the physical sciences", Univ. Press, Manchester (1989).

[10] Saether, G., Bendiksen, K., Müller, J. and Froland, E., "The Fractal Statistics of Liquid Slug Lengths", in: Int. J. Multiphase Flow 16, pp. 1117 - 1126 (1990).

[11] Franca, F., Acikgoz, M., Lahey R. T. Jr. and Clausse, A., "The Use of Fractal Techniques for Flow Regime Identification", in: Int. J. Multiphase Flow 17, pp. 445 - 522 (1991).

[12] Prasad, R. R., Meneveau, C. and Sreenivasan, K. R., "Multifractal Nature of the Dissipation Field of Passive Scalars in Fully Turbulent Flows", in: Phys. Rev. Lett. 61, No. 1, pp. 75 - 77 (1988).

[13] Sreenivasan, K. R., "Fractals and Multifractals in Fluid Turbulence", in: Annu. Rev. Fluid Mech. 23, pp. 539 - 600 (1991).

[14] Procaccia, I., "The Characterization of Fractal Measures as Interwoven Sets of Singularities: Global Universality at the Transition to Chaos", in: Dimensions and Entropies in Chaotic Systems, edited by G. Meyer-Kress, Springer-Verlag, Berlin (1989).

[15] Lauterborn, W. and Parlitz, U., "Methods of chaos physics and their application to acoustics", in: J. Acoust. Soc. Am. 84 (6), pp. 1975 - 1993 (1988).

[16] Meneveau, C. and Sreenivasan, K. R., "Simple Multifractal Cascade Model for Fully Developed Turbulence", in: Phys. Rev. Lett. 59, No. 13, pp. 1424 - 1427 (1987).

[17] Delhaye, J.-M.: "Contribution à l´étude des écoulements diphasiques eau-air et eau-vapeur", Thèses, Université de Grenoble (1970).

DESCRIPTION OF THE FLOW CONDITIONS USED IN THE TESTS

Table I

Flow condition	E_1	E_7	C	E_3
diameter [m]	0.04	0.04	0.01	0.04
u_{sg} [m/s]	0.02	0.02	0.08	4.0
u_{sl} [m/s]	1.3	0.002	0.04	1.5
flow pattern	finely dispersed bubble (II)	bubble (I)	only Taylor bubbles	churn (IV)
local void fraction α	0.01	0.1	0.5	0.7
fractal dimension D_0	0.2	0.4	0.82	0.94

FIGURES

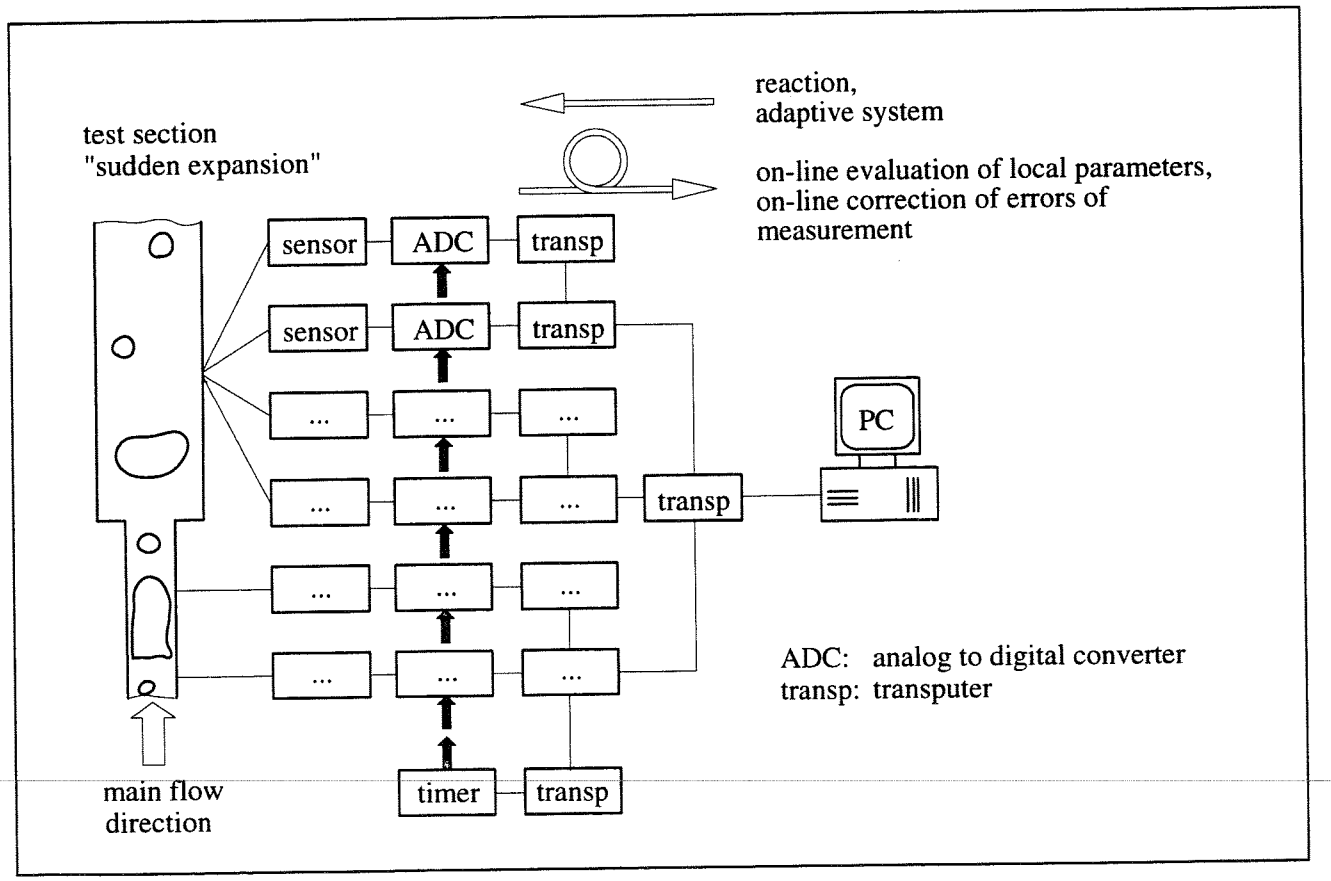

Fig. 1 Transputer-based measuring system

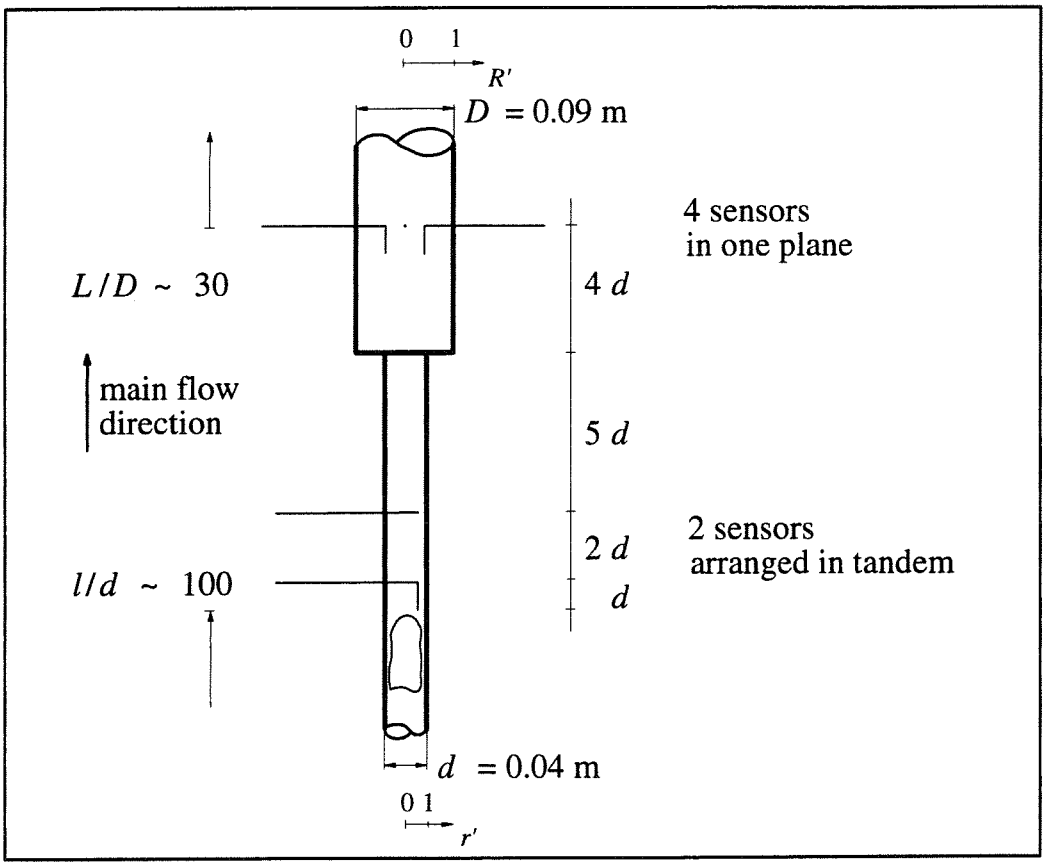

Fig. 2 Test section "sudden expansion"

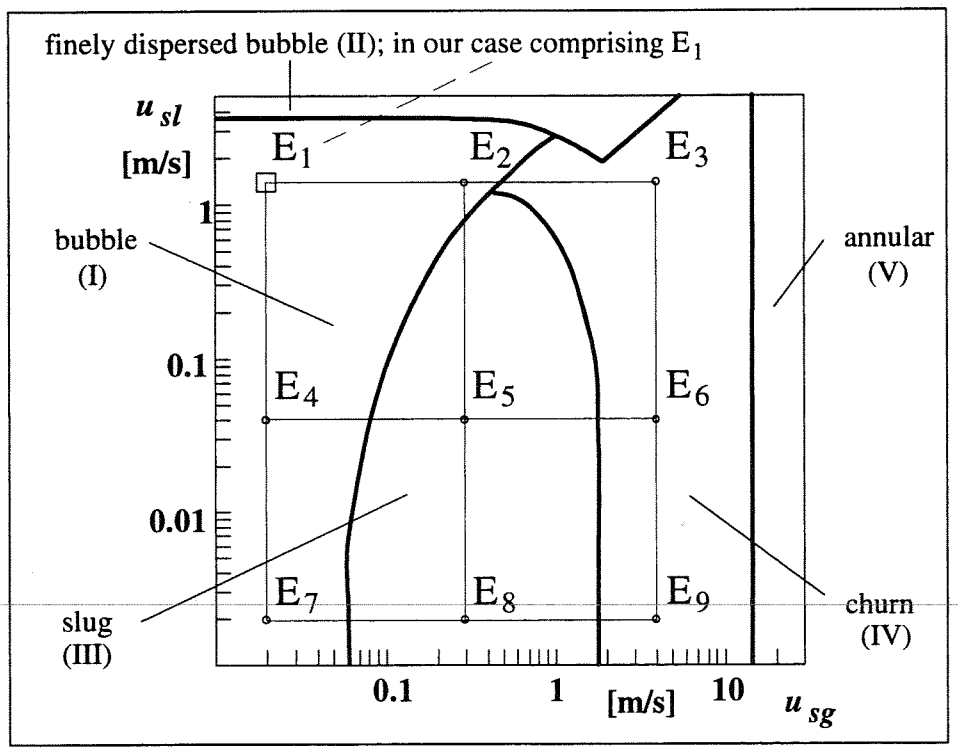

Fig. 3 Flow map for vertical air-water two-phase flow under atmospheric conditions [2]; applied to the entrance of the test section "sudden expansion"

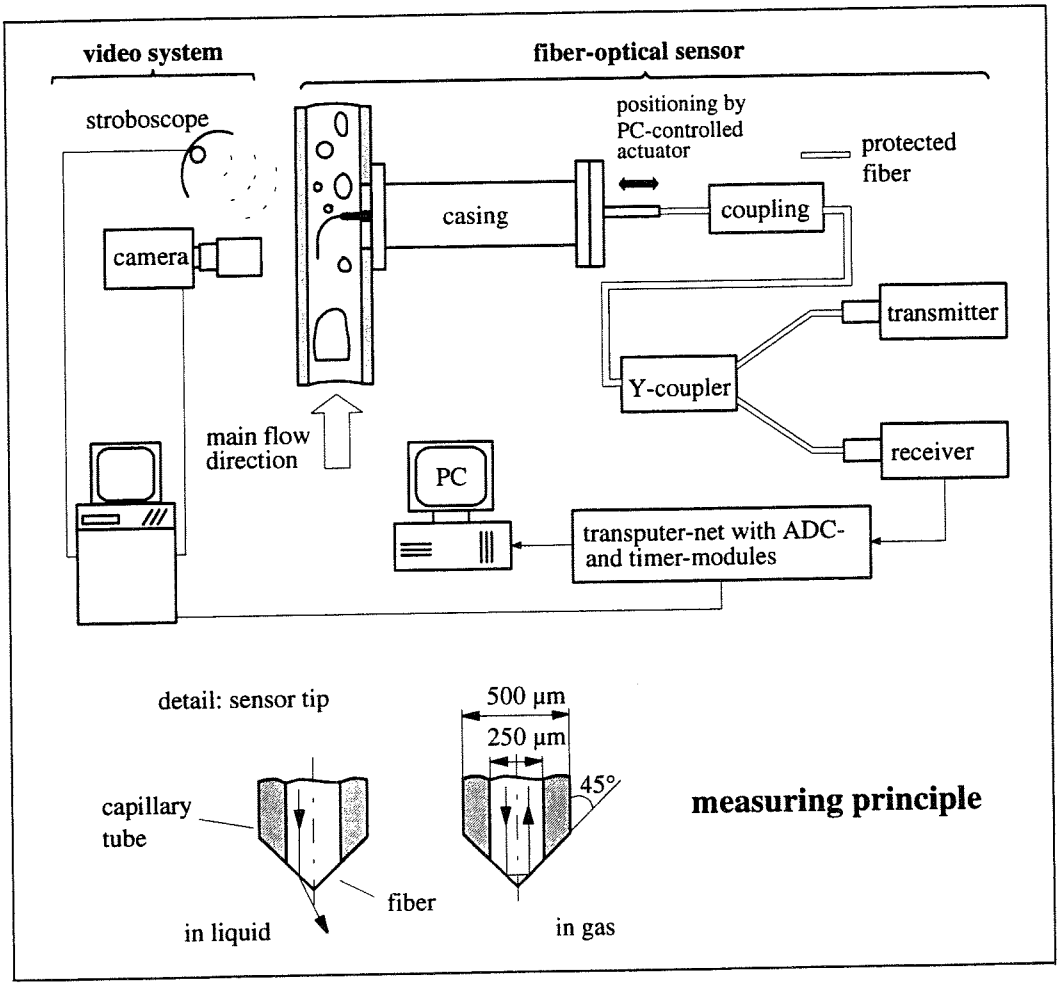

Fig. 4 Measuring technique

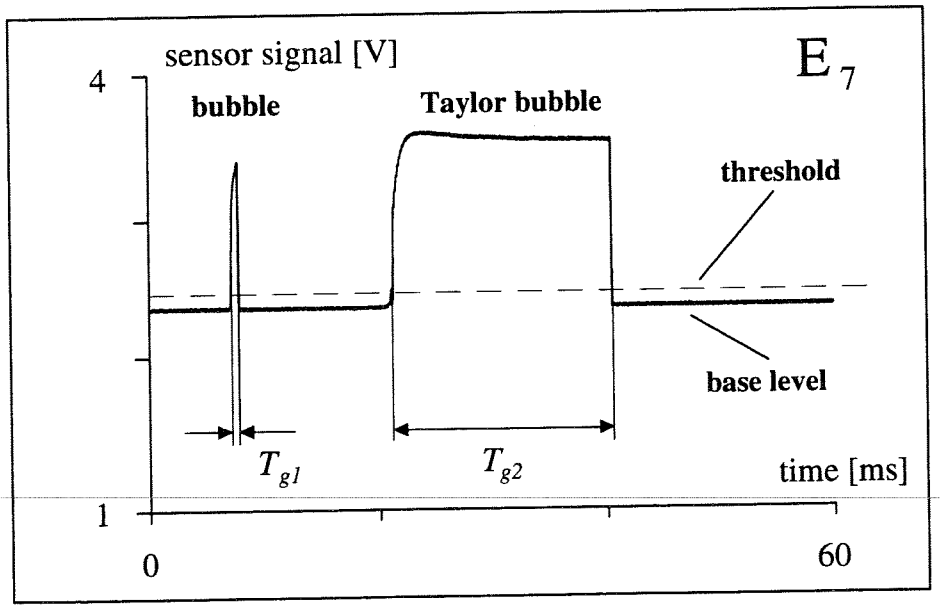

Fig. 5 Signal processing by a single threshold method

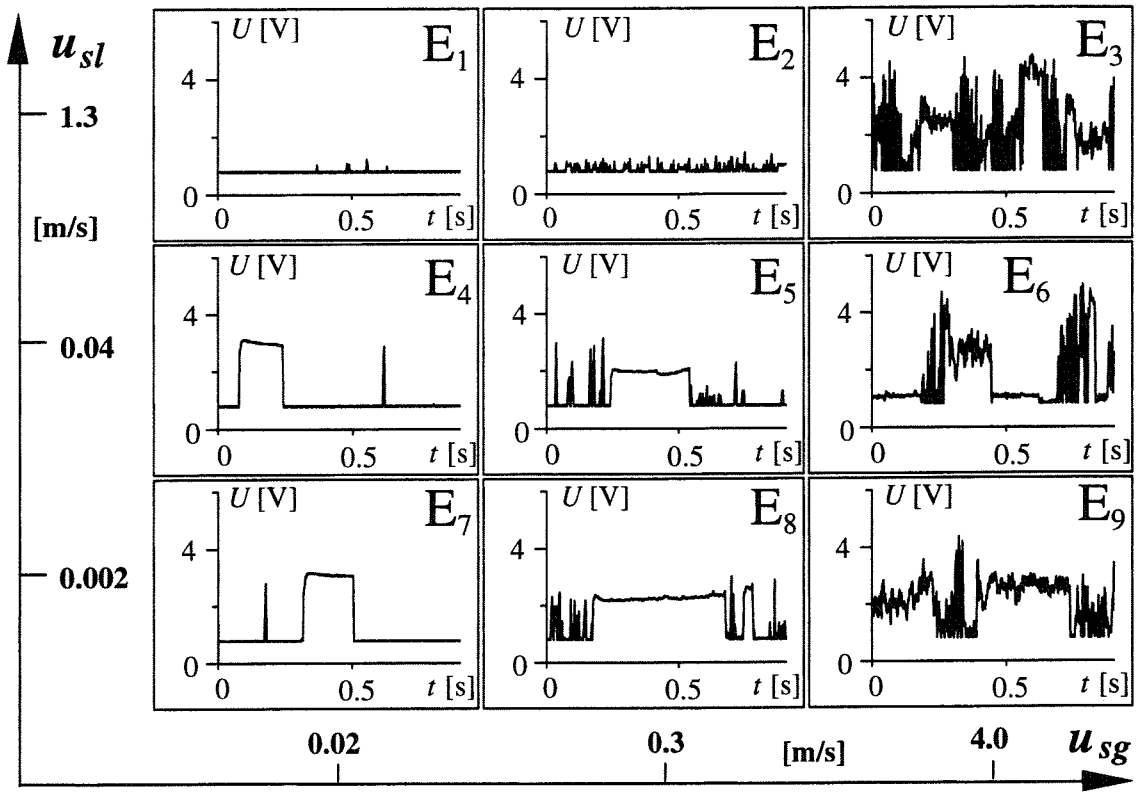

Fig. 6 Influence of the flow condition on the sensor signal (type-I sensor, $r' = 0$)

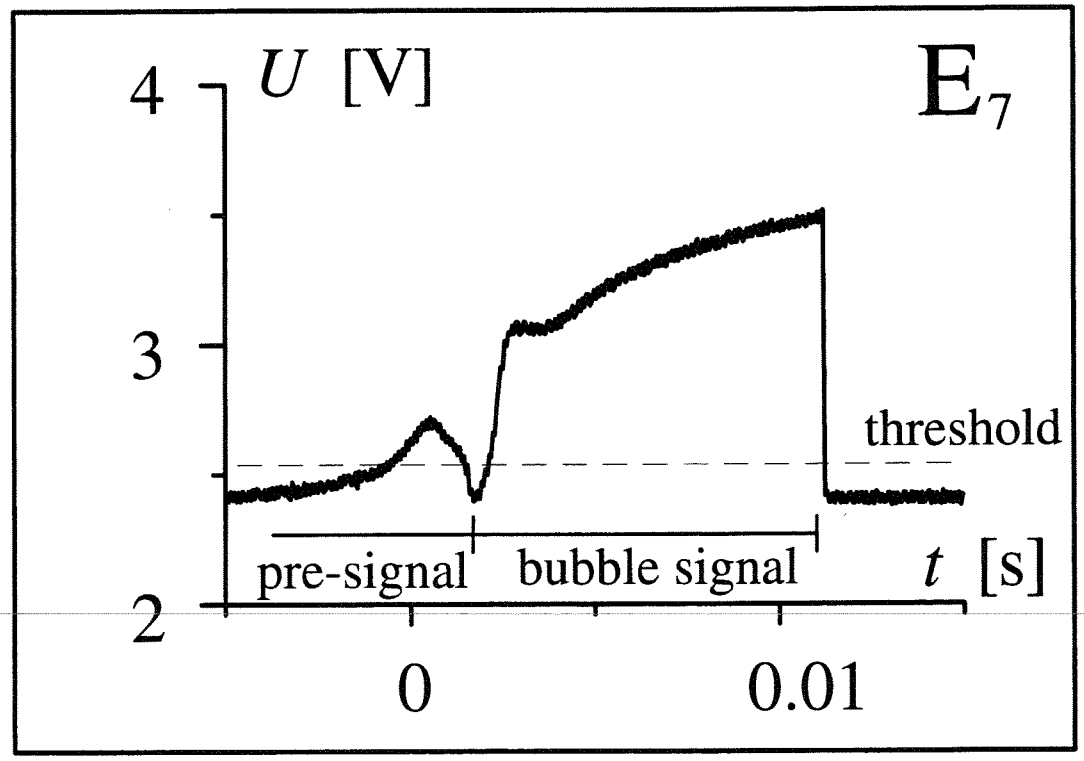

Fig. 7 Pre-signal (extraordinarily high for demonstration purposes)

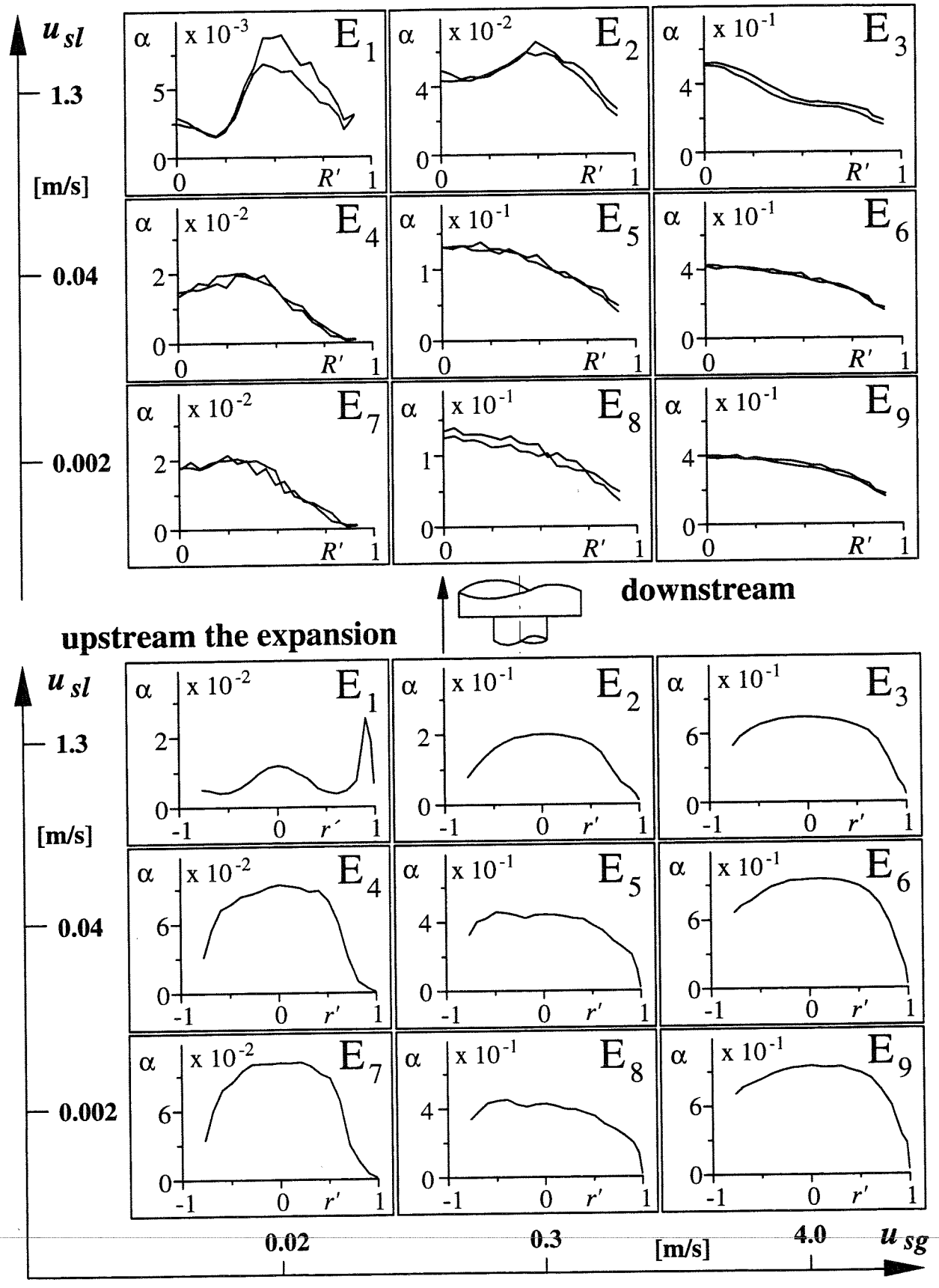

Fig. 8 Local void fraction in the test section "sudden expansion" (radial positions upstream the expansion restricted to $r' > -0.8$ to avoid right angle type-I sensor touching the wall)

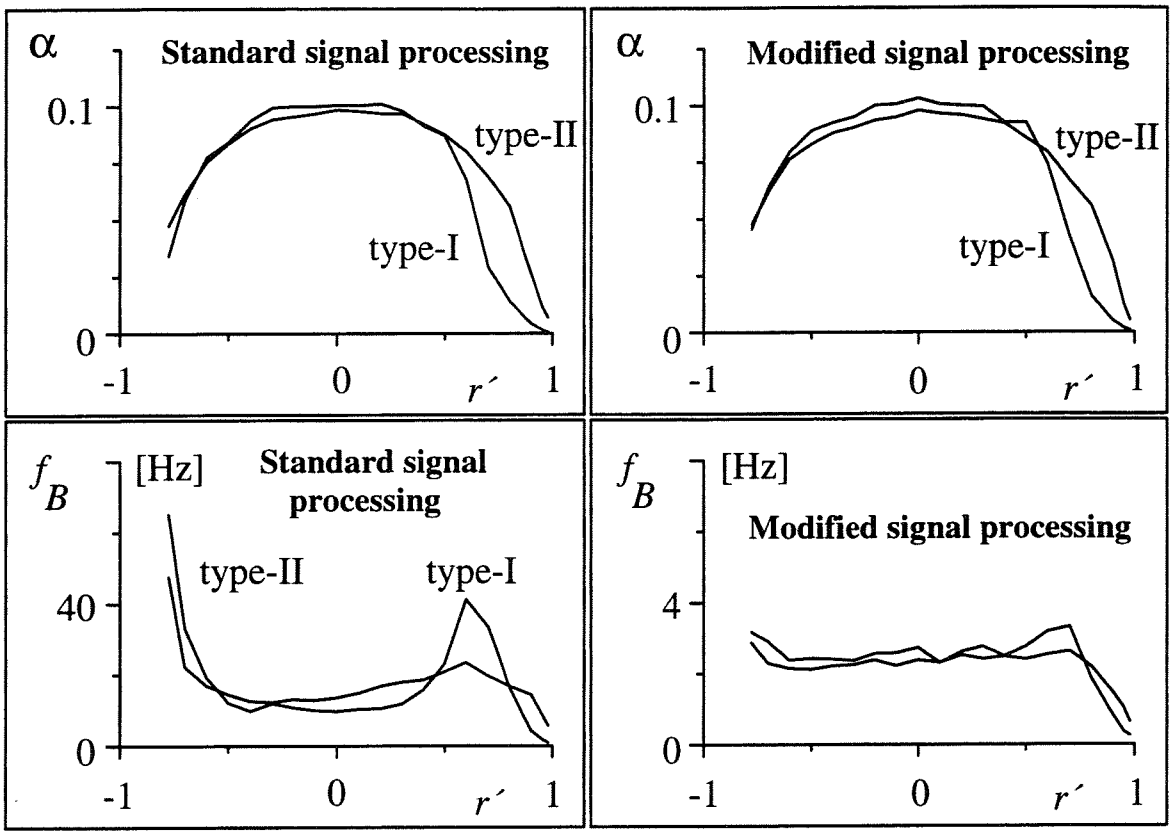

Fig. 9 On-line correction of errors of measurement by modified signal processing; flow condition E7

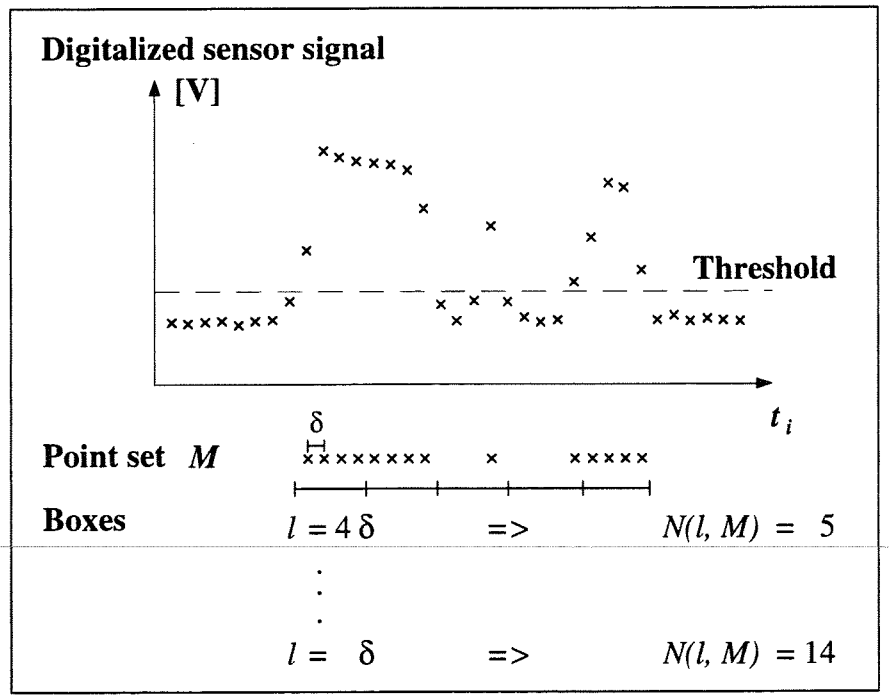

Fig. 10 Box-counting method, applied to the time-trace of the local phase function (the gas phase evaluated)

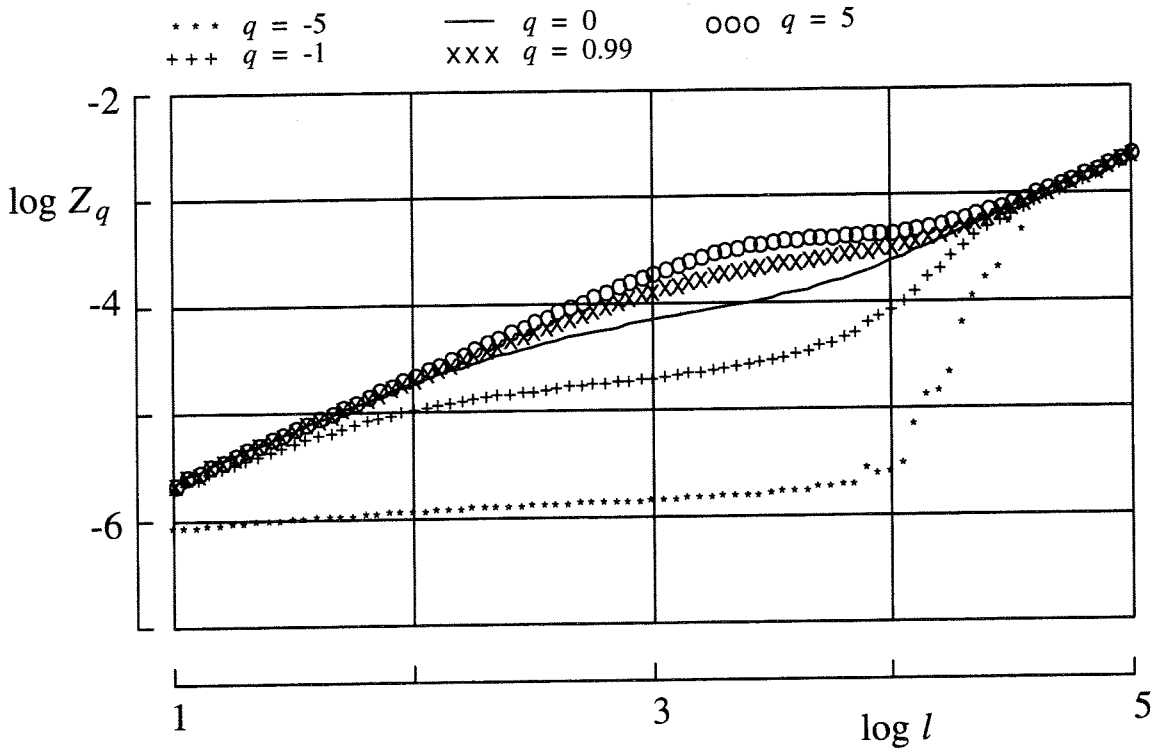

Fig. 11 Results of box-counting for flow condition E_7 (the gas phase evaluated)

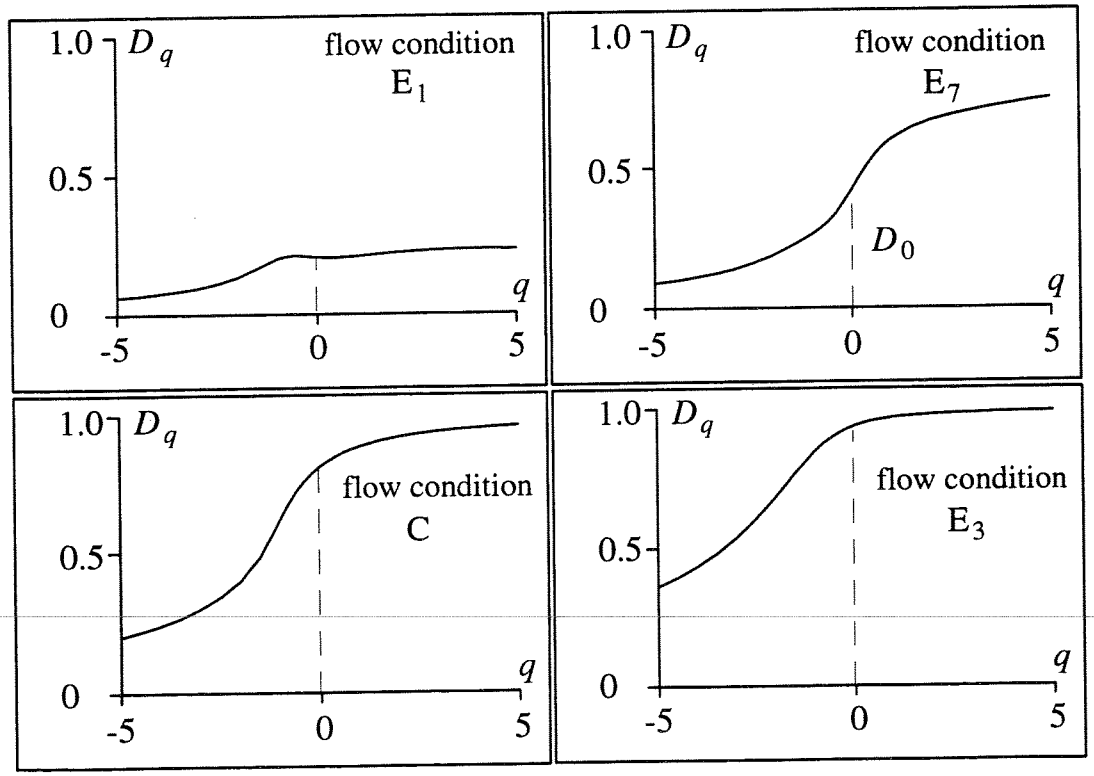

Fig. 12 Generalized dimensions (D_q-curves)

HOLOGRAPHIC MEASURING METHODS APPLIED TO TWO-PHASE FLOW

F. Mayinger, P. Gebhard

TU München, Lehrstuhl A für Thermodynamik, 80290 München

ABSTRACT

In contrast to photography by which only the two-dimensional irradiance distribution of an object is recorded, holography allows the recording and reconstruction not only of the amplitude but also of the phase distribution of the wave-fronts. Since approximately twenty years this image-forming method has been in use, which found admission to measuring techniques in heat and mass transfer and two-phase flow in the last ten years. The holography uses two-dimensional registration tools, namely photographic plates, from which three-dimensional information can be reconstructed. This has special advantages in studies of transient two-phase flow. Holography combined with the well-known interferometry using the phase-shift of the light-wave allows the registration of temperature and concentration fields, and became a very valuable tool in heat and mass transfer. After a short discussion of the basic optical set-ups Examples of measurements taken in two-phase flow with condensing bubbles demonstrate the practical application.

The pulsed laser holography represents one of the more suitable non invasive measurements methods for the study of the injection of liquids into a transparent environment. With one single hologram, taken in a very short time (about 30 ns), it is possible to record – to freeze – the three dimensional scene of what is happening in the control volume for later analysis. The method can be applied in the range of drop sizes from 20 μm up to some millimeters. From this holograms the shape of the spray, the spray angle, the droplet size and the distribution can be evaluated.

By taking double pulsed holograms two sucessive scences of the spray are recorded on the same holographic plate at an pulse interval of 0.2 to 0.8 ms. This kind of holograms are used to determine the drop velocities in value and direction. The large amount of information contained in these holograms is evaluated by digital image processing.

1. INTRODUCTION

Optical methods have many advantages over other measuring techniques. They are non-invasive and do not interact with the material to be investigated and by this not affecting the process under study. Their instant signals make them specially suited to transient situations provided that the registration method is quick enough and has a high sampling frequency. Furthermore, during the measurement with most optical methods it is possible to visualize the process in the test section on-line. Increasing possibilities of computer-aided data processing have caused a new revival of optical techniques in many areas of mechanical and chemical engineering. For a description of complicated phenomena in fluid dynamics or in transfer processes by a computer program a detailed insight with high local and temporal resolution into the thermo- and fluiddynamic situations is necessary. Here optical measuring methods deliver comprehensive and valuable information.

These techniques have a long tradition in heat transfer but their application to two-phase flow started much later.

Optical methods are using changes of light waves as sensoric signals, which are due to interaction between the light and the material. Such changes and interaction consequences

can be attenuation, scattering, deflection or reflection. Depending on the mode of registration we distinguish between image-forming and non-image-forming methods. The latter ones allow only a spotwise record of the events and the first one is registering usually a two-dimensional picture of situations or processes on a surface or in a volume as well-known from photography. Since approximately twenty years a new image-forming method is in use, the holography, which found admission to measuring techniques in heat and mass transfer and two-phase flow in the last ten years. This holography is using two-dimensional registration tools, namely photographic plates, from which however three-dimensional information can be reconstructed. This has special advantages for studies of transient two-phase flow.
Holography combined with the well-known interferometry using the phase-shift of the light-wave allows the registration of temperature- and concentration fields, and by this became a very valuable tool in heat and mass transfer.
From the spotwise working methods the Phase-Doppler-Anemometry, a modification of the Laser-Doppler-Anemometry is best known from the literature for two-phase flow application in dispersed flow. Mie-scattering is another method used in two-phase flow for example to detect spray characteristics.
It is not possible to present all optical methods being used in heat transfer and two-phase flow within a given time and a limited space. Even the concentration of such a survey on optical methods being applicable to transient conditions would cover a wide field of different techniques. Therefore, the author apologises for restricting this presentation on optical methods with which he has a longer experience and to which he contributed to their development to a certain extent.

2. HIGH-SPEED HOLOGRAPHY

In 1949 Gabor /1/ invented a new optical recording technique which he called "holography". In contrast to photography by which only the two-dimensional irradiance distribution of an object is recorded, holography allows the recording and reconstruction not only of the amplitude but also of the phase distribution of the wave-fronts. Making use of this unique property, completely new interference methods could be developed. As holography demands a highly coherent light source it can be only performed by using a laser.
The general theory of holography is very comprehensive and for a detailed description one must refer to the literature /2-4/. Here only the principals necessary for understanding the holographic measurement techniques can be mentioned. In fig. 1 the holographic two-step image-forming process of recording and reconstructing of an arbitrary wave-front is illustrated.
The object is illuminated by a monochromatic light source and the reflected, scattered light falls directly onto a photographic plate. This object wave usually has a very complicated wave-front. According to the principal of Huygens one can, however, regard it to be the superposition of many elementory spherical waves. In order to simplify the matter, only one wave is drawn in fig. 1. This wave is superimposed by a second one called "reference wave". If both waves are mutually coherent they will form a stable interference pattern when they meet on the photographic plate. This system of fringes can be recorded on the photographic emulsion. After the chemical processing of the plate –in a developing bath and in a fixer–, it is called "hologram". The amplitude is recorded in the form of different contrast of the fringes and the phase in the spatial variations of the pattern.

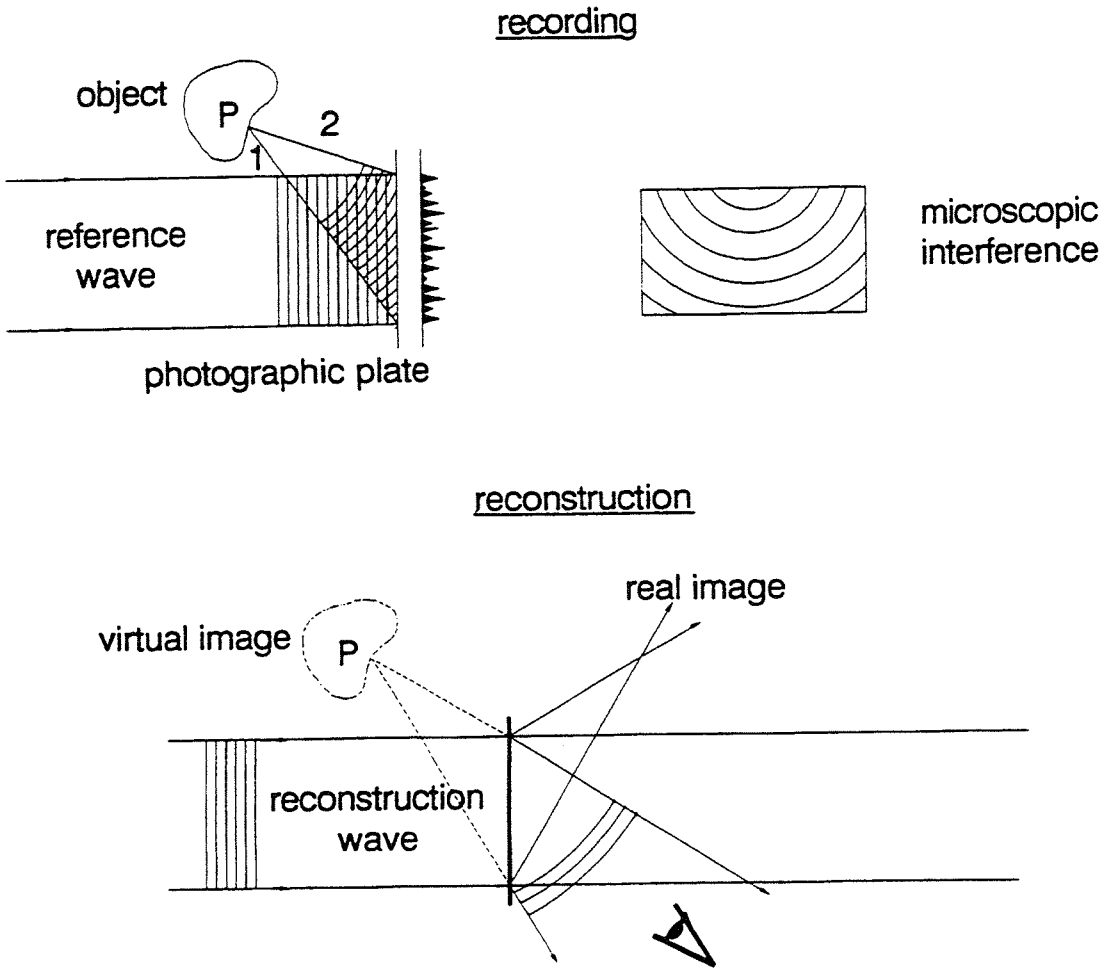

Fig. 1: Holographic two-step image forming process

If the plate is subsequently illuminated by a light beam similar to the original reference wave the microscopic pattern acts like a diffraction grating with variable grating constant. The light transmitted consists of a zero-order wave, travelling in the direction of the reconstructing beam plus two first-order waves. One of these first-order waves travels in the same direction as the original object wave and has the same amplitude and phase-distribution. Thus a virtual image is obtained. The other wave goes in the opposite direction and creates a real image of the object. The virtual image can be looked at with the naked eye and the real image can be studied with reconstruction devices for example with a microscope.

This holographic technique can be used instead of the photography for example for recording a swarm of droplets produced in an injection nozzle. The holograhic set-up for such a study is shown in fig. 2.

It consists of a pulsed ruby laser emitting pulses of a period of 30 ns and a lens- and mirror-system for expanding, dividing and guiding the laser beam through the measuring object and onto the holographic plate. The laser beam is first expanded by means of the lens **AL** and then divided in the beam splitter **ST** to produce the object beam and

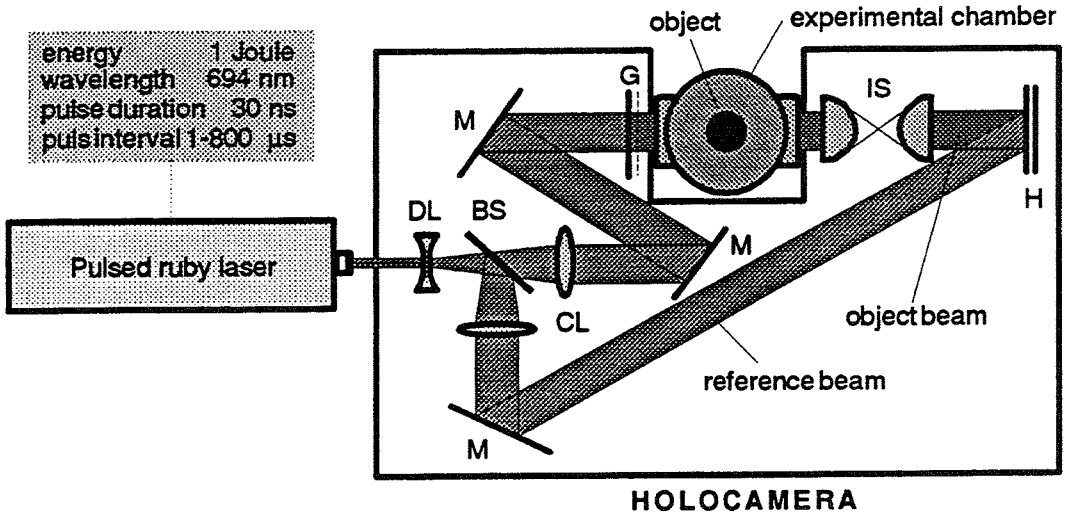

Fig. 2: Optical arrangement for the recording of pulsed laser holograms /6/

the reference beam. The object beam travels via a collecting lens, two mirrors and a screen through the object - in this case the spray coming out of a nozzle - and passes after the object an imaging lens before it falls onto the holographic plate. There it is superimposed by the reference wave which is splitted off by the beam splitter **ST** and falls via the collecting lens **SL** and a mirror onto the photographic plate by-passing the object. So an instantaneous picture of the situation in the spray can be registered. If the electronic system of the ruby laser allows to emit more than one laser pulse within a very short period of time sequences of the spray behaviour can be stored on the photographic plate from which the velocity of the droplets with respect to amount and direction as well as changes in the size and geometrical form of the droplets can be evaluated. This evaluation, however, needs a very sophisticated and computerised procedure.
For evaluating the hologram it first has to be reconstructed as demonstrated in fig. 3. To do this for the special application of studying a nozzle spray, the holographic plate is replaced to the old position after chemical processing and is now illuminated by a continuously light emitting helium-neon-laser, sending its light via the path of the reference beam described in fig. 2. This new beam is now called reconstruction beam. If the holographic plate is replaced in the same orientation as it stood when the exposure occurred one can look at it with the naked eyes and can see a virtual image of the droplet spray exactly at the place where it was produced before by the injecting nozzle. For a quantitative evaluation one needs a closer examination by a camera, for example by a video camera. To do this the holographic plate has to be turned by 180°, when positioning to the old place and by illuminating with reconstruction beam a real image of the spray is produced, however, on the other side of the holographic plate. This real image has a three-dimensional extension and the video camera can be focussed to any plane within the image. For technical evaluation the camera, fixed at a certain position, is focussed to the mid-plane and then for getting information from other planes of the spray the

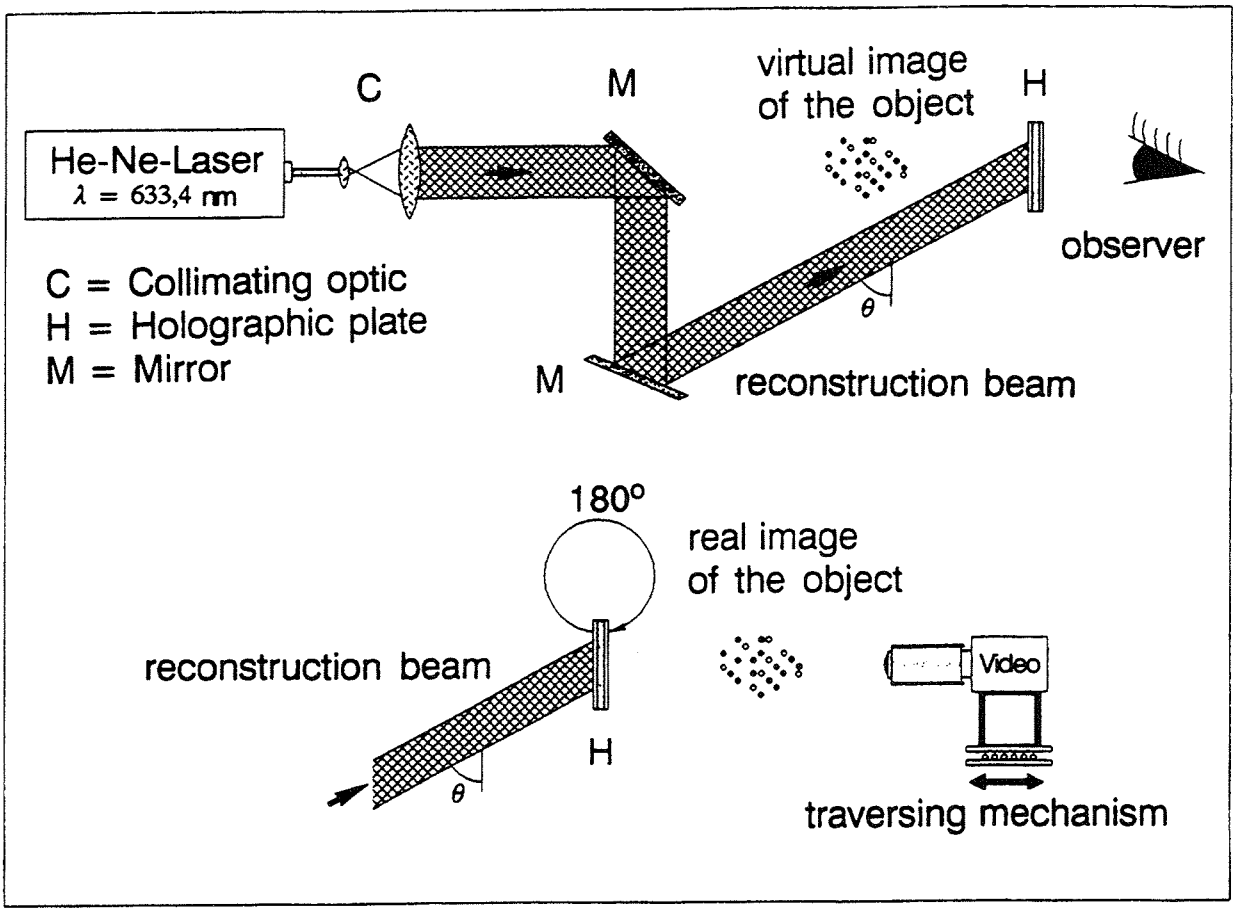

Fig. 3: Optical arrangement for the reconstuction of pulsed laser holograms /6/

camera is moved forward or backward with fixed focus of the lens. So plane by plane of the spray cloud can be evaluated. The virtual picture one would see with the naked eye is demonstrated in fig. 4.

It looks like a photographic picture of a spray with a veil near the nozzle orifice and a swarm of droplets separating from this veil when it breaks up. The quantitative evaluation works via the above-mentioned video camera and a computer system as shown in fig. 5 and uses the real picture. Main components of this evaluating systems are a digitiser, a graphic monitor, a video camera and a PC. The video camera is scanning the real image of the reconstructed hologram **O** and sends its information to the digitiser **D**. It changes the electrical signal from a analogue character to a digital one and stores it in a frame memory. Now the computer **C** can use the digitalised information for performing the image reprocessing. The digitiser simultaneously produces an analogue picture in a false-colour (red-green-blue) reproduction.

The procedure going on in the computer is briefly outlined in fig. 6. After a first positioning of the camera, noise-signals are eliminated without suppressing the gradients of the grey-colour. By this a first "clean" picture (with a minimum of noisy signals) is arising. Then the rest of pixels still originating from noisy signals is filtered out.

In the next step gradients out of the less or more intensive grey-colours of the pixels surrounding the holographic reproduction of the droplets or of the contour of the veil are evaluated. So it can be distinguished between well focused parts and such ones which

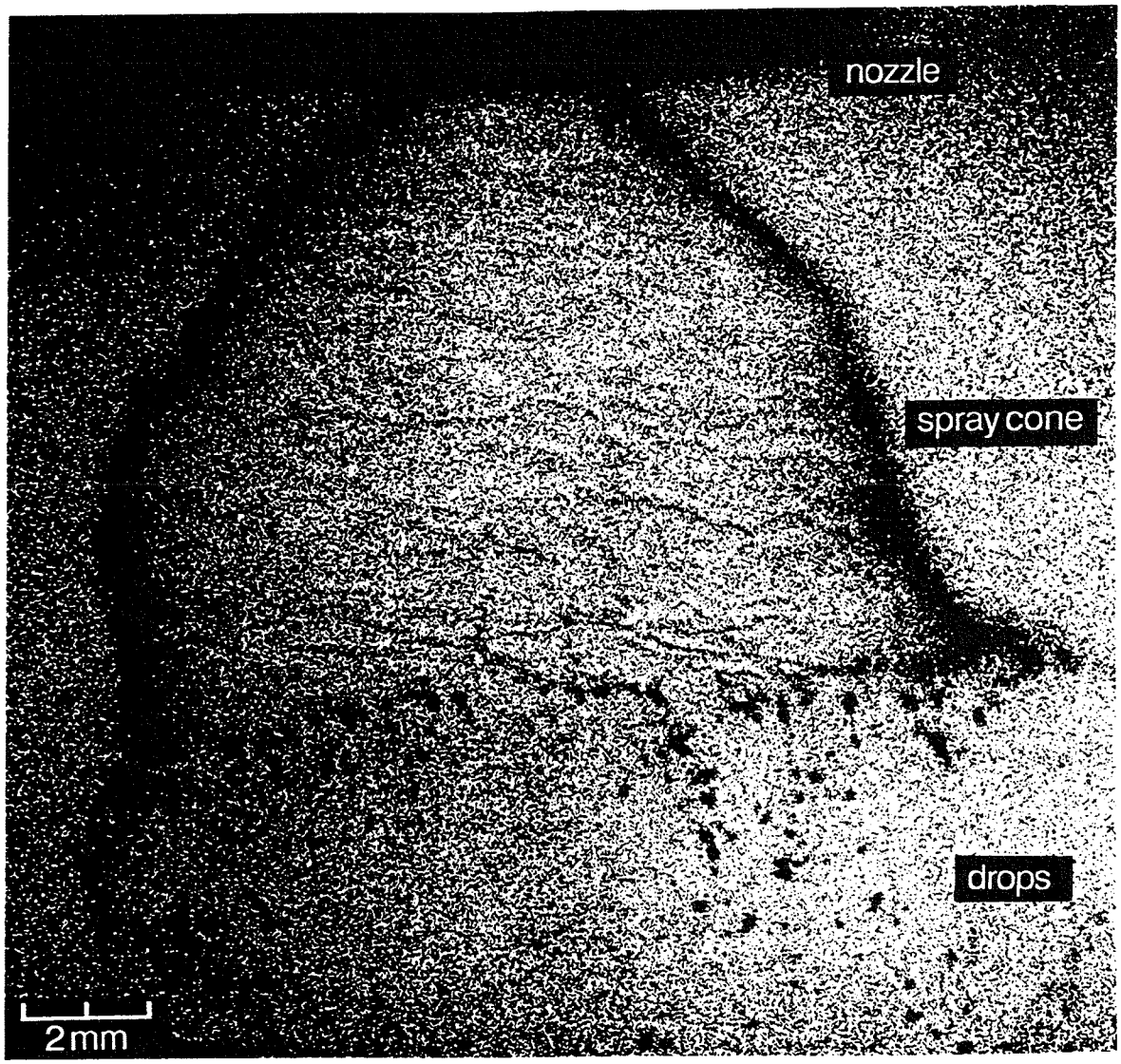

Fig. 4: Photography of a reconstruction of a pulsed laser hologram /6/
Object: Spray of a hollowed cone spiral nozzle.

are out of focus. Then all pixels having a grey-colour below a certain pre-defined value are treated as zero. By this reproductions of droplets which are out of the interesting focus-plane can be eliminated and a "picture" is electronically produced containing only reproductions of droplets which were within a very narrow tolerance within the focussing plan of interest.

By this procedure it happens that the contours of some droplets do not have a closed and continuous outline, because pixels may have been extinguished spotwise during the gradient checking procedure. Therefore a next step follows in which the open contours are filled with colour to produce closed outlines of the droplet reproductions. To be sure not erroneously to create new spots by this process which could be interpreted as droplet reproductions, the situation after the contouring is compared with that which existed before reproductions of droplets out of focus were eliminated. A "droplet" in the new picture is only accepted if it existed already before in the old picture. Finally the remaining droplet-reproductions are filled with colour and now the evaluation with

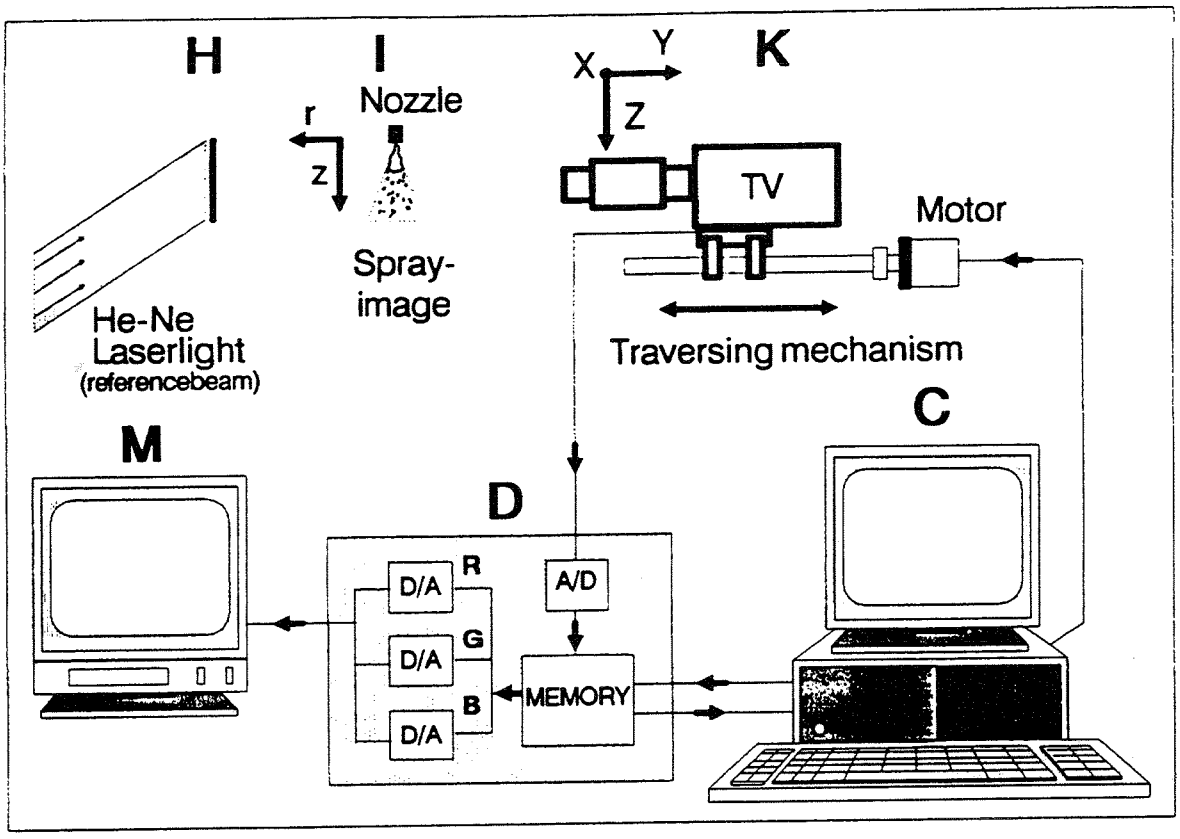

Fig. 5: Digital image processing system for the evaluation of pulsed laser holograms /5/

respect to droplet-size, -form and -concentration can go on.
After this plane in the holographic picture has been evaluated the video-camera is moved within a small step and the whole procedure starts again. So plane by plane of a spray-cloud can be evaluated and a three-dimensional picture of the two-phase flow situation is arising which was fixed on the holographic plate within a few nanoseconds. For more detailed information reference is made to the work by Chávez and Mayinger /5, 6/.
More downstream of the nozzle only droplet clouds can be observed. By evaluating a great number of such droplet clouds with the above-mentioned procedure information can be extracted with respect to the dependency of the droplet diameter from the mass-flow-rate through the nozzle and the pressure of the atmosphere into which the spray is injected. An example of such an evaluation gives fig. 7.
If two exposures of a droplet spray are illuminated onto the same holographic plate within a short period of time also the velocity of the droplets can be determined from such an hologram, however, with a much more complicated procedure which is described in detail in /6/. The data produced by this opto-electronic process are of high accuracy as fig. 8 demonstrates. Especially the suspicion that the computerised processing of the double exposure hologram produces a large scattering in the velocity-data is misproved by this figure. Even the influence of the pressure of the atmosphere in which the droplets are travelling is clearly brought out.

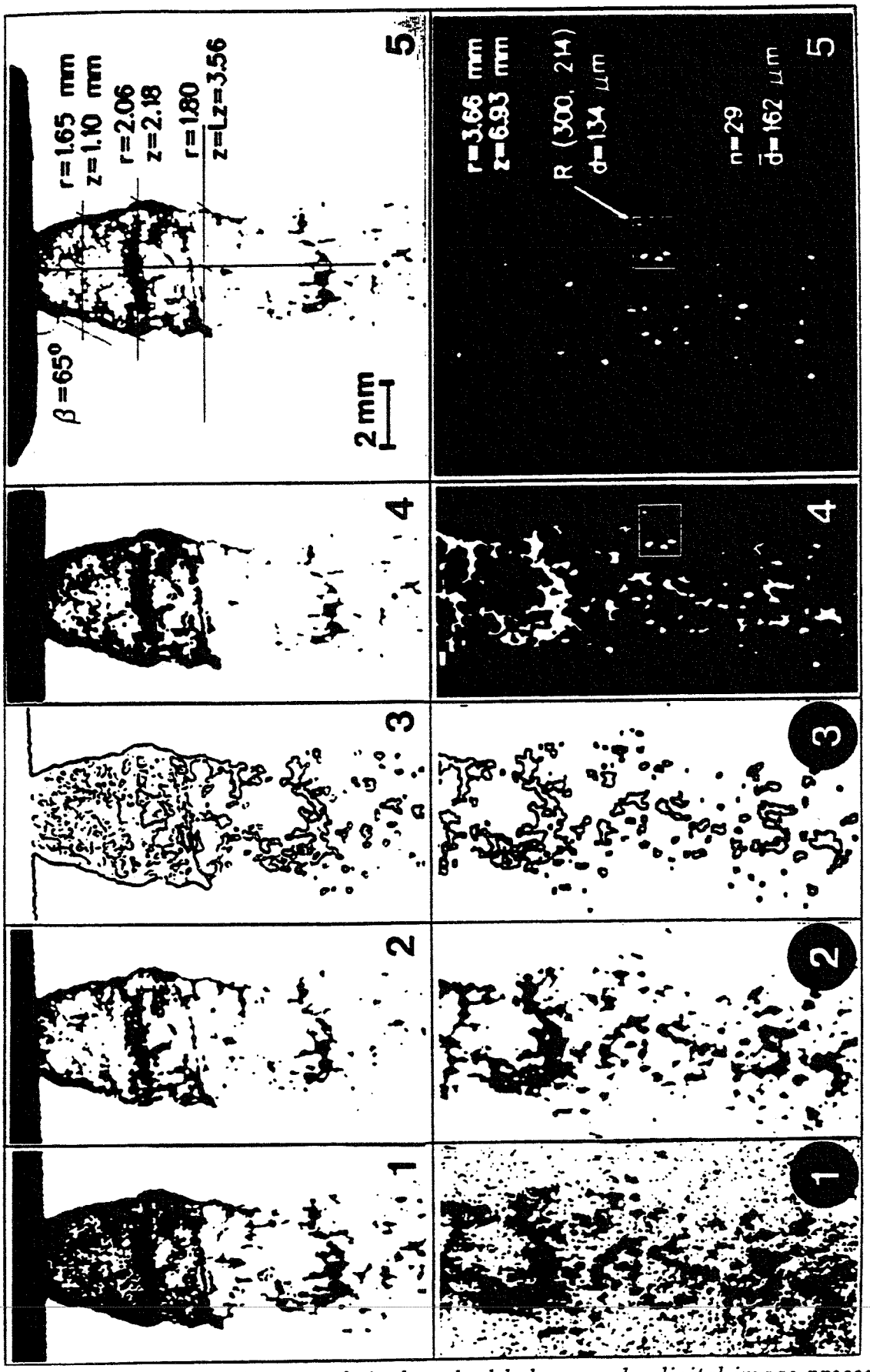

Fig. 6: Evaluation of single pulsed holograms by digital image processing /5/

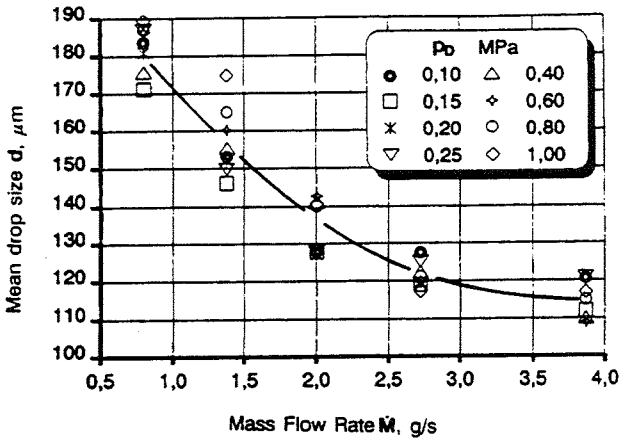

Fig. 7: Mean droplet diameter as a function of the mass flow rate at different ambient pressures

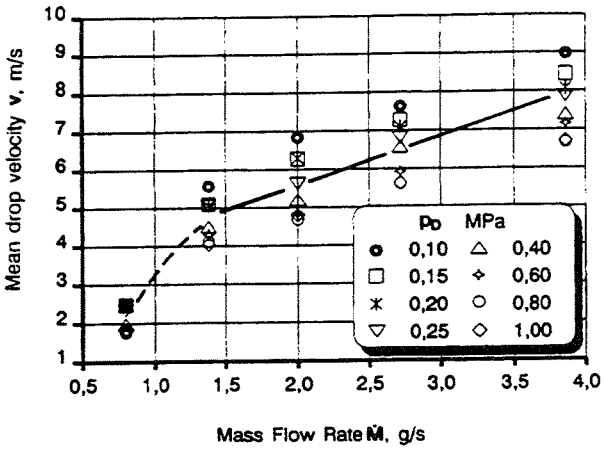

Fig. 8: Mean droplet velocity as a function of the mass flow rate at different ambient pressures

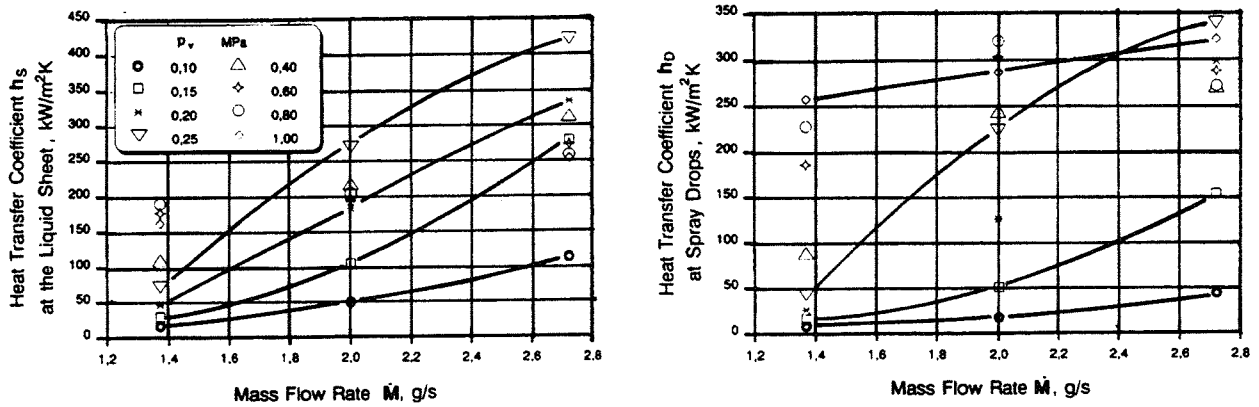

Fig. 9: Heat transfer coefficient at the liquid sheet and at the droplets as a function of the mass flow rate at different vapor pressures /6/

If the droplets are moving in a vapour atmosphere of the same substance as the liquid and if the temperature of the liquid is below the saturation temperature condensation occurs at the phase-interface which makes the volume of the droplet growing. By using a simple energy balance the condensation heat transfer can be calculated from this growth of volume versus time. The accuracy and the reproducibility of the described opto-electronic measuring technique are good enough to determine these heat transfer coefficients at the veil and at the droplet-cloud as fig. 9 demonstrates. The heat transfer data are averaged values from all droplets, being reproduced in a hologram.

3. HOLOGRAPHIC INTERFEROMETRY

For convective heat transfer processes the temperature gradient in the boundary layer near the heat emitting or absorbing wall is of special interest because from the temperature gradient at the wall, supposing a laminar sublayer the heat transfer coefficient

$$h = \frac{-k \left(\frac{dT}{dy}\right)_w}{T_w - T_\infty} \tag{1}$$

can be directly derived if, in addition, the temperature of the wall or of the bulk and the thermal conductivity of the fluid are known. This temperature gradient can be measured by interferometric optical methods, like the Mach-Zehnder interferometry, as well-known from the literature.
A new interferometry method is the combination of holography and interferometry. A most commonly used arrangement of optical set-ups for this holographic interferometry is shown in fig. 10.

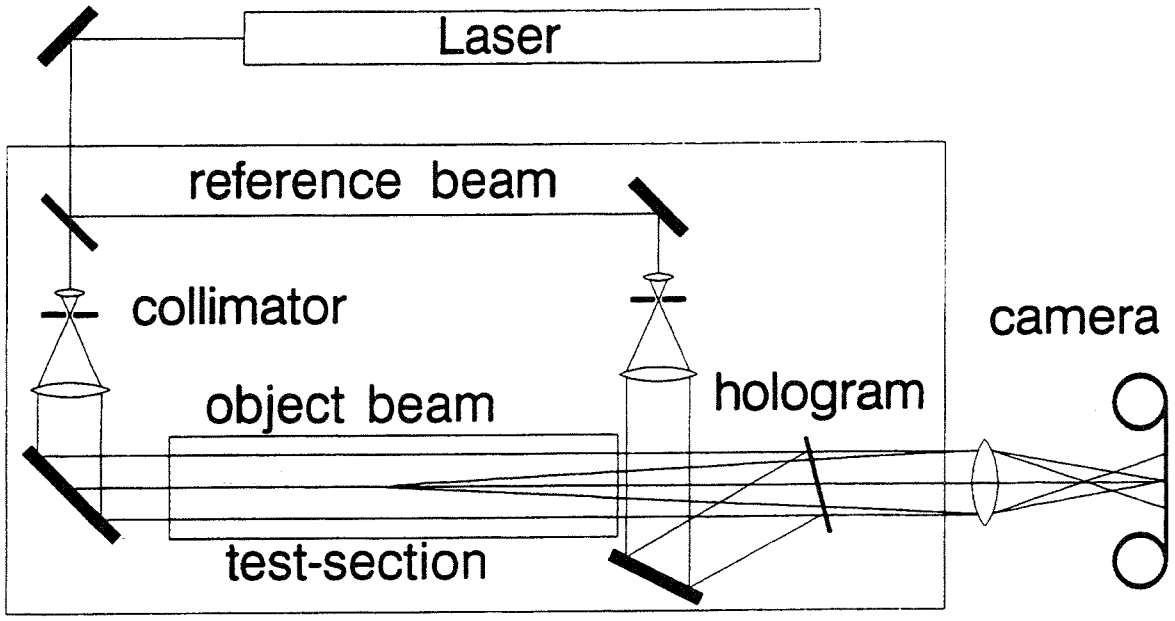

Fig. 10: Optical set-up for holographic interferometry

A helium-neon-laser or an argon-laser serves as a light source emitting continuously monogramatic and coherent light. By means of a beam splitter the laser beam is divided into an object- and a reference-beam in a similar way as we learnt before. Both beams are then expanded to parallel waves by a telescope which consists of a microscope objective and a collimating lens. The object-wave passes through the test section in which the temperature is to be examined whereas the reference-wave directly falls onto the photographic plate. There are many possibilities for arranging the optical set-ups to form a holographic interferometer which cannot be discussed here in detail. Reference is, therefore, made to the literature for example /7, 8/.

Several procedures exist to produce interferograms; here only a sophisticated one will be explained, which can be used for high-speed cinematography and by which transient heat transfer phenomena can be examined. It is called "real-time-method" because it allows to observe a process to be investigated continuously in real time. The method is illustrated in fig. 11.

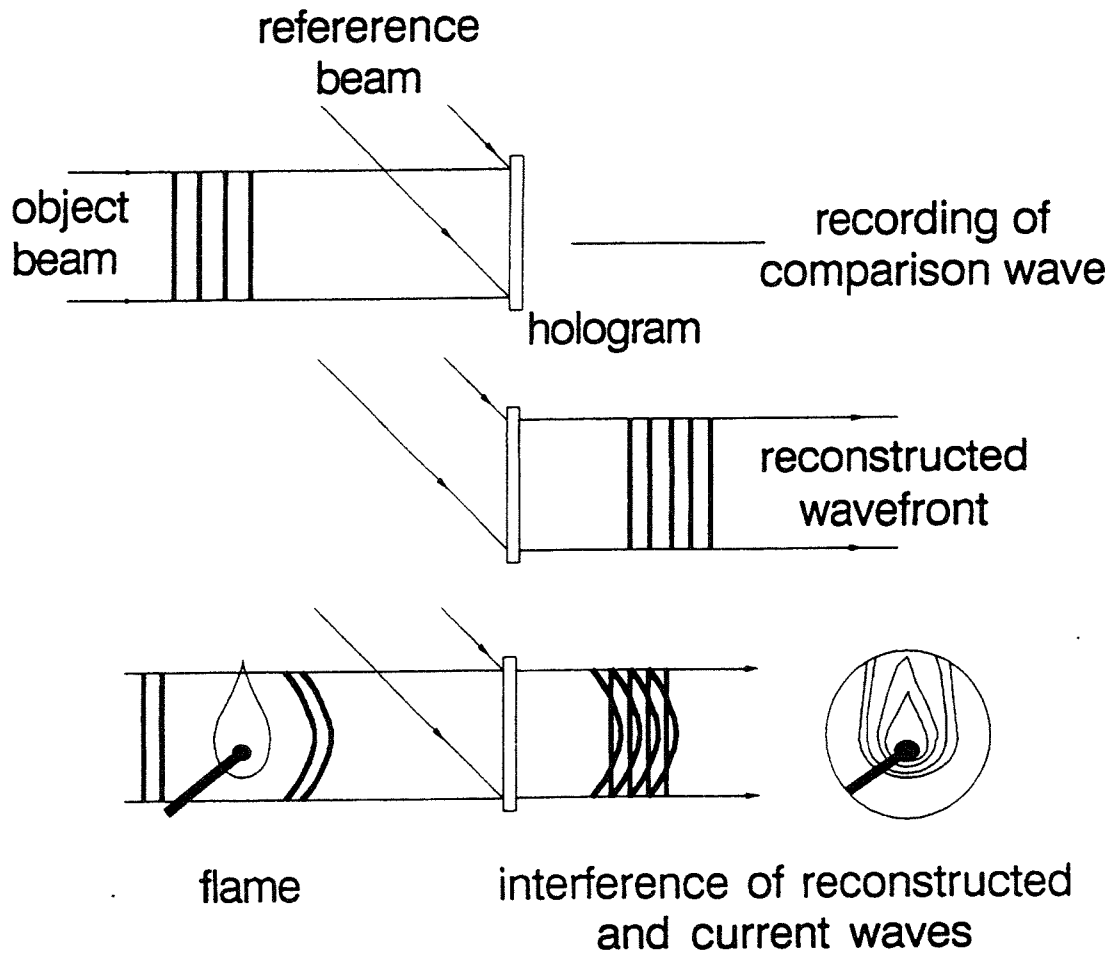

Fig. 11: Real time method for holographic interferometry

After the first exposure, by which the comparison-wave is recorded and during which there is no heat transfer in the test section –for two-phase flow experiments, even only single- phase flow may exist– the hologram is developed and fixed. Remaining at its place or repositioned accurately, the comparison-wave is reconstructed continuously by illuminating the hologram with the reference-wave. This reconstructed wave can now be superposed onto the momentary object-wave. If the object-wave is not changed and the hologram is precisely repositioned, no interference fringes will be seen at first (infinite-fringe-field adjustment).

Now the heat transfer process which is to be examined and for two-phase flow for example the boiling with bubble formation, or the condensation can be started. Due to the heat transport process a temperature field is formed in the fluid and the object-wave receives an additional phase shift passing through this temperature field. Behind the hologram both waves interfere with each other and the changes of the interference pattern can be

continuously observed or photographed on still or moving film.
The real-time-method demands an accurate reconstruction of the comparison-wave; therefore, the hologram must be repositioned precisely at its original place. This can be done by using a well-adjustable plate-holder, which, nowadays, can be purchased from the market. It is recommended to use a plate-holder where the final adjustment can be done via a remote control for example with quartz crystals. The adjustment of the repositioned holographic plate gets its feed-back control signals on an optical basis because the adjustment has to be done in such a way that the interference fringes –at first visible due to non-precise position of the plate– disappear during this procedure. This, certainly, has to be done without the heat transfer process having started, however, the pressure and the temperature are existing under which the system is operated during the experiments. A series of holographic interferograms taken with this method is illustrated in fig. 12, where the bubble formation at a heated surface in water with slow horizontal flow was studied. The water is slightly subcooled, i.e. the bulk temperature of the water was below the saturation temperature and, therefore, the bubble is condensing again after detaching from the heated surface and departing from the superheated boundary layer as one can observe by following the holographic interferograms versus a period of 7 ms in fig. 12. The horizontal black and white fringes in fig. 12 represent lines of constant temperature in a first approximation.

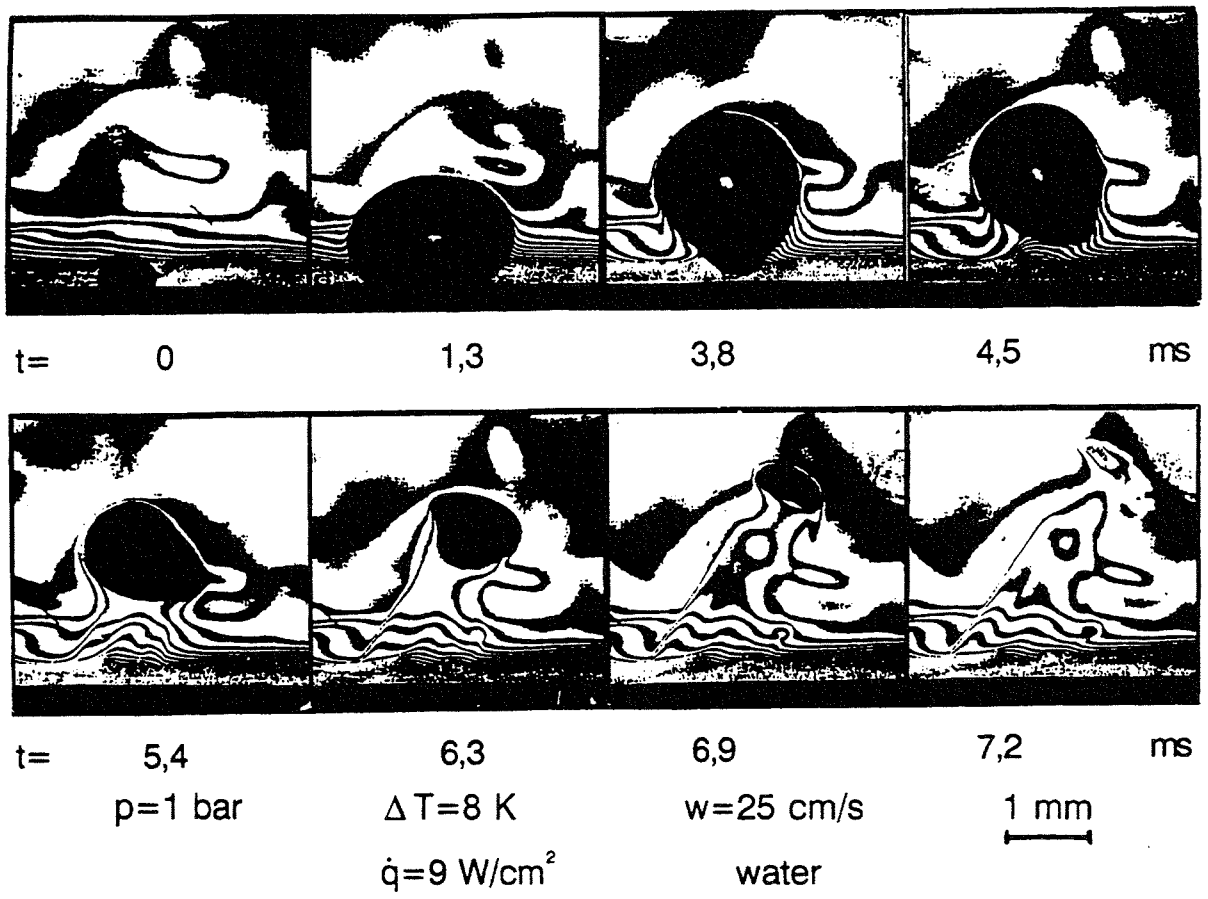

Fig. 12: Interferogram of subcooled boiling on a heated wall /12/

From this figure, however, we can also learn something about the limitation with which

this and all other interferometric methods are afflicted. The temperature field near the heated wall in the fluid is not only shifting the phase of the light-wave, it is also deflecting the light beam when travelling through it. This deflection has the consequence that with very high gradients at the wall –as it is the case in subcooled boiling– the zone immediately adjacent to the wall cannot be seen. With lower heat fluxes this deflection is not a problem in interferometry.
For learning the procedure of evaluating such an interferogram a more simple example shall be used as that in fig. 12. Fig. 13 shows the interference fringes in a subchannel of a tube-shell heat exchanger formed by three heat emitting tubes. The interference fringes here represent exactly isotherms in the fluid around the tubes and it can be clearly seen that the spacing of these isotherms is differnt at positions of narrow and of wider gap-size in the subchannel. Wide-spreading of the isotherms means a low temperature gradient and as we know from experience a low heat transfer coefficient.

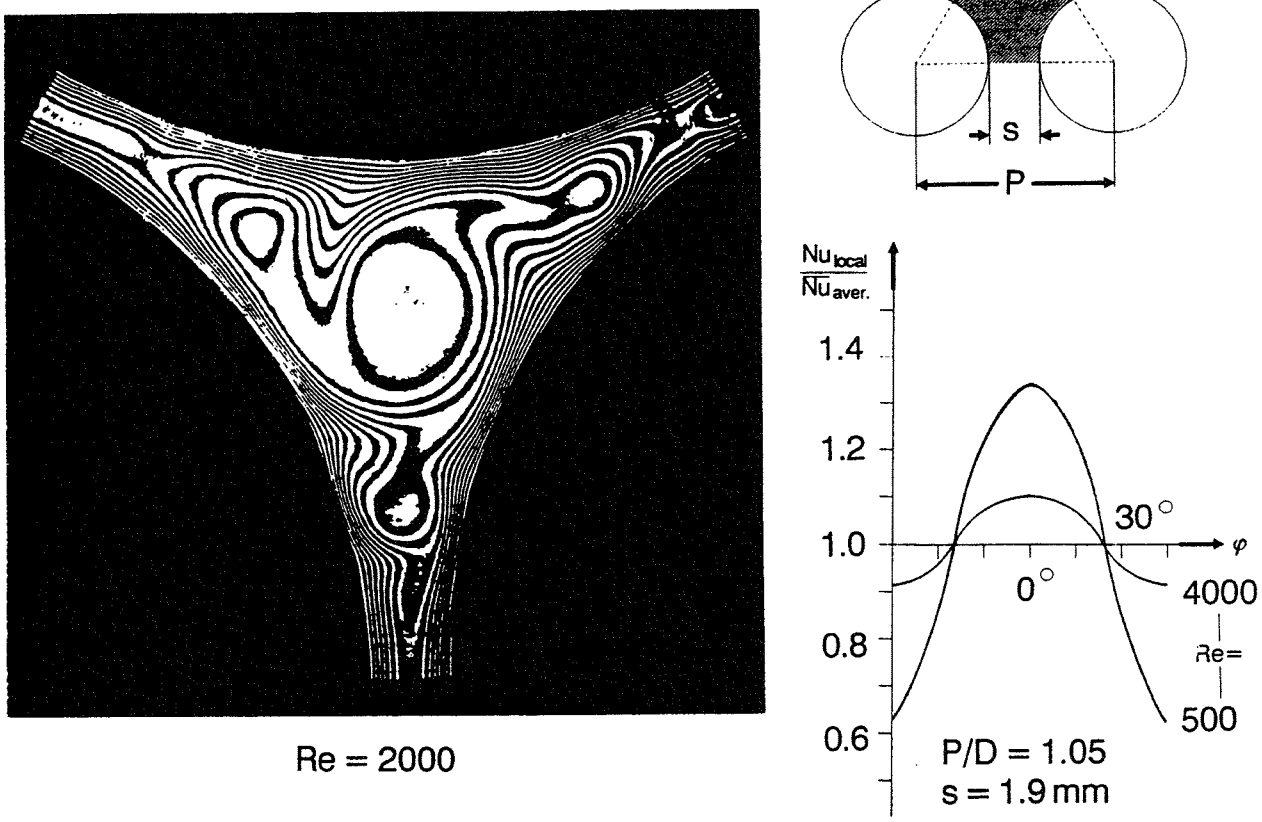

Fig. 13: Temperature field between three heated tubes with coaxial flow

This temperature field in the subchannel is of two-dimensional nature with good approximation. For the sake of simplicity only the evaluation of the simple case of a two-dimensional temperature field will be discussed here. It is also assumed that the holographic interferogram is produced with parallel object-waves. The evaluation of the interference patterns is than quite similar to that of a Mach-Zehnder-interferometer /9/. Therefore, here only the basic equations will be given. In the holographic interferometry

the object-waves passing through the test section at different time are superposed and, therefore, reveal the changes in optical path-length between the two exposures. Expressed in multiples S of a wave-length λ, this change is calculated to

$$S(x,y)\,\lambda \;=\; l\;[\;n(x,y)_2 \;-\; n(x,y)_1\;] \tag{2}$$

where l is the length of the test section in which the refractive index n is varied because of temperature changes. The refractive index distribution $n(x,y)$ during the recording of the two waves is –as mentioned above– assumed to be two-dimensional (no variation in light direction). Equation (2) shows that initially only local variations can be determined. Only if the distribution of the refractive index $n(x,y)_1$ during the recording of the comparison wave is known, absolute values can be obtained. Therefore, one usually establishes a constant refractive index field (constant temperature) while recording the comparison wave.

$$S(x,y)\,\lambda \;=\; l\;[\;n(x,y)_2 \;-\; n_\infty\;] \tag{3}$$

To obtain absolute values for the temperature field, the temperature at one point in the fluid has to be determined by thermocouple measurements. This is usually done in the undisturbed region or at the wall of the test chamber. Equ. (3) is the equation of ideal interferometry. It is assumed that the light beam propagates in a straight line. Passing through a boundary layer, the light beams, however, are deflected because of refractive index gradients. This deflection is used for the various Schlieren- and shadowgraph-methods. The light deflection can be converted into an additional phase shift S, if a linear distribution of the refractive index is assumed to be within this small area.

$$\Delta S \;=\; \frac{n_0\;\lambda\;l}{12\;b^2} \tag{4}$$

In this equation b is the fringe width and n_0 is the average refractive index.
In many applications an ideal, two-dimensional field cannot be found. Often the boundary layer extends over the ends of the heated wall, or there are entrance effects or temperature variations along the path of the light beam (axial flow in the test section). Therefore, only integrate values are obtained. Having corrected the interferogram, the obtained refractive index field can be converted into a density field The relation is given by the Lorentz-Lorenz-formula where N is the molar refractivity and M the molecular mass.

$$\frac{n^2-1}{n^2+2}\;\frac{1}{\rho} \;=\; \frac{N}{M} \tag{5}$$

If there is only one component in the test section and the pressure is kept constant, the density variations can only be caused by temperature changes. If the fluid is a gas, the situation is very simple because its refractive index is very near to 1, which reduces Equ. (5) to the Gladstone-Dale-equation:

$$\frac{2}{3}(n-1)\;\frac{1}{\rho} \;=\; \frac{N}{M} \tag{6}$$

With the simple Boyle-Mariotte-law and R as the gas constant we then obtain the following formula, which relates the fringe shift to the temperature:

$$T(x,y) = \left[\frac{S(x,y)\ 2\ \lambda\ R}{3\ N\ p\ l} + \frac{1}{T_\infty} \right]^{-1} \tag{7}$$

For liquids the procedure is a little more complicated because we have to take in account the real behaviour of the thermodynamic properties as a function of temperature. Therefore, we have to use an equation of state for the refractive index n or we have to take the refractive index from tables interpolating the data with simple equations. Fortunately, there are good data banks available in the literature for most of the fluids. However, it is also not difficult to measure the refractive index in a simple optical set-up.
With an equation for the refractive index as function of the temperature we then can use Equ. (2) and we get the connection between the pattern of the interference fringes and the temperature field, as shown in Equ. (8):

$$S(x,y)\ \lambda = \frac{dn}{dT}\ [T(x,y) - T_0] \tag{8}$$

Often local heat transfer coefficients are of special interest. In this case the temperature gradient at the wall is determined and assuming a laminar boundary layer next to the wall or the phase-interface the heat transfer coefficient is obtained by using Equ. (1).
The assumption that the temperature field is two-dimensional and constant along the path of the beam travelling through the fluid is not valid in case of temperature fields around curved surfaces, like bubbles. The refractive index n is then a function of the radius r, and we have to use Equ. (2) in its differential form

$$S\ \lambda = \int_0^1 (n - n_0)\ dz \tag{9}$$

and we write it in spherical or cylindrical co-ordinates:

$$S(y)\ \lambda = \int_0^z [n(r) - n_0]\, dz \tag{10}$$

For spherical and cylindrical symmetry Equ. (10) can be solved and integrated as described, for example, in /12/ after transforming it in the form

$$S(y)\ \lambda = 2 \sum_{k=i}^{N-1} \Delta\ n_k \left[\left(r_{k+1}^2 - r_i^2\right)^{1/2} - \left(r_k^2 - r_i^2\right)^{1/2} \right] \tag{11}$$

In temperature fields with very high gradients the deflection of the laser beam, which is demonstrated in fig. 14, too, cannot be neglected, as it is done in the evaluating procedure described in /10/. High temperature gradients are especially found in the liquid boundary layer around vapour bubbles, in particular if condensation occurs. In such a case a complicated correction procedure for this deflection has to be used which is described by Nordmann and Mayinger /11/ and by Chen /12/. With the equations

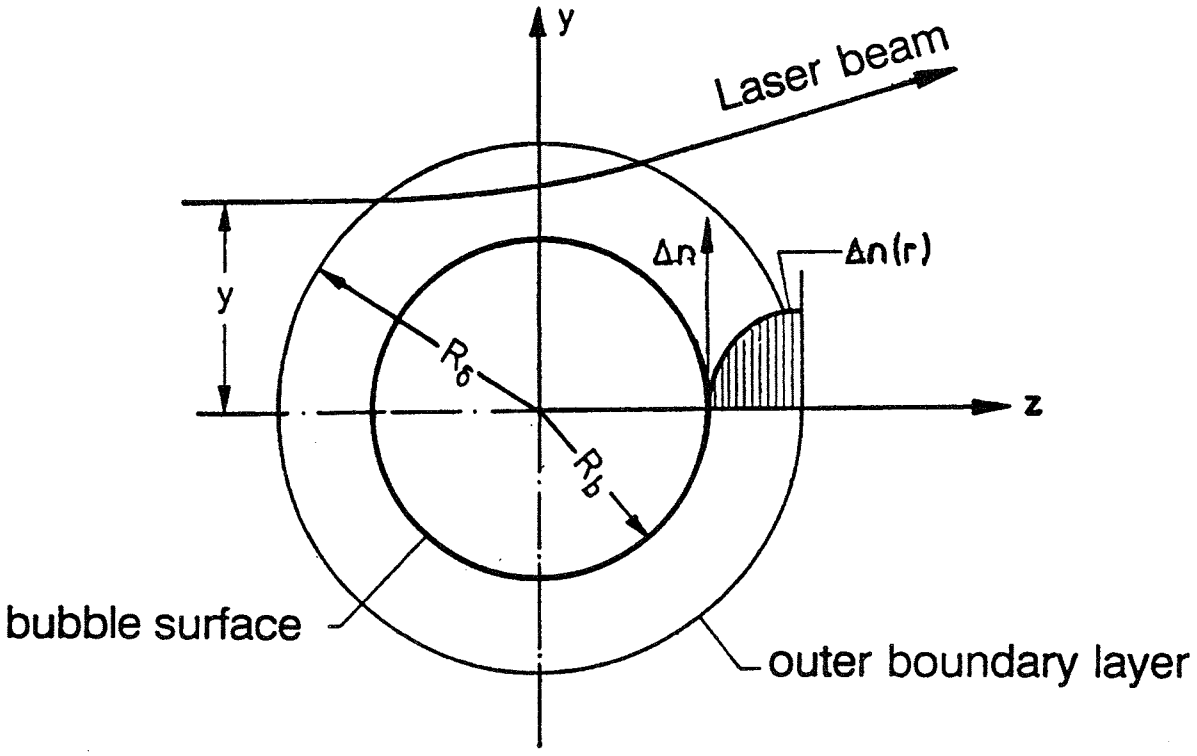

Fig. 14: Beam deflection and optical conditions in a temperature field /12/ around a spherical bubble

and corrections described there, even temperature fields around very tiny bubbles can be evaluated.

With high heat transfer coefficients the boundary layers at the phase-interface are usually very thin –in the order of a few hundredth of a millimeter– and it is difficult to investigate them with the interferometric procedure described up to now, because only a few interference fringes would be observed within this narrow area. Therefore, here another interference method has to be used, the so-called "finite fringe method". In this method, after the reference hologram was produced, a pattern of parallel interference fringes is created by tilting the mirror in the reference-wave of fig. 15, or by moving the hologram there within a few wave-lengths. The direction of the pattern can be selected as one likes and it is only depending on the direction of the movement of the mirror or of the holographic plate.

This pattern of parallel interference fringes is then distorted by the temperature field due to the heat transfer process. The distortion or deflection of each fringe from its original –parallel– direction is, in a first rough approximation, the temperature gradient and gives by using Equ.(1) the heat transfer coefficient. A short description how these interference patterns are evaluated is given in fig. 16. This figure also demonstrates for the example of a temperature field around a burning flame how these distorted interference fringes look like, depending on the original orientation of the parallel pattern. A detailed description of the mathematical procedure how to evaluate these pattern of finite fringes and how to determine the temperature gradients from it, is given in /11/ and /12/.

Fig. 17 demonstrates the possibilities of using these techniques in a flow with a bubble

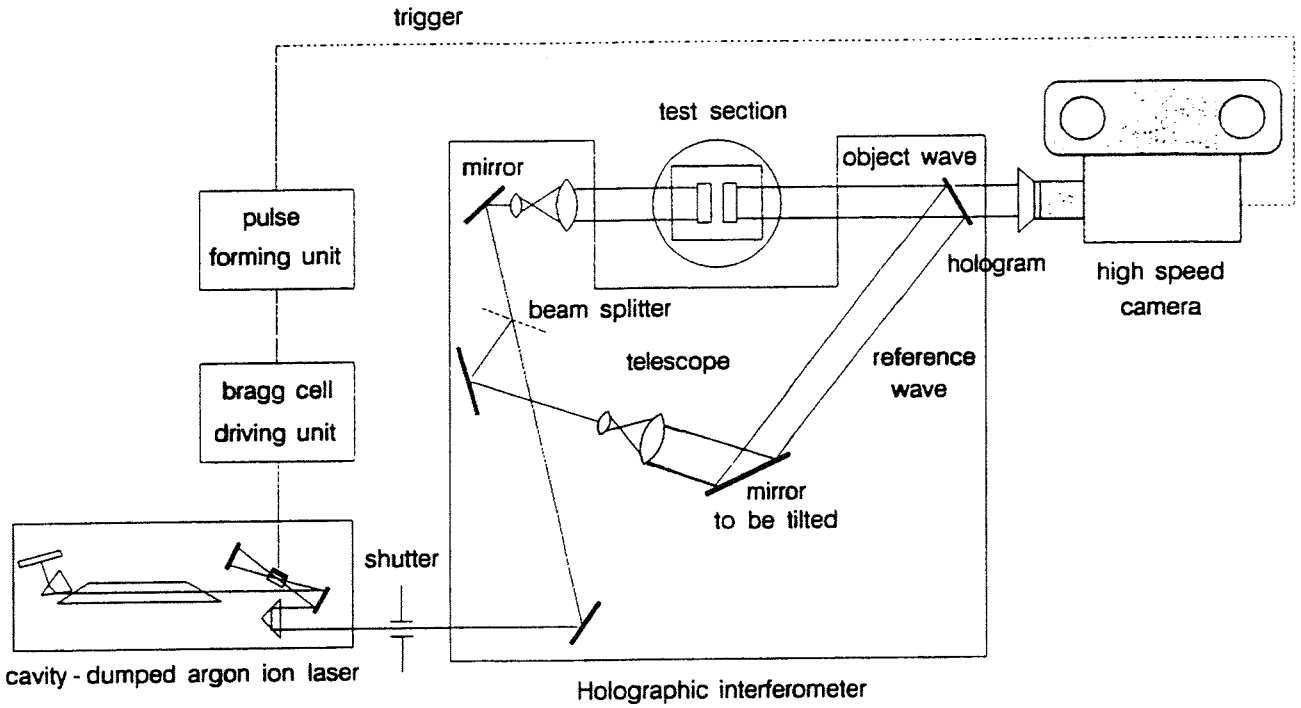

Fig. 15: Arrangement for holographic interferometry with finite fringe method

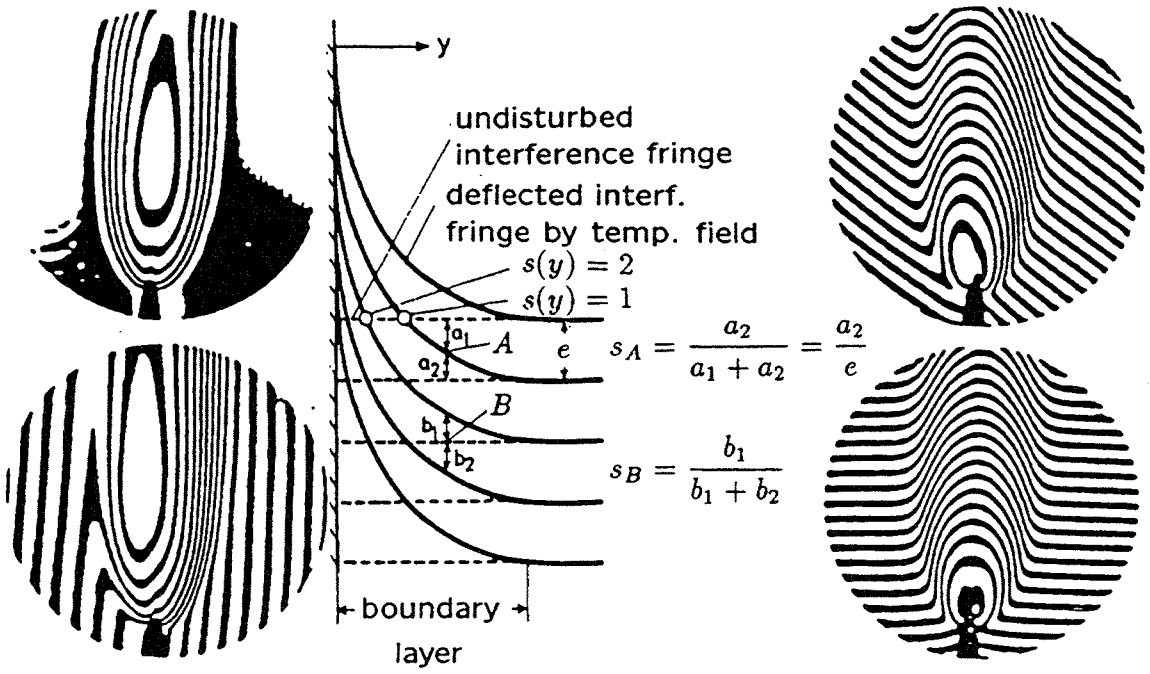

Fig. 16: Finite fringe interferograms (temperature field around a flame) and their evaluation

condensing in a liquid. By combining this method with the high-speed cinematography

it allows an inertialess and precise evaluation of the heat transfer coefficient at the phase-interface of a condensing bubble. Holographic interferometry certainly can only be used if the flow situation is not too complicated and if the bubble population is not too numerous, so that individual bubbles can be identified. It is not possible to look inside the bubbles, because the light is totally reflected at the phase-interface.

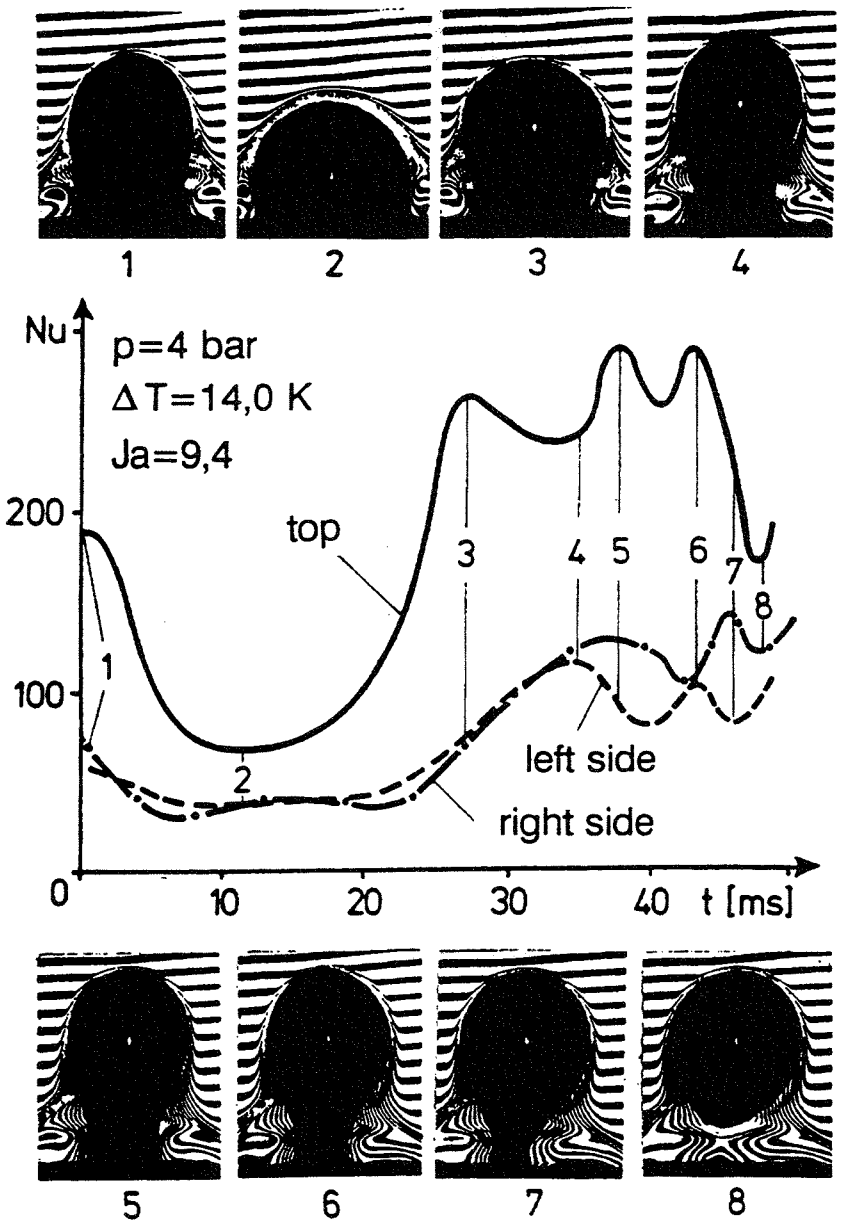

Fig. 17: High speed cinematography of interferograms around a condensing bubble /11/ and the evaluated heat transfer at the phase interface

As explained in the Equs. 2 - 5 the phase shift is a function of the change in the density of the fluid. In pure substances the density is a function of temperature and pressure. In multi-component systems also the concentration influences the density. In our evaluation procedures up to now we worked on the assumption that the alteration of the density is affected by a temperature change only and, therefore, the variations in the refractive

index within the test section could be treated as temperature distributions. When the variations in the refractive index are caused not only by a temperature-, but also by a concentration- or pressure-change these simple evaluation of the interference pattern, described up to now is not possible any more. Therefore, coupled heat and mass transfer processes can be examined by interferometric methods only if one of the two fields is obtained by an additional measuring method. Only by assuming identical profiles of the temperature and of the concentration the interferograms can be evaluated without additional measurements as El-Wakil /13/ did.
There is, however, one method to determine the temperature and the concentration field by optical means alone, which is called the "two-wave lengths interferometry". This is done by applying their dependence of the refractive index on the wave-length of the light to determine the temperature- and concentration-fields by means of separate interferograms, taken at different wave-lengths. Ross and El-Wakil /14/ used this two wave-lengths interferometry in a modified Mach-Zehnder-interferometer for the study of the evaporation and combustion of fuels. Panknin and Mayinger /7, 8/ used this basic idea and developed a two-wave lengths method for the holographic interferometry. The problem with the two-wave-lengths interferometry is that the two interferograms have to be superimposed very accu rately. Here, the peculiarity of the holography allowing the recording of different interference pattern on one and the same plate is a great help to overcome these difficulties. A simple set-up for the holographic two-wave lengths interferometry is shown in fig. 18. It resembles very much the arrangement of fig. 10 and actually the only difference is that two lasers are used as light sources in fig. 18. The beams of the He-Ne-laser ($\lambda_j = 6.328\mathring{A}$) and of the Argon laser ($\lambda_k = 4.579\mathring{A}$) intersect and, therefore, only one shutter is needed and equal exposure times at both wave lengths are guaranteed. The beams are then superimposed by means of a beam splitter. By this one gets two object - and two reference-waves at the different wave-lengths. It has to be mentioned that not only the object wave λ_j is reconstructed by the reference-wave λ_j, but also a false objective-wave λ_k is obtained and vice versa. These unwanted waves, however, emerge at different angle from the hologram and can, therefore, easily be separated from the original waves. For the evaluation of the interferograms here only some simple equations shall be presented. For a more detailed study reference is made to the work by Panknin /8/. In gas we can use the Gladstone-Dale-equation, Equ. (6), and the ideal gas law which relates the fringe shift to the temperature- and concentration-distribution in a heat and mass transfer boundary layer.

$$S(x,y)\,\lambda \;=\; \frac{3\,p\,l}{2\,R}\,N_m\,\left[\frac{1}{T(x,y)} \;-\; \frac{1}{T_\infty}\right] \tag{12}$$

The molar refractivity N_m for a mixture of two gaseous components is given by

$$N_m \;=\; N_a\,C_a \;+\; N_b\,C_b\;; \qquad with \quad C_a \;+\; C_b \;=\; 1 \tag{13}$$

where N_a and N_b are the molar refractivities of the components in their pure form and C is the concentration of the component in the mixture. During the recording of the comparison wave the temperature distribution T in the test section is constant and there are only two components of the mixture.
Combining Equ. (12) and (13) we obtain for each wave-length

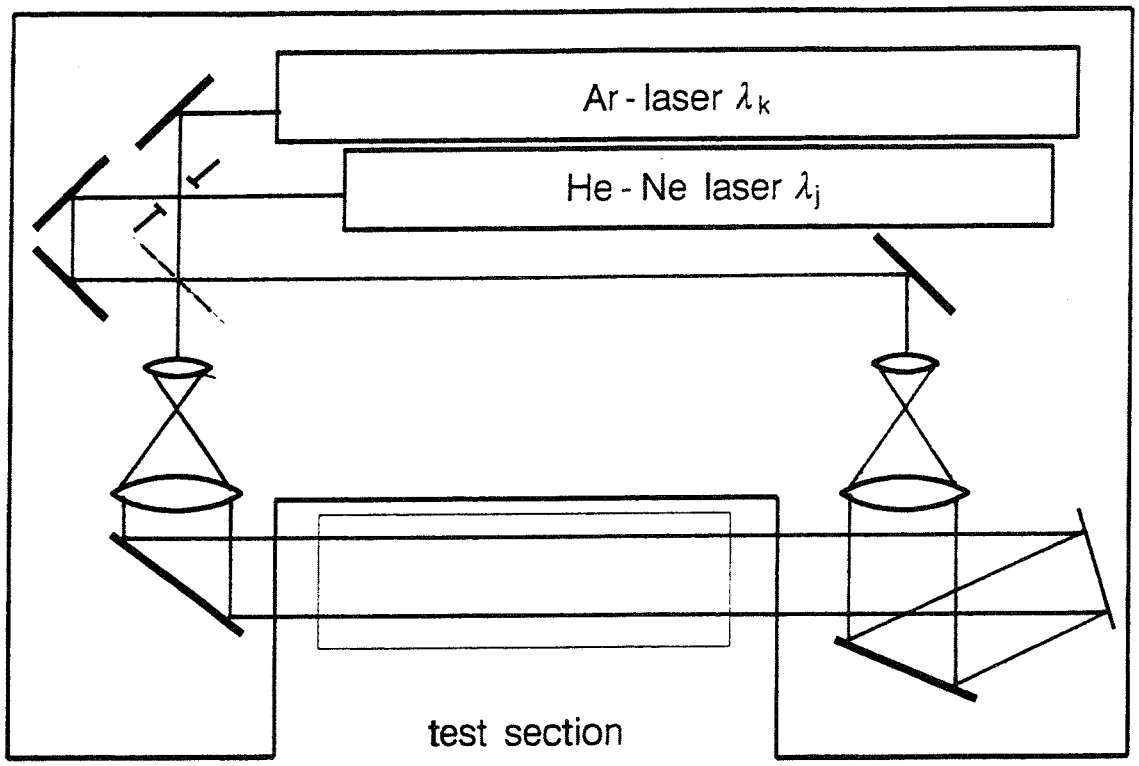

Fig. 18: Optical set-up for holographic two-wavelenght interferometry

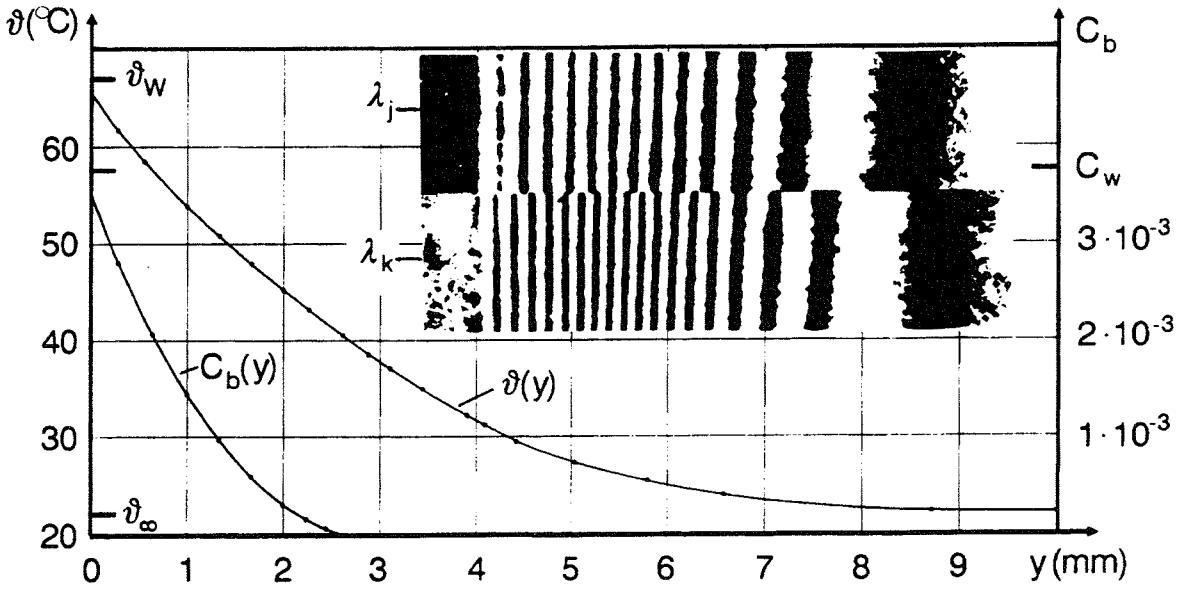

Fig. 19: Temperature and concentration profiles in a laminar boundary layer /7/

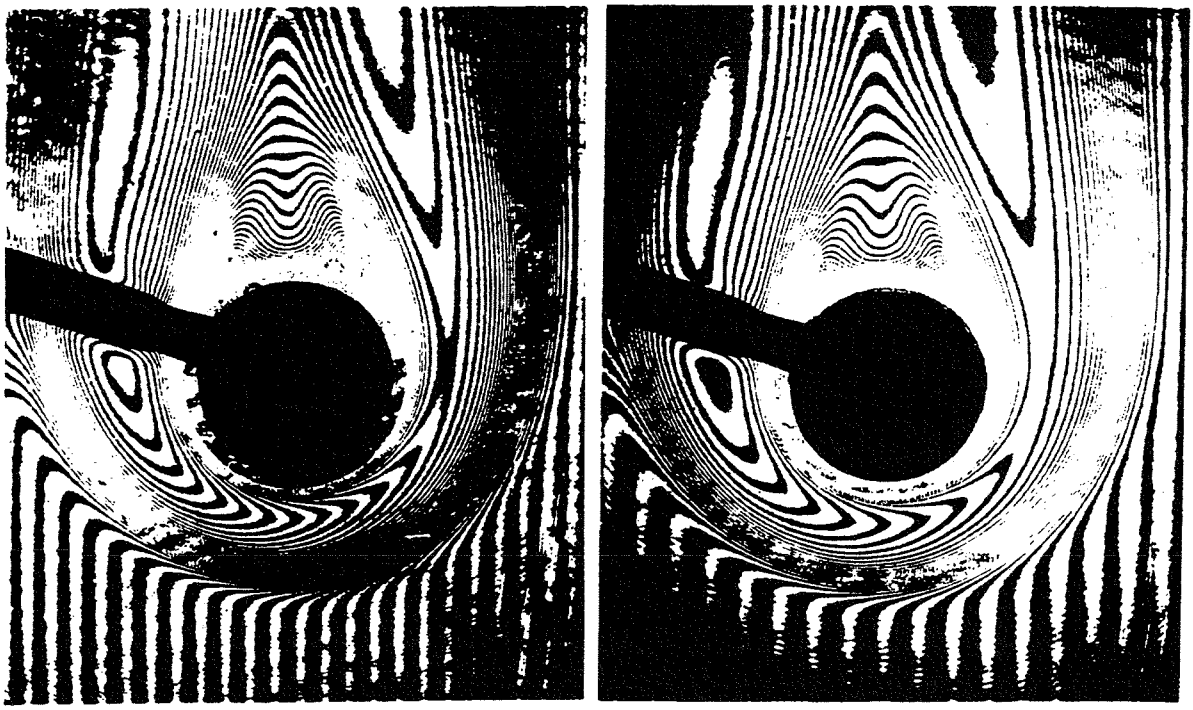

Fig. 20: Finite fringe interferogram of a flame taken with two different laser beams /8/ of the wavelength λ_j (right) and λ_k simultaneously

$$S(x,y)\ \lambda\ =\ \frac{3\ p\ l}{2\ R}\ \left[\frac{1}{T(x,y)}\ (N_a\ +\ C_b(x,y))\ (N_b\ -\ N_a)\ -\ \frac{N_a}{T_\infty}\right] \tag{14}$$

eliminating $C_b(x,y)$. The temperature $T(x,y)$ can be calculated:

$$S_j(x,y)\ \frac{\lambda_j}{N_{bj}\ -\ N_{aj}}\ -\ S_k(x,y)\ \frac{\lambda_k}{N_{bk}\ -\ N_{ak}}\ =$$

$$\frac{3\ p\ l}{2\ R}\left[\frac{1}{T(x,y)}\ -\ \frac{1}{T_\infty}\right]\ \left[\frac{N_{aj}}{N_{bj}\ -\ N_{aj}}\ -\ \frac{N_{ak}}{N_{bk}\ -\ N_{ak}}\right] \tag{15}$$

After determining the temperature distribution only one interferogram is used to calculate the concentration profile.
Equ. (15) shows that there is a difference between the phase shifts for the two wave-lengths which is used for the measurement of the temperature. This difference is usually very small. Therefore, the two wave-lengths used should be as far apart as possible. The dependence of $N_{(a,b)}$ is also very small and gets larger proportions only in the vicinity of an absorption line which, however, is usually not in the visible range. This limits the choice of substances to those lengths used. Some test fluids suitable for this technique are naphtalene, carbondisulphide, bencene and hexane. The position of the fringes has to be determined very accurately at the same plate in the two interferograms.
A simple application example of the two-wave-lengths technique is given in fig. 19. In order to demonstrate the differences in the phase shift only the upper and lower halfes

of each interferogram are shown and the evaluation is made at the intersection of the pictures. The interferograms show the heat and mass transfer boundary layer at a heated vertical wall with free convection. The mass transferred was naphtalene into air.

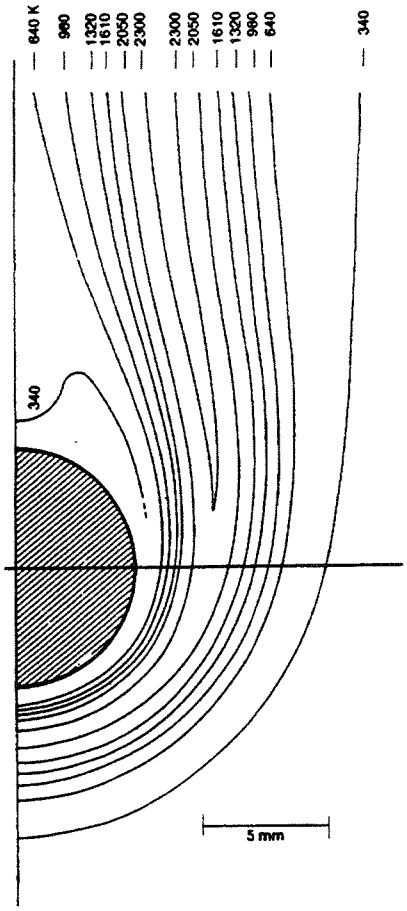

Fig. 21: Evaluation of the temperature field in a flame from the interferogram of fig. 20

Heat and mass transfer experiments were also performed in a burning flame with hexane flowing out of a horizontal porous cylinder and oxidising after evaporation. Fig. 20 shows the two interferograms obtained with the two wave-lengths as emitted by the He-Ne-laser and the Argon-laser. In this interferogram the finite fringe method was used as described before. The temperature field in this flame evaluated from the interferograms in fig. 20 is given in fig. 21, which clearly demonstrates the benefit of this optical method by instantaneously presenting a complete information about the temperature distribution in the flame.

4. CONCLUDING REMARKS

Optical Methods are expected to experience a powerfull revival due to three reasons: Sophisticated theoretical treatment of heat- and mass transfer processes with large computer codes needs very detailed information about temperature- and concentration-fields in the areas of interest - like in boundary layers - for assessing and improving the physical models used in the code and for verifying the code itself. An optically determined pattern of isotherms is a very stringent touchstone for the reliability and accuracy of the code.

Modern developments in power and process engineering make transient situations more and more interesting, especially for controlling procedures and safety deliberations. Optical measuring techniques work inertialess.
A former draw-back of the image-forming optical measuring techniques, the laborious and time-consuming evaluation does not exist anymore. A personal computer can evaluate a hologram or an interferogram within a few seconds which took manpowers of several hours before. The costs of such an evaluating equipment are relatively moderate.
So theoretical analysis and optical measuring techniques could form a new phalanx for investigating heat and mass transfer processes.

5. Literature

1. **Gabor, D.**, A New Microscopic Principle, Nature 161, p. 777, 1948, Microscopy by Reconstructed Wavefonts, Proc. Rcy. Soc. A 197, p. 454, 1949, Microscopy by Reconstructed Wavefonts II, Proc. Phys. Soc. 3 64, p. 449, 1951.
2. **Kiemle, H., and D. Röss (1969)**., Einführung in die Technik der Holographie, Akademische Verlagsgesellschaft, Frankfurt.
3. **Smith, H.M., (1969)**., Principles of holography, Wiley (Interscience), New York.
4. **Caulfield, H.J. and Sun Lu (1971)**.,The applications of holography, Wiley (Interscience), New York.
5. **Chávez, A., Mayinger, F. (1990)**., Evaluation of pulsed laser holograms of spray droplets by applying image processing, 9th International Conference on Heat Transfer, 1990, p. 187.
6. **Chávez, A., Mayinger, F. (1992)**., Measurement of direct-contact condensation of pure saturated vapour on an injection spray by applying pulsed laser holography, Int. J. Heat Mass Transfer, Vol. 35 No. 3, pp 691-702, 1992.
7. **Mayinger, F., Panknin W. (1974)**., Holographie in Heat and Mass Transfer, 5th Int. Heat Transfer Conference, VI, 28, Tokio.
8. **Panknin, W. (1977)**., Eine holographische Zweiwellenlängen-Interferometrie zur Messung überlagerter Temperatur- und Konzentrationsgrenzschichten, Diss. Universität Hannover.
9. **Hauf, W., Grigull, U. (1970)**., Optical Methods in Heat Transfer, Advances in Heat Transfer, Vol. 6, p. 133.
10. **Hauf, W., Grigull, U., Mayinger, F. (1991)**., Optische Messverfahren in der Wärme- und Stoffübertragung, Springer Verlag, Berlin.
11. **Nordmann, D., Mayinger, F. (1981)**., Temperatur, Druck und Wärmetransport in der Umgebung kondensierender Blasen, VDI Forschungsh., Nr. 605, VDI Verlag, Düsseldorf.
12. **Chen, Y. M., (1985)**., Wärmeübergang an der Phasengrenze kondensierender Blasen, Diss. Techn. Universität München.
13. **El-Wakil, M.M., Myers, G.E., Schilling, R.J. (1966)**., An Interferometric Study of Mass Transfer from a Vertical Plate at Low Reynolds Numbers, J. of Heat Transfer, Vol. 88, p. 399.
14. **El-Wakil, M.M., Ross, P.A. (1960)**., A Two Wavelength Interferometric Technique for the Study of Vaporization and Combustion on Fuels, Liquid Rockets and Propellants, Progress in Astronautics and Rocketry, Vol. II, Academic Press, New York.

A Method for Impedance-Supported Reconstruction of Mixture Composition

F. Mayinger, F.Klug and Günter Kiederle
Lehrstuhl A für Thermodynamik, Technische Universität München
D-80290 München
Tel. +0049-89-2105-3436
Fax. +0049-89-2105-3451
E-mail may@thermo-a.mw.tu-muenchen.de

ABSTRACT

A new method is presented, which makes it possible to extend the application of the impendance methods to situations in which no information of the multi-phase mixture is available. The method is not based on tomography, but works also with spatially distributed sensors, having the form of strips integrated in the wall in a non-intrusive way. These strips are acting as electrodes, producing various capacity fields which can be varied over the cross section of the channel within a very short time. The temporal signals of these strip-electrodes are composed into a multi-dimensional field of vectors.

By comparing the multi-dimensional vector field with a matrix of reference data a situation of optimum simularity can be evaluated and from this the flow pattern (bubbly-, annular-, spray-, stratified-flow,...) can be identified. Knowing the flow pattern, the evaluation of the signals can be continued for determining the local volumetric void fraction. The sensor and the method can be used as a universal fully automatisized instrument for measuring multi-phase flow in chemical engineering and in petrol engineering.

The method proved to be a very reliable technique and has been tested in a series of experiments. It was shown that it gives the local void fraction with an error less than 2 - 8 %, depending on the number of capacitive fields produced during a measuring cycle. If the measuring cycle can be extended to 1 s the error is down to 2 % and at shorter cycle periods - for example 0.1 s - the error goes up to 5 - 8 %.

Especially in horizontal flow - also with very wavy situations - the local void fraction can be measured with very good accuracy. With bubbly flow the variation of the bubble concentration over the cross section must be taken into account if very precise data are needed. Therefore, here a measuring cycle has to consist of a larger number of evaluated capacitive fields which means that the minimum measuring time is longer than the above mentioned 0.1 s.

But using not only the dielectric constant (capacitive method) as a sensoric signal but also the electric conductivity (impedance method) also mixtures of oil, gas and water - or in general multi-phase mixtures with gas and liquid components of different electrical properties - can be investigated.

1 IMPEDANCE METHOD

The impedance method is widely applied for measurement of volumetric concentrations in multi-phase flows. It is based on the different electrical properties (permittivity, conductivity) of the flow components and their effect on the measured impedance (capacitance, conductance) of an appropriate sensor. In non-conducting fluids, the capacitance of the sensor is measured; in conducting fluids conductance can be measured, either additionally or exclusivly. The majority of these applications comes from the field of two-phase flows, especially from capacitance measurement in non-conducting fluids. Popular applications employ parallel plate electrodes, Auracher [1]. The using of ring electrodes is described by Özgü et.al.[2], helical electrodes have been tested by Geraets et.al.[3], Abouelwafa et.al.[4]. A method of electrode excitation was proposed by Merilo et.al.[5] and incorporates the use of 6 strip-electrodes fed by a 3-phase voltage generator.

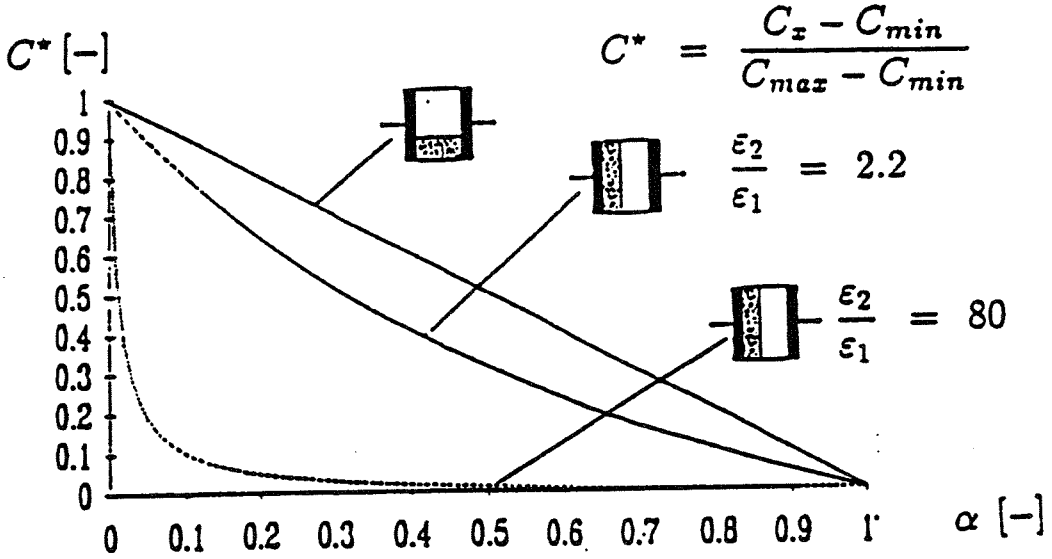

Figure 1: Dependence of the capacitance on the flow pattern

Although the impedance method offers a number of advantages like simultanous responce and no need for moving parts, its sensitivity to the flow pattern sometimes limits the range of application. The dependence of the impedance to

the flow pattern, i.e. to the phase distribution within the sensing volume is illustrated in fig.1. It shows the capacitance of a parallel plate capacitor filled with two dielectrics of permittivities ε_1, ε_2, calculated for the component interface perpenticular (case I) or parallel to the electrodes (case II)[6]. The normalized capacitance C^*

$$C^* = \frac{C_{meas} - C_{min}}{C_{max} - C_{min}} \tag{1}$$

in case I is calculated by parallel connection of the 2 particular capacitances C_1, C_2, in case II however, by their serial connection.

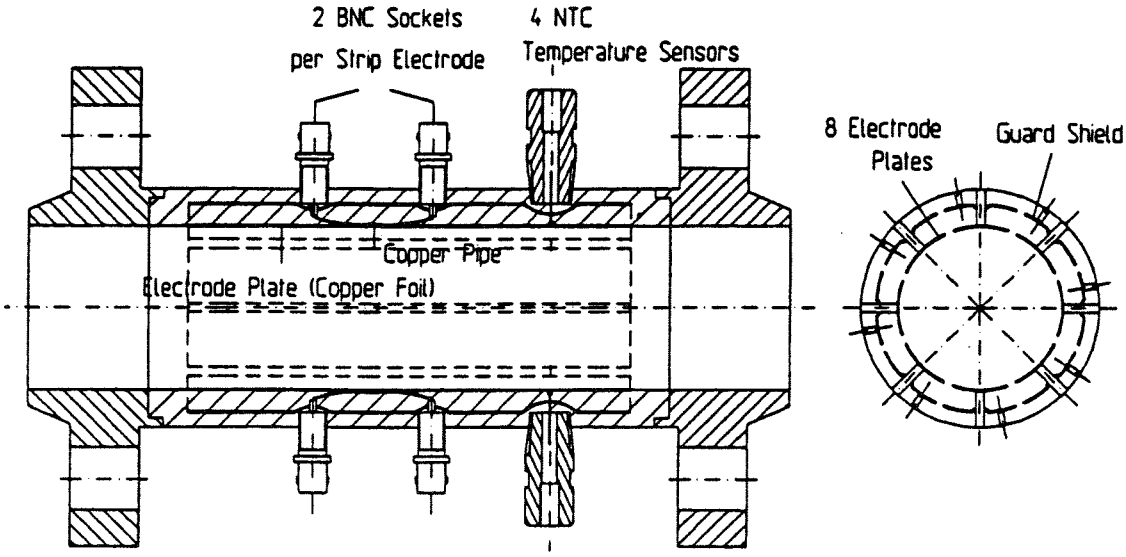

Figure 2: Non-intrusive probe (Ø54mm, L = 300 mm) with 8 plate electrodes

As Fig.1 clearly shows, the difference between the total capacitance $C^*(\alpha)$ for these two cases depends on the permittivity ratio $\varepsilon_1/\varepsilon_2$ of the flow components (α denotes the volume fraction of component 1). In gas-water flows, where $\varepsilon_1/\varepsilon_2 \approx 80$, the two curves differ so much, that the determination of the void fraction α by capacitance measurement, without any information about occuring flow pattern is connected with uncertainties far too high, and therefore becomes unreasonable. For the generally occuring flow conditions, especially with dispersed flow components a number of analytical models [7] - [10] are known for calculation of the permittivity ε of a mixture of two fluids of particular permittivities $\varepsilon_1, \varepsilon_2$. The course of C^* for these flow mixtures lies always between the two cases shown above [6]. Summarizing it can be said, that the

sensitity of the impedance method to the distribution pattern of the components leads to different characteristics for every flow regime. In flow situations, where this curves differ too much, more information about the flow is needed.

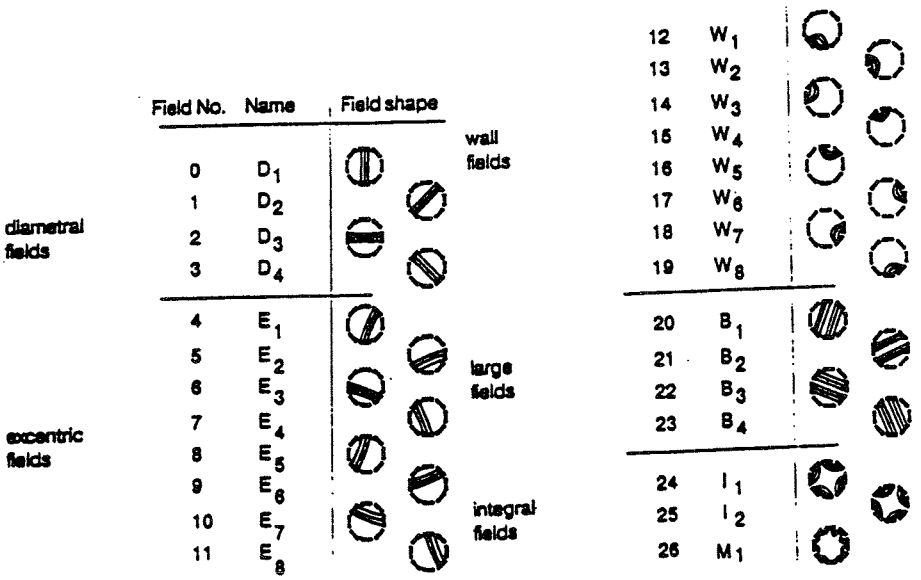

Figure 3: Measuring fields used with the impedance probe

To overcome the insufficiences mentioned above, a new approach is made for concentration measurement in multi-phase flows [10]. Although the proposed method has been originally developed with respect to offshore applications in oil-water-gas mixtures, it can be easily applied to a much wider field of multi-component flows. The main part of the described measuring technique is a non-intrusive impedance probe consisting of eight plate electrodes mounted near the surface of the inner side of the tube made of glass-fiber reinforced plastics. To reduce influences from outside the sensor a guard shield was also included. The influence of the temperature is captured by 4 circumferentially distributed NTC temperature sensors, directly mounted on the electrode plates (see fig.2).

With this probe, the impedance between different combinations of electrodes – the so-called measuring fields – is measured. For every measuring field, the impedance – as an intregral parameter – is determined by the component distribution within the whole sensing volume of the probe. However the individual domains of the sensing volume make different contributions to the total amount of the flow-influenced probe impedance. Therefore characteristic distribution patterns for the spacial sensitivity [11] can be observed, which allows one to classify the multitude of measuring fields into several groups.

Each group consists of a certain number of fields, which depends upon the degree of field symmetry, the fields being "rotated" against each other by an angle $\Delta\psi = k \cdot 360°/8$. These are the diametral fields $D_1 - D_4$, eccentric fields $E_1 - E_8$, wall fields $W_1 - W_8$, large fields $B_1 - B_4$, intregral fields I_1, I_2 and the Maltese-cross shaped field M_1 see fig.3. Although a much higher number of fields is theoretically possible the conducted tests proved, that the 27 fields shown above are sufficient to ensure a good and unambiguous performance over the flow regimes of practical relevance.

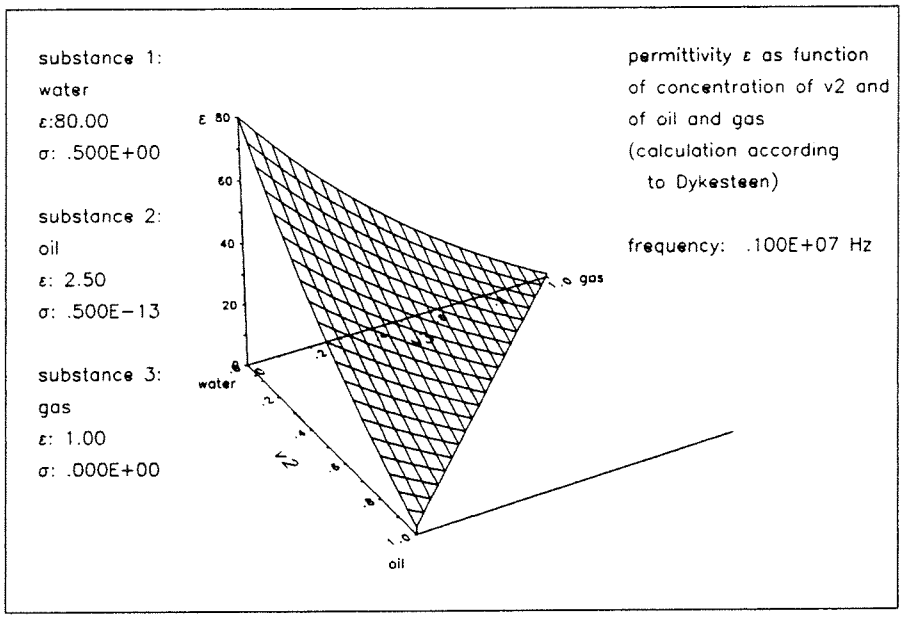

Figure 4: Calculated permittivity of a water-oil-gas mixture at 1 Mhz measurement frequency

Within each measurement cycle, the probe impedance for m fields is recorded. This measurement vector V, consisting of m impedance readings, is compared to a stored reference matrix M of dimension m × n. M consists of the $(m \cdot n)$ impedance values representing n different flow compositions over several flow regimes. Within every flowregime, the component concentration is increased gradually, the stepwidth depending on the overall accuracy of the measurement setup (typ. 2%). In this way the column numbers contain the encoded information about the flow regime and the flow composition.

It proved useful to generate both V and M with normalized, relative impedance values, $0 \leq Z_{ij} \leq 1$ as described in equation (1). This ensures good comparability and achieves independance of the actual probe dimensions. In the next step V and M are compared, calculating the error

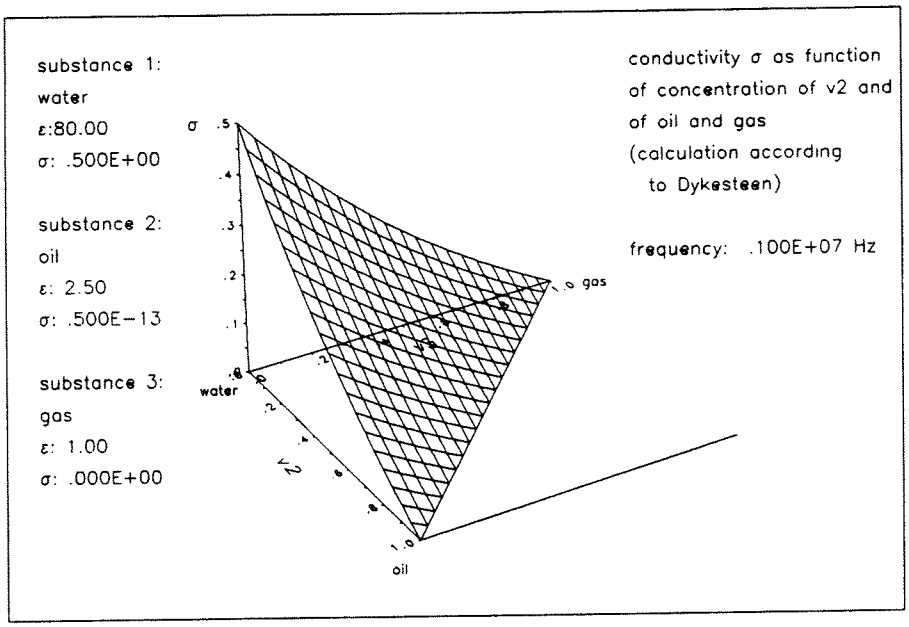

Figure 5: Calculated conductivity of a water-oil-gas mixture at 1 Mhz measurement frequency

$$s(j) = \sum_{i=1}^{m} (|V_i - M_{ij}|)^{1/2} \tag{2}$$

for every column of M. Due to the use of dimensionless impedances which lead to small error values in the range $s(j) < 1$ over most interesting flow regimes, eq. (2) shows a sharper detection of the minimum, compared to the sum over error squares, often used fore this purpose. The reconstruction is finally performed by determining the best-fit column ($s(j_0) = min\{s(j)\}$). The flow composition and the occuring flow regime are then determined by decoding the address of the determined column j_0.

2. 3-PHASE MEASUREMENT

To determine the void fraction of a three phase flow, i.e. oil, water and gas, two independend electrical informations are needed. Following Dykesteen [10] the complete usage of the measured impedance, consisting of capacity and conductivity, is enough. Fig. 4 shows the calculated capacity shape of a three-component mixture of water ($\varepsilon \approx 80$), oil ($\varepsilon \approx 2$) and gas ($\varepsilon \approx 1$). Figure 5 shows the calculated specific conductivity shape of a three-component mixture of water ($\sigma \approx 0.5$), oil ($\sigma \approx 0.5$ E-13) and gas ($\sigma \approx 0$). It has been shown, that the shapes of the two parts of the impedance are different enough to detect the void fractions

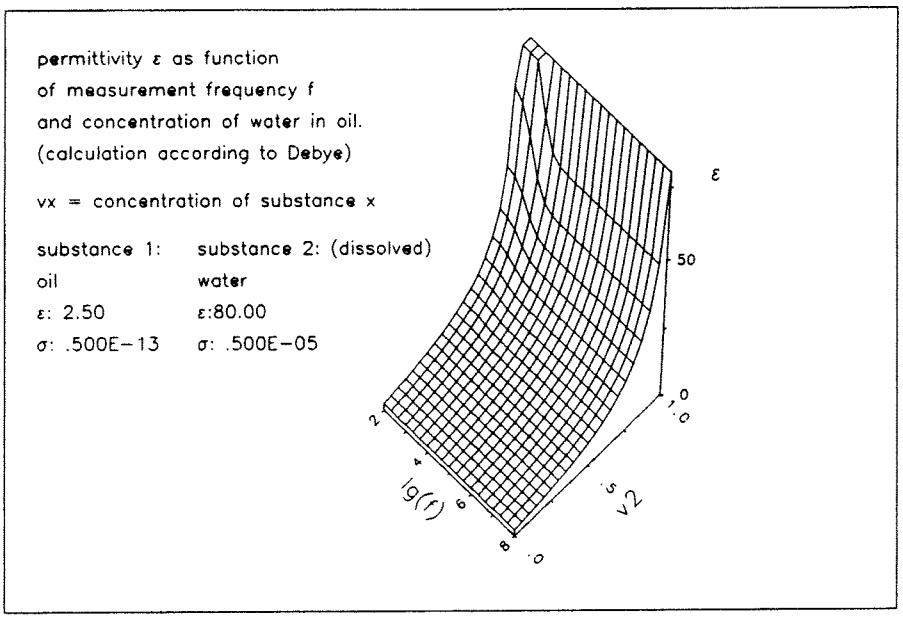

Figure 6: Calculated conductivity of a water-oil mixture with changing measurement frequency from 100 Hz to 100 MHz

α for gas and β for water. The measurement of the capacity gives a line of concentration ratios and the measurement of the conductivitiy gives another line of different concentration ratios, which meat at the actual mixture concentration. By using the HP impedance meter both values are simultaneously captured.

If there occur additional influences – like the flow pattern as mentioned above – a third information about the water-oil ratio will be available by changing the measurement frequency, because there is a change in conductivity of the water according to the frequency, but no change for oil and gas (see Fig.6). This will be very important for situations where no information for sure is available about the carrier phase of the oil-water mixture.

3. GENERATION OF THE REFERENCE MATRIX

The reference matrix can be generated in different ways: by numerical calculation or by calibration.

3.1 Numerical Calculation

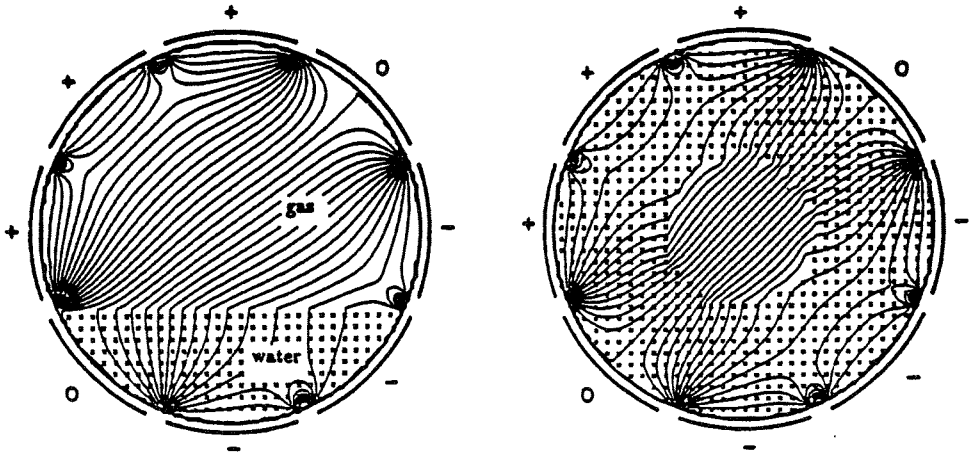

Figure 7: Equipotential lines in the probe for stratified (left side) and annular two-phase flow of water and air

The numerical method [10], [12] is based on the solution of Poisson's equation for a domain of permittivity ε and a space-charge density ϱ:

$$\nabla^2\varphi = \Delta\varphi = -\frac{\varrho}{\varepsilon} \tag{3}$$

In the special case, with no free charges ϱ equation (3) becomes

$$\Delta\varphi = 0 \tag{4}$$

Δ represents the Laplace operator and φ describes the potential. In cartesian coordinates, and if one of the three dimensions can be regarded infinitive, equation (4) simplifies to

$$\frac{\partial^2\varphi}{\partial x^2} + \frac{\partial^2\varphi}{\partial y^2} = 0 \tag{5}$$

The calculation of the 3-dimensional field can be accomplished by the use of a finite-difference method [13]. The Capacitance C_{AB} between any two of a given set of electrodes is determined by the existing electrical field between the assembly, i.e. by the potential distribution between the electrodes. In this way the impedances between any electrodes can be calculated for every specific flow

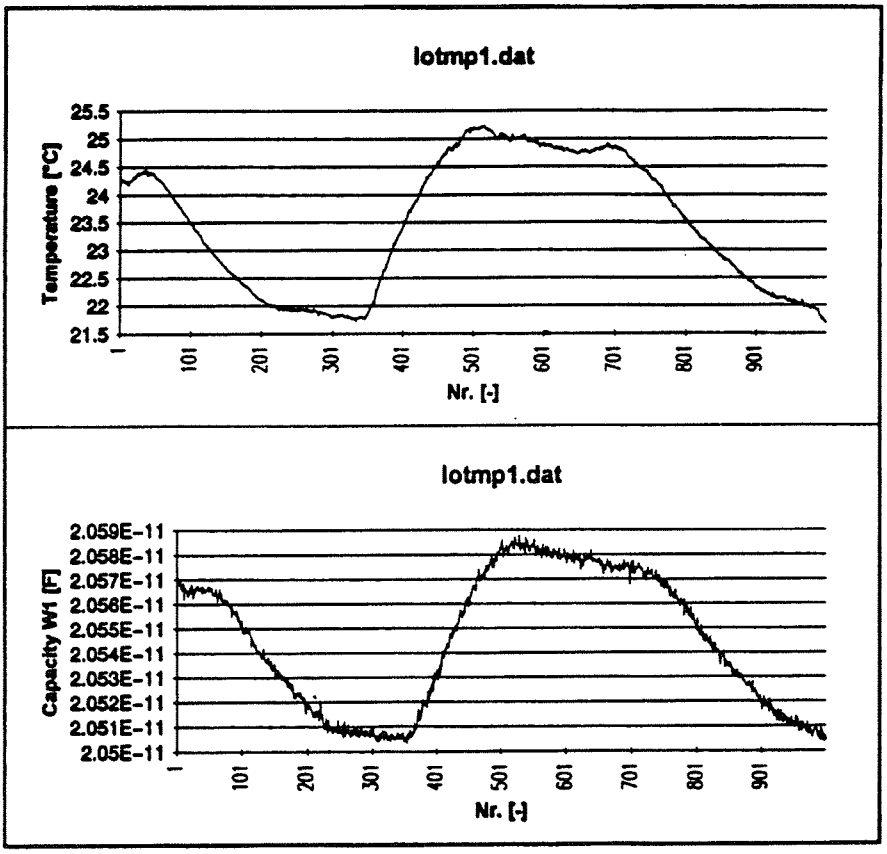

Figure 8: Temperature dependence of a wall field during a time cycle of 36 hours in an isolated room

distribution within the probe so that the distribution of the impedances for every measuring field is obtained. Fig. 7 shows calculated equipotential lines for stratified and annular two-phase flow of water and air.

The problem of any numerical method is to include effects of the set-up like coated electrodes or the shape of the electrodes which causes movements of the charges inside the electrodes not described by the simple theory. Due to this the calculation of the impedance has to be added to calibrations with the real probe.

3.2 Calibration

A very important part of the calibration is the determination of the minimum impedance Z_{min} of the probe correspondig to the filling with a gas only. This minimum impedance depends strongly on the design of the probe, i.e. the thickness of the coating of electrodes and its uniformity. The distance of the

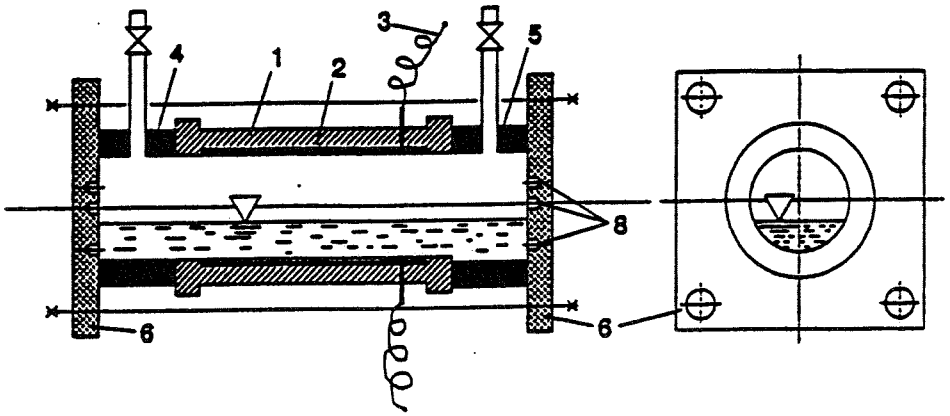

Figure 9: Apparatus for stationary calibration. Impedance probe (1), electrodes (2), electrical connections (3), tubes (4),(5), plexyglass planes (6), positioning bores for phantomes (8)

plate electrodes is the mean factor for the sensitivity of the wall fields. On the other hand environment influences like temperature or adsorption of humidity by the sensor plastics can change the minimum impedance by a multiple of the difference of (Z_{max} - Z_{min}). All these influences must be measured or – if this it not possible – avoided. Fig.8 shows the temperature dependence of a wall field. The change of capacity caused by 3 degrees C represents about 10 % of the measurement range.

In the second step the reference matrix is generated. This can be done under two conditions:

- real flow conditions
- stationary conditions

In the first case, the impedance probe is exposed to a multi-phase flow of the required regime and flow components. During a stepwise alteration of the flow composition the impedance values for all measuring fields are captured. For this calibration procedure, a multi-phase measurement technique is required as reference for the actual volumetric flow composition. In this case quick closing valves has been used for stationary flow and a 5Ci γ-ray densitometer for stationary and instationary flow. In flow regimes with fluctuating component concentrations, e.g. slug flow, it has to be ensured, that representative values of the void fraction are recorded. If the reference matrix is generated by calibration in real flows, the flow itself can be regarded as a "black box", and no

further assumptions concerning the phase distribution are required. By consequence even exotic flows can be covered. The maximum possible reconstruction accuracy is determined by the accuracy of the reference measurement used for calibration.

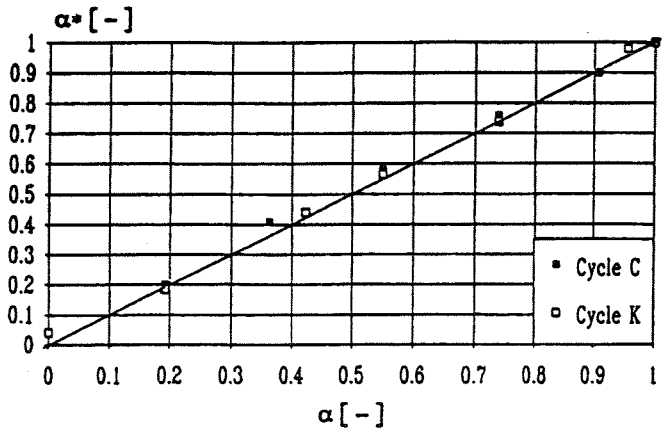

Figure 10: calculated void fraction α^* versus reference void fraction α for stratified flow of oil and gas comparing the complete cycle K (27 fields) and the short cycle C (8 fields)

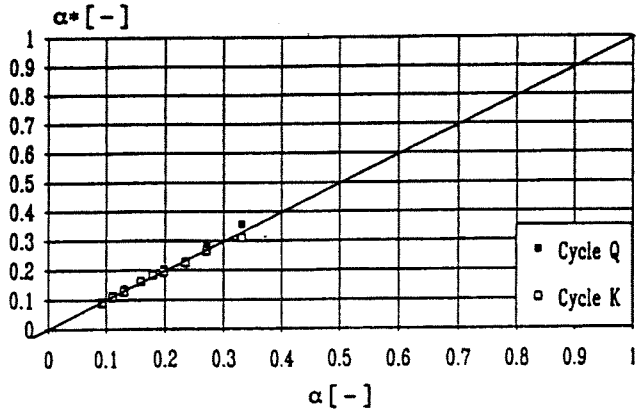

Figure 11: calculated void fraction α^* versus reference void fraction α for bubbly flow of water and gas comparing the complete cycle K (27 fields) and the short cycle Q (4 fields)

If multi-phase test facilities are not available, a modified calibration procedure, the stationary calibration can be used instead. In this case the component distribution is simulated by phantoms. The phantoms could be either geometricly exact designed parts like acrylic pipes or sticks representing, e.g. annular

flow, or averaging parts like plastic foams representing bubbly flow. Though the density distribution of the exactly defined parts is well known, the distribution of the foams has to be measured by a reference technique also. This is done by the simultanous measurement of a γ-ray densitometer and the impendance meter of the probe filled with the foam.

The third stationary calibration method is the stepwise decrease of the void fraction by injecting equal amounts of liquid by the help of a syringe while flanging the probe between two planes of plexiglass (see Fig.9). This kind of calibration has to be repeated for several inclinations of the probe corresponding to flow pattern changing from stratified flow to slug or plug flow.

It is essential, that the void fraction steps $\Delta\alpha$ between adjacent impedance vectors stored in the reference matrix remain under a certain magnitude, which is determined by the overall accuracy of the impedance measurement (typically $\Delta\alpha = 2\%$). This is achieved by interpolation algorhithms applied to the data obtained.

4. EXPERIMENTAL DATA

The experimental data shown below have been obtained with an impedance probe in the stratified, bubbly and annular flow regime. The measurements were carried out in oil-gas and water-gas flows of ambient pressure with tap water, SHELL Ondina 15 oil and air. The multi-phase test loop was equipped with horizontal and vertical test sections of 10 m length. Liquid flow rates could be adjusted in the range of $0.3 \leq \dot{V}_l \leq 4l/s$, gas flow rates were between $0 \leq \dot{V}_g \leq 9l/s$. Thus a void fraction of $0 \leq \alpha \leq 0.88$ could be covered. The reconstruction was based on capacitance measurement at a frequency 100 kHz, using a HP 4284A impedance meter. This allowed for a measurement time $t_{meas} \approx 30ms$ per field at a basic accuracy in the range of 0.1%.

According to the description of the reconstruction technique given above, it is to be expected, that the best results are obtained, if cycles with a large number of measuring fields are employed. However this is connected with a long measuring time (up to 1.8s) per cycle. Under many practical conditions, this is not tolerable, especially if in the time history of the void fraction fluctuations have to be tracked.

In order to increase the measurement rate per cycle some short cycles had been composed of few fields, containing a maximum of information corresponding to a special flow pattern (for detailed information see [6], [12]). The short cycles had been cheked for three flow patterns: for stratified flow (Fig.10), for bubbly flow (Fig.11) and for annular flow.

While keeping the inaccuracy of the reconstruction below 10% the measurement speed could be accelarated by factors of 4 to 8. This causes a measurement strategy of two steps. In the first step a complete cycle is used to determine the

flow pattern and the void fraction. With the information about the flow pattern a shorter cycle is used for a faster detection of the void fraction.

5. DISCUSSION AND CONCLUSIONS

The results presented in this paper demonstrate the excellent performance of the new developed, impedance-based reconstruction technique for multi-phase flows. This improved technique avoids the disadvantages of the conventional impedance method by multi-channel measurement with the help of numerous fields and a non-intrusive, multi-electrode probe. All the calculation steps and control functions for the impedance meter are easily performed by a regular size PC. The method detects the occouring flow regime and the volumetric flow composition. Its application range can also easily be extended to three-phase flows.

The required reference matrix can be generated by calibration or numerical calculation or a combination of both. The best results are obtained by a combination of stationary calibration of the sensor itself and the calibration for the void fraction in a real two-phase flow. To speed up the measurement rate a sophisticated combination of measurement fields is created using preinformation about the flow pattern.

References

[1] Auracher, H.; Daubert, J.: "A Capacitance Method for Void Fraction Measurements in Two-Phase Flow", 2nd Int. Conf. on Multi-Phase Flow, London(1985).

[2] Özgü, M.R.; Chen, J.C.; Eberhardt, N.: "A Capacitance Method for Measurement of Film Thickness in Two-Phase Flow", Rev. Sci. Instrum. 44 No 12, pp 1714 -1716(1973).

[3] Geraets, J.M.; Borst, J.C.: "A Capacitance Sensor for Two-Phase Void Fraction Measurement and Flow Pattern Identification", Int. J. Multiphase Flow, Vol 14, No 3, pp 305 -320 (1988).

[4] Abouelwafa, M.; Kendall, J.M.: "The Usage of Capacitance Sensors for Phase Percentage Determination in Multiphase Pipelines", IEEE Trans. Instr. Meas., Vol IM-29, No 1, pp 24-27 (1980).

[5] Merilo, M.; Dechene, R.L.; Cichowlas, W.M.: "Void Fraction Measurement With Rotating Electric Field Conductance Guage", Trans. ASME J. Heat Transfer Vol 99, pp 330-332 (1977).

[6] Klug, F.: "Ein Meßverfahren zur impedanzgestützten Rekonstruktion der Gemischzusammensetzung in Mehrphasenströmungen", Diss.

Technical University of Munich, VDI Fortschrittsberichte Reihe 3, Nr. 327, Düsseldorf (1993).

[7] Maxwell, J.C.: "A Treatise on Electricity and Magnetism", Vol. 1, Claredon Press Oxford (1892).

[8] Bruggemann, D.A.G.: "Berechnung verschiedener physikalischer Konstanten von heterogenen Substanzen", Ann. d. Physik, 24, pp 636-679, Leipzig (1935).

[9] Beek, L.K. van: "Dielectric Behaviour of Heterogeneous Systems", Progress in Dielectrics, Vol. 7 (1967).

[10] Dykesteen, E. et.al.: "Non-Intrusive Three-Component Ratio Measurement Using an Impedance Sensor", J. Physics E., Sci. Instrum. 18 (1985).

[11] Bair, M.S., Oakley, J.P.: "Comparison of Excitation Methods for Electrical Capacitance Tomography", 1st Meeting European Concerted Action on Process Tomography, Manchester, March 26-29 (1992).

[12] Klug, F.; Mayinger, F.: "Impedance Based Flow Reconstruction - A Novel Flow Composition Measuring technique for Multi-Phase Flows", Proc. NURETH-5 Meeting, Salt Lake City, Sept 21-24 (1992).

[13] Philippow, E.: "Grundlagen der Elektrotechnik", 8. Auflage, Hüthig Verlag, Heidelberg (1980).

Symbols

C	[F]	capacitance
C^*	[-]	relative capacitance
L	[m]	length of probe
M		Matrix
Q	[As]	charge
s	[-]	error value
V		vector
$\dot{V}$	$[m^3/s^{-1}]$	flow rate
w	[m/s]	velocity
x, y		cartesian coordinates
Z	[Ω]	impedance
Ø	[m]	diameter of probe
α	[-]	volumetric viod fraction
ε	[-]	permittivity
ϱ	$[Asm^{-3}]$	space-charge density
σ	$[\Omega^{-1}m^{-1}]$	specific conductivity
φ	[V]	potential
ψ	[-]	angle

Indices

g	gas
i	row
i	row
j	column
l	liquid
s	superficial

Visualization and Measurement of Multi-phase and Liquid Metal Flows by Real-time Neutron Radiography

N.Takenaka[1], T.Fujii[1], A.Ono[2], Y.Motomura[3] and A.Turuno[4]

[1] Department of Mechanical Engineering
[2] Faculty of Cross-Cultural Studies
[3] Graduate School of Science and Technology
Kobe University
Rokkodai, Nada, Kobe, 657 Japan
Telephone:(078)881-1212, Facsimile:(078)803-1131

[4] Department of Research Reactor
Tokai Research Establishment, Japan Atomic Energy Research Institute
Tokai, Naka, Ibaraki, 319-11 Japan

ABSTRACT

Flow visualization is a useful method to study thermal hydraulics phenomena. When the flow is under high pressure and high temperature conditions or the fluid is a liquid metal, the flow visualization is often difficult by optical rays. Since most of metal are visible by a thermal neutron ray and some elements are quite opaque to it, the real-time neutron radiography can be applied to visualize flows in metallic tubes and containers and flows in a liquid metal. In this report, visualization and measurement results are presented on multiphase flows in metallic tubes and containers and flows in a liquid metal by real-time neutron radiography.

1. INTRODUCTION

Flow visualization is a useful method to study thermal hydraulic phenomena. Many optical visualization and measurement methods have been developed for transparent single phase fluids like gas and water. However, these methods are not often applicable to multiphase flows and are difficult to apply liquid metal flows.

The thermal hydraulic systems may be classified into three cases from a view of the visualization techniques;

1. flows of both the working fluids and the wall of a tube or a vessel are transparent to optical rays,
2. those which can be simulated by the transparent systems, and
3. those in which either the working fluid or the wall is opaque to optical rays and are difficult to be simulated by the transparent systems.

Multiphase flows under high pressure and temperature conditions are often in metallic tubes or vessels. A liquid metal is opaque to visible rays. Heat and mass in multiphase flows are transferred through metallic wall. Flows in industrial machines are often in metallic bodies. These flows are often difficult to be simulated by the transparent systems and are included in case 3. New techniques have been developed for the flow

visualizations of case 3 and some of them are radiography techniques.

Radiography is a technique to visualize the structure of an object by the difference of the attenuation rates of radio rays to the materials of the object. A radio ray is attenuated exponentially in an object depending on the characteristics of the ray and the materials of the object. The ray intensity is expressed as

$$N = N_0 \exp(-\mu x) \quad (1)$$

where N_0 is the initial intensity of the ray, N is the intensity in the object at the distance x and μ is the attenuation coefficient which is determined by both the radio ray and the irradiated material. Mass attenuation coefficient μ_m, which is defined as

$$\mu_m = \mu/\rho \quad (2)$$

where ρ is the density of the material, is often used to indicate the transparency of the ray to the material. The material is more transparent for smaller value of μ_m and is more opaque for larger value.

Figure 1 shows the mass attenuation coefficients of thermal neutron rays and a X-ray of 125 keV for various elements [1]. The X-rays of near 100 keV has been often used for non-destructive examinations as well as Roentgen. The mass attenuation coefficients of a X-ray increases with increasing atomic number. On the other hand, those of neutron rays depend much on each element. They are large for small atomic number elements of H, B and Li and for some special elements such as Cd, Gd, Sa, Eu etc. but they are small for high atomic number elements such as Pb, Bi etc..

Applications of neutron radiography have been proposed for many non-destructive examinations since the attenuation characteristics of neutron rays in materials are much different from those of X-rays, i.e., the image difficult to be visualized by X-rays can possibly be visualized by neutron rays. Many applications have been reported and most of them were presented in the proceedings of world neutron radiography conferences [2]. Some of them are methods to obtain still images on a film and others are real-time methods taken by a video camera. The real-time neutron radiography are applicable to observe the dynamic behaviors of the flows which are difficult to be observed by the other methods.

It can be seen from Fig. 1 that the thermal neutron ray is attenuated by water and that it penetrates through most of metals. Therefore, the real-time neutron radiography is suitable for visualizing the dynamic behaviors of water in a metallic bodies. It is also suitable to seen through a liquid metal flow. By image-processing the visualized neutron radiography images, void fraction in gas-liquid two-phase flows and flow vector fields can be obtained

The authors have been studying following projects by the real-time neutron radiography;

a) visualization of multiphase flows and measurement of the void fraction distributions,

b) visualization of liquid metal flows, and

c) visualization of two-phase flows in industrial machines.

Some of the visualized and image processed results are presented on the cases a) and b) in this report. According to the case c), two-phase flow

cooling systems for a space-craft, a plate-fin heat exchanger for a cryogenic fluid and a compressor, heat exchangers and a capillary tube in an air-conditioner were visualized.

2. NEUTRON RADIOGRAPHY SYSTEM AND EXPERIMENTAL PROCEDURE

Three neutron radiography systems were used. One is an accelerator based system in Sumitomo Heavy Industries (SHI) and two are reactor based systems at JRR-3M in Japan Atomic Energy Research Institute (JAERI) which is one of the highest neutron flux system in the world and in Pennsilvania State University (Penn. State). Details of the systems can be found in the proceedings [2]. The thermal neutron fluxes of the systems are 10^6 n/m^{2}s in SHI, 1.5×10^8 n/m^{2}s in JAERI and 5×10^6 n/m^{2}s in Penn. State.

Thermal neutron rays generated by an accelerator or a nuclear reactor was collimated by a duct made of polythylene to obtain a parallel neutron beam. Then the beam was irradiated to the test section. The radiography image of the object was converted to a optical ray image by a scintilation converter and was recorded by a high sensitivity video camera. The speed of the video camera was 30 frame/sec. Schematic diagram of the neutron radiography system in JAERI is shown in Fig.2.

The experimental apparatus was remote-controlled outside of the irradiation room. Tubes for water and gas and wires for electrical inputs and signals were equipped between the irradiation room and the operator room. The water, the gas and the electrical inputs were supplied and controlled from the operator room to the test section. The electrical signals were recorded in the operator room.

3. TEST SECTIONS AND VISUALIZED AND IMAGE PROCESSED RESULTS

3.1 Flow Patterns of Gas-Liquid Two-phase Flow and Fluidized Bed

Figure 3 (a) shows example of nitrogen gas-water two-phase flow in a vertical stainless steel tube of 25 mm in inner diameter and 1 mm in thickness The flow pattern map obtained by the neutron radiography observation is shown in Fig.3 (b) where solid lines indicate the flow pattern transition boundaries predicted by Mishima and Ishii [3]. Examples of flow patterns in a boron oxide powder fluidized bed in a vertical aluminum tube of 23 mm in inner diameter and 1 mm in thickness are shown in Fig.4. They were visualized by SHI system. The neutron flux was low in SHI system but the flow patterns in a metallic tube can be well observed. It was shown that an accelerator system can be applicable to multiphase flow visualization.

Figures 5 (a),(b) show a test section and consecutive pictures in a fluidized bed of polystyrene particles in an alminum vessel visualized by JAERI system. Dynamic behaviors of bubbling are clearly seen.

3.2 Void Fraction Distribution of Gas-Liquid Two-phase Flow

Two-dimensional void fraction distributions of gas-liquid two-phase flows were measured by the image processing methods. The one-dimensional void fraction distribution can be obtained by integrating them. The three-dimensional distribution is obtainable by the CT-method if the flow is steady and the test section can be rotated.

Two-dimensional distribution of the brightness in a two-phase flow image by radiography is expressed as below,

$$S(x,y) = G(x,y)\exp[-\rho_w \mu_w t_w(x,y)-\{1-\alpha(x,y)\}\rho_L \mu_L t(x,y)-\alpha(x,y)\rho_G \mu_G t(x,y)] + O(x,y) \quad (3)$$

where $G(x,y)$ and $O(x,y)$ are the gain and the offset which are detemined by the non-flatnsess of the beam and the imaging system and $\alpha(x,y)$ and $t(x,y)$ are the void fraction and the thickness measured along the beam direction. The suffixes of $_w$, $_G$ and $_L$ means wall, gas and liquid. Before the two-phase experiment, the offset $O(x,y)$ can be measured without the neutron beam and the distribution of the brightness in the test section filled with liquid, $S_0(x,y)$, i.e. $\alpha(x,y)=0$, and that filled with gas, $S_1(x,y)$, i.e. $\alpha(x,y)=1$, can be measured. From the two-phase image, $S(x,y)$, with the images of $O(x,y)$, $S_1(x,y)$ and $S_0(x,y)$, $\alpha(x,y)$ can be expressed as

$$\alpha(x,y) = \frac{\log[S(x,y)-O(x,y)] - \log[S_0(x,y)-O(x,y)]}{\log[S_1(x,y)-O(x,y)] - \log[S_0(x,y)-O(x,y)]} \quad (4)$$

Therefore, the two-dimensional void fraction distribution can be obtained by image-processing four images.

Figures 6 (a),(b) show a test section and image processed results of two-dimensional time-averaged void fraction distribution in a rectangular aluminum vessel of 30x90 mm² and 10 mm in thickness obtained by JAERI system. Water and nitrogen gas were injected at the lower corner of the vessel and a two-dimensional gas-liquid two-phase flow was formed in the test section. The void fraction distributions obtained by Eq.(4) was time-averaged for 256 frames, i.e. 8.53 sec, to obtain time-averaged distributions. These results can be used as a bench mark test for two-dimensional two-fluid model analyses.

Figures 7 (a)-(c) show experimental apparatus for a water flushing flow in an aluminum nozzle, calculated results of axial symmetric distribution of the void fraction and one-dimensional void fraction distribution obtained by SHI system. Hot water was injected in the convergent-divergent nozzle and the water flushed near the throat of the nozzle. One-component two-phase flow was expanded to atmosphere in the divergent part. Assuming the two-phase flow is axial symmetric, axial symmetric void fraction was calculated by the CT-method. Integrating radially, one-dimensional void fraction distributions were also obtained. The results were used to test one-dimensional two-fluid model codes. Calculated results by Mini-TRAC-PF1 and -BF1 codes [4] were compared with the experimental results in Fig.7 (c). In the present experimental conditions, the inlet pressures from 0.4 to 0.8 MPa and the inlet subcoolings from 3 to 40 K, BF1 predicted the experimental results better than PF1.

Figures 8 (a),(b) show an experimental apparatus and some slices of three-dimensional void fraction distribution of a dispersed flow formed by impinging mist flows generated by two nozzles in an alminum container. The container was rotated and 100 images were taken every 1.8° rotation. Each slices was reconstructed by CT-method.

It is shown that one-, two- and three-dimensional void fraction of gas-liquid two-phase flow in a metallic conduit can be measured by neutron radiography.

3.3 Liquid Metal FLows

Figures 9 (a)-(d) show a test section for a forced circulation flow in the lead-bismuth eutectic and visualized and processed results. The test section shown in Fig.9 (a) is a two-dimensional model of a liquid target for a high energy accelerator studied by Takeda [5] in Paul Scherrer Institute. The vessel was made of braze and the wall thickness was 2 mm. The thickness of lead-bismuth is 10 mm. The circulation was induced by a bubble pump. The flow was visualized by a tracer method by JAERI system and a dye-injection method by SHI system. In the tracer method, cubes about 2 mm made of gold-cadmium intermetallic compound, $AuCd_3$, were used, which has a large neutron attenuation coefficient and the similar density to the liquid metal and wets well to it. The tracers in the liquid metal which was suspended in the flow can be clearly seen as a small dots in Fig.9 (b). To obtain a vector field, consecutive two processed frames in 1/30 sec were used and space correlation functions between two frames were calculated at each point. The flow vector can be obtained at the peak of the correlation function. An example of the vector field is shown in Fig.9 (c). An example of the visualizaion by a dye-injection is shown in Fig.9 (d). The dye of liquid lead-bismuth-cadomium alloy, which has high neutron attenuation coefficient, the similar density to the liquid metal and solvable to it, was injected into the fluid and the dye followed the flow.

Figures 10 (a),(b) show a test section and images of the solidification of the liquid metal. The molten lead-bismuth eutectic in the vessel was cooled by water at one side and was solidified from the side. By inserting the dye of a lead-bismuth-cadmium alloy, the solid-liquid interface was clearly visualized since the dye was diffused in the liquid phase but did not penetrate into the solid phase. An examples of the visualized interfaces are shown in Fig.10 (b). The dye was injected three times and the growing interface was observed.

It is shown that real-time neutron radiography is applicable to visualization of a liquid metal flow which is difficult by the other methods.

4. CONCLUSION

Multiphase and liquid metal flows were visualized by the neutron radiography and visualized images were image-processed. Many experimental results which were difficult to visualize or measure by the other methods can be obtained. It was shown that the real-time neutron radiography is efficiently applicable to thermal hydraulics researches.

REFERENCES

1. "Neutron Radiography 1981,1986", Reidel Pub. Comp., 1981,1986.
   "Neutron Radiography (3), (4)", Kluwer Acad. Pub., 1990, 1994.
2. "Neutron Radiography Handbook", Reidel Pub. Comp., 1981.
   "Practical Neutron Radiography", Kluwer Acad. Pub., 1992.
3. K.Mishima and M.Ishii, "Flow Regime Transition Criteria Consistent with Two-fluid Model for Vertical Two-phase Flow", NUREG/CR-3338, ANL-83-42, 9183
4. H.Akimoto et. al.,MINI-TRAC Code: "A Driver Program for Assessment of Constitutive Equations of Two-Fluid Model", JAERI-M. 91-086, 1991 (in Japanease)

5. Y.Takeda, Thermofluid Behaviour of the Lead Bismuth Eutectic Target for the Spallation Neutron Source at SIN, Nuclear Instrument Methods in Physical Research A237 (1985)

Acknowledgements
The authors wish to express their cordial acknowledgements to researchers in Sumitomo Heavy Industries and Pennsilvania State University for their supports in neutron radiography experiments. Their acknowledgements are also extended to Messrs S.Ueda, H.Yamano, Y.Nakamura for their aids in the experiments.

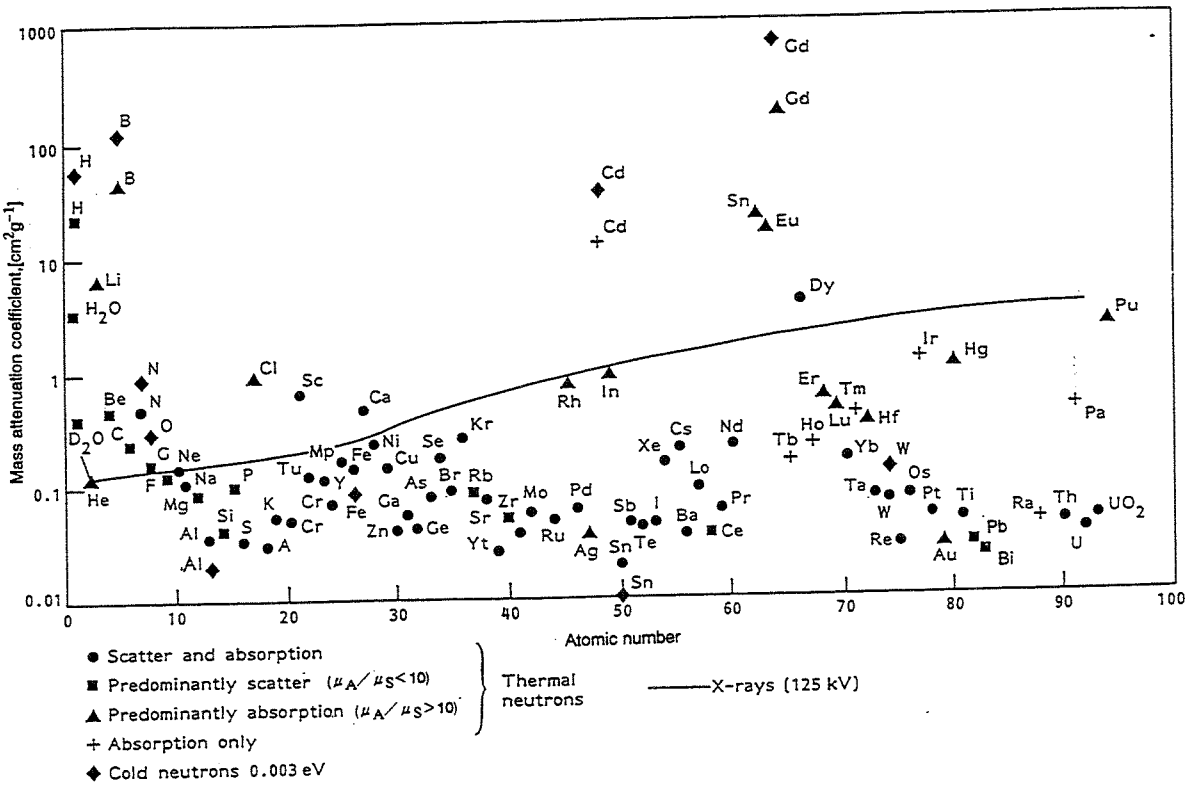

Fig. 1 Mass attenuation coefficient of neutron and X-rays

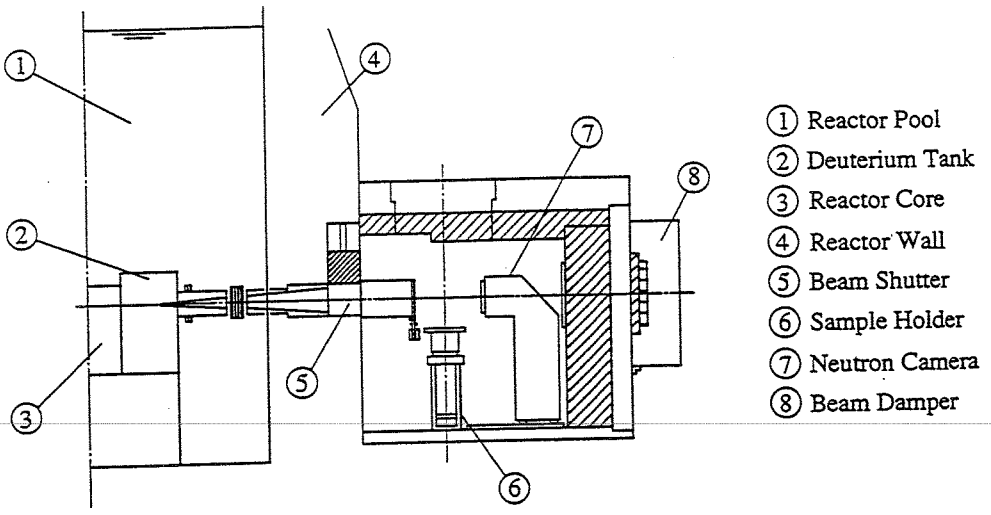

Fig. 2 Schematic diagram of neutron radiography system at JRR-3M in JAERI

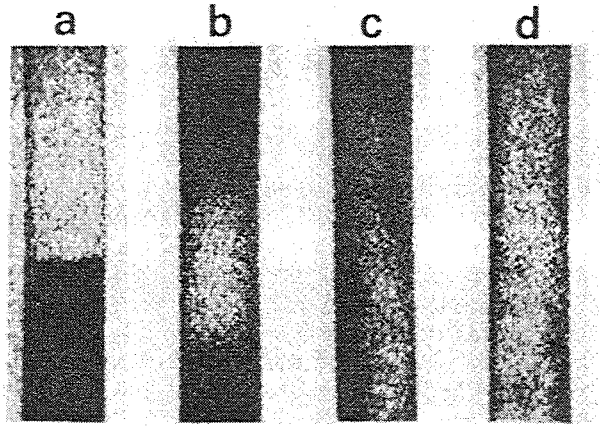

Fig. 3(a) Flow patterns of gas-liquid flow in a vertical tube (SHI)
(a) tube half filled, (b) slug flow, (c) froth flow, and (d) annular flow

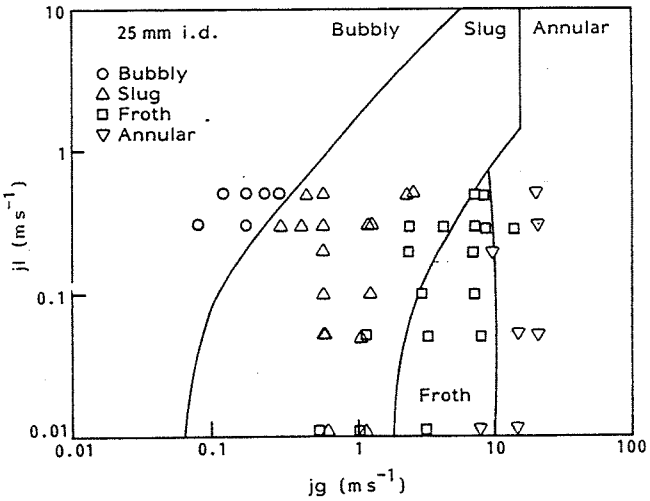

Fig. 3(b) Flow pattern map (SHI)

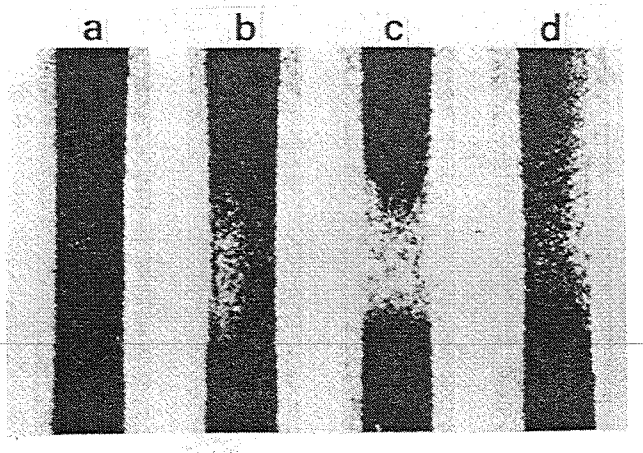

Fig. 4 Flow patterns in fluidized bed in a vertical tube (SHI)
(a) no gas injection, (b) bubbles observed, (c) slugging, and (d) flow pattern

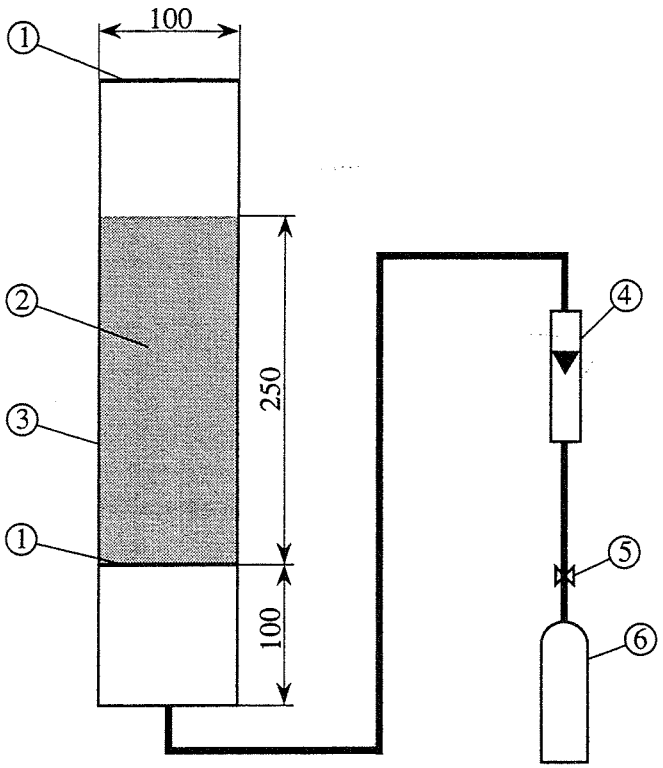

Fig. 5(a) Test section for fluidized bed in a vessel

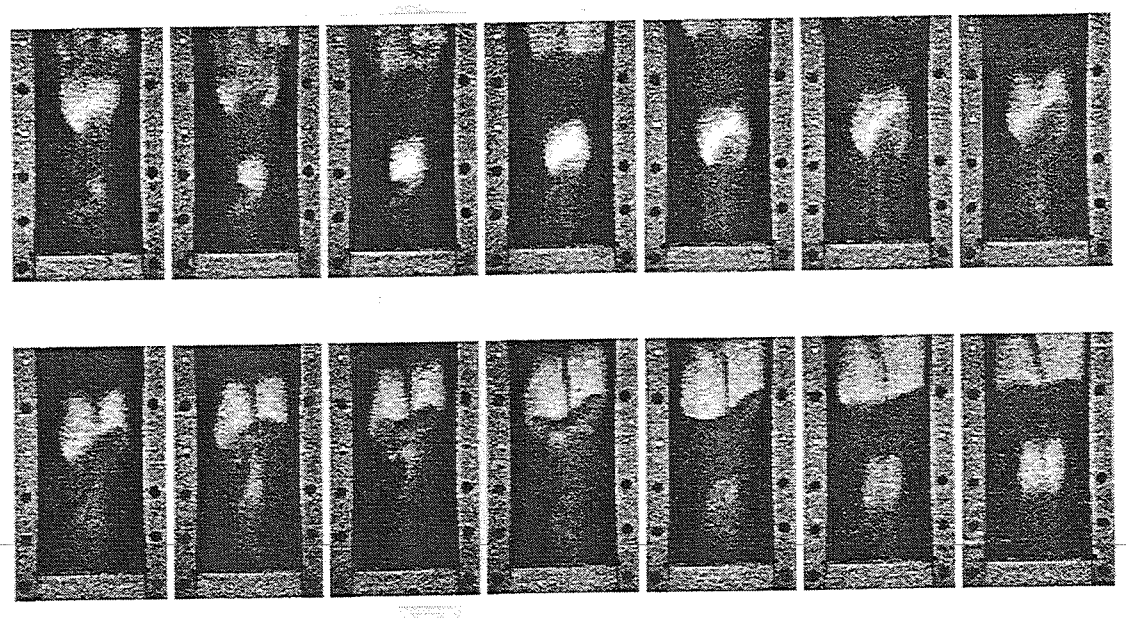

Fig. 5(b) Bubbling in fluidized bed in a vessel (JAERI)

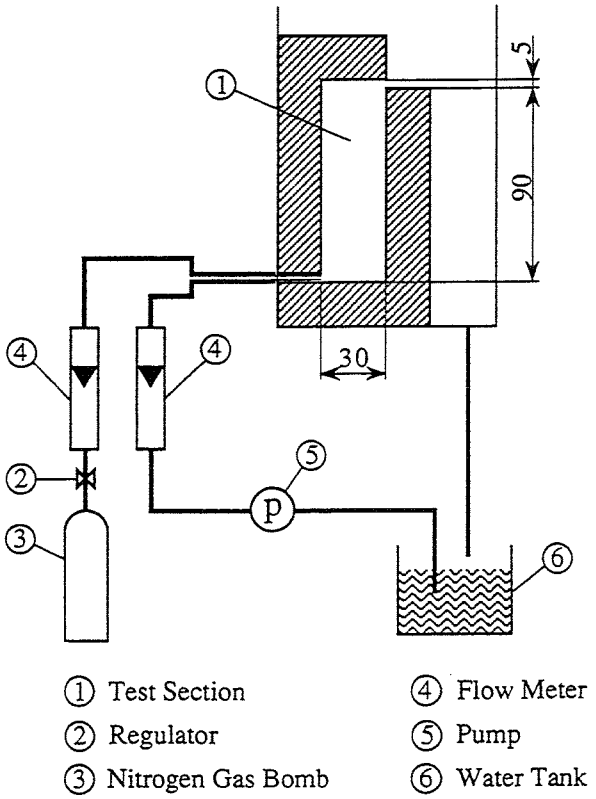

Fig. 6(a) Test section for gas-liquid two-phase flow in a vessel

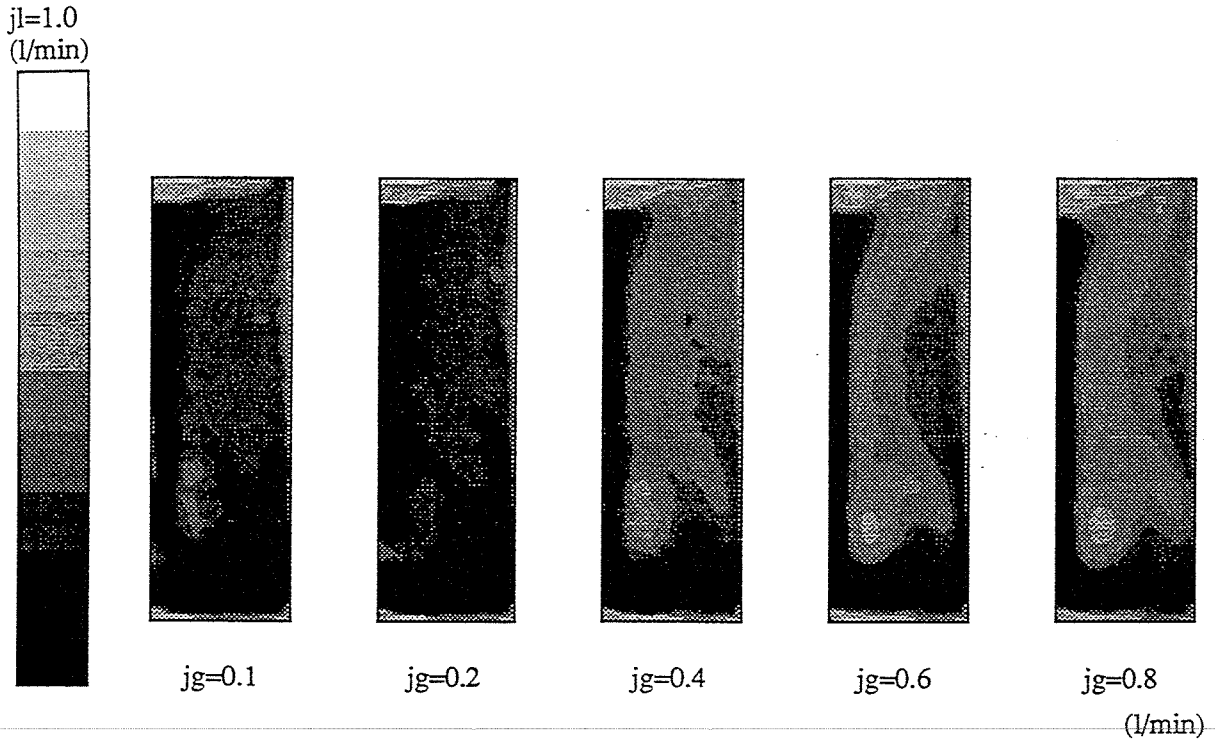

Fig. 6(b) Two-dimensional time-averaged void fraction distribution of gas-liquid two-phase flow in a vessel (JAERI)

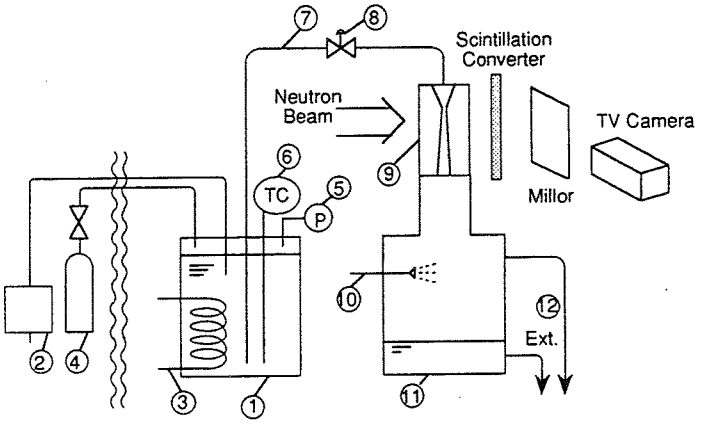

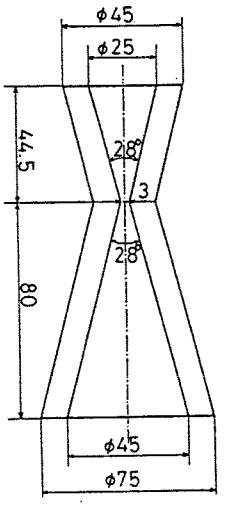

The details of the tested nozzle

1. Pressure tank
2. pump
3. heater
4. nitrogen gas bomb
5. pressure transducer
6. themocouples
7. pipe line
8. air-operation ball balve
9. nozzle
10. water splay
11. drain tank
12. drain pipes

Fig. 7(a) Experimental apparatus for flashing flow in a nozzle

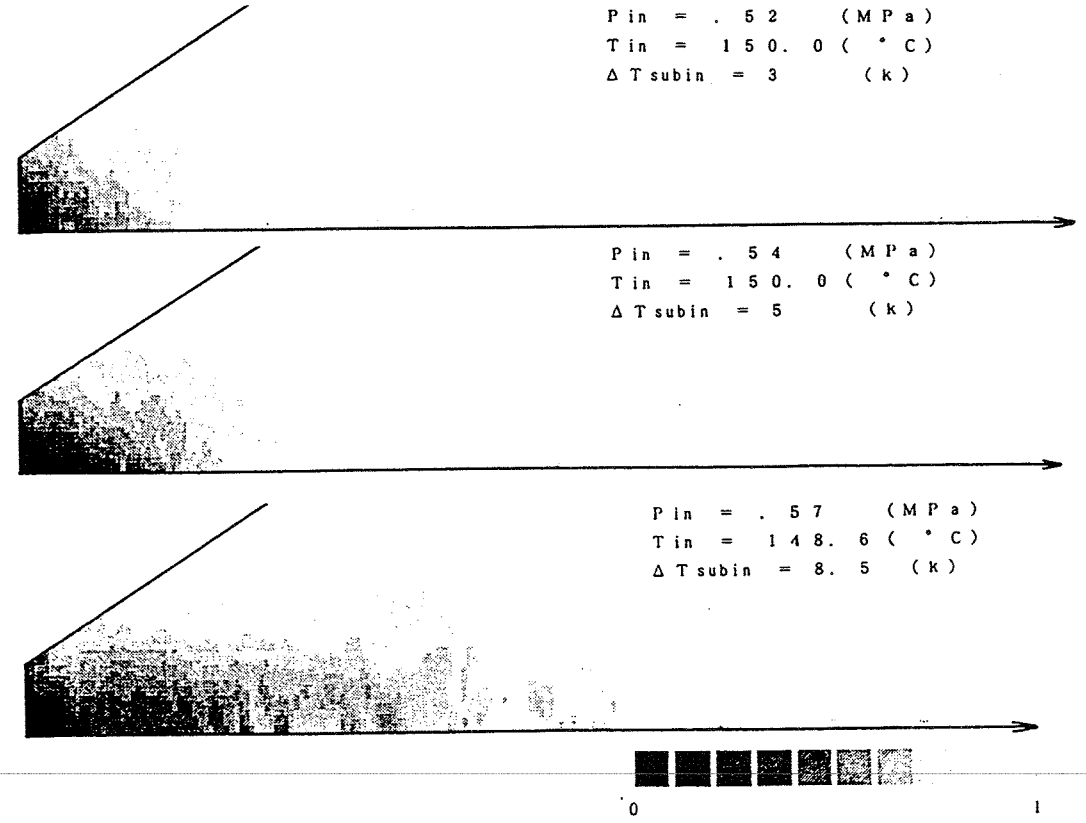

Fig. 7(b) Axial symmetric void fraction distribution in a nozzle (SHI)

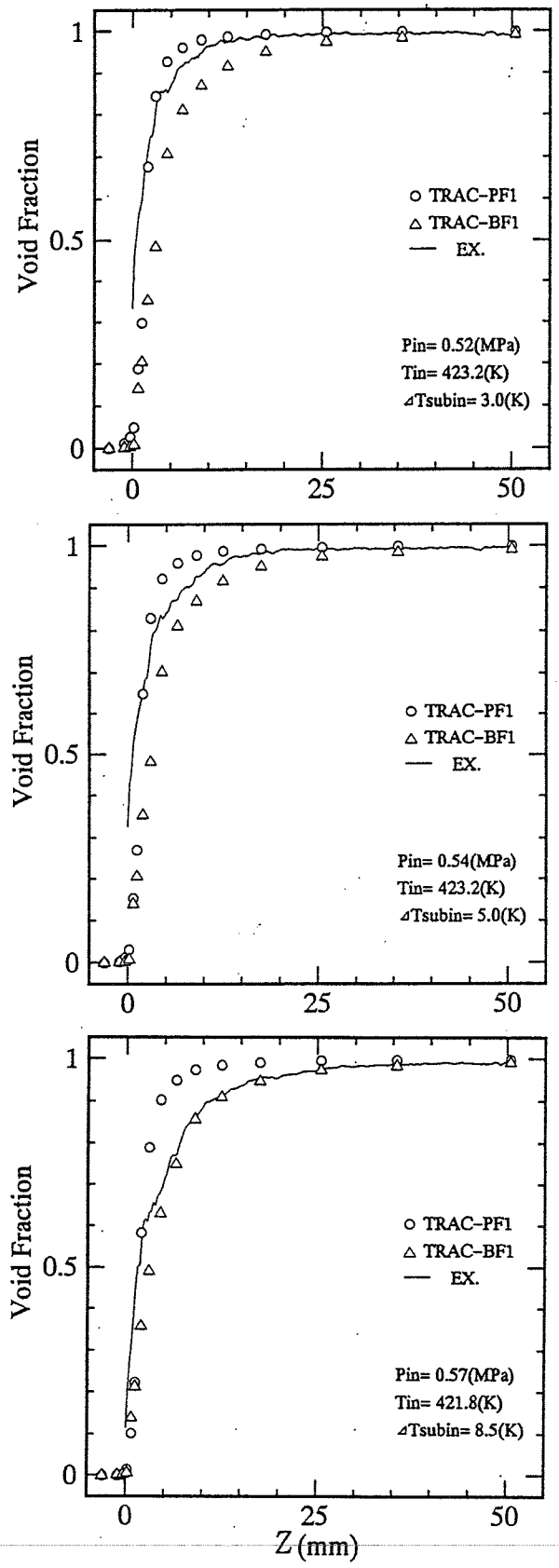

Fig. 7(c) One-dimensional void fraction distribution (SHI)

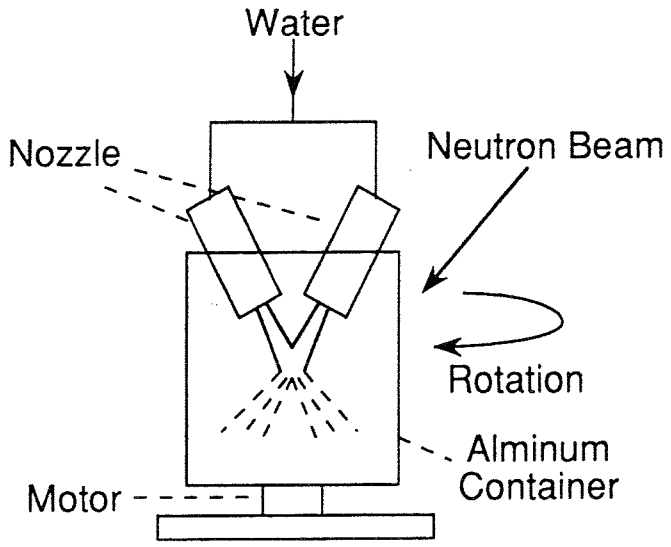

Fig. 8(a) Test section for three-dimensional dispersed flow

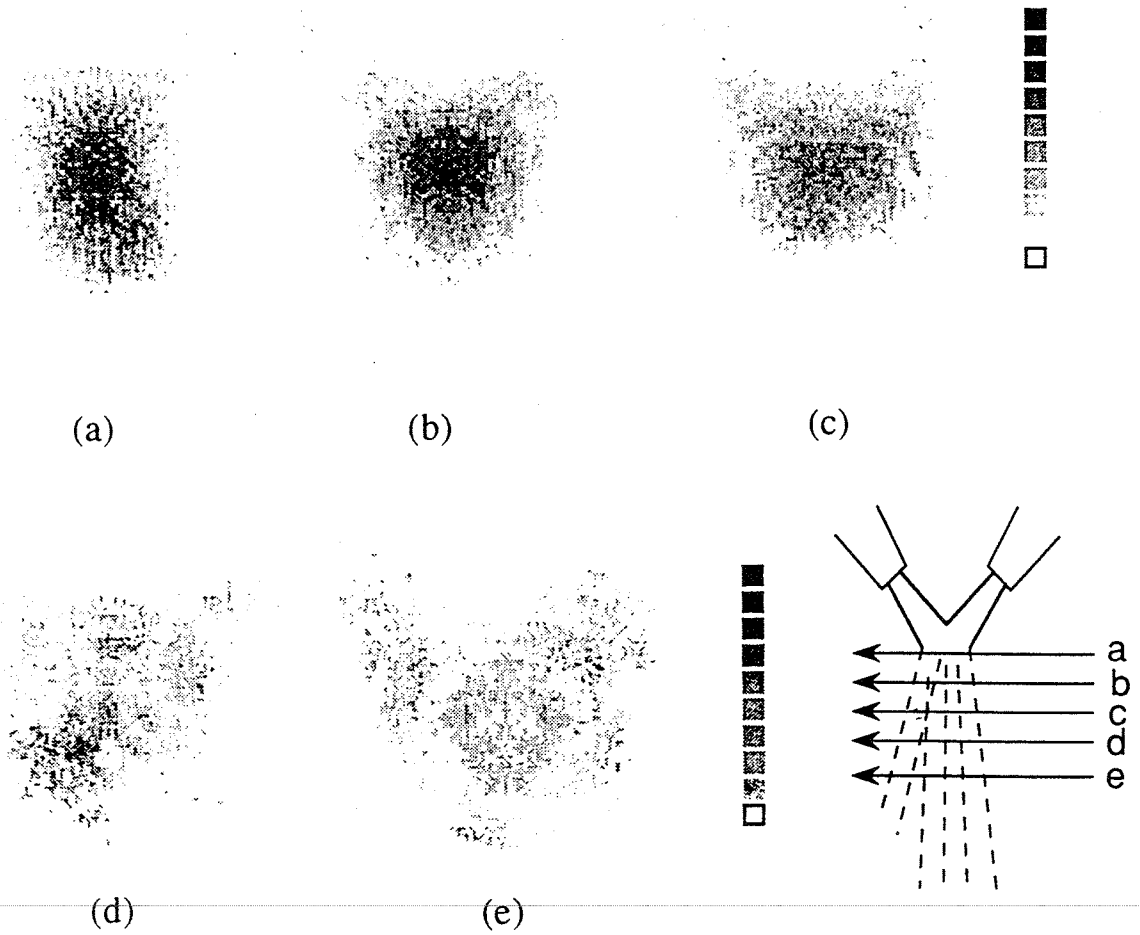

Fig. 8(b) Three-dimensional void fraction distribution (SHI)

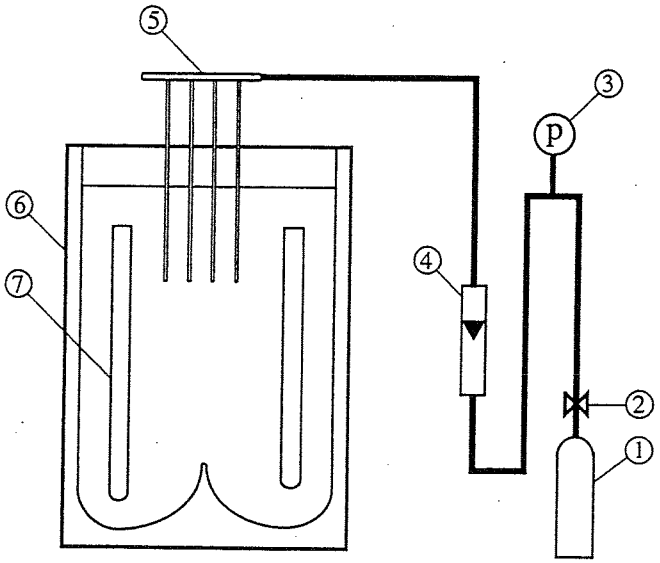

① Nitrogen Gas Bomb
② Regulator
③ Pressure Gauge
④ Flow Meter
⑤ Bubble Pump
⑥ Test Section
⑦ Spacers

Fig. 9(a) Test section for forced circulation flow in liquid metal

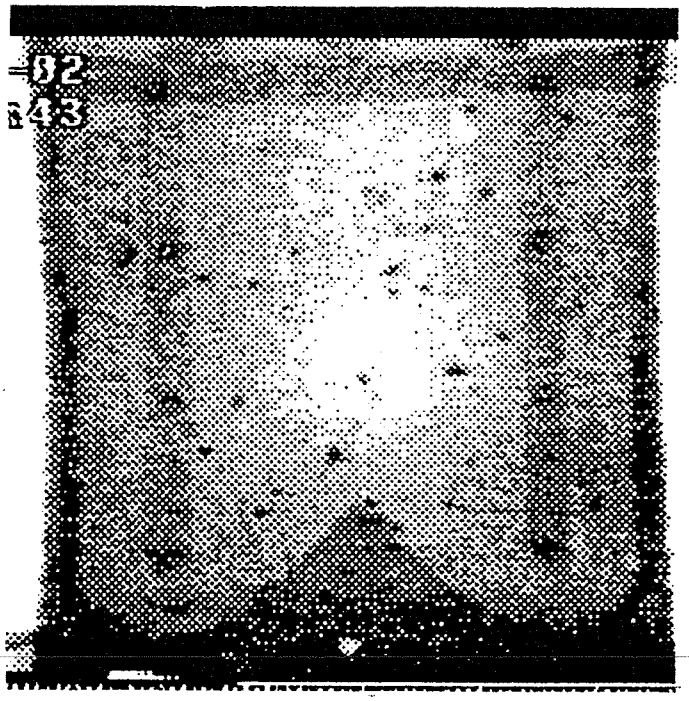

Fig. 9(b) Visualization of forced circulation flow in liquid metal by tracer method { JAERI)

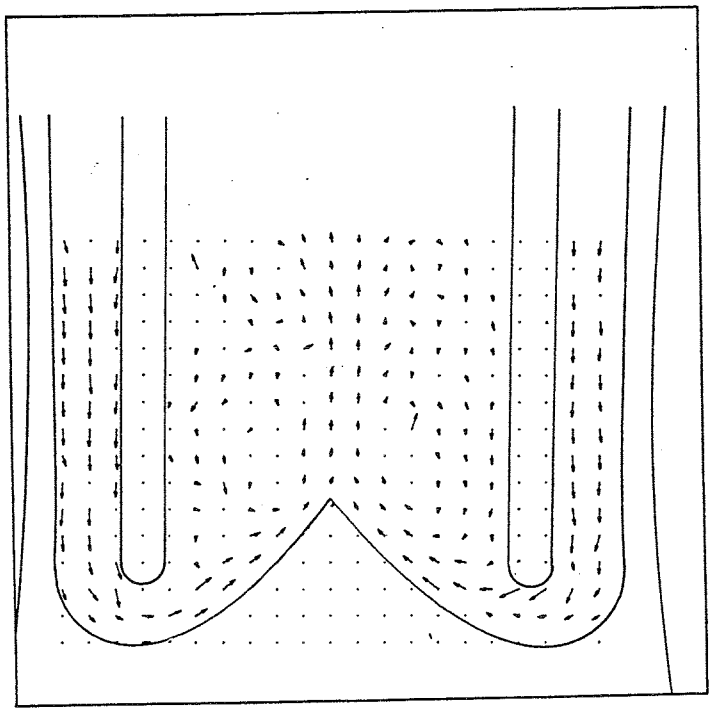

Fig. 9(c) Vector field of forced circulation flow in liquid metal (JAERI)

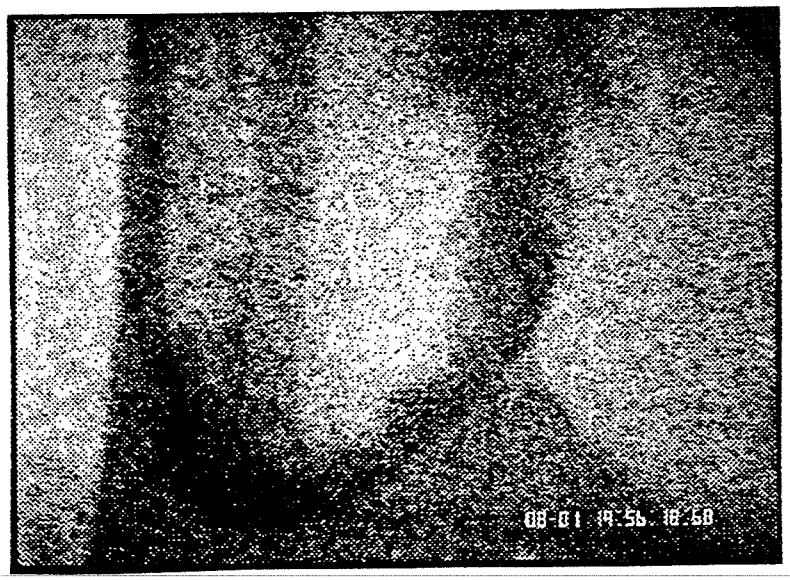

Fig. 9(d) Visualization of forced circulation flow in liquid metal by dye-injection method (SHI)

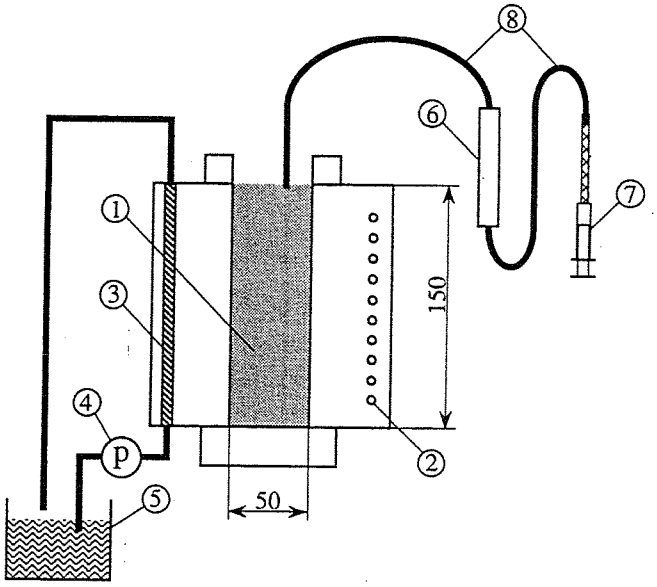

① Liquid Metal (Pb-Bi)
② Electric Heater
③ Heat Exchanger
④ Pump
⑤ Water Tank
⑥ Liquid Dye Tank
⑦ Injector
⑧ Copper Pipe

Fig. 10(a) Test section for solidification of liquid metal

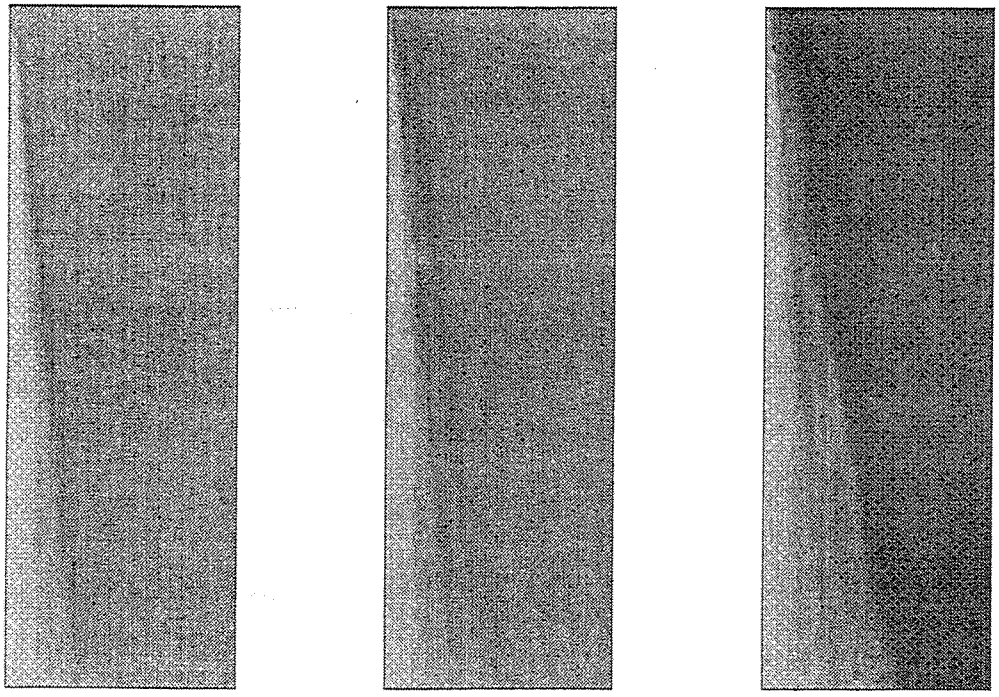

1min45sec 3min10sec 4min30sec

Fig. 10(b) Visualization fo solidification interface in liquid metal by dye-injection method (Penn. State)
Time starts at the begining of cooling

POOL AND FORCED CONVECTIVE VAPORIZATION OF LIQUID MIXTURES

Dieter Steiner

Institut für Thermische Verfahrenstechnik
Universität Karlsruhe, Kaiserstr. 12, D-76128 Karlsruhe
Federal Republic of Germany

ABSTRACT

Vaporization of liquid mixtures is characterized by the decline of heat transfer, which depends on the mixture composition. As the total heat transfer is a function of the convective evaporation and the nucleate boiling mechanisms, the effect of liquid composition and the other variables of each mechanism have been analysed in this article. The analysis has been performed to identify the fundamental changes in nucleate flow boiling compared to nucleate pool boiling and to boiling of the pure components. In the nucleate pool boiling region, the influence of mixture composition on the basic variables bubble-departure diameter, frequency of departure and boiling site density is presented. Models of the heat transfer process which take mass transfer into account are compared with experimental data both of nucleate pool boiling and of nucleate flow boiling to predict the available data.

1. INTRODUCTION

Vaporization of liquid mixtures in pool boiling and in the presence of forced flow is frequently used in industrial applications, such as in reboilers to supply vapours to distillation columns (e.g. kettle reboilers, column internal reboilers, horizontal thermosiphons and vertical tube-side reboilers), evaporators to vaporize a liquid, and various types of evaporators in refrigerating plants and for heat pump systems. Although many experimental data and heat transfer correlations exist, prediction of heat transfer of wide-boiling mixtures results in large uncertainties up to now, as reported by Palen [1]. This is due to a close relation between mass and heat transfer processes. When a mixture is vaporized, the composition of the more volatile components at the vapour-liquid interface is lower than the mean liquid composition in the bulk $\bar{x}$, because the equilibrium vapour composition of the more volatile components $\bar{y}$ is greater than that of $\bar{x}$. As a consequence, the composition of the less volatile components at the interface is higher than in the bulk of the liquid. Therefore, back-diffusion of these components takes place away from the interface into the bulk liquid, and the interfacial composition is affected by the amount of mass transfer. Hence the depletion of less volatile components in the interface layer results in a rise of the local bubble-point temperature. This affects the heat transfer rate in such a manner that the heat transfer coefficient of a mixture may be considerably lower than the molar average of the pure components. This reduction was reported by Cichelli and Bonilla [2] in 1945 after investigating binary mixtures.

Additionally, there is a further difficulty in the analysis of the experimental data because two mechanisms of heat transfer occur as long as the critical boiling regime is not exceeded. The first one is convective evaporation. In this case the heat transfer coefficient depends on buoyancy or flow variables, respectively, and the physical properties of the mixture. The second one is nucleate boiling, which is dependent on the heat flux (wall superheat), the pressure and the composition of the mixture. If these variables are not systematically varied in a sufficiently large range, the different mechanisms cannot be detected. The derived correlations then contain an array of variables and cannot be used for other conditions than the tested ones. Therefore, there is still a lack of knowledge referring to the basic principles of vaporization of liquid mixtures.

2. COMPARISON OF EXPRIMENTAL RESULTS WITH MODELS

In this paper only the behaviour of saturated liquid mixtures without miscibility gap and without surfactant component is considered.

2.1 Convective Evaporation

Convective evaporation occurs if the thermal resistance of the boundary layer near the wall is lower than in nucleate boiling. In this case, superheating of the liquid at the wall no longer suffices to meet the condition for the activation of boiling sites and bubble formation. Both in natural convection (pool of liquid with no appreciable velocity) and in forced flow the heat transfer coefficient can be predicted with well-known equations by inserting physical properties of the mixture as given in Appendix A. Gropp [3] experimentally verified that the mass transfer resistance of the liquid side, although higher than the one of the vapour side, has comparatively little effect on convective evaporation of mixtures of normal viscosity. Using the liquid-side kinetic separation factor K_1 as a measure of the depletion of the volatile component 1 in the boundary layer, this dimensionless number is defined as

$$K_1 \equiv \frac{\tilde{y}_{1,Ph} - \tilde{x}_1}{\tilde{y}_{1,Ph} - \tilde{x}_{1,Ph}} \qquad (1).$$

K_1 may be written in the form

$$K_1 = \exp(-\phi_1) \qquad (2).$$

The ratio of vaporization flux and diffusion flux is expressed as

$$\phi_1 = \frac{\mathring{n}}{\tilde{\rho}_1 \beta_1} \qquad (3).$$

$\mathring{n}$ is the molar mass flux which passes through the interface, β_1 is the liquid-phase mass transfer coefficient, $\tilde{\rho}_1$ the molar density of liquid mixture. The analytically and experimentally obtained results for a binary mixture of $CCl_3F/C_2Cl_3F_3$ with a bulk mole fraction $\tilde{x}_1 = 0.48$ are presented in Fig. 1. As the experiments are performed with falling films, K_1 is plotted against the film Reynolds number

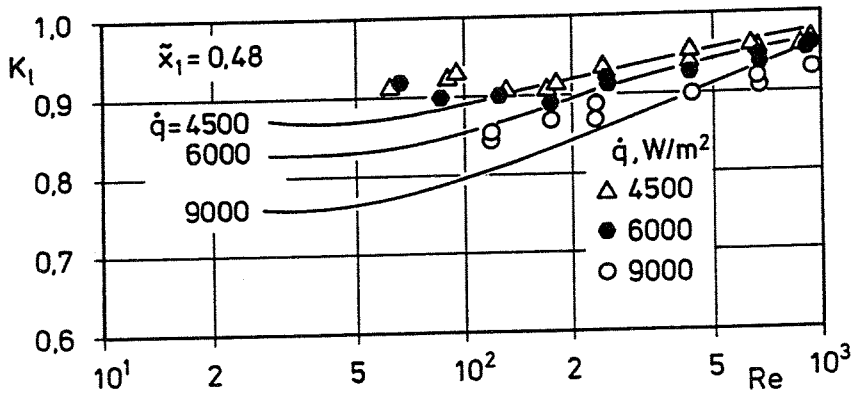

Fig. 1: Kinetic separation factor K_1 (analytical results and experimental date) as a function of the film Reynolds number. Heat flux $\dot{q}$ is parameter. Gropp [3].

2.2 Nucleate Boiling

Heat transfer in the nucleate boiling regime is governed by the activation of the cavities on the wall surface, bubble growth and bubble departure. If the boiling surface is immersed in a pool of liquid, this process is referred to as pool boiling. In the case of flow boiling, the liquid boils during the flow in a channel.

2.2.1 Models of Heat Transfer During Nucleate Boiling

Several mechanistic models are given in the literature. One model has been developed by Mikic and Rohsenow [4], where a microconvection region was postulated in which vapour-liquid exchange takes place. Colder liquid at $T_s(z)$ is brought into contact with the heat transfer surface initiating transient heat conduction. The average heat flux over the area of microconvection is given by

$$\mathring{q} = 2\sqrt{\pi}\sqrt{(\lambda\rho c_p)_l}\ \sqrt{f}\,K\,d_d^2\,(n/A)\,\Delta T\ , \tag{4}$$

where f is the frequency of bubble departure, d_d is the average bubble-departure diameter, $\pi K d_d^2$ is the area of influence of neighboring bubbles, n/A is the number of boiling sites per unit area of the heating surface, ΔT ist the wall superheat ($T_w - T_s(z)$). Mikic and Rohsenow [4] and Han and Griffith [5], who used a similar bulk convection model, assumed K = 1. Judd and Lavdas [6] determined K = 0.25 to 2 depending on heat flux and subcooling.

A different model is the latent heat transport model as used by Rallis and Jawurek [7], by Beer [8] and other authors. The equation can be written as

$$\mathring{q} = \frac{\pi}{6}\rho_v\,\Delta h_v\,f\,d_d^3\,n/A \tag{5}.$$

Another method of heat flux prediction is known as microlayer evaporation model. This microlayer evaporation represents a significant proportion of heat transfer in nucleate boiling. Moore and Mesler [9] postulated that bubbles grow out of a thin superheated microlayer underneath them. Van Strahlen [10] also used this model. Judd and Hwang [11] proposed the following equation

$$\mathring{q} = \rho_l\,\Delta h_v\,f\,V_{FF}\,n/A \tag{6}.$$

Assuming that the evaporated volume of microlayer is related to the bubble volume

$$V_{FF} = c\,\frac{\pi}{6}\,d_d^3 \tag{7}$$

where c < 1, the following is obtained

$$\mathring{q} = \frac{\pi}{6}c\,\rho_l\,\Delta h_v\,f\,d_d^3\,n/A \tag{8}.$$

Further equations have been published, for example combinations of the models given above.

In these mechanistic models, the heat flux or rather the heat transfer coefficient can be determined only if the dependence on the variables bubble frequency f, departure diameter d_d and boiling site density n/A is known. The prediction of heat transfer in nucleate boiling of mixtures requires the relation between f, d_d and n/A, and the composition of the mixtures. This is the fundamental assumption made by many previous research groups.

Tolubinskiy and co-workers [12 to 16] made experimental studies of the effect of composition on the variables mentioned above for various mixtures at atmospheric pressure [12 to 14].

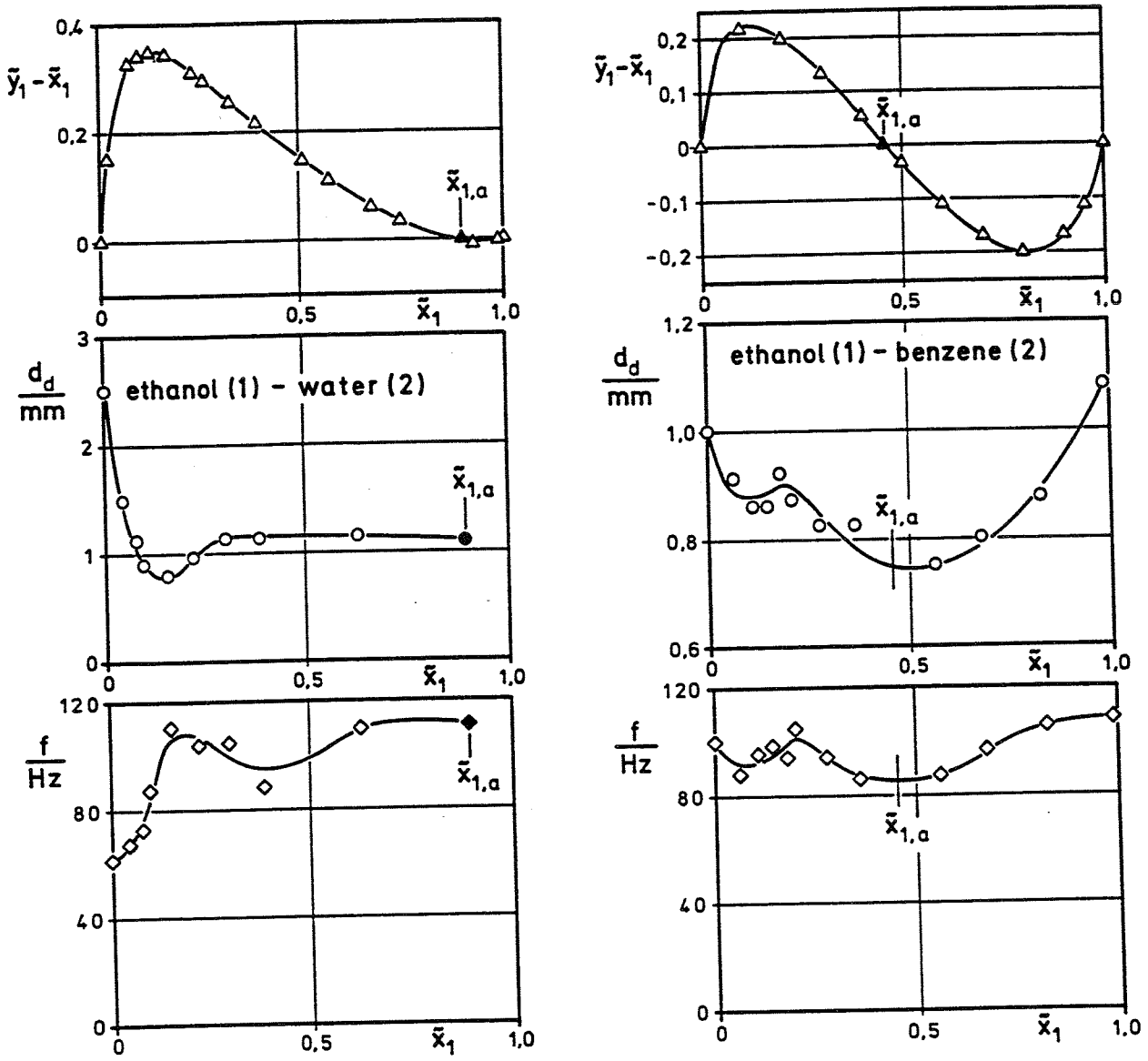

Fig. 2: Vapour-liquid composition difference, bubble-departure diameter and frequency of bubble departure as a function of liquid composition. Atmospheric pressure. Tolubiskiy et al. [12, 14].

The effect of pressure on the heat transfer rate has been determined in other papers [15,16]. The authors studied the following non-azeotropic mixtures: Methanol/water [12], ethanol/n-butanol [12], water/glycerine [13]. Mixtures with azeotropic points were also investigated, for example ethanol/water [12, 14] and ethanol/benzene [12, 14 to 16]. They discovered that, with non-azeotropic mixtures, the departure diameter d_d can be higher (water/glycerine) or lower (methanol/water; ethanol/n-butanol) than the linear averaged diameter of the pure components. For the investigated azeotropic mixtures, the mixture departure diameter is lower than the linear averaged diameter with a relative minimum as presented in Fig. 2.

The bubble frequency f is higher than the linearly averaged frequency of the mixtures water/-glycerine and methanol/water. However, for the mixture ethanol/n-butanol, the bubble frequency is lower than the linear averaged value. The azeotropic mixtures investigated yield a higher frequency in the case of ethanol/water than the linear averaged ones. In the case of ethanol/benzene, the frequency is dependent on the composition as presented in Fig. 2. Tolubinskiy and co-workers [12] defined the product d_d f as growth rate of vapor bubbles of the mixture and proposed

$$d_d f/(d_d f)_{id} = \left[1 - \frac{(y_1 - x_1)^2}{y_1 (1-x_1)}\right]^{1.15} \quad (9)$$

where

$$(d_d f)_{id} = (d_d f)_1 x_1 + (d_d f)_2 x_2 \quad (10).$$

x_1, y_1 are the mass fractions of liquid and vapour, respectively. Subscript 1 refers to the component with the lowest boiling point at given pressure.

Unfortunately, data of the boiling site density n/A have not been reported by Tolubinskiy and co-workers [12 to 16]. Although these authors investigated the effect of pressure on mixture boiling heat transfer [15, 16], no data are published representing the variables bubble departure diameter and frequency as function of pressure. However, Stephan and Körner [17] made experimental studies of the effect of pressure on the frequency of bubble departure. The results are shown in Fig. 3 for the pressures 0.1 and 0.3 MPa.

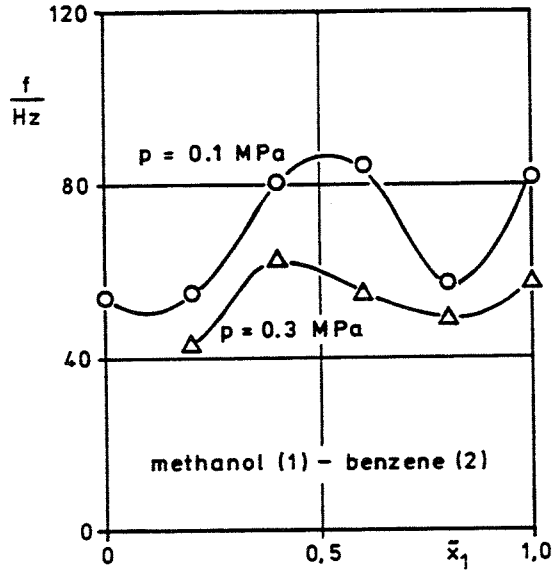

Fig. 3: Frequency of bubble departure as a function of liquid composition at two different pressures. Stephan et al. [17].

Both for the pure components and for the mixture the frequency decreases with increasing pressure. This is verified for a larger number of substances, as summarized by Weckesser [18]. The effect of composition on f, as shown in Fig. 3, is typical of mixtures with an azeotropic point.

There are more publications dealing with the effect of mixture composition on bubble-departure diameter and frequency at atmospheric pressure, for example by Valent and Afgan [19], which contain no new information. However, comparing the results of d_d for the same mixture and global variables as published by different authors, remarkable differences in the numerical values are obtained.

To obtain more generally applicable results, Bier and co-workers [18, 20] investigated the bubble-departure diameter d_d the frequency f and the boiling site density n/A of mixtures over a considerable pressure range. Weckesser [18] experimentally studied the mixture n-butane/i-pentane with a difference of boiling point temperature of 28.5 K at normal pressure. The mixture and the pure components boiled on a horizontal copper plate within the reduced pressure range[1)] $p_r = 0.057$ to 0.2. The results are presented in Fig. 4.

---

1) The critical pressure in the relation p_r is always the critical pressure of the respective mixture

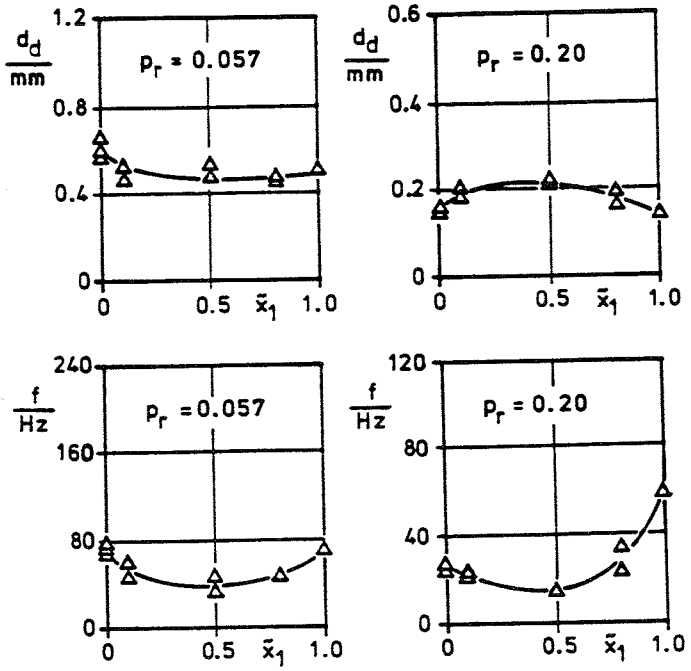

Fig. 4: Bubble-departure diameter and frequency of bubble departure of the mixture n-butane/ i-pentane as a function of liquid composition. Parameter is the reduced pressure. Weckesser [18].

At the reduced pressure [1] $p_r = 0.057$, the bubble departure diameter d_d of the mixture is lower than the linear averaged value, whereas at $p_r = 0.2$, the diameter d_d is higher than the values of the pure components. However, the bubble departure frequency of the mixture is always lower than the linearly averaged value. The hydrocarbon mixtures propene/propane, propane/n-butane, ethane/propane and ethane/n-butane with various differences in boiling point temperature were investigated by Bednar [20]. The test section used is a horizontally mounted copper tube with an outside diameter of 8 mm. The experiments were carried out in the reduced pressure range $p_r = 0.03$ to 0.4 . Bednar investigated bubble-departure diameters and boiling site densities. The results of the bubble-departure diameter as function of mole fraction $\tilde{x}_1$ are given in Fig. 5.

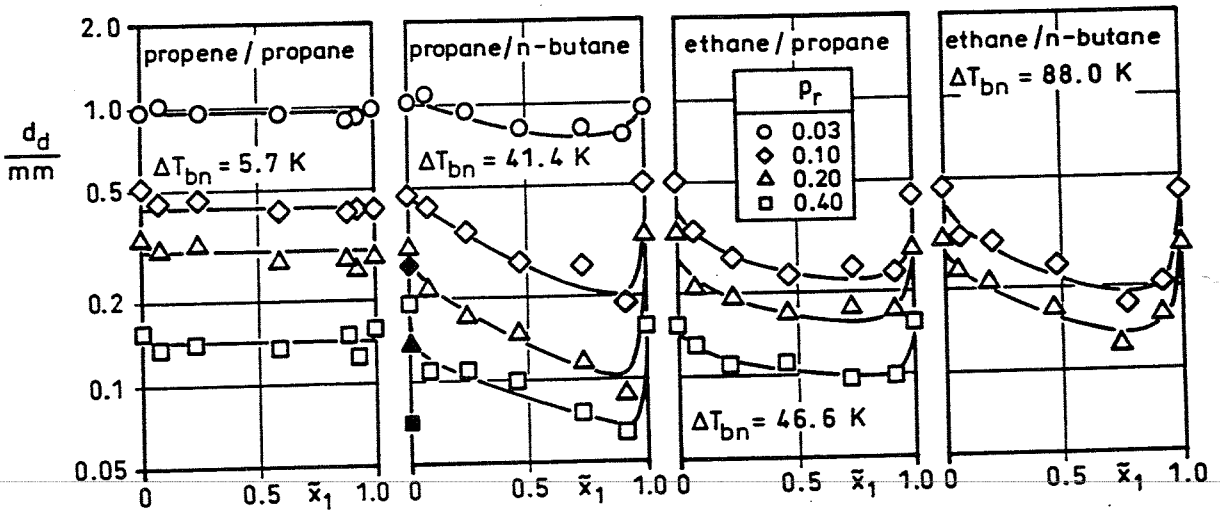

Fig. 5: Bubble-departure diameter as a function of liquid composition with reduced pressure as parameter. Open symbols are data of Bednar [20], full symbols are data of Weckesser [18].

[1] Footnote see page 5

The binary mixture propene/propane, with a difference in boiling point temperature of 5.7 K at normal pressure, has bubble-departure diameters that, as an average, follow a straight line that does not depend on composition. This results from the small difference in equilibrium composition between vapour and liquid. The effect of the difference in equilibrium composition between vapour and liquid on the bubble-departure diameter is noticeable in the dependence on the mixture composition as may be seen in Fig. 5 for the other binary mixtures. Additionally, the data of Weckesser [18] of n-butane are plotted in Fig. 5 for the reduced pressures [1] p_r = 0.1, 0.2 and 0.4. The data of the bubble-departure diameter of Weckesser [18] obviously are lower than the data of Bednar [20] by roughly a factor of 2. Bednar concluded that bubble-departure diameters measured on a horizontal plate and on a horizontal tube do not have the same numerical value. This is probably due to the quite different flow fields. The dependence of boiling site density n/A on mixture composition is presented in Fig. 6 for the reduced pressure 0.1. The experimental results for the other investigated reduced pressures p_r = 0.03 and 0.2 are similar.

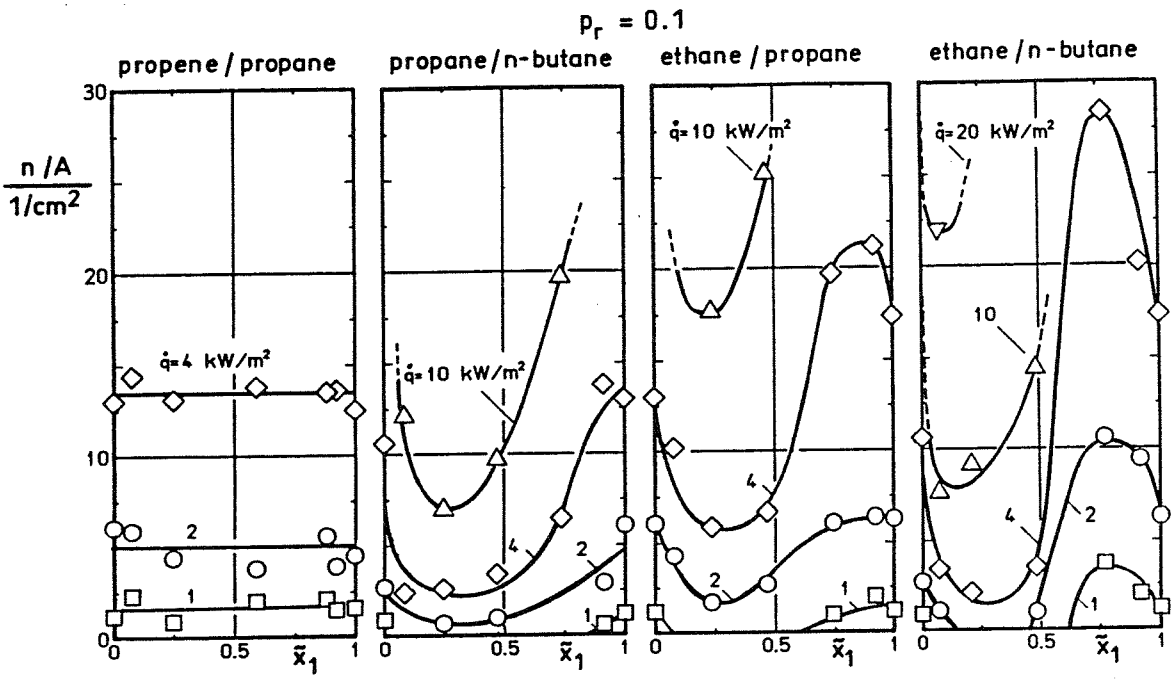

Fig. 6: Boiling site density as a function of liquid composition. Bednar [20]

For propene/propane, the density n/A takes an approximately constant value and therefore is not a function of composition at given reduced pressure and heat flux. All the other binary mixtures show a dramatic effect of composition on the density n/A. In their tendency, these results can be compared to the study of Hui and Thome [22] with the azeotropic mixtures ethanol/water and ethanol/benzene at 0.101 MPa pressure. Their results, too, showed large changes with a relative maximum and minimum as function of composition for the mixture ethanol/benzene. The present knowledge can be summarized as follows:

a. The prediction of the bubble-departure diameter d_d, the bubble departure frequency f and the boiling site density n/A as functions of composition for binary and multicomponent mixtures is presently still impossible. This is especially true for the boiling site density.

b. Thus, the fundamental philosophy concerning nucleate boiling processes, i.e. the successful understanding of d_d, f and n/A, which may lead to improved methods for heat transfer coefficient predictions, is extremely difficult to realize. Therefore, an enormous experimental effort would be necessary to obtain the required data which are representative for various types of mixtures as function of variables.

[1] Footnote see page 5

A different method of heat transfer prediction was proposed by Grigorjev and other Russian researchers. Grigorjev et al. [22] discussed an equation for the critical radius at nucleation in a binary mixture and concluded that the heat transfer coefficient as function of composition may possess not only relative minima but also relative maxima. Furthermore, the effect of mixture composition on nucleation at boiling was analysed in another paper of Grigorjev [23]. The ratio of the critical bubble radius at nucleation with conditions in the bulk of the mixture and the critical bubble radius at interface conditions has been used by Yusufova et al. [24] to characterize the measured heat transfer coefficients of mixtures at pressures up to 2.9 MPa.

The degradation of mixture-boiling heat transfer coefficients relative to the pure component values was taken into account by Stephan and Körner [25] using thermodynamic arguments only. The work necessary to produce a vapour bubble in an infinite binary liquid mixture contains, besides the pure fluid term $\Delta\tilde{h}/T$, a second term $(\tilde{y}_1 - \tilde{x}_1)\frac{\partial^2 G}{\partial \tilde{x}^2}\frac{\Delta\tilde{x}_1}{\Delta T}$. This term is assumed to be responsible for the mass transfer between the bubble interface and the bulk composition, as Stephan [26] explained. In a binary mixture with small differences in vapour-liquid composition $(\tilde{y}_1 - \tilde{x}_1)$, the temperature difference to obtain the same heat flux with the binary mixture and with each of the pure components is given by Stephan and Körner [25] as

$$\Delta T_{id} = \Delta T_1 \tilde{x}_1 + \Delta T_2 \tilde{x}_2 \qquad (11).$$

$\Delta T_i = T_W - T_{si}$ is the difference between the wall surface temperature and the saturation temperature of the respective component i. However, in a real mixture, an excess wall superheat ΔT^E, which is proportional to the mass transfer driving force $(\tilde{y}_1 - \tilde{x}_1)$, must be taken into account. The driving wall superheat is therefore given as

$$\Delta T = \Delta T_{id} + \Delta T^E \qquad (12).$$

The excess wall superheat of a binary mixture has to be calculated as

$$\Delta T^E/\Delta T_{id} = \left|K_{12}\,(\tilde{y}_1 - \tilde{x}_1)\right| \qquad (13).$$

In the pressure range 0.1 to 1 MPa the following pressure influence was found

$$K_{12} = A_0\,(0.88 + 0.012\ \text{p/MPa}) \qquad (14).$$

At a given heat flux the ratio of wall superheat of a mixture which follows the ideal mixing law, Eq. (11), to the wall superheat of a real mixture is given by

$$\frac{\Delta T_{id}}{\Delta T} = \frac{\alpha_{nb}}{\alpha_{id}} \qquad (15).$$

From Eqs. (12) to (14) follows

$$\frac{\alpha_{nb}}{\alpha_{id}} = \frac{1}{\left[1 + A_0\,(0.88 + 0.012\ p)\left|\tilde{y}_1 - \tilde{x}_1\right|\right]} \qquad (16).$$

In general, A_0 is an empirical constant which is different for every binary mixture. Stephan [26] proposed the following extension for multicomponent mixtures

$$\frac{\alpha_{nb}}{\alpha_{id}} = \frac{1}{1 + \left|\sum_{i=1}^{n-1} K_{in}\,(\tilde{y}_i - \tilde{x}_i)\right|} \qquad (17).$$

For calculation purposes, the subscript i = 1 is alloted to the component with the lowest boiling point and the subscript n to the component with the highest boiling point. The heat transfer coefficient α_{id} is determined from the linear molar mixing law, which is equivalent to Eq. (11), by

$$\frac{1}{\alpha_{id}} = \sum_{i=1}^{n} \frac{\tilde{x}_i}{\alpha_{nb,i}} \qquad (18) .$$

The dependence of the heat transfer coefficient on the variables as given in Eq. (16) and (17) and those variables that were determined experimentally showed a remarkable discrepancy.

This discrepancy led to the extension of the equations given above by Calus and Leonidopoulos [27]. They based the correction in wall superheat on the analytical work of Scriven [28] and the work of van Strahlen [29] on nucleate boiling in binary mixtures. Van Strahlen took into account that the growth rate of bubbles is controlled by heat and mass diffusion. Furthermore, Calus and Leonidopoulos [27] concluded that the loss of the more volatile component in the liquid layer near the bubble gives a smaller effective driving temperature difference than the apparent ΔT at bulk conditions. The correction in the effective wall superheat has the form

$$\Delta T^E/\Delta T_{id} = (x_1-y_1)\left(\frac{\kappa}{\delta}\right)_l^{0,5}\left(\frac{c_{pl}}{\Delta h_v}\right)\left(\frac{dT_s}{dx_1}\right)_{x_1} \qquad (19) .$$

All the quantities in Eq. (19) are written with mass fractions. Substituting Eq. (19) into Eq. (12) and (15) yields

$$\frac{\alpha_{nb}}{\alpha_{id}} = \frac{1}{\left[1-(y_1-x_1)\left(\frac{\kappa}{\delta}\right)_l^{0,5}\left(\frac{c_{pl}}{\Delta h_v}\right)\left(\frac{dT_s}{dx_1}\right)_{x_1}\right]} = N_{Sn} \qquad (20) .$$

N_{Sn} is the Scriven number. It should be noted that α_{id}, Eq. (18), is now to be calculated by using mass fractions in the liquid phase. Equation (20) was compared with measured data of n-propanol/water mixtures and showed a reasonable agreement. However, Thome [30] proposed an analytically derived equation similar to Eq. (20), as

$$\frac{\alpha_{nb}}{\alpha_{id}} = (N_{Sn})^{7/5} \qquad (21)$$

where α_{id} has to be calculated by using liquid mole fractions. He compared this equation with experimental data of nitrogen/argon, ethanol/benzene, ethanol/water and acetone/water all at 1 bar absolute pressure. The comparison showed that the results of the non-aqueous mixtures deviate less from the experimental data than the aqueous mixtures, where the deviations are sometimes considerable. Although Calus and Leonidopoulos [27] took account of the effect of mass diffusion in the Eq. (20) given above, an extension of this equation to multicomponent mixtures has not been attempted.

Schlünder [31] derived an equation from the assumption that the dominant mass transfer resistance is in the liquid phase near the growing bubble. Further, he postulated that the effective driving temperature difference of bubble activation and growth is the difference $(T_W - T_{Ph})$, where T_W is the wall surface temperature, T_{Ph} is the interfacial temperature, which is taken as local bubble-point temperature. This superheat and the heat transfer coefficient following the ideal mixing law, α_{id}, gives the actual heat flux

$$\mathring{q} = \alpha_{id}\,(T_W - T_{Ph}) \qquad (22) .$$

The evaluation of experiments carried out at the same heat flux $\mathring{q}$ gives

$$\mathring{q} = \alpha_{nb} (T_W - T_s (\underline{\tilde{x}}, p)) \tag{23}$$

where $T_s (\underline{\tilde{x}},p)$ is the bubble-point temperature of the liquid mixture at bulk conditions, composition vector $\underline{\tilde{x}}$ and pressure p, respectively. Substituting Eq. (23) in (22) gives

$$\frac{\alpha_{nb}}{\alpha_{id}} = \frac{1}{1 + \frac{\alpha_{id}}{\mathring{q}} (T_{Ph} - T_s)} \tag{24}$$

By use of parameter B_0, which is the ratio of the heat rate required as latent heat to produce bubbles and the total heat rate, i.e.

$$B_0 = \mathring{q}_b A_b / \mathring{q} A \tag{25}$$

and by taking into account the mass transfer in the liquid phase and by making a number of simplifying assumptions, Schlünder [31] obtained:

$$\frac{\alpha_{nb}}{\alpha_{id}} = \frac{1}{1 + \frac{\alpha_{id}}{\mathring{q}} (T_{s2} - T_{s1})(\tilde{y}_1 - \tilde{x}_1) \left(1 - \exp\left(\frac{- B_0 \mathring{q}}{\beta_{11} \tilde{\rho}_l \Delta \tilde{h}_v}\right)\right)} \tag{26}$$

Schlünder [31] derived that an extension to multicomponent mixtures is possible as

$$\frac{\alpha_{nb}}{\alpha_{id}} = \frac{1}{1 + \frac{\alpha_{id}}{\mathring{q}} \left[\sum_{i=1}^{n-1} (T_{sn} - T_{si})(\tilde{y}_i - \tilde{x}_i) \left(1 - \exp\left(\frac{- B_0 \mathring{q}}{\beta_{li} \tilde{\rho}_l \Delta \tilde{h}_v}\right)\right)\right]} \tag{27}$$

In Eq. (26) and (27),

β_{li} is the mass transfer coefficient of component i in the mixture. In the current state of art $\beta_{li} = 2 \cdot 10^{-4}$ m/s, is given,

$\tilde{\rho}_l$ is the molar density of liquid mixture, and

$\Delta \tilde{h}_v$ is the molar differential latent heat of vaporization. This is the molar vapour enthalpy at the equilibirum composition $\tilde{y}$ ($\tilde{x}$) minus the molar liquid enthalpie at composition $\tilde{x}$.

The other quantities have been already defined in the text. On the basis of experimental data, a comparison is possible between the real effects of heat flux, pressure and composition and those predicted by the equations given above.

2.2.2 Pool Boiling Characteristics

Among the essential characteristics of nucleate pool boiling of mixtures are weaker effects of heat flux and of pressure on the heat transfer coefficient compared to the case of the pure components. Representative results of Bayer [32] are given in Fig. 7 for pure CHF_3 (1) and two mixtures CHF_3/C_2F_5Cl having an average bulk composition of $\tilde{x}_1 = 0{,}083$ and $0{,}507$, respectively.

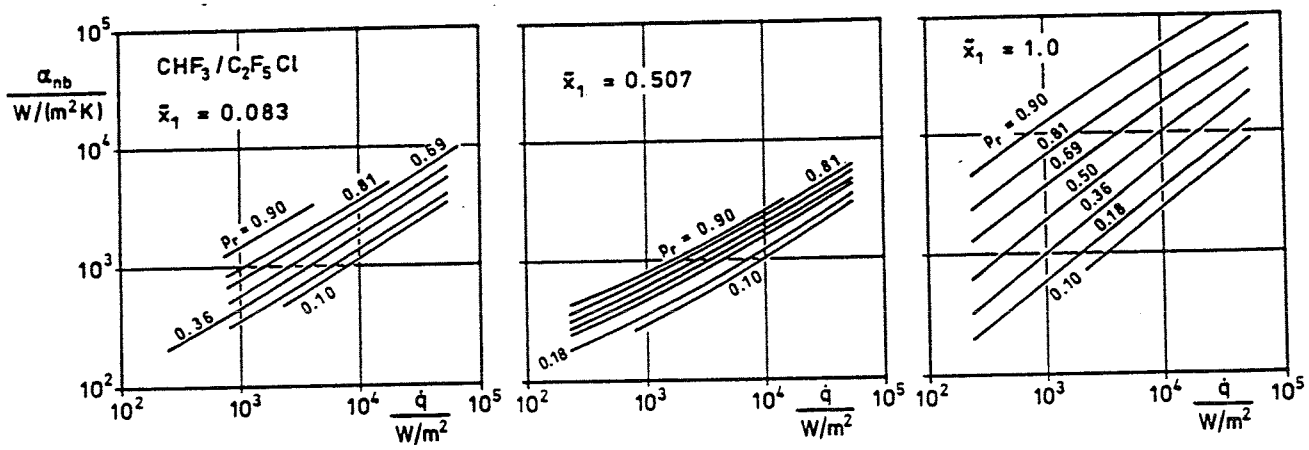

Fig. 7: Pool boiling heat transfer coefficient as a function of heat flux at various reduced pressures. Bayer [32]

From these plots, it may be derived that the slope n of the curves α_{nb} as a function of the heat flux $\dot{q}$ depends significantly on the composition $\tilde{x}_1$. In other words, the ratio α_{nb}/α_{id} is also affected by the heat flux $\dot{q}$, as presented in Fig. 8.

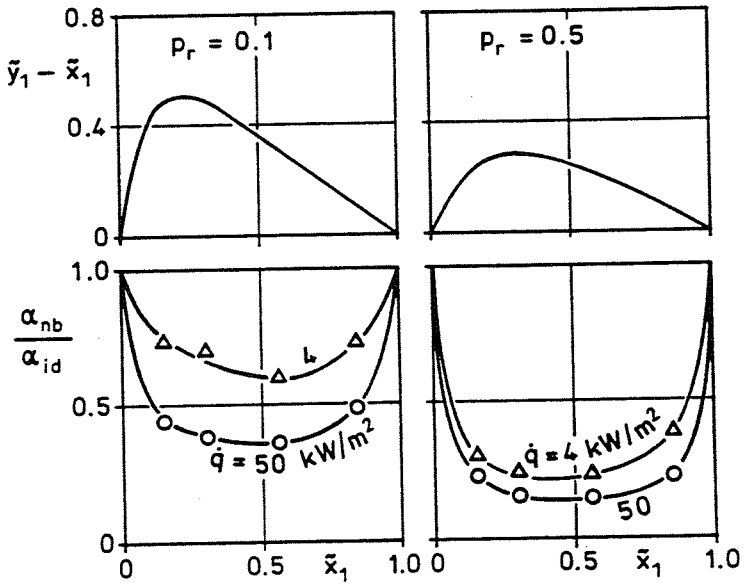

Fig. 8: Dependence of the reduced heat transfer coefficient in pool boiling on heat flux and liquid composition. CHF_3/C_2F_5Cl mixture. Bayer [32]

In many mixtures studied, the ratio α_{nb}/α_{id} decreases as the heat flux rises if the other variables are kept constant. This functional dependence is only represented correctly by the model of Schlünder, equations (26) and (27). Various experimental investigations showed an effect of pressure on the mixture heat transfer coefficient as shown exemplarily in Fig. 7. From experimental results, it can be concluded that at a given heat flux and composition, the ratio α_{nb}/α_{id} goes down with rising pressure as presented in Fig. 8. This decrease has been experimentally verified by Schmadl [33], who measured at reduced pressures [1] of up to $p_r = 0.97$. However, Fig. 8 shows

[1] Footnote see page 5

that this drop is not a simple function of the difference in vapour-liquid composition $(\tilde{y}_1 - \tilde{x}_1)$ as assumed in some models. If that were true, the decline of α_{nb}/α_{id} with rising pressure would be less marked because of a reduced driving composition difference $(\tilde{y}_1 - \tilde{x}_1)$.

In Eq. (20) of Calus and Leonidopoulos, the ratio α_{nb}/α_{id} is a weak function of pressure due to the pressure influence in the physical properties. Equation (16) of Stephan and Körner contains an adequate pressure dependence in the investigated pressure range. The best agreement between the experimentally determined and the predicted pressure effect, however, is given by Schlünder's Eqs. (26) and (27) because of $\alpha_{id} = f(p_r)$. The experimental results with the mixture CHF_3/C_2F_5Cl, the azeotropic mixture CHF_2Cl/C_2F_5Cl, the hydrocarbon mixtures C_2H_6/C_3H_8, C_3H_8/C_4H_{10} and the calculated curves using Schlünder's Eq. (26) are presented in Fig. 9.

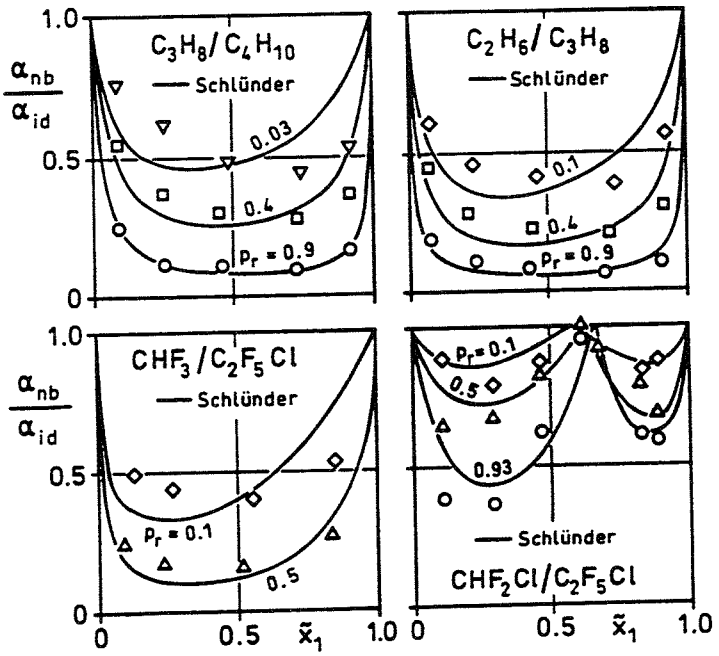

Fig. 9: Calculated and experimentally determined reduced heat transfer coefficients in pool boiling using Schlünder's equation. Heat flux $\mathring{q} = 20$ kW/m^2. Bednar [20], Bayer [32], Bieling [34].

The deviation obviously is acceptable for each mixture. However, it must be mentioned that these results are achieved by the assumption that B_0/β_{li} is an individually adjustable parameter, although Schlünder [31] proposed $B_0 = 1$ and $\beta_{li} = 2 \cdot 10^{-4}$ m/s for all components i.

In Fig. 10 the results of many studies are plotted. They show that B_0/β_{li} is a function of reduced pressure. Moreover, the available results show that the parameter B_0/β_{li} is affected by the difference in boiling-point temperature at atmospheric pressure. Binary mixtures with a large difference in normal boiling-point temperatures show the tendency of a smaller effect of pressure on B_0/β_{li}. The adjusted parameters B_0/β_{li} of these mixtures roughly agree with the proposed value $B_0/\beta_{li} = 5000$ s/m. However, binary mixtures with a small difference in normal boiling point temperatures yield values which are higher than the proposed one by a factor of up to 100. Further information is not available at the moment. No sytematic information is known about the parameter B_0/β_{li} in multicomponent mixtures either.

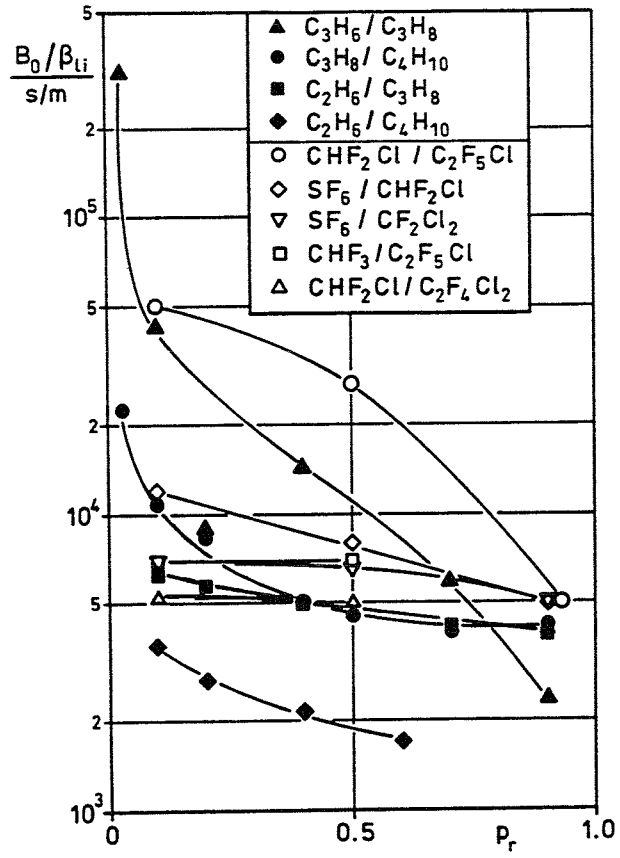

Fig. 10: Parameter B_0/β_{li} in Schlünder's equation as a function of reduced pressure. Recalculated from measured data at $\mathring{q} = 20$ kW/m^2. Bednar [20], Bayer [32], Bieling [34], Rott [35].

2.2.3 Flow Boiling Characteristics

As long as the wall superheating is sufficiently high flow nucleate boiling takes place. Experiments have to be performed and analysis of heat transfer results needs to be done in order to identify the fundamental changes in the phenomenon of flow boiling of mixtures as compared to pure component boiling. Results of local-point heat transfer coefficients in the bottom segment of a horizontal tube are presented in Fig. 11 for SF_6/CF_2Cl_2 mixtures as investigated by Niederkrüger [36].

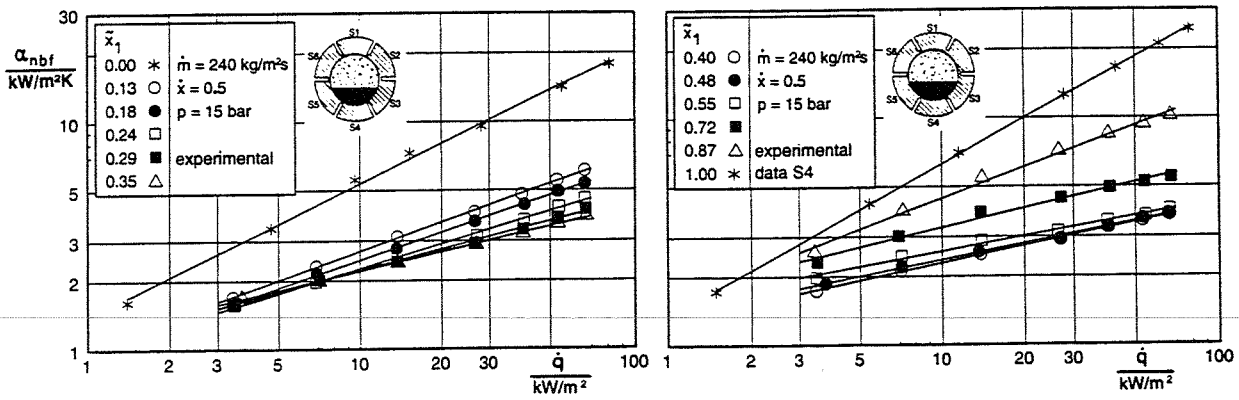

Fig. 11: Dependence of the local heat transfer coefficient in nucleate flow boiling on the heat flux at various liquid compositions. Niederkrüger [36].

The data of the plotted segment no. 4 are those of a wall that always is completely wetted. The values determined from such a set-up should therefore be representative for vertical flow boiling as well. This was verified for pure components where the pressure effect on the heat transfer coefficient, i.e. the pressure function, is - within statistical uncertainties - identical with the equation of vertical tube heat transfer as demonstrated by Niederkrüger, Steiner et al. [37]. It can be ascertained from Fig. 11 that, for a given composition and other fixed variables, the heat transfer coefficient can be approximated by the relationship $\alpha_{nbf} \sim \dot{q}^n$. The slope n, however, depends on the composition of the mixture.

Niederkrüger [36] systematically investigated the effect of mass velocity, $\dot{m}$, and vapour fraction, $\dot{x}$, on the heat transfer coefficient. From the results it can be concluded that in the developed flow nucleate boiling region of mixtures the heat transfer coefficient generally is, except for small deviations, not affected by mass velocity, as shown in Fig. 12.

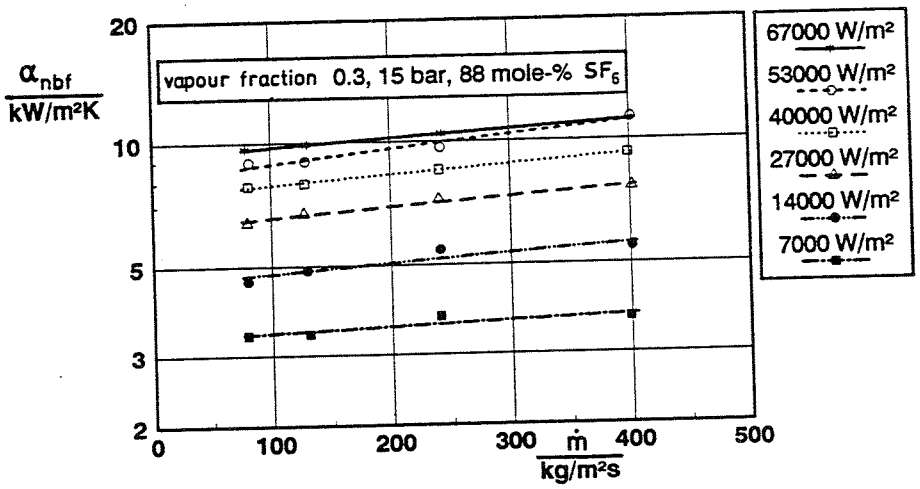

Fig. 12: Nucleate flow boiling heat transfer coefficient showing no significant dependence on mass velocity. SF_6/CF_2Cl_2 mixture. Niederkrüger [36].

A further important flow variable is the vapour fraction, $\dot{x}$. The vapour fraction is representative of the amount by which the average liquid-phase velocity increases when comparing single-phase velocity and two-phase velocity at a given mass velocity. Although in the experiments the vapour fraction was increased from 0.1 to 0.7, the heat transfer coefficient was only slightly reduced, see Fig. 13.

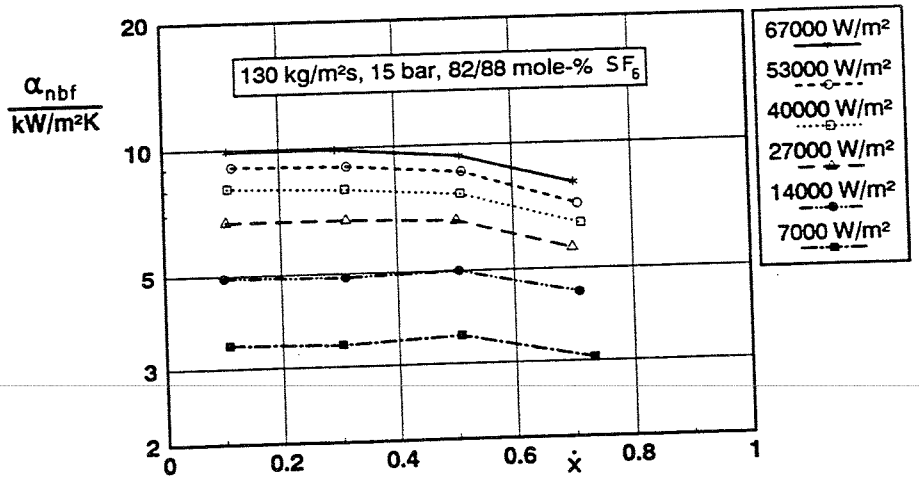

Fig. 13: Dependence of nucleate flow boiling heat transfer coefficient on the vapour fraction $\dot{x}$. SF_6/CF_2Cl_2 mixture. Niederkrüger [36].

However, this reduction is not due to changes in flow conditions. It is a result of the boiling process. At the given overall composition, the vapour produced is enriched with the more volatile component, which results in depletion of this component in the remaining liquid and hence heat transfer reduction. It has been experimentally proved and demonstrated with flash calculations by Niederkrüger, Steiner et al. [37] that with increasing vapour fraction the change in liquid composition becomes larger. The independence of the heat transfer coefficient of mass velocity and vapour fraction in the fully developed nucleate flow boiling region was also verified by Jain and Dhar [38] with CF_2Cl_2/CF_3Cl mixtures.

In nucleate flow boiling, the heat transfer coefficient of the mixture is generally lower than that of a mixture following the linear mixing law of the corresponding pure components. Results are plotted in Fig. 14 for two heat fluxes.

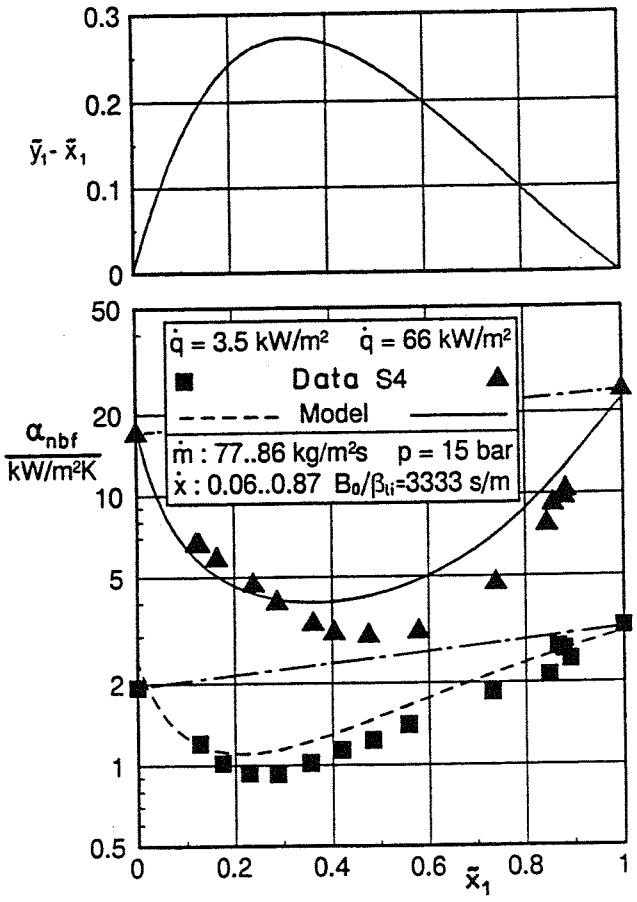

Fig. 14: Dependence of the nucleate flow boiling heat transfer coefficient on liquid composition at two heat fluxes. SF_6/CF_2Cl_2 mixture. Niederkrüger [36].

The magnitude by which the heat transfer coefficient is reduced depending on composition obviously is dependent on heat flux. Moreover, the minimum of the heat transfer coefficient does not always correspond to the maximum of the difference in vapour-liquid composition. The experimental data of Niederkrüger [36] and of Celata, Cumo et al. [39] in a vertical tube with the mixture $CF_2Cl_2/C_2F_4Cl_2$ demonstrated that the degree of the heat transfer reduction depends also on the pressure in such a way that it increases with pressure.

In addition to the independent variables in nucleate pool boiling, as discussed in chapter 2.2.2, analysis of the nucleate flow boiling process yields the flow variables mass velocity and vapour fraction. This has to be taken into consideration in nucleate flow boiling models to predict the observed drop in heat transfer.

Bennett and Chen [40] extended the pure-fluid method of Chen [41] to mixtures. The correlation for binary mixtures is given by

$$\alpha_{fb} = \alpha_{LO}\, F \left(\frac{\Delta\tilde{T}}{\Delta T_s}\right)_{mac} + \alpha_{nb}\, S\, N_{Sn} \qquad (28)\ .$$

This equation is based on the assumption that, for mixtures, each of the two terms is affected in separate ways by mass transfer. The first term on the right-hand side of Eq.(28) is corrected by the effective temperature at the liquid-vapour interface. The correction N_{Sn} for the second term is the known increase in phase temperature of the growing vapour bubbles.

Chen [41] clearly separated the mechanisms of convective evaporation and nucleate boiling in heat transfer. However, the simple additive model required the suppression of the nucleate boiling component, introduced as the factor S. Though already ascertained for pure fluids by Steiner and Taborek [42], the suppression hypothesis must be revised. This could also be confirmed for Eq.(28) by recalculating the experimental data of the mixture SF_6/CF_2Cl_2 as given by Niederkrüger [36], see Fig. 15.

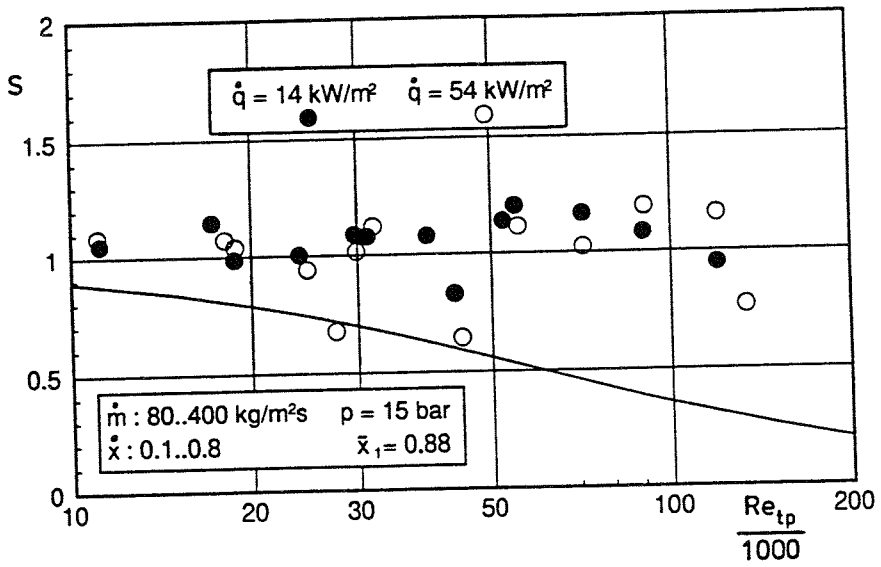

Fig. 15: Suppression factor S of the Bennett-Chen equation showing no dependence on the two-phase Reynolds number. SF_6/CF_2Cl_2 mixture. Niederkrüger [36].

Additionally, the convective component of heat transfer, the first term, is corrected by the ratio $(\Delta\tilde{T}/\Delta T_s)_{mac}$, which is a function of mass transfer. This assumption could be neither confirmed by analysis nor by experiment, as was already discussed in chapter 2.1, as long as the liquid phase has a normal viscosity. If the liquid mixture is highly viscous, however, the mass transfer resistance on the liquid side has a significant effect because the diffusion coefficient is roughly inversely proportional to dynamic viscosity. Ross, Radermacher et al. [43] also concluded from their experiments in the convective region with $C_2H_4F_2/CF_3Br$ mixtures that mass transfer resistance is negligible in turbulent flow evaporation. Because of these two aspects, we have not used or modified Eq. (28) of Bennett and Chen any further.

Instead, the degradation of heat transfer coefficients was calculated from the equation of Schlünder [31]. In the case of nucleate flow boiling, the heat transfer coefficient is to be calculated from

$$\frac{\alpha_{nbf}}{\alpha_{id}} = \frac{1}{1 + \frac{\alpha_{id}}{\mathring{q}} \left[\sum_{i=1}^{n-1} (T_{sn} - T_{si})(\tilde{y}_i - \tilde{x}_i) \left(1 - \exp\left(\frac{-B_0 \mathring{q}}{\beta_{li} \tilde{\rho}_l \Delta\tilde{h}_v} \right) \right) \right]} \qquad (29) .$$

Comparison of nucleate flow boiling with pool boiling data of a given mixture shows that the heat transfer coefficients are not identical even though all parameters (heat flux, pressure, composition, wall material, wall roughness) remain the same. This results mainly from the contribution of the pure components to the mixture heat transfer as given in α_{id}. The heat transfer coefficient of the pure components has to be calculated with nucleate flow boiling equations only. The heat transfer coefficient in flow to pool nucleate boiling appeared to be a function of molecular weight, as given by Steiner [44], see Appendix B. At a reduced pressure of 0.1, fluids with a molecular weight, $\tilde{M}$, greater than approximately 60 have a higher heat transfer coefficient in nucleate flow boiling than in pool boiling. For fluids with $\tilde{M}$ less than than circa 60, the reverse is true. For example, the mixture SF_6/CF_2Cl_2 has a ratio α_{nbf}/α_{nb} of about 1.65 for the component CF_2Cl_2 and 2.07 for the component SF_6.

On the basis of 668 data sets, measured heat transfer coefficients have been compared with the ones calculated from Eq. (29). The results showed that the reduction in heat transfer could be predicted rather well with an adjusted parameter $B_0/\beta_{li} = 3333$ s/m for all the values taken by the variables. However, an effect of mass velocity was observed. At certain conditions, defined by the ratio of heat flux and mass velocity, the decline of the heat transfer is so considerable that convective evaporation gives higher heat transfer coefficients than those resulting from nucleate flow boiling. This led to a remarkable contribution of convective evaporation to the total heat transfer in this range of composition where the drop is largest, as shown in Fig. 16.

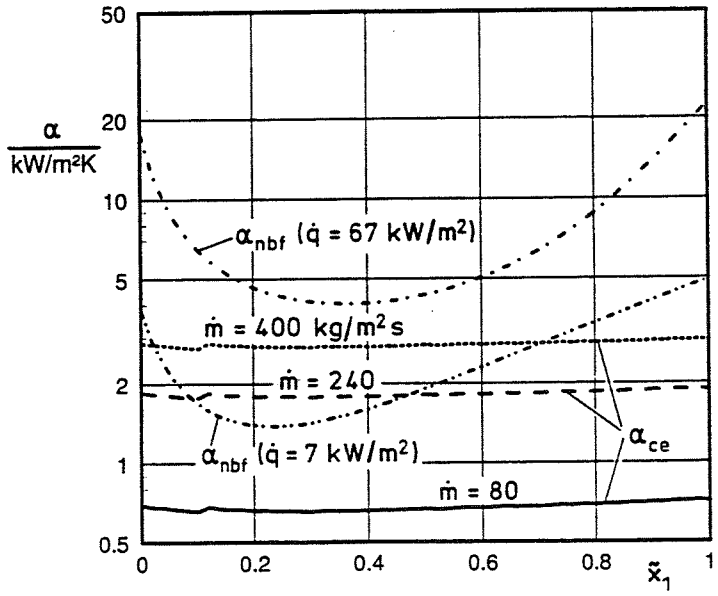

Fig. 16: Calculated convective evaporation and nucleate flow boiling heat transfer as a function of liquid composition. SF_6/CF_2Cl_2 mixture, p = 15 bar, $\mathring{x} = 0.5$. Niederkrüger [36].

Therefore, the heat transfer in convective vaporization, where the flow may be induced by forced or by natural circulation, has to be determined from the superposition of both mechanisms according to

$$\alpha_{fb} = \sqrt[3]{\alpha_{ce}^3 + \alpha_{nbf}^3} \qquad (30) .$$

The equation for the convective evaporation heat transfer coefficient, α_{ce}, is given in Appendix A. The nucleate flow boiling contribution, α_{nbf}, needs to be calculated only if a certain wall superheat or a certain heat flux, $\mathring{q}_{onb}$, required for the onset of nucleate boiling, are exceeded. The following equation approximately applies where T_s ($\underline{\tilde{x}}$, p) is the boiling-point temperature at $z = 0$:

$$\mathring{q}_{onb} = \frac{2\,\sigma\,T_s\,\alpha_{LO}}{r_{cr}\,\tilde{\rho}_v\,\Delta\tilde{h}_v} \qquad (31)\,.$$

The values to be inserted for the properties are those to be calculated for the mixture composition at the tube entrance ($z = 0$). $\tilde{\rho}_v$ is the molar density of the vapour mixture, $\Delta\tilde{h}_v$ is the molar differential latent heat of vaporization, σ is the surface tension of mixture. r_{cr} is a given parameter with $r_{cr} = 0.3 \cdot 10^{-6}$ m for all mixtures. The liquid single-phase heat transfer coefficient α_{LO} is based on $\mathring{m}$ as total flow and calculated with mixture properties at tube entrance conditions ($z = 0$).

The results are presented in Fig. 17. The dominant contribution to the heat transfer coefficient at the lowest mass velocity is that of nucleate flow boiling. This is the lowest curve calculated from Eq. (29). Convective evaporation has only a small additional contribution. The experimental data at higher mass velocities are close to the calculated curve, using Eq. (30), which is significantly affected by convective contribution.

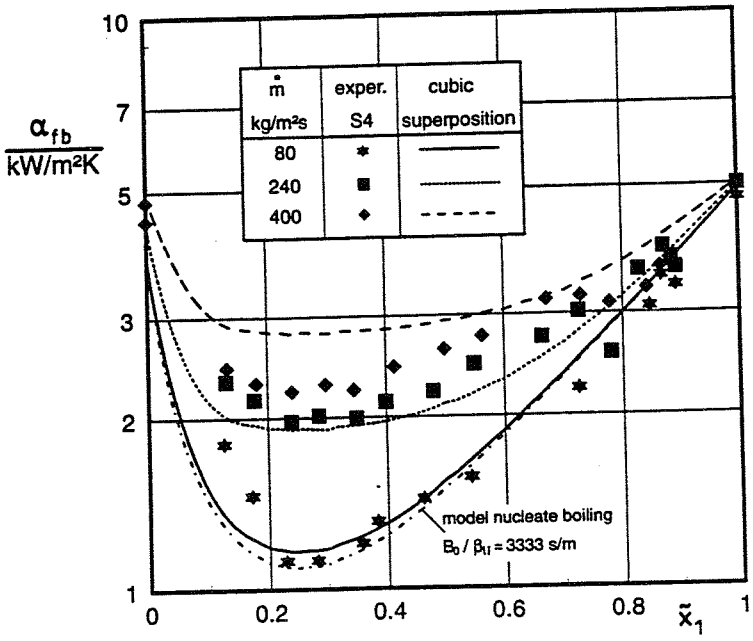

Fig. 17: Comparison of measured heat transfer coefficients in convective vaporization with calculated results. Parameter is the mass velocity. SF_6/CF_2Cl_2 mixture, $\mathring{q} = 7$ kW/m^2, $p = 15$ bar, $\mathring{x} = 0.5$. Niederkrüger [36].

Contrasting with the pool boiling results discussed above, the application of forced convective vaporization allows for the possibility of reducing the decline of the heat transfer coefficient using sufficiently high mass velocities.

CONCLUSIONS

The two major types of saturated mixture vaporization to be considered are pool and forced convective vaporization. The analysis of experimental data showed that the convective evaporation and the nucleate boiling mechanism also occur together in mixture vaporization.

Heat transfer of convective evaporation at pool and forced flow conditions is not significantly affected by mass transfer resistance. Therefore, the postulated correction of the effective temperature at the liquid-vapour interface, as given for example by Bennett and Chen [40], may be neglected as long as the liquid mixture has a low or normal viscosity. The heat transfer coefficient in this region may be predicted from well-known equations by inserting physical properties of the mixture. The concept that complete understanding of the mechanistic nucleate boiling process with the variables bubble-departure diameter, frequency of departure and boiling site density as a function of the mixture composition will lead to an accurate model has been shown to be less suitable as discussion of the data shows.

Analysis of reduced heat transfer coefficients in nucleate pool boiling, α_{nb}/α_{id}, shows a dominant effect of mixture composition, pressure and heat flux. In view of these data, the liquid side mass transfer controlled model of Schlünder [31] is up to now the best available one. The best accuracy between measured and calculated data is achieved if the parameter B_0/β_{li} is assumed to be a function of reduced pressure. In fully developed nucleate flow boiling the heat transfer coefficient is shown to be not affected by mass velocity and vapour fraction. Therefore, the drop of the reduced heat transfer coefficient, α_{nbf}/α_{id}, as a function of mixture composition can be predicted from equations developed for pool boiling. However, the analysis showed that the additive model of Bennett and Chen [40] requires suppression of the nucleate boiling component, introduced as factor S. This suppression hypothesis could not be confirmed by mixture data.

The best accuracy between measured and predicted data was achieved by using Schlünder's [31] equation. However, in this equation, where the linear mixing law is applied, the contribution of the pure components, has to be calculated from nucleate flow boiling heat transfer coefficients only.

The total heat transfer in convective vaporization, where the flow may be induced by forced or natural circulation, has to be calculated by taking into account the contribution of convective evaporation and nucleate flow boiling by an asymptotic superposition model. As a consequence, the drop of the mixture heat transfer can be reduced by using sufficiently high mass velocities.

NOMENCLATURE

A	heat transfer surface, m^2
A_0	factor in equation (14)
B_0	parameter
c_p	specific heat capacity, J/kg K
C_F	factor in nucleate flow boiling
d	inside tube diameter, m
d_d	average bubble departure diameter, m
D	outside tube diameter, m
f	frequency of bubble departure, Hz
F	enhancement factor in Chen correlation
F_{pf}	nucleat flow boiling pressure correction factor
F_{pn}	nucleate pool boiling pressure correction factor
F_{tp}	two-phase flow enhancement factor
g	acceleration due to gravity, m^2/s
Gr	Grashof number
Δh_v	latent heat of vaporization, J/kg
$\Delta \tilde{h}_v$	molar differential latent heat of vaporization, Jmol
K_l	kinetic separation factor, liquid side
K_{in}	factor in equation (17)
$\mathring{m}$	mass velocity, kg/m^2s
$\tilde{M}$	molecular weight, kg/kmol
$\mathring{n}$	molar flux, $kmol/m^2s$

$n(p_r)$ nucleate pool boiling exponent
$n_f(p_r)$ nucleate flow boiling exponent
n/A boiling site density, m^{-2}
N_{Sn} Scriven number
Nu Nußelt number
p pressure, Pa
p_{cr} critical pressure, Pa
p_r reduced pressure $(= p/p_{cr})$
Pr Prandtl number
$\mathring{q}$ heat flux, W/m^2
r radius, m
R_a arithmetic mean roughness height (ISO 4287/1, 1984), m
Re Reynolds number
S suppression factor in Chen correlation
T temperature, K
T_b bulk temperature, K
T_s boiling-point temperature, K
T_{si} boiling-point temperature of component i, K
T_W wall surface temperature, K
ΔT temperature difference, K
$\mathring{x}$ vapour fraction
x_i liquid mass fraction of component i
$\tilde{x}_i$ liquid mole fraction of component i
$\tilde{x}$ liquid mole fraction vector $(\tilde{x}_1, \tilde{x}_2 \ldots \tilde{x}_n)$
y_i vapour mass fraction
$\tilde{y}_i$ vapour mole fraction
z coordinate in main flow direction, m
α heat transfer coefficient, W/m^2K
β_{li} mass transfer coefficient of component i in the liquid phase, m/s
δ diffusivity, m^2/s
η dynamic viscosity, kg/ms
κ thermal diffusivity, m^2/s
λ thermal conductivity, W/Km
ρ density, kg/m^3
$\tilde{\rho}$ molar density, $kmol/m^3$
σ surface tension, N/m

Subscripts

b bubble
ce convective evaporation
cr critical
fb flow boiling
GO based on $\mathring{m}$ as total flow as vapour
id ideal (linear) mixing law
l liquid base
LO based on $\mathring{m}$ as total flow as liquid
nb nucleate pool boiling
nbf nucleate flow boiling
Ph interphase vapour-liquid
tp two-phase vapour-liquid
v vapour base

REFERENCES

[1] J.W. Palen, Shell-and-tube reboilers. In: "HEDH-Heat Exchanger Design Handbook", Hemisphere Publ. Corp., New York (1983).

[2] M.T. Cichelli and C.F. Bonilla, "Heat transfer to liquids boiling under pressure", Trans. Am. Inst. Chem.Engrs., 41 (1945), 755-787.

[3] U. Gropp, "Wärme- und Stoffübergang bei der Oberflächenverdampfung und beim Blasensieden eines binären Kältemittelgemisches am Rieselfilm", Diss. Univ. Karlsruhe (1985).

[4] B.B. Mikic and W.M. Rohsenow, "A new correlation of pool-boiling data including the effect of heating surface characteristics", J. Heat Transfer, 91 (1969), 245-250.

[5] C.-Y. Han and P. Griffith, "The mechanism of heat transfer in nucleate pool boiling", Int. J. Heat Mass Transfer, 8 (1965), 887-913.

[6] R.L. Judd and C.H. Lavdas, "The nature of nucleation site interaction", Trans. ASME, 102 (1980), 461-464.

[7] C.J. Rallis and H.H. Jawurek, "Latent heat transport in saturated nucleate boiling", Int. J. Heat Mass Transfer, 7 (1964), 1051-1068.

[8] H. Beer, "Beitrag zur Wärmeübertragung beim Sieden", Prog. Heat Mass Transfer, 2 (1969), 311-370.

[9] D.F. Moore and R.B. Mesler, "The measurements of rapid surface temperature fluctuations during nucleate boiling of water", AIChE J. 7 (1961), 620-624.

[10] S.J.D. van Stralen, "The mechanism of heat transfer in nucleate pool boiling", Int. J. Heat Mass Transfer, 8 (1965), 887-914.

[11] R.L. Judd and K.S. Hwang, "A comprehensive model for nucleate pool boiling heat transfer including microlayer evaporation", J. Heat Transfer, 98 (1976), 623-629.

[12] V.I. Tolubinskiy and Yu. N. Ostrovskiy, "Mechanism of heat transfer in boiling of binary mixtures", Heat Transfer Sov. Res., 1 (1969), 6-11.

[13] V.I. Tolubinskiy, Yu. N. Ostrovskiy and A.A. Kriveshko, "Heat transfer to boiling water-glycerine mixtures", Heat Transfer Sov. Res., 1 (1970), 22-24.

[14] V.I. Tolubinskiy and Yu. N. Ostrovskiy, "On the mechanism of boiling heat transfer (vapour bubbles growth rate in the process of boiling of liquids, solutions, and binary mixtures)", Int. J. Heat Mass Transfer, 9 (1966), 1463-1470.

[15] V.I. Tolubinskiy, A.A. Kriveshko, Yu. N. Ostrovskiy et al., "Effect of pressure on the boiling heat transfer rate in water-alcohol mixtures", Heat Transfer Sov. Res., 5 (1973), 66-68.

[16] V.I. Tolubinskiy, Yu. N. Ostrovskiy, V. Ye. Pisarev et al., "Boiling heat transfer rate from a benzene-ethanol mixture as a function of pressure", Heat Transfer Sov. Res., 7 (1975), 118-121.

[17] K. Stephan and M. Körner, "Blasenfrequenzen beim Verdampfen reiner Flüssigkeiten und binärer Flüssigkeitsgemische", Wärme-Stoffübertragung, 3 (1970), 185-190.

[18] M. Weckesser, "Untersuchungen zur Blasenbildung bei freier Konvektion", Diss. Univ. Karlsruhe (1990).

[19] V. Valent and N. Afgan, "Dynamik des Blasenwachstums und Wärmeübergangs beim Sieden binärer Gemische von Äthylalkohol-Wasser", Wärme-Stoffübertrag., 6 (1973), 235-240.

[20] H. Bednar, "Wärmeübergang beim Blasensieden von binären Kohlenwasserstoffgemischen", Diss. Univ. Karlsruhe (1993).

[21] T.O. Hui and J.R. Thome, "A study of binary mixture boiling: boiling site density and subcooled heat transfer", Int. J. Heat Mass Transfer, 28 (1985), 919-928.

[22] L.N. Grigorjev and A.G. Usmanov, "Wärmeübergang in binären azeotropen Gemischen (in Russia)", Inzenerno-Fizitseskij Zurnal, 11 (1959), 114-118.

[23] L.N. Grigorjev, "Studies of heat transfer of two component mixtures" (in Russia), Teplo Masso Perenos, 2 (1962), 120-127.

[24] V.D. Yusufova and A.I. Chernyakhovsky, "Heat transfer in boiling mixtures" (in Russia), Vth All-Union Heat and Mass Transfer Conference, Minsk (1976), Vol. III, Part 1, 92-97.

[25] K. Stephan and M. Körner, "Berechnung des Wärmeübergangs verdampfender binärer Flüssigkeitsgemische", Chem.Ing.Tech., 41 (1969), 409-417.

[26] K. Stephan, "Wärmeübergang beim Verdampfen von Gemischen in natürlicher Strömung", vt verfahrenstechnik, 14 (1980), 470-474.

[27] W.F. Calus and D.J. Leonidopoulos, "Pool boiling - Binary liquid mixtures", Int. J. Heat Mass Transfer, 17 (1974), 249-256.

[28] L.E. Scriven, "On the dynamics of phase growth", Chem. Engng. Sci., 10 (1959), 1-13.

[29] S.J.D. van Stralen, "The mechanism of nucleate boiling in pure liquids and in binary mixtures", Int. J. Heat Mass Transfer, 9 (1966), 995-1046.

[30] J.R. Thome, "Nucleate pool boiling of binary mixtures - An analytical equation", AIChE Symp. Ser.,77 (1981), 238-250.

[31] E.-U. Schlünder, "Über den Wärmeübergang bei der Blasenverdampfung von Gemischen", vt verfahrenstechnik, 16 (1982), 692-698.

[32] A. Bayer, "Untersuchungen zum Blasensieden von binären Stoffgemischen in einem großen Druckbereich", Diss. Univ. Karlsruhe (1988).

[33] J. Schmadl, "Wärmeübergang beim Blasensieden binärer Stoffgemische unter hohem Druck", Diss. Univ. Karlsruhe (1982).

[34] V. Bieling, "Zum Wärmeübergang beim Blasensieden des Kältemittelstoffsystems R22/R115 in einem großen Druckbereich", Diss. Univ.-Gesamthochschule Paderborn (1986).

[35] W. Rott, "Zum Wärmeübergang und Phasengleichgewicht siedender R22/R114-Kältemittel-Gemische in einem großen Druckbereich", Diss. Univ.-Gesamthochschule Paderborn (1990).

[36] M. Niederkrüger, "Strömungssieden von reinen Stoffen und binären zeotropen Gemischen im waagerechten Rohr bei mittleren und hohen Drücken", Fortschr.-Ber. VDI-Z., Reihe 3 (1991), Nr. 245, 1-249.

[37] M. Niederkrüger, D. Steiner and E.-U. Schlünder, "Horizontal flow boiling experiments of saturated pure components and mixtures of R846-R12 at high pressures", Int. J. Refrig., 15 (1992), 48-58.

[38] V.K. Jain and P.L. Dhar, "Studies on flow boiling of mixtures of refrigerants R12 and R13 inside a horizontal tube", Proc. XVI. Int. Congr. Refrig., Paris (1983), B1, 287-293.

[39] G.P. Celata, M. Cumo and T. Setoro, "Forced convective boiling in binary mixtures", Int. J. Heat Mass Transfer, 36 (1993), 3299-3309.

[40] D.L. Bennett and J.C. Chen, "Forced convective boiling in vertical tubes for saturated pure components and binary mixtures", AIChE J., 26 (1980), 454-461.

[41] J.C. Chen, "Correlation for boiling heat transfer to saturated fluids in convective flow", Ind. Eng. Chem. Process Design Develop., 5 (1966), 322-329.

[42] D. Steiner and J. Taborek, "Flow boiling heat transfer in vertical tubes correlated by an asymptotic model", Heat Transfer Eng., 13 (1992), 43-69.

[43] H. Ross, R. Radermacher, M. di Marzo et al., "Horizontal flow boiling of pure and mixed refrigerants", Int. J. Heat Mass Transfer, 30 (1987), 979-992.

[44] D. Steiner, "Wärmeübertragung beim Sieden gesättigter Flüssigkeiten", VDI-Wärmeatlas, Abschnitt Hbb, VDI-Verlag, Düsseldorf (1988). Translated in English: VDI-Heat Atlas, Sect. Hbb, VDI-Verlag, Düsseldorf (1993).

[45] J. Rheinländer, "Konvektive Wärmeübertragung bei Auftriebsströmung an senkrechten, geneigten und horizontalen Platten, horizontalen Zylindern und an Kugeln", VDI-Wärmeatlas, Abschnitt Fa, VDI-Verlag, Düsseldorf (1988). Translation: VDI-Heat Atlas, Sect. Fa, VDI-Verlag, Düsseldorf (1993).

[46] D. Gorenflo, "Behältersieden (Sieden bei freier Konvektion)", VDI-Wärmeatlas, Abschnitt Ha, VDI-Verlag, Düsseldorf (1988). Translation: VDI-Heat Atlas, Sect. Ha, VDI-Verlag, Düsseldorf (1993).

[47] K. Stephan and P. Preußer, "Wärmeübergang und maximale Wärmestromdichte beim Behältersieden binärer und ternärer Flüssigkeitsgemische", Chem. Ing. Tech., 51 (1979), 649-679.

APPENDIX A: Heat Transfer Coefficient of the Convective Evaporation Component

Evaporation at pool conditions

The heat transfer due to natural convection in the *laminar region* has to be calculated from

$$Nu = 0.6\,(Gr\,Pr)^{1/4} \qquad (A1)\,.$$

The Grashof number is defined as

$$Gr = \frac{gD^3\,\rho_b}{\eta_l^2}(\rho_b - \rho_W) \qquad (A2)\,,$$

where ρ_b is the liquid density determined at bulk conditions of the mixture. Pr is the Prandtl number,

$$Pr = \eta_l\,c_{pl}/\lambda_l \qquad (A3)\,.$$

The buoyancy-induced convection is considered laminar as long as

$Gr\,Pr \le 2{\cdot}10^7$.

Beyond this critical Rayleigh number (Ra = Gr Pr), the following *turbulent* equation must be used

$$Nu = 0.15\ (Gr\ Pr)^{1/3} \qquad (A4)\ .$$

If the heating surface is a tube with the outside diameter D, Nu is defined as

$$Nu = \frac{\alpha_{ce}\, D}{\lambda_l} \qquad (A5)\ .$$

For other geometries, the characteristic length must be used, see for example VDI-Wärmeatlas [45], section Fa.

Evaporation at convective conditions

For flow in vertical tubes the liquid phase heat transfer coefficient α_{LO} is enhanced. The two-phase flow enhancement factor F_{tp} is given as

$$\frac{\alpha_{ce}}{\alpha_{LO}} = F_{tp} = \left(\left[(1-\mathring{x})^{1.5} + 1.9\ \mathring{x}^{0.6}\ (1-\mathring{x})^{0.01} \left(\frac{\rho_l}{\rho_v}\right)^{0.35} \right]^{-2.2} + \left[\frac{\alpha_{GO}}{\alpha_{LO}}\ \mathring{x}^{0.01} \left(1+8(1-\mathring{x})^{0.7} \left(\frac{\rho_l}{\rho_v}\right)^{0.67} \right) \right]^{-2} \right)^{-0.5} \qquad (A6)\ .$$

In Eq. (A6), α_{LO} and α_{GO} are local single-phase heat transfer coefficients that must be determined at a certain position z. They are based on $\mathring{m}$ as total mass velocity for the liquid (L) and vapour (G), respectively. They can be obtained from recommended equations where flow may be induced by forced or natural circulation.

Property values:

All the properties required for calculation are those of the mixture at bulk composition and at point z in the evaporator tube assuming local equilibrium. For the case of horizontal and inclined tubes, where wetting is incomplete, see VDI-Wärmeatlas [44], section Hbb.

APPENDIX B: Heat Transfer Coefficient of the Pure Components in the Nucleate Boiling Region

Nucleate pool boiling

Heat transfer is a strong function of the wall superheat ΔT. In many correlations the heat flux $\mathring{q}$ is used as basis. For each pure component i of the mixture, the heat transfer must be calculated as follows

$$\frac{\alpha_{nb,i}}{\alpha_{nb,o}} = F_{pn} \left(\frac{\mathring{q}}{\mathring{q}_o}\right)^{n(p_r)} \left(\frac{R_a}{R_{a,o}}\right)^{0.133} \qquad (B1)\ .$$

For all fluids, except water,

$$F_{pn} = 1.2\ p_{r,i}^{0.27} + \left(2.5 + \frac{1}{1 - p_{r,i}}\right) p_{r,i} \qquad (B2)$$

$$n(p_r) = 0.9 - 0.3\ p_{r,i}^{0.3} \qquad (B3)\ .$$

The normalized conditions (subscript o) to calculate the base pool boiling heat transfer coefficient $\alpha_{nb,o}$ are: $p_{r,o} = 0.1$, $R_{a,o} = 0.4 \cdot 10^{-6}$ m, $\mathring{q}_o = 20000$ W/m^2.

The Stephan-Preußer method [47] or Table 1 in section Ha of the VDI-Wärmeatlas [46] are recommended to determine $\alpha_{nb,o}$. The other conditions are given in the VDI-Wärmeatlas [46], section Ha.

Nucleate flow boiling

The heat transfer coefficient of each pure component i of the mixture in vertical tubes has to be calculated from

$$\frac{\alpha_{nbf,i}}{\alpha_{nb,o}} = C_F \, F_{pf} \left(\frac{\mathring{q}}{\mathring{q}_o}\right)^{n_f(p_r)} \left(\frac{d_o}{d}\right)^{0.4} \left(\frac{R_a}{R_{a,o}}\right)^{0.133} \tag{B4}$$

where

$$C_F = 0.36 \, \tilde{M}^{0.27} \tag{B5}$$

$$F_{pf} = 2.186 \, p_{r,i}^{0.45} + \left[3.4 + \frac{1.7}{1-(p_{r,i})^7}\right] p_{r,i}^{3.7} \tag{B6}$$

$$n_f(p_r) = 0.8 - 0.1 \cdot 10^{(0.76 \, p_{r,i})} \tag{B7} .$$

Eq. (B7) has to be used for all fluids except cryogenics. The following normalized parameters have to be used for nucleate flow boiling:

$\mathring{q}_o = 20\,000$ W/m^2 for hydrocarbons, organics, refrigerants.

$p_{r,o} = 0.1$, $d_o = 0.01$ m, $R_{a,o} = 1 \cdot 10^{-6}$ m .

Other fluids see section Hbb of VDI-Wärmeatlas [44].

The base pool boiling heat transfer coefficient $\alpha_{nb,o}$ has to be determined from the Stephan-Preußer method [47] or the Table 3 of section Hbb of the VDI-Wärmeatlas [44]. For each pure component i, the reduced pressure is defined as

$$p_{r,i} = p/p_{cr,i} \tag{B8}$$

where $p_{cr,i}$ is the critical pressure of the component i.

Equations for heat transfer coefficients in horizontal and inclined tubes are given in the VDI-Wärmeatlas [44], section Hbb.

UPSTREAM CRITICAL HEAT FLUX IN FLOW BOILING INSIDE A TUBE

S. Yokoya, M. Watanabe, and M. Shoji

Department of Mechanical Engineering
The University of Tokyo
Hongo 7-3-1, Bunkyo-ku, Tokyo 113, Japan

ABSTRACT

In forced convection boiling inside an uniformly heated tube, critical heat flux generally appears at an exit of the tube, but it is occasionally detected at some upstream locations. In the present paper, experimental findings on this phenomenon of upstream critical heat flux are described.

Three types of stainless steel tubes, which have the same diameter of 5 mm and the same length of 1000 mm but different inner surface roughness, were used separately as test tube. The tube was vertically set and directly heated by an electric current. Using Freon 115 as a test liquid, boiling tests were conducted by varying the parameters widely as follows:

Density ratio (that is the system pressure): ρ_v/ρ_l = 0.1 to 0.4,
Mass flow rate: G = 545 to 6540 kg/m^{2}s,
Inlet enthalpy (liquid inlet subcooling): ΔH_i = -30 to 60 kJ/kg.

Critical heat flux was detected as a heat flux when the wall temperature increases abruptly. Thirteen thermocouples of K type spot welded on the outer tube surface with a uniform distance in the liquid flow direction were used.

From these experiments, the following is found:

1. The phenomenon of upstream critical heat flux is reproducible and autonomous.
2. The upstream critical heat flux is likely to appear in a tube with rough surface.
3. The upstream critical heat flux is likely to occur at low inlet enthalpy at high pressure and high mass flow rate.
4. The upstream critical heat flux is, in general, higher than the one predicted to occur at an exit of the tube for the same inlet enthalpy.
5. The upstream region where the wall temperature is high in post critical heat flux becomes wider as the heat flux increases.

NOTE: *This paper had not been received before the Proceedings were assembled. If received on or before August 23, 1994, handouts will be given to each participant of the Symposium.*

CRITICAL HEAT FLUX OF SUBCOOLED FLOW BOILING WITH AND WITHOUT INTERNAL TWISTRED TAPE UNDER CIRCUMFERENTIALLY NON-UNIFORM HEATING CONDITION

H.Nariai [1] , F.Inasaka[2] and H.Kinoshita[1]

[1]The University of Tsukuba
Institute of Engineering Mechanics
Tsukuba, Ibaraki 305, Japan
Telephone:+81-298-53-5256,Facsimile:+81-298-53-5256

[2]Ship Research Institute
Nuclear Technology Division
Shinkawa 6-38-1, Mitaka, Tokyo 181, Japan
Telephone:+81-422-41-3139,Facsimile:+81-422-41-3136

ABSTRACT

Critical heat flux (CHF) of subcooled flow boiling with water in tubes with and without internal twisted tape under circumferentially non-uniform heating condition was experimentally investigated using direct current heating of stainless steel tube. Thirty four CHF data under uniform heating condition and seventy three data under non-uniform heating condition were presented in this paper. The CHF in smooth tube without internal twisted tape under non-uniform heating condition was slightly higher than that under uniform heating condition. The reason was explained by the lower average quality at the burnout point under non-uniform heating condition than that under uniform heating condition. When average qualities are the same, the CHF under non-uniform heating condition coincides with that under uniform heating condition. Leontiev et al's data also showed the same characteristics. The CHF in tube with internal twisted tape under non-uniform heating condition was much higher than that under uniform heating condition, though the average qualities were almost the same for both cases. The higher CHF under non-uniform heating condition was explained by the alternate development and disruption of bubble boundary layer in the flow along the twisted tape.

1. INTRODUCTION

High heat flux components of fusion reactors are subjected to very high heat flux and the cooling channel is under non-uniform heat flux condition since the heat by irradiation comes in, in general, from one side of the wall. Subcooled flow boiling with water has the high possibility to remove the high heat load, and the critical heat flux (CHF) is the most important factor to determine the upper limit of the coolability. In order to enhance the CHF, an internal twisted tape is usually inserted in the cooling channel. However, the researches on the CHF of subcooled flow boiling with water with internal twisted tape under non-uniform heating condition have been very scarce. Recently, Koski et al [1] , Milora et al [2] , Araki et al [3] , Schlosser et al [4] [5] reported the CHF in tube with internal twisted tape under non-uniform heating condition using such an electron beam apparatus. They estimated that the peak heat flux at the CHF should be considerably higher than that predicted by the existing CHF correlations under uniform heating condition. The precise mechanism of the CHF has, however, not been made clear.

The CHF of subcooled flow boiling under circumferentially non-uniform heating condition has been investigated by several researchers using direct current heating of the tube simulating a cooling channel. Ornaskii et al [6] conducted the experiments with the narrow smooth tube of 0.5 mm inside diameter and 14 mm length. The heat flux of circumferentially 120 ° of the tube was higher than that of remaining part, and they obtained the CHF by 50 to 80 % higher than that under uniform heating condition. Leontiev et al [7] conducted the experiments under the pressure of 6.86 to 13.7 MPa using a smooth tube with an eccentric hole, which was 6 mm inside diameter and 415 mm length. The derived CHF data were slightly higher than those under uniform heating condition. They also pointed out that the average qualities under non-uniform heating condition

were lower than those under uniform heating condition. Recently, Nariai et al [8] [9] conducted the experiments both in smooth tube and in tube with internal twisted tape under non-uniform heating condition. The dimension of the test tube was 6 mm inside diameter and 100 mm length. The tube thickness was made thin by circumferentially 180° and 90° , in order to simulate the non-uniform heating condition. They obtained the higher CHF data under non-uniform heating condition particularly in tube with internal twisted tape than those under uniform heating condition. They pointed out the necessity to define the multiplication factor for non-uniform heating condition.

This paper presents the details of the experimental data with the thinned part angle of 270° , 180° and 90° under both uniform and non-uniform heating conditions and also gives the detailed discussion on non-uniformity effects. The higher CHF in smooth tube under non-uniform heating condition was explained by the lower average qulity. It was well predicted by the empirical correlations under uniform heating condition when we use the same average qualities. The CHF in tube with internal twisted tape under non-uniform heating condition was confirmed to be higher with the increase of non-uniformity. The cause was estimated to be the alternate development and disruption of bubble boundary layer in the flow along the twisted tape.

2. EXPERIMENTS

2.1 Experimental Apparatus

Experiments were conducted with vertical test tube made of stainless steel, which was directly heated by a DC power source. Figure 1 shows a schematic drawing of the experimental apparatus. Water circulates from water tank through a pump, a flow meter, a test section, and a heat exchanger. Figure 2 shows the details of the test tube. In order to simulate the circumferential non-uniform heating condition, a part of the tube wall was made thin by electrochemincal machining. The cross section in the figure shows the case of a thinned part angle, $\beta = 180°$. Dimensions of the test tube were 6 mm of the inside diameter, and about 0.35 mm and 0.15 mm of the tube wall thickness for the thicker and thinner parts, respectively. For the experiments involving an internal twisted tape, a tape made of zirconia, was inserted in the test tube.

2.2 Experimental Condition

Experimental conditions in the present study are as follows:

Mass velocity of water (nominal values)	G	: 5000, 9000 kg/m^{2}s
Inlet temperature of water (nominal)	Tin	: 40 ℃
Pressure at tube outlet (nominal)	P	: 0.1, 0.6, 1.1, 1.5 MPa
Thinned part angle	β	: 270° , 180° , 90° and 0 (uniform heating)
Twisted tape ratio	y	: 2.64, 3.47, and ∞ (smooth tube)

After a combination of these parameters was set, the electric power was increased step by step allowing steady state thermal conditions to be reached. The CHF was determined as the heat flux just before burnout occurred. The average heat flux at the CHF was calculated from the electric power, that was applied to the tube, divided by the surface area of the tube wall, and the heat flux at the thinner and thicker walls were calculated from the electric power applied to each wall using the electric resistance ratio. As the heat flux at the thicker part of the wall was higher, burnout occurred first at that part of the tube.

2.3 Experimental Results

Tables I and II show the experimental data both under non-uniform and under uniform heating conditions, respectively. In Table I, 73 data were presented under non-uniform heating condition. The symbols $q_{c,H}$ and $q_{c,L}$ mean the thicker and thinner part of the heat flux, respectively. The symbol $q_{c,av}$ means the average heat flux of the tube. The heat flux ratio $q_{c,H}/q_{c,av}$, which was tentatively introduced by authors as expressing the intensity of non-uniformity of the test tube, is also presented. The symbol x_{ex} is the average quality of the water at tube outlet or the burnout point. In Table II, 34 data were presented under uniform heating condition. The symbol $q_{c,unif}$ means the average heat flux at burnout under uniform heating condition.

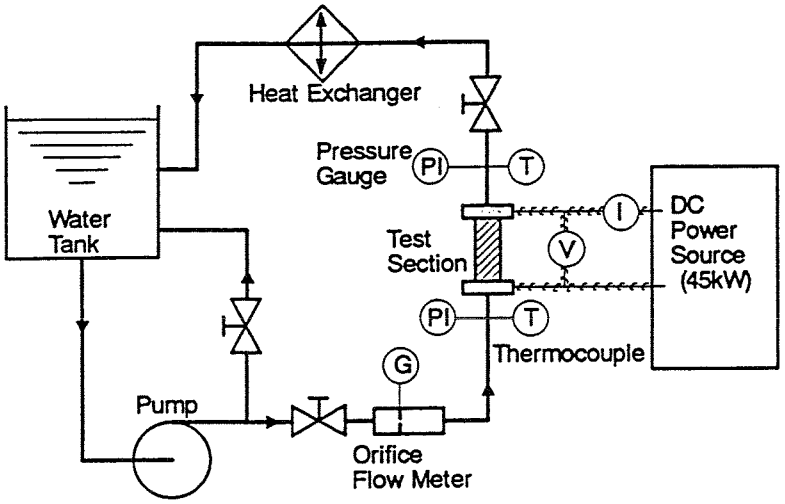

Fig. 1 Schematic drawing of experimental apparatus

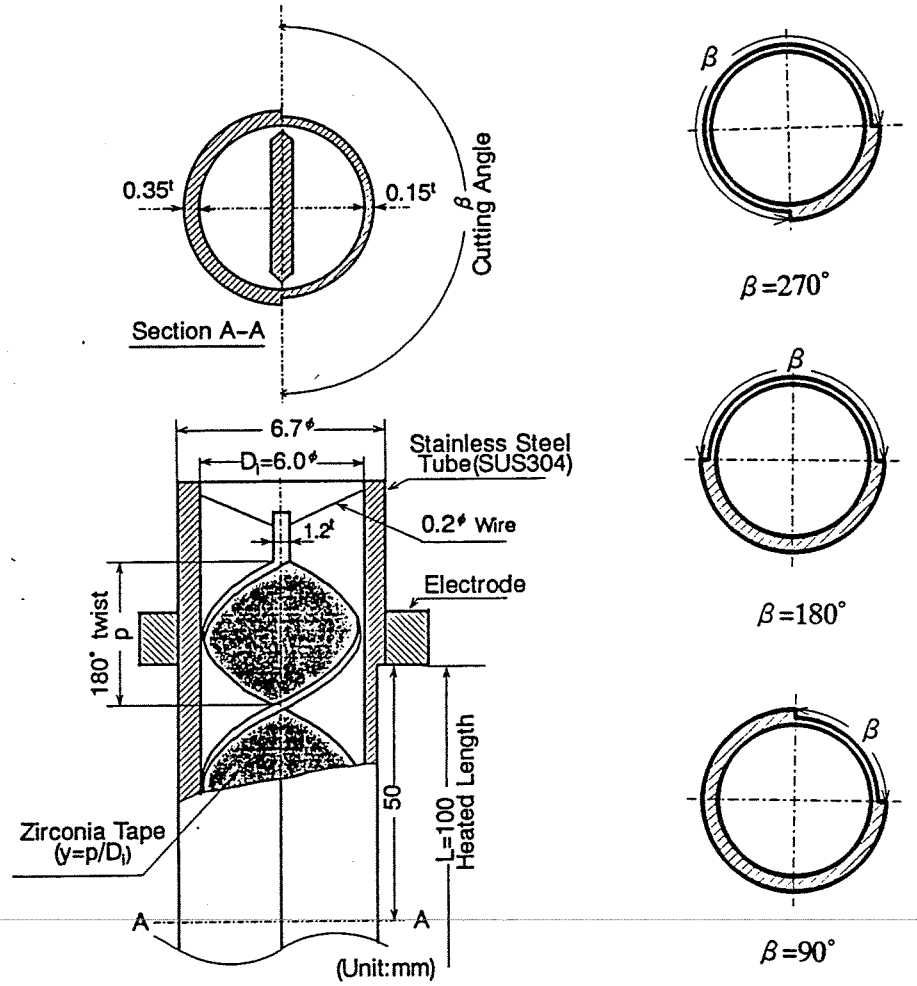

Fig. 2 Configuration of the test tube

Table I CHF Data (Non-Uniform Heating Condition)

No	G (Mg/m^2s)	P (MPa)	Tin (℃)	β	y	$q_{c,H}$ (MW/m^2)	$q_{c,L}$ (MW/m^2)	$q_{c,av}$ (MW/m^2)	$q_{c,H}/q_{c,av}$	X_{ex}
1	4.92	0.1	40.7	270	∞	11.2	4.5	5.8	1.93	−0.08
2	4.88	0.6	36.2	270	∞	16.8	6.2	8.5	1.97	−0.19
3	4.85	1.1	40.0	270	∞	18.8	7.6	10.2	1.84	−0.24
4	4.88	1.5	39.6	270	∞	18.4	8.1	10.5	1.75	−0.28
5	4.93	0.1	40.2	180	∞	9.0	3.9	6.2	1.47	−0.07
6	4.47	0.6	40.3	180	∞	15.0	5.9	10.3	1.46	−0.17
7	4.70	0.6	41.8	180	∞	15.8	6.2	10.8	1.46	−0.17
8	4.49	1.1	40.9	180	∞	16.8	6.8	11.7	1.43	−0.22
9	5.34	1.1	42.6	180	∞	17.9	8.4	13.1	1.37	−0.22
10	5.18	1.5	39.4	180	∞	17.3	7.0	12.1	1.43	−0.27
11	5.07	1.5	41.7	180	∞	17.8	8.9	13.3	1.34	−0.26
12	4.93	0.1	39.9	90	∞	8.4	4.0	7.1	1.18	−0.07
13	4.86	0.6	43.1	90	∞	14.1	5.6	11.9	1.18	−0.16
14	4.82	1.1	43.4	90	∞	15.9	6.6	13.6	1.17	−0.21
15	5.19	1.5	43.0	90	∞	16.2	6.6	13.9	1.17	−0.25
16	4.92	0.1	40.7	270	2.67	16.2	7.3	9.0	1.80	−0.05
17	5.13	0.6	42.4	270	2.67	21.6	8.5	11.4	1.89	−0.14
18	5.01	1.1	39.7	270	2.67	26.3	10.6	14.4	1.83	−0.19
19	5.17	1.5	41.0	270	2.67	27.1	11.4	15.2	1.78	−0.22
20	4.92	0.1	40.1	180	2.67	11.1	4.9	7.7	1.45	−0.06
21	4.92	0.1	40.4	180	2.67	10.1	4.9	7.2	1.41	−0.06
22	4.81	0.6	40.5	180	2.65	16.5	6.7	11.4	1.44	−0.15
23	4.88	1.1	40.0	180	3.46	22.2	9.2	15.8	1.41	−0.18
24	5.02	1.5	49.4	180	2.65	22.6	8.6	15.7	1.44	−0.20
25	4.92	0.1	40.1	90	2.67	8.8	3.8	7.4	1.19	−0.06
26	4.95	0.6	41.4	90	2.67	13.5	6.1	11.6	1.16	−0.15
27	5.54	1.1	42.0	90	2.64	16.8	7.1	14.4	1.17	−0.20
28	5.03	1.5	44.4	90	2.64	19.8	9.5	17.4	1.14	−0.20
29	4.92	0.1	40.0	270	3.47	13.5	5.5	7.0	1.92	−0.07
30	4.87	0.6	39.5	270	3.47	22.7	8.7	11.9	1.91	−0.15
31	4.64	1.1	41.2	270	3.47	24.1	9.8	13.1	1.84	−0.20
32	5.04	1.5	39.3	270	3.47	25.3	9.6	13.4	1.89	−0.24
33	4.92	0.1	39.7	180	3.47	11.9	5.2	8.2	1.45	−0.06
34	4.92	0.1	39.8	180	3.47	12.1	5.1	8.2	1.47	−0.05
35	5.11	0.6	42.8	180	3.47	19.8	8.4	13.9	1.42	−0.13
36	5.10	1.1	40.1	180	3.47	23.5	9.7	16.7	1.41	−0.17
37	5.08	1.5	40.7	180	3.47	22.3	8.5	15.5	1.44	−0.22
38	4.92	0.1	40.8	90	3.47	9.2	4.1	7.7	1.18	−0.05
39	4.63	0.6	38.7	90	3.47	13.8	6.3	11.9	1.16	−0.15
40	5.16	1.1	43.2	90	3.47	17.7	7.8	15.3	1.16	−0.18
41	4.80	1.5	44.4	90	3.47	18.9	8.4	16.4	1.15	−0.19

Table I CHF Data (Non-Uniform Heating Condition) (continued)

No	G (Mg/m^2s)	P (MPa)	Tin (℃)	β	y	$q_{c,H}$ (MW/m^2)	$q_{c,L}$ (MW/m^2)	$q_{c,av}$ (MW/m^2)	$q_{c,H}/q_{c,av}$	X_{ex}
42	8.65	0.1	40.8	270	∞	15.2	6.2	8.0	1.91	−0.08
43	8.65	0.6	39.7	270	∞	23.5	9.7	12.8	1.84	−0.19
44	8.81	1.1	35.4	270	∞	23.4	10.4	13.4	1.75	−0.26
45	8.64	1.5	40.5	270	∞	26.3	11.1	14.8	1.78	−0.29
46	8.62	0.1	41.9	180	∞	12.2	4.8	8.2	1.50	−0.08
47	8.62	0.1	40.9	180	∞	11.3	5.3	8.0	1.42	−0.08
48	8.42	0.6	41.9	180	∞	19.7	9.4	14.5	1.36	−0.18
49	8.59	0.6	42.0	180	∞	18.9	9.4	14.0	1.35	−0.18
50	8.72	0.6	42.0	180	∞	19.2	10.0	14.4	1.33	−0.18
51	8.63	1.1	43.4	180	∞	21.4	9.9	15.6	1.37	−0.24
52	8.28	1.1	43.1	180	∞	21.4	11.2	16.3	1.31	−0.23
53	8.50	1.5	42.5	180	∞	23.2	11.6	17.5	1.32	−0.27
54	8.61	1.5	42.0	180	∞	22.8	9.7	16.4	1.39	−0.28
55	8.62	0.1	41.3	90	∞	12.1	5.4	10.3	1.18	−0.07
56	8.57	0.6	42.4	90	∞	19.1	8.3	16.4	1.16	−0.18
57	8.39	1.1	41.8	90	∞	21.9	7.6	18.5	1.19	−0.23
58	8.98	1.5	43.3	90		21.0	9.2	18.2	1.15	−0.27
59	8.62	0.1	41.4	270	2.67	22.4	8.6	11.5	1.95	−0.06
60	8.80	0.6	42.4	270	2.67	33.8	12.9	17.8	1.89	−0.15
61	8.57	0.1	40.9	180	2.67	15.2	6.9	10.7	1.43	−0.06
62	8.57	0.1	40.7	180	2.67	15.8	7.8	11.4	1.39	−0.06
63	8.57	0.6	41.0	180	2.65	22.4	9.3	15.8	1.42	−0.16
64	8.60	1.1	55.0	180	2.64	28.9	11.2	20.3	1.42	−0.17
65	8.55	0.1	40.7	90	2.67	13.4	5.7	11.4	1.18	−0.06
66	8.57	0.6	40.5	90	2.67	19.6	8.5	16.9	1.16	−0.16
67	8.64	0.1	40.3	270	3.47	18.2	7.6	9.7	1.87	−0.07
68	8.63	0.6	36.4	270	3.47	27.9	11.6	15.3	1.82	−0.18
69	8.57	0.1	41.5	180	3.47	16.6	7.3	11.5	1.44	−0.06
70	8.71	0.6	40.7	180	3.47	21.9	8.9	15.3	1.43	−0.17
71	8.51	1.1	39.1	180	3.47	23.0	10.6	16.9	1.36	−0.22
72	8.57	0.1	41.5	90	3.47	15.1	7.0	12.9	1.17	−0.05
73	8.66	0.6	39.0	90	3.47	20.3	8.9	17.5	1.16	−0.16

Table II CHF Data (Uniform Heating Condition)

No	G (Mg/m^2s)	P (MPa)	Tin (℃)	y	$q_{c,unif}$ (MW/m^2)	X_{ex}
81	4.93	0.1	41.1	∞	8.5	−0.06
82	4.93	0.1	39.8	∞	8.5	−0.06
83	4.90	0.6	38.3	∞	12.5	−0.16
84	4.87	1.1	40.5	∞	15.7	−0.21
85	5.09	1.1	41.6	∞	15.6	−0.20
86	4.79	1.1	41.2	∞	14.9	−0.20
87	4.59	1.5	41.2	∞	15.8	−0.23
88	4.96	1.5	41.9	∞	16.1	−0.24
89	4.93	0.1	40.6	2.71	9.2	−0.04
90	4.93	0.1	40.5	2.71	10.1	−0.04
91	4.77	0.6	40.7	2.64	12.4	−0.15
92	5.09	1.1	40.9	2.64	14.6	−0.19
93	4.76	1.5	43.1	2.64	15.9	−0.21
94	4.92	0.1	42.2	3.47	8.6	−0.05
95	4.93	0.1	40.3	3.47	8.5	−0.05
96	4.93	0.6	40.7	3.47	13.3	−0.14
97	4.61	1.1	39.6	3.47	14.3	−0.19
98	5.32	1.1	39.6	3.47	14.5	−0.20
99	5.09	1.5	39.8	3.47	14.6	−0.24
100	8.63	0.1	40.1	∞	11.2	−0.07
101	8.58	0.6	43.3	∞	16.9	−0.17
102	8.67	1.1	44.7	∞	20.6	−0.22
103	8.69	1.5	43.4	∞	20.8	−0.26
104	8.59	1.5	43.5	∞	22.1	−0.25
105	8.47	1.5	43.1	∞	20.0	−0.26
106	8.62	0.1	40.8	2.71	13.2	−0.05
107	8.58	0.1	39	2.67	12.7	−0.06
108	8.67	0.6	43.1	2.64	19.7	−0.15
109	8.35	1.1	44.4	2.64	21.2	−0.20
110	8.57	0.1	40.7	3.47	12.8	−0.05
111	8.58	0.1	39.3	3.47	13.9	−0.06
112	8.63	0.1	40.5	3.47	12.6	−0.06
113	8.57	0.6	44.3	3.47	18.0	−0.15
114	9.02	1.1	40.3	3.47	19.3	−0.22

3. EXPERIMENTAL RESULTS

3.1 CHF in Smooth Tube

Figures 3 and 4 show the CHF data in smooth tube without internal twisted tape under non-uniform heating and uniform heating conditions against average qualities at tube outlet for mass velocities of 5000 and 9000 kg/m^{2}s, respectively. The solid line means the relation between the heat flux and the average quality at tube outlet during the increase of heat flux under nominal experimental condition specified in the figure. Scatters of $q_{c,av}$ and $q_{c,unif}$ from this solid line mean the scatters of experimental conditions from the nominal values. In the figures, $q_{c,H}$ and $q_{c,L}$ are also shown. When thinned part angle β increases or the non-uniformity increases, the average quality at tube outlet decreases and $q_{c,H}$ increases. The dotted line shows the prediction by Modified Tong correlation which Inasaka and Nariai [10] proposed for smooth tube under uniform heating condition as Eqs. (1) to (3).

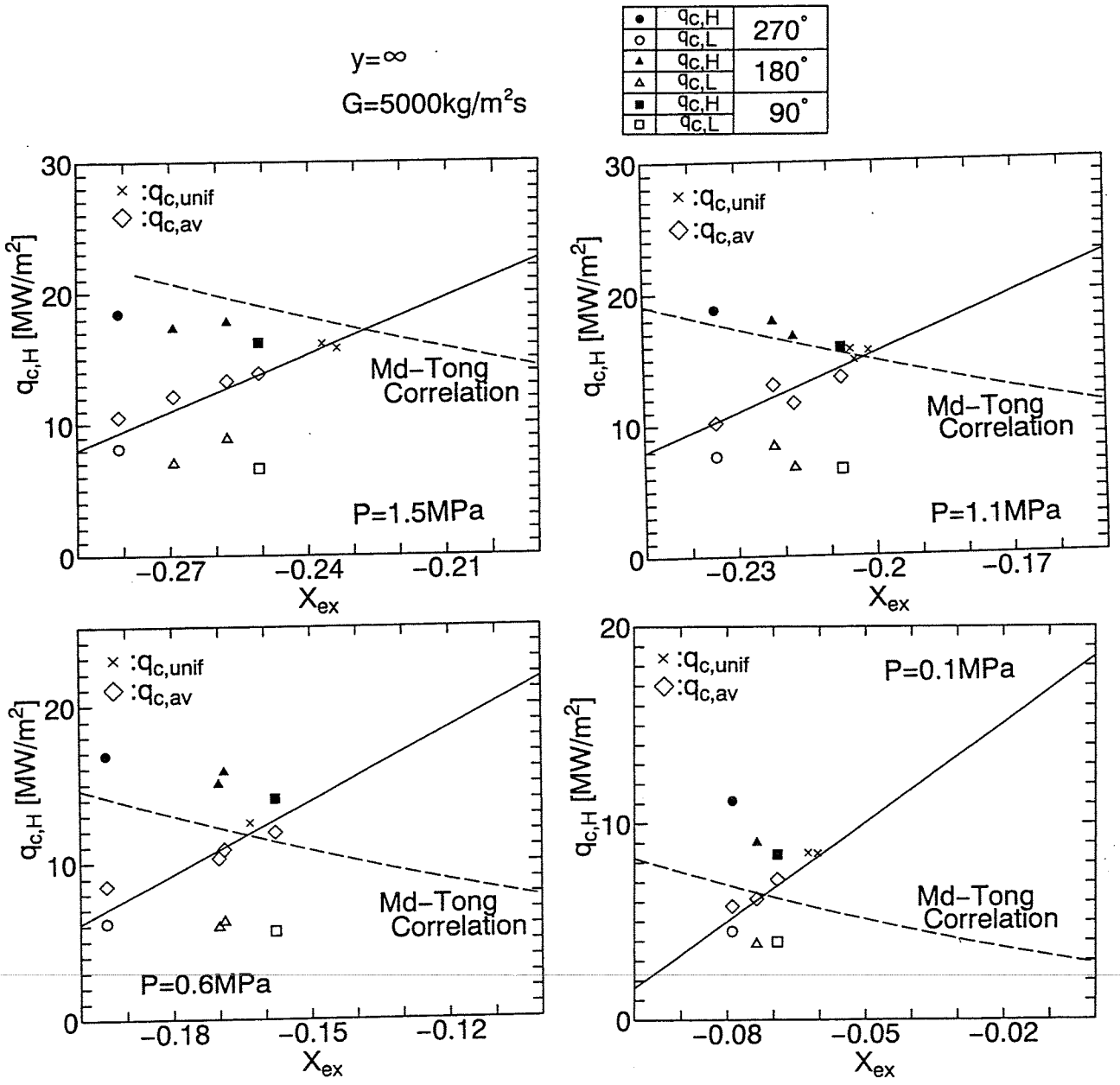

Fig. 3 CHF in smooth tube under non-uniform heating condition (G=5000 kg/m^{2}s)

$$\frac{q_{c,sm}}{H_{fg}} = C\frac{G^{0.4}\mu_f^{0.6}}{D^{0.6}} \tag{1}$$

$$\frac{C}{C_{Tong}} = 1 - \frac{52.3 + 80x_{ex} - 50x_{ex}^2}{60.5 + (P\times 10^{-5})^{1.4}} \tag{2}$$

$$C_{Tong} = 1.76 - 7.433x_{ex} + 12.222x_{ex}^2 \tag{3}$$

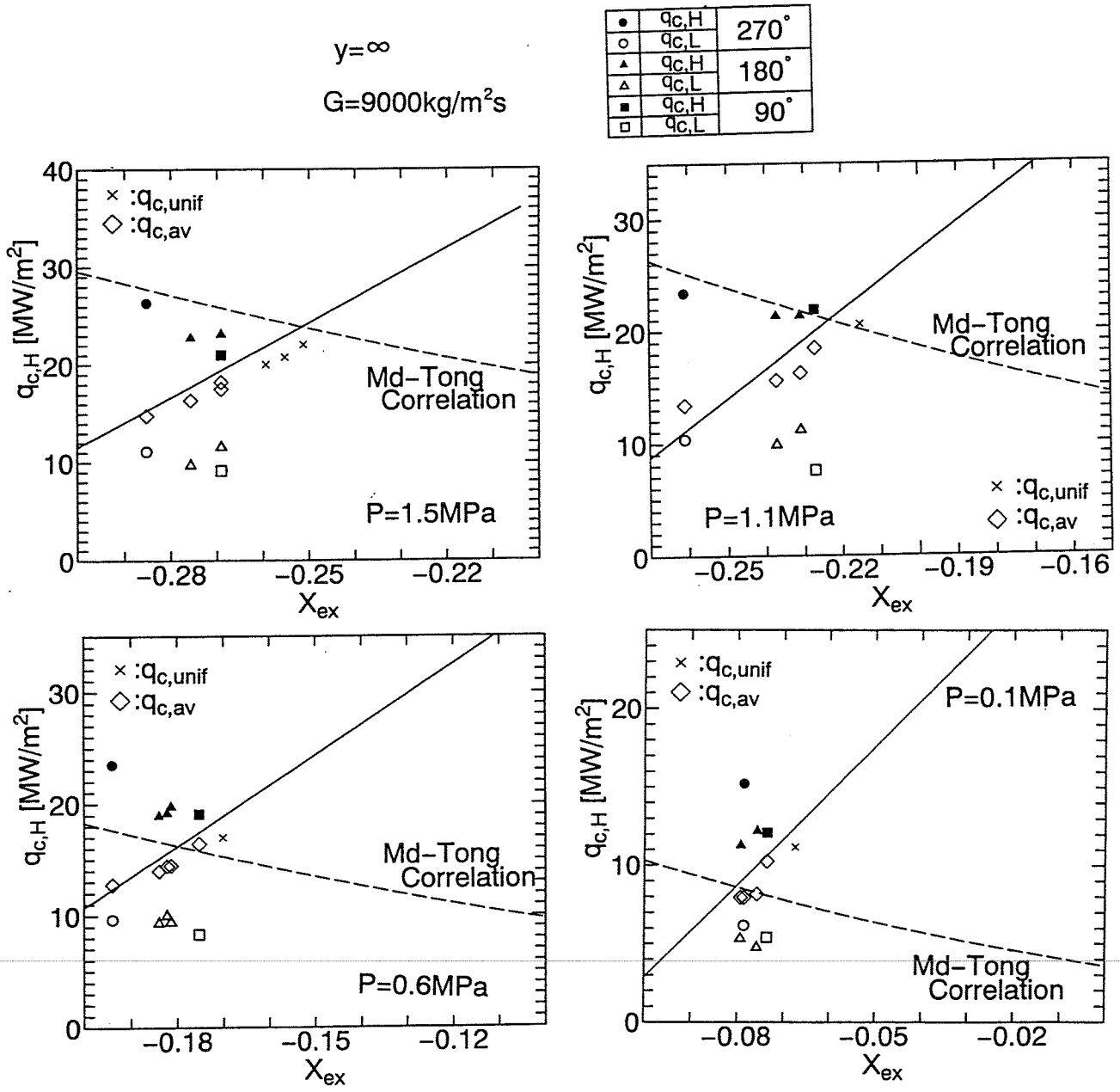

Fig. 4 CHF in smooth tube under non-uniform heating condition (G=9000 kg/m²s)

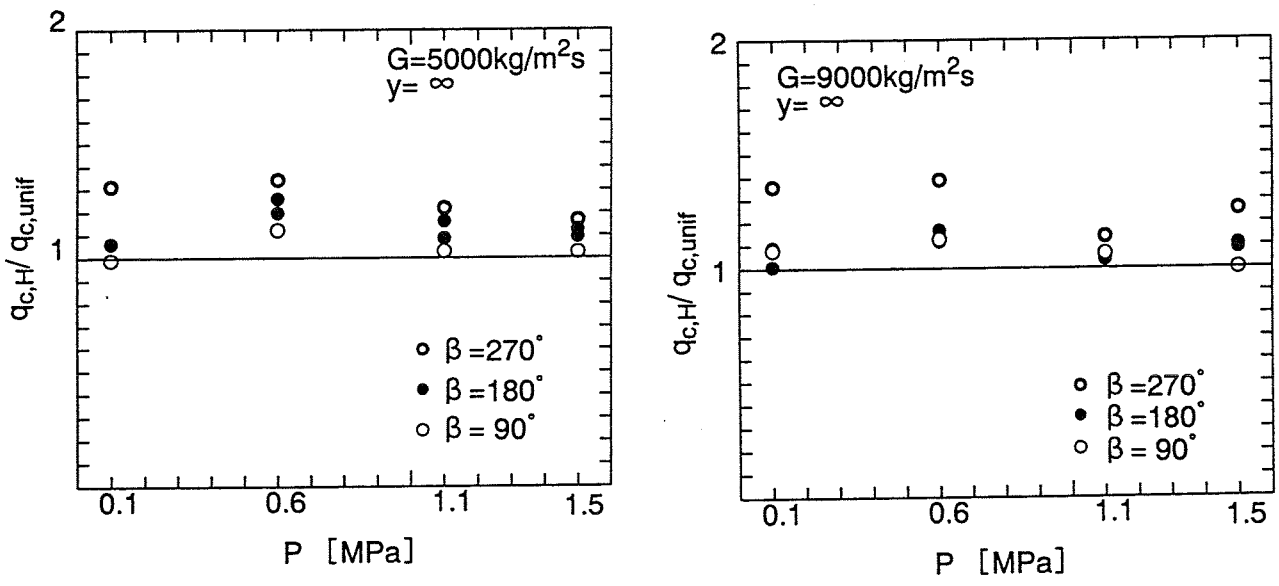

Fig. 5 CHF ratio of non-uniform to uniform heating condition in smooth tube

The symbol $q_{c,sm}$ expresses the CHF in smooth tube. This correlation was confirmed to agree with experimental data for wide pressure range from ambient to more than 20 MPa. Strictly speaking, however, it predicts a little lower for lower pressure than 1 MPa and a little higher for higher pressure than 1 MPa. It agreed well at around 1 MPa pressure [11] . Taking the characteristics into account, we can see that the CHF under non-uniform heating condition agrees well with that under uniform heating condition when exact average quality is considered.

Figure 5 shows the ratio of $q_{c,H}$ to $q_{c,unif}$ against pressure. As shown in the figures, $q_{c,H}$ is by 20 to 30 % higher than $q_{c,unif}$ at large β.

3.2 CHF in Tube with Internal Twisted Tape

Figures 6 and 7 show the CHF in tube with internal twisted tape , twisted tape ratio of which is either of 2.64 and 3.47, respectively, under non-uniform and uniform heating conditions against average quality at tube outlet for mass velocity of 5000 kg/m^{2}s. The meaning of the solid line and the signs is the same as in Figs. 3 and 4. In these figures, the average qualities do not decrease with the increase of β, and they almost coincide with the value under uniform heating condition. The most important characteristics are that $q_{c,H}$ is much higher than that under uniform heating condition though the average qualities are almost the same. Further, $q_{c,H}$ increases with the increase of β.

The dotted line means the predicitons by Nariai-Inasaka correlation in tube with internal twisted tape under uniform heating condition [12] . The correlation is expressed as in Eqs. (4) and (5).

$$\frac{q_{c,sw}}{q_{c,sm}} = [1 + 0.01\theta \cdot \exp\{-(P \times 10^{-6})\}]^{1/6} \tag{4}$$

$$\theta = \frac{\pi^2 V^2}{2 g_o y^2 D} \tag{5}$$

The symbol $q_{c,sw}$ means the CHF with internal twisted tape. For the CHF value $q_{c,sm}$ in smooth tube, we used Modified Tong correlation (1) in present paper. Reflecting the characteristics of Modified Tong correlation, the predictions by Nariai-Inasaka correlation give a little lower for

pressure below 1 MPa and a little higher for pressure above 1 MPa.

Figure 8 shows the CHF for mass velocity of 9000 kg/m^{2}s. Though we could not get enough data at high pressure because of the upper limit of power source, only 0.1 and 0.6 MPa data are presented in the figure. The characteristics are almost the same as in Figs. 6 and 7.

Figure 9 shows the ratio of $q_{c,H}$ to $q_{c,unif}$ against pressure. We can see that $q_{c,H}$ become 1.8 times of $q_{c,unif}$ when β increases. Figure 10 shows the relation between $q_{c,H}$ and $q_{c,unif}$ as a different figure to Fig. 9. Higher heat flux $q_{c,H}$ becomes 1.8 times of $q_{c,unif}$ when β becomes 270 ° .

4. DISCUSSION

As described in Introduction, Leontiev et al and Ornatskii et al conducted experiments under non-uniform heating condition. Figure 11 shows the cross section of the tube and the CHF data by Leontiev et al [7] . In this tube, the ratio of $q_{c,H}$ to $q_{c,av}$ was 1.5. As shown in the figure, $q_{c,H}$

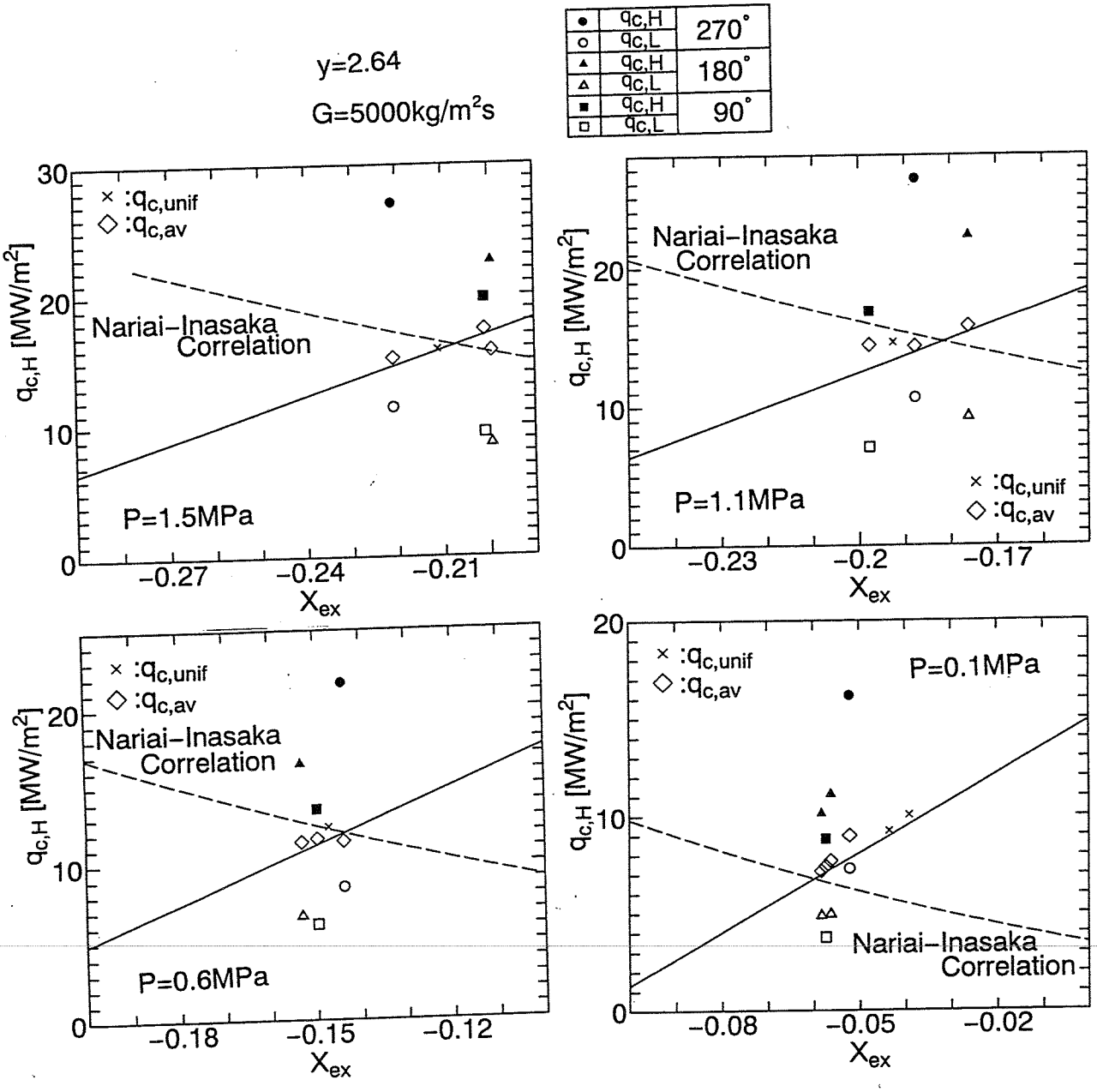

Fig. 6 CHF in swirl tube under non-uniform heating condition (y=2.64, G=5000 kg/m^{2}s)

under non-uniform heating condition coincided with experimentally derived $q_{c,unif}$ under uniform heating condition. This result agrees with authors' one.

Figure 12 shows the cross section of the test tube and the CHF data by Ornatskii et al. In their experiments, $q_{c,H}$ is higher than $q_{c,unif}$ [6] . The reason is not certain. However, inside diameter of the tube was very small, and tube wall thickness was larger comparing with inside diameter. How precise the heat flux distribution around the tube wall could be estimated , may be a problem.

The CHF of subcooled flow boiling is generally determined by the development of bubbles along the tube wall. In the case of smooth tube, the bubble boundary layer develops axially from inlet to outlet. Condensation of bubbles is mainly governed by the temperature of the cold water in core region, which is closely related to the average quality, and then circumferential non-uniformity does not directly affect on the CHF. The CHF will be predicted by the same correlation as under uniform heating condition when we use the same average qualities.

In the case of the CHF in tube with internal twisted tape, the flow along the twisted tape experiences the higher and the lower heat flux alternately. The alternate development and disruption

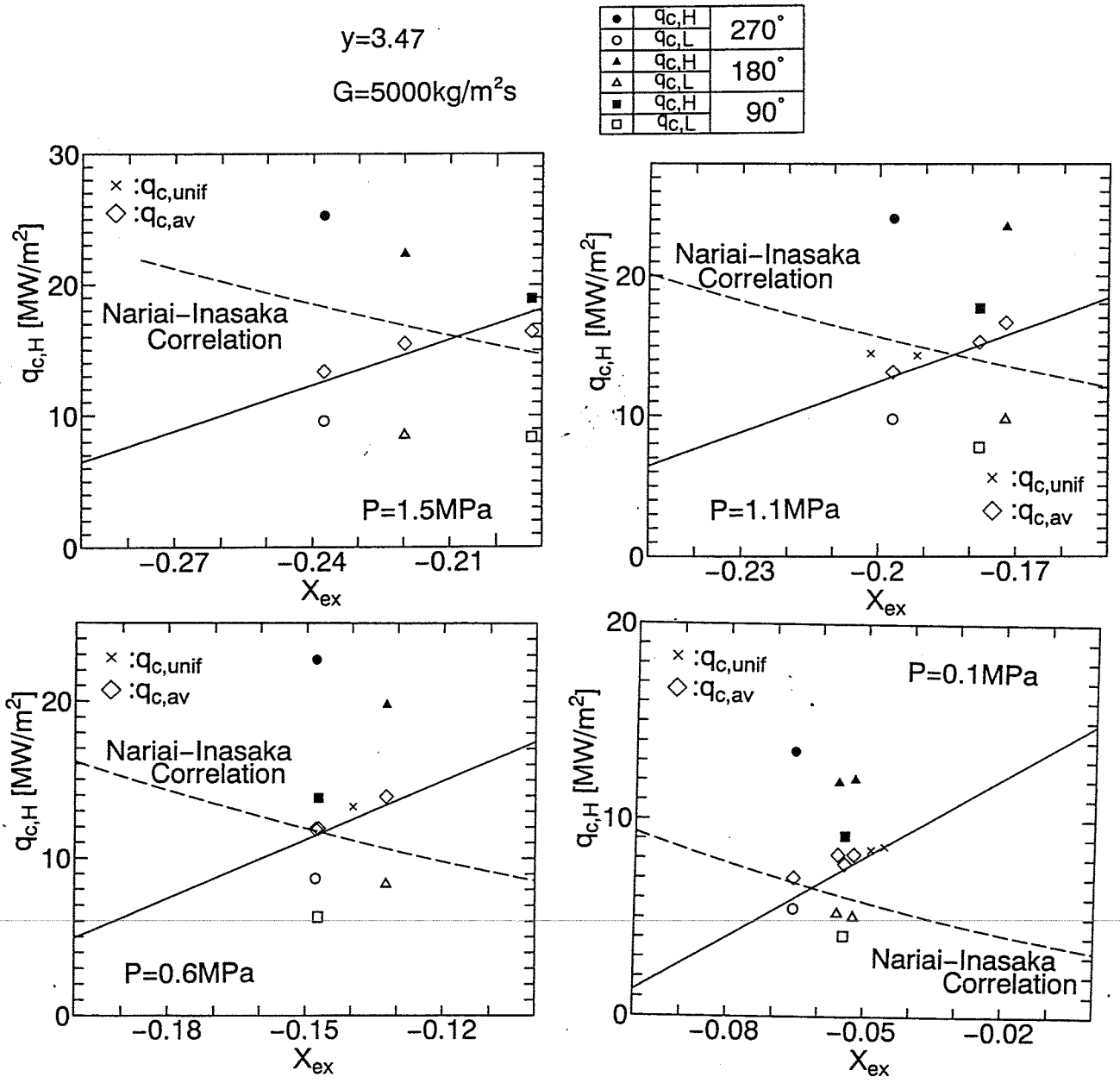

Fig. 7 CHF in swirl tube under non-uniform heating condition (y=3.47, G=5000 kg/m²s)

of the buble boundary layer makes the CHF higher. The higher CHF with the increase of β is explained by the decrease of development period and also the increase of disruption period. This is discussed basing on the observation of the initiation point of burnout by authors [13] .

5. CONCLUSION

The CHF of subcooled flow boiling with water in tube with and without internal twisted tape under circumferentially non-uniform heating condition were experimentally investigated. The CHF in smooth tube without internal twisted tape was slightly higher than that under uniform heating condition. The lower average quality under non-uniform heating condition was the reason for that. The CHF under non-uniform heating condition coincides with that under uniform heating condition when the exact average quality is taken into account. The CHF in tube with internal twisted tape under non-uniform heating condition was much higher than that under uniform heating condition, though the average qualities were almost the same for both cases. The higher CHF was explained by the alternate development and disruption of bubble boundary layer in the flow along the twisted tape.

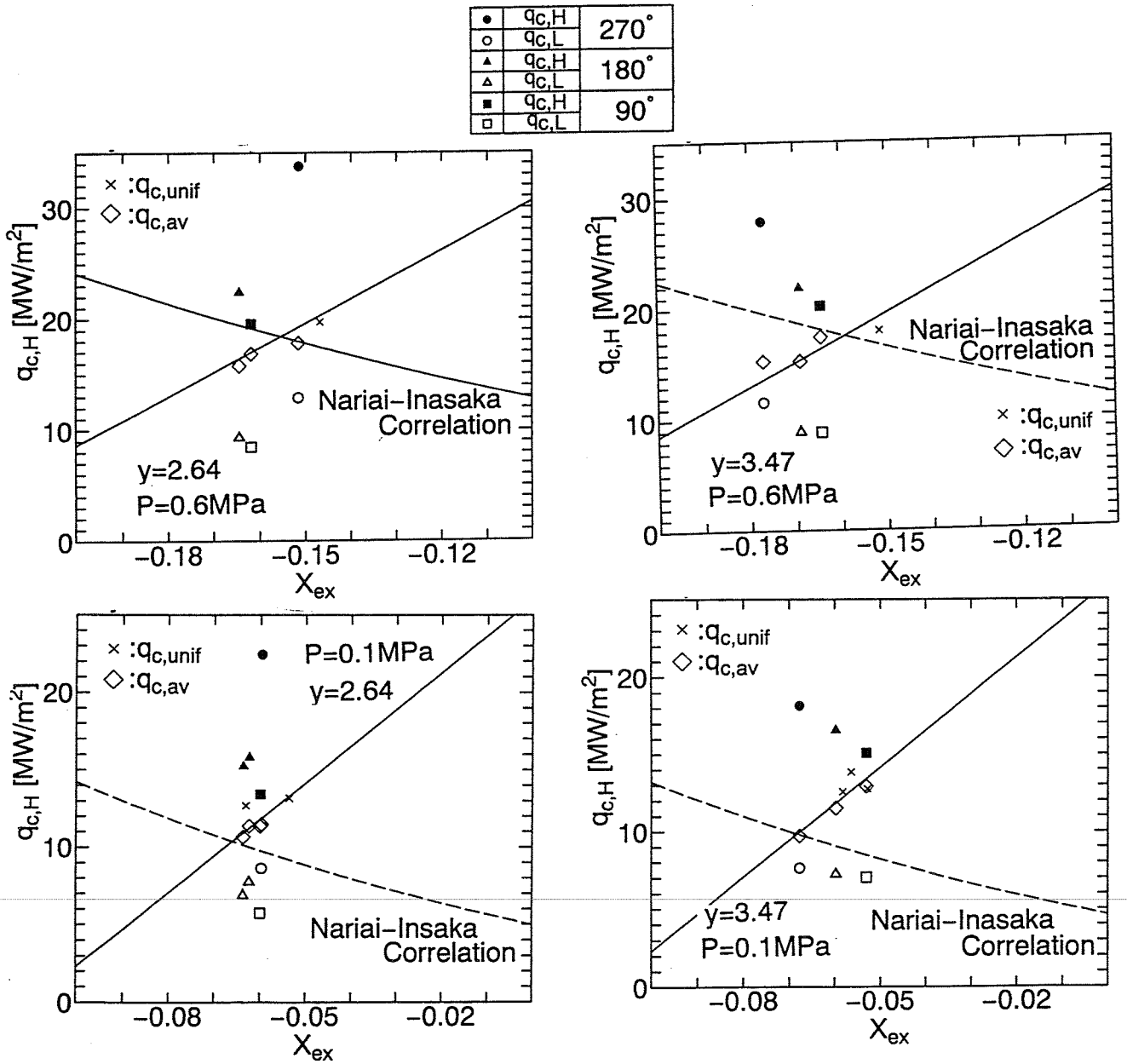

Fig. 8 CHF in swirl tube under non-uniform heating condition (G=9000 kg/m^{2}s)

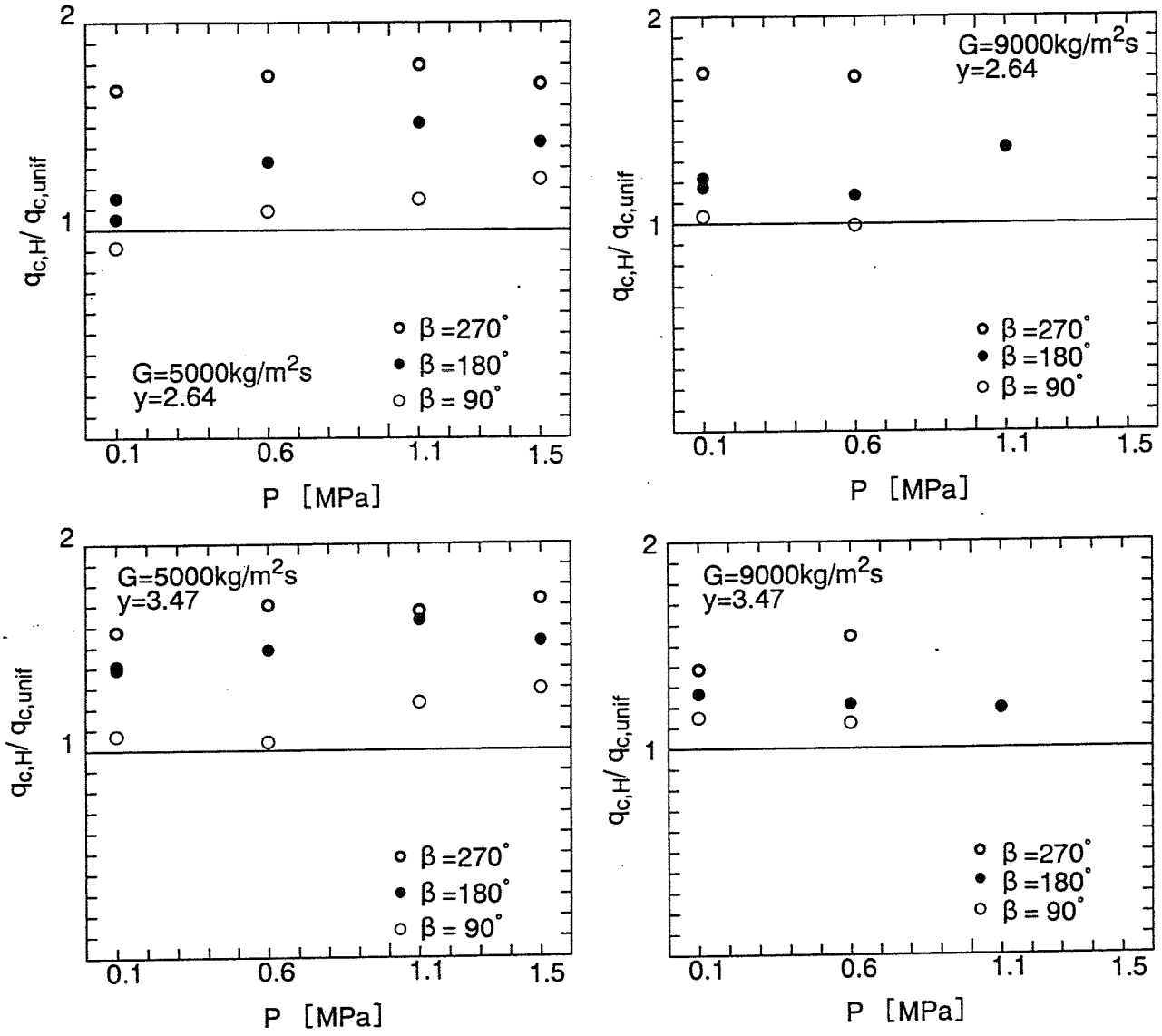

Fig. 9 CHF ratio of non-uniform to uniform heating conditon in swirl tube

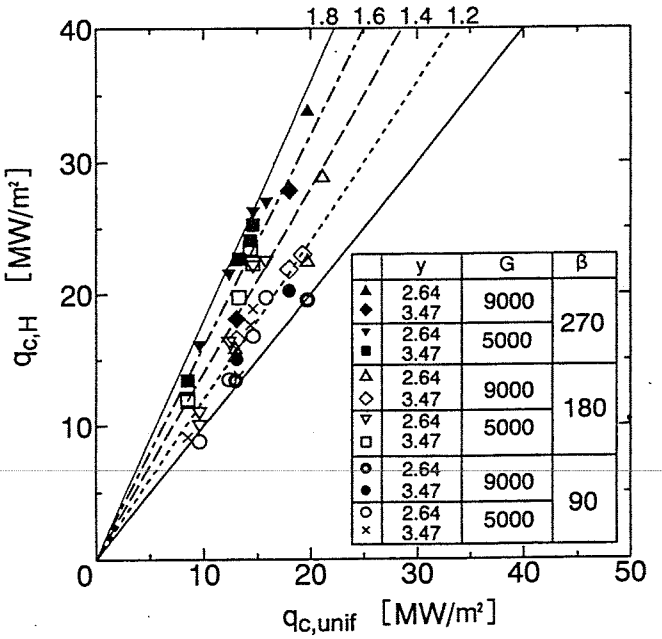

Fig. 10 The relation of CHF under non-uniform with uniform heating condition

ACKNOWLEDGEMENTS

The authors would like to give their hearty appreciation to Dr. Koichi Seimiya of Mechanical Engineering Laboratory in Tsukuba, for making the thinned tubes by electrochemical machining, and to Mr. Mamoru Mohri of the Nikko Co. for making the twisted tape made of zirconia.

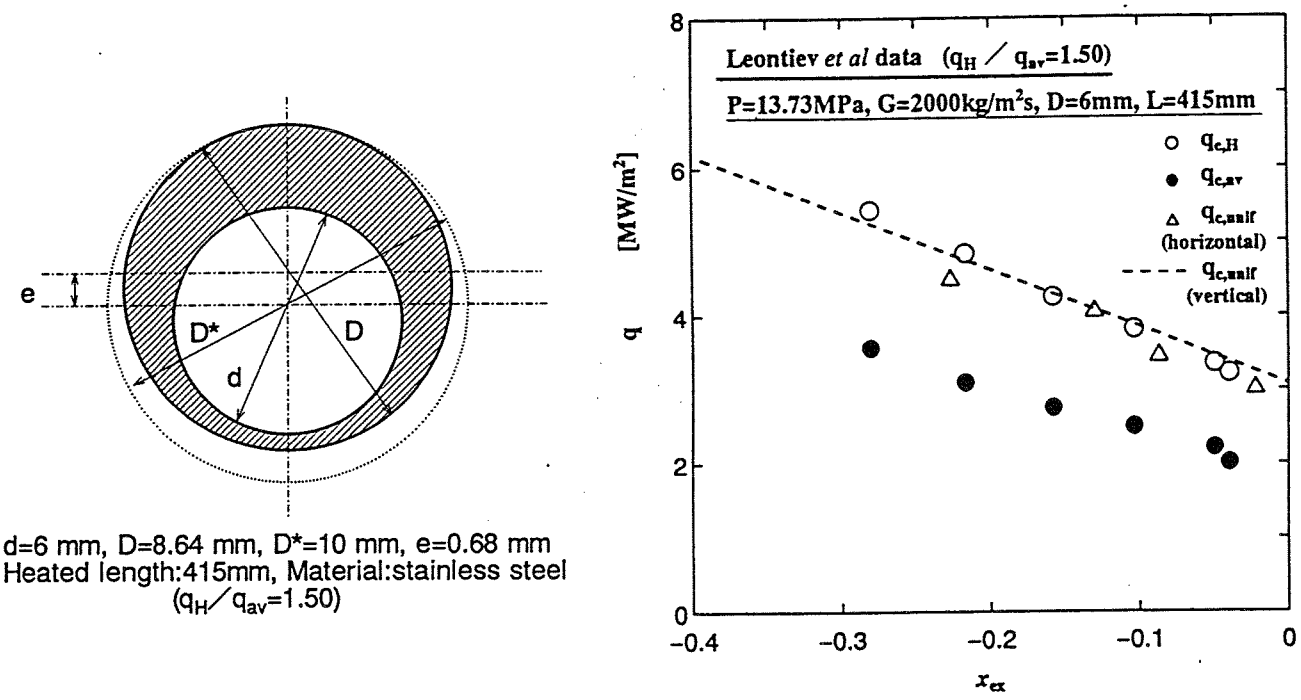

Fig. 11 Cross section of the test tube and experimental results by Leontiev et al.

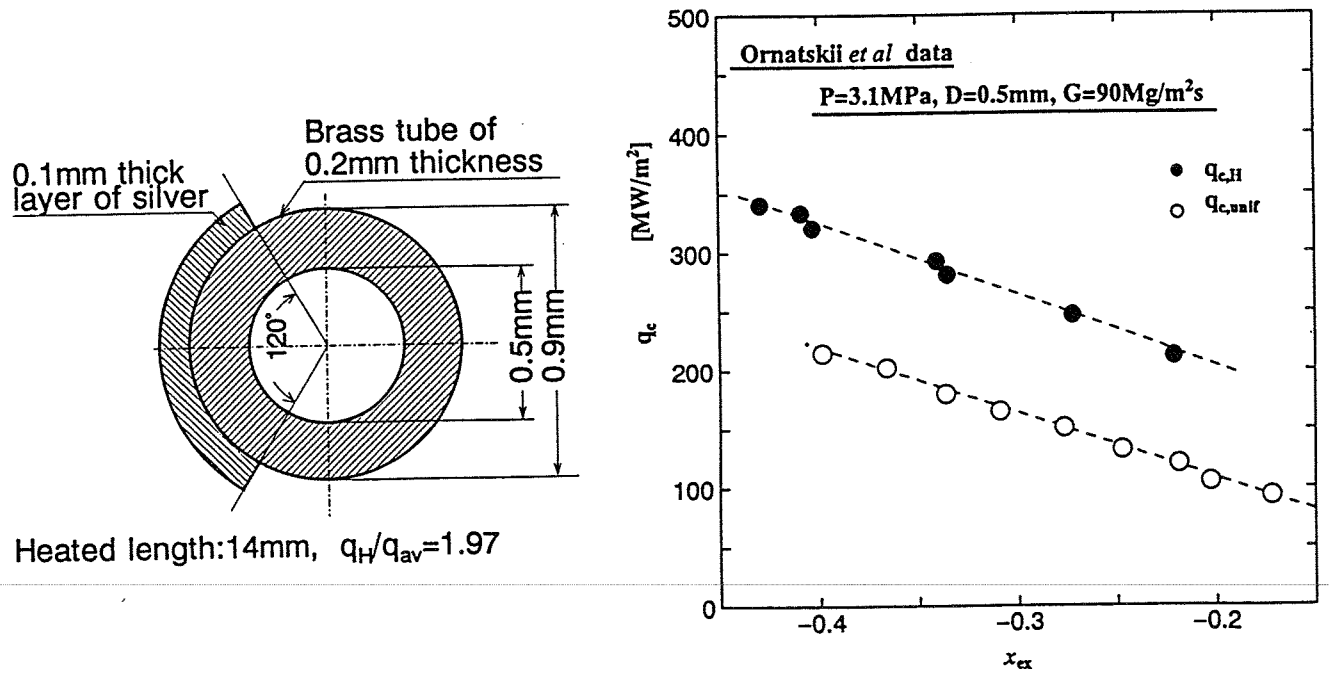

Fig. 12 Cross section of the test tube and experimental results by Ornatskii et al.

NOMENCLATURE

D : tube inside diameter
G : mass velocity of water
g_c : standard gravitational acceleration
H_{fg} : latent heat of evaporation
P : pressure
q_c : critical heat flux
Tin : inlet temperature
V : velocity of water
x_{ex} : average quality of tube outlet
y : twisted tape ratio
β : thinned part angle of the test tube
μ_f : viscosity

Subscripts
av : average
H : higher heat flux
L : lower heat flux
unif : uniform heating condition
sm : smooth tube
sw : swirl tube with internal twisted tape

REFEENCES

[1] J.A. Kosky and C.D. Croessman,"Critical Heat Flux Investigations for Fusion-Relevant Conditions with the Use of a Rastered Electron Beam Apparatus", ASME Paper 88-WA/NE-3, ASME (1988).
[2] S.L. Milora, S.K. Combs, and C.A. Foster,"A Numerical Model for Swirl Flow Cooling in High-Heat Flux Particle Beam Targets and the Design of a Swirl-Flow-Based Plasma Limiter", in: Nuclear Engineering and Design/Fusion, 3, p.301 (1986).
[3] M. Araki, M. Ogawa and M. Akiba,"Experimental Evaluation of Critical Heat Flux under One-Sided Heating Condition", in: Proc. of the 2nd Specialists' Workshop on High Heat Flux Components Thermal-Hydraulics, Rome, Italy (1992).
[4] J. Schlosser, A. Cardella, P. Massmann, P. Chappuis, H.D. Falter, P. Deschamps, and G.H. Deschamps, "Thermal-Hydraulic Tests on NET Divertor Targets Using Swirl Tubes", in: 7th Proc. of Nuclear Thermal Hydraulics, ANS Winter Meeting, San Francisco, p.26 (1991).
[5] J. Schlosser and J. Boscary,"Thermal Hydraulics Tests at NET/ITER Relevant Conditions on Divertor Targets Using Swirl Tubes", in: Proc. of the 3rd Specialists' Workshop on High Heat Flux Component Cooling, Cadarache, France, p.5a-1 (1993).
[6] A.P.Ornatskii and L.S. Vinyarskii,"Heat Transfer Crisis in a Forced Flow Underheated Water in Small-Bore Tubes", in: High Temperature, 3, p.400 (1965).
[7] A.I. Leontiev, I.L. Mostinsky, V.S. Polonsky, M.A. Styrikovich and I.M. Chernika, "Experimental Investigation of the Critical Heat Flux in Horizontal Channels with Circumferentially Variable Heating", in: Int. J. Heat Mass Transfer, 24, 5, p.821 (1981).
[8] H. Nariai, F. Inasaka, A. Ishikawa and W. Fujisaki,"Critical Heat Flux of Subcooled Flow Boiling in Tube with Internal Twisted Tape under Non-Uniform Heating Condition", in: Proc. of the 2nd JSME-KSME Thermal Engineering Conf., 3, p.285 (1992).
[9] H. Nariai and F. Inasaka,"Critical Heat Flux of Subcooled Flow Boiling in Tubes with and without Internal Twisted Tape under Non-Uniform Heating Condition", in: Proc. of the 6th Internat. Topical Meeting on Nuclear Reactor Thermal Hydraulivs (NURETH-6), Grenoble, France, Vol.1, p.715 (1993).
[10] F. Inasaka and H. Nariai,"Critical Heat Flux and Flow Characteristics of Subcooled Flow Boiling in Narrow Tubes", in: JSME Int. J. , 30, p.1595 (1987).
[11] F. Inasaka and H. Nariai,"Evaluation of Subcooled Critical Heat Flux Correlations for Tubes with and without Internal Twisted Tapes", in: Proc. of the 5th Internat. Topical Meeting on Nuclear Reactor Thermal Hydraulics (NURETH-5), Salt Lake City, USA, 4, p.919 (1992).
[12] H. Nariai, F. Inasaka, W. Fujisaki and H. Ishiguro,"Critical Heat Flux of Subcooled Flow Boiling in Tubes Internal Twisted Tapes", in: Seventh Proc. of Nuclear Thermal Hydraulics, ANS, p.38 (1991).
[13] H. Nariai, F.Inasaka, A. Ishikawa and H. Kinoshita,"Effect of Internal Twisted Tape on Critical Heat Flux of Subcooled Flow Boiling under Non-Uniform Heating Condition", in: Proc. of the 10th International Heat Transfer Conference, Brighton, England (to be published) (1994).

CRITICAL HEAT FLUX IN TIGHT BUNDLE GEOMETRIES

F.J. Erbacher[1], X. Cheng[1], U. Müller[1], W. Zeggel[2]

1) Kernforschungszentrum Karlsruhe GmbH
Institut für Angewandte Thermo- und Fluiddynamik
Postfach 3640, D-76021 Karlsruhe, Federal Republic of Germany
2) Technische Universität Braunschweig
Institut für Raumflug- und Reaktortechnik
Hans-Sommer-Str. 5, D-38106 Braunschweig, Federal Republic of Germany

ABSTRACT

The critical heat flux (CHF) in small diameter tubes and in tight hexagonal 7- and 37-rod bundles has been investigated in the KRISTA test facility using Freon 12 as the working fluid. Measurements in tubes show that the influence of the tube diameter on CHF cannot be described as suggested by the earlier publications with sufficient accuracy. Under comparable conditions the CHF value in bundles is lower than in tubes. The influence of spacers (grid spacers, wire wraps) on CHF has been found to be governed by local steam qualities. A comparison of the test results with some CHF prediction methods shows that the Look-up table method reproduces the test results in circular tubes most accurately. The CHF prediction in rod bundles depends strongly on subchannel analysis models, especially the mixing coefficient. By using subchannel analysis the effect of non-uniform radial power distributions on CHF is discussed.

1. INTRODUCTION

Although a great quantity of experimental and theoretical studies concerning the Critical Heat Flux (CHF) has been performed for a number of years, knowledge of the precise nature of CHF is still incomplete. This is mainly due to the very complex nature of the two-phase flow with heat transfer. A large number of experimental CHF data has been obtained for a wide range of test conditions, but test data for small diameter test channels, especially tight hexagonal rod bundles, under high pressures and high mass fluxes are scarce.

A program of experimental and analytical investigation on CHF behaviour of small flow channels (circular tubes and tight rod lattices) has been performed at the Institut für Angewandte Thermo- und Fluiddynamik (IATF) of the Kernforschungszentrum Karlsruhe (KfK), in cooperation with the Technical University Braunschweig (TUBS) and Siemens-AG KWU-Group (Siemens/KWU). The experiments were carried out in the KRISTA test facility of IATF/KfK with Freon 12 as the working fluid.

The experimental program at the KRISTA test facility comprises CHF tests in circular tubes with different diameters (4.2, 8.0, 11.9 mm), in 7-rod bundles with different spacers and in 37-rod bundles. The tests in circular tubes serve to extend the CHF data base published in the literature, e.g. [1], to determine the effect of tube diameter on CHF and to perform an assessment of fluid-to-fluid modeling laws. The tests in 7-rod bundles are designed to investigate the difference of CHF in bundles compared to CHF in tubes, to investigate the effect of spacers (grid spacers and wire wraps) on CHF and to assess CHF prediction methods for tight rod bundles. The objective

of the experimental work on the Freon cooled 37-rod bundles is to assess scaling laws and bundle correlations including predictions by subchannel codes and table data, to verify the application of CHF tables to rod bundles, especially of the most recently developed Canadian CHF table [2] and to study the effect of heat flux distributions on CHF including the effect of heated length.

2. KRISTA TEST FACILITY AND TEST SECTIONS

The KRISTA test facility at IATF/KfK shown schematically in figure 1 is used to perform CHF tests in circular tubes, 7-rod bundles and 37-rod bundles. It has the following performance characteristics (water-equivalent values in parentheses):

- electrical power: up to 500 kW (7500 kW)
- mass flow: up to 50,000 kg/h (70,000 kg/h)
- pressure: up to 3.5 MPa (21 MPa)

The KRISTA test facility consists of two separate loops which are interconnected via the Freon storage tank and the purification system. A refrigeration system connected to the heat exchangers provides a wide range of inlet temperature. The small loop (right part in figure 1) is used for the circular tube and the 7-rod bundle tests while the large loop serves for the 37-rod bundle tests.

Figure 2 shows a circular tube test section. The electrically heated part is located between two copper clamps. The temperature of the tube wall is measured by Chromel/Alumel thermocouples (0.25 mm o.d.) which are located over the whole length of the test section as shown on the diagram. In the region where CHF is more likely to occur, the thermocouples are located more densely. Three tubes with different inner diameters (4.2, 8.0, and 11.9 mm) were used to investigate the effect of the tube diameter on CHF. The heated length was varied from 0.36 m up to 1.0 m by changing the position of the lower copper clamp.

Figure 3 shows details of the 7-rod bundle test channel. Pressure taps are located at various positions along the length of the test channel. The total length is 1.24 m of which 0.6 m is heated with a uniform axial power. Two bundles with different spacers (grid spacer and wire wrap) were used. To minimize the influence of the grid spacers on CHF, a large distance between the CHF detection level and the last upstream grid spacer was chosen. In the bundle with wire wraps, the axial wire lead is 190 mm.
The fuel rod simulators are electrically indirectly heated and shown in figure 4. They consist of a magnesium oxide (MgO) core, a helical-wound heating ribbon, a boron nitride (BN) insulator and a stainless steel cladding. The present fuel rod simulators are designed to have a uniform axial heat flux. The diameter of the rod is 9.5 mm. The rods are arranged in a hexagonal array with the pitch of 10.9 mm. To detect the CHF occurrence thermocouples (0.5 mm o.d.) are embedded in grooves inside the cladding. A plasma spraying process and a subsequent polishing provides a smooth outer surface of the cladding. Eight thermocouples were installed in each of the rods. The junctions were located 15 mm or 20 mm upstream from the end of the heated length. More details of the 7-rod test section can be found in the previous publication [3].

Figure 5 shows the 37-rod test section. The outer pressure vessel is designed for pressures up to 4 MPa. The grid spacers are arranged at axial intervals of 300 mm. The fuel rod simulators are similar to those of the 7-rod test section except for the rod diameter which is 9.0 mm for the 37-rod test section. The total length of the rod bundle is 1240 mm of which 600 mm is heated. The rods are arranged in a hexagonal array with a pitch of 10.6 mm (P/D=1.178). The radial power distribution within the bundle was chosen to be identical with that of the water cooled bundle

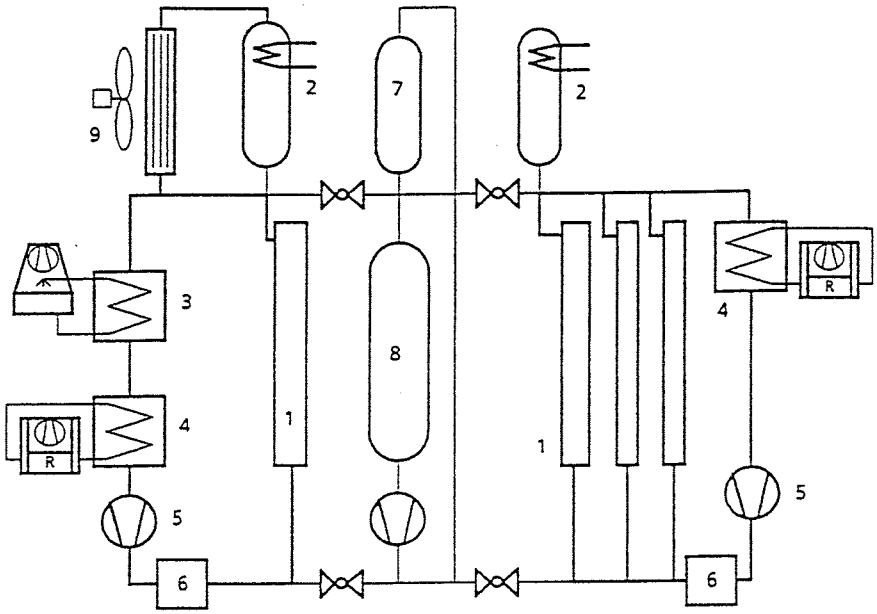

Large Freon-Loop
(80 m^3/h)

1 test section
2 pressurizer
3 heat exchanger (cooling tower)
4 heat exchanger (refrigerator)
5 pump

Small Freon-Loop
(15 m^3/h)

6 preheater
7 purification
8 Freon tank
9 air condenser

Figure 1: schematic diagram of the KRISTA test facility

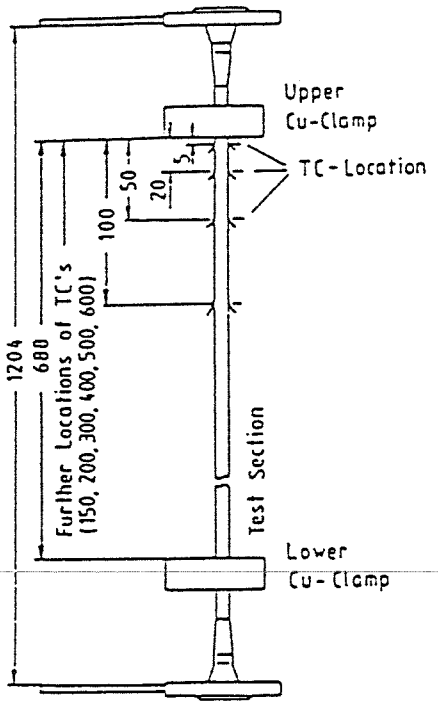

Figure 2: circular tube test section

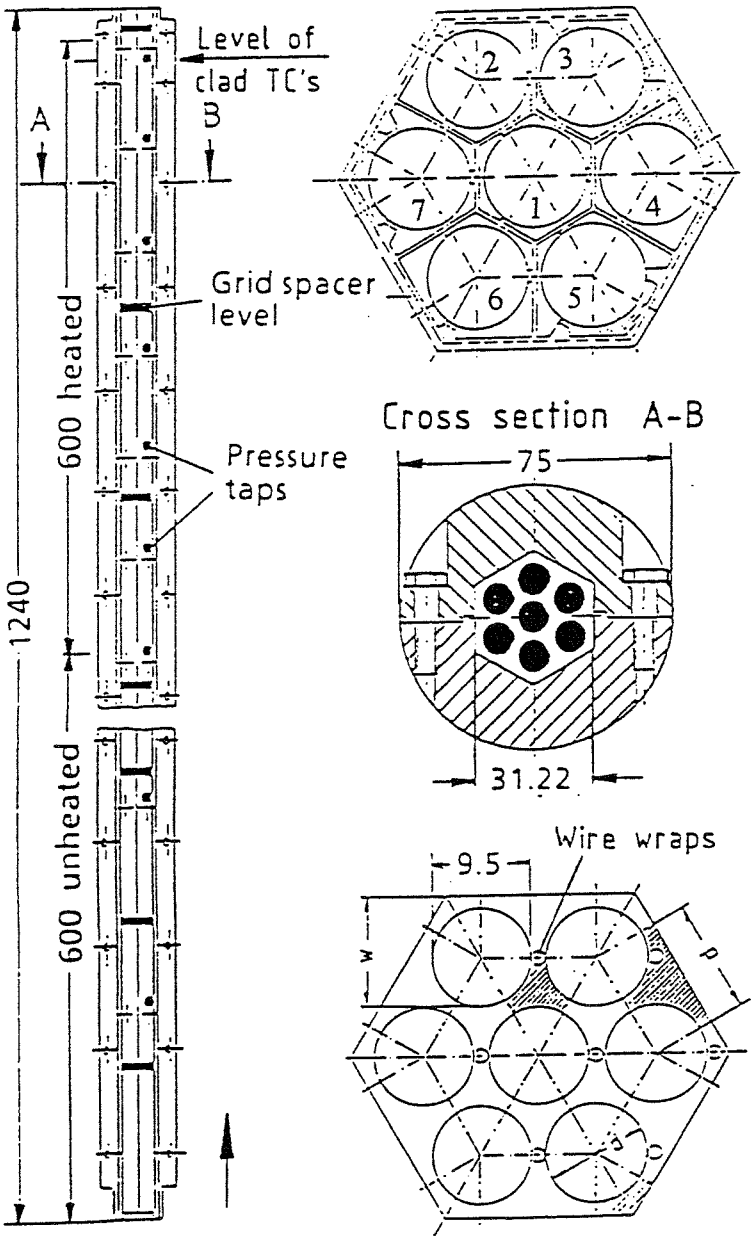

Figure 3: 7-rod bundle test section

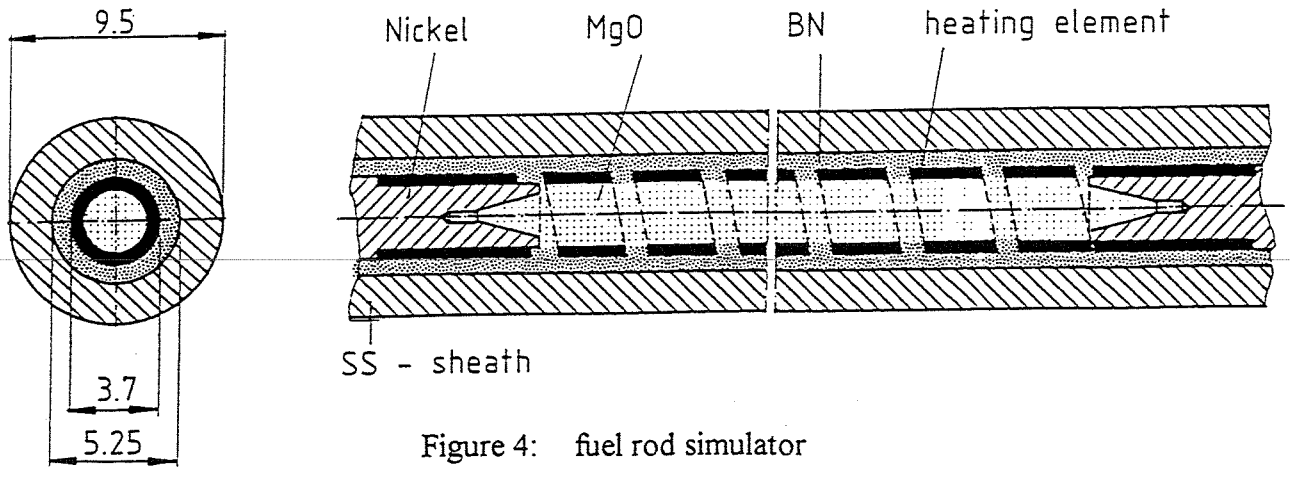

Figure 4: fuel rod simulator

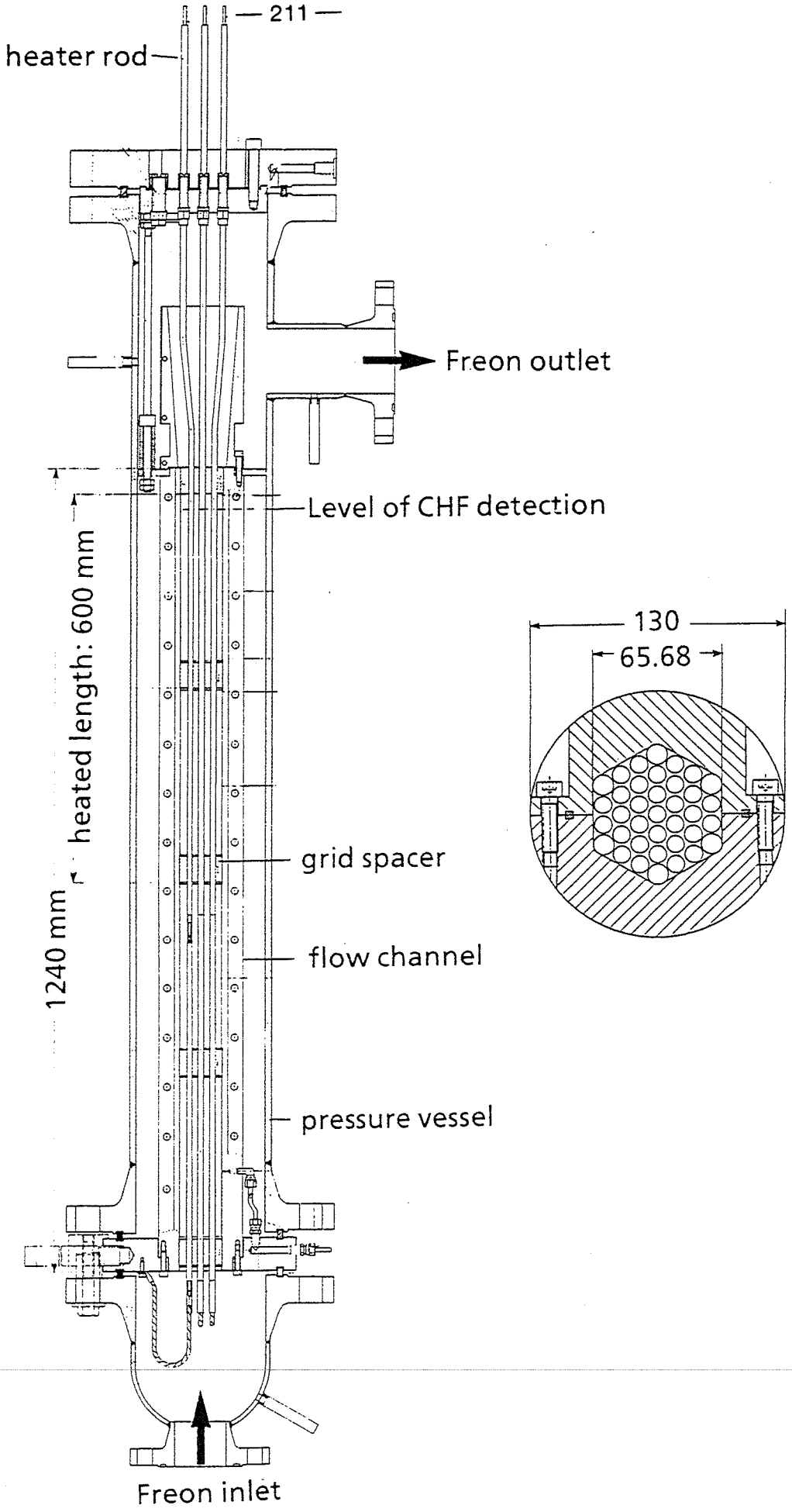

Figure 5: 37-rod bundle test section

which was used by Siemens/KWU [4]. The corner positions are equipped with unheated tubes of 10.2 mm outer diameter. The heating power of the 7 central rods was 20% higher compared to the surrounding rods. This ensured that CHF occured at the inner 7 rods.

Table I: matrix of the test parameters

parameter	circular tubes	7-rod bundles	37-rod bundle
pressure (MPa)	1.05, 1.78, 2.30, 2.72, 3.0		1.07, 1.59, 2.35, 2.76
mass flux (Mg/m^2s)	1.0, 2.0, 3.0, 4.0, 6.0		1.4, 2.1, 2.8, 3.4, 4.1
inlet temperature (^0C)	from -15^0C to saturation temperature		
diameter (mm)	4.2, 8.0, 11.9	9.5	9.0
pitch/diameter (-)	---	1.147	1.178
heated length (mm)	320 - 1000	600	600

The test conditions for all the three test sections are summarized in table I. The following test procedure was adopted: By heating the pressurizer the desired pressure was established and controlled by a pressure controller. The desired mass flux was obtained by adjusting the mass flow control valves. The heat exchangers, refrigeration system and preheater served to set the desired inlet fluid temperature. During the course of a CHF test run, the heating power was slowly increased until CHF is indicated by a temperature excursion. The temperature limit to trigger the shut-off of the power supply was set at about 200^0C.

3. THEORETICAL ANALYSIS

3.1 Scaling law

Performing experiments in Freon 12 as a model fluid requires to transfer the test results to water-equivalent values by using suitable scaling laws. A thorough assessment [3, 5] of the existing scaling laws for application to circular tubes and to rod bundles has indicated that the Ahmad [6] scaling law is well suited for fluid-to-fluid modeling. Figure 6 shows the conversion factors for the pressure F_P, the mass flux F_G and for the critical heat flux F_Q. The conversion factors are defined as the ratio of the values of the original fluid (water) to the model fluid (Freon 12). In the present work the Ahmad scaling law was used to transfer the Freon data to water-equivalent conditions.

3.2. CHF prediction methods

Three methods for the CHF prediction are currently available:

- empirical correlations,
- CHF look-up tables, and
- semi-empirical theoretical models.

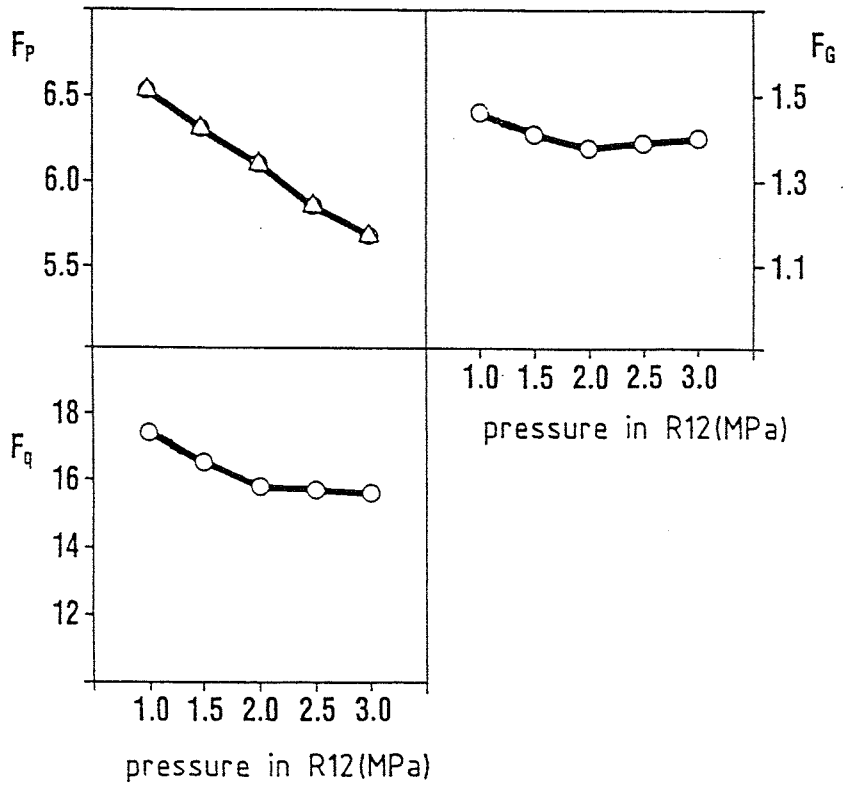

Figure 6: conversion factors for water/Freon 12

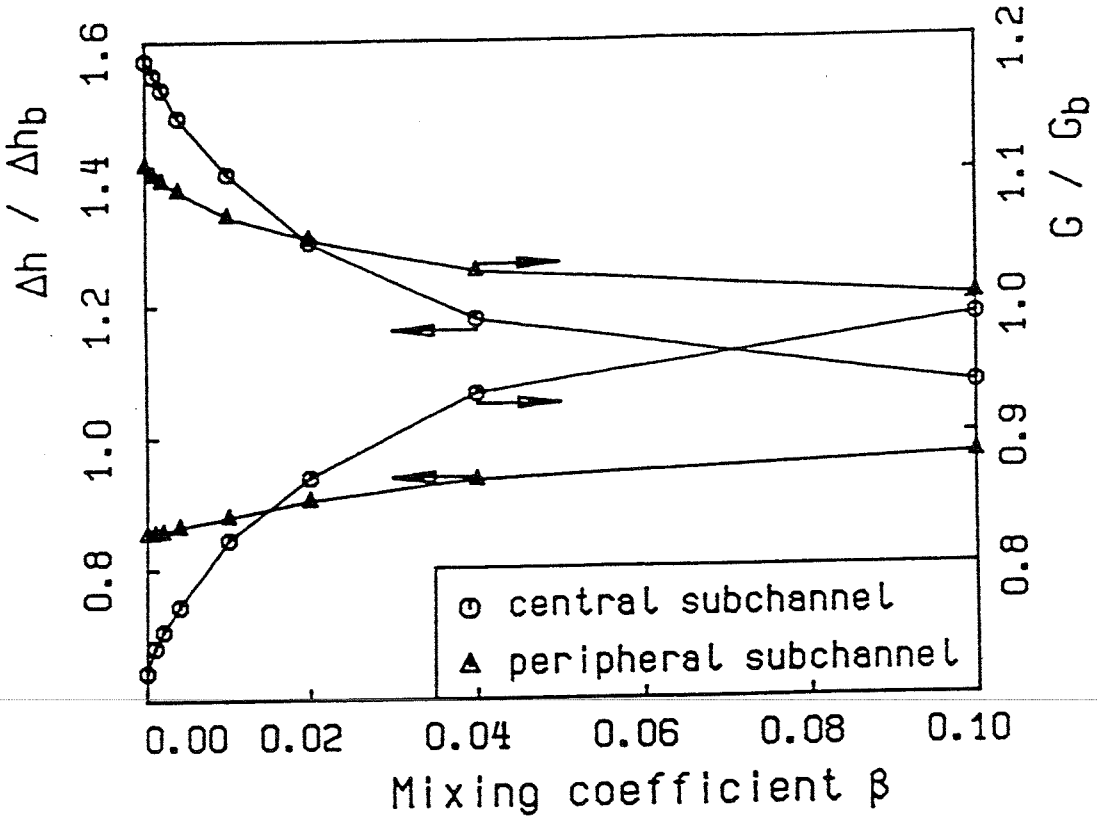

Figure 7: local flow parameters versus mixing coefficient

Table II summarizes the prediction methods selected in the present work to show to what extent they can reproduce the test results in circular tubes as well as in rod bundles. The CHF correlations of Katto & Ohno [7] and of Shah [8] were developed for circular tubes. They are based on dimensionless numbers and applicable to Freon 12 and to the present test conditions. The EPRI-1 correlation [9] has been developed for square LWR element lattice, while the most recent KfK-3 correlation [10] was adapted to the experimental data in hexagonal tight lattices. The KfK-3 correlation consists of two different sets of equations which are valid for the gridded bundles and for the wire wrapped bundles, respectively. Both the EPRI-1 and the KfK-3 correlations were developed for water conditions. To transfer the test data in Freon 12 to water-equivalent values, the scaling law of Ahmad was used.

Table II: CHF prediction methods

	circular tubes	7-rod bundles	37-rod bundle
correlations	Katto & Ohno [7] Shah [8]	EPRI-1 [9] KfK-3 [10]	KfK-3 [10]
CHF tables	Groeneveld [11]		Groeneveld [2]
CHF models	Weisman & Pei [12]	Weisman & Ying [13]	---

Much work was done to develop look-up tables for circular tubes by Canadian and by Russian authors. Based on dimensionless numbers, Groeneveld et.al [11] developed a CHF table for non-aqueous fluids, e.g. Freon 12. Moreover the authors suggested to extend the application of the CHF table to rod bundles by using a suitable subchannel analysis code for calculating subchannel flow conditions. For the 37-rod bundle, the most recently developed CHF look-up table [2] was compared with the test results.

During the last years, semi-empirical CHF models have been reported. One of them is the "near wall bubble crowding model" of Weisman & Pei [12]. Turbulent interchange between the bubble layer and the core regions was considered to be the limiting mechanism for the onset of CHF. They postulated that CHF occurs when the void fraction in the bubble layer exceeds the critical value of 0.82. Weisman & Ying [13] modified this model and applied it to rod bundles at PWR conditions. They achieved satisfying results.

3.3. Subchannel analysis

The prediction of the CHF data in rod bundles is based upon the local condition approach. The local flow conditions are provided by the subchannel code COBRA-IV-TUBS [14]. The present simulation utilizes constitutive relationships which are described as follows.

The pressure drop arises partially from the friction as the coolant flows past the flow channel and partially from the drag induced by spacers. The friction factor of single phase flow in 7-rod bundles was determined experimentally both for a bare 7-rod bundle and for a wire wrapped bundle [3]. For the bare 37-rod bundle, the friction factor is correlated by the Blasius equation. The pressure loss of the grid spacer is taken into account by giving an individual loss coefficient for every subchannel type. This pressure loss coefficient in 7-rod bundles was also determined experimentally [3]. To determine the two-phase pressure drop, a multiplier factor ϕ was introduced which was computed by applying the homogeneous-equilibrium-mixture model (HEM) [15] for the 37-rod bundle and the Armand's model [3] for the 7-rod bundles.

For the simulation of the 37-rod bundle tests, no subcooled void correlation has been included. The void fraction for positive steam quality was calculated by using the HEM. Regarding the 7-rod bundle tests, void fraction was computed by the Armand's model [3].

The interchange of mass, energy and momentum between subchannels, known as mixing, can be split into two phenomena. First, there is a net mass flux between the subchannels which is caused by a radial pressure gradient. Secondly, there is natural mixing causing exchange of enthalpy between neighbouring subchannels but does not result in a net mass flow. The latter one can be represented by the mixing coefficient β which is defined as the total transversal mass flow caused by natural mixing divided by the mean axial mass flux. The total transversal mass flux consists of a turbulent share and a molecular contribution which, however, can be neglected compared to the turbulent share for high Reynolds numbers. It is well known that the mixing coefficient is dependent on flow conditions and on subchannel geometry. Nevertheless, experimentally verified models of mixing coefficient in two-phase flow regime are not available up to now.

A sensitivity study was performed to determine the sensitivity of calculated subchannel flow conditions in 7-rod bundles to the proposed mixing coefficient. Figure 7 shows the ratio of the enthalpy gain Δh and of the mass flux G in subchannels to the bundle average values vs. the mixing coefficient β. The enthalpy gain is defined as the difference between the exit and the inlet enthalpy. The enthalpy gain in central subchannels is higher and the mass flux is lower than in peripheral subchannels, so that the central subchannel is regarded as the hot subchannel or the critical subchannel. The lower values of β result in higher enthalpy gain and lower mass flux in central subchannels. Increasing in β value leads to both the enthalpy gain and the mass flux approaching the bundle average conditions. In single-phase flow, the β value is approximately 0.005 for the 7-rod bundles [3]. Higher β values for two-phase flow are expected. Therefore, two values of mixing coefficient i.e. 0.004 and 0.02 were chosen for the present 7-rod bundles. Because of large expenditure involved in terms of computing time, only one value of the mixing coefficient (0.005) was used for computing the local flow conditions in the 37-rod bundle.

4. EXPERIMENTAL RESULTS AND DISCUSSIONS

4.1. Circular tubes

Details of the tube tests can be found in the previous publications [3, 16]. Figure 8 shows results typical of a 8 mm tube and for a constant pressure of 1.78 MPa. CHF increases with decreasing exit steam quality x_{ex}. The curves for different mass fluxes cross over due to the DNB/dryout transition. At low qualities (DNB region) an increasing mass flux strengthens turbulence, improves bubble transport from the heated wall and leads to higher CHF. At higher qualities, typical of annular flow, an increasing mass flow increases the entrainment rate, thus reducing the film flow rate and resulting in a lower CHF. For the 4.2 mm and the 11.9 mm tubes the same dependency of CHF on mass flux and on exit quality has been observed.

Regarding the influence of exit steam quality, mass flux, pressure and heated length, the test results obtained in the present work confirm the observations made in other works [1, 17].

The influence of the tube diameter on CHF has not yet been fully explained. Most authors predict an increase in CHF with decreasing diameter and describe this relationship by an exponential function:

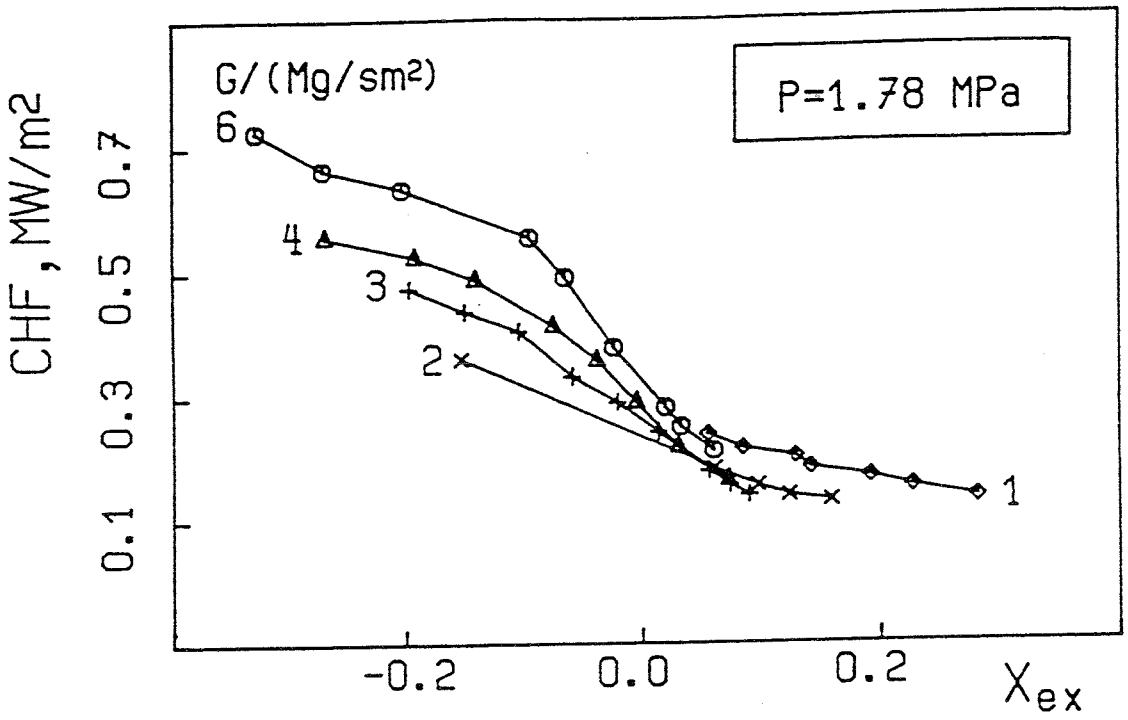

Figure 8: CHF results in 8 mm circular tubes

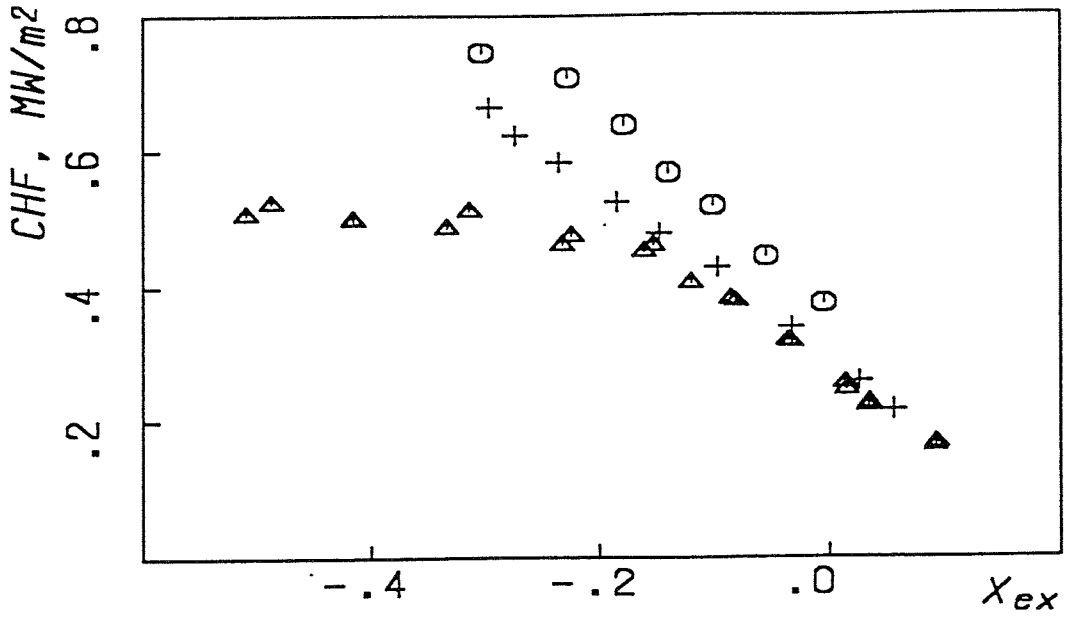

Figure 9: Influence of the tube diameter on CHF: P = 2.3 MPa, G = 4 $Mg / m^2 s$
⏀ - D = 4.2 mm, ▲ - D = 8.0 mm, + - D = 11.9 mm

$$\frac{q_c}{q_{c,D=8mm}} = \left(\frac{8mm}{D}\right)^{\varepsilon}$$

Usually the exponent ε is assumed to be constant and independent of any other thermal-hydraulic and geometric parameters. (e.g. ε=1/3 [2].)

A comparison of the results obtained in three different diameter tubes are presented in figure 9. Obviously, the influence of tube diameter on CHF cannot be described by a simple exponential function. In contrast to previous publications, the influence of tube diameter is more complex and depends on the thermal-hydraulic and geometric conditions. These results emphasize the need for more research work to study the influence of tube diameter on CHF in Freon and in water.

Table III: Comparison of the test results in 8 mm tubes with the CHF predictions $(CHF)_c/(CHF)_m$

Predictions ↓	N	μ	σ
Katto & Ohno	420	1.104	0.185
Shah	420	1.138	0.117
Groeneveld table	358	1.006	0.045
Weisman & Pei	404	0.995	0.153

Table III shows a comparison of the test results in a 8 mm circular tube with the prediction methods summarized in table II. The comparison is based on the constant inlet steam quality. In table III the letter N stands for the number of the data points, μ for the mean value and σ for the standard deviation of the ratio of the predicted CHF value to the measured one. The best agreement is obtained between the measured data and the table data of Groeneveld et.al [11]. Therefore the look-up table method is proven as the best prediction method for circular tubes. The correlations of Katto & Ohno and of Shah overpredict the test results. On the average the CHF model of Weisman & Pei agrees well with the present test results, but the scatter is large.

4.2. 7-rod bundle with grid spacers

Figure 10 shows the CHF results versus the exit steam quality of the central subchannels compared to the CHF data obtained from the 4.2 mm tube. The steam quality of the central subchannel was computed by COBRA-IV-TUBS with two different values of mixing coefficient. The curve with the lower β value (0.004) lies much higher than with higher β values. This indicates a strong influence of the mixing coefficient on the presentation of the test results as well as on the CHF prediction in rod bundles.

The hydraulic diameter of the central subchannel is 4.3 mm and comparable to the 4.2 mm tube diameter. However, the CHF data in the 7-rod bundle are lower than in tubes, especially for high mixing coefficients. This comparison underlines that CHF data obtained in circular tubes should not be applied directly to rod bundles.

Table IV shows a comparison of the test results with the CHF prediction methods summarized in table II. The comparison is based on a constant inlet steam quality. Both the EPRI-1 and KfK-3 correlations underestimate the CHF test results, especially for the lower β value (0.004). The agreement between the measured and the calculated CHF data is improved with the higher β-value (0.02). The CHF look-up table of Groeneveld et.al [11] and the model of Weisman & Pei

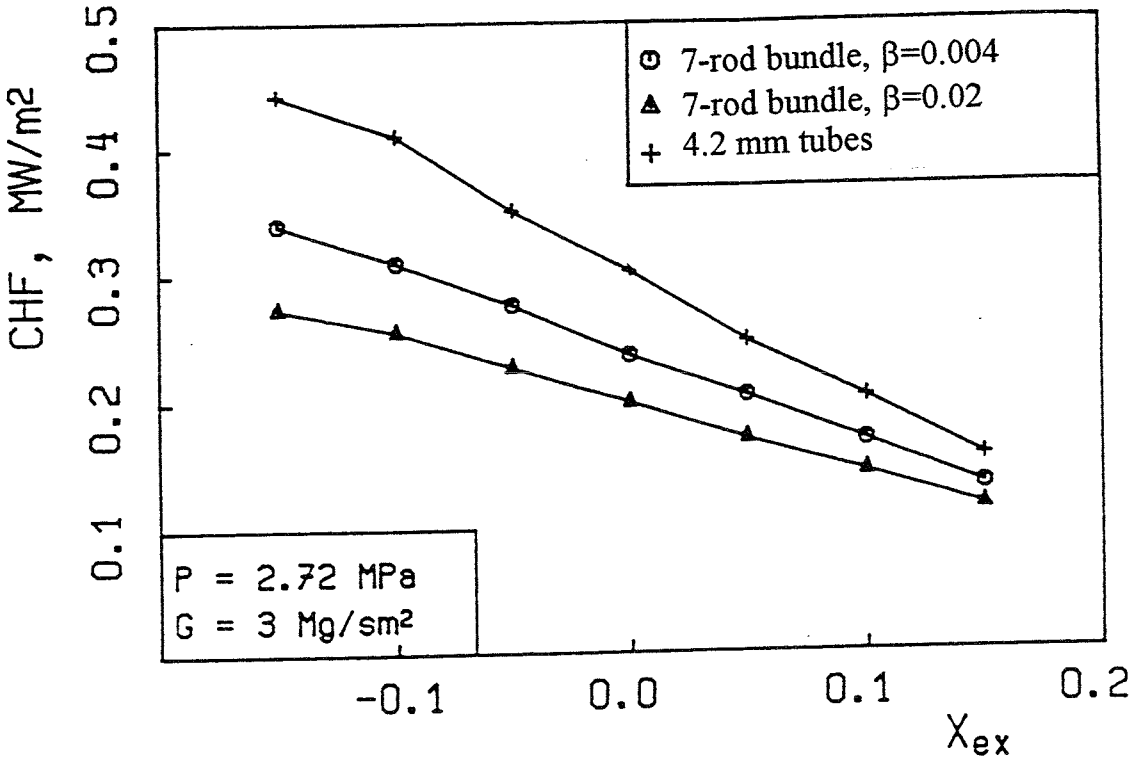

Figure 10: CHF in the gridded 7-rod bundle compared to that in circular tubes

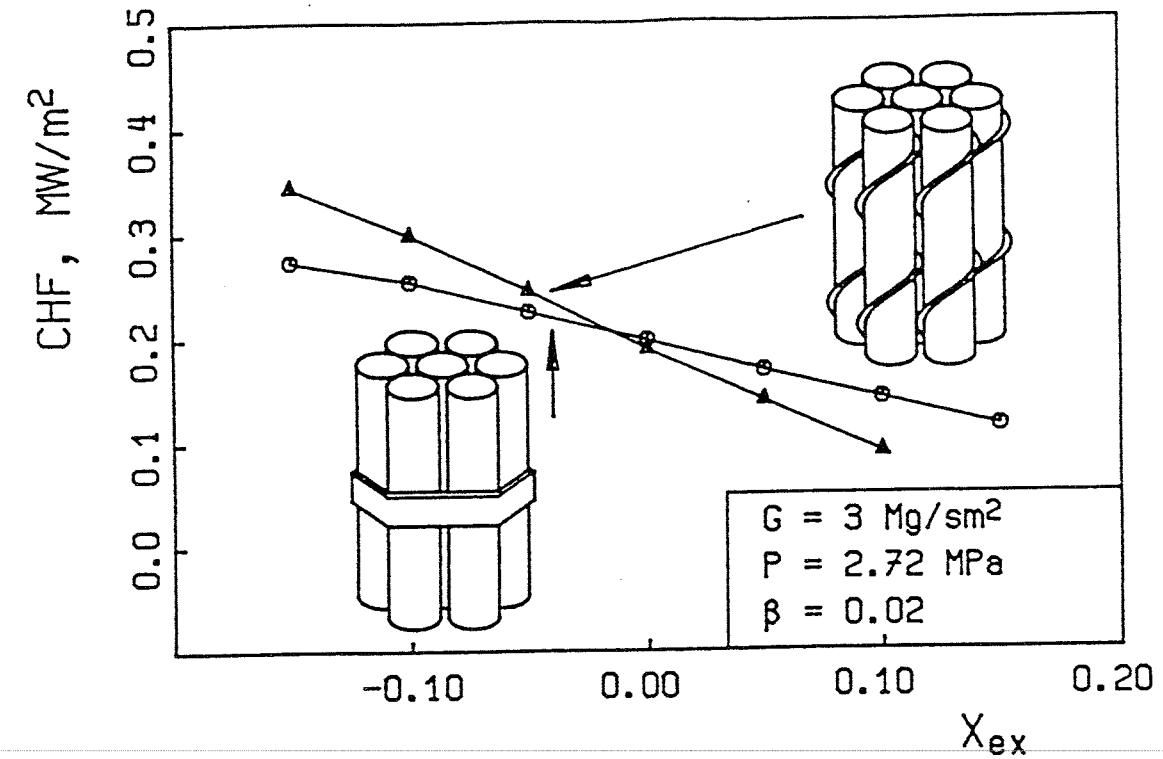

Figure 11: CHF in 7-rod bundles with grid spacers and wire wraps

[12] show a satisfying agreement with the test results by using the lower β value (0.004). With the higher mixing coefficient (0.02), both methods overpredict the measured CHF data.

Table IV: Comparison of the test results in the gridded 7-rod bundle with the CHF predictions $(CHF)_c/(CHF)_m$

predictions↓	β = 0.004			β = 0.02		
	N	μ	σ	N	μ	σ
EPRI-1	145	0.793	0.043	134	0.892	0.051
KfK-3	147	0.766	0.075	145	0.873	0.087
Groeneveld table	214	1.030	0.054	214	1.142	0.050
Weisman & Pei	202	1.039	0.122	204	1.163	0.104

4.3. 7-rod bundle with wire wraps

Figure 11 shows the CHF values versus the exit quality for the wire wrapped bundle compared with the CHF values of the gridded bundle. It is evident that the slope of the curve valid for the bundle with wire wraps is steeper than that for the bundle with grid spacers. Both curves cross over at an exit steam quality close to zero. In addition, it was found that the cross-over quality decreases with decreasing mixing coefficient β.

For low steam qualities CHF of the bundle with wire wraps is higher compared to that of the bundle with grid spacers. A opposite influence of spacers on CHF is found for high steam qualities. This could be due to the complicated influence of wire wraps on local flow conditions near the wall in connection with the flow-regime transition. At low steam qualities with bubble flow, wire wraps tend to enhance the bubble transport from the heated wall and result in a higher CHF. At higher steam qualities with annular flow, wire wraps tend to injure the liquid film on the heated surface and accelerate the dryout of the heated surface. This influence nowadays cannot be described theoretically. Obviously, CHF correlations developed for gridded bundles cannot be applied to wire wrapped bundles.

Figure 12 shows the comparison of the water converted test results by using the Ahmad's scaling law with the KfK-3 correlation [10] which is also valid for wire wrapped bundles. A satisfying agreement is obtained. The deviation between the predicted and the measured CHF values for all the data points is less than 20%.

4.4. 7-rod bundles with non-uniform radial power distributions

In both 7-rod bundles with grid spacers and with wire wraps experimental studies were performed on the influence of the radial power distribution on CHF. Results obtained with two different non-uniform power distributions are presented in figure 13 for the gridded bundle and in figure 14 for the wire wrapped bundle. Initially rod #1 (see figure 3) was disconnected from the power supply. Subsequently the power supply to four peripheral rods (#2, #3, #4 and #7) was disconnected leaving only three heated rods (#1, #5 and #6). For comparison the results obtained in bundles with uniform power distribution are also presented in figure 13 and figure 14 with CHF as a function of the inlet steam quality.

The CHF value in the gridded bundle with a high mass flux (G=3Mg/m^2s) is hardly affected by disconnecting the power supply to the four peripheral rods. In contrast, CHF increases when the central rod is disconnected from the power supply. At a low mass flux of Mg/m^2s the CHF value in the bundle with non-uniform power distributions is always higher than that in the bundle

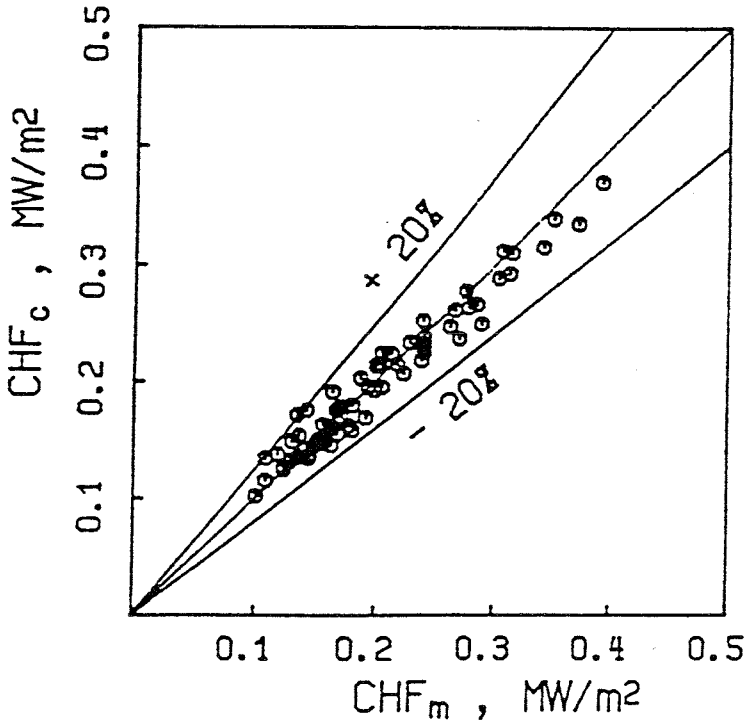

Figure 12: comparison of water-equivalent CHF data of the wire wraped bundle with the KfK-3 correlation

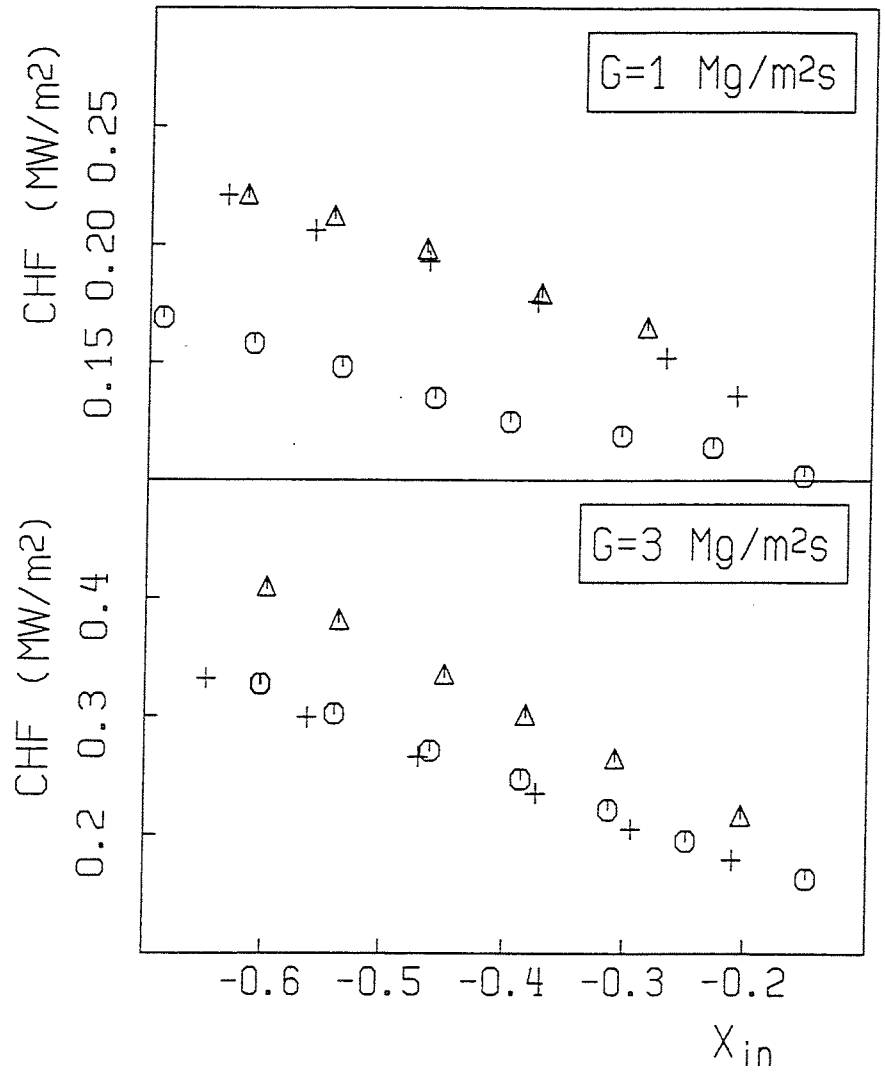

Figure 13: CHF in the gridded 7-rod bundle with different radial power distributions
⏀ uniform power distribution; ▲ unheated central rod; + four unheated peripheral rods

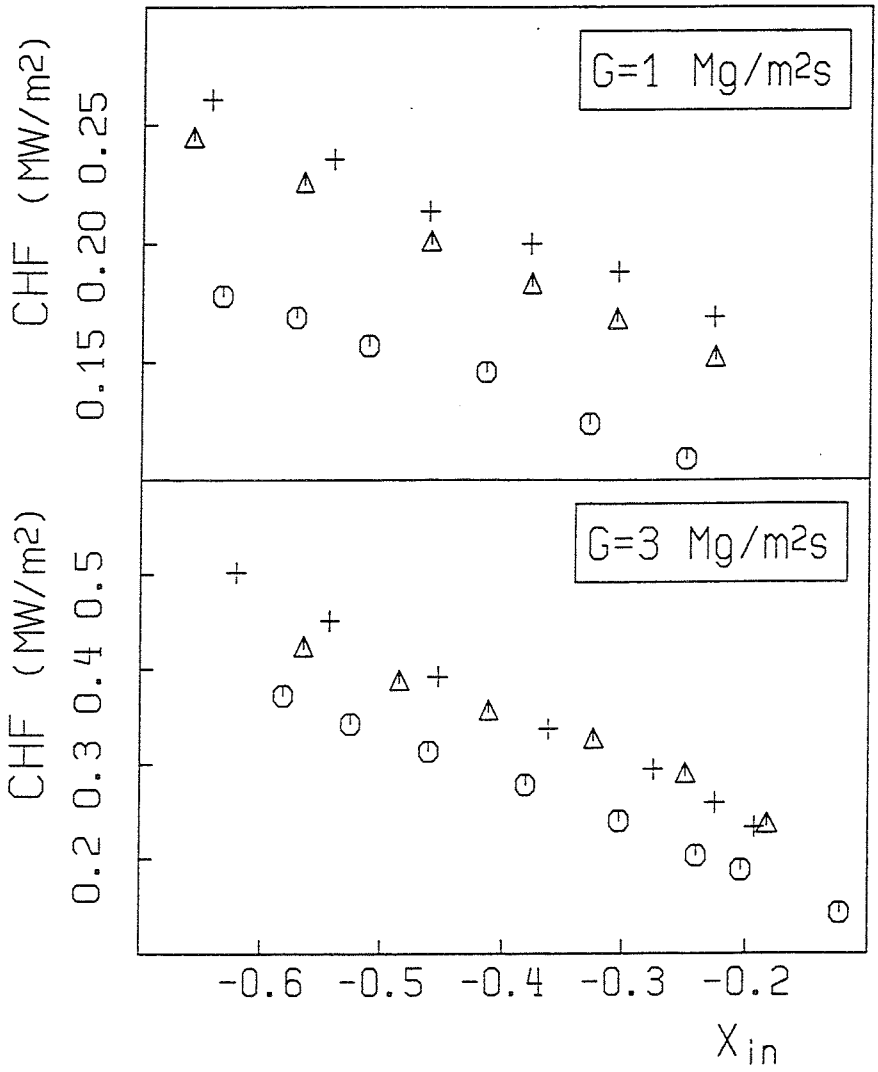

Figure 14: CHF in the wire wrapped 7-rod bundle with different radial power distributions
⓪ uniform power distribution; ▲ unheated central rod; + four unheated peripheral rods

with uniform power distribution. In the wire wrapped 7-rod bundle CHF increases at high as well as at low mass fluxes when the power distribution changes over from uniform to non-uniform.

Table V: local parameters of the hot subchannel calculated with COBRA-IV-TUBS (P=1.78 MPa, X_{in}=-0.438)

	bundle with grid spacers				bundle with wire wraps			
power distributions ↓	$G_b = 1Mg/m^2s$ $q = 0.135MW/m^2$		$G_b = 3Mg/m^2s$ $q = 0.271MW/m^2$		$G_b = 1Mg/m^2s$ $q = 0.150MW/m^2$		$G_b = 3Mg/m^2s$ $q = 0.313MW/m^2$	
	X_{ex}	G	X_{ex}	G	X_{ex}	G	X_{ex}	G
uniform	0.213	0.854	0.041	2.139	0.148	0.903	-0.014	2.627
1 unheated rod	-0.015	0.974	-0.161	2.939	0.077	0.954	-0.124	3.151
4 unheated rods	0.121	0.987	0.007	1.933	-0.076	1.025	-0.146	2.380

The experimental results can be qualitatively explained by subchannel analysis. Table V shows the local parameters of the hot subchannel obtained by using the COBRA code with a mixing coefficient of 0.004. In the bundle with the unheated central rod the thermal imbalance between the central subchannel and the peripheral subchannels is reduced. The local parameters of the central subchannel are closer to the bundle average values, i.e. the steam quality decreases and the mass flux increases. Both effects lead to a higher CHF. Similar results were also obtained in the wire wrapped bundle.

In the 7-rod bundle with grid spacers and with four unheated peripheral rods the CHF value for the high mass flux $3Mg/m^2s$ is nearly the same as that with uniform power distribution. At the low mass flux 1Mg / m^{2}s the non-uniform power distribution with unheated peripheral rods leads to higher CHF values. In the bundle with four unheated peripheral rods the thermal imbalance between the hot subchannel and other subchannels is strong which leads to an increase in energy exchange between subchannels and finally to a reduction of the exit steam quality of the hot subchannel. This effect results in a higher CHF. The distribution of mass flux in subchannels is affected by the pressure boundary condition, i.e. the pressure drop in the hot subchannel has to be equal to that in other subchannels. The total pressure drop consists of three portions: friction, gravitation and acceleration. At high mass fluxes the friction pressure drop prevails. Due to higher void fraction and lower density, mass fluxes in the hot subchannel have to be reduced, so that the pressure boundary condition is filled. As the COBRA code predicted (table V) the mass flux in the hot subchannel is much lower than the bundle average value. The effect of lower mass fluxes results in a lower CHF. Both effects, lower steam qualities and lower mass fluxes compensate with each other, so that the CHF value remains nearly unchanged.

In the wire wrapped 7-rod bundle the energy exchange between subchannels is much stronger than in the gridded 7-rod bundle. The thermal imbalance between subchannels diminishes. The effect of decreasing local qualities in the hot subchannel is dominant in contrast to the effect of decreasing mass fluxes. Therefore, the CHF values in the wire wrapped bundle with four unheated peripheral rods are much higher than those with uniform power distribution.

With decreasing mass fluxes the pressure drop due to the gravitation becomes more and more important. To fill the pressure boundary condition the density difference or the enthalpy difference between the hot subchannel and other subchannels must be reduced. Therefore, mass fluxes in the hot subchannel tend to increase, so that the thermal imbalance, finally the density difference between subchannels decreases. Both effects, decreasing steam qualities and increasing mass fluxes lead to a higher CHF.

4.5. 37-rod bundle

Regarding the influence of thermal-hydraulic conditions on CHF, the test results obtained in the 37-rod bundle are consistent with the data in 7-rod bundles. For comparison of the test results with the CHF look-up table [2] and the KfK-3 correlation [10] the test results were converted to water-equivalent conditions with the Ahmad's scaling law. The average values of the ratio of calculated to measured CHF values depending on mass flux are summarized in table VI. Both the CHF look-up table and the KfK-3 correlation reproduce the test results well. On the average, the CHF look-up table underpredicts the test results about 5%, whereas the CHF value calculated by the KfK-3 correlation is about 4% higher than the measured one. The ratio of the calculated to the measured CHF results exhibits a maximum at mass fluxes of 2 to 3 Mg/m^2s. This is probably due to mixing effects which depend on the axial velocity. Investigations to clarify the influence of mixing correlations on CHF in the 37-rod bundle are under way.

Table VI: Comparison of the test results in the 37-rod bundle with the CHF predictions $(CHF)_c/(CHF)_m$

G (Mg/m^2s)	look-up table		KfK-3 correlation	
	N	μ	N	μ
1.4	27	0.943	8	1.012
2.1	27	0.958	10	1.010
2.8	29	0.970	10	1.077
3.5	23	0.942	9	1.064
4.2	24	0.903	9	1.011
Σ	130	0.945	46	1.036

A better agreement of predicted and measured data may be achieved when including subcooled boiling correlations in COBRA-IV-TUBS. The subchannel analysis considers thermal equilibrium across the whole cross section of one subchannel. In a real flow, however, a significant temperature gradient is expected. The temperature near the heated surface reaches saturation, which causes vapour bubble formation, while the bulk flow remains subcooled. The vapour distribution model used in the present simulation disregards this phenomenon. The presence of a vapour fraction is only considered when the mean subchannel enthalpy is above the saturation state, i.e. steam qualities $x \geq 0$.

The Freon test results in 37-rod bundle were compared with the water data which were obtained by Siemens/KWU [4] in a geometrically similar 37-rod bundle as used in the present work. The most important difference of the water test section to the Freon rod bundle is the heated length of 1200 mm compared to 600 mm of the Freon test section. With respect to the different heated lengths of the water and Freon test sections, the steam quality at the middle level of the heated length of the water test section was chosen to compare the CHF data. Due to the chosen test sequence of the Freon tests only different steam qualities are available up to now to be compared. Therefore, quantitative statements about the comparison of the present experiments are premature. Further Freon tests will be carried out under inlet conditions comparable to water tests.

5. SUMMARY AND CONCLUSIONS

Experimental and theoretical investigations on critical heat flux were performed in circular tubes and in tight hexagonal rod bundles using model fluid Freon 12. The results obtained so far can be summarized as follows:

- The results in tubes as well as in rod bundles are in agreement with those in earlier publications and with initial expections regarding the influence of pressure, mass flux and steam quality on CHF.
- In contrast to previous work, the influence of the tube diameter on CHF has been found to be a complex function of flow parameters and of the diamteter itself. More research work to study the influence of the tube diameter on CHF is necessary.
- For circular tubes the CHF look-up table is proven to be the best prediction method. The Ahmad's scaling law is verified successfully to transfer CHF data from Freon 12 to water conditions.
- The influence of different spacers on CHF has been found to be governed by the local steam quality. In comparison to grid spacers, wire wraps appear advantageous at low steam qualities, whereas they lead to lower CHF at high steam qualities.
- In both 7-rod bundles with grid spacers and with wire wraps non-uniform radial power distributions lead to a higher CHF except for the case of gridded bundle with higher mass fluxes where CHF is hardly affected by disconnecting four peripheral rods. The influence of the non-uniform radial power distribution on CHF can be qualitatively explained by subchannel analysis.
- CHF predictions in rod bundles are affected substantially by the subchannel analysis. Further work is necessary to assess subchannel analysis models, especially the mixing coefficient in two-phase flow regime.
- The results of the present work demonstrates the suitability of Freon tests in combination with subchannel analysis, Ahmad's fluid-to-fluid scaling law, and water CHF tube tables to predict CHF in water cooled rod bundles.

REFERENCES

1 T. Müller-Menzel, W. Zeggel
CHF in the parameter range of advanced pressurized water reactor cores
Nuclear Engineering & Design, 90 (1987), pp.265-273

2 L.K.H. Leung, D.C. Groeneveld
1993 update of the critical heat flux table for upward flow of steam-water mixtures in uniformly heated tubes (version LW-T-1993)
International working group meeting on CHF fundamentals, TU Braunschweig, FR Germany, March 1993

3 X. Cheng
Experimentelle Untersuchungen zur kritischen Heizflächenbelastung in 8 mm-Kreisrohren und 7-Stabbündeln
Kernforschungszentrum Karlsruhe: KfK 4884, FR Germany, July 1991

4 S. Bethke
Darstellung kritischer Siedezustände
PhD thesis, Institut für Raumflug- und Reaktortechnik, TU Braunschweig, 1991

5 A. Katsaounis
Literaturbewertung zur Fluidähnlichkeit für die kritische Heizflächenbelastung
Technical Report GKSS 81/E/10, GKSS-Forschungszentrum Geesthacht GmbH, FR Germany, 1981

6 S.Y. Ahmad
Fluid-to-fluid modeling of critical heat flux: A compensated distortion model
Int. J. Heat Mass Transfer, Vol.16 (1973), pp.641-662

7 Y. Katto, H. Ohno
An improved version of the generalized correlation of critical heat flux for the forced convection boiling in uniformly heated vertical tubes
Int. J. Heat Mass Transfer, Vol. 27 (1984), pp. 1641-1648

8 M.M. Shah
Improved general correlation for critical heat flux during upflow in uniformly heated vertical tubes
Heat and Fluid Flow, Vol.8, No.4, Dec.1987

9 C.F. Fighetti, D.G. Reddy
Parametric study on CHF data, Vol.2: A generalized subchannel CHF correlation for PWR and BWR fuel assemblies
Electric Power Research Institute, EPRI-NP-2609-Vol.2, Jan. 1983

10 M. Dalle Donne
CHF-KfK-3: A critical heat flux correlation for triangular arrays of rods with tight lattices
Kernforschungszentrum Karlsruhe: KfK-4826, FR. Germany, Feb. 1991

11 D.C. Groeneveld, S.C. Cheng, T. Doan
1986 AECL-UO critical heat flux Look-Up table
Heat Transfer Engineering, Vol.7, Nos.1-2. 1986, pp.46-62

12 J. Weisman, B.S. Pei
Prediction of critical heat flux in flow boiling at low qualities
Int. J. Heat Mass Transfer, Vol.26 (1983), pp.1463-1477

13 J. Weisman, S.H. Ying
A theoretically based critical heat flux prediction for rod bundles at PWR conditions
Nuclear Engineering and Design 85 (1985), pp.239-250

14 H.J.- Kirchhoff
Validation thermohydraulischer Gleichungen für wendeldrahtgestützte Brennelemente bei Natriumkühlung
PhD thesis, Institut für Raumflug- und Reaktortechnik, TU Braunschweig, 1991

15 F.J. Erbacher, W. Zeggel, H. Grubel, S. Bethke
Critical heat flux experiments using Freon and water in hexagonal 37-rod bundles
Proc. of the Nureth-6 Topical Meeting, Grenoble, France, October 1993

16 X. Cheng, F.J. Erbacher, E. Staron, W. Zeggel
Critical heat flux in circular tubes at high pressures and high mass fluxes
Proc. of the Nureth-5, Vol.1, pp.121-126, Salt Lake City, Utah, USA, September 1992

17 D. Blumenröhr, F.J. Erbacher, D.C. Groeneveld, W. Zeggel
An experimental investigation into forced convection burnout in Freon, with reference to burnout in water. Uniformly heated round tubes with vertical up-flow
European Two-Phase Flow Group Meeting. June 1992, Stockholm, Sweden

EXPERIMENTAL INVESTIGATION ON DRYOUT UNDER OSCILLATORY FLOW CONDITION IN VERTICAL AND HORIZONTAL TUBES

M. OZAWA and H. UMEKAWA

Department of Mechanical Engineering, Kansai University,
Yamate-cho 3-3-35, Suita, Osaka 564, Japan

ABSTRACT

Critical heat flux (CHF) in a boiling channel under oscillatory flow instability was significantly lower compared with that under steady state condition. In order to verify the effects of the amplitude and the period of the flow oscillation on the CHF, systematic experiments were conducted by imposing a flow oscillation with a predetermined amplitude and a period. When the oscillation period and amplitude were large enough beyond certain limits, substantial reduction of the CHF occurred and the CHF reached almost 40 % of the steady state value. There was no significant difference between the vertical flow and the horizontal flow when the mean mass flux was at relatively higher level.

1. INTRODUCTION

Critical heat flux (CHF) is one of the most important design factors of nuclear reactors, conventional boilers, and other various boiling two-phase flow systems. In the past three decades, extensive works on the CHF have been conducted, especially, with the development of nuclear reactors [1-5]. Recently, increasing attention has been given to the development of small scale gas-fired boilers. Main feature on such development is directed to the size reduction of boilers, which essentially results in the increase in the thermal load in the furnace [6] and gives rise to the CHF problem at relatively low pressure and low mass flux conditions.

CHF problems arise also in waste-heat boilers of Diesel engines and in fluidized bed boilers for coal combustion and incineration of waste materials. In such systems, horizontal and/or serpentine tubes are usually used. In horizontal channel systems, the CHF becomes significantly lower compared with that in the vertical flow system owing to the phase stratification [7-9] at low level of the mass flux.

Boiling channel systems are usually composed of many parallel channels where flow instabilities, such as so-called density wave oscillation, take place under certain operating conditions. The density wave oscillation has been widely investigated mainly concerned with nuclear reactors, and many computer codes for the prediction of the threshold conditions have been developed so far. The flow instabilities and/or flow oscillation, in general, reduce the CHF to a lower level[2,10-13]. Figure 1 is an example which shows the reduction of the CHF owing to the density wave oscillation, where q_{cro} is given by Katto's correlation and $\Delta G_{max}/G_o$ represents the dimensionless amplitude defined in the following section. These data were obtained in the natural circulation experiment using liquid nitrogen. The detailed discussion on this figure can be found elsewhere[14].

As is well known, the amplitude of the density wave oscillation increases with the increase in the heat flux, and finally the flow reversal appears during the limit cycle oscillation, which may enhance the premature dryout. On the contrary, the period of oscillation decreases with the increase in the heat flux, which may enhance the rapid cooling and/or rewetting after the dryout. Thus, the CHF problems under flow oscillation should be analyzed taking account of these both effects. However, the oscillation amplitude and the period are closely related with each other, and are strong functions of the system configuration. Thus the experiment of CHF under flow instability gives only qualitative information about the reduction of the CHF.

Challenging approaches has been conducted almost 30 years ago by Sato et al. [15], and

Ishigai et al. [16] by imposing a predetermined flow oscillation on the mean flow. Other approaches can be found in the investigations of premature dryout under flow transient and/or flow reversal transient, for example, by Ishigai et al. [17] and Smith et al. [18], respectively.

Although various approaches to the premature dryout have been conducted so far, the relationships between the premature dryout and the flow oscillation, namely the effects of the amplitude and the period on the reduction of the CHF, are still not well understood owing to the limitation of the parameter range in the experiments. Thus in this investigation, systematic experiments have been conducted on the dryout under forced flow oscillation in a vertical and a horizontal tubes. In this paper, the experimental results are presented, and a phenomenological discussion are described on the CHF under forced flow oscillations.

2. EXPERIMENT

Main parts of the test loop are a reserve tank of ion-exchanged water, a magnet pump, a calming section, a test section, a separator, and a flow oscillator as shown in Fig.2. Water filled in the reserve tank was degassed by boiling prior to experiments. Controlling the water temperature in the reserve tank by regulating the heater input and the cooling water, the inlet subcooling was kept constant throughout the experiment. The mass flow rate supplied to the mixing chamber was controlled by regulating the pump speed and the valve.

The water from the mixing chamber passed through the calming section of the dimension 5.0mm I.D. and 1.0m in length, and enter the test section of the dimension 5.0mm I.D., 6.0mm O.D. and 900mm in the heated length. In the test section, water was heated by Joule heating of the AC power. Two-phase mixture formed in the heated section flowed through a sight section of 5.0mm I.D. and 50.0mm in length and a riser section of 10.0mm I.D. and 150mm in length, and then entered into the separator. The separator was opened to the atmosphere, and thus all the experiments were conducted under the atmospheric pressure.

The test section was SUS304 tube and the outer wall temperature was measured by using C-A thermocouple of 0.1mm diameter at every 50mm location along the test section. The pressure drops at the calming section (the pressure tap distance was 500mm) and the test section (1140mm) were measured by D.P. cells continuously and were recorded by a pen recorder. The pressure drop in the calming section was used for monitoring the flow oscillation. Most of the parts of the test loop were thermally insulated from the ambient air.

The flow oscillator unit was mounted at the mixing chamber. The oscillator unit was composed of a cylinder and a piston which was driven by using the geared motor and the linkage mechanism. Then, the mass flux through the test section is given by the sum of the mean value G_o and the

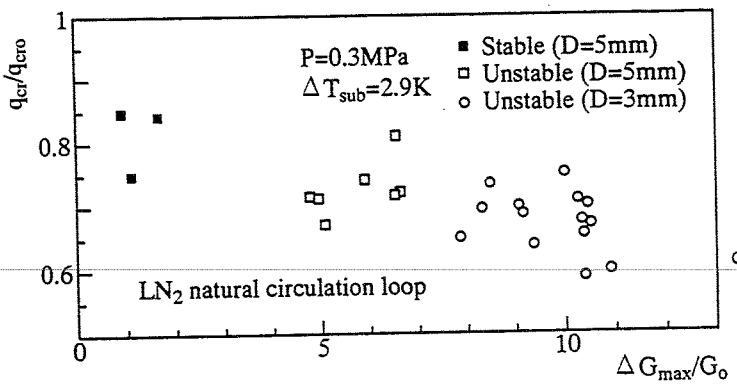

Fig.1 CHF under density wave oscillation (experimental results obtained in a natural circulation loop of liquid nitrogen).

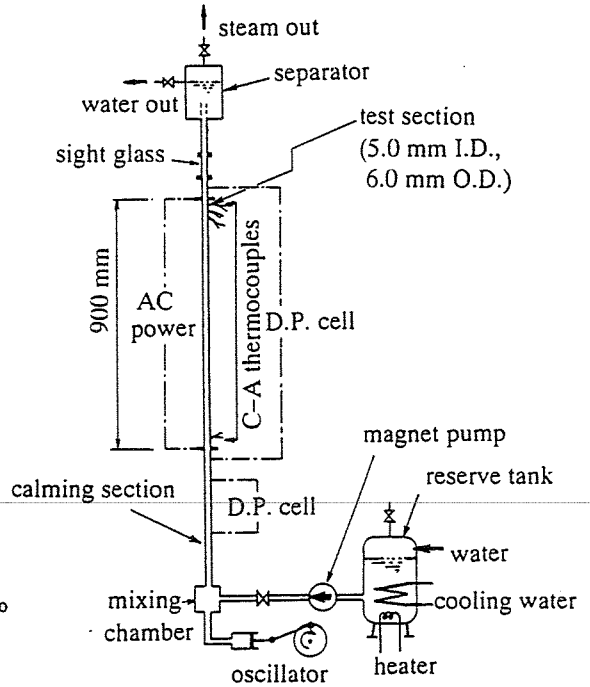

Fig.2 Experimental apparatus.

fluctuating component,

$$G = G_o + \Delta G_{max}\sin(2\pi t/\tau) \ . \qquad (1)$$

In the present investigation, two series of experiments were conducted; i.e. the vertical flow and the horizontal flow experiments. Figure 2 represents the test loop for the vertical flow experiment. In the case of the horizontal flow experiment, the test section and the calming section were set horizontally. Other parts of the system were not changed in principle. In the horizontal flow experiment, tube wall temperatures were measured at three circumferential points, i.e., the top, the side and the bottom walls of the test tube, at every location along the test tube. Experiments were carried out by increasing the heat flux successively under predetermined constant values of the mean mass flux, the period and the amplitude of oscillation. The CHF condition was detected by a burnout detector mounted at the heated section exit. The preset level of the burnout detector was 200deg.C.

Experimental range was as follows: the exit pressure was the atmospheric pressure and the inlet subcooling was ΔT_{sub}=20.0K throughout the present experiment. The mean mass flux was in the range G_o=70 to 450kg/m^{2}s, and the heat flux was in the range up to 514kW/m^2. The dimensionless amplitude $\Delta G_{max}/G_o$ and the period τ of the flow oscillation were $\Delta G_{max}/G_o$=0.209 to 3.77 and τ=2.0, 4.0 and 6.0s, respectively.

3. CHF UNDER STEADY STATE CONDITION

Prior to the discussion of the experimental results under oscillatory flow condition, the experimental results under steady state condition, i.e. constant mass flux condition, are presented in this section. The experimental CHF data are plotted on the dimensionless heat flux versus mass flux plane in Fig.3 which is the same coordinate system as Mishima et al. [12,13,19]. The dimensionless heat flux and mass flux are defined by $(q_{cr}/h_{LG})/\sqrt{(g\lambda_C\rho_G\rho_{LG})}$ and $G_o/\sqrt{(g\lambda_C\rho_G\rho_{LG})}$, respectively, where $\lambda_C=\sqrt{(\sigma/[g\rho_{LG}])}$. Experimental results for the vertical flow are represented by the solid circles and those for horizontal flow by open circles. Both results of the CHF increase with the increase in the dimensionless mass flux. The broken lines in Fig.3 correspond to the condition of constant exit qualities, X_{ex}=1 and 0, and the dot-dash line corresponds to the flooding-CHF condition given by Mishima [19]. The flooding-CHF condition corresponds to the limiting case of zero inlet mass flux, which gives the lowest boundary of the CHF. As is pointed out by Mishima, when the flow oscillation has an

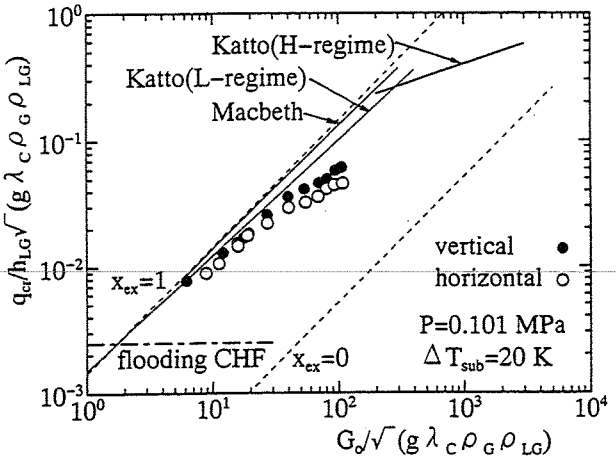

Fig.3 CHF under steady state condition.

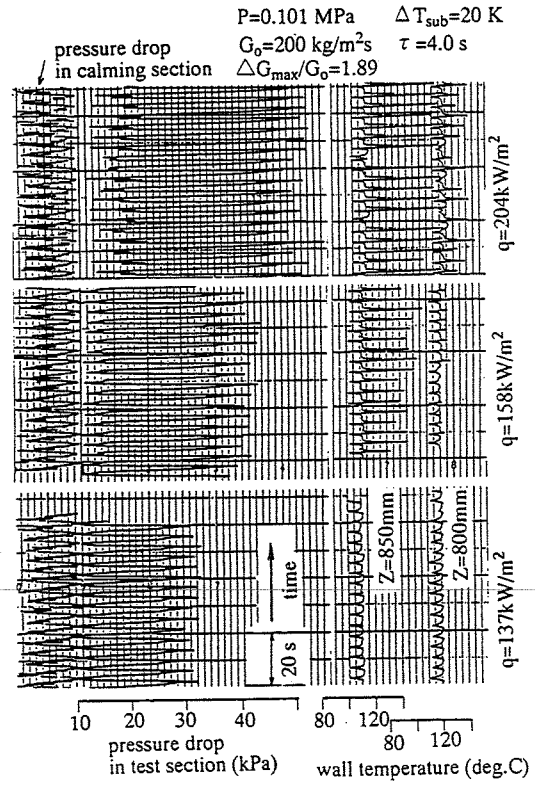

Fig.4 Typical recording trace.

extremely large amplitude, e.g. in the case of pressure drop oscillation, the CHF approaches to the line of X_{ex}=0. In the figure the correlation lines by Katto (L-regime and H-regime)[5,20] and Mcbeth [21] are also drawn. Experimental CHF data approximately agree with Katto's correlation for relatively lower mass flux(L-regime) and Mcbeth's one, but depart from the correlation lines with the increase in the mass flux.

The CHF data for the horizontal flow are slightly lower than those for vertical flow. Robertson [8] reported that the CHF for the horizontal flow became far below than that for the vertical flow. This may be true when the Froude number defined by Eq.(2) [22] is lower than 7 to 10 as is pointed out by Kefer et al. [9].

$$Fr=(x_{cr}G_o/\rho_G)/\sqrt{(gD\rho_{LG}/\rho_G)}. \quad (2)$$

In the present case, the Froude number under the CHF condition is larger than 10, for example Fr=12 when G_o=100kg/m^{2}s. Based on the flow pattern map presented by Kefer [9], the presented data are estimated to be in annular flow region with almost uniform circumferential distribution of the liquid film. Thus the dryout takes place almost the same location at the top, side and bottom walls of the tube, which has been verified in the present experiment.

4. CHF UNDER OSCILLATORY FLOW CONDITION

4.1 General Feature of Temperature Fluctuation

In this section, is discussed the behavior of wall temperature fluctuation under the oscillatory flow condition. Figure 4 shows the recording trace of the pressure drop in the calming section, that in the test section, and the wall temperatures at the position 50mm (Z=850mm from the heated section inlet) and 100mm (Z=800mm) upstream the heated section exit. The fluctuation of the first pressure drop corresponds to the flow oscillation at the heated section inlet. The presented examples in Fig.4 are obtained for the vertical flow experiment.

When the heat flux is enough low and the oscillation amplitude of the mass flux was also low enough, i.e. $\Delta G_{max}/G_o$ is far less than unity, the wall temperature retains almost constant value or shows small increase during the half cycle when the mass flux is lower than the mean value. Increasing the amplitude of the flow oscillation to induce the flow reversal process, for example in the case of $\Delta G_{max}/G_o$=1.89 as in the case in Fig.4, the wall temperature becomes to fluctuate. When the heat flux imposed on the test section is low enough, q=137kW/m^2 as shown in the bottom column, the wall temperature decreases periodically. The time of this temperature decrease corresponds to the time of a minimum value of the pressure drop. Thus, this temperature decrease is mainly caused by the enhanced heat transfer due to the rapid ejection of two-phase mixture in the heated section. Increasing the heat flux further as shown in the middle column in Fig.4, the wall temperature becomes to show the sharp increase just after the decrease in the wall temperature. This sharp increase in the wall temperature represents the dryout.

This phenomenon is postulated on the basis of the visual observation at the sight section as follows: During the decreasing process in the mass flux from the inlet, the quality in the heated section increases. Then, two-phase mixture in the heated section is rapidly ejected toward the riser and the separator, and thin liquid film on the heated wall breaks up to induce the dryout. Then the wall temperature increases rapidly. In the next increasing process of the mass flux from the inlet, the steam flow rate from the heated section decreases and the flow reversal from the riser section begins to penetrate into the heated section. The heated wall is rewetted again. Finally, the heated section returns to the convective boiling condition. These process repeats periodically. When the heat flux is relatively low and/or the oscillation period is short enough, the rate of the temperature rise is not high, and the temperature rise is limited in a certain amount during this dryout.

Increasing the heat flux further, the rate of temperature rise becomes large as shown in the top column in Fig.4, and the wall temperature exceeds a certain limit, i.e. 200 deg.C. The heat flux at this stage is defined as the CHF in the present study. Such conditions were always observed, at first, at the exit of the heated section. Increasing the heat flux further, the dryout

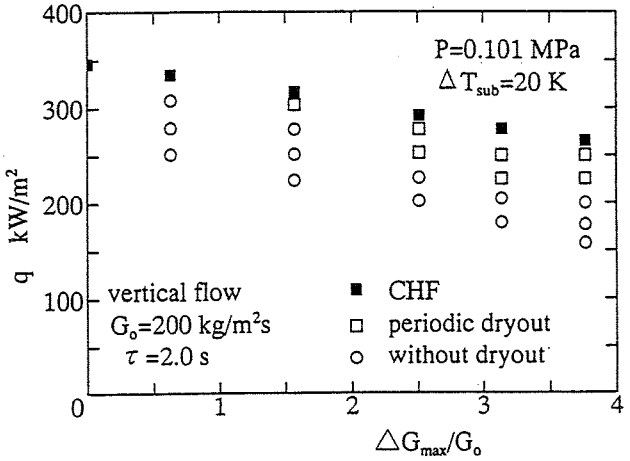

Fig.5 Mode of temperature fluctuation (vertical flow, τ =2.0s).

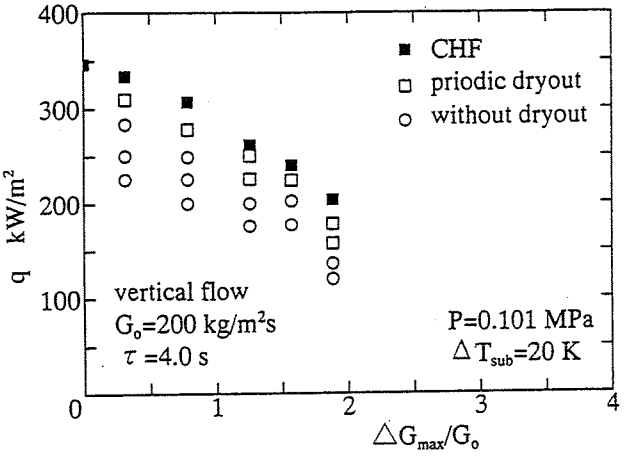

Fig.6 Mode of temperature fluctuation (vertical flow, τ =4.0s).

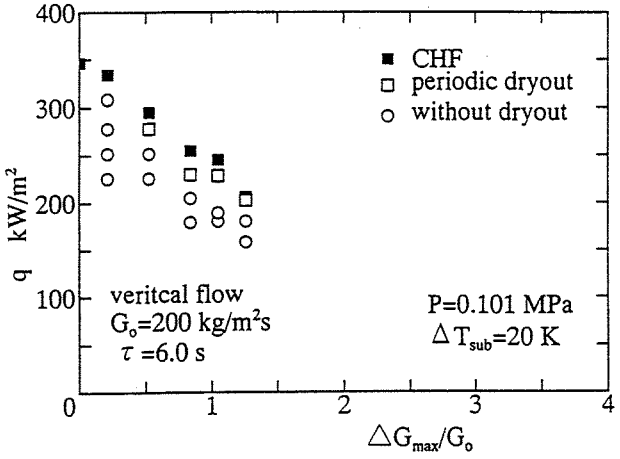

Fig.7 Mode of temperature fluctuation (vertical flow, τ =6.0s).

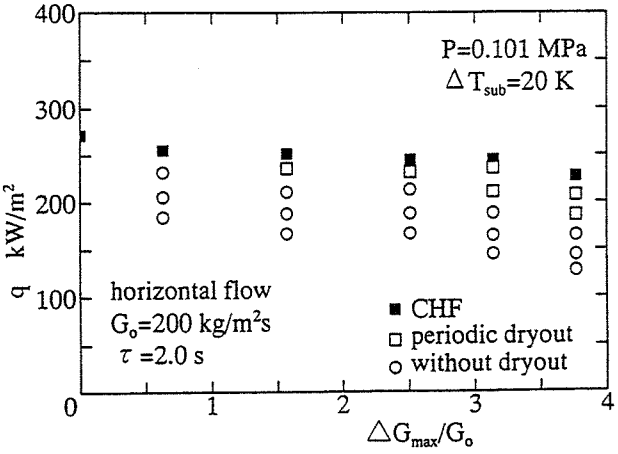

Fig.8 Mode of temperature fluctuation (horizontal flow, τ =2.0s).

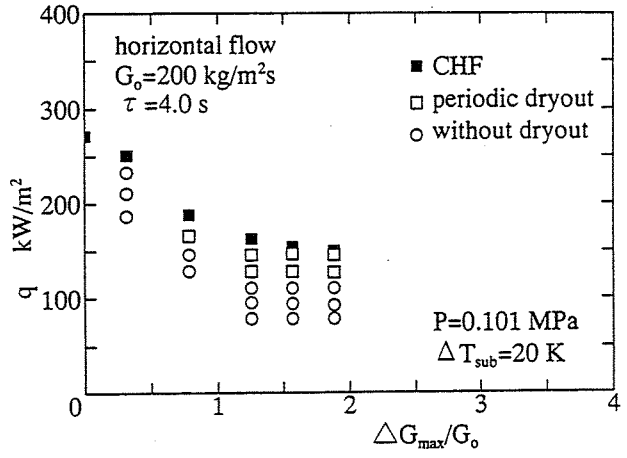

Fig.9 Mode of temperature fluctuation (horizontal flow, τ =4.0s).

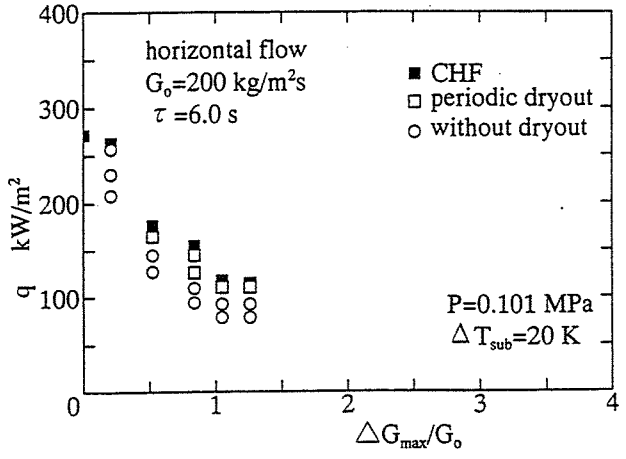

Fig.10 Mode of temperature fluctuation (horizontal flow, τ =6.0s).

region extended upstream. These tendencies of the wall temperature fluctuation were also observed in the horizontal flow, and the substantial differences were not observed between the two series of experiments.

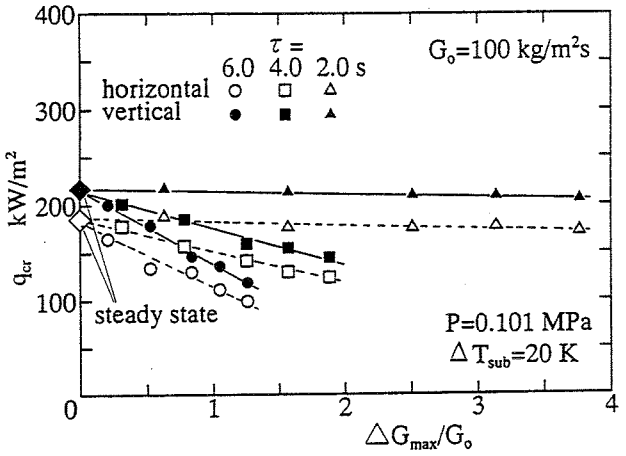

Fig.11 CHF under oscillatory flow condition (mean mass flux G_o=100kg/m^{2}s).

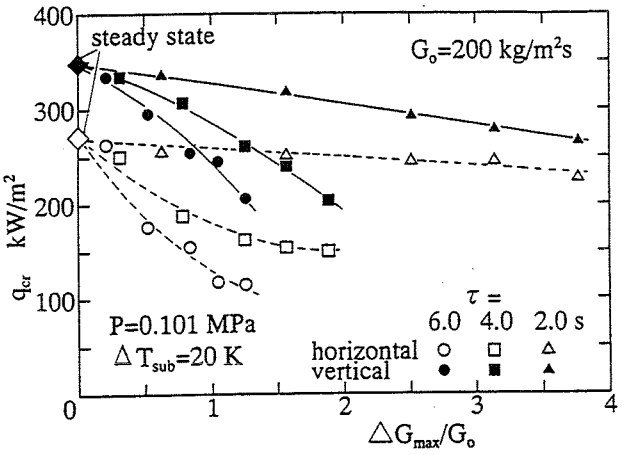

Fig.12 CHF under oscillatory flow condition (mean mass flux G_o=200kg/m^{2}s).

The mode of temperature fluctuation is classified into three regimes; i.e. almost constant and/or periodic decrease owing to the rapid ejection of two-phase mixture but without dryout, periodic dryout but relatively small increase of the wall temperature, and then the CHF condition defined above. These three regimes are plotted on the heat flux q versus dimensionless amplitude $\Delta G_{max}/G_o$ plane in Figs.5 to 7 for the vertical flow and in Figs.8 to 10 for the horizontal flow. Increasing the heat flux, the mode changes from the stable condition without dryout, the periodic dryout and to the CHF condition. The heat fluxes at the transitions from the stable condition to the periodic dryout and from the periodic dryout to the CHF condition decrease with the increase in the dimensionless amplitude. The decrease in the heat flux at the transition and the CHF condition becomes much significant with the increase in the oscillation period. In the case of the horizontal flow shown in Figs.8 to 10, similar tendencies are observed as in the vertical flow, while the CHF and the transition boundary of the heat flux are lower than those in the vertical flow.

4.2 Critical Heat Flux

Figures 11 to 13 show the CHF under various periods τ and dimensionless amplitudes $\Delta G_{max}/G_o$. Referring to the case of the period τ =2.0s in Fig.11, the CHF decreases slightly from the steady state value (data corresponding to $\Delta G_{max}/G_o$=0) with the increase in the dimensionless amplitude $\Delta G_{max}/G_o$. Increasing the period to τ =4.0s and to 6.0s, the reduction of the CHF becomes large compared with that in the case of τ =2.0s.

In the case of the horizontal flow, data for τ =2.0s show gradual decrease in the CHF with the increase in the dimensionless amplitude. The increase in the oscillation period τ results in the substantial reduction of the CHF. Comparing the data for the vertical flow and those for horizontal flow, substantial difference in character cannot be found between them. Thus, even in the case with flow oscillation, the phase stratification did not occur in the present experiment, which was also confirmed by the fact that no significant difference in the behavior of the wall temperature was observed between the circumferential locations. Such tendencies are also observed in cases of the mass flux G_o=200kg/m^{2}s in Fig.12 and G_o=300kg/m^{2}s in Fig.13, while the reduction ratio from the steady state value becomes larger with the increase in the mass flux, especially in the case of τ =2.0s.

The CHF q_{cr} under oscillatory flow condition is normalized by the steady state value q_{cro} of the CHF and is plotted against the dimensionless amplitude $\Delta G_{max}/G_o$ in Figs.14 and 15. Referring to the case of the oscillation period τ =2.0s, the normalized CHF q_{cr}/q_{cro} decreases significantly with the increase in the mean mass flux, while the reduction of the CHF for G_o=100kg/m^{2}s is only 5% in the present range of experiment. Increasing the oscillation period, the effect of the mean mass flux on the reduction of the CHF becomes less significant. In a certain case, when the period is large enough, τ =6.0s, the reduction of the CHF reaches almost 40% of the steady state value.

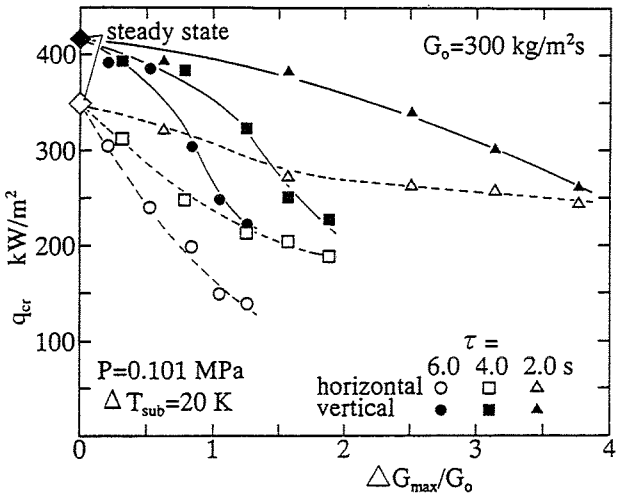

Fig.13 CHF under oscillatory flow condition (mean mass flux G_o=300kg/m²s).

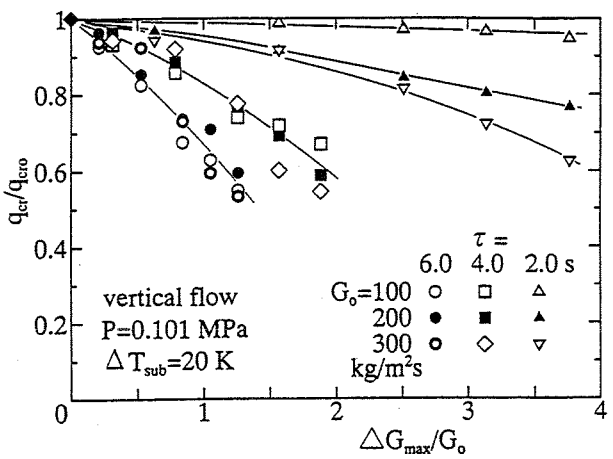

Fig.14 Reduction of CHF (vertical flow).

The rate of temperature rise is closely related to the tube wall heat capacity and the heat transfer coefficient during the dryout. Providing the lumped-parameter model of the heat capacity, one-dimensional energy balance in the radial direction at the tube wall and the heat flux q at the inner wall are expressed by Eqs.(3) and (4), respectively.

$$q_{ext} - q = C_W \rho_W[(D_o^2-D^2)/4D]dT_W/dt \tag{3}$$

$$q = h(T_W - T_S) . \tag{4}$$

Substituting Eq.(4) into Eq.(3), the behavior of the tube wall temperature against the stepwise input of q_{ext} is given by the next equation under constant values of h,

$$\theta = (q_{ext}/h)[1-\exp(-t/\tau_W)] \tag{5}$$

where θ is a wall superheat, $\theta = T_W - T_S$, and τ_W is a time constant which characterizes the temperature response of the tube wall and is given by $\tau_W = C_W \rho_W[(D_o^2-D^2)/4D]/h$.

The wall temperature increases during the dryout. When the dryout period is sufficiently long so as to exceed a certain limit, in this case θ=100K, the critical dryout-period t_D can be calculated on the basis of Eq.(5). Then, the critical dryout-period is given by

$$t_D = \tau_W \ln(1/[1-h\theta/q_{cr}]) . \tag{6}$$

Now we assume the following simplified model: The dryout occurs during the half cycle of the mass flux less than the mean value neglecting the dynamic behavior of two-phase flow. When this critical dryout-period is less than the half of the oscillation period, i.e. t_D/τ <0.5, the wall temperature does not exceed the critical value. On the contrary, the value t_D/τ is larger than 0.5, the wall temperature exceed the critical value. Then the condition t_D/τ =0.5 gives a critical condition. Rearrangement of Eq.(6) gives the critical heat flux as follows,

$$q_{cr} = h\theta/[1-\exp(-0.5\tau/\tau_W)] \tag{7}$$

where the wall superheat θ is set to be 100K. The heat transfer coefficient h is given by the Dittus-Boelter's equation for steam flow and is assumed to be a function of the mean mass flux. The calculated results are shown in Fig. 16. Under the constant value of the mean mass flux, the increase in the oscillation period induces the decrease in the CHF. On the other hand, the CHF increases with the increase in the mean mass flux under constant period of oscillation. The increase in the mean mass flux induces the increase in the heat transfer coefficient h, but results in the decrease in the time constant τ_W. The tendency of the curves suggests that the former effect is significant compared with the latter effect on the CHF. As can be easily understood

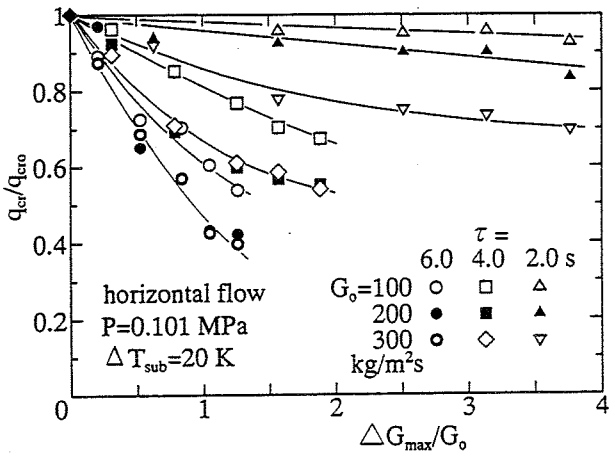

Fig.15 Reduction of CHF (horizontal flow).

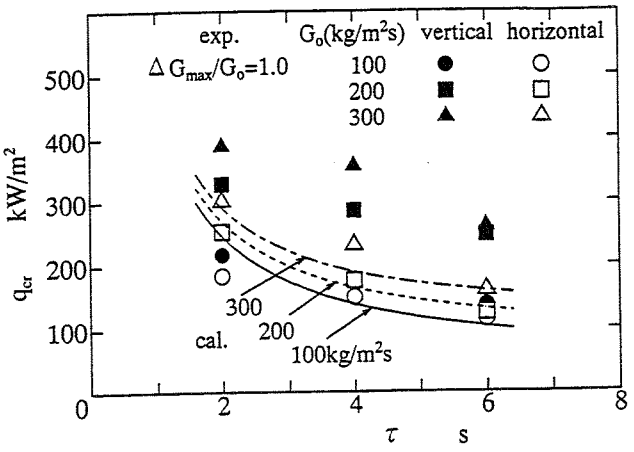

Fig.16 CHF obtained by simplified model.

from the definition of τ_W, the increase of the tube wall thickness, and/or heat capacity results in the decrease in the reduction ratio of the CHF. The effect of the wall heat capacity on the CHF can be found in the recent experimental results by Umekawa el al.[23]. In Fig.16, the experimental results are also plotted in the case of $\Delta G_{max}/G_o$=1.0 for reference. The calculated values represent the qualitative trend of the experimental data against the oscillation period as well as the mean mass flux. Thus, the effect of the oscillation period on the CHF can be explained phenomenologically on the basis of this simplified model. In order to obtain quantitative prediction of the CHF under such oscillatory flow condition, it is essential to analyze and/or simulate the dynamic behavior of two-phase flow and the related behavior of the tube wall temperature. Further investigation on this subject is now going on and the results will be presented near future including the numerical simulation.

5. CONCLUSION

Experimental investigation on the critical heat flux was conducted under oscillatory flow condition with predetermined amplitude and the period. When the oscillation period was relatively short, the reduction of the CHF was relatively small against the increase in the amplitude. But when the oscillation period was long enough, the CHF decreased significantly from the steady state values. In the present range of experiment, no substantial difference was observed between the vertical and horizontal flows. This was mainly because the diameter of the tube was relatively small and thus the flow regime in the horizontal flow was annular flow with relatively uniform film thickness as in the case in the vertical flow. The application of the present results will be limited to the CHF under the density wave oscillation. When the system suffers from the pressure drop oscillation and the flow excursion, the reduction of the CHF becomes extremely large beyond the present data, which is out of scope of the present investigation. On the basis of the rather simplified model, the effects of oscillation period on the reduction of CHF were discussed. Further investigation is necessary on the thermal-hydraulics of two-phase flow during the transient condition.

ACKNOWLEDGEMENTS

This work was partly supported by the Kansai University Research Grant (1992 and 1993). The authors wish to their thanks to Messrs. A. Miyazaki, M. Miyoshi, N. Ishida and Y. Yoshioka, and Prof. A. Tomiyama for their assistance and useful suggestion on this research program.

NOMENCLATURE

C_W : specific heat of tube material

D : inner diameter of tube
D_o : outer diameter of tube
Fr : Froude number
g : gravitational acceleration
G : mass flux
G_o : mean mass flux
ΔG_{max} : amplitude of mass flux oscillation
h : heat transfer coefficient at inner wall of tube
h_{LG} : latent heat of vaporization
P : pressure
q : heat flux
q_{cr} : critical heat flux
q_{cro} : critical heat flux under steady state condition
q_{ext} : heat flux imposed by electricity
t : time
t_D : dryout period
T_S : saturation temperature
T_W : wall temperature
ΔT_{sub} : subcooling
X_{cr} : flow quality at CHF condition
X_{ex} : flow quality at test section exit

Greek symbols:

ρ_G : density of vapor
ρ_{LG} : density difference between liquid and vapor
ρ_W : density of tube material
σ : surface tension
τ : oscillation period
τ_W : characteristic time constant
θ : wall superheat

REFERENCES

[1] L.S.Tong, "Boiling Heat Transfer and Two-Phase Flow", John Wiley & Sons, New York(1965).
[2] J.G.Collier, "Convective Boiling and Condensation", McGraw-Hill, London(1972).
[3] L.S.Tong and G.F.Hewitt, "Overall Viewpoint of Flow Boiling CHF Mechanisms", ASME paper, 72-HT-54(1972).
[4] R.T.Lahey and F.J.Moody, "The Thermal-Hydraulics of a Boiling Water Nuclear Reactor", ANS(1977).
[5] Y.Katto, "Critical Heat Flux", in: Advances in Heat Transfer, J.P.Hartnett and T.F.Irvine,Jr., Eds., Vol.17, 2-64, Academic Press, Orlando(1985).
[6] S.Ishigai, et al., "Jaggy Fireball in Tube-Nested Combustor: An Advanced Concept for Gas-Firing and Its Application to Boilers", in: ASME HTD-Vol.199, Heat Transfer in Fire and Combustion Systems, 189-195(1992).
[7] S.Ishigai, T.Takagi and S.Ichiyama, "Dryout at Entrance of Heated Section for the Horizontal Flow of Low-Pressure Steam-Water Mixture", in: JSME 1967 Semi-International Symp., Paper No.258, 45-53(1967).
[8] J.M.Robertson, "Dryout in Horizontal Hairpin Waste-Heat Boiler Tubes", in: AIChE Symp. Ser. No.131, Vol.69, 55-62(1973).
[9] V.Kefer, W.Koehler and W.Kastner, "Critical Heat Flux(CHF) and Post Dryout Heat Transfer in Horizontal and Inclined Evaporator Tubes", in: Int. J. Multiphase Flow, 15-3, 385-392(1989).
[10] A.E.Bergles, R.F.Lopina and M.P.Fiori, "Critical-Heat-Flux and Flow Pattern Observations for Low-Pressure Water Flowing in Tubes", in: Trans. ASME, J. Heat Transf., 89, 69-74(1967).
[11] K.Kitayama, et al., "Boiling Transition under Thermal Hydraulic Instability in Rod Bundle",

in: Proc. 3rd. Int. Topical Meeting on Reactor Thermal Hydraulics, Newport, Paper No.9c(1985).
[12] K.Mishima, H.Nishihara and I.Michiyoshi, "Boiling Burnout and Flow Instabilities for Water Flowing in a Round Tube under Atmospheric Pressure", in: Int. J. Heat Mass Transfer, 28-6, 1115-1129(1985).
[13] K.Mishima and H.Nishihara, "Critical Heat Flux at Low Velocity and Pressure Conditions, in: Proc. 2nd Int. Topical Meeting on Nuclear Power Plant Thermal Hydraulics and Operations, Tokyo, 1.1-1.8(1986).
[14] H.Umekawa, M.Ozawa and N.Ishida, "Critical Heat Flux and Post-Dryout Heat Transfer in a Boiling Channel of Liquid Nitrogen", to be submitted in: Trans. JSME, Ser.B, (1994).
[15] T.Sato, Y.Hayashida and T.Motoda, "The Effect of Flow Fluctuation on Critical Heat Flux", in: Proc. 3rd Int. Heat Transf. Conf., Chicago, Vol.4, 226-233(1966).
[16] S.Ishigai, et al., "Critical Heat Flux of Oscillatory Flow in a Vertical Tube", in: Preprint of the 43th Annual Conf. of the JSME-Kansai, Paper No.408, 23-25(1968).
[17] S.Ishigai, et al., "Effect of Transient Flow on Premature Dryout in Tube", in: Proc. 5th Int. Heat Transf. Conf., Tokyo, Vol.4, B6.13, 300-304(1974).
[18] R.A.Smith, F.A.Price and P.Griffith, "An Analysis of Critical Heat Flux in Flow Reversal Transients", in: Trans. ASME, J. Heat Transfer, 98, 153-158(1976).
[19] K.Mishima, "Boiling Burnout at Low Flow Rate and Low Pressure Condition", Ph.D. Thesis, Kyoto University, Kyoto(1984).
[20] Y.Katto, "A General Correlation of Critical Heat Flux for the Forced Convection Boiling in Vertical Uniformly Heated Round Tube", in: Int. J. Heat Mass Transf., 21, 1527-1542(1978).
[21] T.Ueda, "Two-Phase Flow", Yokendo Pub., Tokyo, 290-293(1981).
[22] G.B.Wallis, "One-Dimensional Two-Phase Flow", McGraw-Hill, New York, p.317(1969).
[23] H.Umekawa, M.Ozawa and A.Miyazaki, "Dryout in a Boiling Channel under Oscillatory Flow Condition", to be submitted in: Trans. JSME, Ser.B, (1994).

DRYOUT OF WATER FILM ON A HEATED TUBE SURFACE CAUSED BY AN OBSTRUCTION IN A BOILING TWO-PHASE VERTICAL UPWARD FLOW

Tohru FUKANO[1], Akikazu GOTO[1], Yutaro TSURUSAKI[2] and Shin-ich MOROOKA[3]

[1]The University of Kyushu
Faculty of Engineering, Department of Mechanical Engineering
Hakozaki 6-10-1, Higashi-ku, Fukuoka 812, Japan
Telephone:(092)641-1101(EX)5440, Facsimile:(092)641-9744

[2]Kawasaki Heavy Industries,LTD
Assembly Section, Prime Mover Divistion
Higashi Kawasaki-cho 3-1-1, Chūō-ku, Kōbe 650-11, Japan
Telephone:(078)682-5366, Facsimile:(078)682-5551

[3]Toshiba Corporation
Nuclear Engineering Laboratory
Ukishima-cho 4-1, Kawasaki-ku, Kawasaki 210, Japan
Telephone:(044)288-8130, Facsimile:(044)299-2853

ABSTRACT

Due to the green house effect caused by CO_2 the dependence on a nuclear power station does not become weak so far. And both the economy and the safety of the nuclear power station are strongly demanded. One of the problem in the thermal design of the nuclear reactor, especially in BWR is caused near the spacer supporting nuclear fuel rods.

The purpose of the present paper is to make clear mechanism to cause the water film breakdown which results in the burnout of heating tube near the spacer and its relation to the flow pattern.

The experimental results shows that the film breakdown occurs near the leading edge,i.e.,just below the spacer as well as the inside of the down part of the gap between the outer surface of the heating tube and the simulated spacer.

1.INTRODUCTION

The dependence on the electric power produced by nuclear power station does not reduced so far because of the expected sharp increase in the energy consumption especially in developing countries in near future in addition to the serious problem of the green house effect of CO_2. Therefore the safety operation of nuclear reactors must be maintained and still more investigated. It is needless to say that we should be very careful not to cause serious problems such as the loss of coolant accident. On the other hand, today the importance is also attached to the economic and efficient points of view in designing both the usual and new type nuclear power plants.

It has been pointed out from the results obtained by using a large scale experimental apparatus that the restriction in thermal design is the heat removal from nuclear rods at the region in close vicinity of the spacer supporting nuclear rods in a boiling water reactor, for example. The coolant in a BWR is considered to flow as liquid film on the nuclear rods at the location where such a serious problem occurs. And therefore the investigation has been made in order to make clear the mechanism to cause the thermal limitation near the spacer[(1)].

According to the experimental research made by one of the present authors, the drainage (quick thinning of liquid film due to the flow down of liquid) is the main cause to generate drypatches just upstream of the obstruction by using a ring type obstruction[(2)]. In this experiment the ring type obstacle was sticked on the heated tube wall, i.e., there was no gap between the ring and the heated tube wall while there are gap of order 1 mm in the spacer of a actual BWR. Shiralkar and Lahey investigated the effect of a projection jutting from the bottom wall of the horizontal rectangular duct

on the liquid film, and they pointed out an important role of the projection to cause drypatch near the projection[3]. In a horizontal duct the interaction of a flat plate type flow obstruction simulating a spacer of nuclear rods and liquid film flowing concurrently with a high speed gas flow was investigated in detail[4]. As a result it is made clear that the liquid film was dried out at the point where the projection contacted with the bottom wall of the rectangular duct.

Based on the informations described above, in the present investigation, we made a detailed observation of the behavior of liquid near the flow obstruction in order to make clear the mechanism of drypatch formation by using a flat-plate type flow obstruction designed by taking into consideration the shape of the spacer in practical use.

2.EXPERIMENTAL APPARATUS AND PROCEDURE

Figure 1 shows a schematic view of the experimental apparatus used in the present experiment. The test section, which was consisted of concentric double tubes, was vertically set in a closed forced convection loop. A working fluid, distilled water, fed by a feed pump 7 flowed into the test section after passing through a pre-heater 10, where the temperature of the working fluid at the inlet of the test section or the inlet subcooling was controlled. Two-phase mixture from the exit of the test section was separated into water and vapor at a separator 2. Both the water and the vapor were corrected at a reservoir 6 after being respectively cooled down below the saturation temperature at each condenser 5 to prevent cavitation bubbles from generating in the feed pump.

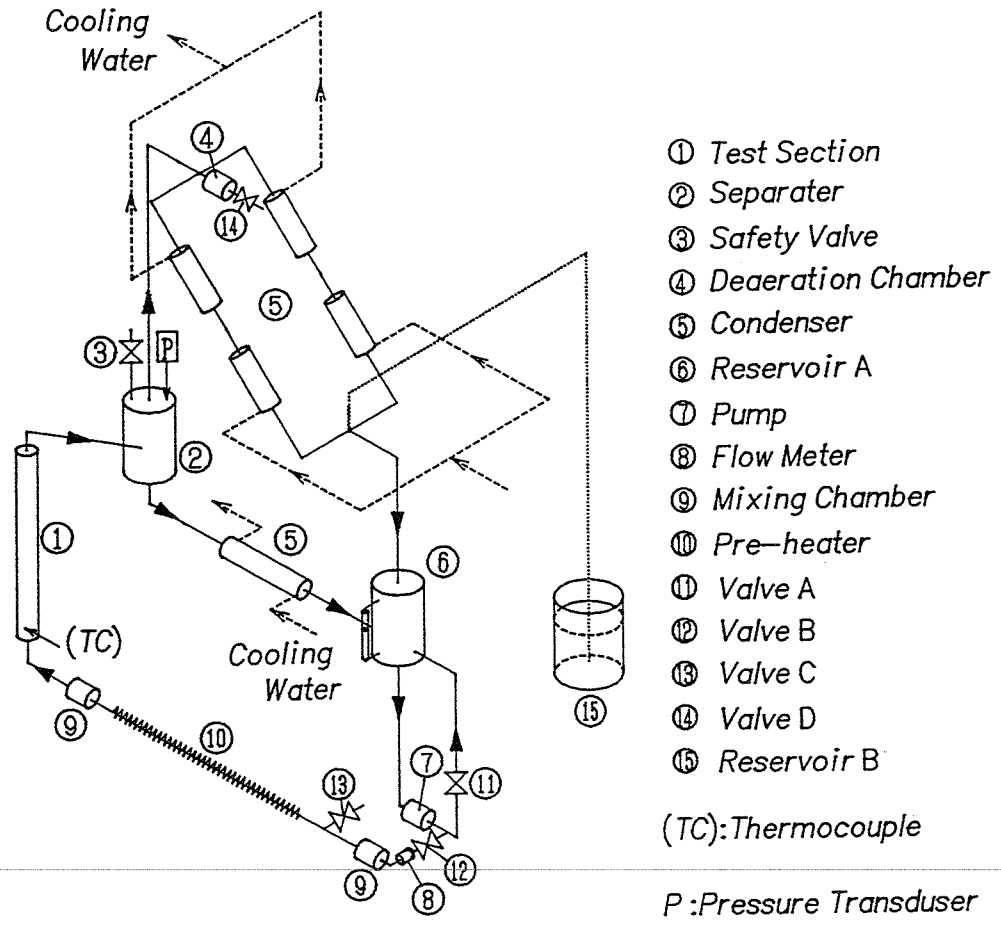

Fig.1 Schematic view of the experimental apparatus

The inner tube of the test section was used as a heater by applying direct current electric power. It was 1970 mm in length, and 16.0 mm in outer diameter. The inside of the inner tube was machined so that the thickness of the tube wall was 1.0 mm except the exit part (upper part) of the test section where the thickness increased toward the upper end to reduce heat flux there. Otherwise the heat input was limited to a considerably small value due to the occurrence of burnout near the top of the test section. The both ends of the tube were silver-soldered to the copper tubes used as power supply electrodes. The outer tube with 30.0 mm outer diameter, 26.0 mm inner diameter and 1.42 m long was made of Pyrex glass so as to observe the flow patterns throughout the heated region.

A plate type obstruction was set at the location of 1.225 m downstream of the start of heating. The geometry of the obstruction was decided so as to simulate a spacer supporting nuclear fuel rods. It is shown in the circle on the right side of Fig.2. In this paper the obstruction is referred to as the spacer. The spacer was supported by six iron pins with diameter of 3.0 mm, each threeat two different axial locations. The pins are referred to as the spacer pin. The tip of the downstream spacer pin was sharpened with an angle of about 45°. On the other hand the that of the upstream spacer pin was flat and contacted flush with the heated tube surface. We used three kinds of spacer geometry, the size of which are tabulated in Fig.2. The thickness, W , and the axial length of the spacer are always 1.0 mm and 30.0 mm, respectively. But the gap between the outer surface of the heated tube and the inner surface of the obstruction was changed from 0.5 mm to 1.5 mm. This gap is referred to as the spacer gap in this paper. There is another path in the reverse side of the spacer gap, which is referred to as the main path.

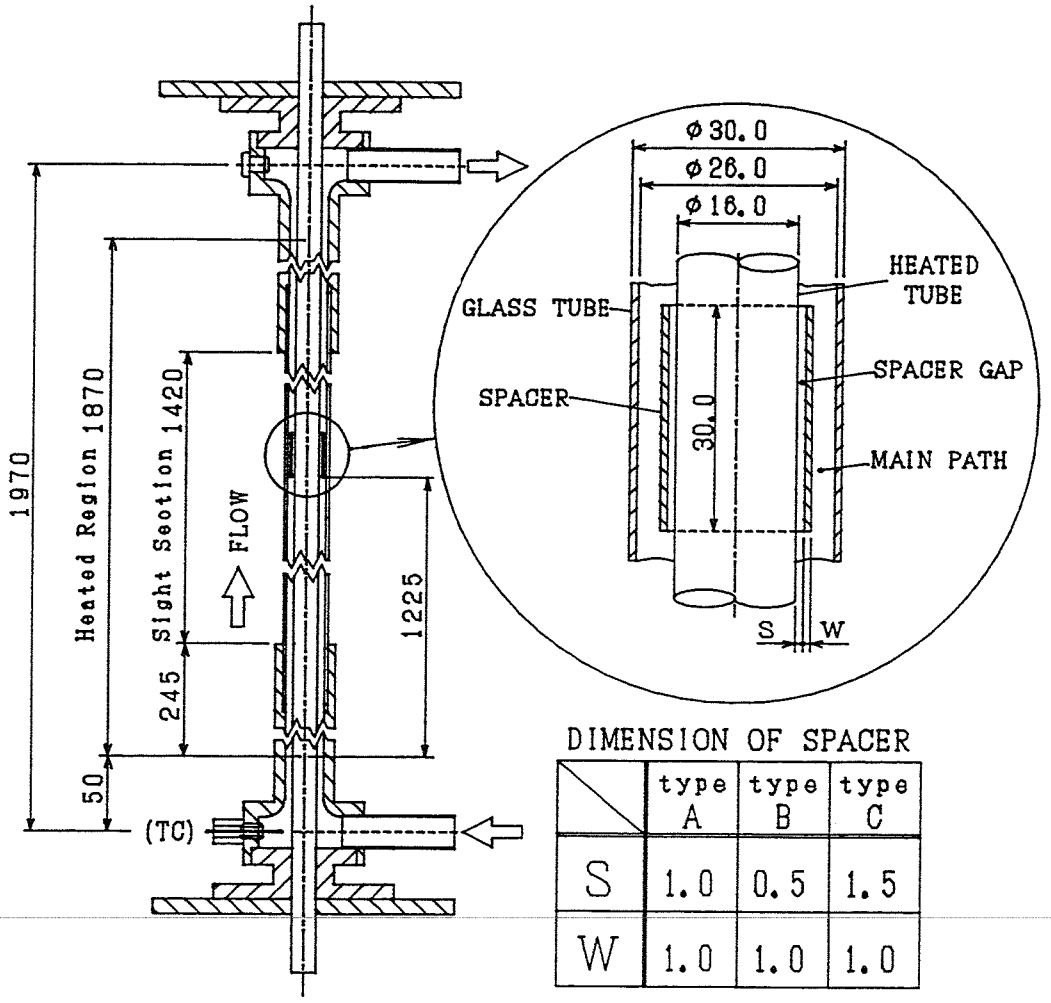

DIMENSION OF SPACER

	type A	type B	type C
S	1.0	0.5	1.5
W	1.0	1.0	1.0

Fig.2 Details of Test Section

Four thermocouples were attached on the inner surface of the heated tube beyond thin mica tape with the thickness of 0.15 mm at different locations near the upstream half part of the spacer as shown in Fig.3. The time varying outputs from the thermocouples were simultaneously recorded on a data acquisition system. By using those data we calculated the outer surface temperatures of the heated tube.

After inlet subcooling and water mass flow rate were set at desired values, heat flux was increased by small power increments. The flow pattern and the process of the formation and reweting of the drypatch was recorded on a high speed video recorder at the speed of (500 ~ 750) frames per second. A still camera was also used for the observation of the flow configuration.

The experimental conditions were decided taking into consideration the operating conditions of steam generator of a boiling water reactor (BWR) except for pressure as follows ; heat flux, q, (0 ~ 300) kW/m^2, inlet water velocity, Uin ; (0.1 ~ 0.25)m/s which corresponds to mass velocity, m ; (98.2 ~ 491.0) kg/m^2s, inlet subcooling, Tsub ; 10℃ and 20℃. The superficial vapor velocity j_G ; (0 ~ about 20 m/s).

The glass wall of the test section was not thermally insulated so as to observe the flow inside. This caused the loss of heat from the glass wall which had temperature higher than the ambient temperature. The heat loss was experimentally examined to be less than 3.3 % of the heat added.

3.EXPERIMENTAL RESULTS AND DISCUSSION

3.1 Flow patterns in the case without the obstruction

The two-phase flow patterns in the annular path were much more complex than those in a single circular tube. We, however, classified them into four typical flow patterns, which are shown in Figs.4 (a)~(d). The definition of the flow pattern is as follows ;

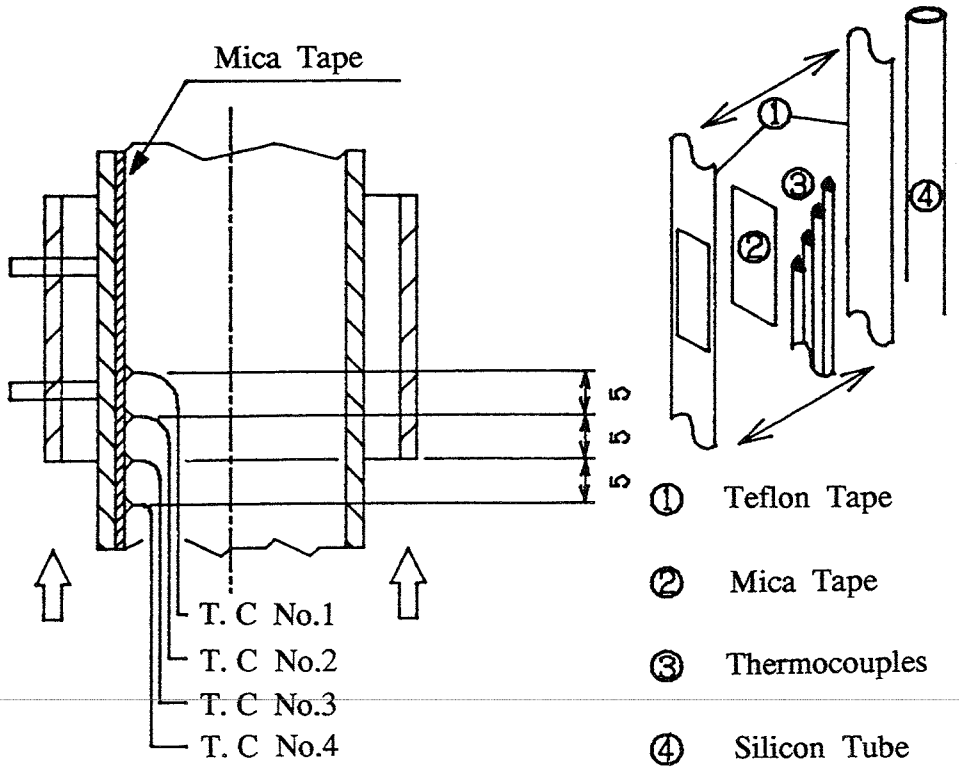

Fig.3 Locations of Thermocouples

Bubbly flow, Fig.4 (a) : The diameter of vapor bubbles is less than the gap size of the annular path, 5 mm in bubbly flow.

Slug flow, Fig.4 (b) : The diameter of large vapor bubbles becomes larger than 5mm and discrete liquid lumps are not observed in this flow regime.

Froth flow, Fig.4 (c) : The large bubbles have a dimension much larger than the diameter the heated tube in this flow regime. Discrete liquid lumps are frequently observed and the flow reversal, i.e., downward flow of liquid in a liquid film on the heated tube is remarkable.

Annular flow, Fig.4 (d): Liquid flows on both the inner wall of the glass tube and the outer wall of the heated tube in the annular flow. It must be noticed that even in this flow the flow reversal of liquid is frequently occurs although it is very short time.

The flow pattern in the test section usually changed from a single liquid flow, the bubbly flow, the slug flow and the annular flow in the order from the bottom to the top of the test section. Fig.5 shows an example of the flow pattern changing along the test section if the heat flux q is fixed, for example, along the one-dot-line in the figure. The location where we intended to set the spacer is shown by a horizontal dotted line. The thick lines indicate the boundaries between the flow patterns. The increase in heat flux, q, corresponds to the increase in the generation of vapor mass flow rate.

Under some experimental conditions, drypatches or dryout of liquid film, were generated on the heated tube wall. They, however, disappeared soon after the thick liquid film or large waves covers the drypatches. That is, the drypatch did not exist for a long time, but it is repetition of dry and rewet of the heated tube wall.

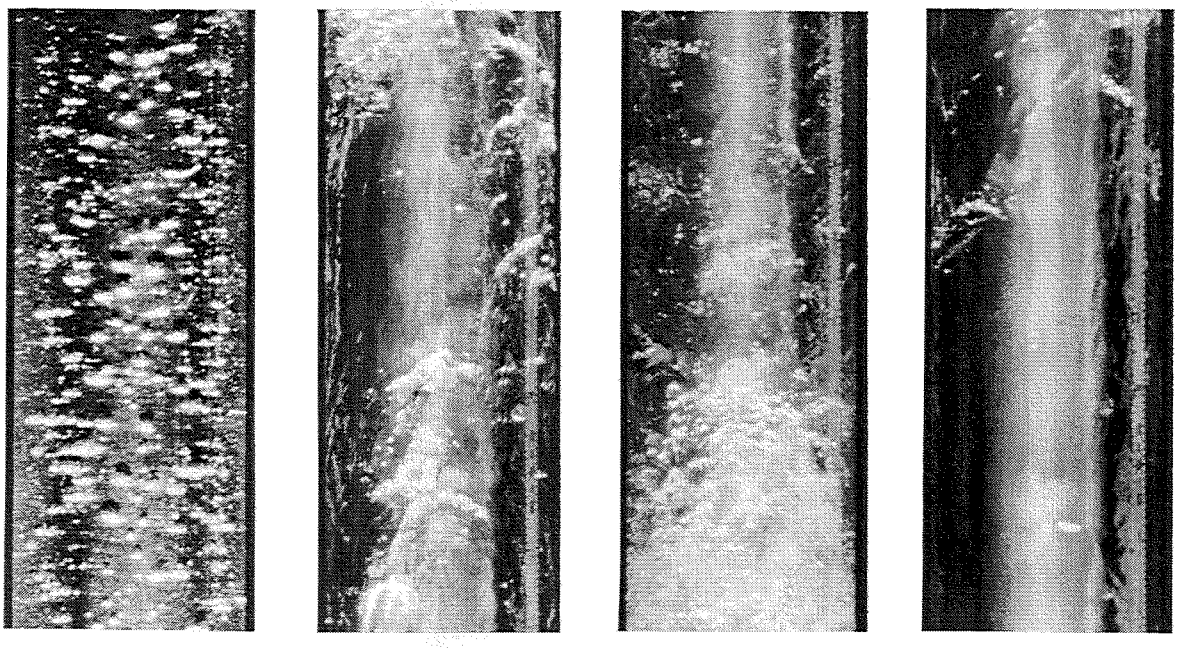

(a) Bubbly Flow (b) Slug Flow (c) Froth Flow (d) Annular Flow

Fig.4 Flow patterns (without spacer)

There are two isolated shadowed areas in Fig.5. They indicate that drypatches were generated in those regions. But the locations of drypatch was not fixed at special points. The experimental conditions of those areas are similar to those pointed out in the previous work[2], except the area close to the top of the heated region. As mentioned before the heated tube used in the present experiment was designed so as to decrease heat flux in the exit part of the heated region, because the maximum heating was always limited by the incipient burnout at the exit region in the previous work[2]. Therefore, in the present experiment the region of drypatch formation was confined in the isolated area.

As clearly seen in Fig.5, the occurrence of drypatch is closely related to the flow pattern, the froth flow and the annular flow. It is noticed that in the transition region between the froth flow to the annular flow the drypatch was not occurred. This result is also the same as that in the previous work[2].

3.2 Drypatch formation in the case with the spacer

Figs. 6 (a) ~ (d) show the flow pattern near the spacer. Fundamentally the flow pattern did not change even if the spacer was inserted. In detail, however, we noticed following interesting behaviors of bubbles and liquid flow from each figure of (a) ~ (d) as follows. In Fig.6 (a) ; the velocity of the bubbles with (1 ~ 2) mm diameter is higher in the main path than in the spacer gap, and the velocity ratio is nearly equal to the area ratio of the two paths. In Fig.6 (b) ; bubbles generated inside the spacer gap grow upstream, i.e., downward, and interrupt liquid from flowing into the spacer gap. In Fig. 6 (c) ; bubbles generated in the spacer gap grow up very quickly and expand up to the outside of the spacer gap. And accordingly, the liquid can not flow into the spacer gap. In Fig.6 (d) ; instead of small bubbles, large part of the spacer gap is occupied by vapor while discrete liquid lumps and liquid film are also noticed on the solid surface in froth flow. This situation is not largely changed even if the flow pattern changes to the annular flow.

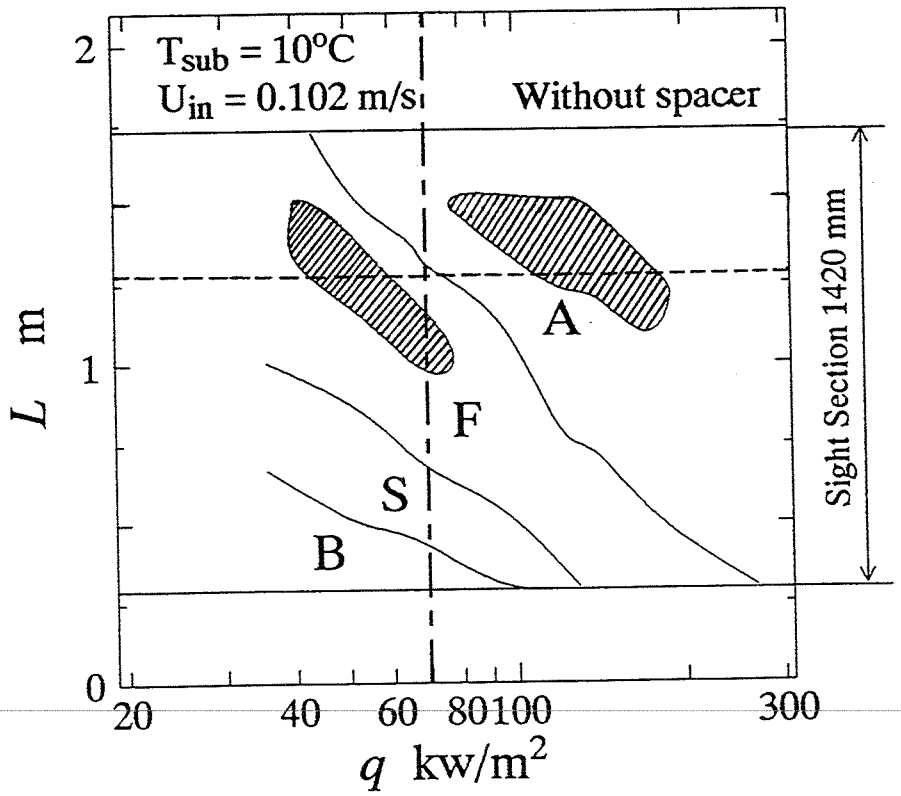

Fig.5 Flow pattern changing along the test section (without spacer)

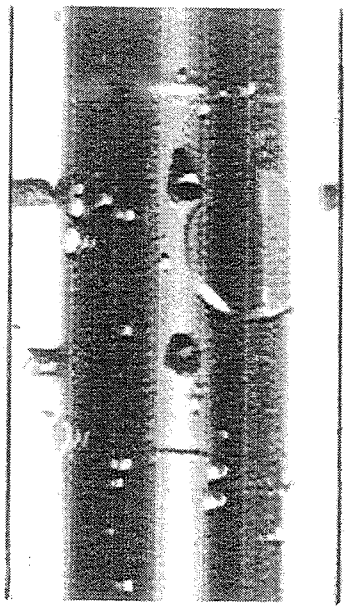

(a) Bubbly Flow
j_G = - m/s
j_L = 0.102 m/s
x = 0.000
q = 22.0 kW/m^2

(c) Slug Flow
j_G = 1.498 m/s
j_L = 0.101 m/s
x = 0.009
q = 50.2 kW/m^2

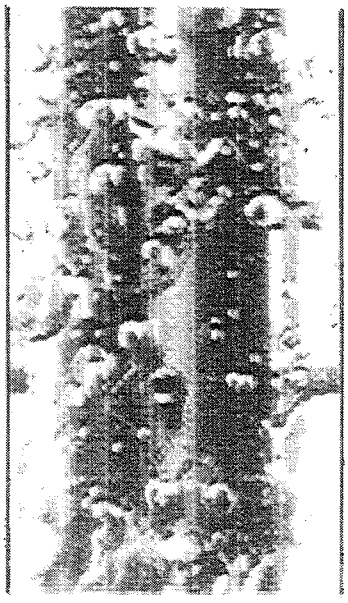

(b) Bubbly Flow
j_G = - m/s
j_L = 0.102 m/s
x = 0.000
q = 36.9 kW/m^2

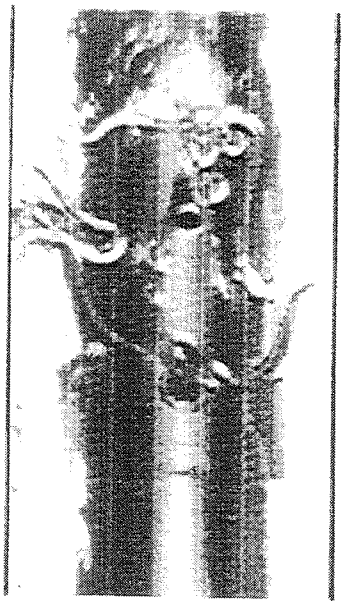

(d) Froth Flow
j_G = 5.095 m/s
j_L = 0.993 m/s
x = 0.031
q = 74.0 kW/m^2

Fig.6 Flow patterns (with spacer, Spacer ; Type A, Tsub = 20℃, Uin = 0.102 m/s)

In the froth flow, the localized incipient drypatch was observed at the spacer pin in the spacer gap as shown by shadowed area in Fig.7 (a). The existence of the drypatch was very shot. this type of drypatch formation is referred to as IDR (inside dry and rewet) in this paper.

If the heat flux increased and the flow pattern became the annular flow, the scale of the drypatch became large and extend outside of the spacer gap as shown in Fig.7 (b). This type of drypatch formation is referred to as UDR (Upstream side Dry and Rewet). The relationship between the drypatch formation and the flow pattern near the spacer is shown in Fig.8. The area map of the generation of UDR is shown in Figs.8(a) for subcooling of Tsub = 10 ℃and (b) for Tsub = 20 ℃. The increase of the vapor velocity j_G corresponds to the increase of heat input, or heat flux, q. The flow pattern of these maps were identified near the spacer. This shows clearly that the location of drypatch formation is limited at the region just upstream (downside) of the spacer as well as on the downward side of the spacer gap in the limited flow pattern, annular flow. In the case of the ring type obstruction the alternate dry and rewet of the heated surface frequently occurred also in the area downstream of ring type obstruction where there is no gap between the heated tube and the ring. In the case of ring type obstacle liquid does not supplied from the upper part of the ring and the thinning of the liquid film is caused by the drainage of the liquid film in the region just upstream of the ring. And accordingly ADR begins under the condition of smaller vapor velocity than in the case of the spacer type obstruction used in the present experiment. That is the ADR is remarkable in the froth flow region in the case of the ring type obstruction. The process of the formation of drypatch and its disappearance in UDR will be discussed later.

The location of drypatch formation along the heated tube is shown in Fig.9. It is noticed that the generation of UDR is limited in the annular flow region and in the area upstream side of the spacer including the spacer gap as mentioned above.

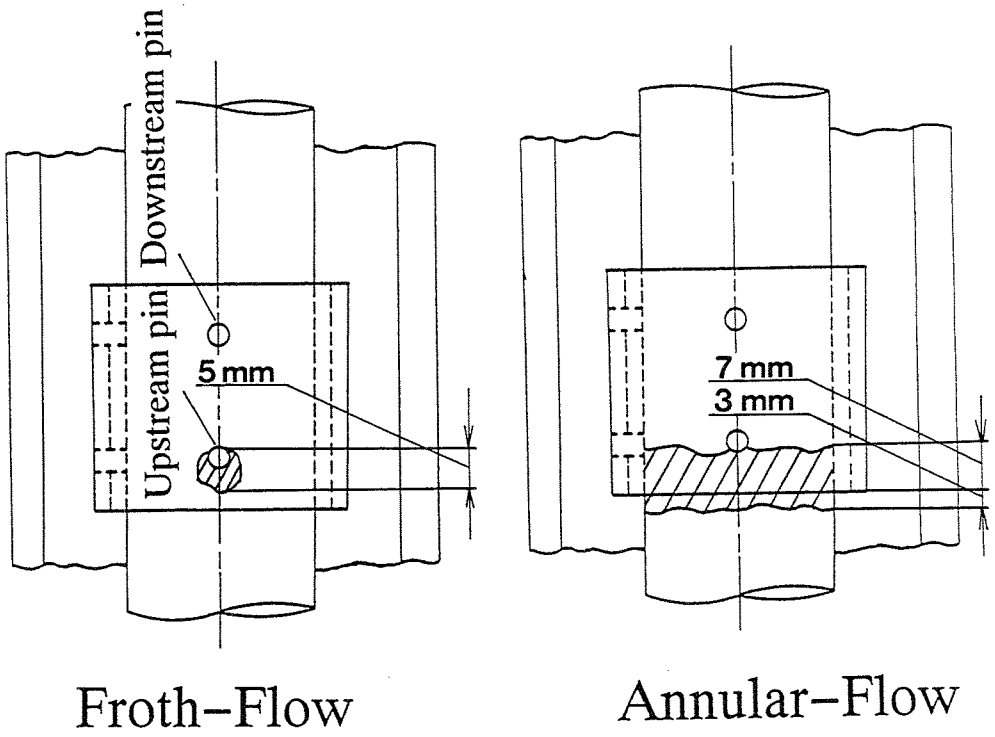

Fig.7 Pattern of drypatch

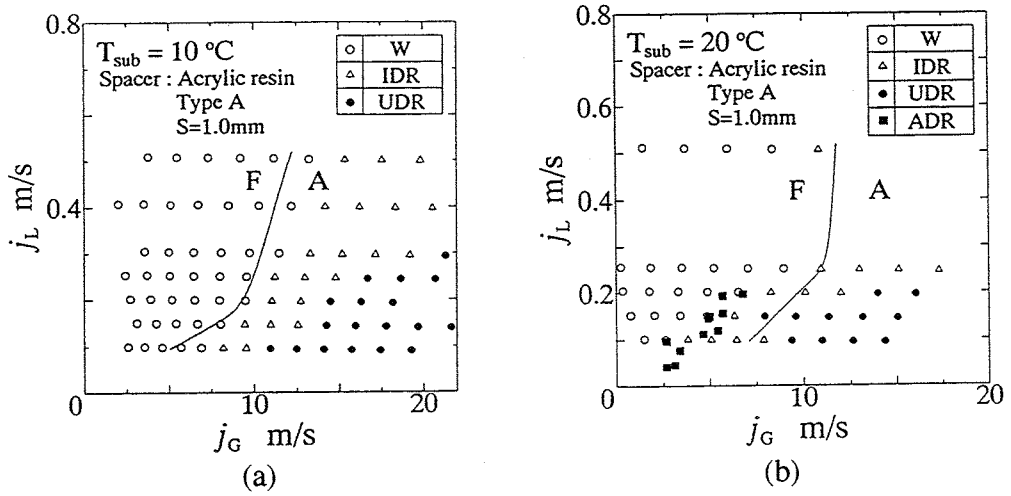

Fig.8 Flow map observed at the spacer

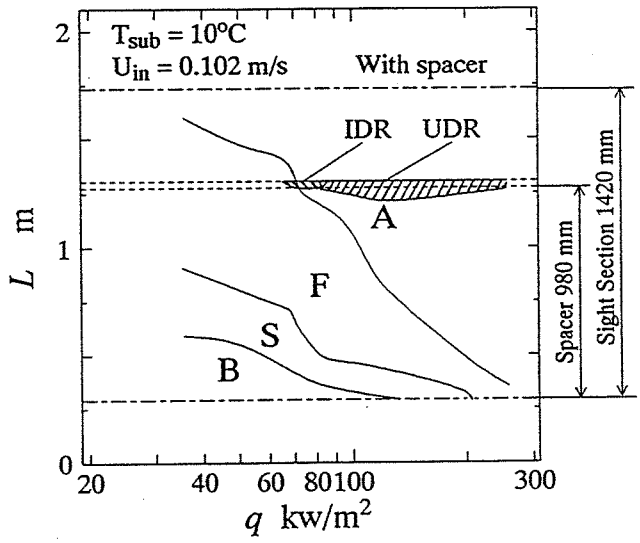

Fig.9 Flow pattern changing along the test section (with spacer)

3.3 Process of drypatch formation and rewet in UDR

Figure 10 shows a sequence of photographs of the drypatch formation and rewet process in the case of UDR at every 25 frame of photos taken by a high speed video recorder at the speed of 750 frames per second. Before we discussed Figs.10 in detail it is better to describe the over all behavior of liquid flow observed when UDR was remarkable. First of all, it must be noticed that flow reversal, i.e., the downward flow of liquid, frequently occurred even in annular flow although it is in short time[5]. Second, we noticed that a wake of the spacer continuously existed in the area behind, i.e., just above the spacer. Liquid impinged on the heated wall from the jet like main stream passing through the main path. And the liquid flowed downward on the heated wall into the spacer gap passing by the wake region. Therefore both the upper part of the spacer gap and the region above the spacer were always covered with full of water.

On the other hand, in the downward part of the spacer gap the thinning of liquid film was quickly developed by the interruption of the downward flow of liquid caused by the spacer pins. As a result drypatch occurred at first at the point when the spacer pin contacted with the heated tube surface as follows. In frame 1 a liquid lump bridges over the spacer gap at the spacer pin. Although the thick liquid film can be seen to accumulate just downstream (upside) of the spacer and any drypatch can not be noticed there. On the other hand, small drypatches appears just below the upstream spacer pin.

This drypatch slowly grows downward a little. After that a considerable large drypatch instantaneously appeared on the circumference of the heated tube near the downward edge of the spacer as shown by a gray color in frame 2 just after the liquid wave is forced to move to the downstream-side-pin by up-going vapor flow in the period of 0.03 second. Then a somewhat thicker liquid waves again come down to the upstream-side-pin from frame 2 to frame 3. And accordingly the area of the drypatch is reduced for a short time in the spacer gap but continues to keep almost the same size as the original one as can be seen by the gray area. From frame 4 to 6 the liquid lump is again blown up by a vapor flow and the drypatch continues to expand out of the spacer gap into the upstream of the spacer. In this sequence of the photos the drypatch upstream of the spacer is biggest in frame 8. Through frame 7 to 9 it is noticed that considerable amount of liquid which passed through the main path impinges on the heated tube surface in the area downstream of the spacer, where wake of the both spacer and spacer gap prevails and flows downward. This liquid flow supplies liquid in the both regions, downstream of the spacer and inside the upper part of the spacer gap, and accordingly drypatch does not occur in those regions.

In frame 9 a considerably large up-going waves reaches at the upstream of the spacer, the drypatch, however, does not easily disappear in the area just upstream of the spacer because the wall temperature must be high due to the dryout of the liquid film on the surface for a rather long period, about 0.3 seconds counted from frame 1. As a result many droplets are entrained from the wave crest at the boundary of the drypatch which is interrupted from going up into the spacer gap. The situation shown in frame 9 can not continue long, and in very short time whole drypatch area is rewet when a large liquid surge continues to stay around the spacer. If we increases the heat flux more, the burnout of the heated tube should take place just upstream of the spacer.

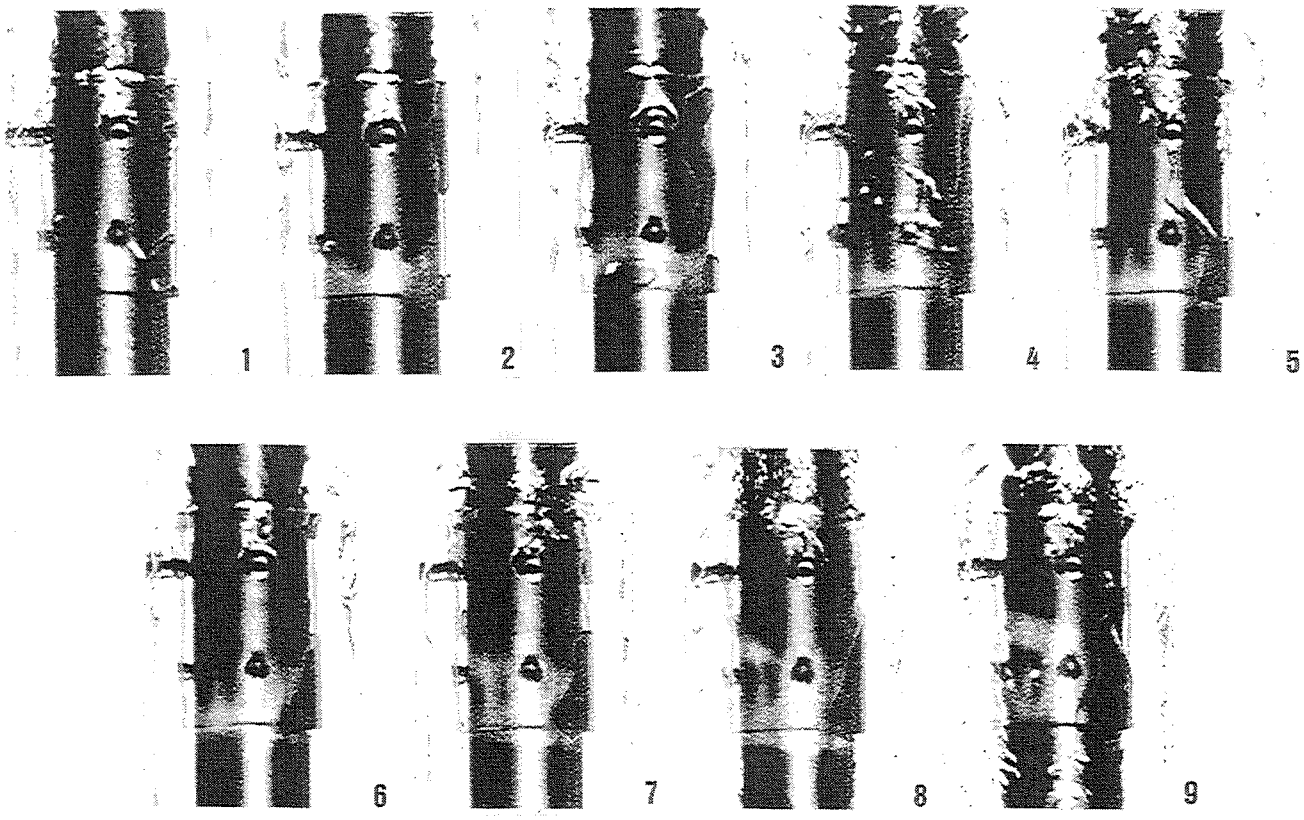

Spacer; Type A (Acrylic resin) j_G = 7.879 m/s, j_L = 0.098 m/s
Tsub = 20 ℃, Uin = 0.102 m/s x = 0.047, q = 92.4 kW/m^2

Fig.10 Process of drypatch formation in UDR

3.4 The effect of size of the spacer gap

We investigate the effects of the size of the spacer gap, S, on the formation of drypatch by using three kind of brass spacer, type A, B and C which are already shown in Fig.2. Figs.11 (a)~(c) show the flow conditions (j_G and j_L) under which UDR occurs, (a) being for S=1.0 mm, (b) for S=0.5 mm and (c) for S=1.5 mm. The mark ● means the generation of UDR and the mark ○ means that the heated tube wall is always covered with liquid. It is noticed that the larger the gap, the broader the area where drypatch occurs. Figs.12 (a) ~ (c) shows the frequency of the generation of UDR under the conditions of the inlet liquid velocities being 0.1, 0.15 and 0.20 m/s, with the different spacer gap size ; S. In general, at first the frequency of the drypatch generation, N, increases with the increase of j_G or the heat flux q, until N takes a maximum value which depends on the liquid inlet velocity, and then decreases. The larger the gap size, the more frequent the drypatch occurrence. This trend is consistent with the results shown in Figs.11 (a) ~ (c). The detailed observation of the flow configuration of liquid near the spacer reveals that the larger amount of liquid adheres on the heated surface in the spacer gap in the case of the smaller spacer gap, the Type B spacer.

The reason why the drypatch is easy to generate in the case of the larger gap size is considered as follows. As already described before the necessary condition of the drypatch formation is the occurrence of the reverse flow of liquid, i.e., the downward flow of liquid due to gravity even in annular flow. The quick thinning of liquid film on the heated tube is caused by the drainage of liquid occurred in the period of the reverse flow. Although the existence of the spacer pin plays and important role to interrupt liquid from going down through it and supplying water in the area below\ the spacer pin and also upstream of the spacer, the most important factor to cause the drypatch formation in the upstream side of the spacer is the existence of the reverse flow.

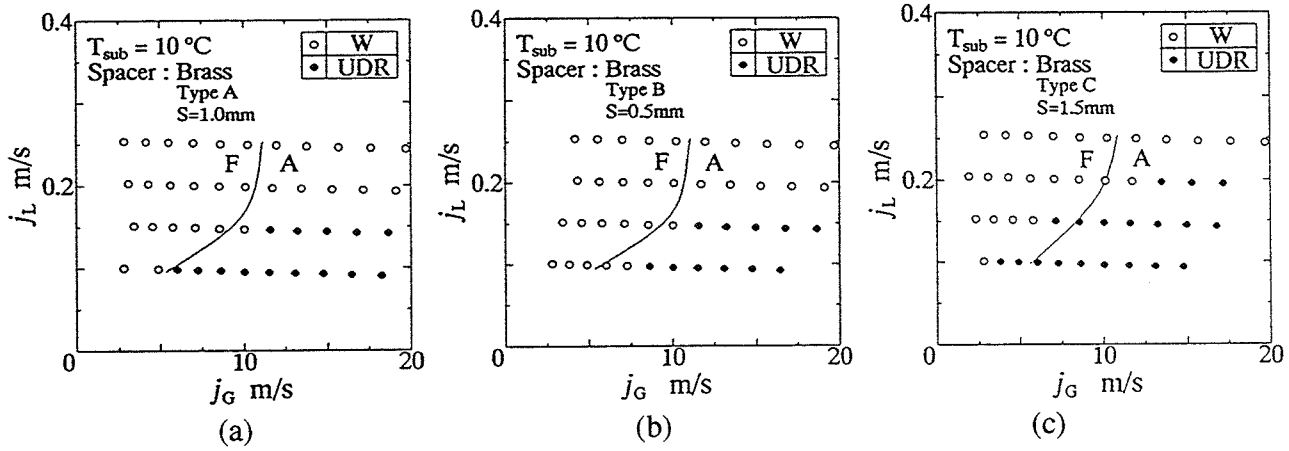

Fig.11 Regime of the generation of UDR

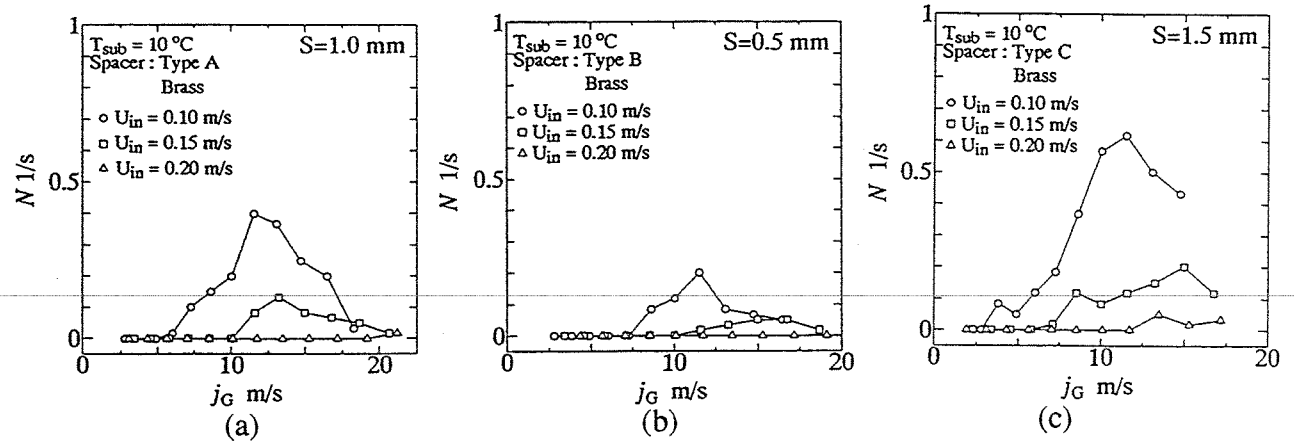

Fig.12 Frequency of the generation of UDR

According to the the careful observation of the reverse flow by using high speed video recorder, we noticed that the downward liquid flow is easier in the case of a larger spacer gap. And accordingly the drypatch is easier to occur in the case of the Type C spacer. Also this fact it must be remember that the reverse flow from the upper part of the spacer is interrupted twice, i.e., by the two spacer pins. From this point of view it is considered that spacers designed so that the spacer pins do not vertically in line with each other should have better performance from a view point of preventing the occurrence of dry patches.

The effect of the material of the spacer on the temperatures of the heated wall, T.C No.1 and TC No.4, is shown in Figs.13 (a) and (b). ΔT means the difference between the outer surface temperature of the heated tube and the saturation temperature which corresponds to the system pressure. It is clearly seen that the temperature becomes lower in the case of the brass spacer which has larger thermal conductivity than acrylic resin of which the other spacer is made. This result means that the spacer acts a roll of cooling fin as well as the flow obstruction causing the drypatch formation.

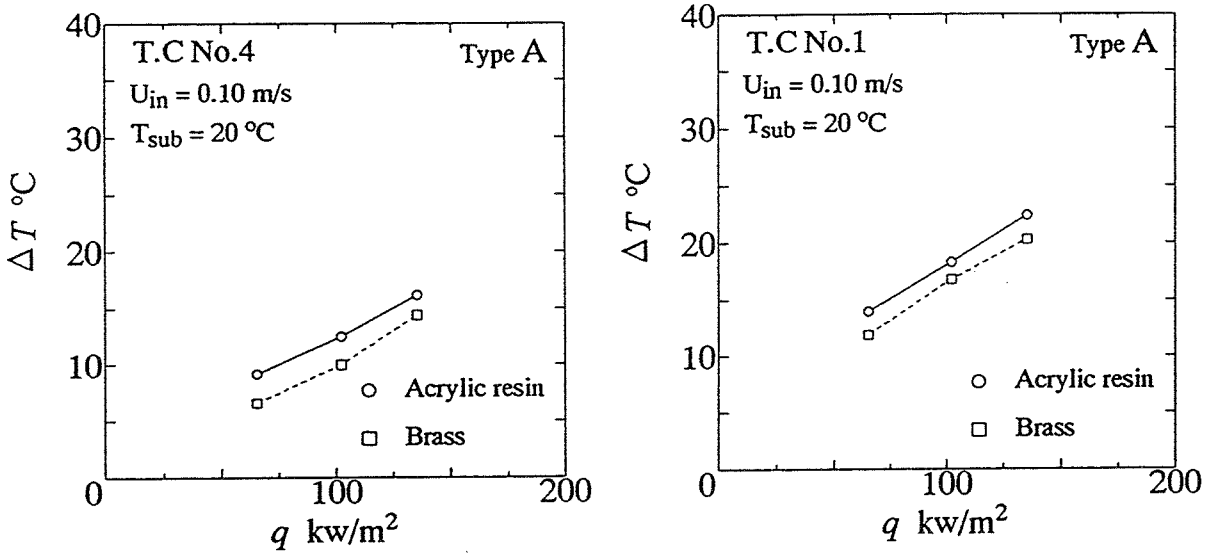

(a) Location of thermocouple (No.1)

(b) Location of thermocouple (No.4)

Fig.13 Temperatures of the heated wall

4.CONCLUSIONS

We experimentally investigated the effects of flow obstruction simulating a spacer of fuel rods of a BWR on the drypatch formation on the heated surface. As a result the followings are obtained.

[1] Drypatches occurs at the limited region, i.e., on the upstream part of the spacer gap and just upstream of the spacer in the limited flow pattern the annular flow region, in the instance when liquid film flows downward due to gravity.

[2] Although the drypatches disappears soon after large wave comes to the spacer, the burnout of the heated tube is probable to occur when the heat flux increases more by even a small amount, and the period of the existence of drypatch becomes longer.

[3] The spacer pin plays an serious role in thinning the liquid film due to the interruption of liquid from supplying liquid and spreading to the region just below the pin, where the incipient drypatch appears.

[4] The spacer as well as the spacer pin can be a fin cooling the heated tube wall at the point the spacer pin contacts.

NOMENCLATURE

j_G	: Superficial Velocity of Gas (Vapor)	m/s
j_L	: Superficial Velocity of Liquid (Water)	m/s
L	: Distance (of Flow direction) from the Inlet Section of Heating Tube	m,mm
m	: Mass Velocity	kg/m^2s
N	: Frequency of the Generation of Drypatch	1/s
q	: Heat Flux	kW/m^2
S	: Spacer Gap	mm
Tsub	: Inlet Subcooling	°C
ΔT	: Difference between Heating Tube Surface Temperature and Saturation Temperature of Water	°C
Uin	: Inlet Mean Velocity of Water	m/s

Flow Pattern

A : Annular Flow
B : Bubbly Flow
F : Froth Flow
S : Slug Flow

Subscript

G : Gas Phase
L : Liquid Phase

REFERENCES

[1] S.Yokobori, M .Ohta, H.Terasaka and S.Morooka, " A phenomenological Study on the Dryout Mechanism in Fuel Rod ", Fourth International Topical Meeting on Nuclear Reactor Thermal-Hydraulics, Nureth-4(1989), 1054-1061.

[2] K.Sekoguchi, O.Tanaka, T.Furukawa, S.Esaki and T.Fukano, " Experimental investigation of the alternate dry and rewet (ADR) on heated tubes with and without an obstruction in flow boiling ", Proc. 6th IHTC Vol. 4, (1978-8) 355-360.

[3] Shiralkar, B.S. and Lahey, Jr.R.T., " The effect of obstacles on a liquid flow ", Trans. ASME, J. Heat Transf., Vol. 95, No. 4, (1973) , 528-533.

[4] T. Fukano, T.Tanaka, K.Kutaragi and M.Kanamori, " The effect of a flat-plate-type obstacle on a thin liquid film flow ", Dynamics of Two-phase Flow, Begel house Inc., (1992), 161-183.

[5] Fukano,T., Kawakami,Y., Itoh,A., and Tominaga,A., " Mechanism of the Disturbance Wave Generation in a Vertical Up- and Down-ward Gas-Liquid Two-Phase Annular Flow ", Transient Phenomena in Multiphase Flow, Hemisphere, (1988), 435-452.

CHARACTERISTICS AND BEHAVIOR OF INTERFACIAL WAVE ON LIQUID FILM IN VERTICALLY UPWARD AIR-WATER TWO-PHASE ANNULAR FLOW (Further Investigation)

K. Ohba, M. Yamaguchi, and K. Nakamura

Department of Mechanical Engineering
Kansai Unversity
3-3-35 Yamate, Suita, Osaka 564, Japan

ABSTRACT

Although knowledge of local and temporal behavior of the interfacial waves on liquid film in two-phase annular flows is very important for obtaining the macroscopic characteristics of flow and heat and mass transfer in such flows, the behavior of individual wave has never directly been obtained because of the lack of an appropriate measurement method. Under such a background, an experimental analysis was made on the behavior of interfacial wave on liquid film in upward air-water two-phase flow through vertical tubes. A pigment luminance technique [1] to visualize the interfacial wave was developed and used in combination with a twin fiber optic liquid film sensor [2] capable making simultaneous measurements of the local thickness and the interfacial wave velocity of liquid film at the crest and the through. A high speed video camera system and a picture analysis system were used to obtain quantitative data from the picture visualized. The vertical tube used in this experiment was a plexiglass tube of about 4.3 m length and 29 mm in inner diameter. A section of mixing air with water consisted of multiholes drilled on the tube wall and encircling the tube cross section, from which water was slowly injected into the air flow to form liquid film. A measurement position was located at 3.5 m downstream, i.e. upward from the air-water mixing section. The white pigment used consisted of spherical particles of titanium oxide having around 5 micrometer in diameter and around 4 g/cm^3 in density. This was intermixed into water by around 0.01% in volume concentration.

As a result, the temporal and local motion of the waves propagating on liquid film was able to be visualized and the temporal and local wave forms were measured. Typical examples of the interfacial waves visualized by this pigment luminance method are shown in Fig. 1. These pictures were printed out from the CRT display of the high speed video tape recorder, and present a change in wave patterns each 10 millisecond. In this Figure, relative brightness could be almost proportional to the thickness of the liquid film [2]. Hence, bright parts correspond to thick film, and dark parts correspond to thin film.

These waves were classified into three types, i.e. (a) a base wave, (b) a fast wave, and (c) a disturbance wave. This classification method is a little different from the ordinary method in which waves are classified into two types, i.e. a ripple wave and a disturbance wave. The ripple wave is equivalent to the base wave in the present classification, and the disturbance wave in the ordinary classification corresponds to a lump of the fast wave and the disturbance wave in our classification together. Under the present experimental conditions, it was very natural to classify them into three types, but not two types, because the fast wave and the disturbance wave showed a clearly different characteristics from each other.

The base wave occupied the most part of the air-water interface and had an imbricate pattern propagating with the lower speed. The typical thickness of the liquid film at the crest and the through were around 0.1 mm and 0.05 mm, respectively, although they varied depending on the volumetric fluxes of air and water.

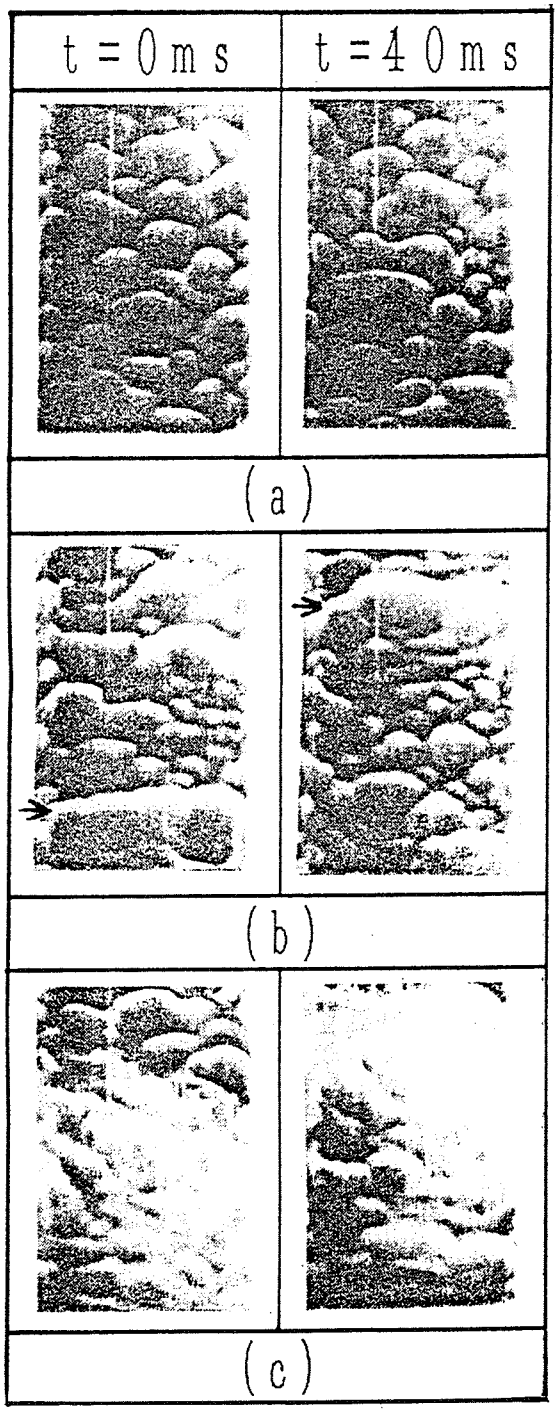

Figure 1.

The fast wave had a wave front encircling the tube cross section and propagated with the highest speed of the three when jl is small. Its speed was about twice higher than that of the base wave. Its wave height, i.e. the film thickness at the crest was about 1 mm. It always incorporated the base wave going in front of it while propagating. It was a single wave with high crest and narrow wave length.

The disturbance wave was a group of several kinds of waves which always agglomerated and disintegrated. It had a large wave width containing droplets and bubbles. Its speed was about five times faster than that of the fast wave when jl was great, while the former was a little slower than the latter when jl was small.

These video tapes were fed to a picture analysis system to convert the spatial luminance pattern into a spatial pattern of liquid film. An assumption of proportionality of the luminance to the film thickness was adopted. Thus, we obtained spatial and temporal pattern of liquid film thickness. From an analysis of these pattern, we obtained wave length, wave velocity, wave period, wave height etc., i.e. a detailed behavior of the individual wave.

From the above measurements and observations, it can be said regarding the mechanism of the generation of various waves that all the wave starts from the basis wave, and that a large amplitude wave with high speed swallows waves with low speed and grows into the fast wave, and that the fast wave is incorporated into the disturbance wave. At least, the disturbance wave gets grown to have much higher speed, and the fast wave vanishes.

References

[1] K. Ohba and K. Obata, Proc. 9th National Symposium on Multiphase Flow, (1990) p.1 (in Japanese).

[2] K. Ohba et al., Japanese Journal of Multiphase Flow, Vol.3, No.2 (1989) pp.50-66 (in Japanese).

NOTE: *This paper had not been received before the Proceedings were assembled. If received on or before August 23, 1994, handouts will be given to each participant of the Symposium.*

INSTABILITY MECHANISMS OF LIQUID SHEETS AND JETS

F. Durst, N. Alleborn and H. Raszillier

Universität Erlangen–Nürnberg
Lehrstuhl für Strömungsmechanik
Cauerstr. 4, D-91058 Erlangen, Federal Republic of Germany
Tel.: (09131) 85–9501, Fax: (09131) 85–9503

ABSTRACT

Many technical processes related to heat and mass transfer, to combustion, spray painting, drying, and chemical reactors rely on the production of a dispersive liquid phase in a gaseous environment by a decay mechanism of liquid sheets or jets. The efficiency of this kind of processes is strongly dependent on the physical properties and the behaviour of the droplets building up the dispersive liquid phase, which in turn are a consequence of the decay mechanisms of the liquid sheet or jet used in their production. The paper reports a systematic linear stability analysis of a hollow cylindrical (viscous) liquid sheet surrounded on both sides, inner and outer, by nonviscous fluids (gases) of different densities, in relative axial motion to it. The dispersion relation giving the absolute and convective instability mechanisms of the sheet is derived. It exhibits the dependence of the stability on several dimensionless quantities characterizing the geometry, the properties of the media and the flow. The stability behaviour of the sheet is investigated numerically by a special continuation algorithm, by which the solution branches of the dispersion relation, relevant for the stability information, can be traced. The results give a stability picture which covers the whole range of sheets between the cylindrical jet and the plane liquid curtain.

1 INTRODUCTION

In many branches of technology atomization of fluids is part of a technological process. This happens e.g. with ink jet printers, with spray coatings or with injection nozzles for i.c. engines. The physical phenomenon common to these processes is the destabilization of a liquid jet or film, in order to generate droplets, preferably of a given size.

On the other side there is the problem in coating technology to keep a liquid film or curtain stable in a wide range of physical, geometrical or operation parameters of the coating procedure.

The generation of droplet (sprays) by destabilization of a cylindical jet and the stabilization of a curtain can be embedded, as two different views, into a broader stability problem, namely that of a hollow cylindrical jet, for which they represent suitable extreme situations. The embedding allows to reveal the physical connection between them and helps to get a deeper insight, by connecting them also to other instability phenomena, like e.g. the Kelvin-Helmholtz instability.

In the present paper a linear stability analysis of the hollow cylindrical jet will be described. The literature on the stability of (full) jets goes back to Rayleigh [9] and includes the fundamental paper of Weber [11]. Work of Crapper and Dombrowski [5] and, recently, of Lee and Chen [6] and Camatte [3] makes some steps toward an extension to the hollow jet. The main problem thereby remains the considerable complexity of the formal result, which makes it very difficult on the one side to avoid errors during the calculations and on the other side to extract from it the relevant physical information. Especially viscosity causes considerable trouble and is, therefore, essentially ignored in this work. In the present paper these problems are tackled by the massive use of symbolic computation tools (MAPLE) in the analytic part of the work, the derivation of the dispersion relation which encodes the stability information, and by a special numerical algorithm (parameter continuation) for its physical decoding.

2 THE HOLLOW CYLINDRICAL JET

2.1 Statement of the Problem and Parameters

A cylindrical fluid film infinitely long in the z-direction, of thickness h, is considered (Fig. 1). The inner radius of the hollow cylinder is a, its outer radius then $b = a + h$.

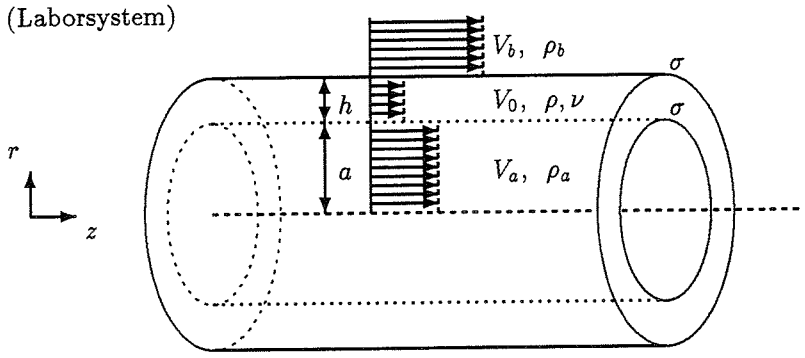

Figure 1: Hollow cylindrical jet in air

The film consists of an incompressible, viscous fluid (liquid) of density ρ and dynamic viscosity μ. The surface tension is considered to have the same value σ for both interfaces. The inner and outer spaces of the hollow cylinder are filled by incompressible, nonviscous fluids (gases) of densities ρ_a and ρ_b, respectively.
The velocities of the fluids will be referred to cylinder coordinates with local unit vectors $(\vec{e}_r, \vec{e}_\varphi, \vec{e}_z)$:

$$\vec{u} = u\,\vec{e}_r + v\,\vec{e}_\varphi + w\,\vec{e}_z. \tag{1}$$

In the laboratory frame (L) the unperturbed flow is characterized by block profiles of the velocities and constant pressures:

$$\vec{u}_0^{(L)}(r,z,t) = V\,\vec{e}_z^{(L)}, \tag{2}$$
$$p_0(r,z,t) = \text{const.} \tag{3}$$

for the liquid film and

$$\vec{u}_{0,j}^{(L)}(r,z,t) = V_j\,\vec{e}_z^{(L)}, \tag{4}$$
$$p_{0,j}(r,z,t) = \text{const.} \quad (j = a,b) \tag{5}$$

for the gases a and b.

The problem is conveniently analyzed in the rest frame (R) of the liquid film, which moves with velocity V relative to the laboratory system (L). In this frame the three unperturbed velocity profiles are

$$\vec{u}_0^{(R)}(r,z,t) = 0, \tag{6}$$
$$\vec{u}_{0,j}^{(R)}(r,z,t) = U_j\vec{e}_z^{(R)}, \tag{7}$$

where $U_a = V_a - V$ and $U_b = V_b - V$. In the following the index (R) of the magnitudes referring to the rest frame of the film will be omitted.

2.2 Linear Stability Analysis

The stability against infinitesimal perturbations will now be analyzed, whereby for simplicity their axial symmetry $(\partial/\partial\varphi = 0)$ will be assumed.

Equations of Perturbation The perturbations of the velocities and pressures in the three flow domains obey linear equations, to which the corresponding interface conditions have to be added:

- the kinematic conditions of the free interfaces
- the dynamic condition of tangential stress vanishing at the interfaces
- the dynamic (normal) condition of capillary pressure jump at the interfaces
- the vanishing of the perturbations far away from the cylinder axis
- the regularity of the perturbation on the axis

2.3 Solution of the Perturbation Equations

Complexification The equations of perturbation, as well as their boundary conditions, are homogeneous, real and linear, with constant coefficients. They can therefore be conveniently complexified in order to facilitate their solution. The (complex) solution is a superposition of exponential modes of the form

$$\begin{aligned}
\vec{u}_c(r,z,t) &= \vec{u}(r)e^{\omega t+ikz} && (8)\\
p_c(r,z,t) &= p(r)e^{\omega t+ikz} && (9)\\
\vec{u}_{c,j}(r,z,t) &= \vec{u}_j(r)e^{\omega t+ikz} && (10)\\
p_{c,j}(r,z,t) &= p_j(r)e^{\omega t+ikz} && (11)\\
\eta_{c,j}(z,t) &= \eta_{0j}e^{\omega t+ikz}; \quad (j=a,b), && (12)
\end{aligned}$$

with complex ω and k, for the perturbations of the velocities, the pressures and the interfaces, respectively.

For the implementation of the conditions at infinity the sign of $\mathrm{Re}\{k\}$ turns out to be important. This can be taken care of either by direct carefull analysis or by the recognition that due to the complexification the information is invariant with respect to the operation

$$\omega \to \omega^*, \quad k \to -k^*, \tag{13}$$

so that only one (complex) halfplane of k (or of ω, respectively) is of physical relevance.

The derivation of the dispersion relation

$$D(\omega,k)=0 \tag{14}$$

describing the stability of the modes is skipped here; it is given in detail in [1].

Dispersion Relation This relation takes the rather complicated form

$$\begin{aligned}
\omega^4 &\left(HG+\frac{1}{k^2abM(ka,kb)^2}\right) && +\\
\omega^3 &\left(HB+GD+\frac{8\nu k^2}{k^2abM(ka,kb)^2}\right) && +\\
\omega^2 &\left(HC+BD+GE+\frac{8\nu^2k^4}{k^2abM(ka,kb)^2}\left(3-\frac{M(ka,kb)}{M(la,lb)}\right)\right) && + \qquad (15)\\
\omega &\left(CD+BE+\frac{32\nu^3k^6}{k^2abM(ka,kb)^2}\left(1-\frac{M(ka,kb)}{M(la,lb)}\right)\right) && +\\
&\left(CE+\frac{16\nu^4k^8}{k^2abM(ka,kb)^2}\left(1-\frac{M(ka,kb)}{M(la,lb)}\right)^2\right) && = 0,
\end{aligned}$$

with the coefficients

$$B = 2ikU_a\frac{\rho_a}{\rho}\frac{I_0(ka)}{I_1(ka)} + 2\frac{\nu k}{a}\left(2ka\frac{X(ka,kb)}{M(ka,kb)} + 1\right), \tag{16}$$

$$D = -2ikU_b\frac{\rho_b}{\rho}\frac{K_0(kb)}{K_1(kb)} + 2\frac{\nu k}{b}\left(-2kb\frac{X(kb,ka)}{M(ka,kb)} + 1\right), \tag{17}$$

$$G = \frac{X(ka,kb)}{M(ka,kb)} + \frac{\rho_a}{\rho}\frac{I_0(ka)}{I_1(ka)}, \tag{18}$$

$$H = -\frac{X(kb,ka)}{M(ka,kb)} - \frac{\rho_b}{\rho}\frac{K_0(kb)}{K_1(kb)}, \tag{19}$$

$$C = -\frac{\sigma}{\rho a^3}ka(1-k^2a^2) - k^2U_a^2\frac{\rho_a}{\rho}\frac{I_0(ka)}{I_1(ka)} + 4\nu^2k^3\left(k\frac{X(ka,kb)}{M(ka,kb)} - l\frac{X(la,lb)}{M(la,lb)}\right), \tag{20}$$

$$E = \frac{\sigma}{\rho b^3}kb(1-k^2b^2) + k^2U_b^2\frac{\rho_b}{\rho}\frac{K_0(kb)}{K_1(kb)} - 4\nu^2k^3\left(k\frac{X(kb,ka)}{M(ka,kb)} - l\frac{X(lb,la)}{M(la,lb)}\right) \tag{21}$$

and

$$M(ka,kb) = K_1(ka)I_1(kb) - K_1(kb)I_1(ka), \tag{22}$$

$$X(ka,kb) = K_1(kb)I_0(ka) + K_0(ka)I_1(kb), \tag{23}$$

where I_ν and K_ν are modified Bessel functions (of, generally, complex argument).

The set of all solutions of this dispersion relation gives the information on the stability behaviour of the system. It is the hope of its analysis that already individual solutions (modes) give a useful amount of stability information by themselves.

The complexity of this relation allows only a numerical investigation of the set of its solutions, except for simpler limit situations. These limit situations thereby serve as control of the correctness of the dispersion relation.

If the investigation is performed in the laboratory system (L) one has to perform in the relation, which refers in the above form to the rest system (R) of the film, the substitution

$$\begin{aligned} \omega^{(R)} &= \omega^{(L)} + ik^{(L)}V, \\ k^{(R)} &= k^{(L)}. \end{aligned} \tag{24}$$

3 LIMIT SITUATIONS

The dispersion relation derived in the previous section has to contain

- the classical results of Rayleigh [9] and Weber [11] on the cylindrical jet,
- the result of Chandrasekhar [4] on the submerged jet and the Kelvin-Helmholtz instability of the individual interfaces for an infinite outer radius b and finite inner radius a,
- the results of Rayleigh [9] for a jet of radius a and those of Chandrasekhar [4] for a radius b, if the density of the (viscous) liquid vanishes,
- the results of Lin, Lian and Creighton [8] and of Squire [10] on the plane curtain, when both film radii a and $b = a + h$ tend to infinity at constant thickness h.

This limit situations are derived in detail in [1].

4 NUMERICAL SOLUTION OF THE DISPERSION RELATION

Algorithm of Parameter Continuation These algorithms have the aim to follow the (connected) branches of solutions of nonlinear (systems of) equations by arguments of continuity and smoothness. The principle of the algorithm used here goes back to Allgower and Georg [2] and is described in [1]. It is thereby a matter of high amount of careful work to describe such a branch, as soon as a point on it is available. But it is a matter of high intuition and art to detect new branches of modes.

In the present paper essentially only temporal instability is investigated, which implies that ω in the dispersion relation is complex, whereas the wave vector k is real. The analysis delivers the complex value of ω:

$$\omega = \omega_r + i\omega_i \tag{25}$$

in terms of the (real) wave number

$$k = k_r\,. \tag{26}$$

Due to the time dependence

$$e^{\omega(k)t} \tag{27}$$

of the perturbation modes, $\mathrm{Re}\{\omega\} = \omega_r$ gives by (positive) sign and by magnitude the presence and the degree of a temporal instability of a mode. Thereby the points $\omega_r = 0$ determine the boundary of stability regions and those $\frac{d\omega_r}{dk} = 0$ the location of the most unstable (dangerous) modes.
The relation

$$\omega_r^{(L)} = \omega_r^{(R)}, \tag{28}$$

$$\omega_i^{(L)} = \omega_i^{(R)} - k_r^{(R)}V, \tag{29}$$

$$k_r^{(L)} = k_r^{(R)} \tag{30}$$

between the magnitudes characterizing the modes in the laboratory (L) and rest (R) frame, show that the temporal stability is frame independent.

5 LINEAR STABILITY ANALYSIS

The flow of a hollow jet is characterized by six numbers:

$$Re = \frac{U_b h}{\nu}, \tag{31}$$

$$We = \frac{\sigma}{\rho U_b^2 h}, \tag{32}$$

$$D_a = \frac{\rho_a}{\rho}, \tag{33}$$

$$D_b = \frac{\rho_b}{\rho}, \tag{34}$$

$$u = \frac{U_a}{U_b}, \tag{35}$$

$$\hat{a} = \frac{a}{h}. \tag{36}$$

The (complex) frequency ω will be normalized in the sequel to

$$\hat{\omega} = \frac{\omega}{\sqrt{\frac{\sigma}{\rho h^3}}} \tag{37}$$

and the (real) wave vector k to

$$\hat{k} = kh\,. \tag{38}$$

5.1 The Full Liquid Jet

For this jet the inner radius vanishes ($a = 0$). Thereby three characteristic numbers get irrelevant, so that only We, D_b, Re survive.

Nonviscous Liquids For a nonviscous jet the Reynolds number is infinite: $Re = \infty$. An insight into the behaviour of its modes is given in Fig. 2 for some values of the Weber number and the relative

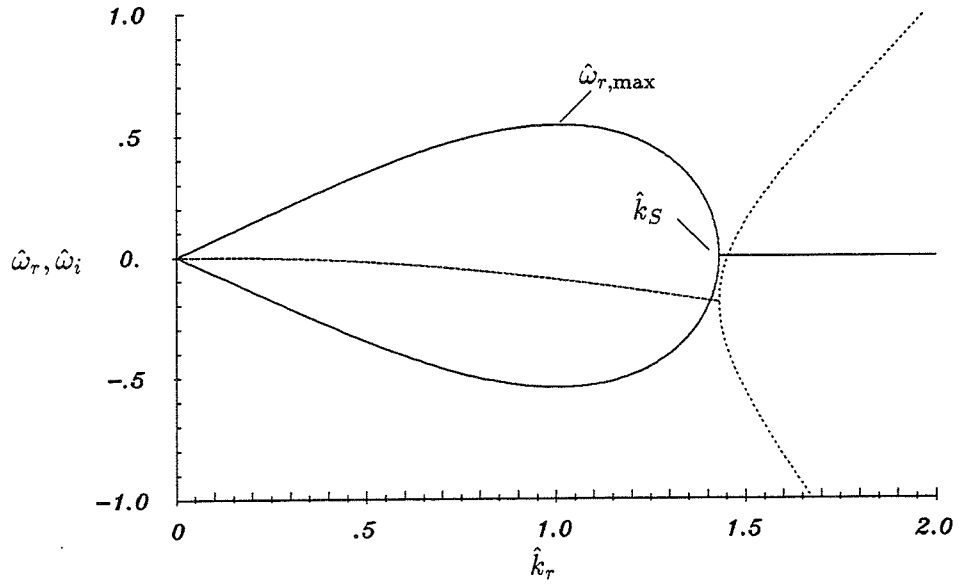

Figure 2: Solutions of the dispersion relation for the liquid jet: $\hat{\omega}_r$ (——), $\hat{\omega}_i$ (· · · · · ·). Characteristic numbers: $D_b = 0.1, We = 0.1, Re = \infty$.

density of the surrounding gas. There is an unstable branch of modes for a wave vector $\hat{k}$ below a value $\hat{k}_S$. The most unstable mode has an amplification rate $\hat{\omega}_{r,max}$. A parameter study shows that they both decrease with increase of capillarity and increase with increasing density of the surrounding gas. Figures 3 and 4 illustrate these facts quantitatively.

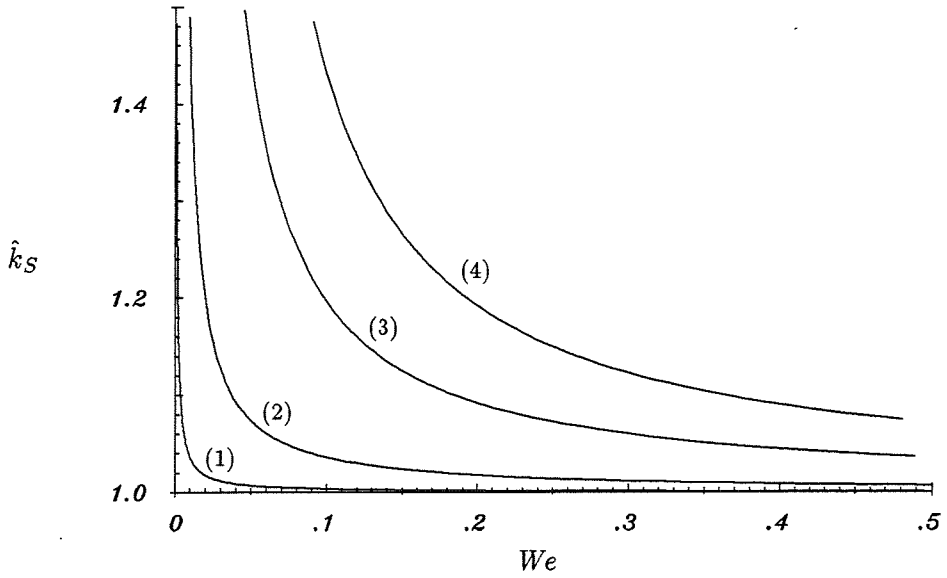

Figure 3: Stability boundary $\hat{k}_S = \hat{k}_S(We)$ for $D_b = 0.001$ (1), $D_b = 0.01$ (2), $D_b = 0.05$ (3) , $D_b = 0.1$ (4).

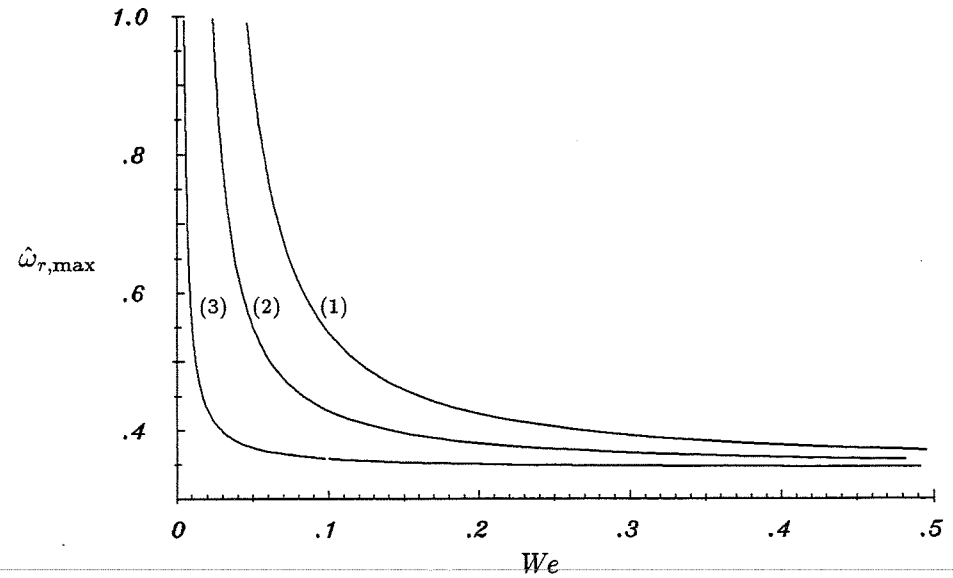

Figure 4: Maximal amplification rate $\hat{\omega}_{r,\max}$, $D_b = 0.1$ (1), $D_b = 0.05$ (2), $D_b = 0.01$ (3).

Viscous Liquids Figure 5 is the correspondent of Fig. 2 for viscous liquids. It shows that here the neutrally stable modes split up due to viscosity and become stable at wave numbers $\hat{k} > \hat{k}_S$, slightly beyond $\hat{k}_S(Re = \infty)$. The detailed behaviour of the stability curve near $\hat{k}_S$ in its dependence on the Reynolds number is shown in Fig. 6.

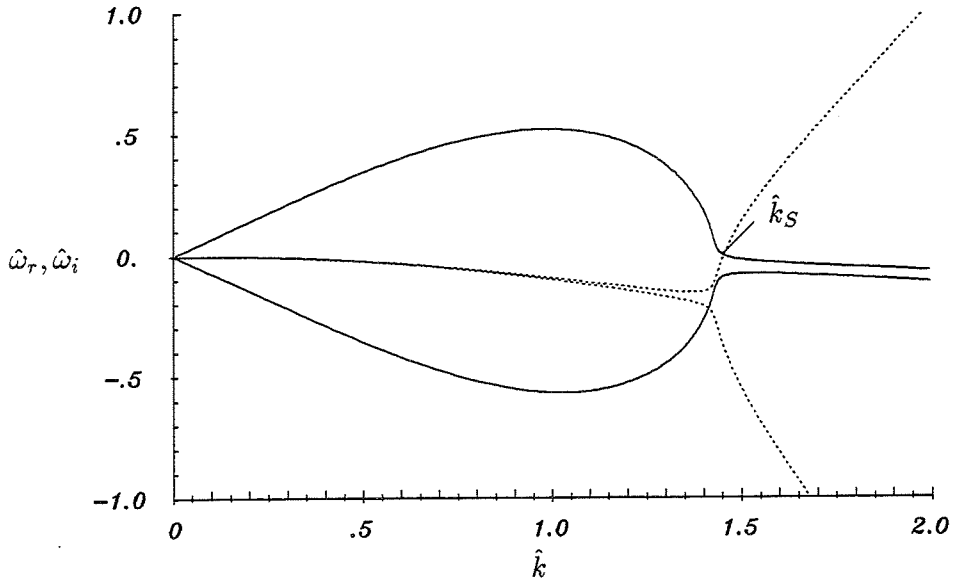

Figure 5: Branches of the dispersion relation for $We = 0.1$, $D_b = 0.1$, $Re = 200$: $\hat{\omega}_r$ (——), $\hat{\omega}_i$ (· · · · · ·).

Whereas the domain of unstable wave lengths is slightly increased by viscosity, the amplification rates and the most dangerous wave vector (inverse wave length) decrease with it, as seen from Fig. 7. The limit value of this vector at $Re = 0$ is $\hat{k}_0 \approx 0.34509429$.

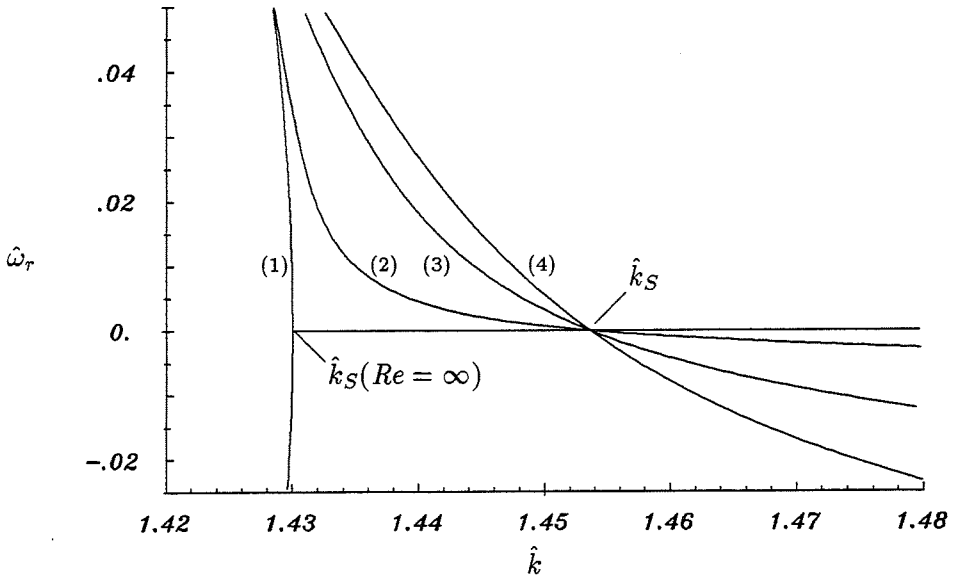

Figure 6: Position of the stability boundary $\hat{k}_S$: $We = 0.1$, $D_b = 0.1$, $Re = \infty$ (1), $Re = 1000$ (2), $Re = 200$ (3) and $Re = 100$ (4).

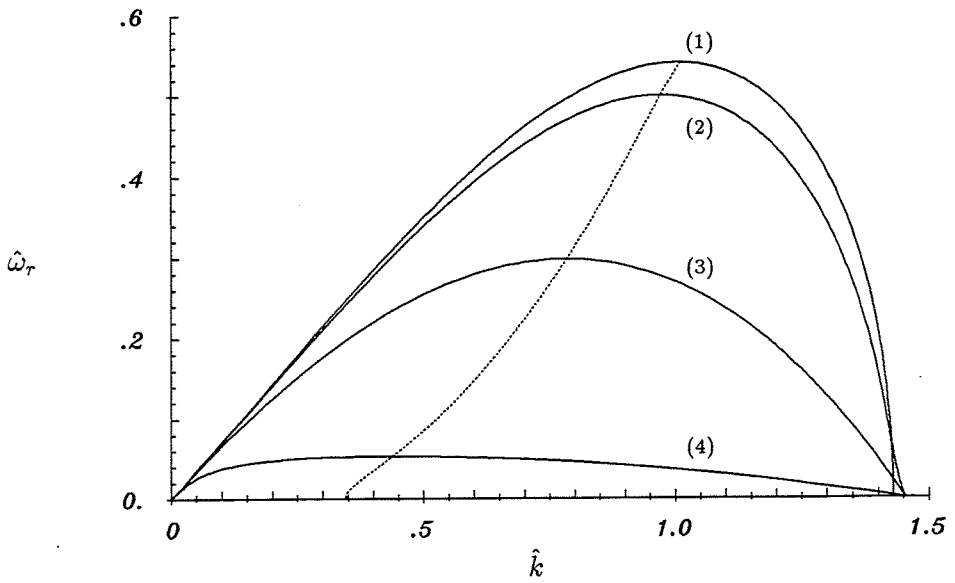

Figure 7: Influence of viscosity: $We = 0.1$, $D_b = 0.1$, $Re = \infty$ (1), $Re = 100$ (2), $Re = 10$ (3) and $Re = 1$ (4). Behaviour of the maximal amplification rate (· · · · · ·).

5.2 The Plane Liquid Sheet

The sheet may be considered as another limit form of a hollow jet, of infinite radius and finite thickness. For simplicity the situation of equal gas densities and (relative) velocities on both sides of the sheet will be considered here.

The sheet (curtain) flow situation possesses under this condition a mirror symmetry, which implies symmetry or antisymmetry of the perturbation modes. Their appearance in the limit is shown by the factorization of the dispersion relation and by amplitude ratios $\vartheta = +1$ and $\vartheta = -1$ of the two interface oscillations corresponding to the two factors (even and odd modes, respectively).

Nonviscous Liquid The modes of the nonviscous sheet have been described by Squire [10]; they are illustrated in Fig. 8. Both branches show finite ranges of instability in the wave vectors: the range for even is smaller, their amplification rate, however higher. Instability range and maximal amplification

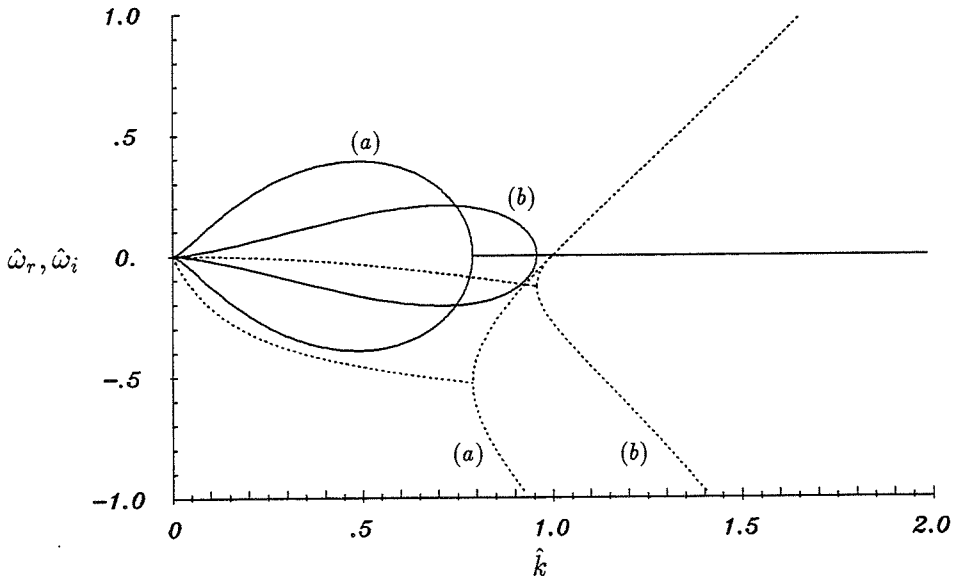

Figure 8: Dispersion curves of the plane liquid sheet: $\hat{\omega}_r$ (——), $\hat{\omega}_i$ (· · · · · ·). Even modes: $\vartheta = +1$ (a), odd modes: $\vartheta = -1$ (b). Characteristic numbers: $We = 0.1, D_a = 0.1, Re = \infty$

rate increase with decreasing Weber number of the sheet and with increase of the (relative) density of the surrounding gas.

Viscous Liquids — Odd Modes Figure 9 shows the amplification rates of the odd modes for different Reynolds numbers. These modes behave qualitatively as those of the jet: viscosity decreases their amplification rate and the most dangerous mode drifts with it towards higher wave lengths. Like for the jet, viscosity increases for these sheet modes the range of instability, yet by an amount independent of the Reynolds number: its boundary point is characterized by $\hat{k}_S = D_a/We$. The situation is illustrated in detail in Fig. 10.

Viscous Liquids — Even Modes Even modes show a completely different aspect, namely a viscosity enhanced instability (C.C. Lin, [7], S. 46ff). There is a drastic increase of the range of instability due to viscosity (Fig. 11). Also for these viscous modes the boundary of the instability range is now given by $\hat{k}_S = D_a/We$. In distinction to the odd modes, there developes in the instability range $\hat{k}_S(Re = \infty) < \hat{k} < \hat{k}_S$, which adds to that of the nonviscous case, a local maximum of amplification rate with increasing viscosity. Its position moves towards small wave vectors. Only

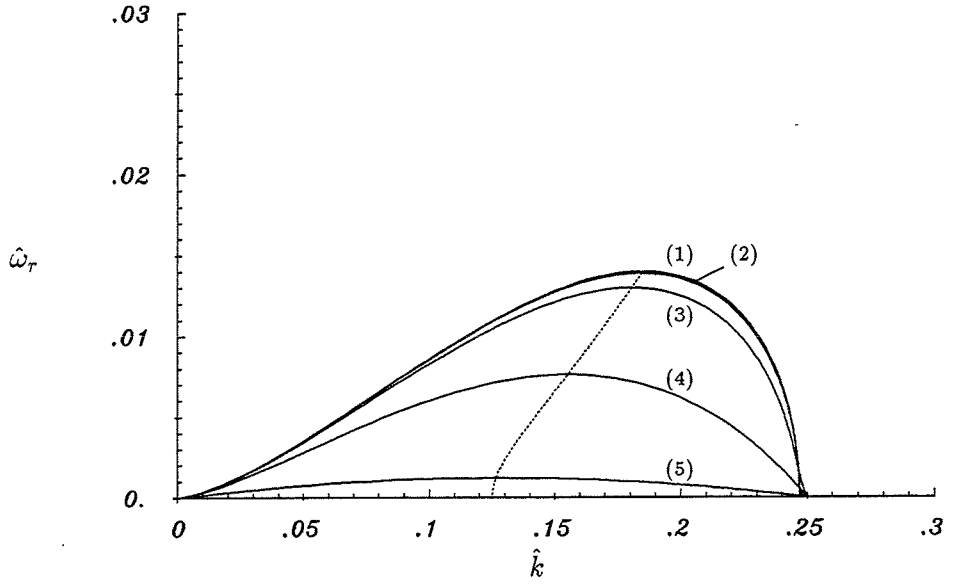

Figure 9: Amplification rate $\hat{\omega}_r$ (odd modes) for $D_a = 0.1$, $We = 0.4$ and $Re = \infty$ (1), $Re = 1000$ (2), $Re = 100$ (3) , $Re = 10$ (4), $Re = 1$ (5).

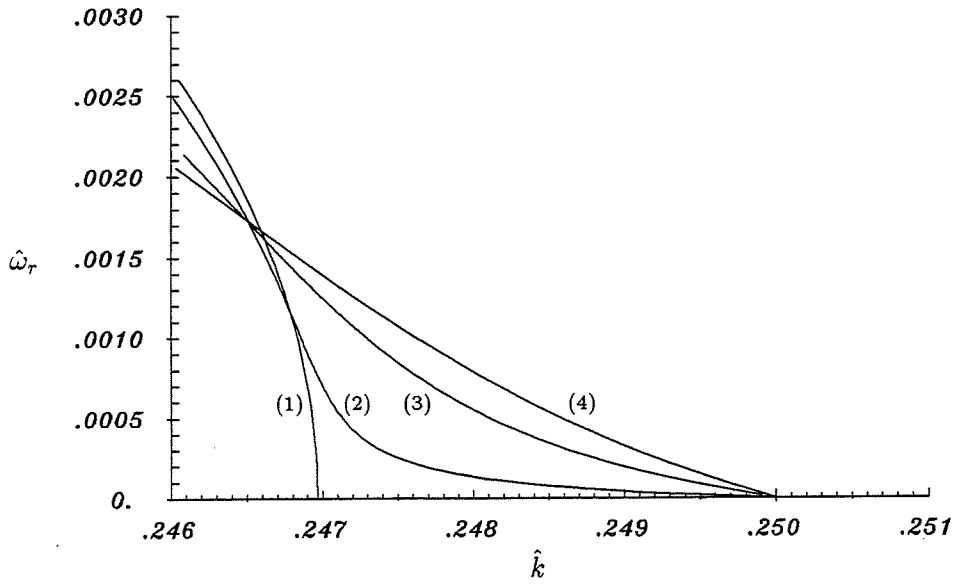

Figure 10: Amplification rate $\hat{\omega}_r$ (odd modes) for $D_a = 0.1$, $We = 0.4$ and $Re = \infty$ (1), $Re = 1000$ (2), $Re = 500$ (3) , $Re = 100$ (4).

below a certain Reynolds number does this rate decrease again. The whole branch of instability disappears with vanishing Reynolds number.

Figure 12 reveals for very low Reynolds numbers a particular capillary phenomenon: for a small range of Weber numbers (here $0.37943 < We < 0.5$) there are two different modes of (local) maximal amplification rates: the smaller one of inertial origin and the larger one due to viscosity.

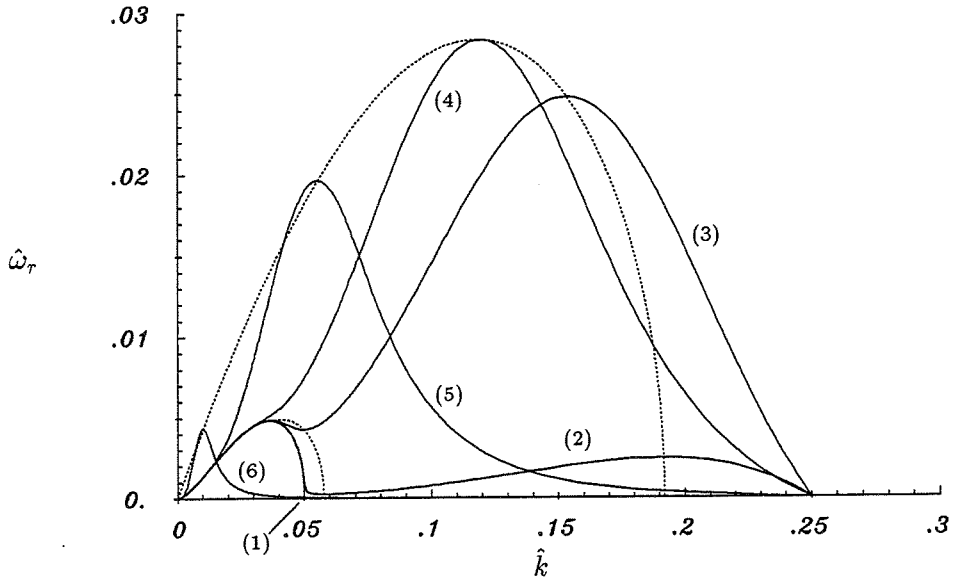

Figure 11: Viscosity enhanced instability: amplification rate $\hat{\omega}_r$ (——) of the even modes for $D_a = 0.1$, $We = 0.4$ and $Re = \infty$ (1) $Re = 0.025$ (2), $Re = 0.001$ (3),$Re = 2.82 \cdot 10^{-4}$ (4), $Re = 1.00 \cdot 10^{-5}$ (5) $Re = 1.00 \cdot 10^{-8}$ (6), Position of the maxima and minima (· · · · · ·).

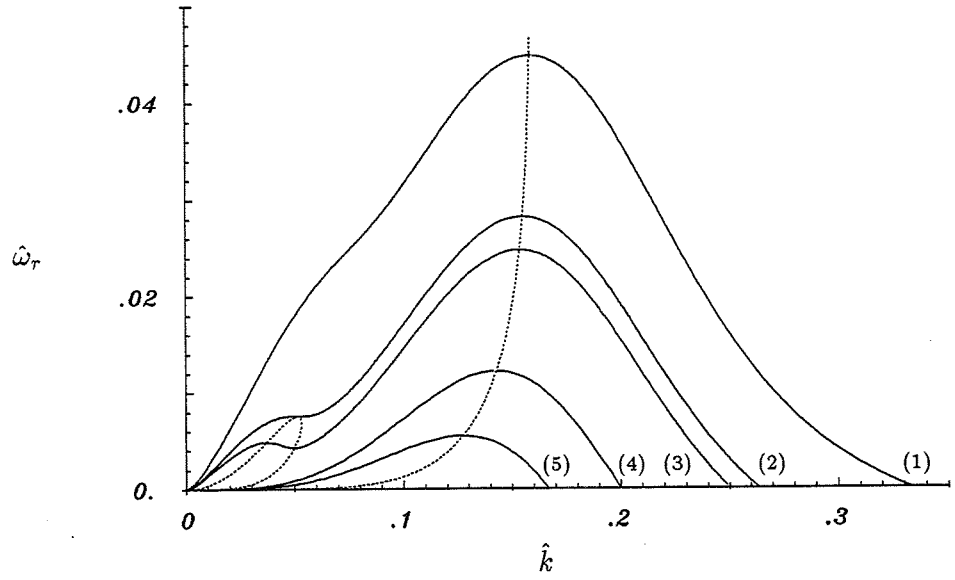

Figure 12: Amplification rate $\hat{\omega}_r$ (even modes) for $D_a = 0.1$, $Re = 0.001$ and $We = 0.3$ (1), $We = 0.37943$ (2), $We = 0.4$ (3) , $We = 0.5$ (4), $We = 0.6$ (5).

5.3 The hollow jet

This jet has as an additional characteristic number, the dimensionless inner radius

$$\hat{a} = \frac{a}{h}. \tag{39}$$

It will, for reasons of simplicity, again be considered only for equal gas densities and velocities:

$$D_a = D_b, \tag{40}$$

$$u = 1. \tag{41}$$

Nonviscous Liquid Figure 13 shows some branches of the dispersion curves for an inner radius $\hat{a} = 10$. There is no decoupling of the branches, which are now connected by bifurcation points. There is an additional unstable branch (iii) present in comparison to those which appear also in a plane sheet ((i) and (ii)). It is separated from the other two branches by neutrally stable modes.

Figure 14 displays information about the localization of the different modes on the two interfaces.

The ranges (i)-(iii) move with change of the curvature $\hat{a}$ of the jet, as do their (locally) maximal amplification rates and their most dangerous wave lengths (see Fig.s 17, 15, and 16).

Viscous Liquid For a viscous hollow jet there are, again, no neutrally stable modes. The change of the stability picture as compared to the nonviscous liquid is dramatic (see 18). There are two connected branches, on which the oscillation amplitudes of the two interfaces have different phase behaviour: $\mathrm{Re}(\vartheta) > 0$ and $\mathrm{Re}(\vartheta) < 0$, respectively. The upper ends $\hat{k}_{Sa}$ and $\hat{k}_{Sb}$ of instability of the two unstable branches are determined by

$$We\left(\frac{1}{\hat{a}^2} - \hat{k}_{Sa}^2\right) + \hat{k}_{Sa}\, D_a \frac{I_0(\hat{k}_{Sa}\hat{a})}{I_1(\hat{k}_{Sa}\hat{a})} = 0 \tag{42}$$

$$We\left(\frac{1}{\hat{b}^2} - \hat{k}_{Sb}^2\right) + \hat{k}_{Sb}\, D_b \frac{K_0(\hat{k}_{Sb}\hat{b})}{K_1(\hat{k}_{Sb}\hat{b})} = 0. \tag{43}$$

for $\mathrm{Re}(\vartheta) > 0$ and $\mathrm{Re}(\vartheta) < 0$, respectively. They are independent of viscosity. The change of their position with $\hat{a}$, from the full jet ($\hat{a} = 0$) to the plane sheet ($\hat{a} \to \infty$) is displayed in Fig. 19. The instability domain of the modes with $\mathrm{Re}(\vartheta) > 0$ decreases monotonously with increasing inner jet radius; its upper end $\hat{k}_S$ tends for $\hat{a} \to \infty$ to the value of the plane sheet. The domain of the modes with $\mathrm{Re}(\vartheta) < 0$ does not decrease monotonously, but goes through a broad and shallow minimum with increasing $\hat{a}$ before it reaches the same limit in the plane case. Figure 20 illustrates the dependence of these domains on the characteristic number D_a/We).

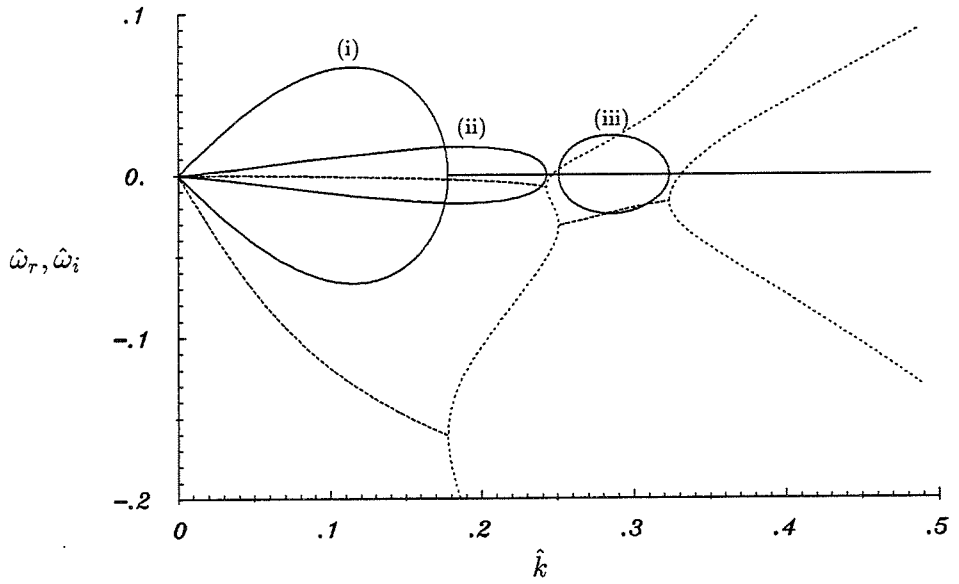

Figure 13: Hollow jet: Stability diagram for $D_a = 0.1$, $We = 0.4$, $\hat{a} = 10$ and $Re = \infty$.

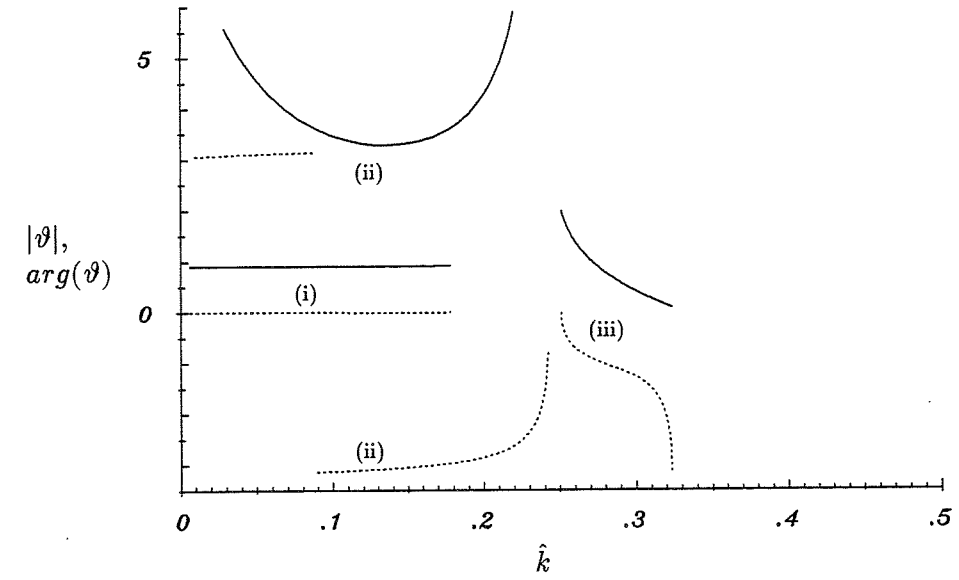

Figure 14: Amplitude ratio $\vartheta = \eta_{0b}/\eta_{0a}$ within the modes with $\hat{\omega}_r > 0$. Magnitude $|\vartheta|$ (——) and phase $\arg(\vartheta)$ (· · · · · ·) for $D_a = 0.1$, $We = 0.4$, $\hat{a} = 10$ and $Re = \infty$.

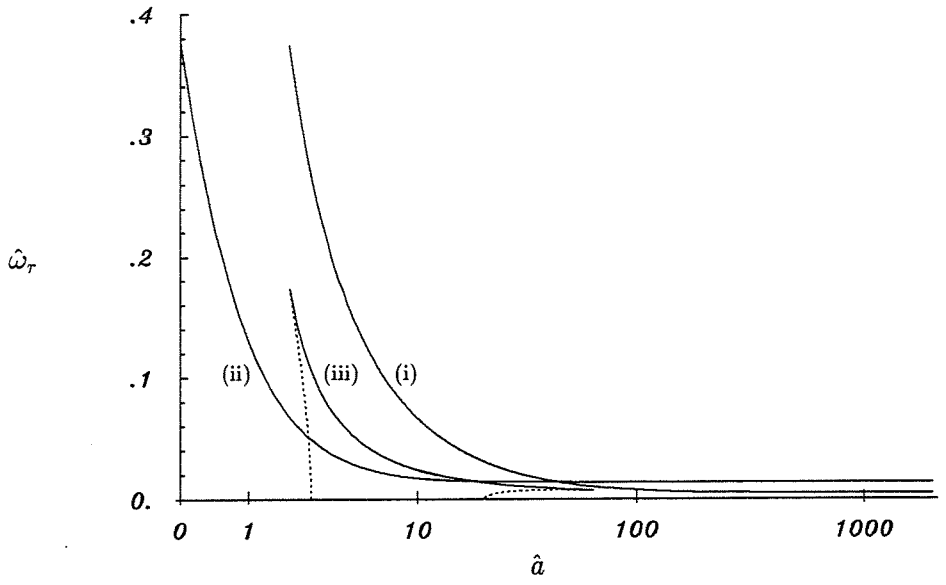

Figure 15: Local extrema of the amplification rate $\hat{\omega}_r$ in dependence on the inner radius $\hat{a}$ for $D_a = 0.1$, $We = 0.4$ and $Re = \infty$. $\hat{\omega}_{r,\,\max}$ (——), $\hat{\omega}_{r,\,\min}$ (· · · · · ·).

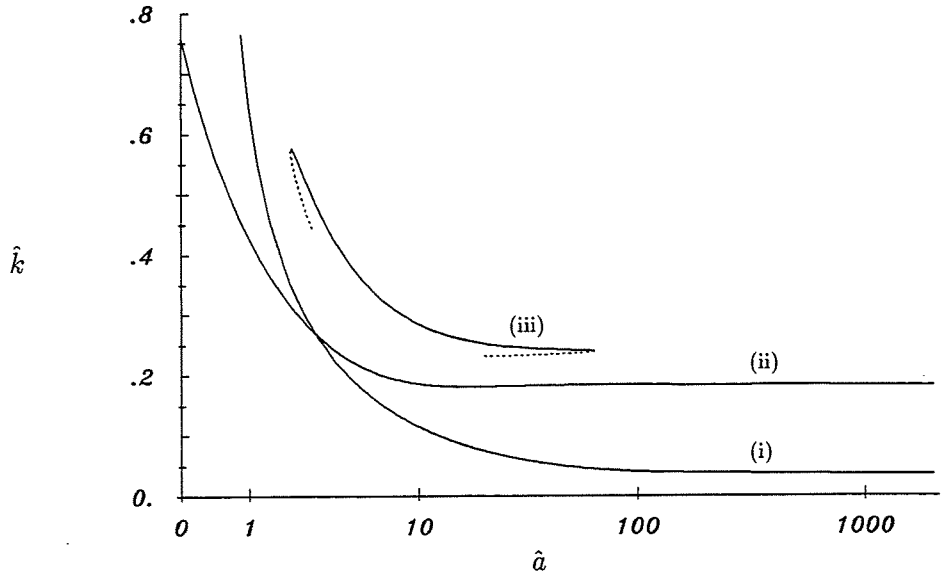

Figure 16: Wave number of the maximal amplification rate $\hat{\omega}_{r,\,\max}$ in its dependence on the inner radius $\hat{a}$ for $D_a = 0.1$, $We = 0.4$ and $Re = \infty$.

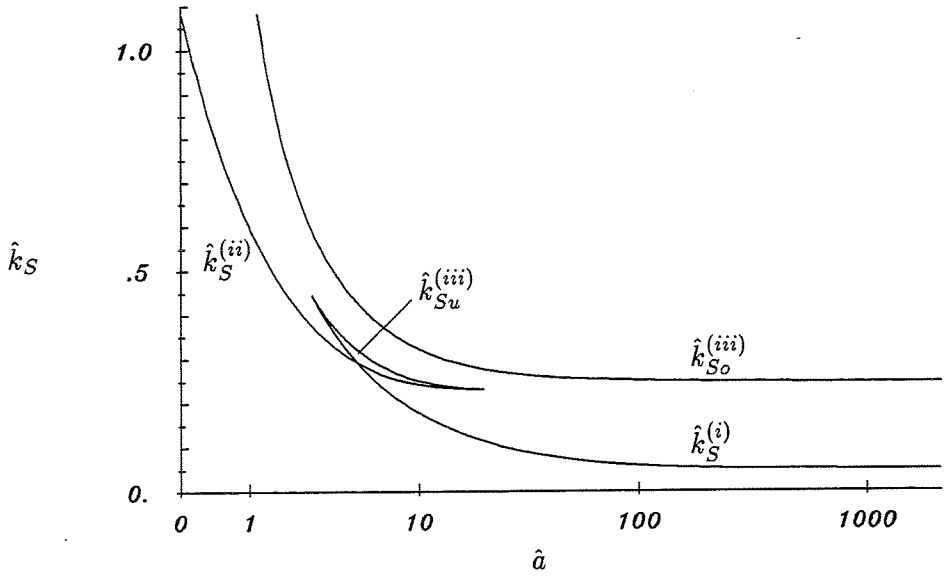

Figure 17: Hollow jet: Boundaries $\hat{k}_S$ of the instability ranges for $D_a = 0.1$, $We = 0.4$, and $Re = \infty$. $\hat{k}_{Su}^{(iii)}$ resp. $\hat{k}_{So}^{(iii)}$: lower resp. upper end of the wave numbers of range (iii). $\hat{k}_S^{(i)}$ and $\hat{k}_S^{(ii)}$: lower ends of the ranges (i) and (ii).

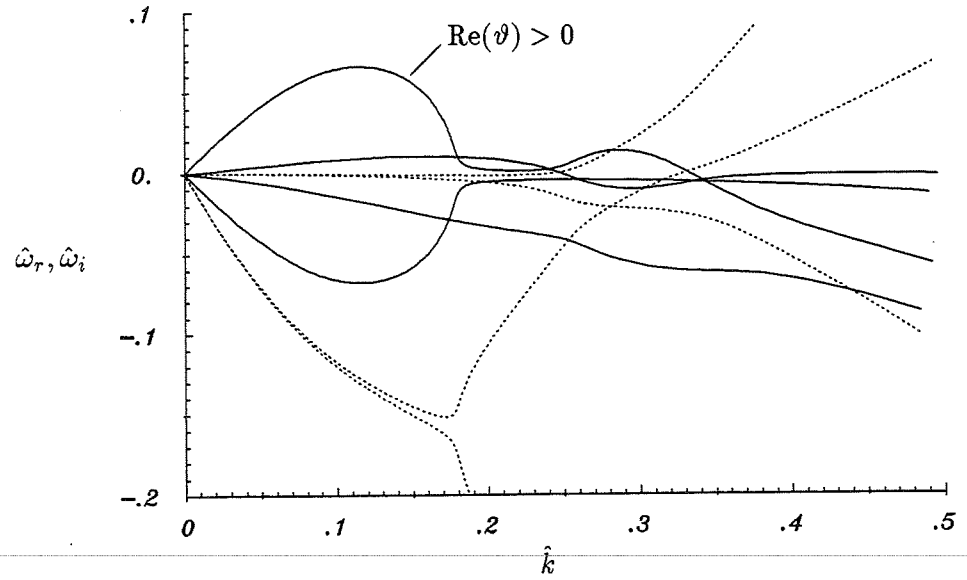

Figure 18: Dispersion relations of the viscous hollow jet: $D_a = 0.1$, $We = 0.4$, $\hat{a} = 10$ and $Re = 10$. $\hat{\omega}_r$ (——), $\hat{\omega}_i$ (· · · · · ·).

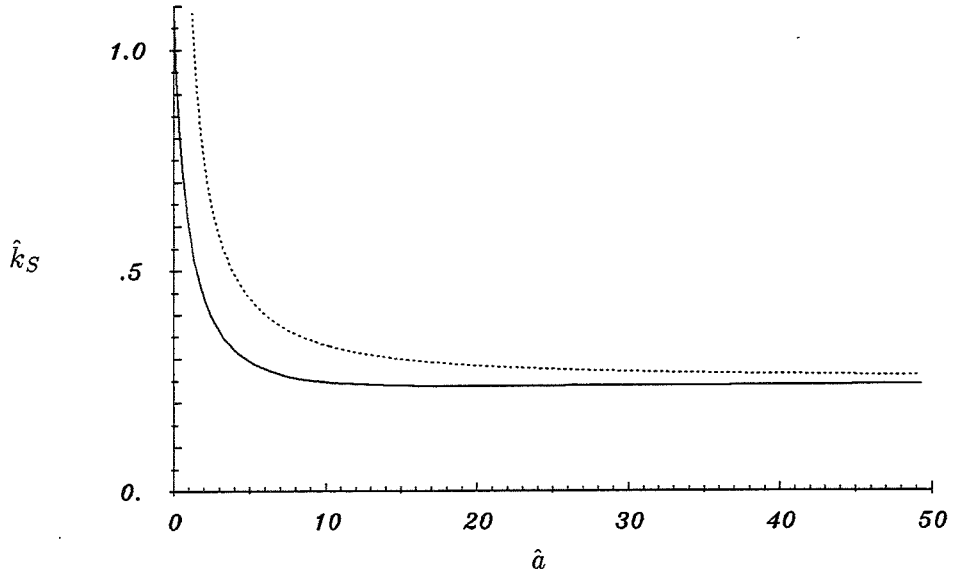

Figure 19: Upper end of instability range of wave vectors, $\hat{k}_S$, in dependence on the inner jet radius $\hat{a}$ for $D_a = 0.1$, $We = 0.4$ and $Re < \infty$ (modes with $\mathrm{Re}(\vartheta) < 0$ ——, modes with $\mathrm{Re}(\vartheta) > 0$ ·····).

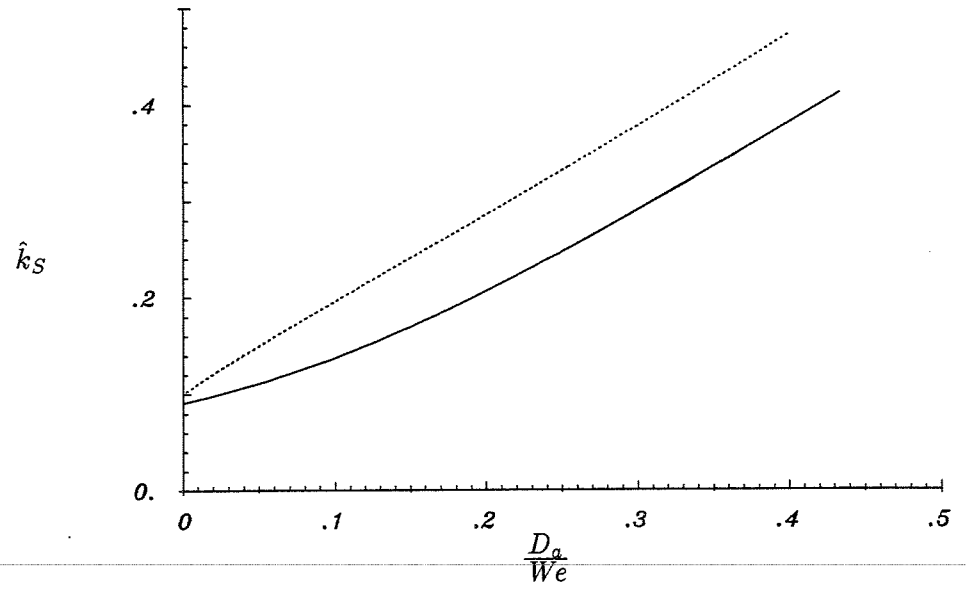

Figure 20: Boundary of stability $\hat{k}_S$ in its dependence on $D_a/\,We$ for $\hat{a} = 10$, and $Re < \infty$ (modes with $\mathrm{Re}(\vartheta) < 0$ ——, modes with $\mathrm{Re}(\vartheta) > 0$ ·····).

6 SUMMARY

In this paper the modes of instability of a hollow liquid jet have been described. The qantitative description leads to rather complicated mathematical expressions, which require a massive use of algebraic computational tools (MAPLE). It has been verified by the derivation, from these expressions, of a number of independently known limit situations, especially the ordinary jet and the plane liquid sheet (or curtain). By a suitably deviced numerical algorithm (parameter continuation) the ranges of wave vectors of the unstable modes of the hollow jet could be derived. Within these ranges the most dangerous mode, of maximal amplification rate, could be characterized and also localized. The dependence of the stability picture on the characteristic numbers: e.g. the density ratios (D_a , D_b), the Weber number (We), the aspect ratio ($\hat{a}$), and especially the Reynolds number (Re), could be traced. The computational technique developed for this purpose allows to perform easily parameter studies of (in)stability required for the design of technical (e.g. coating or atomization) devices.

REFERENCES

[1] N. Alleborn. Die Stabilität von Flüssigkeitsstrahlen und zylindrischen Filmen. Diplomarbeit, Universität Erlangen–Nürnberg, Lehrstuhl für Strömungsmechanik, 1994.

[2] E. L. Allgower and K. Georg. *Numerical Continuation Methods — An Introduction.* Springer–Verlag, Berlin, 1990.

[3] P. Camatte. *Etude des instabilites d'une nappe liquide de geometrie annulaire en pulverisation assistee.* PhD thesis, Faculte des Sciences de l'Universite de Rouen, Mai 1992.

[4] S. Chandrasekhar. *Hydrodynamic and Hydromagnetic Stability.* Dover, New York, 1961.

[5] G. D. Crapper and N. Dombrowski. Kelvin–Helmholtz wave growth on cylindrical sheets. *J. Fluid Mech.*, 68(3):497–502, 1975.

[6] J.-G. Lee and L.-D. Chen. Linear stability analysis of gas-liquid interface. *AIAA Journal*, 29(10):1589–1595, October 1991.

[7] C. C. Lin. *The Theory of Hydrodynamic Stability.* Cambridge University Press, Cambridge, 1955.

[8] S. P. Lin, Z. W. Lian, and B. J. Creighton. Absolute and convective instability of a liquid sheet. *J. Fluid Mech.*, 220:673–689, 1990.

[9] Lord Rayleigh. On the instability of jets. *Proc. London Math. Soc.*, 10:4–13, 1879.

[10] H. B. Squire. Investigation of the instability of a moving liquid film. *Brit. J. Appl. Phys.*, 4:167, 1953.

[11] C. Weber. Zum Zerfall eines Flüssigkeitsstrahls. *Ztschr. f. angew. Math. und Mech.*, 11(2):136–154, April 1931.

SHOCKS IN HIGH SPEED TWO–PHASE FLOW

G.H. Schnerr, S. Adam and G. Mundinger

Universität Karlsruhe (TH)
Institut für Strömungslehre und Strömungsmaschinen
Postfach 6980, D–76128 Karlsruhe, Federal Republic of Germany
Telephone: (0721) 608–3026, Facsimile: (0721) 696727

ABSTRACT

The work presented concentrates on Laval nozzle flows of water vapor/carrier gas mixtures with shocks caused by heat addition after nonequilibrium condensation. Experiments in an atmospheric supersonic wind tunnel and numeric simulations of the two–phase flow are carried out to study the interaction of the shock with the homogeneous condensation process in a nozzle with constant exit Mach number 1.2. Depending on the reservoir conditions we observe steady diabatic flow with a shock within the zone of nucleation and subsonic heat addition or supersonic heat addition ahead of the shock. The variation of the back pressure at the nozzle exit affects the shock position and the condensate formation in a different manner. For high relative humidities we present three modes of self–excited periodic flow oscillation. One of these modes is yet unknown and unsymmetric with respect to the nozzle axis.

1. INTRODUCTION

This investigation deals with transonic flows of water vapor/carrier gas mixtures in Laval nozzles. The fast expansion in these nozzles leads to high supersaturation of the vapor component and to a sudden collapse of the metastable state in the divergent nozzle part. This phenomenon is of basic interest for technical applications, e.g. in turbo machinery and power plants. If the latent heat release to the flow exceeds a critical value shocks are formed which move upstream into the oncoming flow and create self–excited modes of periodic shock formation.

Steady flows in circular arc nozzles with homogeneous condensation have been investigated experimentally and numerically by Schnerr [1, 2] and Dohrmann [3]. A numerical method to calculate both steady and unsteady Laval nozzle flows recently was developed by Mundinger [4], where the two–phase flow is calculated by solving the 2–D Euler equations and four additional equations for the homogeneous droplet formation and the microscopic droplet growth. Further details about the computational method may be found in [4] and Schnerr et al. [5]. The phenomenon of self–excited flow oscillations in nozzle flows of moist air was discovered by Schmidt [6]. Schnerr et al. presented different modes of the flow oscillation and investigated the frequency dependence on the most important controlling parameters, the nozzle geometry and the reservoir conditions [5, 7].

Herein we investigate experimentally and numerically diabatic flows in a nozzle with constant exit Mach number 1.2, where the temperature gradient in flow direction decreases to zero

and compare them with condensing flows in a circular arc nozzle with approximately constant temperature gradient throughout the whole sub– and supersonic flow region. The nozzle is extended by a channel with constant cross sectional area. Here condensing flows with sub– or supersonic heat addition may exist, which lead either to subsonic or supersonic outflow. We investigate flows with different water vapor content, where we observe a shock in the zone of nucleation ahead of the condensation onset or a shock, which limits the region of supersonic heat addition. We also discuss the influence of the back pressure at the nozzle exit on the shock position and we present three different modes of self–excited periodic flow oscillation.

2. DIABATIC FLOW IN THE CIRCULAR ARC NOZZLE S2

Steady diabatic flows of water vapor/carrier gas mixtures in circular arc nozzles have been extensively studied in an intermittent atmospheric supersonic wind tunnel [1, 2] and by numerical simulations [3]. Figure 1 shows typical schlieren photographs of flows with homogeneous condensation in the circular arc nozzle S2 (throat height $2 \cdot y^* = 30\ mm$, radius of wall curvature $R^* = 400\ mm$). In this nozzle type the temperature gradient is nearly constant up to the region where condensation occurs ($(-dT/dt) \approx (-dT/dt)^* = 8.14°C/cm$). Low values

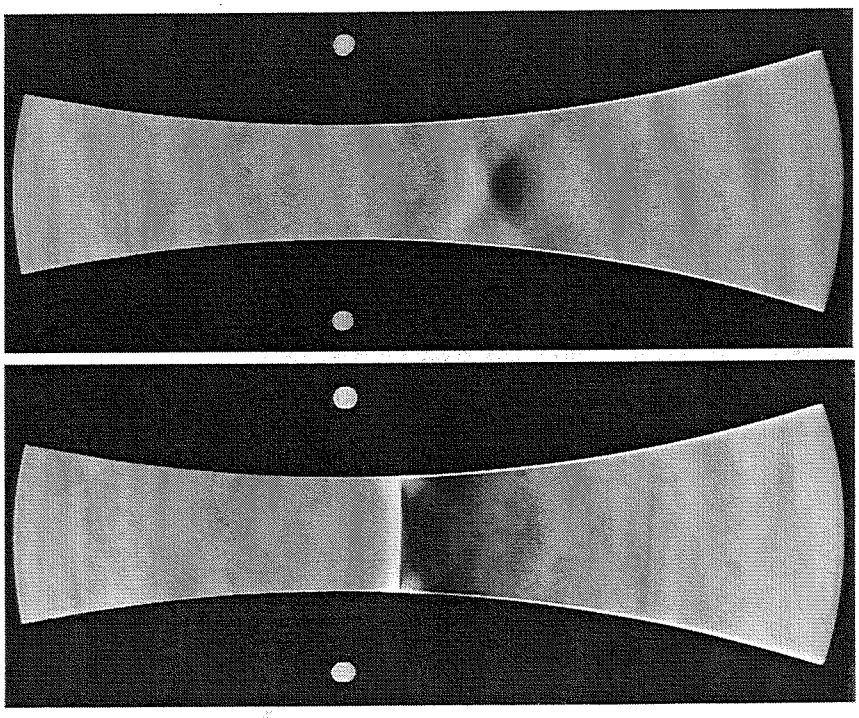

Figure 1: Schlieren pictures of steady diabatic flows in the nozzle S2 (flow from left to right, the white dots indicate the location of the nozzle throat). Reservoir conditions of the moist air: top – $T_{01} = 300\ K$, $p_{01} = 1.011\ bar$, $\phi_0 = 35.3\ \%$, $x = 7.8\ g/kg$; bottom – $T_{01} = 287\ K$, $p_{01} = 1.012\ bar$, $\phi_0 = 73.4\ \%$, $x = 7.3\ g/kg$.

of the relative humidity cause only a weak compression in the supersonic flow region (Fig. 1 – top, $\Phi_0 = 35.3\ \%$). For $\Phi_0 = 73.4\ \%$ the condensation onset moves towards the nozzle throat and creates a steady normal shock followed by a sudden expansion (dark region).

In Fig. 2a the calculated static pressure along the nozzle axis is compared with the isentropic flow ($x = 0\ mm$ corresponds to the nozzle throat position). The frozen Mach number distribution depicts the extension of the local subsonic flow region behind the shock (Fig. 2b). With increasing supersaturation the nucleation rate J rapidly reaches its maximum value of

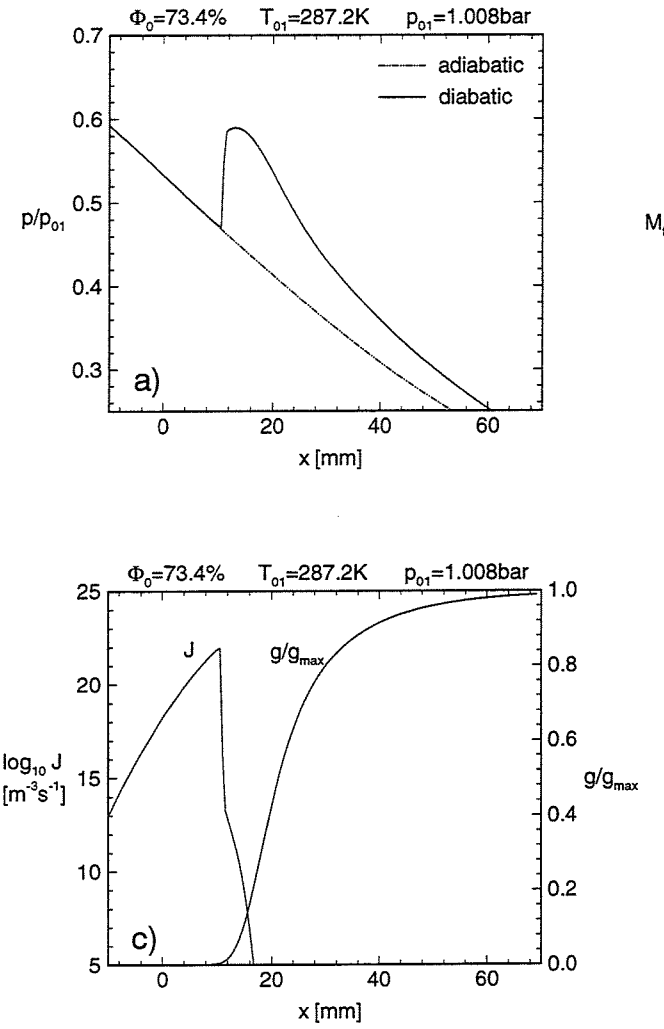

Figure 2: Numerical simulation corresponding to the experiment shown in Fig. 1b (nozzle S2 – throat position at $x = 0\ mm$); plotted along the nozzle axis:
2a (top left) – pressure ratio p/p_{01} compared with the isentropic expansion;
2b (top right) – frozen Mach number M_f;
2c (left) – nucleation rate J and condensate mass fraction g/g_{max}.

about $10^{22}\ m^{-3}s^{-1}$ ahead of the shock (Fig. 2c). The temperature increase across the shock reduces the supersaturation and decreases the nucleation rate to about $10^{13}\ m^{-3}s^{-1}$. By the growth of the homogeneously formed nuclei to droplets the condensate mass fraction g/g_{max} increases to macroscopic relevant values. As a first gasdynamic approximation the shock indicates the onset of condensation. At $x \approx 70\ mm$ nearly the whole water vapor is condensed ($g/g_{max} \approx 1$).

3. STEADY DIABATIC FLOW IN A NOZZLE WITH CONSTANT EXIT MACH NUMBER — RELATIVE HUMIDITY $\Phi_0 = 35.6\ \%$

With respect to technical applications nozzles designed for a constant exit Mach number are important. Here we investigate such a nozzle (A1) with a throat height of $2 \cdot y^* = 90\ mm$, a radius of wall curvature at the nozzle throat of $R^* = 300\ mm$ and a constant exit Mach number of $M_{exit} = 1.2$ (for isentropic flow). In contrast to the nozzle S2 the temperature gradient monotonically decreases to zero at the nozzle exit. The critical temperature gradient is $(-dT/dt)^* = 5.43°C/cm$ (1-D theory). Behind the divergent part ($0\ mm \leq x < 89\ mm$) the nozzle is extended by parallel walls, i.e. a constant cross sectional area ($89\,mm \leq x \leq 194\,mm$).

3.1 Comparison with diabatic flows in the circular arc nozzle S2 and with adiabatic flow

In order to clarify the influence of the nozzle geometry, i.e. of the decreasing temperature gradient on the shock and on the condensation process we compare diabatic flows in the nozzles S2 and A1. Figure 3 shows the schlieren photograph of the condensing flow in the nozzle A1 with $\Phi_0 = 35.6\ \%$ corresponding to the value of Φ_0 in Fig. 1a. In contrast to the weak supersonic compression in the circular arc nozzle S2 we observe a steady shock in the divergent nozzle section similar to that of Fig. 1b.

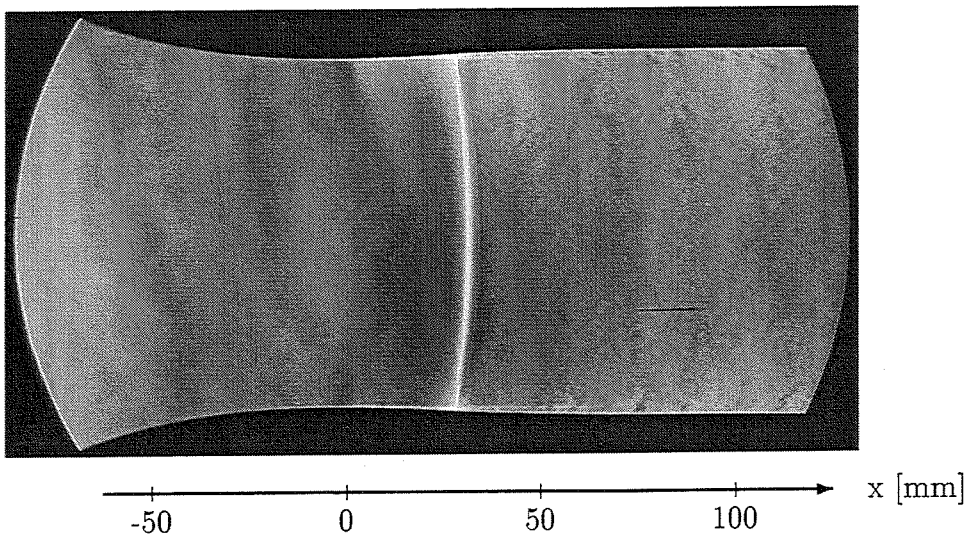

Figure 3: Schlieren picture of steady diabatic flow in the nozzle A1 (flow from left to right, location of the nozzle throat: $x = 0\,mm$). Reservoir conditions of the moist air: $T_{01} = 298.7\,K$, $p_{01} = 1.004\ bar$, $\phi_0 = 35.6\ \%$, $x = 7.3\ g/kg$.

The measured pressure distribution along the nozzle axis is compared with the adiabatic flow with an aerodynamic shock at exactly the same position (Fig. 4a). In the diabatic case the expansion into vacuum tanks behind the nozzle controls the pressure at the nozzle exit. In the numerical calculation (Fig. 4b) the constant back pressure is a boundary condition with two different values at the nozzle exit.

The identical pressure distributions up to a short distance behind the shock indicates that

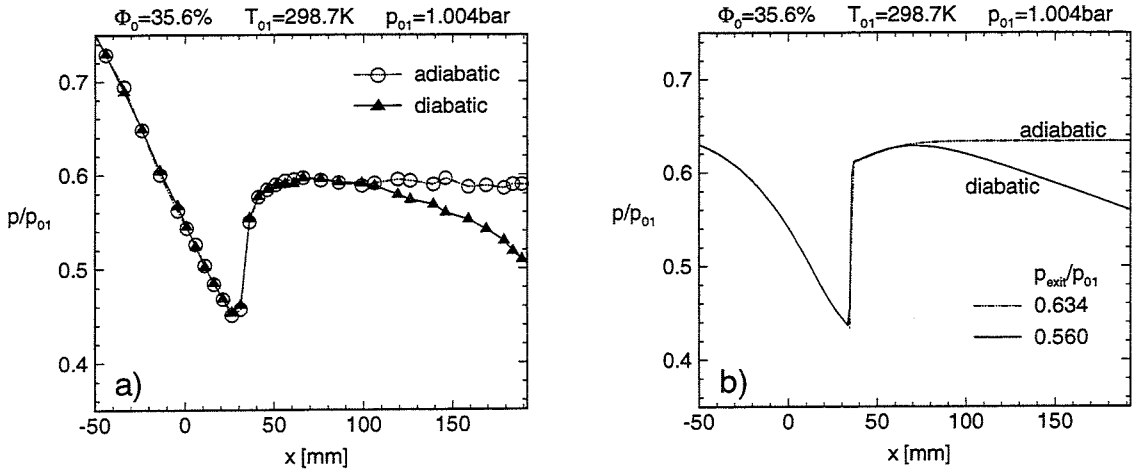

Figure 4: Pressure distribution along the axis of nozzle A1; steady diabatic flow corresponding to Fig. 3 compared with adiabatic flow (location of the nozzle throat: $x = 0\,mm$). Fig. 4a (left): experimental pressure distribution; Fig. 4b (right): numerical pressure distribution.

there is no heat exchange in the shock region. Downstream of the shock the pressure slightly increases. Then the condensation process starts and the pressure decreases monotonically, i.e. the subsonic flow is accelerated. Obviously the heat release in the divergent nozzle part is not strong enough to accelerate the flow to supersonic speed and therefore the flow remains subsonic up to the nozzle exit, which is a characteristic difference to the flow in the circular arc nozzle S2.

Figures 4a and 4b depict some differences of the experimental and numerical results. For numerical reasons the nozzle shape in the subsonic flow region used for the calculation is not identical to that of the experiments. However the influence on the transonic/supersonic flow field is neglegible. In addition, the experimental pressure distribution is influenced by the boundary layer. The increase of the displacement thickness across the shock decreases the pressure behind.

3.2 Variation of the back pressure

The influence of different back pressures on the shock position and on the heat release is investigated by numerical calculation of flows in the nozzle A1 for constant reservoir conditions but different back pressures (Figure 5). The solid line ($p_{exit}/p_{01} = 0.560$) corresponds to the pressure distribution of Fig. 4b.

For the high value of $p_{exit}/p_{01} = 0.576$ the shock moves only a little bit upstream, about $2mm$. Decreasing the back pressure to $p_{exit}/p_{01} = 0.539$ does not affect the shock position. This definitely is not possible in adiabatic flow where an exit pressure variation of $\Delta p_{exit}/p_{01} = \pm 0.5\,\%$ causes a symmetric variation of the shock position of about $\pm 13\,mm$. With decreasing back pressure the frozen Mach number at the nozzle exit tends to unity (Fig. 5b), which is the limit for heat addition in steady subsonic flow. For p_{exit} lower than the local critical value (as

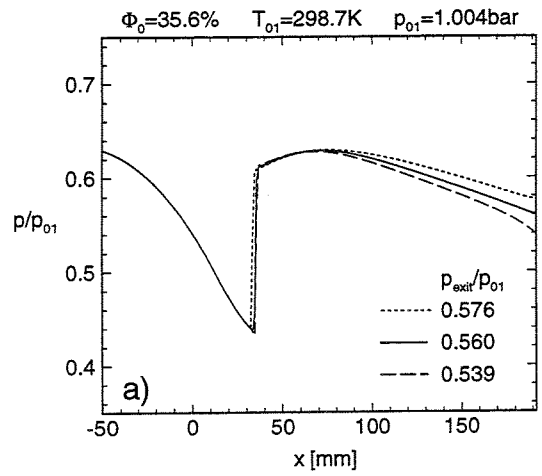

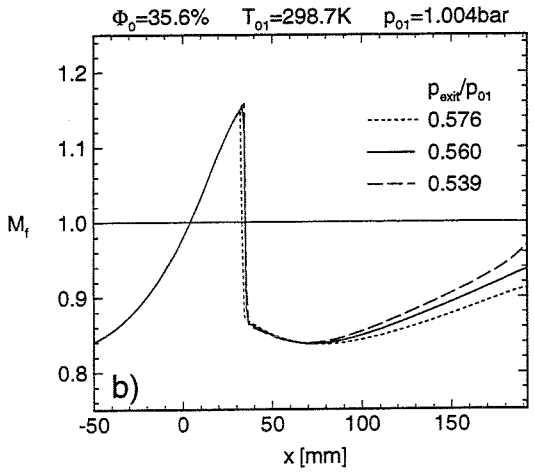

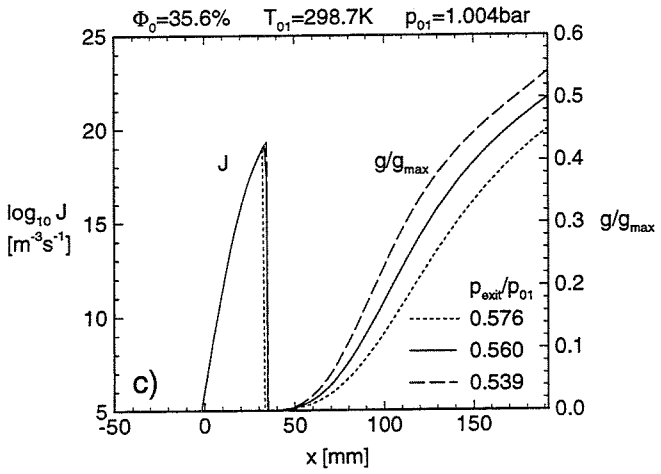

Figure 5: Numerical simulation corresponding to the experiment shown in Fig. 3 (nozzle A1 – throat position at $x = 0\,mm$); plotted along the nozzle axis:
5a (top left) – pressure ratio p/p_{01} for different back pressures;
5b (top right) – frozen Mach number M_f;
5c (left) – nucleation rate J and condensate mass fraction g/g_{max}.

in the experiments) the expansion to supersonic speed occurs just at the nozzle exit. Figure 5c shows that the nucleation rate reaches a peak value of only $10^{19}\,m^{-3}s^{-1}$ which is about 3 orders of magnitude less compared with the nozzle S2 (Fig. 2c), where the higher values of Φ_0 and of the temperature gradient lead to a higher supersaturation. As in the nozzle S2 significant heat release does not start ahead of the shock (Fig. 5c). The main difference to the flow in the nozzle S2 is the much smaller rise of the condensate mass fraction g/g_{max} and the significantly lower value of g/g_{max} at the nozzle exit.

Obviously, the main influence of the back pressure variation is the control of the condensate formation whereas the shock position changes only slightly. The appropriate cut of the nucleation rate allows steady heat addition to the subsonic flow which then leads to the given back pressure at the nozzle exit.

4. COMPARISON OF THE 2–D FLOW FIELDS IN THE NOZZLES S2 AND A1

The 2–D distributions of M_f, J and g/g_{max} of the flows in the nozzle S2 ($\Phi_0 = 73.4\ \%$) and in the nozzle A1 ($\Phi_0 = 35.6\ \%$, $p_{exit}/p_{01} = 0.560$) are plotted in Fig. 6 in different scales.

In both nozzles the shock is almost normal whereas the constant Mach number contours depict clearly 2–D structures. This causes different values of the nucleation rate J at the nozzle wall and the nozzle axis, respectively, because J depends on the thermodynamic state and is therefore constant for a given Mach number. In the nozzle S2 the nucleation rate J increases towards the wall just ahead of the shock and the condensate mass fraction increases towards the wall too. In the nozzle A1 the curvature of the constant Mach number contours changes its sign ahead of the shock, which causes the opposite tendency, J and therefore g/g_{max} decrease towards the nozzle wall.

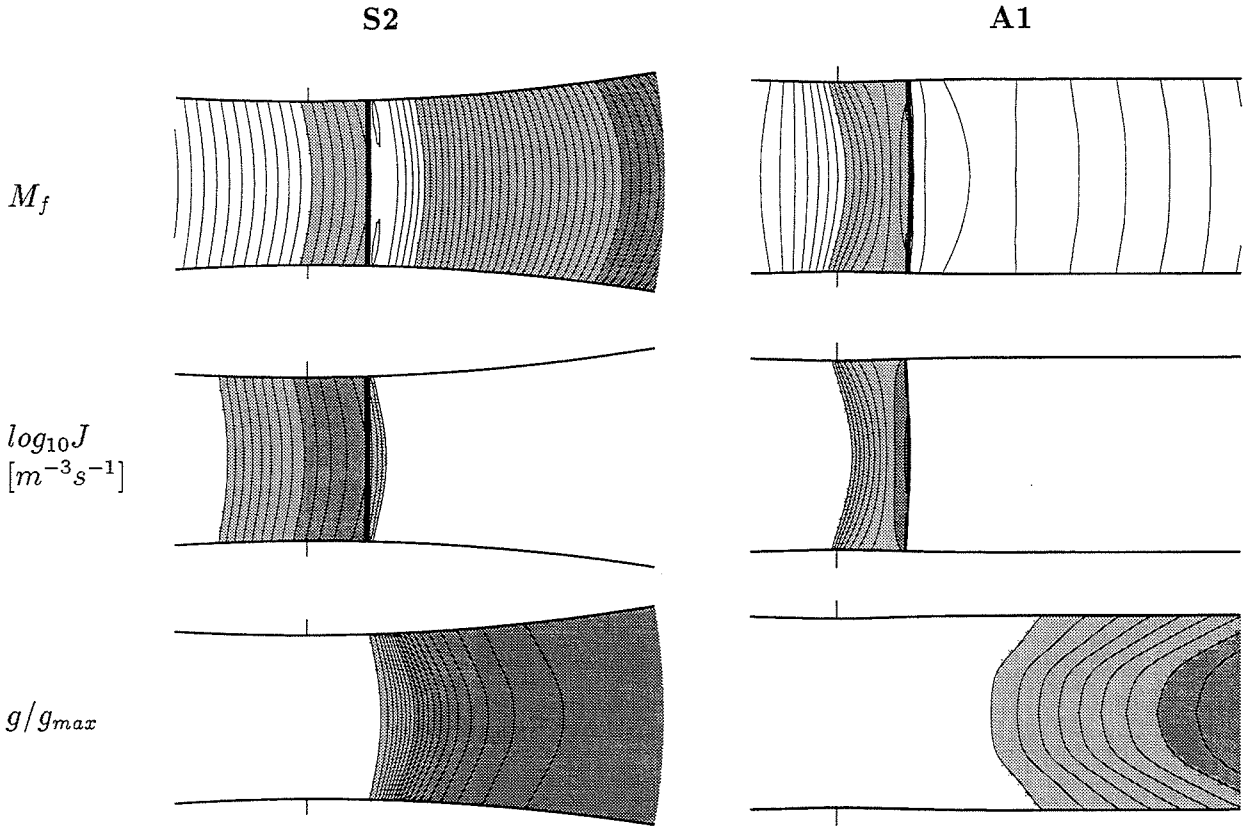

Figure 6: Left column – flow in nozzle S2 corresponding to Figs. 1b, 2 ($\Phi_0 = 73.4\ \%$); right column – flow in nozzle A1 corresponding to Figs. 3, 5 ($\Phi_0 = 35.6\ \%$). 2–D distribution of: frozen Mach number M_f (top) – increment of isolines $\Delta M_f = 0.02$, light shaded area $M_f \geq 1.0$, dark shaded area $M_f \geq 1.5$; nucleation rate $\log_{10} J\ [m^{-3}s^{-1}]$ (middle) – $\Delta \log_{10} J = 1$, light shaded area $\log_{10} J \geq 10$, dark shaded area $\log_{10} J \geq 18$; condensate mass fraction g/g_{max} (bottom) – $\Delta g/g_{max} = 0.05$, light shaded area $g/g_{max} > 0.05$, dark shaded area $g/g_{max} > 0.4$.

In the nozzle A1 the great distance between the shock and the onset of condensation (the $g/g_{max} = 0.05$ contour) indicates the slower growth of the droplets and the lower level of g/g_{max} at the nozzle exit.

5. STEADY DIABATIC FLOW IN THE NOZZLE A1 — RELATIVE HUMIDITY $\Phi_0 = 25.9\%$

In order to investigate supersonic heat addition we decrease the relative humidity Φ_0 to 25.9%. In principle we expect supersonic outflow or weak shocks near the nozzle exit depending on the given back pressure. Comparison of the measured pressure distribution of the adiabatic and diabatic flow by Fig. 7 shows that the onset of condensation is shifted downstream into the constant cross sectional region and that the heat release leads to an increase of p/p_{01} as typical for supersonic heat addition. The adiabatic pressure distribution demonstrates the growing displacement thickness of the boundary layer.

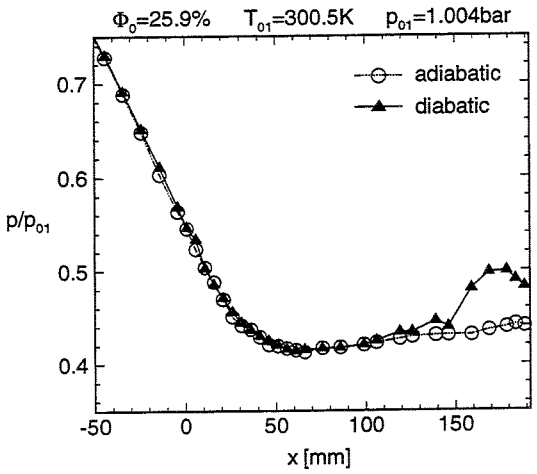

Figure 7: Experimental pressure distribution along the axis of nozzle A1 of steady diabatic and adiabatic flow (location of the nozzle throat: $x = 0\,mm$). Reservoir conditions: $T_{01} = 300.5\,K$, $p_{01} = 1.004\,bar$, $\phi_0 = 25.9\,\%$, $x = 5.9\,g/kg$.

For the same reservoir conditions numerical simulations with different back pressures are shown in Fig. 8. The low back pressure $p_{exit}/p_{01} = 0.534$ yields a weak shock near the nozzle exit (Fig. 8a). The supersonic heat addition ahead of the shock reduces the shock strength, so the pressure increase across the shock is only about 4 % of p_{01}. Here the shock position is obviously in the zone of relevant condensation (Fig. 8c). In contrast to the shock behaviour discussed in the previous sections 2–4 now the shock position varies significantly depending on the back pressure. The temperature and pressure increase across the shock is sufficient to decrease the droplet growth such that the remaining heat addition leads to the given static pressure at the nozzle exit.

6. UNSTEADY FLOWS IN THE NOZZLE A1

In the nozzle S2 the flow may still be steady for relative humidities $\Phi_0 \approx 70\,\%$ (Fig. 1b). For higher values of Φ_0 we observe three different modes of self-excited periodic flow with oscillating or periodically formed shocks. These modes and the frequency dependence on the supply conditions and the nozzle geometry are summarized in [5] and [7].

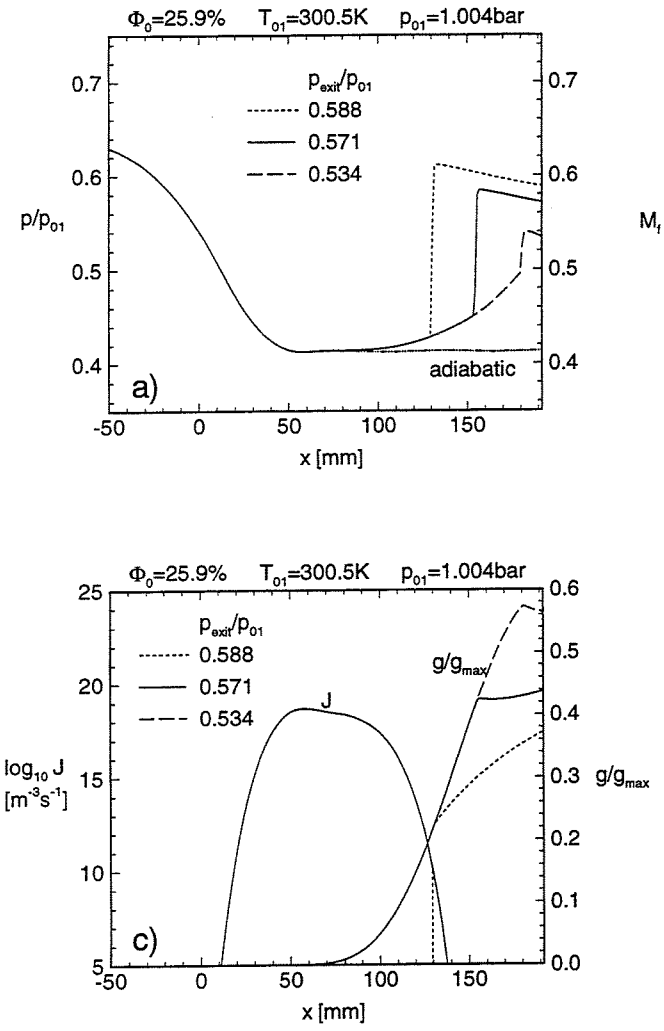

Figure 8: Numerical simulation corresponding to the experiment shown in Fig. 7 (nozzle A1 – throat position at $x = 0\,mm$); plotted along the nozzle axis:
5a (top left) – pressure ratio p/p_{01} for different back pressures;
5b (top right) – frozen Mach number M_f;
5c (left) – nucleation rate J and condensate mass fraction g/g_{max}.

However, for a relative humidity Φ_0 greater than about 45% the flow in the nozzle A1 is unsteady, where a continuous compression occurs in the nozzle S2 for the same conditions. Increasing Φ_0 we first observe an oscillation of the shock in the divergent nozzle section analogous to mode 3 in the nozzle S2. For values of Φ_0 above 50 % we obtain a flow oscillation corresponding to mode 1 in the nozzle S2. Schlieren photographs of one period are shown in Fig. 9 with time increasing from the top to the bottom. In the divergent nozzle section the latent heat release causes the formation of a shock which moves upstream into the convergent nozzle section, where it accelerates and dies out. Schlieren streak registration yields the frequency of $f = 225\ Hz$. Even for high values of Φ_0 mode 1 is observed in the nozzle S2. In the nozzle A1, however, for $\Phi_0 > 75$ % the flow shows a completely different behaviour. Now the moving shocks are not symmetrical with respect to the nozzle axis. Two different phase positions of this mode are shown in Fig. 10. In the upper schlieren photograph a system of oblique shocks moves opposite to the main flow direction from right to left. In the region of the nozzle throat we observe an unsteady Mach reflection. As the time increases a shock seems to separate

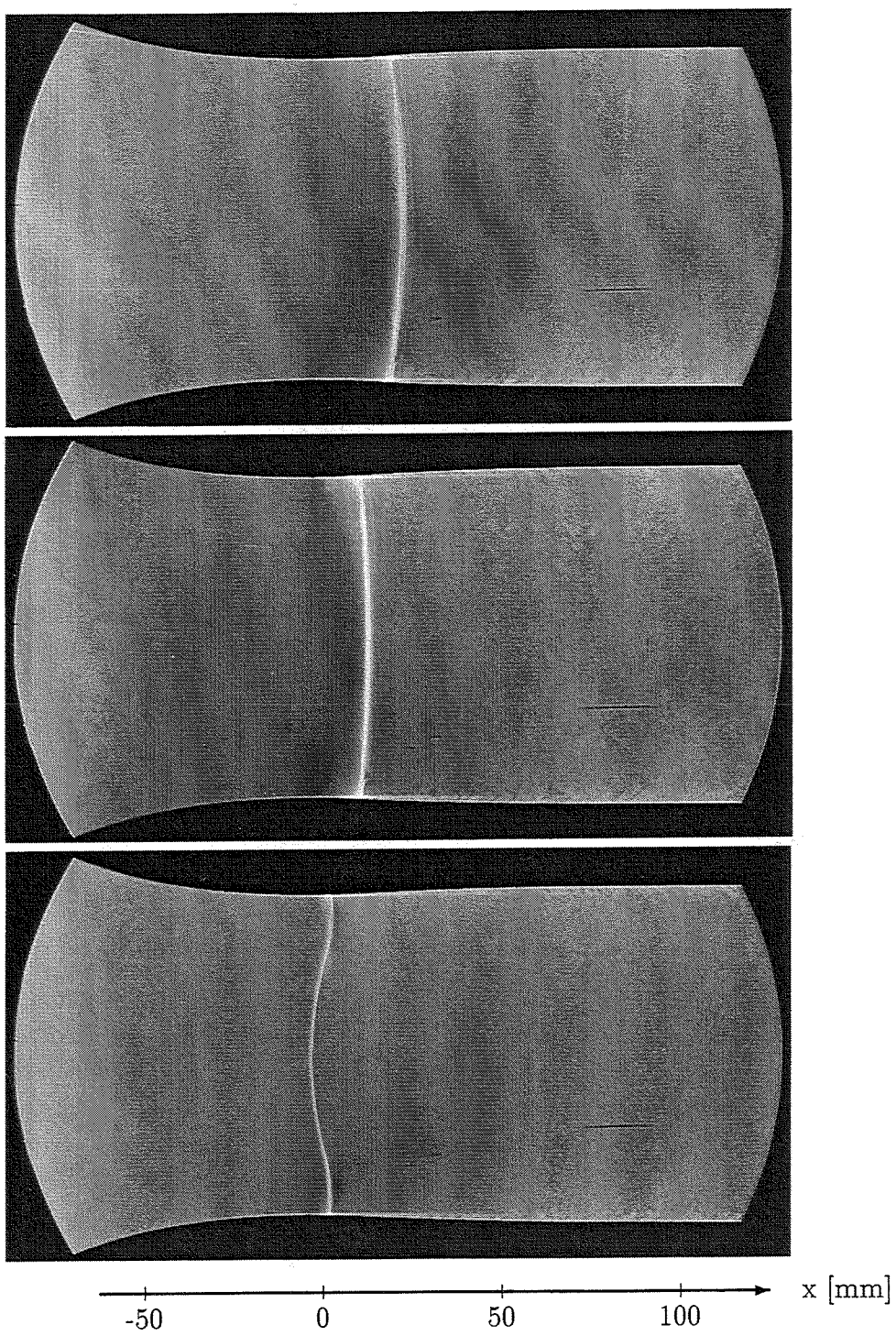

Figure 9: Schlieren pictures of self–excited periodic diabatic flow in the nozzle A1, symmetric flow oscillation (time increases from top to bottom, flow from left to right, location of the nozzle throat: $x = 0\ mm$). Reservoir conditions of the moist air: $T_{01} = 292.8\ K$, $p_{01} = 0.998\ bar$, $\phi_0 = 51.6\ \%$, $x = 7.4\ g/kg$; frequency $f = 225\ Hz$.

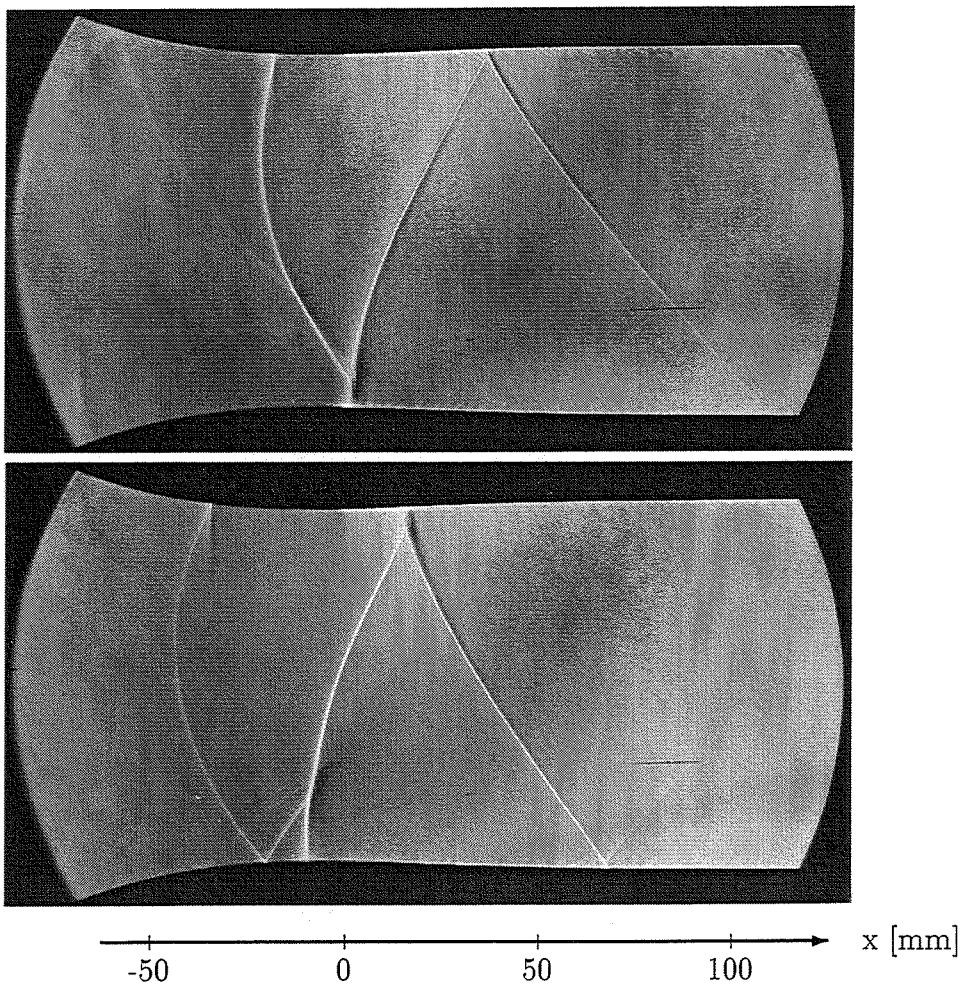

Figure 10: Schlieren pictures of self–excited periodic diabatic flow in the nozzle A1, unsymmetric flow oscillation (time increases from top to bottom, flow from left to right, location of the nozzle throat: $x = 0\ mm$). Reservoir conditions of the moist air: $T_{01} = 288.2\ K$, $p_{01} = 1.000\ bar$, $\phi_0 = 82.0\ \%$, $x = 8.8\ g/kg$; frequency $f = 905\ Hz$.

(lower schlieren photograph). The left hand part of the upper picture shows the previous pressure wave. For this unsymmetric mode the frequency is much higher, here about 905 Hz.

7. CONCLUSION

In order to control flows with shock formation caused by nonequilibrium condensation, we investigated transonic two–phase flows of water vapor/carrier gas mixtures in a Laval nozzle with a constant exit Mach number. For a relative humidity $\Phi_0 = 35.6\ \%$ we obtained a shock ahead of the condensation onset which terminates the zone of significant nucleation. Then the appropriate subsonic heat addition leads to the given back pressure at the nozzle exit. A

variation of the back pressure leads to very small changes of the shock position because here the heat release is controlled by the cut of the nucleation rate. For $\Phi_0 = 25.9\,\%$ the shock location after supersonic heat addition is far behind the zone of relevant nucleation. A variation of the back pressure clearly shifts the shock because in this case the shock controls the heat addition and not the nucleation rate.

Self–excitation already develops for relative humidities $\Phi_0 > 40\,\%$ in the nozzle A1. For $\Phi_0 > 75\,\%$ we observed a yet unknown unsymmetric mode of flow oscillation, which has to be studied in further investigations. Numerical calculation will yield informations about the unsteady interaction of the flow with the condensation process.

8. ACKNOWLEDGEMENT

This work was partially supported by the Deutsche Forschungsgemeinschaft (contract Zi 18/35–1,–2).

9. NOMENCLATURE

English symbols:

f	:	frequency
g	:	condensate mass fraction
J	:	nucleation rate
M_f	:	frozen Mach number
p	:	pressure
R	:	radius of wall curvature
t	:	time
T	:	temperature
x	:	mixing ratio
x	:	cartesian coordinate

Greek symbols:

Φ_0	:	relative humidity

Subscripts:

$_{exit}$	:	value at the nozzle exit
$_{max}$	:	maximum value
$_{01}$	:	reservoir value
*	:	critical value at Mach number 1

10. REFERENCES

[1] G.H. Schnerr: "2-D transonic flow with energy supply by homogeneous condensation: Onset condition and 2-D structure of steady Laval nozzle flow", in: Experiments in Fluids, 7, pp.145-156, (1989)

[2] G.H. Schnerr: "Homogene Kondensation in stationären transsonischen Strömungen durch Lavaldüsen und um Profile", Habilitationsschrift, Universität Karlsruhe (TH), Germany (1986)

[3] U. Dohrmann: "Ein numerisches Verfahren zur Berechnung stationärer transsonischer Strömungen mit Energiezufuhr durch homogene Kondensation", Dissertation, Universität Karlsruhe (TH), Germany (1989)

[4] G. Mundinger: "Numerische Simulation instationärer Lavaldüsenströmungen mit Energiezufuhr durch homogene Kondensation", Dissertation, Universität Karlsruhe (TH), Germany (1994)

[5] G.H. Schnerr, St. Adam and G. Mundinger: "Frequency Control of Shock Oscillations in High Speed Two–Phase Flow", in: Proc. of the Fourth Triennal Intern. Symp. on Fluid Control, Measurement and Visualization (FLUCOME'94), Toulouse, August 29 – September 2, 1994 (ed. Hebrard, P.). ONERA–CERT (1994)

[6] B. Schmidt: "Beobachtungen über das Verhalten der durch Wasserdampfkondensation ausgelösten Störungen in einer Überschall–Windkanaldüse", Dissertation, Universität Karlsruhe (TH), Germany (1962)

[7] G.H. Schnerr, St. Adam and G. Mundinger: "New Modes of Periodic Shock Formation in Compressible Two–Phase Flows", in: Proc. of IUTAM Symposium on "Waves in Liquid/Gas and Liquid/Vapor Two–Phase Systems", Kyoto, May 9–13, 1994 (ed. Morioka, S.). Kluwer Academic Publishers (1994)

THERMO-HYDRAULIC INSTABILITIES DURING START-UP IN NATURAL CIRCULATION BOILING WATER REACTORS (EFFECT OF THE NUMBER OF CHANNELS ON INSTABILITIES)

M. Aritomi [1], J. H. Chiang [1], T. Ishikawa [1], M. Mori [2] and H. Tabata [3]

[1] Research Laboratory for Nuclear Reactors, Tokyo Institute of Technology
2-12-1 Ohokayama, Meguro-ku, Tokyo, 152 Japan
Telephone +81-3-5734-3063, Facsimile +81-3-5734-2959

[2] Tokyo Electric Power Company
1-1-3 Uchisaiwai-cho, Chiyoda-ku, Tokyo, 100 Japan
Telephone +81-3-3501-8111, Facsimile +81-3-3592-1580

[3] Japan Atomic Power Company
1-6-1 Ohtemachi, Chiyoda-ku, Tokyo, 100 Japan
Telephone +81-3-3201-6631, Facsimile +81-3-3212-5720

ABSTRACT

The authors have been investigating transient behavior of natural circulation in boiling two-phase flow by simulating the start-up process in natural circulation BWRs with the aim of establishing their rational start-up procedure. In this paper, the following thermo-hydraulic instabilities are particularly dealt with; (1) out-of-phase geysering induced by condensation of a large bubble and (2) in-phase natural circulation oscillation induced by hydrostatic head fluctuation in steam separators, which have never been understood well enough and may be induced during their start-up according to start-up procedure and reactor configuration. At first, geysering is experimentally investigated in three and four parallel boiling channels with the same thermo-hydraulic condition for both natural and forced circulations, as compared with the results in two channels, in order to confirm its driving mechanism proposed in our previous works and to understand the effect of the number of channels on the flow stability map. Next, geysering is also investigated experimentally in three channels with different heated lengths among channels to clarify the effect of a power distribution in the core on the flow stability map. Finally, natural circulation oscillation is experimentally investigated in three and four channels to verify its driving mechanism proposed in our previous works.

1. INTRODUCTION

1.1 Background

On realizing widely that the safety of current LWRs is too dependent on active engineered safety features to enhance their reliability, many concepts have been proposed for the next generation LWRs in which passive and simplified safety functions are actively introduced. A concept of natural circulation BWRs, e.g. the SBWR[1], has been proposed as one such case. It seems to be promising in that the primary cooling system can be simplified but simultaneously it also brings some disadvantages. Aritomi et al. provided a discussion concerning advantages and disadvantages on eliminating recirculation pumps[2].

From the consideration, it was clear that establishment of a rational start-up procedure is one of the most important problems in achieving natural circulation BWRs because they have to be heated

by fission energy from start-up under low temperature and pressure conditions. Thermo-hydraulic instability was experienced during start-up in thermal natural circulation boilers using fossil fuel. Although there were no published papers about this instability, it was estimated that the instability might be a kind of geysering. In thermal natural circulation boilers, so long as the dryout phenomena, which induce heat transfer tube failure, can be avoided, flow instability during the start-up is not a significant problem. This countermeasure was worked out: The output from burners decreased down to a partial load of about 25% which did not induce dryout phenomena and increased up to the rate power after the pressure in the steam header reached up to about 0.3MPa. On the other hand, if thermo-hydraulic instabilities were to occur during start-up in natural circulation BWRs, they would hamper their operation for raising power output because void fraction fluctuation in the reactor core would oscillate the reactivity.

1.2 Previous Works

The authors have also been investigating thermo-hydraulics during start-up in natural circulation BWRs simulating both normal and abnormal start-up conditions. It was found from the results that three kinds of thermo-hydraulic instabilities may occur according to reactor configuration and start-up procedure[2]; (1) out-of-phase geysering induced by condensation of a large bubble, (2) in-phase natural circulation instability induced by hydrostatic head fluctuation in steam separators and (3) out-of-phase density wave instability.

Thermo-hydraulic instabilities in boiling two-phase flow have been investigated for a long time. Boure, Bergles and Tong[3] and Aritomi[4] have reviewed previous works and classified instabilities into their driving mechanisms. Lahey and Drew[5] reviewed a number of reports concerning thermo-hydraulic instabilities in BWRs. Since the density wave instability has been investigated by many researchers, its driving mechanism has been understood and analytical methods have been established. On the other hand, the geysering and natural circulation oscillation have not been investigated extensively.

Griffith is believed to have been the first to have investigated geysering[6]. He presented an aspect of geysering induced in the case where liquid in a vertical column with a closed end was heated near the bottom as follows:

> Superheated liquid suddenly vaporizes and leads to a large slug bubble which grows as it moves toward the exit due to the decrease in hydrostatic head. The vapor is mixed with subcooled liquid in an upper plenum and is condensed therein. The pressure in the column decreases, subcooled liquid reenters into the column and thereafter the non-boiling condition is restored. It is a feature of geysering that such a process repeats periodically.

Nakanishi et al. investigated geysering in a single channel under forced circulation conditions and found that geysering was only generated at velocities lower than 0.02m/s[7].

In contrast with this, our study indicated that geysering appeared in velocities up to about 0.2m/s[2]. Geysering in parallel channels has never been understood well enough to design a way to prevent it from occurring. The authors have been investigating geysering in twin parallel boiling channels under both natural and forced circulation conditions and proposed its driving mechanism [8]. In order to verify the proposed driving mechanism, the effect of subcooling in the outlet plenum on its occurrence was also investigated in twin parallel boiling channels under forced circulation conditions[9].

Fukuda et al. had investigated thermo-hydraulic instability like natural circulation oscillation for development of the prototype advanced thermal reactor, 'FUGEN'[10]. Although they concluded that the stability map of this instability could be evaluated by the same linear analysis method as used for the density wave instability, it was made clear from our experiment that this instability cannot be analyzed by a linear analysis because it was governed by non-linear phenomenon.

Moreover, the period of flow oscillation is about ten times of the time required for passing through the heated section[2]. Hence, natural circulation oscillation was experimentally investigated in twin parallel boiling channels under natural circulation conditions. From the results, its driving mechanism was proposed[11].

Finally, by considering our proposed driving mechanisms of geysering and natural circulation oscillation, it was inferred that an increase in the system pressure would suppress these instabilities. This inference was experimentally confirmed[12].

1.3 Purpose of This Paper

Based on our proposed driving mechanism of geysering, it is inferred that geysering occurs most readily in twin channels and geysering may be not induced in natural circulation BWRs where there are many fuel assemblies. Geysering was, however, induced in the thermal boilers which had many boiling tubes. In this paper, geysering was experimentally investigated in three and four parallel channels with the same thermo-hydraulic conditions under both natural and forced circulation conditions and the results were compared with the ones in twin channels[8],[9] in order to examine the effect of the number of channels on its stability map. In addition, the experiments were also carried out for the heated lengths different in each channel to investigate how power a distribution in the core influences the occurrence of geysering.

Finally, natural circulation oscillation was experimentally investigated in three and four parallel channels and the results were compared with those in twin channels[11] to verify its proposed driving mechanism.

2. EXPERIMENTAL APPARATUS

Figure 1 illustrates a schematic diagram of the loop which carries boiling fluid in both natural and forced circulations by switching a pneumatic ball valve. The loop was operated at atmospheric pressure, and water was used as the test fluid. The whole circulation rate was measured by an orifice flowmeter. In this set of experiments, circulating fluid temperature was regulated by precoolers and preheaters installed in a separator tank. The steam generated in a test section was separated in the separator tank and was liquefied through a condenser also attached therein. In the separator, the exit of a channel connecting with the outlet plenum was higher than the liquid level to simulate a separator of the SBWR. The experimental conditions are tabulated in **Table I.**

The geometry and dimensions of the test section are presented in **Fig.2**, which gives details of four parallel channels between the inlet and outlet plenums. Each channel consisted of a heater, two electrodes and an orifice flowmeter for measuring flow oscillation. The heater rod was made of a thin stainless steel tube (6mm O.D. and 0.3mm thick), installed concentrically in the test section made of Pyrex glass (15.6mm I.D.) and heated by a DC current.

The experiments were performed in three and four channels under both natural and forced circulations. In experiments for three channels, one outer channel was closed. The following two conditions were investigated; (1) the same thermo-hydraulic condition among channels and (2) heated lengths different in each channel. For the later condition, non-heated risers located in the downstream of the heated section were the same length in every channel because it was clear from our previous work[9] that the non-heated riser length influences the stability map of geysering and its amplitude.

3. RESULTS AND DISCUSSIONS

3.1 Geysering in Multi Parallel Channels with the Same Condition among Channels

Our proposed driving mechanism of geysering appearing in twin parallel boiling channels was as follows:

Whenever geysering appears, a large bubble covering the whole flow cross section such as a slug bubble exists. The large bubble grows with absorption of many small bubbles and a decrease in the hydrostatic head enhances the vaporization and increases the velocity in this channel step by step. As soon as the large bubble arrives at the outlet plenum where subcooled water is filled with, it is rapidly condensed and vanishes and the pressure in the channel results in a decrease. Consequently, water reenters rapidly from the inlet plenum as the pressure drop corresponds to that in the other channel. If the reentering rate is superior to the whole circulation one, flow reversal, which means that water reenters from the outlet plenum, is induced in the other channel. Both channels are filled with liquid and a non-boiling condition is restored for a while. In the other channel, water becomes saturated first and a large bubble is formed because hotter water reenters from the outlet plenum. It is a feature of geysering in twin parallel channels that such phenomena repeat periodically and alternatively in both channels. The condensation rate of the bubble superior to the whole circulation rate is necessary for geysering to occur. The formation of a large bubble and the subcooling in the outlet plenum are required for satisfying this indispensable condition. Flow reversal plays an important role for the occurrence of geysering.

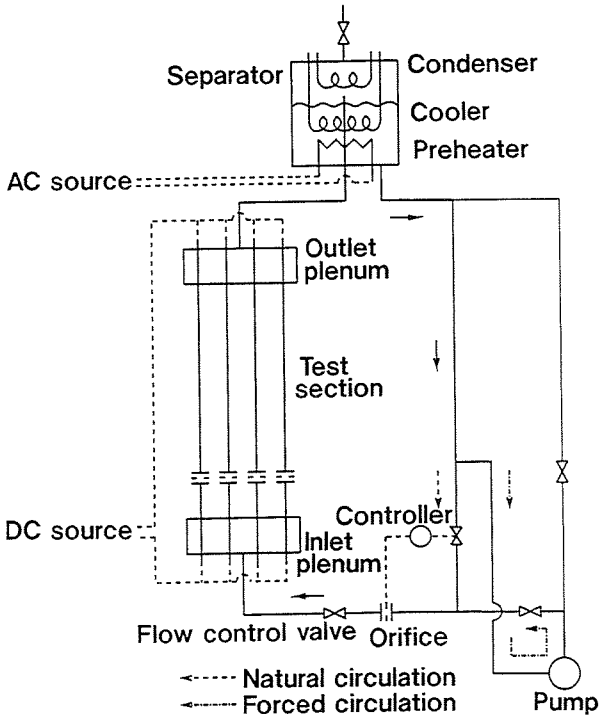

Fig.1 A schematic diagram of flow loop

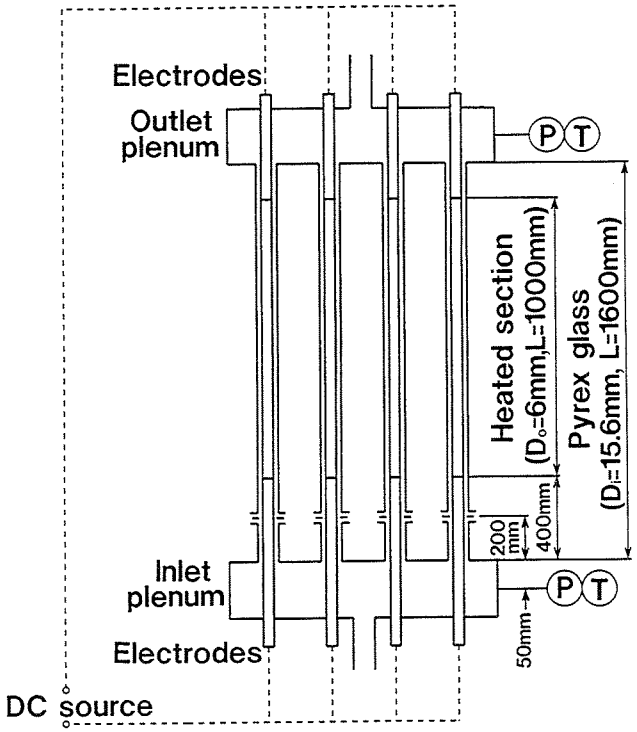

Fig.2 Test section

Table I Experimental conditions

Test fluid	Water
System pressure	Atmospheric pressure
Number of channels	Two, three and four
Heat flux	0 - 200kW/m^2
Subcooling	10K
Heated length	1.0m
Inlet velocity (Only for forced circulation)	0 - 0.5m/s

According to this mechanism, geysering is induced most readily in twin channels because an increase in the number of channels makes the whole circulation rate higher and the flow reversal rate lower. Therefore, it is thought that geysering may not be induced in natural circulation BWRs where there are many fuel assemblies. As mentioned above, geysering was however induced in the thermal boilers which had many boiling channels. It is the first purpose of this paper to clarify the effect of the number of channels on the stability map of geysering.

Geysering was experimentally investigated in three and four parallel channels with the same thermo-hydraulic condition in every channel. It was clear from our previous works[8],[9] that the unstable region for heat flux and the period of flow oscillations in a forced circulation were identical to those in a natural one. Typical measurements of geysering in three and four parallel boiling channels under both natural and forced circulation conditions as compared with those in twin channels in **Figs.3** and **4**, which are velocities in each channel, $u^{(i)}$, and the whole circulation velocity converted by the whole cross sections of the test section, u_t. Regardless of circulation methods, flow oscillations with a phase delay of 180° appear periodically in two channels, and the phase delays are about 120° in three channels and about 90° in four channels. The flow oscillation with a phase delay of 180° in a pair of two by two channels was not observed in four channels. When subcooled water reentered rapidly from the inlet plenum, in the other channels, hotter water reentered from the outlet plenum or the water almost stagnated and continued to heat up. Consequently, a large bubble coalesced first in one of the other channels, geysering occurred therein and then it followed in the other channels. This is the reason why geysering with a phase delay of 120° or 90° appeared in three or four channels.

Although periods and amplitudes of geysering are almost constant in two channels under a certain condition, they are not always constant in three and four channels because the heterogeneity of two-phase flow such as coalescence and condensation of a large bubble becomes notable in that there is the freedom of flow rate distribution in multi channels over three.

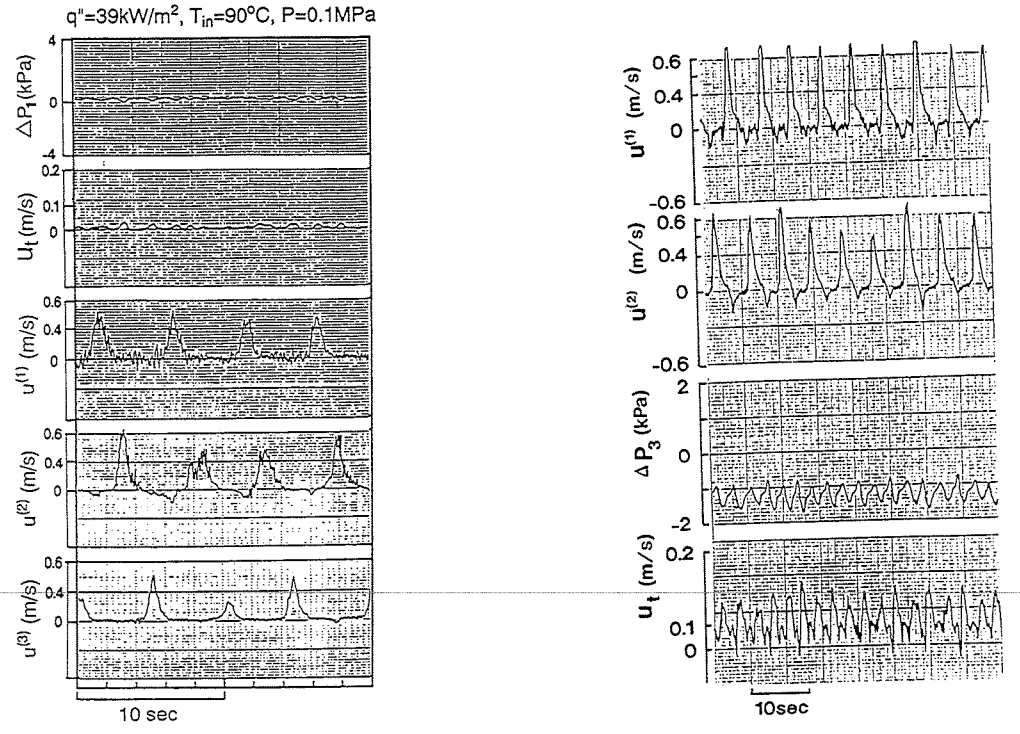

(a) Three parallel boiling channels **(b) Twin parallel boiling channels**

Fig.3 Experimental results in natural circulation

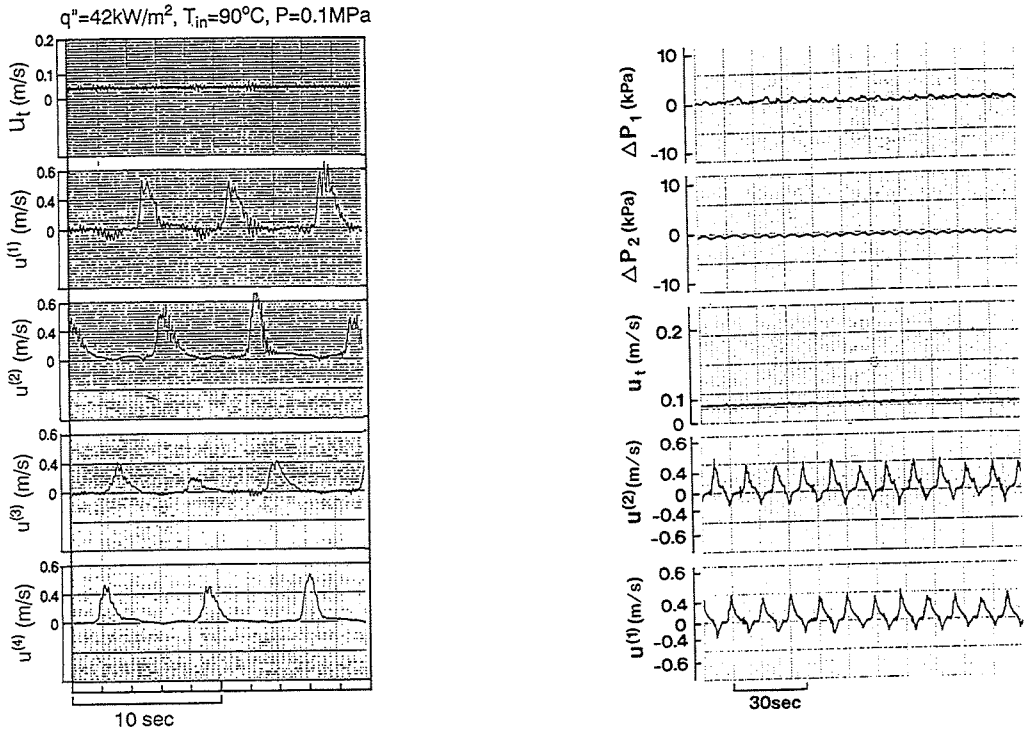

(a) Four parallel boiling channels **(b) Twin parallel boiling channels**

Fig.4 Experimental results in forced circulation

Under natural circulation conditions as shown in **Fig.3**, when geysering is induced in each channel, the whole circulation rate increases temporally. This fact indicates that the whole circulation rate oscillates through the influence of the occurrence of geysering. Hence the frequency of the whole circulation oscillation is times that of the number of channels, e.g. twice in two channels, three times in three channels and four times in four channels as compared with the frequency of flow oscillation in each channel. The amplitude of its oscillation decreases with an increase in the number of channels because of an increase in the whole circulation rate. Regardless of circulation methods, flow reversal rates were greatest in two channels but were not in three and four channels. However, during one cycle of flow oscillation in one channel, the frequency when flow reversal or stagnation occurs increases with an increase in the number of channels, e.g. once in two channels, twice in three channels and three times in four channels.

Although the circulation rate is maintained in forced circulation under the non-boiling condition where every channel is filled with water, it becomes almost zero in natural circulation. The circulation rate is induced at the beginning of subcooled boiling and is increased by an increase in void fraction due to coalescence of a large bubble. In two channels, the regions where only geysering occurs in natural circulation agrees with that where it does in forced circulation[8]. **Figure 5** shows the natural circulation characteristics in three and four channels and its unstable region. **Figure 6** illustrates the unstable regions in reference to the number of channels, where geysering appears alone and together with natural circulation. It can be seen from the figure that the stability map of geysering against heat flux is independent of the number of channels. Next, the stability maps of three and four channels in forced circulation were investigated, and the results are demonstrated in **Fig.7**. The marked region is where geysering periodically appears in two channels. The unstable region where periodic geysering appears is identical to the one in two channels. In three and four channels, however, geysering without periodicity appears at higher heat fluxes, because the heterogeneity of two-phase flow, such as coalescence and condensation of a large bubble, becomes more remarkable due to an increase in the freedom of flow rate distribution.

Consequently, the flow fluctuates greatly and geysering is induced at random at higher heat fluxes than its upper limitation for two channels. It is clear from these results that the stability map of geysering is independent of the number of channels regardless of circulation methods. Let us consider this reasoning. As the number of channels increases, the flow reversal rate decreases because of an increase in the whole circulation rate, and the amount of hotter water reentering from the outlet plenum decreases. On the other hand, the period while circulation rate is low becomes longer because the frequency when geysering occurs in other channels increases, and a large bubble therefore coalesces readily at a low velocity.

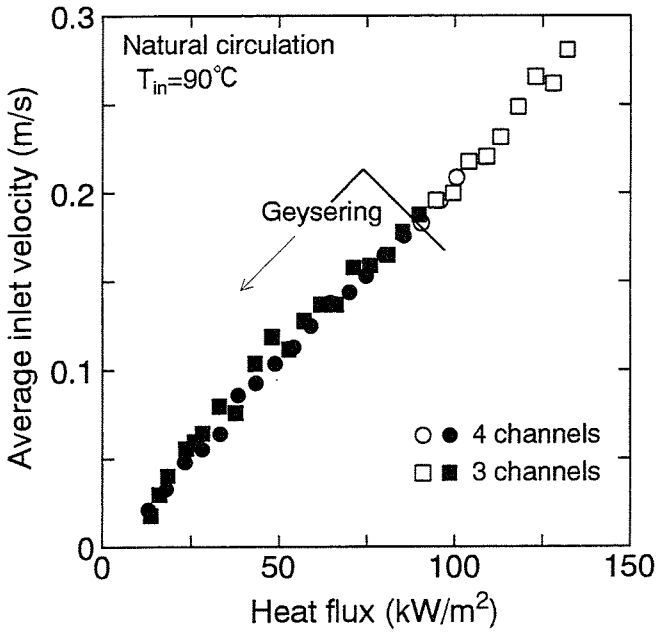

Fig.5 Stability map of geysering in multi channels under natural circulation conditions

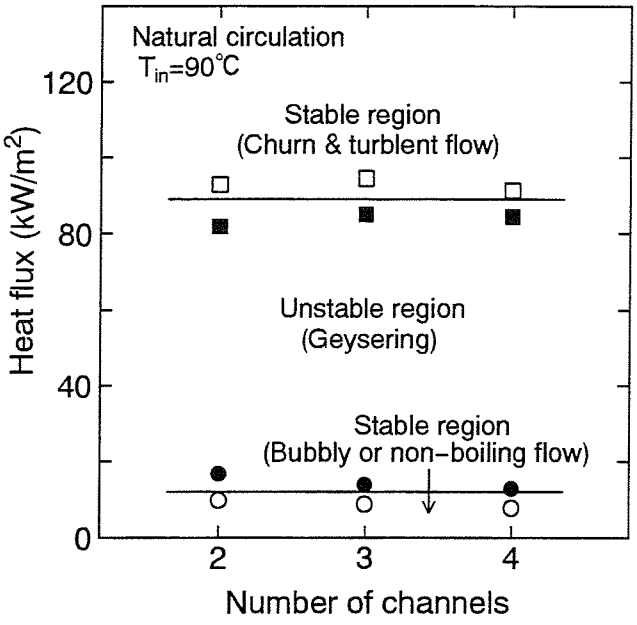

Fig.6 Effect of the number of channels on stability map

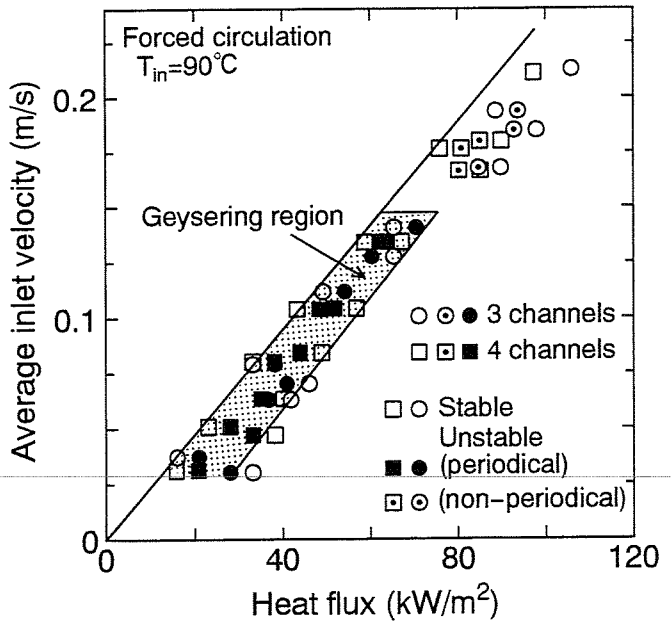

Fig.7 Stability map of geysering in multi channels under forced circulation conditions

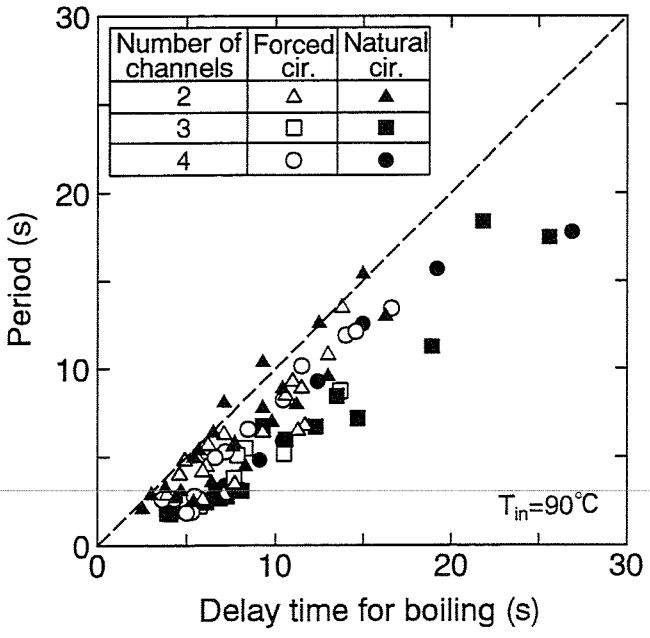

Fig.8 Periods of geysering in multi channels

The effect of the number of channels on the period of geysering was investigated experimentally. The delay time for boiling is introduced:

$$\tau_B = \frac{\rho_l (i_{lsat} - i_{in})}{q'''} \quad , \tag{1}$$

where ρ_l is the liquid density, i_{lsat} the liquid saturated enthalpy, i_{in} the liquid enthalpy in the inlet plenum and q''' the calorific power per unit volume. **Figure 8** shows experimental results of geysering periods in reference to the delay time for boiling, where data obtained in two channels are added. Although data are somewhat scattered because the volume of a large bubble and condensation rate vary and the amount of hot water reentering from the outlet plenum is not constant, it can be seen from the figure that the periods can be almost arranged with the delay time for boiling regardless of the number of channels and circulation methods.

Next, flow reversal rates of geysering, which significantly influenced geysering occurrence in two channels, were also investigated. The results in natural circulation are shown in **Fig.9** where data obtained in two channels are added. It is seen from the figure that the flow reversal rate is very high in two channels but that it is not high in three and four channels. The flow reversal rate is induced by the difference of the volumetric condensation rate from the whole circulation rate which increases with an increase in the number of channels. Furthermore, since the amplitude of the whole circulation rate oscillation in three and four channels becomes smaller than that in two channels, the flow reversal rate in forced circulation is scarcely different from that in natural one. The results of flow oscillation amplitude in forced circulation are shown in **Fig.10**. In contrast with the flow reversal, the amplitude increases with an increase in the number of channels. In natural circulation, the same tendency was also observed but was not conspicuous as compared with that in forced circulation. Since the flow reversal decreases with an increase in the number of channels, the inertia of inlet velocity increases. Consequently, the reentering rate due to the condensation of a large bubble becomes higher. This is the reason why the flow reversal rate decreases but the amplitude increases with an increase in the number of channels.

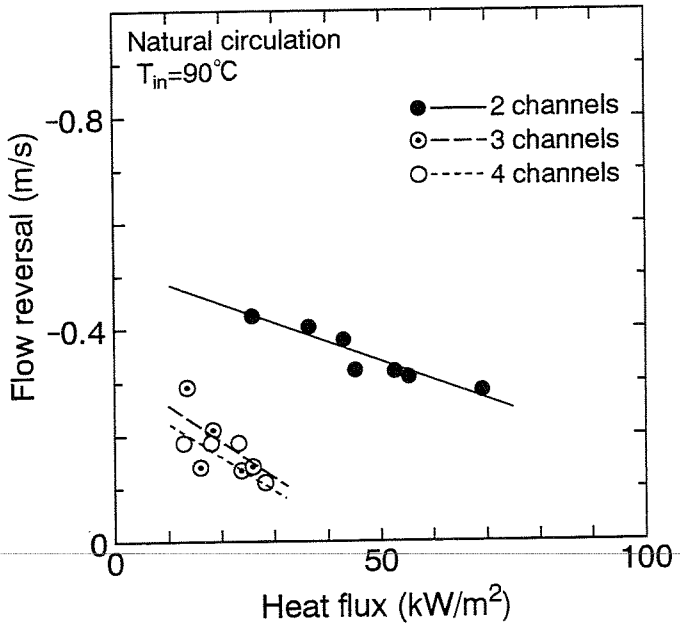

Fig.9 Flow reversal rates of geysering in multi channels

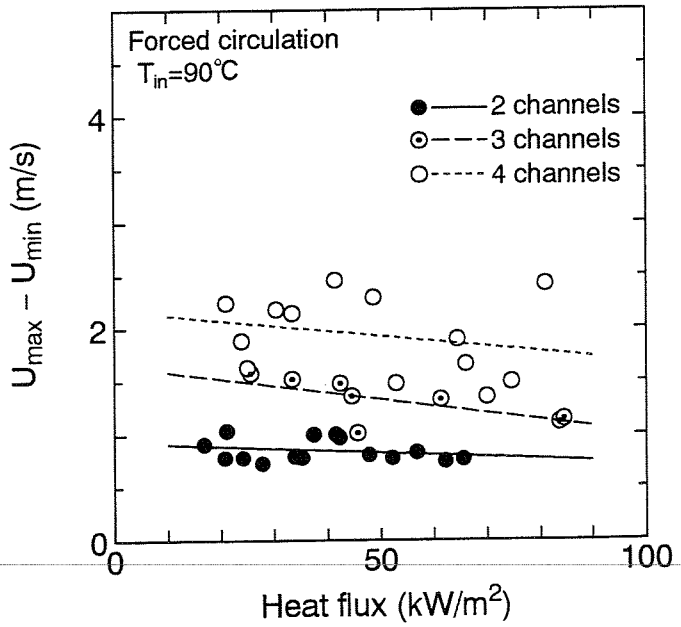

Fig.10 Flow oscillation amplitude of geysering in multi channels

From above-mentioned results, the driving mechanism of geysering in multi parallel channels is clarified as follows: When subcooled water is heated and subcooled boiling is induced, a large

bubble covering the whole channel is formed in the non-heated riser if velocity is low. Then, the growth of a large bubble decreases the hydrostatic head and increases the circulation rate. When the bubble reaches the outlet plenum, if water therein is subcooled, it is rapidly condensed and vanishes and the pressure in the channel is rapidly decreased. Consequently, water reenters rapidly from the inlet plenum as the pressure drop corresponds to that in other channels. This high reentering rate induces the flow reversal or low flow rate in other channels. In other channels, when subcooled boiling is induced, if flow rate is low enough for a large bubble to coalesce and geysering is induced. Therefore, the occurrence of flow reversal is not an indispensable condition but low flow rate enough to form a large bubble is an indispensable condition after subcooled boiling occurs.

In this work, experiments were conducted only on two, three and four channels. However, by considering the experience of geysering in thermal natural circulation boilers which have many boiling tubes, the following is supposed: In multi parallel boiling channel systems operated in natural circulation, while water fills in the channel, fluid is almost stagnant. After subcooled boiling occurs, fluid begins to flow due to a decrease in the hydrostatic head. This aspect is not changed for the number of channels. Consequently, the number of channels does not influence the stability map of geysering. In contrast with this, in forced circulation, even while water fills in the channel and non-boiling condition is restored, fluid flows at the average velocity. Hence, an increase in the channels hampers a decrease in circulation rate in each channel, so this stabilizes the flow against geysering. In three and four channels, this effect is canceled by an increase in a duration at low circulation rate induced by geysering in other channels. As a result, the effect of the number of channels on the stability map of geysering does not appear in two, three and four channels.

3.2 Geysering in Multi Parallel Channels with Different Conditions from Each Channel

Power distribution exists in the core of natural circulation BWRs. If outputs are different in each channel, the static characteristics between an output and a circulation rate in each channel is different from that under the same output condition. It has never been understood how this effect influences the stability map of geysering. Therefore, experiments were also carried out on lengths heated differently in each channel to simulate the power distribution. Since it was clear from our previous work[9] that geysering occurs more readily as a non-heated riser downstream of the heated section becomes longer, the riser lengths were made equal in every channel. The experimental conditions are shown in **Table II**.

Geysering was experimentally investigated in parallel boiling channels whose heated lengths were 0.5m, 0.5m and 1.0m. With increasing heat flux, geysering appeared periodically in Ch.1 and Ch.2 whose phase delay was 180° and geysering appeared at random in Ch.3 as shown in **Fig.11 (a)**. Since the heat input in Ch.3 was higher by twice than that in the other channels and the circulation rate was higher, it was difficult for a large bubble to coalesce. The region where such an oscillation mode appears is called "*A*" region in this paper. As heat flux increases further, geysering is induced at random in every channel as shown in **Fig.11 (b)**. In this case, large bubbles formed at random in each channel and the periodicity of geysering occurring in one channel becomes poor. The region where such a oscillation mode appears is called "*B*" region. With a further increase in heat flux, churn & turbulent flow appeared at the exit of Ch.3 and geysering was suppressed therein, so that geysering with periodicity was again observed in Ch.1 and Ch.2 whose phase delay was 180° , and Ch.3 played a role of a bypass, as shown in **Fig.11 (c)**. The region where such a oscillation mode appears is called "*C*" region.

Next, geysering was experimentally investigated in three parallel boiling channels whose heated lengths were 0.5m, 1.0m and 1.0m. With increasing heat flux, geysering with periodicity appeared in every channel but the phase delay was not 180° and 120° as shown in **Fig.12 (a)**. The reversal was induced twice in a period in Ch.1 where the heat input was a half of that in the other channels and the circulation rate was lower. The region where such a oscillation mode appears is called "*A'*"

Table II Experimental conditions for different heated lengths

	Case 1	Case 2
Heated lengths	0.5, 0.5 and 1.0m	0.5, 1.0 and 1.0m
Number of channels	Three	Three
Heat flux	10 - 200kW/m^2	10 - 200kW/m^2
Inlet subcooling	10K	10K

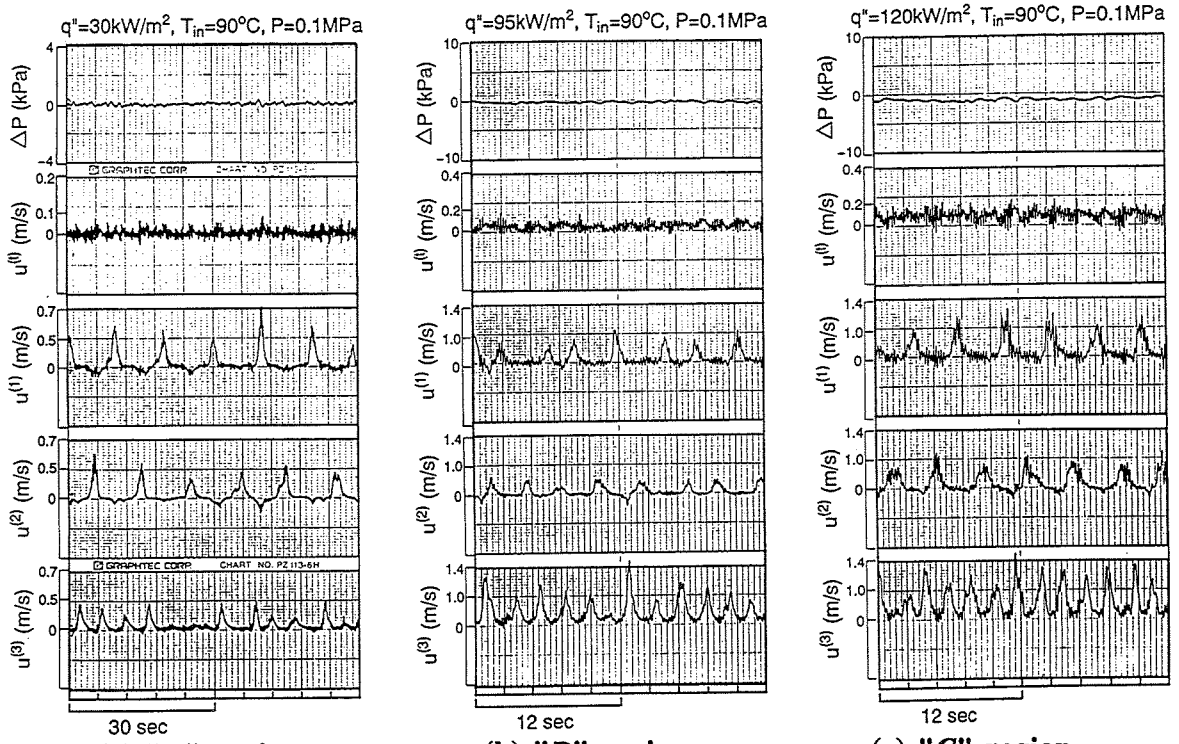

(a) "*A*" region (b) "*B*" region (c) "*C*" region

Fig.11 Measured results in multi channels of heated lengths of 0.5m, 0.5m and 1.0m

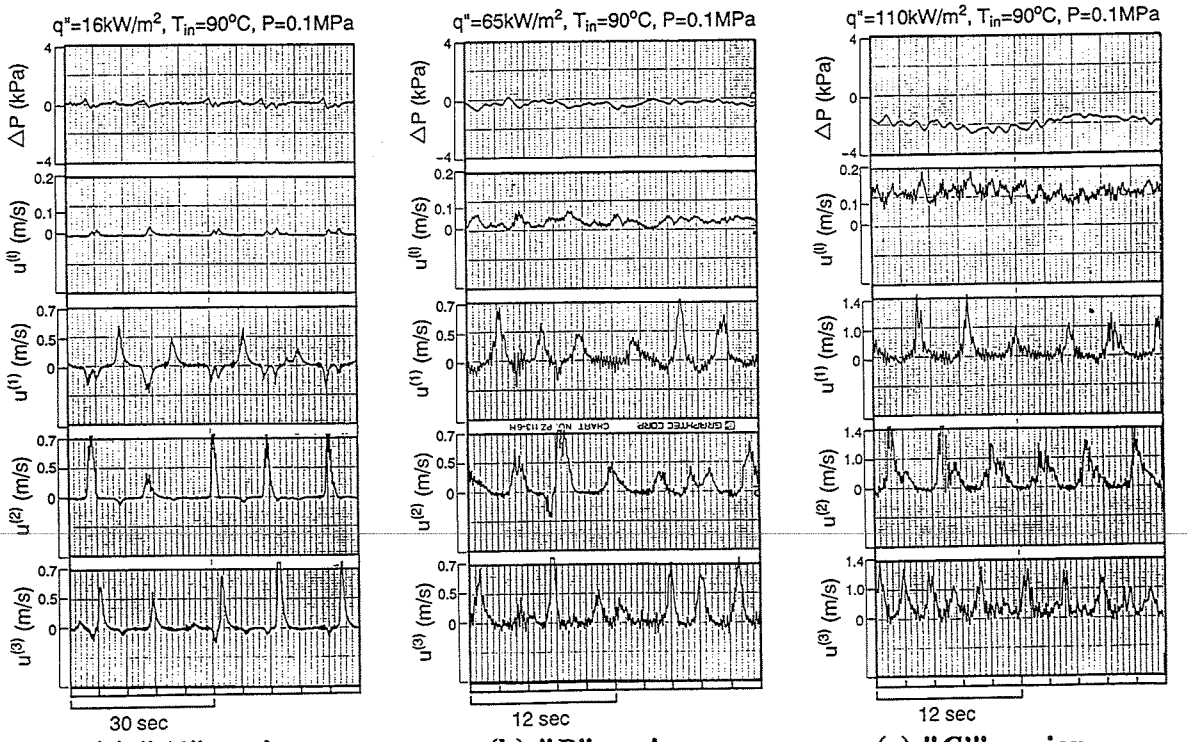

(a) "*A'*" region (b) "*B*" region (c) "*C'*" region

Fig.12 Measured results in multi channels of heated lengths of 0.5m, 1.0m and 1.0mflow

region. As heat flux further increases, geysering without periodicity is induced in every channel because large bubbles form at random in each channel as shown in **Fig.12 (b)**. This oscillation mode is similar to that shown in **Fig.11 (b)**. With a further increase in heat flux, churn & turbulent flow appeared at the exit of Ch.3., and geysering was suppressed therein. Although heated lengths were equal in Ch.2 and Ch.3, the flow reversal rate in Ch.2 was higher than that in Ch.3 and a large bubble could be formed therein. Geysering was induced periodically in Ch.1 and Ch.2 as shown in **Fig.12 (c)**. A rapid velocity rise in Ch.1 due to the condensation of a large bubble influenced more strongly in Ch.2 than in Ch.3 because Ch.2 was adjacent to Ch.1. Ch.3 played a role of a bypass. The region where such a oscillation mode is called "*C'*" region.

Let us consider the results mentioned above. **Figure 13 (a)** and **(b)** show a relationship between the region of geysering occurrence in forced circulation with the same condition and the natural circulation rate in reference to the heat flux. In all region shown in the figures, the condition in channels whose heated length is 0.5m are the unstable ones. However, in "*C*" and "*C'*" regions, the conditions in channels whose heated lengths are 1m are the stable ones.

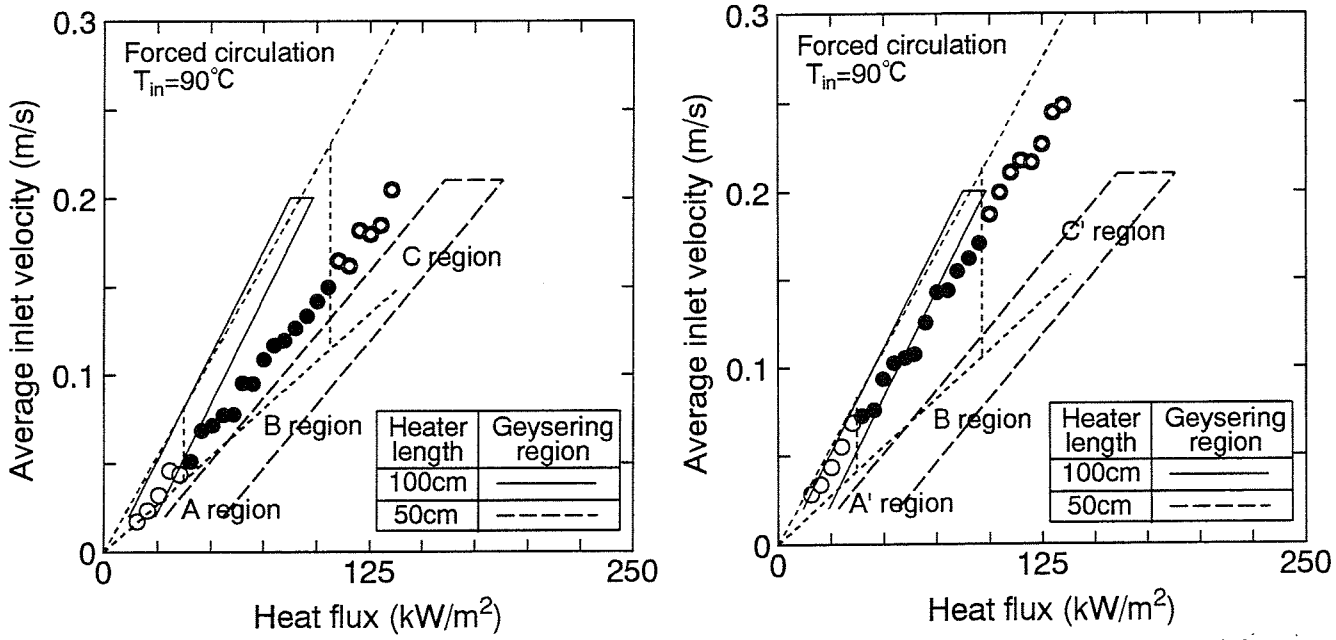

(a) Heated lengths of 0.5m, 0.5m and 1.0m **(b) Heated lengths of 0.5m, 1.0m and 1.0m**

Fig.13 Comparison of stability maps in different heated lengths among channels with the ones for the same heated length in every channel

The following insights are thought from the stability maps and our observations:

(1) In the case where the conditions are unstable in only two channels, e.g. "*C*" region, geysering with a phase delay of 180° periodically appears therein.

(2) In the case where the condition is unstable in only one channel, e.g. "*C'*" region, geysering periodically appears in this channel and this affects the flow in the adjacent channel and geysering may also occur, even if its condition is the stable one.

(3) In the cases where the conditions are unstable in every channel, geysering is induced in every channel but its aspects are very complex: Geysering with a phase delay of 180° periodically appears as a pair of two channels such as "*A*" region, geysering periodically appears in every channel but their phase delays are random such as "*A'*" region, and it appears at random in every channel such as "*B*" region. Namely, geysering occurs periodically at a low circulation rate. In contrast with this, as the circulation rate becomes higher, geysering without the periodicity appears because a large bubble is formed at random due to the heterogeneity of two-phase flow becomes notable.

As a result, the unstable region of geysering in parallel boiling channel systems with a power distribution can be estimated by evaluating the relationship between heat flux and circulation rate in each channel and by comparing this condition with the stability map of geysering in two channels with the same condition.

3.3 Natural Circulation Oscillation in Multi Parallel Channels

The driving mechanism proposed in our previous work[11] is as follows:

> Under conditions of an insufficient vaporization rate, two-phase mixture flows heterogeneously in a long vertical non-heated channel connecting the outlet plenum with the separator tank such as a steam separator. Namely, the growth of a slug bubble in its absorption of many small bubbles with higher drift velocity decreases the hydrostatic head, so that the circulation rate increases. At high circulation rate, the vapor accumulated therein flows out into the separator tank, the hydrostatic head therefore increases and the circulating rate decreases. These phenomena repeat periodically and statically. As heat input increases and two-phase mixture flows steadily in the long vertical non-heated channel, this instability is suppressed.

If the above-mentioned mechanism is correct, it is supposed that the stability map of natural circulation oscillation can be estimated from a relationship between the whole circulation rate and the whole power. Hence, the natural circulation oscillation was experimentally investigated in three and four parallel channels in order to verify our proposed mechanism. **Figure 14** shows the natural circulation characteristics between the whole circulation rate and the total power. In this figure, the regions, where natural circulation oscillation occurs, are also illustrated. As the number of channels increases, for the same total power, the heat flux becomes lower and void fraction in parallel channels decreases, so that the whole circulation rate is reduced.

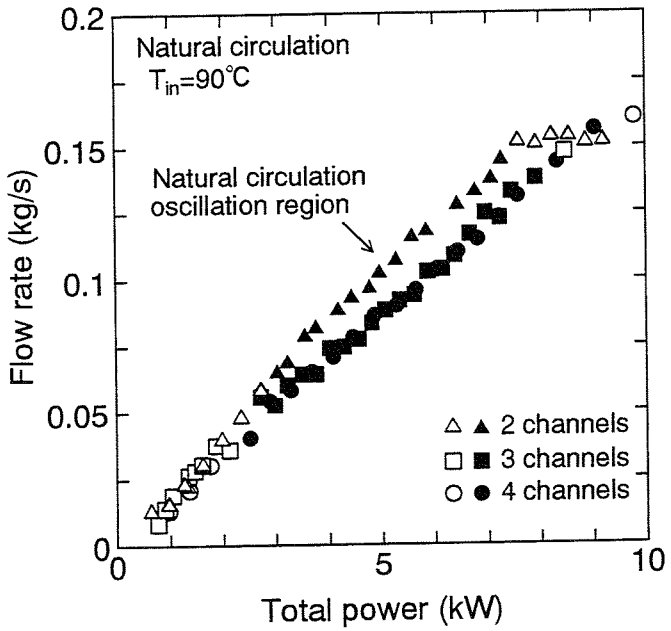

Fig.14 Stability map of natural circulation oscillation

Figure 15 (a) and (b) show the effect of the number of channels on the stability map of natural circulation oscillation in reference to the whole circulation rate and the total power respectively. It can be seen from the figure that the upper limits of the whole circulation rate, where natural circulation oscillation is induced, are almost equal in two, three and four channels. It is seen from **Fig.15** (b) that the region where natural circulation oscillation appears becomes wider with an increase in the number of channels. Let us consider this fact. In the case of low input power, the

whole circulation rate increases higher with an increase in the power. However, as the whole circulation rate becomes over a certain value, two-phase friction loss in the connection channel is not negligibly small and the circulation rate does not increases against increasing the power. Consequently, saturated boiling occurs steadily in the heated section and mixture flows steadily in the connection channel, so that natural circulation oscillation is suppressed. This is the reason why the upper limits of the whole circulation rate, where natural circulation oscillation occurs, is almost equal in two, three and four channels. It is seen from our observation that the lower limit where natural circulation oscillation appears is influenced by characteristics of geysering. Since the periods of geysering are identical in two, three and four channels, as the number of channels increases, the frequency of vapor inflow becomes higher and thus slug bubbles coalesce more readily. As a result, the lower limit of the whole circulation rate becomes lower with an increase in the number of channels. The above-mentioned fact supports our proposed driving mechanism of natural circulation oscillation.

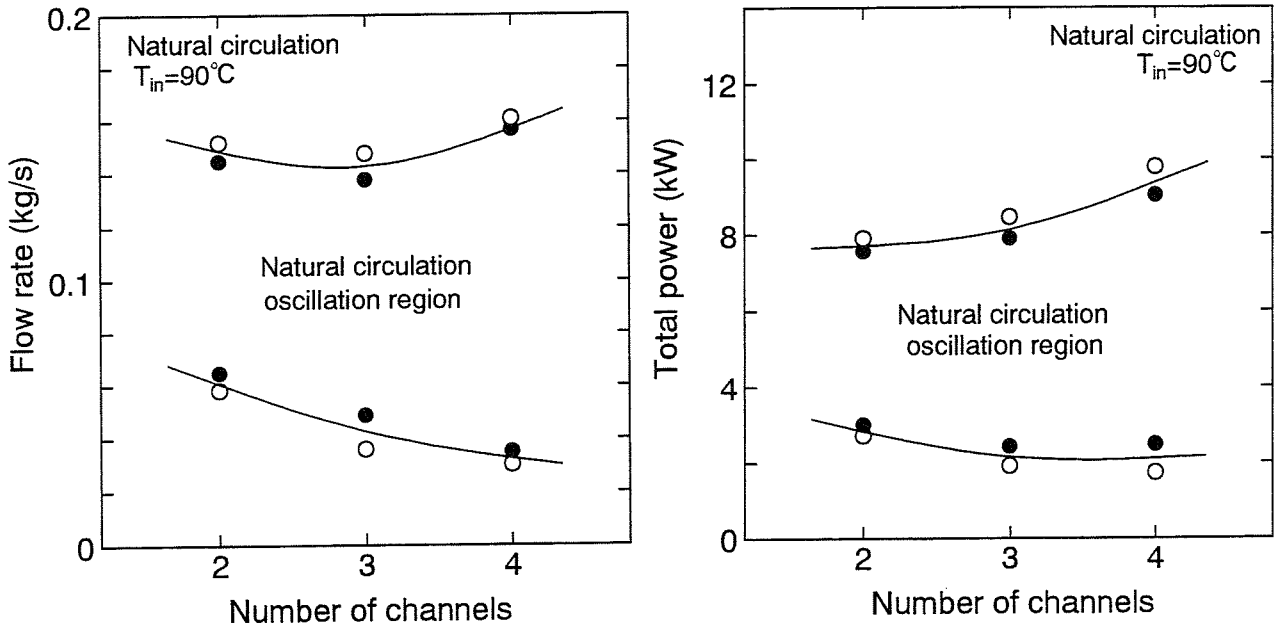

(a) Flow rate **(b) Total power**

Fig.15 Effect of number of channels on stability map

Although geysering and natural circulation oscillation are discussed respectively up to now, the conditions where geysering is induced together with natural circulation oscillation exist. Typical measurements are demonstrated in **Fig.16**, where $\triangle P_1$ is differential pressure between the outlet plenum and the separator tank, $\triangle P_2$ differential pressure between inlet and outlet plenums, $u^{(i)}$ inlet velocity in each channel and u_t the whole circulation rate. The phase difference between u_t and $\triangle P_1$ is 180° . It is geysering that $u^{(1)}$ and $u^{(2)}$ oscillates with phase delay of 180° as u_t is increasing, **Figure 17** shows the flow stability map for every instability. It is supposed that in multi parallel boiling channels the lower limit where natural circulation instability appears may be identical to the lower limit where geysering is induced.

4. CONCLUSIONS

Geysering was experimentally investigated in three and four parallel boiling channels with the same condition for both natural and forced circulations as compared with the results in twin

channels, and the following insights were clarified:

(1) Regardless of circulation methods, geysering appears periodically, and their phase delays are 180° in two channels, about 120° in three channels and about 90° in four channels.

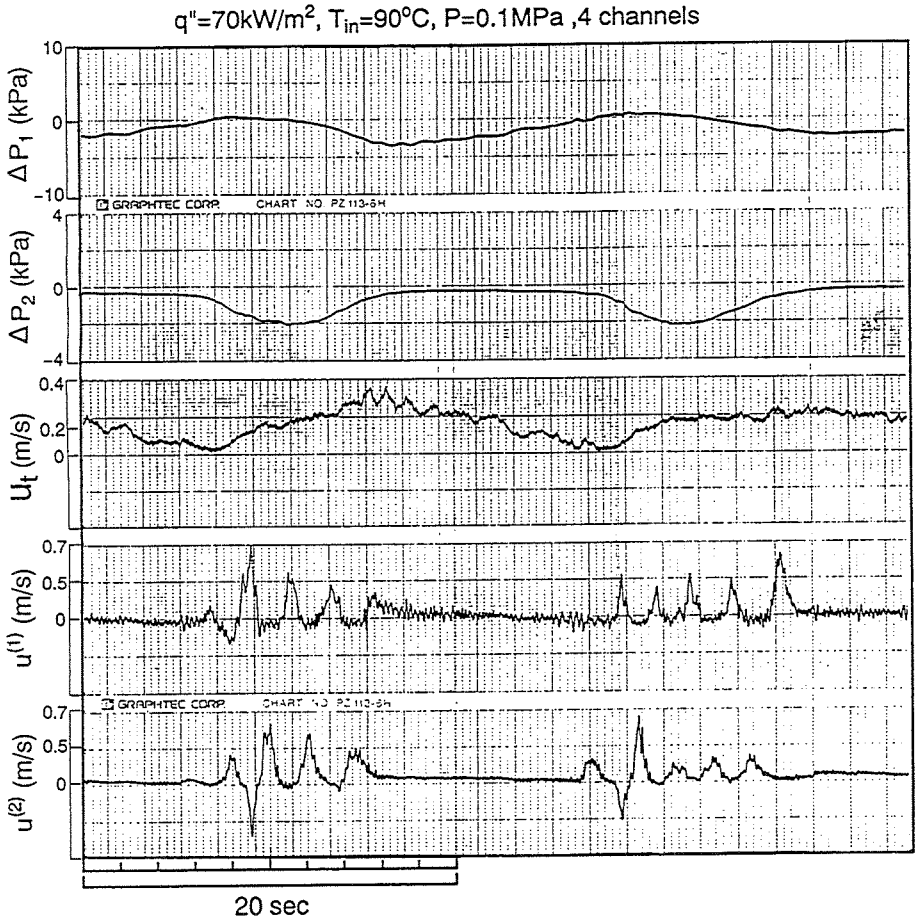

Fig.16 Typical measurement

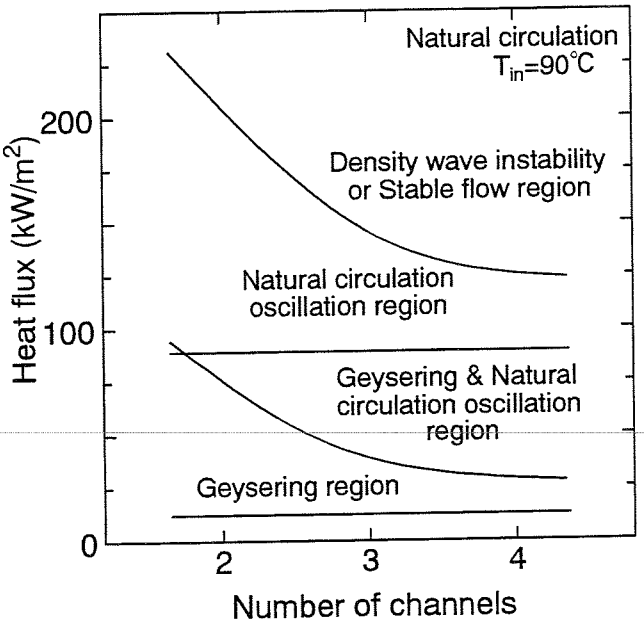

Fig.17 Flow stability map

(2) The periods can be almost arranged with the delay time for boiling regardless of the number of channels and circulation methods.
(3) Flow reversal rate decreases with an increase in the number of channels which is induced by the difference between the volumetric condensation rate of a large bubble and the whole circulation rate.
(4) The stability map of geysering in multi channels is independent of the number of channels regardless of circulation methods because the following effects compensate; a decrease in hotter water reentering and an increase in the frequency when the circulation rate is low.

Geysering was also investigated experimentally in three parallel boiling channels with the heated lengths different among channels, and the following point was made clear:

(5) The unstable region of geysering in parallel boiling channel systems with a power distribution can be estimated by evaluating the thermo-hydraulic conditions in every channel and by comparing these conditions with the stability map of geysering in twin channels with the same condition.

Natural circulation oscillation was experimentally investigated in three and four channels, and the following insight was clarified:

(6) As for the stability map of natural circulation oscillation, since natural circulation oscillation is suppressed by stable two-phase flow in the connection channel, the upper limits of total power, where it occurs, are identical regardless of the number of channels. This fact supports its driving mechanism proposed in our previous work.

This work was performed in the Tokyo Institute of Technology in collaboration with the Tokyo Electric Power Company and the Japan Atomic Power Company.

REFERENCE

[1] J.D.Duncan, SBWR, A Simplified Boiling Water Reactor, *Nucl. Engrg. Des.*, **109** p.73 (1988).
[2] M.Aritomi, J.H. Chiang, T.Nakahashi, M.Wataru and M.Mori, Fundamental Study on Thermo-Hydraulics during Start-up in Natural Circulation Boiling Water Reactors, (I) Thermo-Hydraulic Instabilities, *J. Nucl. Sci. Technol.*, **29,** p.631 (1992).
[3] J.A.Boure, A.E.Bergles and S.L.Tong, Review of Two-Phase Flow Instability, *Nucl. Engrg. Des.*, **25**, p.165 (1973).
[4] M.Aritomi, Handbook of Two-Phase Flow; 6. Flow Stability, *Corona Co.*, (1989.5) 171-205 (in Japanese).
[5] R.T.Lahey,Jr. and D.A.Drew, An Assessment of the Literature Related to LWR Instability Model, *NUREG/CR-1414* (1980).
[6] P.Griffith, Geysering in Liquid-Filled Lines, *ASME Paper 62-HT-39* (1962).
[7] S.Nakanishi, S.Ishigai, M.Ozawa, Y.Mizuta and H.Tarui, Flow Instability in Boiling Channels (2nd Report, Geysering), *Trans. JSME*, **44,** p.4252 (1978) (in Japanese).
[8] M.Aritomi, J.H.Chiang and M.Mori, Fundamental Studies on Safety-Related Thermo- Hydraulics of Natural Circulation Boiling Parallel Channel Flow Systems under Startup Conditions (Mechanism of Geysering in Parallel Channels), *Nuclear Safety*, **33** p.170 (1992).
[9] M.Aritomi, J.H.Chiang and M.Mori, Geysering in Parallel Boiling Channels, *Nucl. Engrg. Des.*, **141**, p.111 (1993).
[10] K.Fukuda and T.Kobori, Two-Phase Flow Instability in Parallel Channels, *Proc. 6th Int. Heat Transfer Conf.*, Toronto, Vol.1, p.369 (1978).
[11] J.H.Chiang, M.Aritomi and M.Mori, Fundamental Study on Thermo-Hydraulics during Start-up in Natural Circulation Boiling Water Reactors, (II) Natural Circulation Oscillation Induced by Hydrostatic Head Fluctuation, *J. Nucl. Sci. Technol.*, **30**, p.203 (1993).
[12] J.H.Chiang, M.Aritomi, R.Inoue and M.Mori, Thermo-Hydraulics during Start-up in Natural Circulation Boiling Water Reactors, *Proc. 5th Int. Topical Meeting on Nuclear Reactor Thermal Hydraulics (NURETH-5)*, Salt Lake City, Vol.1, p.119 (1992).

FINE PARTICLE SEPARATION BY HETEROGENEOUS CONDENSATION OF WATER VAPOR ON AEROSOL PARTICLES

S. Schabel, S. Heidenreich, B. Sachweh, H. Büttner, F. Ebert

Universität Kaiserslautern, Lehrstuhl für Mechanische Verfahrenstechnik und Strömungsmechanik, Postfach 3049, D-67653 Kaiserslautern, Germany

ABSTRACT

Investigations have been carried out to extend the fundamental knowledge about heterogeneous condensation and to turn this effect to account for technical separation of fine particles in the 100 nm region. A laboratory-setup was built for these experiments, in which heterogeneous condensation is forced by adiabatic mixing of two saturated gas flows with different temperatures. One gas flow is heated and subsequently saturated by atomization of tab water. This water contains fine particles which serve as condensation nuclei. The second gas flow is saturated in countercurrent flow with water in a packed column. Both flows are mixed in a coaxial nozzle. Thereby the inner flow is warm and the outer one cold which reduces condensation at the wall. The experimental setup allows the variation of the parameters Re-number, mixing ratio, mass of condensable water vapor, gas temperature and the measuring of their dependence on number concentration and droplet size. The measuring equipment consists of a Differential-Mobility-Particle-Sizer, a High-Sensitivity-Laser-Aerosol-Spectrometer and an Optical-Particle-Counter with digital signal processing for in-situ droplet measurement at high number concentrations. The results of the investigations show, that nuclei with diameters of about 80 - 100 nm can be enlarged to droplets with mean diameters of about 2 - 5 μm. The droplet diameters decrease with increasing Re-numbers and the number concentration of the droplets increases with increasing supersaturation.

1. INTRODUCTION

The requirements for technical separation of fine particles have risen extremely in the last years due to increasing clean-air demands. Additionally, there is a tendency to improve the air quality of clean-rooms which requires new and efficient techniques for particle separation. Investigations have been carried out to examine support techniques for separating those particles in standard inertia separators. One possibility is droplet growth by heterogeneous condensation on submicron particles. If the particle sizes increase to about 5 μm, an efficient separation in a gas cyclone is possible for example. Our experiments aim at contributions to the fundamental knowledge of this process. First experimental results have shown that this method could be of good promise for fine particle separation with less expenditure than usual. A basic problem for our research is measuring droplet diameters and concentrations when high number concentrations are present. To overcome this problem, in-situ measurement is absolutely necessary.

2. EXPERIMENTAL SETUP AND MEASURING EQUIPMENT

In a laboratory-scale setup heterogeneous condensation is forced by adiabatic mixing of two saturated gas flows with different temperatures. The first gas flow is heated with an electrical heater up to about 200 °C. Subsequently the air is saturated by atomization of tab water in a conditioner. The tab water contains fine particles, which are released by this process. In this way we obtain the condensation nuclei for the experiments at number concentrations higher than 10^5 cm^{-3} and with a mean diameter of about 100 nm. The second gas flow is cooled and saturated in a packed column operated in countercurrent flow with water. Nearly no residue particles are produced in this process. With this techniques we obtain one gas flow with a temperature of about 50 °C and the other of about 18 °C. Figure 1 shows the flow sheet of the experimental setup. Both gas flows are coaxially fed into a mixing tube by a specially designed nozzle. The inner flow is the warm one containing the condensation nuclei. Underneath the nozzle mouth first condensation occurs in an annular mixing layer, so that condensation at the wall can be minimized. Downstream a complete mixture of both gas flows should be reached within a short mixing length. This assures constant supersaturation in a cross section of the pipe. If differences in supersaturation occur, the lower particle size activated will vary, here an undesirable effect. The aim is to obtain an adjustable, but spatially homogeneous supersaturation in the entire cross section.

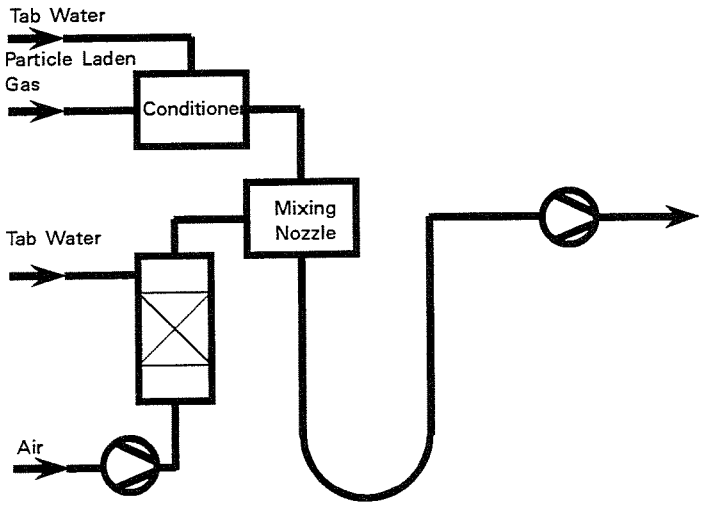

Figure 1: Flow sheet of the laboratory plant

A nozzle designed by Büttner [2] is used for this purpose, which has a large ratio of inner diameter to outer diameter. The present ratio of 0.89 contributes to high turbulence intensities and a short mixing length. Figure 2 shows a schematic of this mixing nozzle.

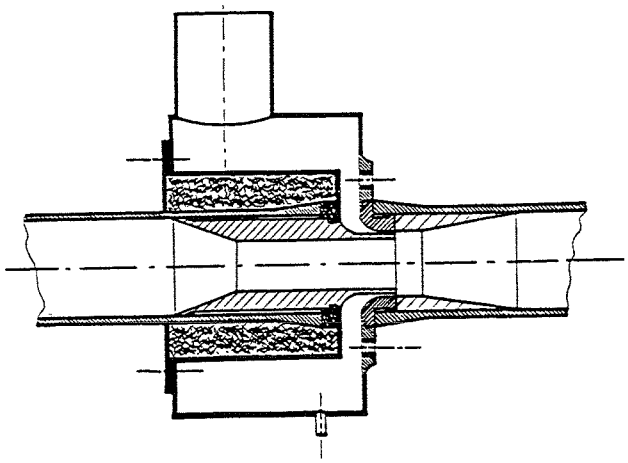

Figure 2: Schematic of the mixing nozzle

Visualization experiments, which are described below, were carried out to get more information about the mixing flow. Downstream the nozzle a pipe with a length of 6 m conducts the gas flow to a suction fan, which realizes volumetric flow rates up to 200 m^3/h. This corresponds to a maximum Reynolds-number of 70,000 respectivly a maximum velocity of 26 m/s. Measurements can be carried out at any distance from the nozzle mouth. The pipe is built from glass tubes with an inner diameter of 50 mm, surrounded by a tube, which can be heated with water and additionally insulated with glass wool. Hence, the wall temperatures are held constant, independent from different ambient conditions.

In the following the control and measurement devices are briefly described: the gas heater is controlled by a computer, which allows convenient adjustment of the warm air temperature. The volumetric flows are measured by standard orifice meters or rotameters. Humidity is measured with psychrometers. All volumetric flows, temperatures and humidities are registered by a computer. Re-number, mixing ratio, mass of condensable water vapor and gas temperature can be varied.

To obtain information about the enlargement of the condensation nuclei, it is necessary to measure the size and the number of the nuclei and of the droplets. We use a TSI Differential Mobility Particle Sizer (DMPS, TSI Model 3932) to measure the particle size distribution of the nuclei. Because the DMPS does not allow temperatures above 30 °C, the sample has to be cooled by instantaneous dilution with cold and dry air. Isokinetic sampling is not mandatory here, because the nuclei diameters are below 1 μm. Figure 3 shows the sampling and dilution device. The sample is taken by a metal probe with an inner diameter of 8 mm. The probe is connected to a heated pipe to avoid early condensation before the gas reaches the ejector diluter (PALAS Model VKL 10), where dry air at room temparature is added. The sample for the DMPS is conducted to a mixing chamber from which a small sample is withdrawn. We prefer the ejector diluter because of its well defined dilution ratio. From our measurements we estimate a maximum error of 5% for the current operational conditions.

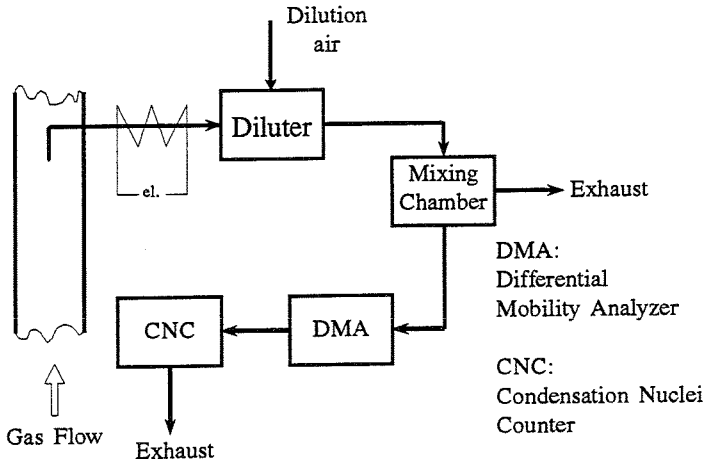

Figure 3: Sampling and dilution device for nuclei size distribution

The measuring of the droplet size distribution was even more difficult. If samples have to be taken from the mixing regime, the same thermodynamic conditions as in the apparatus have to be adjusted to avoid evaporation or condensation, what is rather difficult to realize. These effects disturb the original droplet size distribution. We prefer *in-situ* measuring. For this purpose a special mount was developed in our group [3]. This mount allows *in-situ* measurement by an optical particle counter (OPC), Umhauer [4]. We extended the measuring range of the OPC to smaller particles replacing the original halogen lamp by a xenon short arc lamp ▪. Digital signal processing [1] allows the investigation of the entire signal shape in addition to the pulse height only. The pulse shape leads to the signal length which can be taken as criterion to distinguish between noise, particle signal and coincidences. A specially developed computer code allowed corrections of the number concentration from the ratio of coincident and non coincident signals. This method bases on the assumption that coincidences are Poisson distributed. Only the non-coincident signals are taken for the calculation of the particle size distribution.

An alternative method to obtain the droplet number concentration and the particle size distribution is the phase-Doppler-anemometry (PDA). For the current operational conditions the application of this method is difficult, because the droplets are small. PDA evaluates the droplet velocities from the measured Doppler frequency and the droplet diameter from the measured phase difference between two signals under different elevation angles. The relation between phase difference and droplet diameter, the phase response, can be calculated by the Lorenz-Mie theory [5]. This relation depends on the optical design, the laser beam wavelength and the refractive index of the continuous and the dispersed phase. For small droplets below 10 μm the phase response is ambiguous. Therefore, it is necessary to search for an optical setup for which this phase difference to diameter relation reaches an optimum in linearity. If the relation is still ambiguous, additional data evaluation can serve to correct the results. Currently we are testing two evaluation methods for correcting the droplet size distribution in an appropriate way [6].

▪ The advice and help from H. Umhauer, Institut für Mechanische Verfahrenstechnik und Mechanik, Universität Karlsruhe, Germany, which we enjoyed during our cooperation is gradefully acknowledged

3. VISUALIZATION

We carried out some visualization experiments to evaluate the efficiency of the nozzle mixing. The setup for these experiments was quite simple. So the nozzle and the pipes were built of acrylic plastics with dimensions which allowed the operation with water flows. Reynolds-similarity to the laboratory setup was observed. The visualization was realized by coloring the inner flow with phenolphthalein and decoloring it with an acidified outer flow. The pH levels were adjusted in a way which enabled an instant color change when an eddie from the inner flow was mixed with fluid from the outer flow. For this reason, the pH level in the outer flow was adjusted at about 3 and the pH level in the inner flow at about 9.5. The main point of interest was the mixing length in which the large scale mixing took place. This parameter is important, because fast and large scale mixing lowers the high local supersaturation. We aim at homogeneous supersaturation across the entire pipe in a short time. Peaks in the local distribution of supersaturation would possibly cause the activation of smaller nuclei then intended. Photographs of the mixing process were taken for further analyzation. We used a green filter to get the maximum contrast on black and white film. The shutter speed was set to 1/60 s what allowed the identification of eddies on the photographs. Longer exposure times, which are equal to a longer time of integration, could not be analyzed because eddies could not be identified. In Fig. 4 a typical visualization result is shown. From Fig. 4 one can assess the realistic working conditions of the mixing nozzle with respect to fast large scale mixing. Because of the high ratio of inner to outer diameter and the diffusor, the two flows create a high degree of turbulence and large eddies. These visible eddies become smaller with increasing volumetric flow ratio. Here, the mixing length is defined as the length which is necessary to decolorize the entire flow. This mixing length is only a few pipe diameters, depending on the Re-number and the volumetric flow ratio.

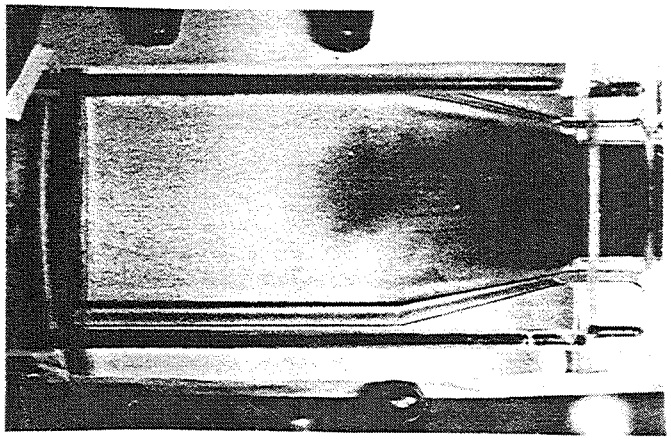

Figure 4: Visualization of the mixing process

This visualization method is qualitative, but the experiments underscore the well working of the mixing nozzle and they show that there is an optimum volume flow ratio for each Re-number at which the mixing length is at it's minimum. Additionally, this optimum volumetric ratio is independend from the Re-number. This is shown in Fig. 5. There, the mixing lengths are plotted versus the volumetric flow ratios for different Re-numbers.

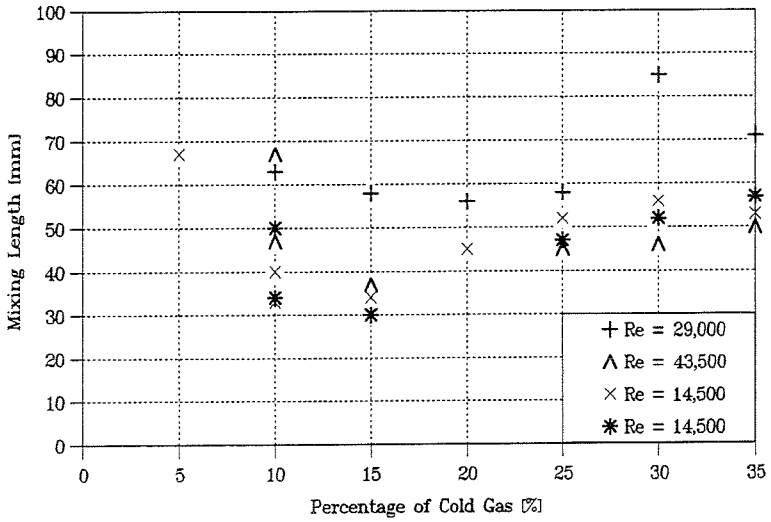

Figure 5: Mixing lengths from visualization experiments

4. EXPERIMENTAL RESULTS

Velocity profiles behind the mixing nozzle were measured using the PDA. Tab water was dispersed into the inner flow at room temperature to get tracer particles. In this way the gas velocities were measured for different Reynolds-numbers and volumetric flow ratios at different distances from the nozzle. Figure 6 shows a typical velocity profile and Fig. 7 the corresponding turbulence profile.

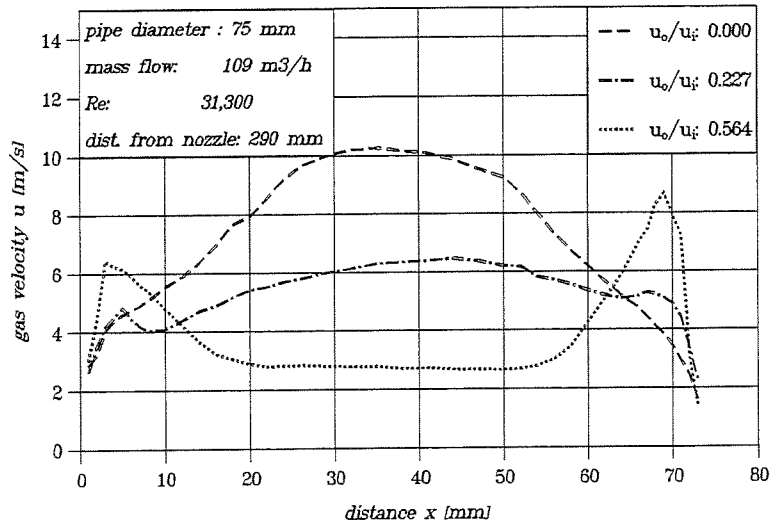

Figure 6: Velocity profiles

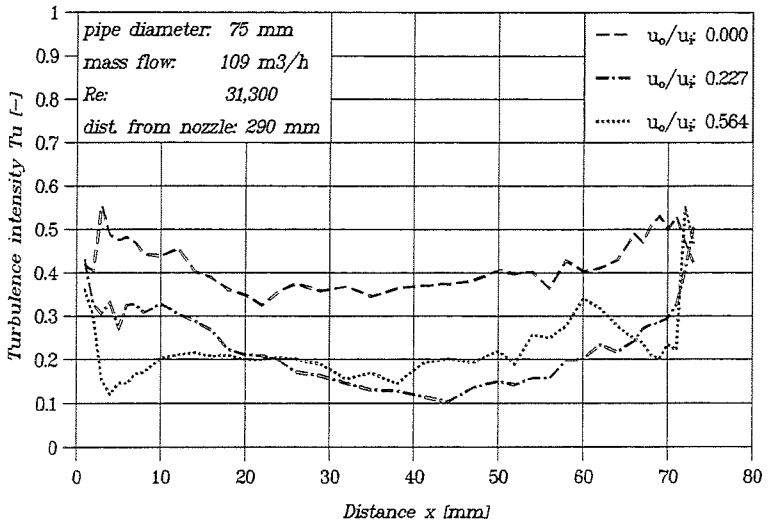

Figure 7: Turbulence profiles

The turbulence measurements show that the turbulence intensity after the mixing nozzle varies between 0.2 and 0.4. The velocity profiles have two characteristic peaks near the wall where the outer flow is injected. This peaks descend with increasing distance from the nozzle and the velocity profile reaches the shape of a turbulent pipe flow. We tried to calculate the mean local supersaturation from the velocity measurements with a simple model [7]. This model is based on Prandtls theory of free turbulence [8], which decomposes the velocity into a time averaged and a fluctuating component, as shown in Eq. (1):

$$u = \bar{u} + u' \qquad (1).$$

For a continuous velocity distribution the longitudinal fluctuating velocities are described in Eq. (2) with the mixing length l

$$u' \approx l \left| \partial u/\partial y \right| \qquad (2).$$

Further the conditions l(y) = const. and $l = k\,x$ are used. We assume homogeneous and isotropic turbulence, negligible pressure change and negligible influence of viscosity and walls. This leads to Eq. (3):

$$\frac{u - u_H}{u_m - u_H} = \frac{T - T_H}{T_m - T_H} = \frac{c - c_H}{c_m - c_H} \qquad (3).$$

From this relation we can calculate profiles for the mean local supersaturation. These calculations are a worst case description, because they lead to the most extreme supersaturation distribution. It is obvious that the assumption of negligible wall influence is not fullfilled. However, a free jet will lead to a larger supersaturation gradient than a confined jet does. The aim of the calculations is to estimate the probability of the occurrence of homogeneous nucleation. Figure 8 shows a supersaturation profile calculated from the measured velocity profile under the described conditions.

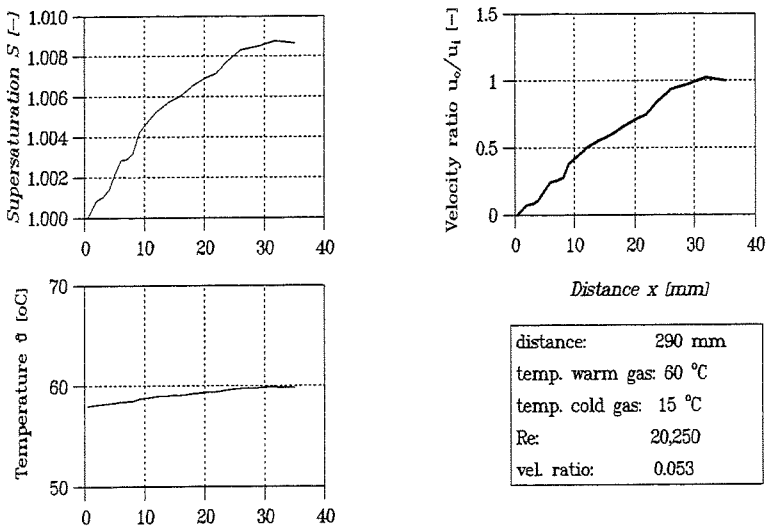

Figure 8: Calculated supersaturation Profile

From this result we conclude that the supersaturation is much below the critical supersaturation in every radial position, which is about 2.6 for the current conditions. Another calculation for a short distance of 1 mm from the nozzle mouth, where the largest temperature gradient is expected, showed that the maximum supersaturation level is below 2.0. This means, that no homogeneous nucleation will occur in the mixing zone.

The most important parameters for the separation of the fine particles are the number and the size of the droplets after the condensation. It should be possible to enlarge all nuclei to a size which can be separated by a cyclone for example. This size should be about 5 μm for good separation. We tried to find out the influence of the parameters Re-number, volumetric flow ratio and temperature of the warm gas flow on droplet number and size. Measurements were carried out for the Re-numbers and temperatures listed in Table I. For each of these states, the volumetric flow ratio was varied with the range which was possible with our plant.

Re	ϑ(warm)				
17.000	53 °C	55 °C	57 °C	61 °C	62 °C
33.000	48 °C	51 °C	52 °C	55 °C	57 °C
48.000	43 °C	46 °C	47 °C	52 °C	54 °C

Table I: Parameters for droplet number and size measurements

The supersaturation and the turbulence intensity in the mixing region depend on these parameters. Thereby, the Re-number and the volumetric flow ratio affect the turbulence intensity while the temperature of the warm gas flow and the volumetric flow ratio control the supersaturation. For this reason, the results are plotted versus the parameters Re-number and supersaturation S. Note that the parameters are not independend in the existing setup. So, the number of the nuclei depends on the temperature of the warm gas flow. A gas with higher temperature needs more water for saturation and the evaporation of this water produces more nuclei. Further the volumetric flow ratio, which we use to adjust the supersaturation level, is coupled with the turbulence intensity in the mixing region.

Figure 9 shows the relative number concentration versus supersaturation for all measurements. Here, the relative number concentration C_M is the number of droplets per mass of the warm gas flow at the temperature after the mixing. This method takes into account the dilution which is caused by the mixing with cold, particle free gas.

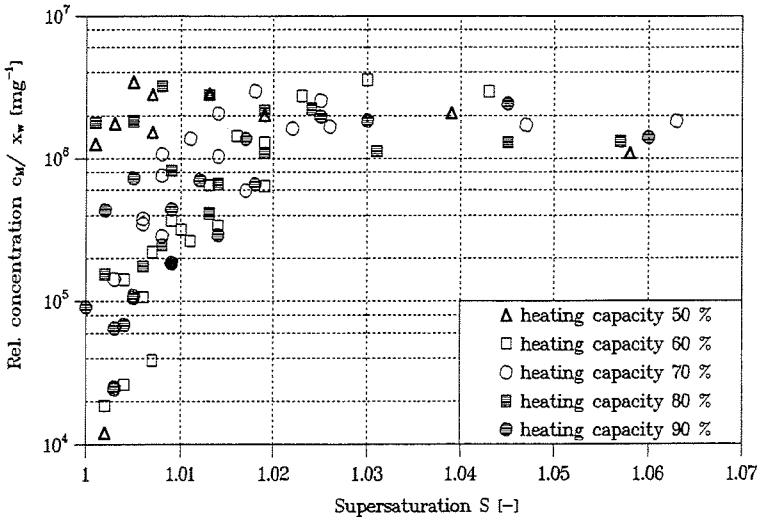

Figure 9: Relative number concentration versus supersaturation for the measurement results

With increasing supersaturation the number of droplets increases because the diameter of the nuclei decreases which are activated. So, with increasing supersaturation an increasing number of nuclei is activated and grows to droplets. The droplet size distribution is narrow and after the condensation all droplets are of the same size. In the region below a supersaturation of 1.02 there is a spread of the results. This can be explained with the accuracy of the psychrometer which decreases for small supersaturations. For supersaturations above 1.02, C_N is almost constant for any Re-number and any temperature of the warm gas flow. From this, one can conclude that all nuclei are activated and enlarged to droplets. This, of course, depends on the nuclei size distribution, which has a mean value of 100 nm.

The droplet size is almost independent from the supersaturation level but there is a dependence from the Re-number. This is because of the fixed measuring position. So the residence time between the mixing nozzle and the OPC depends on the gas velocity. The droplet diameter to Re-number relation is shown in Fig. 10. The diameter to Re relation, respectively the relation of the radius R to the residence time t can be calculated for the growth in the continuum region with equations given by Barrett and Clement [9]. This leads to Eq. (4):

$$\frac{d}{2} = R \sim \sqrt{t} \quad \Rightarrow \quad d \sim \frac{1}{\sqrt{Re}} \qquad (4).$$

So the decreasing droplet diameter d for increasing Re-number can be explained with the shorter residence time for higher Re-numbers.

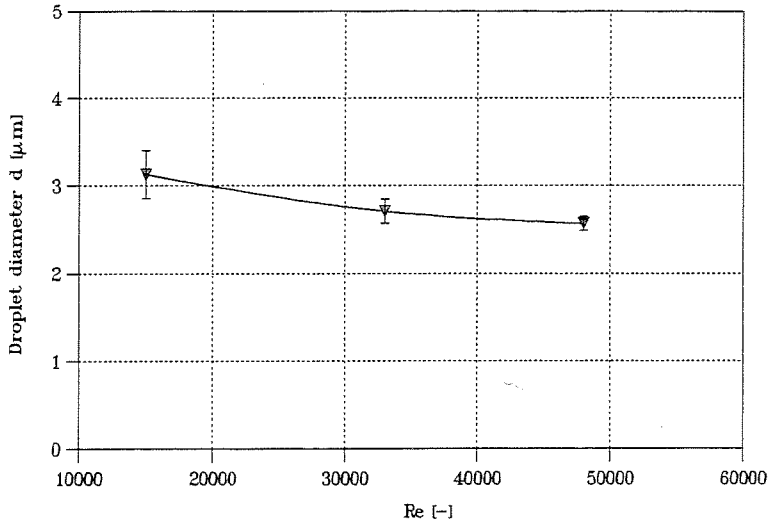

Figure 10: Droplet diameter to Re-number relation

5. SUMMARY AND CONCLUSION

Investigations have been carried out to extend the fundamental knowledge about separation of fine particles supported by heterogeneous condensation of water vapor in technical separators. For the experiments a laboratory apparatus was built, where heterogeneous condensation is forced by mixing of two saturated gas flows with different temperatures. One gas flow is heated and subsequently saturated by atomization of tab water. This water contains fine particles which serve as condensation nuclei. The second gas flow is saturated with water by countercurrent flow in a packed column. Both flows are mixed in a coaxial nozzle with the inner flow warm and the outer one cold which reduces condensation at the wall. The ratio of the inner to outer diameter of the nozzle is 0.89. This large ratio contributes to intensive turbulence in the mixing zone and causes herewith a high degree of turbulence and a short mixing length.

The experimental-setup allows the variation of the parameters Reynolds-number, mixing ratio, mass of condensable water vapor and gas temperature and to determine their dependency on number concentration and droplet size.

The measuring equipment consists of a Differential Mobility Particle Sizer for measuring number and diameter of the condensation nuclei and an Optical-Particle-Counter with digital signal processing for *in-situ* droplet measurement at high number concentrations. Droplet diameters and velocities are also registered by a phase-Doppler-anemometer.

A model of the mixing nozzle was built in acrylic plastics to study the turbulent mixing. For this purpose visualization experiments were carried out with water flows under Reynolds-similarity visualized by coloring the inner flow with phenolphthalein and decoloring it with an acidified outer flow. The visualization experiments underscore the realistic working conditions of the mixing nozzle.

The results of the investigations show that nuclei with diameters of about 80 - 100 nm can be enlarged to droplets with mean diameters of about 2 - 5 μm. The droplet diameters decrease with increasing Re-numbers because of a shorter residence time. The number concentration of the droplets increases with increasing supersaturation, until all nuclei are activated. This state can be reached for the used nuclei with a mean diameter of 80 nm with a supersaturation level of 1.02.

NOMENCLATURE

C Number concentration per unit volume
c Number concentration per unit mass
d_M Droplet diameter
k Constant
l Turbulent mixing length
R Droplet radius
S Supersaturation
t Relaxation time
T Temperature
Tu Turbulence intensity
u Velocity
$\bar{u}$ Time averaged component of the local velocity
u' Fluctuating component of the local velocity
x Distance from the pipe wall
x_w Water content

ϑ Temperature

Subscripts

i Inner flow
o Outer flow
H Value at the center of the pipe

REFERENCES

[1] Sachweh, B.: "Erweiterung des Meßbereiches eines Optischen Partikelzählers durch moderne, digitale Signalverarbeitung", Ph.D. Thesis, Kaiserslautern, Germany (1991)

[2] Büttner, H.: "Untersuchungen über den Einfluß von Kondensationsvorgängen in naßarbeitenden Abscheidern", Ph.D. Thesis, Kaiserslautern, Germany (1978)

[3] Denzer, W.: "Untersuchungen zur Tropfenkoaleszenz in turbulenter Rohrströmung", VDI Fortschritt-Berichte; Reihe 7, Nr. 114 (1987)

[4] Umhauer, H.: "Partikelgrößen-Zählanalyse durch Streulichtmessung bei rein optischer Meßvolumenbegrenzung", in: J. Aerosol Sci, 14, p. 344 (1983)

[5] Flögel, H.-H.: "Modifizierte Laser-Doppler-Anemometrie zur simultanen Bestimmung von Geschwindigkeit und Größe einzelner Partikeln", VDI Fortschritt-Berichte; Reihe 3, Nr. 140 (1987)

[6] Schabel,S., Doicu, A., Ebert, F.:"Correction of Particle Size Distributions from PDA-Measurements for Continuous Distributions less than 10 μm", in: Seventh International Symposium on Applications of Laser Techniques to Fluid Mechanics, Lisboa 1994

[7] Amelin, A. G.: "Theory of fog condensation", Jerusalem (1967)

[8] Abramovich, G. N.: "The Theory of Turbulent Jets", M.I.T. Press, Cambridge, Massachusetts (1963)

[9] Barrett, J. C. and Clement, C. F.:" Growth Rates for Liquid Drops", in: J. Aerosol Sci. Vol. 19, No. 2

DEPENDENCE OF HEAT TRANSFER BY DIRECT CONTACT CONDENSATION ON LIQUID SIDE TURBULENCE IN STRATIFIED TWO PHASE FLOW

H. Ruile

Techniche Universität München
Lehrstuhl Thermische Kraftanlagen
Arcisstrasse 21, D-80290 München, Germany
Telephone: (089) 2105-3262, Fax: (089) 2105-3272

ABSTRACT

Heat transfer by direct contact condensation of saturated steam on a subcooled water layer is a function of liquid side turbulence. Detailed experimental investigations were made on the heating of the water layer by direct contact condensation at pressure levels up to 2.0 MPa. Local velocities, turbulence intensities and temperatures were measured in a horizontal open channel geometry to show the influence of initial turbulence generated by cylinder grids and turbulence generated by interfacial shear stress on the heat transfer. The increase of turbulent heat transfer by changing the initial turbulence intensity is clearly visible in the measured temperature profiles.

1. INTRODUCTION

During a postulated small break loss of coolant accident in a pressurized water reactor the injection of cold emergency core cooling (ECC) water with low injection rates leads to stratified steam water two phase flow in the cold leg of the primary loop. For analysing the pressurized thermal shock the temperature distribution within the water layer has to be known. Direct contact condensation (DCC) of saturated steam heats the cold ECC water and therefore will reduce the thermal stress. The heat transfer however is limited to the turbulent transport properties at the free interface.
At the injection point high turbulence was generated depending on injection rate and steam flow. Hence the local condensation heat transfer has to be explored as a function of the initial turbulence intensity .

2. TURBULENCE CENTERED CONDENSATION MODELS

In absence of noncondensible gases during condensation heat and respectively mass transfer is dominated by liquid side turbulence. Liquid side turbulence is generated by wall shear stresses, interfacial shear and in addition naturally by initial conditions and disturbances. A lot of experimental studies have been carried out on local condensation rates in horizontal stratified two phase flows. In the first period empirical correlation's based on dimensionless parameters (Reynolds number, Prandtl number, Froude number) were developed. Further investigations resulted in condensation models correlated with turbulent time and length scales. Bankoff [7] used in a power law for the heat transfer the interfacial shear velocity $u_i = \sqrt{\tau_i / \rho}$ and the water depth h.
Most successfully applied was the surface renewal model [4] in which turbulence brought eddies from liquid bulk to the surface where unsteady heat conduction for a period T occurred. It can be shown that the heat transfer coefficient α can be expressed as a function of thermodynamic quantities and the renewal time T:

$$\alpha = \frac{2}{\pi}\sqrt{\lambda c_p \rho T} \qquad (1)$$

Modelling the renewal time T the discussion raised whether the turbulence is controlled by large or small eddies. At least Theofanus [10] suggested that the small eddy model may be more relevant for flows with high turbulence. In this case the eddies are in the size of the Kolmogorov mircoscale. The renewal period T is defined:

$$T = \sqrt{\frac{\nu}{\varepsilon}} \tag{2}$$

where ν is the kinematic viscosity and ε the turbulent energy dissipation. The problem was now shifted to the determination of ε.
For the one-dimensional pipe flow the dissipation is related to the pressure drop and the mean velocity v_b:

$$\varepsilon = \frac{1}{\rho}\frac{dp}{dx} v_b \tag{3}$$

The total pressure loss in a pipe flow is the sum of friction and geometry. Therefore Hobbhahn [5] developed a condensation model where ε is combined with wall friction, interface friction and changes in geometry.
Next step in modelling the dissipation rate was using a turbulence model for the water layer. Here the dissipation is defined as:

$$\varepsilon = \overline{uv}\frac{dU}{dy} \tag{4}$$

In this case the dissipation rate and hence the heat transfer near the free surface becomes close to zero.
Hughes & Duffey [6] used the standard Prandtl mixing length $l=\kappa y$ theory for analysing the dissipation distribution in a developed turbulent water flow. In this case the dissipation rate ε will be:

$$\varepsilon = \left(l^2 \left|\frac{\partial U}{\partial y}\right| \frac{\partial U}{\partial y} \right) \frac{\partial U}{\partial y} \tag{5}$$

They found for flows with and without interfacial shear that the dissipation near the wall scales as $\varepsilon \propto u_*^4 / \nu_l$ and in the full turbulent region as $\varepsilon \propto u_*^3 / h$. whereas u_* is the friction velocity. Wall shear and interface friction were used building an average characteristic shear stress scaled with the wall region:

$$\varepsilon = \left(\frac{1}{4\rho_l^2 \upsilon_l} \right) (\tau_w + \tau_i)^2 \tag{6}$$

Hughes & Duffey got good results for relative shallow flows where the wall shear dominates.
The application of these correlation on horizontal pipe flow with high local turbulence at injection location remained difficult because free turbulence dominates and the flow isn't developed as provided in the model.

3. EXPERIMENTAL TEST FACILITY

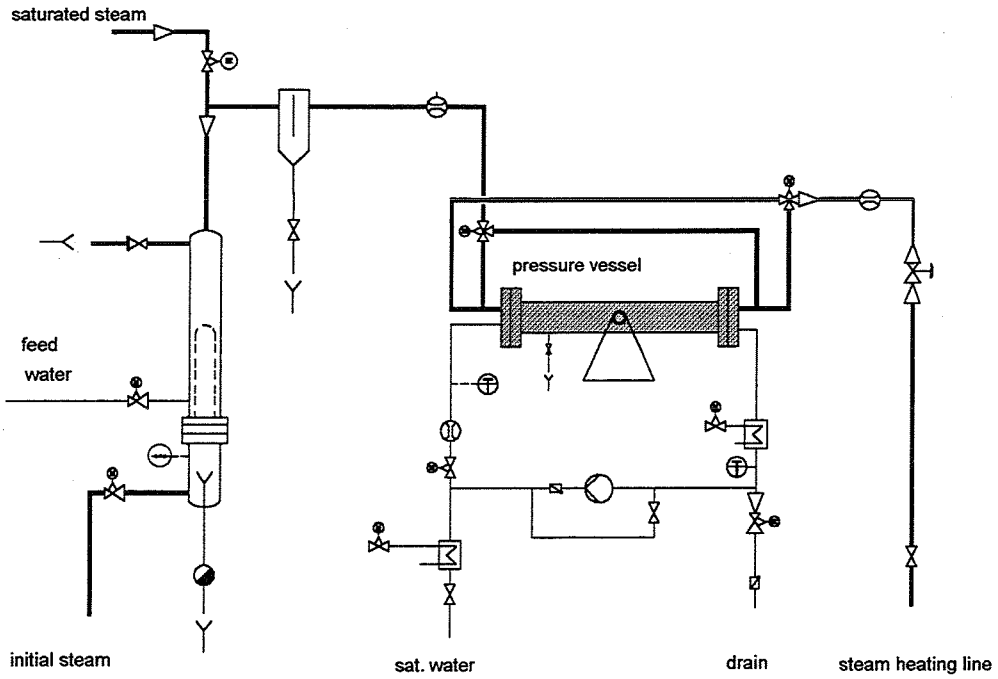

Fig. 1: Steam and water supply of the test facility

The steam water experiments were conducted in a rectangular open channel 1.0 m long and 0.08 m wide insulated with 40 mm foam glass. The channel is supported in a pressure vessel supplied from the heating power plant of the University (fig. 1). Using a steam converter saturated steam could be produced at any pressure level up to 6 MPa. After passing a water separator the steam mass flow is measured by vortex flow meter combined with a Pt100 resistant thermometer. The thermodynamic properties were calculated at saturation point. Concurrent and countercurrent steam water flow could be realized. The steam flow area in the pressure vessel would be too large to realize remarkable steam velocities. So the open channel was covered to reduce the steam flow area to A_D=102.15 cm².

The water level in the open channel is about 40 mm but depends strongly on steam flow which could accelerate and decelerate the water flow. The water circulates in a loop containing a heat exchanger and a centrifugal pump. The mass flow is detected by two corriolis mass flow meter.

For minimizing additional turbulence by instrumentation only one measurement location at the end of the open channel was selected as shown in fig. 2. For the determination of the local heat transfer coefficient as a function of local turbulence parameters the discharge into the open channel has to be axial movable. At the measurement location 12 NiCr-Ni thermocouples (∅ 0.5mm) mounted on a stalk in the symmetry plane give a sufficient resolution of the vertical temperature distribution in the water layer. Through a glass window in the channel bottom the vertical velocity distribution is recorded by Laser-Doppler Anemometry (LDA) with backscattering method.

The LDA (TSI) consists of a 4W Argon laser, a two component fibre optic probe (beam spacing 50 mm) traversing normal to the channel bottom and the TSI flow analyser IFA650 with auto correlation technique. With a focal distance of 350 mm the beam cross angle is 3.97° and with a beam diameter of 2.82 mm the length of the measuring volume becomes 1.7 mm. Hence the resolution of the velocity and turbulence profile is limited to this length.

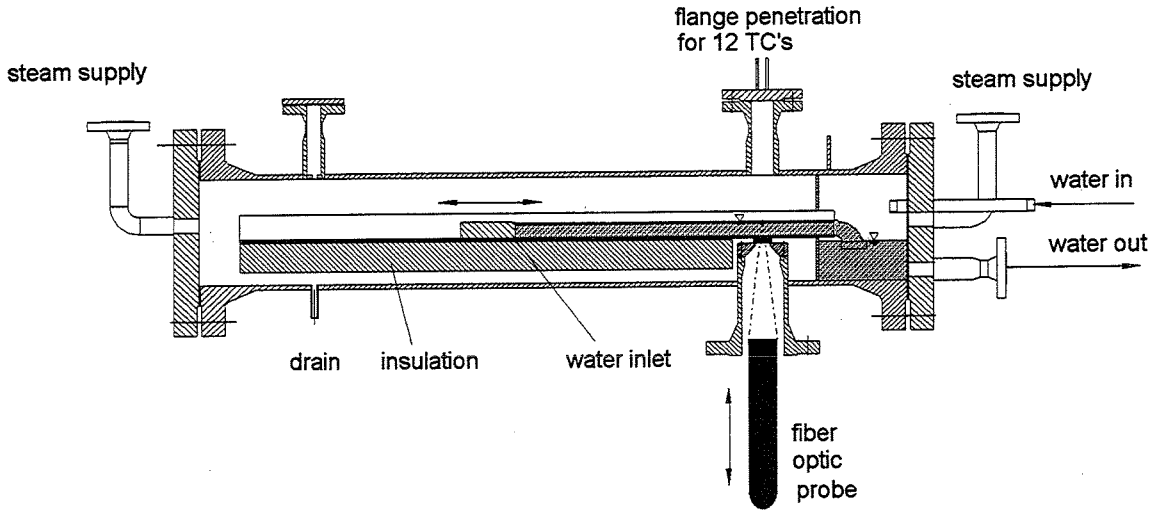

Fig. 2: Schematic view of the open channel supported in a pressure vessel. The cold water is lead by a flexible tube to the movable water discharge head

4. EXPERIMENTS

Experiments are performed to show the influence on heat transfer by free turbulence and by turbulence generated by interfacial shear stress.
Detailed investigations on turbulent boundary conditions were conducted for adiabatic flow in a Plexiglas channel with same dimensions. The inlet water flow should have lowest turbulence intensities and a flat velocity profile. Diffuser, grids, honeycombs and fine meshes were built in the water inlet configuration for equalizing the leaving water flow. The used arrangement results in very low turbulence intensities. Fig. 3 shows the horizontal and vertical velocity and turbulence distribution at water inlet for adiabatic flattened flow. Entering the open channel the water flow has not yet developed to a plug profile rather the profile is high heterogeneous due to the honeycombs and meshes. Uberoi and Wallis [11] showed similar effects for different grid types in a low turbulence wind tunnel. About 100 mm after flow exit the profile is flattened while the turbulence intensity is very low and dominated by wall shear effects.

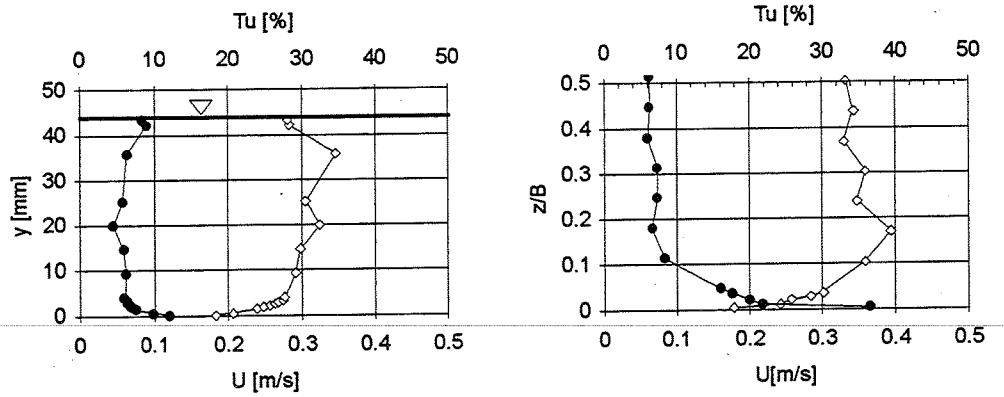

Fig. 3: Vertical and horizontal velocity (◊) and turbulence intensity (•) distribution for low turbulence flow at x= 50mm (adiabatic flow)

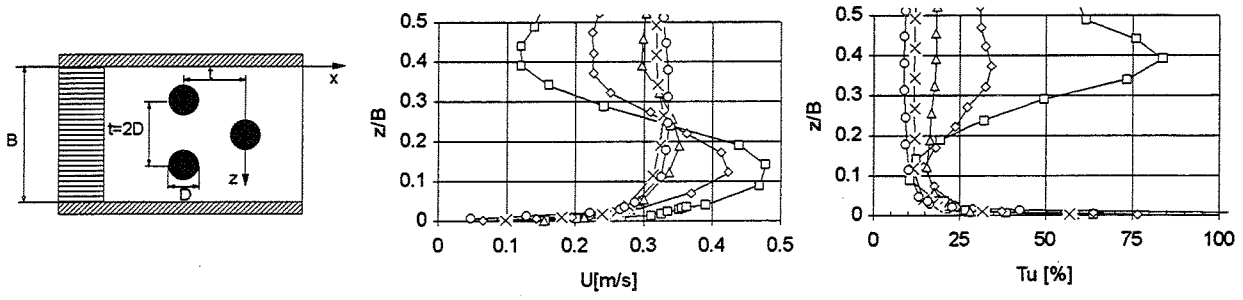

Fig. 4: Cylinder configuration used for high turbulence generation (D=16 mm). Horizontal velocity and turbulence distribution for flow with cylinder grid (□: x=60mm, ◊: x=100 mm, Δ: x=200mm, x: x=300mm, o: x=400mm) (adiabatic flow)

Additional turbulence was generated by installing cylinders in front of the water inlet configuration within the open channel. The cylinders were moved with the discharge head. Fig. 4 shows the used cylinder configuration (cylinder diameter is 16 mm) and the measured velocity and turbulence profiles at different axial locations.
The velocity profiles indicates clearly that the flow is symmetrically to the channel center line and free stream turbulence dominates. The well known velocity distribution for a cylinder cross flow is measured. The velocity defect behind the cylinder grid leads to an acceleration of the flow near the wall. The local turbulence increased up to 80% while the mean turbulence becomes 44% at x= 60mm. The profiles were smoothing down fast and were flattened at x=400 mm.
With the known turbulence profile the heat transfer experiments were conducted in two series. The influence of free turbulence is shown in the experimental series A at 0.45 Mpa with cocurrent steam mass flow. The open channel cover wasn't buildt in so the steam velocity was less than 0.5 m/s and the influence of interfacial shear could be neglected. The boundary conditions are given in Table 1

Table 1: Boundary conditions for series A

system pressure	0.45 MPa
water mass flow	0.80 kg/s
steam mass flow	0.08 kg/s
Inlet temperature	70.00 °C
steam temperature	147.00 °C
flow direction	cocurrent
turbulence	none | cylinder grid

In series B the influence of interfacial shear depending on steam density should be demonstrated. Therfore the steam velocity was kept nearly constant and the system pressure was increased from 4.5 Mpa over 1.0 Mpa up to 1.9 Mpa. The channel cover was buildt in and higher steam velocities were available. To enlarge the influence of interfacial shear countercurrent steam water flow was realized. At the axial location of 800 mm the developed velocity, temperature and turbulence profiles in the water layer were measured . The subcooling at the different pressure levels remained nearby constant

(90K). The experiments were conducted in steam water countercurrent flow. Table 2 shows the used boundary conditions for series B. The system boundaries could be kept constant in a range of 1-1.5%. The repetition accuracy is within the same range of standard deviation σ.

Table 2: Boundary conditions for series B

p_{sys} [MPa]	$\dot{m}_l$ [kg/s]	T_0 [°C]	$\dot{m}_v$ [kg/s]
0.45	0.9	67	0.05
1.00	0.9	85	0.10
1.90	0.9	116	0.17

5. DATA ANALYSIS

Most important in the analysis of the heat transfer coefficient was the exact determination of the mean water level h because at the interface boundary layer the most of the heat transfer and so the highest temperature rise occured.
For determining the mean water level there are three independent criteria: first the vanishing of the LDA-signal, second the temperature and temperature fluctuation (steam temperature measurement is nearly without fluctuation) and at least the comparison of the measured mass flow with the integrated velocity profile. By this way the accuracy of determining the mean water level is in a range of 1-2%.
The mean liquid temperature was calculated by integrating the energy flow. Assuming constant thermal properties the local mean temperature of the water layer was determined by:

$$\overline{T}_x = \frac{\int_0^h T_y U_y dy}{\int_0^h U_y dy} \tag{7}$$

The total heat flux was evaluated by integrating of the velocity and the temperature profiles.

$$\dot{Q} = B\rho c_p \int_0^h U(T_y - T_0)dy \tag{8}$$

So the local heat transfer coefficient can be evaluated by the measured and known quantities as:

$$\alpha(x) = \frac{\Delta\dot{Q}_x}{B\Delta x(T_s - \overline{T}_x)} \tag{9}$$

whereas $\overline{T}_x$ is the mean liquid temperature in the flow section Δx.

6. RESULTS

Series A:
In series A the axial distribution of turbulence and heat transfer were investigated. At system pressure of 4.5 MPa and steam water cocurrent flow (enlarged steam flow cross area) two different initial turbulence intensities were realized. Free stream turbulence dominates and interfacial drag could be neglected. Fig. 5 shows the axial temperature profiles for low and high turbulence flow.

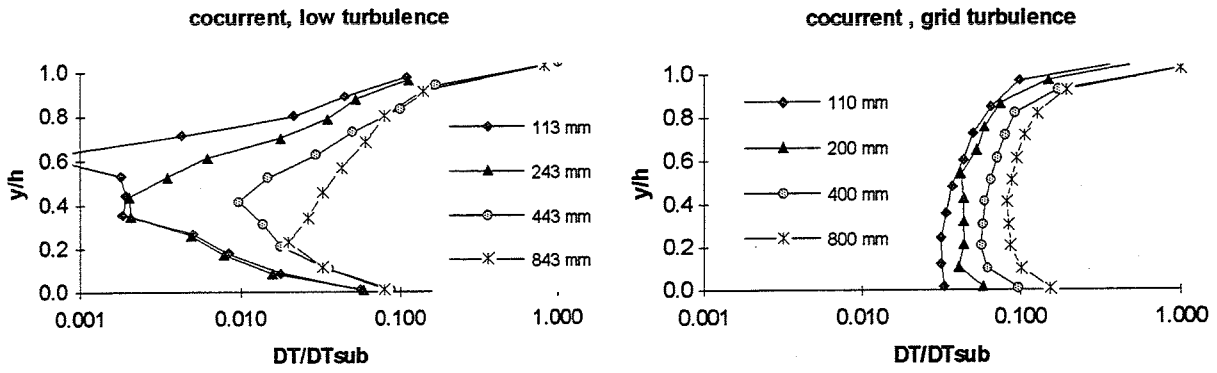

Fig. 5: Heating of the water layer as a function of initial turbulence intensity.

The turbulent heat transport is enhanced by the grid generated turbulence resulting in a steeper temperature profile. Fig. 5 shows although a remarkable heat transfer through the channel bottom plate. The isolation with foam glas seems to be not ideal. By integrating the local temperature and turbulence profiles the distribution of the mean liquid temperature and turbulence intensity along the water flow path are available (Fig. 6).
The local heat transfer coefficient is shown in Fig. 7. For low turbulence flow the heat transfer is in the same order as reported by Bankoff [3]. The higher turbulence leads to a significant increase of the heat transfer coefficient at channel inlet. After turbulence decaying the thermal stratification dominates and reduces in a remarkable way the heat transfer even for low turbulence flow.

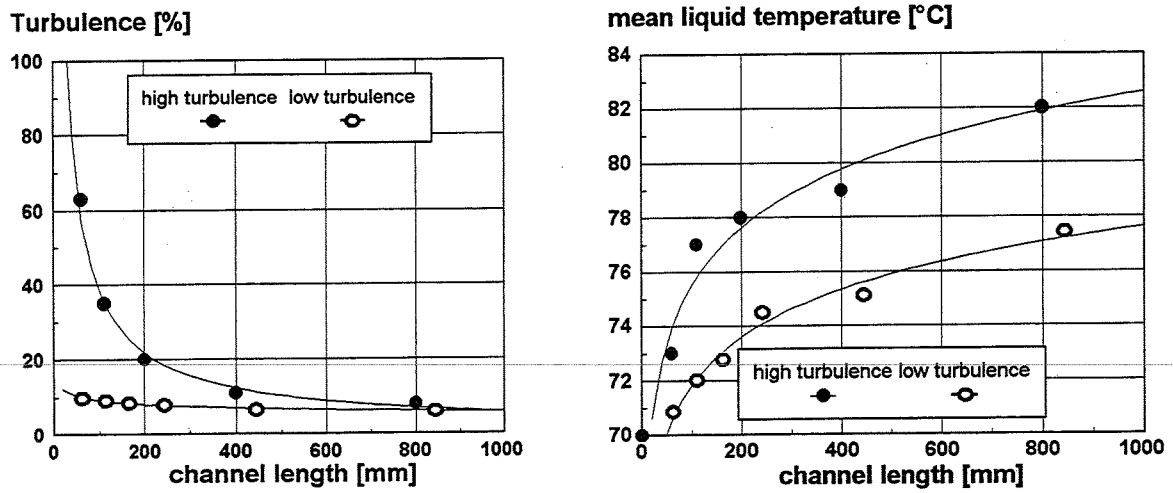

Fig. 6 Axial distribution of mean liquid temperature and turbulence intensity for low and high turbulence intensity

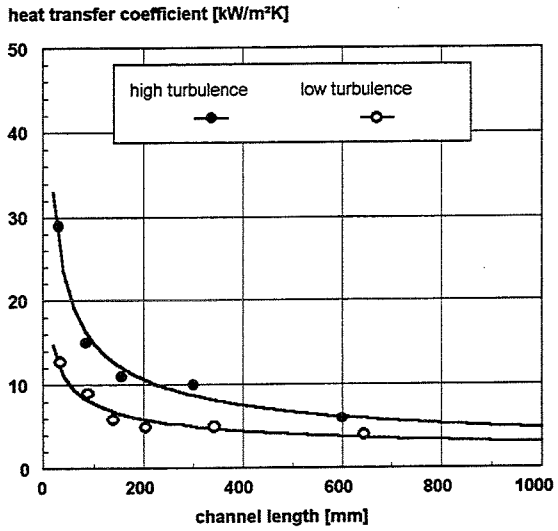

Fig. 7 Influence of local turbulence intensity on heat transfer by direct contact condensation

Series B:
Series B should show the influence of interfacial drag on heat transfer and temperature distribution in the water layer. The interface shear stress is not measured so we used Bankoffs correlation [7] for determining the interfacial shear stress

$$\tau_i = 4.065 f_{i,a} \frac{\rho_D}{2} (\overline{U_b} - U_i)^2 \tag{10}$$

whereas $f_{i,a}$ is friction factor for horizontal flow

$$f_{i,a} = 0.14 \cdot 10^{-5} Re_l + 0.021 \tag{11}$$

the increasing of system pressure results in a increasing of the interface shear stress (table 3).

Table 3: Interface boundaries depending on system pressure

p_{sys} [MPa]	Re_l	Re_v	ρ_v [kg/m³]	τ_i [N/m²]
4.5	32900	13800	2.42	1.12
10	41200	29400	5.05	2.81
19	54400	50000	9.56	5.05

The experiments in series B were performed with nearly constant subcooling. Because the viscosity of the water depends on the temperature the liquid Reynolds number increase with system pressure. Nevertheless the main influence on shear stress takes the steam density. The countercurrent steam flow decelerates the water velocity near the interface resulting in a growing of the water level. At

2.0MPa the water level reaches a height of 50 mm, whereas at 4.5MPa the water level was at 44 mm. Fig. 8 shows the velocity and the turbulence distribution of series B.
The higher shear stress develops a characteristic velocity profile that leads to flow reversal at the interface. The drag forces at the interface agitate the interface resulting in higher turbulence intensities. These profiles are totally different to the known profiles at wall boundary. The interface is source of high turbulence and in opposite to adabatic flow no place where vertical fluctuations could be damped.

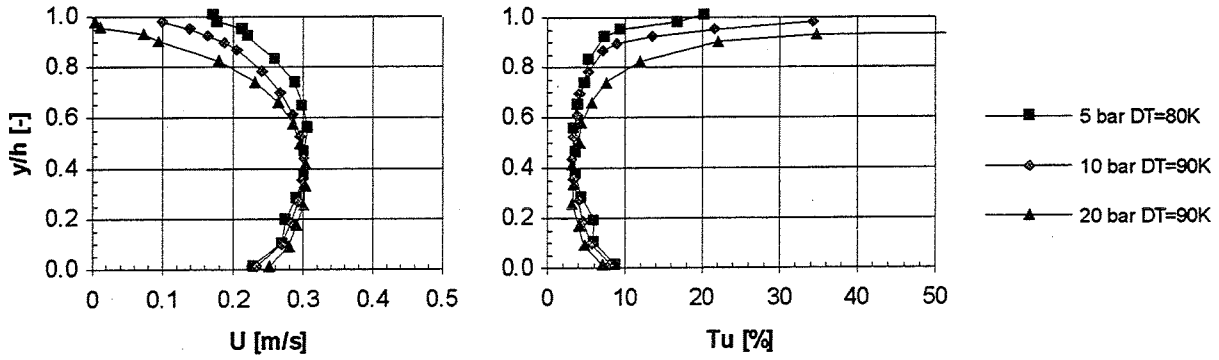

Fig. 8: Velocity and turbulence distribution for increasing interface shear stress

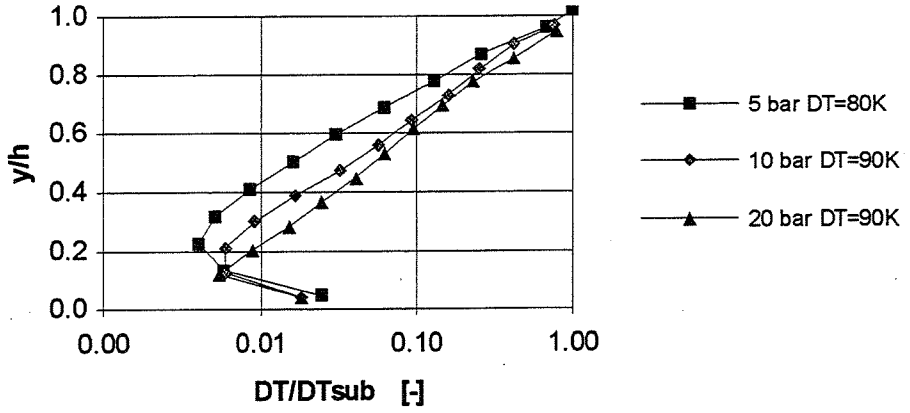

Fig. 9: Temperature profile for increasing interface shear stress

This phenomena is continuing in the temperature profile as shown in fig. 9. The agitation of the interface results in a better mixing of the water layer. The relevant turbulence and dissipation rate for the heat transfer is kept to the turbulence source at the interface. The influence of wall shear is negligible.

7. CONCLUSION

As postulated in the surface renewal theory heat transfer by direct contact condensation is dominated by liquid side turbulence. Two different turbulent initial conditions for the open channel flow were realized to show the influence of high and low turbulence intensities on the heat transfer for steam water cocurrent flow. The high turbulences generated by a cylinder grid decays exponentially to the value of the undisturbed flow. Along the flow path the improved turbulent transport leads to "homogeneous" heating of the water layer whereas for low turbulent flow thermal stratification

arises. The excellent turbulent mixing just behind the cylinder grid results in a remarkable increase of the heat transfer coefficient.
Experiments with increasing interfacial shear stress show clearly an growing of turbulence near interface resulting in a very good mixing within the water layer. In contrast to film or shallow water flow dissipation generated by wall shear is negligible.
For flows with low initial turbulence intensity a strong thermal stratification develops. Interfacial shear could influence it only in a small way. Recent condensation models do not simulate this effect.

ACKNOWLEDGEMENTS

The research reported herein is part of work sponsored by the Federal Minister for Research and Technology (BMFT) under contract number 1500906.

NOMENCLATURE

B	m	channel width
D	m	diameter
DT	K	mean heating
DTsub	K	initial subcooling
U	m/s	mean velocity
T	s	renewal time; temperature
Tu	%	turbulence intensity
c_p	kJ/kgK	specific heat capacity
h	m	water level
l	m	mixing length
$\dot{m}$	kg/s	mass flow
u,v	m/s	fluctuating velocities
x,y,z	m	Cartesian coordinates

Greek symbols

α	W/m^2K	heat transfer coefficient
ε	W/m^3	Dissipation
κ	-	empirical constant in mixing length model
λ	W/mK	thermal conductivity
ν	m^2/s	kinematic viscosity
ρ	kg/m^3	density
$\rho\overline{uv}$	N/m^2	Reynolds stress
σ	-	standard deviation
τ	N/m^2	shear stress
τ_i	N/m^2	shear stress at interface

Indices

b	bulk
i	interface
l	liquid
v	vapour
w	wall
0	initial

REFERENCES

[1] Ahmed. A., Ostowari C., "Longitudinally and transversely spaced cylinders in cross flow", in J. Wind Eng. and Industrial Aerodynamics, Vol. 36 , pp 1095-1104 (1990)

[2] Banerjee, S., Rashidi, M., Hetsroni G., "Mechanisms of heat and mass transport at gas liquid interfaces", in Int. J. Heat Mass Transfer, Vol.34 (7) , pp 1799-1810 (1991)

[3] Bankoff, S.G., Lim, I.S., Tankin, R.S., Yuen, M.C., "Cocurrent steam/water flow in a horizontal channel", NUREG/CR-2289, Northwestern University, Evanston (1981)

[4] Higbie, R., "The rate of absorption of a pure gas into a still liquid during short periods of exposure", in AIChE Journal,. Vol. 31, pp 365-389 (1935)

[5] Hobbhahn, W., "Beschreibung der Direktkontaktkondesation von Dampf an unterkühltem Wasser mit Anwendung in der Störfallberechnung von Druckwasserreaktoren"., Dissertation, Bochum (1990)

[6] Hughes, E.D., Duffey, R.B., "Direct Contact Condensation and momentum transfer in turbulent separated flow", in Int. J. Multiphase Flow , Vol. 17(5), pp 559-619 (1991)

[7] Kim H.J., Lee S.C., Bankoff S.G., "Heat transfer and interfacial drag in countercurrent steam-water stratified flow", in . Int. J. Multiphase Flow, Vol. 11(5), pp 593-606 (1985)

[8] Ogino F., Tominari Y., Mizushina T., "Heat transfer mechanism in a thermally stratified turbulent flow". in Proc. of 7th Int. Heat Transfer conference, Vol. 2, pp 443-448, Munich (1982)

[9] Sonin, A.A., Shimoko, M.A., Chun, J-H., "Vapor condensation onto a turbulent liquid", in Int. J. Heat Mass Transfer, Vol.29 (9), pp 1319-1332 (1986)

[10] Theophanous T.G., "Conceptual models of gas exchange", In Gas Transfer at water surfaces, ed. W. Brutsaert, G.H. Jirka, Reidel/North-Holland, Amsterdam, pp. 271-281 (1984)

[11] Uberoi, M.S., Wallis, S., "Effect of grid geometry on turbulence decay", in The physics of fluids, Vol. 10(6), pp 1216-1224 (1967)

THEORETICAL AND EXPERIMENTAL STUDIES ON THE PSEUDO-DROPWISE CONDENSATION OF BINARY VAPOR MIXTURE

K. Hijikata [1], Y. Fukasaku [1] and O. Nakabeppu [1]

[1] Tokyo Institute of Technology
Faculty of Engineering, Department of Mechano-Aerospace Engineering
2-12-1 Ohokayama, Meguro-Ku, Tokyo 152, Japan
Telephone: (03) 5734-3172, Facsimile: (03) 3729-0628

ABSTRACT

If a water and ethanol vapor mixture condenses, it can be observed that drops or streaks will appear in the condensate film though they are miscible each other. This condensation phenomenon is clearly different from that of conventional pure vapor dropwise condensation, because experiments have shown that the droplets rise from the undulating film and always move around on the film. Moreover, the dimensions of the droplet for the binary vapor mixture are an order of magnitude larger than that for water vapor. In this paper, both experimental and theoretical analysis on the pseudo-dropwise condensation are reported. Drop formation on a horizontal plane was observed and perturbation theory was used in the analysis of the condensate film. Special attention was paid to the Marangoni effect of both temperature and concentration change in the film. The result indicates that the condensate film is stable for negative Marangoni numbers, but unstable for positive Marangoni numbers and small wave numbers. The experimentally observed modified wave number, $k/(Ma/Pr)$ coincides with the one predicted by analysis within a small discrepancy.

1. INTRODUCTION

Research on the condensation of the binary vapor mixtures have aimed to improve cycle efficiencies of energy systems[1] which use binary vapors mixtures as the working fluid. However, because of the formation of a concentration boundary layer, the heat transfer rate in binary vapor mixtures is reduced, thus reducing possible cycle efficiency. Moreover, since the ideal refrigerants - CFCs - are limited in use because of the recent awareness about their environmental problems, substitute refrigerant or new technique to enhance heat transfer is getting necessary. For this reason, research on the condensation having the unique characteristics becomes important.

Hayashi et al.[2] used immiscible liquids to study film-drop mixed condensation. However, non-filmwise condensation can also occur with miscible liquid mixtures. For example, when a water-ethanol binary vapor mixture condenses, the droplets or streaks have been observed in the condensing film[3,4]. Since both liquids are complete miscible and will wet a copper surface, this film-drop condensation phenomenon is different from conventional dropwise condensation. Here, this paper defines this type condensation as pseudo-dropwise condensation. This observation about miscible binary mixtures suggests that they may have the advantage of high heat transfer rate due to dropwise condensation. This phenomena has been observed[5], but no one has yet explained theoretically the reason for its existence. Therefore, in this work, the drop growth mechanism in the pseudo-dropwise condensation is investigated both theoretically and experimentally.

The pseudo-dropwise condensation on a horizontal plate was observed with a microscope and the wave number of the droplets was compared with theoretical prediction. A perturbation method was employed for the theoretical analysis, with special attention paid to the Marangoni effect when both temperature and concentration change. This paper presents a comparison of the results from perturbation theory and experiments. Instability wave number and dependency on properties are also discussed.

2. EXPERIMENT OF A WATER-ETHANOL VAPOR MIXTURE CONDENSATION

2.1 Pseudo-Dropwise Condensation on a Vertical Flat Plate

Figure 1 shows a picture of pseudo-dropwise condensation on a vertical plate. For the same degree of subcooling, $\Delta T = (T_{sat} - T_w)$, both pure water and pure ethanol vapor should experience filmwise condensation. However, as Fig. 1 shows, the binary vapor mixture of water and ethanol (ethanol concentration = 26 mol%) experiences pseudo-dropwise condensation. The droplets do not, remain stationary on the cooling wall, and a liquid film covers the wall simultaneously. This feature is different from that of the conventional dropwise condensation for pure vapors.

The droplets appear to rise from the base liquid film and grow by coalescence. However, beyond a critical size, the droplet condensate flows due to gravity. In order to observe this process in detail without the effect of gravity, an experimental apparatus having a horizontal flat plate was designed.

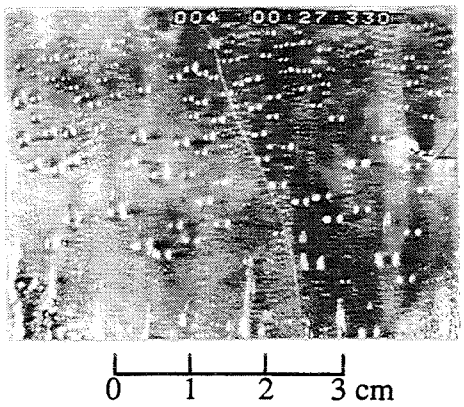

Fig. 1 Pseudo-Dropwise Condensation on a horizontal plate. ΔT = 15 K, C_{et} = 26 mol%, P_{sat} = 150 mmHg

2.2 Experimental Apparatus

Figure 2 shows a schematic diagram of the experimental apparatus. A horizontal surface was used to condense the binary vapor mixture. A copper cylinder block measuring 30 mm in diameter and 60 mm height served as the condenser, which was cooled at one end with water and surrounded by thermal insulator. The condensing surface on the opposite end of the block was polished with 1500 grade emery paper and ϕ1.0 μm alumina polishing liquid, and washed with pure ethanol and water to eliminate contamination. Thermocouples were set along the center axis of the condenser block. The heat flux was measured from the temperature gradient.

A boiler under the condenser block generated the binary vapor mixture from a liquid mixture with a suitable concentration. The vapor then moved to a condensation chamber, condensing on the polished surface. To remove the accumulated condensate periodically, a rotating rubber blade wiper was used. The behavior of condensate was observed through a window 5 mm above the condensing surface using a microscope connected with a CCD camera and a video recorder.

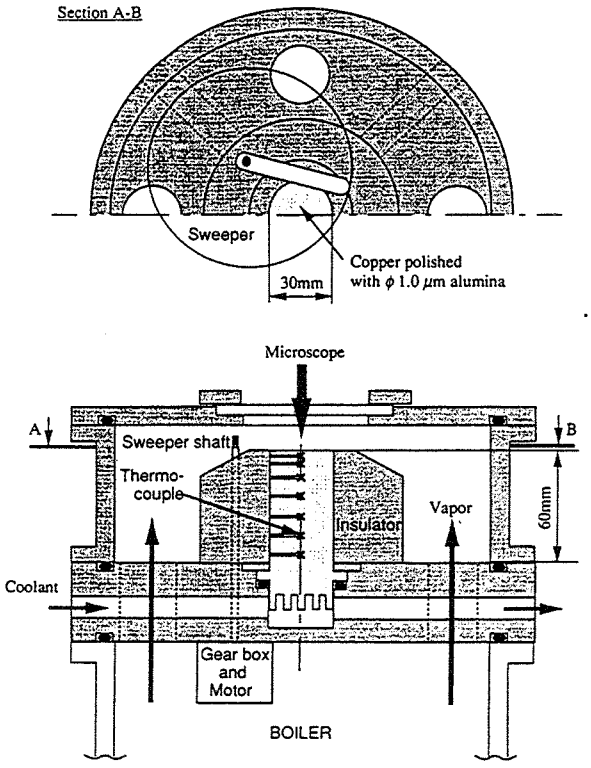

Fig 2 Experimental Apparatus

2.3 Experimental Conditions

The total vapor pressure was kept at 135 mmHg throughout the experiment. The sweeping frequency was varied from 0.2 to 4 Hz. Ethanol concentrations in the vapor mixture were 0, 25,35,45,55 and 100 mol%. The temperature difference between the bulk vapor and the condensing surface, $(T_{sat} - T_w)$, which depends on the ethanol concentration, was 0.6 to 12K.

2.4 Observation of Dropwise Condensation

Figure 3 shows the transition of a condensing film for a water-ethanol binary system, where the ethanol concentration, subcooling, $T_{sat} - T_w$, and sweeping frequency were 25 mol%, 11.0 K and 1.38 Hz, respectively. The time after the condensate is wiped off is shown below each picture.

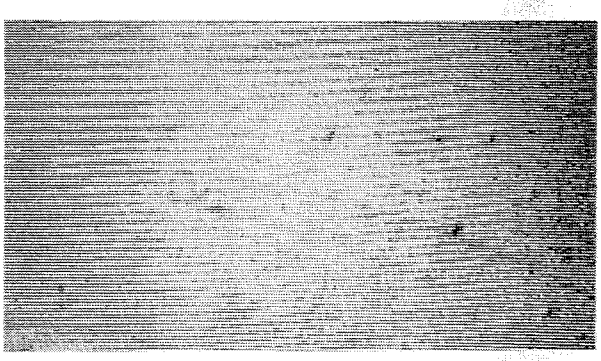

Fig. 3 (1) 0.03 sec 1mm

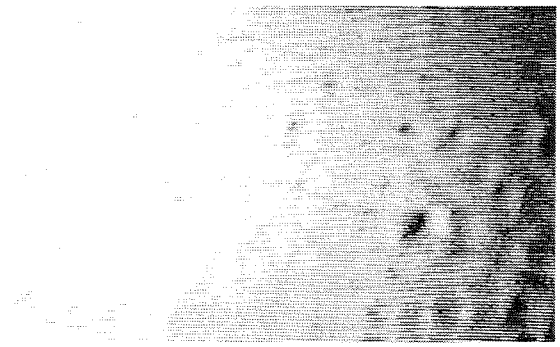

Fig. 3 (2) 0.10 sec 1mm

Fig. 3 (3) 0.17 sec 1mm

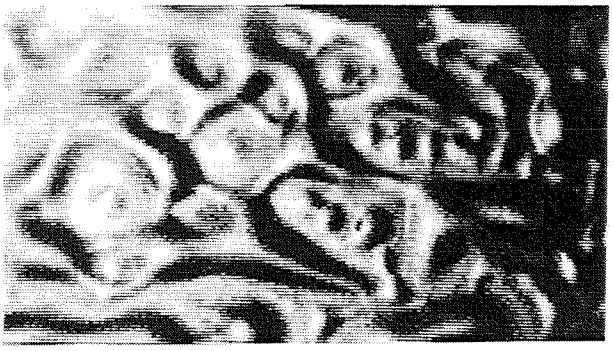

Fig. 3 (4) 0.27 sec 1mm

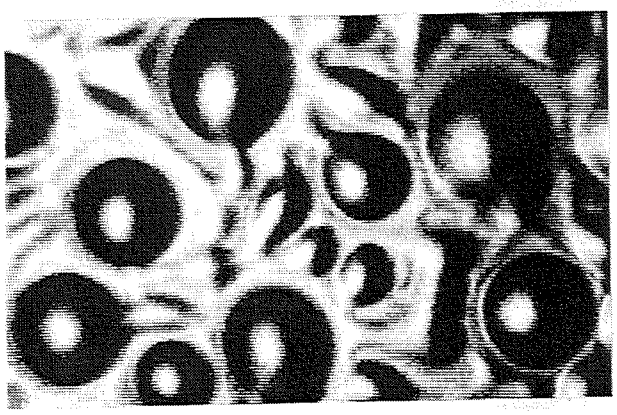

0.57 sec 1mm

Fig. 3 (5) Condensation of Water-Ethanol mixture

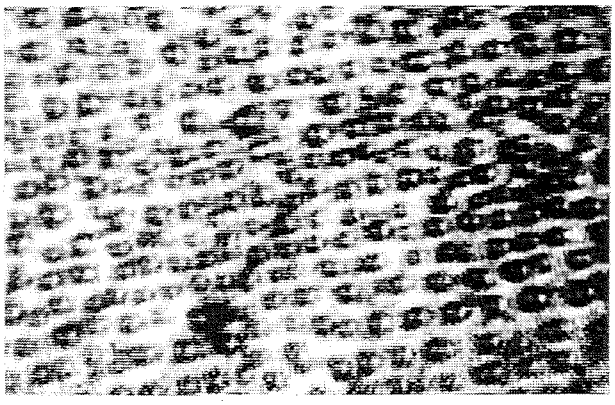

0.1mm

Fig. 4 Dropwise Condensation of Water

The wiper rotated in a clockwise direction, moving from right to left in the pictures. Only a small portion for the condensing surface is represented in the pictures, however the appearance of condensate film in all regions was uniform except at differing times due to the motion of the wiper. Fig.3 (1) indicates a flat condensate film immediately after wiping. The initial thickness of the film could not be measured. After 0.1 s the condensate film surface becomes uneven in the right side of Fig.3 (2).

The white surfaces show the light source facing surfaces and the dark surfaces are the surfaces which are in shadow. These indicate hills and valleys in the condensate film. After 0.17 s, the amplitudes of the surface undulations become larger and the crater like formations become arranged in a honeycomb shape - Fig.3 (3). After 0.27 s, the honeycomb arrangement has appear over the entire Fig.3 (4), and on the right hand side, a section of the honeycomb structures have begun to change into a hemispherical droplet. The new droplet formation progress toward the left side, and after 0.57 s, many droplets are distributed over the whole condensate film area as shown in Fig.3 (5). The droplets grow and move on the surface by coalescing with each other.

For comparison, Fig. 4 shows ordinary dropwise condensation of pure water vapor on same surface. The picture was taken 0.4 s after wiping, where sub cooling of the surface and wiping frequency were 12.8 K and 1.82 Hz, respectively. The size of droplets is approximately 20 times smaller than that of water-ethanol vapor. In addition, the water droplets are directly formed on the condensation surface, staying at the same position. These differences indicate that condensation droplet formation mechanics are different between pure vapor and binary vapors.

Experiments were also carried out by changing the inclination angle of the condensing surface and the same pseudo-dropwise condensation was observed. This fact shows that the flow of the condensate due to gravity is not essential to the drop formation.

Figure 5 shows the relationship between the wave length of the honeycomb structure on the film, λ, and film thickness, δ, which is measured from the temperature gradient at the wall surface and the sweep period. Except for the pure vapor cases, every experiment showed pseudo-dropwise condensation, and showed that the wave length of the disturbance increased as film thickness increased. This data is replotted as Sh versus Ma/Pr ratio in Fig.6, where the wave length has been non- dimensionalized by film thickness δ. Although the effect of Sh is not clear, the figure shows that for large Ma/Pr ratio, the non-dimensional wave lengths are smaller. This data will be discussed further after the theoretical analysis.

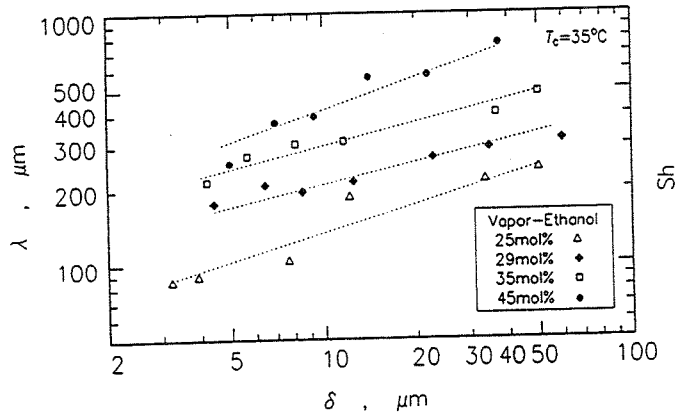

Fig. 5 Film thickness vs. wave length of disturbance.

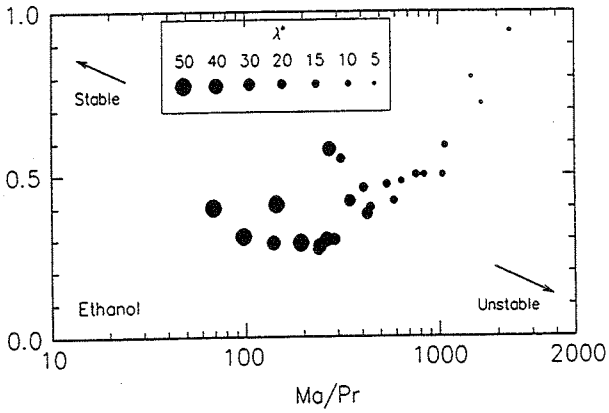

Fig. 6 Wave length of the disturbance for various experimental condition.

3. INSTABILITY ANALYSIS ON CONDENSATE FILM OF A BINARY VAPOR MIXTURE

Observing the condensate film revealed that many droplets grow from small disturbances on the smooth condensate film. Therefore, a theoretical analysis using perturbation theory was conducted to understand this phenomenon. The model used here is two dimensional and assumes that a binary vapor mixture of miscible liquids condenses on a horizontal infinite liquid film, whose thickness, H, is constant. At an equilibrium state, the liquid velocity is zero, the concentration in the liquid is constant, and the temperature profile is linear due to released latent heat. The diffusion resistance in the vapor phase is considered by assuming the appropriate mass transfer coefficient at the vapor liquid interface.

3.1 Governing Equations and Boundary Conditions

Since the primary quantity of velocity is zero, convection terms in governing equations of first order variables can be neglected. Therefore the conservation equations become as follows.

continuity equation :

$$\frac{\partial u}{\partial x} + \frac{\partial v}{\partial y} = 0 \qquad (1)$$

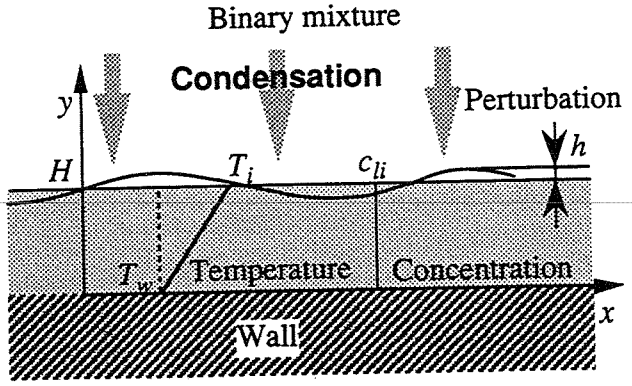

Fig 7 Schematic diagram of the Field

momentum equation:

$$\frac{\partial u}{\partial t} = -\frac{1}{\rho}\frac{\partial P}{\partial x} + \nu\left(\frac{\partial^2 u}{\partial x^2} + \frac{\partial^2 u}{\partial y^2}\right) - g\frac{\partial h}{\partial x} \tag{2}$$

$$\frac{\partial v}{\partial t} = -\frac{1}{\rho}\frac{\partial P}{\partial y} + \nu\left(\frac{\partial^2 v}{\partial x^2} + \frac{\partial^2 v}{\partial y^2}\right) \tag{3}$$

energy equation :

$$\frac{\partial T}{\partial t} = \kappa\left(\frac{\partial^2 T}{\partial x^2} + \frac{\partial^2 T}{\partial y^2}\right) \tag{4}$$

mass diffusion equation :

$$\frac{\partial c}{\partial t} = D\left(\frac{\partial^2 c}{\partial x^2} + \frac{\partial^2 c}{\partial y^2}\right) \tag{5}$$

The boundary conditions are assumed as follows,
at $y = 0$ (cooling wall)

$$u = v = 0 \tag{6}$$

$$T = T_w \tag{7}$$

$$\frac{\partial c}{\partial y} = 0 \tag{8}$$

at $y = H+h$ (vapor-liquid interface)

tangential stress balance: $$\mu\left(\frac{\partial u}{\partial y}+\frac{\partial v}{\partial x}\right)=\frac{\partial \sigma}{\partial c}\frac{\partial c_i}{\partial x}+\frac{\partial \sigma}{\partial T}\frac{\partial T_i}{\partial x} \tag{10}$$

normal stress balance: $$-P + 2\mu\frac{\partial v}{\partial y} = \sigma\frac{\partial^2 h}{\partial x^2} \tag{11}$$

energy balance: $$-\lambda\frac{\partial T}{\partial y}\propto\left(c_{g\infty} - c_{gi}\right) \tag{12}$$

phase equilibrium: $$T_i = T_s + \alpha_g c_{gi}\ ,\ T_i = T_s + \alpha_l c_{li} \tag{13}$$

The tangential stress is normally zero at the interface, but it is generated by surface tension changes along the surface. The surface tension varies according to both temperature and concentration change. The pressure and the normal stress at the interface are balanced against the surface force caused by the curvature. It is assumed that latent heat released by condensation is caused by the mass transfer via diffusion in the vapor phase, which is proportional to the concentration difference between the bulk and the interface, $c_{g\infty} - c_{gi}$. Moreover, phase equilibrium is assumed at the vapor-liquid interface with Eq.(13).

3.2 Normalization

Normalization by film thickness, H, characteristic velocity, ν/H, and temperature difference ΔT $(= T_i - T_w)$ gives the following non-dimension parameters;

$$Pr = \frac{\nu}{\kappa}\ ,\ Sc = \frac{\nu}{D}\ ,Ga = \frac{H^3 g}{\nu^2}\ ,\ Sh = \frac{CH}{\alpha_g \lambda}\ ,\ Ma = \left(\frac{\partial \sigma}{\partial c}\frac{1}{\alpha_l} + \frac{\partial \sigma}{\partial T}\right)\frac{\left(T_\infty - T_i\right)\cdot H}{\kappa\mu}\ ,\ K = \frac{\sigma H}{\rho\nu^2} \tag{14}$$

where Pr, Sc and Ga are Prandtl number, Schmit number and Galilee number, respectively. The variable Sh is the modified Sherwood number representing dimensionless mass transfer coefficient of the vapor phase. The C in Sh is a proportional constant in Eq.(12). Ma is the modified Marangoni number corresponding to the surface tension change by the temperature and concentration change. Usually $\partial\sigma/\partial T$ is negative for a pure substance, but $\partial\sigma/\partial c$ can be either negative or positive depending on the combination of two substances, therefore Ma can become positive for a binary mixture. A dimensionless parameter for the absolute value of surface tension is defined as K.

3.3 Derivation of Solutions

All variables (u, v, P, c and T) are perturbed as follows:

$$f(x,y,t) = f_0 + f_1(y)\cdot \exp(ikx + \omega t) \tag{15}$$

where k is the x-direction wave number and ω is the perturbation growth rate. Subscripts 0 and 1 correspond to primary and perturbed terms, respectively. Substituting Eq.(15) into the governing equations, the following ordinary differential equations are derived:

$$\left(\frac{d^2}{dy^2} - k^2\right)\left(\frac{d^2}{dy^2} - k^2 - \omega\right) v_1(y) = 0 \tag{16}$$

$$\left(\frac{d^2}{dy^2} - k^2 - \mathrm{Pr}\cdot\omega\right) T_1(y) = \mathrm{Pr}\cdot v_1(y) \tag{17}$$

The solutions to these differential equations are:

$$v_1(y) = C_1 e^{ky} + C_2 e^{-ky} + C_3 e^{my} + C_4 e^{-my} \tag{18}$$

$$T_1(y) = \frac{\mathrm{Pr}}{k^2 - n^2}\left(C_1 e^{ky} + C_2 e^{-ky}\right) + \frac{\mathrm{Pr}}{m^2 - n^2}\left(C_3 e^{my} + C_4 e^{-my}\right) + C_5 e^{ny} + C_6 e^{-ny} \tag{19}$$

where

$$m^2 = k^2 + \omega, \quad n^2 = k^2 + Pr\cdot\omega \tag{20}$$

and C_1~C_6 are integral constants. By substituting Eq.(17) into the boundary conditions, they become, at y = 0

$$v_1 = \frac{dv_1}{dy} = T_1 = 0 \tag{21}$$

at y = 1+h (vapor-liquid interface)

$$\omega\frac{d^2 v_1}{dy^2} + k^2\left(\omega - \frac{Ma}{\mathrm{Pr}}\right)v_1 - k^2\omega\frac{Ma}{\mathrm{Pr}}T_1 = 0 \tag{22}$$

$$\omega\frac{d^3 v_1}{dy^3} + \omega\left(-3k^2 - \omega\right)\frac{dv_1}{dy} - k^2\left(Ga + k^2 K\right)v_1 = 0 \tag{23}$$

$$Sh\cdot v_1 + \omega\frac{dT_1}{dy} + \omega\, Sh\cdot T_1 = 0 \tag{24}$$

By substituting the theoretical solutions, Eq. (18) and (19) into these boundary conditions, the integral constants are calculated. This procedure yields the following simultaneous equations using coefficient a_{ij}.

$$\begin{cases} a_{11}C_1 + a_{12}C_2 + a_{13}C_3 + a_{14}C_4 + a_{15}C_5 + a_{16}C_6 = 0 \\ \vdots \\ a_{61}C_1 + a_{62}C_2 + a_{63}C_3 + a_{64}C_4 + a_{65}C_5 + a_{66}C_6 = 0 \end{cases} \tag{25}$$

Eq.(25) can be rewritten as follows:

$$\begin{bmatrix} a_{11} & \cdots & a_{16} \\ \vdots & \ddots & \vdots \\ a_{61} & \cdots & a_{66} \end{bmatrix}\begin{bmatrix} C_1 \\ \vdots \\ C_6 \end{bmatrix} = \begin{bmatrix} 0 \\ \vdots \\ 0 \end{bmatrix} \tag{26}$$

Because the right-hand side of Eq.(26) is zero, the following condition is necessary to obtain a nontrivial solution.

$$\begin{vmatrix} a_{11} & \cdots & a_{16} \\ \vdots & \ddots & \vdots \\ a_{61} & \cdots & a_{66} \end{vmatrix} = 0 \tag{27}$$

This equation gives the relation between the growth rate ω and the wave number k, because each coefficient a_{ij} is a function of k and ω.

3.4 Results and discussion

From the numerical calculation of Eq.(27), the relation between the growth rate ω and the wave number k is obtained as shown in Fig. 8. From the definition of perturbed terms in Eq.(15), it is clear that the perturbation is amplified for positive growth rate ω and damped for negative ω. The curve at $Ma/Pr = 500$ in the figure, for instance, passes through both positive and negative growth rate areas. This implies that specified disturbances having a particular wave number can grow. The Marangoni effect (Ma/Pr) plays an important role with respect to the stability of a condensate film because the curve largely depends on the value of Ma/Pr and a larger Ma/Pr makes the condensate film more unstable.

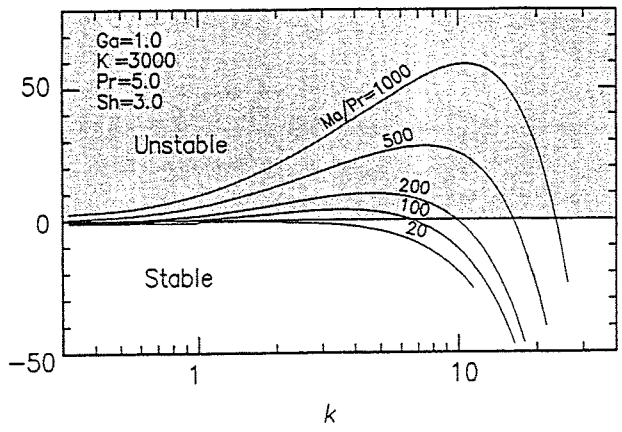

Fig. 8 Typical relation between wave length k and growth rate ω

Figure 9 shows the velocity profile in the liquid and the temperature distribution at the interface for the unstable case at $Ma/Pr = 200$ and $k = 6.2$. It is important to note that the directions of the variables and not the absolute values have meaning in those type of figures.

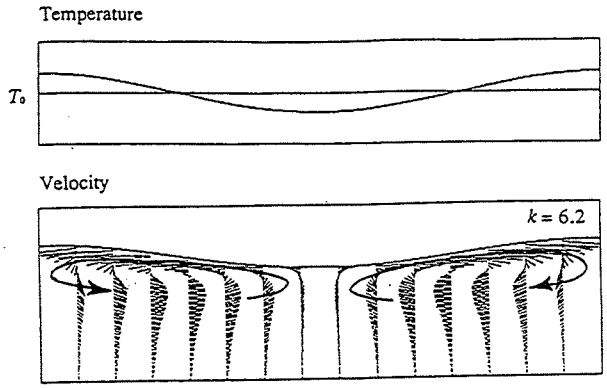

Fig. 9 Velocity profile and Temperature distribution at the interface (unstable case)

The surface temperature at a hill on the liquid film becomes higher than that of the primary unperturbed state (i.e. zeroth order state with no perturbation terms), because heat conducts from surface to cooling wall and temperature gradient in the film has a positive value. From the phase diagram of water and ethanol system, the higher temperature generates a higher water concentration and a lower temperature generates a higher ethanol concentration. Therefore, at the interface on a hill, the concentration of water exceeds the primary unperturbed condition. Because the surface tension of the water is larger than that of ethanol, the liquid near the interface is pulled by the surface tension difference and moves from the valley to the hill. This is Marangoni convection due to the concentration change induced by temperature change.

In the condensation of the water-ethanol vapor mixture, the Marangoni effect raises the higher part of the film and lowers the lower part. That is, Marangoni convection destabilizes the film. On the contrary, gravity and the normal component of surface tension stabilize the film by generating a flow from the hill to the valley. This stabilizing effect appears in the flow from the hill to the valley inside the liquid film. The relation of the Marangoni convection effect and the stabilizing effect decides the instability of the whole film. Under the conditions listed for Fig.9, the Marangoni effect overcomes the stabilizing effect and make the condensate film unstable.

In order to see the effect on instability of absolute value of surface tension, gravity, heat conduction and mass transfer rate in the vapor phase, the relationships between the growth rate ω and the wave number k were calculated by changing the value K, Ga, Pr and Sh. Since the stability curve does not depend on both K and Ga, surface tension itself and gravity do not influence the condensation film stability.

Figure 10 shows the effect of Pr on the relation between wave length and growth rate ω. Large Pr makes the system more unstable. Large Pr implies a large temperature gradient in the film and the fluctuation of the surface temperature according to the fluctuation of film height will also be large. Because the Marangoni effect increases as temperature difference increases, the film becomes unstable.

Large Sh number makes the condensate film slightly more stable as shown in Fig.11. The reason is as follows: when the heat flux at the interface changes due to the fluctuation of the film

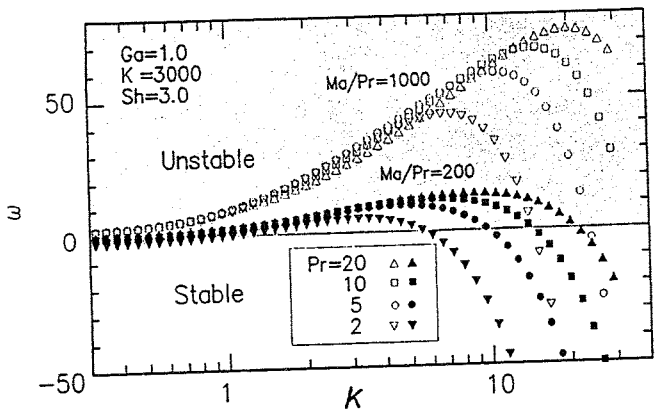

Fig. 10 The effect of Pr number on the k-ω curve

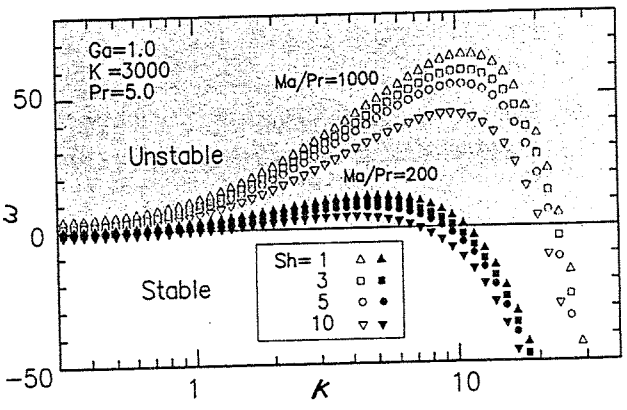

Fig. 11 The effect of Sh number on the k-ω curve.

height, the concentration and temperature change are small for the large Sh, as is implied in Eqs.(12) and (13). Then, Marangoni effect is small and the liquid film is stable.

Using these results, the neutral stability curve is plotted versus Ma/Pr according to the wave number k as shown in Fig. 12. In the region above this curve (indicated with $\omega = 0$), the growth rate ω is positive and the film can change to the dropwise shape, but in the region below the curve the condensate film remains flat. This relationship corresponds to that of the Rayleigh number versus wave number for the ordinary Benard cells stability problem. However, unlike the Bernard cells problem, there is no absolute minimum value of Ma/Pr in the figure, which means that no critical value of Ma/Pr for instability exists. That is, the analysis permits instability to exist at low wave number if Ma/Pr is positive.

Experimental data is also plotted in Fig. 12 and is the same data as shown Fig. 6. Each data was callected at a moment when the disturbance was recognized with the eye, and the wave number k is nondimensionalized by a fixed film thickness just before wiping. In the actual experiment, the condensate film thickness is increasing with time. Therefore, wave number k of same disturbance is increasing with time. Simultaneously, the ratio Ma/Pr , which is proportional to the film thickness, increases with time as well. Therefore, the progress of condensation can be represented by 45 degree lines passing on data point. Hence, it is important to read Fig. 12 along 45 degree lines, and it provides a way to predict the progression of a perturbation. A disturbance with wave number on the line A is damped because the line A passes once through the unstable region, but reenters the stable region again. On the other hand, in the region above line B, a disturbance always grows as the film thickness increase, because they are always in the unstable region.

The experiment was carried out for a variety of vapor concentrations and wiper rotation speeds, but the data is nearly on the same line indicated by C. This line is parallel to and located slightly above line B, which connects with the zero growth rate curve and gives a critical value for instability.

A dotted line indicated by $\omega = \omega_{max}$ in Fig.12 shows the maximum growth rate wave number curve. If the wave number for a given Ma/Pr is closer to this curve, the growth rate becomes faster. It is reasonable that the experimental data are all located in the region where disturbances are always unstable and grows at fastest rate in the region, because only the fastest growing disturbances can be observed.

The quantity $k/(Ma/Pr)$ can be defined to characterize the wave number during actual condensation. By this modified wave number all data is reduced to one number, 7.3×10^{-4}, regardless of the various experimental conditions. While, the analysis yields a critical wave number, 1.8×10^{-3}, corresponding to line B in Fig. 12, the critical wave number is slightly

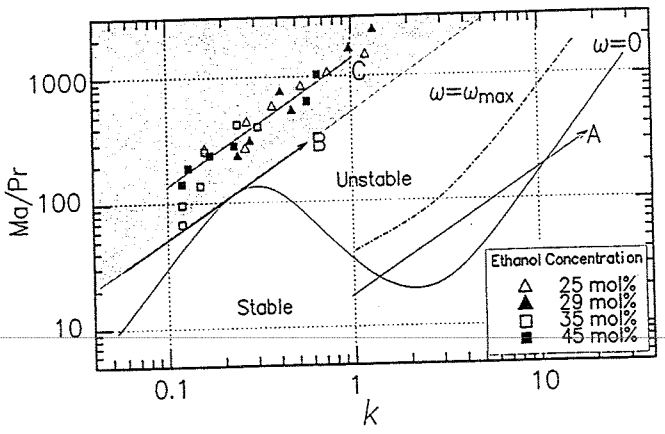

Fig. 12 Stability Curves of Ma/Pr versus wave number k

larger than the measured modified wave number.

The small discrepancy is expected between experiment and analysis. The discrepancy originates from the differences in parameters and assumption in the analysis. For example, Sherwood number changes from 0.7 to 0.3 in the actual experiment. The assumption for film thickness, temperature distribution, etc. may also be different from those in the experiment. However, the analysis shows that the measured modified wave number can be predicted and the Marangoni effect is dominant over the drop formation mechanism.

CONCLUSION

The pseudo-dropwise condensation phenomena of the water-ethanol binary mixture was investigated and following conclusions were obtained.

(1) The droplets in the pseudo-dropwise condensation are generated by the instability of the condensing film.

(2) The wave length of this instability is explained by the theory considering the surface tension change due to the concentration and temperature.

NOMENCLATURE

c	concentration (mol%)
D	diffusivity (kg/(m s))
Ga	Galilee number
g	gravity acceleration (m2/s)
H	initial Film thickness (m)
h	amplitude of perturbation (m)
K	dimensionless surface tension
L	latent heat (J/kg)
Ma	modified Marangoni number
P	pressure (Pa)
Pr	Prandtl number
Sc	Schmit number
Sh	Sherwood number
T	temperature (K)
u	velocity in horizontal direction (m/s)
v	velocity in vertical direction (m/s)
x	direction parallel to the wall (m)
y	direction vertical to the wall (m)

Greek letters

α	physical constant related to phase diagram (K/mol%)
δ	condensing film thickness (m)
κ	Thermal diffusivity
λ	heat conductivity (W/(m K))
μ	viscosity (kg/(m s))
ν	kinetic viscosity (m^2/s)
ρ	density (kg/m^3)
σ	surface tension (N/m)
ω	perturbation growth rate (1/s)

subscripts

0	primary term
1	perturbed term
g	vapor phase
i	interface
sat	saturation
l	liquid phase
w	cooling wall
∞	at the bulk

REFERENCES

[1] Hijikata K., Himeno N. "Condensation of Azeotropic and Nonazeotropic Binary Vapor Mixtures", in: Annual Review of Heat Transfer, vol.3, C. L. Tien, Ed. Hemisphere Publishing Co. p.39 (1990)

[2] Hayashi Y., Takimoto A., Tada Y. and Teranishi T. "Condensation of Binary Vapors of Immiscible liquids", in: Energy Conversion and Utilization with High Efficiency, Researches Pursed by Grant-in-Aid on Priority-Area Research Supported the Ministry of Education, Japan, p.235 (1993)

[3] Fujii T., Koyama S., Shimizu Y. Watabe M. and Nakamura Y., "Gravity Controlled Condensation of an Ethanol and Water Mixture on a Horizontal Tube", in: Trans. of JSME, Series B, vol.55, No.509, Hemisphere publishing Co. p.210 (1989)

[4] Hijikata K., Nakabeppu O. and Fukasaku Y., "Condensation Characteristics of a Water-Ethanol binary Vapor Mixture", in: Proc. 29th National Heat Transfer Symposium of Japan, p742 (1992)

[5] Mirkovich V.V., Missen R.W., "A Study of the condensation of Binary Vapors of Miscible Liquids", in: Canadian J. of Chemical Engineering, vol.39, p86 (1961)

GAS-LIQUID TWO-PHASE FLOW BEHAVIOR IN HEAT EXCHANGERS OF A REFRIGERATING MACHINE

Takamoto Saito[1)], Keizo Tanaka[1)], Eiji Hihara[1)] and Fumio Matsuoka[2)]

[1)]Department of Mechanical Engineering, The University of Tokyo
7-3-1, Hongo, Bunkyo-ku, Tokyo 113, Japan
[2)]Mitsubishi Electric Corporation
5-14-10, Ofuna, Kamakura, Kanagawa 247, Japan

ABSTRACT

Void fraction of refrigerant flowing in a refrigerating cycle was experimentally investigated. The refrigerant is confined in a sampling section by closing the valves mounted at the both ends, and the void fraction was determined from the measurement of mass of refrigerant. The relation among void fraction, quality, and slip ratio was obtained. The Smith's relation was found to correlate also data for refrigerant 22 in a horizontal tube. Based upon the examination of the correlations of void fraction, a fundamental heat pump cycle was simulated. The calculated refrigerant distribution in a condenser and an evaporator coincides with the measurement results.

1. INTRODUCTION

After the oil crisis a large number of thermal cycles were discussed from viewpoint of saving energy consumption. Since ozone hole in the stratosphere became of big concern, several kinds of refrigerants were examined for their influence on environment as well as thermal characteristics. Refrigerant mixtures are also considered as more efficient refrigerant or as alternatives CFCs or HCFCs. In the research and development, it is desirable that performance characteristics are given by computer simulation as well as by experiments. Recently, as for a heat pump or a refrigerating machine, such a system that a compressor drives a number of indoor heat exchangers has been widespreading. Local refrigerant behavior should be taken into consideration for adequate operation of these machines under heat load change, and refrigerant distribution in each heat exchangers is one of the most important factors for the machine performance. The first part of this report is on refrigerant flow parameter measurements, and the second part is concerned with a refrigeration cycle simulation. [1]

2. EXPERIMENTS ON VOID FRACTION

It is important to know the state of refrigerant flowing in heat exchangers, including void fraction, quality and slip ratio between vapor, and liquid phase. Many researches have been executed for air-water or steam-water two-phase flow in a tube, [2] but experimental data are few for refrigerant HCFC.

2.1 Experimental Method

The schematic diagram of experimental apparatus is shown in Fig. 1. R-22 is used as a working fluid. The condenser is composed of 5 concentric tubes (C1-C5). The inside wall surface of inner tube is smooth, if not otherwise specified. The refrigerant flow in the inner tube is cooled by water flowing in the outer tube. The evaporator is composed of 5 tubes (E1-E5). The refrigerant evaporates by electric Joule-heating of tube wall. Geometry of the heat exchanger tubes is listed in Table I. Sampling sections are insulated and are located between tube C3 and tube C4 for the condenser, and between tube-E2 and tube-E3 for the evaporator. At both ends of the sampling sections, pneumatic valves and ball valves are mounted, which are open in operation. The quality in the sampling sections can be adjusted by controlling compressor speed, expansion valve, electrical input in the evaporator and flow rate of the cooling water.

After a stationary state is reached, pneumatic valves in evaporator and condenser are closed simultaneously, and the refrigerant is confined in the sampling sections. The compressor is pulled down after closing ball valves. The sampling sections are removed from the line, and the mass, M, of the confined refrigerant is measured. The average void fraction, α, in the sampling section is calculated by Eq.(1),

$$M = V\alpha\rho_g + V(1-\alpha)\rho_l \tag{1}$$

where V is the volume in the sampling section. The average slip ratio, s, is calculated in Eq.(2).

$$\alpha = \frac{x}{x + s(1-x)\rho_l/\rho_g} \tag{2}$$

The experimental conditions are summarized in Table II.

2.2 Correlations

The relations of void fraction versus quality, and those of slip ratio versus quality under constant flow rate conditions are shown in Figs. 2 and 3, respectively, including evaporator and condenser. For the same quality, as a whole, the void fraction decreases with increase of pressure. The slip ratio in the evaporator scatters rather widely compared with that in the condenser. The characteristics of the void fraction versus quality under constant pressure conditions (P=1.2MPa in the condenser) are shown in Fig. 4. The void fraction increases with mass flux. Considering that the pressure drop of the liquid flow is equal to that of the vapor flow for separate flow, the void fraction is determined by the balance of shear stress at the wall and at the interface. With increase of mass flux, the interfacial shear stress increases and the void fraction becomes larger. The slip ratio becomes smaller with the increase of mass flux, as shown in Fig. 5. Correlations [3] ~ [9] of void fraction, proposed by several researchers, are summarized in Table III . Their comparison with the experimental data for P=0.386MPa is shown in Fig. 6. Within the range of our experimental conditions, the Smith's model, and the Taitel-Dukler's model agree better with the data. All experimental data on the condenser and evaporator can be correlated in the form,

$$s = 667.5\left(\frac{1-x}{x}\right)^{-0.398}\left(\frac{\rho_l}{\rho_g}\right)^{0.122}\left(\frac{GD}{\mu_h}\right)^{-0.497} \tag{3}$$

where the two-phase viscosity, μ_h , is defined by

$$\frac{1}{\mu_h} = \frac{x}{\mu_g} + \frac{1-x}{\mu_l} \tag{4}$$

Deviations between Eq.(3) and the data are within about 15%, as indicated in Fig. 7. If equation are formulated for the condenser and the evaporator, respectively, the following equations are obtained.

Condenser:

$$s = 2152 \left(\frac{1-x}{x}\right)^{-0.442} \left(\frac{\rho_l}{\rho_g}\right)^{0.122} \left(\frac{GD}{\mu_h}\right)^{-0.604} \tag{5}$$

Evaporator:

$$s = 248.9 \left(\frac{1-x}{x}\right)^{-0.444} \left(\frac{\rho_l}{\rho_g}\right)^{0.122} \left(\frac{GD}{\mu_h}\right)^{-0.397} \tag{6}$$

Fig. 8 shows the effect of heat flux on the void fraction. A portion ($E2$) of evaporating tube located just upstream of the sampling section is not heated. In this case, the quality is constant in the tube $E2$ and sampling section. The influence of heat flux at upstream is not obvious within the present experimental conditions.

Internally grooved tubes (groove depth : 0.15mm) are used for evaporator, in order to investigate the effect of surface configuration on void fraction. The void fraction is not influenced by mass flux. It is smaller than that for a smooth tube, as shown in Fig. 9, due to the increase of shear stress at the wall. Experiments, concerned with inner surface configuration, are being performed further.

3. COMPUTER SIMULATION OF CYCLE PERFORMANCE

3.1 Experimental Apparatus

Taking an air-conditioner as an example, calculation methods of refrigerant behavior have been studied by a number of researchers. [10] In this study refrigerant behavior in heat exchangers is focused.

Schematics of the apparatus and the structure of heat exchangers are given in Figs. 10 and 11. The compressor is of a rotary type, and has a displacement volume of 10.4 cm^3. The condenser is composed of horizontal tubes which are connected by bends, and are arrayed in a vertical plane. The refrigerant enters from the top and the bottom of tube array. It flows in two ways, and discharges from the same exit at the middle. The evaporator has two vertical arrays of horizontal tubes. The refrigerant enters from the middle of front array, and discharges from the middle of the rear array. The refrigerant (R-22) flow exchanges heat with air flow. The standard conditions are given in Table IV.

3.2 Computation Model of Heat Exchangers

One-dimensional steady flow is assumed in heat exchangers. Conservation equations for each control volumes are given below.(Fig. 12)

Mass conservation:

$$G_{\ell o} + G_{go} = G_{\ell i} + G_{gi} \tag{7}$$

Momentum conservation:

$$G_{\ell o} u_{\ell o} + G_{go} u_{go} = G_{\ell i} u_{\ell i} + G_{gi} u_{gi} - \pi D(\Delta \ell)\, \tau_w - A(P_o - P_i) - N_1 g \sin\theta \tag{8}$$

Energy conservation:

$$G_{\ell o}h_{\ell o} + G_{go}h_{go} = G_{\ell i}h_{\ell i} + G_{gi}h_{gi} - \pi D(\Delta\ell)\, q_w - N_2 g \sin\theta \tag{9}$$

where

$$G_\ell = G(1-x) \tag{10}$$

$$G_g = Gx \tag{11}$$

$$u_\ell = G_\ell/[\,\rho_\ell A(1-\alpha)] \tag{12}$$

$$u_g = G_g/(\,\rho_g A\,\alpha) \tag{13}$$

$$N_1 = A\,\Delta\ell[\,\rho_{\ell i}(1-\alpha_i) + \rho_{go}\,\alpha_i]/2 + A\,\Delta\ell[\,\rho_{\ell o}(1-\alpha_o) + \rho_{go}\,\alpha_o]/2 \tag{14}$$

$$N_2 = A\,\Delta\ell[\,\rho_{\ell i}(1-\alpha_i)u_{\ell i} + \rho_{gi}\,\alpha_i u_{gi}]/2 + A\,\Delta\ell[\,\rho_{\ell o}(1-\alpha_o)u_{\ell o} + \rho_{go}\,\alpha_o u_{go}]/2 \tag{15}$$

Heat transfer at refrigerant side is calculated as follows. In the condenser, the Dittus-Boelter equation is adopted for the single-phase region, and the Fujii's equation is used for the two-phase region. [11] In the evaporator, Yoshida's equation [12] is applied. Heat transfer coefficient at air side including fin efficiency was measured for air flow. The details are referred to Appendix.
The refrigerant flows in the two passages so as to make pressure drop between the inlet and the outlet equal. The two-phase flow shear stress, τ_w, at the wall is expressed in the following equation:

$$\tau_w = {\phi_g}^2 \tau_{wg} \tag{16}$$

where the shear stress, τ_{wg}, of the gas flowing alone in single-phase flow within tube is expressed by the Colburn's equation. [2]

$$\tau_{wg} = 0.046\left(\frac{G_g D}{\mu_g A}\right)^{-0.2} \frac{1}{2\rho_g}\left(\frac{G_g}{A}\right)^2 \tag{17}$$

The two-phase multiplier, ϕ_g, is expressed by Chisholm's equation [13]:

$$\begin{aligned} {\phi_g}^2 &= 1 + 21X_{tt} + {X_{tt}}^2, \\ X_{tt} &= \left(\frac{1-x}{x}\right)^{0.9}\left(\frac{\rho_g}{\rho_l}\right)^{0.5}\left(\frac{\mu_l}{\mu_g}\right)^{0.1} \end{aligned} \tag{18}$$

For bend effect, ϕ_g is multiplied by a factor to make pressure drop calculation coincide with experiment. Correlations of Smith [3] and Zivi [4] for slip ratio are applied. Dynamic characteristics of the compressor influence the cycle performance, and a large number of researches [14] have been executed. Usually the relation between inlet and outlet of compressor is simply expressed as polytropic change, and volumetric efficiency is considered for compressor performance, but they should be evaluated more in detail. For example, refrigerant amount in compressor shell is important, although evaluation is difficult. The compressor can be modeled as shown in Fig. 13. In each divided section conservation equations of mass and energy are considered.

3.3 Results

As examples of computational results of case 1, the distributions of pressure drop, refrigerant mass, and temperature for the standard condition are described in Figs. 14 and 15 for the condenser and evaporator, respectively.

As for characteristics of pressure drop, the following relations are found.

In condenser:

frictional loss $\simeq$ gravitational loss $>$ acceleration loss

In evaporator:

frictional loss $\gg$ gravitational loss $>$ acceleration loss

Let's compare the characteristics in the condenser and evaporator. In the condenser, the gravitational loss is large, and the accelerational loss is small. The gravitational loss depends on the amount of liquid phase in a tube and on geometric configuration like bend. Therefore, it is larger in the lower passage than in the upper passage. As a result, pressure drop between the inlet and outlet in the lower passage should coincide with that in the upper one. Consequently the frictional loss in the lower passage should be smaller than in the upper passage, and the flow rate in the lower passage becomes smaller than that in the upper passage. As shown in the temperature distribution diagram (Fig. 14), condensation completes more upstream in the lower passage than in the upper passage, and the refrigerant amount is larger in the lower passage. The accelerational loss in the condenser is smaller, because the flow velocity decreases as condensation proceeds. In the evaporator, the frictional loss is distinguished, because the specific volume is large due to lower pressure, and the vapor velocity is large. Consequently, the gravitational component is relatively small, and difference of the flow rate between passages are smaller than that in the condenser. In case 2 of a slower compressor speed condition 52 Hz (Fig. 16 and Fig. 17), the gravitational loss becomes relatively larger, especially in the condenser. In order to balance pressure drop in passages, the flow rate difference between the passages becomes conspicuous with decrease of compressor speed. Refrigerant mass in heat exchangers is calculated based on the slip ratio relations of Zivi and Smith. Smith's model gives the result of larger mass in heat exchanger than Zivi's model, as shown in Table V. Mass distribution given in Figs. 14, 15, 16 and 17 is calculated by using the Smith's model.

Conclusion

1. Relation between void fraction and quality of refrigerant (R-22) flow in a horizontal tube was measured.
2. Several models of slip ratio are compared with the data. The Smith's model and the Taitel-Dukler's model are fitted better with the data in a horizontal tube.
3. Flow distribution in multi-passage heat exchangers of a refrigerating machines can be reasonably evaluated in simulation.
4. Flow rate difference among passages is bigger in the condenser than in the evaporator. This tendency is explained by the characteristics of the frictional loss and gravitational loss in heat exchangers.

Acknowledgement

The authors acknowledge Mr.S.Saito and Mr.T.Suzuki of the University of Tokyo for his contribution in fabricating the test apparatus, performing the experiments, and readjusting the data, and the research engineers of Mitsubishi Electric Co. for manufacturing the test apparatus.

Nomenclature

A	:	heat transfer area	Subscripts		
D	:	tube diameter	g	:	gas, vapor
G	:	mass flux	l	:	liquid
P	:	pressure	i	:	inlet
s	:	slip ratio	o	:	outlet
u	:	velocity			
V	:	volume			
x	:	quality			
α	:	void fraction			
ρ	:	density			

References

[1] F.Unezaki, E.Hihara, F.Matsuoka, and T.Saito, "Modeling of a heat pump cycle", Trans. JSME (B), 58, 556 (1992), 3760.

[2] T.Ueda, "Gas Liquid Two-Phase Flow", (1981) Yokendo.

[3] S.L.Smith, "Void Fractions in Two-Phase Flow: A Correlation Based upon an Equal Velocity Head Model", Proc.Instn.Mech.Engrs., 184, Pt 1. 36, (1969,70), 647.

[4] S.M.Zivi, Estimation of Steady-State Void-Fraction by Means of the Principle of Minimum Entropy Production", Trans.ASME, Ser.C, 86, (1964), 247.

[5] S.Levy, "Steam Slip-Theoretical Prediction from Momentum Model", Trans.ASME, Ser.C, 82, (1960), 113.

[6] S.G.Bankoff, "A Variable Density Single-Fluid Model for Two-Phase Flow with Particular Reference to Steam-Water Flow", Trans. ASME, Ser. C, 82, (1960), 265.

[7] J.R.S.Thom, "Prediction of Pressure Drop during Forced Circulation Boiling of Water",Int.J.Mass Transfer, 7, (1964), 709.

[8] N.Zuber, and J.Findlay, "Average Volumetric Concentration in Two-Phase Flow Systems",Trans. ASME, Ser C, 87, (1965), 453.

[9] A.E.Dukler, and Y.Taitel, "A Model for Predicting Flow Regime Transitions in Horizontal and Near Horizontal Gas-Liquid Flow", A.I.Ch.E. Journal 22, (1976), 47.

[10] T.Fukushima, and S.Miyamoto, "Analysis of Transient Behavior of a Vapor Compression Refrigeration Cycle", Trans. JAR, 2-2 (1985), 111.

[11] T. Fujii, H.Honda, and S.Nozu, "Condensation of Fluorocarbon Refrigerants inside a Horizontal Tube - Proposals of Semi-Empirical Expressions for the Local Heat Transfer Coefficient and the Interfacial Friction Factor - ", Refrigeration, 55-627 (1980), 3.

[12] S.Yoshida, K.Nishikawa, T.Matsunaga, and H.Nakada, "Heat Transfer to Refrigerant in Horizontal Tubes of Evaporator", Refrigeration,58-666(1983), 331.

[13] D.Chisholm, and A.D.K.Laird, "Two-Phase Flow in Rough Tubes", Trans. ASME, 80-2 (1958), 276.

[14] T.Yanagisawa, T.Shimizu, M.Fukuda, and K.Ikeda, "Mathematical Model of Variable Speed Refrigerant Compressor to Predict its Transient Behavior", Trans. JAR, 9-1, (1992), 65.

Appendix

Single phase region: Dittus-Boelter equation [2]

$$Nu = 0.023\ Re^{\,0.8} Pr^{\,0.4} \tag{19}$$

Two phase region: Fujii's equation [11] in condenser :

$$Nu = \mathrm{Max}\{Nu_F, Nu_B\} \tag{20}$$

Forced convection condensation region

$$Nu_F = 0.018 \left(Re_l \sqrt{\frac{\rho_l}{\rho_g}} \right)^{0.9} \left(\frac{x}{1-x} \right)^{0.1x+0.8} Pr_l^{\ \frac{1}{3}} \left(1 + \frac{AH}{Pr_l} \right) \tag{21}$$

$$A = 0.071 Re_l^{\ 0.1} \left(\frac{\rho_l}{\rho_g} \right)^{0.55} \left(\frac{x}{1-x} \right)^{0.2-0.1x} Pr_l^{\ \frac{1}{3}} \tag{22}$$

$$H = C_{pl} \frac{T_s - T_o}{L} \tag{23}$$

$$Re_l = 4W(1-x)/\pi d\mu_l \tag{24}$$

Volumetric convection condensation region

$$Nu_B = 0.725 \left(\frac{G_a Pr_l}{H} \right)^{\frac{1}{4}} \frac{(1 + 3 \times 10^{-3} \sqrt{Pr_l} C^{(3.1 - \frac{0.5}{Pr_l})})^{0.3}}{(1+DB)^{\frac{1}{4}}} \tag{25}$$

$$B = \frac{(1 + 1.6 \times 10^{11} (\frac{H}{Pr_L})^5)^{\frac{1}{4}}}{\sqrt{\frac{\rho_l}{\rho_g}}} \left(\frac{(G_a Pr_l / H)^{\frac{1}{4}}}{\overline{W}_l \left(\frac{x}{1-x} \right)} \right)^{1.8} \tag{26}$$

$$C = 0.47 \left(\frac{\rho_l}{\rho_g} \right)^{0.5} \left(\frac{H}{Pr_L} \right)^{\frac{1}{12}} \left(Re_L \frac{x}{1-x} \right)^{0.9} / \left(\frac{G_a Pr_l}{H} \right)^{\frac{1.1}{4}} \tag{27}$$

$$D = 20 \exp\left(-\frac{\overline{W}}{3000} \right) \tag{28}$$

Yoshida's Equation [12] : in evaporator

$$k/k_l = 3.7 \left[B_0 \times 10^4 + 0.23\ (B_0 \times 10^4)^{0.89} \left(\frac{1}{X_{tt}} \right)^{2.0} \right]^{0.44} \tag{29}$$

$$k_l = 0.023(\lambda_l / D) [\ G\ (1-x)\ D\ /\ (\mu_l)\ ]^{0.8} Pr_l^{\ 0.4} \tag{30}$$

Table I Geometry of heat exchange tubes

Tube	Inner diameter (mm)	Length (mm)
C1,C2,C4,C5	5.8	1450
C3	5.8	1090
E1,E2,E4,E5	8.12	1450
E3	8.12	1000
Sampling section	8.53	802

Table II Experimental conditions for void fraction measurements

Pressure (MPa) \ Mass flux (kg/m^2s)	311	246	182	158	125	92.7
1.45	o	o				
1.36	o	o				
1.20	o	o	o			
0.52					o	
0.386					o	o

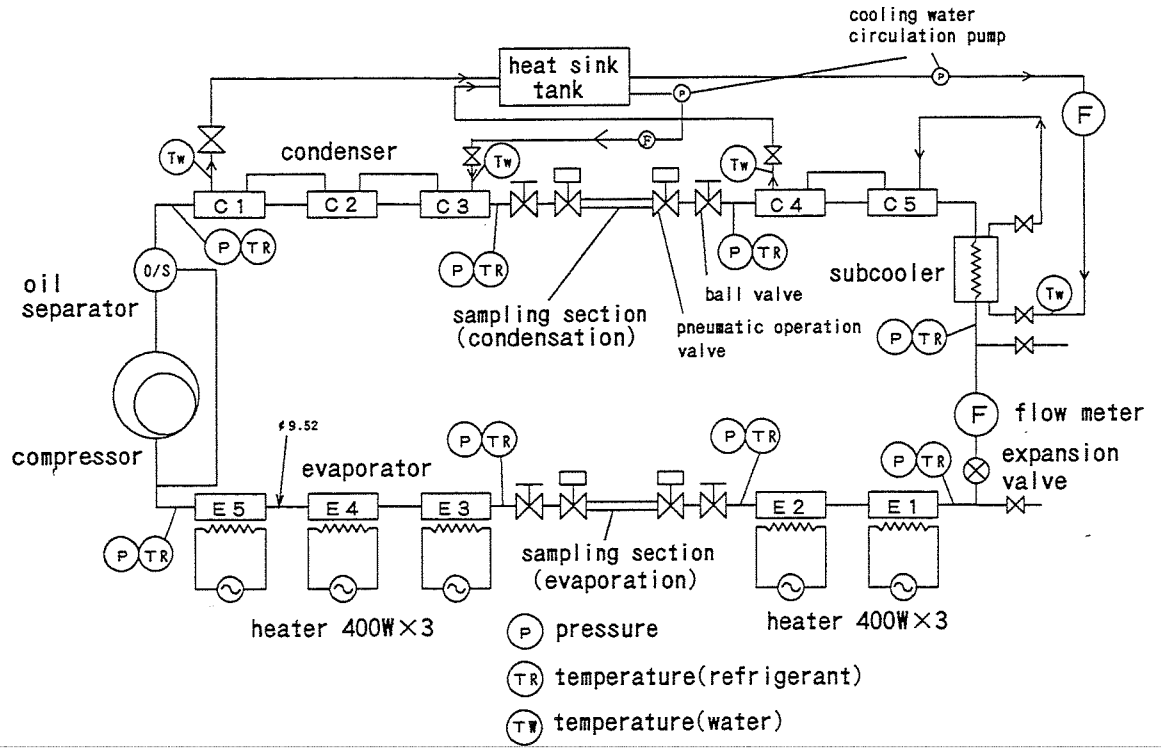

Fig. 1 Schematic diagram of the experimental apparatus for void fraction measurement

Table III Correlations of void fraction

Homogeneous flow model

$$\alpha = \frac{x}{x + (1-x)(\rho_g/\rho_l)} \tag{31}$$

Smith [3]

$$\alpha = \left[1 + \frac{\rho_g}{\rho_l} e \left(\frac{1}{x} - 1\right) + \frac{\rho_g}{\rho_l}(1-e)\left(\frac{1}{x} - 1\right)\left\{\frac{\rho_g/\rho_l + e(1/x-1)}{1+e(1/x-1)}\right\}^{\frac{1}{2}}\right]^{-1} \tag{32}$$

$$e = 0.4 \tag{33}$$

Zivi [4]

$$\alpha = \left[1 + \frac{\rho_g}{\rho_l} e \left(\frac{1}{x} - 1\right) + \left(\frac{\rho_g}{\rho_l}\right)^{\frac{2}{3}}(1-e)\left(\frac{1}{x} - 1\right)\left\{\frac{1+e(1/x-1)\rho_g/\rho_l}{1+e(1/x-1)}\right\}^{\frac{1}{2}}\right]^{-1} \tag{34}$$

$$e = 0.2 \tag{35}$$

Levy [5]

$$\frac{x^2}{\alpha} \cdot \frac{\rho_l}{\rho_g} + \frac{(1-x)^2}{(1-\alpha)^2} - \frac{1}{2} \cdot \frac{(1-x)^2}{(1-\alpha)^2} - \frac{1}{2} = 0 \tag{36}$$

Bankoff [6]

$$\alpha = K \frac{x}{x + (1-x)\rho_g/\rho_l} \tag{37}$$

$$K = 0.71 + 1.45 \cdot 10^{-8} p(atm) \tag{38}$$

Thom [7]

$$\alpha = \frac{\gamma x}{1 + x(\gamma - 1)} \tag{39}$$

$$\gamma = \frac{\rho_l/\rho_g}{s} \tag{40}$$

$$s = 0.93\left(\frac{\rho_l}{\rho_g}\right)^{0.11} + 0.07\left(\frac{\rho_l}{\rho_g}\right)^{0.561} \tag{41}$$

Zuber-Findlay [8]

$$<\alpha> = \frac{x/\{x + (1-x)\rho_g/\rho_l\}}{C_0 + V_{Gj}/\{x/\rho_g + (1-x)/\rho_l\}G} \tag{42}$$

$$C_0 = 1.13 \tag{43}$$

$$V_{Gj} = \sqrt{2}\left[\frac{\sigma(\rho_l - \rho_g)}{\rho_l{}^2}\right]^{\frac{1}{4}} \tag{44}$$

Taitel-Dukler [9]

$$\tau_{wg}\frac{S_g}{A_g} - \tau_{wl}\frac{S_l}{A_l} + \tau_i S_i\left(\frac{1}{A_l} + \frac{1}{A_g}\right) + (\rho_l - \rho_g)g\sin\theta = 0 \tag{45}$$

Table IV Experimental conditions for refrigerating cycle analysis

air temperature	condenser	35 ℃*, 24 ℃**
	evaporator	27 ℃*, 19 ℃**
air flow rate	condenser	28.0 m^3/min
	evaporator	7.2 m^3/min
compressor speed		88Hz
superheat in evaporator		5 ℃
subcooling in condenser		5 ℃

* dry-bulb temperature ** wet-bulb temperature

Table V Refrigerant mass in condenser and evaporator

	Smith		Zivi	
	condenser	evaporator	condenser	evaporator
case1	484.4g	100.3g	452.8g	75.8g
case2	619.1g	106.0g	590.9g	81.1g

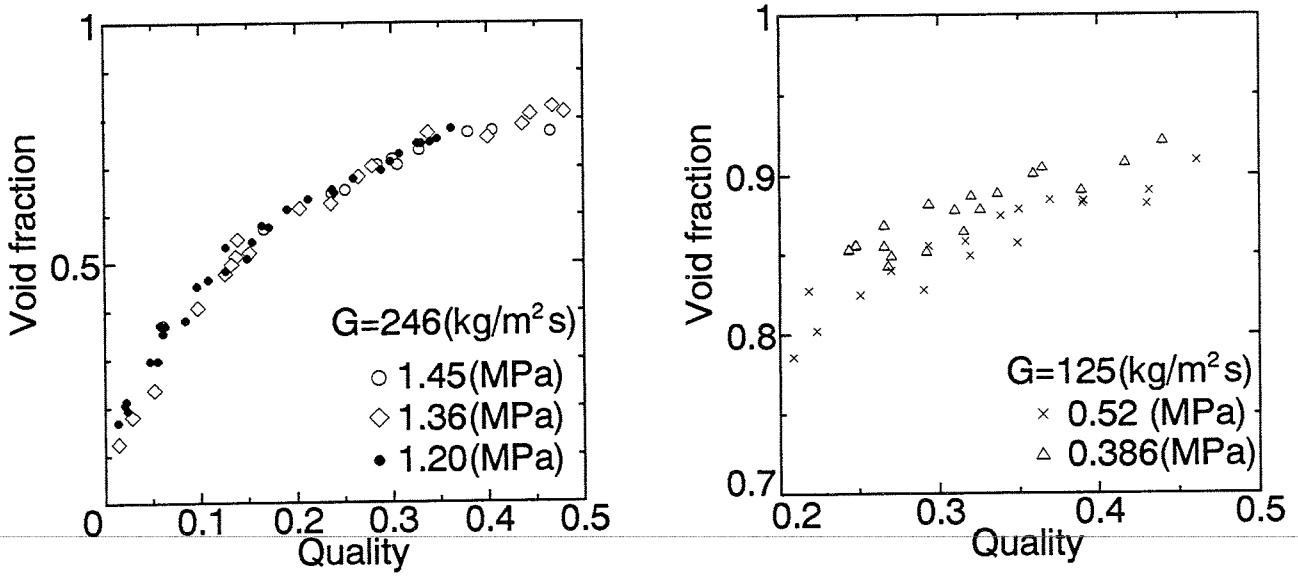

Fig.2 Void fraction versus quality for :
(a) G=246 kg/m^2s (condenser) (b) G=125 kg/m^2s (evaporator)

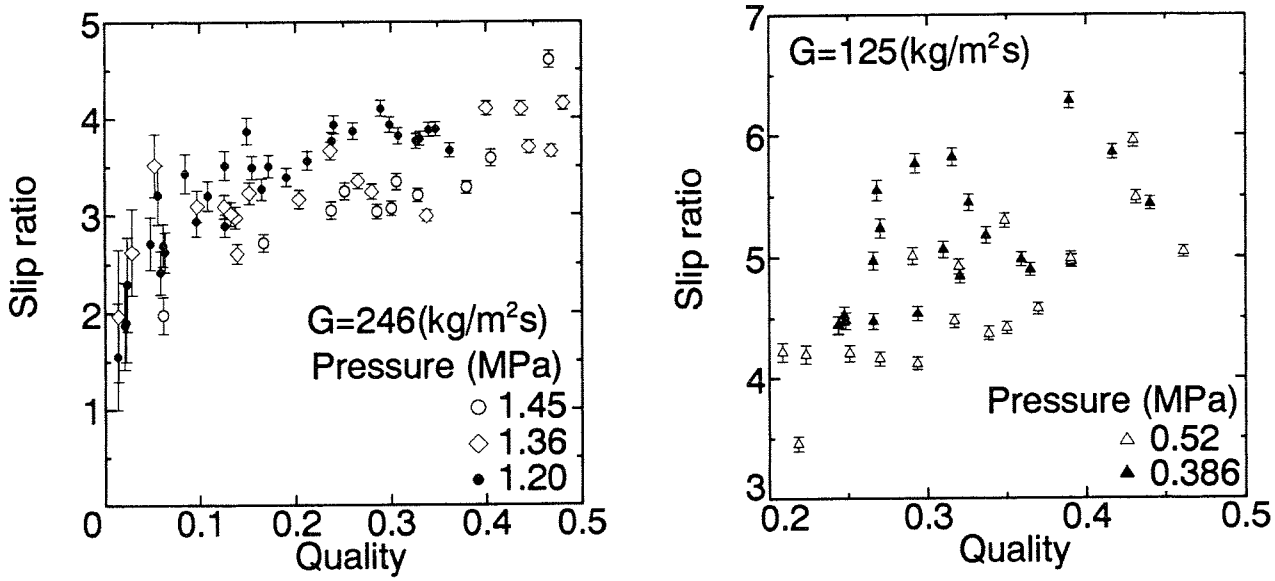

Fig.3 Slip ratio versus quality for :
(a) G=246 kg/m^{2}s (condenser) (b) G=125 kg/m^{2}s (evaporator)

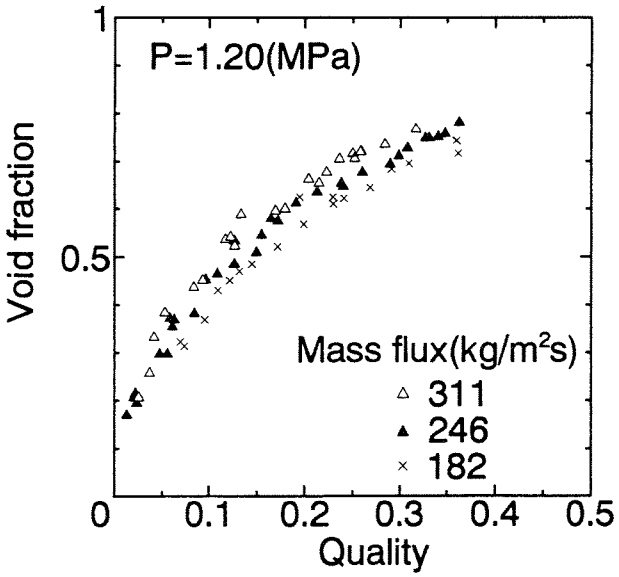

Fig.4 Void fraction versus quality at P=1.20 MPa

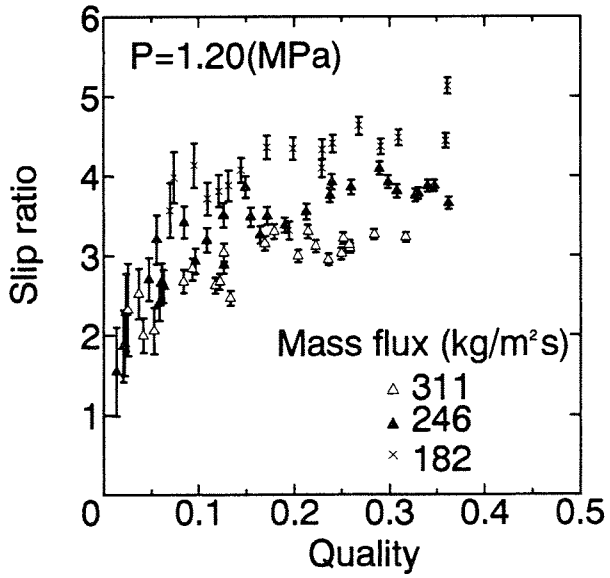

Fig.5 Slip ratio versus quality at P=1.20 MPa

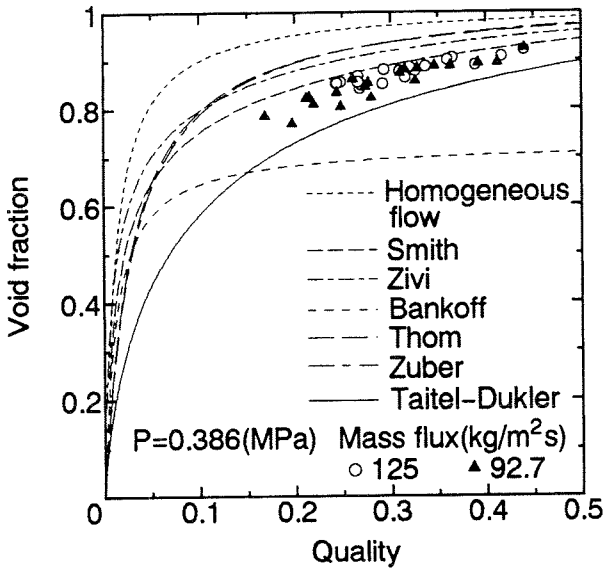

Fig.6 Comparison between the present data and the existing correlations for void fraction

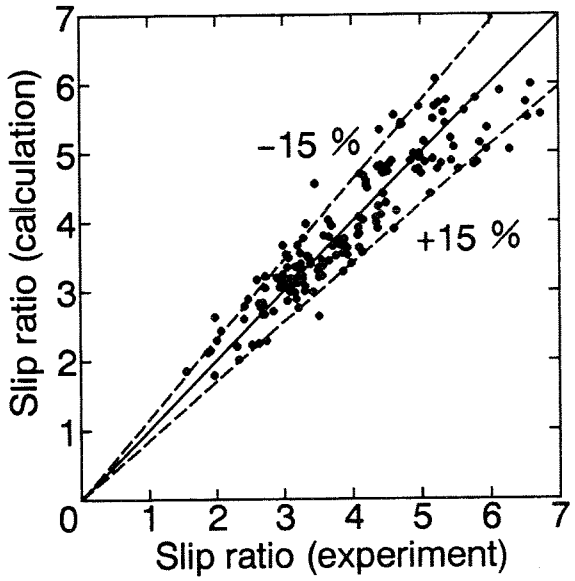

Fig.7 Comparison of Eq.(3) with the experimental data

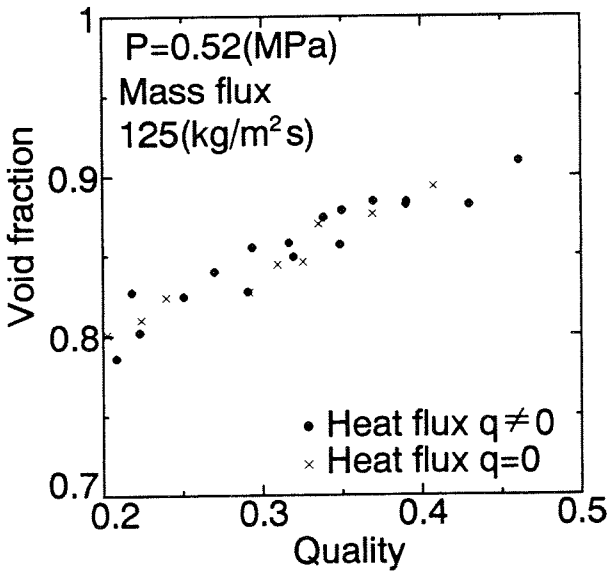

Fig.8 Effect of heat flux on void fraction

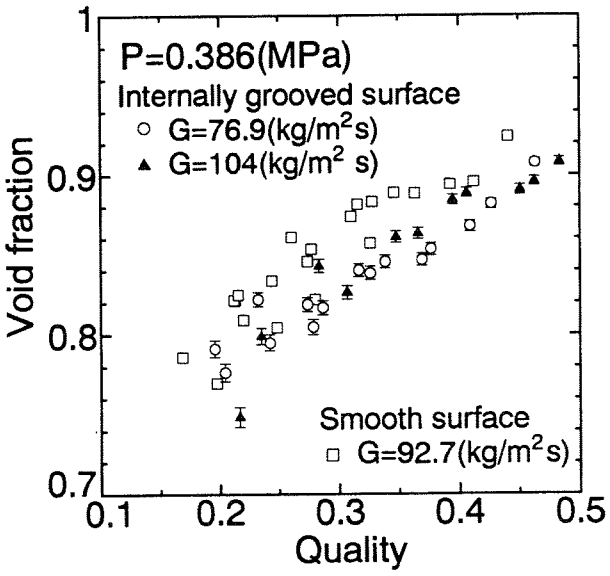

Fig.9 Effect of wall surface configuration on void fraction

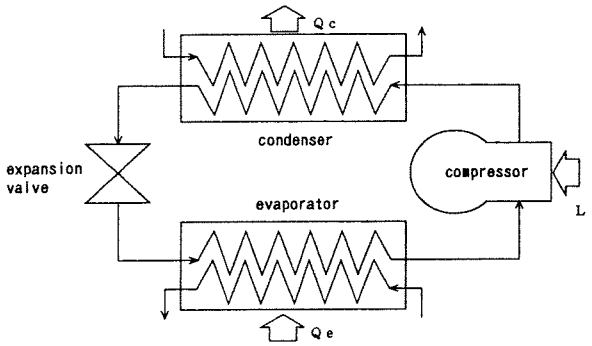

Fig.10 Refrigeration cycle

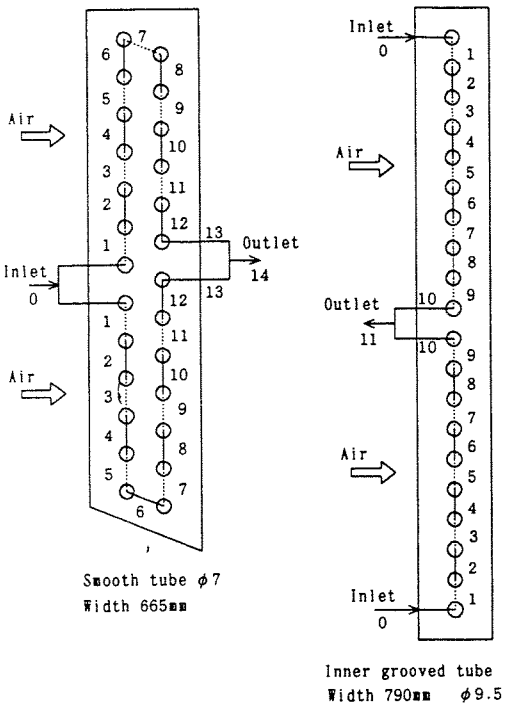

Fig.11 Condenser and evaporator

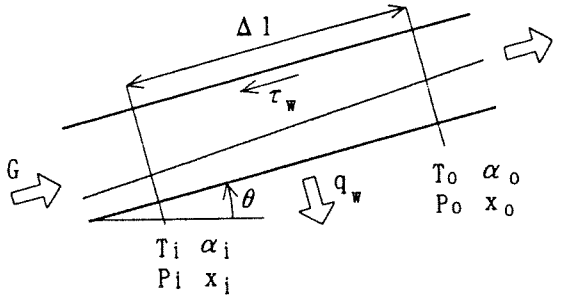

Fig.12 Heat exchanger model

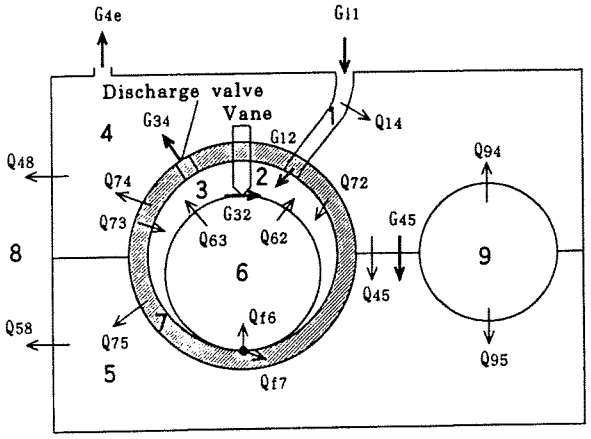

1:Suction tube
2:Suction room
3:Compression room
4:Gas in shell
5:Oil
6:Rotor
7:Cylinder
8:Ambient
9:Motor

Fig.13 Compressor model

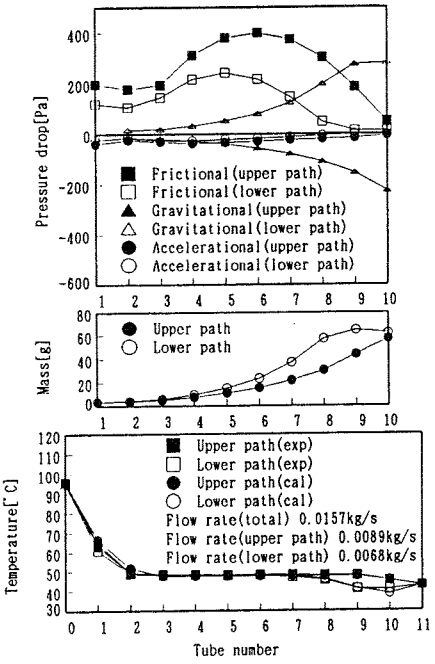

Fig.14 Distributions of present drop, refrigerant mass, and temperature in condenser at a compressor speed of 88 Hz

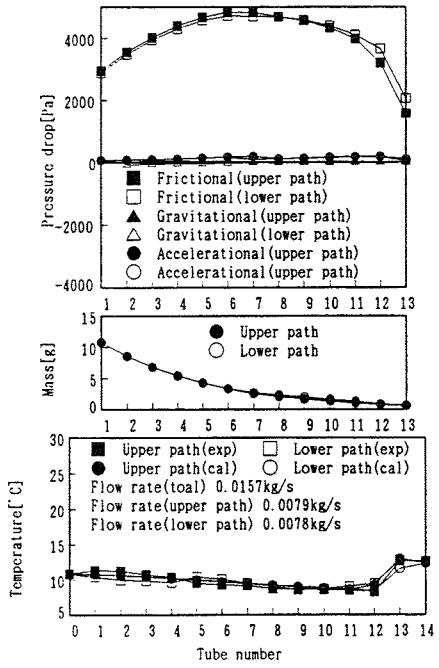

Fig.15 Distributions of present drop, refrigerant mass, and temperature in evaporator at a compressor speed of 88 Hz

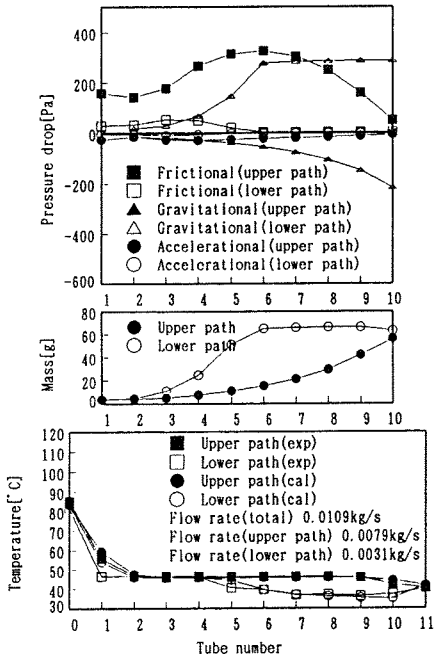

Fig.16 Distributions of present drop, refrigerant mass, and temperature in condenser at a compressor speed of 52 Hz

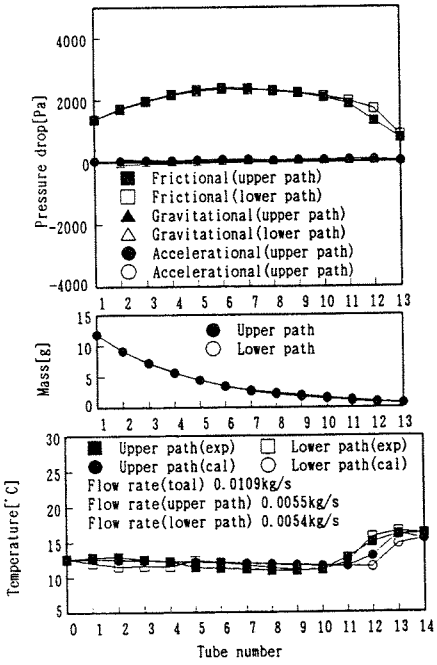

Fig. 17 Distributions of present drop, refrigerant mass, and temperature in evaporator at a compressor speed of 52 Hz

FLOW VISUALIZATION FOR STEAM/HELIUM/SPRAY WATER INJECTION INTO MODEL CONTAINMENT

Tadashi Hirose[1], Mark Rodgers[2]

[1]Systems Safety Department
Nuclear Power Engineering Corporation
Fujita Kanko Toranamon Building (5F)
Minato-ku, Tokyo 105, Japan
Telephone: (03) 5470-5461, Facsimile: (03) 5470-5466

[2]Computer Software Development Co., Ltd.
Mitsubishi-Juko Shinjuku Building (4F)
15-1 Tomihisa cho
Shinjuku-ku, Tokyo 162, Japan
Telephone: (03) 3225-6455, Facsimile: (03) 3225-7145

ABSTRACT

The NUclear Power Engineering Corporation (NUPEC) was established in March 1976 with the support of the Ministry of International Trade and Industry (MITI) and is involved in the safety analyses of severe accidents in Japan's Light Water Reactors. Among NUPEC's many projects is a MITI sponsored investigation into the integrity of a containment vessel under various accident scenarios. This study includes experiments investigating the mixing and distribution phenomena of hydrogen within the containment vessel.
During the experiment, steam and a light gas (helium) are injected into a 1/4th scale model PWR containment for 30 minutes. The cooling spray is also active during some of the experiments. Parameter measurements are taken and these results have been visualized.
In this presentation, we describe NUPEC 's hydrogen mixing and distribution experiments and outline the results of two of these tests. A short description of computer code models for such large scale tests is also given. Furthermore, a visualization of these tests is described, emphasizing the importance of considering visualization as an integral part of scientific analysis. Hardware and software requirements are discussed and references to visualizations created by NUPEC will be made. A video presentation will be shown which will include material used in the OECD's International Standard Problem ISP-35 workshop.

1. INTRODUCTION

NUPEC was established in March 1976 with the support of the MITI and is involved in the on-going safety analyses of severe accidents in Japan's Light Water Reactors. Among NUPEC's many projects is a MITI sponsored investigation, evaluating the integrity of a containment vessel under various accident scenarios. Post-Three Mile Island investigations have shown the importance of evaluating the hydrogen distribution processes within a containment. The "Hydrogen Mixing and Distribution Test"[1] is one part of this project and has provided valuable experimental data on the phenomena of hydrogen mixing within a containment.

As part of its role in fostering international co-operation in the area of nuclear safety, the OECD sponsors projects referred to as "International Standard Problems" or ISPs. In 1992, NUPEC proposed one of its hydrogen mixing and distribution experiments (the M-7-1 test) to the OECD and this was accepted as ISP-35. 13 organizations from 10 countries took part in this code validation exercise. As part of this ISP project, NUPEC decided to visualize the results of its tests.

This paper gives a description of NUPEC's hydrogen mixing and distribution experiments, outlining some of the results of these tests. In particular the M-7-1 test, a steam/helium/spray water mixing problem is detailed. Computer code models for such tests are described. The issue of data visualization as an analy-

sis tool is addressed. An outline of the visualization process is described, identifying techniques as well as detailing hardware and software requirements.

2. DESCRIPTION OF THE TEST FACILITY

NUPEC's test facility, located at the Tadotsu Engineering Laboratory in the south of Japan, consists of a 1/4th linearly scaled, steel containment with multiple compartments representing the rooms of an actual dry-type, 4-loop PWR plant. The model containment has a free volume of 1300m^3 with an internal diameter of 10.8m and an internal height of 19.4 m. Fig.1 shows a flow diagram for the test facility.

The containment wall is made of 12mm thick non-painted steel. The outside of the containment wall is insulated from the atmosphere. Each of the 3 floors inside the containment is also 12mm thick, the walls are mostly 4.5mm. Fig. 2 shows the layout of the compartments within the containment. A computer generated model of these compartments is also shown in Fig. 3.

During the tests, a heated steam /helium (used to simulate hydrogen to prevent accidental ignitions) mixture is injected into the containment over the 30 minute test period. A sophisticated instrumentation system measures the transient helium gas concentration and gas temperature in each compartment. The system pressure was also measured as well as wall temperatures at over 200 locations. Gas velocity measurements were not possible in a wet environment.

3. DESCRIPTION OF THE EXPERIMENTS

An extensive test program was conducted in the NUPEC facility, injecting varied rates of steam and helium into the containment. Some of the tests also involved the dome spray, used to simulate the cooling system of the containment. All injection rates were determined using either volumetric or area scaling ratios of actual plant values. The test matrix covered a wide spectrum of H_2-distribution scenarios, as shown in Table I.

Data on the thermal-hydraulic phenomena of multi-phase flow in the form of steam/helium/spray water in a large scale test facility was recorded over a 2 hour period. As this study was primarily parameter based, it was useful in providing an extensive set of experimental data for computer code validation.

Fig. 4 shows the injection rates for two of these tests. The top figure shows the injection rates for the M-4-3 test. The bottom two figures show the M-7-1 test injection rates. The cooling spray was active during the M-7-1 test. Table II gives the operating conditions for both tests.

During ISP-35, the M-4-3 test was used by participants as an open test to calibrate their computer models. The test results were distributed to participants to allow them to compare their simulated results with the experimental data before starting the "blind" M-7-1 exercise.

4. OUTLINE OF TEST RESULTS

Pressure, helium concentration and gas temperature time histories for the M-7-1 test are shown in Fig. 5. In the case of helium concentration and gas temperature, each figure shows the time history for all 25 compartments in one graph. This method allows an immediate identification of the compartment with maximum temperature/concentration and the time at which it occurs. Some of the graphs are labeled with compartment numbers. One drawback of this method is that there is no indication of the relative location of compartments in 3-D space.

By evaluating the helium concentration time histories in Fig.5, it is clear that a main flow path exists through compartments 8, 15 & 21. This flow path includes the injection compartment (8) and the 2 compartments directly above it. The mixing effect of the spray creates a well mixed environment within the containment. Comparing the helium concentration figures to those of the M-4-3 test, shown in Fig. 6, the strong mixing effect of the spray is clearly visible. The range of concentrations within the containment at any time is much narrower for the M-7-1 test than the M-4-3 test.

The pressure plots are also shown in Figs. 5 & 6. These plots show the efficiency of a spray in reducing the pressure within a containment. The cooling spray can clearly be seen to be the dominant effect for the M-7-1 test. The falling pressure is also reflected in the temperature plots. Both these phenomena can be clearly seen in NUPEC's visualizations.

Also noticeable from the M-7-1 test results is the fact that after 35 minutes, there is a very well mixed condition within the containment. This again is due to the mixing of the spray water.

Gas temperatures are seen to fall steadily for the M-7-1 test, as shown in the lower plot of Fig. 5. Again a well mixed environment inside the containment can be seen.

Although these graphs give a full time history of the helium concentration and gas temperatures, there is

no indication as to the flow patterns that led to these thermal-hydraulic states.

In summary, the results of these tests have provided valuable data on the thermal-hydraulic phenomena within a containment vessel for steam/helium/spray water injection. The data has allowed researchers to confirm that natural convection, steam release and cooling water spray affect the hydrogen. It has also aided researchers in identifying main flow paths and distribution patterns, essential for understanding and application to large scale facilities. Finally, data has been provided to allow verification of computer codes used for prediction of hydrogen mixing and distribution problems.

A short description of the modeling methods used in these codes now follows.

5. MODELING THE TEST FACILITY

In the computer modeling of this problem, each of the 25 compartments in the test facility corresponds to 1 control volume. Most of these control volumes correspond to physical compartments of the facility but in some cases, large volumes were divided-up for convenience. The flow paths were modeled and user-defined values were assigned to the loss coefficients. Boundary and initial conditions were also defined.

5.1 Modeling Hydrogen Mixing Problems

Modeling of hydrogen mixing problems in irregular shaped test facilities is possible with the use of modern thermal-hydraulics computer codes. Currently, two general approaches for modeling the mixing process are used[2] : lumped-parameter models, where specified volumes (called control volumes) are assumed to be well mixed and field models where equations of motion and transport are solved for incremental regions of flow.

To analyze large scale experiments such as NUPEC's test facility, lumped-parameter codes such as MELCOR, CONTAIN or MAPHY-BURN are typically used in Japan since they greatly reduce the computer time required to solve problems. These models assume that specified control volumes are well-mixed. These volumes usually correspond to the compartments within the containment although sometimes two or more compartments are lumped together.

Flow between compartments is usually modeled by 1-D equations for flow. These flows are regulated by user defined parameters called "flow loss coefficients". The equations for mass, energy and momentum balance are solved for each of the constituents in each compartment[3].

To ensure both user experience and modeling assumptions are reliable when using lumped-parameter models, code validation with experimental data is important. Thus the blind ISP-35 test was a good opportunity for participants to test their codes and modeling experience against NUPEC'S data.

6. VISUALIZATION

Visualization of data is an essential part in many of today's scientific fields. It is a process that often allows scientists/researchers to see data that is not obvious through standard analysis techniques. Modern technology allows man to conduct experiments and research which is far more complicated than most people can conceive. Visualization allows us to bring this information back to a reference frame that we all understand: 2-D or 3-D colour images.

The following requirements were considered essential for an effective visualization: Firstly, a 3-D model of the test facility was required to enable the viewer to picture the layout of the facility. Secondly, a view of the main thermal-hydraulic parameters in each compartment was needed. Finally, it was necessary to show how these parameters changed over time, allowing the mixing and distribution patterns to be identified.

Having identified these requirements, the next stage was to consider the data for visualization.

6.1. Creating the Visualization

NUPEC's visualization process involved combining the multi-phase data from the mixing and distribution tests with a 3-D model of the test facility. Fig. 7 shows a flow diagram for the overall visualization process.

6.2. Data Selection for Visualization

The selection of data for visualization can be considered as a 2 phase process. Phase one involved a comprehensive analysis of the experiment. The complex distribution patterns involved in injecting a heated

steam–helium mixture into a relatively large vessel needed to be understood. Phase two involved selecting suitable parameters that fully described these phenomena.

We considered the essence of visualizing data as presenting data in a manner that imparts maximum information to the viewer. Pretty pictures are of no value to researchers if they don't focus on advancing his understanding. By only showing one parameter (e.g. helium concentration, gas temperature) for each compartment at a time, we could describe the phenomena of multi–phase flow and at the same time, the viewer would not be confused by an excess of information.

7. HARDWARE & SOFTWARE REQUIREMENTS

To model large quantities of data a powerful computer with a special board called a graphics accelerator is required. A software package that converts numerical data into images is also required. For this purpose, NUPEC used an Iris Crimson VGXT from Silicon Graphics Inc. This 64–bit workstation has a "Reality Engine" capable of rendering 180,000 polygons per second. This will produce real–time, photo–realistic graphics. While using this high–powered graphics workstation, NUPEC found itself using its maximum capabilities on numerous occasions.

The graphics accelerator of the Iris Crimson allows large amounts of data to be rapidly displayed on the screen. To view NUPEC's visualizations it was necessary to run animations to represent the 30 minute time histories of the main thermal–hydraulic parameters. The hardware of the Iris Crimson was capable of showing these animations in real time. If a slower computer had been used, a typical scenario could have taken up to 1000 times longer to record.

The "Application Visualization System"[4] (AVS) developed by AVS Inc. (Waltham, MA) is a software package which allows researchers to construct their own visualization applications without requiring specialized programming expertise. By connecting software components, called modules, into a flow network, numerical data can be converted into graphic images. The modules are in fact specific functions used to represent sets of data as velocity field arrows, particles or simple colours. Once data has been read into the network, a 3–D geometry representation of the data is produced, which can then be rotated, scaled or coloured as required.

8. CREATING THE GEOMETRIC MODEL

One feature of lumped–parameter models is that there is often no geometric correspondence between the actual facility and the computer model. Consequently, the geometric model of NUPEC's test facility had to be created using a standard FEM mesh generator. Using the graphical user interface, geometric data from the engineering drawings of the test facility could be entered into the package with a mouse, rather like a CAD system.

There are 2 main ways to create geometric models:

1. A solid model consisting of small cubes or hexahedra which fit together to make up the structure
2. A surface model consisting of flat planes that "cover" the surface of the structure.

It was decided to construct a solid model, although a surface model could just as easily have been used. Each compartment of the facility was created separately. The files containing the coordinates of each compartment were then merged into one large file containing data for the whole test facility.

Using an interface programme, the nodal and connectivity data was converted to an AVS compatible format. Fig. 3 shows such an example of a computer generated model of the inside of the containment vessel.

9. VISUALIZING TECHNIQUES

One frequently used technique for visualizing data is called "colourizing". Instead of representing data as numbers, the data is translated into a number that represents a colour. Displaying high temperatures in red and low temperatures in blue is an example of colourizing.

This technique was used in creating NUPEC's visualizations. Simple to understand, it allows large quantities of process data to be represented as a pattern of colours.

Since the quantity of NUPEC's data to be viewed was large, different scenarios of the same data set were created. This involved such techniques as only displaying part of the full model, thus enabling the viewer to examine particular regions of interest. Another method is to rotate the view point, thus showing the same data from a different perspective. This has been found to be an effective way to reshow data.

9.1. Visualizing the M-7-1 Test Data

To visualize the helium data, each compartment of the containment was assigned a colour to represent its concentration. Using a colour scale ranging from red (indicating high concentration) to blue (indicating low concentration), the actual concentration could be evaluated. As time passed, the injection process caused the concentration of helium gas in the compartments to increase, thus the colour assigned to each compartment would change from blue to red. A suitable colourbar was developed as a legend allowing the full range of concentrations to be assigned numerical values.

As can be expected, the release compartment could be seen to change colour first. The mixing and distribution process of the helium gas within the containment could clearly be seen. Fig. 8 and Fig. 9 show the helium concentration in the lower part of the containment. The distribution of helium gas in this region can easily be identified.

A similar scenario was used to visualize the gas temperature in each room. Again the convection effects of injecting heated gases could clearly be seen. The visualization, in effect, showed what a video camera might have recorded if the gases were to be seen. Fig. 10 shows a visualization of the gas temperatures throughout the containment. The cooling effect of the dome spray is clearly visible.

The cooling spray droplets were represented as small moving particles. These particles were released from the top of the dome and had a significant cooling effect on the injected gases. The AVSFLOW package was used to model these moving particles.

In order to visualize the coupled effects of a steam-helium mixture, another scenario was developed with the helium gas represented as small particles. The number of particles in any compartment indicated the gas concentration with the gas temperature represented by the colour of the particles. As release proceeded, the particles could be seen filling the compartments. The cooling effects of the spray could be seen as the particles changed colour from red to blue. Fig. 11 shows an example of this visualization. The differences in particle density and colour indicate the relative concentrations and temperatures in each compartment.

To show a time history of the data, an animation looping over the full set of data was created. The graphics hardware of the Iris Crimson was powerful enough to run this series of time histories as a smooth animation. This animation was recorded to video-tape for later playback.

10. ANALYSIS OF THE TEST DATA

NUPEC's visualization was used to effectively analyze many aspects of the M-7-1 test. Watching the visualization, the heated steam-helium mixture could be seen to rise in a vertical column from the injection point towards the dome. The mixing and distribution patterns could be identified by tracing the progress of the helium gas. With conventional analytical techniques, identifying flow paths could involve searching through many sets of graphs whereas with data visualization, it was easy to watch the advance of the "red front" of high concentrations.

The visualization highlighted the flow patterns inside the containment. By following colour changes, the mixing and distribution effects could be clearly identified. The exact location and time of maximum concentrations could be identified by searching for the red colored regions. Branches and dead-ends could be quickly identified.

NUPEC's visualization was shown in video form at the 2nd Workshop for ISP-35 in Nov. 1993 in Tokyo. The impressions of the participants confirmed the benefits in visualizing the data. As well as showing the thermal-hydraulic phenomena of hydrogen mixing and distribution, many points for discussion were resolved by referring to the visualized data; comparing overlay plots and checking figures could have taken days longer.

As a method of comparing simulated results to experimental data, the visualization was most useful. Each participant's data set could be compared to the test data for all 25 compartments at one time. This considerably reduced the time required to compare the data sets. Differences between the 2 data sets were instantaneously recognizable.

Once the visualization has been created, it is a simple process to interchange the simulated data with experimental data. By running one visualization for the simulated data alongside a visualization for the experimental data it would be possible to compare analytical and experimental results. It would also be possible to view steam concentration results extracted from a computer simulation. These results, although not available from the test, could be examined using visualization techniques.

11. CONCLUSIONS

NUPEC has successfully conducted a series of hydrogen mixing and distribution experiments in a 1/4

scale model of a PWR containment. During the experiments, a heated steam/helium mixture was injected into the lower region of the containment. The cooling spray was also active. The thermal-hydraulic phenomena in this multi-phase flow experiment were recorded and analyzed.

During the analysis stage, NUPEC found scientific visualization to be a very effective tool in identifying the phenomena involved in a steam/helium/spray water environment. During the ISP35 project, the visualization allowed participants to "watch" the M-7-1 test and to quickly compare their own code results with the actual test data. This led to a greater understanding of the project.

Rather than include all parameters in the same scenarios, NUPEC visualized parameters separately. While this could be regarded as not showing the actual conditions within the containment, a more important objective of visualization is to impart as much knowledge as possible to the viewer. This technique is to be recommended in all visualizations.

The success of this visualization has confirmed NUPEC's beliefs that scientific visualization needs to be considered as an integral part of any analysis project. It is important to use a high level of skill during the visualization process, to ensure an accurate analysis.

NUPEC is now planning to extend the use of its visualizing techniques to other areas of research. In the near future, virtual reality and parallel processing machines will be introduced to further enhance the visualization capabilities of its' researchers.

REFERENCES

[1] K.Takumi, A.Nonaka, S.Moriya and J.Ogata: "Proving Test on the Reliability for Reactor Containment Vessel Part (1) Hydrogen Mixing and Distribution Test", Hydrogen Behavior in Water Cooled Nuclear Power Reactors, edited E.Della Logia. (CEC), ISSN1018-5593.

[2] Committee on Hydrogen Combustion: "Technical Aspects of Hydrogen Control and Combustion in Severe Light-Water Reactor Accidents," National Academy Press, Washington.D.C., 1987.

[3] IAEA/CEC Joint State of the Art Report: "Hydrogen in Water-Cooled Nuclear Power Plants," Vienna, Austria, December, 1990.

[4] AVS User's Guide, Release 4, Advanced Visual Systems Inc., 300 Fifth Ave., Waltham, MA 02154, USA.,May 1992

Table I Test Matrix

M-1 Series	Natural Circulation
M-2 Series	Helium Mixing & Distribution Test
M-3 Series	Confirmation Test of Steam Injection Effect
M-4 Series	**Helium Mixing & Distribution Test with Steam**
M-5 Series	Helium Mixing & Distribution Test with CV Spray
M-6 Series	Confirmation Test of Steam/CV Spray Injection Effect
M-7 Series	**Helium Mixing & Distribution Test with Steam & CV Spray**
M-8 Series	Upper Break Test
M-9 Series	Confirmation Test for Validity of Measurement Points

TABLE II Operating Conditions for NUPEC's Tests

Initial Conditions	M-7-1	M-4-3
C/V Dome Pressure	139.8 kPa	101.3kPa
C/V Dome Temperature	67.3°C	6.6°C
C/V Humidity	100%	100%
Outer Ambient Temperature	11°C	11°C
Operating Conditions		
Gas Mixture Temperature	115°C	115°C
Spray Supply Temperature	40 °C	None
Duration of Injection	30 min.	30 min.
Location of Injection	Comp. #8	Comp. #8

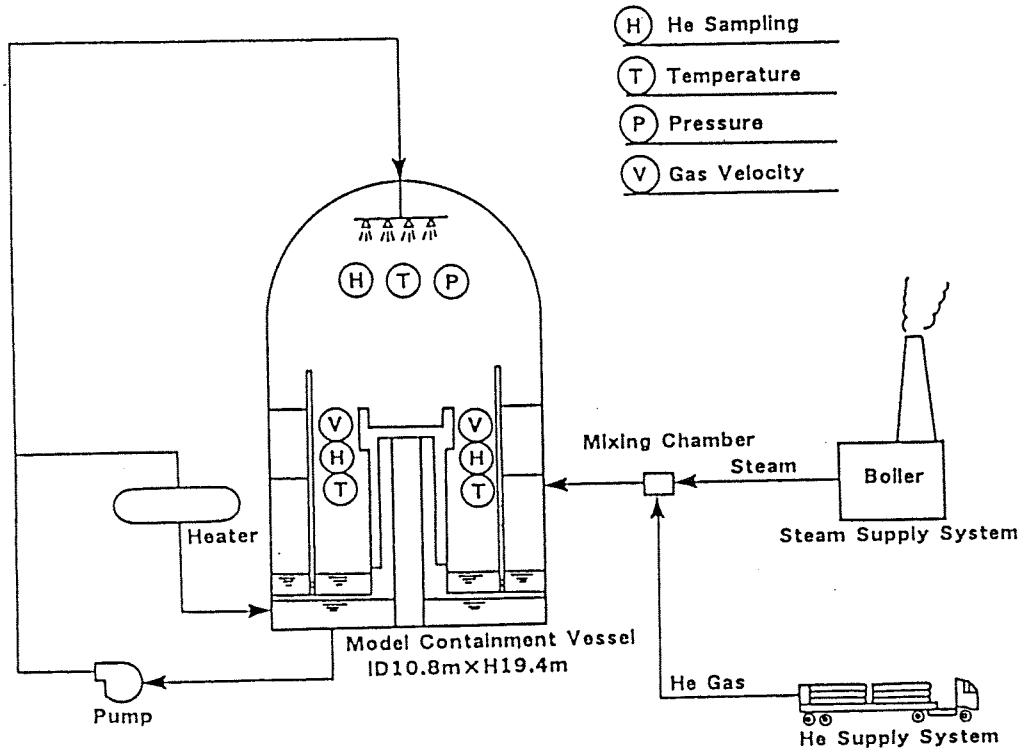

Fig. 1 Flow Diagram for Test Facility

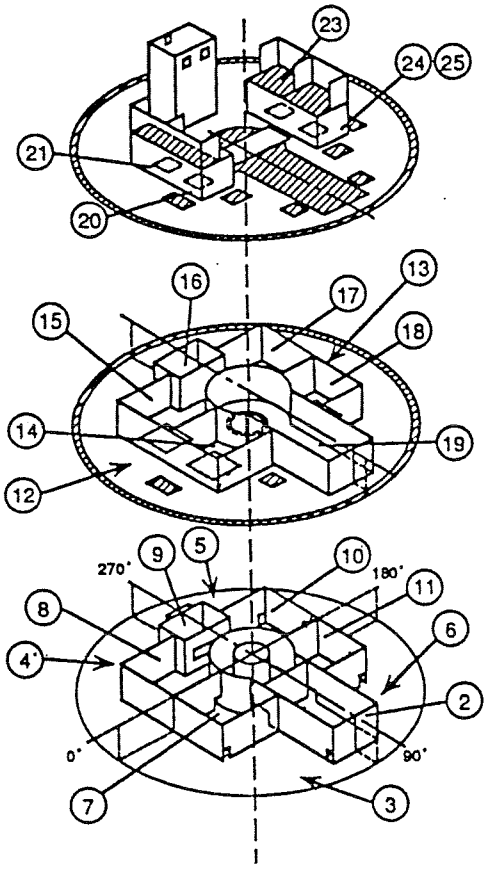

Fig. 2 Layout of Compartments

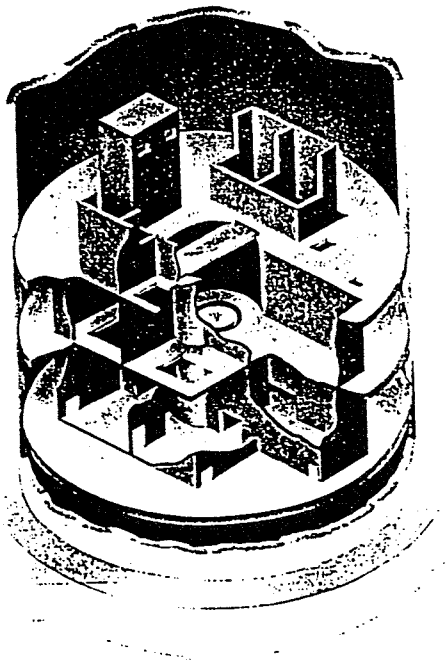

Fig. 3 Computer Model of Test Facility

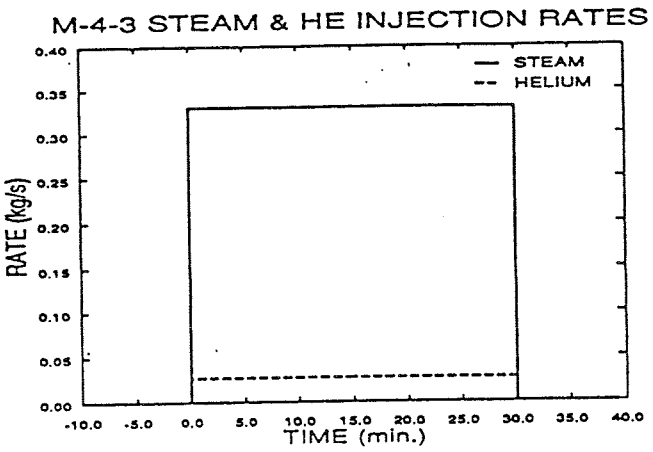

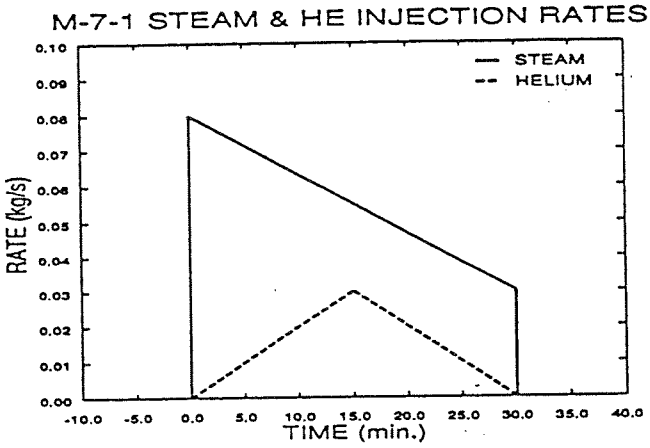

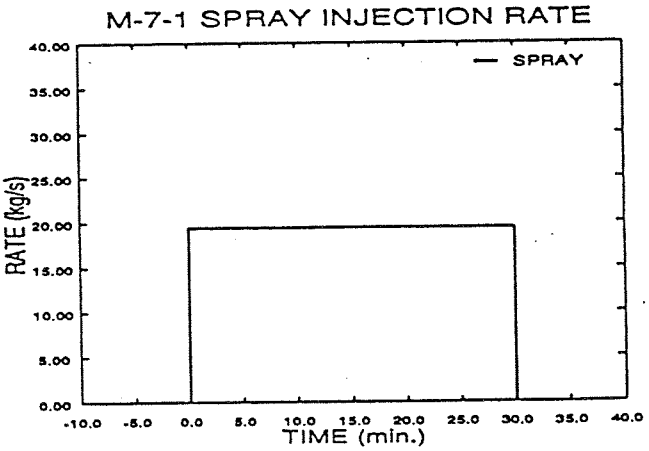

Fig. 4 Injection Rates

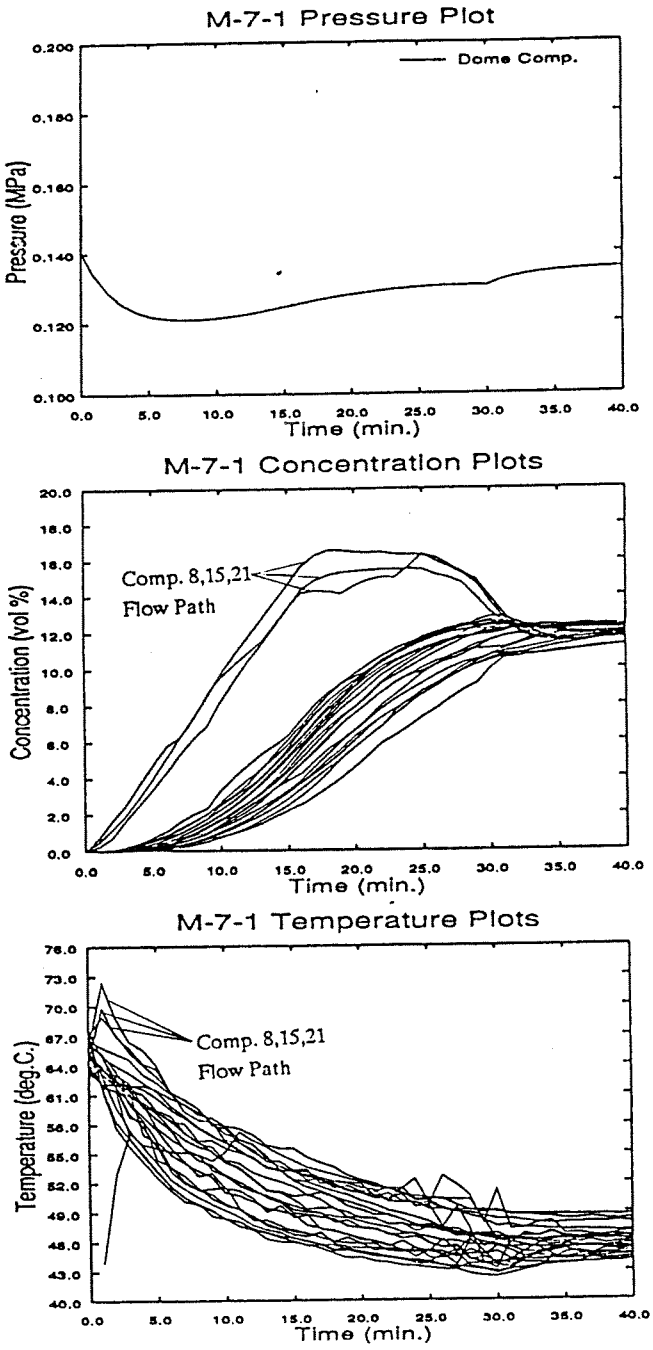

Fig. 5 M-7-1 Test Results

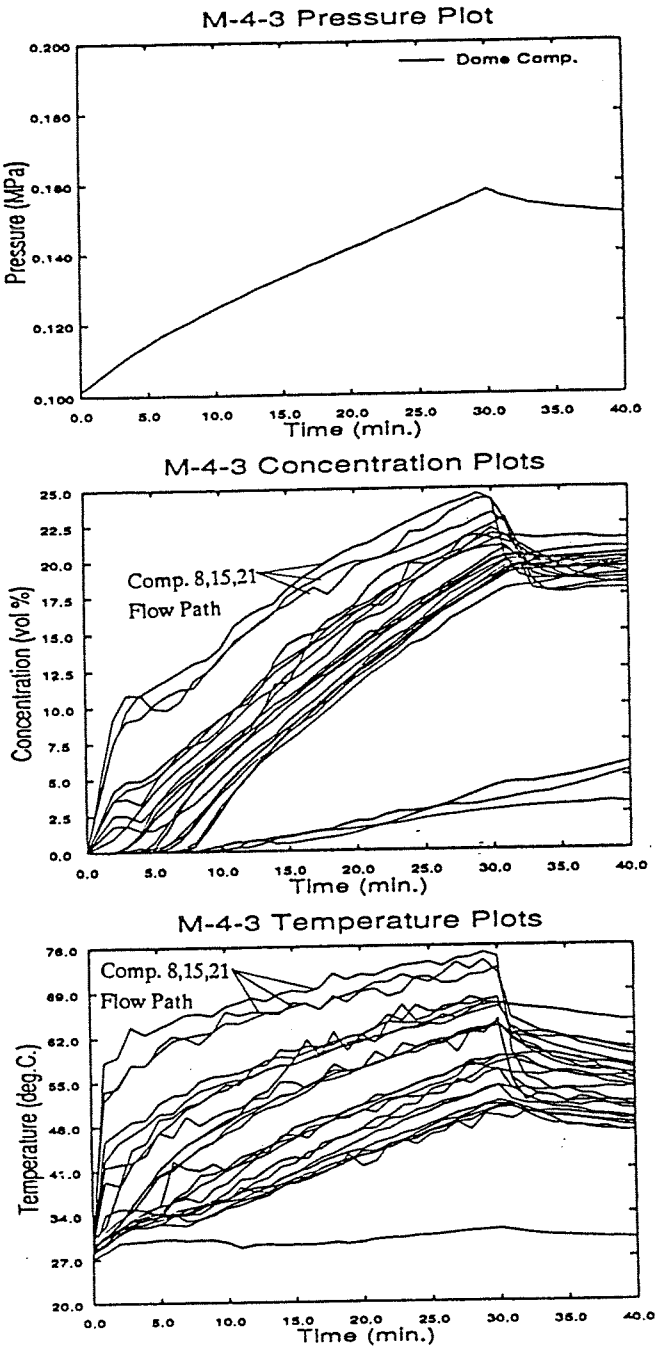

Fig. 6 M-4-3 Test Results

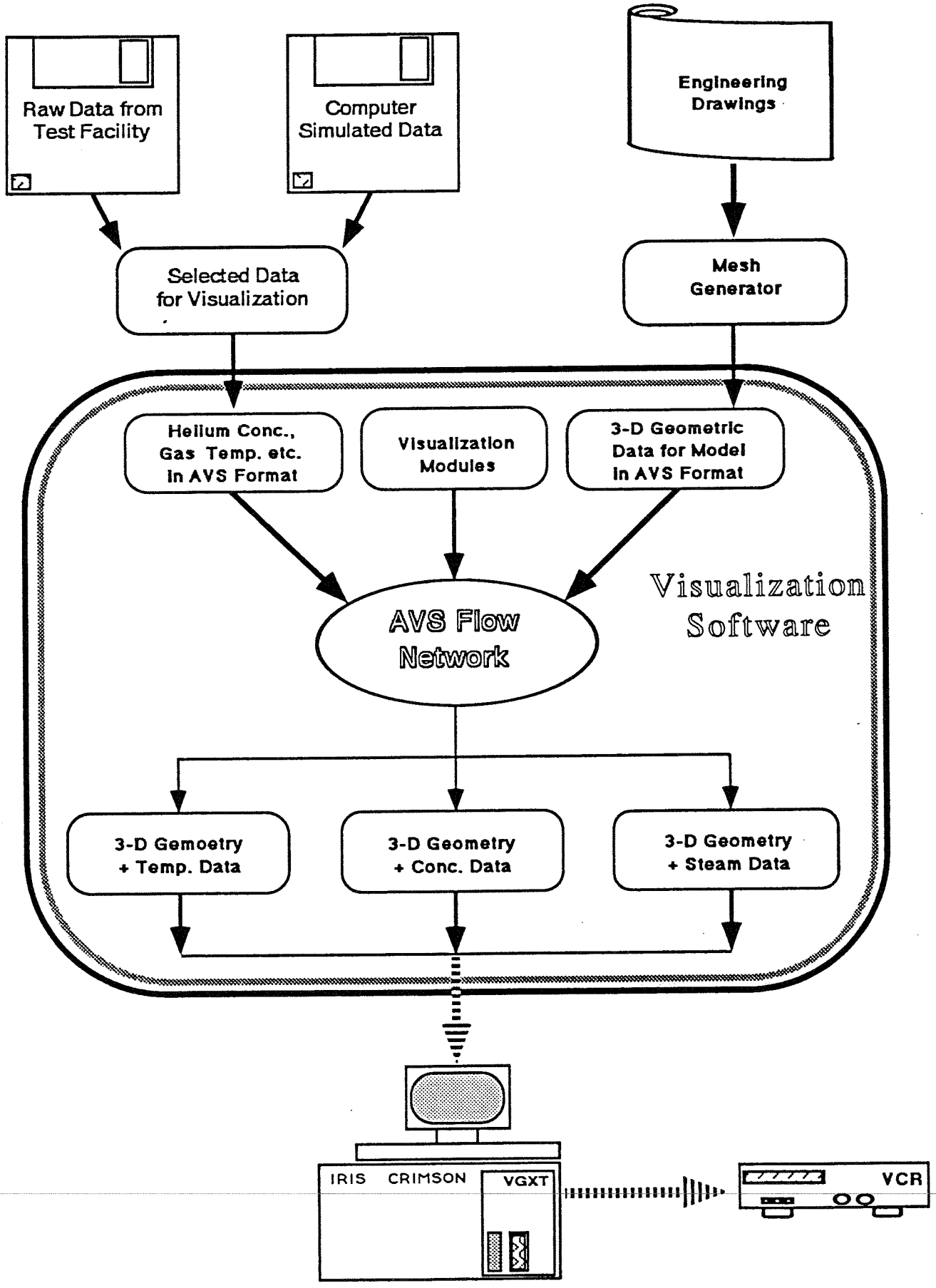

Fig. 7 Flow Diagram of Visualization Process

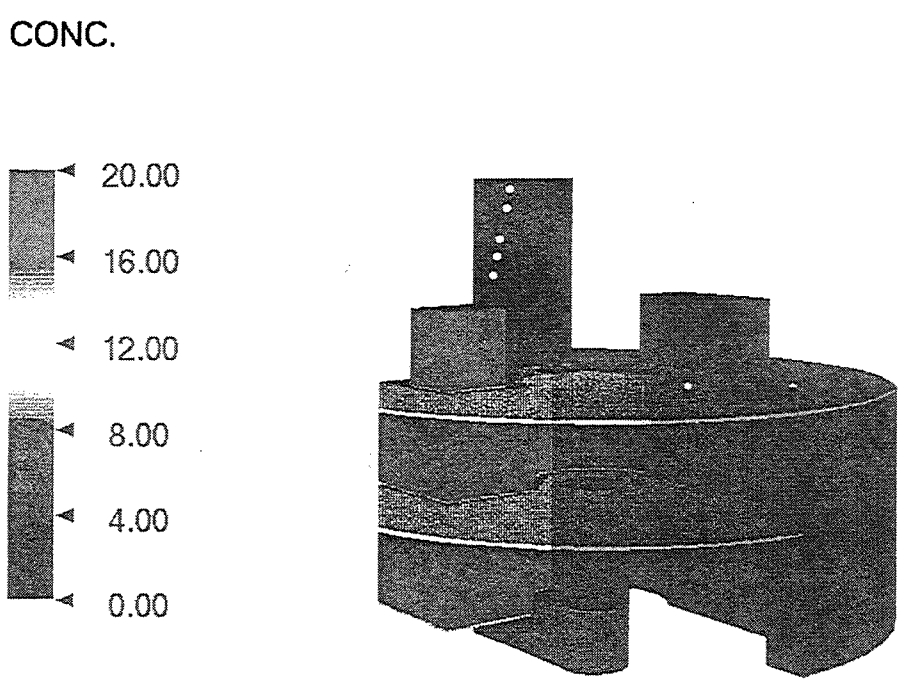

Fig. 8 Sample Visualization of Helium Concentration

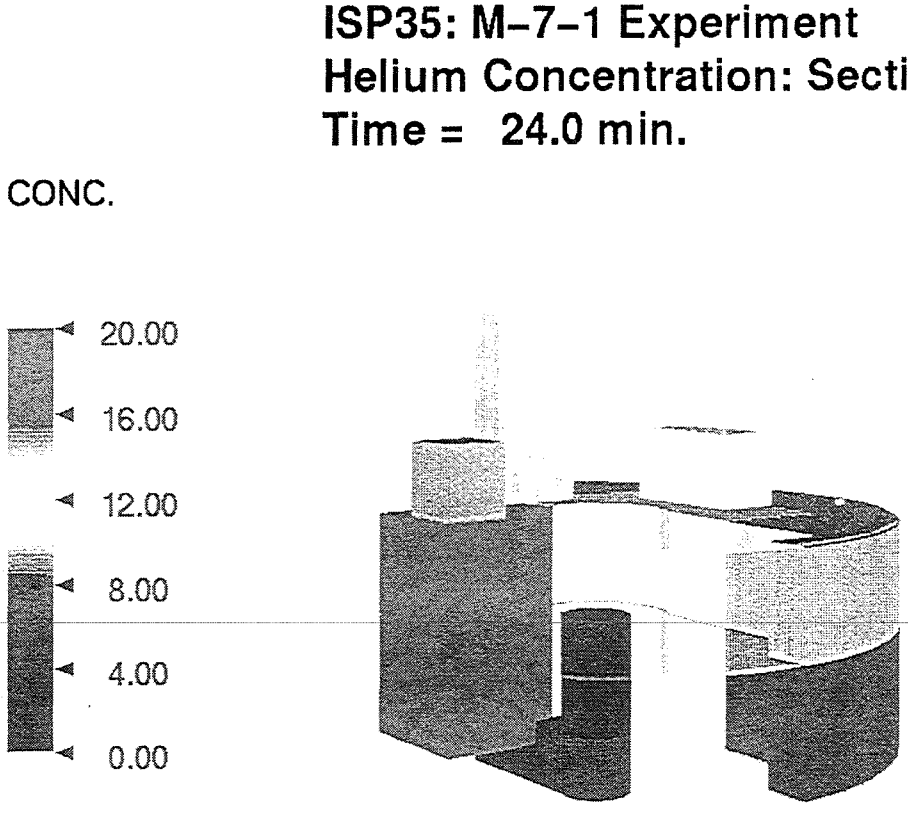

Fig. 9 Sample Visualization of Helium Concentration

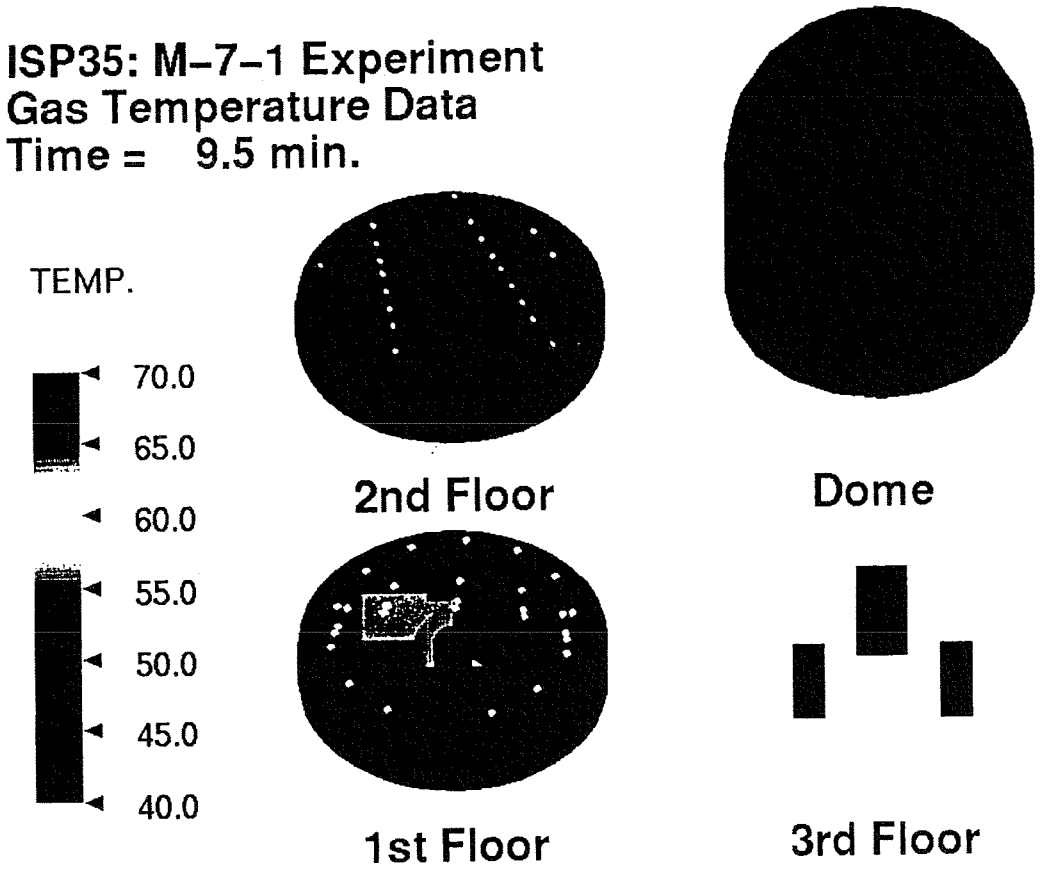

Fig. 10 Sample Visualization of Gas Temperature

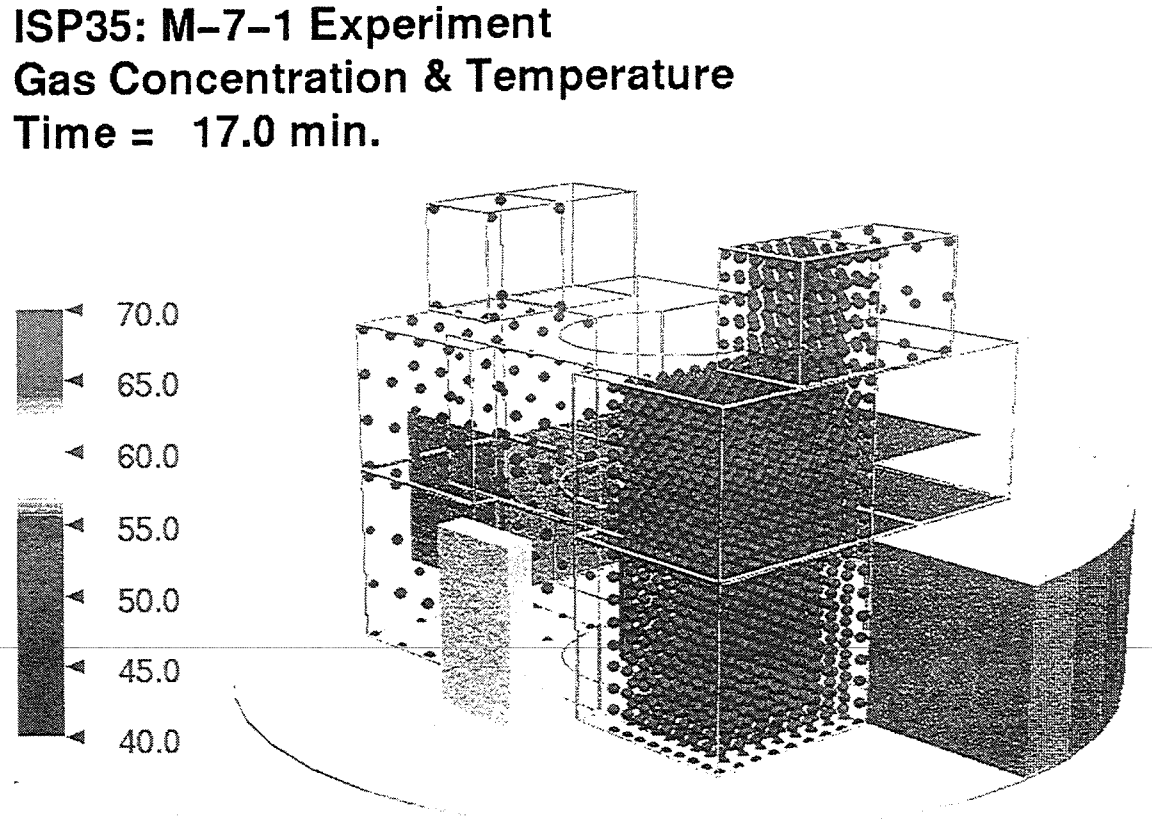

Fig. 11 Sample Visualization of Combined Parameters

STUDY OF STEAM LEAKING WITH CONDENSATION BETWEEN A PIPING AND INSULATOR

W. S. Hsu[1] and S. Toda[2]

[1]The University of Tohoku
Faculty of Engineering, Department of Nuclear Engineering
Aramaki-Aoba, Aoba-ku, Sendai 980-77, Japan
Telephone:(022)222-1800 Ext. 4670, Facsimile:(022)268-1539

[2]The University of Tohoku
Faculty of Engineering, Department of Nuclear Engineering
Aramaki-Aoba, Aoba-ku, Sendai 980-77, Japan
Telephone:(022)222-1800 Ext. 4668, Facsimile:(022)268-1539

ABSTRACT

An experimental study was performed to evaluate the effect of steam leakage through a defect on temperature distributions of pipes in nuclear power plants, where the initial occurrence of steam leakage should be monitored even in operation as early as possible. In the experiment, a SUS 304 pipe 2000 mm long, 114.3 mm in outer diameter and 2.1 mm thick was used, and insulators were made of calcium silicate with thickness of 40 mm. Steam was leaked from a defect of the pipe, which was simulated by a pin hole of 0.5 mm diameter opened at the center of the test pipe, and flowed with condensation in the gap space between the pipe and insulators. Transient changes of temperature distributions on the surface of the insulators were measured by the infrared ray thermography, and the two-phase-flow of steam with condensing through narrow gaps and in porous thermal insulators were analyzed. At the early stage, a small area of the surface near the location of the defect was at a high temperature, and with time, this high temperature zone was spread until a steady temperature distribution was achieved. The final distribution depended on the relative location between the defect and the gap positions of the insulators. For the purpose of contrast, the experiment in which heated air was used as working fluid was also conducted. A new method to predict the location of the defect based on these patterns of temperature distribution was proposed through this study.

1. INTRODUCTION

There is a fair possibility for steam leakage to occur on pipes in nuclear power plant because of the numerous joints and welds dispersed in them. It is, therefore, quite important for safety's sake to deal with the steam leakage before falling into critical condition. The methods often used to detect the steam leakage can be categorized as follows; (1) pipe flow rate and container pressure monitoring, (2) ultrasonic flaw detection, (3) eddy current test, (4) magnetic-particle test, (5) penetrant test, and (6) radiographic test.

The monitoring method is applied when a power plant is in operation and the other methods when in periodical inspection. It is difficult to detect steam leakage by the monitoring method if the leakage flow is small. Since the pipes are surrounded with insulators, it is almost impossible to make a static and close examination of them by the methods of (2) to (6) when the plant is operating.

On the other hand, the concept of LBB is being applied to the piping of nuclear power plant. The concept of leak-before-break is that if any through-wall cracks were to occur, they would be detected well by leakage before they could grow to a size at which catastrophic rupture would occur. It can always be guaranteed under the following conditions[1]:

(1)Highly qualified piping. Material selection, design, fabrication, inspection, testing and welding should be optimized to secure sufficient fracture toughness of the piping components.

(2)Leak detection capability. Reliable fluid leakage monitoring system is needed to ensure LBB.

Therefore, in order to extend the application of the LBB concept, it is necessary to develop a monitoring system which can detect the small leakage sensitively. In this study, a new method to detect leakage based on the temperature distribution is evaluated through the following procedures:

(1) fabricating the experimental apparatus to simulate steam leakage from a pipe.

(2) performing the experiment simulating steam leakage by using heated air as working fluid.

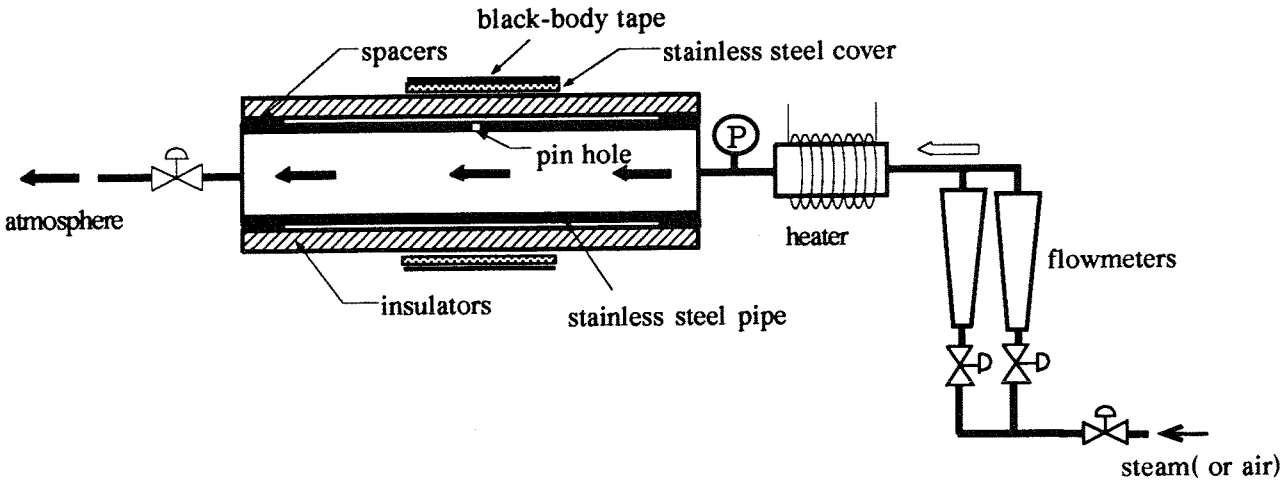

Fig. 1. Experimental apparatus

(3) using steam instead of heated air to evaluate the behavior of leakage with condensation.
(4) determining the location of leakage by monitoring temperature distribution on heated insulator surface.

2. EXPERIMENTAL APPARATUS

Steam leakage is followed by a complicated thermodynamic process such as condensation and resultant two-phase-flow. Therefore, in the first step of our study, we simplified the process by using heated air instead of steam and investigated experimentally the hydrodynamics of single-phase-flow in a narrow channel between pipe and insulators. When the nature of air leakage was elucidated, we then took into account the effect of phase change, which would occur for steam in the second step.

Figure 1 illustrates the instrumentation employed in the steam and air experiments. Test section consisted mainly of stainless steel pipe and insulators surrounding the pipe. The pipe was made of SUS 304 with length of 2000 mm, outer diameter of 114.3 mm, and thickness of 2.1 mm to simulate that joining a reactor pressure vessel to a recirculation pump in a nuclear power plant. And then a defect was simulated by piercing a pin hole of 0.5 mm diameter in the center of the stainless steel pipe. The thermal insulators used in the experiments were made of calcium silicate with thickness of 40 mm, which are widely taken advantage of in the nuclear power plants. The space between pipe and insulators was maintained at 1 mm by inserting spacers into it. Heated air was supplied by a compressor at pressures of 0.2 to 0.4 MPa, and its temperature was controlled at 42 to 66 °C in the heater section. Jet Reynolds numbers varied from 18000 to 20000 and the range of z/D tested was $2.0 < z/D < 82$. Before the heated air entered the test section, we introduced it through an orifice plate and regulation section with length of 1000 mm in order to make uniform its temperature profile. It is reasonable to assume that the heated air issued from the pin hole would impinge upon the insulators, and then travel through the narrow space between stainless steel pipe and insulators, and finally flow into atmosphere through the gap between insulators. The air is cooled, while the surrounding instruments are heated through the heat exchange process between the heated air and the surrounding instruments. This means that there is a possibility to detect the location of leakage by means of monitoring temperature rise of the instruments such as stainless steel cover. As shown in Fig. 2, five chromel-alumel thermocouples were placed longitudinally along the pipe at 50 mm intervals to obtain the local temperature distribution in the gap between insulators. The radial temperature distributions were measured by moving the location of the five thermocouples from A to B, where A was between insulators and pipe, and B was outside insulators. Furthermore, 108 thermocouples, 12 points in circumferential direction and 9 points in longitudinal direction, were placed along longitudinally the outside cover (location C) at 250 mm intervals and circumferentially at 50 mm intervals to measure the global temperature distribution of the cover. Since it could be expected that the temperature distribution of cover would vary with the direction of the pin hole, the stainless steel pipe and insulators were designed so as to permit rotation at angles (both θ_p and θ_i) of up to 180° as shown in Fig. 3, where θ_p and θ_i were angles of pin hole and gap between insulators with respect to vertical, respectively.

In the second step, instead of heated air, steam was used as working fluid in order to evaluate the effect of condensation during leakage. Steam was supplied by an electric boiler, of which mass flow rate and temperature were maintained at 10.5 kg/h and 107 °C, respectively. Θ_p, θ_i and test section pressure P controlled by adjusting the

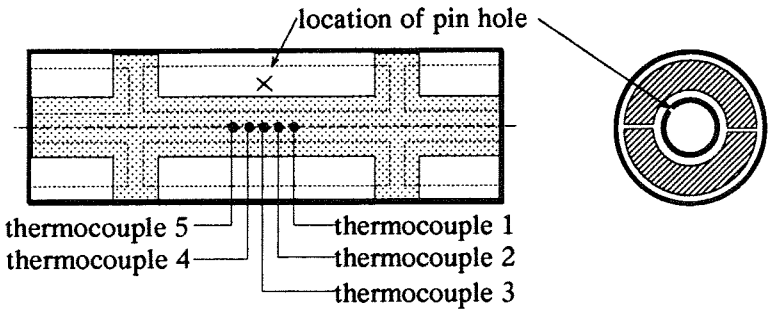

Fig. 2. Arrangement of thermocouples

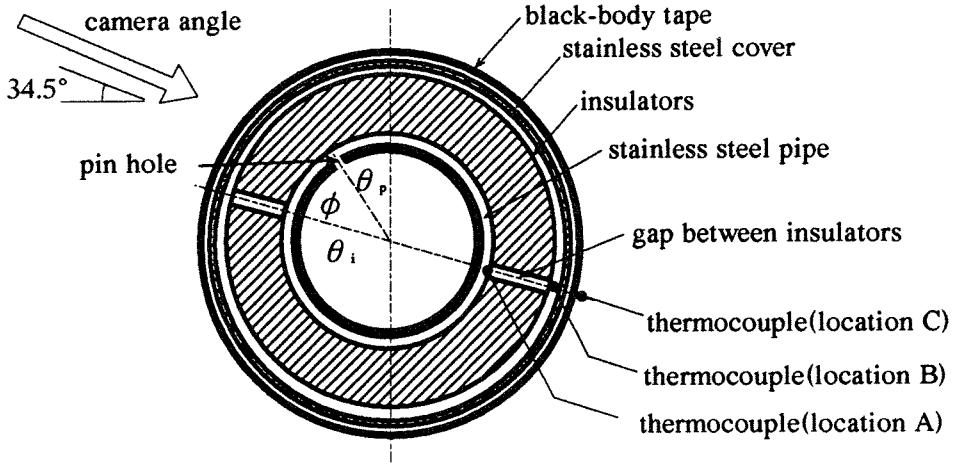

Fig. 3. Test section

exit valve were varied as parameters in this experiment. However, steam pipe lines in a nuclear power plant are so long and the gaps between insulators are so narrow (below 1 mm) that it seems impossible to obtain temperature distribution by using thermocouples. Hence, an infrared ray thermography (Avio TVS-2000), which could catch temperature distribution with accuracy of 0.1 °C at a rate of 0.033 second was also utilized in this experiment. Further, in order to make easier the measurement of temperature on the stainless steel cover by thermography, we attached a black-body tape with 1.0 emissivity to the stainless steel cover. The camera lens of the infrared ray system was arranged at an angle of 34.5° with the centerline of the pipe to avoid interruptions such as pipe supporter (Fig. 3).

3. RESULTS AND DISCUSSIONS

The values of working fluid temperature T at location A, B and C, obtained in the present experiments are represented in dimensionless form using the following effective temperature;

$$\eta = \frac{T - T_{atm}}{T_{in} - T_{atm}} \tag{1}$$

where η, T_{in} and T_{atm} were the effective temperature, the fluid temperature at inlet of test section, and the atmosphere temperature, respectively.

3.1 Results of Heated Air Experiments

Results for pipe without insulators. The temperature distribution of the bare pipe was measured by an infrared ray thermography. It is found that the temperature in the upper half of the pipe was higher than in the lower. This result indicates that heat transfer by natural convection was dominant inside the test section. Fluctuation in η near the pin hole was also observed; therefore it is reasonable to suppose that vortices were formed on the inner surface of the pipe around the pin hole due to leakage flow.

Temperature distributions of insulators. Temperature distributions on the insulator surface were also measured by an infrared ray thermography for $\theta_p = 0^\circ$ with varying ϕ from 0 to 90 degree. The temperature distribution of the insulator was affected by that of the pipe; therefore a higher η in the upper part of the insulator was observed as was in the bare pipe. Local maximum in η was measured at the gap between insulators. The value in η decreased with increasing ϕ since the leakage air was cooled during the process in which it passed through the space between the pipe and the insulators.

Temperature distribution at location A. Figure 4 shows η for $\theta_p = 0^\circ$ with P = 0.32 MPa, where P is the test section pressure. As the diagram indicates, for $30^\circ \le \phi \le 90^\circ$, the values in η have maxima at the location of thermocouple 3 where the pin hole is located, while for $\phi > 90^\circ$, the maxima tends to disappear. The fact may be explained as follows. For small ϕ in the present experiment, η was primarily contributed by leakage temperature. However, for large ϕ, as the leakage fluid traveled through a long and narrow channel between the pipe and insulators, temperature profiles became flat due to spread of the flow. As a result, the variation in η among adjacent thermocouples diminished; and accordingly the curves of η became flat. It means that with increasing ϕ, temperature profiles became flat and close to one another. Therefore, it is possible to predict the circumferential location of a pin hole based upon these temperature distribution patterns. It is very interesting to see that for $\phi = 0^\circ$, the maximum of η appeared not above the pin hole but somewhere in the vicinity of it. The phenomenon may be explained as follows. Goldstein et al.[2] found the length of potential core to be 5 to 8 jet diameters with a single, round and impinging jet for jet Reynolds numbers ($10000 < Re_j < 40000$). In the present study with Re_j = 18000-20000, for $\phi = 0^\circ$, thermocouple 3 was expected to lie within the potential core. On the assumption that the process in which heated air issued from the pipe to the atmosphere to be an isentropic one, the temperature difference between its source and exit can be determined by Eq. (2)

$$\frac{P_e}{P_o} = \left(\frac{T_e}{T_o}\right)^{\frac{\varkappa}{\varkappa-1}} \tag{2}$$

where P , T, $\varkappa$ are pressure, temperature and specific heat ratio, respectively. Source and exit positions are denoted by subscript o and e, respectively.

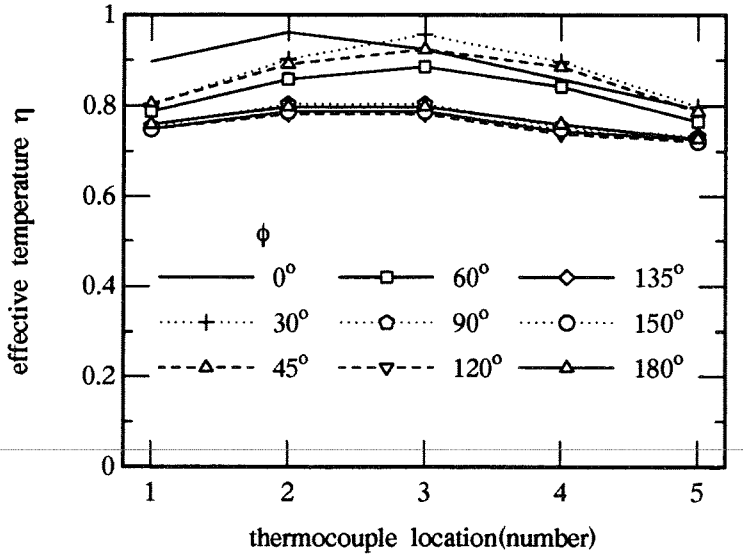

Fig. 4. Effect of angle ϕ

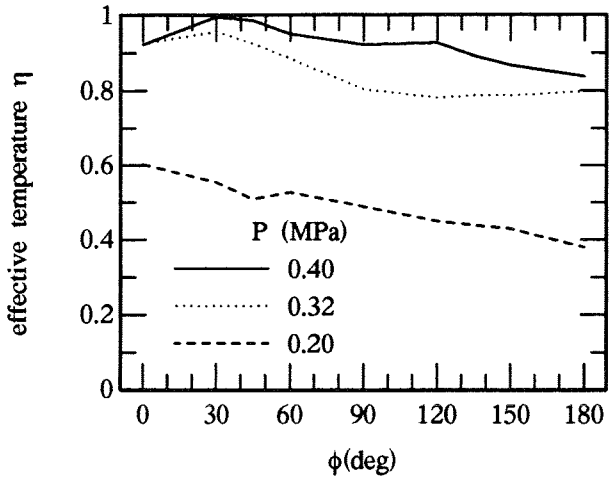

Fig. 5. Effect of inlet pressure on η

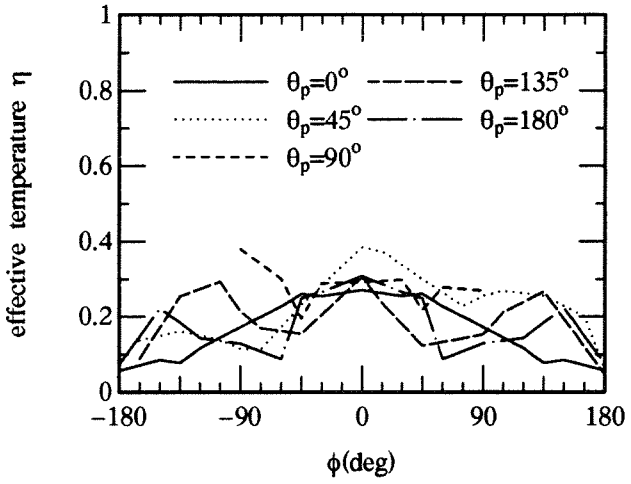

Fig. 6. Effect of location of pin hole

From Eq. (2), with jet source pressure of P_o = 0.2 to 0.4 MPa, the temperature at the jet exit could be expected to be 59 to 102 °C lower than that at the jet source on the presumption that the impingement point pressure was maintained at 1 atm and the experiment was controlled to be an adiabatic and reversible process. However, making allowance for the heat conduction of the stainless steel pipe and the higher pressure on the impingement point than 1 atm, the value of $T_o - T_e$ measured in the present study was not so large as obtained from Eq. (2). In fact, in this experiment for $\phi = 0^o$, $T_o - T_e$ was about 2 to 6 °C. It means that the fluid temperature within potential core was lower than in the neighborhood of the core since the latter might be influenced by the heat transfer from the heated pipe. The values in effective temperature also exhibit a dependence on P as shown in Fig. 5. As the diagram indicates, η increased with increasing P form 0.2 to 0.4 MPa. For P>0.32 MPa, maximum temperature appeared not at the impingement point ($\phi = 0^o$) but at $\phi = 30^o$ due to the effect of potential core discussed above. However, as the pressure decreased, this effect diminished and finally disappeared.

Temperature distribution at outside gap between insulators (location B). At location B for $\phi = 0^o$ (z/D= 82), with thermocouples beyond core length, leakage air mixed a part of room air; and therefore the temperatures measured at this location were lower than those measured at location A. In Fig. 6 the values in η are considered as functions of φ for various θ_p. As the diagram indicates, for small φ, η was dominantly affected by the jet temperature, while for large φ, the influence of pipe temperature on η became important.

Temperature distribution of stainless steel cover (location C). Figure 7 shows a sample of isotherms on the stainless steel cover surface when θ_p and φ were 180 and 90 degrees, respectively. At the bottom of the cover, since the jet impinged straightly on the stainless cover, a relatively high η was observed. At the top of the cover, a relatively high η was also observed because the leakage air was heated during the process in which it

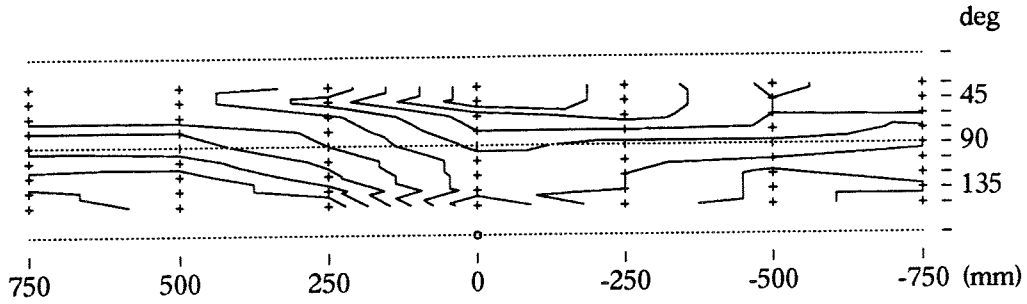

Fig.7. Isotherms on surface of stainless steel cover

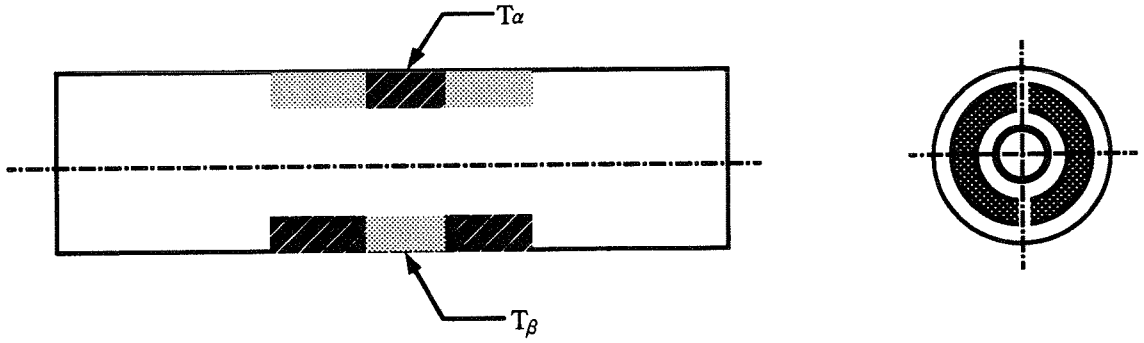

Fig. 8. Surface temperature of stainless steel cover

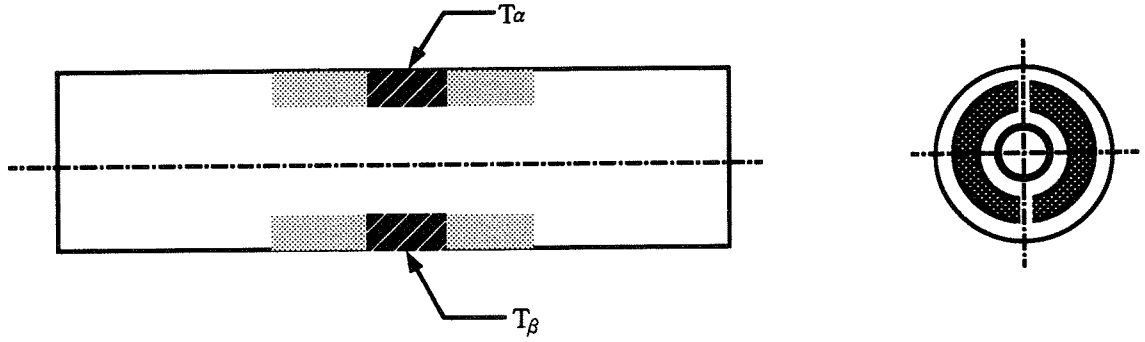

Fig. 9. Surface temperature of stainless steel cover

passed through the space between the upper pipe and the insulators. On the other hand, for $\theta_p=0^o$ a higher η was observed at the top cover due to direct impingement on the cover, and a lower η was observed at the bottom cover because the leakage air was cooled during the process in which it flowed through the space between the lower pipe and the insulators. That is, these isotherms can be categorized into two distinct patterns as θ_p varies. The one as

shown in Fig. 8 with a higher T_α and a lower T_β, where T_α and T_β are the top and bottom temperatures of the cover, predicts that a pin hole exists in the vicinity of the location represented by T_α, and in the other case with a higher T_α and a higher T_β as shown in Fig. 9 indicates existence of a pin hole in the vicinity of T_β.

3.2 Results of Steam Experiments

Results for pipe without insulators. The temperature distribution of the bare pipe in which steam flowed was uniform. The fact indicates that convection of steam was not so obvious inside the pipe. As shown in Fig. 10, lower temperature was measured near $\theta = 180^\circ$ for the reason that a part of the steam condensed and accumulated at the bottom.

Temperature distributions of insulators. Temperature distribution of insulators which surrounded the pipe with $\theta_i = 90^\circ$ without pin hole was also obtained by thermography (Fig. 11). The temperature distribution of insulators was dependent on that of the bare pipe as observed in the experiment for heated air. A local maximum in η was also observed (Fig. 10) at the gap between insulators as was in the case for heated air.

Temperature distribution of stainless cover (location C). Transient and steady state experiments for steam leakage with $\theta_p = 0^\circ$, 180° and $\phi = 90^\circ$ were performed in order to make a comparison with those for heated air. We found that the patterns of temperature distributions were quite different between them. Figures 12 to 16 are a series of thermographs illustrating the temperature distributions of stainless steel cover at different time steps from the start of steam leakage with $\theta_p = 0^\circ$. As shown in Fig. 12, the temperature distribution of the stainless steel cover in the direction of the leaking fluid had the shape of a circle when t = 350 seconds (t_p). The time step t_p was what it required for steam to go through insulator and arrive at the observed surface. Since no remarkable temperature rise could be observed for $t < t_p$, we may say that t_p was the shortest time for a defect to be detected for $\theta_p = 0^\circ$ by means of thermography. The value in t_p is a function of the size and the location of the defect, the leakage fluid pressure, the material and the thickness of the insulator; accordingly, various kinds of system yield various values in t_p. As t increased, the circle spread and gradually developed into concentric circles. When t = 379 seconds (t_i) as shown in Fig. 13, a temperature rise in the form of a straight line at the gap between insulators became visible as well. When t = 419 seconds as shown in Fig. 14, the concentric circles expanded more widely around the pin hole and at the same time, the shape of rosaries began to appear along the gap. As t = 444 seconds as shown in Fig. 15, the shapes of concentric circles and rosaries extended into each other and then began to coalesce. For $t > 9021$ seconds (t_s) as shown in Fig. 16, the temperature distribution grew into a level one, and in consequence the patterns of the temperature observed until now vanished. Since no more change could be perceived through the medium of thermography even for $t > t_s$, it is appropriate to say that t_s was the duration for the present system to reach steady state. Now, we shall discuss the transport properties such as relative permeability and effective thermal conductivity of the porous medium in order to obtain an insight about the steam leakage process for $0 < t < t_s$ (Figs. 11 to 16). Assuming that the insulator is an isotropic porous medium, a relative permeability $k_{rw}(S_w)$ can be defined as the ratio between the effective permeability, k_w and the permeability at saturation, k_{sat} by Eq. (3)

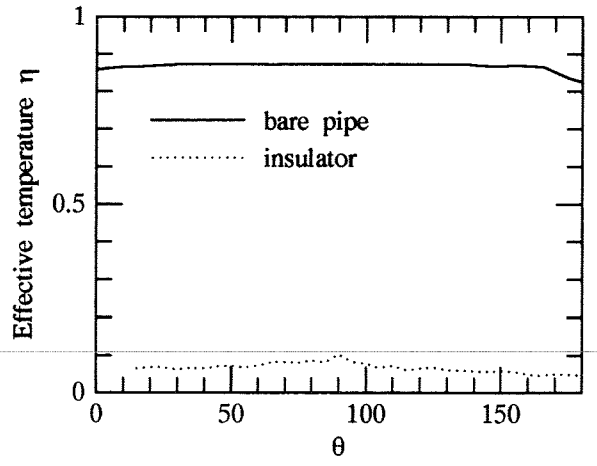

Fig. 10. Temperature distributions of the bare pipe and insulator without pin hole

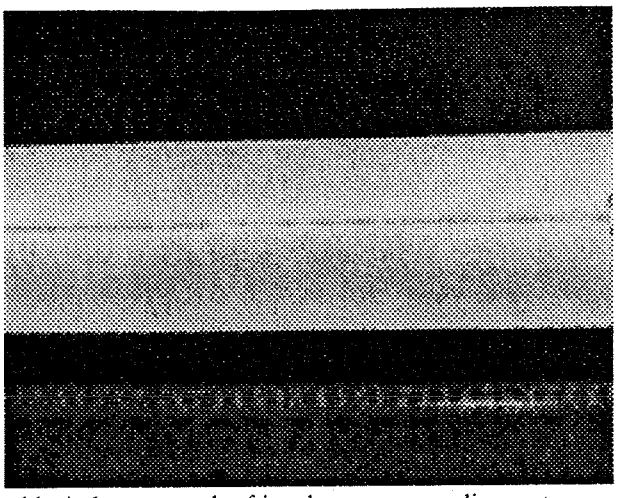

Fig. 11. A thermograph of insulators surrounding a steam pipe

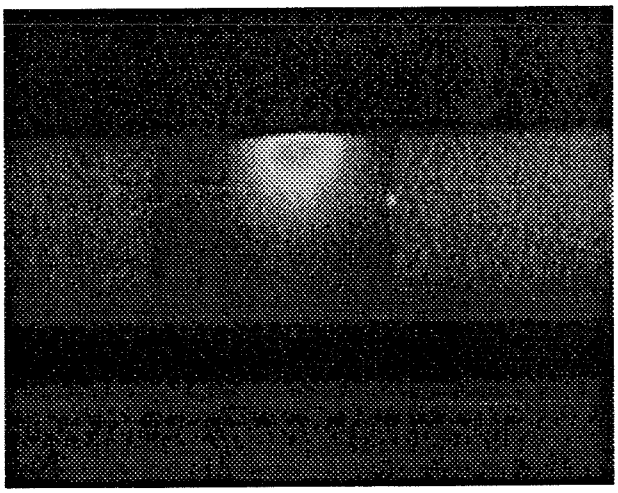

Fig. 12. A thermograph of stainless steel cover 350 seconds after steam leakage with $\theta_p = 0^o$

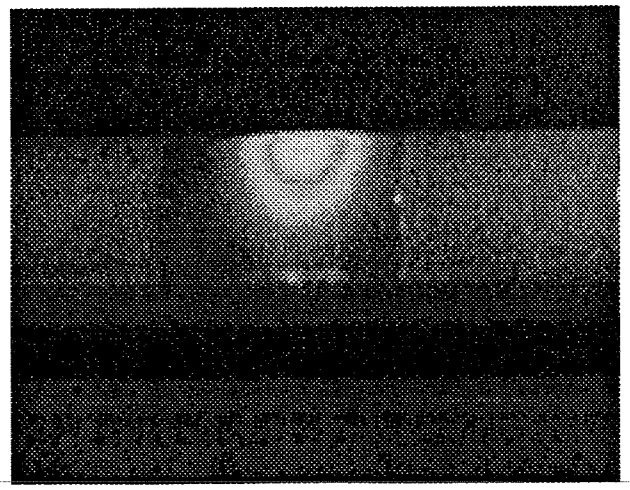

Fig. 13. A thermograph of stainless steel cover 379 seconds after steam leakage with $\theta_p = 0^o$

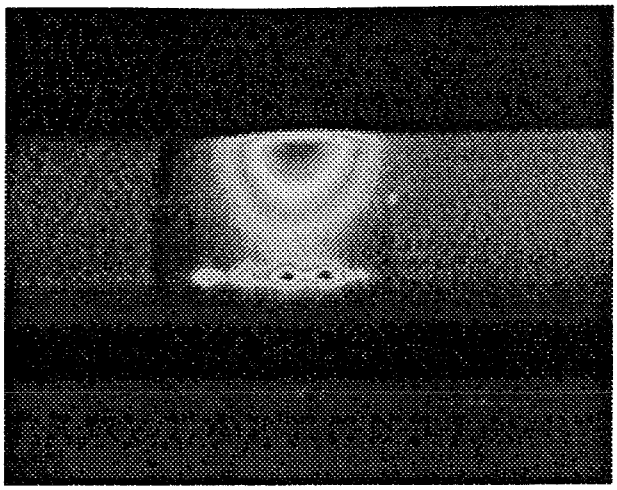

Fig. 14. A thermograph of stainless steel cover 419 seconds after steam leakage with $\theta_p = 0^o$.

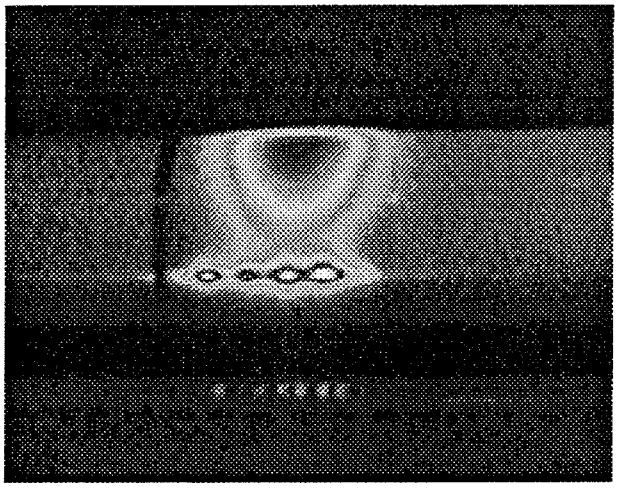

Fig. 15. A thermograph of stainless steel cover 444 seconds afeter steam leakage with $\theta_p = 0^o$

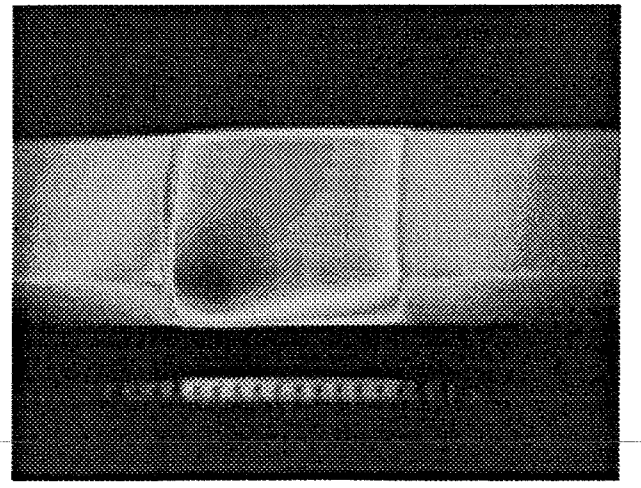

Fig. 16. A thermograph of stainless steel cover 9021 seconds after steam leakage with $\theta_p = 0^o$

$$k_{rw} = \frac{k_w}{k_{sat}} \tag{3}$$

where subscript w denotes the properties for water. Similarly, the relative permeability for vapor can be defined by Eq. (4).

$$k_{rv} = \frac{k_v}{k_{sat}} \tag{4}$$

The relative permeability, as a function of saturation, has to be determined empirically for each particular porous medium of interest. However, typical relative permeability curves (Fig. 17) suggested by Jacob Bear and Yehuda Bachmat[3] can be used to illustrate the phenomenon represented by Figs. 11 to 16. Jacob Bear and Yehuda Bachmat refer to the fact that $k_{rw} = 0$ for $S_w < S_{w0}$, where S_{w0} is the irreducible water saturation, at which the liquid phase is discontinuous and no pressure can be transmitted. Similarly, for vapor phase, $k_{rv} = 0$ for $S_v < S_{v0}$, where S_{v0} is the residual vapor saturation. At the time right after leakage, the whole steam entered the insulators and then condensed and formed discontinuous rings around the grain contact points. In spite of the latent heat released by condensation within insulator, no outstanding temperature rise at the outer surface of the insulator was noticed. As $t > t_p$, the temperature within insulator ascended to an extent such that a part of leakage steam passes through the insulator without condensation, or it became possible for a part of condensate close to the outer surface of insulator reevaporated and departed from it, and then we could detect temperature rise by thermography. As t increases, S_w increased and simultaneously S_v decreased due to condensation. As a result, k_{rv} became lower and it means that lower steam could go through the porous medium. In fact, for $t > t_i$, a part of leakage steam could not enter the insulator but altered its course to the gap between insulators. For $t > t_s$, as S_w increased and S_v decreased to a value

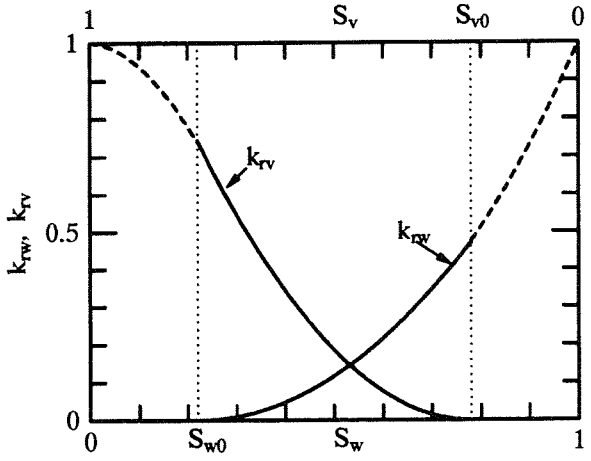

Fig. 17. Typical relative permeability curves.

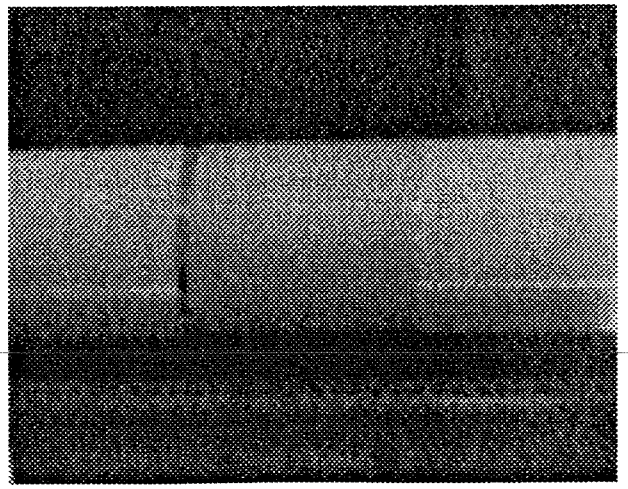

Fig. 18. A thermograph of stainless steel cover 276 seconds after steam leakage with $\theta_p = 180^\circ$

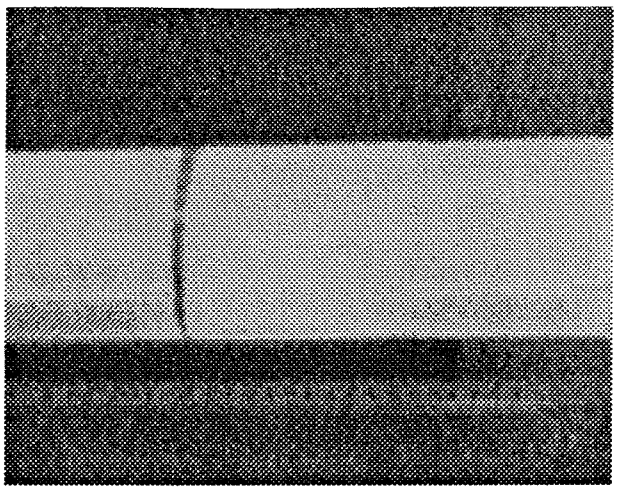

Fig. 19. A thermograph of stainless steel cover 574 seconds after steam leakage with $\theta_p = 180^o$

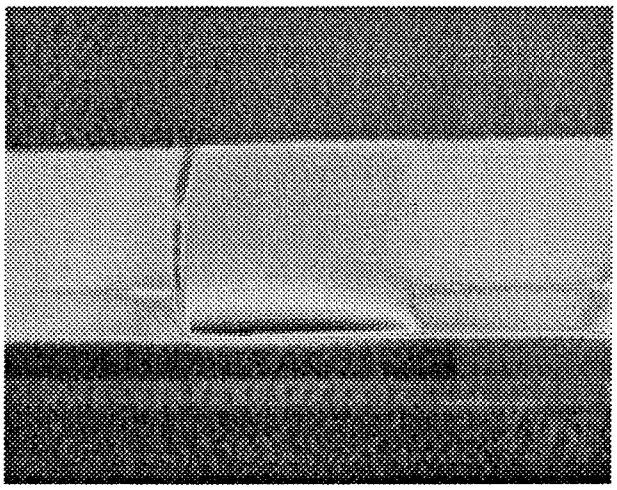

Fig. 20. A thermograph of stainless steel cover 1016 seconds after steam leakage with $\theta_p = 180^o$

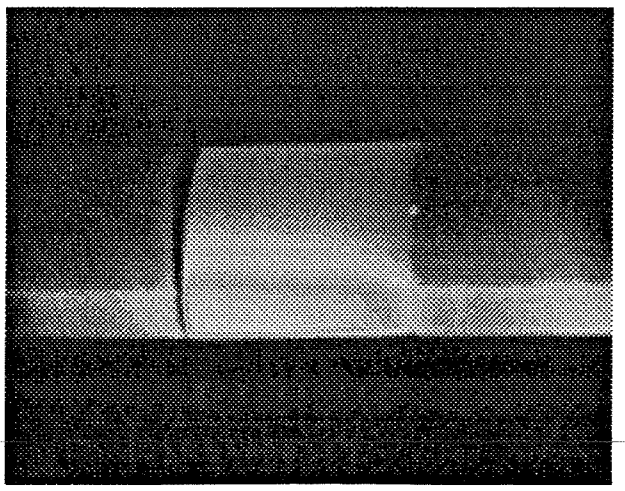

Fig. 21. A thermograph of stainless steel cover 9900 seconds after steam leakage with $\theta_p = 180^o$

of S_{v0}, i.e., $k_{rv} = 0$, leakage steam could not enter the insulator any more. At this time, the whole leakage steam detoured from the insulators and flowed to the gap composed by them. On the other hand, the effective thermal conductivity of three-phase mixtures, --vapor, liquid and solid-- which are of primary interest in our experiment has been addressed by several investigators and is summarized in a recent work by O. A. Plumb[4]. O. A. Plumb stated that above a water saturation of about 20%, the effective thermal conductivity increases approximately linearly with water saturation. In our case, for $t < t_s$, the phenomenon that the temperature of the insulator became higher with increasing t resulted from an increase of effective thermal conductivity associated with an increase of water saturation. For $t > t_s$, as S_v reduced to a minimum, S_{v0}, the water saturation close to the outer surface of the insulator remained constant and thus the heat transfer through insulator became conduction dominated. As a result, an unvaried and uniform pattern of temperature distribution was obtained.

Figures 18 to 21 are a series of thermographs illustrating the temperature distributions of stainless steel cover at different time steps from the start of steam leakage with $\theta_p = 180^\circ$. When t = 276 seconds (t_i), a temperature rise in the form of a straight line was spotted along the gap between insulators. When t = 574 seconds (t_p), a temperature rise at the bottom became visible as well. Owing to the camera angle of the infrared ray system, the pattern of temperature distribution observed looked like half of an ellipse rather than a circle. For the same reason, in this case with $\theta_p = 180^\circ$, t_p was larger than t_i contrasting strikingly with above case with $\theta_p = 0^\circ$. As t = 1016 seconds, the shapes of temperature rise at the gap and at the bottom began to coalesce as described in previous case for $\theta_p = 0^\circ$ with t = 444 seconds. The fact that the temperature rise along the gap grew far more slowly for $\theta_p = 180^\circ$ than for $\theta_p = 0^\circ$ may be explained as follow. As water saturation increased, the discontinuous condensates within insulator coalesced each other and then grew until a continuous water phase was formed. The saturation at which this occurs is called equilibrium water saturation. Above this critical saturation, the saturation is called funicular and flow of water is possible[3]. For $\theta_p = 180^\circ$, as condensed water was in the state of funicular saturation, flow of water in the same direction of leakage (downward in this case) caused by gravitation decreased the water saturation within the insulator close to the pin hole and simultaneously increased the relative permeability for steam; on the contrary, for $\theta_p = 0^\circ$, flow of water in the reverse direction of leakage increased the water saturation within the insulator close to the pin hole and decreased the relative permeability for steam. Consequently, more steam entered the insulator in the case for $\theta_p = 180^\circ$ than in the case for $\theta_p = 0^\circ$. As we observed in the case for $\theta_p = 0^\circ$, an immediate temperature rise at the gap appeared since a great deal more steam was obstructed from passing through the insulator and made a detour to the gap. We shall present the transient changes of temperature at the gap and at the pin hole for both $\theta_p = 0^\circ$ and $\theta_p = 180^\circ$ in Fig. 22.

4. METHOD FOR MONITORING DEFECT IN OPERATION

4.1 In the Case for Heated Air

In the present study, the cover temperature was always affected by the temperature of leakage air. The temperature of the leakage air was high just after leakage air was released from the pin hole, while it would be heated by the upper part of the pipe or be cooled by the lower one when the leakage air traveled through a long path

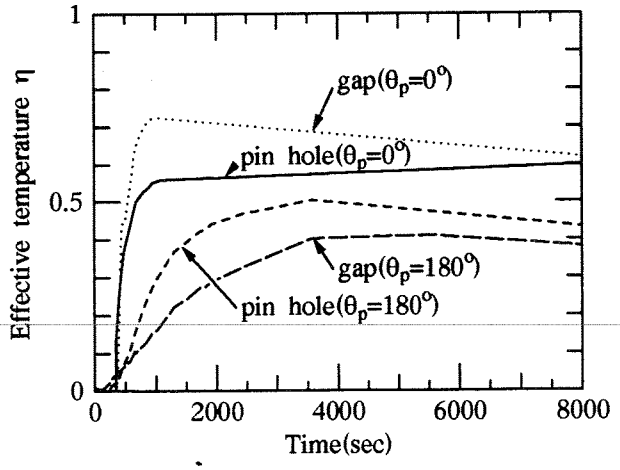

Fig. 22. Stainless steel cover temperature transients for $\theta_p = 0^\circ$, 180°

between the pipe and insulators. Therefore, it is necessary to obtain beforehand the orientation of gap between insulators and the temperature distribution of the bare pipe in order to determine the location of the defect. It is easy to know the orientation of the gap since it has been decided in the designing stage, while it is almost impossible to measure directly the temperature distribution of the bare pipe during operation due to the surrounding insulators. It can, however, be determined by numerical analysis taking fluid temperature as a parameter. And besides, for the sake of contrast in temperature distribution, it is important to place gaps on the hottest side and the opposite one (the top and the bottom in the present study). By observing the patterns of T_α and T_β, one can keep track of the occurrence of a defect in a heated air pipe and determine its location in operation.

4.2 In the Case for Steam with Condensation

In this experiment, a temperature rise at the top of stainless cover was detected earlier than at the gap for a defect located at the top of the pipe. As leakage time increased, the shapes of temperature distribution at the top and at the gap coalesced and finally disappeared. On the other hand, for a defect occurred at the bottom, a temperature rise at the gap was detected earlier than at the bottom of the stainless steel cover owing to the arrangement of camera angle. As leakage time increased, the temperature rise at the bottom became remarkable compared with that at the gap. It required much more time for the shapes of temperature distribution at the bottom and at the gap to coalesce each other, however. By observing the patterns of transient change of temperature distribution, one can monitor the occurrence of a defect in a steam pipe and designate its location even in operation as we can in the case for heated air.

5. CONCLUDING REMARKS

Concluding remarks resulting from this experimental investigation are the followings;

(1) The temperature distributions of the bare pipe and insulator surface without leakage were measured by an infrared ray thermography for both heated air and steam. The temperature distribution of the insulator surface was elementally affected by that of the bare pipe.

(2) The temperature distributions of stainless steel cover with leakage fluid were obtained by an infrared ray thermography as well. It is found that for both heated air and steam, as θ_p varied, the isotherms for these two cases could be categorized into two distinct patterns, respectively. By observing these patterns of temperature distribution, one can monitor the occurrence of a defect in a steam (or heated air) pipe and designate its location even in operation.

(3) For the sake of contrast in temperature distribution, it is important to arrange the gaps between insulators to the hottest side and the opposite one (the top and the bottom in the present study) for heated air, or to adjust the camera lens of infrared ray system at a proper angle with pipe axis for steam.

6. REFERENCES

[1]Y. Asada, K.Takumi, H.Hata and Y.Yamamoto, Jr., "Development of criteria for protection against pipe breaks in LWR plants", in: Int. J. Pres. & Piping, 43, p.95 (1990).

[2]R. Gardon and J. Cobonpue: "Heat transfer between a flat plate and jets of air impinging on it", in: Proc. 2nd Int. Heat Transfer Conference, ASME, New York, p.454 (1962).

[3]Jacob Bear and Yehuda Bachmat: "Introduction to modeling of transport phenomena in porous media", Kluwer Academic Publishers, Netherlands (1991).

[4]O. A. Plumb: "Heat transfer during unsaturated flow in porous media", in: Convective heat and mass transfer in porous media, Cluwer Academic Publishers, p.435, Netherlands (1991).

[5]Milan Vukovic and Andjelko Soro: "Determination of hydraulic conductivity of porous media from grain-size composition", Water Resources Publications, Colorado (1992).

[6]S. Toda, W.S. Hsu, H. Hashizume and Y. Hori: "Study of thermal fluid leaking between piping and insulators: Basic experiment by air", in: Proc. 2nd ASME/JSME Nuclear Engineering, p.131, San Francisco (1976).

[7]C. H. A. Molenda, P. Crausse and D. Lemarchand, Jr., "Heat and humidity transfer in non saturated porous media: capillary hysteresis effects under cyclic thermal conditions", in: Int. J. Heat Mass Transfer, 36, p.3077 (1993).

[8]Shahryar Montakef and Maher A. El-Masri, Jr., "Simultaneous heat and mass transfer with phase change in a porous slab", in: Int. J. Heat Mass Transfer, 29, p.1503 (1986).

[9]H. A. Dinulescu and E. R. G. Eckert, Jr., "Analysis of the one-dimensional moisture migration caused by temperature gradients in a porous medium", in: Int. J. Heat Mass Transfer, 23, p.1069 (1980).
[10]Andrew P. Shapiro and Shahryar Motakef, Jr., "Unsteady heat and mass transfer with phase change in porous slabs: analytical solutions and experimental results", in: Int. J. Heat Mass Transfer, 33, p.163 (1990).
[11]C. L. D. Huang, Jr., "Multi-Phase moisture transfer in porous media subjected to temperature gradient", in: Int. J. Heat Mass Transfer, 22, p.1295 (1979).
[12]Daniel A. de Vries, Jr., "The theory of heat and moisture transfer in porous media revisited", in: Int. J. Heat Mass Transfer, 30, p.1343 (1987).
[13]V. Prasad, N. Kladias, A. Bandyopadhaya and Q. Tian, Jr., "Evaluation of correlations for stagnant thermal conductivity of liquid-saturated porous beds of spheres", in: Int. J. Heat Mass Transfer, 32, p.1793 (1989).
[14]D. A. Nield, Jr., "Estimation of the stagnant thermal conductivity of saturated porous media", in: Int. J. Heat Mass Transfer, 34, p.1575 (1991).
[15]Y. Ogniewicz and C. L. Tien, Jr., "Analysis of condensation in porous insulation", in: Int. J. Heat Mass Transfer, 24, p.421 (1981).
[16] Chao-Yang Wang and C. Beckermann, Jr., "A two-phase mixture model of liqid-gas flow and heat transfer in capillary porous media--I. Formulation", in: Int. J. Heat Mass Transfer, 36, p.2747 (1993).
[17] Chao-Yang Wang and C. Beckermann, Jr., "A two-phase mixture model of liqid-gas flow and heat transfer in capillary porous media--II. Application to pressure-driven boiling flow adjacent to a vertical heated plate", in: Int. J. Heat Mass Transfer, 36, p.2759 (1993).
[18]J. C. Hsieh, T. S. Chen and B. F. Armaly, Jr., "Nonsimilarity solutions for mixed convection from vertical surfaces in porous media: variable surface temperature or heat flux", in: Int. J. Heat Mass Transfer, 36, p.1485 (1993).
[19]Jiin-Yuh Jang and Jin-Sheng Leu, Jr., "Variable viscosity effects on the vortex instability of free convection boundary layer flow over a horizontal surface in a porous medium", in: Int. J. Heat Mass Transfer, 36, p.1287 (1993).
[20]Jiin-Yuh Jang and Jiing-Lin Chen, Jr., "Variable porosity effect on vortex instability of a horizontal mixed convection flow in a saturated porous medium", in: Int. J. Heat Mass Transfer, 36, p.1573 (1993).
[21]A. K. Stubos, C. Satik and Y. C. Yortsos, Jr., "Effects of capillary heterogeneity on vapor-liquid counterflow in porous media", in: Int. J. Heat Mass Transfer, 36, p.967 (1993).
[22]Jiin-Yuh Jang and Jiing-Lin Chen, Jr., "Thermal dispersion and inertia effects on vortex instability of a horizontal mixed convection flow in a saturated porous medium", in: Int. J. Heat Mass Transfer, 36, p.383 (1993).
[23]Zeng-Guang Yuan and Kent S. Udell, Jr., "Steam distillation of a single component hydrocarbon liquid in porous media", in: Int. J. Heat Mass Transfer, 36, p.887 (1993).
[24]K. Vafai and S. Whitaker, Jr., "Simultaneous heat and mass transfer accompanied by phase change in porous insulation", in: Int. J. Heat Transer, 108, p.132 (1986).
[25]K. Vafai and S. Sarkar, Jr., "Condensation effects in a fibrous insulation slab", in: Int. J. Heat Transfer, 108, p.667 (1986).
[26]Toshikazu Yano, Eiji Matsushima and Asao Okamato, Jr., "Evaluation of leak flow rate and jet impingement related to leak before break", in: J. Nuclear Engineering and Design, 111, p.197 (1989).
[27]C. Maricchiolo and P. P. Milella, Jr., "Prediction of lead areas and experimental verification on carbon and stainless steel pipes", in: J. Nuclear Engineering and Design, 111, p.47 (1989).

7. NOMENCLATURE

D	jet exit diameter (0.5 mm in the present study)
k_{rv}	relative permeability for vapor
k_{rw}	relative permeability for water
k_{sat}	permeability at saturation
k_v	effective permeability for vapor
k_w	effective permeability for water
P	test section pressure
Re_j	$= u_j D / \nu$, jet Reynolds number
S_v	vapor saturation
S_{v0}	residual vapor saturation
S_w	water saturation
S_{w0}	irreducible water saturation
t	time after leakage
t_p	time for a temperature rise to be detected in the vicinity of the pin hole
t_i	time for a temperature rise to be detected at the gap between insulators
t_s	time for a particular system to reach steady state in temperature distribution of the stainless cover
T_{in}	fluid temperature at inlet of the test section
T_{atm}	atmosphere temperature
T_α	temperature of the top cover on the circumference crossing impingement line
T_β	temperature of bottom cover on the circumference crossing impingement line
u_j	average jet exit velocity
z	distance from jet exit
η	effective temperature defined by Eq. (1)
θ_p	angle of pin hole with respect to vertical shown in Fig. 3
θ_i	angle of insulators' gap with respect to vertical shown in Fig. 3
ϕ	$\theta_i - \theta_p$
$\varkappa$	specific heat ratio
ν	kinematic viscosity

NON-EQUILIBRIUM BEHAVIOR OF DISTURBANCE WAVES ON EVAPORATING FILM FLOW

S. Nakanishi[1], S. Yamauchi[2], and T. Sawai[2]

[1] Himeji Institute of Technology
Department of Chemical Engineering
2167, Shosha, Himeji, Hyogo 671-22, Japan

[2] Takamatsu National College of Technology

ABSTRACT

The behavior of the disturbance waves on an evaporating film flow was investigated experimentally. A new type of hydrodynamic non-equilibrium was confirmed through the two kinds of experiments; steam-water two-phase flow and Freon R113 two-phase flow in a vertical evaporating tube. The notion of new hydrodynamic non-equilibrium was identified as the imbalance in the liquid distribution between the disturbance waves and the base film. The new hydrodynamic non-equilibrium introduced here was also investigated by the simulation experiment with an air-water shear flow in the horizontal rectangular duct, at which the part of the base film in the liquid was removed. After removing, it was found that the imbalance condition occurring in the liquid film affected the behavior of the disturbance waves because the imbalance was recovered by redistribution of a part of the disturbance waves to the base film. This phenomenon was also observed in an unheated section following the evaporating tube, which supported the new type of hydrodynamic non-equilibrium in the evaporating tube. Through the above experiments, it is concluded that the notion presented here is an inherent characteristic to understand the behavior of the disturbance waves on an evaporating film flow. Moreover, the disturbance waves in steam-water two-phase flow were found to be related to the complexity of the film flow by estimating the attractor dimension of its reconstructed trajectory.

NOTE: *This paper had not been received before the Proceedings were assembled. If received on or before August 23, 1994, handouts will be given to each participant of the Symposium.*

EXPERIMENTAL INVESTIGATIONS ON THERMAL NONEQUILIBRIUM EFFECTS OF TWO-PHASE EXPANSION FLOWS

J. Huhn and M. Wein

Technische Universität Dresden
Institut für Thermodynamik und Technische Gebäudeausrüstung
Mommsenstraße 13, D-01062 Dresden, Federal Republic of Germany
Telephone: (0351) 463-4036, Facsimile: (0351) 463-7105

ABSTRACT

Measurements of local void fractions using the resistivity probe technique were conducted to investigate the influence of thermal nonequilibrium effects in expansion flows through nozzles of initially subcooled hot water. The steady-state, quasi-one-dimensional model used for calculation is based on a set of conservation equations applied to phase and mixture. Isothermal flow implying metastable liquid states is assumed to consider delayed nucleation. The transition from single to two-phase flow is determined by a pressure undershoot correlation. Vapor generation is controlled by simulation of bubble growth. Calculations compare quite well with presently available experimental data.

1. INTRODUCTION

Two-phase flows are of much interest in the power and process industries. The accurate prediction of two-phase flow transients is essential for the thermal hydraulic dimensioning of safety devices as well as analysis of hypothetical ruptures of vessels or pipes.

In the homogeneous equilibrium model (HEM), Wallis [1], the two-phase mixture is regarded as a single-phase fluid incorporating equal phase velocities and temperatures. This model shows reasonable results for two-phase flows undergoing relatively slow processes, such as flow through long pipes. By way of contrast it fails in describing two-phase flows where there is insufficient time to reach equilibrium conditions, e.g. blowdown through short tubes and nozzles. This holds true as well for the slip flow model proposed by Moody [2], which accounts for different phase velocities but is also based on the assumption of thermodynamic equilibrium.

A number of models have been suggested to account for mechanical and thermal nonequilibrium effects like retarded phase-change. Henry *et al.* [3], [4] performed low-quality steam-water experiments in constant area ducts and proposed a function that can be determined experimentally to consider deviation from thermodynamic equilibrium. Another expression for the critical flow rate and the pressure ratio calculated from upstream stagnation conditions especially for nozzles, orifices and short tubes was presented by Henry and Fauske [5]. Vessel blowdown experiments of saturated and subcooled water conducted by Sozzi and Sutherland [6], clearly revealed the influence of thermodynamic nonequilibrium for short discharge geometries. Schrock *et al.* [7] presented experimental results on flashing flow of water through convergent-divergent nozzles and considered some nucleation delay, however without specifying a general formulation to determine locations of flashing inception.

Calculation procedures allowing thermal nonequilibrium in the way of simulating delayed bubble nucleation and bubble growth were used for example by Edwards [8], Wolfert [9] and Riznic

and Ishii [10]. Shin and Jones [11] proposed a method to determine the number and the size of bubbles in flashing flow which is based on a wall cavity model. Their nucleation model was applied by Blinkov *et al.* [12] who developed a calculation procedure for choked nozzle flow with subcooled water inlet conditions. They obtained good agreement with experimental data and confirmed that consideration of thermal nonequilibrium is essential while mechanical nonequilibrium can be neglected. They also found that bulk nucleation has a negligible effect for flashing flow through small nozzles.

A critical review of early two-phase flow models was presented by Wallis [13]. With respect to the numerous uncertainties about the real physics, he emphasized the necessity of experimental efforts to provide detailed measurements.

Methods of measurement in two-phase flow were presented by Bergles *et al.* [14]. As special focus is put on local changes of void fraction inside nozzles, only intrusive methods such as the electrical resistivity probe technique turning the different conductivities of liquid and vapor into account are applicable. By means of dual or multiple sensor probes this method has been employed not only to measure local void fractions but interfacial area as well as velocity and mean radius of bubbles, Revankar and Ishii [15] and Kalkach-Navarro *et al.* [16]. Kobori and Terada [17] utilized single-needle probes in blowdown tests and showed different types of signal conditioning. Due to restricted space and severe flow conditions, similar probes have been used in this study.

It is the purpose of this paper to describe preliminary experiments on bubbly flows of initially subcooled hot water through nozzles. Measured void fraction distributions are presented along with a simple calculation procedure used to recalculate the experiments.

2. EXPERIMENTAL SETUP AND PROCEDURES

The experiments were conducted at the local district heating test facility, Fig. 1, which provided relatively stable nozzle upstream conditions. Inlet temperatures were varied within a range of 391.15 to 407.15 K at pressures of 0.550 to 0.582 MPa and were held constant during measurements within maximum fluctuations of ±1 K and ±0.01 MPa, respectively.

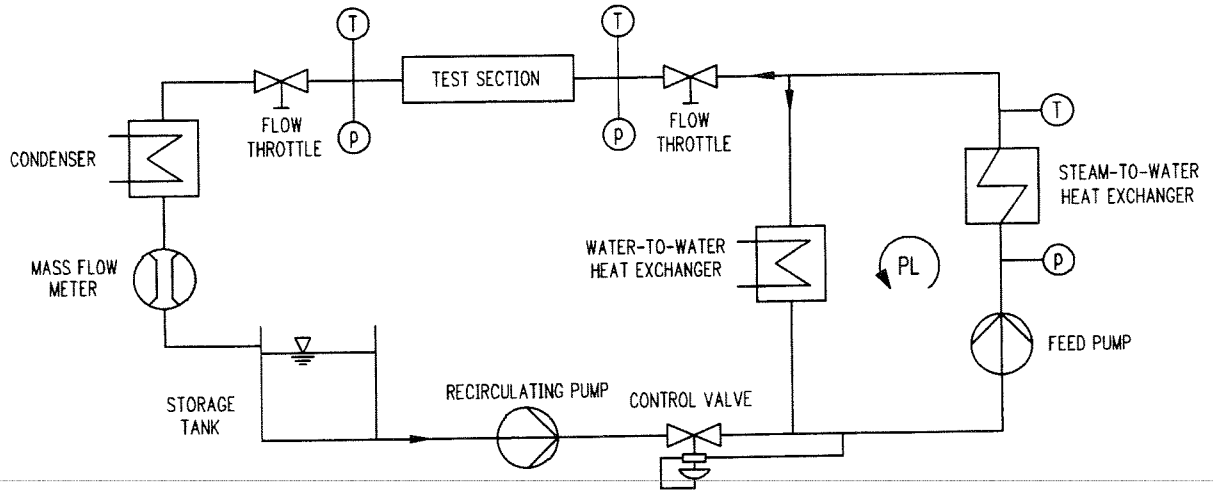

Fig. 1. Test facility with experimental loop on the left and primary loop (PL) on the right

Subcooled hot water was taken from the primary loop and was led to the horizontal test section where it was vented through the test nozzle. Next the water was routed through a condenser to

an atmospheric reservoir. Thus the nozzle back pressure approximately corresponded to the ambient pressure. After leaving the storage tank the water was fed back to the primary loop.

As a further reduction of the back pressure was not possible, the assumed critical flow conditions could not be proved definitely. But as chosen inlet conditions always complied with Burnell's [18] criterion for the critical pressure ratio as a function of inlet temperature

$$\frac{p^*}{p_0} = 1 - \frac{75.48 - 0.14\left(T_0 - 273.15K\right)/K}{186.36}, \tag{1}$$

one can proceed on the assumption of critical flow.

The test nozzle had a 4.5 mm diameter throat, an axial length of 21 mm and was of axissymmetric conical shape with a convergent angle of 6.82°. The inlet was sharp-edged with an abrupt expansion at the throat to be inserted horizontally into a steel disc orifice perpendicular to the pipe (I.D. 80 mm) axis.

Temperature and pressure were measured with Iron-Constantan thermocouples and strain gauges, respectively. Maximum uncertainties were within ± 0.7 % with respect to temperature, and ± 1.8 % regarding pressure. The flow rate was determined within an uncertainty of ± 2.4 % downstream of the condenser by counting the sweep frequency of a tipping device. The local void fraction was measured using a single-needle resistivity probe. This was connected via a long stick inside the steel pipe and was moved by an adjusting screw fixed at the downstream bend.

Figure 2 shows the probe-tip, consisting of a tungsten-wire projecting out of the end of a small ceramic tube glued into telescopically arranged hypodermic needles with increasing inside diameter. While these stainless steel tubes were used as common ground, the non-isolated exposed wire tip represented the signal-conductor.

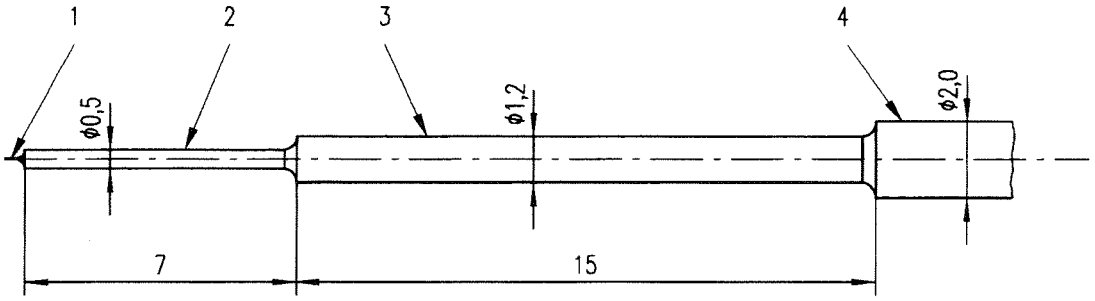

Fig. 2. Probe tip #1; 1: Tungsten-wire (ø125µm); 2: Insulating cappillary ceramic tube; 3,4: Hypodermic needles

There are two competitive demands on the probe construction: on the one hand the probe should be as small as possible to minimize disturbance effects and on the other hand it should possess enough strength to withstand the severe flow conditions near the nozzle throat. Lateral vibrations of the delicate probe front part caused by velocity fluctuations, thermal stress as well as erosive effects on glued probe joints resulted in relatively short duty-cycles.

The sensor was connected in series with a high-Ohmic resistor supplied with low dual current voltage. The voltage drop across the ends of the resistor indicates changes of local resistivity and thus the presence of vapor bubbles or liquid phase at the probe tip. The continuous analog probe signals were conditioned by amplification and comparison with an appropriate reference voltage to be subsequently shaped to square waves using a Schmitt trigger circuit. The digitized signals were stored and processed on a microcomputer.

In this way time averaged local void fractions were obtained by relating the elapsed time that vapor bubbles contact the probe tip, i.e. the width of the square waves, to the total sample time:

$$\alpha = \frac{\sum_i \tau_{B,i}}{\tau_{tot}}.$$

By moving the probe along the pipe axis the nozzle was scanned to find loci of flashing inception and to measure the void fraction distribution up to the nozzle throat.

3. CALCULATION MODEL

A simple calculation model was developed to simulate critical flow of initially subcooled hot water through nozzles with consideration of nonequilibrium effects.

3.1 Basic Considerations and Assumptions

The horizontal flow is assumed to be at steady-state and adiabatic. In the presence of vapor the flow is supposed to be ideally dispersed. As pressure drop of flows through short nozzles with small length to diameter ratios is dominated by the acceleration term, pressure loss caused by friction can be neglected.

Figure 3 illustrates the assumed change of state of hot water during a rapid expansion process. The liquid phase follows an isothermal path starting in the subcooled region according to its initial temperature T_0 and pressure p_0. It then passes the saturated liquid line reaching metastable states until, at a distinct pressure p_n, nucleation of vapor bubbles occurs. The formed vapor phase is supposed to be saturated.

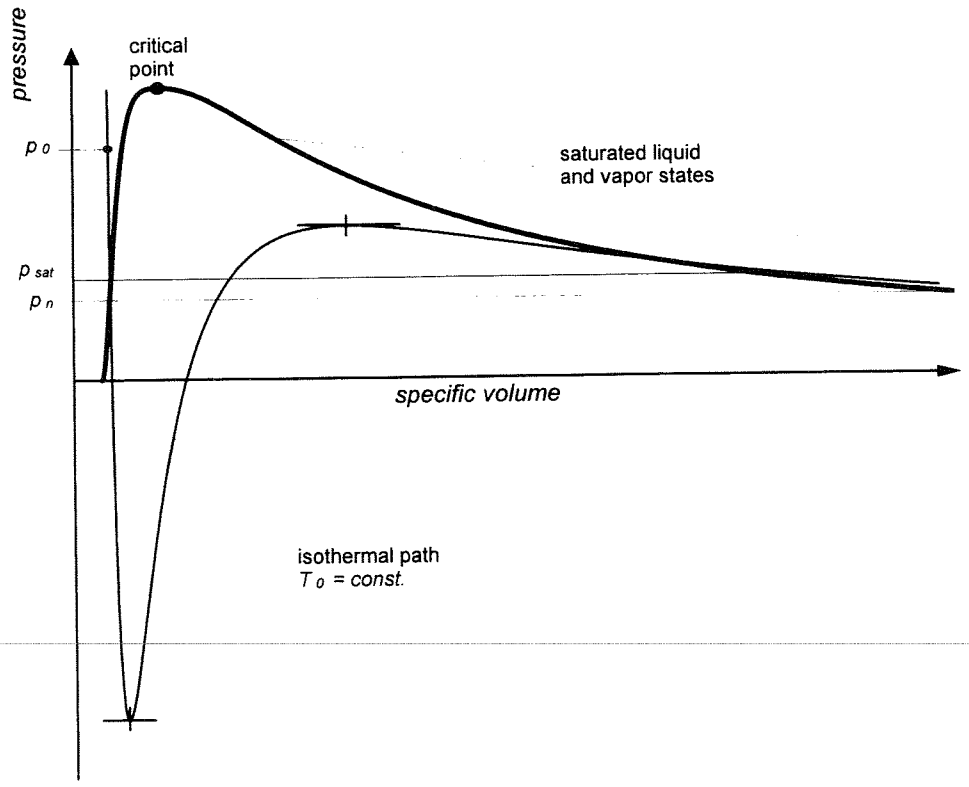

Fig. 3. Isothermal expansion process in the *p-v* diagram

3.2 Balance and Constitutive Equations

The singular pressure loss caused by the sudden contraction at the nozzle inlet is calculated applying the correlation of Kays, which includes the inlet acceleration term:

$$\Delta p_0 = (1+\zeta)\frac{\rho_{L,0}\, w_0^2}{2}, \tag{3}$$

where the inlet velocity w_0 is calculated according to the measured flow rate and $\zeta = 0.5$ is the head loss coefficient.

The quasi-one-dimensional conservation equations for steady-state flow are used in their entire form expressed below or in combination according to different assumptions:

- continuity-equation for the vapor phase:

$$\frac{d}{dz}(\alpha\, \rho_V\, w_V\, A) = \Gamma_V\, A, \tag{4}$$

- continuity equation for the liquid:

$$\frac{d}{dz}\left[(1-\alpha)\, \rho_L\, w_L\, A\right] = -\Gamma_V\, A, \tag{5}$$

- momentum equation for the vapor phase:

$$\frac{d}{dz}(\alpha\, \rho_V\, w_V^2\, A) + \alpha\, A\frac{dp}{dz} = \Gamma_V\, w_L\, A, \tag{6}$$

- momentum equation for the liquid:

$$\frac{d}{dz}\left[(1-\alpha)\, \rho_L\, w_L^2\, A\right] + (1-\alpha)\, A\frac{dp}{dz} = -\Gamma_V\, w_L\, A, \tag{7}$$

- energy equation for the mixture:

$$\frac{d}{dz}\left\{\left[\alpha\, \rho_V\, w_V\left(h_V + \frac{w_V^2}{2}\right) + (1-\alpha)\, \rho_L\, w_L\left(h_L + \frac{w_L^2}{2}\right)\right] A\right\} = 0. \tag{8}$$

The mixture density is given by:

$$\rho_M = \alpha\, \rho_V + (1-\alpha)\, \rho_L. \tag{9}$$

The governing set of equations can be reduced by one, if further homogeneous flow is assumed. This seems to be well founded for rapid expansion flows with flashing as there is not sufficient time to form substantial differences in phase velocities. Thermodynamic properties are calculated using the IFC-1967 formulation.

To determine the onset of flashing inception, the semi-empirical model of Alamgir and Lienhard [19] was used. Based on the heterogeneous nucleation theory, their correlation was developed to describe the static decompression undershoot during rapid decompression of water from long pipes:

$$p_n = p_{sat} - 0.252\,\frac{\sigma^{3/2}\,(T_0/T_c)^{13.73}}{1 - v_L/v_V}\left[\frac{1+14\,(dp/d\tau)^{0.8}}{k\, T_c}\right]^{1/2}, \tag{10}$$

with saturation specific volumes of vapor and liquid at initial temperature. Equation (10) correlates experimental data within a scope of $0.62 \le T_0/T_c \le 0.935$ and 400 MPa/s $\le dp/d\tau \le 1.803\cdot 10^5$ MPa/s. It is assumed that the formation of bubbles starts at locations where the calculated static pressure remains under the limiting pressure p_n.

For steady-state flow conditions the total change of pressure is equal to its convective change. Thus the following expression for the depressurization rate, utilizing mean values of velocity and first order rearward differences for the change in pressure, can be obtained:

$$\frac{dp}{d\tau} = \frac{\partial p}{\partial \tau} + w\frac{\partial p}{\partial z} \approx \overline{w}\frac{\Delta p}{\Delta z}.$$

Turbulence effects on pressure undershoot as proposed by Abuaf and Jones [20] were not taken into account, reflecting the reducing influence of convergent flow geometries on turbulent fluctuations.

According to Kolev [21] the rate of mass exchange from the liquid to the vapor phase for a two-phase flow without relative motion between vapor bubbles and surrounding liquid is given by

$$\Gamma_V = \rho'' N_B \frac{dV_B}{d\tau}. \tag{11}$$

The bubble number density was adopted from Wolfert [9] and was assumed to remain constant during flashing: $N_B \approx 5 \cdot 10^9\ m^{-3}$. Numerical simulation of bubble growth in superheated liquid was realized by applying the conduction-controlled heat-transfer model of Plesset and Zwick [22]:

$$\frac{dR_B}{d\tau} = \left(\frac{3a_L}{\pi}\right)^{1/2} Ja\,\tau_n^{-1/2}, \tag{12}$$

where the time of bubble growth τ_n is determined starting with the moment where the transition from single phase to two-phase flow occurs, i.e. the limiting pressure given by Eq. (10) is reached. The Jakob number is defined by

$$Ja = \frac{\rho_L c_{p,L}(T_L - T_{sat})}{\rho''(h'' - h')}. \tag{13}$$

The assumption of simultaneously generated spherical bubbles yields a relation between bubble radius and void fraction:

$$R_B = \left(\frac{3\alpha}{4\pi N_B}\right)^{1/3}. \tag{14}$$

The evaporation rate is obtained after integration of Eq. (12) and by introducing Eq. (14) into (11):

$$\Gamma_V = 24\left(\frac{3\alpha}{4\pi}\right)^{1/3} N_B^{2/3}\,\rho''\,Ja^2\,a_L. \tag{15}$$

3.3 Calculation Procedure

The above presented calculation model has been implemented in a computer program developed to check experimental data. Measured inlet stagnation conditions and mass flow rate are input parameters. The choice of thermal behavior is an option in the program.

The set of differential equations describing single and two-phase flow is integrated using a Runge-Kutta method of fourth order. The calculation procedure is terminated at points where the negative pressure gradient approached very large values. For critical flow conditions these points should coincide with the nozzle exit plane.

4. COMPARISON BETWEEN CALCULATION MODEL AND EXPERIMENTAL RESULTS

The calculation model has been set up with the main intention to recalculate experimental results and to give a simple tool to predict flow conditions for proceedings in experimental work with similar nozzle geometries.

The assumption of either thermal equilibrium or nonequilibrium strongly affects numerical simulation. If the expansion is assumed to occur in a thermal equilibrium manner, large void generation results in reaching critical conditions far in front of the exit plane. The consideration of departure from thermal equilibrium as proposed in section 3 leads to more reasonable results. The large negative pressure gradient appears in the vicinity of the nozzle throat as expected for critical flow conditions. Figure 4 illustrates these effects on the axial pressure profiles along the nozzle axis.

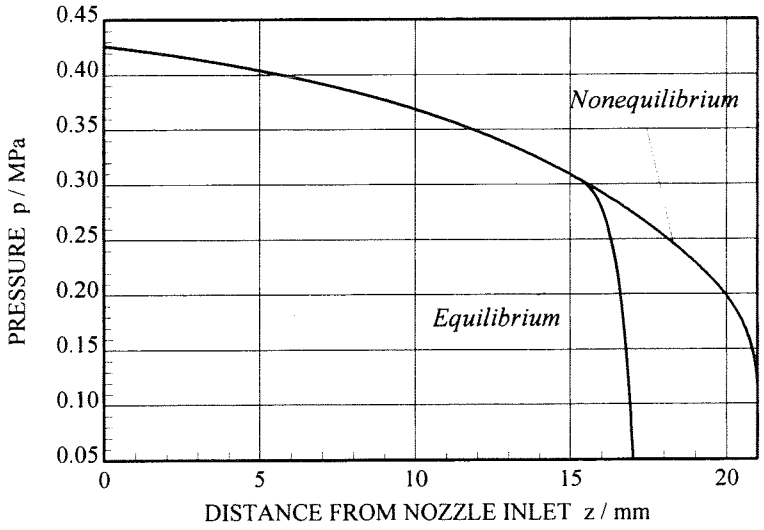

Fig. 4. Comparison between calculated pressure distributions, assuming thermal equilibrium and nonequilibrium; *R1*: $p_0 = 0.557$ MPa, $T_0 = 407.15$ K, $\dot{m}_{exp} = 0.38$ kg/s.

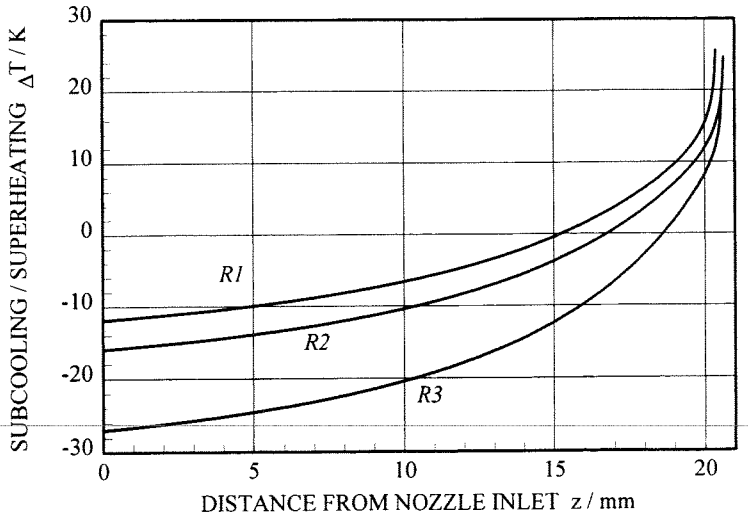

Fig. 5. Subcooling / superheating of liquid phase assuming thermal nonequilibrium; *R1*: $p_0 = 0.557$ MPa, $T_0 = 407.15$ K, $\dot{m}_{exp} = 0.38$ kg/s, *R2*: $p_0 = 0.565$ MPa, $T_0 = 403.15$ K, $\dot{m}_{exp} = 0.39$ kg/s, *R3*: $p_0 = 0.573$ MPa, $T_0 = 391.15$ K, $\dot{m}_{exp} = 0.42$ kg/s.

Figure 5 shows the calculated subcooling or superheating respectively of the liquid phase along the nozzle axis. With nearly equal pressures and increasing subcooling at the nozzle inlet the saturation temperatures are reached closer to the nozzle exit plane. The amount of superheating indicates the deviation from thermal equilibrium.

Figures 6 and 7 compare measured and calculated void fraction profiles. The large scatter in experimental void fraction data is supposed to be due to unavoidable fluctuations of inlet conditions.

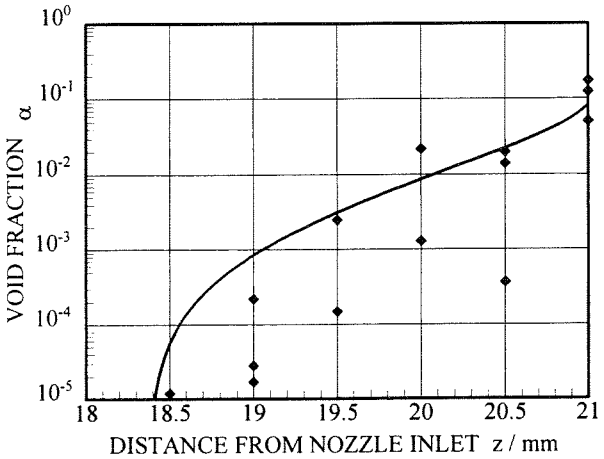

Fig. 6. Comparison between measured and calculated distributions of void fraction;
R1: $p_0 = 0.557$ MPa, $T_0 = 407.15$ K, $\dot{m}_{exp} = 0.38$ kg/s.

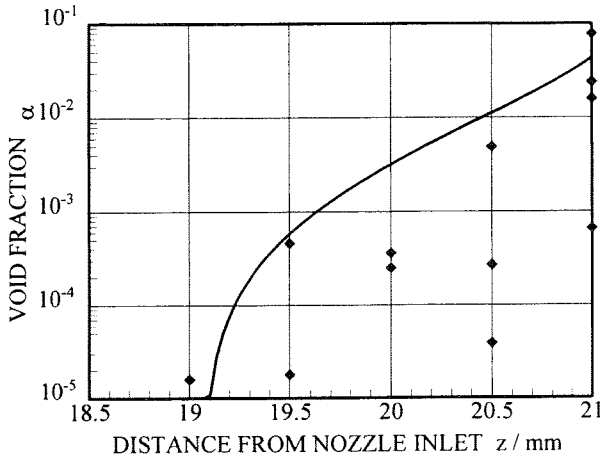

Fig. 7. Comparison between measured and calculated distributions of void fraction;
R2: $p_0 = 0.565$ MPa, $T_0 = 403.15$ K, $\dot{m}_{exp} = 0.39$ kg/s.

Locations of flashing inception are displaced closer to the nozzle exit with increasing subcooling at the nozzle inlet which leads to lower void fractions at the nozzle throat and thus higher flow rates.

5. CONCLUSION

The critical discharge of initially subcooled hot water through a nozzle has been studied utilizing the resistivity-probe technique to measure local void fractions.

The quasi-one-dimensional, steady-state model used to recalculate experiments is based on a set of balance equations for phases and mixture and implies the bubble growth model of Plesset and Zwick. It considers nucleation delay according to the pressure undershoot model of Alamgir and Lienhard. Further a constant bubble number density has been chosen to match calculated void fraction distributions with measured data.

As the number of experiments is too small to derive quantitative relations, further experiments are planned on a new test section with improved instrumentation and data acquisition. Temperatures are measured with resistance temperature detectors. Inlet and nozzle back pressures are read on piezoresistive transducers. The flow rate is measured with a electromagnetic flowmeter. Furthermore the test section is equipped with a sight glass armature, wherein interchangeable nozzles can be mounted and the discharged two-phase jet can be observed.

ACKNOWLEDGEMENT

Most of the above presented experiments were conducted and evaluated by Dr. P. Röllig [23]. Our recent work is financially supported by the Deutsche Forschungsgemeinschaft under research contract Di 485/2-3.

NOMENCLATURE

Latin symbols

A	m^2	cross-sectional area
a	$m^2\ s^{-1}$	thermal diffusivity
c	$J\ kg^{-1}\ K^{-1}$	specific heat
h	$J\ kg^{-1}$	specific enthalpy
Ja	-	Jakob number
k	$J\ K^{-1}$	Boltzmann constant
$\dot{m}$	$kg\ s^{-1}$	mass flow rate
N	m^{-3}	number density
p	Pa	pressure
R	m	radius
T	K	temperature
v	$m^3\ kg^{-1}$	specific volume
V	m^{-3}	volume
w	$m\ s^{-1}$	z-direction velocity
z	m	axial coordinate

Greek symbols

α	-	void fraction
Γ	$kg\ m^{-3}\ s^{-1}$	rate of mass exchange
ρ	$kg\ m^{-3}$	density
σ	$N\ m^{-1}$	surface tension
τ	s	time
ζ	-	head loss coefficient

Subscripts

0	initial / inlet values
B	bubble
c	critical state
exp	experimental
i	index
L	liquid
M	mixture
n	nucleation
p	at constant pressure
sat	saturation conditions
tot	total
V	vapor / evaporation

Superscripts

$'$	saturated liquid
$''$	saturated vapor
$*$	critical flow
$\bar{}$	average

REFERENCES

[1] G.B. Wallis: "One-Dimensional Two-Phase Flow", McGraw-Hill, New York (1969).

[2] F.J. Moody: "Maximum Two-Phase Vessel Blowdown from Pipes", in: Trans. ASME, J. Heat Transfer, Vol.88, p.285 (1966).

[3] R.E. Henry, H.K. Fauske, and S.T. McComas: "Two-Phase Critical Flow at Low Qualities Part I - Experimental", in: Nucl. Sci. Engng., 41, p.79 (1970).

[4] R.E. Henry, H.K. Fauske, and S.T. McComas: "Two-Phase Critical Flow at Low Qualities Part II - Analysis", in: Nucl. Sci. Engng., 41, p.92 (1970).

[5] R.E. Henry and H.K. Fauske: "The Two-Phase Critical Flow of One-Component Mixtures in Nozzles, Orifices, and Short Tubes", in: Trans. ASME, J. Heat Transfer, Vol.95, p.179 (1971).

[6] G.L. Sozzi and W.A. Sutherland: "Critical Flow of Saturated and Subcooled Water at High Pressure", in: ASME Non-Equilibrium Two-Phase Flows Symp., p.19 (1975).

[7] V.E. Schrock, E.S. Starkman, and R.A. Brown: "Flashing Flow of Initially Subcooled Water in Convergent-Divergent Nozzles", in: Trans. ASME, J. Heat Transfer, Vol.99, p.263 (1977).

[8] A.R. Edwards: "Conduction Controlled Flashing of a Fluid and the Prediction of Critical Flow Rates in a One-dimensional System", UKAEA, Health & Safety Branch, R147, (1968).

[9] K. Wolfert, M.J. Burwell, and D. Enix: "Non-Equilibrium Mass Transfer Between Liquid and Vapour Phases During Depressurization Processes", in: Second CSNI Specialists Meeting on Transient Two-Phase Flow, Paris (1978).

[10] J.R. Riznic and M. Ishii: "Bubble Number Density and Vapor Generation in Flashing Flow", in: Int. J. Heat Mass Transfer, Vol.32, No.10, p.1821 (1989).

[11] T.S. Shin and O.C. Jones: "Nucleation and Flashing in Nozzles - 1, A Distributed Nucleation Model", in: Int. J. Multiphase Flow, Vol.19, No.6, p.943 (1993).

[12] V.N. Blinkov, O.C. Jones, and B.I. Nigmatulin: "Nucleation and Flashing in Nozzles - 2, Comparison with Experiments Using a Five-Equation Model for Vapor Void Development", in: Int. J. Multiphase Flow, Vol.19, No.6, p.965 (1993).

[13] G.B. Wallis: "Critical Two-Phase Flow", in: Int. J. Multiphase Flow, Vol.6, p.97 (1980).

[14] A.E. Bergles, J.G. Collier, J.M. Delhaye, G.F. Hewitt, and F. Mayinger: "Two-Phase Flow and Heat Transfer in the Power and Process Industries", Hemisphere Publishing Corporation (1981).

[15] S.T. Revankar and M. Ishii: "Theory and Measurement of Local Interfacial Area Using a Four Sensor Probe in Two-Phase Flow", in: Int. J. Heat Mass Transfer, Vol.36, No.12, p.2997 (1993).

[16] S. Kalkach-Navarro, R.T. Lahey Jr., D.A. Drew, and R. Meyder: "Interfacial Area Density, Mean Radius and Number Density Measurements in Bubbly Two-Phase Flow", in: Nuclear Engineering and Design, 142, p.341 (1993).

[17] T. Kobori and M. Terada: "Application of Needle Contact Probe to Blow-down Test", in: Second CSNI Specialists Meeting on Transient Two-Phase Flow, Paris (1978).

[18] J.G. Burnell: "Flow of Boiling Water Through Nozzles, Orifices and Pipes", in: Engineering, Vol.164, p.572 (1947).

[19] Md. Alamgir and J.H. Lienhard: "Correlation of Pressure Undershoot During Hot-Water Depressurization", in: Trans. ASME, J. Heat Transfer, Vol.103, p.52 (1981).

[20] N. Abuaf, O.C. Jones Jr., and B.J.C. Wu: "Critical Flashing Flows in Nozzles With Subcooled Inlet Conditions", in: Trans. ASME, J. Heat Transfer, Vol.105, p.379 (1983).

[21] N.I. Kolev: "Transiente Zweiphasen-Strömung", Springer-Verlag, Berlin (1986).

[22] M.S. Plesset and S.A. Zwick: "The Growth of Vapor Bubbles in Superheated Liquids", in: J. Appl. Phys., Vol.25, p.474 (1954).

[23] P. Röllig: "Untersuchungen zum Zustandsverhalten schnell expandierender bzw. kritischer Einkomponenten-Zweiphasenströmungen (flüssig/gasförmig)", Diss., TU Dresden, Dresden (1992).

CAVITATION IN CENTRIFUGAL PUMPS

G. Kosyna[1], M. Oldenburg[2], V. Schütte[2], and A. Dreiß[1]

[1] Pfleiderer-Institut für Strömungsmaschinen
Technische Universität Braunschweig
Langer Kamp 6, D-38106 Braunschweig, Germany

[2] Institut für Strömungsmaschinen
Technische Universität Magdeburg
Universitätsplatz 2, D-39106 Magdeburg, Germany

ABSTRACT

The subject of this paper are experimental and theoretical investigations of the cavitation in centrifugal pumps. For the present, two-dimensional conditions for the streamflow are considered (cylindrical blades). Bubble-cavities in the impeller inlet and the leading edge cavities on the blades are mathematically modeled and experimentally verified.

The calculation of bubble-cavities is carried out by integrating the Raleigh-Plesset-equation along the streamlines of the inviscous mixture. The development of fixed cavities attached at the leading edge of the blades is determined by means of analogous integral method for film-boiling. To determine the effects in the wake at the end of the fixed cavities, the notional spherical cavity concept is used.

The experimental investigations are concentrated on the visual analysis of the cavity, the instationary pressure measurements along the blades and on the behaviour of the pump by decreasing NPSH-values. Eventually different impellers are used to prove the calculation method, particularly to precalculate the $NPSH_R$ - value (decrease of head by 3%).

NOTE: *This paper had not been received before the Proceedings were assembled. If received on or before August 23, 1994, handouts will be given to each participant of the Symposium.*

FLOW VISUALIZATION IN A CAVITATING FLOW

M. Dues[1], A. Gebhardt[2], S. Kallweit[1], T. Scheffler[1], H. Siekmann[1], T. Uchiyama[3]

[1]Technical University, Berlin, Institute of Hydraulic Turbomachinery and Fluid Mechanics
Straße des 17. Juni, 10623 Berlin, Federal Republic of Germany
Telephone: (030) 314 25262, Facsimile: (030) 314 21472

[2]Laser Bearbeitungs- und Beratungszentrum NRW GmbH (LBBZ)
Steinbachstraße 15, 52074 Aachen, Federal Republic of Germany
Telephone: (0241) 8906 417, Facsimile: (0241) 8906 280

[3]Nagoya University, School of Informatics and Sciences
Furo-Cho, Chikusa-Ku, Nagoya 464-01, Japan
Telephone: (0081) 52 781 5111, Facsimile: (0081) 52 782 9793

ABSTRACT

Cavitation is known as one of damaging phenomena in hydraulic turbomachinery and hydraulic apparatus. One aim of the hydraulic design is to avoid or to minimize cavitation. On the other hand, cavitation has a possibility to be utilized for water purification by separating volatile ingredients from the water in a generated cavitating area. The production of cavitating regions in water flows is therefore of specific interest for this purification technique.

For investigating possible solutions of the generation of cavitating areas some experimental methods are introduced. The laser-Doppler velocimetry (LDV) as a pointwise measuring technique disregards the unsteady flow behaviour near the cavitating area. Whole flow field measurements with the LDV-technique show only their periodic unsteady behaviour. By combining the laser light sheet method with digital image processing techniques a qualitative view on the unsteady flow field near multiphase flows is obtainable. With a pulsed laser light sheet and an analog or digital evaluation of the acquired picture, the flow velocity vectors are obtained. In this paper, these techniques are used for a comparison of the cavitating flow field produced by two devices: static guide vanes and rotating impeller blades.

1. INTRODUCTION

Since the worldwide consumption of water is growing steadily, the development of new technologies of water purification is much demanded.

One method to separate volatile ingredients from water utilizes the different volatilities of the mixture components. This is done by the controlled production of cavitating areas wherein the volatile ingredients enriches themselves [1]. A purification, for example of water polluted by chlorinated hydrocarbons, is possible by extracting the generated vapour [2]. The realization of cavitating areas with a minimum loss of energy is described in [3], where different cavitation generators were examined using LDV and high speed photography. However, the LDV results describe only the periodic unsteady behaviour of the flow near the cavitating area, whereas the high speed photography gives only a qualitative view of the flow field.

In this contribution experimental investigation techniques, which are able to measure the unsteady whole flow field qualitatively and quantitatively, are applied to a multiphase flow test facility.

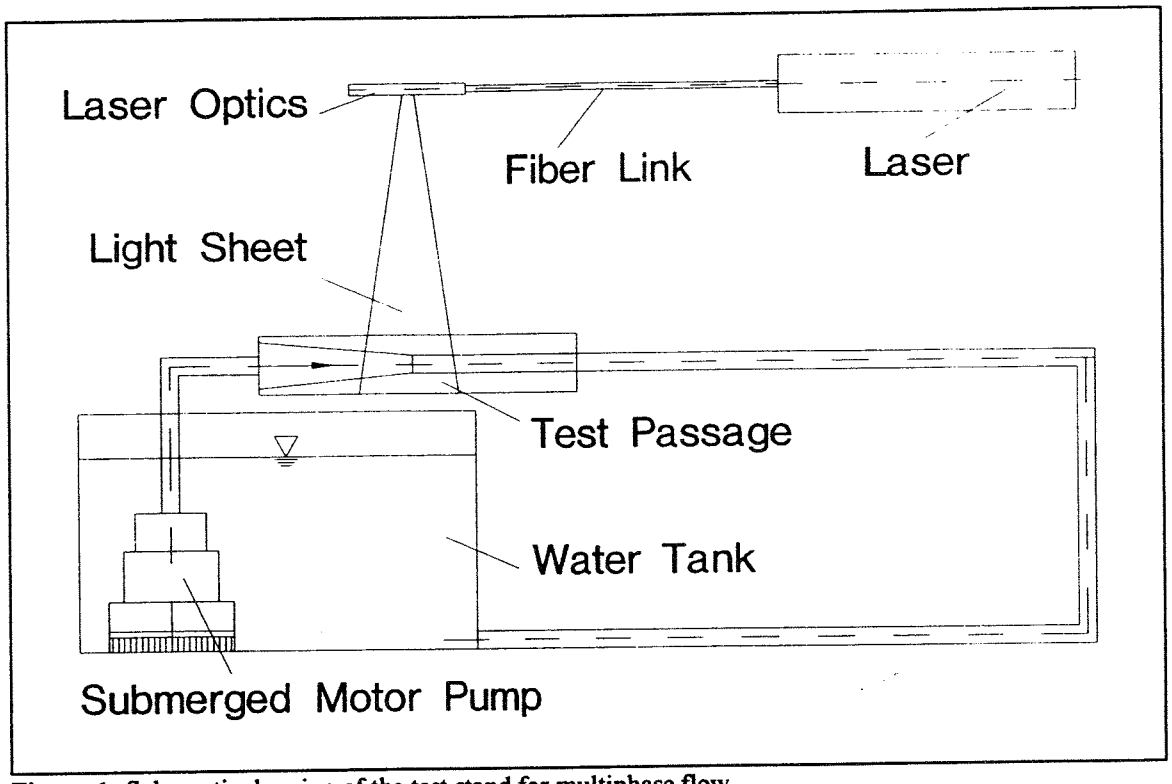

Figure 1: Schematic drawing of the test stand for multiphase flow

2 EXPERIMENTAL SETUP

2.1 Test Stand

The test stand (**figure 1**) is a water loop consisting of a test passage, a water tank with a submerged motor pump and a pipe system which connects these two parts. The whole test stand is made of PVC. The pressure of the system is equal to the ambient pressure. The test passage is shown in detail in **figure 2**. The water flows from the left through a test section which is shaped as a nozzle and is made of transparent Acrylic glass,

to the right of the test passage. The submerged motor pump produces a water single phase flow through the nozzle in the test section. In order to generate a multiphase flow, a small motor at the beginning of the test passage drives an impeller in the test passage upstream of the

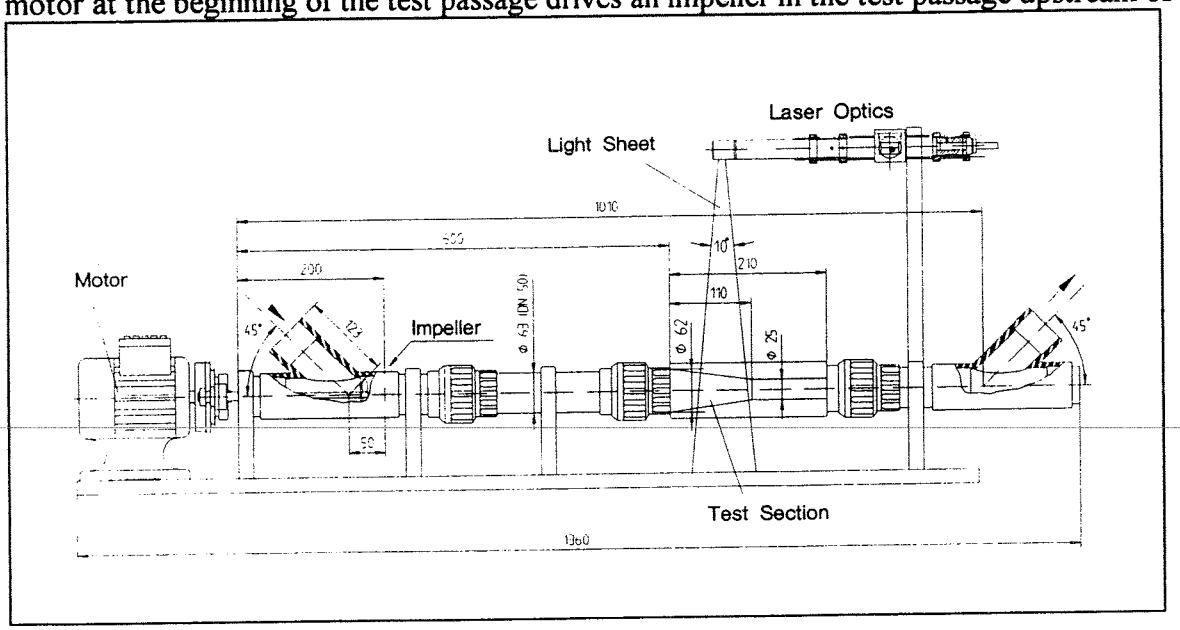

Figure 2: Test passage of the test stand for multiphase flow

test section. This impeller has two blades and produces high circumferential velocity components which lead to a multiphase flow in the test section.

The other possibility to produce cavitation is the use of static guide vanes as a cavitation generator (**figure 3**), which can be mounted in the beginning of the nozzle. The seven static guide vanes turn the flow from 0° to 80° in circumferential direction. By using the technique of rapid prototyping the cavitation generator is made of stereo lithographic resin.

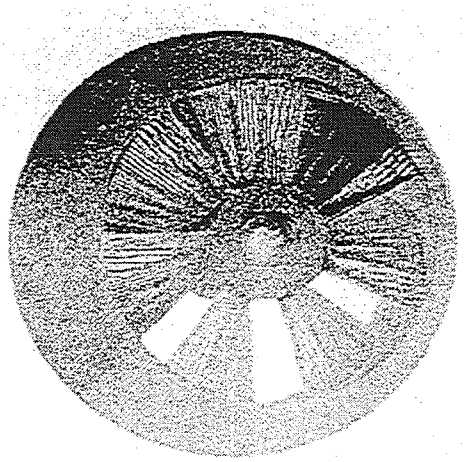

Figure 3: Cavitation Generator

The test section can be investigated by using a thin laser light sheet. Small particles which are added to the flow scatter the laser light back and are used to visualize the flow field near the cavitating area. The laser light sheet can be adjusted in the axial direction to visualize the axial and circumferential velocity components or in an radial orientation to visualize the circumferential and radial velocity components in the laser light plane.

2.2 Laser Optics

The laser light, used for flow visualization, is produced by a two watt output power Argon laser. By coupling the laser light into a fiber link a very flexible positioning of the laser light sheet plane is realized. At the end of the single mode fiber link are two possibilities to illuminate the flow with the laser light:

The first possibility is the use of the continuous wave laser light. A light sheet optic generates a continuous light plane with an angle of 15° and a thickness of about 1 mm by using a decoupling optic and a cylinder lens. This method allows the visualization of the trajectories of the tracer particles in the investigated light plane. The trajectories can be evaluated by combining this method with digital image processing techniques.

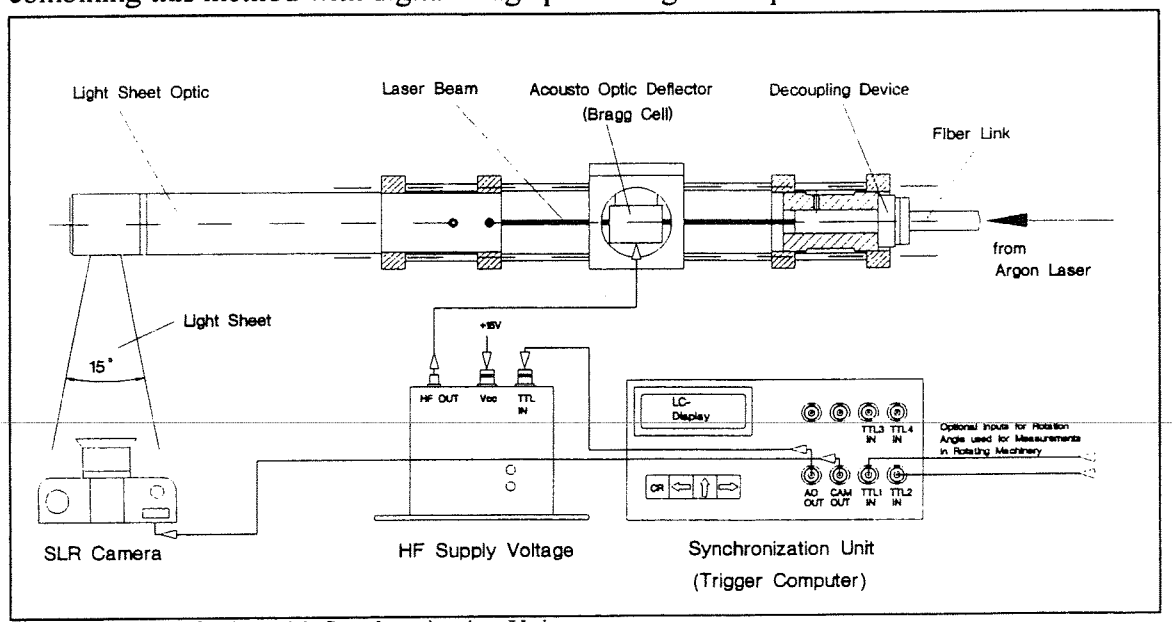

Figure 4: Laser Optics with Synchronization Unit

The other possibility is to pulse the laser beam in order to produce a pulsed light sheet. This pulsed light sheet generates multiple pictures of one tracer particle at different locations in the flow. These pictures can be used by correlation techniques to produce a quantitative flow field. **Figure 4** shows the laser optics. The laser beam is decoupled from the fiber link and is pulsed by an acousto optic deflector (Bragg cell). This deflector is controlled by a function generator which produces TTL-pulses with the possibility of using varying time delay between the pulses and a varying length of the pulses. The variation of the pulse timing is necessary to investigate flow fields with a wide range of velocities. A function generator is often not as variable as required by these pulsing techniques. Therefore special equipment like a synchronization unit (trigger computer) is developed to allow a wider variation of the pulse timing. This trigger computer based on a digital signal processor controls the time between the pulses, the number of pulses and the start of the first pulse and is especially needed for the application in hydraulic turbomachinery.

2.3 Image Acquisition

A CCD camera with a high light-sensitivity takes pictures of the illuminated tracer particles in the light plane. With a frame grabber based on a personal computer the pictures are digitized in a resolution of 786x576 in interlaced mode or 384x256 in non-interlaced mode by quantization with 8 bit (256 grey levels). The low resolution in the non-interlaced mode reduces the resolution of obtainable velocity vectors in the case of the pulsed light sheet. When the continous light sheet is used, the electronic shutter of the CCD camera is adjusted so that parts of the flow trajectories are produced. The CCD camera is placed in front of the test section in the case of an axial arrangement of the light sheet plane. The obtained images of the flow can be processed with the PC or with a transputer based parallel computing device.

3. MEASURING TECHNIQUES

3.1 Trajectory Recognition

The combination of the laser light sheet method with digital processing techniques allows a fast qualitative view on the flow field. The digitized image obtained by the continuous light sheet plane shows parts of the tracer particle trajectories. The length of the trajectories depends on the time the electronic shutter of the CCD camera was left open. With use of special filtering techniques like binomial Laplacian, Laplacian-of-Gaussian and anisotropic diffusion [4], these trajectories are enhanced. A thresholding operation binarizes the trajectories after enhancing the image. On the binarized image a tracking algorithm, which combines the trajectories, produces a direction field of the flow. By taking the shutter time into account a quantitative result is possible, but due to the inaccuracy of the video time base, the produced flow field is investigated only in a qualitative matter. The binarization is also possible with the aid of a neural network [5], which is moved pixel by pixel across the whole picture and detects parts of the trajectories. This net has a multi layer perceptron architecture and is trained by the common backpropagation algorithm [6]. The net consists for its minimal performance of 16 neurons in the input layer, 8 neurons in the hidden layer and 16 neurons in the output layer. In the training phase the net is trained with typical trajectory patterns obtained from former light sheet pictures. The net learns how to map these patterns onto binary templates [7]. Afterwards, in the recall phase, the net is able to recognize new trajectories and to produce a binarized picture which is transformed in a direction field using the tracking algorithm. A parallel computing device based on T800-Transputers is used to decrease the interrogation time. The algorithms for enhancing the picture, recognizing the trajectories and tracking, work all in the spatial domain on local data, so that they can be parallelized easily.

3.2 Particle Image Velocimetry (PIV)

The whole flow field showing unsteady behaviour can be investigated by the particle image velocimetry. It is useful to distinguish between two steps of PIV measurements [8]:

- data acquisition and
- data evaluation.

For the data aquisition the laser light sheet is pulsed as described in section 2.2. An analog single lens reflex camera (SLR) takes pictures of the illuminated tracer particles in the light plane. The common technique uses only two pulses with an adjustable time between them during the exposure time of the camera. The pulsing time is variable and depends on the mean velocity of the flow. The image shows two times the same tracer particle shifted by a time and velocity dependent distance. With use of the distance and the pulse frequency the velocity vector in a small interrogation region can be calculated. The distance between the two pictures of the tracer particles can be obtained by tracking [9] or correlation [10] methods. From a number of about 10-15 particles for each interrogation spot, the use of correlation methods is advisable [11]. The location of the side peaks of the two dimensional autocorrelation function defines the mean distance in the interrogation area. There are several methods to calculate the two dimensional autocorrelation function (ACF) of the analog film material. One uses the Wiener-Khintchine [12] theorem by transforming the interrogation spots in the frequency domain using the two dimensional Fast Fourier Transform (FFT). The square of the amplitudes in the frequency domain is then transformed back into the spatial domain using an inverse FFT. This finally produces the ACF. By a clipping algorithm the side peaks of the ACF can be found. The whole procedure can be numerically calculated by digitizing or scanning the analog film material. However, the Fourier Transform (FT) of the interesting region is also obtainable by optical methods. **Figure 5** shows the PIV evaluation device [13] which carries out the first FT in real time by using a laser light beam of the same diameter like the interrogation area. The produced Youngs' fringes are orientated vertical to the mean direction of the flow and the distance of the fringes is anti-proportional to the mean distance in the interrogation spot. These fringes are digitized and the second FT, including the clipping, is done numerically in a common PC. The data evaluation of a common 24x36 mm film material with a distance of 0.5 mm between each interrogation spot needs on a normal PC about nine hours. The combination of the PC and the parallel computing device would speed up the procedure by a factor of about three and will be done in the near future.

Another method (multiple exposure) uses a multiple pulsed laser beam [14]. The image with several pictures of each tracer particle is also evaluated by the described method. The difference is, that after the calculation of the ACF, side peaks of higher order must be suppressed by the clipping algorithm. Only the side peak which lies next to the main peak of the ACF has to be taken into account.

3.3 Digital Particle Image Velocimetry (DPIV)

The analog PIV has the disadvantage that the film material has to be developed before evaluation. However, the optical restrictions to produce PIV images which are evaluable are evident. For generating detectable Youngs' fringes the diameters of the particle pictures on the film material have to be in the range of 20 μm. The mean distance between them has to be adjusted to about 200 μm with use of the variable pulsing frequency of the laser light sheet in the data acquisition phase. The need to minimize the time between data acquisition and evaluation and the control of the described optical parameters during the measurement, suggests the use of CCD cameras in combination with a digital image processing system. The spatial resolution and the quantization of the flow velocity and flow angle of the obtained vector field depend on the resolution of the CCD camera and on the computer system which

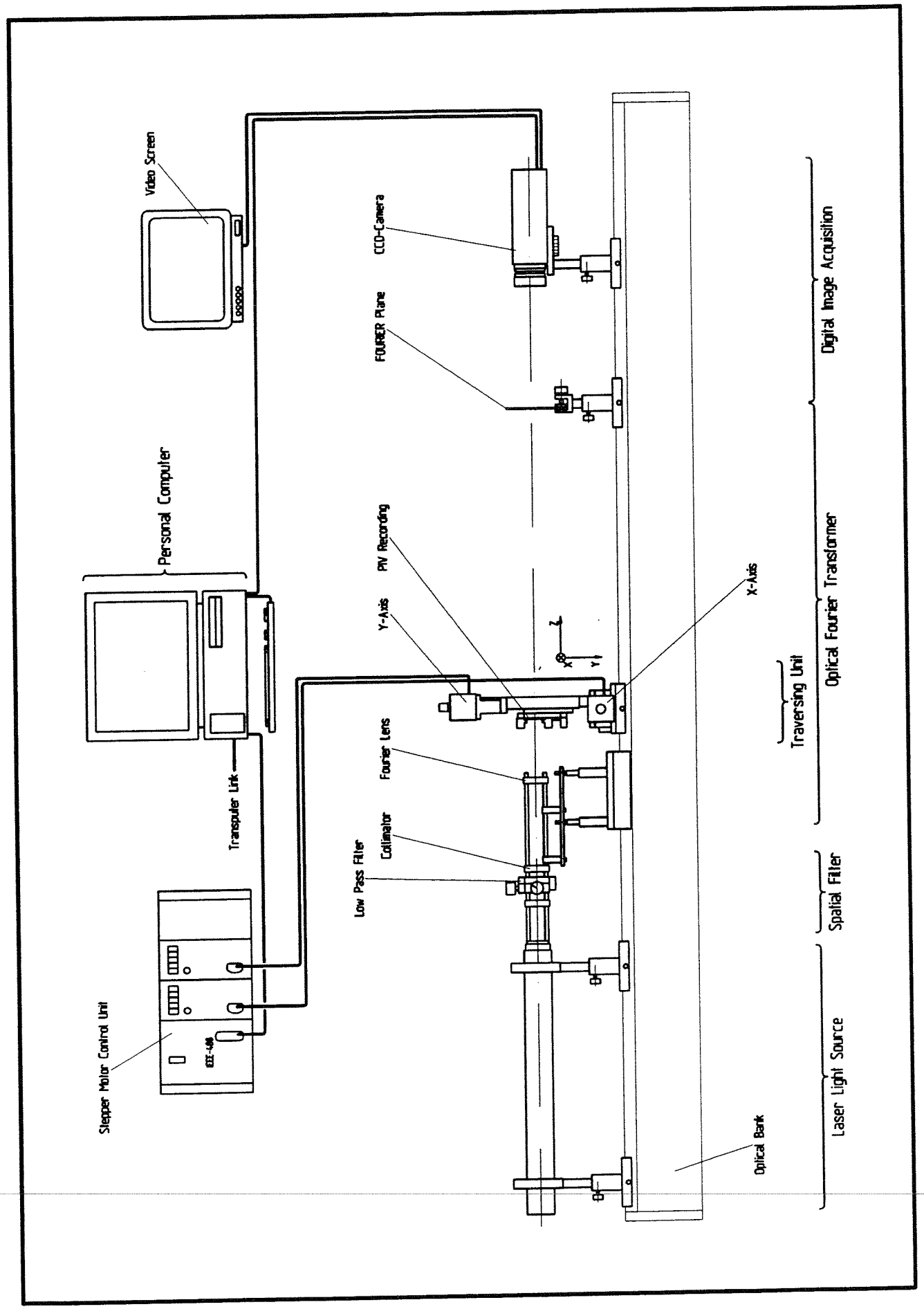

Figure 5: PIV Evaluation Device

has to calculate each interrogation spot. A standard low resolution camera produces only a small amount of velocity vectors where its quantization follows from the resolution of the interrogation spot [15]. CCD cameras with the highest possible number of pixels, at this time 2048x2048 pixels, show half the resolution of a high light-sensitivity analog film. The CCD camera used in the following investigations has a resolution of 768x576 pixels. In non-interlaced mode the used multiple pulse illuminated pictures have a low resolution of 384x256 pixels and produce by a minimum interrogation spot extent of 32x32 pixels only 12x8 vectors or with half overlapping 24x16 vectors.

4. RESULTS

For the qualitative investigations of the flow field near the cavitation region tracer particles with a diameter of about 50 μm and a density of 1.002 g/l are used. The shutter time is adjusted to 1/125 s and the f#-number to 2.8. The light sheet is fixed in a distance of 1.5 mm out of the center of the nozzle. This is done to reduce the light reflection from the cavitation area. If the light sheet is adjusted in the center of the tube, the backscattered light from the cavitating area is brighter than the backscattered light of the tracer particles.

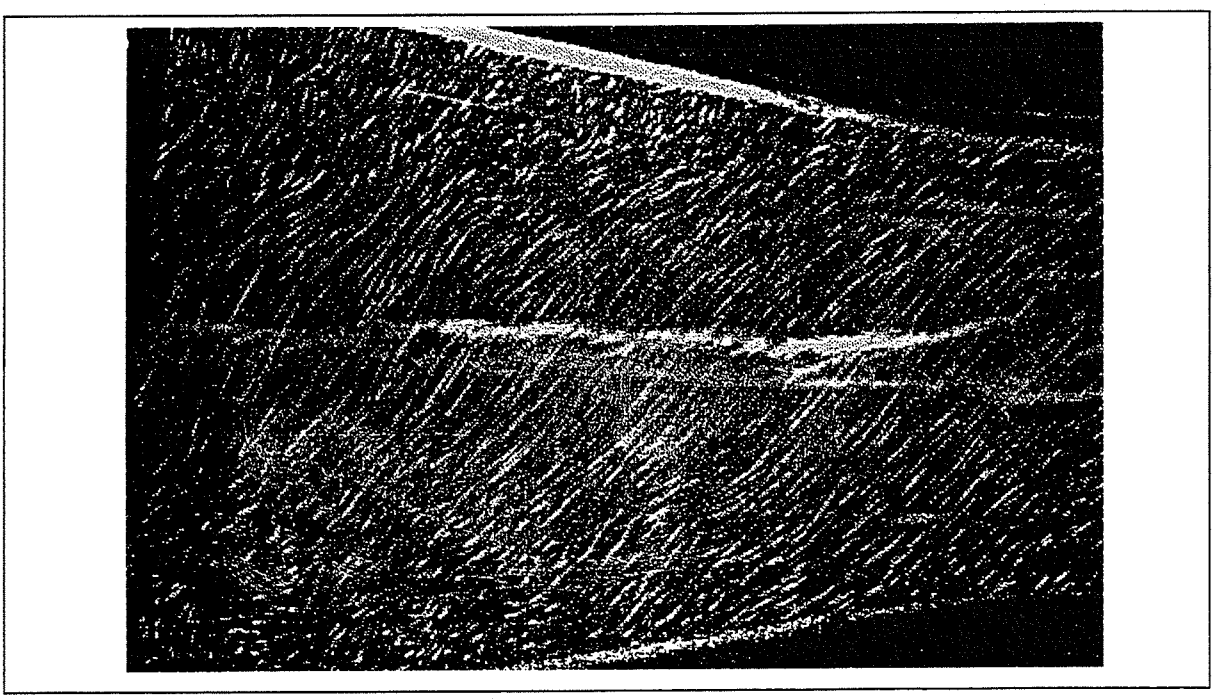

Figure 6: Flow Field behind the Cavitation Generator

Figure 6 shows the flow field in the region of the nozzle behind the cavitation generator. High circumferential velocity components are detectable in the inner region of the nozzle. The flow angle in this region is about 20° against the circumferential direction and the pathlines show a regular behaviour. In the outer regions near the wall of the nozzle the flow is much disturbed. In this region a geometric problem between the plane light sheet and the curved nozzle arises. Caused by the circumferential velocity components in this region the pathlines leave the light plane and only the small points of tracers who enter or leave the light plane are detectable. The pathlines near the cavitating area produced by the rotating impeller (**figure 7**) are more regular compared to the near region of the flow behind the cavitation generator. In the inner region of the nozzle the flow angle in **figure 7** is about 40° and in the outer regions higher axial components are detectable compared with **figure 6**. The larger flow angle is a result of the high axial velocity component produced by the impeller. Due to the long distance between the impeller and the nozzle, the high circumferential component near the wall is reduced by friction.

impeller and the nozzle, the high circumferential component near the wall is reduced by friction.

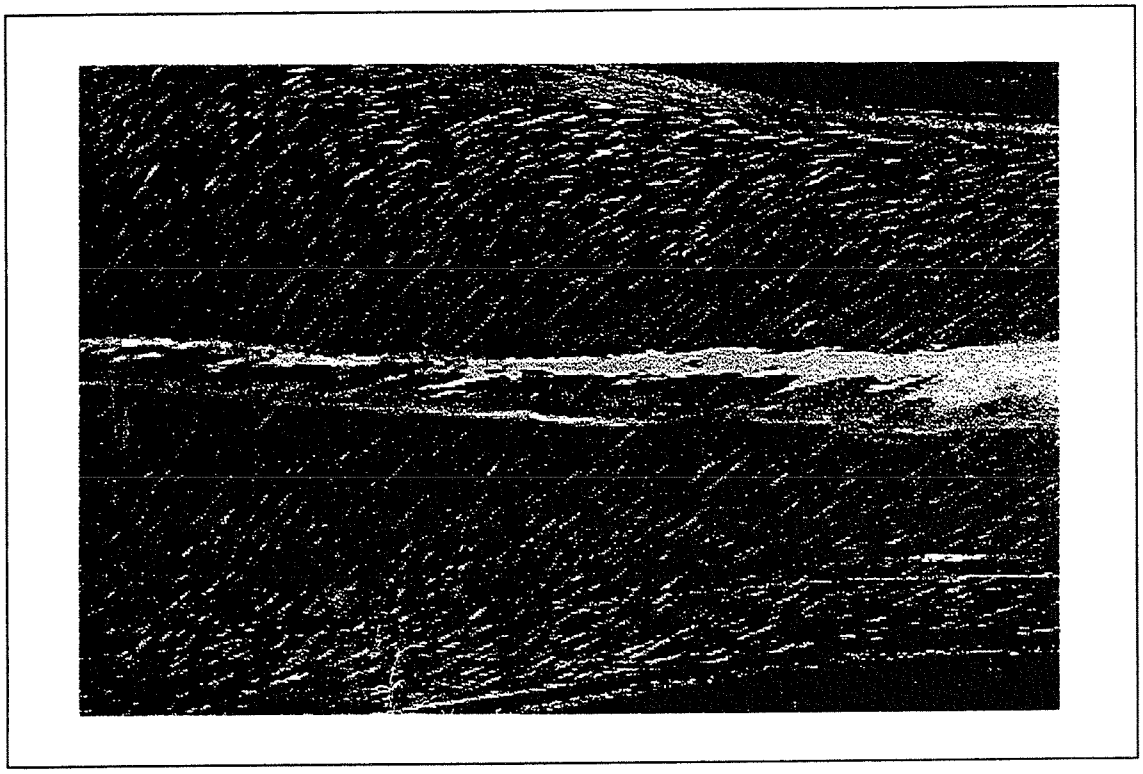

Figure 7: Flow Field in the Nozzle produced by the Impeller

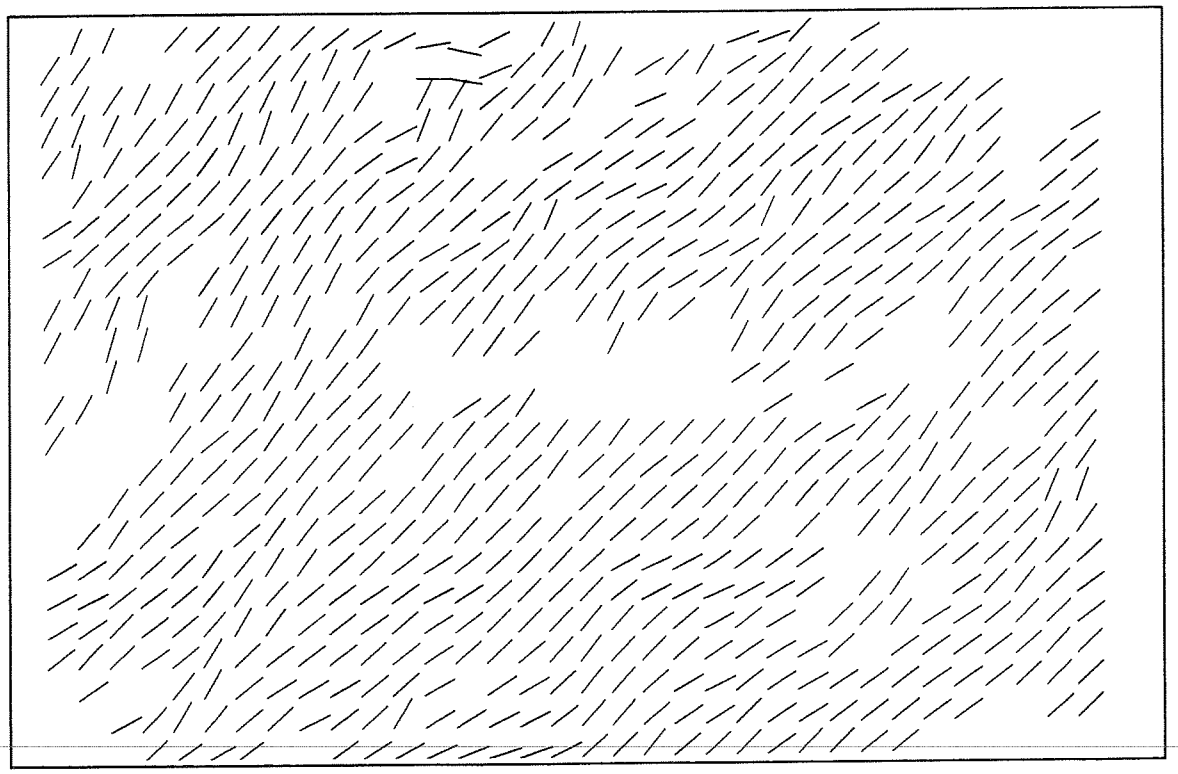

Figure 8: Direction Field of the Flow in Figure 6

Figure 8 shows the direction field of the flow in **figure 6**. The recognized and tracked trajectory parts are placed on an equidistant grid. As described for **figure 6** the regular flow in the inner region and the higher turbulent flow in the outer region is obvious. This leads to a strong unsteady behaviour of the vapour area. The direction field of **figure 7** is shown by

figure 9. The whole flow field is more regular than the one obtained by the cavitation generator and as a result the unsteady behaviour of this cavitating area is not so strong.

A comparison of the spatial extent of the two cavitation areas is possible with **figure 10** and **figure 11**. The cavitating region behind the cavitation generator (**figure 10**) is shaped irregular. The beginning is characterized of an unsteady fluctuating movement of the cavitating region.

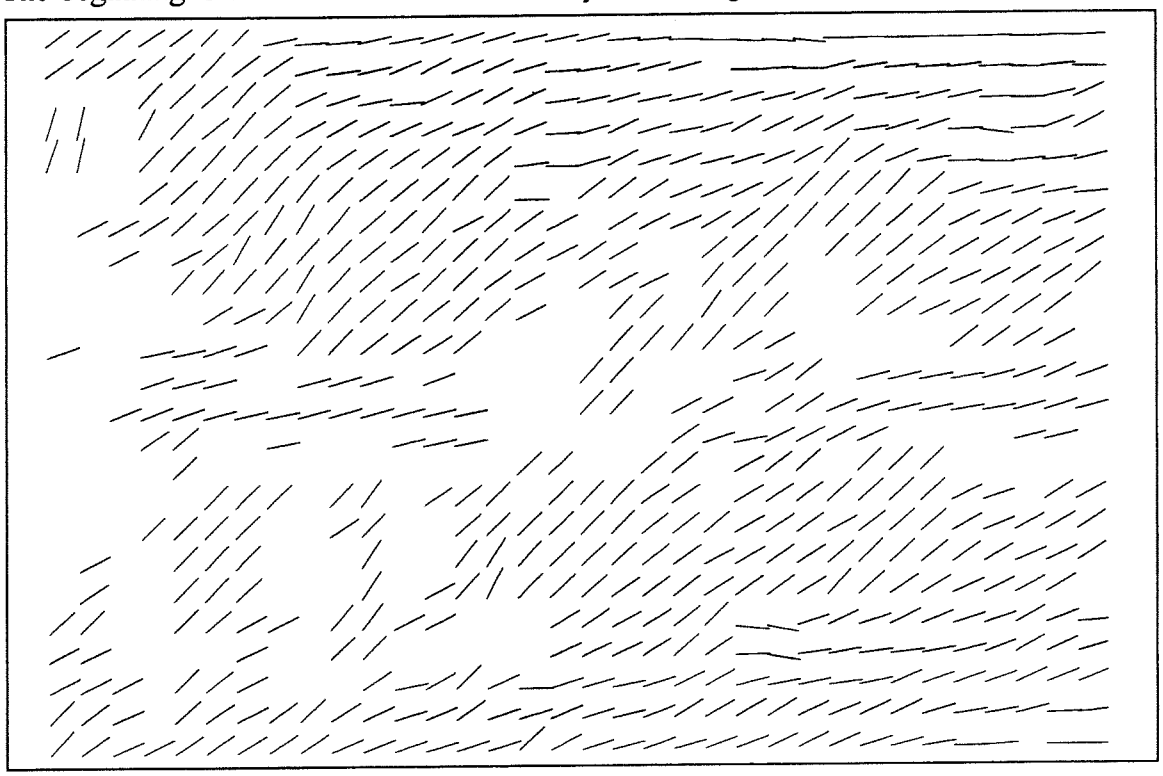

Figure 9: Direction Field of Figure 7

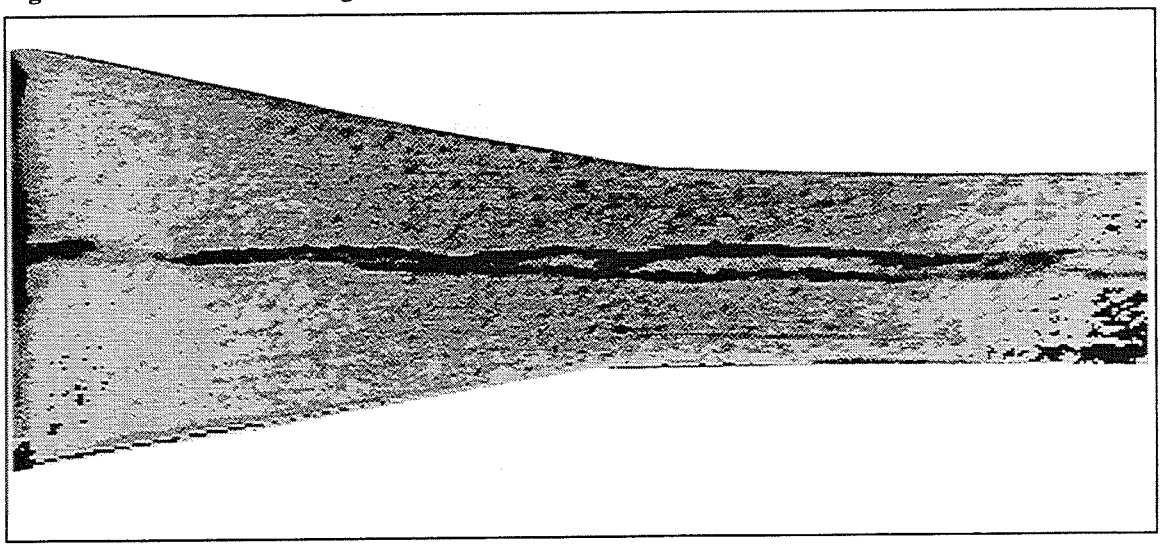

Figure 10: Spatial Extent of the Cavitating Area produced by the Cavitation Generator

Behind the nozzle the flow is homogenized and the unsteady behaviour is attenuated. The cavitating region produced by the impeller is shaped more regular and the unsteadiness is much lower (**figure 11**). The spatial extent of the vapour region behind the nozzle is bigger compared to the same area produced by the cavitation generator.

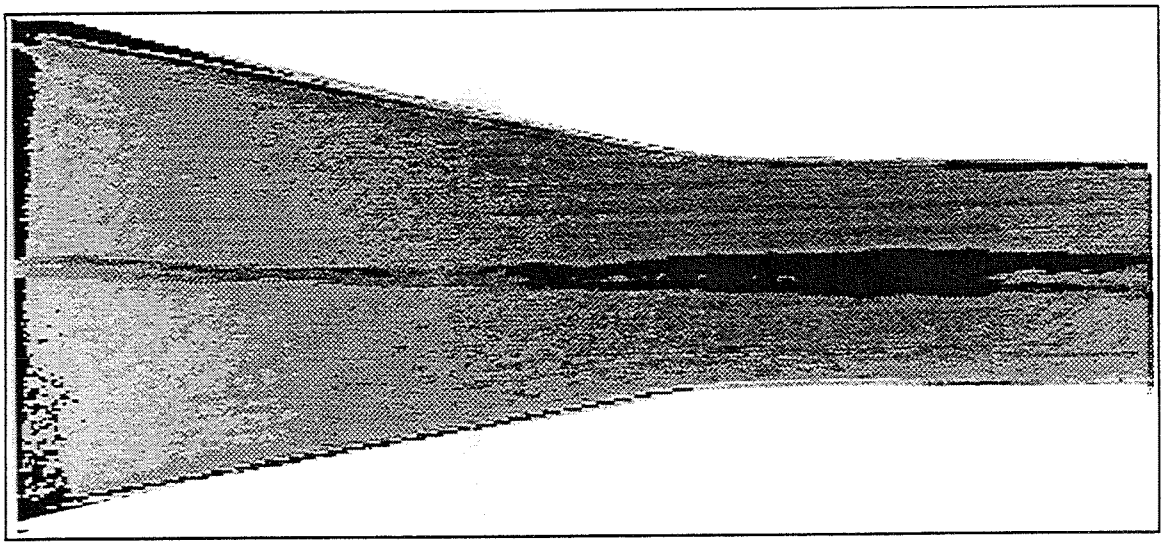

Figure 11: Spatial Extent of the Cavitating Area produced by the Impeller

Figure 12 is a PIV-measurement of the flow through the nozzle without cavitation. The measurement was done to check the parameters for the latter measuring of the flow field produced by the cavitation generator. By using the analog PIV-technique **figure 13** was obtained.
The effects of a regular flow in the inner region is also shown by the quantitative flow field. The unsteadiness in the near of the nozzle wall leads to fluctuating velocity vectors and in that

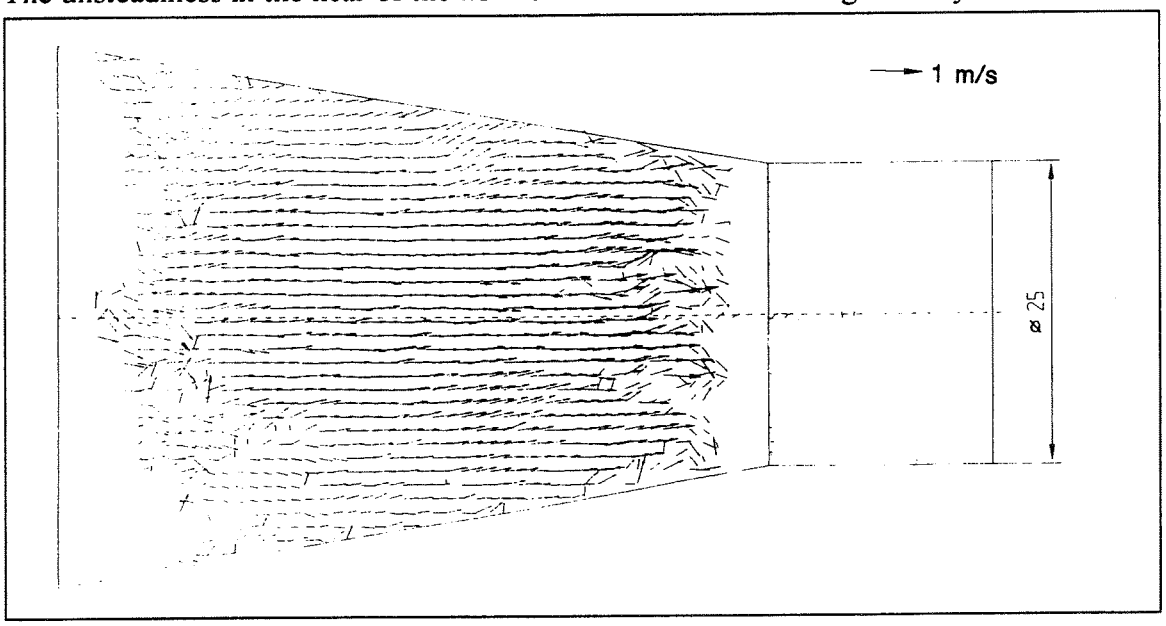

Figure 12: PIV-Measurement of Nozzle Flow
region swirl effects are visible.

5. CONCLUSIONS

The generation of cavitation is possible by utilizing static guide vanes as well as rotating impellers. The unsteady effects in the flow field are stronger, if static guide vanes are used. The spatial extent of the vapour region generated by the impeller is bigger, compared to a static cavitation generator. Also the pressure loss is evident and has to be taken into account in the designing phase of a plant which utilizes these technique. However, the use of a rotating impeller recquires additional energy, a motor and a more complicated construction. The presented investigation techniques can be used in normal water flows and in multiphase flows.

Some difficulties arise if the PIV-technique is applied to multiphase flows due to bad signal noise ratios but in the near future improvements are expected.

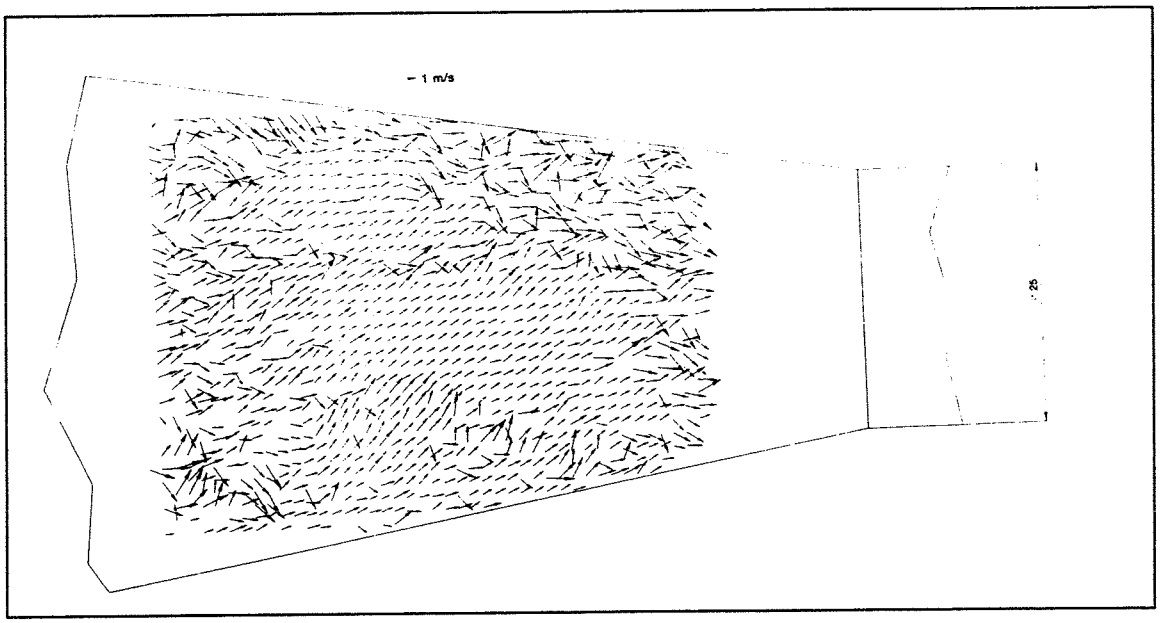

Figure 13: PIV-Measurement of Flow Field behind the Cavitation Generator

6. ACKNOWLEDGEMENTS

We want to thank Dr.-Ing. A. Gebhardt from the Laser Bearbeitungs- und Beratungszentrum (LBBZ) for the possibility to use the rapid prototyping method to produce the cavitation generator.

7. REFERENCES

[1] BENZ, H., MOESSNER, P., SIEKMANN, H.: Generation of Cavitation to Separate Liquid Mixtures, 1st International Congress of Fluid Handling Systems (INTERFLUID), 10-12 September 1990.

[2] BENZ, H., MOESSNER, P., SIEKMANN, H.: Abschlußbericht zum BMFT-Forschungsvorhaben "Untersuchungen zur Entfernung chlorierter Lösungsmittel aus Wasser durch Verdampfen im Kavitationsgebiet", Institut für Maschinenkonstruktion, TU Berlin, 1992.

[3] BENZ, H.: Untersuchung strömungstechnischer Bauteile zur Erzeugung von Kavitationsströmungen zum Zwecke der Stofftrennung, Dissertation TU-Berlin, 1993.

[4] JÄHNE, B.: Digitale Bildverarbeitung, 2. Auflage, Springer Verlag Berlin, 1991.

[5] RUMELHART, D., MCCLELLAND, J.: Parallel Distributed Processing, Volume 1: Foundations, MIT-Press, 1989.

[6] PAO, H.: Adaptive Pattern Recognition, Addison Wesley, 1989.

[7] EBINGER, G., KALLWEIT, S., DUES, M., SIEKMANN, H.: Anwendung des Laserlichtschnitt-Verfahrens zur qualitativen Untersuchung der Durchströmung von Kreiselpumpen, Preprint GALA Braunschweig, 1993.

[8] ADRIAN, R.: Particle-Imaging Techniques for Experimental Fluid Mechanics, Annual Review Fluid Mechanics 23, 1991.

[9] KHALAGHI, B.: Study of the intake tumble motion by flow visualization and particle tracking velocimetry, Experiments in Fluids 10, 1991.

[10] LIU, Z., LANDRETH, C, ADRIAN, R., HANRATTY, T.: High resolution measurement of turbulent structure in a channel with particle image velocimetry, Experiments in Fluids 10, 1991.

[11] HINSCH, K.: Particle Image Velocimetry (PIV), Speckle Metrology, ed. Sirohi, R.S., Marcel Dekker Inc. New York, 1993.

[12] FLANNERY, B., PRESS, W., TEUKOLSKY, S., VETTERLING, W., Numerical Recipes in C - The Art of Scientific Computing, Cambridge University Press 1990.

[13] SCHEFFLER, T.: Konzipieren und Entwerfen eines optischen PIV-Auswertesystems, Diplomarbeit TU Berlin, 1994.

[14] CENEDESE, A., PAGLIALUNGA, A.: Digital direct analysis of a multiexposed photograph in PIV, Experiments in Fluids 8, 1990.

[15] WILLERT, C., GHARIB, M.: Digital particle image velocimetry, Experiments in Fluids 10, 1991.

NUMERICAL PREDICTION OF TWO-PHASE-FLOW PUMP PERFORMANCE BY A BUBBLY FLOW MODEL WITH FIXED CAVITY

K. Minemura and T. Uchiyama

Nagoya University
School of Informatics and Sciences, Department of Informatics for Natural Sciences
Furo-cho, Chikusa-ku, Nagoya 464-01, Japan
Telephone: (052)789-4783, Facsimile: (052)789-4802

ABSTRACT

To predict the behavior of air-water two-phase flows in centrifugal pumps, the authors have proposed a three-dimensional numerical method on the basis of an inviscid bubbly flow model with slippage between two-phases. The model is extended in this study by assuming that the bubbles in high void fraction regions coalesce with each other to adhere to the neighboring impeller walls so as to form a fixed cavity. The numerical results for a radial-flow pump are favorably compared with the experiments when the pump loses its function due to an air-filled blockade, and with the results estimated by an inviscid one-dimensional two-fluid model.

1. INTRODUCTION

Related to the safety analysis of nuclear reactors, a number of researchers have investigated experimentally[1] and theoretically[2] the characteristics on centrifugal pumps operating under gas-liquid two-phase flow conditions, as reviewed by the author[3]. Recently the crude oil pumps in submarine fields are being developed to make the pumps maintain their pumping activity even under the gaseous oil contained a fair amount of gas[4], and effects of design parameters on the characteristics were studied experimentally by Kosmowski[5][6] and Furukawa[7].

To comply with industrial demands for designing such a pump, more definite methods for simulating the two-phase mixture flows in the pump should be developed. The authors have proposed a three-dimensional numerical method to analyze the flows[8] and a related method for predicting the change in the head developed by the impeller due to the inlet void fraction[9] on the basis of an inviscid bubbly flow model with slippage between two-phases[10][11], in which the mixture is assumed to be a bubbly flow entraining homogeneously fine bubbles. The calculated results agree well with the trend of measured values, however, such a predominating region as the local void fraction is more than four times inlet void fraction locally appears along the blade in the impeller inlet region when the inlet void fraction increases greatly.

Since densely crowded bubbles should coalesce to form a lump, the model is extended in this study by assuming that the bubbles in a predominating region of high void fractions easily coalesce with each other to grow into a large mass and adhere to the neighboring impeller blade wall just as a fixed cavity under cavitating conditions, where such bubbles are hardly swept out to stay there. It will, however, be shown that the numerical results for a radial-flow pump by this model are quite similar with those by the previous bubbly flow model, with regard to degradation in the head developed by the impeller and also the distributions of pressures and void fractions. On the other hand, the cavity obtained expands progressively its volume and finally tends to fill rapidly the section. It will be described this rapid expansion of the cavity is equivalent to the limit of pumping activity, when the entrained gas blocks the impeller passage and the pump loses its function, as reported in the author's experimental work[12]. Using the model, the effects of outlet blade angle and rotational speed of the impeller are discussed in this paper. Besides, an one-dimensional two-fluid model by Furuya[2] is also employed in this study by making some modifications so that the performance of low specific-speed pumps can be estimated for wider rage of inlet void fractions.

2. PROBLEM FORMULATION

2.1 Assumptions

The following assumptions are employed in the formulation.

(1) The air-water two-phase mixture is a bubbly flow entraining homogeneously fine bubbles except for fixed cavity regions.
(2) The bubble movements are represented by Basset-Bousinesque-Oseen's formula except for fixed cavity regions and gravity effects, and the drag coefficient of a bubble is identical with that of a solid particle.
(3) The mixture flow is steady in a relative frame of reference, which rotates around an axis with a constant velocity, and inviscid except for the drag force between the two phases.
(4) Neither fragmentation nor coalescence of bubbles arises except for the coalescence in such regions as the local void fraction exceeds a critical level.
(5) Bubbles maintain their spherical shape and change their volume adiabatically according to the pressure that surrounds them. The liquid phase is incompressible.
(6) Neither mass nor heat transfer takes place between the two phases.
(7) The change of void fractions in an absolute frame of reference is quasi-steady.
(8) The mass and momentum of the gas-phase are very small and negligible compared with those of the liquid-phase.
(9) Bubbles in such regions as the local void fraction exceeds a certain limit coalesce with each other to adhere to the neighboring impeller walls, generating a fixed cavity there. Neither interfacial forces on the cavity surface except for the normal stress (i.e., the pressure) nor bubble entrainment from the cavity into the flow exists.

The above assumptions, except for (9), are the same as those employed in solving bubbly flows[10][11] and the previous paper[8].

2.2 Equations of Motion of a Bubble and Void Fraction

Using assumptions (1) to (5), the behavior of bubbles can be analyzed by tracking a bubble released from various initial positions on a pump inlet section.

The equation of motion of a bubble, moving with velocity $\boldsymbol{v}$ in a water flow field $\boldsymbol{w}$, can then be given by the following equation[8].

$$(4/3)\pi d(\rho_g R_b^3 \boldsymbol{v})/dt = -(4/3)\pi R_b^3 \nabla p + (1/2)\rho_l \pi R_b^2 C_D \mid \boldsymbol{w} - \boldsymbol{v} \mid (\boldsymbol{w} - \boldsymbol{v})$$
$$+ \rho_l (2/3)\pi \{D(R_b^3 \boldsymbol{w})/Dt - d(R_b^3 \boldsymbol{v})/dt\} + \rho_g (4/3)\pi R_b^3 \{\boldsymbol{\omega} \times (\boldsymbol{\omega} \times \boldsymbol{r}) + 2\boldsymbol{\omega} \times \boldsymbol{v}\} \qquad (1)$$

where the first term of the right-hand side is the force due to the pressure gradient, the second the drag force, the third the force due to virtual mass, and the fifth the force due to the potential field. And, $D/Dtn = \partial/\partial t + \boldsymbol{w}\cdot\nabla$, $\quad d/dt = \partial/\partial t$.

By integrating numerically Eq. (1) from the pump inlet to the outlet as an initial value problem on the basis of the assumptions (4) to (6), trajectories of the bubble as well as the change in the bubble radius along them are known at any location in the flow field.

In this study, a three-dimensional finite element method using tetrahedral elements is employed to determine the flow properties in the field, and the field is partitioned into hexahedral elements before each of these elements is re-partitioned into six tetrahedrons. These hexahedral elements are used as control volumes to obtain void fraction α, which is defined by the volumetric ratio of the whole bubbles existing in each control volume to this volume itself. Since the solutions of Eq. (1) give bubble trajectories and a mean bubble volume in each control volume $(4/3)\pi \bar{R}_b^3$ along them, the total number of bubbles existing in each control volume can be evaluated. The number, divided by the volume of the control volume, namely the number density of bubbles, n_b, yields the value of α in any control volume by the following equation[8][11].

$$\alpha = (4/3)\,\pi \bar{R}_b^3 n_b \qquad (2)$$

2.3 Governing Equations of Air-Water Two-Phase Mixture

From assumptions (7) and (8), the equation of continuity for the bubbly flow in a relative frame of reference can be written with liquid-phase velocity $\boldsymbol{w}$ and void fraction α as:

$$\nabla\cdot\{(1-\alpha)(\boldsymbol{w}+\boldsymbol{\omega}\times\boldsymbol{r})\}=0 \tag{3}$$

By examining the conservation of circulation in the bubbly flow field[8], the velocity $\boldsymbol{w}_a$ ($=\boldsymbol{w}+\boldsymbol{\omega}\times\boldsymbol{r}$) in the absolute frame of reference is found to have a potential ϕ if the flow in the pump inlet is assumed to be irrotational. Then, Eq. (3) can be reduced to the quasi-harmonic equation, namely,

$$\nabla_a\cdot\{(1-\alpha)\nabla_a\phi\}=0 \tag{4}$$

The equation of motion of the two-phase mixture in a system rotating with a constant angular velocity $\boldsymbol{\omega}$ is expressed by the following equation under the assumptions (1), (3), (6) and (8)[8].

$$(1-\alpha)\boldsymbol{w}\cdot\nabla\boldsymbol{w}+(1-\alpha)\boldsymbol{\omega}\times(2\boldsymbol{w}+\boldsymbol{\omega}\times\boldsymbol{r})=-\nabla p/\rho_l \tag{5}$$

Divergence of Eq. (5) yields a Poisson equation as

$$\nabla^2 p=-\rho_l\nabla\cdot\{(1-\alpha)\boldsymbol{w}\cdot\nabla\boldsymbol{w}+(1-\alpha)\boldsymbol{\omega}\times(2\boldsymbol{w}+\boldsymbol{\omega}\times\boldsymbol{r})\} \tag{6}$$

After both values of $\boldsymbol{w}$ and α are known at all the nodes, the pressure p can then be evaluated at every node with Eq. (6). On the cavity surface, the pressure remains constant, because the pressure gradients there become zero from Eq. (5) for $\alpha=1$.

2.4 Region for Calculation and Boundary Conditions

In this calculation, the velocity potential ϕ in Eq. (4) is solved, in the flow field with a given distribution of void fractions, by using a three-dimensional finite element method with simplex tetrahedral elements. The flow region for calculation consists of the spaces between blades and the passages before and after them, as shown in Fig. 1.

In the case of radial-flow pumps, the following boundary conditions should be satisfied.

$$(1-\alpha)\boldsymbol{n}\cdot\nabla_a\phi=\begin{cases} w_{az} & \text{on } B_1 \\ -w_{ar} & \text{on } B_2 \\ \pm\boldsymbol{n}\cdot\boldsymbol{\omega}\times\boldsymbol{r} & \text{on } B_3 \text{ and } B_4 \\ 0 & \text{on } B_5 \text{ and } B_6 \end{cases} \tag{7}$$

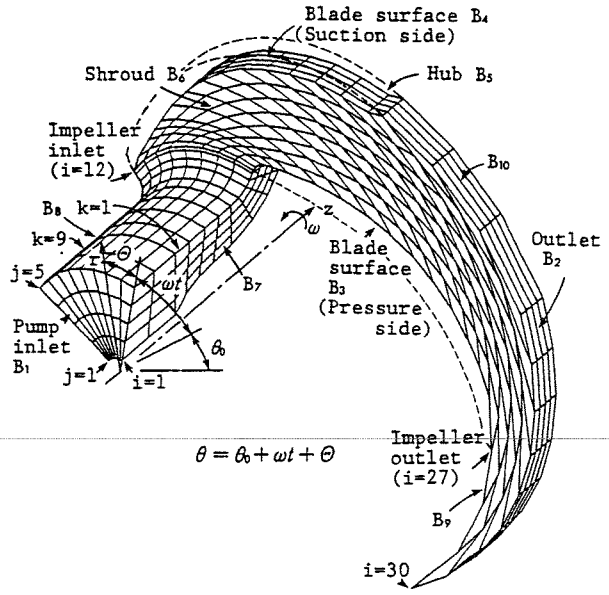

Fig. 1 Flow region for calculation

where B_1 and B_2 are the inlet and outlet sections, B_3 and B_4 the surfaces of the adjacent blades, B_5 and B_6 the hub and shroud surfaces. On the remainder of the boundary, B_7 to B_{10}, the periodic conditions should be met as follows:

$$\begin{aligned} &\phi(z,\theta+2\pi/N,r)=\phi(z,\theta,r)-\Gamma/N \\ &\partial\phi(z,\theta+2\pi/N,r)/\partial n=-\partial\phi(z,\theta,r)/\partial n \end{aligned} \tag{8}$$

where the circulation Γ is determined so as to satisfy the Kutta condition; that is, with the flows from both sides of the trailing edge joining smoothly. This condition can be realized iteratively by making the pressures at the trailing edge coincide on the pressure and suction sides of the blade[8].

If we assume that, under two-phase flow conditions, the water flows with the same velocity as the air without swirl through the inlet section B_1, and that distributions of void fractions are uniform there, then $w_{az}=const.$ on B_1. On the other hand, the velocity w_{ar} on the section B_2 of radial-flow pumps is determined so as to conserve the mass flow rate of the mixture as well as to satisfy the radial-equilibrium equation;

$$dw_{ar}^2/dz=(\omega/\pi)(d\Gamma/dz)-(1/2\pi r)^2(d\Gamma^2/dz) \tag{9}$$

which is derived under the assumptions of circumferentially uniform distributions of the velocities and void fractions on B_2.

2.5 Conditions for Calculation

The governing equations and boundary conditions described above are now applied to the flows in the radial-flow impeller pump as shown in Fig. 2. Though the normal outlet blade angle $\beta_2=18°$, the blade geometry are changed only in the latter half of the impeller as $\beta_2=30,\ 50,\ 70°$ so that the effects of the angle are investigated. The characteristics of the original pump, of which the specific speed and normal rotational speed are listed on the top of Table 1, has been well clarified for two-phase flow conditions by observations of bubbly flows[12], pressure measurements on the wall inside the casing for the open impeller[13], measurements of bubble size[14] and void fractions[15] in the impeller.

The flow is analyzed for the conditions at the rated flow capacity ($\phi=0.08$) for water single-phase flow, besides at higher ($\phi=0.1$) and lower capacities ($\phi=0.06$) for the normal impeller, and for three kinds of rotational speed including the rated speed ($n=1750\ rpm$).

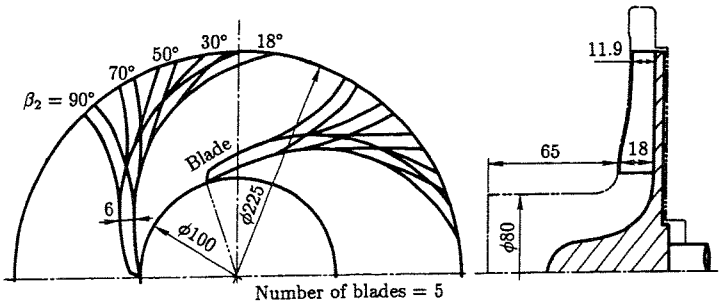

Fig. 2 Shape and dimensions of impeller employed

Table 1 Specific speed and suction pressure of pump

Reference	Flow type	Specific speed $[m,m^3/min,rpm]$	Rotational speed n $[rpm]$	Inlet pressure p_0 $[kP_a]$
This study	Radial	180	1,750	54 ~ 100
Furukawa [7]	Radial	156	1,100	50 ~ 100
Furuya [2]	Mixed	655	3,580	137 ~ 826
	Mixed	637	18,000	620

Under two-phase flow conditions the mass flow rate is taken to remain unaltered. For every condition, static pressure in the pump inlet is $54kPa$, at which no cavitation occurs.

Bubbles at the pump inlet section (B_1) are assumed to flow with the same velocity as the water, and have a uniform radius R_{b0} determined with the correlation formula based on the size measurements of bubbles in the impeller[14], namely, $2R_{b0} = 0.34,\ 0.3,\ 0.27mm$ for $n = 1500,\ 1750,\ 2000rpm$, respectively. Initial positions of bubbles are arrayed circumferentially in 18 rows and radially in 10 rows at a total of 180 points. A value of α_0 is realized by changing the number of releasing bubbles per unit time on each bubble trajectory as described in our previous paper[8].

2.6 Head Developed by Impeller

After the distributions of the flow properties in the pump are obtained by the method described, the theoretical pump head H_{th} is calculated, as the increase in the angular momentum of the mixture within the impeller per unit mass flow rate, by the following equation[8].

$$H_{th} = \frac{u_2 \int_{A_2}(1-\alpha_2)w_{ar2}w_{a\theta 2}dA_2 - u_1 \int_{A_1}(1-\alpha_1)w_{ar1}w_{a\theta 1}dA_1}{g \int_{A_2}(1-\alpha_2)w_{ar2}dA_2} \tag{10}$$

3. FIXED CAVITY AND NUMERICAL PROCEDURE

3.1 Generation of Fixed Cavity

According to the calculations by the bubbly flow model[8], the void fractions obtained are distributed unevenly in the impeller, as an example is shown in Fig. 3, when the pump ($\beta_2 = 18°$) is operated at the rated capacity ($\phi = 0.08$) and speed ($n = 1750rpm$). The figure contains the results for the inlet void fraction $\alpha_0 = 0.02,\ 0.05,\ 0.07$ on a section just after the impeller inlet. The void fractions increase toward the shroud near the suction side of the blade. On the basis of the assumption (9), bubbles in such a high void fraction region are assumed to coalesce with each other to form a lump and adhere to the neighboring wall, producing a cavity there. The cavity is numerically generated as follows:

After the void fraction in every control volume is evaluated, the representative value of the void fraction on every nodal point is also deduced by a method usually used in finite element methods, for example, a least squares method[16]. These values on every node are available to obtain contour lines expressing equi-void fraction curves by using a linear interpolation method, giving the distribution of the void fraction in the flow field. The cavity is thus represented by the high void fraction region enclosed by a contour line corresponding to the critical void fraction α_{cr}. Since the cavity surfaces are determined iteratively together with the calculations to obtain a solution of the liquid-flow field, as described in section 3.2, a relaxation factor γ should be used to determine the displacement of the cavity surface as $\gamma\delta$, so as to prevent as excessive cavity and restrain the divergence of the solution, in which δ is the displacement of the cavity surface newly estimated at any nodal point. The cavity generated is regarded as being a part of the impeller wall in the successive calculations. In this study, the relation $\gamma = 0.2$ is used.

3.2 Numerical Procedure

Calculations for inlet void fraction α_0 are performed as the following steps.

(1) As an initial step ($i = 0$), calculate the distributions of α_i with the values p_0 and $\boldsymbol{w}_0$ and the cavity form, which are the converged solutions in the previous calculation.
(2) Generate the cavity form as described in section 3.1.
(3) If the form has not converged, re-partition the flow field outside the cavity, and obtain the void fractions in each element α_i' using coordinates of the element centroid by interpolating α_i.

(4) Solve Eq. (4) on the field of α_i' by FEM to obtain ϕ_i, and calculate $\boldsymbol{w}_i$ by differentiating ϕ_i. Calculate pressure p_{i+1} with Eq. (6) for the field of α_i' and $\boldsymbol{w}_i$.
(5) If the pressures on the trailing edge do not satisfy the Kutta condition, modify circulation Γ_i and return to step (4) to obtain the flow properties.
(6) Calculate the void fraction α_i on the field of α_i', $\boldsymbol{w}_i$ and p_i by using Eqs. (1) and (4), and return to step (2).

After the cavity form for α_0 converges, the same procedure is repeated to obtain the solutions for the inlet void fraction increased by $\Delta\alpha_0\,(=0.001)$.

4. CALCULATED RESULTS AND DISCUSSION

4.1 Change in Fixed Cavity Form Due to Inlet Void Fractions

Distributions of the void fractions calculated by the previous bubbly flow model, shown in Fig. 3, agree well with the trend of those measured[15], but the values are 40% lower than the measured ones. This difference is attributed to neglect of fluid viscosity, as pointed out in the previous paper[8]. In this study the cavity is formed on the basis of the void fractions calculated by this model. It means that the void fractions cited are regarded as being equivalent to the value increased by the corresponding reduction in the void fractions (40%), for example, the calculated void fraction of 0.20 corresponds to the measured value of 0.50.

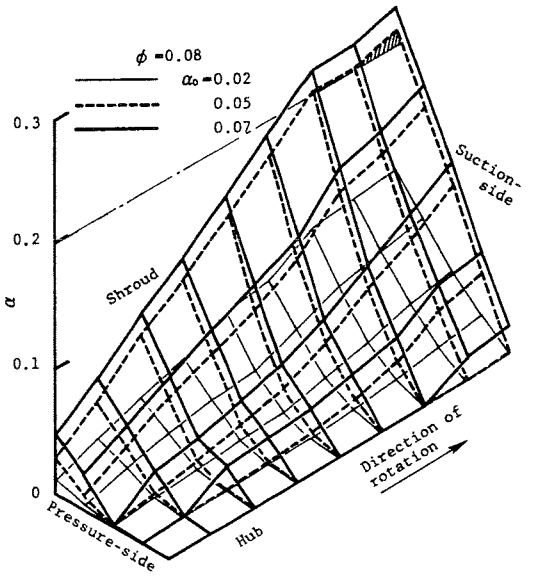

Fig. 3 Distributions of void fractions on section just after impeller inlet
(by bubbly flow model, $r/r_1 = 1.1$, $\phi = 0.08$)
(The shaded region is regarded as a fixed cavity in this study)

According to the observations[11] under the same running condition ($\alpha_0 = 0.05$), an air-filled hollow occupies nearly the same circumferential extent on the shroud with that shaded in Fig. 3, in which the region of $\alpha \geq 0.2$ is shaded for the case of $\alpha_0 = 0.05$. In this study, the critical void fraction α_{cr}, beyond which the bubbles are assumed to coalesce and adhere to the neighboring impeller wall to produce a fixed cavity, is thus taken to be 0.2. Effects of the change on α_{cr} are discussed later.

The result, for the normal condition ($\phi = 0.08$, $1750rpm$) of the impeller $\beta_2 = 18°$, by the cavity model is shown in Fig. 4, when $\alpha_0 = 0.075$, the highest value for obtaining a convergent solution. In the figure we plot the cavity form and contour lines of void fractions $\alpha/\alpha_0 = const.$ for various meridional sections, dislocating circumferentially from the suction side of the blade to the pressure one. The cavity region, shaded in the figure, is seen to exist on the shroud near the suction side just after the impeller inlet, corresponding to the predominant region of the

high void fractions calculated by the bubbly flow model (Fig. 3). The cavity is rather thin in an axial direction, and its maximum thickness is 22% less than the depth of the flow passage. Near the cavity the contour lines of void fractions are seen to parallel almost the cavity surface.

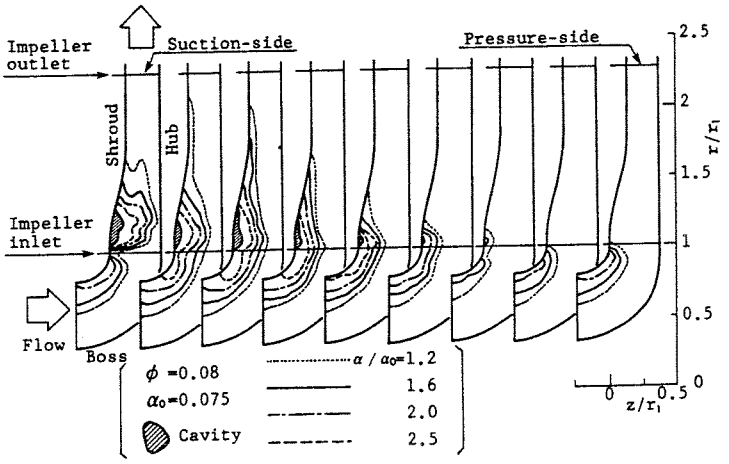

Fig. 4 Fixed cavity form and distributions of void fractions on meridional section ($\phi = 0.08$)

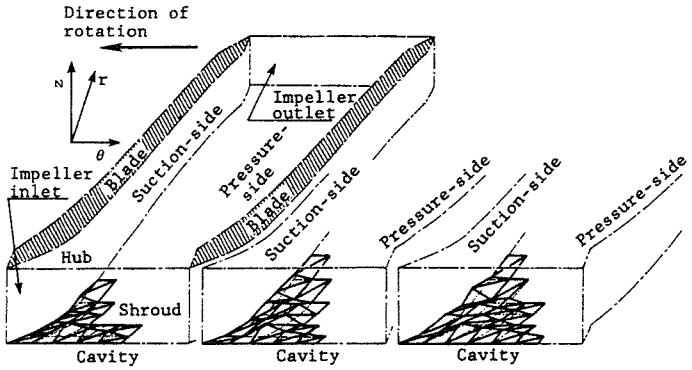

(a) $\alpha_0 = 0.06$ (b) $\alpha_0 = 0.068$ (c) $\alpha_0 = 0.075$

Fig. 5 Fixed cavity form within impeller ($\phi = 0.08$)

Figure 5 shows pictorial drawings of the cavity form corresponding to Fig. 4, though the scale in an axial direction (z) is taken to be slightly larger than that in a circumferential one (θ) because of the thin cavity in the axial one. The result for $\alpha_0 = 0.06$, just after the cavity appears ($\alpha_0 = 0.05$), is plotted in Fig. 5(a), where the cavity exists in a region on the shroud from the mid-channel between the blades to the suction side and just after the impeller inlet.

When α_0 is slightly increased further to $\alpha_0 = 0.068$, the cavity enlarges in a radial direction along the suction side and thickens as shown in Fig. 5(b). When $\alpha_0 = 0.075$, the highest value of α_0, the cavity is seen to extend toward the pressure side as well as thicken as shown in Fig. 5(c). As compared with the cavity observed on the shroud under the same pump operating condition[11], the width appears to be as great as in the circumferential direction, but somewhat smaller in the radial direction.

When α_0 is changed at the flow capacity $\phi = 0.06$ or 0.1 different from the normal one ($\phi = 0.08$), the extent of the cavity and contour lines of void fractions show almost similar changes to those for $\phi = 0.08$, so their illustration is omitted here. For every ϕ the cavity appears on the suction side of the blade in the same way as observed earlier[11], and a high void fraction region also exists in the neighborhood of the cavity as expected from the measurements of void fractions[15].

4.2 Change in Volume of Fixed Cavity

When increasing inlet void fraction α_0, the cavity volume V_v also increases as shown in Fig. 6, when the normal impeller ($\beta_2 = 18°$) is operated at the rated speed (1750 rpm). In the figure, the volume V_v is expressed non-dimensionally by the cube of impeller inlet radius r_1, and the results for three kinds of flow capacities, $\phi = 0.06$, 0.08 and 0.1, are superimposed with different symbols.

The results for the normal flow capacity ($\phi = 0.08$), plotted by the symbol ○, show that the cavity appears at $\alpha_0 = 0.05$ and its volume increases almost linearly with increasing α_0 for the range of $\alpha_0 \leq 0.071$. Beyond this limit the volume grows explosively, in which the culculation was made with an increment of the inlet void fraction reduced to $\Delta\alpha_0 = 0.0005$. When $\alpha_0 > 0.075$, however, the cavity expanded locally in the region just after the impeller inlet and monotonously from the shroud to the hub, and no converged solution could be obtained. According to the experiments[12], the pump rapidly loses its head at the nearly same value as this ($\alpha_0 = 0.07$) (see Fig. 11) and no longer functions when α_0 is slightly increased further. This rapid degradation is attributable to the fact that an air-filled hollow, generated just after the impeller inlet, expands with an increase of α_0 and finally shuts off the water flow there[12]. The limits of the calculation as shown in Fig. 6 can then be considered to correspond to the loss of pumping activity.

The results for a lower ($\phi = 0.06$) and higher capacity ($\phi = 0.1$) are also shown in Fig. 6 with the symbols △ and □, respectively. The volume V_v changes, owing to α_0, in a way almost similar to that for $\phi = 0.08$. When ϕ becomes greater, however, the cavity appears at a value of less α_0 and V_v grows at a greater rate, so that the rapid growth of the cavity arises at a less α_0. Irrespective of different ϕ, such a growth occurs almost at the same α_0 as when the pump ceases to function, as will be seen in Fig. 11.

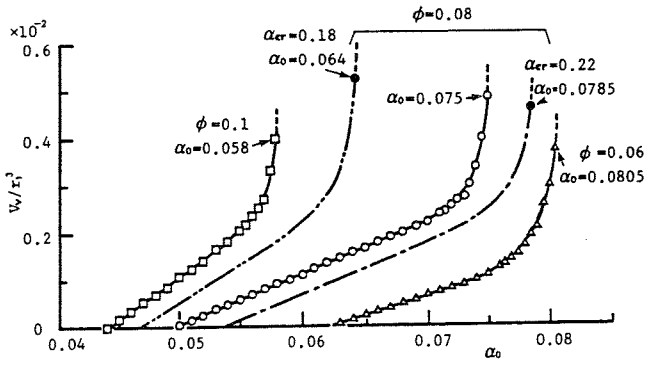

Fig. 6 Change in cavity volume due to α_0 and α_{cr}

When the critical value of void fractions α_{cr} is altered as $\alpha_{cr} = 0.18$ or 0.22 at the normal flow capacity ($\phi = 0.08$), the cavity volume appears to change in a similar way as shown in Fig. 6. It is, however, evident that the cavity appearance and its rapid growth take place at a larger value of α_0 with the increase of α_{cr}. Although omitted illustration, the application of the value $\alpha_{cr} = 0.2$ is confirmed with another pump, which has the same geometry and dimensions except for the number of impeller blades (7 blades). In spite of the sensitiveness due to the alternations in α_{cr}, the fixed cavity model with the value $\alpha_{cr} = 0.2$ is thus considered to be available for the design problem to determine the optimum two-phase pump geometry.

When the blade angle β_2 is increased, the cavity appears nearly at the same value of α_0 but its incipient volume somewhat increases, as shown in Fig. 7, when the pump is operated in the normal capacity ($\phi = 0.8$). With an increases in β_2, the rapid growth of the cavity arises at a smaller value of α_0, as $\alpha_0 = 0.0675$, 0.0575, 0.055 for $\beta_2 = 30$, 50, 70°, respectively. This is attributable to the increase in the pressure gradient within the impeller with increasing of β_2. These limits are comparable to those of the Furukawa's experiment[7], in which a radial-flow

pump, having nearly the same specific speed as listed in the middle of Table 1, degrades rapidly its performance at $\alpha_0 = 0.1,\ 0.077,\ 0.062$ for β_2=25, 40, 60°, respectively.

When the running speed n of the pump with $\beta_2 = 30°$ is altered to 1500 or $2000rpm$, the cavity also takes place almost at the same $\alpha_0(= 0.049)$ with the result for $n = 1750rpm$, as plotted with a chain line in Fig. 7. The volume V_v increases at a less rate with increasing in n and tends to grow rapidly at a larger α_0. From the results it is evident that the pumps operated at a higher speed can maintain its function up to a greater α_0, as expected from the experiment[12]. When the speed n increases, the air bubbles crash into smaller sizes at the impeller inlet[16] so that the bubbles may easily be discharged from the impeller.

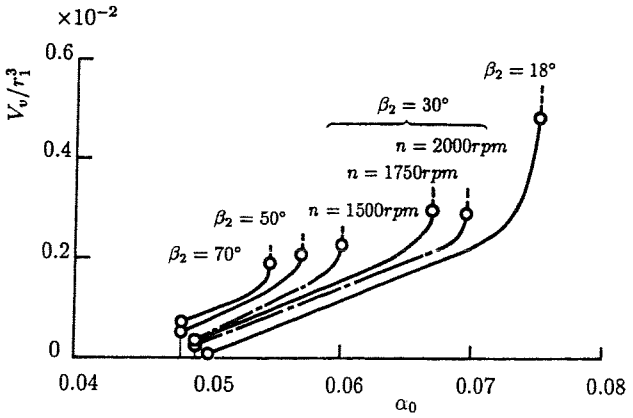

Fig. 7 Effects of β_2 and n on cavity volume

4.3 Distributions of Pressure

Meridional distributions of the pressure calculated for the normal flow capacity ($\phi = 0.08$) are shown in Fig. 8, when the pump ($\beta_2 = 18°$) is operated at the rated speed ($n = 1750rpm$). The non-dimensional isobaric lines for α_0 =0, 0.06 and 0.075, connecting points having the same value of $\Delta\psi_r$, on the suction surface, those on the mid-surface between the pressure and suction surfaces, and those on the pressure surface, are compared with different kinds of line in Figs. 8(a), (b) and (c), respectively, where the cavity regions are shaded by hatching and enclosed with lines corresponding to the isobaric lines. Though the cavity deforms the isobaric lines near the shroud, the distributions are almost the same as those obtained by the bubbly flow model except for a surrounding region of the cavity.

Pressure distributions on blade-to-blade sections, corresponding to those in Fig. 8, are plotted in Fig. 9, where Fig. (a) shows the results on the shroud, which is maximally affected due to α_0. Owing to the existence of the cavity shaded by hatching, the isobaric lines near the cavity shift downstream, and this effect spreads downward, firstly to the suction side of the blade and finally to the center of the flow passage in the course of flow. As the result, a convex shape of the iso-baric lines appears in the center of the passage near the impeller outlet, though the bubbly flow model yields only parallel lines[8]. Such changes due to α_0 agree well with the measurement[13], though the calculation shows a somewhat smaller shift of the isobaric lines. Figure 9(b) presents the results on a mid-surface between the shroud and the hub, indicating less effects of the cavity.

When the flow capacity is made lower ($\phi = 0.06$) or higher ($\phi = 0.1$), resultant pressure distributions for different α_0 change almost in the same manner with those at the normal capacity ($\phi = 0.08$).

When the angle β_2 is increased from $\beta_2 = 18°$ to 30 or 70°, such a deformation due to α_0 decreases, as shown in Fig. 10, where the results for the $\alpha_0 = 0$ and the maximum are compared. With the increase of β_2, the cavity tends to lengthen along the suction side of the blade. This is attributable to the steeper pressure gradient in a radial direction so that the bubbles may accumulate more easily in the inlet region. Besides, the cavity decreases its circumferential

extent with increasing in β_2, and also thins as 19% and 9% less than the impeller depth for $\beta_2 = 30$ and 70°, respectively.

When the pump with $\beta_2 = 30°$ is operated at a higher speed, the cavity form calculated remains almost the same as that in Fig. 10(b), though the cavity length along the shroud tends somewhat to shorten.

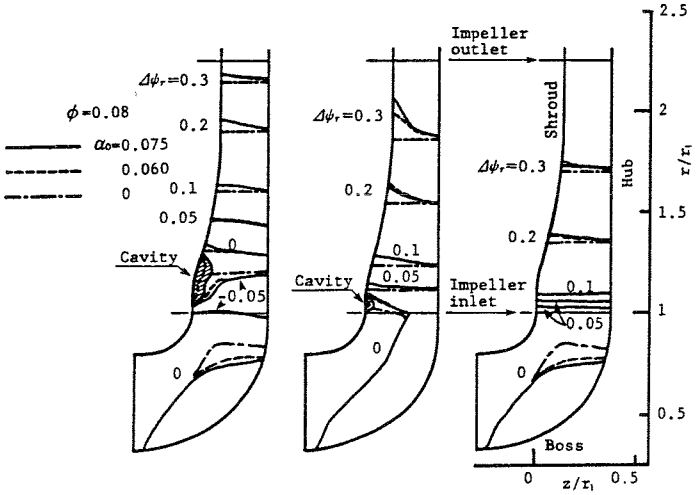

Fig. 8 Pressure distributions on meridional sections ($\phi = 0.08$)

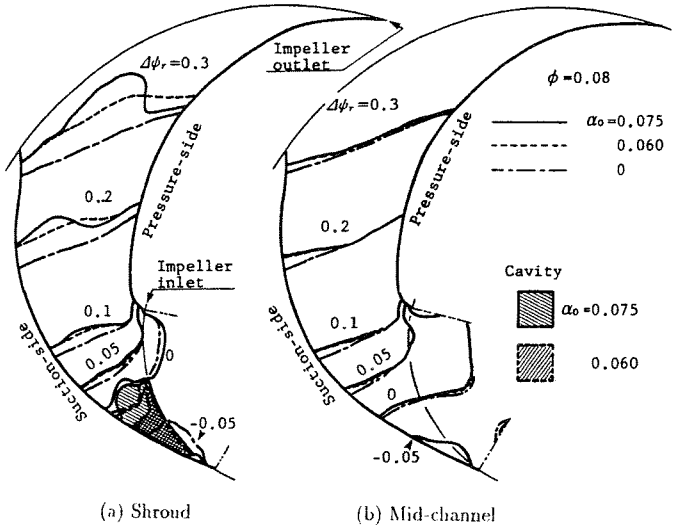

Fig. 9 Pressure distributions on blade-to-blade sections ($\phi = 0.08$)

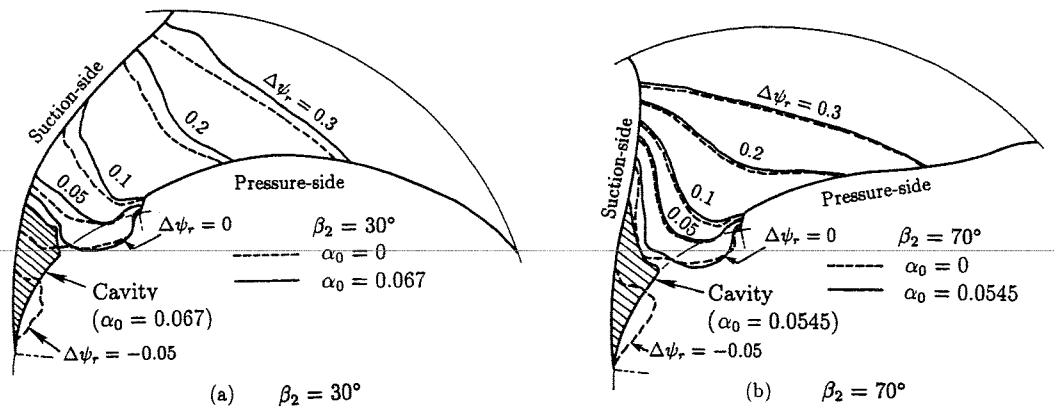

Fig. 10 Effects of β_2 on pressure distributions ($\phi = 0.08$)

4.4 Change in Head Developed by Impeller

As described in section 2.6, calculated velocities and void fractions on the sections just before the impeller inlet and just after the outlet yield the head developed by the impeller H_{th}. The evaluated non-dimensional head ψ_{th} decreases slightly with increasing α_0 and remains unaltered in the range greater than a certain value of α_0, as shown in Fig. 11, where the head divided by that in the single-phase flow ψ_{th0}, (ψ_{th}/ψ_{th0}), is plotted against inlet void fraction α_0 by thick solid lines, and compared with that calculated by the bubbly flow model with dotted lines connecting the symbol ○ . The results for the normal flow capacity ($\phi = 0.08$) are shown in the middle of Fig. 11. The results calculated both by this fixed cavity model and by the bubbly flow model substantially coincide even when the cavity exists i.e., $\alpha_0 \geq 0.05$. Such cavity effects on the head are quite similar to those of the void caused by cavitation, when the flow around the void is calculated based on the assumptions of steady and inviscid flow by using two-dimensional singularity methods[17][18]. According to such calculations the head obtained remains unaltered owing to the change in extent of the void, as long as the void exists in the neighborhood of the leading edge on the suction side.

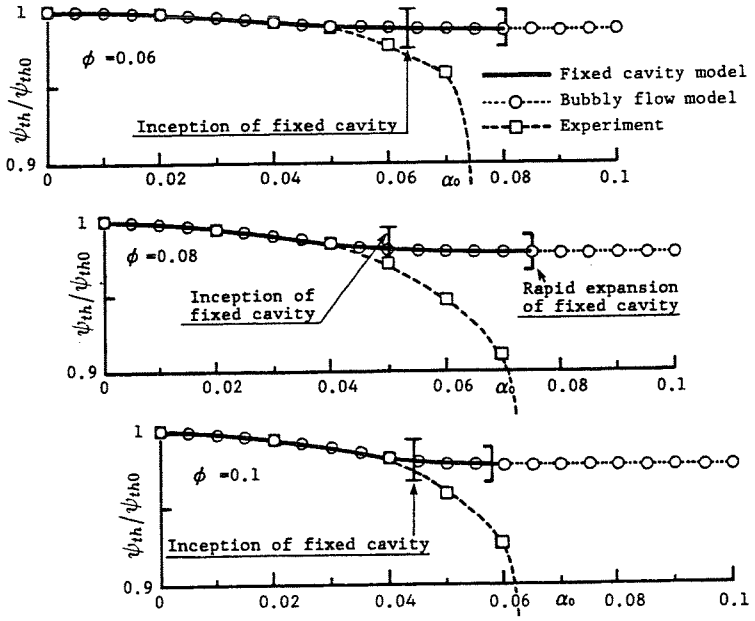

Fig. 11 Relationship between theoretical head ψ_{th} and α_0

Figure 11 also shows experimental results[14] indicated by the symbol □. When $\phi = 0.08$, they coincide with the calculations by this fixed cavity model within the range of $\alpha_0 \leq 0.04$. When $\alpha_0 \geq 0.05$, however, the measured values decrease more. From the observations, the cavity region was found to be present already at $\alpha_0 = 0.051$, and the rapid drop in pump performance occurred when α_0 was increased a little further than 0.071.

The results for a lower flow capacity ($\phi = 0.06$) are shown above in Fig. 11. The relationship between the head ratio and α_0 is similar to that for the normal flow capacity. The maximum value of α_0, at which a converged solution can be obtained, is 0.0805. This is slightly larger than with a rapid drop in pump performance ($\alpha_0 = 0.07$). The results for a higher capacity ($\phi = 0.1$) are shown below in Fig. 11. The α_0 maximum value of 0.058 is slightly smaller than for the rapid drop in performance ($\alpha_0 = 0.06$).

Figure 12 shows the results for the pump with different outlet blade angle β_2. The head curves shift upwards with the increase in β_2, though the changes in the head due to α_0 is almost similar with each other. When the running speed n is increased for the pump with $\beta_2 = 30°$, the calculated head ψ_{th} increases a little within the range of $\alpha_0 > 0.036$ as plotted with chain lines in Fig. 12.

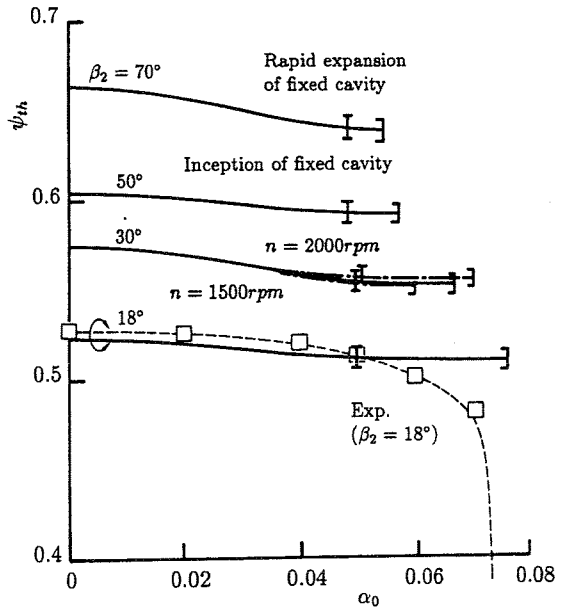

Fig. 12 Effects of β_2 and n on pump head and α_0

4.5 Head Estimated by One-Dimensional Method

To ascertain the resultant effects of pump design parameters on the head, an inviscid and incompressive one-dimensional two-fluid model by Furuya[2] is applied to the pump employed in this calculation. The result obtained for the pump with $\beta_2 = 18°$ and $n = 1750rpm$ is plotted with a thick broken line shown in Fig. 13(a). The head calculated corresponds to the theoretical head for an infinite number of blades $\psi_{th\infty}$, because the outlet flow angle from the impeller exit is replaced with the outlet blade angle β_2 in this model. Besides the mixture in the impeller flows in a mechanically similar manner for different running speed n owing to the assumption of incompressibility, no effects of n on $\psi_{th\infty}$ thus appears. The constitutive equation for the friction between two phases employs Hench-Johnston's drag coefficient of a bubble[19] (which is abbreviated to H-J in the following) for the range of $\alpha \leq 0.3$, Zuber-Hench's coefficient[20] (abbreviated to Z-H) for the range of $\alpha \geq 0.4$ and the value interpolated linearly using both coefficients for the middle range of $0.3 < \alpha < 0.4$. For reference, the results solved separately with H-J and Z-H coefficients are plotted with thin lines.

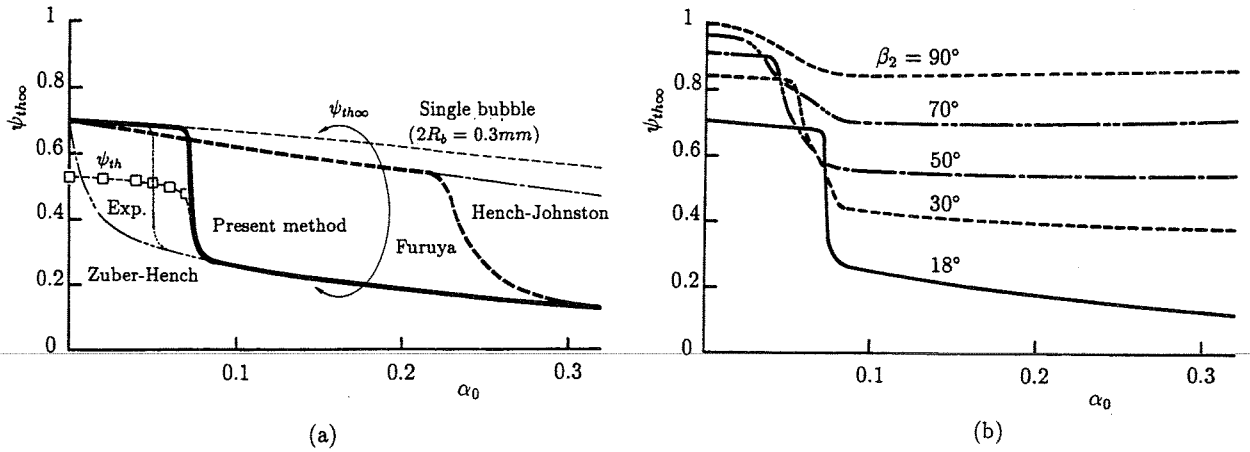

Fig. 13 Theoretical head $\psi_{th\infty}$ based on one-dimensional method

Calculated void fractions α increase monotonously towards the impeller exit[2] and head $\psi_{th\infty}$ degrades sharply at $\alpha_0 \approx 0.23$, as seen in Fig. 13(a). The degradation thus means that a

predominant region of high void fractions of $\alpha \geq 0.3$ exists in the impeller, but the region differs greatly from the calculated results with the cavity model and observed one[12]. Since the pump performance is substantially affected not by the flow states within the impeller but by those at the impeller exit, predicted values of the head is considered to be not necessarily injured by the reason. The void fraction at which the head degrades sharply, however, is much higher than the measured one, which is indicated with the mark □ in the figure. This discrepancy arises largely from the fact that the pump for calculations with the cavity model is a low specific-speed radial-flow type operating at a suction pressure as low as the atmospheric one, while the pump for those with the one-dimensional model is a high specific-speed mixed-flow type running at pressurized suction pressure, as cited on the bottom of Table 1. Namely, such a pump, as its specific speed or intake pressure is high, can keep its function up to a greater inlet void fraction, as pointed out by Kastner and his co-workers[21].

When Furuya's method is applied to the pumps with $\beta_2 \geq 50°$, however, the head degrades at much less value of α_0 and differs from the trend of the experiment, just behaves as same as Z-H curve in Fig. 13(a). It may be caused by the fact that H-Z coefficient was obtained in a static diffuser entraining much greater bubbles ($2R_b = 3.18mm$), being about ten times as large as the minute bubbles observed within the impeller[13]. When the predicted values α_0 by the cavity model for the incipient and the limit of the rapid cavity growth are applied to the model, the head obtained degrades at a less value of α_0, being 60% less than the experiment, as shown with a dotted line in Fig. 13(a). In this calculation, the drag coefficient of a single bubble for the diameter $2R_b = 0.3mm$, being observed most frequently in the impeller[13], Z-H coefficient and a linearly interpolated value of them are used for the ranges of $\alpha \leq 0.05$, $\alpha \geq 0.0755$ and $0.05 < \alpha < 0.0755$, respectively.

Using the drag coefficient of a single bubble for $\alpha < 0.08$, Z-H value for $\alpha > 0.1$ and an interpolated value for $0.08 < \alpha < 0.1$ instead, the head calculated agrees fairly well with the trend of the experiment, as plotted with a thick solid line in Fig. 13(a). Figure 13(b) shows thus the results when these coefficients are applied to the pumps with $\beta_2 = 30, 50, 70, 90°$ to obtain $\psi_{th\infty}$. The resultant head demonstrates that the pump with a greater β_2 can maintain still a higher head after the degradation though it degrades at a less value of α_0, being expected in the experiment[7] for a pump nearly with the same specific speed as that in this study.

5. CONCLUSIONS

A bubbly flow model with a fixed cavity has been proposed, and applied to a radial-flow low-specific-speed pump. And the one-dimensional two-fluid model is also carried out. The results obtained are summarized as follows.

(1) On the shroud just after the impeller inlet, a fixed cavity appears at a certain value of α_0 according to the flow capacity ϕ ($0.06 \leq \phi \leq 0.1$), and its volume increases linearly with an increase in α_0. When α_0 is increased beyond a certain limit, the cavity grows rapidly at the inlet so as to fill the flow passage.

(2) When the calculated cavity grows so rapidly, the pump performance also deteriorates sharply at almost the same value of α_0 owing to air blockade of the impeller passage. The limit of this rapid deterioration can then be simulated by using the proposed model.

(3) The impeller heads calculated both by this fixed cavity model and by the bubbly flow model substantially coincide even when the cavity exists.

(4) The larger the outlet blade angle and the smaller the running speed of the pump, the less the range in which the pump keeps its function becomes.

(5) By using the drag coefficients of a single bubble and Zuber-Hench, the theoretical head for low specific-speed pumps can be estimated with the one-dimensional two-fluid model. The impellers with a larger outlet blade angle can keep a higher head after the degradation.

NOMENCLATURE

A : flow area of impeller
C_D : drag coefficient of a bubble $= C_D(Re)$
g : acceleration of gravity
H_{th} : theoretical pump head
$\dot{m}$: mass flow rate of mixture
N : number of blades
n : number of revolutions per minute
$\boldsymbol{n}$: unit vector perpendicular to boundary surface
n_b : number of bubbles in unit volume
p : absolute pressure
Re : Reynolds number of bubble $= 2R_b \mid \boldsymbol{w} - \boldsymbol{v} \mid /\nu$
R_b : radius of bubble
r : radial coordinate
t : time
u : peripheral speed of impeller
$\boldsymbol{v}$: velocity vector of bubble
V_v : volume of fixed cavity
$\boldsymbol{w}$: velocity vector of water
z : axial coordinate
α : void fraction
α_{cr} : critical void fraction for appearance of fixed cavity
β : blade angle
Γ : circulation $= 2\pi r w_{a\theta}$
θ : angular coordinate
ν : kinematic viscosity of water
ρ : density
ϕ : velocity potential or non-dimensional expression of pump flow rate $= \dot{m}/(\rho_m A_2 u_2)$
ψ_{th} : non-dimensional expression of pump head $= H_{th}/(u_2^2/g)$
$\Delta\psi_r$: non-dimensional pressure coefficient $= (p - p_0)/(\rho_l u_2^2)$
$\boldsymbol{\omega}$: angular velocity of impeller

Subscripts

0 : pump inlet or liquid single-phase flow
1 : impeller inlet
2 : impeller outlet
a : condition in an absolute frame of reference
g : gas phase
l : liquid phase
m : air-water two-phase flow
r : radial component
z : axial component
θ : circumferential component
∞ : infinite number of blades

REFERENCES

[1] K.A. Nilsson: "LWR Recirculation Pump Performance Under Two-Phase Flow Conditions", in: Proc. of Cavitation and Polyphase Flow Forum (ASME), R.L. Waid Eds., p.39 (1977).
[2] O. Furuya: "An Analytical Model for Prediction of Two-Phase (Noncondensable) Flow Pump Performance", in: Trans. ASME, J. Fluid Eng., 107, 1, p.139 (1985).
[3] K. Minemura and M. Murakami: "Developments in the Research of Air-Water Two-Phase Flow in Turbomachinery", in: JSME Int. J., Series II, 31, 4, p.615 (1988).

[4] S.D. Donno, et al.: "The S.B.S. Project-Development of a Subsea Booster System for the Exploitation of Deep Water Oil Fields", in: Proc. of the 5th Deep Offshore Technol.(ASME), p.357 (1985).
[5] I. Kosmowski: "Problems when Conveying Liquid-Gas Mixtures and Conclusions for the Construction of Centrifugal Pumps", in: Oper. Probl. Pump Stations Power Plants, 1, p.21.1 (1982).
[6] I. Kosmowski: "Einfluß des Gehäuses von Turbopumpen auf die Förderung gasbeladener Flüssigkeiten", in: Energietechnik, 34, 4, p.141 (1984).
[7] A. Furukawa, S. Sato, H. Ikeda and Y. Takamatsu: "Some Experiments on Improving the Liquid/Gas Two-phase Flow Performance of a Centrifugal Pump", in: Technology Reports of Kyushu University(in Japanese), 63, 5, p.535 (1990).
[8] K. Minemura and T. Uchiyama: "Three-Dimensional Calculation of Air-Water Two-Phase Flow in Centrifugal Pump Impeller Based on a Bubbly Flow Model", in: Trans. ASME, J. Fluid Eng., 115, 4, p.766 (1992).
[9] K. Minemura and T. Uchiyama: "Prediction of Pump Performance under Air-Water Two-Phase Flow Based on a Bubbly Flow Model", in: Trans. ASME, J. Fluid Eng., 115, 4, p.781 (1992).
[10] L. Noordzij and L. van Wijngaarden: "Relaxation effects, caused by relative motion, on shock waves in gas-bubble/liquid mixtures", in: J. Fluid Mech., 66, 1, p.115 (1974).
[11] Y. Matsumoto, H. Nishikawa and H. Ohashi: "Performance of Cascade of Blades in Two-phase Flow (Modeling and Numerical Calculation)", in: JSME Int. J., Series II, 31, 4, p.652 (1988).
[12] M. Murakami and K. Minemura: "Effects of Entrained Air on the Performance of a Centrifugal Pump (1st Report, Performance and Flow Conditions)", in: Bulletin of JSME, 17, 110, p.1047 (1974).
[13] K. Minemura, M. Murakami and T. Kataoka: "Pressure Distribution in a Centrifugal Impeller Handling Air-Water Mixtures", in: Bulletin of JSME, 26, 220, p.1727 (1983).
[14] K. Minemura, M. Murakami and H. Katagiri: "Characteristics of Centrifugal Pumps Handling Air-Water Mixtures and Size of Air Bubbles in Pump Impellers", in: Bulletin of JSME, 28, 244, p.2310 (1985).
[15] K. Minemura and M. Murakami: "Distributions of Velocities and Void Fractions in a Radial-Flow Pump Impeller Handling Air-Water Two-Phase Mixtures", in: Proc. of Cavitation and Multiphase Flow Forum (ASME), p.35 (1986).
[16] H. Daiguji: "Numerical Analysis of 3-D Potential Flow in Axial Flow Turbomachines", in: Bulletin of JSME, 26, 215, p.763 (1983).
[17] H. Nishiyama: "Theoretical Analysis for Passage and Exit Flow of Two Dimensional Centrifugal Impeller with Leading Edge Cavitation (Effects of Blade Number and Blade Angle) (in Japanese) ", in: Trans. JSME, 54, 503-B, p.1703 (1988).
[18] R. Imai, Y. Tsujimoto and O. Furuya: "Non-linear Analyses of Cavitating Flows through a Centrifugal Impeller by a Singularity Method (in Japanese)", in: Trans. JSME, 56, 522-B, p.454 (1990).
[19] J.E. Hench and J.P. Jhonston: "Two-Dimensional Diffuser Performance with Subsonic, Two-Phase, Air-Water Flow", in: Trans. ASME, J. Basic Eng,. 94, 1, p.105 (1972).
[20] N. Zuber and J.E. Hench: "Steady State and Transient Void Fraction on of Bubbling Systems and Their Operating Limits, Part I Steady State Operation", GE Rep., No.62 GL 100 (1962).
[21] W. Kastner and G.J. Seeberger: "Pump Behavior and Its Impact on a Loss-of Coolant Accident in a Pressurized Water Reactor", in: Nucl. Technol., 60, p.268 (1983).

THE EFFECT OF GAS INJECTION ON THE FLOW OF IMMISCIBLE LIQUIDS IN HORIZONTAL PIPES

M. Nädler and D. Mewes

Institut für Verfahrenstechnik, Callinstraße 36, D-30167 Hannover, Germany

ABSTRACT

The flow of two immiscible liquids and the influence of an additional inserted gas phase in horizontal pipes is investigated. The experiments are carried out in a transparent horizontal pipe with an inner diameter of 59 mm and a total length of 48 m. Experimental results are presented for the flow regimes of the two phase and three phase flow of oil, water and gas mixtures. The effect of phase inversion on the pressure drop is measured. The experimental results obtained for the three phase flow of oil, water and air indicate that drag reduction is possible by injecting gas in laminar flowing mixtures of oil and water. In the aerated slug flow regime of oil, water and air a water dominated and an oil dominated flow system can be distinguished. The pressure drop of the three phase flow system is of the same order of magnitude as the pressure drop of the two phase flow of gas and the dominating liquid phase.

1 INTRODUCTION

In the chemical and petroleum industry the design of tubular reactors and pipelines for liquid transportation requires the knowledge of the flow characteristics of cocurrently flowing immiscible liquids. The flow behaviour of the system of two immiscible liquids, such as oil and water, is complicated due to the existence of various flow regimes and the occurence of phase inversion phenomena, where the dispersed phase becomes the continuous phase. When the flowing oil-water mixture reaches the phase inversion point where the continuous phase is inverted from water to oil or vice versa, an abrupt increase of the frictional pressure drop of the oil-water mixtures is observed. The viscosity and hence the pressure drop of the flowing emulsions can be considerably higher than that of the pure oil. In order to avoid operating an oil-water pipeline at phase inversion conditions, the prediction of these conditions is required. Investigations of the various flow regimes occuring in the pipeline flow of two immiscible liquids were carried out by Russel et al. [1, 2], Charles et al. [3, 4], Guzhov et al. [5] and Arirachakaran et al. [6].

Russel et al. [1] conducted their experiments in a horizontal pipeline with an inner diameter of $d = 25.4\ mm$ using a white mineral oil ($\varrho_{f2} = 834 \frac{kg}{m^3}, \eta_{f2} = 18\ mPas$) and water as the liquid phases. In their investigations they found that emulsification of the oil-water mixtures along the pipeline can occur while the oil-water mixture is flowing downstream and that in case of emulsification an increasing pressure drop is possible.

The effect of liquid viscosity on the flow regimes of horizontal flow of water and oil in a 25.4 mm diameter pipe was investigated by Charles et al. [3, 4]. In order to avoid effects due to difference in density of the liquids used, they added carbon tetrachloride to each oil until the water density ($\varrho_{f2} \approx 998 \frac{kg}{m^3}$) was reached. By increasing the oil viscosity from $\eta_{f2} = 6.3\,mPas$ to $\eta_{f2} = 65\,mPas$ they observed no significant effect of the oil viscosity on the flow regimes. In their investigations of the pressure drop Charles et al. [3, 4] found that the introduction of water into an originally laminar flowing oil leads to drag reduction down to a minimum pressure drop, after which further water introduction results in an increasing pressure drop which exceeds the pressure drop for the pipeline flow of the pure oil. The results of Charles et al. [3, 4] indicate that a maximum drag reduction is obtained for input water fractions $\dot{\varepsilon}_{f1} = \frac{\dot{V}_{f1}}{\dot{V}_{f1}+\dot{V}_{f2}}$ in the range from $\dot{\varepsilon}_{f1} = 0.4$ to $\dot{\varepsilon}_{f1} = 0.6$, where flow regimes of concentric oil-in-water and of oil-slugs-in-water are observed.

A flow pattern map for the horizontal pipe flow of immiscible liquids was presented by Guzhov et al. [5] who investigated the flow of water and a transforma oil ($\eta_{f2} = 22mPas, \varrho_{f2} = 896 \frac{kg}{m^3}$) in a horizontal 18 m long pipe with 39.4 mm inner diameter. Based on their observations, Guzhov et al. [5] distinguished between eight flow regimes five of which are the flow of different types of oil-in-water and water-in-oil emulsions.

By measuring the pressure drop they obtained two peaks in a plot of the pressure gradient versus the input oil fraction $\dot{\varepsilon}_{f2} = \frac{\dot{V}_{f2}}{\dot{V}_{f1}+\dot{V}_{f2}}$. The first peak observed for input oil fractions of about $\dot{\varepsilon}_{f2} \approx 0.4$ was contributed to an inversion from a continuous oil phase to a continuous water phase, while the second peak occuring in the range of input oil fractions from $\dot{\varepsilon}_{f2} = 0.8$ to $\dot{\varepsilon}_{f2} = 0.9$ was assumed to be due to initial turbulence of the oil phase. In the region of phase inversion the measured pressure drop is approximately between 10 % and 20 % higher than the pressure drop in case of pure oil.

Extended investigations of the two-phase flow of oil and water in a horizontal pipe were carried out by Arirachakaran et al. [6]. They conducted their experiments in pipes with inner diameters of $d = 26.6\,mm$ and $d = 41\,mm$ using six different oils with viscosities covering the range from $\eta_{f2} = 4.7\,mPas, (\varrho_{f2} = 850 \frac{kg}{m^3})$ to $\eta_{f2} = 2116\,mPas, (\varrho_{f2} = 899 \frac{kg}{m^3})$.

In order to present the flow regimes observed, Arirachakaran et al. [6] revised the flow pattern map given by Guzhov et al. [5]. Comparing the flow regime boundaries observed in their own study and those of Guzhov et al. [5] they found different boundaries for the occurence of phase inversion. While the results of Guzhov et al. [5] indicated that the phase inversion is a function of the input water fraction as well as of the mixture velocity, Arirachakaran et al. [6] stated that the phase inversion occurs independently of the mixture velocity at a constant input water fraction.

In the region of phase inversion Arirachakaran et al. [6] observed a much stronger increase in the pressure drop as reported by Guzhov et al. [5]. In the investigations of the two phase flow pressure drop of dispersions, Arirachakaran et al. [6] measured values in the order of magnitude of the pressure drop of the single phase flow of the fluid being the continuous phase in the dispersion. According to the results for the pressure drop of the dispersions, Arirachakaran et al. [6] recommended to use the viscosity of the continuous phase in order to calculate the pressure drop of a dispersion, assuming a homogeneous mixture and applying the equations known for single phase pipe flow.

As known from published results, emulsions with volume fractions of the dispersed phase higher than 0.5 often behave as non-Newtonian shear-thinning power-law fluids which for pipeline flow of these emulsions can result in drag reduction behaviour [7, 8] where the drag reduction

behaviour increases with an increase in the dispersed phase concentration [8].
In particular in the region of phase inversion highly shear thinning emulsions are observed.
In the oil-water-gas slug flow the mixing effects can be sufficiently high to disperse one liquid in the other, so that emulsions are formed and a phase inversion is possible ([9, 10, 11, 12, 13]). There are only a few investigations on the effect of such phase inversion phenomena on the three phase flow of oil, water and a gas phase with differing results. Therefore, there is still a lack of knowledge of the effect of gas injection into the flow of two immiscible liquids in horizontal pipes. In order to extend the knowledge of the effect of gas injection on the flow of immiscible liquids in horizontal pipes experimental investigations are carried out. In these investigations shown in the next section the flow behaviour of oil-water mixtures, the pipeline flow of these immiscible liquids and the three phase flow of oil, water and gas are considered.

2 Experimental

In the experimental investigations water and oil are used as the liquid phases. The oil being used is a mineral white oil (Shell Ondina 17) with Newtonian flow characteristics. The emulsions are prepared at room temperature by using tap water and the oil. For stabilizing the emulsions, the non-ionic emulsifier Triton X-100 (iso-octyl phenoxypolyethoxy ethanol) is used. The emulsions are prepared by the agent-in-water method where the emulsifier is first dissolved in the water. The emulsifier concentration is 0.2% by volume based on the water. Thereupon the water and the oil are agitated in a vessel by means of a turbine type stirrer rotating at a controlled speed. The flow behaviour of the emulsions is measured by means of a Haake RV-12 coaxial cylinder viscosimeter with the NV sensor system. The measurements are carried out at shear rates in the range from $16\frac{1}{s}$ to $2628\frac{1}{s}$. In the experiments the water concentration in the oil-water mixture

$$\varepsilon_{f1} = \frac{V_{f1}}{V_{f1} + V_{f2}} \tag{1}$$

which is the volume of the water phase V_{f1} related to the total volume of the liquid mixture, is varied in the range from $\varepsilon_{f1} = 0$ (pure oil) to $\varepsilon_{f1} = 1.0$ (pure water) in steps of 10 % as shown in Fig. 1. Fig. 1 depicts the flow diagram for the emulsions investigated. The shear stress increases by increasing shear rates. The water as well as the oil shows Newtonian flow behaviour. The mixtures of oil and water with water concentrations above $\varepsilon_{f1} > 0.6$ also show Newtonian flow behaviour while mixtures with lower water concentrations show shear thinning behaviour. The non-Newtonian emulsions seem to follow the power law equation $\tau = K\,\dot{\gamma}^n$ where K is the power law constant and n is the power law index. The lowest value for the power law index observed in this study is approximately in the order of $n \approx 0.5$ for the water concentration of $\varepsilon_{f1} = 0.1$ in the region of phase inversion.

For all shear rates, the highest values are obtained in case of water fractions of about $\varepsilon_{f1} = 0.1$, where the phase inversion from an oil-in-water to a water-in-oil emulsion is observed. For water concentrations between $\varepsilon_{f1} = 0.1$ and $\varepsilon_{f1} = 0.3$, the emulsion becomes unstable resulting in oil-in-water dispersions for water concentrations above $\varepsilon_{f1} > 0.3$.

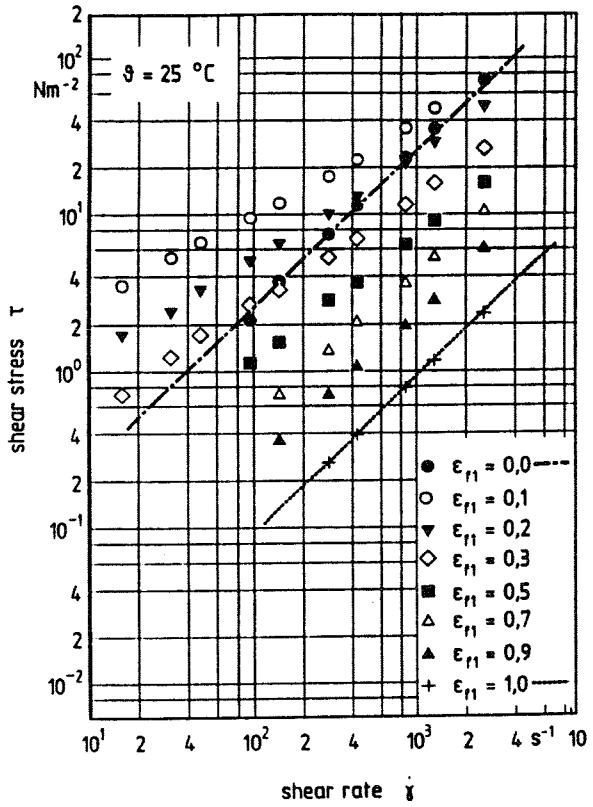

Fig. 1: The flow behaviour of two phase mixtures of water and oil

The pipeline flow measurements are conducted in the experimental setup shown in Fig. 2.

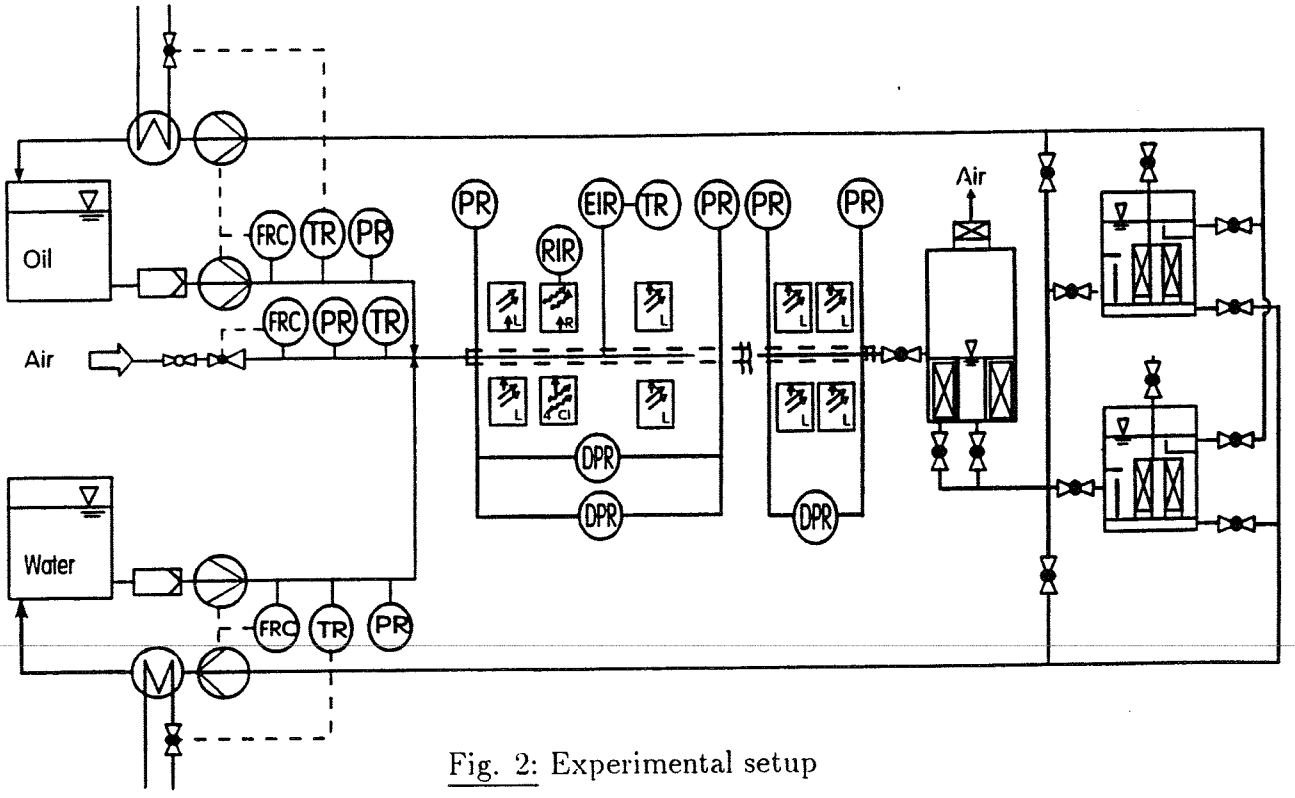

Fig. 2: Experimental setup

By means of this experimental setup, the two-phase flow of water and oil as well as the three-phase flow of oil, water and gas in various compositions is investigated. In contrast to the rheological investigations the investigations on the pipeline flow are conducted without any Triton X-100. Water and oil are conveyed from separate supply vessels into the pipeline. The volumetric flow rates of the liquids are regulated by varying the number of revolutions of the centrifugal pumps. In the three phase flow experiments the gas phase is air which is supplied by a compressor network. The volumetric flow rates of all phases can be regulated independently and are measured by turbine flow meters and orifice gauges.

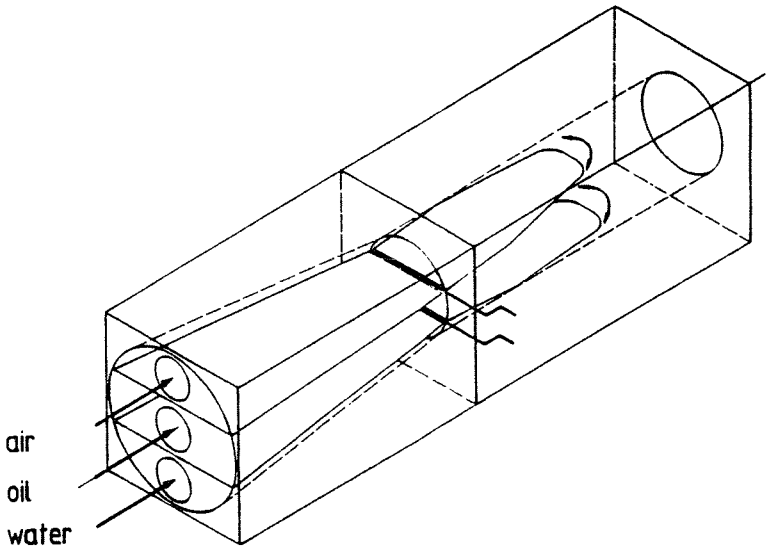

Fig. 3: Schematic diagram of the entrance nozzle

The pure phases of oil, water and gas are fed into the pipeline by a nozzle which is shown in Fig. 3. The nozzle is cone-shaped. It has three sections separated by baffle plates. Each baffle plate consists of two parts, the second of which can be inclined upwards and downwards. This design has been selected to prevent the formation of emulsions due to mixing effects taking place in the entrance nozzle. For the experiments shown in this paper, the baffle plates are inclined so that the mixing between the phases within the nozzle and just behind is reduced to a minimum.

By means of these baffle plates, the phases are fed into the pipeline in layers corresponding to their density. The pipeline is manufactured of perspex with an internal diameter of 59.0 mm. The total length of the multiphase flow pipeline between the entrance nozzle and the separation unit is approximatly 48 m. The multiphase pipeline consists of two legs connected by an U-bend with a leg length of 25 m and 23 m, respectively. The measurements in the first leg are taken behind an entrance length l_e of approximately 12 m ($l_e/d \approx 225$). The measurements in the second leg are taken behind a length of approximately 15 m between the bend and the upstream pressure taping ($l_e/d \approx 680$ from the entrance nozzle).

2.1 Flow regimes of the two phase flow of oil and water

The flow regimes observed in the experimental investigation of the two phase flow of water and oil are shown schematically in Fig. 4, the resulting flow pattern map is given in Fig. 5. In the following there is distinguished between dispersions and emulsions. The flow is identified as a

dispersion if there are layers of one continuous phase in which the other phase is nonuniformly dispersed. For emulsions, one continuous phase is flowing in the entire pipe cross-sectional area, while the other phase is uniformly dispersed in nearly equally sized droplets within the continuous phase.

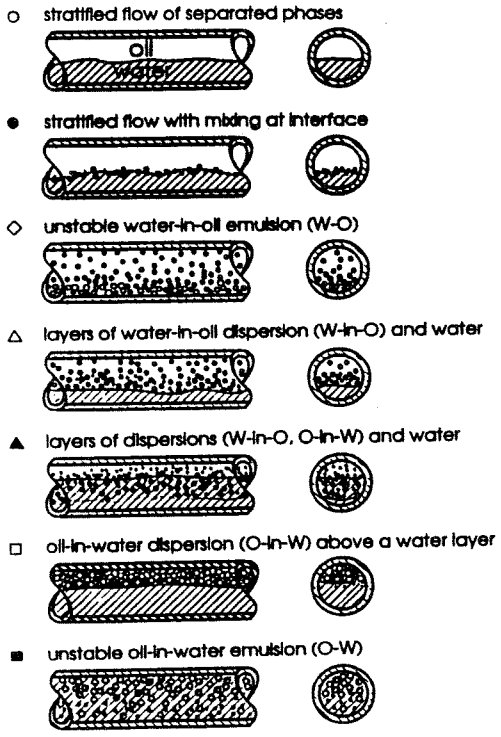

Fig. 4: Schematic diagram of flow regimes of the two phase flow of water and oil

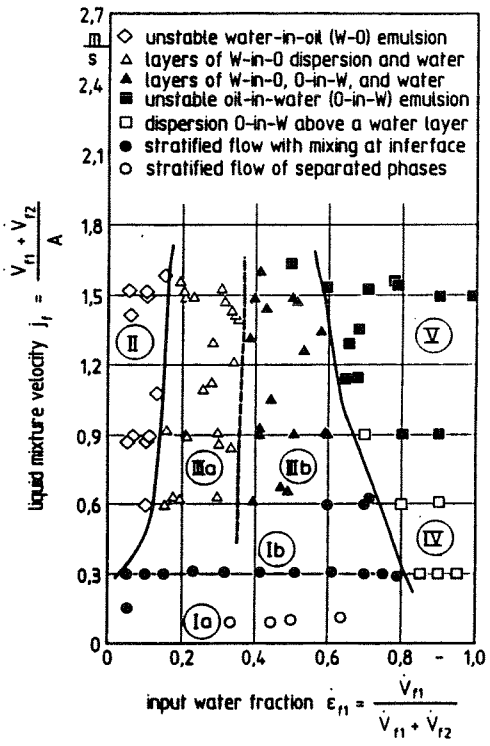

Fig. 5: Flow pattern map for the two phase flow of water and oil

In Fig. 5 the flow regimes distinguished in the present study are shown in a plot of the liquid mixture velocity j_m versus the input water fraction $\dot{\varepsilon}_{f1}$ as proposed by Guzhov et al. [5]. The mixture velocity

$$j_f \equiv \frac{1}{A}\left(\dot{V}_{f1} + \dot{V}_{f2}\right) \tag{2}$$

is defined as the sum of the volumetric flow rates $\dot{V}$ of the water phase, denoted with the index "$f1$", and the oil phase, denoted with "$f2$", related to the pipe cross sectional area A. The input water fraction

$$\dot{\varepsilon}_{f1} = \frac{\dot{V}_{f1}}{\dot{V}_{f1} + \dot{V}_{f2}} \tag{3}$$

is defined as the volumetric flow rate of the water phase $\dot{V}_{f1}$ related to the total volumetric flow rate of the water and the oil phase $\dot{V}_{f1} + \dot{V}_{f2}$.
In the range of mixture velocities less than $j_f = 0.3\ \frac{m}{s}$, the stratified flow regime is observed where water ($\varrho_{f1} \approx 998\ \frac{kg}{m^3}$) and oil ($\varrho_{f2} \approx 841\ \frac{kg}{m^3}$) are flowing in layers correponding to their density (region Ia in Fig. 5). In the stratified flow regime an increase of the liquid

mixture velocity leads to the formation of an interfacial region consisting of oil and water droplets dispersed within the water and the oil layer, respectively (region 1b). The size of the droplets dispersed deceases significantly while the mixture flows downstream. In the first leg the decrease of the size of the droplets of the dispersed phase with increasing entrance length agrees with the results reported by Collins & Knudsen [14]. In the second leg the droplet size seems to be nearly constant. This supports the assumption of Karabelas [15] that a maximum stable drop diameter is formed after an entrance length of 600 times the internal pipe diameter.

Increasing the mixture velocity above $j_f = 0.3\ \frac{m}{s}$ results in an increasing heigth of the mixing zone and finally in a dispersion filling the whole pipe cross-sectional area. In case of input water fractions less than $\dot{\varepsilon}_{f1} < 0.2$, the flow of unstable water-in-oil emulsions is observed which consist of small water droplets homogeneously dispersed in a continuous oil phase in the total pipe cross sectional area (region II). In this region the emulsions look like a viscous gel for input water fractions between $\dot{\varepsilon}_{f1} = 0.1$ and $\dot{\varepsilon}_{f1} = 0.2$.
By increasing the input water fraction, dispersions of water-in-oil are observed. The amount of water dispersed within the oil increases with increasing distance from the top of the pipe and reaches a maximum above the bottom of the pipe where a continuous water film is flowing (region IIIa).
An increase of the input water fraction above $\dot{\varepsilon}_{f1} = 0.35$ leads to a decreasing height of the layer consisting of a water-in-oil dispersion and an increasing height of the water layer where the upper part of the water layer consists of an oil-in-water dispersion (region IIIb).
In case of liquid mixture velocities less than $j_f = 0.9\ \frac{m}{s}$ a further increase of the input water fraction results in the flow regime of oil droplets in water (region IV) while in case of higher mixture velocities unstable emulsions of oil-in-water are observed (region V).
In the region of phase inversion the external phase inverts from oil to water or vice versa. This region is assosciated with region IIIa as well as with region IIIb. The points of phase inversion obtained by means of visual observations are shown in Fig. 5 by the dashed line. According to the results of these observations a phase inversion for input water fractions in the order of $\dot{\varepsilon}_{f1} \approx 0.35$ is expected. In contrast to this the measurements of the impendance of the oil-water mixtures flowing in the pipe show a first abrupt change in conductivity for input water fractions in the range from $\dot{\varepsilon}_{f1} = 0.05$ (for $j_f = 0.3\ \frac{m}{s}$) to $\dot{\varepsilon}_{f1} = 0.2$ (for $j_f = 1.5\ \frac{m}{s}$) and a second abrupt change in conductivity for input water fractions in the range from $\dot{\varepsilon}_{f1} = 0.6$ (for $j_f = 1.5\ \frac{m}{s}$) to $\dot{\varepsilon}_{f1} = 0.8$ (for $j_f = 0.3\ \frac{m}{s}$). The corresponding points for phase inversion determined by means of the conductivity measurements are shown in Fig. 5 by the solid lines. The different methods of determining phase inversion may be one reason for the scatter of the values of input water fraction required for phase inversion reported in the literature. Nevertheless, the determination of phase inversion by means of conductivity measurements is the more accurate one as shown in the next section.

2.2 The Pressure drop of the two phase flow of oil and water

Due to the significant change in the droplet size of the dispersed phase observed in the first leg, in the present paper only results for the pressure drop of the oil-water mixtures obtained in the second leg are considered. In Fig. 6 the pressure drop for the pipeline flow of oil-water mixtures is shown as a function of the input water fraction.
As shown in other investigations mentioned above, the highest values of the pressure drop are measured in the region where phase inversion takes place. Therefore, the maxima of the

pressure drop may be used to confirm the region of phase inversion. The absolute maxima of the pressure drop are measured for input water fractions from $\dot{\varepsilon}_{f1} \approx 0.1$ to $\dot{\varepsilon}_{f1} \approx 0.2$. At this point the pressure drop is higher than the values for the pipe flow of the pure oil with the same velocity $j_{f2} = j_f$.

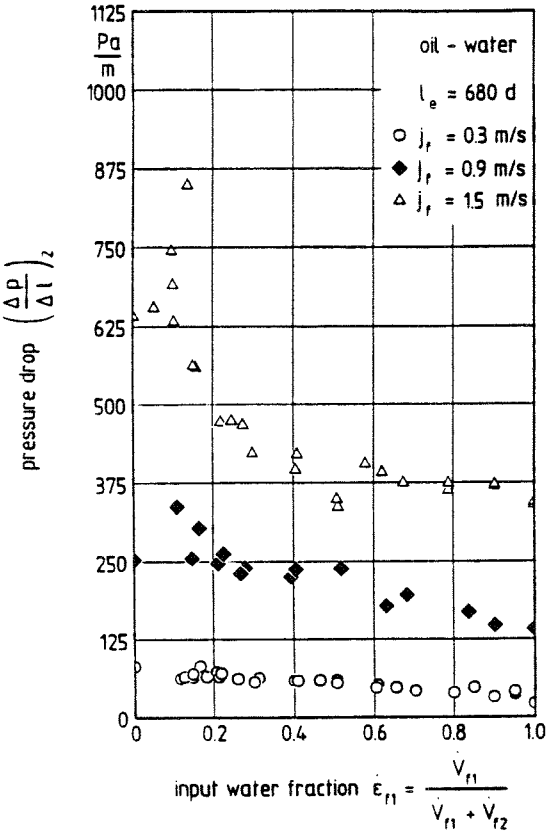

Fig. 6: Pressure drop of the two phase flow of water and oil

For input water fractions in the range from $\dot{\varepsilon}_{f1} = 0.35$ to $\dot{\varepsilon}_{f1} = 0.6$. the pressure drop of the two phase flow of oil and water is less than the pressure drop of the pure oil. This range of pressure drop reduction is in agreement with the results of Charles et al. [3, 4] mentioned above. After passing this region of a minimum pressure drop, a further increase of the input water fraction results in a second increase of the pressure drop up to a second maximum. This increase of the pressure drop is associated with an inversion from region III to the flow regime of oil-in-water emulsions (region V). The second maximum of the pressure drop occurs for input water fractions where the oil is fully dispersed in the water phase. In case of liquid mixture velocities of $j_f = 0.9\frac{m}{s}$ and less, the values of this second maximum are lower than the values obtained for the pure oil. After passing the second maximum a further increase of the input water fraction results in continuously decreasing values of the pressure drop down to the pressure drop of the single phase flow of the water.

Comparing the results for the maximum shear stress obtained in the rheometer experiments and the results for the maximum pressure drop in the region of phase inversion the corresponding input water fractions are in agreement. It is indicated that emulsification of the oil-water mixtures along the pipe takes place. Therefore, there is a sufficient mixing effect in the pipeline

so that the liquids which are fed into the pipeline in layers correponding to their density are dispersed forming emulsions. This is in agreement with the results of Russel et al. [1, 2].

2.3 The Pressure drop of the three phase flow of oil, water and air

The three phase flow experiments are conducted in several test series each consisting of several test runs. In a test serie the total volumetric flow rate of the liquid phases $\dot{V}_f = \dot{V}_{f1} + \dot{V}_{f2}$ and hence the superficial liquid velocity $j_f = \frac{\dot{V}_{f1}+\dot{V}_{f2}}{A}$ is kept constant while the superficial air velocity $j_g = \frac{\dot{V}_g}{A}$ which is the volumetric flow rate of the gas phase $\dot{V}_g$ related to the pipe cross sectional area A is varied. Each test run is conducted for a constant input water fraction $\dot{\varepsilon}_{f1}$ defined by equation (3).
The results shown in Figs. 8 to 13 are obtained for test series carried out with constant superficial liquid velocities of $j_f = 0.3\,\frac{m}{s}$, $j_f = 0.9\,\frac{m}{s}$ and $j_f = 1.5\,\frac{m}{s}$, respectively.
Even in case of small superficial air velocities $j_g \approx 0.1\frac{m}{s}$ the intermittent flow regime is observed. Therefore, all results shown in Figs. 8 - 13 are obtained either in the elongated bubble flow regime, where unaerated liquid plugs seperated by elongated gas bubbles are flowing, or in the aerated slug flow regime where gas entrainment into the liquid plugs occurs. The flow of liquid slugs filling the whole cross-sectional area of the pipe and elongated gas bubbles is schematically shown in Fig. 7.

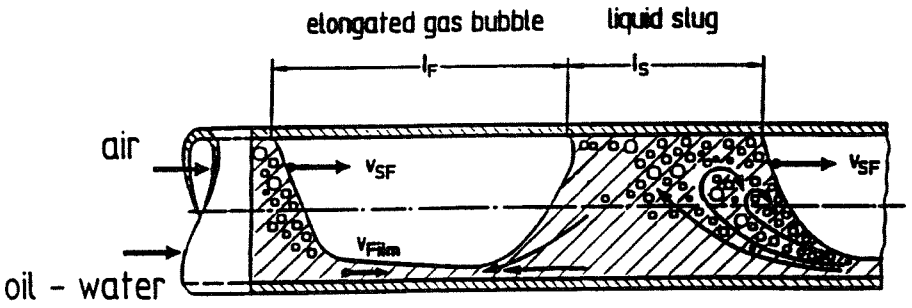

Fig. 7: Schematic diagram of a the slug flow

The transition from the elongated bubble to the plug flow regime is observed for superficial air velocities in the range from $j_g = 0.4\frac{m}{s}$ to $j_g = 1.0\frac{m}{s}$. First, it should be noted that in all tests conducted in the aerated slug flow regime and presented in these Figs. 8 - 13 there is always a water layer observed flowing on the bottom of the pipe if the input water fraction is above $\dot{\varepsilon}_{f1} > 0.3$.
According to the results shown in Fig. 6, the highest values of the pressure drop of the three phase flow are expected for input water fractions where maxima of the pressure drop of the pipeline flow of water and oil are observed.
Therefore, for a superficial liquid velocity of $j_f = 0.3\frac{m}{s}$, the highest values are expected for oil flowing alone in the pipe and i.e. $\dot{\varepsilon}_{f1} = 0$. This is confirmed by the results shown in Figs. 8, 9.

Pressure drop of three phase flow for a superficial liquid velocity of $j_f = 0.3\ m/s$, ($\frac{l_e}{d} \approx 680$)

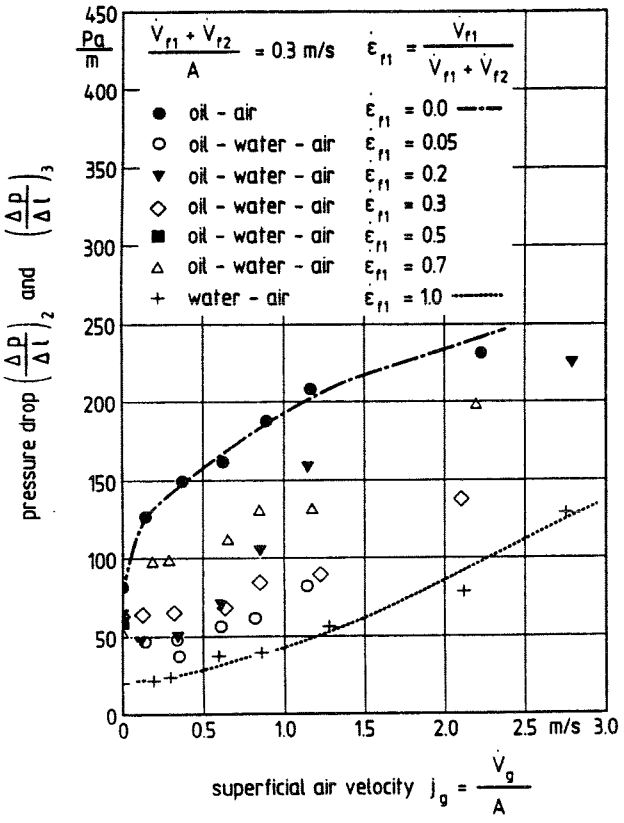

Fig. 8: low gas velocities

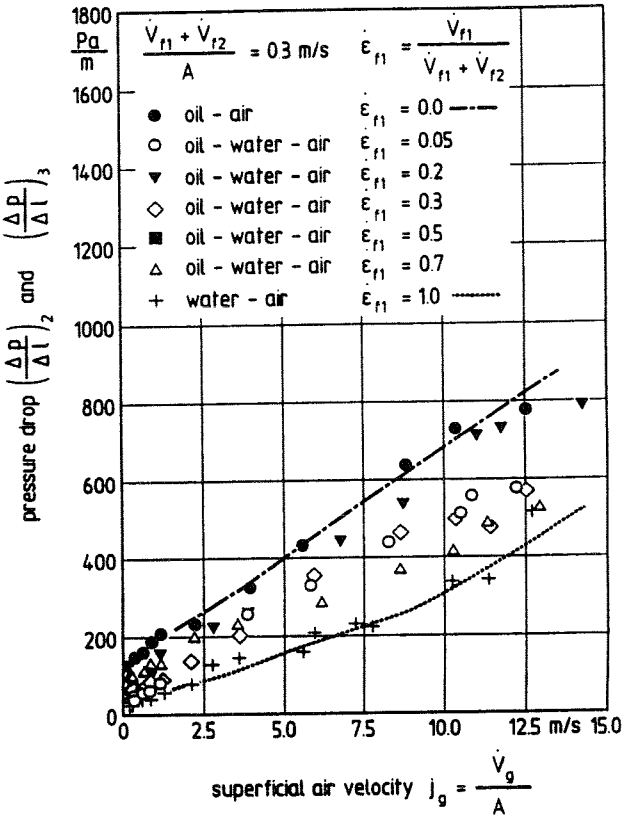

Fig. 9: high gas velocities

The highest and the lowest values of the pressure drop are measured for the two phase flow of oil-air and water-air mixtures, respectively. Considering the values of the pressure drop obtained for input water fractions of $\dot\varepsilon_{f1} = 0.05$ (marked by open circles) and $\dot\varepsilon_{f1} = 0.2$ (marked by solid triangles) in the range of superficial air velocities less than $j_g = 3.0\frac{m}{s}$ (Fig. 8), at first decreasing values of the pressure drop and after passing a minimum increasing values of the pressure drop are observed with increasing superficial air velocity. The pressure drop reduction is up to 50 % in comparison with the pressure drop of the two phase pipeline flow of water and oil. The minimum pressure drop is obtained for a superficial air velocity of $j_g \approx 0.3\frac{m}{s}$ and hence just before the transition from the elongated bubble flow regime to the aerated slug flow regime is observed. Up to this gas velocity the liquid mixture is flowing laminar while in the aerated slug flow regime the liquid mixture is flowing turbulent.

In the aerated slug flow regime the values of the pressure drop of the three phase flow of oil, water and air increase with decreasing input water fractions (Fig. 9), where the decreasing water fractions result in increasing flow averaged oil holdups in the pipeline. The effect of increasing input water fractions on the pressure drop of the three phase flow is similar to the effect on the pressure drop of the two phase flow of water and oil as shown in Fig. 6.

As it is indicated by the results shown in Fig. 1, the oil-water mixtures can show shear-thinning behaviour. The conditions for maximum drag reduction in case of the three phase flow of oil, water and air (Fig. 8) seems to be similar to the conditions observed in the investigations of gas injection into non-Newtonian shear thinning suspensions and polymer solutions reported e.g. by Farooqi et al. [16] and Chhabra et al. [17].

In their studies the effect of drag reduction is contributed to the increasing liquid velocity by increasing rates of air injection which in case of shear-thinning liquids results in a decrease of the apparent viscosity. Furthermore, increasing the rate of air injection leads to increasing flow averaged void fractions and in the intermittent flow regime it results in increasing length of the elongated gas bubbles (Fig. 7) and hence a reduction of the wetted area of the pipe wall. If the pressure gradient along the elongated gas bubble is negligible a net reduction in overall pressure drop over the flow system is possible. The results of the present paper support the assumption that such a mechanism can also exist in the three phase flow of oil, water and gas.

In Figs. 10 and 11 the results for a test series carried out for a superficial liquid velocity of $j_f = 0.9\,\frac{m}{s}$ are shown.

Pressure drop of three phase flow for a superficial liquid velocity of $j_f = 0.9\,m/s$, $(\frac{l_e}{d} \approx 680)$

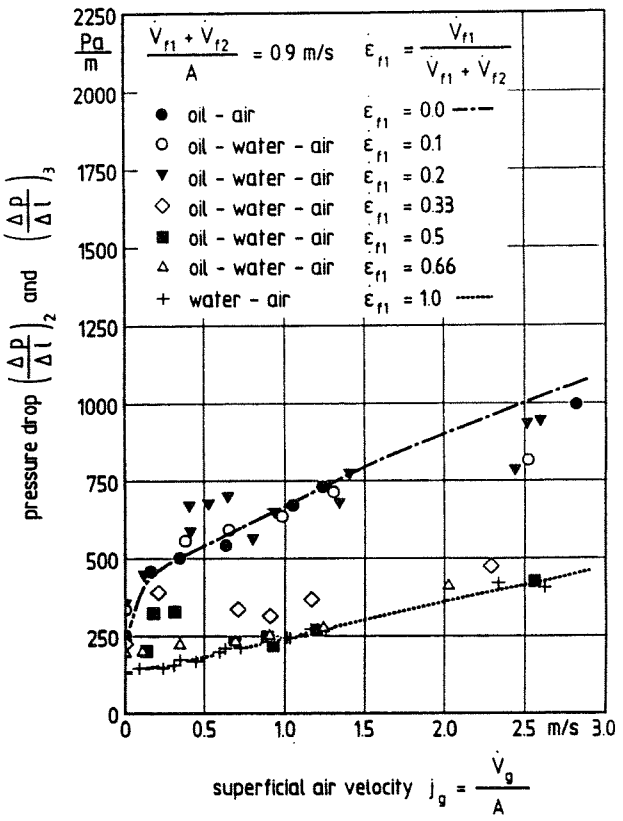

Fig. 10: low gas velocities

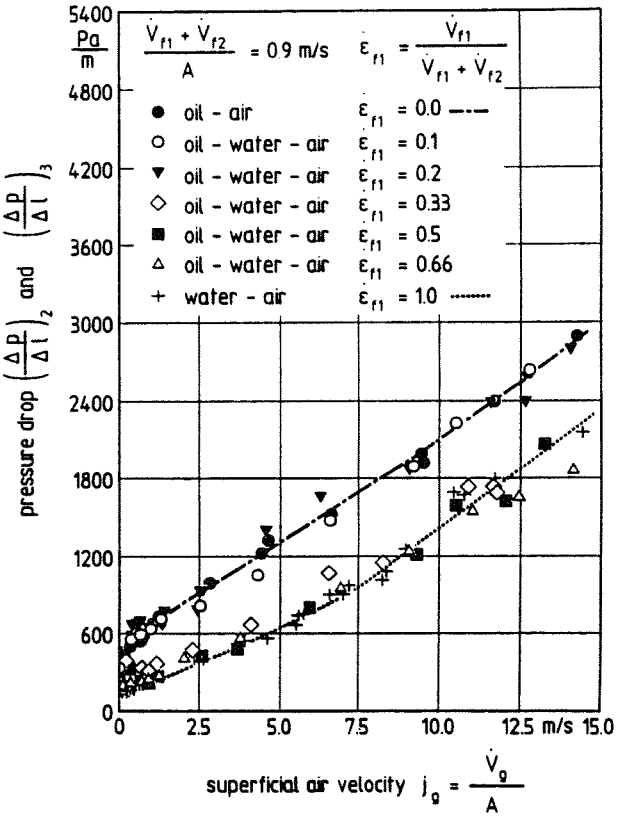

Fig. 11: high gas velocities

The transition from the elongated bubble flow regime to the aerated slug flow regime is observed for a superficial air velocity of $j_g \approx 0.5\,\frac{m}{s}$. Independent of the input water fraction in the elongated bubble flow regime, the values of the pressure drop increase with increasing superficial air velocity. In contrast to the results obtained for superficial liquid velocity of $j_f = 0.3\,\frac{m}{s}$, in case of the superficial liquid velocity of $j_f = 0.9\,\frac{m}{s}$ even low gas injection rates result in a turbulent flow regime and no pressure drop reduction can be determined.

According to results for the effect of air injection into shear thinning fluids reported by Chhabra et al. [17], in case of initially turbulent flowing liquids an increasing rate of air injection is expected to result in increasing values of the pressure drop so that no drag reduction occurs. Therefore, one may assume that in case of the superficial liquid velocity of $j_f = 0.9\ \frac{m}{s}$ and $j_f = 1.5\ \frac{m}{s}$ all oil-water mixtures investigated are flowing turbulent even in the range of smallest gas velocities.

In case of an input water fraction between $\dot{\varepsilon}_{f1} = 0.2$ and $\dot{\varepsilon}_{f1} = 0.5$ in the transition region from the elongated bubble flow regime to the slug flow regime, maxima in the values of the pressure drop are observed (Fig. 10). This increase is contributed to the flow of viscous water-in-oil emulsions.
In the elongated bubble flow regime it is visually observed that a fraction of the area of the pipe wall along the liquid slug wetted by the oil is greater than the area wetted by the water. For superficial air velocities in the range from $j_g = 0.5\ \frac{m}{s}$ to $j_g = 1.0\ \frac{m}{s}$, decreasing values of the pressure drop down to minimal values are measured in case of input water fractions of $\dot{\varepsilon}_{f1} = 0.3$ and $\dot{\varepsilon}_{f1} = 0.5$ (Fig. 10). The minima for the pressure drop are of the same order of magnitude as the pressure drops of the two phase flow of oil and water. By further increasing gas entrainment into the liquid slugs, the pressure drop finally reaches values in the order of magnitude of the two phase pressure drop of water and air. The visual observations indicate that by increasing gas entrainment in case of input water fractions between $\dot{\varepsilon}_{f1} = 0.3$ and $\dot{\varepsilon}_{f1} = 0.7$, there is a sufficient mixing effect resulting in a dispersion of oil in the water, so that the water becomes the continuous and the dominant phase (Fig. 10).
In the aerated slug flow regime (Fig. 11) an increasing of the gas injection rate and hence the turbulence within the liquid slugs results in a decrease of the apparent viscosity so that the values of the pressure drop of the three phase flow approach the values for the two phase flow of water and air for corresponding superficial liquid and gas velocities as shown in Fig. 11.
In contrast to this for input water fractions of $\dot{\varepsilon}_{f1} = 0.1$ and $\dot{\varepsilon}_{f1} = 0.2$, the pressure drop of the three phase flow is of the same order of magnitude as the pressure drop of the two phase flow of oil and air. According to the results shown in Fig. 5 and Fig. 6, these input water fractions are associated with the phase inversion region where the values of the pressure drop for the pipeline flow of oil and water are higher than the values of the single phase flow of oil for the same liquid mixture velocity. This leads to the assumption that in the three phase flow the oil becomes the dominant liquid phase and hence the three phase flow behaves as the two phase flow of oil and gas if the pressure drop of the two phase pipeline flow of water and oil is higher than that of the pure oil.

While in case of superficial liquid velocities of $j_f = 0.3\ \frac{m}{s}$ and $j_f = 0.9\ \frac{m}{s}$ for the single phase flow of the oil the laminar flow regime is obtained, in case of $j_f = 1.5\ \frac{m}{s}$ the oil flow is turbulent. The results measured for the superficial liquid velocities of $j_f = 1.5\ \frac{m}{s}$ are shown in Figs. 12 and 13.
As observed in the results obtained for the superficial liquid velocities of $j_f = 0.9\ \frac{m}{s}$ (Fig. 10) an abrupt increase in the pressure drop is also observed for a superficial liquid velocity of $j_f = 1.5\ \frac{m}{s}$. A local pressure drop maximum occurs in the transition region from the elongated bubble to the slug flow regime. In case of a superficial liquid velocity of $j_f = 1.5\ \frac{m}{s}$ this is only observed for an input water fraction of $\dot{\varepsilon}_{f1} = 0.3$ (Fig. 12).

Pressure drop of three phase flow for a superficial liquid velocity of $j_f = 1.5\,m/s$, $(\frac{l_s}{d} \approx 680)$

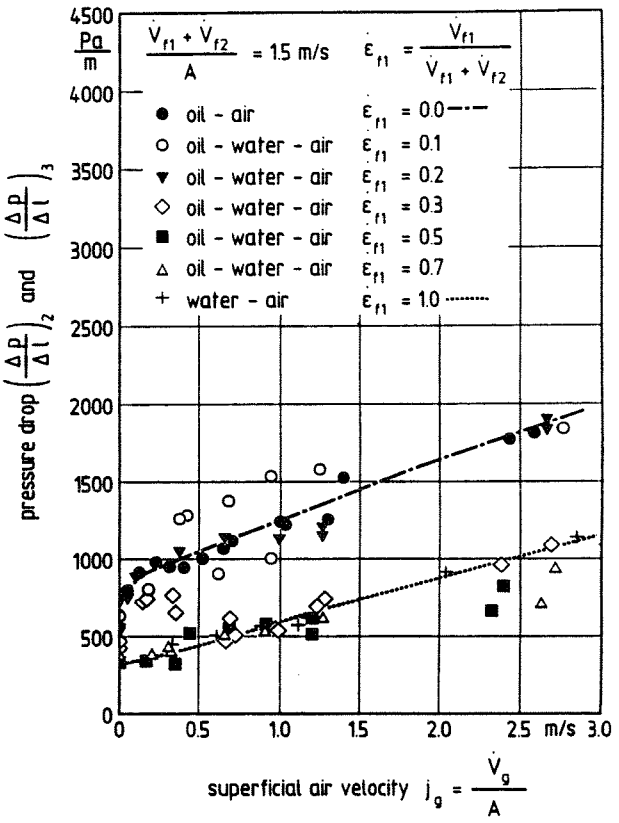

Fig. 12: low gas velocities

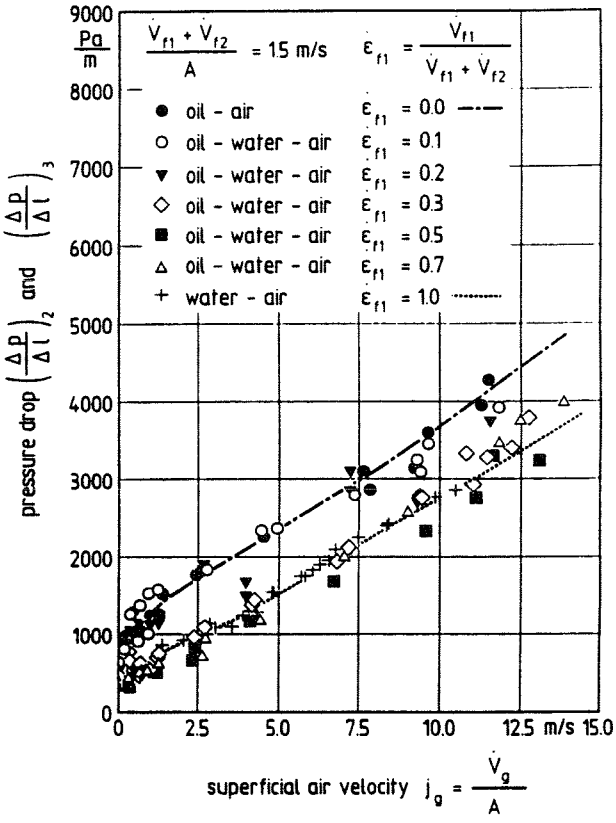

Fig. 13: high gas velocities

In the aerated slug flow regime of the three phase flow in case of the superficial liquid velocity of $j_f = 1.5\,\frac{m}{s}$ (Fig. 13) similar results are obtained in case of initially turbulent flowing liquids as observed in Fig. 11 for the superficial liquid velocity $j_f = 0.9\,\frac{m}{s}$. As shown in Figs. 11 and 13 in the aerated slug flow regime two types of flow regimes can be distinguished by comparing the values of the pressure drop. For input water fractions $\dot{\varepsilon}_{f1} < 0.3$, an oil dominated sytem is obtained where the values of the pressure drop of the three phase slug flow are of the same order of magnitude as the values of the two phase slug flow of oil and air. For input water fractions above $\dot{\varepsilon}_{f1} \geq 0.3$, a water dominated system is obtained if the values of the pressure drop in three phase slug flow are of the same order of magnitude as the values for water-air slug flow for correponding volumetric flow rates of the air and the liquid mixture.
The critical input water fractions observed in Fig. 8 - 13, where the flow inverts from an oil dominated system to a water dominated system, are of the same order of magnitude as the input water fractions for phase inversion in the pipeline flow of the oil-water mixtures (Fig. 6).

3 Conclusion

According to the experimental results for the flow regimes and the pressure drop of the two phase flow of oil-water mixtures, different flow regimes of dispersions can be distinguished:
In case of phase inversion maxima values of the pressure drop of the pipeline flow of water and oil are measured.

The results obtained in the three phase slug flow of oil, water and air indicate that there is a sufficient mixing effect to disperse one liquid in the other and that this mixing can cause a change of the continuous phase within the liquid slugs.
The results of this study are not sufficient to make any conclusions regarding the effect of phase inversion on the flow characteristics of the three phase flow of oil, water and gas. Nevertheless, the results indicate that in case of injecting gas in an initially laminar flowing shear thinning liquid mixture of oil and water drag reduction is possible. The drag reduction increases by increasing the rate of air injection up to maximum gas velocities where the transition from the laminar to the turbulent flow regime within the liquid slugs takes place. In case of initially turbulent flowing liquid mixtures of oil and water, an increasing rate of air injection results in increasing values of the pressure drop.
In the aerated slug flow two flow situations can be distinguished by means of the measured pressure drop:

- In case of a continuous water phase in the liquid slugs, the pressure drop of the three phase flow of oil, water and air is of the same order of magnitude as the pressure drop of the two phase flow of water and air for corresponding superficial liquid and gas velocities. In this case a continuous water layer is flowing above the bottom of the entire pipe.

- In case of a continuous oil phase in the liquid slugs the pressure drop of the three phase flow is of the same order of magnitude as the pressure drop of the two phase flow of oil and air.

The results of the present study indicate that in the three phase flow water becomes the dominant liquid phase if the pressure drop of the two phase flow of water and oil with equal input water fraction and equal superficial liquid velocity is lower than the pressure drop of the oil flowing alone in the pipe with the same velocity. In case of a pressure drop of the pipeline flow of water and oil higher than that of the pure oil, in the three phase flow the oil is expected to become the dominant liquid phase.
According to these results it is recommended that in case of a lack of knowledge of the behaviour of the three phase flow of oil, water and air, the pressure drop of the three phase flow should be approximated by the pressure drop of the two phase flow of water and air in a water dominated system and by the pressure drop of oil and air in an oil dominated system. Therefore, equations are necessary for predicting the critical input water fraction resulting in a water dominated system with a lower pressure drop.
In order to understand the behaviour of the multiphase slug flow of oil, water and gas in pipes further investigations of this multiphase flow are required.

Acknowledgement

The authors wish to acknowledge the financial support of the BMFT (Bundesministerium für Forschung und Technologie) for a program on technical development of Multiphase Transportation Systems.

References

[1] T. Russel, G.W. Hodgson, G.W. Govier: Horizontal pipeline flow of mixtures of oil and water; Can. J. Chem. Engng. 37 (1959) 1, 9/17

[2] T. Russel, M.E. Charles: The effect of the less viscous liquid in the laminar flow of two immiscible liquids; Can. J. Chem. Engng. 37 (1959) 1, 18/24

[3] M. Charles, G.W. Govier, G.W. Hodgson: The horizontal flow of equal density oil-water mixtures; Can. J. Chem. Engng. 39 (1961) 2, 27/36

[4] M. Charles, G.W. Govier , G.W. Hodgson: Complexities inherent in the study of two-phase flow; Can. J. Chem. Engng. 39 (1961) 2, 67/71

[5] A. Guzhov, A.D. Grishin, V.F. Medredev, O.P. Medredeva: Emulsion formation during the flow of two immiscible liquids; Neft. Choz. (1973) 8, 58/61, (in Russian)

[6] S. Arirachakaran, K.D. Oglesby, M.S. Malinowsky, O. Shoham, J.P. Brill: An analysis of oil/water flow phenomena in horizontal pipes; SPE Paper 18836, SPE Proc. Prod. Operating Symp. Oklahoma 1989

[7] R. Pal, Y. Yan, J. Masliyah: Rheology of Emulsions; in: L.L. Schramm (ed.) Emulsions, Advances in Chemistry Series 231 (1992), 131/169

[8] R. Pal: Pipeline Flow of Unstable and Surfactant-Stabilized Emulsions; AIChE J. 39 (1993) 11, 1754/1764

[9] M. Galaymov, N.L. Karpushin: Change in the viscosity of the liquid phase during the movement of gas-water-oil mixtures in pipelines; Transport, Khranenie Nefti, Nefteproduktov (1971), 14/16 (in Russian)

[10] A. Bacharov, R.S. Andriasov, V.A. Sakkarov: Investigation of the motion of gas-water-oil mixtures in horizontal pipes; Neftepromyslovoe delo 6 (1972), 27/30, (in Russian)

[11] A. Hall: Multiphase Flow of Oil, Water and Gas in Horizontal Pipes; Ph. D. Thesis, Imperial College, Univ. London, London 1992

[12] K. Lunde, S. Nuland, M. Lingelem: Aspects of three-phase flows in gas condensate pipelines; Paper I1, 30th European Two-Phase Flow Group Meeting, Hannover 1993

[13] M. Nädler, D. Mewes: Multiphase slug flow in horizontal pipes; Paper I2, 30th European Two-Phase Flow Group Meeting, Hannover 1993

[14] S. Collins, J.G. Knudsen: Drop-size distributions produced by turbulent pipe flow of immiscible liquids; AIChE J. 16 (1970) 6, 1072/1080

[15] A. Karabelas: Droplet size spectra generated in turbulent pipe flow of dilute liquid/liquid dispersions; AIChE J. 24 (1978) 2, 170/180

[16] S. Farooqi, N.I. Heywood, J.F. Richardson: Drag Reduction by Air Injection for Suspension Flow in a Horizontal Pipeline; Trans. Inst. Chem. Engrs. 58 (1980) 1, 16/27

[17] R. Chhabra, S.I. Farooqi, J.F. Richardson: Isothermal Two-Phase Flow of Air and Aqueous Polymer Solutions in a Smooth Horizontal Pipe; Chem. Eng. Res. Des. 62 (1984), 22/32

MODELING AND SIMULATION OF DROPLET BEHAVIOR IN ANNULAR MIST FLOW

I.Kataoka[1], K.Matsuura[2], A.Tomiyama[3] and A.Serizawa[2]

[1]Institute of Atomic Energy
Kyoto University
Uji, Kyoto 611, Japan
Telephone:(0774)32-3111Ext.2325, Facsimile:(0774)33-3234

[2]Department of Nuclear Engineering
Kyoto University
Sakyo-ku, Kyoto 606, Japan
Telephone:(075)753-5823, Facsimile:(075)753-5845

[3]Department of Mechanical Engineering
Kobe University
Rokkodai, Kobe 657, Japan
Telephone:(078)881-1212Ext.5344, Facsimile:(078)881-0036

ABSTRACT

Droplet behavior in gas-liquid annular mist flow was analyzed and modeled. Based on the modeling, Lagrangian simulation of droplet was carried out. Previous correlations of droplet deposition coefficient were surveyed and systematic comparisons were carried out. The predicted values of deposition coefficient considerably differ among the correlations. In view of this survey, modeling and formulation of droplet flow were carried out. For Eulerian simulation, basic conservation equations of dispersed phase in droplet flow were derived which reasonably reflect the physical aspects of droplet flow. For Lagrangian simulation of droplet, basic equations were formulated and was derived. Based on the simplified model, Lagrangian simulation of droplet in mist flow was carried out and results indicated this method reasonably predicted the diffusion phenomenon of droplets in turbulent field observed in the experiment.

1.INTRODUCTION

Annular mist flow is one of the most important flow regimes in gas-liquid two-phase flow. In many industrial equipments such as boiler, nuclear reactor, chemical plant, this flow regime is often encountered both in normal and anomaly conditions. Therefore, considerable researches have been carried out on this flow regime both experimentally and analytically [1,2] and a lot of knowledge has been accumulated. However, due to the complexity of the phenomena, there are still some subjects to be studied further. Among such subjects, droplet behavior such as deposition and entrainment of droplets are quite important. Recently, detailed analytical model such as three fluid model has developed and numerical analyses of various thermohydrodynamic characteristics of annular dispersed flow such as film dryout, become possible based on this model. In calculation using three fluid model [3,4], consitutive equations of droplet deposition rate and droplet entrainment rate from liquid film are most crucial in predicting the various phenomena in annular dispersed flow. Of course, there have been considerable experimental and analytical works on deposition and entrainment phenomena [1-14]. However, experimental data and correlations still show considerable scatters. Furthermore, due to the difficulties of experimental techniques, most of experiments are limited to low pressure and low temperature condition under simple geometries such as round tube or rectangular duct. On one hand, much more detailed experiments and analyses are needed. On the other hand, as a method for compensating the limitation of experiments, numerical analyses of annular dispersed flow and droplet behavior becomes more and more impor-

tant along with remarkable progresses of computer and numerical technologies. Using such method, detailed analyses of annular dispersed flow and droplet behavior under high pressure and high temperature, under complicated flow geometries become possible. However, in order to carry out such numerical analyses accurately and reasonably, it is needed to have adequate understanding of previous research works. Furthermore, indispensable are accurate and appropriate modeling and consistent mathematical formulations of phenomena of annular dispersed flow and droplet behavior.

In view of these, in this paper, survey and researches are carried out particularly on the droplet behavior and deposition rate in annular dispersed and droplet flows. Firstly, the survey of previous correlations of droplet deposition coefficient and systematic comparisons of these correlations are carried out. Secondly, basic conservation equations of mist flow are derived which are consistent with detailed simulation of droplet behavior. Then, basic equations for droplet behaviors in turbulence field are formulated. Finally, based on these formulation, preliminary simulation for droplet behavior in turbulence field is carried out and turbulent diffusion of droplets is simulated and compared with experimental data.

2.COMPARISON OF PREVIOUS CORRELATIONS OF DROPLET DEPOSITION COEFFICIENT [15]

Deposition rate of droplet is one of the most important parameters in analyzing thermohydrodynamic characteristics of annular dispersed flow and droplet flow. In particular, in analysis based on three fluid model [3,4], this parameter is the key parameter in predicting various phenomena in annular dispersed flow, such as dryout heat flux and post dryout heat transfer. There have been considerable researches on droplet deposition rate and various correlations have been proposed. However, due to the complexity of the droplet deposition phenomenon, experimental data show considerable scattering and resultantly, there are discrepancy among the correlations. The correlations proposed so far were derived based on the experimental data under various ranges of experimental conditions. They are expressed in various dimensional or dimensionless parameters. Therefore, there have been no systematic comparisons among these previous correlations of droplet deposition rate. However, in order to make the prediction of various phenomena in annular dispersed flow more accurate, it is quite important to evaluate the previous correlations of droplet deposition and develop reliable correlation based on further experimental research, physical modeling, and numerical analyses. For this purpose, here, the survey of typical previous correlations of droplet deposition rate and systematic qualitative comparisons among these correlations are carried out.

2.1 Previous Correlation of Droplet Deposition Rate

Usually, droplet deposition rate is given in terms of droplet deposition coefficient K(m/s) and averaged mass density of droplet in the gas core, C(Kg/m^3) which is given by

$$\dot{d} = K\ C \tag{1}$$

Therefore, correlations of deposition coefficient K have been proposed by various researchers [4-14] based on various experimental data and modelings. Comprehensive literature survey was carried out and following typical correlations were chosen for the comparisons purpose.

Alexander & Coldren's Correlation [5]

This correlation is one of the oldest correlation of deposition coefficient. It is based on the experimental data obtained in air-water system in 0.0472 diameter tube under atmospheric pressure. It is given in dimensional form as

$$K = 0.00410\ u_G^{1.17} \qquad K:m/s,\ u_G:m/s \tag{2}$$

Goldmann et al's Correlation [6]

This correlation is obtained based on the experimental data of dryout heat flux for steam-water system under high pressure. In deriving this correlation, it is assumed that at dryout point,

mass flux due to deposition of droplet is equal to the mass flux due to evaporation.

$$K/u_G = 0.023\ Re_G^{-0.2} \tag{3}$$

Here, Re_G denotes Reynolds number of gas (vapor) phase.

Paleev & Fillipovich's Correlation [7]

This equation is based on the experimental data of deposition rate for air–water two–phase flow under atmospheric pressure in horizontal rectangular passage of which hydraulic diameter is 4mm. This correlation is given in dimensionless form based on the physical consideration of droplet deposition coefficient. It takes into account of the effect of density ratio between gas and liquid and the effect of droplet mass density. This correlations is often used for the evaluation of droplet deposition rate as one of standard correlations of droplet deposition coefficient since it agrees with experimental data for relatively wide range of experimental data.

$$K/u_G = 0.022\ Re_G^{-0.25}\ (C/\rho_L)^{-0.26}\ (\rho_L/\rho_G)^{0.26} \tag{4}$$

Here, ρ_L and ρ_G are density of liquid and gas phases respectively.

Namie & Ueda's Correlation [8]

Namie and Ueda carried out detailed analyses of droplet behavior in the turbulent gas field and together with detailed experimental data they derived the correlation of droplet deposition coefficient. Their correlation considers the effects of droplet size and its distribution, droplet mass concentration, and many other parameters in droplet flow. The exact form of their correlation is very complicated and some of the parameters are given in graphical form. The approximate expression of their correlation is given by

$$K/u_G = Re_G^{-0.3}\ f(a)\ 10^{-0.012Ge} \tag{5}$$

Here, f(a) is the function which represent the effect of droplet diameter and given in graphical form.

Yanai's Correlation [9]

This correlation is proposed as one of the constitutive equations in the method of dryout heat flux based on three fluid model by Yanai. Using this correlation, Yanai predicted the dryout heat flux and compared his own experimatnal data of dryout heat flux in round tube for steam–water system. Therefore, this correlation is derived indirectly by dryout heat flux and the method of dryout heat flux. It is given by

$$K/u_G = Re_G^{-0.5} \tag{6}$$

Hutchinson & Whalley's Correlation [10]

This correlation is derived by research group in Harwell Laboratory, UK. This correlation is one of the most standard correlations of droplet deposition coefficient and quoted and used most often up to now. In this correlation, the droplet deposition coefficient is not dependent of gas flux nor droplet mass concentration but only the function of surface tension. based on the experimental data mainly for steam–water experiments, the deposition coefficient is given in graphical form. Katto [16] gives the approximate expression of this correlation which is given by

$$\begin{aligned} K &= 0.405\ \sigma^{0.915} \quad \sigma<0.0383 \\ &= 9.48\times10^{4}\ \sigma^{4.7} \quad \sigma>0.0383 \end{aligned} \qquad K:\ m/s,\quad \sigma:n/m \tag{7}$$

McCoy & Hanratty's Correlation [11]

McCoy and Hanratty carried out a comprehensive survey of the experimental researches on droplet deposition coefficient. Based on previous experimental data and their own, they derived this correlation along with detailed physical analyses of droplet behavior. The characteristic feature of this correlation is that it is given in terms of dimensionless relaxation time τ_+ which repre–

sent the time scale of droplet's following the turbulent motion of gas phase.

$$K/u_f = 3.25\times10^{-4}\ \tau^{+2} \qquad \tau^+<22.9$$
$$= 0.17 \qquad \tau^+>22.9 \tag{8}$$

$$\tau^+ = \frac{d_P^2 u_f^2 \rho_G^2}{18\mu_G^2}\ \frac{\rho_L}{\rho_G} \tag{9}$$

where u_f denotes friction velocity which is given by the wall shear stress of gas phase flow.

Saito's Correlation [12]

Similar to Yanai's correlation, this correlation is derived in order to predict dryout heat flux for steam water system based on three fluid model. Saito surveyed the previous correlations and experimental data of deposition coefficient and derived this correlation assuming that the deposition coefficient is only the function of mass concentration of droplet.

$$K = 1.698\times10^{-2} - 2.117\times10^{-4}C + 2.896\times10^{-6}C^2 - 2.192\times10^{-8}C^3 + 7.778\times10^{-11}C^4 - 1.027\times10^{-13}C^5 \tag{10}$$

Andreussi's Correlation [13]

This correlation is basically same type of correlation as McCoy & hanratty's correlation. In this correlation, the effect of mass concentration of droplet is introduced as

$$K/u_f = 0.115/(1 + 2.3\ C/\rho_G) \tag{11}$$

Whally & Hewitt's Correlation [14]

This correlation is also derived by research group in Harwell Laboratory, UK. In this correlation, the effects of gas flux and mass concentration of droplet is taken into account. Moreover, this correlation is given in dimensionless form which is given by

$$K/u_C^* = 87\ \{\mu_L^2/(D\sigma\ \rho_L)\}^{0.5} \tag{12}$$

Here, u_c^* is the friction velocity considering the mass concentration in gas core and given by following equation.

$$u_C^* = (\tau_i/\rho_C)^{0.5} \tag{13}$$

$$\rho_C = \rho_G\ (G_e + G_G)/G_G = C + \rho_G \tag{14}$$

where G_e and G_G are mass flow rate of droplet and gas respectively and τ_i is interfacial shear stress on liquid film which is given by "triangular relationship" among interfacial shear stress, liquid film thickness and entrainment rate which is proposed by Harwell research group.

Sugawara's Correlation [4]

Sugawara developed computer code called "FIDAS" which predict hydrodynamics characteristics of annular dispersed flow based on three fluid model. In this code, he developed this correlation of droplet deposition coefficient based of the physical analyses of droplet deposition phenomenon and previous experimental data particularly high pressure steam water system. This correlation also takes into accounts of mass concentration of droplet and confirmed through the dryout heat flux prediction in high pressure steam water flow.

$$K/u_G = 0.009\ Re_G^{-0.2}\ (C/\rho_G)^{-0.5}\ Pr_G^{-2/3} \tag{15}$$

2.2 Comparison of Correlations

Systematic comparisons among the correlations of droplet deposition coefficient described above were carried out. Since those correlations are expressed in various dimensionless and dimensional parameters, comparisons were made under various flow conditions. Here, in view of applications to nuclear reactor thermohydraulics, comparisons were carried out for water-steam

system of which conditions were listed below.

Pressure: 1.0 and 7.1 Mpa Mass Flux: 500 – 2000 Kg/m^2/s
Hydraulic Diameter of Flow passage: 5 –20 mm
Steam Quality: 0.2 –0.6 Entrainment Ratio: 0.02 – 1.0

Some examples of the comparisons were shown in Figs.1 through 4. In Figs.1 and 2, quality is fixed and entrainment ratio (ratio between droplet mass flow rate and total mass flow rate of liquid) are varied from 0.02 to 1.0. On the other hand, in Figs.3 and 4, entrainment ratio is fixed and quality is varied from 0.2 to 0.6. Here, entrainment ratio and quality represent mass concentration of droplet and gas velocity respectively which are related by

$$u_G = x\,G\,/\,\rho_G \tag{16}$$

$$C = E(1-x)G/u_G \tag{17}$$

As these figures show, the droplet deposition coefficients given by above mentioned correlations scatter considerably ranging one or two order of magnitude. This indicates that the accurate evaluation of droplet deposition coefficient is still very difficult and a lot of research efforts are needed in order to develop a reliable correlation.

The dependence of droplet deposition coefficient on entrainment ratio is shown in Fig.1 and 2. As shown in these figures, the correlations are divided into two groups in regard to the dependence on the entrainment ratio (or droplet mass concentration). In one group, the deposition coefficient decreases with increasing entrainment ratio (Paleev's correlation etc.). In the other group, the deposition coefficient does not depend upon entrainment ratio (Hutchinson's correlation etc.). It is interesting and important whether the deposition coefficient depend upon entrainment ratio (or mass concentration of droplet). As shown in Figs.1 and 2, the general trend of deposition coefficient surveyed here indicates that deposition coefficient decreases with increasing entrainment ratio for small entrainment ratio while it is almost independent of entrainment ratio for large entrainment ratio.

The dependence of deposition coefficient on steam quality (gas flux) is shown in Fig.3 and 4. As shown in these figures, most correlations show the dependency on the quality except for Hutchinson's correlation and Saito's correlation. The dependency on the quality also differs from correlation to correlation. As described in previous section, this is due to the dependency on gas flux and the exponent of gas flux varies from 0.5 to 1.2 depending on the correlation.

When the system pressure decreases, the discrepancy among the correlations becomes larger as shown in Fig.2. There are no dependence on the hydraulic diameter within the present range of comparisons. The dependence on the mass flux is small. However, there is tendency that for small mass flux, the discrepancy among the correlations become smaller.

As shown above, the results of systematic comparisons among the previous correlations of droplet deposition coefficient indicate that there are serious discrepancy among the correlations and dependencies on entrainment ratio (mass concentration of droplet) and quality (gas flux) and other parameters differ considerably from one correlation to other. Much more researches both theoretically and experimentally are needed for the better prediction of droplet behaviors and thermohydraulic characteristics of annular dispersed flow.

3.DERIVATION OF BASIC EQUATIONS OF DROPLET FLOW [17]

In order to accurately analyze the thermohydrodynamic phenomena in annular flow, it is quite important to formulate rigorous basic equations for mass, momentum and energy conservations. There have been several researches on averaging methods for gas–liquid two–phase flow, and rigorous and reliable basic equations have been already obtained [18–20]. Presently, the basic equations based on the two–fluid (or three fluid) model are most often used in the analyses of gas–liquid two–phase flow. This model treats gas and liquid phase separately and basic equations for each phase are formulated. Using this two–fluid (or three fluid) model, it has become possible to analyze steady and transient behaviors of gas–liquid two–phase flow with certain accuracy.

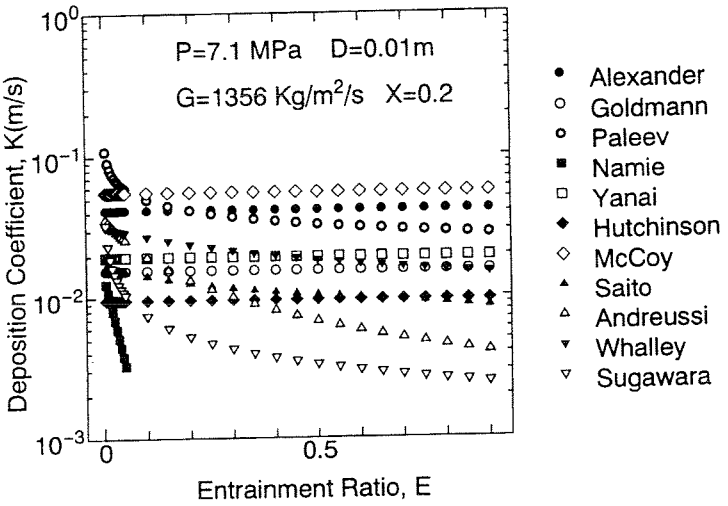

Fig.1 Comparison among Previous Correlations (Effect of Entrainment Ratio, 7MPa, 1356Kg/m²/s, X=0.2)

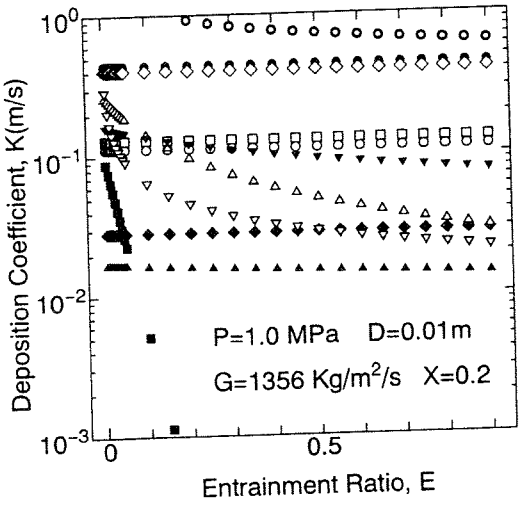

Fig.2 Comaprison amon Previous Correlations (Effect of Entrainemnt Ratio, 1MPa, 1356Kg/m²/s, x=0.2)

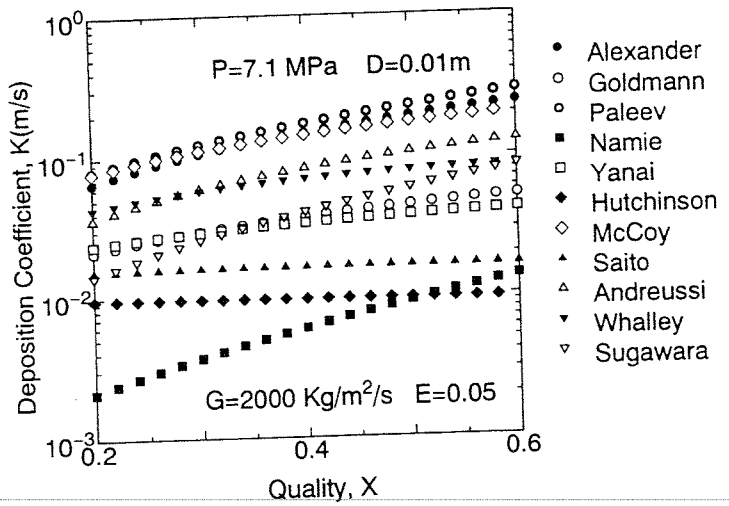

Fig.3 Comparison among Previous Correlations (Effect of Quality, 7MPa, 2000Kg/m²/s, E=0.05)

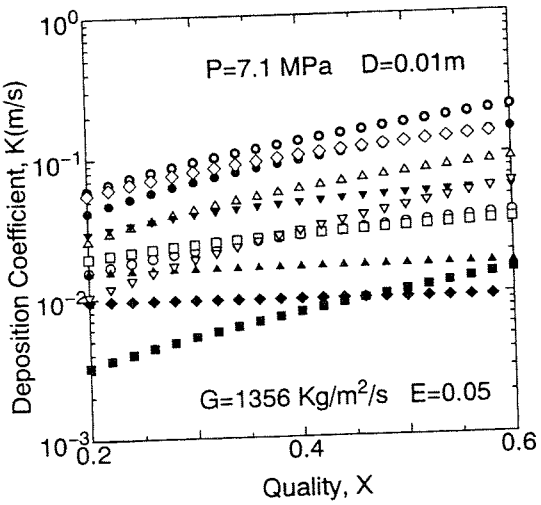

Fig.4 Comaprison amon Previous Correlations (Effect of Quality, 7MPa, 1356Kg/m²/s, E=0.05)

The previous basic equations are ,of course, are very rigorous in their original form, and can be applied to gas–liquid two–phase flow in any flow regime. However, when these basic equations are applied to droplet flow, they are too rigorous to interpret the physical meaning of certain terms in the basic equations.

For example, in the momentum equation based on two–fluid model, the averaged pressure gradient terms appear in both phases. However, for dispersed phase such as bubbles and droplets, it is difficult to understand the physical meaning of averaged pressure gradient (of course its definition is possible) and body force acting on the bubbles and droplets due to the averaged pressure gradient.

Moreover, the averaged physical quantities (averaged velocity, averaged density etc.) for dispersed phase which appear in the previous basic equations based on two–fluid model, are averaged values considering the distribution within droplet. However, it is possible to assume the uniformity of physical quantities (temperature, pressure, velocity) within dispersed phased for the dispersed flow in practical applications where phase change rate and chemical reaction rate are not so large at interface and there are no internal heat generation within the dispersed phase. In addition to this, in the experiments for velocity measurement of dispersed flow using electrical resistivity probe, anemometer and LDV, we usually measure the velocity at surface of droplet and obtain averaged velocity assuming that velocity within droplet is equal to the velocity at interface. Therefore, basic equations of dispersed phase we need in the practical analyses of gas–liquid dispersed flow are those averaged over dispersed phase assuming that droplet can be treated as a particle with constant distribution of physical quantities within it.

Finally, one of the application of present study is mentioned here. Recently, more detailed analyses of two–phase flow are required for the safety and performance of various industrial equipments. For this purpose, more accurate constitutive equations become needed. Along with experiments, numerical simulation for droplet behavior becomes very useful method for obtaining such constitutive equations Numerical simulation of each droplet or bubble in Lagrangian scheme become possible due to the progresses in numerical method and computer capacity. However, in the previous basic equations based on two–fluid model, dispersed phase is also treated as continuous fluid. Therefore, it is not easy to apply the constitutive equations for dispersed phase obtained by Lagrangian analyses to the two–fluid model basic equations. The present study is a part of such project for more detailed analyses of gas–liquid two–phase flow in corporation with Lagrangian simulation of droplets.

3.1 Derivation of averaged Basic Equation of Droplet Phase

Here, averaged basic equations of mass, momentum and energy conservations for dispersed phase are considered. Averaged basic equations for continuous phase (gas phase in droplet flow) are same as those obtained previously. Averaged basic equations of droplet phase are obtained by averaging local instant basic equations [19] which are given by

(mass)

$$\phi_d\{\frac{\partial \rho_d}{\partial t}+\mathrm{div}\,(\rho_d \boldsymbol{v}_d)\}=0 \tag{18}$$

(momentum)

$$\phi_d\{\frac{\partial}{\partial t}(\rho_d \boldsymbol{v}_d)+\mathrm{div}\,(\rho_d \boldsymbol{v}_d \boldsymbol{v}_d)\} = \phi_d(-\mathrm{grad}\,P_d+\mathrm{div}\,\tau_d+\rho_d \boldsymbol{g}) \tag{19}$$

(energy)

$$\phi_d[\frac{\partial}{\partial t}\{\rho_d(E_d+\frac{1}{2}\boldsymbol{v}_d^2)\} +\mathrm{div}\,\{\rho_d(E_d+\frac{1}{2}\boldsymbol{v}_d^2)\boldsymbol{v}_d)\}]$$

$$=\phi_d\{-\mathrm{div}\,\boldsymbol{q}_d-\mathrm{div}\,(P_d \boldsymbol{v}_d) +\mathrm{div}\,(\tau_d\cdot \boldsymbol{v}_d)+\rho_d \boldsymbol{g}\cdot \boldsymbol{v}_d+Q_d\} \tag{20}$$

Here, suffix d denotes dispersed phases and ϕ_d is the characteristic function of dispersed phase which gives unity where dispersed phase exists and otherwise gives zero [17].

Averaging Eqs.(18) through (20) for the time interval T, we obtain time averaged basic equations for dispersed phase. In averaging, we assume that physical quantities are uniform within each dispersed phase (within droplet). This can be given by following relations.

$$\mathrm{div}\,(\rho_d \boldsymbol{v}_d) = 0 \tag{21}$$

$$\mathrm{div}\,(\rho_d \boldsymbol{v}_d \boldsymbol{v}_d) = 0 \tag{22}$$

$$\mathrm{div}\,\tau_d = 0 \tag{23}$$

$$\mathrm{div}\,\{\rho_d (E_d + (1/2)\,\boldsymbol{v}_d^2)\,\boldsymbol{v}_d\} = 0 \tag{24}$$

$$\mathrm{div}\,(P_d \boldsymbol{v}_d) = 0 \tag{25}$$

$$\mathrm{div}\,(\tau_d \cdot \boldsymbol{v}_d) = 0 \tag{26}$$

These assumptions are considered to be valid for gas–liquid dispersed flow where phase change rate and chemical reaction rate are not so large at interface and there are no internal heat generation within the dispersed phase. For pressure field within the dispersed phase, we consider the force at the gas–liquid interface and assume uniform pressure within each dispersed phase. This is expressed by the following equation.

$$-\mathrm{grad}\,P_d = -P_{di}\,\boldsymbol{n}_{di} a_i \tag{27}$$

Similarly, for heat flux field within the dispersed phase, we consider the heat flux at gas–liquid interface and assume uniform heat flux within each dispersed phase which is given by

$$-\mathrm{div}\,(\boldsymbol{q}_d) = -\boldsymbol{q}_{di} \cdot \boldsymbol{n}_{di} a_i \tag{28}$$

Here, a_i is local instant interfacial area concentration [19] and $\boldsymbol{n}_{di}$ is outward unit normal vector at interface. Suffix i denotes the value at gas–liquid interface.

Averaging Eqs.(18) through (20) for time interval T using above mentioned relations (Eqs.(21) through (28)) and averaging method for differential terms including gas–liquid interfaces within time interval T [19], we obtain time averaged basic equations for dispersed phase for practical use. We denote time averaging for time interval T by —— hereafter. Furthermore, we define phasic averaging of dispersed phase which is given by

$$\overline{\overline{A_d}} = \overline{\phi_d A_d} / \alpha_d \qquad \text{(Phasic averaging of phase)} \tag{29}$$

Here, α_d is volumetric fraction of dispersed phase given by

$$\alpha_d = \overline{\phi_d} \tag{30}$$

All these relations mentioned above, we finally obtain the time averaged basic equations for dispersed phase which are given by

(mass)

$$\frac{\partial}{\partial t}(\alpha_d \overline{\overline{\rho_d}}) + \mathrm{div}\,(\alpha_d \overline{\overline{\rho_d \boldsymbol{v}_{dm}}}) = \frac{1}{T}\sum_{j=1}^{N} \frac{\rho_{dij}\,\boldsymbol{n}_{dij} \cdot (\boldsymbol{v}_{ij} - \boldsymbol{v}_{dij})}{|\boldsymbol{n}_{dij} \cdot \boldsymbol{v}_{ij}|} \tag{31}$$

(momentum)

$$\frac{\partial}{\partial t}(\alpha_d \overline{\overline{\rho_d \boldsymbol{v}_{dm}}}) + \mathrm{div}\,(\alpha_d \overline{\overline{\rho_d \boldsymbol{v}_{dm} \boldsymbol{v}_{dm}}}) = -\mathrm{div}\,(\alpha_d \overline{\overline{\rho_d \boldsymbol{v}_{dm} \boldsymbol{v}_{dm}}})$$

$$+ \alpha_d \overline{\overline{\rho_d}}\,\boldsymbol{g} - \frac{1}{T}\sum_{j=1}^{N} \frac{P_{dij}\,\boldsymbol{n}_{dij}}{|\boldsymbol{n}_{dij} \cdot \boldsymbol{v}_{ij}|} + \frac{1}{T}\sum_{j=1}^{N} \frac{\rho_{dij}\,\boldsymbol{n}_{dij} \cdot (\boldsymbol{v}_{ij} - \boldsymbol{v}_{dij})\,\boldsymbol{v}_{dij}}{|\boldsymbol{n}_{dij} \cdot \boldsymbol{v}_{ij}|} \tag{32}$$

(energy)

$$\frac{\partial}{\partial t}(\alpha_d \overline{\overline{\rho_d E_{dm}}}) + \mathrm{div}(\alpha_d \overline{\overline{\rho_d E_{dm} v_{dm}}}) = -\mathrm{div}(\alpha_d \overline{\overline{\rho_d E'_{dm} v'_{dm}}})$$

$$-\frac{1}{T}\sum_{j=1}^{N}\frac{q_{dij}\cdot n_{dij}}{|n_{dij}\cdot v_{ij}|} + \frac{1}{T}\sum_{j=1}^{N}\frac{\rho_{dij} n_{dij}\cdot(v_{ij}-v_{dij}) E_{dij}}{|n_{dij}\cdot v_{ij}|} + \alpha_d \overline{\overline{Q_d}} \tag{33}$$

Here, N denotes the number of interfaces passing a measuring point within time interval T and suffix j denotes j th interface. v_i is velocity of interface. Mass averaged quantities and fluctuating quantities are defined by

$$v_{dm} = \overline{\overline{\rho_d v_d}} / \overline{\overline{\rho_d}} \tag{34}$$

$$\overline{\overline{\rho_d v'_d v'_d}} = \overline{\overline{\rho_d (v_d - v_{dm})(v_d - v_{dm})}} \tag{35}$$

$$E_{dm} = \overline{\overline{\rho_d E_d}} / \overline{\overline{\rho_d}} \tag{36}$$

$$\overline{\overline{\rho_d E'_d v'_d}} = \overline{\overline{\rho_d (E_d - E_{dm})(v_d - v_{dm})}} \tag{37}$$

In obtaining Eq.(33), we assumed that kinetic energy is negligible compared with thermal energy.

The right hand side of Eq.(31) corresponds to interfacial mass transfer term (phase change rate) which is rewritten by

$$\frac{1}{T}\sum_{j=1}^{N}\frac{\rho_{dij} n_{dij}\cdot(v_{ij}-v_{dij})}{|n_{dij}\cdot v_{ij}|} = \dot{m}_d \overline{a_i} \tag{38}$$

where $\dot{m}_d$ is phase change rate of dispersed phase (evaporation, condensation) per unit interfacial area. The third term in the right hand side of Eq.(32) represents interfacial momentum transport term due to the pressure distribution around bubble and droplet. More concretely, it corresponds to buoyancy force, drag force, transverse lift force (such as Magnus force etc,) and virtual mass force. It can be rewritten by

$$-\frac{1}{T}\sum_{j=1}^{N}\frac{P_{dij} n_{dij}}{|n_{dij}\cdot v_{ij}|} = -\alpha_d(\alpha_d \overline{\overline{\rho_d}} + \alpha_c \overline{\overline{\rho_c}})\, g - C_D(1/2)\,\overline{\overline{\rho_c}}(v_{cm}-v_{dm})^2 \overline{a_i}$$

$$-C_T \overline{\overline{\rho_c}}(v_{cm}-v_{dm})\,\mathrm{grad}\, v_{cm} + C_{VM}\overline{\overline{\rho_c}}\left\{\frac{D_d}{Dt}(v_{dm}-v_{cm})\right\} \tag{39}$$

The fourth term in the right hand side of Eq.(32) corresponds to the interfacial momentum transport due to phase change, that is

$$\frac{1}{T}\sum_{j=1}^{N}\frac{\rho_{dij} n_{dij}\cdot(v_{ij}-v_{dij}) v_{dij}}{|n_{dij}\cdot v_{ij}|} = \dot{m}_d v_{di} \overline{a_i} \tag{40}$$

The second term in the right hand side of energy conservation equation (Eq.(33)) represents the interfacial energy transport term due to the temperature gradient at interface and given in the form of interfacial heat transfer term which is given by

$$-\frac{1}{T}\sum_{j=1}^{N}\frac{q_{dij}\cdot n_{dij}}{|n_{dij}\cdot v_{ij}|} = -h_i(T_{cm}-T_{dm})\overline{a_i} \tag{41}$$

where h_i is interfacial heat transfer coefficient and T_{cm} and T_{dm} are averaged temperatures of continuous and dispersed phase respectively. The third term in the right hand side of Eq.(33) corresponds to interfacial energy transport term due to phase change which is rewritten by

$$\frac{1}{T}\sum_{j=1}^{N}\frac{\rho_{dij} n_{dij}\cdot(v_{ij}-v_{dij}) E_{dij}}{|n_{dij}\cdot v_{ij}|} = \dot{m}_d E_{di} \overline{a_i} \tag{42}$$

3.2 Characteristics of Basic Equations for Droplet Phase

The basic equations of dispersed phase in gas–liquid two–phase flow based on simplified assumptions obtained in previous sections have some characteristics in the physical interpretation of their terms which are described below.

The averaged physical quantities of dispersed phase in the present equations are defined using the values at the interface due to the assumption of uniform distribution in each dispersed phase. For example, some averaged quantities are defined by following equations.

$$\alpha_d = \frac{1}{T}\sum_{j=1}^{N/2}(t_{2j}-t_{2j-1}) \tag{43}$$

$$\overline{\alpha_d \rho_d} = \frac{1}{T}\sum_{j=1}^{N/2}(t_{2j}-t_{2j-1})\,\rho_{d,2j-1} \tag{44}$$

$$\overline{\alpha_d \rho_d v_{dm}} = \frac{1}{T}\sum_{j=1}^{N/2}(t_{2j}-t_{2j-1})\,\rho_{di,2j-1}\,v_{di,2j-1} \tag{45}$$

$$\overline{\alpha_d \rho_d E_{dm}} = \frac{1}{T}\sum_{j=1}^{N/2}(t_{2j}-t_{2j-1})\,\rho_{di,2j-1}\,E_{di,2j-1} \tag{46}$$

Here, t_{2j-1} and t_{2j} are the times when the j th dispersed phase arrives and departs a measuring point, respectively as shown in Fig.5. For example, speaking of velocity, the averaged velocity defined Eq.(46) is given by only the interfacial velocities when the bubbles and droplets passes the measuring probe. This averaged value well corresponds to the actual velocity measurements in the experiments. In the practical measurements of velocity of dispersed phase, we usually use electrical resisitvity probe, anemometer, and laser doppler anemometer. What these probe usually measure for dispersed phase is interfacial velocity of dispersed phase and velocity within the dispersed phase is assumed to be equal to the interfacial velocity. Therefore, the measured averaged velocity (and other properties) of dispersed phase is well represented by Eqs.(36) through (46). Therefore, when we compare the experiment with analysis in dispersed gas–liquid two–phase flow in detail, the present basic equations are much more appropriate in regard to consistency between measured and predicted values.

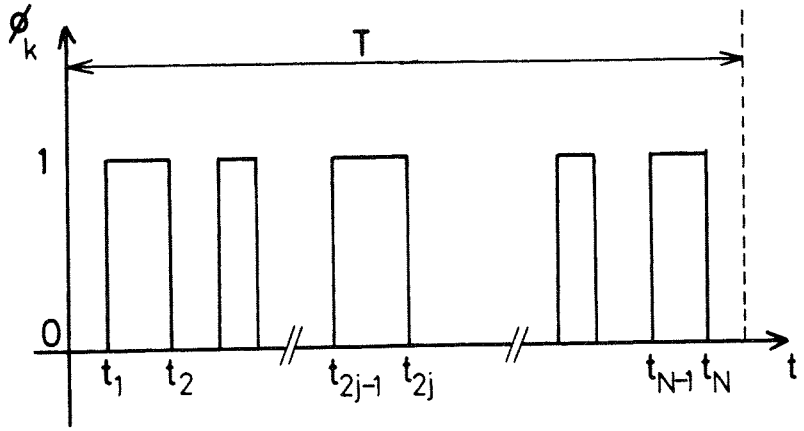

Fig.5 Situation of Passing of Interface through Measuring Point

In the momentum equation of dispersed phase, Eq.(32), the averaged pressure gradient term does not appear which is one of the most characteristic difference from previous equations. Although dispersed phase (droplet) consists of continuous fluid, each dispersed phase (droplet) does not connected each other. Therefore, it is difficult to interpret the force exerted on dispersed phase due to the averaged pressure gradient of dispersed phase unlike continuous phase. Of course, there exists an interaction between dispersed phases. However, it is considered that dispersed phases interact each other not directly but through the continuous phase. In gas–liquid two–phase flow where the particle concentration is not so high, it is reported that the similar basic equations to the present ones was obtained in which pressure gradient term does not appear in the momentum equation of dispersed phase (solid particle phase) [21,22].

Such feature of momentum equation of dispersed phase (no averaged pressure gradient term) makes averaged pressure modeling in two–fluid model much easier. In the previous two–fluid model where dispersed and continuous phases are treated as continuous fluid, there appear averaged

pressure gradient terms in momentum equations of both phases. Therefore, in order to get the closure relation, we need modeling of the relation between averaged pressures of both phases. Usually, the averaged pressures are assumed to be equal. However, this assumption causes the ill-posed problem which is still serious and unresolved problem in two-fluid model [23]. On the other hand, in the present equations, the averaged pressure gradient term does not appear in the dispersed phase momentum equation but appears only in the continuous phase equation. Therefore, there needs no modeling for the averaged pressures of both phases. Furthermore, as shown in the following section, the present equations do not cause ill-posed problem unlike the previous equations.

Another characteristic feature of momentum equation of dispersed phase is that there are no divergence term of viscous stress unlike the continuous phase. Viscous stress is proportional to the velocity gradient in Newtonian fluid. This force is reasonable in continuous phase. However, in the dispersed phase, it is difficult to interpret physically the averaged viscous stress in the dispersed phase since each dispersed phase (bubble and droplet) does not connected each other. Therefore, this feature is considered to be reasonable for dispersed phase.

Similar discussion is possible regarding to molecular heat diffusion term in the energy equation of dispersed phase, Eq.(33). In the equation, there are no divergence term of heat flux due to the molecular heat diffusion. In the continuous phase, it is natural to consider the heat flux due to the molecular heat diffusion proportional to the averaged temperature gradient. However, in the dispersed phase, each dispersed phase is not connected each other. Therefore, it is quite difficult to consider physically the heat flux due to the molecular heat diffusion from one dispersed phase to another dispersed phase. Of course, there are some energy transfer between dispersed phases. However, it is not transferred from one dispersed phase to another dispersed phase directly but it is transferred through continuous phase. In this regards, the present equation of dispersed phase energy conservation is reasonable in physical interpretation of molecular heat diffusion term.

As mentioned in Introduction, the present basic equations can be applied to the more detailed analyses of dispersed gas-liquid two-phase flow in cooperation with numerical simulation of bubble or droplet in Lagrangian scheme. Averaging method in the present basic equations is based on the assumption that bubble and droplet are taken as a particle. Therefore, the present equations are consistent with the averaged basic equations in Lagrangian analyses. As an example, we will show in below that for droplet flow, averaged momentum equation in Lagrangian simulation of droplets is identical to the momentum equation in the present basic equation

In Lagrangian simulation of droplet, the equation of motion for each droplet is given by

$$\rho_d V_d \frac{d v_d}{d t} = -C_D \frac{1}{2} \rho_c (v_d - v_c)^2 A_d + g \rho_d V_d \tag{47}$$

where, V_d and A_d are volume and projected area of each droplet and C_D is drag coefficient of single droplet. Here, for simplicity, the main interacting force is assumed to be the drag force acting on the droplet.

Now, we consider averaging Eq.(47) in appropriate control volume containing N droplet. The droplet population balance in the control volume is given by

$$\frac{\partial N}{\partial t} + div (N v_d) = 0 \tag{48}$$

Averaging Eq.(47) for N droplets in the control volume under the condition of Eq.(48), we approximately obtain

$$\frac{\partial}{\partial t} (\alpha_d \overline{\rho}_d v_{dm}) + div (\alpha_d \overline{\rho}_d v_{dm} v_{dm}) = -div (\alpha_d \overline{\rho_d v_{dm} v_{dm}}) - C_D K \frac{1}{2} \overline{\rho_c (v_d - v_c)^2 a_i} + \alpha_d \overline{\rho}_d g \tag{49}$$

Here, we used the relations for void fraction and interfacial area which are given by

$$\alpha_d = N V_d \tag{50}$$

$$a_i = K N A_d \tag{51}$$

where K is the coefficient related to the ratio between surface area and projected area of droplet.

Comparing Eq.(49) with Eq.(32), the momentum equation of present basic equation is consistent with averaged momentum equation in Lagrangian simulation of each droplet, in particular, with

respect that there are no gradient term of averaged pressure of dispersed phase in both equations.

As discussed above, the present basic equations of dispersed phase are very reasonable and consistent in physical interpretation, although they are derived based on several simplifications and assumptions.

4. LAGRANGIAN SIMULATION OF DROPLET BEHAVIOR [24]

In the previous section, the basic conservation equations of dispersed phase (droplet) in annular mist flow were derived in Eulerian coordinate. Using these basic equations, the average thermohydrodynamic behavior of annular mist flow can be simulated. However, due to the averaging, some of the detailed information of droplet behavior are lost in these averaged equations. Droplet deposition rate which are surveyed in Section 2. and many other important parameters must be given as constitutive equations. Therefore, along with such Eulerian simulation, Lagrangian simulation of droplet behavior is also very important. In such simulation, some detailed parameters such as droplet deposition rate, droplet diffusion coefficient in turbulent gas field can be simulated. Although this method takes a lot of computation time, recent remarkable progresses in computer and numerical technology make such calculation practically possible. Since in this method, the trajectory of each droplet is calculated, the number of the droplets to be simulated is limited at present computational capacity. Therefore, complete simulation of mist flow in actual annular mist flow using this method is not possible. However, this Lagrangian simulation becomes a powerful tool to predict detailed parameters in annular mist flow along with experiment and theoretical analyses. As described in previous section, the basic conservation equations in Eulerian coordinate derived here are consistent with the basic equation of Lagrangian simulation. Therefore, combining this Lagrangian simulation and Eulerian simulation mentioned in previous section, the detailed simulation of annual mist flow become practically possible.

In view of these, in this section, some preliminary results of Lagrangian simulation of droplet are carried out and droplet diffusion coefficient of droplet in turbulent field is predicted and compared with experimental results.

4.1 Basic Equations for Lagrangian Simulation

Here, as a first step, Lagrangian simulation of droplet in simplified flow conditions is carried out. The case treated here is the diffusion of small droplet introduced into the centerline of fully developed steady state turbulent gas flow with high velocity in round tube. Since the gas velocity is high and droplet is small, main force acting on the droplet is assumed the drag force due to the local velocity difference between droplet and gas. Therefore, Equation of motion of droplet Eq.50) become simplified to

$$m_d \, dv_d/dt = - C_D \rho_c (v_d - v_c) \, | v_d - v_c | \, \pi D_d^2 / 4 \tag{52}$$

Where D_d is droplet diameter and m_d is mass of a droplet. For drag coefficient of droplet, Ishii's correlation [25] is used which is given by

$$C_D = 24 \, (1+0.1 Re_d^{0.75}) / Re_d \qquad \text{(For viscous regime)} \tag{53}$$

$$C_D = \frac{2}{3} D_d \sqrt{\frac{g \Delta \rho}{\sigma}} \left\{ \frac{1+17.67 \, (1-\alpha)^{3.5}}{18.67 \, (1-\alpha)^3} \right\}^2 \qquad \text{(Distorted particle regime)} \tag{54}$$

where Re_d is defined by

$$Re_d = D_d \rho_c | \mathbf{v}_d - \mathbf{v}_c | / \{ (1+2.5 \alpha_d) \, \mu_c \} \tag{55}$$

Here α_d is volume fraction of droplet.

In Eq.(52), local velocity of continuous phase (gas phase) is given by the sum of averaged velocity and turbulent velocity

$$\mathbf{v}_c = \overline{\mathbf{v}}_c + \mathbf{v}_c' \tag{56}$$

Averaged velocity of gas phase can be obtained by solving averaged momentum equation of gas phase. In order to give the turbulent velocity, it is assumed that direction of turbulent velocity is equilateral and Monte Carlo method is used for giving the direction of turbulent velocity. the magnitude of turbulent velocity is given by solving the conservation equation of turbulent kinetic energy in mist flow which is given by

$$\frac{1}{R-y}\frac{\partial}{\partial y}\{(R-y)(1-\alpha_d)(\frac{\nu_c}{2}+\beta_2\sqrt{k}\,l_{TP})\frac{\partial k}{\partial y}\}+\beta_1\sqrt{k}\,l_{TP}(1-\alpha_d)(\frac{\partial \overline{V}_c}{\partial y})^2 \qquad (k=(1/2)\,\mathbf{v}_c'^2)$$

$$-\gamma_1(1-\alpha_d)\frac{(\sqrt{k})^3}{l_{TP}} - K_2\alpha_d\frac{(\sqrt{k})^3}{D_d}+K_1\frac{3}{4D_d}\alpha_d C_D|v_d-v_c|^3 = 0 \tag{57}$$

Here, $l_{TP}$is the mixing length of two-phase flow and given by

$$l_{TP} = 0.4y + (1/3)\alpha_d D_d \tag{58}$$

where y is distance from the wall. The coefficients in Eq.(57) are given by

$$\beta_1=0.56,\quad \beta_2=0.38,\quad \gamma_1=0.18,\quad K_1=0.075,\quad K_2=1.0 \tag{59}$$

the conservation equation of turbulent kinetic energy and constitutive equations in gas phase in mist flow described above are derived based on the previous researches of the formulation and modeling of basic equation of turbulence in two-phase flow [26–28]. Using similar basic equations and constitutive equations, turbulence structure of bubbly flow is satisfactorily predicted [28,29].

Another important parameter in Lagrangian simulation of droplet is the relaxation time of droplet, t_R, which is the time duration of interaction between droplet and turbulent eddy of gas. Here, it is given be the ratio of mixing length and magnitude of turbulent velocity.

$$t_R = a\,l_{TP}/|\mathbf{v}_c'| \tag{60}$$

Here, a is the coefficient which will determined in collaboration with experimental data.

4.2 Lagrangian Simulation of Droplet and Prediction of Diffusion Phenomenon of Droplet

In order to compare with the experimental results of Ginsberg [30], Lagrangian simulation of droplet is carried out under following conditions.

Pipe diameter: 0.19 m Gas flux: 2.05 – 8.19 m/s, Gas Reynolds number, Re_G: 25000 – 100000
Droplet diameter: 80 –200 micron
Droplet injection: Centerline of pipe
Measuring Points of droplet distribution: 1.22 and 1.44 m from injection

trajectories of 10000 droplets are simulated using basic equations in previous section. The Distribution of droplet flux at 1.22 m and 2.44 m from injection points are calculated and compared with experimental data of Ginsberg [30]. Under such conditions the number density (therefore the volume fraction of droplet) is very small. Therefore, for the simplicity of calculation, the volumetric fraction of droplet in Eq.(58) is approximated to negligible in the present calculation. Further more, the coefficient of relaxation time is assumed to be 0.3, since prediction best fitted the experimental data for this value. Some example of simulation results are shown in Figs.6 and 7. In Fig.6, the simulated trajectories of droplets are shown. As shown in Fig.7, experimental distribution of droplet flux is well predicted by the present simulation for the location of 1.22 m. Foe 2.44m, droplet flux distributions of experiment and prediction agree qualitatively but some discrepancy are shown. This is partly attributable to the experimental error due to the difficulties in measuring small droplet flux, since experimental data in Fig.7 do not satisfy continuity of droplet mass flow rate.

Although the Lagrangian simulation here is preliminary based on the simplified assump-

tions. The results show that simulation reasonably predict the droplet diffusion phenomenon in turbulent flow filed of gas phase.

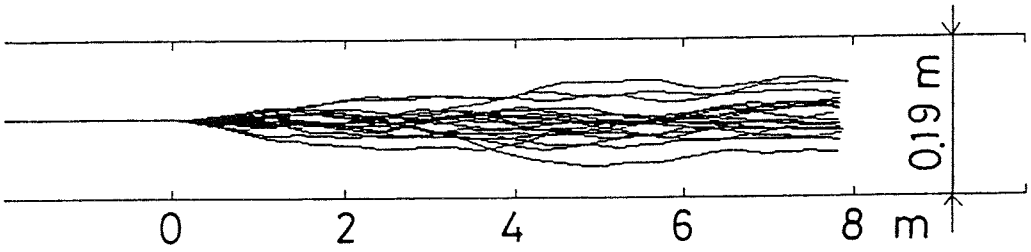

Fig.6 Trajectories of Droplets by Lagrangian Simulation for Re_G=100000 and D_d= 150 micron

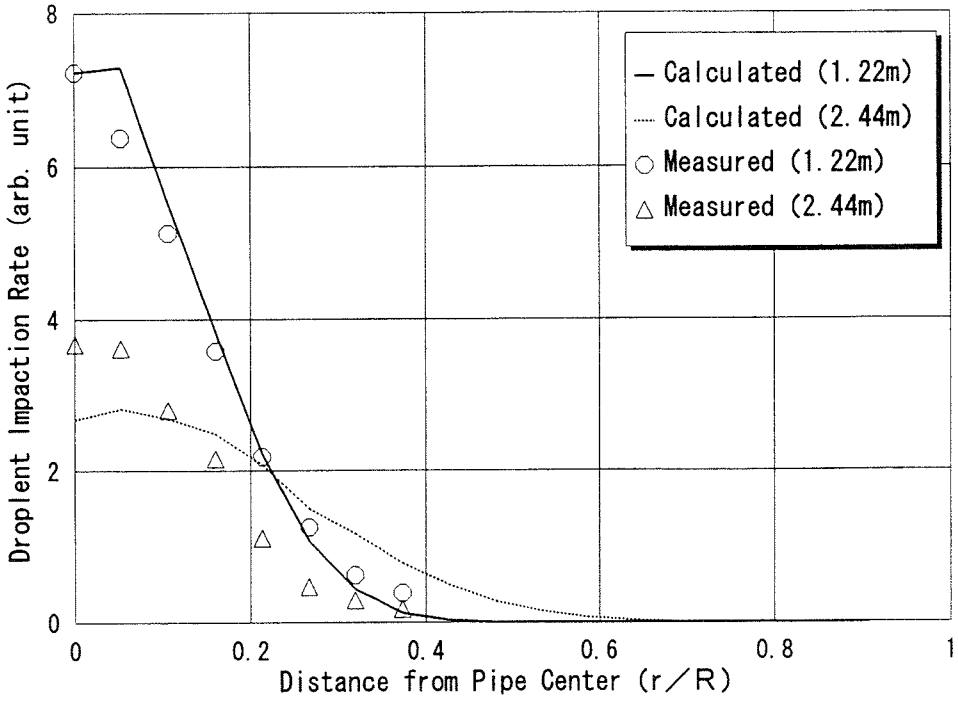

Fig.7 Comparison of Predicted and measured droplet Flux Distributions (Re_G=100000, D_d=150 micron, N=10000, a=0.3)

5. CONCLUSIONS

In order to develop accurate prediction method of thermohydrodynamic of annular mist flow, survey of previous researches, modeling and simulations of droplet behavior of annual mist flow were carried out.

The previous correlation of droplet deposition rate in annular mist flow were surveyed and systematic comparisons among these correlations were carried out. The results of comparisons show that considerable discrepancies (one or two order of magnitude) still exit and effects of droplet concentration and gas flux and other parameters are considerably differ form correlation to correlation.

Basic averaged equation of mass, momentum and energy conservations in dispersed phase (droplet) of annular mist flow were formulated in Eulerian coordinate. Based on the assumptions reasonable to dispersed phase, the obtained basic equations well reflect the physical aspects of averaged behavior of mist flow. They are shown to be consistent with averaged parameters obtained in experiment and lagrangian simulation of droplet behavior.

Lagrangian simulations of droplets were carried out based on the equation of motion of

droplet and turbulent equations of mist flow. Results of simulation well agreed with experimental data of droplet diffusion phenomenon in turbulent gas flow.

REFERENCES

[1] G.F.Hewitt & N.S.Hall-Taylor: "Annular Two-Phase Flow", Pergamon Press, Oxford (1970).
[2] J.G.Collier: "Convective Boiling and Condensation,"McGraw-Hill, New York (1972).
[3] P.B.Whalley, "The Calculation of Critical heat Flux in rod Bundle", in: Int. J. Multiphase Flow, 3, p.501 (1977).
[4] S.Sugawara: "Study on Flow and dryout phenomena in Forced Convection Boiling Two-Phase Flow", Ph.D Thesis, Tokyo Inst. technology, (1990).
[5] L.G.Alexander & C.L.Coldren, "Droplet Transfer from Suspending Air to Duct Walls", in: Industrial Engineering Chemistry, 43, p.1325 (1951).
[6] K.Goldmann, H.Firstenberg & C.Lombardi, "Burnout in turbulent Flow- A Droplet Diffusion Model", in: Trans. of ASME, J. Heat Transfer, 83, p.158 (1961).
[7] I.I.Paleev & B.S.Fillipovich, "Phenomena of Liquid transfer in Two-Phase Dispersed Annular Flow", in: Int. J. Heat Mass Transfer, 9, p.1089 (1966).
[8] S.Namie & T.Ueda, "Droplet transport in Mist Flow, 2nd Rpt. Analysis of Droplet Transport and Consideration of Transport Rate", in: Trans. JSME, 38-312, p.2126 (1972).
[9] M. Yanai: "Study on Boiling Heat transfer in Pipe Flow", Ph.D. Thesis, Kyoto University (1971).
[10] P.Hutchinson & P.B. Whalley, "A possible Characterization of Entrainment in Annular Flow", in: Chem. Eng. Sci., 28, p.974 (1973).
[11] D.D.McCoy & T.J.Hanratty,"Rate of Deposition of Droplets in Annular Two-Phase Flow", in: Int. J. Multiphase Flow, 3, p.319 (1977).
[12] T.Saito, E.D.Hughes & M.W.Carbon, "Multi-Fluid Modeling of Annular Two-Phase Flow", in: Nucl. Eng. Des., 50, p.225 (1978).
[13] P.Andreussi & B.J.Azzopardi, "Droplet Deposition and Interchange in Annular Gas-Liquid Flow", Int. J. Multiphase Flow, 9, p.697 (1983).
[14] P.B.Whalley & G.F.Hewitt: "The Correlation of Liquid Entrainment Fraction and Entrainment Rate in Annular Two-Phase Flow," Rept. AERE-R9187, Harwell (1978).
[15] I.Kataoka, A.Tomiyama & T.Sakaguchi, Multiphase Flow Symp. '93, Fukuoka, Japan, p.213 (1993).
[16] Y.Katto, in: Int. J. Heat Mass Transfer, 27, p.883 (1984).
[17] I.Kataoka & A.Tomiyama, 4th Int.Topical Mtg. on Nuclear Thermal, Hydraulics, Operation & Safety, Taipei, Taiwan, Vol.1, 8-C-1 (1994).
[18] M. Ishii, Thermo-Fluid Dynamic theory of Two-Phase Flow, Eyrolles, Paris (1975).
[19] I. Kataoka, International Journal of Multiphase Flow, 12, p.745 (1986).
[20] J.M. Delhaye, et al., Thermohydraulics of Two-Phase Systems for Industrial Design and Nuclear Engineering, hemisphere, Washington, D.C. (1981).
[21] S.L. Soo, Fluid Dynamics of Multiphase Systems, Blaisdell, Waltham, Mass. (1967).
[22] R.W. Lyczkowski, D. Gidaspaw, and C.W. Solbrig, "Multiphase Flow Models for Nuclear, Fossil and Biomass Energy Production," Advances in Transport Processes, Vol.II, Wiley Eastern Limited p.198 (1982).
[23] H.B. Stewart and B. Wendroff, J. Comp. Phys., 56, p.363 (1984).
[24] K.Matsuura, I.Kataoka & A.Serizawa, Multiphase Flow Symp. '94, Tsukuba, Japan, to be presented (1994).
[25] M.Ishii & T.C.Chawla: "Local Drag Laws in Dispersed Two-Phase Flow", ANL79-105, NUREG/CR-1230 (1979).
[26] I.kataoka & A.Serizawa, Int. J. Multiphase Flow, 15, p.843 (1989).
[27] I.Kataoka, D.C.Besnard & A.Serizawa, Chem. Eng. Communication, 117, p.221 (1992).
[28] I.kataoka, D.C. Besnard & A.Serizawa, Nucl. Eng. Design, 141, p.145 (1993).
[29] I.Kataoka & A.Serizawa, 31st National Heat Transfer Symp. Japan, Sapporo, Japan, p.166 (1994).
[30] T.Ginsberg: "Droplet Transport in Turbulent Pipe Flow", ANL 7694 (1971).

VOLUMETRIC FRACTIONS AND PHASE VELOCITIES OF GAS-LIQUID-SOLID THREE PHASE FLOW IN VERTICAL PIPES

T. Sakaguchi, H. Minagawa, A. Tomiyama, and M. Ushio
Kobe University
Department of Mechanical Engineering, Faculty of Engineering
Rokkodai Cho, Nada, Kobe 657, Japan
Telephone:(078)881-1212, Facsimile:(078)881-0036

ABSTRACT

An experimental database of the volumetric fractions of each phase and the averaged phase velocities in the gas-liquid-solid three phase slug flow in vertical round pipes were obtained. They were plotted against total volumetric flux of the three phase flow. Their characteristics for the volumetric fluxes were clarified in detail. They were also compared with the results obtained for gas-liquid two phase slug flow and liquid-solid two phase flow. The effect of the third phase added to these two phase flows were investigated. The variables such as local velocities and phase distributions of each phase, rising velocity and lengths of the large bubble, wake and liquid slug were also measured to understand the characteristics of the three phase slug flow.

1. INTRODUCTION

The gas-liquid-solid three phase flow is one of the most complex multiphase flows so that it has a lot of characteristics to be clarified. The three phase flow, however, plays an important role in many practical engineering devices such as air-lift pumps for mining manganese nodules on the deep sea bed, and preheaters and evaporators of coal liquefaction plant. In addition to these practical applications, the three phase flow would be utilized in near future to provide an intelligent function to the gas-liquid or liquid-solid two phase flow by adding the solid or gas phase to them as a third phase[1]. There have been, however, few experimental data[2]-[6].

In the present study, we presented an experimental database of the volume-averaged volumetric fractions of each phase and averaged phase velocities in the air-water-spherical particles three phase slug flow in a vertical round pipe of 20.9 mm I.D. and of 10m length. Measured data with aluminum ceramic particles whose mean diameter and density are 2.57 mm and 2380 kg/m^3, respectively, were presented in this report. In the present experimental conditions, most solid particles were contained in the liquid phase. Gas-liquid two phase slug flow and liquid solid two phase flows are, therefore, basic two phase flows for such three phase flows. Since the knowledge of these two phase flows are bases for understanding the characteristics of the three phase flow, characteristics of the gas-liquid and liquid-solid two phase flows were examined before the three phase flow. The effects of the volumetric fluxes on the volume-averaged volumetric fractions of each phase and averaged phase velocities were discussed.

Characteristics variables for the slug flow, such as local velocities and phase distributions of each phase, rising velocity and lengths of the large bubble, wake and liquid slug are referred to as slug characteristics henceforth. They were measured using a vertical pipe of 30.6 mm I.D. and with aluminum ceramic particles whose mean diameter and density are 4.17 mm and 2400 kg/m^3, respectively. Some of the macroscopic characteristics of the volumetric fractions and averaged phase velocities were explained by making use of the slug characteristics variables.

2. EXPERIMENTAL APPARATUS AND UNCERTAINTIES

Air, water and aluminum ceramic spherical particles were used as the gas, liquid and solid phase, respectively. The vertical round pipes made from transparent acrylic resin were used to directly observe the flow.

A schematic diagram of the experimental apparatus is shown in **Fig.1**. The air from a compressor was fed to the test section through a cooler, a filter, a regulator valve, and a critical flow

nozzle. The mixing section is shown in **Fig.2**. Air was injected through the circumference of the porous pipe whose pore diameter was 200-300 μm. The air flow rate was controlled and measured with a pressure at the upstream side of the critical flow nozzle. Solid particles accumulated in a hopper were supplied with water from a tank by a Mohno pump (a). Additional water was supplied from the bottom by a Mohno pump (b) to prevent them from settling down and piling on the bottom. Excess water was drained away by a Mohno pump (c). The solid flow rate was controlled by the vibration frequency of the feeder. The water flow rate was controlled by the rotating speeds of the three Mohno pumps. The volume-averaged volumetric fractions in the test section of 2m length were measured by a quick-closing valve method[5]. The solid and liquid flow rates were measured with graduated cylinders. The gas flow rate was corrected to the value corresponding to the static pressure at the centers of the two measuring sections, supposing that the gas phase experienced isothermal volume change.

Slug characteristics were measured at the test section located at about 7.5m downstream of the mixing section of the 30.6 mm pipe. Two kinds of electric probes made of ϕ0.4 mm stainless steel needle were installed in the test section as shown in **Fig.3** (a) and (b). Hereafter, we will call them type (a) and type (b) probe, respectively. The type (a) probe, which consists of two right-angled electrodes, were used to detect the time when large bubbles and liquid slugs reached to their positions. The electrodes were insulated except for their tips. Four type (a) probes were installed along the test section. Rising velocity and lengths of each large bubble and liquid slug were obtained from the detected times. The type (b) probe, which also consisted of two parallel conductive electrodes, was used to detect liquid film thickness around the large bubbles in terms of the film-thickness dependent electric resistance between the two electrodes. The relation between the film thickness and the electric resistance was calibrated in advance. Four type (b) probes were installed in the test section as shown in **Fig.3** (b) to detect the film thickness at four positions simultaneously.

Video images of the flow were recorded using 8mm video recorders. Axial distribution and local velocities of solid particles in slug units were obtained by processing the recorded images.

The volumetric fluxes ranged $\langle J_G \rangle$=0, 0.30-0.60 m/s, $\langle J_L \rangle$=0.50-0.90 m/s, and $\langle J_S \rangle$=0, 0.0017-0.060 m/s. Here, < > is the area-averaging operator[7] and the subscripts G, L and S denote the gas, liquid and solid phase, respectively.

Then, we summarize experimental uncertainty. We could not make the length between the two quick-closing valves long enough to capture a lot of slug units. It induced errors on the volumetric fraction measurement. The inevitable random error introduced by the present system which includes the random error introduced by the instrumentation[8] was evaluated for averaged volumetric fractions. Their relative values were 3.68, 2.48 and 10.6% for the gas, liquid and solid phase, respectively. On the other hand, the source of fixed error was not detected. Hence, the uncertainties estimated at 95% confidence were ±7.36, 4.96 and 21.2 % of the observed values, respectively. The uncertainties for slug characteristic variables such as rising velocities, lengths and film thickness were estimated about ±12% of the averaged values at 95% confidence.

3. EXPERIMENTAL RESULTS OF VOLUMETRIC FRACTIONS AND PHASE VELOCITIES

Measured volumetric fractions, $\langle \alpha_i \rangle$ (i=G, L, S), were instantaneous volume-averaged values in the test section. They will be referred to as "volumetric fraction" for simplicity. Relation between the volumetric fractions and the volumetric fluxes is shown in **Fig.4** with total volumetric flux $\langle J_T \rangle$ ($=\langle J_G \rangle+\langle J_L \rangle+\langle J_S \rangle$) on the abscissa in order to discuss their relations organically. This figure is based on the experimental condition of D=20.9 mm, d_S=2.57 mm and ρ_S=2380 kg/m^3. The upper, middle and lower frame shows $\langle \alpha_G \rangle$, $\langle \alpha_L \rangle$ and $\langle \alpha_S \rangle$, respectively. The ordinate axis of the lower frame is three times magnified so as to clarify the characteristics of $\langle \alpha_S \rangle$. Solid symbols in the figure denote the volumetric fractions for gas-liquid two phase slug flow. Gray symbols are for liquid-solid two phase flow, and open symbols for gas-liquid-solid three phase slug flow. The difference in symbol shape (circle, triangle and square) corresponds to $\langle J_L \rangle \cong$ 0.50, 0.70 and 0.90 m/s, respectively.

Curved lines in the figure were drawn with the least squares method for the combinations of representative values of the volumetric fluxes; $\langle J_G \rangle$ = 0, 0.30, 0.45 and 0.60 m/s, $\langle J_L \rangle$ = 0.50, 0.70 and 0.90 m/s, and $\langle J_S \rangle$ = 0, 0.010, 0.020 and 0.050 m/s. Thin lines are for gas-liquid and liquid-solid two phase flows and thick lines for three phase flows. Lines are also classified into four types; broken lines are for the case of constant values of $\langle J_G \rangle$, or $\langle J_G \rangle$ and $\langle J_S \rangle$ with $\langle J_L \rangle$ as a parameter, solid lines for constant $\langle J_L \rangle$ or $\langle J_L \rangle$ and $\langle J_S \rangle$ with $\langle J_G \rangle$ as a parameter, dotted lines for constant $\langle J_L \rangle$ or

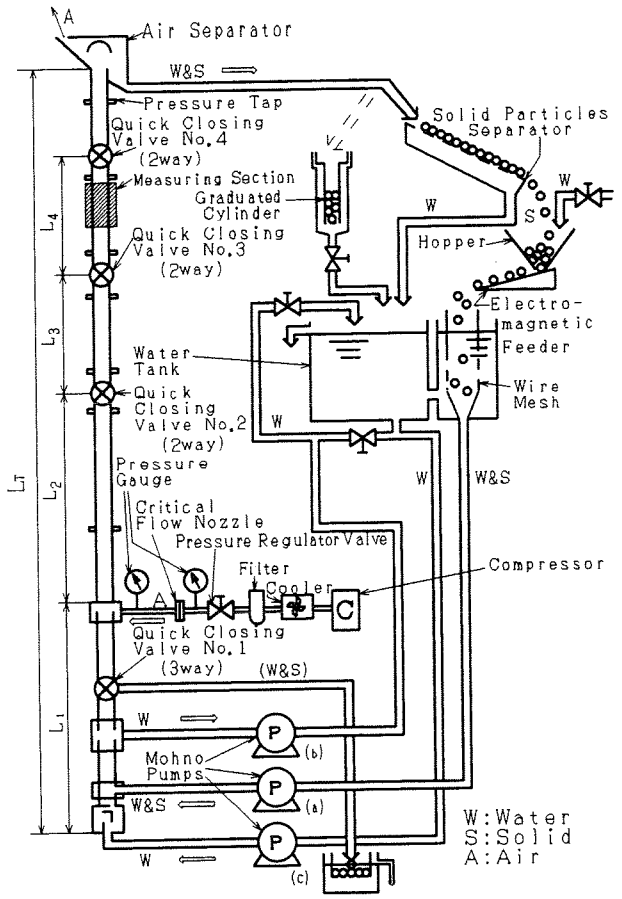

D (mm)	L_T (mm)	L_1 (mm)	L_2 (mm)	L_3 (mm)	L_4 (mm)
20.9	9820	853	3599	2002	2020
30.6	9965	974	3583	2003	2002

Fig.1 Experimental apparatus

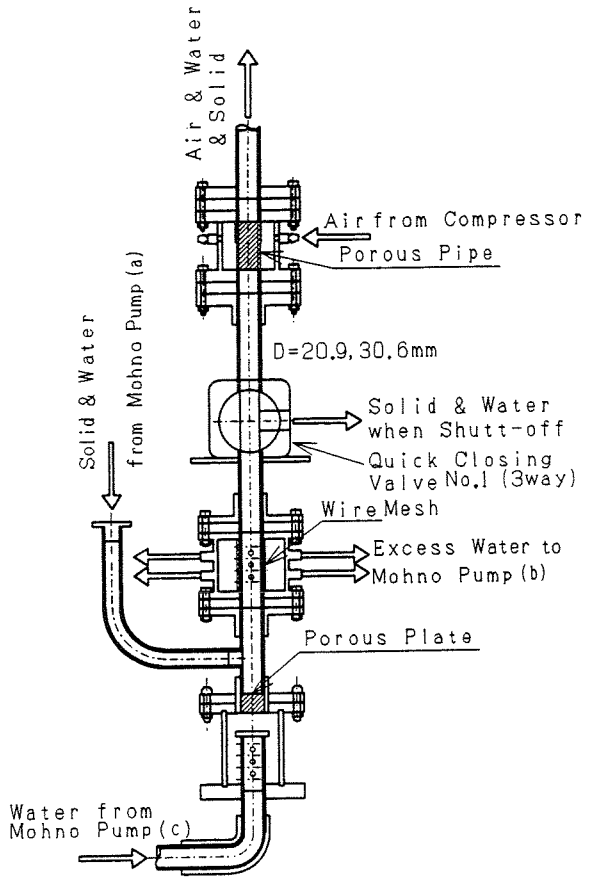

Fig.2 Mixing section

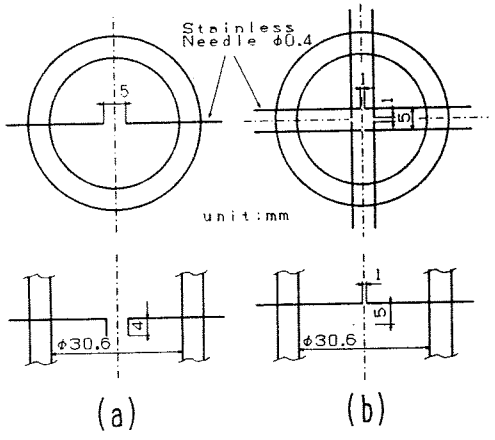

Fig.3 Electric probes

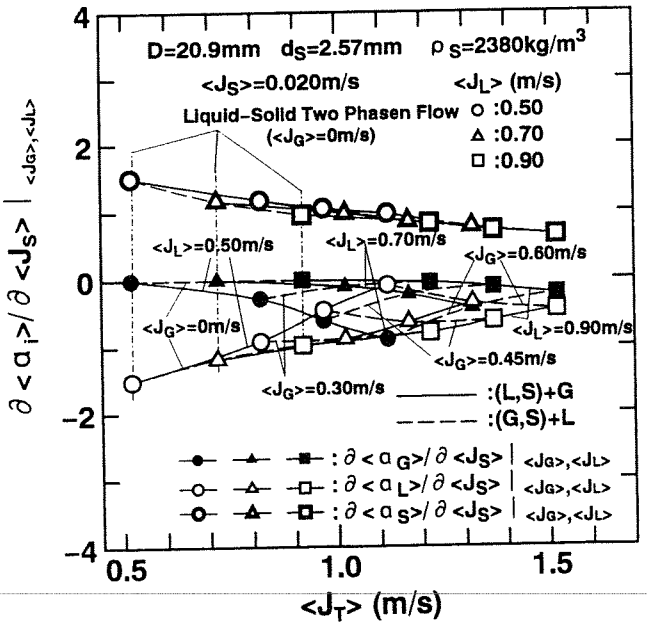

Fig.5 Increasing/decreasing rates of volumetric fractions when solid phase is increased

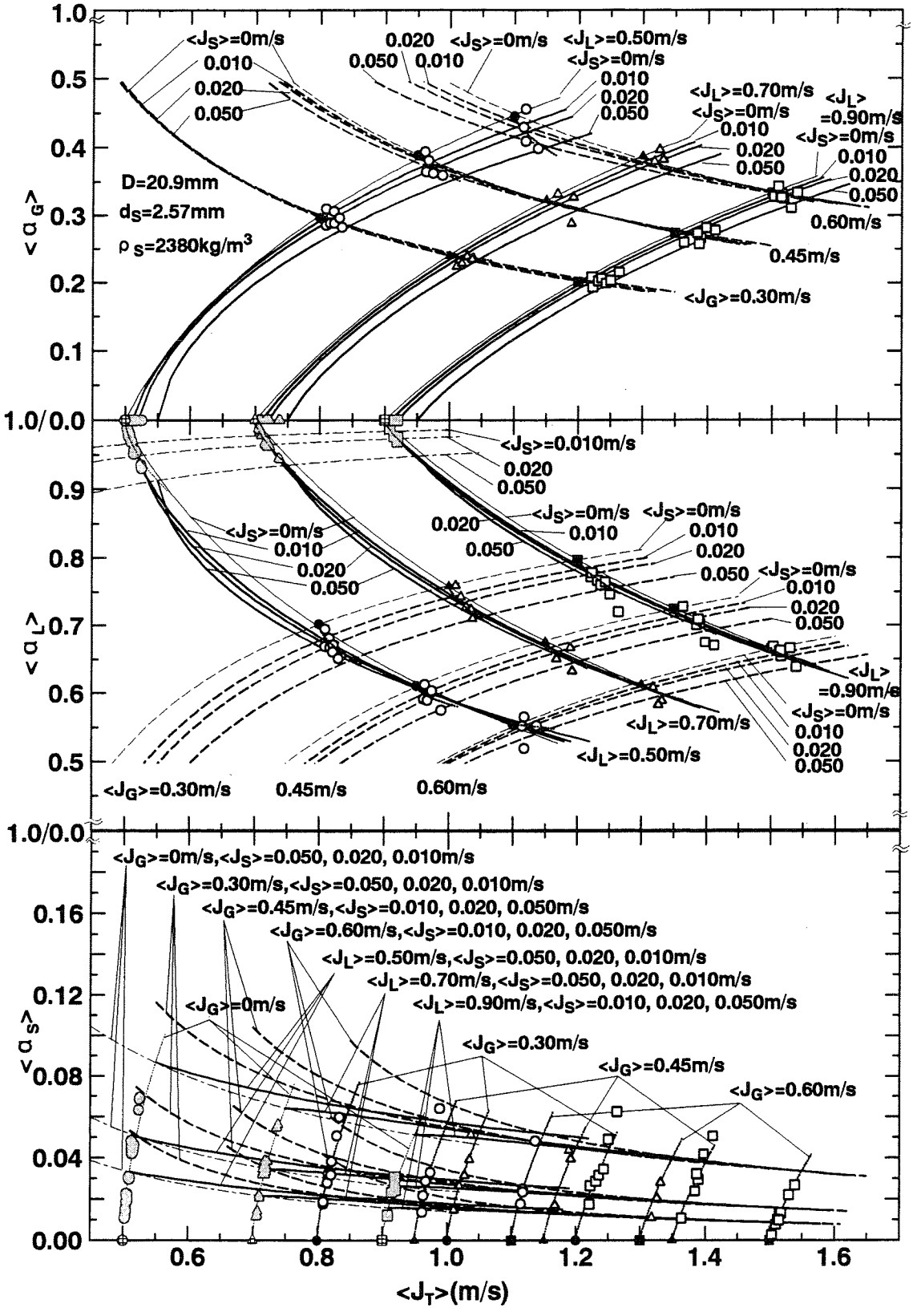

Fig.4 Volumetric fractions

$\langle J_G \rangle$ and $\langle J_L \rangle$ with $\langle J_S \rangle$ as a parameter, and alternate long dotted dash lines for constant $\langle J_S \rangle$ with $\langle J_L \rangle$ as a parameter. Since the curved lines were drawn using representative values of the volumetric fluxes shown in **Fig.4**, they do not necessarily agree well with each measured data whose volumetric flux is a little bit different from the representative value.

3.1 Volumetric fractions in gas-liquid two phase slug flow

Six thin lines in the upper frame for gas-liquid two phase slug flow form distorted rhomb patterns. These lines and solid symbols appear at symmetrical position about the abscissa ($\langle \alpha_G \rangle$=0, $\langle \alpha_L \rangle$=1) in the middle frame of the figure, because the relation $\langle \alpha_G \rangle+\langle \alpha_L \rangle=1$ always holds for gas-liquid two phase flow. In the lower frame, these six thin lines and solid symbols appear on the abscissa ($\langle \alpha_S \rangle$=0). The characteristics of $\langle \alpha_G \rangle$ and $\langle \alpha_L \rangle$ in gas-liquid two phase flow can be summarized as follows:

1. When $\langle J_L \rangle$ is increased at constant $\langle J_G \rangle$, $\langle \alpha_G \rangle$ decreases with increasing $\langle J_T \rangle$. The decreasing rate of $\langle \alpha_G \rangle$ with respect to $\langle J_T \rangle$ under constant $\langle J_G \rangle$, $\left|\partial\langle \alpha_G \rangle/\partial\langle J_T \rangle|_{\langle J_G \rangle}\right|$ decreases with increasing $\langle J_T \rangle$. Since $\left|\partial\langle \alpha_G \rangle/\partial\langle J_T \rangle|_{\langle J_G \rangle}\right|=\left|\partial\langle \alpha_G \rangle/\partial\langle J_L \rangle|_{\langle J_G \rangle}\right|$, the above mentioned characteristics also hold for the decreasing rate of $\langle \alpha_G \rangle$ with respect to $\langle J_L \rangle$. Since $\langle \alpha_G \rangle+\langle \alpha_L \rangle=1$, the characteristics of $\langle \alpha_L \rangle$ and its increasing rate ($\partial\langle \alpha_L \rangle/\partial\langle J_T \rangle|_{\langle J_G \rangle}$ $=\partial\langle \alpha_L \rangle/\partial\langle J_L \rangle|_{\langle J_G \rangle}$) are the same as those of $\langle \alpha_G \rangle$ and its decreasing rate.
2. When $\langle J_G \rangle$ is increased at constant $\langle J_L \rangle$, $\langle \alpha_G \rangle$ increases with $\langle J_T \rangle$ or $\langle J_G \rangle$. The increasing rate of $\langle \alpha_G \rangle$ under constant $\langle J_L \rangle$, $\partial\langle \alpha_G \rangle/\partial\langle J_T \rangle|_{\langle J_L \rangle}=\partial\langle \alpha_G \rangle/\partial\langle J_G \rangle|_{\langle J_L \rangle}$, is large when $\langle J_T \rangle$ or $\langle J_G \rangle$ is small, and small when $\langle J_T \rangle$ or $\langle J_G \rangle$ is large. Of course, $\langle \alpha_L \rangle$ and its decreasing rate ($\left|\partial\langle \alpha_L \rangle/\partial\langle J_T \rangle|_{\langle J_L \rangle}\right|=\left|\partial\langle \alpha_L \rangle/\partial\langle J_G \rangle|_{\langle J_L \rangle}\right|$) have the same characteristics.
3. The values of $\partial\langle \alpha_G \rangle/\partial\langle J_G \rangle|_{\langle J_L \rangle}$ and $\partial\langle \alpha_L \rangle/\partial\langle J_L \rangle|_{\langle J_G \rangle}$ are in the same order. When $\langle J_G \rangle$ is small or $\langle J_L \rangle$ is large, $\partial\langle \alpha_G \rangle/\partial\langle J_G \rangle|_{\langle J_L \rangle}$ is the larger, and when $\langle J_L \rangle$ is small or $\langle J_G \rangle$ is large, $\partial\langle \alpha_L \rangle/\partial\langle J_L \rangle|_{\langle J_G \rangle}$ is the larger. If the values of $\langle J_G \rangle$ and $\langle J_L \rangle$ are just the same, the value of $\partial\langle \alpha_G \rangle/\partial\langle J_G \rangle|_{\langle J_L \rangle}$ is the larger in this experimental range. The roles of the gas or the dispersed phase and the liquid or the continuous phase are thus slightly different, whereas in ordinary models such as the drift flux model, the value of volumetric fractions are affected only by $\langle J_T \rangle$, and not by each value of $\langle J_G \rangle$ and $\langle J_L \rangle$.

3.2 Volumetric fractions in liquid-solid two phase flow

Measured $\langle \alpha_S \rangle$ for liquid-solid two phase flow denoted by gray symbols are located near the ordinate in the lower frame. Six thin lines for liquid-solid two phase flow form rectangular-like patterns. Since $\langle \alpha_S \rangle+\langle \alpha_L \rangle=1$, these thin lines and gray symbols also appear at the upper of the middle frame of the figure. The characteristics of $\langle \alpha_S \rangle$ and $\langle \alpha_L \rangle$ in liquid-solid two phase flow are summarized as follows:

1. When $\langle J_L \rangle$ is increased under constant $\langle J_S \rangle$, $\langle \alpha_S \rangle$ slightly decreases with increasing $\langle J_T \rangle$. The decreasing rate of $\langle \alpha_S \rangle$ with respect to $\langle J_T \rangle$ under constant $\langle J_S \rangle$, $\left|\partial\langle \alpha_S \rangle/\partial\langle J_T \rangle|_{\langle J_S \rangle}\right|$ decreases with increasing $\langle J_T \rangle$. Since $\left|\partial\langle \alpha_S \rangle/\partial\langle J_T \rangle|_{\langle J_S \rangle}\right|=\left|\partial\langle \alpha_S \rangle/\partial\langle J_L \rangle|_{\langle J_S \rangle}\right|$, the above mentioned characteristics also hold with respect to $\langle J_L \rangle$. Since $\langle \alpha_S \rangle+\langle \alpha_L \rangle=1$, $\langle \alpha_L \rangle$ and its increasing rate ($\partial\langle \alpha_L \rangle/\partial\langle J_T \rangle|_{\langle J_S \rangle}=\partial\langle \alpha_L \rangle/\partial\langle J_L \rangle|_{\langle J_S \rangle}$) have the same characteristics.
2. When $\langle J_S \rangle$ is increased under constant $\langle J_L \rangle$, $\langle \alpha_S \rangle$ increases with $\langle J_T \rangle$ or $\langle J_S \rangle$. The increasing rate of $\langle \alpha_S \rangle$ under constant $\langle J_L \rangle$, $\partial\langle \alpha_S \rangle/\partial\langle J_T \rangle|_{\langle J_L \rangle}=\partial\langle \alpha_S \rangle/\partial\langle J_S \rangle|_{\langle J_L \rangle}$, is large when $\langle J_T \rangle$ or $\langle J_S \rangle$ is small, and small when $\langle J_T \rangle$ or $\langle J_S \rangle$ is large. Of course, the characteristics of $\langle \alpha_L \rangle$ and its decreasing rate ($\left|\partial\langle \alpha_L \rangle/\partial\langle J_T \rangle|_{\langle J_L \rangle}\right| =\left|\partial\langle \alpha_L \rangle/\partial\langle J_S \rangle|_{\langle J_L \rangle}\right|$) are the same.
3. The values of $\partial\langle \alpha_S \rangle/\partial\langle J_S \rangle|_{\langle J_L \rangle}$ are much larger than $\partial\langle \alpha_L \rangle/\partial\langle J_L \rangle|_{\langle J_S \rangle}$. This is because the unit increment of volumetric flux causes a large increment on $\langle J_S \rangle$ in ratio, as $\langle J_S \rangle$ is much smaller than $\langle J_L \rangle$.

The features 1 and 2 for both gas-liquid two phase slug flow and liquid-solid two phase flow are common, however feature 3 is different.

3.3 Volumetric fractions in gas-liquid-solid three phase slug flow

Volumetric fractions in the gas-liquid-solid three phase slug flow are denoted by open symbols

in **Fig.4**. Thick lines represent the change of volumetric fractions of the three phase flow. It is easily found from **Fig.4** that if $\langle J_S \rangle$ is kept constant, $\langle \alpha_G \rangle$ is large when $\langle J_G \rangle$ is large or when $\langle J_L \rangle$ is small, while $\langle \alpha_L \rangle$ is large when $\langle J_L \rangle$ is large or $\langle J_G \rangle$ is small. This feature is identical with that of gas-liquid two phase flow. It also holds in the three phase flow that $\langle \alpha_S \rangle$ is large when $\langle J_S \rangle$ is large or when $\langle J_L \rangle$ is small, while $\langle \alpha_L \rangle$ is large when $\langle J_L \rangle$ is large or $\langle J_S \rangle$ is small under constant $\langle J_G \rangle$, which is also identical with the feature of liquid-solid two phase flow. The characteristics of volumetric fractions will be investigated more precisely for each volumetric flux below.

3.3.1 When $\langle J_l \rangle$ is increased at constant $\langle J_G \rangle$ and $\langle J_S \rangle$ Thick and broken lines in **Fig.4** run roughly parallel to the thin broken lines for the two phase slug flow. Thus, the characteristics summarized in 3.1, No.1 also hold for the three phase flow under constant $\langle J_S \rangle$. At the same time, the characteristics of the liquid-solid two phase flow summarized in 3.2 No.1 hold for $\langle \alpha_L \rangle$ and $\langle \alpha_S \rangle$ in three phase flow under constant $\langle J_G \rangle$.

The decreasing rate $|\partial\langle \alpha_G \rangle/\partial\langle J_L \rangle|_{\langle J_G \rangle,\langle J_S \rangle}$ tends to decrease with increasing $\langle J_S \rangle$ when $\langle J_G \rangle$ is large. As a result, the crossing of lines occurs when $\langle J_G \rangle$ is large; for the cases of $\langle J_G \rangle$=0.45 and 0.60 m/s in **Fig.4**, the values of $\langle \alpha_G \rangle$ for gas-liquid two phase flow is larger than those for three phase flow when $\langle J_L \rangle$ is small, but when $\langle J_L \rangle$ becomes large, the crossing occurs, and $\langle \alpha_G \rangle$ for three phase flow exceeds that for two phase flow. In this region, $\langle \alpha_G \rangle$ increases with $\langle J_S \rangle$ if $\langle J_T \rangle$ or $\langle J_G \rangle$ is kept constant. Of course, $\langle J_L \rangle$ decreases at the same time. When $\langle J_G \rangle$=0.30 m/s, $\langle \alpha_G \rangle$ lines for three phase flow nearly agree with that for two phase flow.

Broken lines for $\langle \alpha_L \rangle$ clearly move down with increasing $\langle J_S \rangle$. Crossing of lines are not found. Therefore, in this experimental range, $\langle \alpha_L \rangle$ always decreases when the volumetric flux of the liquid phase is decreased, and that of the solid phase is increased under constant $\langle J_T \rangle$.

On the other hand, $\langle \alpha_S \rangle$ slightly decreases with increasing $\langle J_L \rangle$ as shown by thick broken lines in the lower frame in **Fig.4**. Its decreasing rate with respect to $\langle J_T \rangle$ or $\langle J_L \rangle$ under constant $\langle J_G \rangle$ and $\langle J_S \rangle$ ($|\partial\langle \alpha_S \rangle/\partial\langle J_T \rangle|_{\langle J_G \rangle,\langle J_S \rangle}=|\partial\langle \alpha_S \rangle/\partial\langle J_L \rangle|_{\langle J_G \rangle,\langle J_S \rangle}|$) is very small compared with $|\partial\langle \alpha_G \rangle/\partial\langle J_L \rangle|_{\langle J_G \rangle,\langle J_S \rangle}|$ or $\partial\langle \alpha_L \rangle/\partial\langle J_L \rangle|_{\langle J_G \rangle,\langle J_S \rangle}$. Thus, in this case, the decrement of the gas phase almost compensates for the increment of the liquid phase. When $\langle J_T \rangle$ or $\langle J_L \rangle$ is small, $\langle \alpha_S \rangle$ for larger $\langle J_G \rangle$ is larger if $\langle J_T \rangle$ and $\langle J_S \rangle$ are kept constant. But when $\langle J_T \rangle$ becomes large (about more than 1.30 m/s), $\langle \alpha_S \rangle$ lines for the same $\langle J_S \rangle$ almost agree regardless of the value of $\langle J_G \rangle$. In this region, value of $\langle \alpha_S \rangle$ is determined only by $\langle J_T \rangle$ and $\langle J_S \rangle$.

3.3.2 When $\langle J_G \rangle$ is increased at constant $\langle J_l \rangle$ and $\langle J_S \rangle$ Thick and solid lines also run roughly parallel to the thin solid lines for gas-liquid two phase flow. Thus, the characteristics summarized for gas-liquid two phase flow in 3.1, No.2 also hold under constant $\langle J_S \rangle$.

The lines for $\langle \alpha_G \rangle$ in the upper frame in **Fig.4** starts from the abscissa, and do not cross each other. Among these lines, line for larger $\langle J_S \rangle$ has smaller values under constant $\langle J_T \rangle$. Thus, in this experimental range, $\langle \alpha_G \rangle$ always decreases when the volumetric flux of the gas phase is decreased, and that of the solid phase is increased under constant $\langle J_T \rangle$. Value of $\partial\langle \alpha_G \rangle/\partial\langle J_G \rangle|_{\langle J_L \rangle,\langle J_S \rangle}$ decrease with increasing $\langle J_S \rangle$ especially when $\langle J_L \rangle$ is small. As a result, when $\langle J_L \rangle$ is small and $\langle J_S \rangle$ is large, $\langle \alpha_G \rangle$ lines much separate from thin line for gas-liquid two phase flow.

The decreasing rate of $\langle \alpha_L \rangle$, $|\partial\langle \alpha_L \rangle/\partial\langle J_G \rangle|_{\langle J_L \rangle,\langle J_S \rangle}$ also decreases with increasing $\langle J_S \rangle$ especially when $\langle J_L \rangle$ is small. Lines for $\langle \alpha_L \rangle$ cross with thin line and with each other when $\langle J_L \rangle$ is small. The $\langle \alpha_L \rangle$ lines for each $\langle J_S \rangle$ starts from the values of $\langle \alpha_L \rangle$ for liquid-solid two phase flow. Hence, they are below gas-liquid two phase $\langle \alpha_L \rangle$ line when $\langle J_T \rangle$ or $\langle J_G \rangle$ is small. When $\langle J_G \rangle$ becomes large, the crossing of lines occurs, and $\langle \alpha_L \rangle$ line comes above that for two phase flow. In this region, $\langle \alpha_L \rangle$ increases when the volumetric flux of the gas phase is decreased, and that of the solid phase is increased under constant $\langle J_T \rangle$.

On the other hand, $\langle \alpha_S \rangle$ slightly decreases with increasing $\langle J_G \rangle$ as shown by thick solid lines in the lower frame in **Fig.4**. Its decreasing rate with respect to $\langle J_T \rangle$ under constant $\langle J_L \rangle$ and $\langle J_S \rangle$ ($|\partial\langle \alpha_S \rangle/\partial\langle J_T \rangle|_{\langle J_L \rangle,\langle J_S \rangle}=|\partial\langle \alpha_S \rangle/\partial\langle J_G \rangle|_{\langle J_L \rangle,\langle J_S \rangle}|$) is much smaller than $\partial\langle \alpha_G \rangle/\partial\langle J_G \rangle|_{\langle J_L \rangle,\langle J_S \rangle}$ or $|\partial\langle \alpha_L \rangle/\partial\langle J_G \rangle|_{\langle J_L \rangle,\langle J_S \rangle}|$. Thus, in this case, the increment of the gas phase is almost compensated by the decrement of the liquid phase. When $\langle J_T \rangle$ or $\langle J_G \rangle$ is small, $\langle \alpha_S \rangle$ for larger $\langle J_L \rangle$ is larger if $\langle J_T \rangle$ and $\langle J_S \rangle$ are kept constant. But when $\langle J_T \rangle$ becomes large (about more than 1.30 m/s), $\langle \alpha_S \rangle$ lines for the same $\langle J_S \rangle$ agree regardless of the value of $\langle J_G \rangle$ as shown in 3.3.1.

3.3.3 When $\langle J_S \rangle$ is increased at constant $\langle J_G \rangle$ and $\langle J_l \rangle$ In this case, $\langle \alpha_G \rangle$ tends to decrease from the value for the gas-liquid two phase flow. However, the decreasing rates of $\langle \alpha_G \rangle$ under constant $\langle J_G \rangle$ and $\langle J_L \rangle$, $|\partial\langle \alpha_G \rangle/\partial\langle J_S \rangle|_{\langle J_G \rangle,\langle J_L \rangle}|$, change with $\langle J_G \rangle$, $\langle J_L \rangle$ and $\langle J_S \rangle$. An

example of the values of $\partial\langle\alpha_G\rangle/\partial\langle J_S\rangle|_{\langle J_G\rangle,\langle J_L\rangle}$ are shown in **Fig.5**. They have negative values when $\langle J_G\rangle>>0$. Their absolute values increase with $\langle J_T\rangle$ under constant $\langle J_L\rangle$. That is, the decreasing rate of $\langle\alpha_G\rangle$ increases with $\langle J_G\rangle$. However, their absolute values decrease with increasing $\langle J_T\rangle$ or $\langle J_L\rangle$ under constant $\langle J_G\rangle$. Consequently, it was confirmed that $\langle\alpha_G\rangle$ steeply decreases with increasing $\langle J_S\rangle$ when $\langle J_L\rangle$ is small and $\langle J_G\rangle$ is large, whereas it slightly decreases when $\langle J_L\rangle$ is large and $\langle J_G\rangle$ is small. Values of $\partial\langle\alpha_G\rangle/\partial\langle J_S\rangle|_{\langle J_G\rangle,\langle J_L\rangle}$ also depends on $\langle\alpha_G\rangle$ itself; $\langle\alpha_G\rangle$ steeply decreases by increasing $\langle J_S\rangle$ when $\langle\alpha_G\rangle$ is large, but it slightly decreases when $\langle\alpha_G\rangle$ is small.

When $\langle J_S\rangle$ is increased, $\langle\alpha_L\rangle$ also decreases from the gas-liquid two phase flow data. This tendency is similar to the liquid-solid two phase flow. The decreasing rate of $\langle\alpha_L\rangle$ under constant $\langle J_G\rangle$ and $\langle J_L\rangle$, $\partial\langle\alpha_L\rangle/\partial\langle J_S\rangle|_{\langle J_G\rangle,\langle J_L\rangle}$, changes with $\langle J_G\rangle$, $\langle J_L\rangle$ and $\langle J_S\rangle$ as shown in **Fig.5**. They have negative values. Their absolute values decrease with increasing $\langle J_T\rangle$ or $\langle J_G\rangle$ under constant $\langle J_L\rangle$. This tendency is opposite to the case of $\langle\alpha_G\rangle$. Their absolute values almost keep constant or slightly increase with $\langle J_T\rangle$ under constant $\langle J_G\rangle$. $\langle\alpha_L\rangle$ fairly decreases with increasing $\langle J_S\rangle$ when $\langle J_G\rangle$ is small or $\langle J_L\rangle$ is large, whereas it slightly decreases when $\langle J_G\rangle$ is large or $\langle J_L\rangle$ is small.

When $\langle J_S\rangle$ is increased, $\langle\alpha_S\rangle$ always increases similarly to liquid-solid two phase flow. Its increasing rate $\partial\langle\alpha_S\rangle/\partial\langle J_S\rangle|_{\langle J_G\rangle,\langle J_L\rangle}$ is the largest when $\langle J_G\rangle=0$, and it decreases with increasing $\langle J_G\rangle$ or $\langle J_L\rangle$. The effects of $\langle J_G\rangle$ and $\langle J_L\rangle$ are almost equivalent. Therefore, $\partial\langle\alpha_S\rangle/\partial\langle J_S\rangle|_{\langle J_G\rangle,\langle J_L\rangle}$ is approximately determined by $\langle J_T\rangle$ as shown in **Fig.5** when $\langle J_S\rangle$ is kept constant. The values of $\partial\langle\alpha_S\rangle/\partial\langle J_S\rangle|_{\langle J_G\rangle,\langle J_L\rangle}$ also decrease with increasing $\langle J_S\rangle$ when $\langle J_G\rangle$ or $\langle J_L\rangle$ are kept constant.

When solid phase is added, $\langle\alpha_S\rangle$ increases and $\langle\alpha_G\rangle$ and $\langle\alpha_L\rangle$ decrease as mentioned above. The increasing rates are related with each other by the following relation,

$$\partial\langle\alpha_G\rangle/\partial\langle J_S\rangle|_{\langle J_G\rangle,\langle J_L\rangle}+\partial\langle\alpha_L\rangle/\partial\langle J_S\rangle|_{\langle J_G\rangle,\langle J_L\rangle}+\partial\langle\alpha_S\rangle/\partial\langle J_S\rangle|_{\langle J_G\rangle,\langle J_L\rangle}=0.$$

Thus, the increasing rate of the solid phase counterbalances the decreasing rates of gas and liquid phases. When $\langle J_L\rangle$ is large and $\langle J_G\rangle$ is small, $\left|\partial\langle\alpha_L\rangle/\partial\langle J_S\rangle|_{\langle J_G\rangle,\langle J_L\rangle}\right|$ is larger than $\left|\partial\langle\alpha_G\rangle/\partial\langle J_S\rangle|_{\langle J_G\rangle,\langle J_L\rangle}\right|$. When $\langle J_G\rangle$ is large and $\langle J_L\rangle$ is small, $\left|\partial\langle\alpha_L\rangle/\partial\langle J_S\rangle|_{\langle J_G\rangle,\langle J_L\rangle}\right|$ is smaller than $\left|\partial\langle\alpha_G\rangle/\partial\langle J_S\rangle|_{\langle J_G\rangle,\langle J_L\rangle}\right|$. The above mentioned tendency changes at $\langle\alpha_G\rangle\cong0.35$. Consequently, when $\langle\alpha_G\rangle$ is below 0.35, the increment of the solid phase is mainly compensated by the decrement of the liquid phase, meanwhile when $\langle\alpha_G\rangle$ exceeds about 0.35, it is mainly compensated by the decrement of the gas phase.

3.4 Phase velocities

The averaged phase velocity of phase i is obtained by

$$\overline{V}_i=\langle J_i\rangle/\langle\alpha_i\rangle, \qquad (1)$$

so that the characteristics of the averaged phase velocity are deeply related to those of the volumetric fraction. **Figure 6** shows relations between averaged phase velocity, $\overline{V}_i$, and the total volumetric flux, $\langle J_T\rangle$. The term "averaged" will be omitted below for simplicity. Gas and liquid phase velocities are shown in the upper frame of **Fig.6**, and solid phase velocity is shown in the lower frame. The symbol shape and color are in the same manner as **Fig.4**. Since we cannot define the value of $\overline{V}_G$ in liquid-solid two phase flow and $\overline{V}_S$ in gas-liquid two phase flow, they are plotted on the abscissas. Curved lines shown in **Fig.4** are also transferred using Eq.(1). Only some samples of them are, however, shown in **Fig.6** as they heavily overlap with each other. Lines were principally drawn for the cases of $\langle J_G\rangle$=0.45 m/s, $\langle J_L\rangle$=0.70 m/s and $\langle J_S\rangle$=0, 0.050 m/s. The alternate long dotted dash line represents $\overline{V}_i=\langle J_T\rangle$. Hence, the increasing rate of this line is unity

In this experimental range, $\overline{V}_G$ is always larger than $\langle J_T\rangle$, and $\overline{V}_L$ is smaller than $\langle J_T\rangle$ except for the case of liquid-solid two phase flow. In most cases, $\overline{V}_S$ for both liquid-solid two phase flow and three phase flow is smaller than $\langle J_T\rangle$. Therefore, $\overline{V}_G$ is always larger than both $\overline{V}_L$ and $\overline{V}_S$. On the other hand, $\overline{V}_L$ is larger than $\overline{V}_S$ for most flow conditions, but when $\langle J_L\rangle$ is large, $\overline{V}_S$ is sometimes greater than $\overline{V}_L$. The phase velocities in the three phase flow almost increase with $\langle J_T\rangle$, but in the strict sense, it is impossible to express them by a single stright line even for $\overline{V}_G$. Their increasing rates are discussed in the following sections.

3.4.1 When $\langle J_i\rangle$ is increased at constant $\langle J_G\rangle$ and $\langle J_S\rangle$ In this case, $\overline{V}_G$ increases approximately linearly to $\langle J_T\rangle$ both in gas-liquid two phase slug flow and in three phase slug flow. The increasing rate of $\overline{V}_G$, $\partial\overline{V}_G/\partial\langle J_L\rangle|_{\langle J_G\rangle,\langle J_S\rangle}$, is a little larger than unity. By comparing two broken lines for $\overline{V}_G$, it is clear that the increasing rate is larger in gas-liquid two phase flow than in

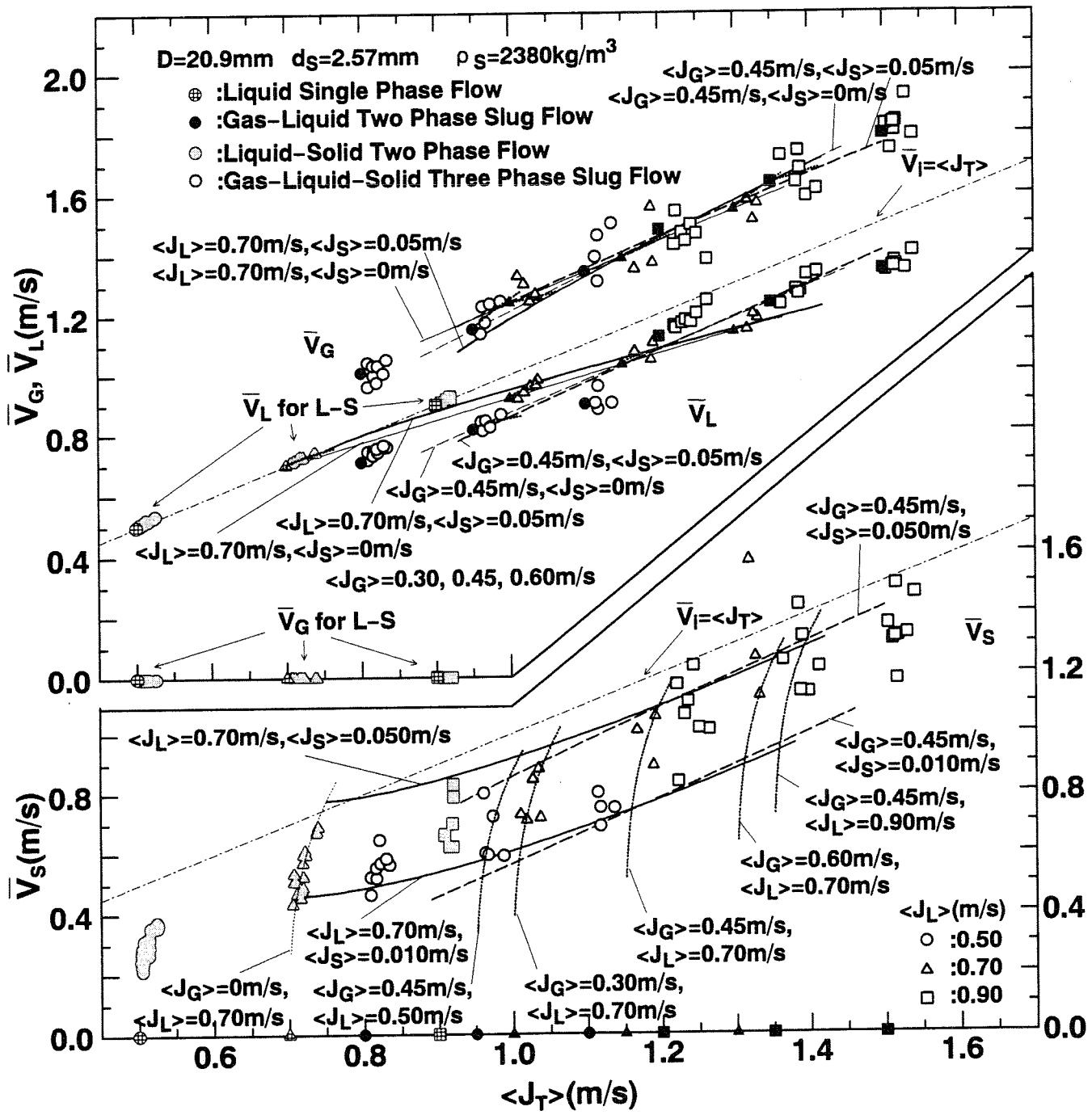

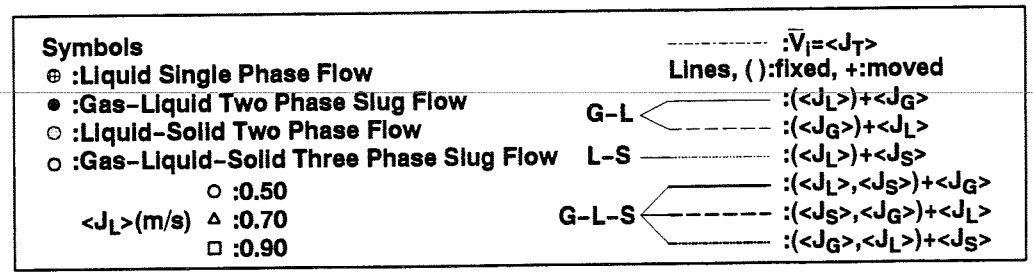

Fig.6 Phase velocities

three phase flow. Therefore, by adding solid phase into gas-liquid two phase flow, the increasing rate of the gas phase velocity decreases. The $\overline{V}_G$ lines make a crossing for the cases of $\langle J_G \rangle$=0.45 and 0.60 m/s, just similar to $\langle \alpha_G \rangle$ lines shown in 3.3.1. The values of $\langle J_T \rangle$ where crossing occurs are the same as the case of $\langle \alpha_G \rangle$ lines. In the region $\langle J_T \rangle$ is larger than the crossing, $\overline{V}_G$ decreases when the volumetric flux of the liquid phase is decreased, and that of the solid phase is increased under constant $\langle J_T \rangle$.

Broken lines for $\overline{V}_L$ show that $\overline{V}_L$ increases approximately linearly to $\langle J_T \rangle$ both in gas-liquid two phase and in three phase slug flow. The increasing rate of $\overline{V}_L$, $\partial \overline{V}_L / \partial \langle J_L \rangle|_{\langle J_G \rangle, \langle J_S \rangle}$, is also larger than unity. But the increasing rate for gas-liquid two phase flow is a little bit smaller than that for three phase flow. Although $\langle \alpha_L \rangle$ lines have no crossing as shown in 3.3.1, $\overline{V}_L$ lines for two and three phase flows have a crossing for the cases of $\langle J_G \rangle$=0.45 and 0.60 m/s. Because $\langle J_G \rangle$ and $\langle J_S \rangle$ are fixed, and only $\langle J_L \rangle$ changes along the broken lines, the values of $\langle J_L \rangle$ on two broken lines are shifted by the difference of $\langle J_S \rangle$ if the value of $\langle J_T \rangle$ is identical. As the relation $\langle \alpha_L \rangle = \langle J_L \rangle / \overline{V}_L$ holds, the values of $\langle \alpha_L \rangle$ are different when the values of $\overline{V}_L$ are the same. This is the reason why $\langle \alpha_L \rangle$ lines have no crossing at a flow condition where $\overline{V}_L$ lines have a crossing.

Two near parallel broken lines in the lower frame of **Fig.6** show the $\overline{V}_S$ lines for $\langle J_S \rangle$=0.010 and 0.050 m/s. Their increasing rates are almost larger than unity. But when $\langle J_G \rangle$=0.30 m/s, they are smaller than unity. Thus, $\partial \overline{V}_S / \partial \langle J_L \rangle|_{\langle J_G \rangle, \langle J_S \rangle}$ increases with $\langle J_G \rangle$. The values of three increasing rates when $\langle J_L \rangle$ is increased are roughly comparable.

3.4.2 When $\langle J_G \rangle$ is increased at constant $\langle J_L \rangle$ and $\langle J_S \rangle$ Solid lines in **Fig.6** represent the change of phase velocities in this case. $\overline{V}_G$ lines are almost linear, and the increasing rate $\partial \overline{V}_G / \partial \langle J_G \rangle|_{\langle J_L \rangle, \langle J_S \rangle}$ is larger than unity. The increasing rate for three phase flow is larger than for gas-liquid two phase flow. The lines have a crossing. The value of $\langle J_T \rangle$ where crossing occurs is large when $\langle J_L \rangle$ is large. In the region $\langle J_T \rangle$ is larger than the crossing, $\overline{V}_G$ line for three phase flow is above the line for two phase flow. In this region, $\overline{V}_G$ increases when the volumetric flux of the gas phase is decreased, and that of the solid phase is increased under constant $\langle J_T \rangle$. As shown in 3.3.2, $\langle \alpha_G \rangle$ lines do not cross in this condition; the reason is just similar to the case of $\langle \alpha_L \rangle$ lines when $\langle J_L \rangle$ increases described 3.4.1.

$\overline{V}_L$ lines for three phase flow starts from the value for liquid-solid two phase flow. Its increasing rate $\partial \overline{V}_L / \partial \langle J_G \rangle|_{\langle J_L \rangle, \langle J_S \rangle}$ is rather smaller than unity. When $\langle J_T \rangle$ or $\langle J_G \rangle$ is small, $\overline{V}_L$ for three phase flow is smaller than that for gas-liquid two phase flow. These lines are again crossed just in the same manner as $\langle \alpha_L \rangle$ lines when $\langle J_G \rangle$ increases.

$\overline{V}_S$ lines for three phase flow also starts from the value for liquid-solid two phase flow. Their increasing rate, $\partial \overline{V}_S / \partial \langle J_G \rangle|_{\langle J_L \rangle, \langle J_S \rangle}$, is very small when $\langle J_L \rangle$ or $\langle J_G \rangle$ is small. In this condition, it is smaller than $\partial \overline{V}_L / \partial \langle J_G \rangle|_{\langle J_L \rangle, \langle J_S \rangle}$. When both $\langle J_L \rangle$ and $\langle J_G \rangle$ are large, it sometimes becomes larger than $\partial \overline{V}_G / \partial \langle J_G \rangle|_{\langle J_L \rangle, \langle J_S \rangle}$.

3.4.3 When $\langle J_S \rangle$ is increased at constant $\langle J_G \rangle$ and $\langle J_L \rangle$ Dotted lines in **Fig.6** represent the change of phase velocities in this case. $\overline{V}_G$ always increases with $\langle J_T \rangle$ or $\langle J_S \rangle$ in this experimental range. The increasing rate, $\partial \overline{V}_G / \partial \langle J_S \rangle|_{\langle J_G \rangle, \langle J_L \rangle}$, is affected by volumetric fluxes; it increases with $\langle J_G \rangle$, and decreases with increasing $\langle J_L \rangle$.

Similarly, $\overline{V}_L$ increases with $\langle J_T \rangle$ or $\langle J_S \rangle$. Its increasing rate, $\partial \overline{V}_L / \partial \langle J_S \rangle|_{\langle J_G \rangle, \langle J_L \rangle}$, is also affected by volumetric fluxes. Contrary to the case of $\overline{V}_G$, the increasing rate increases with $\langle J_L \rangle$, and decreases with increasing $\langle J_G \rangle$. When $\langle J_G \rangle$ is small or $\langle J_L \rangle$ is large, $\partial \overline{V}_L / \partial \langle J_S \rangle|_{\langle J_G \rangle, \langle J_L \rangle}$ is larger than $\partial \overline{V}_G / \partial \langle J_S \rangle|_{\langle J_G \rangle, \langle J_L \rangle}$. They change places when $\langle \alpha_G \rangle$ reaches about 0.35. Of course, this corresponds to the tendency of the decreasing rates of $\langle \alpha_G \rangle$ and $\langle \alpha_L \rangle$ mentioned in 3.3.3.

The dotted lines in the lower frame simply increase with $\langle J_T \rangle$ or $\langle J_S \rangle$. Its increasing rate, $\partial \overline{V}_S / \partial \langle J_S \rangle|_{\langle J_G \rangle, \langle J_L \rangle}$ is much larger than unity. Therefore, solid phase velocity increases more intensely by adding the solid phase than adding the gas or liquid phase in this range.

3.4.4 Quantitative comparison of increasing rate of each phase velocity The increasing rate of each phase velocities are here compared. For the gas phase, $\partial \overline{V}_G / \partial \langle J_S \rangle|_{\langle J_G \rangle, \langle J_L \rangle}$, is larger than both $\partial \overline{V}_G / \partial \langle J_G \rangle|_{\langle J_L \rangle, \langle J_S \rangle}$ and $\partial \overline{V}_G / \partial \langle J_L \rangle|_{\langle J_G \rangle, \langle J_S \rangle}$ when $\langle J_G \rangle$ is large, but it becomes the smallest when $\langle J_G \rangle$ is small. $\partial \overline{V}_G / \partial \langle J_G \rangle|_{\langle J_L \rangle, \langle J_S \rangle}$ and $\partial \overline{V}_G / \partial \langle J_L \rangle|_{\langle J_G \rangle, \langle J_S \rangle}$ are comparable, but the

former is a little larger than the latter.

The increasing rate of $\overline{V}_L$, $\partial\overline{V}_L/\partial\langle J_L\rangle|_{\langle J_G\rangle,\langle J_S\rangle}$, is always larger than $\partial\overline{V}_L/\partial\langle J_G\rangle|_{\langle J_L\rangle,\langle J_S\rangle}$. On the other hand, $\partial\overline{V}_L/\partial\langle J_S\rangle|_{\langle J_G\rangle,\langle J_L\rangle}$ is the largest when $\langle J_G\rangle$ is small, but it becomes smallest when $\langle J_L\rangle$ is small and $\langle J_G\rangle$ is large.

$\overline{V}_S$ increases steeply with $\langle J_S\rangle$. Therefore $\partial\overline{V}_S/\partial\langle J_S\rangle|_{\langle J_G\rangle,\langle J_L\rangle}$ is much larger than both $\partial\overline{V}_S/\partial\langle J_G\rangle|_{\langle J_L\rangle,\langle J_S\rangle}$ and $\partial\overline{V}_S/\partial\langle J_L\rangle|_{\langle J_G\rangle,\langle J_S\rangle}$. In this experimental range, $\partial\overline{V}_S/\partial\langle J_L\rangle|_{\langle J_G\rangle,\langle J_S\rangle}$ is always a little larger than $\partial\overline{V}_S/\partial\langle J_G\rangle|_{\langle J_L\rangle,\langle J_S\rangle}$.

4. DETAILED CHARACTERISTICS OF THE THREE PHASE SLUG FLOW

In order to understand the characteristics of the three phase slug flow including the volumetric fraction and phase velocity in more detail, the slug characteristics variables were also measured. The ensemble averaged value of the variables were obtained for 200 slug units and denoted by the tilde ~ . Slug characteristics variables were measured using 30.6mm diameter pipe with 4.17mm ceramic particle as the solid phase. However, the aforementioned characteristics of the volumetric fractions and phase velocities were confirmed to also hold for the case of D=30.6mm and d_S=4.17mm. The slug unit in the three phase slug flow is illustrated in **Fig.7**. It consists of large bubble part, wake part and liquid slug part. These parts are denoted by the subscripts b, w and ls, respectively, henceforth. In **Fig.8**, slug characteristic variables are plotted for the common abscissa of $\langle J_T\rangle$.

4.1 Large bubble rising velocity

The ensemble averaged rising velocity of large bubbles, $\tilde{V}_b$, is shown in **Fig.8(a)**. This velocity was measured using the type (a) proves as the rising velocity of the bottom ends of large bubbles. Averaged gas phase velocities $\overline{V}_G$ are simultaneously plotted. $\tilde{V}_b$ is always larger than $\overline{V}_G$ in this experimental range. This is probably because the gas phase exists in the wake part and liquid slug part in the form of small bubbles as well as in large bubble part. It was observed that the small bubbles in the liquid slugs were overtaken by large bubbles of the following slug unit. The averaged gas phase velocity is the volumetric weighted mean value of velocities of all bubbles. Therefore, the averaged gas phase velocity becomes smaller than large bubble velocity due to smaller rising velocity of small bubbles. However, the characteristics of $\tilde{V}_b$ is similar to those of $\overline{V}_G$. For example, $\tilde{V}_b$ increases with $\langle J_T\rangle$, and the increasing rates of $\tilde{V}_b$ for volumetric fluxes are basically similar to those of $\overline{V}_G$. When $\langle J_S\rangle$ increases, $\tilde{V}_b$ also increases. Under constant $\langle J_G\rangle$, the increasing rate $\partial\tilde{V}_b/\partial\langle J_S\rangle|_{\langle J_G\rangle,\langle J_L\rangle}$ is large when $\langle J_L\rangle$ is small, and it decreases with increasing $\langle J_L\rangle$. Under constant $\langle J_L\rangle$, the increasing rate $\partial\tilde{V}_b/\partial\langle J_S\rangle|_{\langle J_G\rangle,\langle J_L\rangle}$ is small when $\langle J_G\rangle$ is small, and it increases with $\langle J_G\rangle$.

4.2 Lengths of large bubble, wake and liquid slug part

The large bubble length, $\tilde{L}_b$, and the total length of liquid slug and wake part, denoted by $\tilde{L}_{ls}+\tilde{L}_w$, are shown in **Fig.8(b)**. In this experimental range, $\tilde{L}_{ls}+\tilde{L}_w$ is larger than $\tilde{L}_b$. Both $\tilde{L}_b$ and $\tilde{L}_{ls}+\tilde{L}_w$ increase with $\langle J_G\rangle$, and decrease with increasing $\langle J_L\rangle$. When $\langle J_S\rangle$ is increased under constant $\langle J_G\rangle$ and $\langle J_L\rangle$, both $\tilde{L}_b$ and $\tilde{L}_{ls}+\tilde{L}_w$ decrease. When $\langle J_L\rangle$ is small or $\langle J_G\rangle$ is large, the decreasing rates of $\tilde{L}_b$ and $\tilde{L}_{ls}+\tilde{L}_w$ are large, whereas when $\langle J_G\rangle$ is small or $\langle J_L\rangle$ is large, their decreasing rates are small. It was confirmed that effects of $\langle J_S\rangle$ on these lengths agree with those on $\tilde{V}_b$ although $\tilde{V}_b$ increases while $\tilde{L}_b$ and $\tilde{L}_{ls}+\tilde{L}_w$ decrease. $\tilde{L}_w$, which were measured using the 8mm video recorder system, is approximately proportional to $\tilde{L}_b$. The proportional constant was from 0.2 to 0.3.

4.3 Film thickness around large bubbles

The film thickness t_f was obtained as the averaged value of each film thickness for four azimuthal directions at a location z=90mm downward from large bubble nose in order to obtain a fully developed film thickness. The relation between $\tilde{t}_f$ and $\langle J_T\rangle$ is shown in **Fig.8(c)**. The value is almost constant for gas-liquid two phase flow. In most cases, $\tilde{t}_f$ increases with $\langle J_S\rangle$ under constant $\langle J_G\rangle$ and $\langle J_L\rangle$. The tendency of the increasing rate of $\tilde{t}_f$ for $\langle J_S\rangle$ is also similar to that of the increasing rates

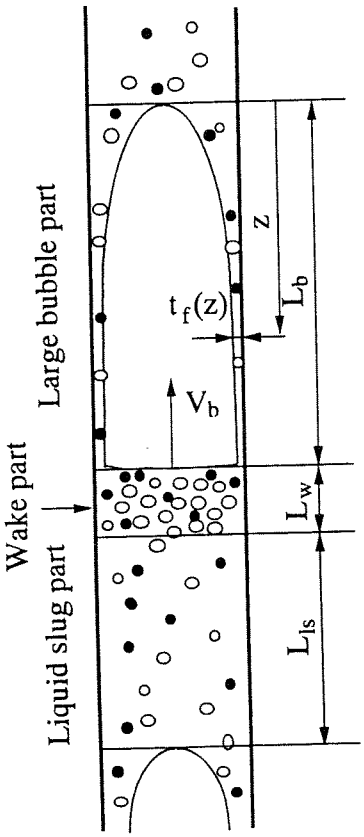

Fig.7 Sketch of slug unit

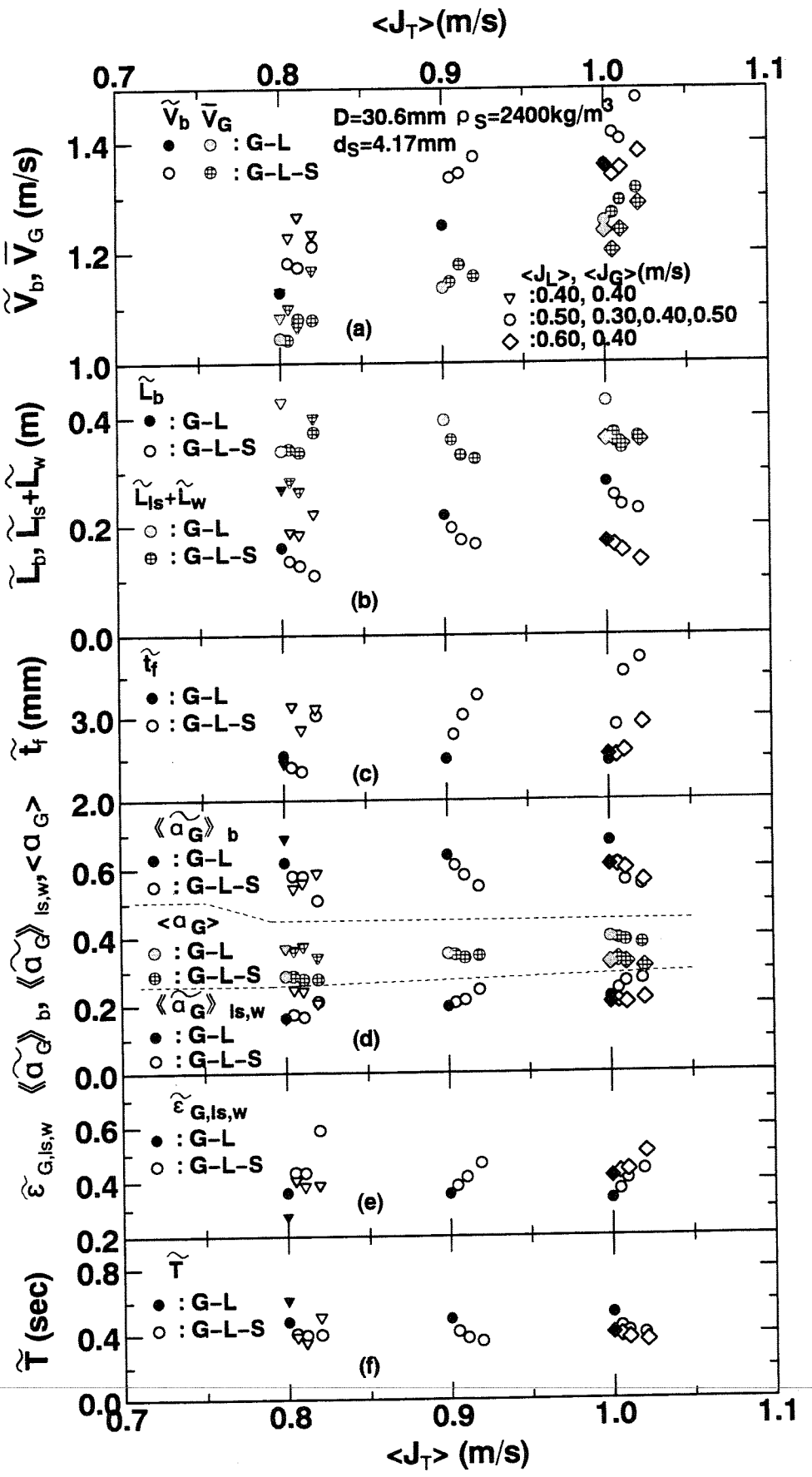

Fig.8 Slug characteristic variables

of $\tilde{V}_b$ for $\langle J_S \rangle$. That is to say, $\partial \tilde{t}_f / \partial \langle J_S \rangle|_{\langle J_G \rangle, \langle J_L \rangle}$ is large for larger $\langle J_G \rangle$ and for smaller $\langle J_L \rangle$.

4.4 Gas phase volumetric fractions in a slug unit

Since small bubbles were rarely observed in the liquid film, we can assume that the volumetric fraction of large bubble is nearly equal to the gas phase volumetric fraction in the large bubble part. Hence, the volumetric fraction of large bubble in the large bubble part was evaluated using the measured film thickness. This volumetric fraction $\langle\langle \alpha_G \rangle\rangle_b$ is the volume averaged volumetric fraction in the large bubble part, and is obtained by using the following equation for each large bubble:

$$\langle\langle \alpha_G \rangle\rangle_b = \frac{1}{Z_2 - Z_1} \int_{Z_1}^{Z_2} \{1 - t_f(z)/(D/2)\}^2 dz \qquad (2)$$

where $t_f(z)$ denotes the liquid film thickness at a location z. Z_1 and Z_2 are the locations of large bubble tail and nose, respectively. Gas volumetric fraction in the liquid slug and wake part, $\widetilde{\langle\langle \alpha_G \rangle\rangle}_{ls,w}$, is derived from the volume balance in slug units :

$$\widetilde{\langle\langle \alpha_G \rangle\rangle}_{ls,w} = \frac{\langle \alpha_G \rangle (\tilde{L}_b + \tilde{L}_{ls} + \tilde{L}_w) - \widetilde{\langle\langle \alpha_G \rangle\rangle}_b \tilde{L}_b}{\tilde{L}_{ls} + \tilde{L}_w}, \qquad (3)$$

$\widetilde{\langle\langle \alpha_G \rangle\rangle}_b$ and $\widetilde{\langle\langle \alpha_G \rangle\rangle}_{ls,w}$ obtained for 200 large bubbles are shown in **Fig.8(d)** as well as $\langle \alpha_G \rangle$. $\widetilde{\langle\langle \alpha_G \rangle\rangle}_b$ ranges from 0.5 to 0.7, whereas $\widetilde{\langle\langle \alpha_G \rangle\rangle}_{ls,w}$ from 0.15 to 0.3. The range of $\langle \alpha_G \rangle$ is between them. For gas-liquid two phase flow, both $\widetilde{\langle\langle \alpha_G \rangle\rangle}_b$ and $\widetilde{\langle\langle \alpha_G \rangle\rangle}_{ls,w}$ increase with $\langle J_G \rangle$ under constant $\langle J_L \rangle$. $\widetilde{\langle\langle \alpha_G \rangle\rangle}_b$ decreases, and $\widetilde{\langle\langle \alpha_G \rangle\rangle}_{ls,w}$ increases with increasing $\langle J_L \rangle$ under constant $\langle J_G \rangle$. When $\langle J_S \rangle$ is increased under constant $\langle J_G \rangle$ and $\langle J_L \rangle$, $\widetilde{\langle\langle \alpha_G \rangle\rangle}_b$ decreases and $\widetilde{\langle\langle \alpha_G \rangle\rangle}_{ls,w}$ increases. When solid phase is increased, large bubbles become thin, and amount of small bubbles increase in the liquid slug and wake part. These tendencies were also confirmed by the VTR observation. Their decreasing and increasing features again agree with the case of $\tilde{V}_b$. That is, when $\langle J_S \rangle$ is increased, $\widetilde{\langle\langle \alpha_G \rangle\rangle}_b$ decreases and $\widetilde{\langle\langle \alpha_G \rangle\rangle}_{ls,w}$ increases more remarkably when $\langle J_G \rangle$ is large or $\langle J_L \rangle$ is small.

The ratio of the volume of gas phase included in the liquid slug and wake part to the whole gas volume in a slug unit, $\tilde{\varepsilon}_{G,ls,w}$, is shown in **Fig.8(e)**. $\tilde{\varepsilon}_{G,ls,w}$ was given by

$$\tilde{\varepsilon}_{G,ls,w} = \frac{\widetilde{\langle\langle \alpha_G \rangle\rangle}_{ls,w} (\tilde{L}_{ls} + \tilde{L}_w)}{\langle \alpha_G \rangle (\tilde{L}_b + \tilde{L}_{ls} + \tilde{L}_w)} \qquad (4)$$

$\tilde{\varepsilon}_{G,ls,w}$ is larger than $\widetilde{\langle\langle \alpha_G \rangle\rangle}_{ls,w}$. This is because the total length of the liquid slug and wake part is much longer than that of large bubble. When $\langle J_S \rangle$ is large, $\tilde{\varepsilon}_{G,ls,w}$ is sometimes greater than 0.5. This means that more than half of the gas phase is included in the liquid slug and the wake part. $\tilde{\varepsilon}_{G,ls,w}$ for gas-liquid two phase flow increases with $\langle J_L \rangle$, and decreases with increasing $\langle J_G \rangle$. Similar to $\widetilde{\langle\langle \alpha_G \rangle\rangle}_{ls,w}$, $\tilde{\varepsilon}_{G,ls,w}$ increases by adding the solid phase. The characteristics of the increasing rate of $\tilde{\varepsilon}_{G,ls,w}$ with respect to $\langle J_S \rangle$ is not clearly affected by volumetric fluxes of the gas and liquid phases.

4.5 Slug period

The slug period, T, was obtained by $(\tilde{L}_b + \tilde{L}_{ls} + \tilde{L}_w)/\tilde{V}_b$. Thus, it represents an averaged time interval of slug unit. For gas-liquid two phase flow, it decreases with increasing $\langle J_L \rangle$, and slightly increases with increasing $\langle J_G \rangle$ as shown in **Fig.8(f)**. It decreases with increasing $\langle J_S \rangle$. Their decreasing rates are again larger when $\langle J_G \rangle$ is large or $\langle J_L \rangle$ is small.

4.6 Effect of slug characteristics on gas phase velocity

The effect of slug characteristic variables on $\bar{V}_G$ (in other words, $\langle \alpha_G \rangle$) will be discussed below. The increment of $\langle J_S \rangle$ results in the increment of the solid volumetric fraction in the liquid-solid mixture defined by $\langle \alpha_S \rangle^* = \langle \alpha_S \rangle / (1 - \langle \alpha_G \rangle)$, which also induces the increment of $\tilde{t}_f$, $\widetilde{\langle\langle \alpha_G \rangle\rangle}_{ls,w}$, $\tilde{\varepsilon}_{G,ls,w}$ and $\tilde{V}_b$, and the decrement of $\widetilde{\langle\langle \alpha_G \rangle\rangle}_b$. Their increment and decrement cause the following two effects which are contrary to each other.

(E1) The increment of $\tilde{V}_b$ contributes the increment of $\bar{V}_G$.

(E2) The increment of $\widetilde{\varepsilon_{G,ls,w}}$ means the increment of volume of gas phase in small bubbles whose rising velocity is smaller than that of a large bubble. Hence, it contributes the decrement of $\overline{V_G}$.

Let us discuss in what flow conditions these two effects become dominant. When volumetric flow fraction of the gas phase, β_G ($=<J_G>/<J_T>$), is large, $<\alpha_G>$ is large. In this case, the value of k defined by $1/(1-<\alpha_G>)$ is also large. Since $<\alpha_S>^*=k<\alpha_S>$, $\partial<\alpha_S>^*/\partial<J_S>|_{<J_G>,<J_L>}$ is approximately equal to k times $\partial<\alpha_S>/\partial<J_S>|_{<J_G>,<J_L>}$. On the other hand, $\partial<\alpha_S>/\partial<J_S>|_{<J_G>,<J_L>}$ is almost constant if $<J_T>$ is kept constant as shown in **Fig.5** and is irrelevant to β_G. Hence, $\partial<\alpha_S>^*/\partial<J_S>|_{<J_G>,<J_L>}$ is large when β_G is large. Namely, $<\alpha_S>^*$ increases steeply with increasing $<J_S>$ when β_G is large. As mentioned above, the steep increment of $<\alpha_S>^*$ leads to the steep increment of $\widetilde{V_b}$. Although $\widetilde{\varepsilon_{G,ls,w}}$ increases at the same time, its increasing rate is not very large, and the value of $\widetilde{\varepsilon_{G,ls,w}}$ is kept small. This is because $\widetilde{L_b}/(\widetilde{L_b}+\widetilde{L_{ls}}+\widetilde{L_w})$ is large, and $(\widetilde{L_{ls}}+\widetilde{L_w})/(\widetilde{L_b}+\widetilde{L_{ls}}+\widetilde{L_w})$ is small. So that when β_G is large, the effect of the decrement of $\overline{V_G}$ due to the increment of $\widetilde{\varepsilon_{G,ls,w}}$ is trivial. Consequently, when β_G is large, the effect (E1) is more prominent than (E2), which causes the steep increment of $\overline{V_G}$. On the contrary, when β_G is small, (E1) becomes less effective while (E2) more effective. Therefore, $\overline{V_G}$ does not increase steeply with $<J_S>$. The above discussion can explain not only the effects of $<J_S>$ on $\overline{V_G}$ mentioned in 3.4.3 but on $<\alpha_G>$ mentioned in 3.3.3, since $\overline{V_G}$ is related to $<\alpha_G>$ by Eq.(1).

4.7 Phase and velocity distributions of solid phase

The axial distribution and local velocities of solid particles in slug units are presented here. The video images were processed for the flow condition shown in **Fig.9**. In this condition, it is relatively easy to observe solid particle positions.

Volume averaged solid volumetric fraction in large bubble part $\langle\langle\alpha_S\rangle\rangle_b$, in wake part $\langle\langle\alpha_S\rangle\rangle_w$ and in liquid slug part $\langle\langle\alpha_S\rangle\rangle_{ls}$ are given in **Fig.9** for 15 sampled slug units. For most slug units, $\langle\langle\alpha_S\rangle\rangle_b$ is the smallest, and smaller than $<\alpha_S>$. This is because more than half volume of large bubble part is occupied by the gas phase in which solid phase does not exist. In most slug units, $\langle\langle\alpha_S\rangle\rangle_{ls}$ is the largest among them.

In **Fig.10**, the ratios of the volume of the solid phase included in each part to the whole solid volume in a slug unit, $\varepsilon_{S,b}$, $\varepsilon_{S,w}$ and $\varepsilon_{S,ls}$ are shown for the same 15 sampled slug units. The $\varepsilon_{S,w}$ becomes the smallest as their length is much smaller than the others. In this flow condition, about sixty percents of solid phase is included in the liquid slug part although each slug unit takes considerably different $\varepsilon_{S,ls}$.

Solid velocities in large bubble part and in liquid slug part are shown in **Fig.11** for consecutive five slug units; the slug units from 1 to 5 shown in **Figs.9** and **10**. We could not measure solid velocity in the wake part in this flow condition because of the difficulties in identifying each particle in the wake part. At the noses of large bubble part, solid velocities are about 1m/s. They decelerate rapidly in the z direction, and at some locations they become negative. At the bottoms of large bubbles, the velocities are from -1 to -0.5m/s. Around wake parts, solid particles accelerate steeply. At the noses of liquid slugs, solid particle velocities become the largest in each slug unit although they are smaller than large bubble rising velocity. In the liquid slug parts, they also decelerate in the z direction. The deceleration is, however, much smaller than in large bubble part.

The averaged values of solid velocities in each part in each slug unit are shown by dotted lines. They are around zero in large bubble part, and about 0.8m/s in the liquid slug part. The averaged solid phase velocity, $\overline{V_S}$ was 0.548m/s in this flow condition. From these results, it is recognized that solid particles rise at larger velocity than their averaged velocity in liquid slugs, whereas they almost stop rising or fall down in large bubble parts.

A feature of $\overline{V_S}$ stated above, namely $\partial\overline{V_S}/\partial<J_L>|_{<J_G>,<J_S>}$ is larger than $\partial\overline{V_S}/\partial<J_G>|_{<J_L>,<J_S>}$ especially when $<J_L>$ is small, can be explained using above discussion. Since solid phase velocity is very small in large bubble part, $\overline{V_S}$ will decrease with increasing $\widetilde{L_b}$. As shown above, $\widetilde{L_b}$ increases with $<J_G>$, and decreases with increasing $<J_L>$. Therefore, the increasing rate of $\overline{V_S}$ when the gas phase is increased becomes smaller than that when liquid phase is increased.

We could measure the solid velocities in the wake part in another flow condition shown in **Fig.12**. In this flow condition, large bubble length was so short that solid falling velocity in the liquid film was not very large even at the bottom. Thus we could identify particles in the wake part. In **Fig.12(a)**, local solid particle velocities are plotted in the same manner as **Fig.11**. The plotted

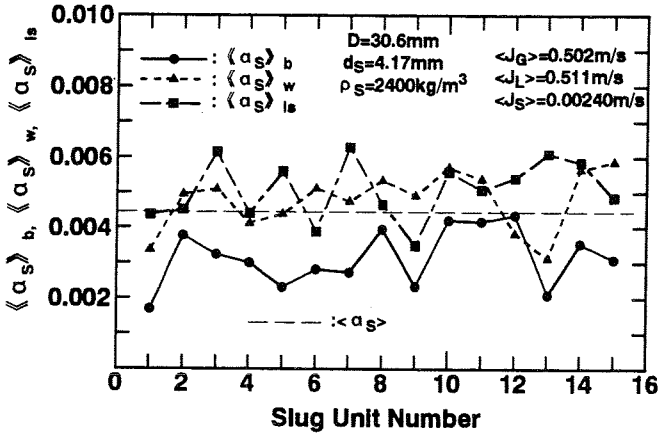

Fig.9 Volumetric fraction of solid phase in each part

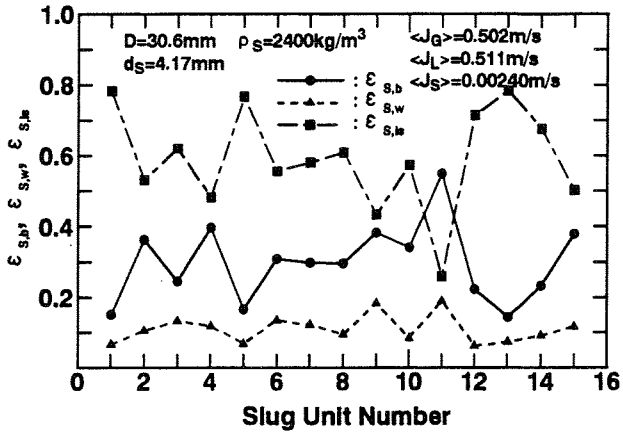

Fig.10 Ratio of solid volume in each part to solid volume in a slug unit

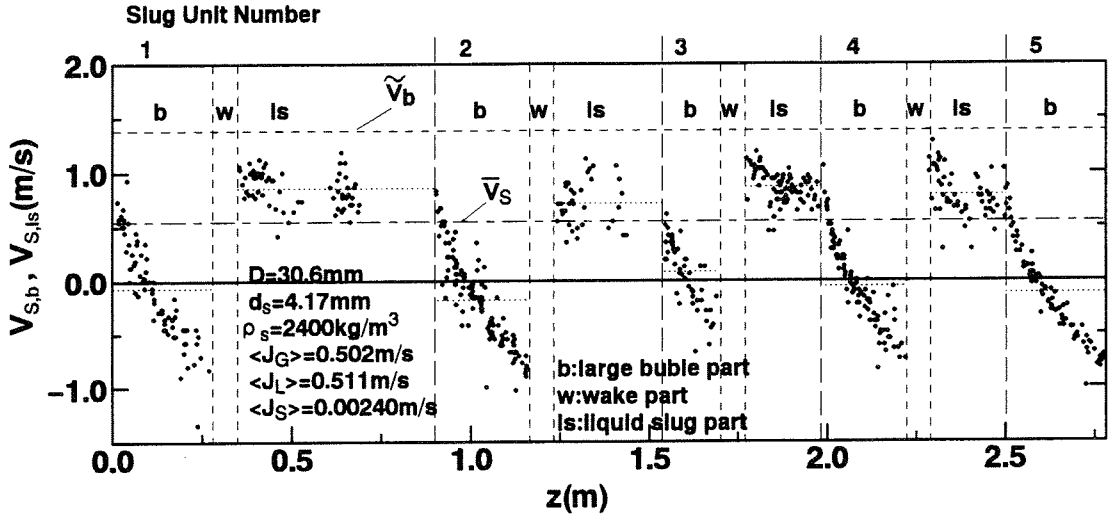

Fig.11 Solid particle velocity in each part

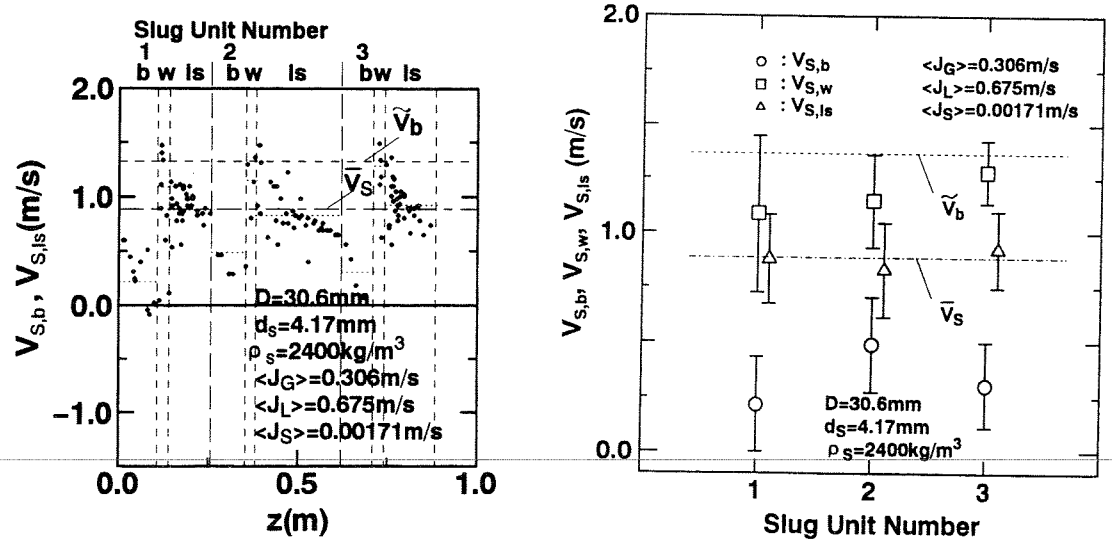

(a) (b)

Fig.12 Comparison of solid particle velocities in each part

data in **Fig.12(b)** are their averaged velocity. The standard deviations are also shown. It is recognized that solid velocity in the wake part is larger than that in the liquid slug part. This is explained by the fact that the solid particles near the pipe axis in the wake part move with nearly the same velocity of large bubble, although velocity of particles near the wall is small.

5. CONCLUSION

The macroscopic characteristics of gas-liquid-solid three phase slug flow were systematically measured using vertical round pipes. We related the volumetric fractions and phase velocities to the total volumetric flux in order to clarify their characteristics organically. Their increasing or decreasing rates for the volumetric flux of each phase under constant volumetric fluxes of the other phases were discussed.

The slug characteristics variables, namely local velocities and phase distributions of each phase, rising velocities and lengths of large bubbles, lengths of wake and liquid slug parts were also measured, and their features were discussed. Some characteristics of the volumetric fractions and averaged phase velocities were explained by making use of the measured slug characteristics.

ACKNOWLEDGEMENT

We wish to acknowledge the financial support by the Technical Research Center of the Kansai Electric Power Co., Inc., and also to express our thanks to Messrs. K. Sahara, T. Saibe, K. Hashimoto and N. Matsumoto for their assistance in experiments.

NOMENCLATURE

- D : Pipe diameter (mm)
- d_S : Particle diameter (mm)
- J : Volumetric flux ($m^3/m^2s=m/s$)
- L : Length (m)
- T : Slug period (sec)
- t_f : Film thickness (mm)
- V : Velocity (m/s)
- z : Downward distance from large bubble nose
- α : Volumetric fraction
- β : Volumetric flow fraction
- ε : Ratio of volume included in a part to the volume included in a whole slug unit
- ρ : Density (kg/m^3)

Subscripts

- b : Large bubble part, large bubble
- G : Gas phase
- L : Liquid phase
- ls : Liquid slug part
- S : Solid phase
- w : Wake part

Others

- $< >$: Area averaging operator
- $\langle\!\langle \rangle\!\rangle$: Volume averaging operator
- $\bar{}$: Phase averaged value
- $\sim$: Ensemble averaged value

REFERENCES

[1] A. Serizawa, et al., "A Dream-Intelligent Multiphase Fluid with Active Functions and Built-in Sensors", in: Proc. 4th Japan-US Seminar on Two-Phase Flow Dynamics, July 5-11, 1992, Berkeley, USA.

[2] M. Weber and Y. Dedegil, "Transport of Solids according to Air-Lift Principle", in: Proc. 4th. Int. Conf. Hydrau. Transp. Solids, Alberta, Canada, pp.H1-1-23, May 1976.

[3] M.Toda, et al., "Transports of Solids by Gas-Liquid Upward Flow in Vertical Pipes", in: Trans. Chem. Eng., 8(4), pp.380-386, 1982.

[4] M. Sadatomi, et al., "Hydraulic Lifting of Coarse Particles in Vertical Pipes (2nd Report, Gas-Liquid-Solid Three Phase Flow)", in: Jpn. J. Multiphase Flow, 4(2), pp.125-140, 1990.

[5] T. Sakaguchi, et al., "Estimation of Volumetric Fractions of Each Phase in Gas-Liquid-Solid Three-Phase Slug Flow in Vertical Pipe", in: Dynamics of Two-Phase Flows, O.C. Jones and I. Michiyoshi Eds., CRC Press, Boca Raton, USA, pp.61-85, 1992.

[6] T. Sakaguchi, et al., "Pressure Drop in Gas-Liquid-Solid Three-Phase Slug Flow in Vertical Pipe", in: Experimental Thermal and Fluid Science, Vol.7-1, pp.49-60, 1993.

[7] N. Zuber and J.A. Findlay, "Average Volumetric Concentration in Two-Phase Flow Systems", in: Trans. ASME, J. Heat Transf., 87(4), pp.453-468, 1965.

[8] ASME, "Measurement Uncertainty", in: ASME Performance Test Codes, ANSI/ASME PTC 19.1-1985, translated by JSME, 1987.

FLOW BEHAVIOR AND MASS TRANSFER IN THREE PHASE FLUIDIZED BUBBLE COLUMNS

Dipl.-Ing. K. Sommer and Prof. Dr.-Ing. M. Bohnet

Technical University of Braunschweig
Institute of Chemical Engineering
Langer Kamp 7
38106 Braunschweig, Germany

ABSTRACT

The most commonly used models for describing bubble columns are the dispersion models. Here, the residence time distribution of one phase is expressed by the dispersion coefficient, which takes values between zero (plug flow model) and infinity (complete stirred reactor). There are only few publications about these coefficients in three phase fluidized bubble columns. In this paper gas hold-up, local solid volume fraction, dispersion coefficients of gas, liquid and solid phases and mass transfer are investigated in a water, air, PMMA or Ca-alginate particle bubble column of 0.142 m diameter at superficial velocities of the gas phase between 0.007 and 0.074 m/s, superficial liquid - velocities between 0 and 0.03 m/s in countercurrent and cocurrent operation mode and solid concentration between 0 and 20 %vol. Gas phase dispersion is measured by the so called frequency curve method, liquid dispersion is determined by measuring steady state concentration distribution of a pH-tracer and the solid dispersion by optical measurement of particle distribution. The mass transfer coefficient between gas and liquid phase is determined by using the sulfite method.

1. INTRODUCTION

Bubble columns are widely used in biotechnology industry particularly for aerobe processes. As the simplest layout bubble columns could be considered as a cylindrical vertical tube. At the bottom a gas phase is dispersed by using a gas sparger and moves in form of bubbles relative to the continuous liquid phase. The liquid nutrient medium flows through the apparatus in co- or countercurrent operation mode. At the top of the column is a zone for the separation of gas and liquid (slurry) phase.

If biomass or intracellular materials are not representing the process products, microorganisms are used as biocatalytic agents remaining in the reactor volume. To discouple the residence time of biomass and substrate microorganisms are immobilized on fluidized carrier particles. The immobilisation allows a simple hold back of the biomass. Therefore, high concentration of catalytic agents and an increase of metabolism products particularly in continuous operation mode can be observed [1]. Applying carrier particles it is also possible to work under unsterilized conditions by increasing the flow rate of the liquid phase to high values. Here the maximal specific growth rate of other cells is lower than the reciprocal residence time of the liquid phase and microorganisms not being immobilized would be washed out. A further advantage of the immobilisation is the lower shear stress which could lead to lower production rates. But especially high concentration of biomass increases the dynamic viscosity of the liquid medium [2].

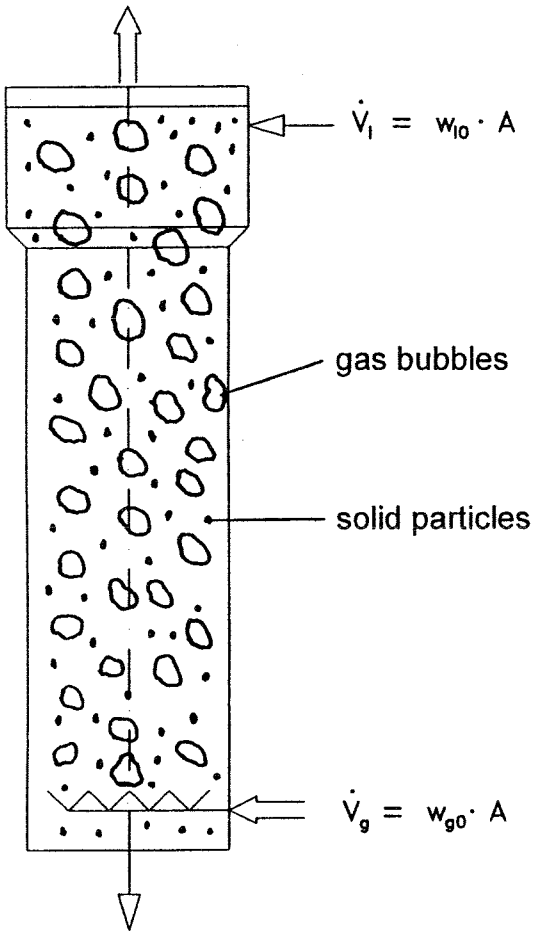

Fig. 1: **Schematic design of bubble columns**

	air, 1 bar	tap water	substratum solution	calcium alginate beads	polymethylmetacrylat beads
T [K]	293	293	293		
ϱ [kg/m³]	1.18	998.3	1007.2	1030	1148
η [10^{-6} kg/(ms)]	17.98	1002.7	1038	-	-
σ to air [N/m]	-	0.072	0.046	-	-
$D_{O_2,l}$ [10^{-9} m²/s]	-	2.63[1]	2.148[1]	-	-
$c^*_{O_2,l}$ [10^{-6} kg/m³]	-	8.5	8.5	-	-
d_{P50} [10^{-3} m]	-	-	-	540	351
w_s [10^{-3} m/s]	-	-	-	3.49	1.00

Table I: **Properties of the test system**

[1] [10]

A technical advantage especially for bioreactors is the absence of moving parts inside the reactor volume. Although the layout of bubble columns is very simple, the design of such apparatus is difficult. No general model has been developed until now that allows a reliable reactor design. The reason for the absence of such a model is the complexity of momentum and mass transfer. Particularly in large reactors dead zones and backmixing can occur.

The aim of this paper is to investigate the influence of the mean solid volume fraction in three-phase fluidized bubble columns on gas and solid hold-ups, dispersion coefficients of the three phases and mass transfer between gas and liquid phase at different superficial velocities of the gas and the liquid phase.

The three-phase system consists of the gas phase (air), the liquid phase (water or substratum solution) and solid phase (calcium alginate or PMMA[2] beads). The properties of the phases are listed in Table I.

2. EXPERIMENTAL SET-UP

The central part of the experimental set-up shown in Fig. 2 is a reactor (a) with a reaction volume of 0.038 m³ (inner diameter 0.142 m) and a hole plate (24 holes, each 1 mm in diameter) as gas sparger (b), the phase separation zone (c) and with pressure taps along the reactor height for measuring axial local gas hold-up profiles. In the centre of the bottom is a liquid in- or outlet (n) with a sieve basket to hold back the solid particles. The piping (k) and the pump (h) allow co- or countercurrent operation mode. The liquid flow rate is measured by using magnetic-inductive flowmeters (i), the flowrate of the gas phase is determined by rotameters (e). To keep the level of the slurry phase nearly constant an expansion tank (m) with a cross area of eight times as large as the reactor has been installed. The slurry surface has a level of 1.748 m.

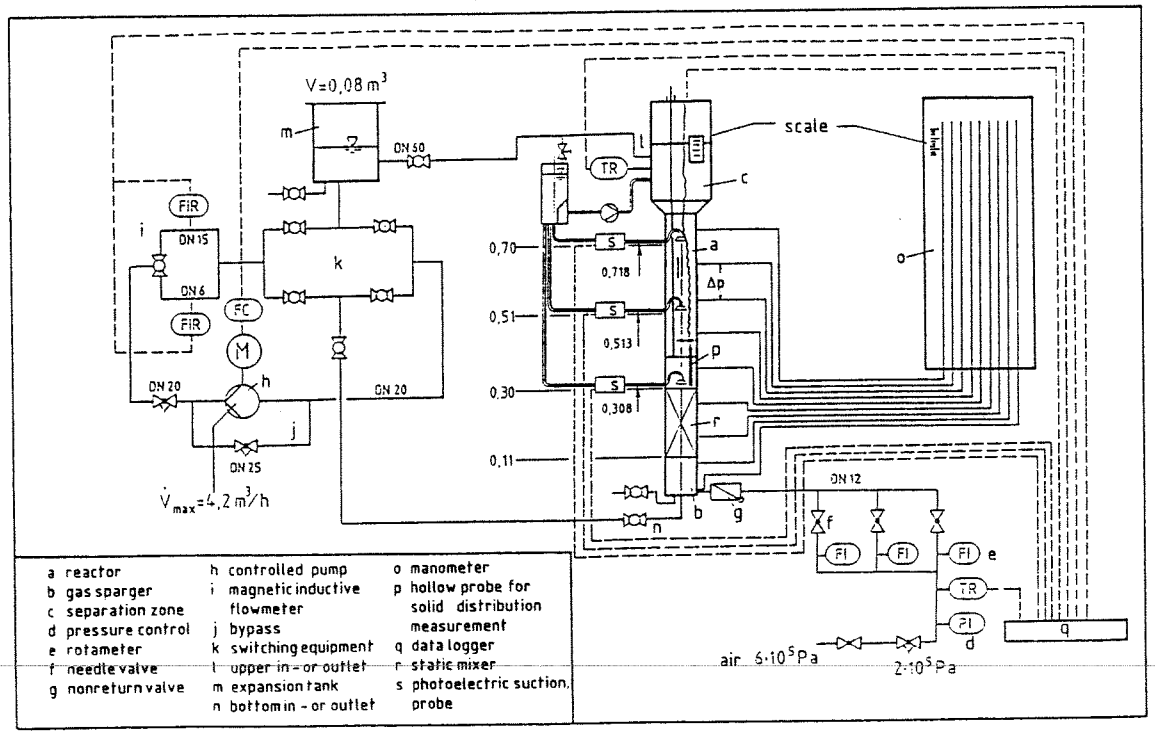

Fig. 2: Experimental set-up

[2]Polymethylmetacrylate

Mean bubble diameters (Sauter-diameter) are measured in three cross sections by photoelectric suction probes [11]. Axial dispersion coefficients of the liquid phase is determined by measuring the axial steady state axial profile of a pH-tracer. Gas phase dispersion is measured by the frequency curve method [12]. An insoluble gas component (methane) is added to the inlet gas flow in form of a sine-shaped signal. The decreasing amplitude along the reactor height is a quantity for the dispersion coefficient of the gas phase. Volumetric oxygen transfer coefficient between gas and liquid phase is determined by measuring axial profile of dissolved oxygen in the nutrient solution and decreasing oxygen volume concentration in the gas phase along the reactor height [13].

3. MASS TRANSFER MODEL

The metabolism of the microorganisms requires mass transfer of substrates and cosubstrates to the immobilized cells. Often the substrate represents the carbon source, e. g. glycerol or glucose, and oxygen is used as cosubstrate. Fig. 3 shows the concentration curve of substrate and oxygen versus the transport line. The mass transport of the oxygen component consists of several parts [14]:

- Transport from the bubble centre through the inner boundary layer between gas and liquid phase by diffusion,
- transport through the interfacial area,
- transport of the dissolved gas component through the outward boundary layer by diffusion,
- transport of the liquid phase to the particles (biocatalytic agents) by convection and dispersion,
- transport through the boundary layer of particles by diffusion
- and absorption of the component by the microorganisms and biochemical reaction.

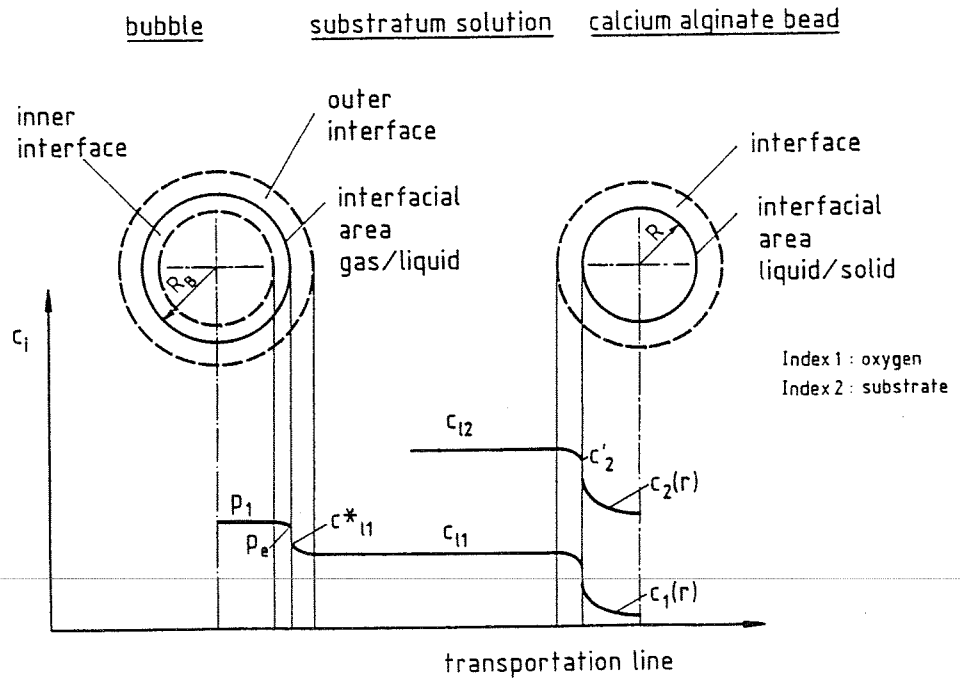

Fig. 3: Concentration curve of substrate and cosubstrate vs. the transportion line

Mathematical models for three phase bubble columns have to be generated by the aid of conservation laws. An unsteady mass balance of a differential disk-shaped reactor element shown in Fig. 4 results in the following modelling equation taking into account the axial dispersion model for the three phases:

$$\begin{aligned} d\dot{M} &= (d\dot{M}_C)_z - (d\dot{M}_C)_{z+dz} + (d\dot{M}_D)_{z+dz} - (d\dot{M}_D)_z + \\ &+ \left[(d\dot{M}_S)_z - (d\dot{M}_S)_{z+dz}\right] + d\dot{M}_{source} - d\dot{M}_{sink} \end{aligned} \tag{1}$$

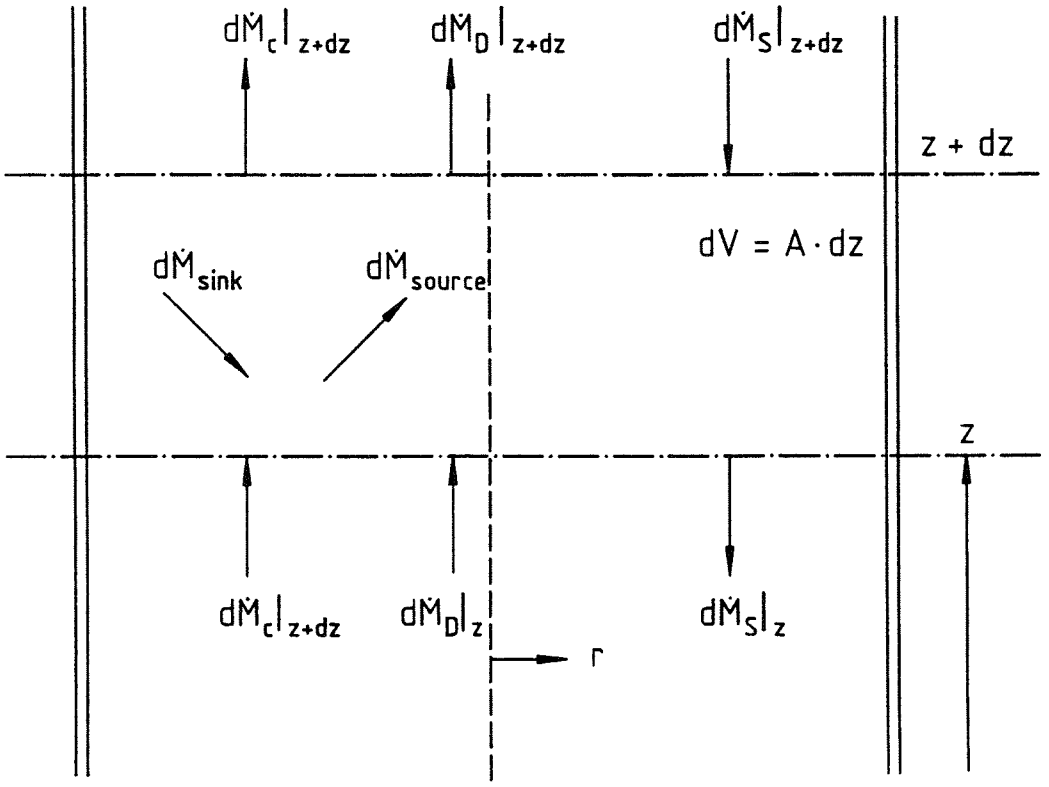

Fig. 4: Disk-shaped reactor element for mass balance

Temporal mass alterations due to the convection (index C) and dispersion (index D) of each phase, or solid sedimentation (index S) are defined by:

$$\begin{aligned} d\dot{M} &= \frac{d(\varepsilon \cdot \rho \cdot c \cdot dV)}{dt} \\ d\dot{M}_C &= \varepsilon \cdot \rho \cdot c \cdot w \cdot A \\ d\dot{M}_D &= -\varepsilon \cdot \rho \cdot E \cdot A \cdot \frac{dc}{dz} \\ d\dot{M}_S &= \varepsilon \cdot \rho \cdot c \cdot w_{SS} \cdot A \end{aligned} \tag{2}$$

with the concentration c of one phase component, the phase velocity w, the terminal settling velocity of the solid phase w_{SS}, the density ϱ of one phase, the phase dispersion coefficient E, the reactor cross area A and the differential reactor volume dV. Assuming

incompressible gas phase yields to:

$$\varepsilon \cdot \frac{dc}{dt} = -\varepsilon \cdot \frac{d}{dz}(w \cdot c) + \varepsilon \cdot \frac{d}{dz}\left(E \cdot \frac{dc}{dz}\right) + \\ + \varepsilon \cdot \frac{d}{dz}(w_{SS} \cdot c) + \\ + (k_{source} \cdot a_{source} \cdot \Delta c_{source}) - (k_{sink} \cdot a_{sink} \cdot \Delta c_{sink}) \quad (3)$$

This equation has to be established for each phase for the substratum and cosubstratum component, the biochemical products, and the component with the slowest reaction step. The difficulties in solving this system of differential equations are the lack of understanding about the fluiddynamics (phase hold-up, dispersion coefficients) and the mass transfer coefficients (volumetric mass transfer coefficient).

4. HYDRODYNAMICS

4.1 Phase Distribution

Gas hold-up Axial gas hold-up profiles are determined by measuring pressure differences between two neighbouring cross sections as shown in Fig. 5 [14].

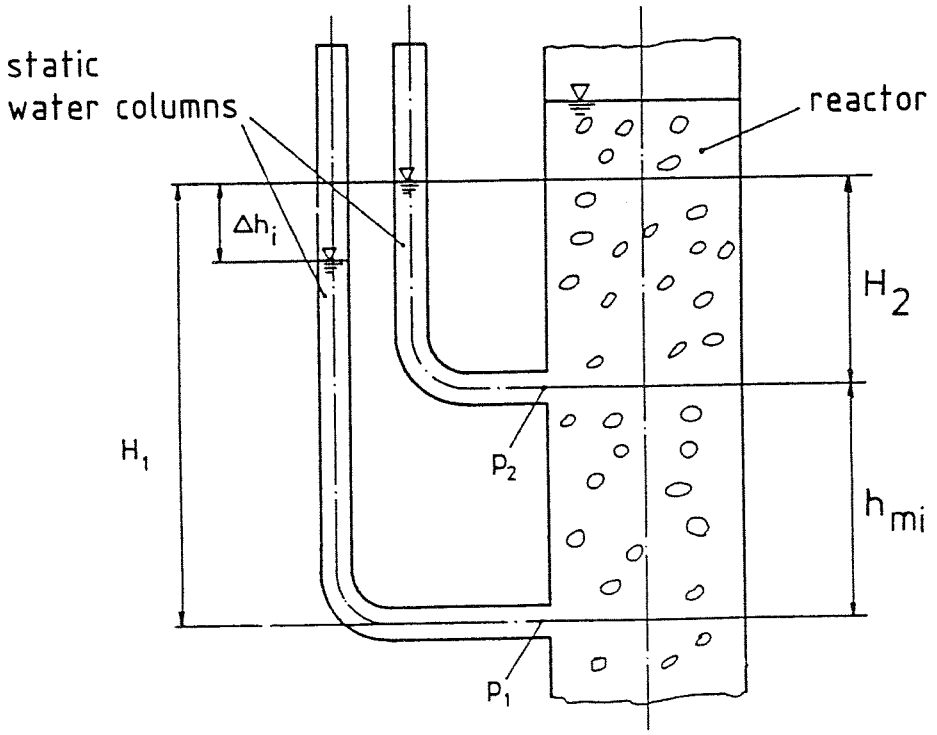

Fig. 5: Measurement of the local gas hold-up

The gas phase hold-up in a volume element i, ε_{gi} in a three phase system is given by

$$\varepsilon_{gi} = \frac{\rho_l}{\rho_g - \rho_l} \cdot \left(-\frac{\Delta h_i}{h_{mi}} + \varepsilon_{si} \cdot \left(1 - \frac{\rho_s}{\rho_l}\right)\right) \quad (4)$$

with the phase densities ϱ_g, ϱ_l and ϱ_s, the pressure difference in units of liquid heights Δh_i and the height of the reactor volume element h_{mi}. The local solid hold-up ε_{si} must be calculated by using the sedimentation/dispersion model of KATO [16].

The influence of the superficial gas velocitiy w_{g0} has been studied before by several authors [15-21]. With increasing gas velocity the gas hold-up rises as shown in Fig. 6. About the influence of solid particles on the gas hold-up the reported results differ considerably. Some authors [17-19] report a decrease of gas hold-up with increasing solid concentration. They explain this phenomenon by an increase of the suspension viscosity and an increase of bubble coalescence. But the solid they used had a much higher density than the particles used in this work.

Fig. 7 shows the axial gas hold-up profiles at different mean solid volume fractions for superficial gas velocitiy of 0.026 m/s. The gas hold-up increases only slightly with increasing solid volume fraction. The reason for this is the small effect of the low density difference between the solid and the liquid phase.

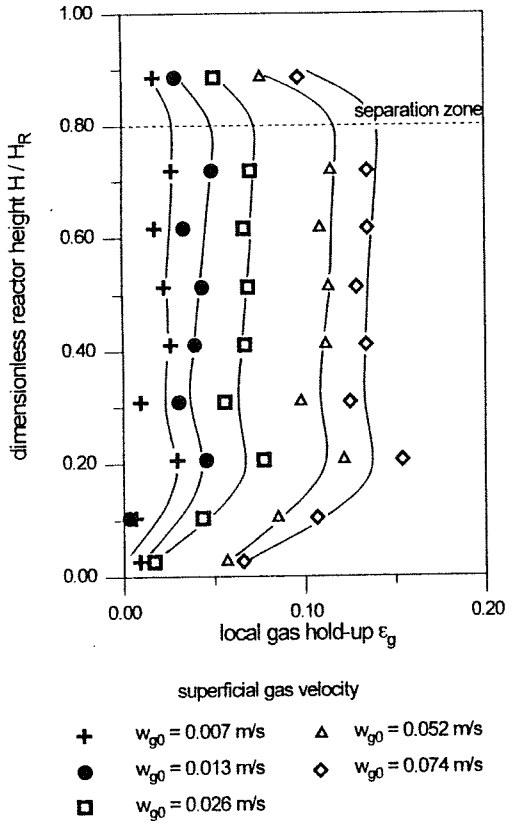

Fig. 6: Dimensionless height vs. the gas hold-up; parameter: superficial gas velocity, $\bar{\varepsilon}_s = 0$

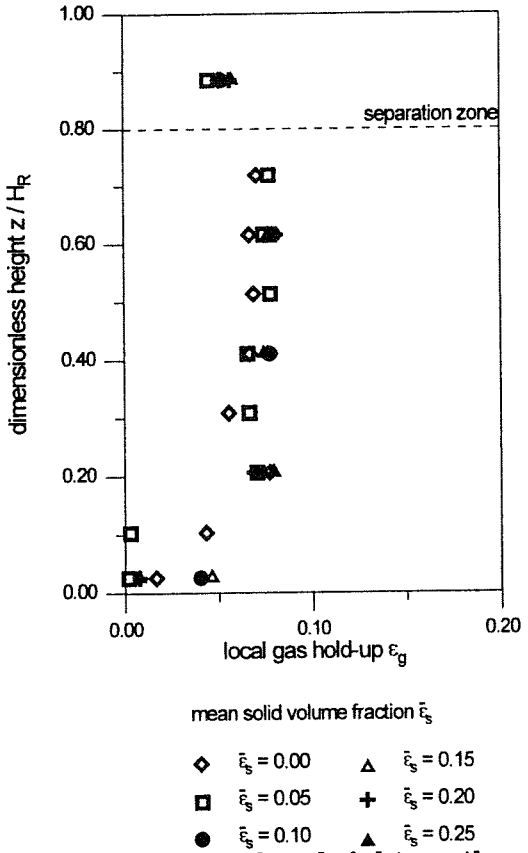

Fig. 7: Dimensionless height vs. the gas hold-up; parameter: mean solid volume fraction $w_{g0} = 0.026$ m/s

Solid volume fraction Solid phase distribution has been the topic of a few publications [22-27]. Often it is assumed that the solid dispersion is equal to the liquid dispersion. Decreasing particle size and decreasing difference between liquid and solid densities yield to steeper axial profiles of the solid volume fraction, which means better solid mixing. This is explained by a decrease in the solid settling velocity.

In this work the axial profile of the solid volume fraction is measured by an optical method [22]. To measure profiles of the local solid volume fraction 5 per cent of PMMA beads were inked by a fluorescent substance (1,1,4,4-tetraphenyle-1,3-butadiene). The set-up shown in Fig. 8 consists of a dielectric UV-mirror (3) revolved on 45 degrees,

which devides a light beam of a UV-lamp (1) into two parts. Wave lengths of about 400 nm are transmitted, smaller wave lengths are reflected through a lens into a glas fiber cable (5). The cable leads to a probe (6) inside the reactor. As the solid phase dyed with fluorescent ink flows through the probe a light beam with a wavelength of 465 nm is emitted. The fluorescent light beam passes an UV-blocking filter (7) with a range of free transmission for wave length over 420 nm. This signal is detected (8) and evaluated (10) by aid of an A/D-converter (9). The probe can be positioned at any arbitrary point inside the reactor.

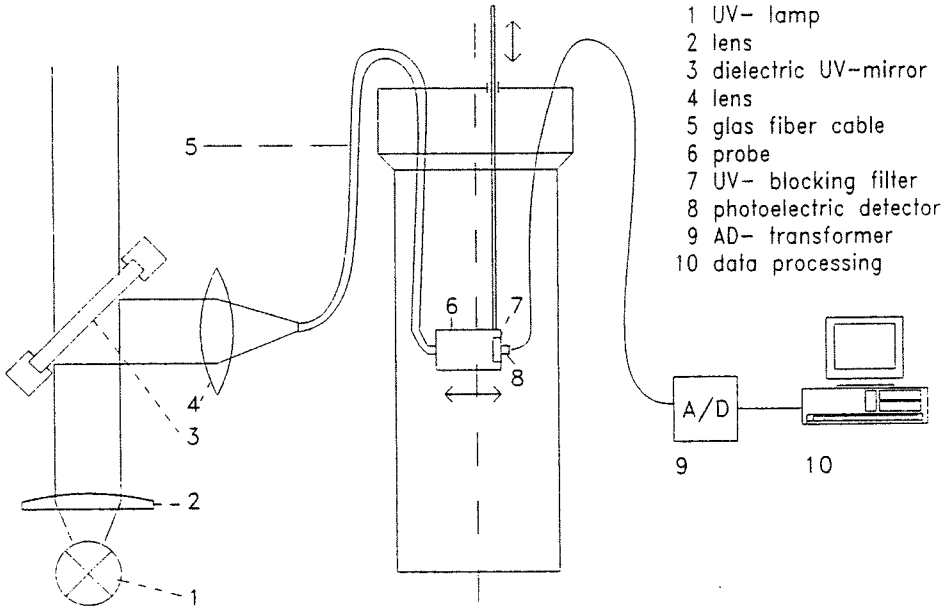

Fig. 8: Experimental set-up for measuring axial solid concentration

Fig. 9 shows the radial profiles of the solid volume fraction at different heights. It is obvious that there is no radial profile. This is explained by the high turbulent mixing of the liquid phase.

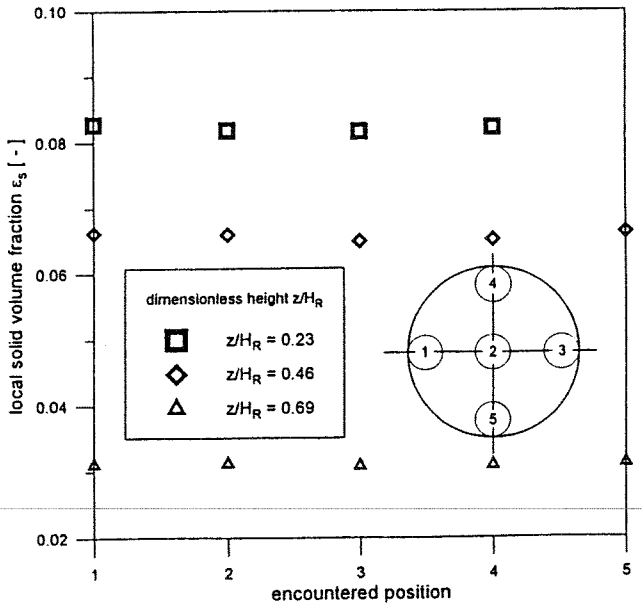

Fig. 9: Radiale profiles of the solid volume fraction at different heights, $\bar{\varepsilon}_s = 0.05$

Fig. 10 shows the axial solid profiles at different superficial liquid velocities in countercurrent operation mode. The influence of the liquid velocity is nearly neglectable. This is due to the much higher circulation velocity of the liquid phase, so that the superficial velocity of the liquid phase has only a small influence. The influence of the superficial gas velocity on particle distribution is shown in Fig. 11. With increasing gas velocity the axial profile of solid volume fraction becomes steeper, because of the increase of energy input. But due to the small difference between the densities of liquid and solid phase it is only a small influence for the system used here.

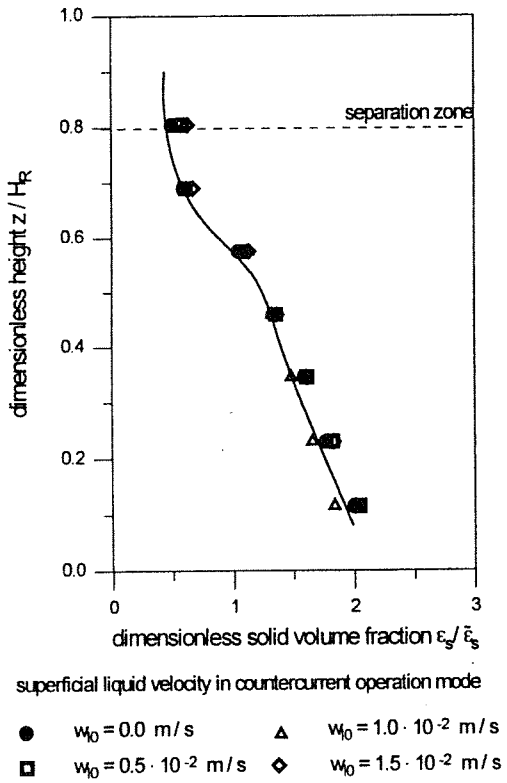

Fig. 10: **Axial solid distribution, parameter: superficial liquid velocity, $\bar{\varepsilon}_s = 0.1$**

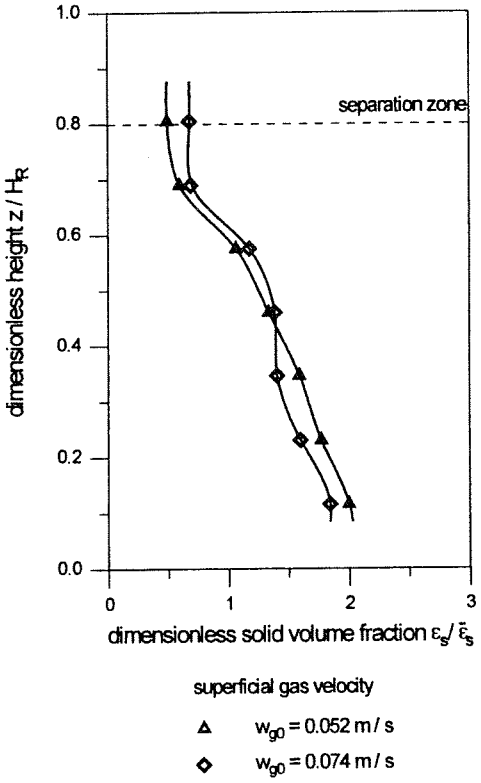

Fig. 11: **Axial solid distribution, parameter: superficial gas velocity, $\bar{\varepsilon}_s = 0.1$**

4.2 Residence time behavior

Regarding their fluiddynamic behavior bubble columns do not act as a complete stirred reactor (no concentration profiles inside the reactor) and not as an ideal plug tube (maximal gradients, plug flow model). Due to the rising bubbles there is a high phase circulation inside the reactor. In small columns with diameters less than 20 cm the mixing behavior of one phase can be described by the aid of only one coefficient, the axiale phase dispersion coefficient.

Gas phase dispersion Bubble columns are often modeled by neglecting gas phase dispersion. This is only permitted for high reactors with small gas hold-ups, where the Bodenstein-numbers of the gas phase Bo_G ($Bo_G = w_G \cdot H_R / (\varepsilon_G \cdot E_G)$) reach high values ($Bo_G \geq 10$) [3]. Gas phase dispersion in bubble columns is considerable and it is generated by different bubble rising velocities, bubble circulation and coalescence or

bubble break up. All these effects are summed up into the axial dispersion coefficient of the gas phase. The influence of the superficial gas velocity and the reactor diameter has been studied by few authors [12, 28-30] before. With increasing superficial gas velocity the gas phase dispersion increases. This effect is explained as follows: In the homogeneous flow regime of the bubbles (for small gas superficial velocities) there is no significant movement of the bubbles in radial direction, and the column diameter is not significant. But at higher gas flow rates bubble clusters are formed, the flow pattern becomes heterogeneous. Large bubbles or bubble agglomerates ascend in the column core region. This causes a liquid circulation and bubbles with low terminal rising velocities are entrained in the downward moving liquid. This effect is more distinguished with increasing superficial gas velocity and rising column diameter. About the influence of solid particles no data are available in the literature.

The gas phase dispersion is determined by using the frequency curve method [12]. It is impossible to mark the dispersed bubbles with a tracer in a cross area inside the reactor. Therefore the inlet gas phase was marked with a insoluble gas tracer (methane) by a sine-shaped tracer signal. The axial dispersion coefficient of the gas phase is given by the decrease of the amplitude of the tracer sign along the reactor height as follows:

$$\frac{A(z)}{A_I} = \exp\left(- \frac{E_g \cdot \varepsilon_g^3 \cdot \omega^2 \cdot z}{w_{g0}^3} \right) \tag{5}$$

with the amplitude of the sine-shaped signal A_I at the gas inlet and A(z) at the reactor height z, and the frequency of the signal ω .

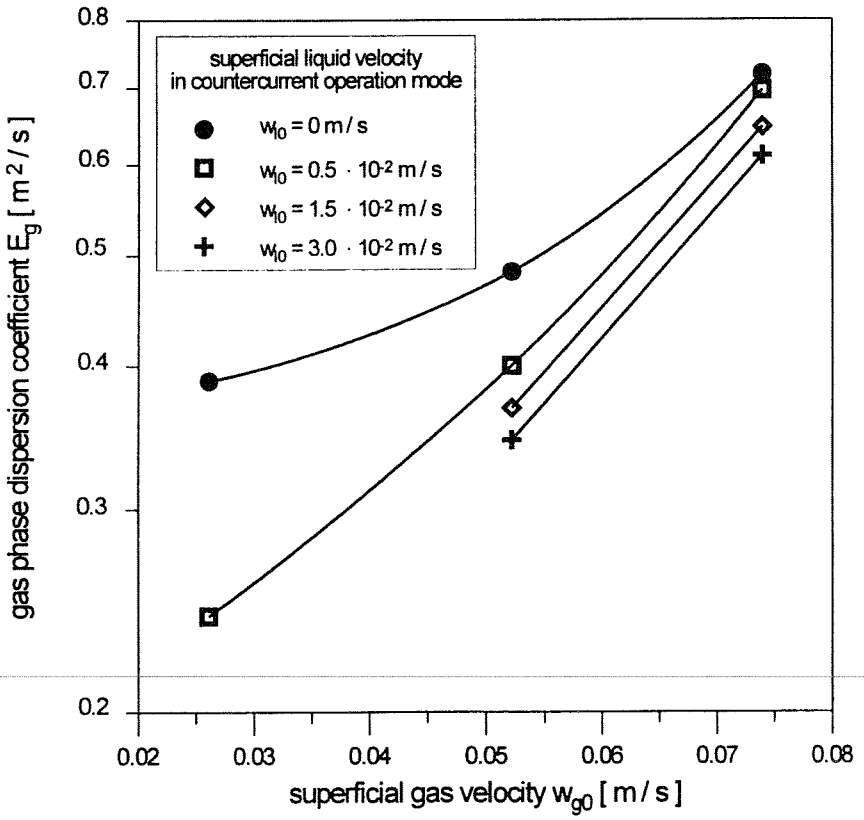

Fig. 12: **Dispersion coefficient of the gas phase, $\bar{\varepsilon}_s$ = 0**

Fig. 12 shows the dispersion coefficient of the gas phase versus the superficial gas velocity at different liquid flow rates in a semi logarithmic plot. It is obvious, that the influence of the superficial gas velocity is significant. The dispersion coefficient rises nearly to the third power of the gas flow rate. The influence of the liquid superficial velocity is only significant at low gas flow rates. This is explained as follows: At high gas flow rates the circulation velocity of the liquid is much higher than the superficial liquid velocity and therefore the liquid flow rate is neglectable. For decreasing gas flow rates the influence of the liquid superficial velocity increases.

The influence of the solid phase volume fraction on gas phase dispersion coefficient is shown in Fig. 13. With increasing solid concentration the gas phase dispersion decreases. This is due to the increasing liquid viscosity with rising solid concentration. This effect may be more significant for higher differences between the densities of the liquid and the solid phases.

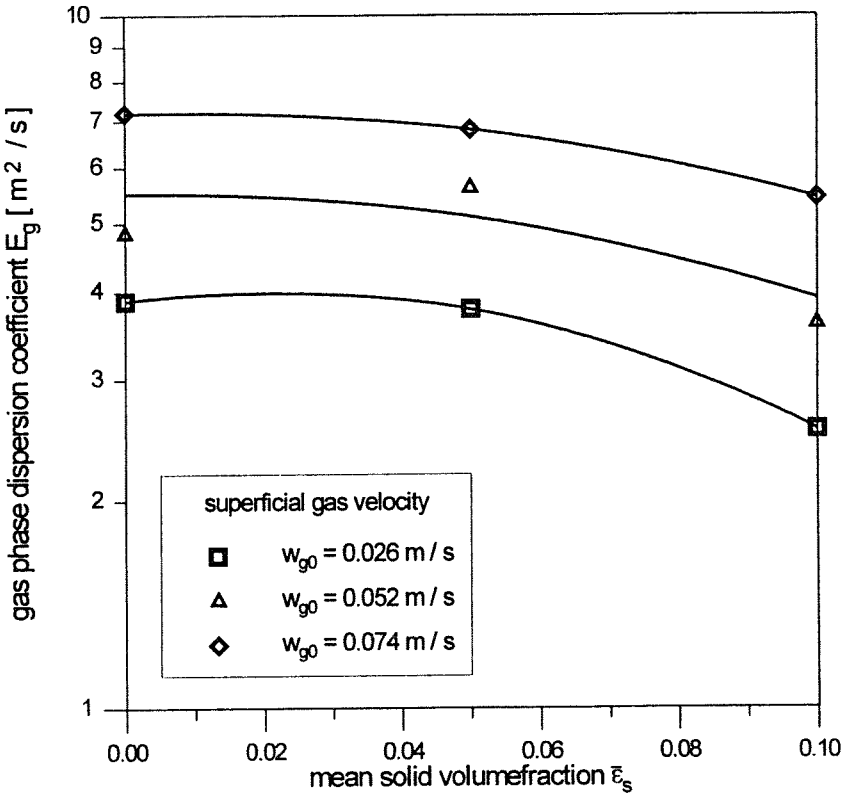

Fig. 13: Dispersion coefficient of the gas phase, $w_{l0} = 0$

Liquid dispersion The liquid dispersion has often been investigated in the last years [31-37]. One reason may be that the dispersion coefficient of the liquid phase is relativly easy to determine. Most of experimental datas for the dispersion coefficient E_l can be described by the equation derivered by Baird and Rice [32]:

$$E_L = K \cdot D_R^{4/3} \cdot (g \cdot w_{g0})^{1/3} \qquad (6)$$

with the reactor diameter D_R. This equation is based on a dimensional analysis and Kolmogoroff theory of isotropic turbulence (the specific energy dissipation per unit mass in bubble columns is defined by $\epsilon = g \cdot w_{g0}$). K is a constant and was found as 0.35 [32].

In this paper the liquid dispersion coefficient is determined by measuring the steady-state axial profile of a pH-tracer. The coefficient can be calculated using a mass balance. Fig. 14 shows the influence of the superficial liquid velocity on the liquid dispersion coefficient. Due to the large circulation velocity of the liquid phase no significant influence can be determined.

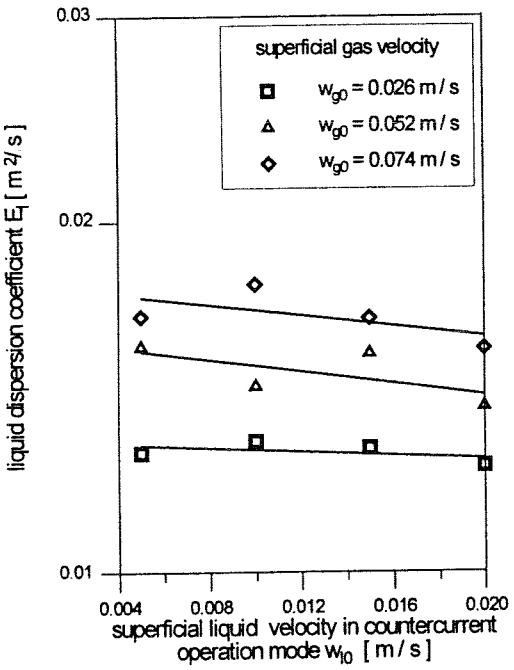

Fig. 14: **Dispersion coefficient of the liquid phase, $\bar{\varepsilon}_s = 0$**

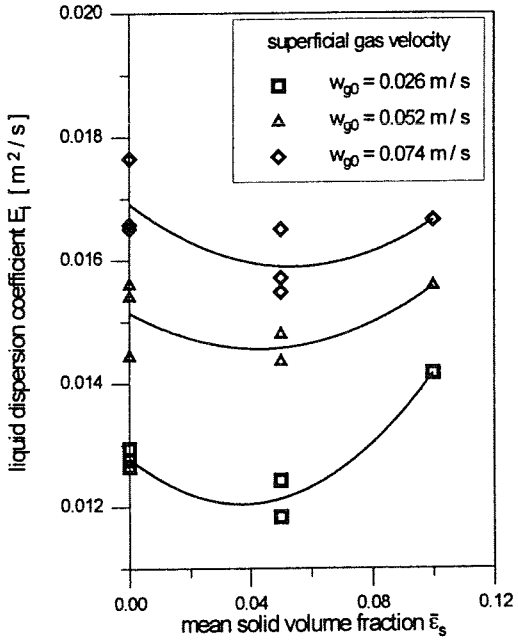

Fig. 15: **Dispersion coefficient of the liquid phase, $w_{l0} = 0$**

The influence of the solid volume fraction at different gas flow rates is shown in Fig. 15. For low solid volume fractions the dispersion coefficient decreases with rising solid concentration. This effect is caused by the increase of the liquid viscosity. With higher volume fractions of the solid phase the dispersion coefficient increases with rising solid concentration. This can be explained as follows: At higher solid volume fractions the bubble flow becomes heterogeneous, which was confirmed by visual observation. Large bubbles and bubble agglomerates rise in the core region. This effects a higher liquid circulation velocity and an increasing liquid dispersion. The influence of the solid volume fraction on the transition from homogeneous to heterogeneous bubble flow decreases with increasing gas flow rate, because the heterogeneous flow pattern is more distinguished with increasing gas flow rate.

Solid dispersion The mass balance of the solid phase in a differential disk-shaped reaktor element supplies a relation between the solid volume fraction and the dispersion coefficient of the solid phase.

$$\varepsilon_s\left(\frac{z}{H_R}\right) = \bar{\varepsilon}_s \cdot \frac{Bo_s - Bo_s^*}{1 - e^{-(Bo_s - Bo_s^*)}} \cdot e^{-(Bo_s - Bo_s^*)\cdot\frac{z}{H_R}} \qquad (7)$$

with the Bodenstein-numbers

$$Bo_s = \frac{w_{l0} \cdot H_R}{(1-\varepsilon_g) \cdot E_s}$$

$$Bo_s^* = \frac{w_{SS} \cdot H_R}{E_s} \qquad (8)$$

with the terminal settling velocity of a particle swarm w_{SS}. The dispersion coefficient of the solid phase versus the superficial gas velocity is shown in Fig. 16. With increasing superficial gas velocity the solid dispersion rises.

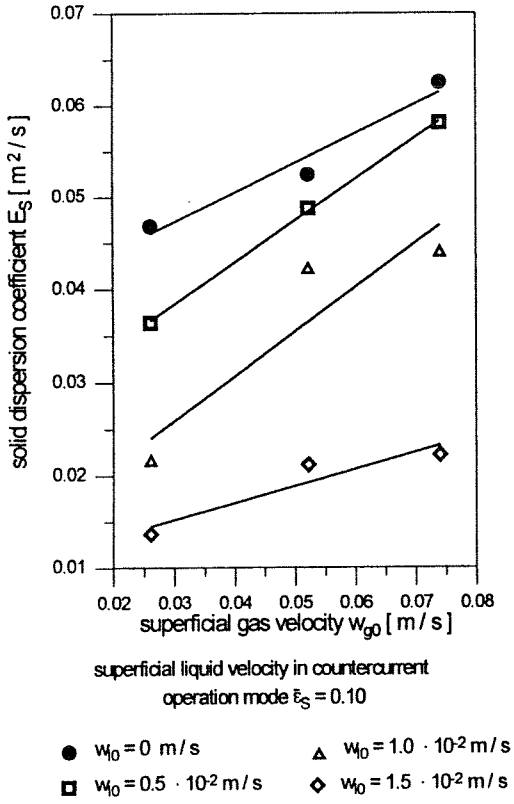

Fig. 16: Solid dispersion coefficient, $\bar{\varepsilon}_s = 0.1$

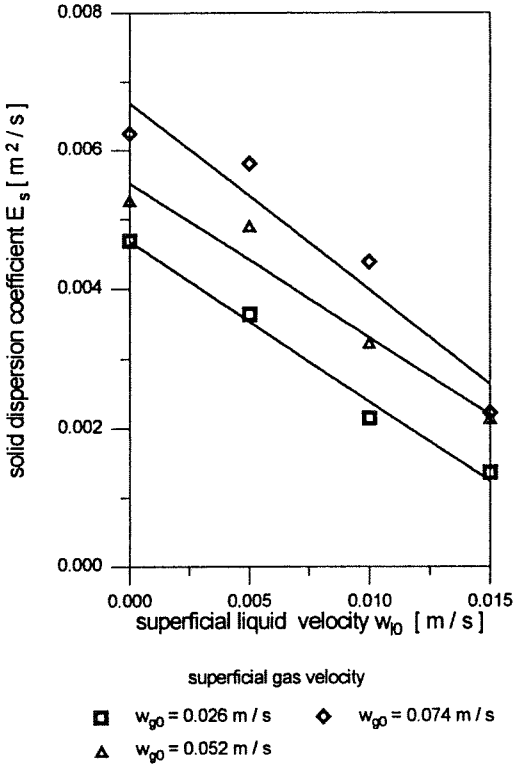

Fig. 17: Solid dispersion coefficient, $\bar{\varepsilon}_s = 0.1$

An increase of superficial liquid velocity in countercurrent operation mode yields to lower solid dispersion as shown in Fig. 17. The axial solid distribution profile becomes less steep with increasing liquid flow rate in countercurrent operation mode. The alteration in the profile of solid distribution is only small, but the dispersion coefficient was found to be insensitive against the local solid volume fraction.

5. MASS TRANSFER

5.1 Mean Bubble Diameter, Specific Interfacial Area

Mass transfer in bubble columns is influenced by the mean bubble diameter, and resulting from that the specific interfacial area a, which is defined as

$$a = \frac{6 \cdot \varepsilon_g}{d_S} \tag{9}$$

with the local gas hold-up ε_g and the Sauter-diameter d_S of the bubbles:

$$d_S = \frac{\sum_{i=1}^{n} n_i \cdot d_i^3}{\sum_{i=1}^{n} n_i \cdot d_i^2} \tag{10}$$

The Sauter-diameter was measured with a suction probe in a cross section between two pressure taps. The probe was able to determine bubble diameters in a range between 2 and 8 mm with an accuray of 5 %. Therefore large bubbles could not be measured, but the influence of large bubbles on the gas/liquid mass transfer is not significant, because the specific interfacial area of large bubbles is much smaller than for small bubbles. Secondary the residence time of larges bubble is much lower than the residence time of small bubbles, because of the higher terminal rising velocity. Radial profiles of bubble diameters in a cross section area could not be observed. The dependence on the reactor height was as expected. Bubble diameter increases with increasing height due to the decrease of hydrostatic pressure.

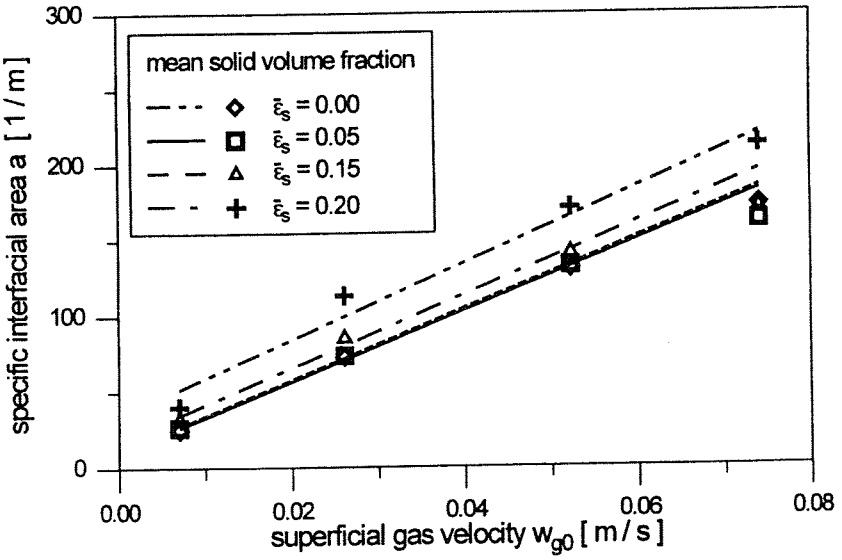

Fig. 18: Specific interfacial area, $w_{l0} = 0$

Fig. 18 shows the influence of the superficial gas velocity on the specific interfacial area at different solid volume fractions. It is obvious, that the specific interfacial area is dependent on the superficial gas velocity similar to the related process variable gas hold-up. The interfacial area increases significantly with increasing gas flow rate. But there is also an influence of the solid volume fraction on a as shown in Fig. 19. With rising solid volume fraction the interfacial area increases slightly especially at low gas flow rates. This

is explained by the slight increasing of gas hold-up with rising solid volume fraction. But it has to be mentioned that bubbles with a diameter about more than eight millimeters could not be measured, so that the coalescence of bubbles, which leads to smaller interfacial areas, has to be neglected.

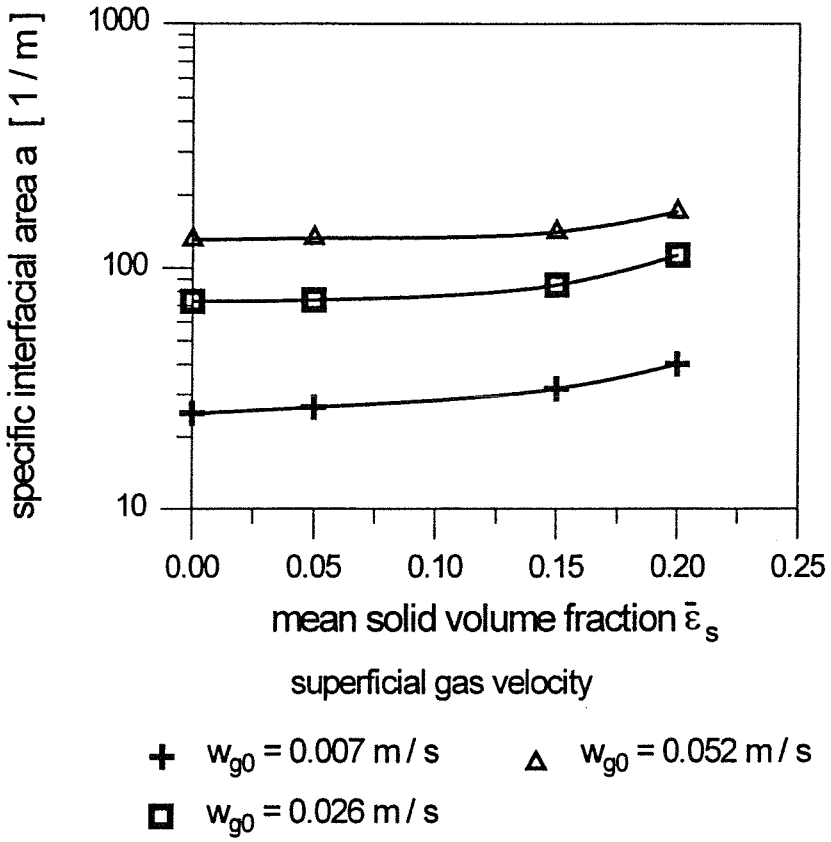

Fig. 19: Specific interfacial area, $w_{l0} = 0$

5.2 Volumetric Oxygen Mass Transfer Coefficient

The design and scale-up of bioreactors require a relationship between the volumetric mass transfer coefficient and the physical and operational parameters of the system. As bubble columns are often used in slow reaction-absorption regime and gas side mass transfer resistance is very small, it is sufficient to describe the mass transfer only by the aid of the liquid side mass transfer coefficient $k_l a$. A number of research works have been done on $k_l a$ [38-43]. These works show that the volumetric mass transfer coefficient $k_l a$ increases with increasing gas velocity. But for solids with only a small difference between liquid and solid densities only a few investigations exist. SUN et al [41] und KOIDE et al. [40] observed a decreasing $k_l a$-value with increasing solid concentration. In this examination the solid phase is represented by calcium alginate beads. Due to the small difference between the densities of the liquid and the Ca-alginate beads it was assumed that the axial concentration gradient is neglectable. This was confirmed by visual observation.

The volumetric oxygen transfer coefficient is measured simulating an oxygen consumption by the aid of a chemical reaction [13]:

$$Na_2SO_3 + \frac{1}{2} O_2 \rightarrow Na_2SO_4 \qquad (11)$$

To check that there is no absorption acceleration due to chemical film reaction, the Hatta-number, which relates the reaction and the absortion velocity, has to be applied as:

$$Ha = \left(\frac{\frac{2}{3} \cdot k_r \cdot D_{O_2,l} \cdot c^*_{O_2,l}}{k_l^2} \right)^{0.5} \tag{12}$$

with the reaction velocity constant k_r, the oxygen diffusion coefficient $D_{O_2,l}$ the equilibrium concentration of the dissolved oxygen $c^*_{O_2,l}$ and the liquid side mass transfer coefficient k_l. To determine $k_l a$ a balance of the oxygen in a disk-shaped reactor element is applied by the aid of the axiale dispersion model as follows:

$$\frac{\partial \dot{N}_{C,O_2}}{\partial z} + \frac{\partial \dot{N}_{D,O_2}}{\partial z} + d\dot{N}_{O_2} = 0 \tag{13}$$

Neglecting the axial phase profiles and assuming the universal law for the gas phase yield to a differential equation for the molar fraction of the oxygen in the gas phase [13]:

$$\frac{\partial^2 y_{O_2}}{\partial z^2} - \left(a_1(z) + a_2(z) \cdot \frac{1}{(1 - y_{O_2})^2} \right) \cdot \frac{\partial y_{O_2}}{\partial z} + a_3(z) \cdot y_{O_2} + a_4(z) = 0 \tag{14}$$

with the coefficients

$$\begin{aligned}
a_1(z) &= \frac{2 \cdot \left(\rho_l \cdot \left[1 - \varepsilon_s - \varepsilon_g \right] + \varepsilon_s \cdot \rho_s \right) \cdot g}{\left[p_u + \left(\rho_l \cdot \left[1 - \varepsilon_s - \varepsilon_g \right] + \varepsilon_s \cdot \rho_s \right) \cdot g \cdot (H_R - z) \right]} \\
a_2(z) &= \left(\frac{\rho_g \cdot V_g}{\tilde{M}_g} \right)_I \cdot \frac{(1 - y_{O_2,I}) \cdot R \cdot T}{\varepsilon_g \cdot E_g \cdot A_R \cdot \left[p_u + \left(\rho_l \cdot \left[1 - \varepsilon_s - \varepsilon_g \right] + \varepsilon_s \cdot \rho_s \right) \cdot g \cdot (H_R - z) \right]} \\
a_3(z) &= \frac{k_l a}{He \cdot \varepsilon_g \cdot E_g} \\
a_4(z) &= \frac{k_l a \cdot c_{l,O_2} \cdot R \cdot T}{\varepsilon_g \cdot E_g \cdot \left[p_u + \left(\rho_l \cdot \left[1 - \varepsilon_s - \varepsilon_g \right] + \varepsilon_s \cdot \rho_s \right) \cdot g \cdot (H_R - z) \right]}
\end{aligned} \tag{15}$$

This equation is solved with the boundary conditions:

$$\begin{aligned}
y_{O_2}(z = 0) &= y_{O_2,I} \\
y_{O_2}(z = H_R) &= y_{O_2,O}
\end{aligned} \tag{16}$$

with the molar fraction of oxygen in the inlet and outlet of the gas phase. The equilibrium concentration of the dissolved oxygen in the liquid phase was calculated by Henry's

law. The mass transfer in a finite volume element ΔV_j with the height Δz_j is defined by:

$$\Delta \dot{N}_{O_2,j} = k_l a \cdot \left(c^*_{l,O_2}(z_j) - c_{l,O_2}(z_j) \right) \cdot A_R \cdot \Delta z_j \qquad (17)$$

By the aid of a balance over the whole reactor the following correlation for $k_l a$ is generated:

$$k_l a = \frac{\left(\frac{\rho_g \cdot w_{g0}}{\tilde{M}_g} \right)_I \cdot \left(\frac{y_{O_2,i} - y_{O_2,o}}{1 - y_{O_2,o}} \right)}{\sum_{j=1}^{n} \left(c^*_{l,O_2}(z_j) - c_{l,O_2}(z_j) \right) \cdot \Delta z_j} \qquad (18)$$

Using measured molar fractions of oxygen in the inlet and outlet gas flow and dissolved oxygen concentration in the liquid phase the volumetric oxygen mass transfer coefficient was calculated by numerical iteration.

Fig. 20 shows the volumetric oxygen mass transfer coefficient versus the superficial gas velocity. $k_l a$ increases with rising gas flow rate. But it also can be seen, that the solid volume fraction has an influence on $k_l a$ as shown in Fig. 21.

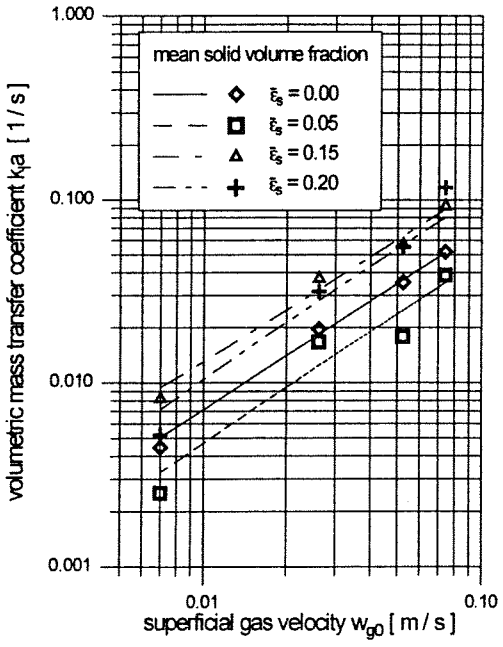

Fig. 20: Volumetric oxygen mass transfer coefficient, $w_{l0} = 0$

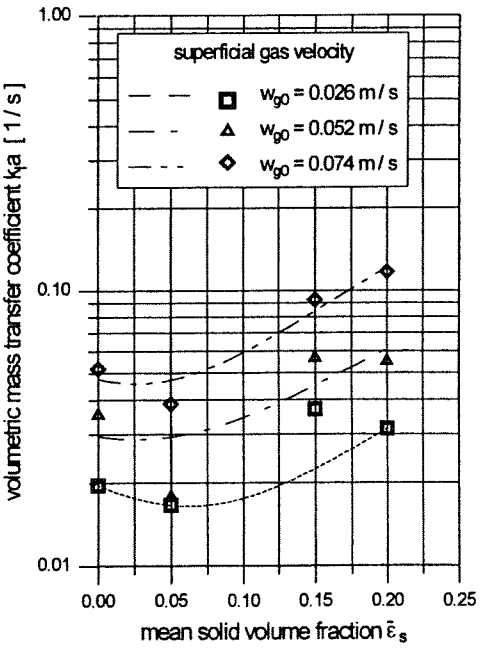

Fig. 21: Volumetric oxygen mass transfer coefficient, $w_{l0} = 0$

At a mean solid volume fraction of 0.05 the volumetric solid oxygen mass transfer coefficient is slightly lower than the $k_l a$-value in a two-phase system. This effect is caused by an accumulation of the particles in the bounbary layer between the gas and the liquid phase. Therefore the mass transfer through the liquid side boundary layer is reduced and k_l becomes lower while the interfacial area is being nearly constant. At higher solid volume fractions the volumetric mass transfer coefficient increases due to the slightly

increasing interfacial area and secondary to the higher turbulence intensity. More particles penetrate into the boundary layer but on the other side particles are constantly eleminated from the layer, which leads to an advanced substitute of the boundary layer and therefore to increased mass transfer coefficients. This effect is especially important for bioreactors, which are often operated at high particle concentrations.

6. CONCLUSIONS

For the design and scale-up of three-phase fluidized bubble columns the following points should be considered. Increasing superficial gas velocity

- increases the gas hold-up,
- leads to better solid distribution,
- increases the gas phase dispersion significantly
- leads to higher liquid dispersion,
- rises the solid dispersion,
- increases the mass transfer between the gas and the liquid phase,
- increases the interfacial area considerably.

Rising superficial velocities of the liquid phase in countercurrent operation mode

- have only a small influence on the solid distribution,
- decrease the gas phase dispersion,
- decrease slightly the liquid dispersion,
- decrease the solid dispersion significantly.

Higher values of the mean solid volume fraction

- have only a small influence on gas hold up,
- decrease the gas phase dispersion,
- decrease the liquid dispersion at low solid concentrations, increases the liquid dispersion at high solid concentrations,
- increase the specific interfacial area especially at low gas flow rates,
- decrease the mass transfer at low solid concentrations, increase the mass transfer at high solid concentrations.

7. NOMENCLATURE

A	[m^2]	area
a	[m^2/m^3]	specific interfacial area
Bo	[-]	Bodenstein-number
c	[kg/m^3]	concentration
D_R	[m]	reactor diameter, D_R = 0.142 m
D	[m^2/s]	diffusion coefficient
d	[m]	diameter
d_{P50}	[m]	mean particle diameter
d_S	[m]	Sauter-diameter
E	[m^2/s]	dispersion coefficient
g	[m/s^2]	acceleration due to gravity, g = 9.81 m/s^2
H_R	[m]	reactor height, H_R = 1.742 m
h	[m]	height of a reactor element
Ha	[-]	Hatta-number
k_l	[m/s]	mass transfer coefficient
M	[kg]	mass
$\dot{M}$	[kg/s]	mass flow

$\tilde{M}$	[kg/kmol]	molar mass
$\dot{N}$	[mol/s]	molar flow
n	[-]	counter
p	[Pa]	pressure
T	[K]	temperature
w	[m/s]	velocity
y	[mol/mol]	molar fraction
z	[m]	axial coordinate

Greek letters

ϵ	[m^2/s^3]	energy dissipation rate per unit mass
ε	[m^3/m^3]	volume fraction
η	[Pa·s]	dynamic viscosity
ϱ	[kg/m^3]	density
σ	[N/m]	surface tension
ω	[1/s]	frequency

Subscripts

g	gas
I	inlet
l	liquid
O	outlet
s	solid
0	superficial

Superscripts

*	equilibrium
-	mean

8. REFERENCES

[1] H. Chmiel: "Bioprozeßtechnik", Gustav Fischer, Stuttgart (1991).

[2] H.-G. Springmann, A. Steiff, P.-M. Weinspach, "Feststoffeinfluß auf den Stofftransport in Suspensionsblasensäulen", in: Chem.-Ing.-Tech., 63, 5, pp. 512/513 (1991).

[3] W.-D. Deckwer, A. Schumpe, "Improved Tools for Bubble Column Reactor Design and Scale-up", in: Chem. Eng. Sci 48, 5, pp. 889/911 (1992).

[4] W.-D. Deckwer, A. Schumpe, "Blasensäulen-Erkenntnisstand und Entwicklungstendenzen", in: Chem.-Ing.-Tech., 57, 9, pp. 754/767 (1985).

[5] W.-D. Deckwer, A. Schumpe, "Transporterscheinungen in Dreiphasen-Reaktoren mit fluidisiertem Feststoff", in: Chem.-Ing.-Tech. 55, 8, pp. 591/600 (1983).

[6] Y. T. Shah, G. J. Stiegel, M. M. Sharma, "Backmixing in Gas-liquid Reactors", in: AIChE J. 24, 3, pp. 369/400 (1978).

[7] R. Torvik, H. F. Svendson, "Modelling of Slurry Reactors. A Fundamental Approach", in: Chem. Eng. Sci. 45, 8, pp. 2325/2332 (1990).

[8] N. W. Geary, R. G. Rice, "Circulation and Scale-up in Bubble Columns", in: AIChE J. 38, 1, pp. 76/82 (1992).

[9] V. V. Ranade, "Flow in Bubble Columns: Some Numerical Experiments", in: Chem. Eng. Sci 47, 8, pp. 1857/1869 (1992).

[10] H. Hikita, S. Asai, Y. Azuma, "Solubility and Diffusity of Oxygen in Aqueous Sucrose Solutions", in: Can. J. Chem. Eng. 56, 6, pp. 371/374 (1978).

[11] T. Pilhofer, H. Jekat, H. D. Müller, "Messung der Größenverteilung fluider Partikeln in Blasensäulen und Sprühkolonnen", in: Chem.-Ing-Tech. 46, pp. 149/174 (1974).

[12] K.-H. Mangartz: "Theoretische und experimentelle Darstellung der Funktion einer Blasensäule unter Einbeziehung von axialer Durchmischung und Stoffübergang", Ph.D. Thesis, TU München (1977).

[13] H.-G. Springmann, A. Steiff, P.-M. Weinspach, "Bestimmung des volumetrischen Stoffübergangskoeffizienten in Suspensionsblasensäulen mit einer modifizierten Sulfit-Oxidationsmethode", in: Chem.-Ing.-Tech. 63, 2, p. 162 (1990).

[14] M. Potthoff: "Einfluß statischer Mischer auf die Strömungsverhältnisse und den Stofftransport in Dreiphasen-Wirbelschicht-Bioreaktoren", Ph.D. Thesis, TU Braunschweig (1992).

[15] S. C. Saxena, N. S. Rao, A. C. Saxena, "Heat Transfer and Gas Hold-up Studies in a Bubble Column: Air-Water-Sand System", in: Can. J. Chem. Eng. 70, 2, pp. 33/41 (1992).
[16] Y. Kato, A. Nishiwaki, T. Fukuda, S. Tanaka, "The Behavior of Suspended Solid Particles and Liquid in Bubble Columns", in: J. Chem. Eng. Japan, 5, 2, pp. 112/118 (1972).
[17] K. Akita, F. Yoshida, "Gas Hold-up and Volumetric Mass Transfer Coefficient in Bubble Columns", in: Ind. Eng. Chem. Proc. Des. Dev. 12, pp. 76/80 (1973).
[18] Y. Kato, S. Morooka, T. Kago, T. Saruwatari, S.-Z. Yang, "Axial Hold-up Distributions of Gas and Solid Particles in Three Phase Fluidized Bed for Gas-Liquid (Slurry)-Solid Systems", in: J. Chem. Eng. Japan, 18, 4, pp. 308/312 (1985).
[19] I. G. Reilly, D. S. Scott, T. de Bruijn, A. Jain, J. Piskorz, "A Correlation for Gas Hold-up in Turbulent Coalescing Bubble Columns", in: Can. J. Chem. Eng. 64, 10, pp. 705/717 (1986).
[20] Y. Sun, T. Nozowa, "Gas Hold-up and Volumetric Mass Transfer Coefficient in a Three Phase Fluidized Bed Bioreactor," in: J. Chem. Eng. Japan, 21, 1, pp. 15/20 (1988).
[21] H. Hikita, S. Asai, K. Segawa, M. Kitao, "Gas Hold-up in Bubble Columns", in: Chem. Eng. J. Lausanne 20, pp. 59/67 (1980).
[22] E. Flaschel, C. Metzorf, A. Renken, "Methode zur Messung der axialen Vermischung des Feststoffs in Flüssigkeit/Feststoff-Wirbelschichten", in: Chem.-Ing.-Tech. 59, 6, pp. 494/496 (1987).
[23] I. G. Reilly, D. S. Scott. T. de Bruijn, D. McIntyre, J. Piskorz, "Axial Solids Concentration in Three Phase Bubble Columns", in: Chem. Eng. Sci. 45, 8, pp. 2293/2299 (1990).
[24] M. N. Badgujar, A. Deimling, B. I. Morsi, Y. T. Shah, N. L. Carr, "Solids Distribution in a Batch Bubble Column", in: Chem. Eng. Commun. 48, pp. 127/153 (1986).
[25] T. Matsumoto, N. Hidaka, S. Morooka, "Axial Distribution of Solid Hold-up in Bubble Column for Gas-Liquid-Solid Systems", in: AIChE J. 35, 10, pp. 1701/1709 (1989).
[26] C. R. Carlos, J. F. Richardson: "Solids Movement in Liquid Fluidized Bed, Part I: Particle Velocity Distribution", in: Chem. Eng. Sci. 23, 8, pp. 813/824 (1968).
[27] P. Murray, L.-S. Fan: "Axial Solid Distribution in Slurry Columns", in: Ind. Eng. Chem. Res. 28, 11, pp. 1697/1703 (1989).
[28] S. A. Shetty, M. V. Kantak, B. G. Kelkar, "Gas-phase Dispersion in Bubble Column Reactors", in: AIChE J. 38, 7, pp. 1013/1026 (1992).
[29] M. Kawagoe, T. Otake, C. W. Robinson, "Gas-phase Mixing in Bubble Columns", in: J. Chem. Eng. Japan, 22, 2, pp. 136/142 (1989).
[30] S. Wachi, Y. Nojima:, "Gas-phase Dispersion in Bubble Columns", in: Chem. Eng. Sci. 45, 4, pp. 901/905 (1990).
[31] R. W. Field, J. F. Davidson, "Axial Dispersion in Bubble Columns", in: Trans IChemE 58, pp. 228/235 (1980).
[32] M. H. I. Baird, R. G. Rice, "Axial Dispersion in Large Unbaffled Columns", in: Chem. Eng. J. Lausanne 9, pp. 171/174 (1975).
[33] R. Badura, W.-D. Deckwer H.-J. Warnecke, H. Langemann, "Durchmischung in Blasensäulen", in: Chem.-Ing.-Tech. 46, 9, p. 399 (1974).
[34] R. Wendt, A. Steiff. P.-M. Weinspach, "Flüssigphasenrückvermischung in Blasensäulenreaktoren", in: Chem.-Ing.-Tech. 55, 10, pp. 796/797 (1983).
[35] A. Schumpe, W.-D. Deckwer, "Flüssigphase-Dispersion in einer über eine Sinterplatte begaste Blasensäule", in: Chem.-Ing.-Tech. 59, 6, pp. 489/491 (1987).
[36] H.-P. Riquarts, "Strömungsprofile, Impulsaustausch und Durchmischung der flüssigen Phase in Blasensäulen", in: Chem.-Ing.-Tech. 53, 1, pp. 60/61 (1981).
[37] W-T. Tang, L.-S. Fan, "Axial Liquid Mixing in Liquid-Solid and Gas-Liquid-Solid Fluidized Beds Containing Low Density Particles", in: Chem. Eng. Sci. 45, 2, pp. 543/551 (1990).
[38] K. Koide, A. Takazawa, M. Komura, H. Matsunaga, "Gas Hold-up and Volumetric Liquid-side Mass Transfer Coefficient in Solid-Suspended Bubble Columns", in: J. Chem. Eng. Japan, 17, 5, pp. 459/466 (1984).
[39] T. Seno, S. Uchida, S. Tsuyutani, "Mass Transfer in Countercurrent and Cocurrent Bubble Columns", in: Chem. Eng. Technol. 13, pp. 113/118 (1990).
[40] K. Koide, K. Shibata, H. Ito, S. Y. Kim, K. Ohtaguchi, "Gas Hold-up and Volumetric Mass Transfer Coefficient in a Gel Suspended Bubble Column with Draught Tube", in: J. Chem Eng. Japan, 25, 1, pp. 11/16 (1992).
[41] Y. Sun, S. Furusaki, "Mean Bubble Diameter and Oxygen Transfer Coefficient in a Three Phase Fluidized Bed Bioreactor", in: J. Chem. Eng. Japan 21, 1, pp. 20/24 (1988).
[42] Y. Kawase, B. Halard, M. Moo-Young, "Liquid Phase Mass Transfer Coefficient in Biorectors", in: Biotechnology and Bioengineering 39, 11, pp. 1133/1140 (1992).
[43] M. K. Popovic, C. W. Robinson, "Mass Transfer Studies of External Loop Airlifts and a Bubble Column", in: AIChE J. 35, 3, pp. 393/405 (1989).

THREE-DIMENSIONAL DETAILED NUMERICAL SIMULATION OF BUBBLY UPFLOW IN A VERTICAL SQUARE DUCT

Akio Tomiyama[1], Akira Sou[1], Iztok Zun[2] and Tadashi Sakaguchi[1]

[1] Kobe University
Faculty of Engineering, Department of Mechanical Engineering
Rokkodai, Nada, Kobe 657, Japan

[2] University of Ljubljana
Faculty of Mechanical Engineering
61000 Ljubljana, Slovenia

ABSTRACT

A three-dimensional detailed numerical simulation of bubbly flow in a vertical duct was carried out in the present study. The simulation was based on the local-instantaneous field equations of the gas-liquid two-phase flow and on the interface tracking method of the volume of fluid (VOF) method. The validity of the numerical method was confirmed by the comparison between measured and calculated terminal rising velocity and shape of a single bubble in an infinite stagnant liquid for a wide range of the Morton and Eötvös numbers. Then, laminar bubbly flow in a vertical square duct was analyzed by making use of a periodic boundary condition and an initial pressure distribution of the two-phase flow. As a result, two typical void distributions, the wall-peak and core-peak distributions, were obtained by varying the Eötvös number. The results of the simulation agreed well with available experimental data on the phase distribution.

1. INTRODUCTION

Numerical simulation of gas-liquid two-phase flow has been usually conducted by coupling averaged field equations such as the two-fluid model and drift-flux model with constitutive equations representing an interaction between the two phases[1]. Since this method has an ability to predict complex transient two-phase flow phenomena in a relatively short CPU time, it has been applied to a wide range of practical problems concerning safety evaluation of nuclear reactors, multidimensional two-phase flow in chemical reaction reactors and so on. However, it would be difficult for us to extract from this method more physical information on the mechanism of two-phase flow than physical experiments can offer. This is because most of the constitutive equations adopted in this method are experimental correlations. On the other hand, recent rapid progress in computer performance and numerical methods gives us a large prospect for realizing a more detailed numerical simulation of two-phase flow without any constitutive equations, that is to say, a simulation based on local-instantaneous field equations. This kind of simulation would yield a lot of knowledge on the flow field available to develop a sophisticated two-phase flow model.

The authors have been, therefore, examining the feasibility of detailed numerical simulation of gas-liquid two-phase bubbly flow through the analyses of a single bubble in a stagnant liquid, a single bubble in a shear field, a Taylor bubble in a vertical pipe, and interaction of two bubbles in train[2]-[5]. These analyses were conducted using the volume of fluid (VOF) method[6], which is based on the local-instantaneous field equations and an interface tracking method. As a result of these previous examinations, we could demonstrate that the following effects on bubble shape and dynamic behavior can be predicted well ; (1) bubble diameter, (2) fluid properties such as density, viscosity and surface tension, (3) gravity, (4) vortex generated by a bubble itself, (5) external shear field of the continuous liquid phase, (6) pipe wall, and (7) indirect interaction of bubbles. The above effects can be considered as the ones governing a laminar bubbly upflow of low void fraction, in which bubble coalescence or break-up will rarely take place. Consequently, it is possible for us now to carry out a detailed simulation of a laminar bubbly flow in a vertical duct.

Hence, three-dimensional simulation of a laminar bubbly flow in a vertical square duct was

carried out in the present study. For this purpose, a program based on the three-dimensional local-instantaneous equations, the interface tracking technique of the VOF method and a modified SOLA method[7] was developed. Comparisons between measured and calculated terminal rising velocity and shape of a single bubble in various stagnant liquids were also conducted to examine the validity of the developed program.

2. FIELD EQUATIONS AND NUMERICAL METHOD

The local-instantaneous field equations for the incompressible gas-liquid two-phase flow in Cartesian coordinates (x, y, z) are given by

$$div\mathbf{V}_k = 0 , \tag{1}$$

$$\rho\frac{D\mathbf{V}_k}{Dt} = -grad p + \rho\mathbf{g} + \mu_k divgrad\mathbf{V}_k , \tag{2}$$

where the subscript k denotes the gas (G) or liquid (L) phase, **V** the velocity vector, t the time, p the pressure, **g** the body force per unit mass, μ the viscosity, and D/Dt the material derivative. Similar to the VOF method, the density ρ in Eq.(2) is defined by using the liquid volumetric fraction, F, in a computational cell as follows :

$$\rho = F\rho_L + (1-F)\rho_G . \tag{3}$$

A cell is filled with the liquid when F=1 or with the gas when F=0. If the value of F lies between 0 and 1, a gas-liquid interface exists in a cell. The location and the curvature κ of the gas-liquid interface are determined from the values of F in the cells surrounding the interface cell. The curvature κ is the sum of the two principal curvatures, κ_1 and κ_2, and is expressed by the following formula of differential geometry [8]:

$$\kappa = \kappa_1 + \kappa_2 = \frac{R(1+Q^2) - 2PQS + T(1+P^2)}{(1+P^2+Q^2)^{3/2}} . \tag{4}$$

When the interface is almost parallel to the x-y plane, the height of the interface in the z direction can be expressed by h=h(x,y). In this case, the terms, P, Q, R, S and T in the above equation are given by

$$P = \frac{\partial h}{\partial x}, Q = \frac{\partial h}{\partial y}, R = \frac{\partial^2 h}{\partial x^2}, S = \frac{\partial^2 h}{\partial x \partial y}, T = \frac{\partial^2 h}{\partial y^2} . \tag{5}$$

Using similar expressions for P, Q, R, S and T, we can calculate κ when the interface is almost parallel to the y-z or z-x plane. Then, the pressure due to the surface tension, p_s, is given by

$$p_s = \kappa\sigma , \tag{6}$$

where σ is the surface tension. The surface tension force per unit volume, $\mathbf{f}_s$, is normal to the interface and directs toward the center of the curvature. Hence, $\mathbf{f}_s$ is expressed by

$$\mathbf{f}_s = \frac{p_s \mathbf{S}}{\Delta x \Delta y \Delta z} , \tag{7}$$

where **S** is the vector of the surface element in the interface cell directing toward the center of the curvature and Δx, Δy and Δz are the cell sizes as shown in **Fig.1**. In order to take into account the effect of surface tension on the pressure and velocity fields, $\mathbf{f}_s$ is added to the right-hand side of Eq.(2) in the interface cells.

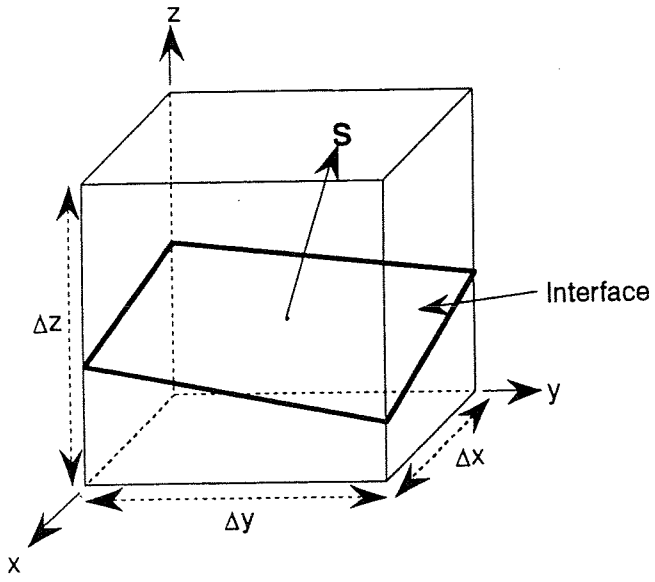

Fig.1 Schematic of an interface cell

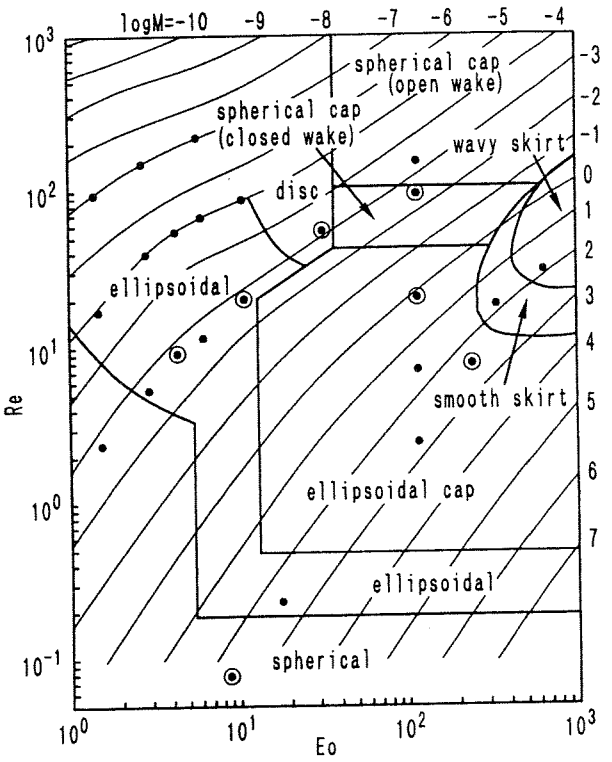

Fig.2 Bhaga's graphical correlation on terminal velocity and shape of bubble [13]

Since F is the liquid volumetric fraction, it satisfies the following volume conservation of the liquid phase:

$$\frac{\partial F}{\partial t} + div(FV_L) = 0 \tag{8}$$

Equation (8) is solved using a donor-acceptor method[6] to advance the interface location.

Equations (1) and (2) are solved by a modified SOLA method proposed by Tomiyama and Hirano[7], which can solve transient incompressible flow more faster than the original SOLA method[9] since the pressure iteration procedure of the modified SOLA method correctly takes into account the pressure boundary conditions. The details of the modified SOLA method are given in Ref.[7].

3. ANALYSIS OF A SINGLE BUBBLE IN A STAGNANT LIQUID

Comparisons between measured and calculated terminal rising velocity and shape of a single bubble in an infinite stagnant liquid were conducted in order to examine the validity of the present numerical method. **Figure 2** shows a graphical correlation of the terminal velocity and shape of a single bubble in a stagnant liquid proposed by Grace[10] and Bhaga and Weber[11]. Three dimensionless numbers, Eo, M and Re, in this figure are the Eötvös, Morton and bubble Reynolds numbers defined by

$$Eo = \frac{g(\rho_L - \rho_G)d^2}{\sigma}, \tag{9}$$

$$M = \frac{g\mu_L^4(\rho_L - \rho_G)}{\rho_L^2\sigma^3}, \tag{10}$$

and

$$Re = \frac{\rho_L V_t d}{\mu_L}, \qquad (11)$$

respectively. Here g the gravity constant, d the equivalent bubble diameter and V_t the terminal rising velocity. The Eötvös number represents the ratio of buoyancy to surface tension whereas the Morton number, which is also called as the property group, represents the effect of fluid properties and gravity. Figure 2 indicates that the nondimensional terminal rising velocity, Re, and shape of a single bubble in a stagnant liquid are uniquely determined by Eo and M.

The initial and boundary conditions of the calculation are shown in **Fig.3**. The initial bubble shape was spherical. The cell sizes were set as $\Delta x=\Delta y=\Delta z$, and the number of cells assigned to the bubble diameter, d, was from 10 to 14. When bubble shape distortion was large, we assigned larger number of cells to the bubble. The lengths of the x, y and z directions were 4d, 4d and 4.5d, respectively. Therefore, when we adopted 14 cells for the bubble diameter, the total number of cells including boundary cells was (56+2)(56+2)(63+2)=218660 where the term, +2, accounts for the contribution of the fictitious boundary cells. The liquid was fed from the top boundary in the downward direction at the uniform velocity V_{in}. In order to prevent the bubble from escaping from the center region of the computational domain, V_{in} was adjusted to be almost equal to the terminal rising velocity. Continuous boundary condition was adopted for the bottom and side boundaries to realize the simulation of a single bubble in an infinite stagnant liquid in the frame of reference moving upward at the constant velocity V_{in}. Since V_{in} was not just equal to the terminal rising velocity of a calculated bubble, the calculated bubble slightly moved in the z direction with an axial velocity W. Hence, the terminal velocity of a calculated bubble was calculated by adding W to V_{in}. As for the calculated bubble shapes, we used resultant steady bubble shapes for the comparison. All the calculations were conducted using a workstation, DEC 3000 AXP model 400 (133MFLOPS, LINPACK double precision (100 x 100)=26.4). Graphics were drawn using AVS, Application Visualization System, on a workstation, Silicon Graphics Iris Indigo.

Comparisons between calculated and Grace's nondimensional terminal velocitiy, Re, were conducted for the conditions denoted by black dots in Fig.2. The results are shown in **Fig.4**. As shown in this figure, we could obtain good predictions of Re for a wide range of flow condition, $1.41 \leq Eo \leq 641$ and $-6.9 \leq \log M \leq 2.9$. This result indicates that various forces acting on the bubble are predicted well by the present numerical method. **Figure 5** shows the comparison of measured and

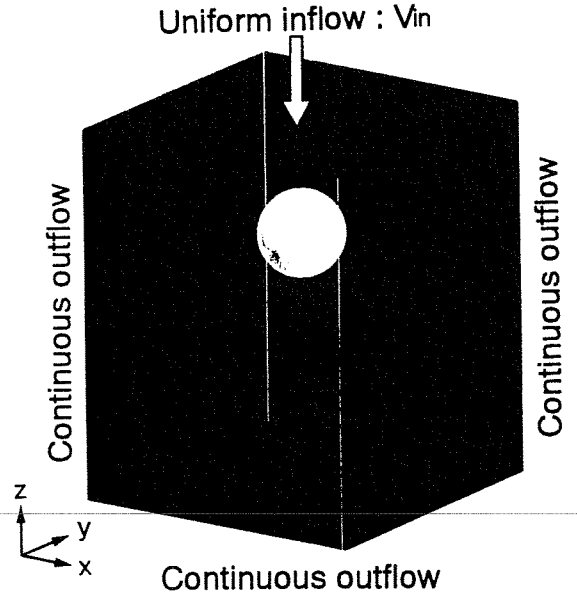

Fig.3 Computational geometry and initial bubble shape

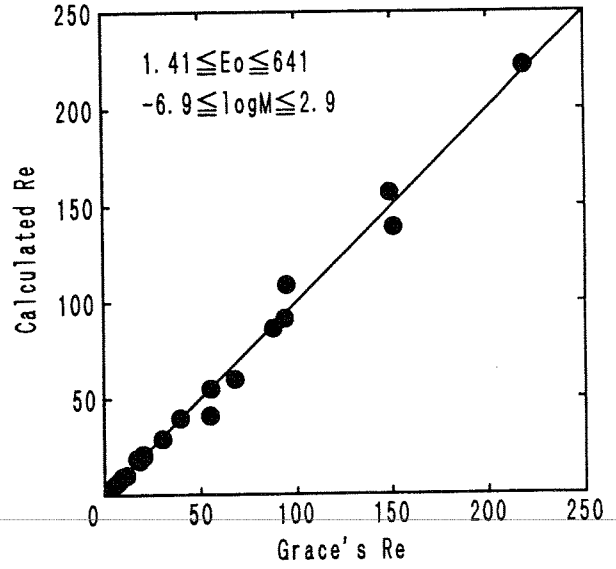

Fig.4 Comparison between Grace's and calculated bubble Reynolds numbers

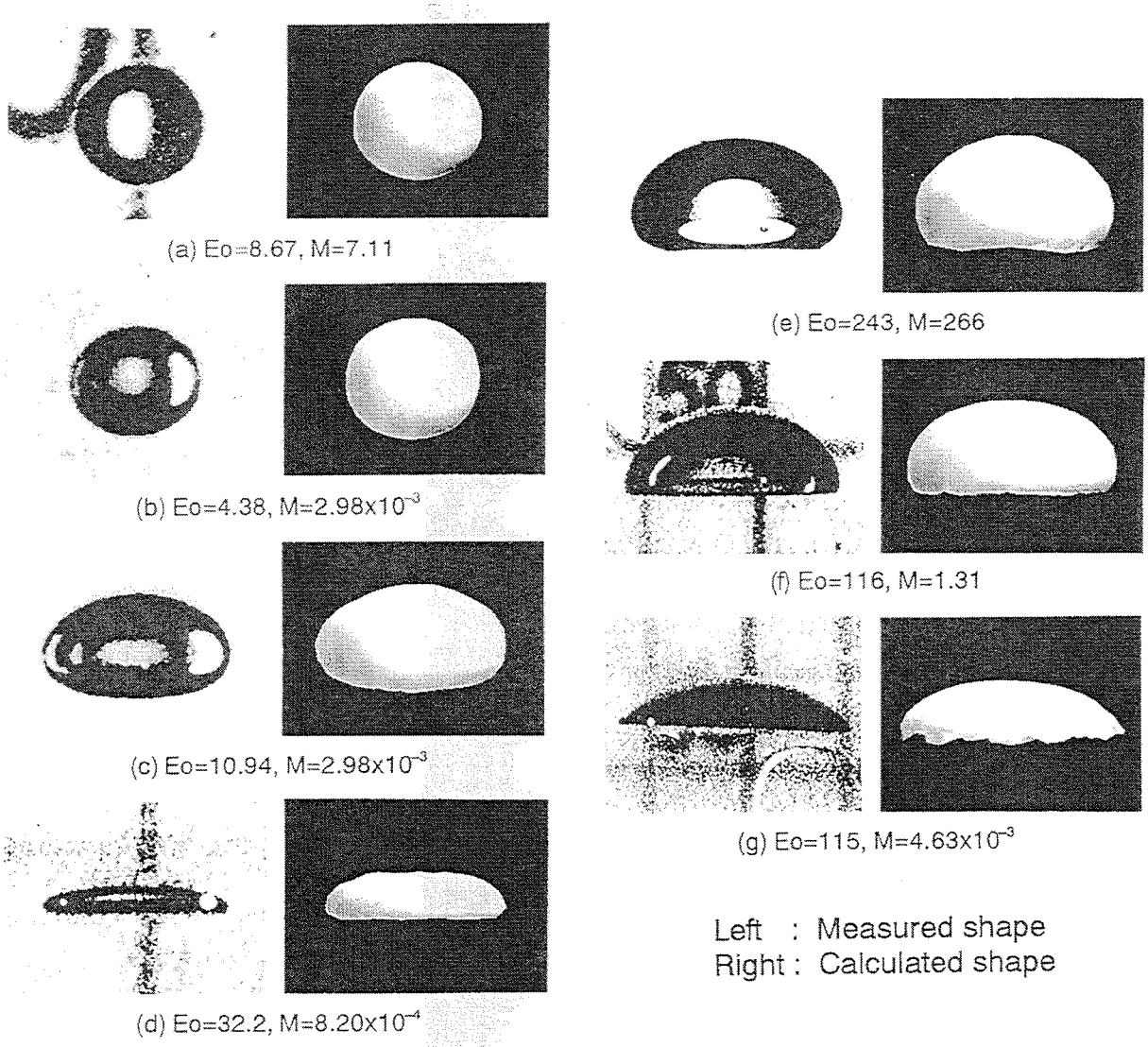

Fig. 5 Comparison between measured and calculated bubble shapes: Photos (a),(d),(e),(f) and (g) are quoted from Ref.[13]

calculated bubble shapes. The conditions for this comparison denoted by open circles in Fig.2 correspond to various bubble shapes under laminar flow condition. The photos of cases (a), (d), (e), (f) and (g) in Fig.5 were quoted from Bhaga and Weber[11]. On the other hand, those of cases (b) and (c) were obtained by the authors using air and glycerol solution at atmospheric pressure and room temperature. As shown in this figure, good agreement was obtained except for cases (d) and (g). When bubble shape distortion is large like cases (d) and (g), the number of cells included in the region between two adjacent gas-liquid interfaces will decrease, which results in the source of numerical error. This is the main reason why the agreement was not so good in cases (d) and (g). Hence, if we can afford to use more computational cells for these cases, we will be able to obtain more good predictions. At any rate, the calculated shapes of cases (d) and (g) also qualitatively agreed well with the measured shapes.

4. SIMULATION OF LAMINAR BUBBLY FLOW IN A SQUARE DUCT

4.1 Numerical Scheme for Bubbly Flow Simulation

Initial and boundary conditions for three-dimensional bubbly flow simulation are shown in **Fig.6** in the form of three-sided figures. No slip boundary condition was adopted for the side walls and periodic boundary condition was applied to the top and bottom boundaries. Therefore, the liquid and bubbles escaping from the top boundary reenter to the computational domain from the bottom boundary. The shape of the duct was square and its size was 4d x 4d. The axial height of the duct was

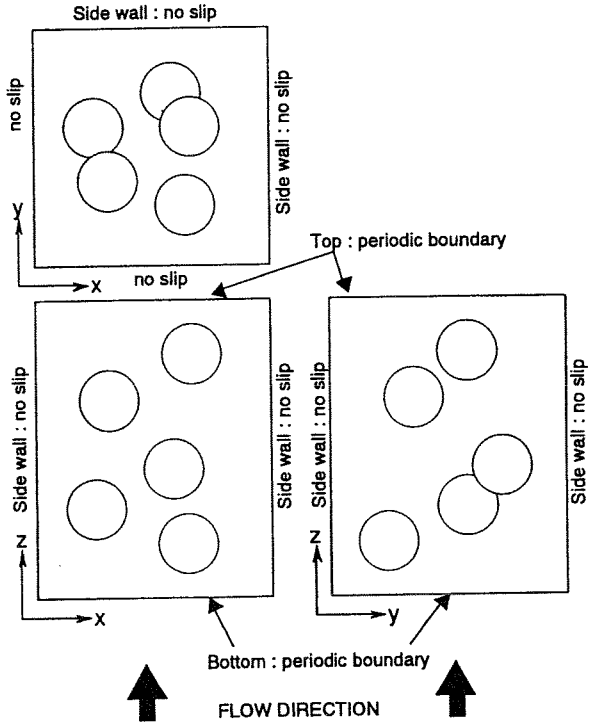

Fig.6 Initial and boundary conditions for bubbly flow simulation

5d. Cubic cells, i.e., $\Delta x=\Delta y=\Delta z$, were used and the number of cells in the x, y and z directions were 48, 48 and 60, respectively. Hence, the total number of cells including the fictitious boundary cells were 157500. The initial bubble shapes were spherical and the number of cells assigned to the bubble diameter was 12. Five bubbles were included in the computational domain so that the volume-averaged void fraction was 3.3%.

The initial distribution of the local total volumetric flux, **J**, defined by

$$\mathbf{J} = F\mathbf{V}_L + (1-F)\mathbf{V}_G = (J_x, J_y, J_z), \tag{12}$$

was specified by using the laminar velocity distribution. The initial lateral components, J_x and J_y, were null. The axial component, J_z, was calculated using the following steady momentum balance :

$$0 = -\frac{dp}{dz} - \rho g + \mu_L\left(\frac{\partial^2 J_z}{\partial x^2} + \frac{\partial^2 J_z}{\partial y^2}\right). \tag{13}$$

It was assumed in the above equation that the pressure was constant in the cross-sectional area of the duct. Hence, dp/dz was assumed as a function of z. Equation (13) constitutes the boundary-value problem of the Poisson equation given by

$$\frac{\partial^2 J_z}{\partial x^2} + \frac{\partial^2 J_z}{\partial y^2} = G, \tag{14}$$

$$J_z = 0 \quad \text{at} \quad x=0,\ x=L,\ y=0,\ \text{and}\ y=L, \tag{15}$$

where L denotes the duct width and the source term G is given by

$$G = \frac{1}{\mu_L}\left(\frac{dp}{dz} + \rho g\right). \tag{16}$$

If the following area-averaged density $\rho(z)$ is substituted into Eq.(16),

$$\rho=\rho(z)=\frac{1}{L^2}\int_{L^2}\{\rho_G(1-F(x,y,z))+\rho_L F(x,y,z)\}dxdy \quad , \tag{17}$$

the source term G becomes constant in the cross-sectional area.

Equation (14) is a linear partial differential equation and the boundary condition (15) is homogeneous so that when G is multiplied by a constant β, the shape of the spatial distribution of $J_z(x,y)$ dose not change at all but only the value of $J_z(x,y)$ changes to $\beta J_z(x,y)$. This feature of Eqs.(14) and (15) was utilized to set up the initial conditions for the velocity and pressure fields. Firstly, the solution of Eqs.(14) and (15) was obtained numerically by setting G=–1. Then, the resultant solution $J_z(x,y)$ was multiplied by β in order to adjust a total volume flow rate to a desired value. In this case, G is equal to $-\beta$. Hence, solving Eq.(16) for dp/dz yields

$$\frac{dp}{dz}=-(\mu_L\beta+\rho g) \quad . \tag{18}$$

The first and second terms of the right-hand side of Eq.(18) represent the frictional and gravitational pressure gradients. The frictional pressure gradient of two-phase flow generally differs from that of single-phase flow. Consequently, the pressure gradient determined by Eq.(18) is not just equal to the pressure gradient that can keep the prescribed flow rate constant in time. Equation (18) is, therefore, modified by using a two-phase friction multiplier Φ^2 to the following equation :

$$\frac{dp}{dz}=-(\mu_L\beta\Phi^2+\rho g) \quad . \tag{19}$$

Since it was difficult to find an appropriate value of Φ^2 before conducting a simulation, the first simulation was conducted using the initial pressure distribution calculated by setting $\Phi^2=1$ in Eq.(19). Then, if the total volume flow rate decreased (or increased) in time, the second simulation was conducted using a new initial pressure distribution calculated using a slightly increased (or decreased) value of Φ^2. That is to say, the value of Φ^2 was determined by a trial and error method until the value of the total volume flow rate did not change in time.

Then, let us summarize parameters for bubbly flow simulation. In addition to Eo and M, characteristics of laminar bubbly flow in a vertical duct would be influenced by geometry of a duct, volume-averaged void fraction and area-averaged total volumetric flux. Among these parameters, the geometry of the duct and the volume-averaged void fraction were fixed in the simulation. Hence, the nondimensional initial value of the local total volume flux $J_z(x,y)$ at the center of the cross-sectional area of the duct,

$$J^*_{zmax}=\frac{J_{zmax}}{V_t} \quad , \tag{20}$$

was selected as a parameter of the simulation in addition to Eo and M.

4.2 Results and Discussion

Bubbly flow under the condition of Eo=5, logM=–3 and $J_{zmax}^*=0.5$ was analyzed. As one can see from Fig.2, a single bubble in a stagnant liquid takes spherical or ellipsoidal shape when Eo=5 and logM=–3. In the case of air-water bubbly flow in a vertical pipe at room temperature and atmospheric pressure, spherical or ellipsoidal bubble corresponds to a relatively small bubble whose equivalent diameter ranges from 1 to 3mm. It is well-known that these small bubbles are apt to flow near a pipe wall, which results in the so-called wall-peak void distribution[12]. It has been also observed that the wall-peak distribution is enhanced by increasing the liquid flow rate[13].

Calculated time evolution of bubble shape and its distribution is shown in **Figs.7 and 8**. Figure 7 is a top view and Fig.8 is a bird-eye's view. The time t^* in the figures is the nondimensional

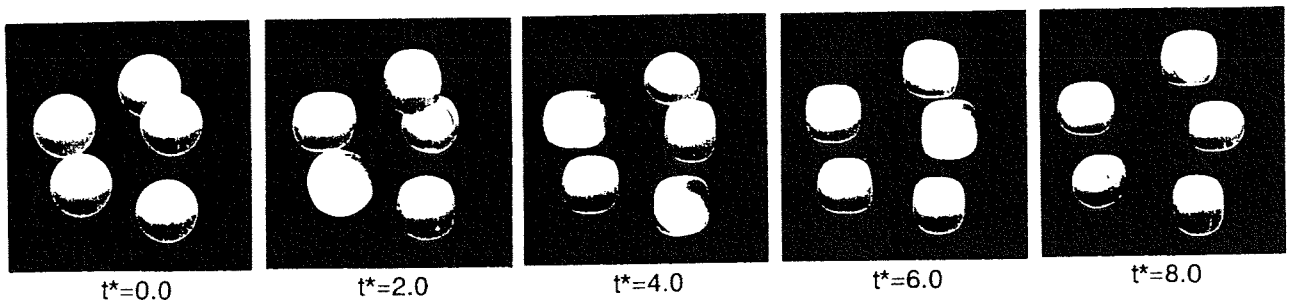

Fig. 7 Top view of calculated bubbly flow : Eo=5, logM=–3, j_{zmax}*=0.5

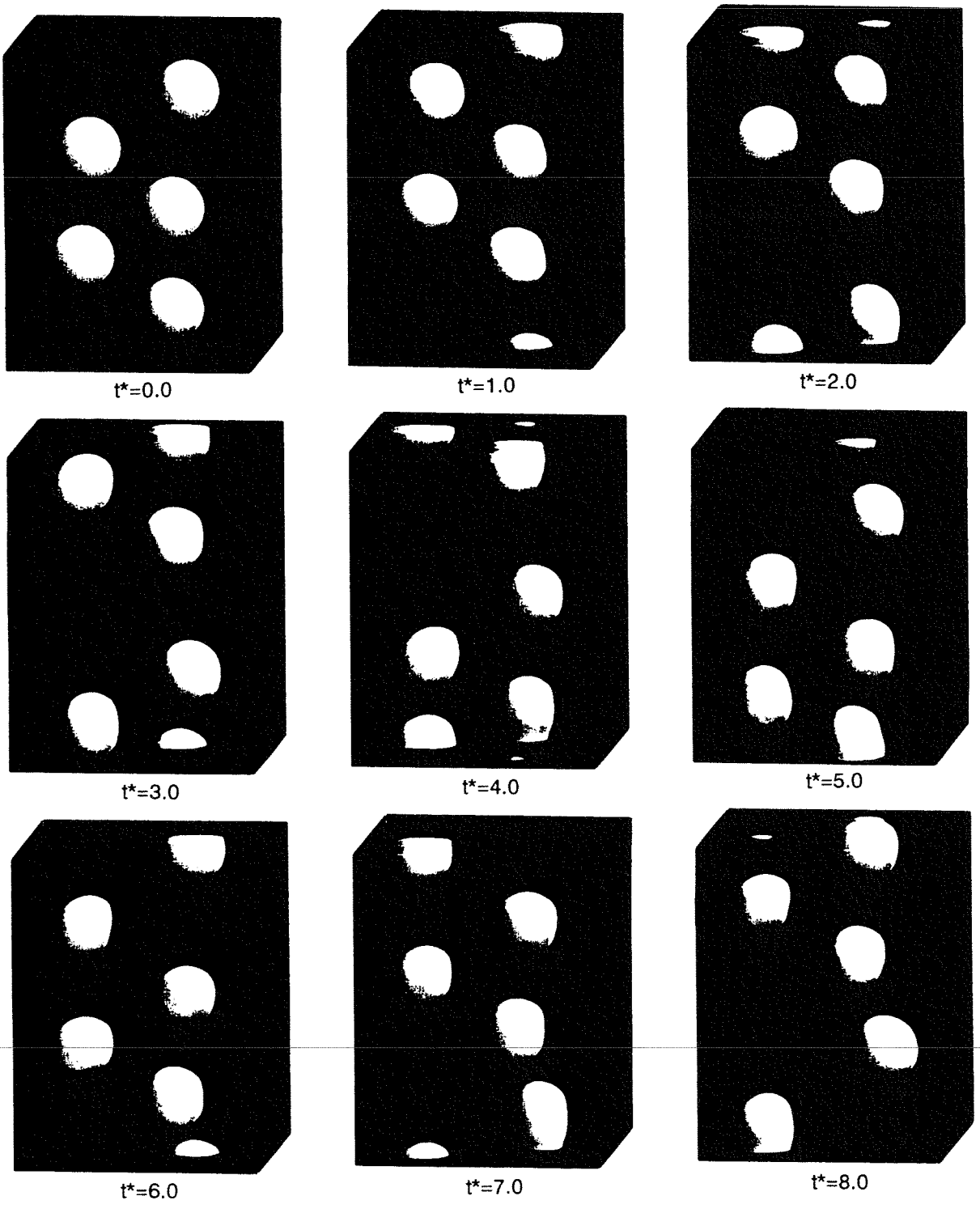

Fig. 8 Bird eye's view of calculated bubbly flow : Eo=5, logM=–3, j_{zmax}*=0.5

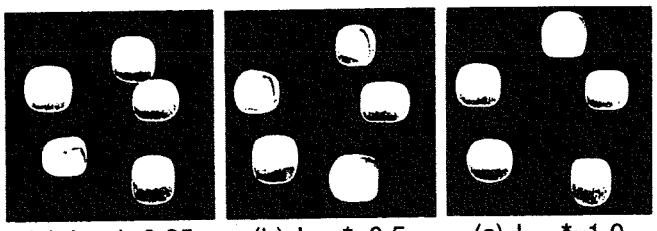

(a) J_{zmax}*=0.25 (b) J_{zmax}*=0.5 (c) J_{zmax}*=1.0

Fig.9 Effect of total volumetric flux on bubble distribution: Eo=5, logM=–3, t*=10

time defined by

$$t^* = \frac{V_t t}{d} . \tag{21}$$

The nondimensional time step size Δt^* for the calculation was 10^{-4} so that the total number of time evolution of this calculation was about 100000. As shown in Fig.7, the bubbles were migrating toward the duct wall and constituted the wall-peak bubble distribution. One can also find that the bubble shape from the top side looks like a square. This square shape was not observed in the previous simulations of a single bubble in an infinite stagnant liquid so that the square shape must be caused by the effect of the duct walls. As the bubbles approached to the pipe wall, they tended to change their shape to ellipsoid having an inclined major axis. This deformation was caused by a large velocity gradient near the duct wall. As a result of the deformation, the projected area of each bubble to the x-y plane decreased. This is the reason why the projected bubble sizes at t*=8 in Fig.7 look somewhat smaller than those at t*=0.

The effect of the total volumetric flux on bubble distribution is shown in **Fig.9 (a),(b) and (c)**. The values of Eo, logM and t* were 5, –3 and 10 for the three cases. Only J_{zmax}* was varied. As shown in this figure, the wall-peak bubble distribution was enhanced by increasing the total volumetric flux. This tendency agreed well with available experimental data on void distribution[13].

Then, another simulation was conducted by increasing the Eötvös number from 5 to 20. The results are shown in **Figs.10 and 11**. When Eo=20 and logM=–3, the shape of a single bubble in a stagnant liquid is ellipsoid or disk. If we consider an air-water bubbly flow in a vertical pipe at room temperature and atmospheric pressure, ellipsoidal or disk-like bubble corresponds to a relatively large bubble whose equivalent diameter is larger than 4 - 5mm. In this case, the bubbles tend to flow near the center of the pipe and form the so-called core-peak void distribution[12]. As shown in Fig.10, the calculated bubbles also formed the core-peak bubble distribution. In addition, Fig.11 clearly shows the process of bubble deformation from spherical shape to wing-like shape due to the liquid velocity gradient. This deformation process and the lateral migration toward higher liquid velocity region agreed well with Kariyasaki's experimental data[14] on a lateral migration of a single bubble in a linear shear field. He observed using viscous liquid and air that the bubble in a linear shear field deformed to wing-like shape and migrated to higher liquid velocity region. **Figure 12** shows the effect of the total volumetric flux on bubble distribution when Eo=20. Although it is not so obvious as Fig.9, the core-peak distribution was slightly enhanced by increasing J_{zmax}*.

Consequently, we could demonstrate that the two typical distributions, the wall-peak and core-peak bubble distributions, can be obtained from the three-dimensional local-instantaneous field equations of the gas-liquid two-phase flow.

5. CONCLUSIONS

A three-dimensional detailed numerical simulation of bubbly flow in a vertical square duct was conducted in the present study. The simulation was based on the local-instantaneous field equations of the gas-liquid two-phase flow, the interface tracking technique of the volume of fluid method and the modified SOLA method. As a result, the following conclusions were obtained:

(1)The present numerical method could give good predictions for the terminal rising velocity and shape of a single bubble in an infinite stagnant liquid under a wide range of the Eötvös and Morton numbers, i.e., $1.41 \le Eo \le 641$ and $-6.9 \le \log M \le 2.9$.

(2)The simulation of laminar bubbly flow in a vertical duct was realized by making use of a periodic

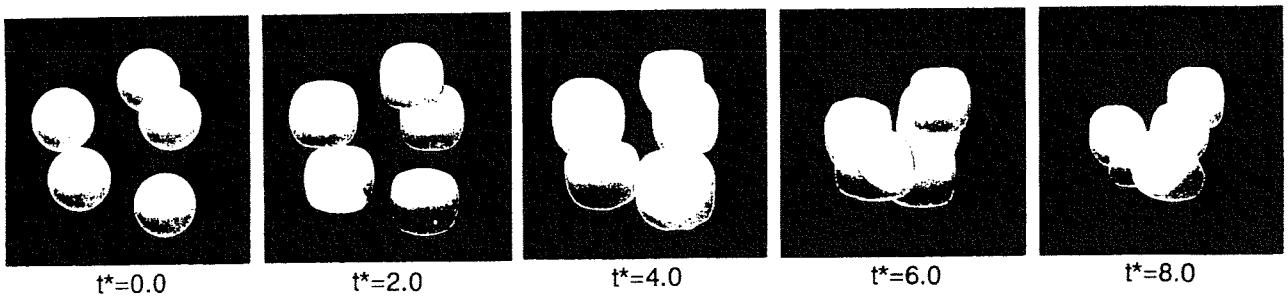

Fig. 10 Top view of calculated bubbly flow : Eo=20, logM=–3, j_{zmax}*=0.5

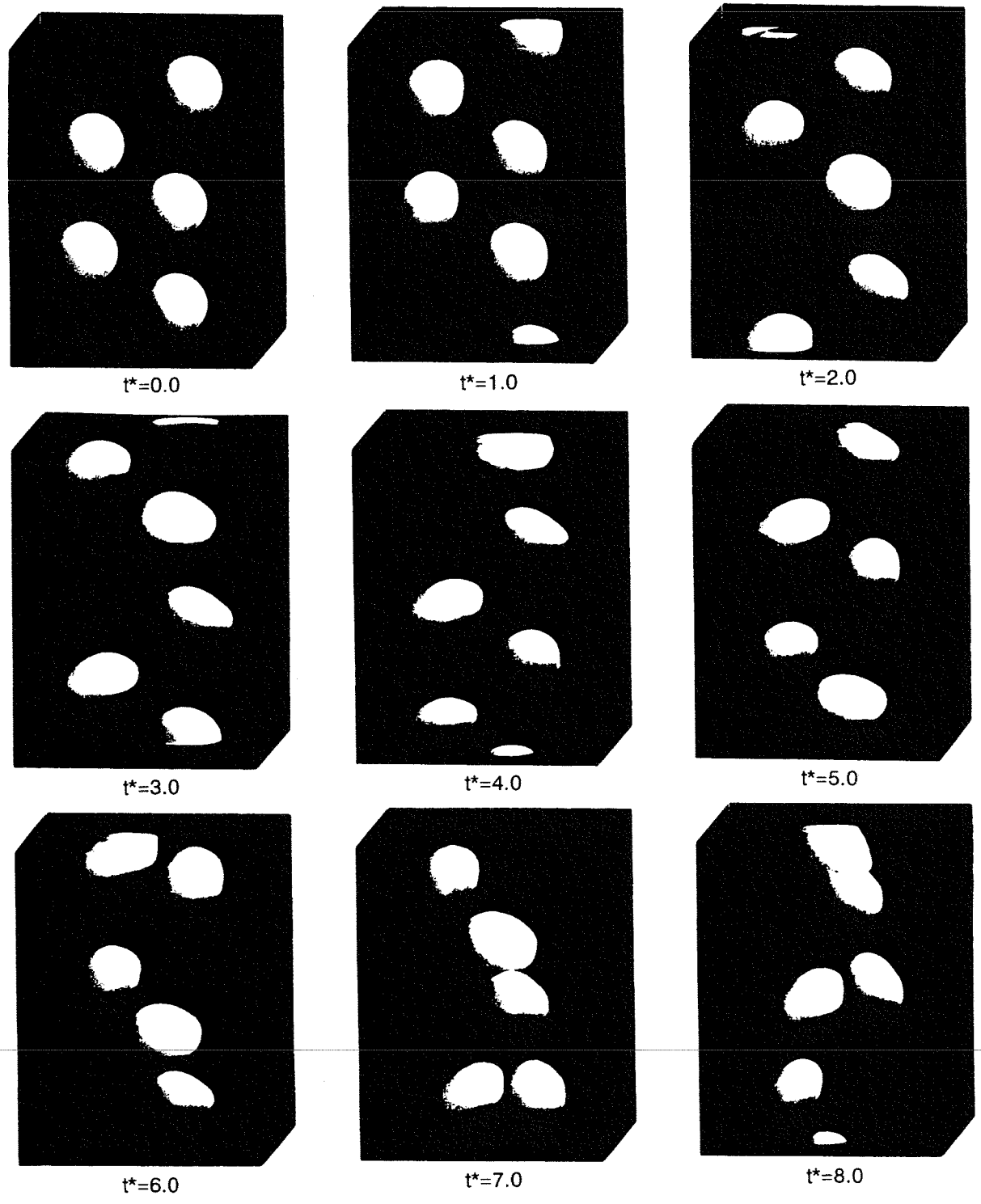

Fig. 11 Bird eye's view of calculated bubbly flow : Eo=20, logM=–3, j_{zmax}*=0.5

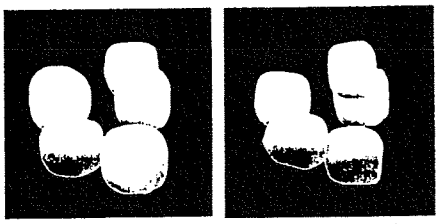

(a) J_{zmax}*=0.5 (b) J_{zmax}*=1.0

Fig.12 Effect of total volumetric flux on bubble distribution: Eo=20, logM=–3, t*=4

boundary condition and an initial pressure distribution which took into account the effect of gravity and wall friction of the two-phase flow.
(3)When the surface tension was high (Eo=5), the wall-peak bubble distribution was obtained by the simulation. On the other hand, the core-peak distribution was formed when the surface tension was low (Eo=20). In addition, each distribution was enhanced by increasing the total volumetric flux. These tendencies on the bubble distribution were in good agreement with available experimental data.

ACKNOWLEDGMENT

The authors wish to express their sincere thanks to Mr. H.Yoshikawa and Mr. A. Toyooka of Kozo Keikaku Engineering Inc. in Tokyo and Mr. V. Alkalaj of Slovene Supercomputing Center, Jozef Stefan Institute, Ljubljana for their kind supports to the present numerical simulation.

NOMENCLATURE

d : equivalent bubble diameter [m]
F : liquid volumetric fraction in a cell [-]
g : body force per unit mass [N/kg]
J : volumetric flux [m/s]
L : width of a square duct [m]
p : pressure [Pa]
Re : bubble Reynolds number [-]
t : time [s]
V_t : terminal rising velocity of a bubble [m/s]
x : a Cartesian coordinate
z : a Cartesian coordinate
Eo : Eötvös number [-]
$\mathbf{f}_S$: force due to surface tension [N/m^3]
h : height of interface in a cell [m]
J : volumetric flux vector [m/s]
M : Morton number [-]
p_S : pressure due to surface tension [Pa]
S : vector of surface element [m^2]
V : velocity [m/s]
V : velocity vector [m/s]
y : a Cartesian coordinate

Greek Symbols

Δt : time step [s]
Δy : cell width in the y direction [m]
Φ^2 : two-phase friction multiplier [-]
μ : viscosity [kg/ms]
σ : surface tension [N/m]
Δx : cell width in the x direction [m]
Δz : cell width in the z direction [m]
κ : curvature of gas-liquid interface [1/m]
ρ : density [kg/m^3]

Subscripts

G : gas phase
L : liquid phase
k : gas or liquid phase

Superscripts

* : dimensionless quantity

REFERENCES

[1] J.M. Delhaye, M. Giot and M.L. Riethmuller: "Thermohydraulics of Two-Phase Systems for Industrial Design and Nuclear Engineering", McGraw-Hill (1981).
[2] A. Tomiyama, A. Sou, H. Minagawa and T. Sakaguchi, "Numerical Analysis of a Single Bubble by VOF Method", in: Trans. JSME, 57, 539, p.1 (1991), in Japanese and reproduced in: JSME Int. J., 36, 1, p.51 (1993).
[3] A. Tomiyama, I. Zun, A. Sou and T. Sakaguchi, "Numerical Analysis of Bubble Motion with the VOF Method", in: Nucl. Eng. Des., 141, p.69 (1993).
[4] A. Tomiyama, A. Sou and T. Sakaguchi, "Numerical Simulation of a Taylor Bubble in a Stagnant Liquid", published in: Proc. Int. Symposium on Numerical Methods in Multiphase Flows, Nevada in USA, June, (1994).
[5] A. Sou, A. Tomiyama and T. Sakaguchi, "Numerical Simulation of Interaction between Deformable Bubble and Continuous Liquid Phase in Two-Dimensional Bubbly Flow", to be published in: Proc. 1st Int. Conf. on Flow Interaction, Hong Kong, Sept. (1994).
[6] C.W. Hirt and B.D. Nichols, "Volume of Fluid (VOF) method for the dynamics of free boundaries", in: J. Comp. Phys., 39, p.201 (1981).
[7] A. Tomiyama and M. Hirano, "An Improvement of the Computational Efficiency of the SOLA Method", in: Trans. JSME, 58, 551, p.2171 (1992), in Japanese, and to be published in: JSME Int. J., (1994).
[8] C. Adachi: "Differential Geometry", Baifu Pub. Company, (1976), in Japanese.
[9] C.W. Hirt, B.D. Nichols and N.C. Romero, " "SOLA" A Numerical Solution Algorithm for Transient Fluid Flows", LA-5852, (1975).
[10] J.R. Grace, "Shapes and Velocities of Bubbles Rising in Infinite Liquids", in: Trans. Inst. Chem. Eng., 51, p.116 (1973).
[11] D. Bhaga and M.E. Weber, "Bubbles in Viscous Liquids : Shapes, Wakes and Velocities", in: J. Fluid Mech., 105, p.61 (1981).
[12] A. Serizawa and I. Kataoka, "Phase Distribution in Two-Phase Flow", in: Proc. ICHMT Int. Seminar on Transient Phenomena in Multiphase Flow, Dubrovnik, Yugoslavia, p.179 (1987).
[13] T.J. Liu, "Bubble Size and Entrance Length Effects on Void Development in a Vertical Channel", in: Int. J. Multiphase Flow, 19, 1, p.99 (1993).
[14] A. Kariyasaki, "Behavior of a Gas Bubble in a Linear Shear Flow", in: Proc. 6th Two-Phase Flow Symposium of Japan, p.49 (1985), in Japanese.

THREE DIMENSIONAL DEFORMATION OF A RISING BUBBLE

Shu Takagi and Yoichiro Matsumoto

Dept. of Mech. Eng., The University of Tokyo
Hongo 7-3-1,Bunkyo-ku, Tokyo 113,JAPAN

ABSTRACT

The numerical method is developed to solve the three dimensional unsteady flow with a free surface . The basic equations are formulated by the physical components of the contravariant velocity with a boundary fitted coordinate system. This method is applied to solve the rising bubble in a quiescent liquid and in a simple shear flow. The density of the gas is assumed to be zero as a limit case of the high density ratio of the liquid and gas. From the experimental observation, it is known that the bubble rising through a quiescent liquid starts showing the unsteady 3-D(spiral or zigzag) motion beyond the critical Reynolds and Weber numbers. In the present study, the calculations are performed for these conditions and the 3-D motions are simulated. The numerical results show that axisymmetric unsteady motion occurs when the bubble shape is upward curved. And the three dimensional deformation of a rising bubble is caused by the asymmetric separation behind the bubble which is developed after the axisymmetric unsteady motion. It is reported by Kariyazaki[1] experimentally that the rising bubble in the shear flow moves in the different directions compared with a solid sphere, which means that the bubble moves in the lower slip velocity region although the solid particle moves in the higher one. Our numerical results reveal that this phenomenon is observed when the bubble deformation is relatively large and that the nearly spherical bubble moves in the same direction of the solid particle.

1. INTRODUCTION

It is known experimentally(Hartunian & Sears[2], Tsuge and Hibino[3]) that the rising bubble in a quiescent liquid changes its motion from axisymmetric to three dimensional(spiral or zigzag) beyond some critical Reynolds and Weber number. It is also known experimentally (Kariyazaki[1]) that the bubble rising through the simple shear flow moves in the different direction compared to the solid particle. Although there are many experimental studies for the unsteady motion of the rising bubble, there are few numerical calculations for the three dimensional motion of the rising bubble in the case of the high density ratio of the liquid and gas. Unverdi & Trygvasson[4] and Tomiyama et al.[5] have obtained a lot of results about the rising bubble by solving the both liquid and gas phases. But these methods are valid only for the low density ratio of O(10), and it is not clear how much accuracy they are keeping for the unsteady motion of the general gas bubble in the liquid which has O(1000) density ratio. Therefore our main purpose is to analyze the unsteady motion of the bubble which has the high density ratio.

It can be assumed that the gas-liquid interface is a free surface, if the density ratio is sufficiently large like the air-water one. In that case, the surface of the bubble is essentially different from that of the solid particle as a source of the vorticity generation. The zero tangential stress condition will be imposed on the bubble surface and the non-slip condition is on the solid particle. Because of this, the order of the vorticity generated on the bubble surface is different from that of the solid particle. The vorticity in the boundary layer is O(1) for the bubble and $O(1/\delta)$ for the solid particle. Here δ is the

boundary layer thickness. As a result, the separation and the vortex shedding which is observed behind the solid particle doesn't exist for the spherical bubble, even though the Reynolds number is very large. The separation behind the bubble strongly depend on the curvature of the surface, and the separation occurs only when the bubble is largely deformed. For example, considering the axisymmetric deformed bubble, the vorticity on the bubble surface is expressed as follows by the tangential velocity(u_ξ) and the surface curvature(κ_ξ) on the axisymmetric plane. (see Ryskin & Leal[6])

$$\omega = 2\kappa_\xi u_\xi \ , \quad \text{where } \xi \text{ is the direction along the surface} \tag{1}$$

From this equation, we can see that the vorticity on the free surface is related to the curvature of the surface.

Another important difference of the bubbles from the particles is the deformation. The bubble deforms to keep the normal stress condition on the surface which includes the surface tension effect. Therefore the bubble shape is decided as a part of the solution of the flow field and this makes the things complicated to treat numerically. The surface tension is the important factor to decide the bubble shape after the initial accelerating stage. Again it is noted that the curvature of the surface is important because the surface tension is proportional to the mean curvature.

As is discussed above, the vorticity on the bubble surface which is calculated from zero tangential stress condition and the surface tension is related to the curvature of the surface. Therefore we have concluded that the more accurate solution can be obtained by increasing the accuracy to calculate the curvature of the surface. Since the theory to treat the curvature of the space is the "Riemannian Geometry", we take the approach to introduce this theory to solve the flow field and in the present study we develop the numerical method to solve the three dimensional free surface flow. The physical components of the contravariant velocity are used as the variables, and the method is applied to analyze the interesting behavior of the three dimensional rising bubble. In addition the special iteration technique for the boundary condition are used to stabilize the solution.

2.ASSUMPTION

The following assumptions are used for the calculation.

(1) The surface tension coefficient of the gas-liquid interface is constant. Therefore, the liquid is assumed to be free of impurities and surfactants.
(2) The liquid phase is the incompressible Newtonian fluid.
(3) The density and viscosity of the liquid phase is sufficiently large compared with those of the gas. So the dynamic pressure and viscous stress of the gas phase is negligible compared with those of the liquid.
(4) The volume of the rising bubble is constant. In the real situation, the rising bubble changes its volume slightly because of the existence of the static pressure gradient. But this will be quite small for the gas bubble rising under atmospheric pressure.

Since our purpose is to simulate the unsteady motion of the gas bubble rising through the liquid which has the high density ratio of O(1000), these are the quite reasonable assumptions .
And with the similar assumptions, Ryskin & Leal[6] and Takagi[7] got very good agreement with the experiment, though their calculations are only for the axisymmetric steady cases.

3.SOLUTION ALGORITHM

The generalized curvilinear coordinate system is used with the unsteady grid movement. So the grid is regenerated at each time step. The solution algorithm is briefly shown here and the detailed one later.

(1) Generate the 3-D grid by expanding the 2-D grid around the axis as shown in Fig.1.
(2) Solve the flow field with the proper boundary condition under the generated grid.
(The velocity of the surface is calculated in this process.)
(3) Move the grid point on the bubble surface by the calculated velocity and decide the shape of the bubble at the new time step.
(4) Repeat the process (1)~(3) with the time development.

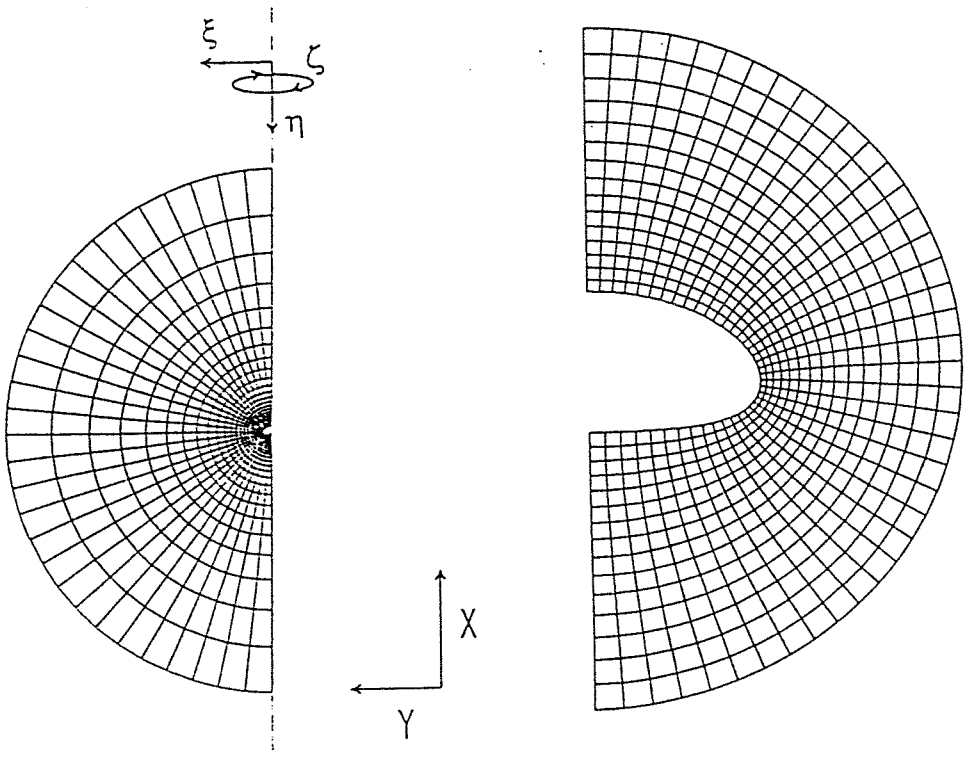

Fig.1 Coordinate System & the Grid near the Bubble

4.DETAILS OF THE SOLUTION ALGORITHM

4-1 Grid Generation

Three dimensional grid is generated by the connection of the two dimensional grid as is explained above. The way of generating the two dimensional grid is the one developed by Duraiswami and Prosperetti[8]. They developed the method to generate the orthogonal grid system. Since our numerical solver doesn't require the orthogonality of the grid, we use the same method without strictly keeping orthogonality and with keeping coincident of the point on the axis. The Laplace equation which is used to generate the grid is as follows.

$$\frac{\partial}{\partial \xi}\left(f\frac{\partial x}{\partial \xi}\right)+\frac{\partial}{\partial \eta}\left(\frac{1}{f}\frac{\partial x}{\partial \eta}\right)=0\ , \qquad (2)$$

The same equation is used for the y direction. The function "f" is called the distortion function and is used to control over the density of the grid. In the present study the distortion function is decided to have more grid points near the surface. This is corresponding to the fact that "f" takes a relatively bigger value near the surface. And the new grid is calculated by Eq(2) at each time step from the former grid data.

4-2 Basic Equations

Since the liquid phase is assumed to be Newtonian and incompressible, three dimensional full Navier-Stokes equation is solved by SIMPLER method. As is mentioned in Introduction, we introduce the contravariant velocity to utilize the theory of Riemaniann Geometry. In general, the contravariant velocity is defined as follows.

$$u^i = \frac{\partial \xi^i}{\partial x^j} v^j \quad , \text{ where } v^j \text{ is the Cartesian Components} \tag{3}$$

These are the mathematical components of the contravariant velocity. Since the transformation matrix is not necessary nondimensional, the magnitude of the contravariant velocity is not always the same as that of the velocity in the physical space. Here the conservation low in the physical curvilinear space is considered and the physical components of the cotravariant velocity is used as the variables. To avoid the numerical instability which is caused by the grid density difference, Koshizuka[9] suggested using the physical components. We define the physical components of the contravariant velocity as follows.

$$u(i) = \frac{u^i}{\sqrt{g^{ii}}} = \frac{1}{\sqrt{g^{ii}}} \frac{\partial \xi^i}{\partial x^j} v^j \quad , \tag{4}$$

where $\sqrt{g^{ii}}$ is the scale factor, which is constructed from the diagonal components of the contravariant metric tensor. In general, the physical components of the contravariant velocity are defined as $u(i) = \sqrt{g_{ii}}\, u^i$, where g_{ii} is the diagonal components of the covariant metric tensor. These two definitions are the same in the orthogonal curvilinear coordinate system. Koshizuka[9] is using this definition following the tensor analysis textbook. We take the other kind of definition, considering the normalization of the contravariant base vector.

With these definition, the Navier-Stokes equation and all the other equations are written by the physical components of the contravariant vector. Since the contravariant velocity in the generalized coordinate system is used here, the partial derivative with respect to the space is not $\frac{\partial u^i}{\partial \xi^j}$. It is defined as the covariant derivative, which is shown below expressed by the mathematical component.

$$u^i_{,j} = \frac{\partial u^i}{\partial x_j} + \Gamma^i_{jk} u^k \quad , \quad \text{where } \Gamma^i_{jk} = \frac{1}{2} g^{il} \left(\frac{\partial g_{kl}}{\partial \xi^j} + \frac{\partial g_{jl}}{\partial \xi^k} - \frac{\partial g_{jk}}{\partial \xi^l} \right) \tag{5}$$

Γ^i_{jk} is called the Christoffel symbol of the second kind and it is related to the curvature of the space. By using these operators and with some other knowledge of the Riemannian Geometry, the Navier-Stokes equation which is used for the descritization is written as Eq.(6). The equation has a rather complicated form, firstly because the physical components are used. Secondly it is modified to be suitable for the SIMPLER algorithm.

$$\begin{aligned} \rho \frac{\partial}{\partial \xi^j} \left[J \sqrt{g^{jj}} \left(u(j) u(i) - \mu \frac{\partial u(i)}{\partial \xi^j} \right) \right] = & -\rho \frac{\partial u(i)}{\partial t} - J \frac{\sqrt{g^{jj}}}{\sqrt{g^{ii}}} \frac{\partial \sqrt{g^{ii}}}{\partial \xi^j} \rho u(j) u(i) - J \frac{1}{\sqrt{g^{ii}}} \Gamma^i_{jk} \sqrt{g^{jj}} \sqrt{g^{kk}} \rho u(j) u(k) \\ & + J F^i - J g^{ij} \frac{\partial p}{\partial \xi^j} - \mu \frac{\partial}{\partial \xi^j} [J g^{il} g^{jm} \{ \frac{\partial}{\partial \xi^l} (g_{mk} \sqrt{g^{kk}}\, u(k)) - \frac{\partial}{\partial \xi^m} (g_{lk} \sqrt{g^{kk}}\, u(k)) \}] \\ & - \mu \frac{\partial}{\partial \xi^j} [J \sqrt{g^{jj}} \frac{\partial u(i)}{\partial \xi^j}] \end{aligned} \tag{6}$$

$$\text{where,} \quad \frac{\partial (u(i))}{\partial t} = \frac{\partial (u(i))}{\partial \tau} - \frac{\partial x^j}{\partial \tau} \frac{1}{\sqrt{g^{ii}}} \frac{\partial \xi^i}{\partial x^k} \frac{\partial \xi^l}{\partial x^j} \frac{\partial v^k}{\partial \xi^l} \quad (\tau\text{: time in calculation space}) \tag{7}$$

J : Jacobian , g^{ij} :contravariant metric tensor , g_{ij} : covariant metric tensor

The stabilized central difference scheme is used to the convective term. Here, we have grid movements in the physical space with the time development and the extra term which is related to the

grid movement is added to the time derivative term in the calculation space. Since we use the contravariant velocity field, this term is defined by the material derivative on the differential manifold and its expression becomes very complicated. But in the Cartesian velocity field, this term can be expressed in a simple manner compared with the contravariant one. Hence, we treat this term by calculating the Cartesian component and transforming it to the contravariant one.

4-3Boundary Condition and Initial Condition

In the present study, the bubble surface is assumed to be a free boundary and the zero tangential stress condition is imposed on it. There are several combinations of the boundary conditions with the variables which is calculated on the surface. Here the two tangential velocity component is calculated from the zero tangential stress condition on the bubble surface. The normal velocity component is calculated from the normal stress condition. And the pressure inside the bubble (p_0) is decided to keep the volume constant. Though we tried some of the other combinations, only this one gave us the stable solution for the rising bubble problem.

In the present method, the treatment of the normal stress condition is extremely important. And without the following iteration technique, we could not get the stable solution for high Reynolds number cases, even though the usual under-relaxation technique is used. For simplicity, we will discuss this technique with the orthogonal curvilinear coordinates, though the actual method is valid also for the nonorthogonal one. The condition of the normal stress balance is expressed as follows.

$$-p + 2\mu e_{22} = -p_0 + T\,, \tag{8}$$

where $$e_{22} = \frac{1}{h_2}\frac{\partial u_{(2)}}{\partial \xi_2} + \frac{u_{(1)}}{h_1 h_2}\frac{\partial h_2}{\partial \xi_1}\,, \quad (h_i = \sqrt{g_{ii}} = \frac{1}{\sqrt{g^{ii}}}\text{: scale factor}), \tag{9}$$

and the surface tension T is defined as follows.

$$T = \sigma(\kappa_1 + \kappa_2) = \sigma\,(G\cdot L + E\cdot N - 2F\cdot M)/(E\cdot G - F^2), \tag{10}$$

where $E = \vec{r}_\xi^{\,2}$, $F = \vec{r}_\xi \cdot \vec{r}_\varsigma$, $G = \vec{r}_\varsigma^{\,2}$, $L = \vec{r}_{\xi\xi}\cdot\vec{n}$, $M = \vec{r}_{\xi\varsigma}\cdot\vec{n}$, $N = \vec{r}_{\varsigma\varsigma}\cdot\vec{n}$,

σ : surface tension , κ_1, κ_2: principal curvature , $\vec{n}$: normal vector on the surface

It is noted that the normal velocity component $u_{(2)}$ is calculated from Eq.(8) through the first term of the right hand side of Eq.(9). In general, it is because the ratio of the pressure and the normal viscous force is large that the numerical instability occurs. That is to say, if the viscosity is small, the small pressure changes during the iteration causes the big changes of the normal velocity (u_2) which is calculated from Eqs.(8), (9), and finally it makes the solution diverge. From this point of view, the change of the normal viscous stress and the pressure should be balanced within the same order during the iteration. To satisfy this requirement, the following formula is used to calculate the normal velocity component.

$$-p + 2\mu e_{22} + \frac{2}{h_2}\frac{\partial u_{(2)}}{\partial \xi_2} = -p_0 + T + \frac{2}{h_2}\frac{\partial u_{(2)}}{\partial \xi_2} \tag{11}$$

Here($\frac{2}{h_2}\frac{\partial u_{(2)}}{\partial \xi_2}$) is a kind of relaxation parameter to make the order of the pressure and the viscous force same. By doing this, the solution can be stabilized extremely.

The pressure inside the bubble (p_0) is decided as follows. Discretizing the Eq.(11), the normal velocity on the bubble surface(u_{2s}) is given by the linear equation of the p_0.

$$u_{2s} = Ap_0 + B\,: \quad \text{here A and B are not the function of } p_0 \tag{12}$$

To keep the bubble volume constant, the total flux from the surface is set to be zero, by integrating this normal velocity all over the surface. Therefore $\int_S u_{2s} ds = \Sigma\, u_{2s\,i,j,k}\cdot \Delta S_{i,j,k} = 0$ is the constraint to keep the volume constant, and using the expression of Eq.(12) the pressure p_0 is

calculated as $p_0 = \frac{\sum(B\,\Delta S)_{i,j,k}}{\sum(A\,\Delta S)_{i,j,k}}$. The bubble volume is kept constant by the calculated pressure(p_0) theoretically . But there exists the small numerical error of the volume changing, which is the $O(10^{-4})$ at each time step. The accumulation of this error is not negligible after a several hundred time steps. To avoid this accumulation, the bubble volume is very slightly modified to the initial bubble volume by the following equations.

$$y_s = y_s \times \sqrt{\frac{(initial\ volume)}{(current\ volume)}} \quad , \quad z_s = z_s \times \sqrt{\frac{(initial\ volume)}{(current\ volume)}} \tag{13}$$

With these procedures mentioned above, the velocity components on the surface are calculated and the bubble shape is changed by moving the grid point on the surface in Lagrangian way. After the movement of the surface grid, the new grid is generated by using cubic spline on the boundary.

The boundary condition at the far-field is given for the quiescent liquid and for the simple shear flow which has the constant velocity gradient normal to the gravity direction. In the quiescent liquid case, the zero velocity condition is imposed as the boundary condition at the far-field. In the shear flow case, since the gravity is acting in x-direction in this calculation, $v_x = -\Omega y$ is imposed as a boundary condition at the far-field. Here v_x is the Cartesian velocity component in x-direction. The contravariant velocity components are calculated from this condition and are used as the boundary condition at far-field. Now $\Omega = 0.1$ is given , which is corresponding to the relatively weak shear compared to the rising velocity of the bubble.

The bubble is initially spherical of the unit length radius and is released in the quiescent liquid with zero velocity. For the shear flow, the steady state solution of the spherical bubble of zero rising velocity is calculated firstly and it is used as a initial condition.

5.Numerical Results and Discussions

5-1 Quiescent Liquid Case

The typical numerical result is shown in Fig. 2. From the experimental results(Clift et al.), it is known that the bubble keeps a steady axisymmetric shape in the range of Re<O(50). The result in Fig.2 is in that range, and it reaches to the nearly steady state after t=5.0. The nearly steady state shape and the flow field around the bubble is compared with the experiment in Fig. 3. This is the case of the Morton number ($M = g\mu^4/\rho\sigma^3$) = 0.065, and the Eotvos number ($E_o = g\rho d_e^2/\sigma$) = 39.4. The Morton number is the one nondimensionalized by the material property. And Eotvos number is the ratio of the gravitational force and the capillary force. For the steady state of the rising bubble, these two numbers are the good criteria to analize the phenomena as is discussed by Clift et al. Good agreement is obtained about the shape and the velocity field around the bubble.

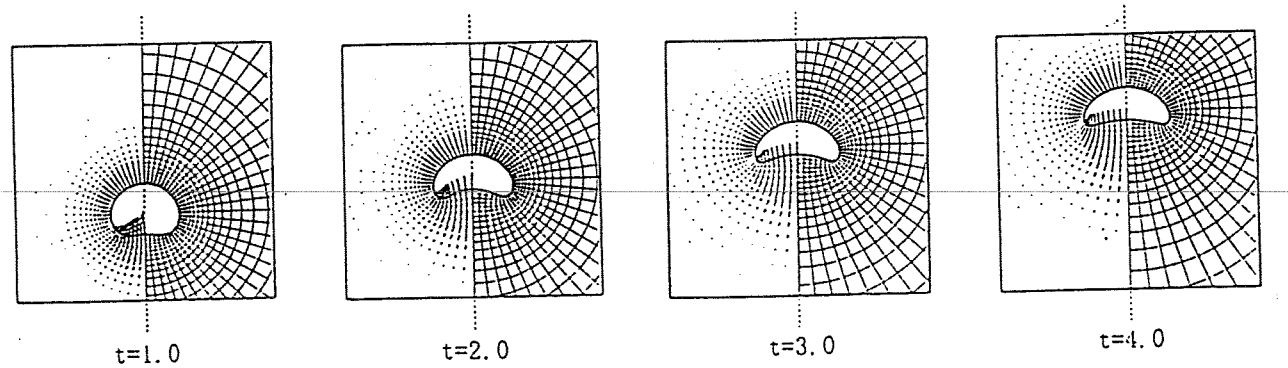

Fig.2 Numerical Result of M=0.065, Eo=39.4

The experiments of Hartunian & Sears[2] and Tsuge & Hibino[3] are famous for the three dimensional (zigzag , spiral) motion of the bubble rising through the quiescent liquid. Hartunial et al. suggested that the bubble starts showing three dimensional unsteady motion over the critical Reynolds number 202 and critical Weber number 3.18. But Tsuge et al. made the farther research and they found that critical Reynolds number 202 is the case that the liquid implies impurities. And they gave the following relations about the critical Reynolds number, critical Weber number and the Morton number.

$$Re_c = 9.0M^{-0.173} \quad , \quad We_c = 21.5Re_c^{-0.32} \quad (14)$$

In the present study, we made the calculation in the following two cases to simulate the three dimensional motion.

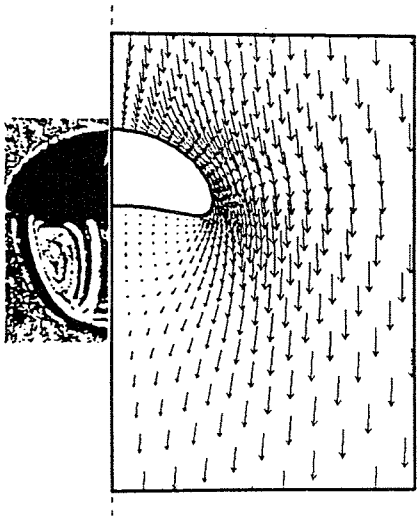

Fig.3 Comparison with Experiment
(Photo: Hnat & Buckmaster[12])

$$\text{Case1: } M = 3.84 \times 10^{-7},\ E_o = 9.6 \quad , \quad \text{Case2: } M = 1.77 \times 10^{-8},\ E_o = 1.77 \quad (15)$$

With these conditions, the steady state solutions of Ryskin & Leal[6] give the values of Re=200, We=8 (case 1) and Re=200,We=4 (case 2) . By using the formula(14) for calculating the critical Reynolds number(hereafter Rec) and critical Weber number(Wec), we get the Rec=116,Wec=4.70 for Case 1 and Rec=197,Wec=3.96 for Case2. Therefore, considering the error of the experimental data, it can be said that Case 1 is for the three dimensional motion and that Case 2 has two possibilities of axisymmetric and three dimensional.

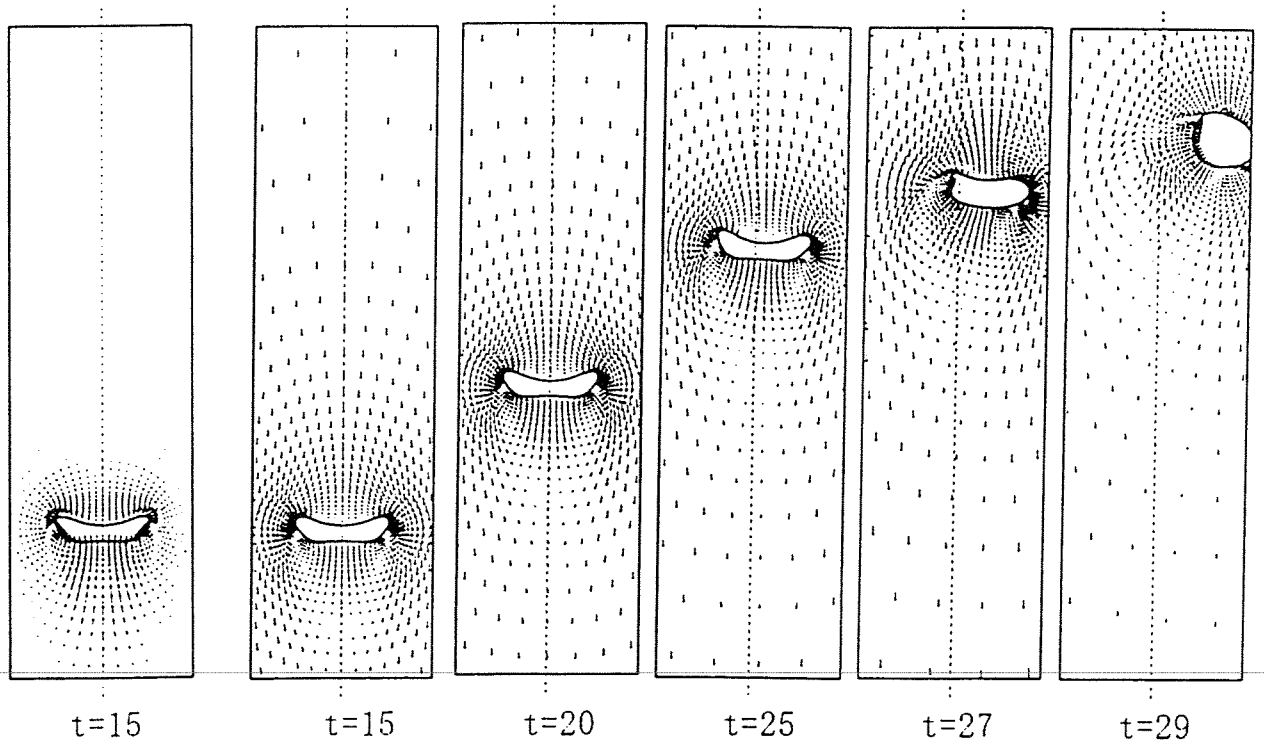

Fig.4 Motion of the Rising Bubble (Case 1)

First, the numerical results of Case1 are shown in Fig. 4 ~Fig. 6. Fig.7 shows the trajectories of the gravity center. From Fig. 4 and Fig. 7 , it is seen that the three dimensional motion occurs after t=20. The first figure of the left side in Fig.4 , which is about time t=15, is the calculated velocity field and the other figures are the relative velocity field subtracted by the rising velocity of the bubble. The numerical results are shown on the two dimensional plane where the asymmetric motion occurs. Some of the three dimensional bubble shapes are shown in Fig.5, and the flow fields around the bubble after the 3-D motion occurs are shown in Fig.6. Here, the time is nondimensionalized by the bubble radius and the terminal velocity which is calculated from the steady states solution of Ryskin & Leal. And the rising velocity of our calculation is nondimensionalised by their terminal velocity. So our solution has a same terminal velocity as Ryskin & Leal if the terminal velocity is 1.0. In Case2, the bubble keeps axisymmetric shape and the three dimensional motion didn't occur in this calculation, as shown in Fig.7 by the trajectories of the gravity center. The bubble shape in the nearly steady state is shown in Fig.8. The rising velocity of the gravity center is shown in Fig.9. Good agreement with Ryskin & Leal [6] is obtained for the terminal velocity in Case2. From the result of Case1 in this figure, it is found that there exists an axisymmetric oscillatory motion before the 3-D motion occurs. This motion is a periodic one and it has a strong relation with the bubble shapes. The bubble shape is also oscillating between the ellipsoidal shape and the upward curved shape with the same frequency. But once asymmetric motion occurs, this oscillating motion vanishes and the 3-D unsteady motion(zigzag motion) begins. The rising velocity in the gravity direction starts decreasing after that and remains almost constant with the small acceleration as shown in Fig.9. But there is no oscillation of the rising velocity in Case2. In this case, the bubble shape is nearly ellipsoidal and the upward curved shape doesn't exist. Therefore, the axisymmetric shape oscillation which causes the periodic fluctuation of the rising velocity is thought to be the important factor for the asymmetric three dimensional motion.

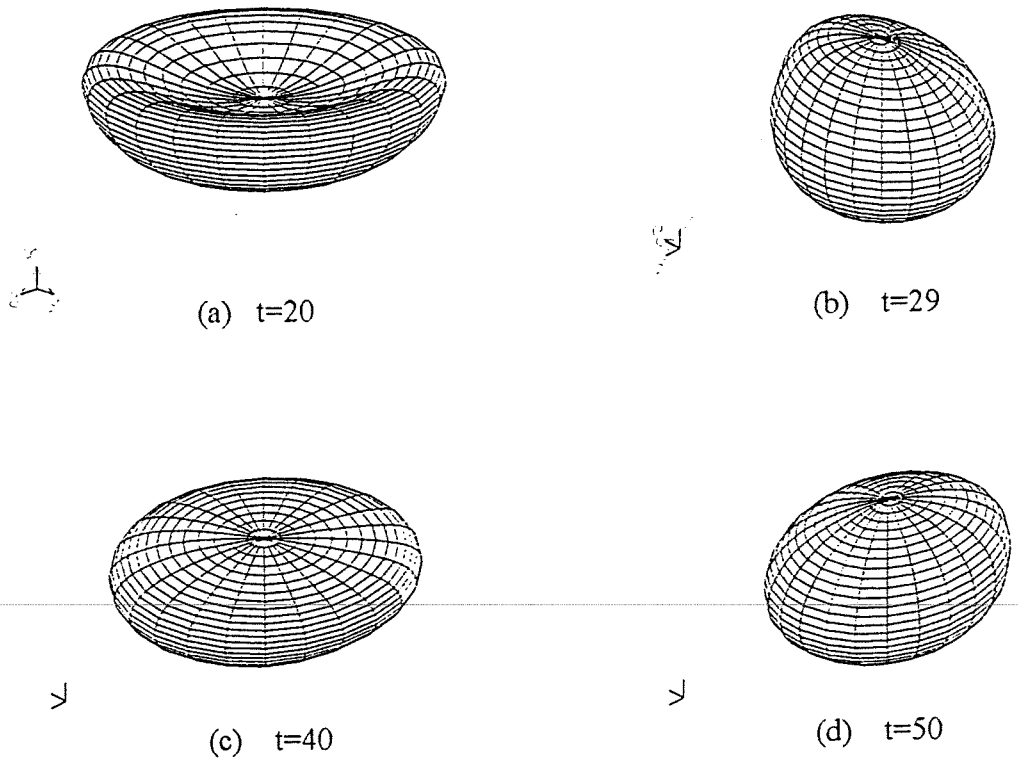

Fig.5 Three Dimensional Bubble Shape (Case1)

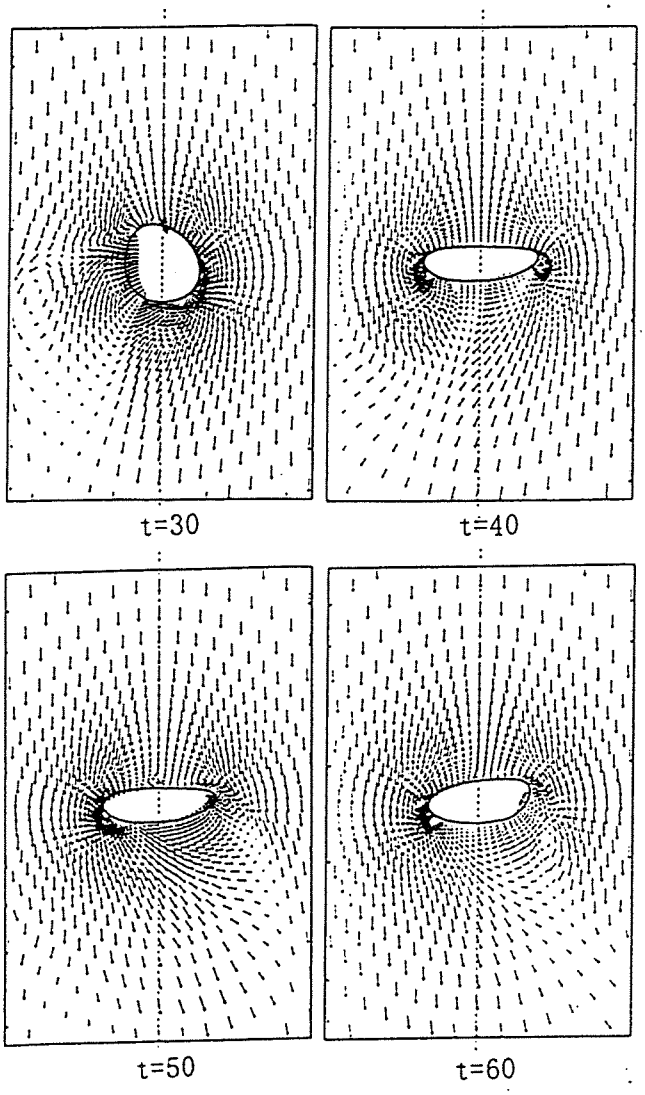

Fig.6 3-D motion of the bubble (Case1)

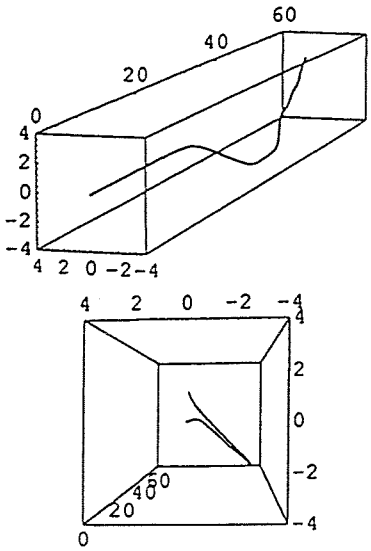

(a) Case 1

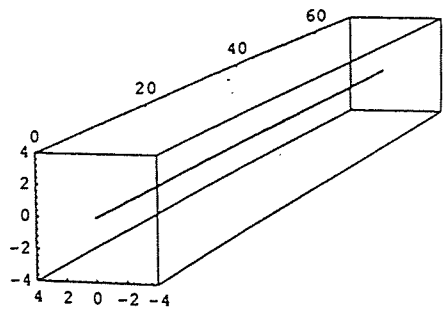

(b) Case2

Fig.7 Trajectories of the Gravity Center

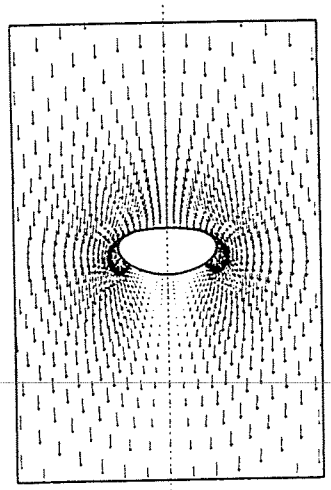

Fig.8 Bubble Shape (Case 2 : t=60)

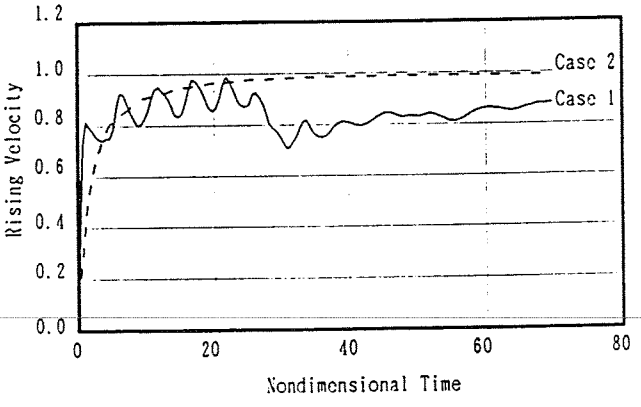

Fig.9 Rising Velocity of the Bubble

(2) Shear Flow Case

Kariyazaki[1] reported by the experiment that the rising bubble in the simple shear flow which has a constant velocity gradient at the far-field feels the opposite lift force compared with the solid sphere because of the deformation effect. Tomiyama et al. also got the same tendency numerically for the two dimensional bubble. Here, we have calculated the three dimensional unsteady motion of the rising bubble in the shear flow. The object of the calculations are sketched in Fig.10. To see the effect of the deformation, the calculation is done for the different Weber number and the same Reynolds number which are calculated by the terminal velocity without shear. So the Weber number is the parameter to see the effect of the deformation to the lift force. Since, the shear at the far-field is given in the y direction in our calculation, the main motion is in the x-y plane.

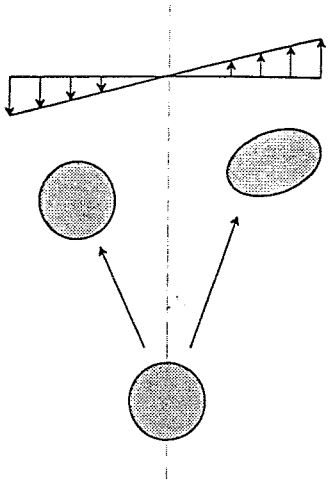

Fig . 10 Bubble in the Shear Flow

The projections of the trajectory of the gravity center to the x-y plane are shown in Fig.11 in the case of Reynolds number 20. The bubble shapes and the flow fields at time t=20 are also shown in Fig.12. The numerical results show that the trajectories strongly depend on the Weber numbers. As was reported by Kariyazaki[1], the deformation affects the direction of the lift force and the bubble moves in the different direction because of that.

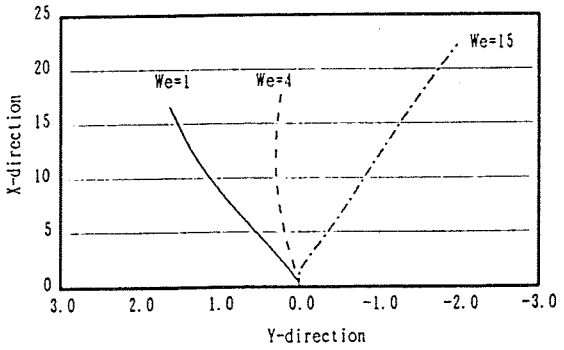

Fig. 11 Trajectories of the Rising Bubble in the Shear Flow (Re=20)

From the Auton's theoretical analysis, it may be said that the spherical bubble moves in the direction of the higher slip velocity. But the deformation makes the another kind of lift forces, and this forces makes the bubble move in the other directions. Tomiyama et al.[5] showed by the calculation of two dimensional bubble that the lift force acting on the bubble is caused by the strong interaction between the flow inside the bubble and that of outside, and they noted the importance of the flow inside the bubble. But our numerical results show that the free surface boundary condition gives us

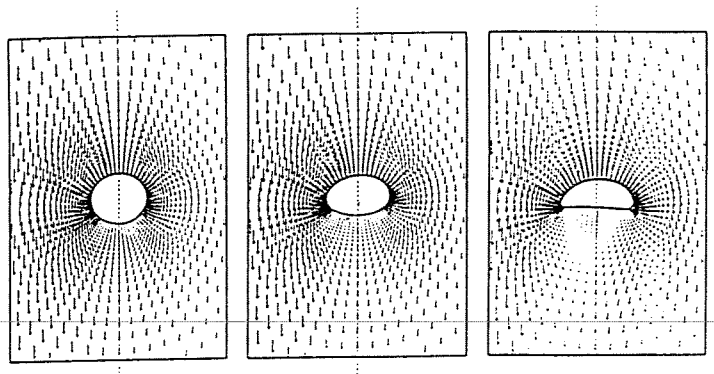

We=1 We=4 We=15

Fig.12 Shapes of the Bubble in the Shear Flow

the same effect, even though the flow inside the bubble is unknown. If the case of the high density ratio of the gas and the liquid is considered, it is not difficult to imagine the situation that the flow around the bubble is important to determine the motion of the bubble. In this sense, it can be concluded that the flow field around the bubble which is solved with the free surface boundary condition is enough and essential to determine the lift force of the light gas bubble.

Next, the numerical results of the low Reynolds number(Re=2) case is shown in Fig.13,14 and that of the high Reynolds number(Re=100) in Fig.15,16. From Fig 13, it is seen that the bubble is not strongly affected by the existence of the shear when the Reynolds number is small(Re=2). Especially for the nearly spherical bubble, that is the case of the low Weber number, the bubble doesn't s0how the typical behavior to move in the direction of the higher slip velocity. These are related to the kinematic reversibility of the Stokes flow. Because of this nature, the lift force doesn't exist for the spherical bubble rising through the shear flow of the Stokes one. Since the Reynolds number is about 2 in the case of Fig13, we may have a small effect of the lift force for the nearly spherical bubble. But it is seen from Fig.13 that this effect is smaller than that of the deformation and the bubble moves farther in the lateral direction due to the deformation, though this effect is also small compared with Fig.11. To the contrary, the lift force is much bigger for the high Reynolds number(Re=100) as shown in Fig.15. And it should be noted that the deformation effect is also very big in this case.

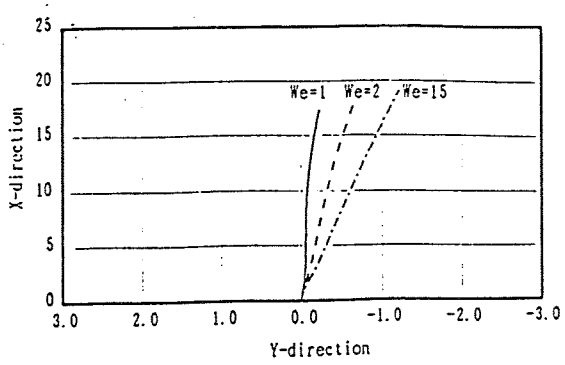

Fig. 13 Trajectories of the Rising Bubble in the Shear Flow (Re=2)

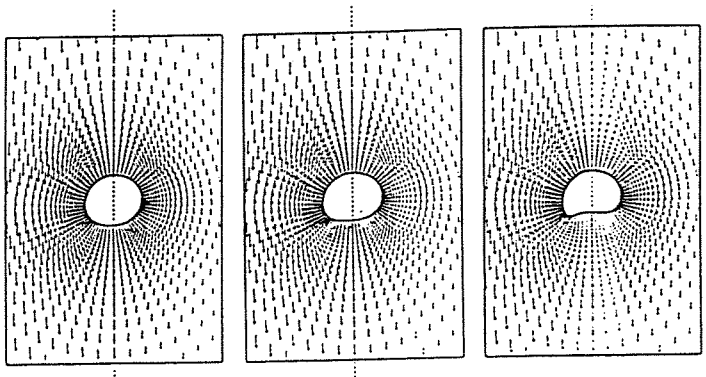

We=1 We=2 We=15

Fig.14 Shapes of the Bubble in the Shear Flow

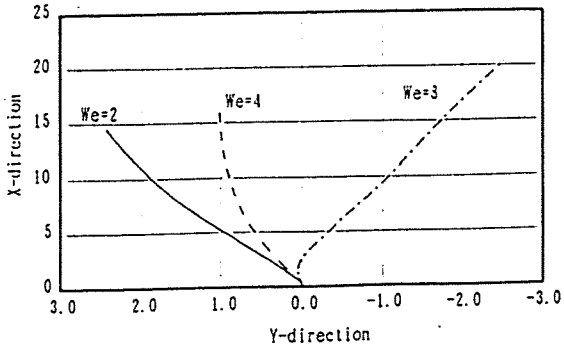

Fig. 15 Trajectories of the Rising Bubble in the Shear Flow (Re=100)

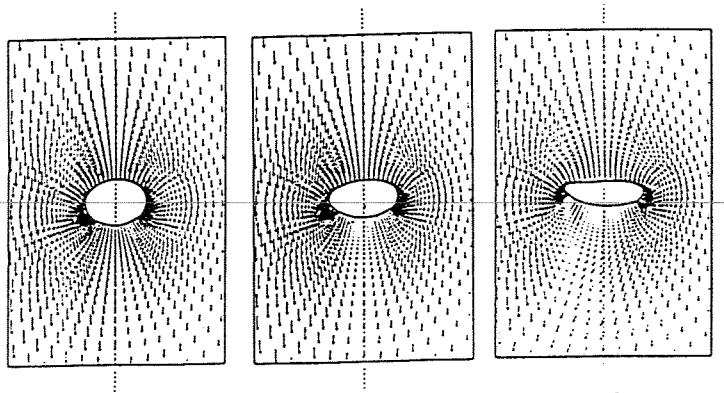

We=2 We=4 We=8

Fig.14 Shapes of the Bubble in the Shear Flow

6.CONCLUSION

[1] The numerical method has been developed to calculate the three dimensional unsteady flow with free surface. The following technique is used to stabilize the solution.

(1) The physical components of the contravariant velocity are used as the variables. And the expression of the viscous term is simplified on the discretization of the momentum equation for SIMPLER method. The time derivative term for the moving grid is also simplified by the Cartesian component of the velocity.

(2) Special iteration technique is used for the normal stress condition, considering the effect of the normal viscous stress. As a result, the numerical instability of the bubble surface which has been pointed out as a big problem is removed.

[2] Rising motions of a single bubble in the quiescent fluid and the shear flows have been calculated by the developed method. And the following results are obtained.

(1) The Quiescent Liquid Case:

The numerical results of the axisymmetric steady shape and the rising velocity are compared with the experiments of others. The results show quantitatively good agreement.

The three dimensional unsteady zigzag motion has been obtained numerically under the condition that the phenomenon is also observed experimentally, and the result is compared with that of the axisymmetric solution. As a result, it is found that the three dimensional asymmetric motion is caused after the axisymmetric unsteady motion which is related to the upward curved shape of the bubble.

(2) The Shear Flow Case:

The three dimensional numerical results reveal that the lift force acting on the bubble strongly depend on the bubble shape and the Reynolds number. The rising bubble in the shear flow moves in the higher slip velocity region if the bubble shape is nearly spherical and the Reynolds number is not small. But with becoming more deformed, it starts moving in the other direction, which is the lower slip velocity region. In low Reynolds number case, the effect of the lift force to the spherical mode is quite small and the bubble moves in the lateral direction mainly due to the deformation. These are the same tendency that the smaller spherical bubbles in the upflow rise near the wall of the pipe and the larger deformed bubble do in the center which is observed experimentally.

ACKNOWLEDGMENTS

A part of this study was done while one of the author S.T. was staying at Johns Hopkins Univeresity in U.S.A. for a year. The authors express their gratitude to Professor A.Prosperetti, Dr.H.Huang, and Dr.H.N.Oguz for the advice to develop the present numerical technique. Authors also appreciate the help of T.Koyanagi for making 3-D graphics of the bubble shape.

REFERENCES

(1)A.Kariyazaki,"Behaviour of a Gas Bubble in a Liquid Flow with a Linear Velocity Profile", in: Trans. J.S.M.E.,**53**,744(1987) (in Japanese)

(2)R.A.Hartunian and W.R.Sears, "On the instability of small gas bubbles moving uniformly in various liquids", in: J.Fluid Mech.**3**,27(1957)

(3)H.Tsuge and S.Hibino, "The Onset Conditions of Oscillatory Motion of Single Gas Bubbles Rising in Various Liquids", in: J.Chemical Eng.Japan,**10**,66(1977)

(4)S.O.Unverdi and G.Tryggvason, "A Front -Tracking Method for Viscous, Incompressible, Multi-fluid Flows", in: J.Comput.Phys.**100**,25(1992)
(5)A.Tomiyama,I.Zun,A.Sou and T.Sakaguchi, "Numerical analysis of bubble motion with the VOF method", in: Nuclear Eng.Design,**141**,69(1993)
(6)G.Ryskin and L.G.Leal, "Numerical solution of free-boundary problems in fluid mechanics", in: J.Fluid Mech.,**148**,1(1984)
(7)S.Takagi, "The behaviour of the single bubble rising through the quiescent liquid", Master Thesis,The Univ. of Tokyo(1992), (in Japanese)
(8)R.Duraiswami & A.Prosperetti, "Orhogonal Mapping in Two Dimensions", in: J. Comput. Phys. **98**,254(1992)
(9)S.Koshizuka: "Boundary-Fitted Coordinate Method for Incompressible Flow Using Riemann Geometry", Doctor Thesis, The Univ.of Tokyo(1990), (in Japanese)
(10)Clift, Grace, and Weber : "Bubbles, Drops, and Particles", Academic Press (1978)
(11)T.R.Auton, "The lift force on a spherical body in a rotating flow", in: J. Fluid Mech. **183**,199(1987)
(12) J.G.Hnat and J.D.Buckmaster, "Spherical cap bubbles and skirt formation", in: Phys. Fluids, **19**, 182(1976)

NUMERICAL SIMULATION OF CAVITATING FLOW

SHEET AND CLOUD CAVITATION

G.H. Schnerr, K. Lanzenberger and R. Schulz

Universität Karlsruhe (TH)
Institut für Strömungslehre und Strömungsmaschinen
Postfach 6980, D–76128 Karlsruhe, Federal Republic of Germany
Telephone: (0721) 608–3026, Facsimile: (0721) 696727

ABSTRACT

Two main types of cavitation can be observed in hydraulic machinery: Sheet cavitation which consists of a vapor region adjacent to the body surface and cloud cavitation formed by small cavitation bubbles, e.g. after sheet cavitation regions and in vortices. The different physical properties of these two cavitation types are treated by two individual models and numerical schemes.

The investigation of sheet cavitation concentrates on the interaction between sheet cavitation and boundary layer. In the actual version of the model the displacement of the incompressible fluid by vaporization and the slip condition at the vapor/liquid interface are taken into account. For modeling of the interface a Chimera grid scheme is used. The complex geometry of the vapor region is treated separately and then overset onto the main flow. The Chimera scheme is applied to a two–dimensional incompressible Navier–Stokes code based on the concept of artificial compressibility.

The cloud cavitation model is based on an averaged two–phase model: In a macroscopic view the fluid is assumed to be viscous and compressible characterized by the volume averaged void fraction. At the microscopic scale clusters of small spherical cavitation bubbles are considered. The macroscopic flow is described by the conservation laws for mass, momentum and bubble number density, while the microscopic bubble radius is obtained from a modified Rayleigh–Plesset–equation. The classical MAC–Method for incompressible flow is modified for cavitating flow. This numerical scheme is applicable to incompressible non–cavitating flows as well as to compressible cavitation regions. It is implemented as an implicit finite–difference–scheme on body fitted coordinates for calculation of unsteady two–dimensional viscous flow. The code will be first applied to internal cavitating flow.

The aim of the future work is to combine the two models in order to investigate the interaction between sheet and cloud cavitation.

1. INTRODUCTION

Cavitating flow has been mainly experimentally investigated in the past. Scaling effects and different experimental conditions (water quality etc.) in several test facilities make it difficult to transfer experimental data from the model to the real size or even to compare

experimental results for identical test configurations (Young [1]). Theoretical models have been worked out for different partial aspects of cavitation, e.g. several analytical solutions have been derived for bubble dynamics [1], but a comprehensive theoretical model for cavitating flow is not available. Therefore and because of the problems with experimental facilities (scaling effects, costs) there is need for a numerical simulation method of cavitating flow. The final aim for the future is a numerical cavitation tunnel.

Cavitation phenomena in hydraulic machinery and on ship propulsors can be divided in the two main types sheet and cloud cavitation. Sheet cavitation usually is observed at the leading edge of a hydrofoil and consists of a large vapor region attached to the body surface. A sheet cavity has a distinct vapor–liquid interface with a smooth shape and is not influenced by the concentration of cavitation nuclei upstream (Gindroz [2]). Clouds of small spherical cavitation bubbles are called cloud cavitation. This type of cavitation is usually observed in tip vortices or in separation vortices. Cloud cavitation occurs at large concentrations of cavitation nuclei upstream and depends on viscous effects like separation and turbulence.

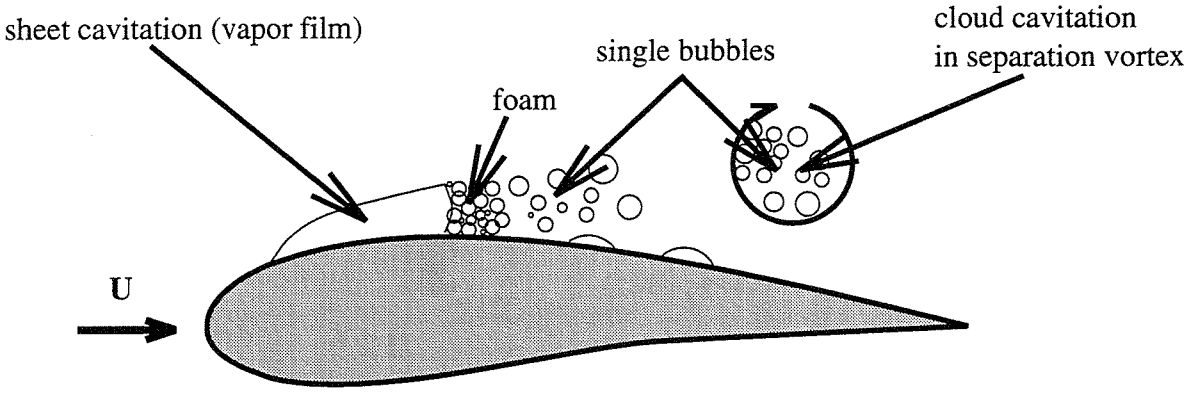

Fig. 1: Cavitating flow over a hydrofoil: Sheet and cloud cavitation

For a cavitating hydrofoil both cavitation types usually coexist (Fig. 1): At the leading edge of the foil a sheet cavity is formed, which becomes unstable and disintegrates into vapor–liquid foam. The foam finally breaks up into clouds of small cavitation bubbles, which are carried with separation vortices into the flow field.

In a comprehensive numerical simulation of such cavitating flow (numerical cavitation tunnel) the interaction of sheet cavitation, cloud cavitation and viscous effects must be taken into account. The physical mechanisms of the two cavitation types are very different and require consequently two different physical models.

Recently several works started on numerical simulation of cavitating flow. These numerical methods are based on different physical models and treat mostly only one cavitation type. Kubota and Kato [3] [4] treat the bubbly ascpect of cavitation, while Avellan [5] and Despande [6] concentrate on sheet cavitation. Starting from two–phase flow pump performance prediction, Minemura [7] and Schütte [8] work on sheet and cloud cavitation in pump impellers.

In this work sheet cavitation as well as cloud cavitation is treated. At the present two different numerical schemes based on different models suited for each individual cavitation type have been developed. These two models will be combined in the future in order to calculate the interaction of sheet and cloud cavitation. In the following the two models and numerical schemes are discussed and first results are presented.

2. SHEET CAVITATION

2.1 Physical Model

Sheet cavitation is observed in hydraulic machines like turbo pumps, water turbines and ship propellers. When, starting from a non–cavitating condition, the pressure is reduced, a stable smooth sheet cavity occurs at the leading edge of the hydrofoil (Fig. 2a). Reducing the pressure further, a sheet cavity develops with a smooth interface at its leading edge and an unstable interface at its trailing edge (Fig. 2b). The instability of the sheet cavitation is caused by a re–entrant jet [9] or by vortex shedding [5].

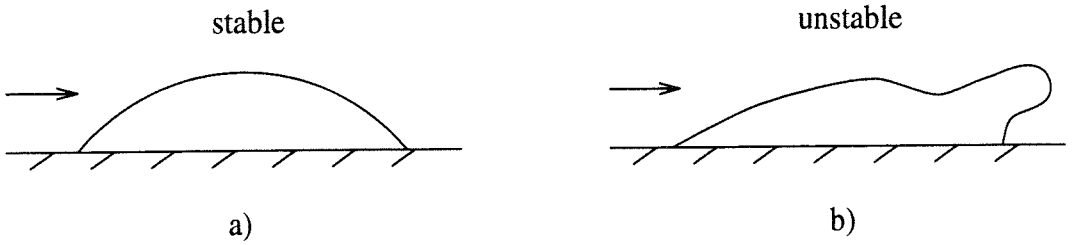

Fig. 2: Stable (a) and unstable (b) sheet cavitation

The conditions inside of the sheet cavity are assumed to be homogeneous. In the whole cavity the pressure is equal to the vapor pressure of the liquid phase. The governing equations for the incompressible main flow are the two–dimensional Navier–Stokes equations:

$$\frac{\partial u}{\partial x} + \frac{\partial v}{\partial y} = 0 \tag{1}$$

$$\frac{\partial u}{\partial t} + u\frac{\partial u}{\partial x} + v\frac{\partial u}{\partial y} = -\frac{1}{\rho}\frac{\partial p}{\partial x} + \nu\left(\frac{\partial^2 u}{\partial x^2} + \frac{\partial^2 u}{\partial y^2}\right) \tag{2}$$

$$\frac{\partial v}{\partial t} + u\frac{\partial v}{\partial x} + v\frac{\partial v}{\partial y} = -\frac{1}{\rho}\frac{\partial p}{\partial y} + \nu\left(\frac{\partial^2 v}{\partial x^2} + \frac{\partial^2 v}{\partial y^2}\right) \tag{3}$$

The boundary condition at the body surface is the no–slip condition. The changing boundary condition from no–slip at the body surface to slip along the interface is very important for the behaviour of the boundary layer and consequently for the sheet cavity. At the vapor/liquid interface, the conditions to be satisfied are that the normal component of stress is the sum of vapor pressure p_v and a contribution from surface tension

$$p = p_v - \frac{2S}{R_K} \tag{4}$$

and that the tangential component of stress is zero:

$$\tau = 0 \tag{5}$$

Here S is the surface tension, R_K the radius of the interface curvature and U the tangential component of the velocity.

2.2 Numerical scheme

MacCormack scheme with application of artificial compressibility The two–dimensional incompressible Navier–Stokes equations are solved using the explicit MacCormack scheme [10]. The first step of this two–step predictor–corrector scheme is a first–order forward discretization in space. The second, corrector, step is a backward first–order scheme, which will be unstable for negative characteristic speeds of propagation, that is for subsonic flows. However, the overall combined scheme is stable and of second order due to the cancellation of the truncation errors of each step. The MacCormack scheme developed for compressible equations is applied to the incompressible Navier–Stokes equations using the method of artificial compressibility. In this method first introduced by Chorin [11], a pseudo–time derivative of pressure is added to the continuity equation which directly couples the pressure and the velocity

$$\frac{\partial p}{\partial t} + \rho\beta^2 \left(\frac{\partial u}{\partial x} + \frac{\partial v}{\partial y} \right) = 0 \, . \tag{6}$$

The parameter β has the dimension of a velocity and represents a pseudo–speed of sound of the transformed system. The incompressible flow equations become hyperbolic, with pseudo–pressure waves propagating with finite speed.

Chimera grid scheme The Chimera scheme is an overset grid scheme approach first applied in aeronautics for the calculation of the flow around wing–body configurations (Buning [12]). Nirschl [13] developed a Chimera grid scheme for the calculation of particle flow. In this study the method will be applied to sheet cavitation. Two different and overlapping grids are used for the main flow configuration (e.g. hydrofoil, nozzle) and for the shape of the sheet cavity.

In Fig. 3 the two grids for a channel with a cylindrical convergent–divergent part are shown. The incompressible Navier–Stokes equations are separately solved on each grid. A bilinear

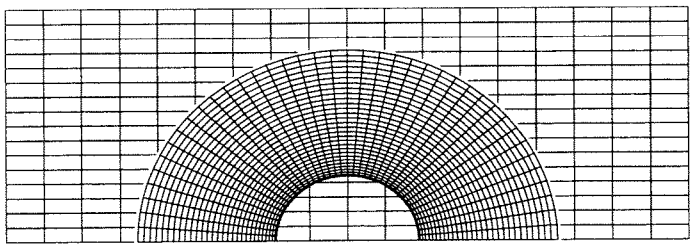

Fig. 3: Chimera scheme: Two overlapping grids for a channel with a cylindrical convergent–divergent part

interpolation scheme is used to relate the two solutions to each other. A grid point P(x,y) of one of the two grids is surrounded by four neighbors of the other grid. The interpolation formula for the variable f at point P(x,y) is

$$f(x,y) = a_1 + a_2 x + a_3 y + a_4 xy \ . \tag{7}$$

The coefficients a_i are determined by the solution of the four linear equations obtained with the four surrounding grid points.

2.3 Results

Noncavitating flow The numerical scheme explained in chapter 2.2 has been tested before applying to sheet cavitation. The results for the fully developed flow in a channel and for the boundary layer at the flat plate agree well with the analytical solutions. As third test case the laminar flow over a backward–facing step was chosen. Flow separation occurs because of the sudden change of the cross sectional area, Fig. 4. The length of the recirculation zone x_r/h depends on the expansion ratio H/h and the Reynolds number Re. The flow in the inlet channel is a two–dimensional fully developed channel flow with a parabolic velocity

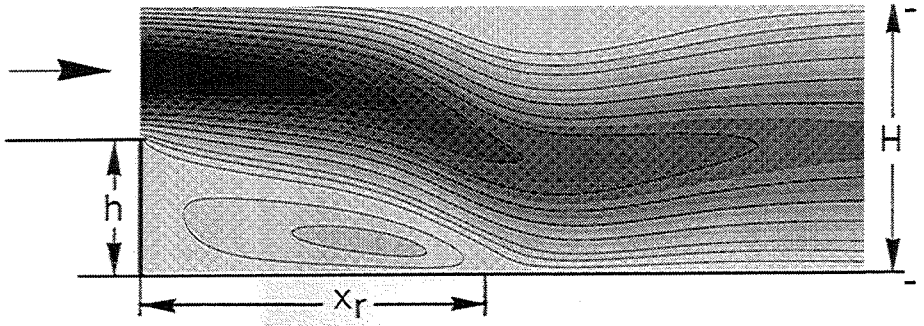

Fig. 4: Isolines of the velocity field (dark – high velocity, light – low velocity) for the flow behind a backward–facing step, $Re = 600$

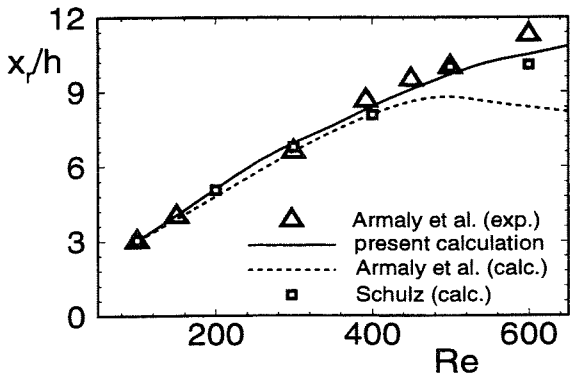

Fig. 5: Comparison of experimental and theoretical results for the reattachment length x_r/h up to $Re_h = 600$

distribution. With the present scheme the backward–facing step flow is investigated in a Reynolds number range of $100 < Re_h < 600$ for the expansion ratio $H/h = 2$. The numerical results agree quite well with experimental results of Armaly et al. [14] (Fig. 5).

The channel flow with a cylindric bump at one wall is very appropriate as test case for the Chimera grid scheme since the kink in the wall geometry makes it difficult to use only one structured grid. The flow field is calculated on two different grids (Fig. 3) for the Reynolds number $Re_d = 80$. In Fig. 6 and Fig. 7, the results from the calculation on the two grids are depicted for the pressure field and the stream lines, respectively. The circular arc is the outer boundary of the spherical mesh. There are no jumps in pressure isolines or in stream lines between the two grids.

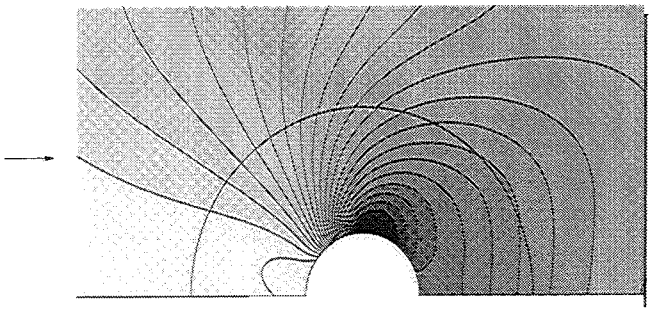

Fig. 6: Isolines of the pressure field in a channel with a cylindrical bump at one wall for $Re_d = 80$ (dark – low pressure, light – high pressure; increment: 15.2 Pa)

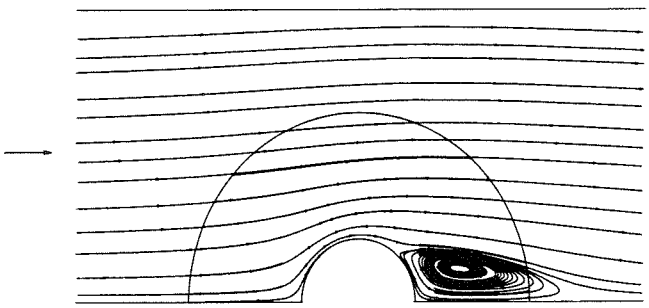

Fig. 7: Stream lines in a channel with a cylindric bump at one wall for $Re_d = 80$

Cavitating flow The flow through a convergent–divergent channel is chosen as first example of the present scheme to cavitating flow. As a first approximation it was tried to modelize the sheet cavity without the Chimera grid scheme. The shape of the sheet cavity is formed by grid adaptation. In Fig. 8 the pressure field without cavitation is depicted for a Reynolds number Re =250. The box at one side of the channel indicates the region where cavitation will occur. On the basis of this non–cavitating pressure field an initial shape of the sheet cavity is assumed. The boundary condition is changed from no–slip at the wall to disappearing shear stress along the liquid/vapor interface. As depicted in the calculated vector field of the velocity (Fig. 9) the boundary layer is accelerated at the leading edge of the sheet cavity and decelerated at the trailing edge. However, the pressure along the interface is not constant. At the trailing edge of the cavity an overestimation of the pressure peak occur due to numerical errors. In order to avoid these grid caused errors, we decided to apply in the following the successfully tested Chimera grid scheme.

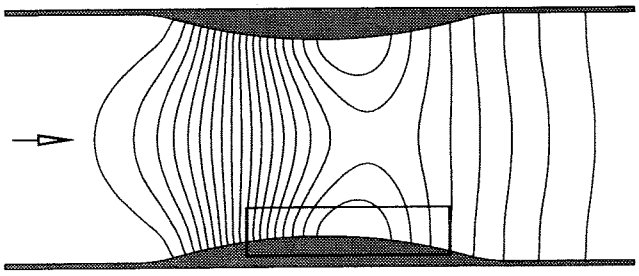

Fig. 8: Isolines of the pressure field in a convergent–divergent channel, Re=250

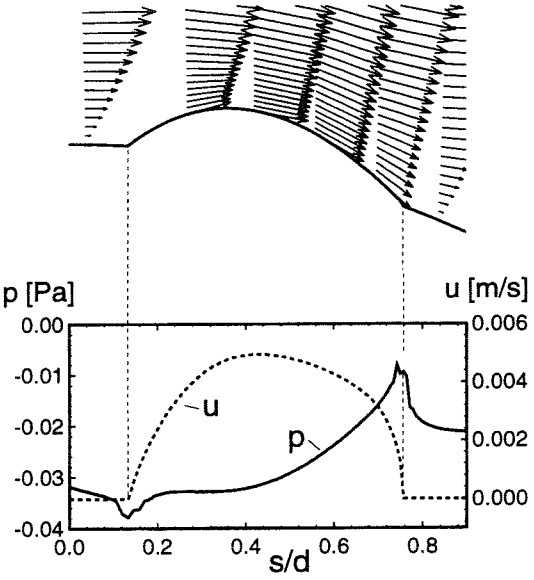

Fig. 9: Sheet cavitation: velocity vectors near the cavity (up); u–component of velocity and the static pressure along the interface (below).

3. CLOUD CAVITATION

3.1 Physical Model

Bubble two–phase flow model In bubbly liquids, e.g. gas bubbles in a liquid, the speed of sound is much lower than the speed of sound of the single components, even at small void fractions. Compressibility effects like shocks or expansion waves can be observed at low flow velocities ($|\vec{w}| \approx 20\frac{m}{s}$ at $p \approx 1bar$). Because of the oscillatoric behaviour of the single bubbles, strong dispersive effects occur in bubbly liquids. Cloud cavitation regions are bubbly liquids consisting of vapor bubbles, but in contrast to bubbly liquids consisting of gas bubbles, cavitation zones are embedded in incompressible main flow (Fig. 1).

With a numerical simulation method for cloud cavitation both, the cavitation zone and the incompressible main flow, must be calculated. This demand is performed by the bubble two–phase flow (BTF) model recently developed by Kubota and Kato [3] [4] for cavitating flow over hydrofoils: The classical MAC–scheme (Harlow and Welch [15]) for incompressible viscous flow has been modified for cavitating flow in order to calculate the cavitation regions and the incompressible main flow simultaneously. Kubota's model is based on the bubbly two–phase aspect of cavitation and has been chosen as starting point for the present work in order to calculate the cloud cavitation regions.

As depicted in Fig. 10, the BTF model is based on two views of the flow: In a macroscopic view the flow is considered as compressible and is characterized by the volumetric void fraction α. At microscopic scale clusters of single spherical bubbles in incompressible liquid are assumed.

In the cluster the bubbles interact on each other and with the main flow. Microscopic and macroscopic view are connected by the void fraction. The void fraction depends on the local bubble number density n (bubbles per volume) and the local bubble radius R. Lines of constant void fraction describe the shape of the cavitation region.

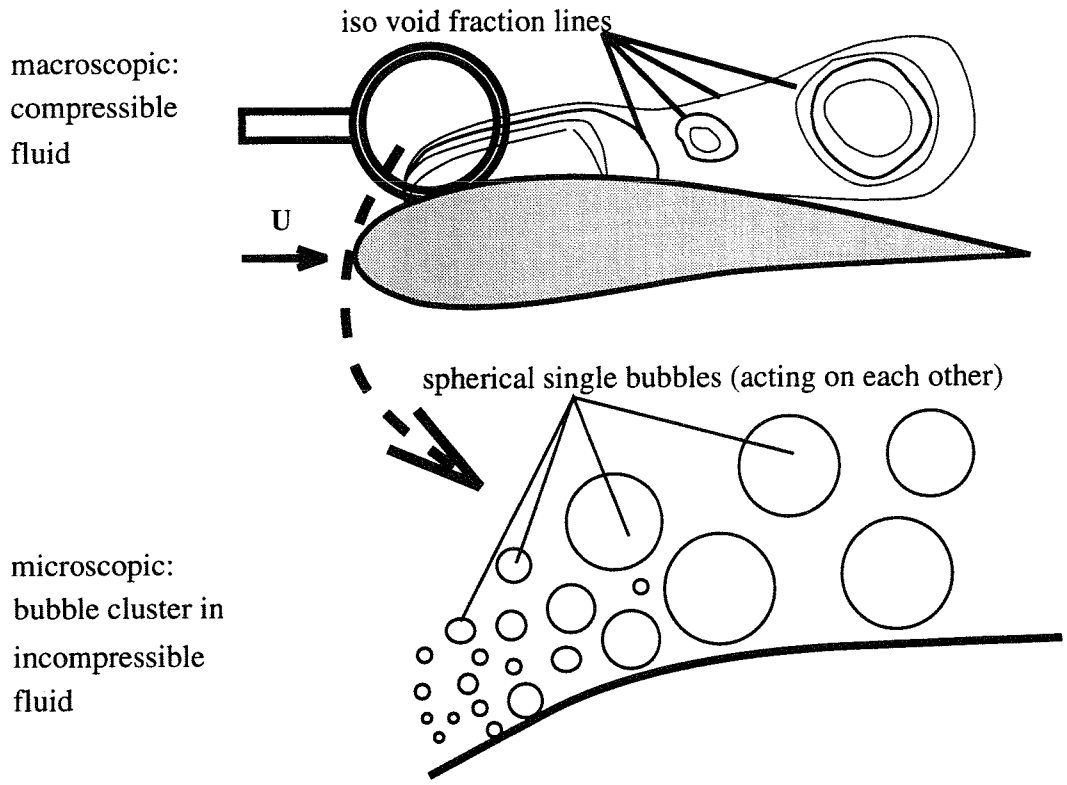

Fig. 10: Bubble two–phase model

Macroscopic scale Governing equations (all equations are nondimensional):

$$\text{void fraction:} \quad \alpha = \frac{volume\ gas}{total\ volume} = \frac{4}{3}\pi n R^3 \tag{8}$$

$$\text{mean density:} \quad \rho = (1-\alpha)\rho_l + \alpha\rho_g \approx (1-\alpha)\rho_l \tag{9}$$

$$\text{mean viscosity:} \quad \mu \approx \mu_l \tag{10}$$

$$\text{mass conservation:} \quad \frac{\partial \rho}{\partial t} + \nabla \cdot (\rho \vec{w}) = 0 \tag{11}$$

$$\text{bubble number conservation:} \quad \frac{\partial n}{\partial t} + \nabla \cdot (n \vec{w}) = 0 \tag{12}$$

$$\text{momentum conservation:} \quad \frac{\partial (\rho \vec{w})}{\partial t} + \nabla \cdot (\rho \vec{w}\vec{w}) = -\nabla p + \vec{D} \tag{13}$$

In Eq. (13) viscous terms are expressed as

$$\vec{D} = \frac{1}{Re}\left(\frac{1}{3}\nabla(\nabla \cdot \vec{w}) + \Delta \vec{w}\right), \tag{14}$$

the Reynolds number is defined as $Re = \frac{\rho_0 u_0 l_0}{\mu}$, with density $\rho_0 = \rho_l$ viscosity μ and typical macroscopic length l_0 (e.g. chord length). In Kubota's work the bubble number density n was set to be constant. For the viscous terms he assumed decreasing viscosity μ with increasing void fraction α and proposed the following relationship:

$$\mu = (1 - \alpha)\mu_l + \alpha\mu_g \tag{15}$$

Equation (15) does not agree with Taylor's results [16], who showed for $\alpha < 0.05$ that the effective viscosity in a bubbly liquid increases with the void fraction:

$$\mu = (1 + \alpha)\mu_l \tag{16}$$

For higher void fractions Baiter [17] assumes a decreasing viscosity with increasing void fraction as depicted in Fig. 11. In the present model the viscosity is set constant and equal to the viscosity of the liquid, Eq. (10).

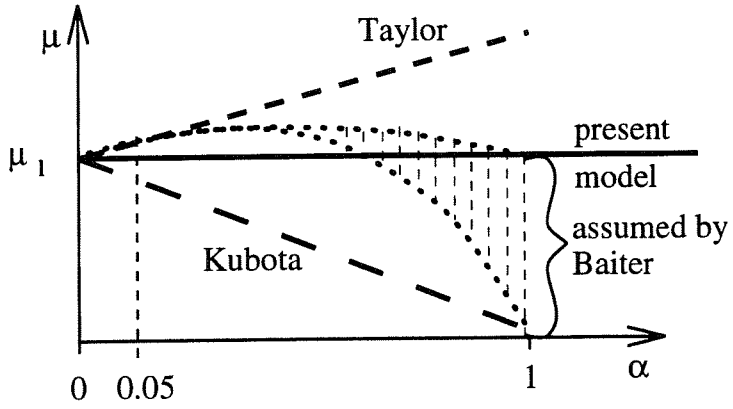

Fig. 11: Effective viscosity in the cavitation region

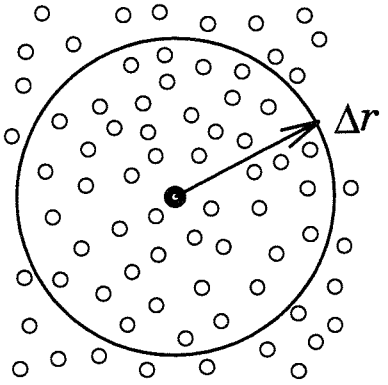

Fig. 12: Spherical bubbles in a cluster inside Δr act on the bubble in the center

Microscopic scale At this scale clusters of single bubbles are treated. The bubbles do not coagulate or break up into smaller bubbles and remain spherical all the time. From the Rayleigh–Plesset equation the growth of a single spherical bubble in an infinite fluid region is given by:

$$R\ddot{R} + \frac{3}{2}(\dot{R})^2 = \lambda(p_i - p_\infty) \tag{17}$$

Here

$$p_i = p_v + p_{g0}\left(\frac{R_0}{R}\right)^3 - \frac{2}{We}\frac{1}{R} - \frac{4}{Re}\frac{\dot{R}}{R} \tag{18}$$

is the internal pressure in the bubble, p_∞ the pressure far away from the bubble and $\lambda = \left(\frac{l_0}{R_0}\right)^2$ the ratio between the typical macroscopic and microscopic length–scales, e.g. R_0 is the initial bubble Radius.

Assuming that a bubble is only affected by other bubbles inside an effecting radius Δr (Fig. 12), Eq. (17) can be modified for a spherical bubble in the center of a bubble cluster (Kubota [4]):

$$(1+2\pi\Delta r^2 nR)R\frac{D^2R}{Dt^2}+\left(\frac{3}{2}+4\pi\Delta r^2 nR\right)\left(\frac{DR}{Dt}\right)^2+2\pi\Delta r^2\frac{Dn}{Dt}R^2\frac{DR}{Dt}=\lambda(p_i-p) \qquad (19)$$

After introducing the bubble number conservation Eq. (12) and the momentum equation (13) into this equation, following relation ship for the radial speed of the bubble surface ω is obtained:

$$\frac{\partial R}{\partial t} = \omega \qquad (20)$$

$$\frac{\partial \omega}{\partial t} = \lambda\frac{p_i-p}{(1+3\phi)R}-\frac{3}{2}\cdot\frac{1+4\phi}{1+3\phi}\cdot\frac{1}{R}(\omega+\vec{w}\cdot\nabla R)^2+\frac{3\phi}{1+3\phi}\nabla\cdot\vec{w}\,(\omega+\vec{w}\cdot\nabla R)$$
$$-2\vec{w}\cdot\nabla\omega-\vec{w}\vec{w}\cdot\nabla\nabla R+\frac{1}{1-\alpha}\nabla R\cdot\left(\nabla p-\vec{D}\right) \qquad (21)$$

In Eq. (21) $\phi=\alpha\left(\frac{\Delta r}{R}\right)^2$ is the bubble interaction coefficient. Kubota set the free parameter Δr equal to the grid spacing and explained this analogous to the subgrid scale model in large eddy turbulence simulations. The presented one-dimensional results (discussed later) showed that the parameter Δr has no grid dependency and should be determined experimentally.

3.2 Numerical Scheme

MAC scheme for incompressible flow In incompressible flow the coupling between the density and the pressure field vanishes and the continuity equation

$$\nabla\cdot\vec{w}=0 \qquad (22)$$

is not time integrable for unsteady problems. This problem is avoided in the classical marker and cell (MAC) scheme [15] for unsteady incompressible viscous flow. By introducing the mass conservation Eq. (11) into the divergence of the momentum equation Eq. (13), an elliptic equation for pressure p is obtained:

$$\Delta p=\frac{\partial^2\rho}{\partial t^2}-\nabla\cdot\nabla(\rho\vec{w}\vec{w})+\frac{4}{3}\frac{1}{Re}\Delta(\nabla\cdot\vec{w}) \quad\Longrightarrow\quad \Delta p=-\nabla\cdot\nabla(\rho\vec{w}\vec{w}) \qquad (23)$$

The second time derivative of the density and the viscous term vanish for incompressible flow. The numerical procedure of the MAC scheme is the following:

1. Time integration of momentum equation Eq. (13) $\Longrightarrow$ velocity field
2. Solution of pressure equation (23) as boundary problem $\Longrightarrow$ pressure field

Modified MAC scheme for cavitating flow The density in cavitating flow depends on the void fraction Eq. (9). The second time derivative of the density in Eq. (23) is given by

the Rayleigh–Plesset equation (19) and the bubble number conservation Eq. (12). Introducing these equations in Eq. (23) a modified pressure equation for cavitating flow is obtained:

$$\begin{aligned}
&\Delta p + \frac{\nabla\alpha}{1-\alpha}\cdot\nabla p - \lambda\delta p \\
&= -\lambda\delta p_i + \frac{3}{2}\delta(1+4\phi)(\omega+\vec{w}\cdot\nabla R)^2 - 3R\delta\phi\nabla\cdot\vec{w}(\omega+\vec{w}\cdot\nabla R) \\
&\quad +6\alpha(1-\alpha)\left[\frac{\nabla\cdot(n\omega\vec{w})}{nR} - \left(\frac{\omega}{R}\right)^2\right] + \frac{\nabla\alpha}{1-\alpha}\cdot\vec{D} + \frac{1}{1-\alpha}\nabla\cdot\vec{D} \\
&\quad +\alpha(1-\alpha)\left[3\frac{\vec{u}\vec{u}\cdot\nabla\nabla R}{R} - \frac{\nabla\cdot\nabla\cdot(\vec{w}\vec{w}n)}{n} - \frac{\nabla\cdot\nabla\cdot(\vec{w}\vec{w}(1-\alpha))}{\alpha}\right]
\end{aligned} \tag{24}$$

In Eq. (24)

$$\delta = \frac{3\alpha(1-\alpha)}{R^2(1+3\phi)} \tag{25}$$

is the dispersion coefficient, increasing δ means decreasing dispersion.

Discretisation scheme Because of the lack of a comprehensive turbulence model for bubbly liquids, no turbulence model is employed. In order to calculate laminar flow at high Reynolds numbers, great attention must be paid to nonlinear convective terms in the Navier–Stokes equation (13). Kawamura and Kuwahara [18] propose an implicit second order upwinding scheme with correction of the third order error. Their laminar calculations for incompressible viscous flow over a circular cylinder agree well with experiments ($Re = 10^5$). The transition point is calculated quite good and the vortex structure is resolved including small eddys.

In the present work, the governing equations are transformed on body fitted coordinates and a finite–difference–scheme on a structured regular grid is performed. Kawamura's and Kuwahara's upwinding scheme is applied to all nonlinear convective terms, and central differences to the first and second order linear terms. This implicit scheme is stable, especially for the time integration of the very stiff Rayleigh–Plesset equation (21). The linear systems resulting from the implicit time integration and the solution of the pressure equation (24) are solved with a biconjugate gradient method (BICO). In order to achieve high computing speed on a vector computer, an optimal vectorized subroutine by the Computing Center of the University of Karlsruhe, Forschungsgruppe Numerik für Supercomputer, is used.

3.3 Results

Investigation of bubbly liquid one–dimensional flow Because of the lack of an analytical solution for cloud cavitation, the capabilities of the BTF model and the new implicit numerical scheme have been checked for one–dimensional flow of bubbly liquid. Based on the theory of small disturbances analytical solutions for bubbly liquids have been derived for the dispersive linear wave propagation in a shock tube and for the dispersive weakly nonlinear propagation of a solitary wave (Schnerr [19]). In the following all calculations were performed for air–water mixtures.

In Fig. 13 the analytical solution for the linear wave propagation is compared with numerical data. The influence of the dispersion because of microscopic bubble oscillations increases

with the undisturbed bubble radius R_0. While the shape of the discontinuity for a bubble size of $R_0 = 0.1mm$ is approximated by oscillations of very high frequencies, for $R_0 = 2.0mm$ the shockwave is divided into single wave packets due to higher dispersion. The numerical results agree very well with the analytical solution, even for high frequencies at lower dispersion. Strong nonlinear and dispersive effects in a shock tube are resolved with the numerical scheme too, as shown in Fig. 14.

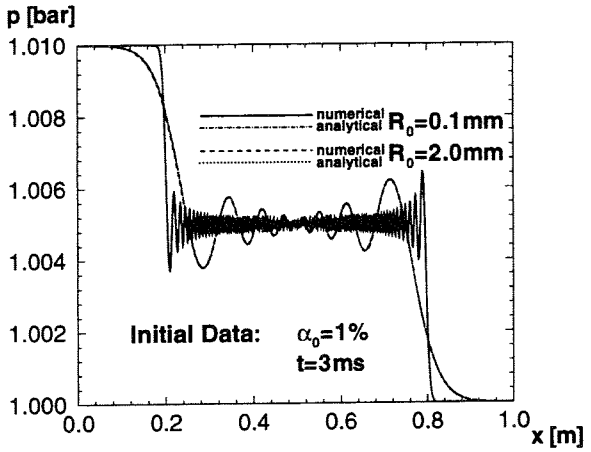

Fig. 13: Bubbly liquid in a shock tube: Linear dispersive wave propagation, $\Delta r = 0$

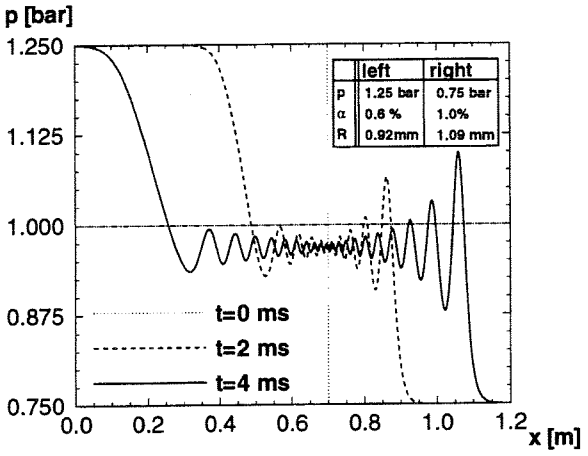

Fig. 14: Bubbly liquid: Strong nonlinear wave propagation in a shock tube, $\Delta r = 0$

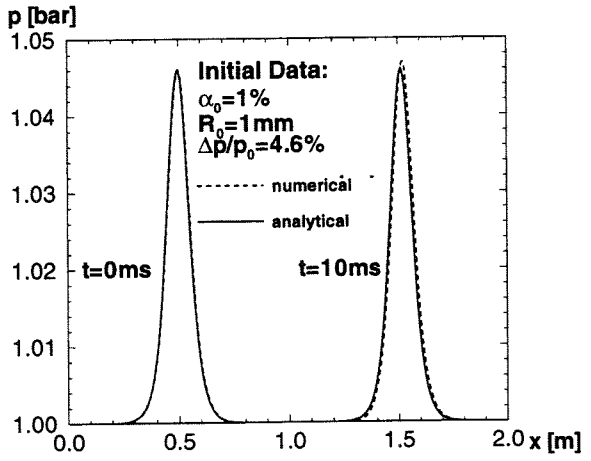

Fig. 15: Weakly nonlinear and dispersive propagation of a solitary wave in bubbly liquid, $\Delta r = 0$

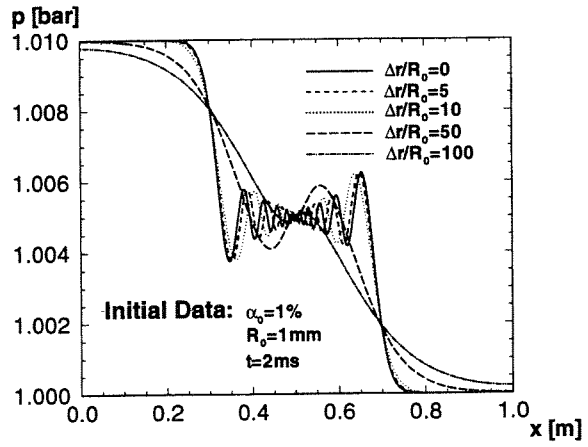

Fig. 16: Influence of effecting radius Δr on wave propagation in a shock tube

In Fig. 15 the propagation of a solitary wave in a bubbly liquid is depicted. The numerical results agree well with the analytical solution for weakly nonlinear wave propagation. Even after a simulation time of $t = 10ms$ the shape of the soliton has only slightly changed.

The influence of the bubble interaction model is shown in Fig. 16. Dispersion increases with Δr, as expected from Eq. (25). $\Delta r = 0$ means that the bubble interaction is neglected and that the original Rayleigh–Plesset equation (17) for a single bubble is solved. In the present calculations the number of gridpoints was varied from 100 up to 2000, but this had no influence on the result. Kubota assumed the effecting radius proportional to the grid spacing. Because of the coarseness of the mesh, Δr was very large in his simulations of cavitating flow. The physical properties of the modified Rayleigh–Plesset equation (19) were changed in such a way that the dispersion was very high and therefore the frequencies to be resolved relative low. The last seems to be the reason, why Kubota successfully employed the explicit Euler scheme to solve the stiff Rayleigh–Plesset equation. This explicit scheme was tested in the present calculations for bubbly liquid too, but it was found to be unconditionally unstable for $\Delta r = 0$. The effecting radius Δr has to be determined by experiments. It has to be checked, if the void fraction α, the bubble radius R or the bubble number density n have an influence on Δr.

Two–dimensional calculations without cavitation A Navier–Stokes code for two–dimensional, incompressible and viscous flow on arbitrary body fitted domains has been implemented. First calculations were performed for the backwards facing step and convergent divergent ducts. As depicted in Fig. 5, the results for the backwards facing step agree well with the experimental data of Armaly et al. [14]. Above a Reynolds number $Re \approx 600$ the flow becomes three–dimensional and both, the pressure correction scheme (section 1) and the present calculation differ from the experimental data.

Two–dimensional calculations of cavitating flow The incompressible Navier–Stokes code has been modified for cavitating flow. In order to check the code, currently two–dimensional cavitating flow through a convergent–divergent duct at Reynolds number $Re = 1000$ is calculated.

4. CONCLUSION

Two models and numerical schemes were presented for simulation of sheet and cloud cavitation. Sheet cavitation is modelized as incompressible flow with a free surface (the liquid/vapor interface). In order to check the explicit MacCormack scheme and the developed Chimera grid technique, non–cavitating flow configurations were successfully calculated. As a first simulation of sheet cavitation the flow through a convergent–divergent channel is presented. The preliminary result of this calculation without Chimera grid scheme has shown that the application of this overlapping grid technique is necessary for the future treatment of sheet cavitation.

Cloud cavitation is modelized by a bubble two–phase flow model which is based on two views of the flow: Macroscopically a compressible fluid and microscopically a bubble cluster in incompressible liquid is assumed. The properties of the model and the numerical scheme have been estimated by one–dimensional calculations for bubbly liquid. Numerical results for dispersive linear wave propagation in a shock tube and dispersive weakly nonlinear propagation of solitary waves have been compared with analytical solutions. The influence of the bubble interaction on dispersion has been investigated and it has been carried out that the free interaction parameter Δr should be estimated by experiments. Two–dimensional calculations

for non–cavitating conditions have been compared with experimental data. The incompressible scheme has been extended for two–dimensional cavitating flow and is currenly validated. The influence of physical parameters like nuclei radius, nuclei density and the ratio between nuclei radius and macroscopic length will be studied with the cavitation code. In order to compare these results with experimental data, high Reynolds number flow ($Re \approx 10^5$) must be calculated.

The models for the individual cavitation types will be combined in the future in order to calculate both sheet and cloud cavitation.

5. NOMENCLATURE

English symbols:

n	:	bubble number density
l	:	length
p	:	pressure
Δr	:	effecting radius
t	:	time
u, v, w	:	components of the velocity vector
$\vec{w}$	:	velocity vector
$\vec{D}$	:	vector of viscous terms
R	:	bubble radius
R_K	:	radius of interface curvature
Re	:	Reynolds number
S	:	surface tension
We	:	Weber number

Greek symbols:

α	:	void fraction
δ	:	dispersion coefficient
λ	:	scale ratio
μ	:	viscosity (dimensional)
ϕ	:	bubble interaction parameter
ρ	:	density
σ	:	cavitation number

Subscripts:

$_0$	:	reference (dimensional)
$_g$	:	gas phase, gas (dimensional)
$_l$	:	liquid phase (dimensional)
$_i$	:	inside bubble
$_v$	:	vapor
$_\infty$	:	infinity

6. REFERENCES

[1] F. R. Young: "Cavitation", McGraw–Hill, London (1989).

[2] B. Gindroz and M. L. Billet. "Influence of the Nuclei on the Cavitation Inception for Different Types of Cavitation on Ship Propellers", in: Cavitation 1993, ASME FED, 177, p. 1 (1993).

[3] H. Kato, N. Takasugi and H. Yamaguchi: "Numerical Analysis of a Cavitating Hydrofoil with Finite Span", in: International Symposium Propulsors and Cavitation, Schiffbautechnische Gesellschaft, Hamburg, Germany, Vol. 1, p. 164 (1992).

[4] A. Kubota, H. Kato and H. Yamaguchi: "A New Modelling of Cavitating Flow: A Numerical Study of Unsteady Cavitation on a Hydrofoil Section", in: Journal of Fluid Mechanics, 240, p. 59 (1992).

[5] P. Dupont and F. Avellan: "Numerical Calculation of a Leading Edge Cavity", in: Cavitation 1991, ASME FED, 116, p. 47 (1991).

[6] M. Deshpande, J. Feng and C.L. Merkle: "Numerical modelling of the thermodynamic effects of cavitation", in: International Cavitation Conference, Institution of Mechanical Engineers, Cambridge (UK) p. 303 (1992).

[7] K. Minemura and T. Uchiyama: "Calculation of Two-Phase Flow Pump Performance by a Bubbly Flow Model with Fixed Cavity", in: Cavitation and Multiphase Flow Forum 1991, ASME FED 109, p. 131 (1991).

[8] V. Schütte: "Modellierung und Berechnung von Blasenströmungen und Kavitation in Laufradkanälen von Kreiselpumpen", in: Pumpentagung Karlsruhe 1992, Karlsruhe, Germany (1992).

[9] R. A. Furness and S. P. Hutton: "Experimental and Theoretical Studies of Two-Dimensional Fixed-Type Cavities", in: Journal of Fluids Engineering, p. 515 (December 1975).

[10] R. W. MacCormack. "The Effect of Viscosity in Hypervelocity Impact Cratering ", in: AIAA Paper 69-354 1969.

[11] A. J. Chorin: "A Numerical Method for Solving Incompressible Viscous Flow Problems", in: Journal of Computational Physics, 2, p. 12, (1968).

[12] P. G. Buning, I. T. Chiu, S. Obayashi, Y. M. Rizk and J. L. Steger: "Numerical Simulation of the Integrated Space Shuttle Vehicle in Ascent", in: AIAA Paper 88-4359-CP (1988).

[13] H. Nirschl. "Mikrofluidmechanik: Numerische und experimentelle Untersuchungen zur Umströmung kleiner Körper". Dissertation, Technische Universität München, Lehrstuhl für Fluidmechanik und Prozeßautomation 1994.

[14] B.F. Armaly, F. Durst and J. C. F. Pereira: "Experimental and theoretical investigation of backward-facing step flow", in: Journal of Fluid Mechanics, 127, p.473 (1983).

[15] F.H. Harlow and J.E. Welch: "Numerical Calculation of Time-Dependent Viscous Incompressible Flow of Fluid with Free Surface", in: Physics of Fluids, 8, p. 2182 (1965).

[16] G. I. Taylor: "The Viscosity of a Fluid Containing small Drops of another Fluid", Proc. Royal Society London, 138, p. 41, (1932).

[17] H.-J. Baiter: "Discussion to H. Kato [3]", in: International Symposium Propulsors and Cavitation, Schiffbautechnische Gesellschaft, Hamburg, Germany, Vol. 2 , p. 21 (1992).

[18] T. Kawamura and K. Kuwahara: "Computation of High Reynolds Number Flow around a Circular Cylinder with Surface Roughness" in: AIAA 22nd Aerospace Science Meeting, AIAA, Reno, AIAA Paper 84-0340 (1984).

[19] G. H. Schnerr, K. Lanzenberger and R. Schulz: "Dispersive und nichtlineare Wellenausbreitung in Blasenflüssigkeiten", in: ZAMM, Accepted to be published.

THEORETICAL AND EXPERIMENTAL ANALYSIS OF VENTING INDUCED PROCESSES IN REACTING AND NON-REACTING TWO-PHASE SYSTEMS

L. Friedel*, N.-J. Kranz*, G. Wehmeier**

*Technische Universität Hamburg-Harburg
Arbeitsbereich Strömungsmechanik
Postfach 21050, D-21071 Hamburg, Deutschland
Telephone: (040) 7718-3252, Facsimile: (040) 7718-2573

**Hoechst AG
Technische Prüfung, G 811
D-65926 Frankfurt am Main, Deutschland
Telephone: (069) 305-5777, Facsimile: (069) 30 90 14

ABSTRACT

Top venting of initially saturated methanol and water and of a reacting methanol-acetic anhydride mixture has been carried out in a semi-technical scale test facility. Measured variables were the pressure in the reactor and the catchtank and mass flow rate and quality in the vent line. The experimental results compare satisfactorily with predictions obtained by using an in-house modified version of the SAFIRE code.

PROBLEM

The adequacy of the various sizing methods for the determination of the required minimum relief area is usually verified by comparing the calculated and measured reactor pressure course during relief. However, this approach does not ensure that the submodels, which are included in the sizing method, especially those describing the reaction kinetics, the phase separation in the reactor and the mass flow rate through the relief area, are correct and physically consistent: For example, the mass flow quality at the top of the reactor, which is an important input parameter to the mass flow rate submodel [1], depends on the phase separation inside the reactor, which in turn depends on the volume flow rate and, thereby, on the mass flow rate. Hence, mass flow rate and quality are coupled by the phase separation process, with increasing mass flow rate leading to decreasing mass flow quality. Therefore, an error in the prediction of the mass flow rate results in a deviation of the calculated value of the mass flow quality that partly or even totally compensates for the effect of the first error on the calculated reactor pressure. Similarly, an inaccuracy in the reaction kinetics may be compensated by imprecisions in the other submodels. Accordingly, each submodel should be verified independently.

In view of the hazards of an emergency discharge of the contents of a chemical reactor directly to the atmosphere—although this actually occurs seldom—not only the reactor pressure but also the values of mass flow rate and mass flow quality during relief are needed for an adequate design of auxiliary downstream processing equipment like catchtanks, separators, flares etc. Consequently, in modern relief system design the accurate prediction of the mass flow rate and quality is as important as of the reactor pressure. This emphasizes the need for

independent verification of the submodels too.

It is our aim to contribute to an improvement on existing models of the well accepted DIERS method and to show their limitations by a detailed comparison of the results of depressurisation experiments with the corresponding calculations.

1. EXPERIMENTAL FACILITIES

The experimental investigation comprises of pressure relief experiments with chemically non-reacting fluids, namely methanol, water and refrigerants (only the results of the methanol and water depressurisations are presented here exemplarily), and with a reacting mixture of methanol and acetic anhydride. The former experiments are used to check the mass flow rate and phase separation submodels, whereas the latter are necessary for the verification of the reaction kinetics submodel alone and in conjunction with the other submodels.

The semi-technical scale test facility principally consists of a reactor with a volume of $0.105\,m^3$, which can be mantle-heated by low pressure steam, and a catchtank with a volume of $2.3\,m^3$, fig. 1. The vessels are connected via a vent line with a nominal diameter of 50 mm, which is mounted at the top of the reactor. Orifice plates with different bore diameters can be inserted into the vent line to simulate various relief areas. The controlled initiation of the depressurisation is achieved with a quick-opening valve. The pressure and temperature are measured in the reactor, vent line and catchtank. Three pitot tubes, which are mounted parallely in a pipe cross section, and a five-beam gamma-densitometer are used for measuring the dynamic pressure and the void fraction in the vent line, respectively. The mass flow rate is derived from the void fraction and the dynamic pressure assuming no slip between liquid and vapour phase velocities. The mass flow quality at the entrance of the vent line is determined from the measured pressure and temperature in the vent line and in the reactor on the assumption of isenthalpic flashing and thermodynamic equilibrium between vapour and liquid phase.

2. MODIFICATIONS TO THE COMPUTER CODE

The employed computer program is an in-house extended version of SAFIRE, originally developed by DIERS [2]. Presently, the extensions include a variable discharge coefficient, which depends on the phase composition of the two-phase flow or the pressure ratio, a new phase separation model, which is based on a sophisticated drift flux model and allows for the gradual rise of the mixture level after start of relief, and a module for the simulation of a catchtank at the end of the vent line [3].

3. EXPERIMENTAL AND NUMERICAL RESULTS FOR A METHANOL DEPRESSURISATION

In fig. 2 the reactor and catchtank pressure during a depressurisation of initially saturated methanol are shown along the values predicted by using the extended SAFIRE code. Here, the discharge coefficient was calculated according to D.W. Sallet [4], taking into account the ratio of the pressure in front of and behind the orifice plate. After actuation of the quick-opening valve the pressure in the reactor rapidly falls from the set pressure of 11.2 bar to about 10 bar due to the discharge of vapour out of the free board space of the reactor. After a delay time of about 200 ms, boiling of methanol in the reactor begins and the pressure rises again, when more vapour is produced per unit time than discharged. At the same time, the

mixture level is rising due to incomplete separation of the generated vapour from the boiling liquid. When the mixture level reaches the entrance of the vent line, a two-phase mixture of vapour and liquid is discharged. After passing a maximum the reactor pressure falls steadily. Later on, complete phase separation begins, the mixture recedes from the top of the reactor and the flow in the vent line changes back to mainly single-phase vapour flow. Finally, the reactor pressure approaches a value of 4 bar.

Most of the time, the difference between the calculated and the measured reactor pressure is small. It is, however, impossible to reproduce the initial phase of the depressurisation—the initial drop and the following increase of the reactor pressure—correctly, because the assumption of thermodynamic equilibrium between the vapour and liquid phase is used in SAFIRE, whereas actually during the boiling delay time after start of relief the deviations from thermodynamic equilibrium are growing [5].

The simultaneously measured pressure in the closed catchtank rises from ambient pressure to approximately 3 bar within 15 s after initiation of relief. The very slow rise during the first 500 ms is likely caused by the condensation of vapour on the cold wall of the catchtank. With increasing relief time the pressure curve flattens and the catchtank pressure approaches the end pressure of 4 bar. The calculated catchtank pressure rises faster than the measured pressure immediately after start of relief. This is possibly due to the use of a constant and initially too small heat transfer coefficient in the calculation of the heat transfer across the catchtank wall, i.e., the initially enhanced condensation of vapour on the wall is neglected. Later on, the difference between the measured and calculated value of the catchtank pressure vanishes.

The mass flow quality at the discharge pipe inlet, determined as outlined above, is shown in fig. 3 as a function of relief time. The measured quality remains at a value of unity during the rise of the level of the flashing mixture, indicating that only vapour is discharged. After about 300 ms the mixture level reaches the top of the reactor and a two-phase flow in the vent line occurs. Accordingly, the quality suddenly drops to approximately 0.2, a value characteristic for stationary annular-mist flow. The following recorded oscillations of the quality are caused by fluctuations of the vapour generation and phase separation processes. With decreasing pressure difference between reactor and catchtank the mass and volume flow rate decrease, too. The vapour generation rate, which during this phase of the depressurisation is proportional to the volume flow rate, also lessens, thus leading to increasing separation of the generated vapour from the boiling liquid. Accordingly, the mass flow quality rises and reaches unity again about 9 s after start of relief, i.e., only vapour flows out of the reactor again.

The calculated mass flow quality amounts, in contrast to the measured value, only to a few percent at the start of relief. It rises gradually and reaches the final value of unity within 12 s. Obviously, the initial phase of relief and the later ocurring oscillations are not reproduced by using the program. This is a consequence of applying the assumptions of completely swollen reactor contents at the start of relief and of quasi-stationary states during later phases of the depressurisation to the phase separation model. The further discrepancies are caused by additional simplifications in modelling the phase separation process. Even for later times the reproduction of the time-averaged measured mass flow quality is not entirely satisfactory; the calculated values amount to only 50% of the measured ones.

The measured and calculated mass flux related to the orifice area are shown as a function of time in fig. 4. After initiation of relief the mass flux steeply rises up to 5000 kg/(m^{2}s), first due to the inception of single-phase vapour flow and then due to the developing two-phase flow. It is, however, not possible to distinguish the two flow periods. Thereafter, the mass

flux altogether drops to about 1000 kg/(m^{2}s) with superimposed minor fluctuations, which correspond to the simultaneous fluctuations of the mass flow quality. Whereas this decrease is caused mainly by the increasing mass flow quality, the further decrease of the mass flux is due to the vanishing difference between reactor and catchtank pressure.

The calculated mass flux of about 4500 kg/(m^{2}s) at the beginning of relief is slightly lower than the highest measured value. With increasing relief time, the mass flux falls continuously to a value of 1000 kg/(m^{2}s) due to the increasing mass flow quality in the discharge pipe. The further decrease of the mass flux is caused principally by the decreasing difference between reactor and catchtank pressure. Altogether, the calculated values are only a little bit below those determined experimentally, if the inaccurately reproduced initial phase of the relief is disregarded.

4. EXPERIMENTAL AND NUMERICAL RESULTS FOR A WATER DEPRESSURISATION

The measured and predicted pressure in the reactor and the catchtank during a depressurisation of initially saturated water are presented in fig. 5. The pressure decrease after opening the relief section at the set pressure of 3.8 bar amounts to less than 0.3 bar before flashing of the water begins, i.e., the superheat of the water at boiling incipience is small. The pressure then rises, because more steam is produced per time unit by vaporisation than removed by the discharge flow. Simultaneously, the level of the flashing water is rising due to only partial separation of the generated steam from the water. When the mixture level reaches the top of the reactor, a two-phase mixture of steam and water is discharged. After that, the pressure decreases gradually with only slight oscillations until the end pressure of 2.5 bar is reached. The differences between the calculated and the measured reactor pressure during the initial phase of the depressurisation are similar to those in the case of the methanol depressurisation and have the same causes.

The simultaneously measured pressure in the catchtank rises very slowly during the first two seconds, most probably because again the inflowing steam is condensing on the much colder catchtank wall. Later on, the pressure rises gradually to the end pressure of 2.5 bar. The difference between the measured and the calculated catchtank pressure increases at first, because the heat transfer across the catchtank wall is underestimated: The heat transfer coefficient is assumed constant in the calculation of the heat flux across the catchtank wall, whereas its actual value is time-dependent. At the beginning of relief the heat of condensation is transferred to the catchtank wall leading to an increase in wall temperature, i.e., the heat transfer from the steam to the wall, which is achieved directly by condensation, regulates the rate of heat loss of the catchtank contents. During later phases of the depressurisation the temperature difference between steam and catchtank wall is much smaller and the condensation of steam on the wall is balanced against the heat transfer from the outside of the wall to the air surrounding the catchtank. Consequently, the rate of heat loss of the catchtank contents is regulated by the latter process, i.e., by free convection. Clearly, a correct description of these two very different modes of heat transfer—condensation and free convection—requires distinct values of the heat transfer coefficient.

The mass flow quality at the entrance of the vent line is shown in fig. 6 as a function of relief time. The measured quality, which is unity at the start of relief, almost immediately falls to ca. 0.2, indicating that the initial period of single-phase steam discharge is very short. During the next 15 s the time average of the oscillating quality rises to about 0.6. Thereafter, the quality rises rapidly to unity and the flow returns to single-phase steam flow. The observed

fluctuations of the quality are greater than during the depressurisation of methanol, fig. 2.

The calculated mass flow quality remains unity for approximately 100 ms after start of relief and then drops to a value of 0.15. It grows with steadily increasing rate, until unity is reached after a time interval of 17 s of two-phase flow in the vent line. During this time the calculated value is always smaller than the measured one, the difference amounting to 0.2 on average. This should lead to a predicted reactor pressure which is higher than the measured pressure. Since the calculated value is actually too small, other errors must compensate for the deviation of the mass flow quality. The observed, apparently chaotic oscillations of the quality can not be reproduced by using the new phase separation model, because it is based on the assumptions of quasi-stationary states and of a linear dependance between vapour generation rate and total volume flow rate in the discharge pipe.

The measured and calculated mass flux related to the orifice cross section is presented as a function of time in fig. 7. After beginning of relief the mass flux rises to 5300 $kg/(m^2s)$ in less than 1 s. This increase is caused mainly by the simultaneous decrease of the mass flow quality. After that, the mass flux falls to a value of about 500 $kg/(m^2s)$, which is reached when the mass flow quality becomes unity again. The observed fluctuations during this time correspond to the fluctuations of the mass flow quality. The overall decrease of the mass flow rate is caused by the combined effects of the vanishing pressure difference between reactor and catchtank and of the increasing value of the mass flow quality.

The predicted value of the mass flux at the start of relief amounts to about 1600 $kg/(m^2s)$ in contrast to the measured value of zero. This follows using a mass flow rate model based on the assumption of stationary flow, which makes it impossible to model the gradual acceleration of the fluid in the vent line directly after actuation of the quick-opening valve. During the first 5 s of relief, the predicted value of the mass flux is smaller than the measured one. After that, the calculated mass flux rises above the measured value and remains there for the rest of the measurement time. Here, the likely cause for the deviation is the difference between the measured and calculated value of the mass flow quality. This is, however, no explanation for the observed difference during the first 5 s.

On summarizing, the time-dependent values of the main parameters of the depressurisation of two non-reacting two-phase systems, i.e., pressure, mass flow quality and mass flow rate, are predicted with different accuracy by using the extended version of SAFIRE. In both cases the measured pressure can be computed fairly accurately, whereas larger deviations still remain with respect to mass flow quality and mass flow rate. Therefore, we conclude that the mass flow rate and mass flow quality models very likely still contain too many simplifying assumptions, which were introduced into the original program because of a lack of detailed knowledge. These assumptions compensate to a large extent for each other in the calculation of the reactor pressure, leading to a seemingly good agreement between measurement and calculation, if only the reactor pressure is considered. If, however, additional parameters like mass flow rate and quality are examined, the deviations become obvious. Since accurate values of mass flow rate and quality are needed for the design of downstream processing equipment, further improvements are necessary. The question is now, if this statement still holds when analysing the results obtained during venting of a reacting system.

5. EXPERIMENTAL AND NUMERICAL RESULTS OF THE DEPRESSURISATION OF A RUNAWAY REACTION

The depressurisation experiment with a runaway chemical reaction was carried out on the basis of the exothermic esterification of acetic anhydride and methanol to acetic acid and

methyl acetate. This reaction was already used in the DIERS Users Group Round-Robin Phase II Tests as a model for vapour pressure systems with a reacting liquid phase [6]. The main non-catalysed exothermic reaction with a reaction enthalpy of 66.3KJ/mol is described by

$$(CH_3CO)_2O + CH_3OH \rightarrow CH_3COOCH_3 + CH_3COOH$$

For our purposes, it seems sufficient to assume that there are no side reactions. The reaction rate k [kmol/m^3 s] will then depend only on the temperature T [K] and the concentrations of acetic anhydride Ac [kmol/m^3] and methanol Me [kmol/m^3]. The dependance of the reaction rate k [kmol/m^3 s] on these variables was determined in an adiabatic temperature rise experiment in a VSP reaction calorimeter. The equation obtained for the reaction rate, which is only valid in conjunction with the physical data used in its derivation, reads

$$k = 3.711 \cdot 10^7\ \mathrm{m^3/(kmol\,s)}\ \exp\left(-9323.2\,\mathrm{K}/T\right) \cdot Ac \cdot Me$$

A prerequisite for a proper recalculation of the relief process is here the correct determination of the state variables at the start of relief. This requires an accurate description of the chemical and thermodynamic processes ocurring before initiation of venting. In fig. 8 the measured and calculated pressure course in the closed reactor are shown. At the beginning of the experiment, when the reactor contains a mixture of methanol and acetic anhydride under its own vapour pressure, the temperature amounts to 65°C. Initially, the pressure rises due to heating of the mixture by the reactor wall, which is kept at a constant temperature of 135°C, and due to the initially slow exothermic reaction. The rising mixture temperature leads to an acceleration of the reaction, which in turn leads to a faster rise of the pressure and temperature, until at last a so-called thermal explosion would take place. At the relief set pressure of approximately 7.5 bar, the rate of pressure rise is about 0.7 bar/s, both measured and calculated. The measured pressure in the closed reactor is, altogether, fairly well reproduced by the calculation, i.e., the modelling of the reaction kinetic and thermodynamic processes in the closed reactor seems to be sufficiently accurate and the state variables at the very start of relief are nearly identical in computation and experiment.

The measured and calculated pressure course in the reactor and in the catchtank after beginning of relief are shown in fig. 9. At the set pressure of 7.5 bar, the temperature amounts to 137°C and the filling level to about 90%. The measured reactor pressure rapidly drops to about 6.7 bar within 200 ms after opening the relief cross section due to the discharge of vapour from the free board volume in the reactor. After that, it rises to a maximum value of 8.7 bar within 6 s. This pressure overshoot is due to the heat generated by the chemical reaction, which exceeds initially the cooling of the mixture due to the discharge flow [7]. Thereafter, the reactor pressure falls steadily and approaches the final value of 3.2 bar. The simultaneously measured catchtank pressure rises from ambient pressure to approximately 3 bar within 15 seconds. With increasing time, the curve flattens and approaches the final reactor pressure.

In the recalculation of this experiment a variable orifice discharge coefficient, which depends on the quality of the two-phase flow, was used. It was calculated according to a correlation proposed by S.D. Morris [8] for two-phase flow through an orifice. Disregarding the first stage of the depressurisation, where the initial pressure decrease due to the delayed onset of vaporisation can not be predicted by using the program, the pressure in the reactor is quite accurately reproduced by the calculation.

Fig. 10 contains a graph of the measured and calculated mass flow quality at the entrance of the vent line during relief. The measured quality amounts to unity immediately after start of relief. After a time of ca. 400 ms the mass flow quality drops to a value of approximately 0.6,

where—except for small fluctuations—it remains for a time of about 3 s. Following a rise to a value of about 0.8 and a drop back to 0.6, the mass flow quality rises again to unity, which is reached after a total time of 6.7 s of the two-phase discharge. During the first 400 ms the discharge flow and the still increasing liquid temperature due to the progressing chemical reaction cause a growing superheat of the liquid until flashing begins and the level of the boiling vapour-liquid mixture rises to the top of the reactor. The temporary rise of the mass flow quality to 0.8 is obviously caused by a major movement of the boiling mixture level. The predicted time interval of ca. 500 ms between start of relief and onset of two-phase flow is somewhat to large. Here, the quality drops to approximately 0.35, which corresponds to only 60% of the measured value, and rises at once, in contrast to the measured value. Altogether, the onset and duration of two-phase flow are reproduced very well, but the calculated values of the mass flow quality still differ from the measured ones.

The measured and calculated mass flux during the depressurisation are shown in fig. 11. The experimental mass flux rises steeply from zero to a value of 1000 kg/(m^{2}s), where it remains for about 3 s. The minor fluctuations during this time as well as the following drop to a value of 700 kg/(m^{2}s) correspond to the simultaneous fluctuations of the mass flow quality, fig. 10. After a time of 7 s the transition to single-phase vapour flow takes place and the mass flux continuously falls due to the diminishing difference between reactor and catchtank pressure. The calculated mass flux amounts to 400 kg/(m^{2}s) directly after start of relief, i.e., a fully developed single-phase vapour flow is assumed. In contrast to the measured value, the mass flux increases to only 670 kg/(m^{2}s) after the onset of two-phase flow and remains below the measured value during the whole period of two-phase flow. Since the differences between the measured and the calculated values are large even for single-phase vapour flow, at least a part of the deviations seems to be caused by the mass flow rate submodel itself. Whereas in the recalculation of this experiment the mass flow quality is reproduced more accurately than in the recalculation of the methanol depressurisation, the differences between the measured and the calculated values of reactor and catchtank pressure and mass flux are larger than in the latter case.

Altogether, essentially the same drawbacks appear in the recalculation of the depressurisation of a runwaway reaction as of chemically inert mixtures. The deviations directly after start of relief are mainly attributed to the simple and unrealistic assumption of thermodynamic equilibrium between the phases and to the use of mass flow models, which are based on the stationary flow assumption and do not allow for pressure waves and gradual acceleration of fluid in the vent line. The differences between measured and calculated values of mass flow rate and quality, which occur during later stages of the depressurisation process, are caused by still remaining simplifications in the mass flow rate and phase separation models. Nevertheless, by using SAFIRE it should be possible to determine the effect of a chemical reaction on the depressurisation process fairly well.

CONCLUSIONS

The transient pressure and mass flow rate during emergency top venting both of a chemically inert system and a reacting two-phase system can be reproduced by using SAFIRE with an accuracy sufficient for technical purposes. Therefore, it should be possible to size the relief area and the vent line for similar systems in the chemical process and related industries. However, the results of this investigation should be checked further in experiments with other reaction systems and on a larger scale.

REFERENCES

[1] F. Hardekopf, D. Mewes: "Flow of Multicomponent Mixtures During Depressurisation of Reactor Vessels", in: Proc. Eurotherm Seminar No. 14, L. Bolle, Ed., Louvain-La-Neuve, Belgium, vol. 1, pp. 14.1–14.29 (1990).

[2] M.A. Grolmes, J.C. Leung, "Code Method for Evaluating Integrated Relief System Phenomena", in: Chem. Eng. Prog., vol. 81, pp. 47–52 (1985).

[3] G. Wehmeier: "Theoretische und experimentelle Untersuchung der Vorgänge bei der Druckentlastung von Chemiereaktoren", Ph.D. Thesis, Univ. Dortmund, BRD (1994).

[4] D.W. Sallet, "Thermohydraulics of Valves for Nuclear Applications", in: Nucl. Sci. Eng., vol. 88, pp. 220–224 (1984).

[5] F. Mayinger, "Stand der thermohydraulischen Kenntnisse bei Druckentlastungsvorgängen", in: Chem.-Ing.-Tech., vol. 53, pp. 424–432 (1981).

[6] J.C. Leung: "Round Robin Testing Vent Sizing Results", in: 5. Official DIERS Users Group Meeting, Seattle, 1989.

[7] L. Friedel, G. Wehmeier: "Modelling of the Vented Methanol-Acetic Anhydride Runaway Using SAFIRE", in: Proc. Eurotherm Seminar No. 14, L. Bolle, Ed., Louvain-La-Neuve, Belgium, vol. 1, pp. 12.1–12.15 (1990).

[8] S.D. Morris, "Discharge Coefficients for Choked Gas-Liquid Flow Through Nozzles and Orifices and Applications to Safety Devices", in: J. Loss. Prev. Proc. Ind., vol. 3, pp. 303–310 (1990).

FIGURES

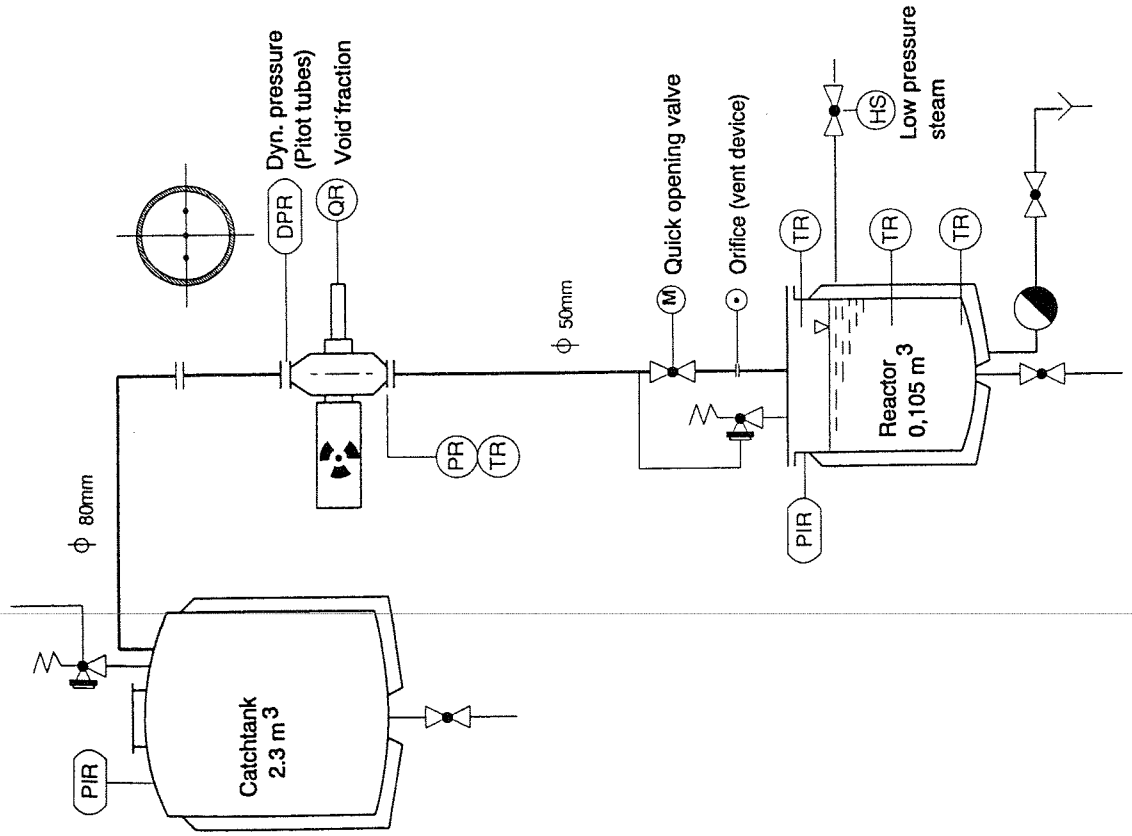

Fig. 1: Semi-technical scale test facility for depressurisation experiments

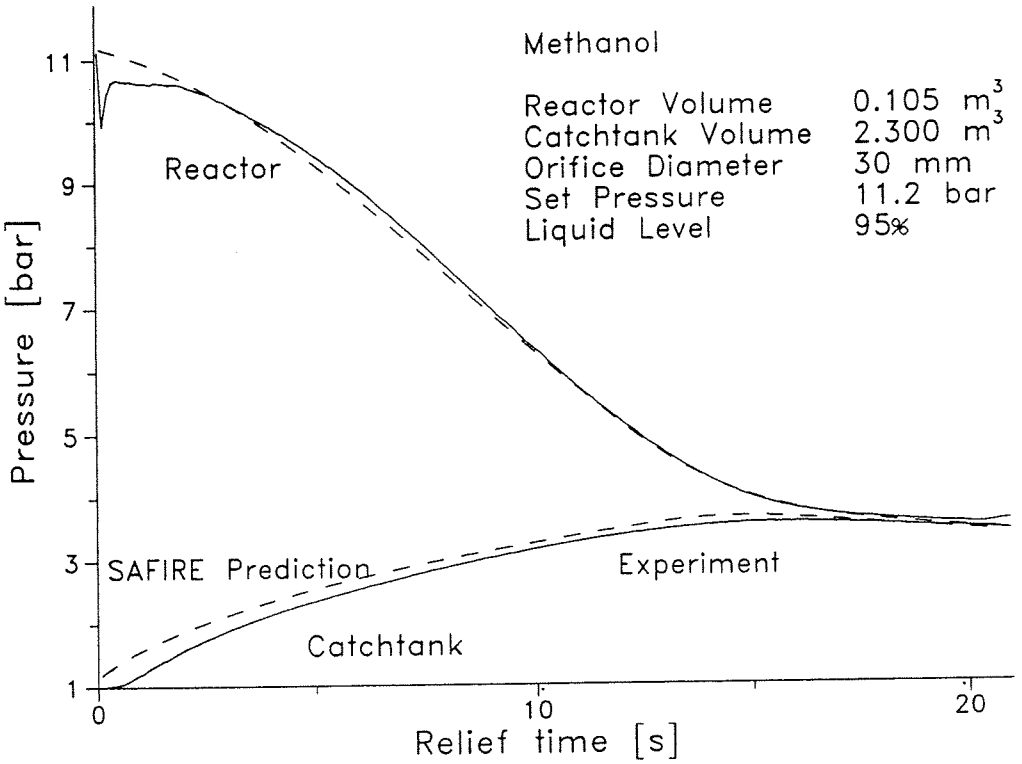

Fig. 2: Measured and calculated pressure in the reactor and catchtank as a function of relief time during venting of methanol

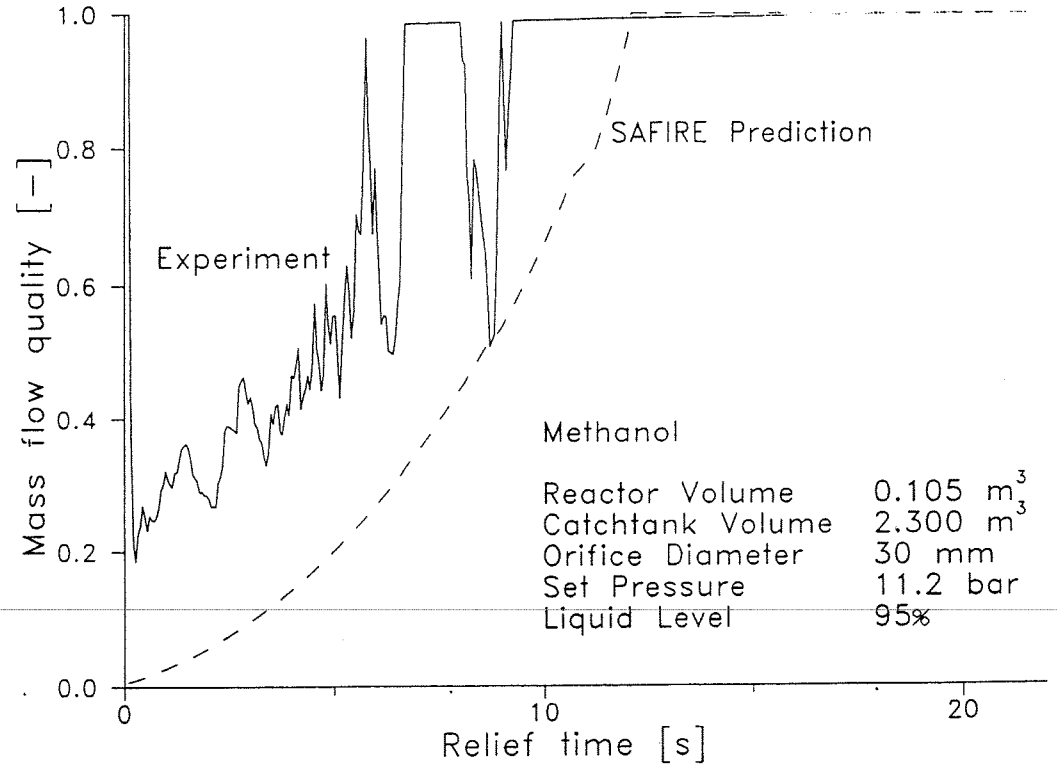

Fig. 3: Measured and calculated mass flow quality at the entrance of the vent line as a function of relief time during venting of methanol

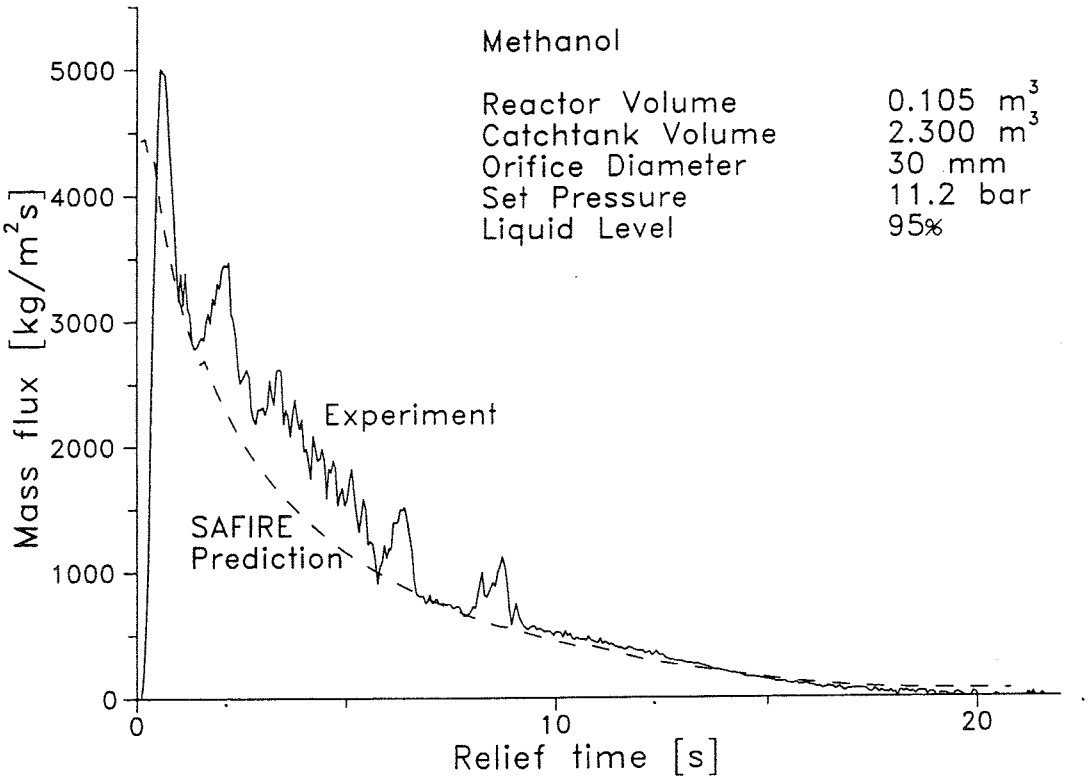

Fig. 4: Measured and calculated mass flux in the orifice as a function of relief time during venting of methanol

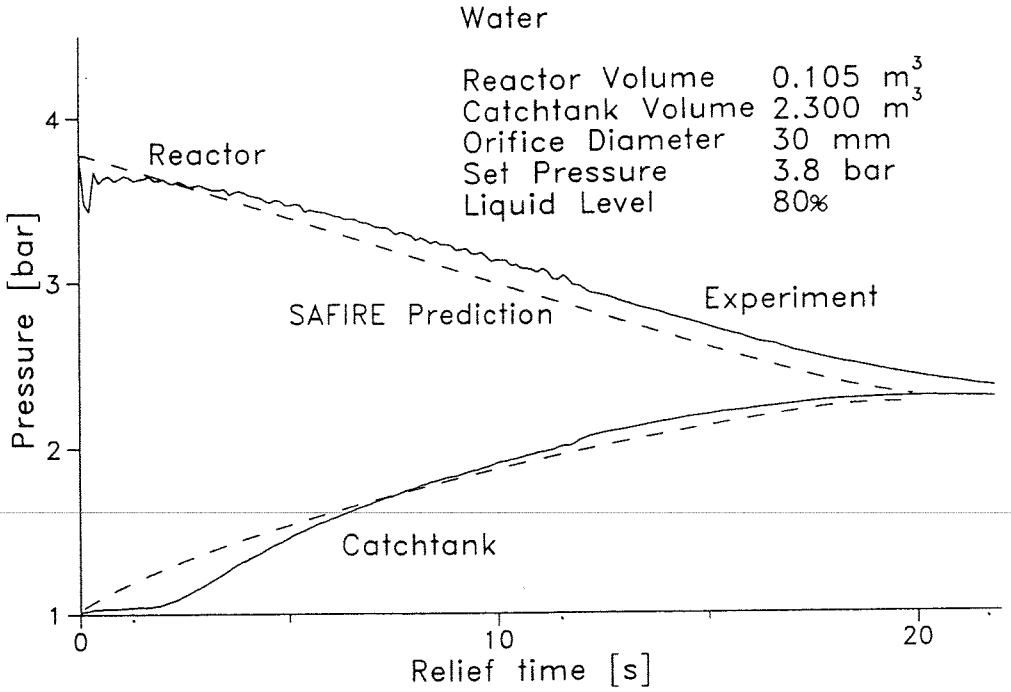

Fig. 5: Measured and calculated pressure in the reactor and catchtank as a function of relief time during venting of water

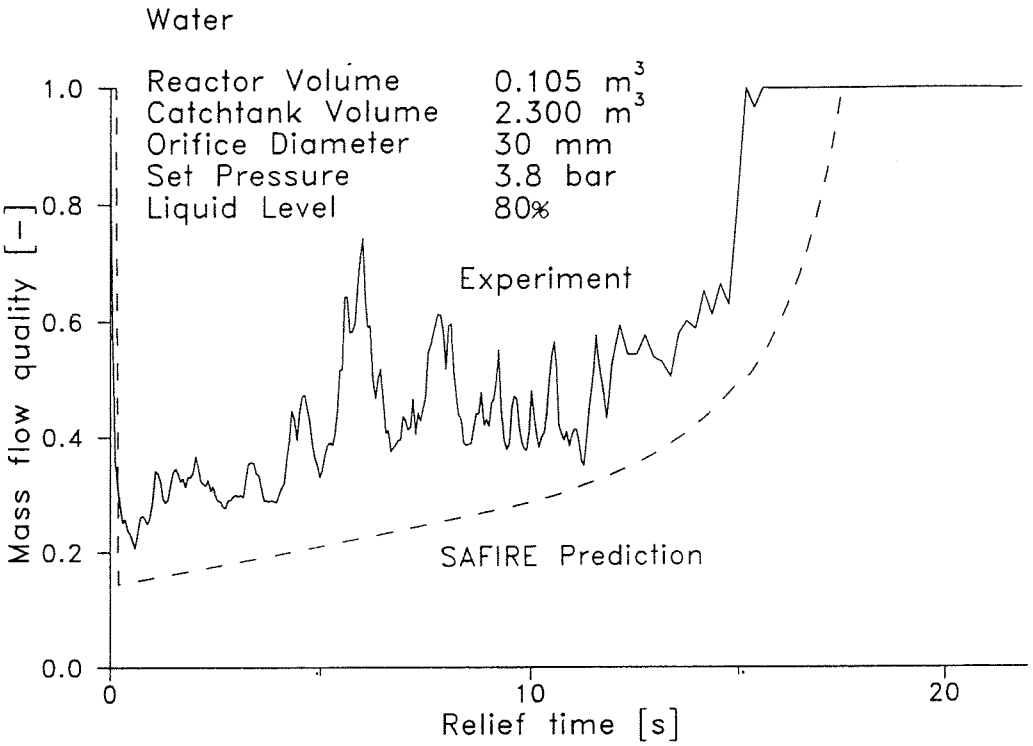

Fig. 6: Measured and calculated mass flow quality at the entrance of the vent line as a function of relief time during venting of water

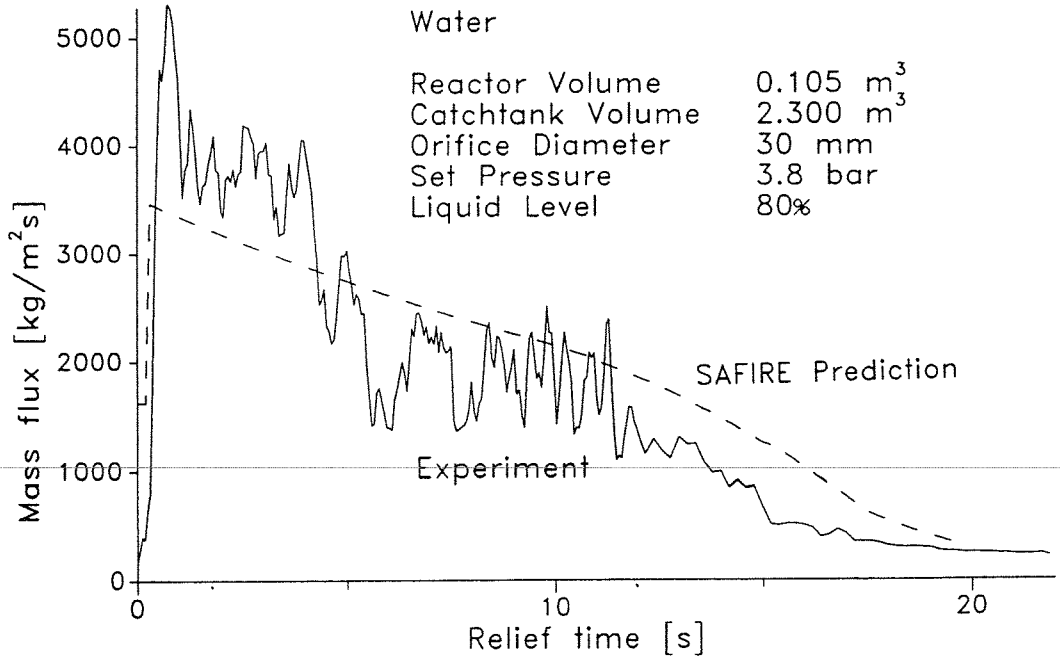

Fig. 7: Measured and calculated mass flux in the orifice as a function of relief time during venting of water

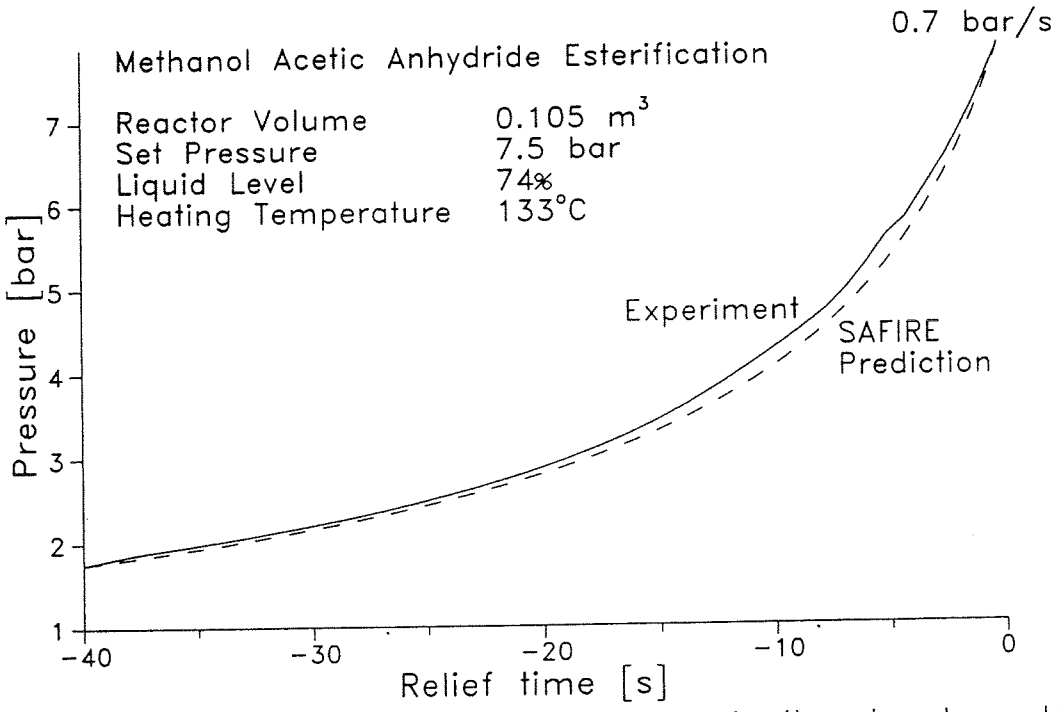

Fig. 8: Measured and calculated pressure in the closed reactor during the self-heating phase of a methanol acetic anhydride esterification

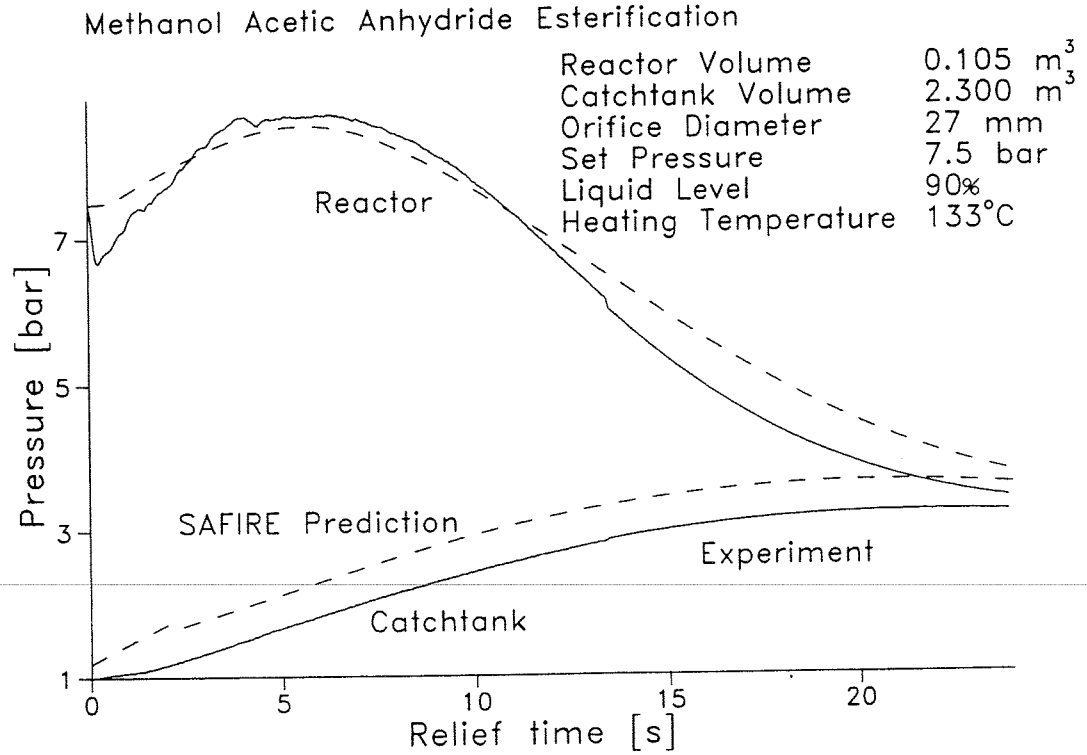

Fig. 9: Measured and calculated pressure in the reactor and catchtank as a function of relief time during venting of a runaway methanol acetic anhydride esterification

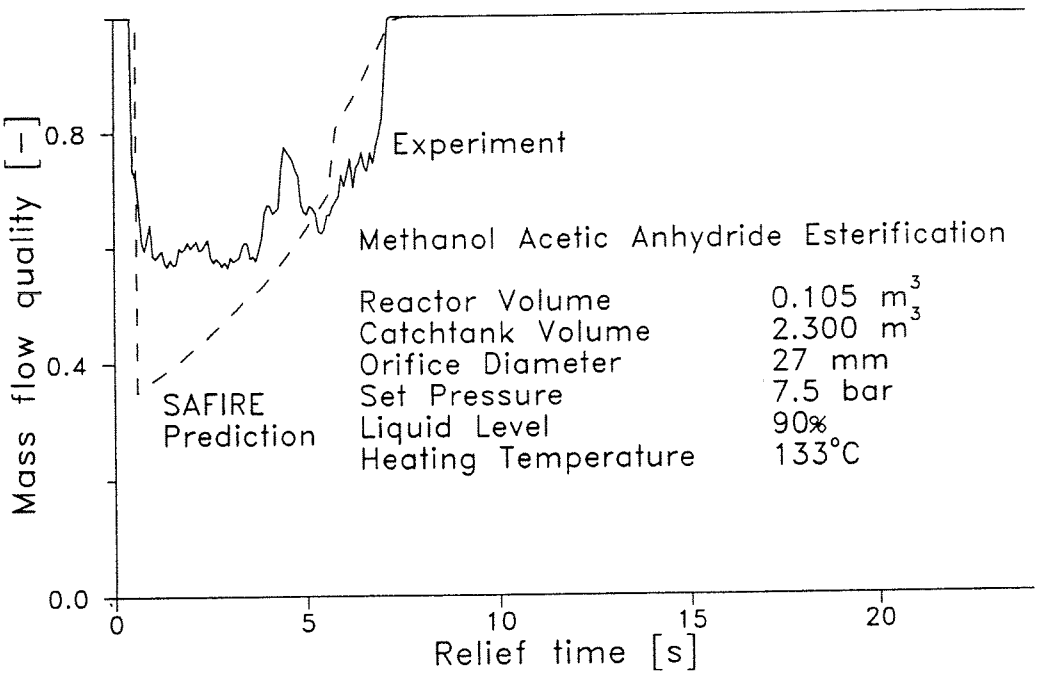

Fig. 10: Measured and calculated mass flow quality at the entrance of the vent line as a function of relief time during venting of a runaway methanol acetic anhydride esterification

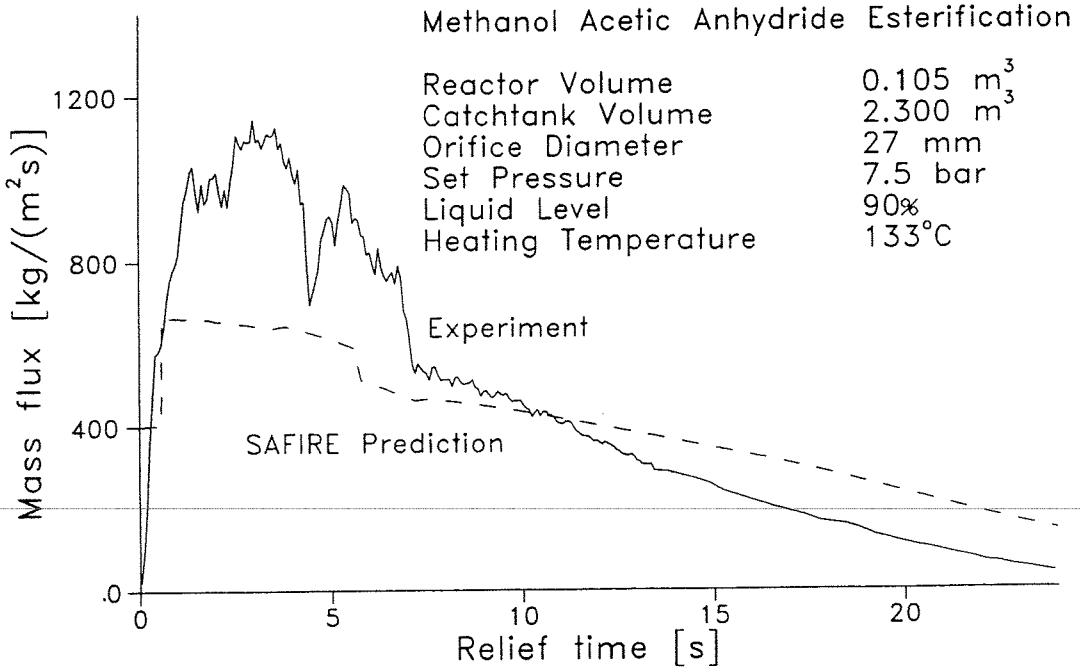

Fig. 11: Measured and calculated mass flux in the vent line as a function of relief time during venting of a runaway methanol acetic anhydride esterification

An Overview of Industry Activities on Multi-Phase Flow Studies for Pressurized Water Reactor in Japan

A. Tsuge, K. Kawanishi, N. Nakamori

Takasago R&D Center, Mitsubishi Heavy Industries, Ltd.
2-1-1 Shinhama, Arai-cho, Takasago City, Hyogo-Rref., Japan
Phone:0794-45-6710, Fax:0794-45-9626

ABSTRACT

An overview is presented on the multi-phase flow studies for pressurized water reactor mainly conducted by Japanese industries. Four major fields are brought into focus.

(1)Small break LOCA Study and Training Simulator
(2)DNB and In-Bundle Void Fraction Measurement
(3)Steam Generator Thermal Hydraulics and Vibrations
(4)New Concept of Passive/Active safety System

1. INTRODUCTION

In Japan, 21 PWR units are under commercial operation and 2 PWR's under construction with twenty four years operational experiences. Multi-phase flow studies and developments during these two and half decade played important roles in establishing PWR reliability and safety.

In addition to the university's academic researches and regulatory side activities on multi-phase flow phenomena, Japanese PWR industries also have conducted extensive research and development on multi-phase flow, aiming for the higher reliability and availability of PWR's.

In this paper, the author forcuses on the major four fields of PWR reliability activities which are mainly conducted by the Japanese PWR industry group with the collaboration with utilities and government.

2. SMALL BREAK LOCA STUDY AND TRAINING SIMULATOR

The Three Mile Island #2 unit's in 1979 made us realize the importance of the small break LOCA study and the operator training for the adequate remedial action under the accident. Japanese PWR industry group ; the five PWR utilities and Mitsubishi Heavy Industries, made a comprehensive R&D program to fully understand the phenomena and to develop the best estimate computer program with the real time simulation capability. The program included three issues, that were an integral experimental study on small break LOCA, a fundamental experiment on a drift flux model applicable to a thermal hydraulic behavior during the small break accident and CANAC-2 code development and the verification[1].

A semi scale test facility named EOS LOOP was built in Takasago Research and Development Center[2][3]. The EOS test facility simulated a PWR with the 1/270 volume as shown in Fig. 2.1. The elevations of the main components are the same as the commercial plant to simulate the phenomena such as natural circulation cooling and reflux condensation cooling. Two serials of tests were conducted which were power operated relief valve (PORV) break tests and cold leg break tests.

In the PORV break accident, water level transient in the pressurizer was important as indicated at Three Mile Island accident. Fig. 2.2 and 2.3 show the collapsed water level and the core water level. It was clear that the pressureizer was almost filled with water even though the water level decreased below the hot leg in the reactor vessel. This phenomenon occurred due to countercurrent limitation at the surge line piping. Steam in surge flow prevented the water drop from the pressurizer to the hot leg. The higher steam flow in the surge line resulted in the lower water level in the pressurizer. The countercurrent limitation velocity in the test was able to be given by the empirical expression by Siddiqui[4].

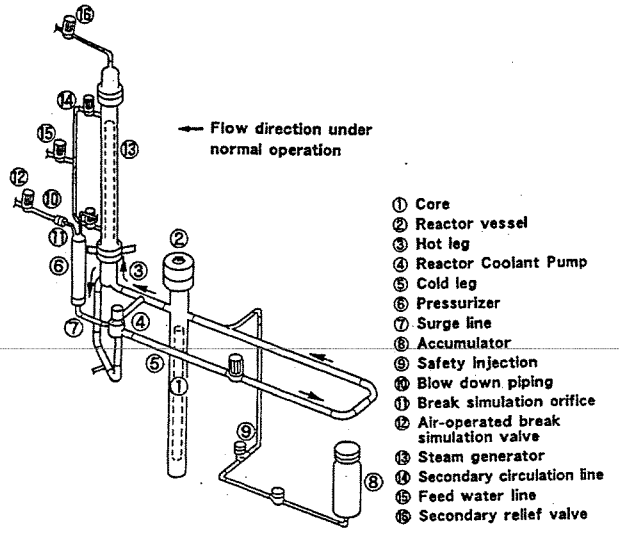

Fig.2.1 Bird's Eye View of EOS Facility[2] [3]

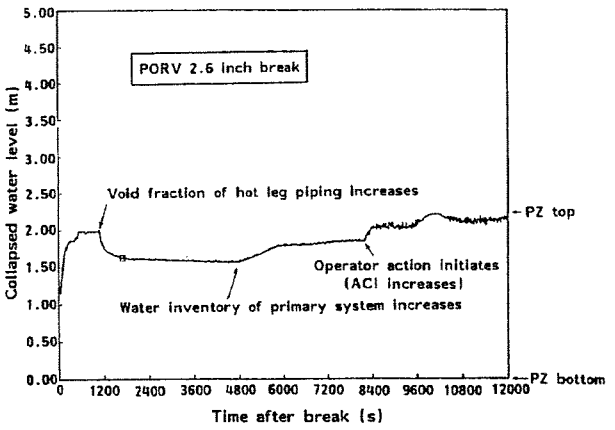

Fig.2.2 Collapsed Water Level in Pressurizer in PORV Break[2]

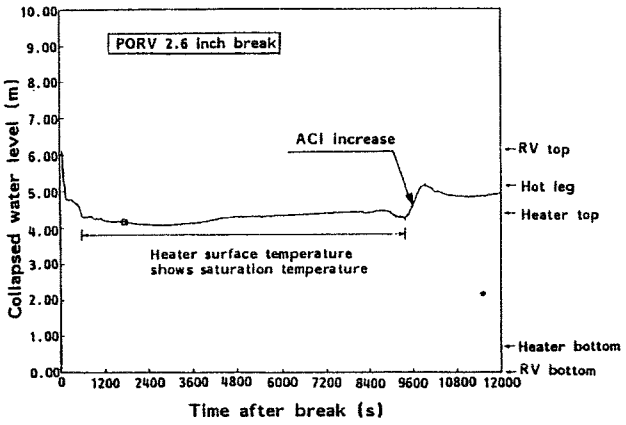

Fig.2.3 Collapsed Water Level in Core in PORV Break[2]

In the cold leg break accident, temporary uncovers of the core fuel assembly that resulted in the temporary fuel temperature rise were seen as shown in Fig. 2.4. This phenomenon occurred in the cold leg break accident due to loop seal formation and clearance in the crossover legs as are seen in Fig. 2.5.

For simulation of the small brak transient, a non-homogeneous two-phase flow model is needed because phase separation effects play an important role in the transient behavior. For this purpose, a drift flux model was applied in the CANAC-2 code. The distribution parameters and the drift velocities were experimentally obtained and a map of the drift flux parameters took the flow regime into consideration[5]. The empirical expression map is applicable to a full range of the two-phase flow that includes the velocity, the tube diameter, the void fraction, the pressure and the gravity direction. The comparison with the data is shown in Fig. 2.6. The map is easy to use because the drift flux parameters are given by the set of simple equations and the comparisons with the data are in good agreement.

The CANAC-2 code has a capability to simulate the small break accident with fast computer running time because of the simple architecture without decreasing the accuracy[1][6]. The special distribution effect was modeled by the elemental control volumes, and appropriately interconnected paths. The sets of the mass, momentum and energy equations in each volume are solved at each time step based on a thermal

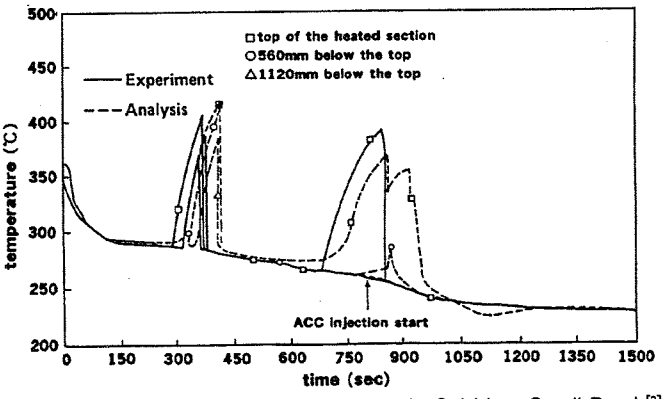

Fig.2.4 Fuel Rod Surface Temperature In Cold Leg Small Break[3]

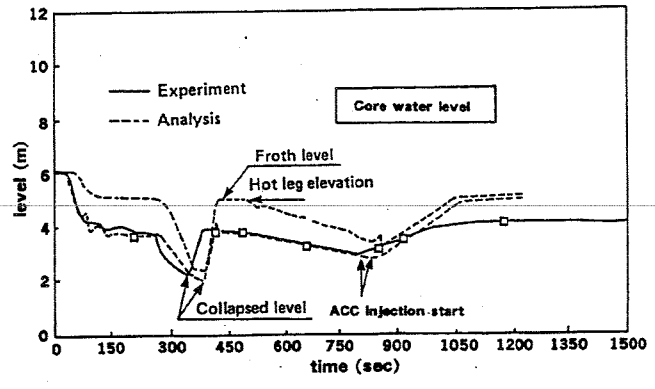

Fig.2.5 Water Level in the Core in Cold Leg Small Break[3]

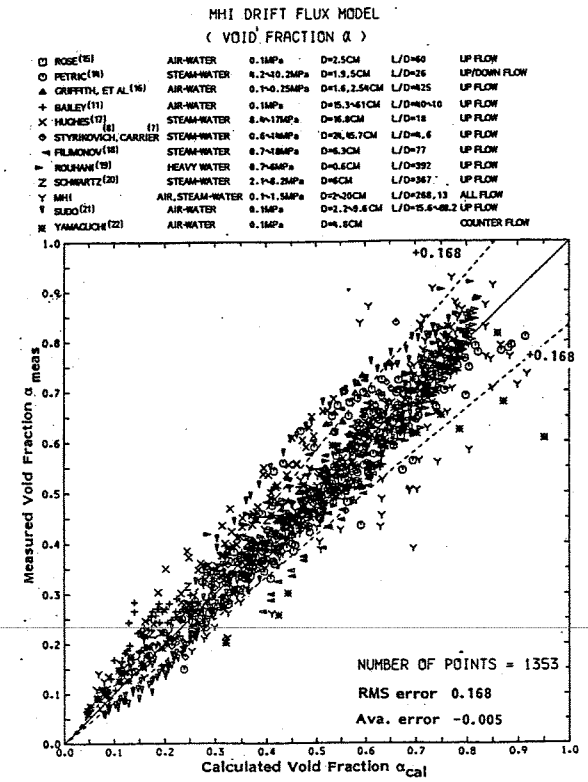

Fig.2.6 Comparison of Drift Flux Correlation to Experimental Data (MHI's Correlations)[5]

NUPEC TAKASAGO Engineering Laboratory is running the new project for the in- bundle void fraction measurements under the prototypical thermal hydraulic condition. The project consists of two test sections : single subchannel and 5 × 5 full length fuel assembly having 150kW and 10MW thermal output respectively[16].

Three dimensional spacial void distribution is measured by specially developed gamma- ray beam computed tomography (CT Scanner). The first experiment was carried out in 1992, and the preliminary report was issued as reference[17].

Fig. 3.1 and Fig. 3.2 show the void measurement system for single channel test and rod bundle test respectively. Both steady state and transient state tests have been carried out covering the conditions in PWR.

The typical detailed void distribution data within a subchannel as is shown in Fig. 3.3, and within the multi- rod bundles as is shown in Fig. 3.4 shall give us more clear insight into the subchannel boiling phenomena, resulting the improvement of subchannel analysis method. These improvements of thermal - hydraulic evaluation should be useful for introducing the reactivity feed back effect due to void generation which is currently not included in the safety analysis[17].The comprehensive test program are under way untill the end of 1994.

3.3 High Speed X- Ray Computed Tomography Scanner for two- phase- flow Visualization

Hori, K. and Kawanishi, K. et al. developed a high speed X- ray computed tomography (CT) scanner for the transient two - phase - flow visualization[18].

The system configuration is shown in Fig. 3.5 schematically. This system consists of the X- ray generating system, the detection system, the data acquisition system, the main controller and the data processing system. The main controller controls the data acquisition system and the X- ray generating system and works as the timing control for the total system.

The X- ray generating system consists of the X- ray generating units, the electronic switching units, the vacuum chamber and the vacuum pump. The eighteen X- ray generating units are installed in the annulus vacuum chamber. Each one has a cathode, a grid and a tungsten target as an anode. A high accelerating voltage up to 100kV is applied between the anode and the cathode to generate the X- ray haveing the required energy. The emission of the electron beam generated from the cathode to the target is normally suppressed by the bias voltage supplied to the grid. Only when this bias voltage is removed, will the electron beam pass through the unsuppressed grid towards the target and generate X- rays. The bias voltage of each grid is removed sequentially and temporarily. Since the electron beam is electronically controlled as described above, the X- ray fan beam is permitted to measure the time- dependent cross- sectional view of the object with a high speed scanning. The present system has the scanning time of 3.6 milliseconds per slice and the scanning rate of 250 slices per second.

The typical reconstructed images of the bubbly flow are shown in Fig. 3.6 and those of the slug flow are shown in Fig. 3.7. These figures are reproductions of the EWS video screen. In each figure, the left strip has the tomograms, the center strip has the tomogram images overlapped slantingly,

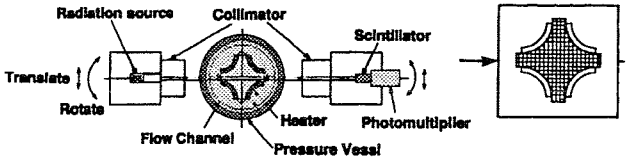

Fig.3.1 Computed Tomography Scanner System for Void Measurement in Single Channel[17]

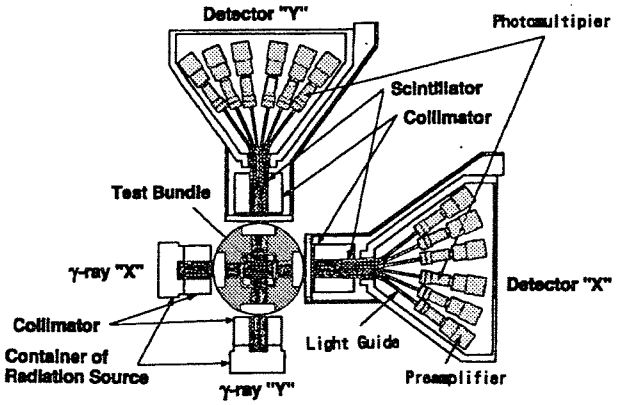

Fig.3.2 Void Measurement System for Rod Bundle Test[17]

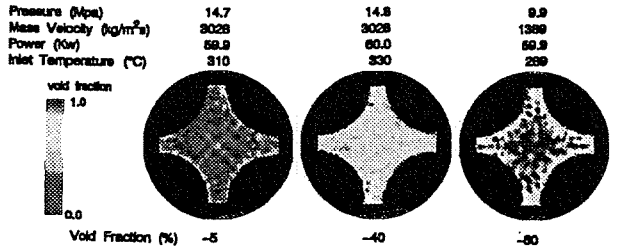

Fig.3.3 Single Channel Test Results by CT Scanners[17]

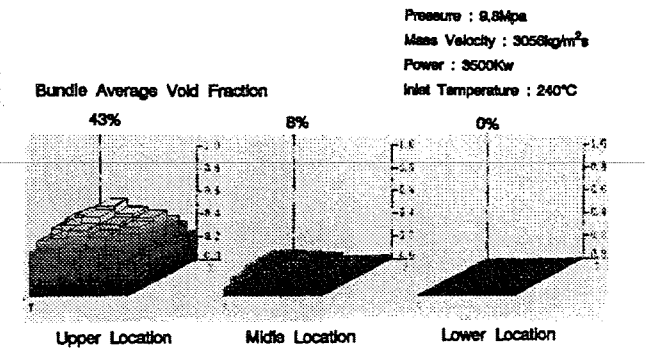

Fig.3.4 Rod Bundle Test Results[17]

equilibrium assumption. The user can select the non-equilibrium option for each volume. The non-equilibrium process is important for realistic simulation, especially for the pressure transient. The drift flux model was applied to calculate the velocities of each phase at the path. Non-condensable gas such as a hydrogen and a nitrogen gas must be taken into consideration because of the heat removal in the steam generator. In the CANAC-2, the gas is treated with as the dissolve gas in the steam and the water. The concentrations of the gas in each phase are determined based on Henry's law.

The CANAC-2 also has a full range heat transfer coefficient module including the non-condensable gas effect and a pressure loss coefficient module for the single phase and the two-phase flows. Break flow is calculated by Henry-Fauske's critical flow model.

The comparisons between the calculation and the integral experimental data as mentioned above were in good agreement. The typical results that are the core water level and the fuel rod surface temperature during the cold leg break experiment are shown in Fig. 2.5 and Fig. 2.4.

The CANAC-2 code has been incorporated in the advanced engineering simulator to give the wider range of simulation capability with operator action. The first advanced engineering simulator was in commission in February 1990 at the Nuclear Training Center #3 ; NTC-3, Tsuruga, JAPAN. The NTC-3 simulator made many opeprators experience the small break LOCA and steam generator tube rupture with their remedial interaction. It is worthy to note that the remarkable remedial operator action which was taken at the Mihama-2 steam generator tube rupture on February 9, 1991, was one of successful proofs of the advanced training simulator. The more the actual nuclear power plants be operated without trouble, the more the role of the engineering training simulator should be important.

The above small break LOCA study by Japanese PWR industry group was succeeded by the ROSA-IV Program in JAERI. ROSA-IV Program producted extensive data base and also deeper insight into the small break LOCA thermal hydraulic phenomena with the Large Scale Test Facility (LSTF). Rererence [7] and [8] introduce the outline of the program.

With the advancement of high performance computer system, more precise physical modeling of multi-phase flow are becoming to be incorporated in the next generation simulatior.

New project on development of super simulator has been launched by Nuclear Power Engineering Corporation with the participation of Japanese utilities, PWR/BWR vendors and academic organization[9]. International collaboration are encouraged.

3. DNB AND IN-BUNDLE VOID FRACTION MEASUREMENT OF PWR FUEL ASSEMBLY

Current fuel bundle two-phase flow studies by Japanese PWR industries can be introduced by overviewing following three areas.

3.1 DNB Study for High Conversion PWR

Mitsubishi Heavy Industries and Kansai Electric Power Co. made feasibility studies on high conversion PWR with semitight core configuration[10][11]. In the study, DNB experiments were performed using both Freon-12 and Water[11]. The scaling factor between Freon and Water was examined introducing some modification to stevens' empirical model for vertical round tubes[12]. Detailed description is in reference[11].

3.2 Proving Test on Thermal-Hydraulic Design Reliability of PWR Fuel Assembly by In-Bundle Void Fraction Measurement

Nuclear Power Engineering Corporation (NUPEC) with the sponsorship by Ministry of International Trade and Industry has finished three years' test program for proving DNB design reliability of PWR fuel[13].

Using 10MW PWR simulation loop with fully instrumented 5 × 5 and 6 × 6 full length PWR fuel assembly, comprehensive data base with 870 data points have been established resulting in the following achievements :

(1)Steady State Test	The obtained DNB data are in good agreement with MIRC-1[14] and NFI-1[15] prediction. The derived DNBR limits are lower than the value, 1.17, which is currently used in the licensing calculations.
(2)Transient Condition Test	It was confirmed that both correlations predict the critial heat flux adequately under transient conditions as well as the steady state. However, it is also recognized that they require further improvements for low flow and low-pressure conditions.
(3)Rod Bow Effect test	It is worthy to note that DNB penalty was not observed for either the contact bow or 85% bow cases.

and the right images are the three-dimensional images reconstructed from the tomograms and information of the bubble rise velocity. The parts of tomograms used to reconstruct the three-dimensional images of bubbles in the right strip are arranged in the left and center strips sequentially from the first one corresponding to the top of the upper bubble. The time sequences are downward in the left and center strips. When the scanning speed of the CT scanner is high enough to freeze a dynamic event of the two-phase flow, the resultant tomogram might be displayed as binary images representing the cross-sectional phase-distribution as shown in these figures.

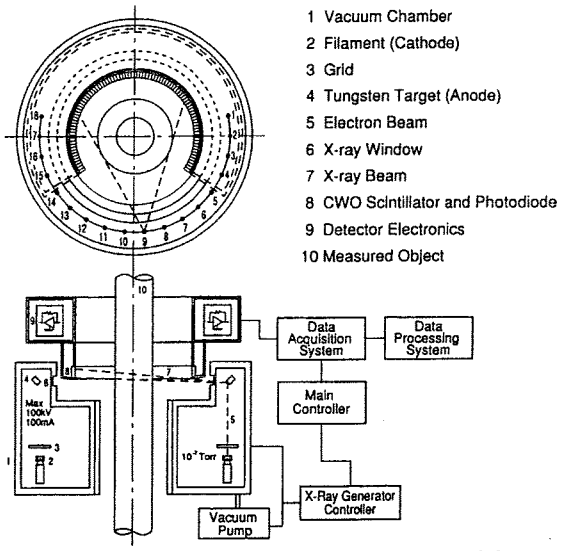

Fig.3.5 High Speed CT System Configuration[18]

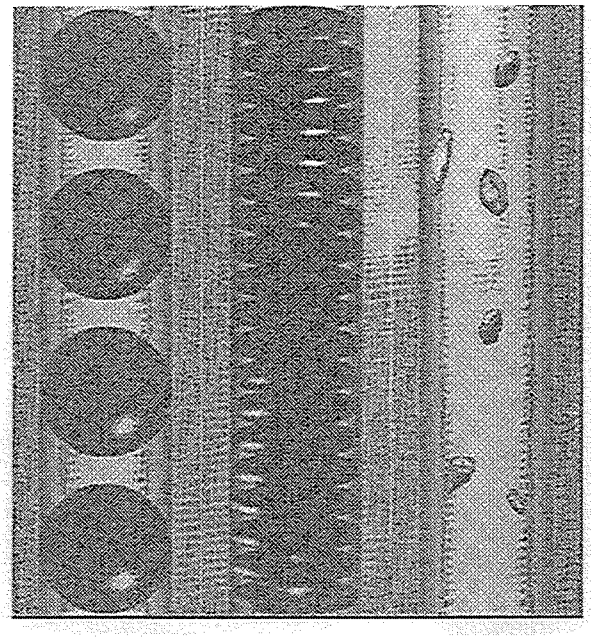

Fig. 3.6 Reconstructed Images of Bubbly Flow[18]

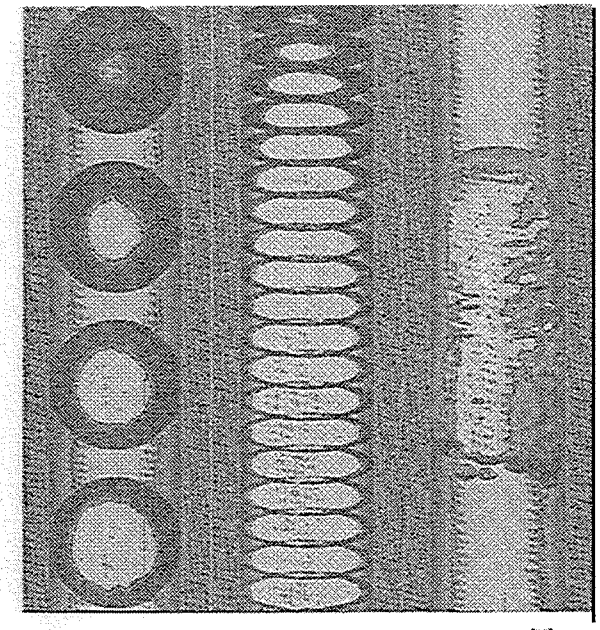

Fig. 3.7 Reconstructed Images of Slug Flow[18]

The history of the cross-sectional void distribution or the size and the number of bubbles can be evaluated from these resultant images. Fig. 3.6 shows the images of the dispersed bubbles of various sizes. Fig. 3.7 shows the larger bullet shaped bubble called a Taylor bubble having the parabolic outline at the head and the entrained small bubbles as observed in the typical slug flow regime.

The history of the void fraction in any cross-sectional area can be evaluated from the reconstructed tomogram data giving the phase distribution. As one example, Fig. 3.8 gives the histories of the total cross-sectional averaged void fraction of two cases.

Fig. 3.8(a) represents the results of the bubbly flow when the air injection rate is small. It is supposed in this case that relatively small numbers of bubbles of small sizes are passing through the measured cross-section. Thus the void fraction fluctuates between 0% and 10%. This figure corresponds to Fig. 3.6. Fig. 3.8(b) gives the results corresponding to Fig. 3.7 of the typical slug flow. When the large air slug passes through the measured cross-section, the void fraction increases close to 100%. After the large air slug passes, the small entrained bubbles give the small void fraction.

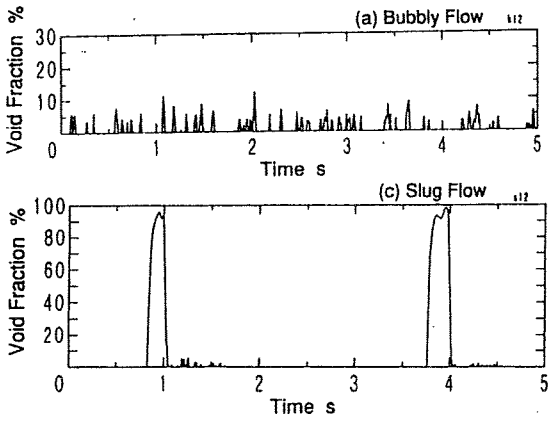

Fig. 3.8 History of Void Fraction[18]

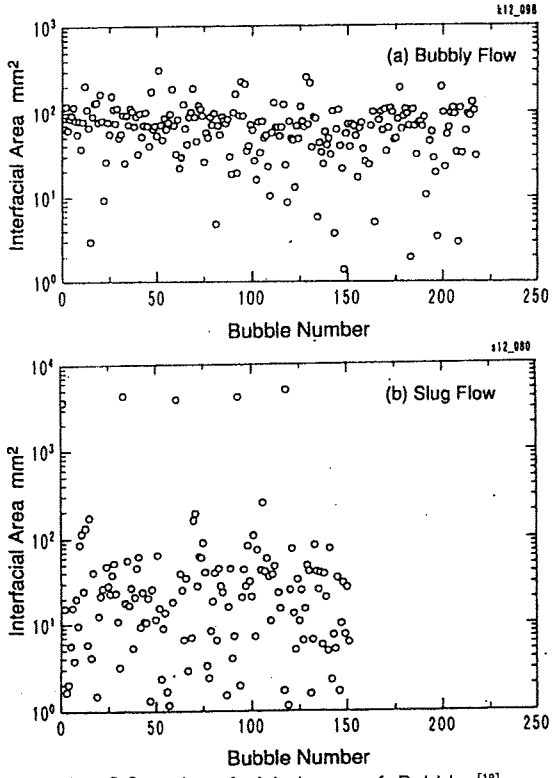

Fig. 3.9 Interfacial Areas of Bubbles[18]

The evaluation of the interfacial area of each bubble is obtained from the three - dimensional reconstructed image data. The results are shown in Fig. 3.9 giving the interfacial area of the bubbles passing thorough the measured cross - section sequentially. Fig. 3.9(a) corresponds to the bubbly flow of Fig. 3.8(a). About 220 small bubbles are observed in this case during the measuring time of about 15 seconds. The interfacial areas of the bubbles are about 100mm^2 in this bubbly flow. Fig. 3.9(b) gives those in the slug flow corresponding to Fig. 3.8(b). The interfacial areas of the air slugs become about 4000mm^2.

This high speed electronically controlled X- ray CT scanner system should provide us a new weapon to approach more precise modeling of two- phase flow phenomena.

4. STEAM GENERATOR THERMAL HYDRAULIC STUDY

The pursuit of steam generator reliability for more than twenty years in Japan[19] forced us to keep continuous research and development activities in the thermal hydraulic area. Here is a brief review of the current achievements.

4.1 Three- Dimensional Two phase Thermal Hydraulics within the secondary Side of PWR Steam Generator and Flow Induced Vibration of U- Tube Bundle

The needs for the reliable thermal- hydraulic computer code to analyze the three- dimensional spacial distribution of void fraction, velocity within the U- tube bundle of PWR steam generator comes from corrosion and flow- induced vibration issues.

Mitsubishi Heavy Industries has been developing FIT- III computer code with the extensive verification test programs[20][21] to check its capability of predicting three- dimensional velocity, quality and void fraction distribution by comparing with several verification tests.

The tube- sheet area study was done using two- dimensional Freon 113 steam generator[22], as are shown in Figs. 4.1 ~ 4.3.

The full bundle study was done using 10MW model steam generator[22] and the three- dimensional Freon steam generator(CLOTAIRE Test)[23].Typical comparison results are shown from Fig. 4.4 and Fig. 4.5.

Development and verification activities for the next generation two- fluid model computer code has been started also, which is expected to be a powerful tool for the detailed examination of the thermal- hydraulic local behaviors within

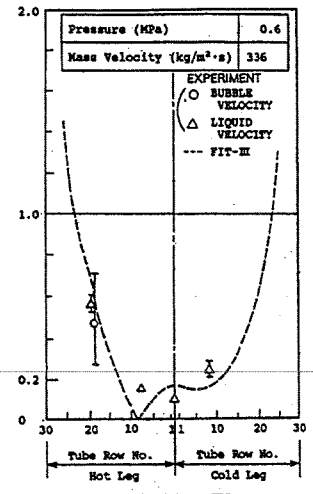

Fig.4.1 Comparison Between Experiment Results and calculation Results of Horizontal Liquid Velocity Distribution Above Tube Sheet(Level 1)[22]

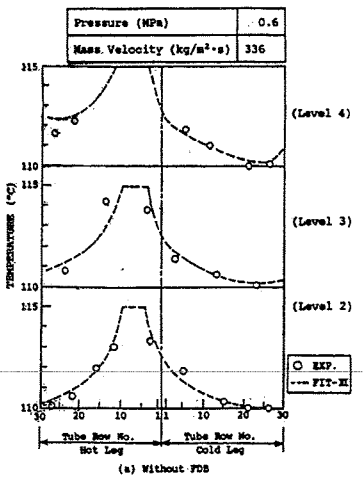

Fig.4.2 Comparison Between Experiment Results and Calculation Results of Temperature Distribution (Level 2~level 4)[22]

the U-tube bundle.

Coupled with those 3D Two-phase flow simulation code development, extensive research has been done on the vibration of tube bundle by two-phase flow for both random excitation and fluid elastic vibration[24][25][26][27].

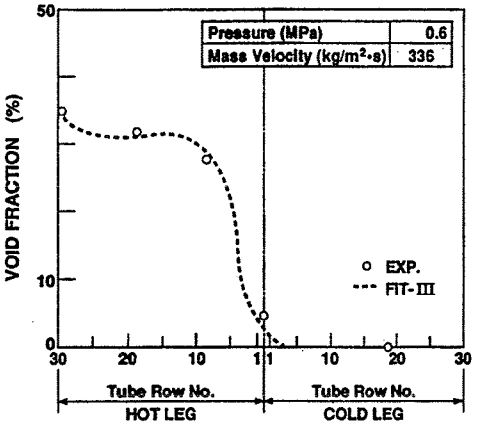

Fig.4.3 Comparison Between Experiment Results and Calculation Results of Void Fraction Below 2nd Tube Support Plate (Level 5) (Without FDB)[22]

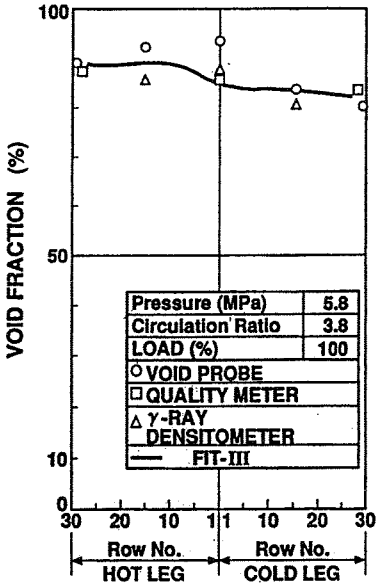

Fig.4.4 Comparison Between Experiment Results and Calculation Results of Void Fraction Distribution Between 6th Tube Support Plate and 7th Tube Support Plate[22]

A new large scale verification test program on the flow induced vibration of tube bundle of steam generator is launched by NUPEC(Nuclear Power Engineering Corporation) sponsored by MITI (Ministry of International Trade and Industry)[28]. In the program, thermal hydraulic distribution and flow induced vibration characteristics will be measured using two dimensional model steam generator equipped with full size U-bend tube bundle subject to Freon R-123 two-phase flow. By the end of 1997, world first data base of two-phase flow and flow induced vibration for the full size of U-bend tube bundle will be established. As the long term academic research activities, it is desirable to pursure more advanced methodology for evaluation of two-phase-flow-induced vibration based on the first principle.

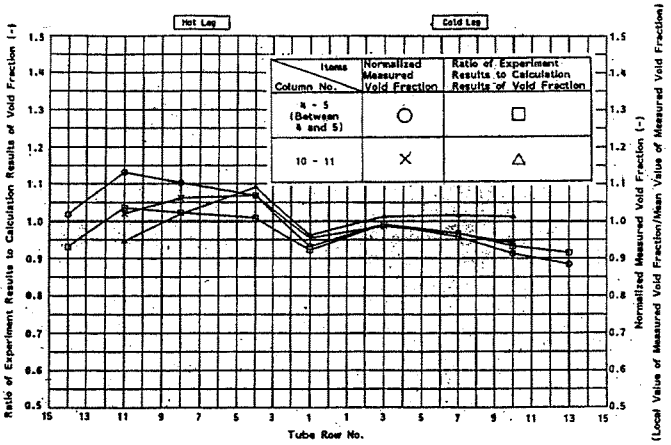

Fig.4.5 Comparison Between Experiment Results and FIT-III Calculation Results of Void Fraction at Entrance of U-Bend Region(CLOTAIRE Test)[22]

4.2 Boilling Behavior in the Tube-to-Tube Support Crevice of PWR Steam Generator

After the first primary-to-secondary side leakage of steam generator tube happened in Mihama-1 in 1972, extensive studies on boiling behavior and chemical concentration mechanisms have been carried out in Japan[29]-[31]. The achievements from the first stage study on crevice boiling was applied to the development of the advanced type of tube-support-configuration, Broached Egg Crate (BEC) patented by Mitsubishi Heavy Industries, which is now commonly used as the flat land broached tube-support over the world.

The current study on the crevice boiling was focused into the optimum procedure to introduce the boric acid into the crevice in order to inhibit the inter-granular-attack (IGA).

Ueno, et al[32][33], performed an extensive research on the advanced boron soaking procedure for steam generator. Both open type crevice and sludge-packed type crevice are studied with the superheat measurements and boron accumulation measurement. The uniqueness of Ueno's study is the

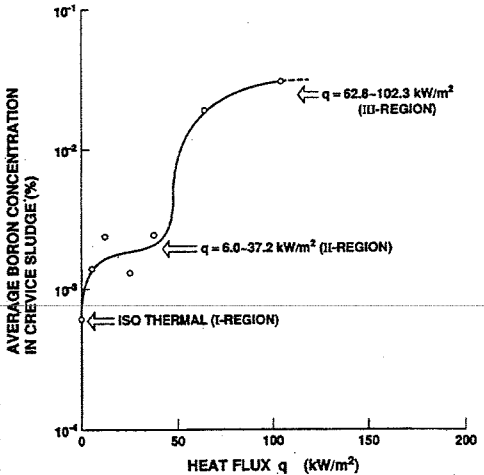

Fig.4.6 Overall Boric and Acid Penetration Into Crevice Sludge[32]

introduction of boron measurements by GDS (Glow Discharge spectrography) and IMA (Ion Micro Analysis) to correlate the incipience of liquid-deficient boiling mechanisms. The typical results are shown in Fig. 4.6 and Fig. 4.7. The horizontal axis of Fig. 4.7 indicates the spattering time through GSD, corresponding to the distance from the tube surface in the sludge thickness direction. The vertical axis corresponds to the boron concentration. As shown in Fig. 4.7, with heat fluxes of q=62.8 & 102.3 kW/m^2, the slope of the boron concentration toward the tube surface tends to decrease. It is thought that the dryout phenomenon occurs on the tube surface. However, with a heat flux of q=25.6 kW/m^2, the slope of the boron concentration toward the tube surface tends to increase, leading to the occurrence of concentration on the tube surface.

It is recommended to the conventional boiling study to introduce such a chemical tracer method as one of the off-line measurement tools for the boiling mechanism.

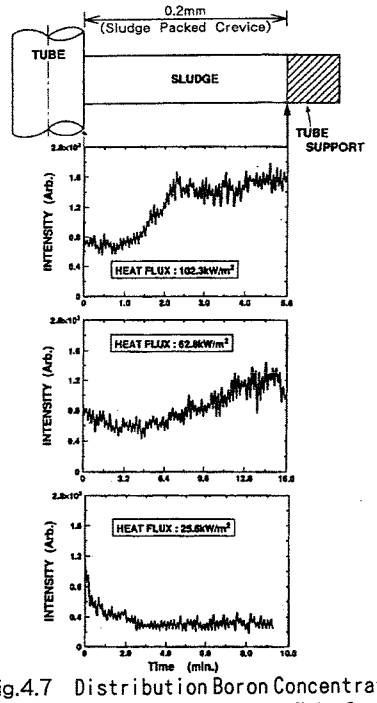

Fig.4.7 Distribution Boron Concentration in Sludge Contacting Tube Surface (Glow Discharge Spectrography)[32]

5. NEW CONCEPT OF PASSIVE/ACTIVE SAFETY SYSTEMS FOR NEXT GENERATION PWR

Responding to the growing need for new concepts to produce nuclear power plants with improved safety, higher reliability and economy, Mitsubishi has proposed a new concept of the hybrid safety system for next generation PWR (New PWR-21)[34], as is shown in Fig. 5.1 and Fig. 5.2, which incorporate the following new concepts.

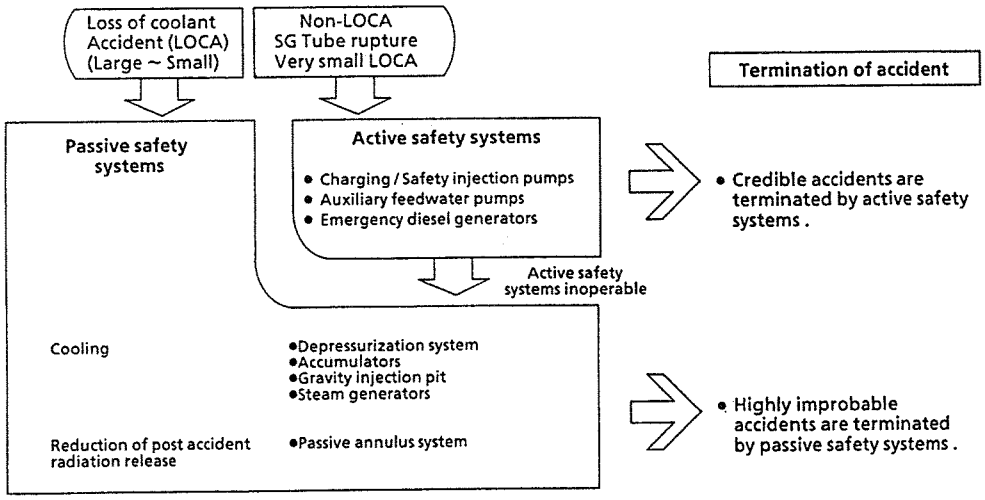

Fig.5.1 Safety Function of Hybrid Safety System[34]

(1)Conventional active safety systems and passive safety systems using new technologies are combined in a way that optimizes reliability and economy.
(2)For Non-LOCA events, such as loss of external power, powerful and flexible active safety systems are used similar to conventional PWR plants.
(3)Passive safety systems actuate if the active safety systems are not available and also in a LOCA event.
(4)Passive safety systems include horizontal steam generators, flow controlled accumulators, improved automatic depressurization systems, gravity injection pit and condensate storage tank as shown in Fig.5.2.

The Mitsubishi hybrid safety system uses horizontal steam generators which provide natural circulation cooling under accident conditions as part of the passive safety design as shown in Fig. 5.3. The horizontal arrangement avoids the possibility of a gas bubble forming in the U-tubes which could obstruct natural circulation. Noncondensable gas is separated from the condensate, is collected in the top of cold side SG channel head, and removed from a vent line connected to the primary gravity injection pit. The secondary side of the steam generators is supplied by gravity from a condensate storage tank.

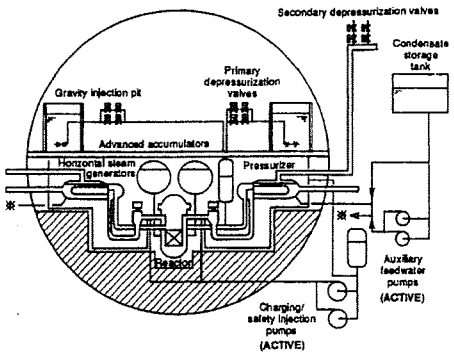

Fig.5.2 Configuration of Hybrid Safety Systems.[36]

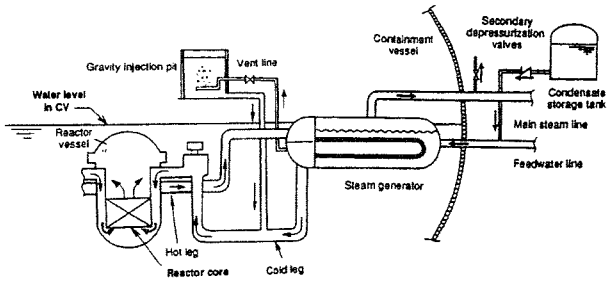

Fig.5.3 Steam Generator Cooling System.[36]

In order to confirm the feasiblity of the Mitsubishi hybrid safety system, various kinds of safety analyses are performed for LOCA events[35]. In parallel with these safety analysis efforts, the following thermal-hydraulic tests are performed[36].

(1)Thermal-hydraulic tests on the horizontal steam generator
(2)Development and Verification test on high performance accumulator
(3)Integrated thermal-hydraulic test using the SLIM test

5.1 Thermal-Hydraulic Tests on Horizontal Steam Generator[36]

The thermal-hydraulic tests of the horizontal steam generator have been performed using the horizontal single tube test rig and the horizontal tube bundle test rig with the objectives. ① to obtain the heat transfer coefficients inside the wall of the tube in detail with parameters of pressure, steam flow rate, water flow rate and noncondensable gas concentration, and ② to confirm the separation of noncondensable gas and water in the cold side channel head and ventilation of noncondensable gas through the vent line connected with the cold side channel head. Furthermore, the method to evaluate the heat removal capacity of the horizontal steam generator is developed by comparing the amount of heat exchange obtained from the tube bundle test rig with that obtained from the single tube test rig. A schematic of the experimental test rig with the main components of the system ; the horizontal steam generator, is shown in Fig. 5.4.

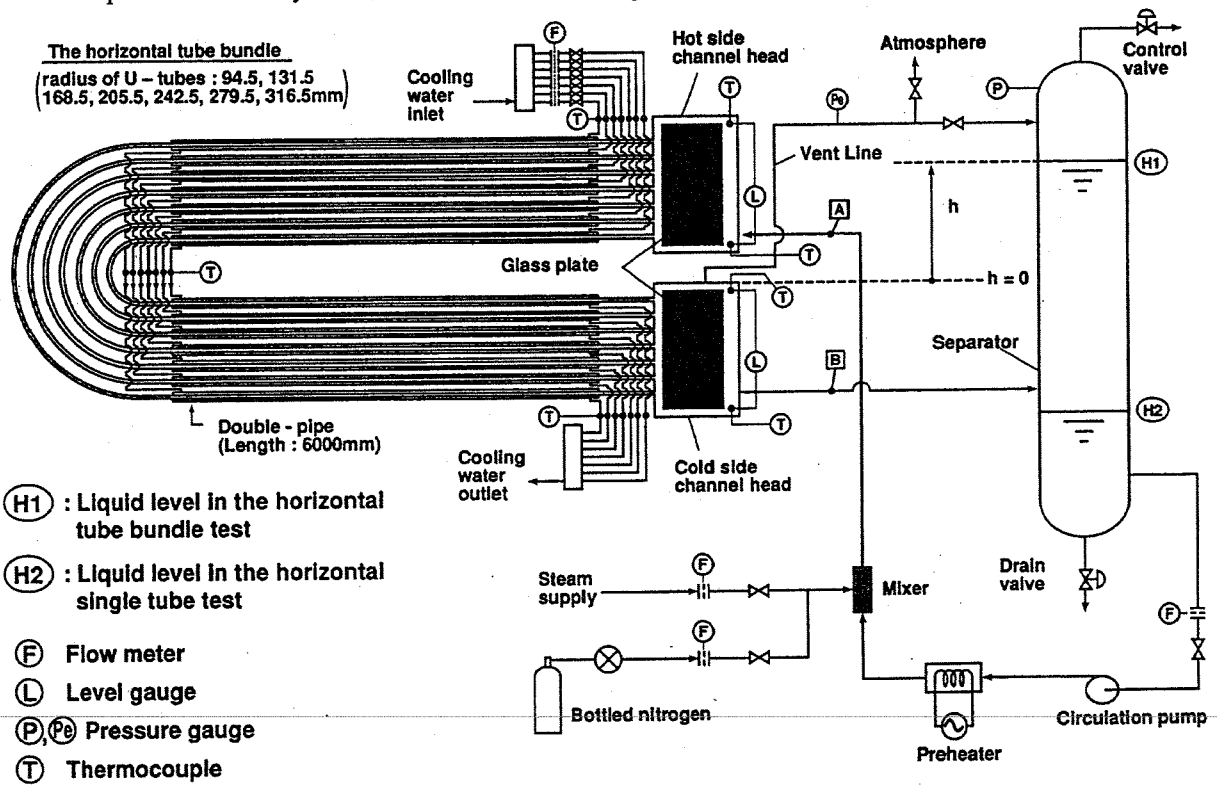

Fig.5.4 Schematic Diagram of Experimental Loop and The Horizonal Tube Bundle Test Rig[36]

Based on the systematic test covering the test condition of the noncondensable gas weight faction, 0.02~0.2% and the pressure range, 0.2~0.4MPa as are shown in Table 5.1, Ueno et.al. proposed a new correlation for the heat transfer coefficient under the existence of noncondensable gas[36].

The correlation agrees well with the experimental data within ± 20%.Using the horizontal seven- tubes bundle test rig in Fig. 5.4, the accuracy of the proposed correlation was confirmed together with the verification of the capability of venting system for the noncondensable gas.

Table 5.1 Experimental Conditions of Horizontal Tube Bundle Test[36]

	P (MPa)	W_g (kg/h)	W_l (kg/h)	C_{N2} (wt%)	P_e (MPa)	h (m)
Case 1	0.2, 0.4	120	0	0.2	0.1	0
Case 2	0.4	182	1200	0.03	0.4	0.27, 0.57
Case 3	0.4	85	1200	0.02	0.4	0.52

5.2 High Performance Accumulator[37]

The passive safety systems use an originally designed, high performance accumulator which is shown in Fig. 5.5. A fluidic flow control device is located in the lower part of the accumulator tank. When the accumulator is full of water, the water flows through both the main flow standpipe and the side connection into the device, and passes through the device without forming a vortex at large flow rate. When the level drops below the top of the standpipe, the large flow path through the standpipe is stopped and the water flows only through the side connection path. The path forms a vortex inside the device that causes a high- pressure drop and reduces flow rate. Thus a high initial flow rate followed by a prolonged injection at a much lower flow rate can be achieved.

This matches the flow rates required in a large break loss of coolant accident because in such an accident the reactor vessel is initially emptied when the water in the core flashes to steam (so- called blowdown phase). In the subsequent refill phase, the accumulators are used to quickly refill the reactor vessel lower plenum, therefore a high flow rate is reguired. However, when the water reaches the core (so- called quenching phase), a large amount of steam is produced which limits the rate at which water can be forced into the core. If a high injection flow rate is used during this quenching phase, the surplus of the injected water is spilled from the break. Consequently a prolonged low flow rate from the accumulators is the most effective way of dealing with this phase of the accident.

The basic design of the high performance accumulator is completed and verified by small scale and large scale accumulator tests with the fluidic flow control device mounted.

Typical performance data is shown in Fig. 5.6.

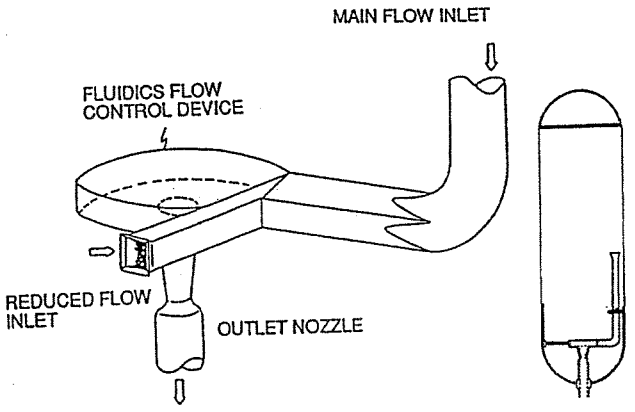

Fig.5.5 Desigh Features of Advanced Accumulator[37]

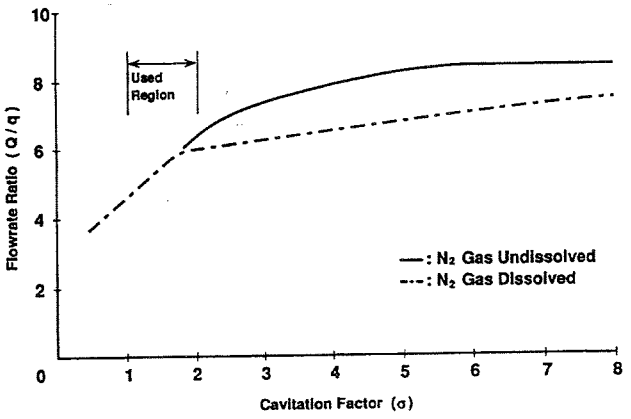

Fig.5.6 Typical Flow Control Performance of the High Performance Accumulator[37]

5.3 Integrated Thermal- Hydraulic Tests Using the SLIM Test Facility[36]

The SLIM test facility at Takasago R & D Center, MHI simulates the New PWR- 21 systems with the volumetric scaling ratio of 1/1000. The objectives of this test are as follows:

(1)Improve understanding of the thermal- hydraulic behavior inside the primary systems and the heat transfer characteristics of the horizontal steam generator during establishment of natural circulation

(2)Establish a data base for the verification of the analytical code to predict the unsteady two- phase flow with noncondensable gas present using a two- fluid model Table 5.2 and Fig. 5.7 shows the SLIM- Facility outline.

The series of test simulating postulated accident have been completed and the evaluation is now under giong.

Table5.2 Volume Distribution in Primary Systems[36]

(Unit : m^3)

	New PWR - 21	SLIM
Core	15.1 (6.9%)	0.0142 (6.4%)
Downcomer	27.6 (12.5%)	0.0242 (10.9%)
Upper plenum	24.3 (11.0%)	0.0512 (23.2%)
Upper head	27.2 (12.3%)	
Lower plenum	17.7 (8.0%)	0.0161 (7.3%)
RV Total	111.9 (50.7%)	0.1057 (47.8%)
Hot Leg	4.4 (2.0%)	0.0044 (2.0%)
Cold Leg	4.0 (1.8%)	0.0053 (2.4%)
Cross Over Leg	11.0 (5.0%)	0.0088 (4.0%)
Piping Total	19.4 (8.8%)	0.0185 (8.4%)
Hot side channel head	22.6 (10.3%)	0.0226 (10.3%)
Cold side channel head	21.3 (9.7%)	0.0213 (9.7%)
U tubes	37.8 (17.2%)	0.0455 (20.6%)
SG Total	81.7 (37.2%)	0.0894 (40.6%)
Reactor coolant pump	7.2 (3.3%)	0.0070 (3.2%)
Total primary volume	220.2 (100%)	0.2206 (100%)

(Remark) Values in parenthesis indicate ratio of volume to total primary volume.

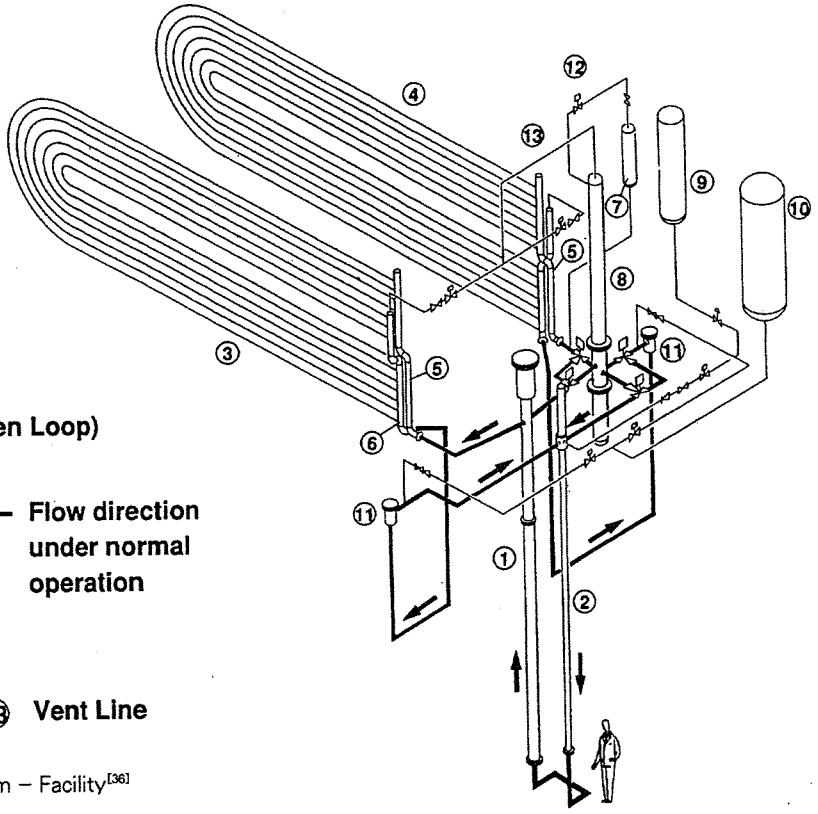

Fig.5.7 Slim – Facility[36]

CONCLUSION

Five major fields of two- phase thermal hydraulic studies on PWR reliability mainly supported by Japanese PWR industry group are overviewed. It is worthy to point out the following achievements and trend.

(1)The reliability and safety of Japanese operating PWRs have been significantly enhanced with the advancement of two- phase hydraulic study and with their implementation to the actual plants.

(2)With the improvement of operating performance of PWRs, the role of operator training simulator has been increased. The thermal hydraulic study on PWR is playing a significant role on the advancement of the engineering simulator.

(3)The introduced new concept of mixed passive/active safety system for next generation PWR (New PWR- 21) can be promising in terms of practical solution to the contradicting requirement for the system safety and the preservation of the property.

REFERENCES

[1]Kuwabara, K., et al., "Small Break LOCAs Analysis Code CANAC- II", Proc, 2nd Int. Topical Mtg. on Nuclear Power Plant Thermal Hydraulics and Operations, Tokyo, Japan, p.2- 41 (1986).

[2]Kawanishi, K., et al., "Experimental Study on PORV Break LOCA in PWR Plants", J. of Nuclear Science and Technology, Vol. 27, No. 2, p.133, (1990).

[3]Kawanishi, K., et al., "Experimental Study on Heat Removal during Cold Leg Small Break LOCAs in PWRs", J. of Nuclear Science and Technology, Vol. 28, No. 6, p.555, (1991).

[4]Siddiqui, C., et al., Int. J. of Multiphase Flow, Vol. 12, No. 4, p.531, (1986).

[5]Kawanishi, K., et al., "An Experimental Study on Drift Flux Parameters for Two- Phase Flow on Vertical Round Tubes", Nuclear Engineering and Design, No. 120, p.447, (1990).

[6]Kawanishi, K., et al., "Small Break LOCA Experiments and Verification of CANAC- 2 Code", Nuclear Engineering and Design, No. 120, p.259, (1990).

[7]ROSA- IV Group, ROSA- IV Large Scale Test Facility (LSTF) System Description for Second Simulated Fuel Assembly, JAERI- M 90- 176, JAERI (1990).

[8]Kukita, Y., et al., Summary of ROSA- IV LSTF First- phase Test Program - Integral Simulation of PWR Small- Break LOCAs and Transients, Nucl. Engrg. Des., 131- 1 (1991) 101- 111.

[9]Akiyama, M., A view on the Future of Nuclear Simulation Systems – Need and Impact of Developing a Supersimulator, XI Annual Simulator Conference, Sandiego, California, April 10 – 14, 1994

[10]Saji, E., et al., Feasibility Studies on High Conversion Pressurized Water Reactors with Semitight Core Configurations, Nuclear Technology, Jan. (1988), Vol. 80, 18- 20.

[11]Akiyama, Y., et al., DNB Experiments for High- Conversion PWR Core Design, Nuclear Engineering and Design, 126 (1991), 267- 275.

[12]Stevens, G. F., et al., A Quantitative Comparison between Burnout Data for Water at 1000 lb/in^2 and Freon 12 at 155 lb/in^2 Uniformly Heated Round Tubes Vertical Upwards, AEWW- R327 (1964).

[13]Sugiyama, S., Oishi, M., et al., Proof Test on Thermal Hydraulic Design Reliability PWR Fuel, Proc. Autumn Annual Conference, Japan Atomic Power Society, Oct. (1990), 251- 256.

[14]Akita, Y., Makihara, Y., Development of New Thermal Design Method for PWR and Up- rating of Mitsubishi 17 × 17, 3- Loop Plant, Proceedings of Second International Topical Meeting on Nuclear Power Plant Thermal Hydraulics and Operations, April (1986), Vol.4- 66.

[15]Nuclear Fuel Industries, Ltd. "New DNB Correlation : NFI- 1", NFK- 8987 (January 1986)(in Japanese).

[16]Hori, K., Miyazaki, K., Kurosu, T., Sugiyama, S., In Bundle Void Fraction Measurement of PWR Fuel Assembly, Proc. of 2nd. ASME/JSME Nuclear Engineering.

[17]Kurosu, T., et al., In Bundle Void Fraction Measurement of PWR Fuel Assembly, Proc. 2nd International Seminar on Subchannel Analysis, PalAlto U.S.A. Nov. 19, 1993.

[18]Hori, K., Kawanishi, K., et al., A High Speed X- Ray Computed Tomography Scanner for Multipurpose Flow Visualization and Measurement, Proc. 4th International Meeting on Nuclear Thermal Hydraulics, Operations and Safety, Taipei, Taiwan, April 5- 9, 1994.

[19]Tsuge, A., Hirano, H., Sato, M., Takamatsu, H., Preventive and Corrective Actions for Tube Degradation and New Steam Generator Design Concept, Proc. 4th International Topical Mtg. on Nuclear Thermal Hydraulics, Operations and Safety, TAIWAN, April 5- 9, 1994.

[20]Hirao, Y., et al., Experimental and Analytical Studies on Thermal- hydraulic Behaviors of the PWR Steam Generator, 3rd ASME- JSME Thermal Engineering Joint Conference, Nevada, U.S.A., March 17- 22, 1991.

[21]Hirao, Y., et al., Development of Thermal- Hydraulic Computer Code for Steam Generator, JSME International Journal Series B, Vol. 36, No. 3, 1993, p.456.

[22]MITI Committee of Investigation on Steam Generator Reliability, Investigation Report of Steam Generator Reliability, 1987.

[23]Bouchter, J.C. (CEA), Campan, J.L. (CEA), Kalra, P. (EPRI), Flow Regimes and Structure Interactions within a Large Scale steam- Generator Simulation : The Clotaire Experiment, International Symposium on Gas- Liquid Two- Phase Flows, ASME Winter Meeting, Dallas, Texas, U.S.A., November 25- 30, 1990.

[24]Nakamura, T. et al., Study on the Vibration Characteristics of a Tube Array Caused by Two- Phase Flow- Part 1 : Random Vibration, Transactions of the ASME, Journal of Pressure Vessel Technology, Nov. 1992, Vol. 114, P.472.

[25]Nakamura, T. et al., Study on the Vibration Characteristics of a Tube Array Caused by Two- Phase Flow- Part 2 : Fluid elastic Vibration, Transactions of the ASME, Journal of Pressure Vessel Technology, Nov. 1992, Vol. 114, P.479.

[26]Nakamura, T. et al., Two- Phase Cross- Flow- Induced Vibration of Tube Arrays, JSME International Journal, Series B, Vol. 36, No. 3, 1993, P.429.
[27]Nakamura, T. et al., Study of Two- Phase Flow Behavior and Turbulent Excitation Mechanism in a U- bend Tube Bundle in Steam Generator, JSME International Journal, Series B, Vol. 36, No. 3, 1993, P.439.
[28]Saitou, T., et al., Verification Test on Flow Induced Vibration in U- bend Tube Bundle of Steam Generator, Proc. Second International Steam Generator and Heat Exchanger Conference, Toronto, Canada, June 13- 15, 1994.
[29]Hirao, Y., et al., Study on Thermal- Hydraulic Behaviour in the Crevice within the Steam Generator, Proceedings of the 27th National Heat Transfer Symposium of Japan, 1990, 841 (in Japanese).
[30]Ueno, T., et al., Study on Thermal- Hydraulic Behaviour in the Crevice within the Steam Generator, Proceedings of the 68th, JSME Fall Annual Meeting, 1990, 443 (in Japanese).
[31]Ueno, T., et al., Study on Concentration Phenomena in the Crevice within the Steam Generator, Proceedings of the 24th Chemical Engineering Fall Annual Meeting, 1991, 485 (in Japanese).
[32]Ueno, T., et al., Improved Boric Acid Penetration Procedure into Tube To Tube- Spport- Plate Crevices in Steam Generator, Third International Topical Meeting on Thermal Hydraulics and Operations, 1988, B9- 34.
[33]Ueno, T., et al., Advanced Boron Soaking Procedure for Steam Generators, Proceedings of the 1st JSME/ASME Joint International Conference on Nuclear Engineering, 1991, 477.
[34]T. Matsuoka et al., Safety Features of the Simplified Mitsubishi Pressurized- Water Reactor, Nuclear Safety Vol. 33, No. 2, April June, 1992.
[35]K. Okabe et al., Analytical Study of the Hybrid Safety System of the New Simplified PWR. International conference on design and safety of advanced nuclear power plants (1992).
[36]Ueno, T., et al., Thermal- Hydraulic Test on Mitsubishi Simplified PWR, Proc. ANS Winter Meg., San Fransisco, California, Nov. 17, 1993, P.193.
[37]Shiraishi, T., et al., Development of the Flow Controlled Accumulator, ANP '92, Tokyo, 1992.

TWO-PHASE FLOW ANALYSES IN BWRs

Toshitsugu Nakao, Terufumi Kawasaki and Akihiko Minato

Energy Research Laboratory, Hitachi Ltd.
7-2-1 Omika-cho, Hitachi-shi, Ibaraki-ken, 319-12 Japan
Telephone:(0294)53-3111,Facsimile:(0294)53-7664

ABSTRACT

Findings from recent studies on two-phase flow analyses in boiling water reactor are summarized. By considering the respective behavior of gas, liquid droplets, liquid film and bubbles, detailed prediction of thermal-hydraulic performances of components is possible. The annular-dispersed flow model for fuel bundle is improved by considering the spacer effect. The critical power of the fuel bundle is in good agreement with measurements. The dispersed flow model is applied to the steam dryer and separator. The calculated wetness fraction in the steam dryer agrees well with air-water tests results. The calculation of droplets behavior using the discrete droplet model is shown to be an effective way to understand characteristics of liquid removal for droplets of different diameters. The two-phase flow analysis in the heat exchanger is done using a two-fluid model. The results show phase separation phenomena well in a three-dimensional flow passsage.

1. INTRODUCTION

Two-phase flow analysess in boiling water reactors (BWRs), have been developed mainly for the reactor core so as to predict boiling transition and thermal margin. However they depend on empirical critical heat flux correlations to predict critical power [1]-[3], so that the ranges of applicability are limited by those of the correlations. For other reactor components related to two phase flow, their developments have been based on full scale tests under reactor conditions. As requirements for higher performance components are raised, the demand for two-phase flow analysis which is applicable to any component geometry is increased in order to reduce the developmental period and cost. Precise models have been developed and applied to some BWR components where movements of gas, liquid film, droplets, and bubbles are considered separately [4]-[7].

The direct cycle BWR nuclear system is a steam generating system consisting of a nuclear core and an internal structure assembled within a pressure vessel, auxiliary systems to accommodate the operational and safeguard requirement of the nuclear reactor, and necessary controls and instrumentation as shown in Fig. 1. Water is circulated through the reactor core, producing saturated steam which is separated from recirculation water, dried in the top of the vessel, and directed to the steam turbine-generator. Figure 2 shows a schematic of the reactor internals. In the pressure vessel, the coolant water passes in the core where it is heated and becomes a two-phase, steam-water mixture. The steam-water mixture enters the plenum located directly above the core and bounded by the separator dome which opens to the separator array of fixed steam separators. The steam is separated from the water and passes through a dryer where any remaining water is removed. The saturated steam leaves the vessel through steam line nozzles located near the top of the vessel body and then it is piped to the turbine. Water collected in the support tray of the dryer is routed through drain lines, joins the water leaving the separators, and flows downward in the annulus between the core shroud and the vessel wall. Flow patterns in the three reactor components are also shown in Fig. 2. The authors have developed some numerical techniques by considering the flow patterns and conponent structure. A numerical method applicable to a heat exchanger, which is used in the rector recirculation system, has also been developed.

Critical power at the boiling transition is an important factor for BWR fuel bundle design. The boiling transition under the high quality condition is considered to be caused by dryout of liquid film

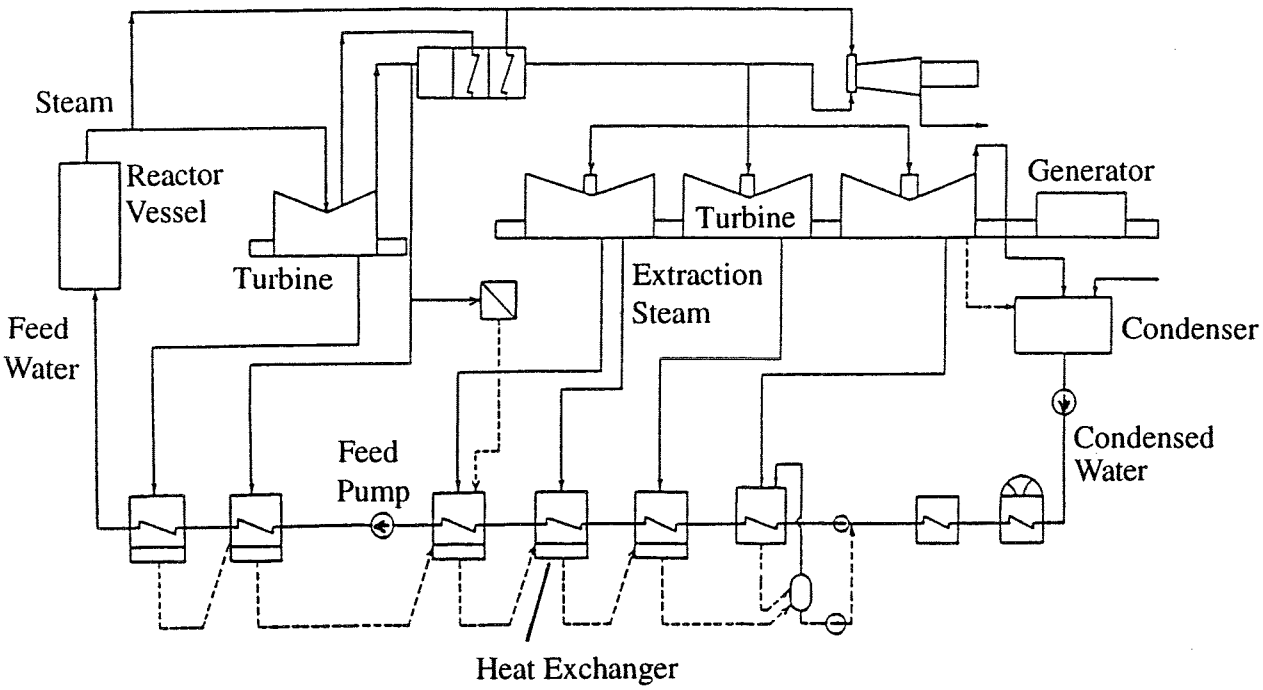

Fig. 1 Boiling Water Reactor System

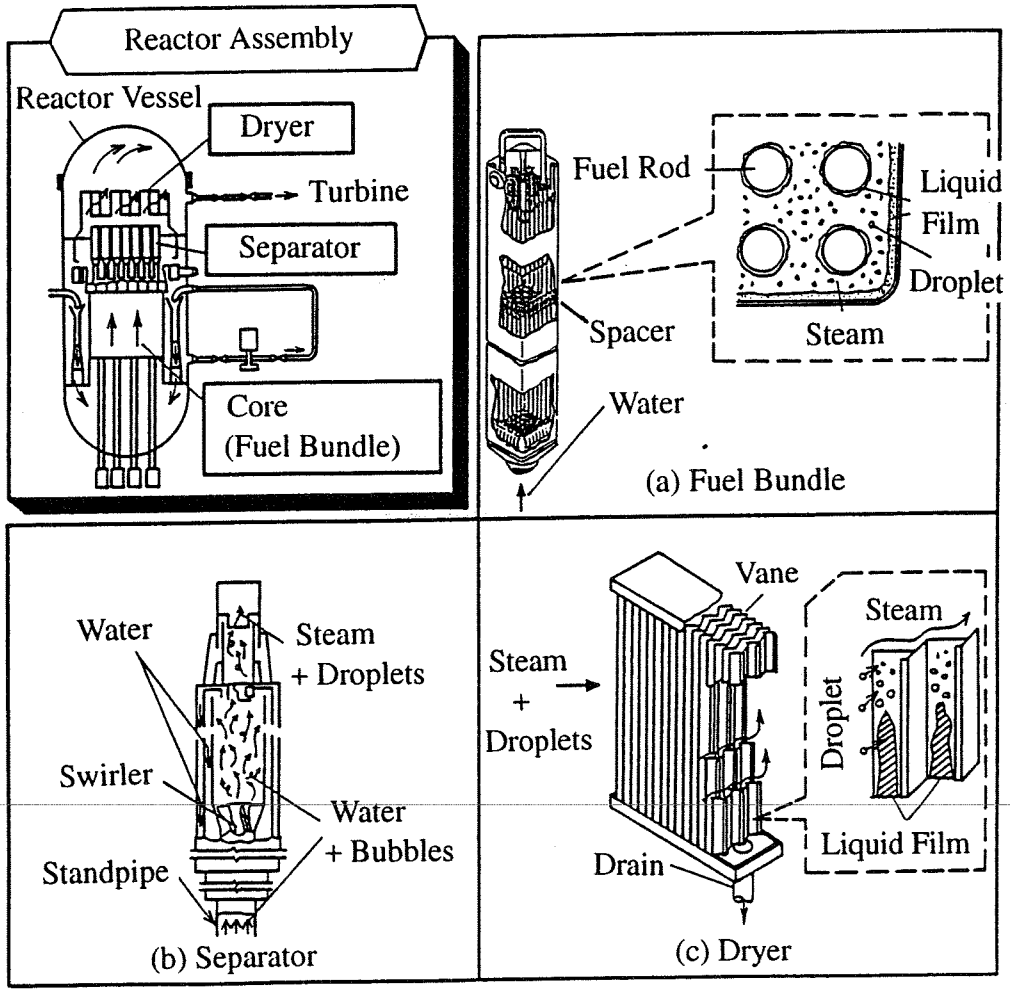

Fig. 2 Reactor Assembly and Flow Pattern

flow on fuel rods. This liquid film vanishing process can be predicted by a liquid film model[8] which takes account of evaporation from the heating rod surface, entrained droplets from the liquid film by steam flow, and liquid droplet deposition onto the film. Spacers affect the occurrence of entrainment and deposition, as well as flow re-destribution in a fuel bundle. Therefore, a detailed study of spacer effects on hydrodynamic characteristics of a liquid film is necessary for accurate prediction of the critical power based on the film flow model. In the present research, liquid film thicknesses in 4X4 and 9X9 fuel bundles were measured to clarify the dependance of deposition and entrainment of droplets on spacer shape. Furthermore, a new spacer model was developed by taking the spacer effects into consideration in the liquid film model [8]. Critical powers predicted by using the film flow model were compared with measured data for a wide variety of designed BWR fuel bundles.

The primary performance of the steam separator is evaluated by its steam-water separating performances, i.e. carryover and carryunder. In the steam dryer, the performace is determined by carryover. It is desirable to reduce both of them. These performances have been estimated in mock-up tests, however, such tests are of long duration and costly. Therefore, it would be better to develop a numerical method to estimate steam-water separation. This report describes studies on dispersed flow analyses for the steam separator and dryer. Some results were compared with experiments.

A multi-dimensional analytical method based on a two-fluid model is becoming a necessity and one-dimensional methods are being replaced with homogeneous or drift-flux models. In a heat exchanger, phase separation due to flow constriction and expansion affect the pressure drop, velocities of gas and liquid, void fraction distribution, heat transfer, and so on. Therefore, numerical calculations of two-phase flow in complicated flow paths should treat three-dimensional flow. In this paper, a three dimensional two-phase flow analysis program using a two-fluid model was adopted in order to analyze the behavior of gas and liquid in a typical heat exchanger.

Finally, this paper summarizes recent research on two-phase flow analyses in BWRs. Some experiments which contributed to the new techniques are also included.

2. FUEL BUNDLE

2.1 Spacer Effects in Annular-Dispersed Flow Region

It has been reported that generally dryout of liquid film occurs just upstream from the spacer installed in a fuel bundle. Therefore, most studies have focused on liquid film behavior in the vicinity of the spacer, meaning drypatch formation close to the spacer was discussed [9]. This dryout occurrence seemed to suggest that bundle critical power decreases with increasing spacer numbers and decreasing spacer pitch. However, most critical power tests have given the opposite results [10]. Spacer effects on dryout depend on not only the spacer configuration and arrangement, but also the droplet concentration of annular-dispersed flow. In this section, spacer effects on liquid film flows are examined to resolve the observed contradiction.

Droplet entrainment tests

Droplet entrainment tests were carried out with a 3X3 simulated fuel rod bundle test section to study entrained droplet behavior from liquid film flows (Fig.3) [11]. The installed spacer was of a "lattice type". Upward liquid film flows were generated by air and water at atmospheric pressure and room temperature. The film thickness across the test spacer was obtained by measuring voltage drop between circular electrodes (Fig.4). The relationship between voltage drop and liquid film thickness was determined using reference electrodes. These reference electrodes had the same electrode pairs as the rod, which were used for measurements of the fuel bundle. The annular shape gap (0.1-0.6mm) was changed by varying the inner diameter of the outer tube. During operation, a very low droplet concentration was observed in the upstream annular-dispersed flow region.

Figure 5 shows typical experimental results of the liquid film thickness distributions on the center rod. These are two interesting points. First, the film thickness has its minimum in the vicinity of the spacer due to flow area reduction. Owing to this reduction, decreased film thickness and increased film velocity are considered to occur in the spacer vicinity. So it should be noted that

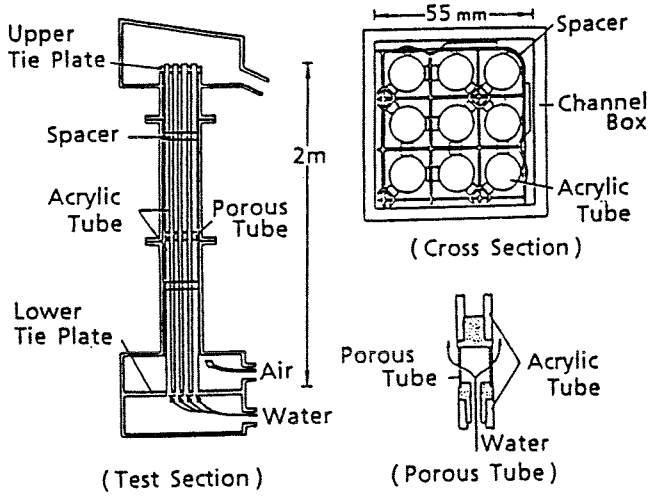

Fig.3 Droplet Entrainment Test Facility

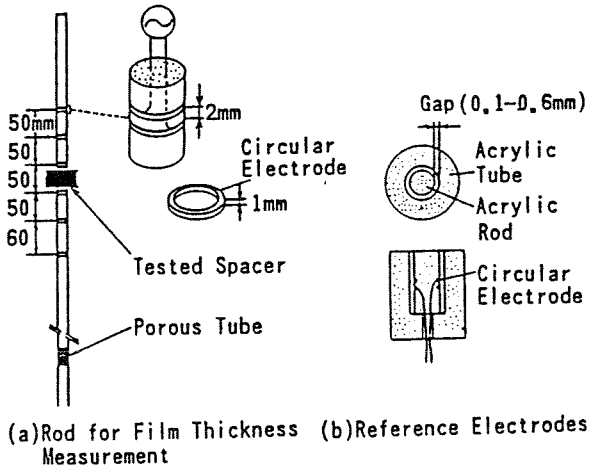

Fig. 4 Film Thickness Measuring Method

dryout does not always occur at the point of minimum film thickness, but rather at the point of minimum film flow rate. Second, as the superficial velocity of water increases, the film thickness behind the spacer does not recover to its upstream level. This film thickness behavior may have a close relationship with the enhanced droplet entrainment rate from the liquid film due to an increase of gas-liquid interfacial shear stress. Though these trends may suggest that the spacer causes a decrease of critical power, no spacer effect on droplet deposition enhancement was seen in these tests.

Droplet deposition and entrainment tests

In order to examine the spacer effects on liquid film flows under high droplet concentration conditions, droplet deposition and entrainment tests were carried out using full-sized (9X9) mock-up fuel rod bundles (Fig.6) [12]. Experimental procedures were the same as those in the small scale 3X3 tests just mentioned, including the liquid film generation, except for two additional spacers in the upstream region from the tested spacer position and use of the "round cell type" for the tested spacer. High droplet concentration is observed in the upstream region from the tested spacer in this case owing to the additional spacers.

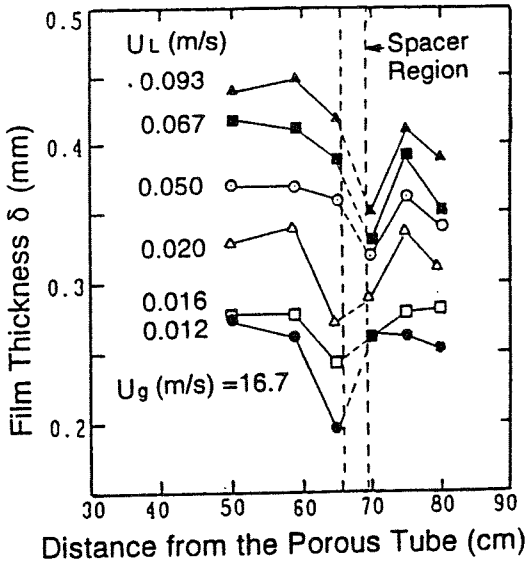

Fig. 5 Film Thickness Distribution on the Center Rod (3X3 Fuel Bundle)

Figure 7 shows that the liquid film thickness distribution varies depending on the rod locations. The bars indicate data dispersion. For an air flow velocity distribution in the fuel bundle cross section, the velocity seems to have its maximum at a position close to the water rods. So the inner rod is covered with the thinnest liquid film. As for the corner rod, its film is the thickest, and, additionally its data dispersion is the largest. Visual observation shows that the dispersion depends on irregularly flowing slugs in the corner subchannel.

The film thickness distributions on the side and inner rods are shown in Fig. 8. The tested spacer was installed between the fourth and fifth electrodes. One of the upstream spacers was placed 500mm upstream from the tested spacer. As for the distribution along the rods, the thickness decreases or remains almost unchanged in the vicinity of the spacer. The film thickness in the vicinity of the spacer was strongly affected by not only droplet behavior, but also reduction of the flow area. Therefore, for the following discussions on droplet deposition and entrainment behaviors, points nearest the up-and down-stream regions are excluded. As for the film thickness across the spacer, the thickness increases somewhat in the downstream region. This is considered to be caused by an increase of deposited droplets on the liquid film due to the turbulence enhancement. A high

droplet concentration is regarded as leading to a droplet deposition rate larger than the droplet entrainment rate.

Figures 9 shows the effect of the number of spacers on the film thickness distributions on the side and inner rods. Case A had the same spacer arrangement as in the above experiments. In case B, the second spacer was installed 150mm upstream from the original tested spacer. From a comparison of film thickness in the downstream region of the original tested spacer, the film of B is found to be thicker than that of A. Under actual BWR conditions, it has been reported that the bundle average quality at the critical power is below 40% [8]. Therefore, more than half of the liquid mass may be carried in the flow of droplets in the annular-dispersed flow. Though the droplet concentration was not measured in this unheated test, the trend correlates well to the dependency of the number of spacers on the critical power in simulated fuel bundle tests [13].

From the experimental results described above, it was concluded that the spacer has the following effects on liquid film flows.

(1) The film thickness has its minimum in the vicinity of the spacer due to flow area reduction. However, it should be noted that dryout does not always occur at the point of minimum film thickness, but at the point of minimum flow rate.

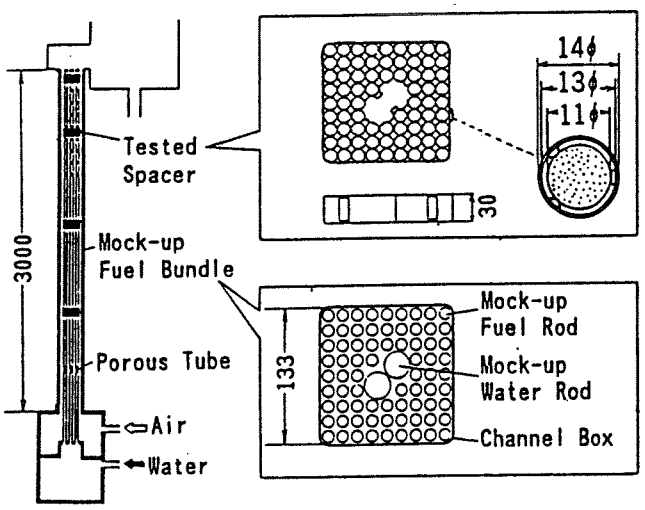

Fig. 6 Droplet Deposition and Entrainment Test Facility (Unit, mm)

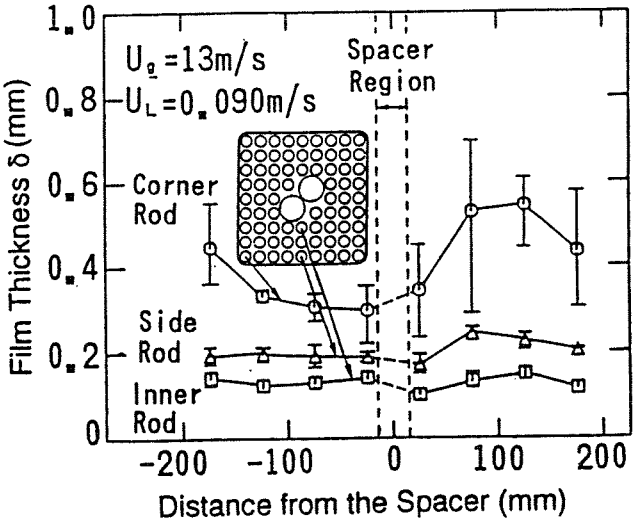

Fig. 7 Dependency of the Rod Location on Film Thickness Distribution

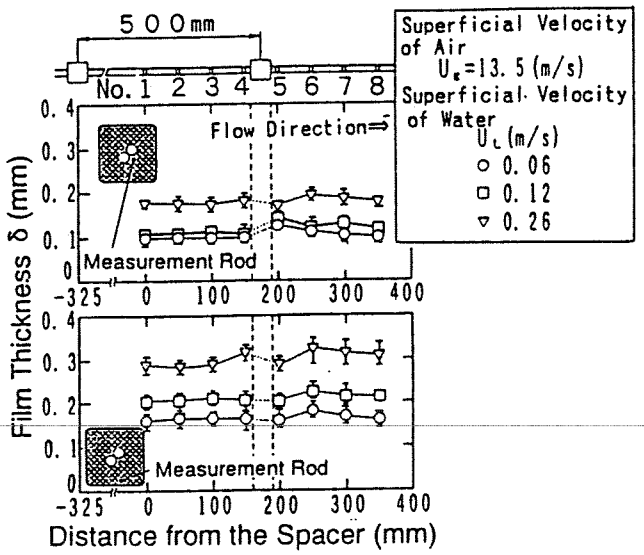

Fig. 8 Liquid Film Thickness Distribution on the Side and Inner Rods

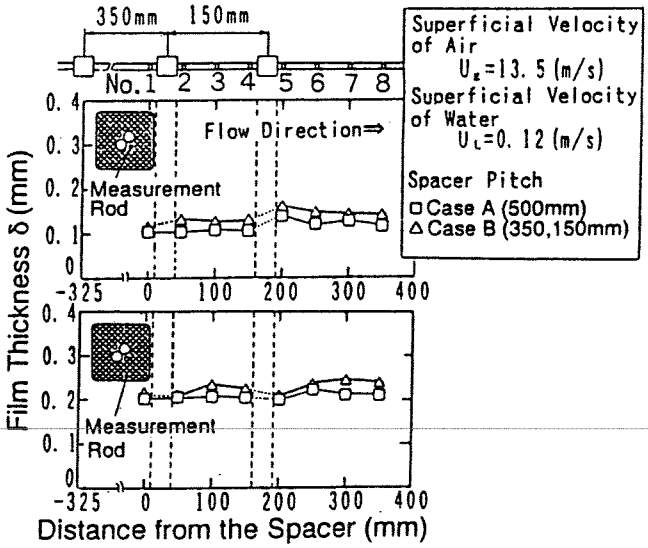

Fig. 9 Dependency of the Spacer Numbers on Liquid Film Thickness Distribution

(2) At very low droplet concentrations, an increase of gas-liquid interfacial shear stress owing to the spacer results in more entrained droplets, which lead to decreased film thickness behind the spacer. On the other hand, at a high droplet concentration, the film thickness behind the spacer increases due to the larger number of deposited droplets. Since the bundle average quality at critical power is below 40% in simulated fuel bundle tests, the spacer may have the ability to increase critical power owing to more deposited droplets .
(3) On increasing the number of installed spacers, thicker films are formed due to increased droplet deposition rate at each spacer. This trend can be attributed to higher critical powers with more spacers.

2.2 Spacer Models

In the previous section, it was found that the liquid film flow rate behind the spacer increases due to the droplet deposition enhancement. This spacer effect on the film dryout has been modeled in order to implement it into SILFEED [12].

In liquid film flow analysis of SILFEED, the mass conservation equation of liquid film flow in steady state is written as:

$$\frac{dW_f}{dz} = P_e(D - E - B), \qquad (1)$$

where W_f is the liquid film flow rate; Pe, the wetted perimeter; z, the distance along the fuel rod; D, the droplet deposition rate; E, the droplet entrainment rate; and B, the evaporation rate. Onset of dryout is assumed to occur where W_f becomes zero on one of the rods as shown in Fig.10. Deposition and entrainment rates are assumed to follow Whalley's model [14]:

$$D = kC, \qquad (2)$$

$$E = kC_{eq}, \qquad (3)$$

where C is the homogeneous droplet concentration in the gas core; C_{eq}, the equilibrium droplet concentration [15]; k, the droplet deposition coefficient [16].

In the annular-dispersed flow region, droplets are carried by the flows in the gas core and some of them deposit on the liquid film due to turbulent diffusivity of this core. The droplet transfer rate in the radial direction is proportional to the gradient of the droplet concentration of the gas core:

$$M_D = (D_P + \varepsilon_P)\frac{dC}{dy}, \qquad (4)$$

where D_P is the molecular diffusivity of droplet; ε_P, the eddy diffusivity of droplet; y, perpendicular distance from fuel rod. The droplet deposition rate D, which denotes the droplet transfer rate at a wall, is represented by the following equation:

$$D = (D_P + \varepsilon_P)\frac{C_{(l)} - C_W}{l}, \qquad (5)$$

where l is thickness of the boundary layer. Since no droplets exist on a fuel rod surface, the droplet concentration at the wall C_W can be treated as zero. The droplet concentration at the boundary layer $C_{(l)}$ is assumed to be equal to the average droplet concentration of the gas core C. Furthermore, the molecular diffusivity D_P can be neglected in Eq.(5), because the molecular diffusivity D_P is about 10^{-3} times as large as the eddy diffusivity ε_P. Accordingly, the droplet deposition rate D is rewritten as the following equation:

$$D = \frac{\varepsilon_P}{l}C, \qquad (6)$$

The eddy diffusivity of droplet ε_P behind a complex spacer configuration has not been presented. Although the eddy diffusivity of single phase flow behind an obstacle has been studied [17], it is important to investigate systemically the dependency of the ε_P on spacer configurations and flow conditions, e.g., droplet size, gas velocity etc. For solid particles in gas flow, it was reported that Schmidt number Sc could be assumed to be constant downstream from an obstacle [18]. Applying this assumption to liquid droplets in the gas core, the following relation holds:

$$Sc = \frac{\varepsilon_{PSP}}{\varepsilon_{gSP}} = \frac{\varepsilon_{PB}}{\varepsilon_{gB}}, \qquad (7)$$

where the subscript B means the value without any spacer (i.e. background value), and SP is the value behind the spacer. ε_g is eddy diffusivity of gas. Since the thickness of the boundary layer l does not change in up-and down-stream regions of the spacer, the droplet deposition coefficient behind the spacer can be estimated by the following equation:

$$k_{SP} = \frac{\varepsilon_{PSP}}{l} = \frac{\varepsilon_{PB}}{l}\frac{\varepsilon_{gSP}}{\varepsilon_{gB}} = \frac{\varepsilon_{gSP}}{\varepsilon_{gB}} k_B, \qquad (8)$$

In this spacer model of SILFEED, ε_{gSP} is estimated by the eddy enhancement model, proposed by Lahey et al. [19] to describe the mass and energy transfer due to mixing and void drift between adjacent subchannels. In their eddy enhancement model, the downstream region was divided into three subregions. Furthermore, a characteristic length λ was defined for describing the eddy intensity of the first region and boundaries of the three subregions.

It is considered that the intensity of the turbulent enhancement downstream depends on not only the spacer configurations, but also the gas core velocity, droplet concentration, etc. Though this spacer model does not take into account three-dimensional configuration of the spacing structures, predicted critical powers by SILFEED correlate well with critical power test data (Fig.11). The test data include different fuel rod arrangements, different "round cell type" spacers and several spacer patches (i.e., 4X4 and 8X8 fuel bundle tests for BWRs[12], 36-rod fuel bundle tests for the Advanced Thermal Reactor [20], and 7-rod fuel bundle tests for the High Conversion Boiling Water Reactor [21]).

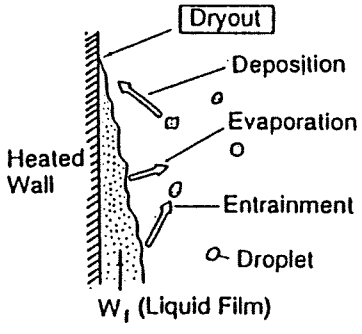

Fig. 10 Mechanism of Dryout Phenomena

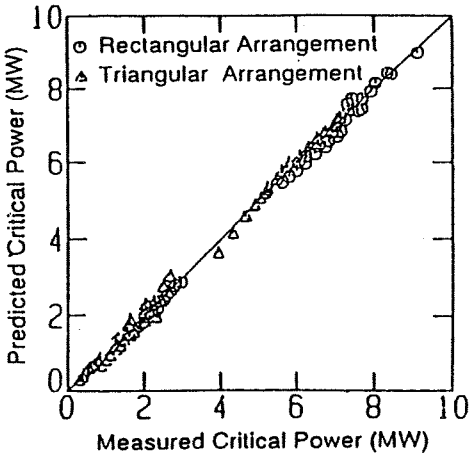

Fig. 11 Comparison of Measured and Predicted Critical Powers

3. STEAM DRYER

Dryers having wave-type vanes are used in the BWR pressure vessel. Steam containing liquid droplets flows through the narrow passages formed by the wave-type vanes where droplets are removed when they collide with the vanes, to flow downwards forming a liquid film. In this paper, the two-dimensional droplet behavior was simulated by dispersed flow analysis and results were compared with experiments.

3.1 Analytical Method

A computer program HIJET-AFIMA [22] , which has been developed for dispersed flow analysis, was used to simulate the liquid droplet behavior in the dryer with wave-type vanes. It can describe movement of liquid droplets as influenced by gas flow and their deposition on the vane surface. The droplets differ in size and velocity direction. To describe droplet movements precisely, the discrete droplet model (DDM) was adopted, in which each of the droplets is treated as a point mass. The droplet tends to go forward, in a straight line, due to its inertia, but both the magnitude and direction of its velocity change due to the drag force of gas flow along the dryer passage. Each droplet is also assumed to be a rigid sphere. The coefficient of drag force C_D for the droplet is derived from previous experiments [23], as given in

$$C_D=(0.63+4.8/\sqrt{Re_d})^2, \tag{9}$$

where Reynolds number is defined as shown in

$$Re_d=d\cdot V_{ad}/\nu, \tag{10}$$

and d is the droplet diameter; V_{ad}, the slip velocity; ν, the kinematic viscosity. In terms of C_D, the motion of the droplet is expressed in

$$\left(\frac{dV_d}{dt}\right)=\frac{6}{8}C_D\frac{\rho_g}{\rho_d}\cdot\frac{1}{d}(V_g-V_d)|V_g-V_d|, \tag{11}$$

where subscripts d and g show droplet and gas. Collision and coalescence of droplets are not taken into consideration due to the low number density of liquid droplets in a typical dryer. The Fluid in Cell (FLIC) method was adopted as a numerical calculation method for inviscid gas flow. Each droplet was traced at every time step in computing the gas flow. When a droplet hits the surface, it was assumed to stay at the collision point and the trace was terminated. The liquid film flow on the vane surface, formed by trapped droplets, was also considered. Interaction between the gas and a droplet was calculated using the velocity of gas in the mesh where the droplet was found.

3.2 Analytical Results

The analyses were performed for droplet movement in the flow passage between two wave-type vanes, as shown in Figs. 12 (a) and (b). The dryer was composed of four-stage vanes. The vane sizes were as noted in the figure. The flow passage was divided into about 4,000 meshes for the gas flow analysis, in which inlet velocity distribution was assumed to be uniform. The size distribution of liquid droplets was obtained experimentally, and is shown in the figure together with gas and liquid conditions. The average droplet size and air velocity were determined by a scale law which was based on the ratio of drag force to inertia force of droplet. The droplet size under reactor operating conditions was estimated from the mean value for annular-dispersed flow. The droplet velocity at the vane inlet was assumed to be the same as the gas velocity. The analytical results are shown in Figs.13 (a)-(c). The droplet positions for three different times after droplet injection are shown. Injected liquid droplets move along the flow passage between the vanes. Larger droplets are concentrated at the first and second stages due to their larger centrifugal force. Smaller droplets, less than 30 μ m of diameter are able to pass through the flow channnel without collisions against the vane surface. This is because the effect of the drag force is exerted more on smaller droplets. As a

result, almost all of the droplets are trapped in the first and second stages.

3.3 Comparison with Measurements

Dispersed flow tests were performed to validate the computational method. The test section is shown in Fig. 14. An acrylic model was constructed having vanes of the same size as in the computations. It had a two-phase flow nozzle in the upstream side. Air was supplied by a compressor through the left end and it entrained droplets at the nozzle. The liquid droplets trapped in the vane stages were measured through a drain nozzle located at the bottom of each vane stage. A comparison of experimental and calculated results is shown in Fig. 15. The vertical axis shows wetness fraction obtained from the amount of trapped droplets at the exit of each vane stage. Almost all of the droplets are found to be trapped in the first stage, with fewer droplets in the third and fourth stages. These results agree well with calculations.

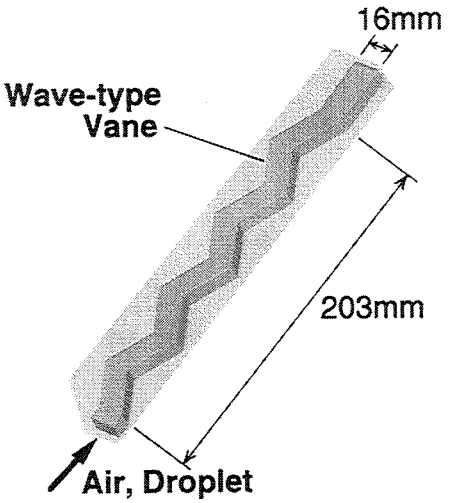

(a) Flow Passage

Air	Density	1.1 kg/m^3
	Velocity	2.0 m/s
Droplet	Density	998 kg/m^3
	Velocity	2.0 m/s

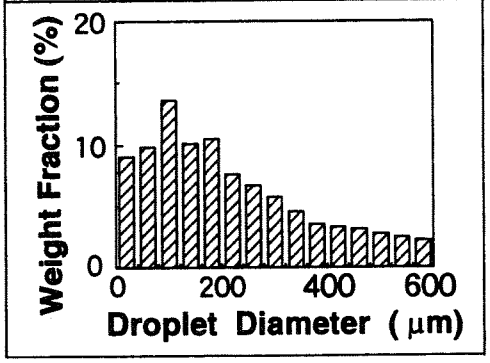

(b) Flow Conditions and Droplet Diameter

Fig. 12 Analytical Conditions

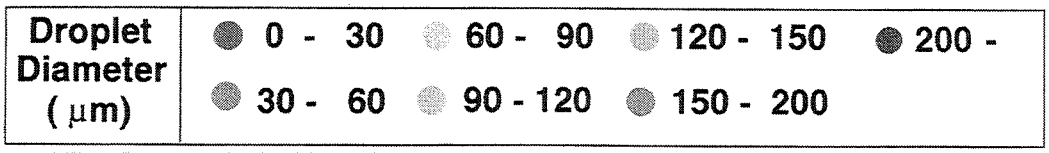

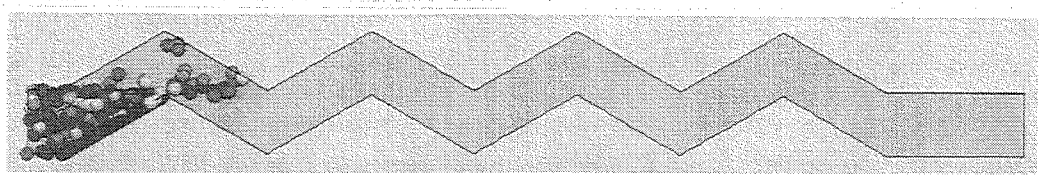

(a) 25ms after Droplet Injection

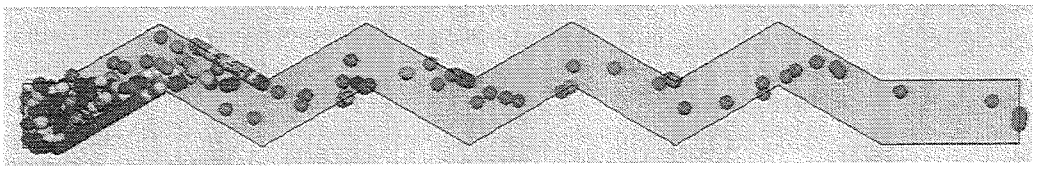

(b) 100ms

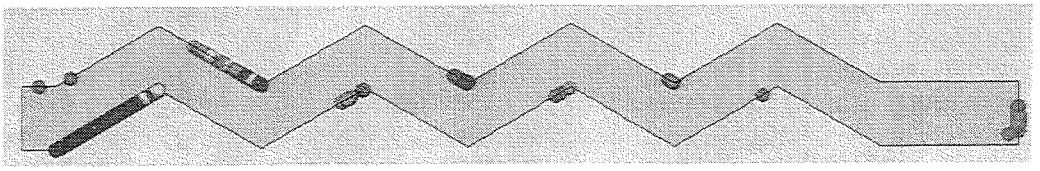

(c) 300ms

Fig. 13 Droplet Positions in Dryer

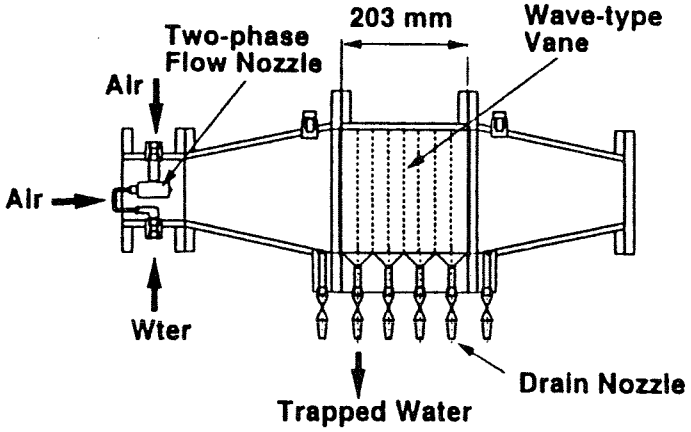

Fig. 14 Schematic of Test Apparatus

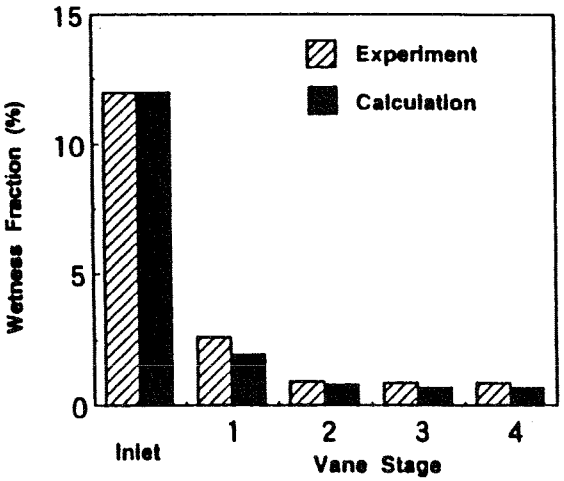

Fig. 15 Comparison with Experiments and Calculations on Wetness Fraction

4. STEAM SEPARATOR

Steam separators are used to remove water from steam in a BWR. In the separator, a two-phase flow (a steam-water mixture) rises through the standpipes to strike vanes which gives the mixture a swirl, forming a vortex where centrifugal forces separate the water from the steam in the barrel. The two-phase flow is an annular dispersed flow there. The steam, including water droplets, leaves the separator at the top and goes into the dryers. The separated water rises along the inside wall of the barrels, flows through pick-off rings, and exits from the discharge passages. Accurate performance predictions require consideration be given to behavior of gas, droplet and liquid film, individually in an annular dispersed flow. This paper describes studies on droplet behavior in annular dispersed flow with swirl of a separator and its modeling. Simulations were carried out using typical conditions of a three-stage steam separator (Fig.16(a)).

4.1. Steam Flow Analysis

The Navier-Stokes equations which are derived from an axially symmetrical two-dimensional flow were solved with a computer program, based on SIMPLE (Semi-Implicit Method for Pressure-Linked Equations) [24]. A numerical technique to simulate swirling turbulent flow in the separator has not been established. Therefore, in order to obtain a simply steady-state flow field at high Reynolds numbers (Re= 10^6), the steam flow was assumed to be non-compressible and turbulent viscosity of Prandtl's mixing length model [24] was adopted. The mixing length was estimated by Karman's constant and the distance from the separator wall. In the first stage of the separator, 40 computational grids were used in the axial direction and 20 grids were used in the radial direction. Boundary conditions were: inlet total mass flow rate W=46 kg/s; quality x=13%. Because the divergent angle of the inlet swirler γ was half that of its tangential angle β, the radial component of the swirler outlet velocity was neglected. The inlet steam velocities in axial and azimuthal directions were assumed to be the same. It was also assumed that the velocities at the separator walls were zero and there was a free condition at the exit.

The results of the steam flow analysis are shown in Fig.16(b). The horizontal axis value (r) is normalized by the barrel diameter D (=0.216 m) and the vertical axis values (u_z,u_θ) are normalized by the inlet absolute velocity of the steam Uo (=7.2m/s), where u_z is the axial steam velocity, and u_θ is the azimuthal velocity. The downstream maximum of u_z is at the center (r/D=0) and u_z gradually decreases with increasing r/D. This is similar to the profile of the n-power law in turbulent flow. The upstream maximum of u_z, however, is not at the center but near the wall (r/D=0.4) because the steam pressure at the center is lower than that near the wall due to steam swirling. The upstream maximum of u_θ ($u_{\theta max}$) is u_θ/Uo=1.1 at r/D=0.3. Since the swirl deteriorates due to viscous friction in the steam, the downstream $u_{\theta max}$ is lower than the upstream $u_{\theta max}$. The u_θ decays at r/D >0.3 because

of viscous friction against the barrel wall. The u_θ is proportion to r/D between r/D=0 and r/D=0.3. This shows a forced vortex. The above velocity profiles are similar to those in swirling pipe flow [25].

4.2. Droplet Tracing Analysis

Centrifugal and drag forces are exerted on a droplet in the swirling steam flow. Since gravity and pressure gradient forces are smaller than those forces in the separator, they were neglected. Newton's momentum equation of the droplet can be obtained for Cartesian coordinates, and is expressed by Eq.(11) which is used also in the steam dryer analysis.

Considering the conditions of the separator inlet, the average D_d was about 1mm (0.1-2.0 mm), which was based on Ueda's empirical correlation for annular dispersed flows [26]. The steam velocity u_g at the droplet location was obtained by linear interpolation from the results of the steam flow analysis. Initial droplet's velocities were assumed to be the same as the inlet gas velocities. The droplet traces were solved using a fourth step and fourth order Runge-Kutta method. When a droplet hit the surface, it was assumed to stay at the collision point and the trace was terminated. The droplet deposition rate to the barrel wall m_D was estimated by summing of the droplet mass flow rate at each collision point.

The results of the droplet tracing analysis are shown in Fig.16(c). The curves are for different diameters of D_d=0.1, 0.5 and 2.0mm, where the initial locations are at r/D=0.25. The droplets move and turn along the swirling flow of the steam-water mixture in the barrel. They move outside because of action from the centrifugal force of the flow. The droplet centrifugal force F_I and the drag force F_D are expressed by Eqs.(12) and (13). The ratio F_I to F_D is written in Eq.(14), where r is the droplet radial location. The subscripts g and d denote steam and droplet, respectively.

$$F_I = \rho_d \frac{\pi}{6} D_d^3 \frac{u_d^2}{r} \tag{12}$$

$$F_D = C_D \rho_g \frac{\pi}{8} D_d^2 \left|u_g - u_d\right|\left(u_g - u_d\right) \tag{13}$$

$$F_I / F_D \propto \frac{\rho_d D_d^2 u_d^2}{18\mu_g r\left(u_g - u_d\right)} \tag{14}$$

The right hand side of Eq.(14) is the Stokes number St, which indicates the strength of the centrifugal force. Since the droplet of D_d=2.0mm has a larger St than those of D_d=0.1 or 0.5 mm, it collides further upstream than the other droplets. When a droplet shifts its initial location outward, it collides further upstream due to larger centrifugal force.

4.3. Droplet Deposition Analysis

Droplets corresponding to the liquid (water) mass flow rate are located on an inlet cross-section of the separator. The number of droplet increases in the radial direction, so that the inlet droplet concentration is uniform on the cross-section in this analysis. The homogeneous droplet concentration in the steam core C and the deposition coefficient K are defined in Eqs.(15) and (16), where W is the mass flow rate, and m_D, the droplet deposition rate was obtained from the droplet tracing analysis.

$$C = \frac{W_d}{W_d / \rho_d + \left(W_g / \rho_g\right) \cdot \left(u_d / u_g\right)} \tag{15}$$

$$K = m_D / C \tag{16}$$

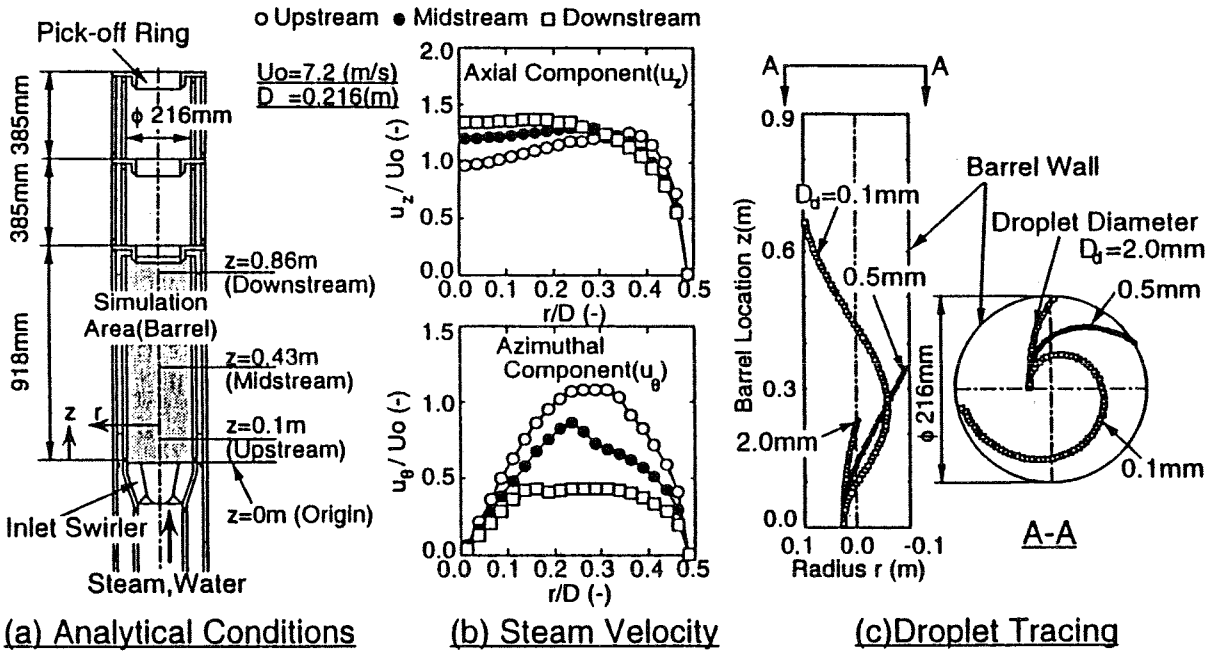

Fig. 16 Steam Flow and Droplet Tracing Analyses

Fig. 17 shows results from the droplet deposition analysis, where the diameter D_d is 1.0mm. Because C=0 at z>0.2, K cannot be defined. Between z=0 and z=0.1 (upstream), m_D becomes larger with increasing z. The m_D becomes smaller with increments of z at z>0.1 (downstream) because C is decreased due to droplets being deposited downstream. The K increases with increasing z between z=0 and z=0.2, and is reasonably proportional to z. In annular dispersed flow, the deposition coefficient without swirl is small and on the order of 0.01m/s. The results show that K with swirl is much higher than that without swirl. The effect of inlet quality on the droplet deposition was finally examined as shown in Fig.17. Deposition coefficients are found to be almost the same for different qualities. These phenomena can be explained by the following reasoning. The droplet Reynolds number is large and C_D is almost constant in the separator, so that the Stokes number is the same. Therefore, the ratio of the droplet's radial velocity to the azimuthal velocity is also the same, making a similar droplet trajectory.

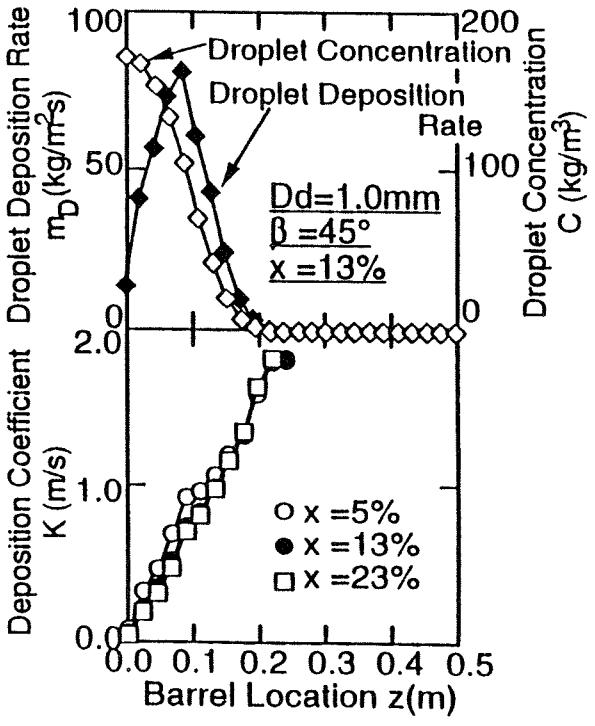

Fig. 17 Droplet Deposition Analysis

5. HEAT EXCHANGER

A calculation, using a two-fluid model, was performed for the two-phase flow behavior in the heat exchanger which is generally used in a power plant. This program was an extended version of the two-fluid model [27]. Figure 18 shows a cross section of a typical heat exchanger. Heat exchange is conducted through numerous heat exchange tubes to transfer heat from the fluid in the primary system to the fluid in the secondary one. The fluid in the primary system (e.g. water and steam) goes into the heat exchanger through the two phase flow inlet pipe and steam inlet pipe, respectively, and it goes out through the drain outlet nozzle. Three-dimensional two-phase flow behavior in the heat exchanger has a large effect on heat transfer, but it has not been analyzed in former studies because of the complicated structure.

5.1 Analytical Conditions

The analytical region is also illustrated in Fig. 18, enclosed by the chain line in the upper region of the heat exchanger. The top row of the heater tubes and baffle plates were included. In the analysis, this region was divided into control volumes with several boundary conditions. The heater tubes were treated by a porous model of control volumes with appropriate volume porosities and surface permeabilities. The baffle plates, which have many small holes penetrating them, were also treated by the porous model with the value of zero for volume porosities and appropriate values for surface permeabilities for each direction. The baffle plates could be assumed to have no volume compared with the control volume size. The total number of control volumes was 1078.

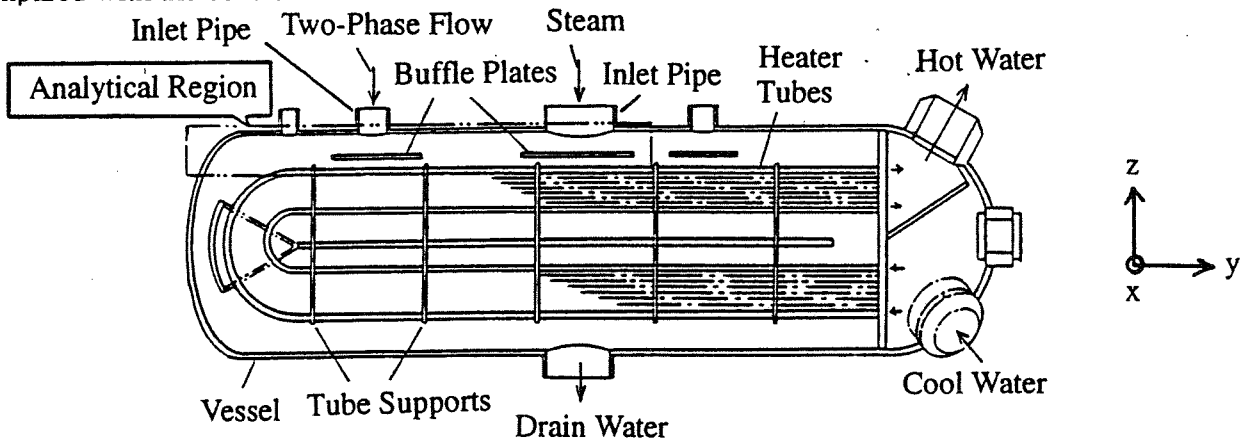

Fig. 18 Cross-Section of Heat Exchanger

Analytical conditions are listed in Table 1. Inlet velocities and void fractions of water and steam were constant at the inlet boundaries for the values as shown in Table 1. Pressure at the inlet boundary was calculated from stored mass and energy in the analytical region. Flow rates of gas and liquid at the exit boundary were calculated from the pressure difference between the inlet and exit boundaries. In all control volumes, velocities of each phase were zero and void fractions were 0.99 in the initial state. That is, the analytical region was assumed to be almost filled with steam in the initial condition.

Table 1 Analytical Conditions

Term	Value
Inlet velocity	
Two-phase flow inlet	1.4 m
Steam inlet	23.4 m
Inlet void fraction	
Two-phase flow inlet	0.27
Steam inlet	0.99
Inlet enthalpy	
Water	0.826×10^6 J/kg
Steam	2.787×10^6 J/kg
Exit pressure	1.38 MPa
Number of control volumes	
Total	1078
x-direction	7
y-direction	22
z-direction	7

5.2 Analytical Results

Calculated results are shown in Figs. 19 and 20. These figures are enlarged three times regarding the z-direction. Figure 19 shows the liquid velocity distribution at the cross-section as regards the y-z plane. The water, flowing from the two-phase flow inlet pipe, dropps straight into

the vessel and does not spread out widely after it impinges on the baffle plate. The water loses kinetic energy due to this impingement and reaches the heater tubes after passing through the baffle plate holes. This behavior is due to gravity and the inertia of the water.

Figure 20 shows the liquid distribution at the same cross-section. Density of the black dots is proportional to the volumetric fraction of liquid. The liquid is accumulated on the upper side of the baffle plate due to flow resistance at the hole inlets, which were represented by the porous expression in the control volumes using surface permeability for the z-direction. The water passes through the baffle plate holes and also accumulates on the top of the heater tubes due to their flow resistance.

According to these results, it becames clear that the water drops straight from the two-phase flow inlet pipe into the vessel without being blown off by the steam which comes from the steam inlet pipe. Moreover, the water does not spread out widely and loses the kinetic energy after it impinges on the baffle plate. A similar flow pattern is observed in full scale air-water experiments.

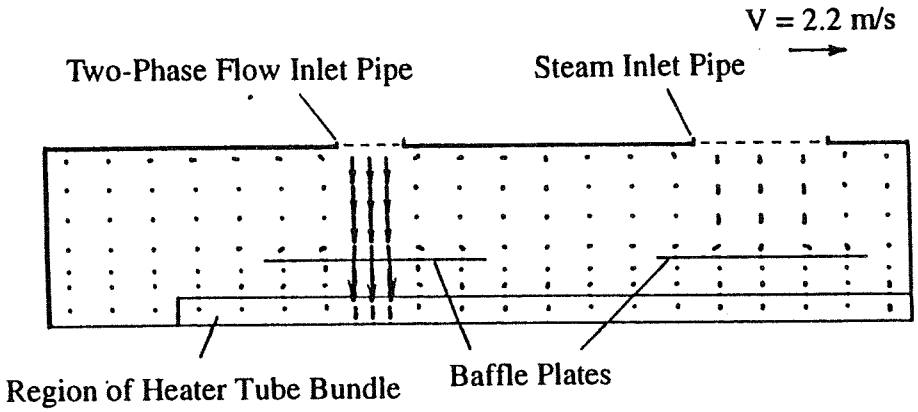

Fig. 19 Volumetric Velocity Distribution of Liquid (y-z Plane)

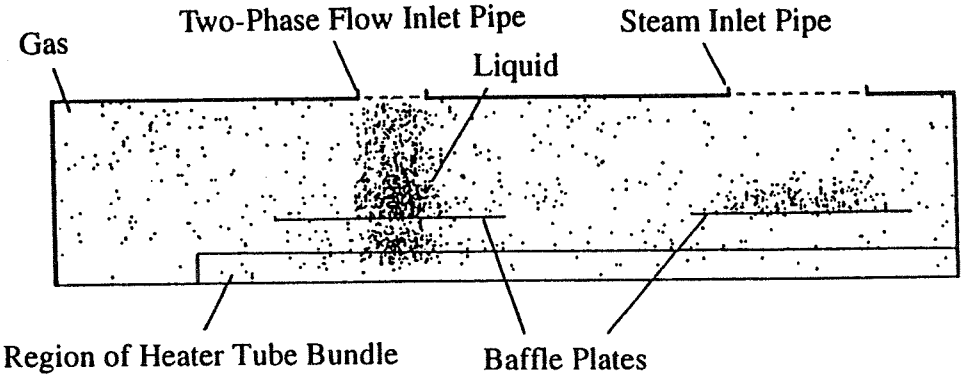

Fig. 20 Liquid Distribution (y-z Plane)

6. SUMMARY

Recent studies on two-phase flow analyses in boiling water reactor were described. By considering the behavior of gas, liquid droplets, liquid film and bubbles respectively, detailed prediction of thermal-hydraulic performances of components were possible. The authors developed an annular dispersed flow model for the fuel bundle, a dispersed flow model for the steam separator and dryer, and a two-phase separation model for the heat exchanger. Validity of calculated results were demonstrated in comparison with experimental results.

REFERENCES

[1] D.S. Rowe: "COBRA Ⅲ: "A Digital Computer Program for Steady State and Transient Thermal-

hydraulic Analysis of Rod Bundle Neclear Fuel Elements", BNWL-1695, (1973).
[2] R.W.Bowring: "HAMBO; A Computer Program for the Subchannel Analysis of the Hydraulic and Burnout Characteristics of Rod Clusters, Part 1, General Description", AEEW-R524, (1967).
[3] A. Faya, et al.:"Development of a Method for BWR Subchannnel Analysis", PB80-171283, (1979).
[4] K. Nishida, O. Yokomizo: "Effect of Spacing Structures on Critical Power in a Nuclear Fuel Bundle", in : Proc. of Int. Seminar on Subchannel Analysis in Nuclear Reactors, H. Ninokata, M. Aritomi, Tokyo, Japan, p.215 (1992).
[5] T. Nakao, et al., "Analysis of Droplet Behavior in a Dryer with wave-Type Vanes", in : J. Nucl. Sci. Tech., 30, 12, p.1303 (1993).
[6] Y. Saito, et al., "Analysis of Droplet Behavior in BWR Separator", in : J. Nucl. Sci. Tech., 31, 4, p.349 (1994).
[7] S. Murata, et al.: "Calculation for Two-Phase Flow Behavior in Heat Exchanger", in : Proc. of the First Int. Con. on supercomputing in Nuclear Applications, Mito, Japan, p.202 (1990).
[8] A. Tomiyama, et al., " Method of Critical Power Prediction Based on Film Flow Model Coupled with Subchannel Analysis", in: J. Sci. Tech., 25, p.914 (1988) .
[9] B.S. Shiralkar, et al., "The Effect of Obstacles on a Liquid Film", Trans. ASME , p.528 (1973).
[10] S. Yokobori, et al.: " A Phenomenological Study on the Dryout Mechanism in a Fuel Rod", Proc. of NURETH-4, p.1054 (1989).
[11] A. Tomiyama, et al.: " Spacer Effects on Film Flow in BWR Fuel Bundle", in: J. of Nuc. Sci. Tech., 25, 2, p.204 (1988).
[12] K. Nishida, et al.: "Spacer Effect on Liquid Film Flow and Critica Power in BWR Fuel Bundle", in : ICONE-1, 1, p.81 (1991).
[13] T. Sakai, S. Sugawara: "Development and Validation of a 3-Dimensional Analysis Code FIDAS", in ; Preprint. 68th Mtg. of Mec. Soc. Japan, B1306, p.400 (1991) (in Japanese).
[14] P.B. Whalley, et al.: "The Calculation of Critical Heat Flux in Forced Convection Boiling", in ; Proc. of 5th Int. Heat Transfer Conf., Tokyo, 4, p.290 (1974).
[15] P. Hutchinson, P.B. Whallet, "Possible Characterization of Entrainment in Annular Flow", in : Chem. Eng. Sci., 28, p.974 (1973).
[16] Y. Katto , " Prediction of Critical Heat Flux for Annular Flow in Tubes Taking into Account the Critical Liquid Film Thickness Concept", in : Int. J. Heat Mass Transfer, 27 ,6, p.833 (1984).
[17] H. Schlichting : "Boundary-Layer Theory", McGraw-Hill, New York (1955).
[18] H. Uchida :"Dennetu Kougaku", Syoukabou, Japan (1969).
[19] R.T. Lahey Jr., et al.: "Out-of Pile Subchannel Measurements in a Nine-Rod Bundle for Water at 1000 psia", Progress in Heat and Mass Transfer, 4, New York Press, (1972).
[20] T. Gotou, et al. : "Application of the Liquid Film Model to the Critical Power Correlation for Core Thermal-Hydraulic Design of ATR", in ; Proc. of ICONE-1, 1 , p.329 (1991).
[21] Y. Yoshimoto, et al.: "Critical Power Experiments of a Tight Fuel Rod Lattice for Light Water Reactors", Proc. of ICONE-1, 1, p.9 (1991).
[22] T. Kawasaki, et al.: "Analysis of Injected Fuel Droplet Behavior in Intake Manifold of Spark Ignition Engine", in : Proc of 12th Int. Vienna Motor Symp., Vienna, Austria, (1991).
[23] R.B. Bird, et al.: "Interphase Transport in Isothermal System", John Wiley & Sons, New York.
[24] S.V. Patankar : "Numerical Heat Transfer and Fluid Flow", Hemisphere Publishing Corporation, (1980).
[25] D.G. Sloan, et al.: "Modeling of Swirl in Turbulent Flow Systems", in : Proc. of Energy Combust. Sci., Kobe, Japan, 12, p. 163 (1986).
[26] T. Ueda, "Study on Entrainment Rate and Droplet Size in Annular Two-Phase Flow", in : Bulletin of the JSME, 45, 389, p.127 (1979) (in Japanese).
[27] A. Minato, et al., "Numerical Analysis Method for Two-Dimensional Two-Fluid Model Using Control Volume Formulation", in : J. Nucl. Sci. Tech., 25, 12, p.901 (1988).

AUTHOR'S INDEX